



**The California Central Coast Research Partnership:
Building Relationships, Partnerships and Paradigms for University-Industry
Research Collaboration.**

FINAL REPORT ON ONR GRANT NO. N00014-04-1-0436

PERIOD OF PERFORMANCE: March 15, 2004 through July 14, 2005

October 14, 2005

DISTRIBUTION STATEMENT A
Approved for Public Release
Distribution Unlimited

Principal Investigator:

Susan Opava, Ph.D.
Dean of Research and Graduate Programs
California Polytechnic State University
San Luis Obispo, California

20051011 101



CALIFORNIA CENTRAL COAST
RESEARCH PARTNERSHIP



**The California Central Coast Research Partnership:
Building Relationships, Partnerships and Paradigms for University-Industry
Research Collaboration.**

FINAL REPORT ON ONR GRANT NO. N00014-04-1-0436

PERIOD OF PERFORMANCE: March 15, 2004 through July 14, 2005

October 14, 2005

DISTRIBUTION STATEMENT A
Approved for Public Release
Distribution Unlimited

Principal Investigator:

Susan Opava, Ph.D.
Dean of Research and Graduate Programs
California Polytechnic State University
San Luis Obispo, California

REPORT DOCUMENTATION PAGE					Form Approved OMB No. 0704-0188	
<p>The public reporting burden for this collection of information is estimated to average 1 hour per response, including the time for reviewing instructions, searching existing data sources, gathering and maintaining the data needed, and completing and reviewing the collection of information. Send comments regarding this burden estimate or any other aspect of this collection of information, including suggestions for reducing the burden, to Department of Defense, Washington Headquarters Services, Directorate for Information Operations and Reports (0704-0188), 1215 Jefferson Davis Highway, Suite 1204, Arlington, VA 22202-4302. Respondents should be aware that notwithstanding any other provision of law, no person shall be subject to any penalty for failing to comply with a collection of information if it does not display a currently valid OMB control number.</p> <p>PLEASE DO NOT RETURN YOUR FORM TO THE ABOVE ADDRESS.</p>						
1. REPORT DATE (DD-MM-YYYY) 14/10/2005		2. REPORT TYPE Final Technical Report		3. DATES COVERED (From - To) 3/15/04 - 7/14/05		
4. TITLE AND SUBTITLE The California Central Coast Research Partnership: Building Relationships, Partnerships and Paradigms for University-Industry Research Collaboration				5a. CONTRACT NUMBER		
				5b. GRANT NUMBER N00014-04-1-0436		
				5c. PROGRAM ELEMENT NUMBER		
				5d. PROJECT NUMBER		
6. AUTHOR(S) Opava, Susan C.; Adams, Nikki L.; Alptekin, Sema E.; Arakaki, Dean; Beckett, Deborah M.; Beckett, Jonathon L.; Bensky, Thomas J.; Birdsong, Charles; Chadwell, Charles B.; Chen, Katherine C.; Crockett, Robert; Davol, Andrew; Delagrammatikas, George; DeTurris, Dianne J.; Echols, Robert; Franklin, Diana; Garcia, Garrett; Goel, Rakesh; Gollery, Steve; Gragson, (Continued on reverse side)				5e. TASK NUMBER		
				5f. WORK UNIT NUMBER		
7. PERFORMING ORGANIZATION NAME(S) AND ADDRESS(ES) California Polytechnic State University Foundation Sponsored Programs Department Foundation Administration Bldg. 15 San Luis Obispo, CA 93407				8. PERFORMING ORGANIZATION REPORT NUMBER		
9. SPONSORING/MONITORING AGENCY NAME(S) AND ADDRESS(ES) George W. Solhan Office of Naval Research Ballston Centre Tower One 800 North Quincy Street Arlington, VA 22217-5660				10. SPONSOR/MONITOR'S ACRONYM(S) ONR		
				11. SPONSOR/MONITOR'S REPORT NUMBER(S)		
12. DISTRIBUTION/AVAILABILITY STATEMENT Available for public release DISTRIBUTION STATEMENT A Approved for Public Release Distribution Unlimited						
13. SUPPLEMENTARY NOTES						
14. ABSTRACT The primary purpose of this initiative is to forge a strong link between private sector R&D and University applied research, to speed the development of new knowledge and the transfer of technology to the public and private sectors. To this end, communications infrastructure and R&D facilities have been developed. Relationships with private companies engaged in R&D have been advanced. Important research has been carried out in areas of interest to the DOD and national security. These areas include nanotechnology, haptics, image analysis, materials, energy efficiency, communications, network technologies, remote sensing, malaria, biofouling and corrosion, and underwater optical sensing.						
15. SUBJECT TERMS Autonomous vehicles, nanotechnology, haptics, image analysis, materials, energy efficiency, communications, network technologies, remote sensing, malaria, biofouling and corrosion, and underwater optical sensing.						
16. SECURITY CLASSIFICATION OF:			17. LIMITATION OF ABSTRACT UU	18. NUMBER OF PAGES 1012	19a. NAME OF RESPONSIBLE PERSON Susan C. Opava	
a. REPORT U	b. ABSTRACT U	c. THIS PAGE UU			19b. TELEPHONE NUMBER (Include area code) 805-756-1508	

Answer 6, continued:

Derek E.; Hall, Garrett; Haungs, Michael; Jansen, Daniel C.; Kasper, Eric; Kelly, Shaun; Khosmood, Foaad; Kitts, Christopher L.; Klisch, Stephen M.; Koutsos, Elizabeth A.; Kozloff, Lyle; Kurfess, Franz; Lehmkuhl, Mike; Lindert, Lisa M.; MacDougall, Neal A.; Macedo, Jose; Mirijamdotter, Anita; Muckenhaupt, Meike; Mukherjee, Parna; Murray, William R.; Niebuhr, David; Niku, Saeed; Pan, Jianbiao; Peterson, Daniel G.; Pohl, Jens G.; Rahim, Ashraf M.; Rogers, Erika; Savage, Richard N.; Schuster, Peter; Schwartz, Peter V.; Seng, John; Shireman, Christopher; Sindorf, Brent; Somerville, Mary M.; Stanley, Jeremy M.; Strohman, Rollin; Taufik; Wendt, Dean E.; Williams, Doug; Wood, Zoe J.; Yu, Xio-Hua; Zhang, Jane

TABLE OF CONTENTS

I.	Title of Project	3
II.	Summary of Project	3
III.	Relevance to ONR Objectives	3-7
	A. Relevant partners	3-4
	B. Strategic locations	5
	C. Relevant R&D focus	5-6
	D. University-industry-government partnership	6
	E. University strengths	6-7
IV.	Summary of Results During the Period of Performance	7-1012
	A. General	7-9
	B. Detailed Research Reports	9-1012
	1. Results of CADRC research	
	• Knowledge Management Using Semantic Web Languages and Technologies.....	10-25
	2. Results of research projects	26-931
	• Molecular Sensors and Defenses against Ultraviolet Radiation.....	26-40
	• Antenna Bandwidth Improvement and Emissions and Mounting Structure Studies.....	41-57
	• Development of Multi-Marker Genetic Testing Protocols for Fresh Versus Cryopreserved Bovine Embryos.....	58-70
	• Real-Time Underwater Monitoring of Sunlight Penetration into the Ocean Water at Avila Bay, California.....	71-81
	• Human Sensing.....	82-215
	• Nonlinear Analytical Modeling and System Verification Utilizing a Combined Slide-Rock Seismic Response of Wine Barrel Stacks.....	216-268
	• Hydrogen and Residual Stress Effects on the Performances of NiTi Shape Memory Alloys.....	269-273
	• Meso-Scale Composites via Solid Freeform Fabrication.....	274-289
	• Development of an HCCI Engine for Combustion Sensing and Control Studies.....	290-449
	• Development of an Autonomous Tactical Reconnaissance Platform....	450-499
	• Improving Power Conversion Efficiencies of Polymer Based Solar Cells.....	500-509
	• Exploring the Design and Fabrication of Nanoscale Architectures Fashioned via Layer-by-Layer Adsorption of Polyelectrolytes.....	510-513
	• Rapid Delivery of Massive Geospatial Data over Internet2.....	514-555
	• Cement Stabilized Recycled Aggregates for Roadway Base.....	556-591
	• Effect of Probiotics on the Species Distribution of Bifidobacterium and Lactobacillus in healthy subjects undergoing Antibiotic Therapy...	592-599
	• Nonlinear Constitutive Equations for Cartilage Growth Analysis.....	600-649
	• Production of Transgenic Quail Expressing Phytase to Increase Nutrient Availability and Reduce Environment Impact.....	650-657

2. Results of research projects – Continued

- Mechanistic Study of the Cyclin-Dependent Kinase PfPK5/Pfcyc-1 from the Malarial Parasite, Plasmodia Falciparum..... 658-660
- Registration of Color Images in Non-Rigid Environments..... 661-689
- Understanding the Adversity of Perchlorate Contamination in Water by Permeation Studies through RO / NF Membranes..... 690-708
- Force Feedback Control for Visually Impaired Wheelchair Users..... 709-733
- Effect of Reflow Profile on SnPb and SnAgCu Solder Joint Shear Strength..... 734-788
- Development of a Micro System Actuator Employing Shape Memory Alloys for Exploring the Nanotechnology World..... 789-805
- Biomechanical 'Leg-form' for Pedestrian Impact Tests..... 806-815
- Construction of Tetrahedral Photonic Bandgap Crystal: Demonstrating Three-dimensional Self-assembly using DNA Linkage..... 816-828
- Large Scale Distributed Wireless Networks..... 829-838
- Investigation of Efficiency Improvement in High-Density Light-Weight DC-DC Converter..... 839-887
- Establishment of a Field Site for Testing Non-Toxic, Fouling-Release Marine Coatings to Aid in the Control of Biofouling and Corrosion.... 888-891
- 3D Digital Data Acquisition and Interaction..... 892-915
- Real Time Error Detection Using Artificial Intelligence..... 916-923
- Screen Data Compression for Improved VNC..... 924-931

3. Results of Internet2 pilot projects 932-1012

- Utilizing Internet2 to Integrate Multimedia Repositories in an Adaptive Learning Environment..... 932-961
- Redundant Peer to Peer File System..... 962-965
- Real-Time Searching on I2..... 966-978
- Virtual Team Collaboration over Internet2..... 979-986
- Remote Monitoring and Control of Cal Poly Dairy Biogas Pilot Project Using Internet2..... 987-992
- Interactive Design and Evaluation of a Learning Environment for Distributed Collaboration over Internet2..... 993-1007
- Developing a Pest Control Advisor Continuing Education Conference for I2..... 1008-1012

FINAL REPORT ON ONR GRANT NO. N00014-04-1-0436
PERIOD OF PERFORMANCE: 3/15/04 to 07/14/05

I. Title of Project

The California Central Coast Research Partnership: Building Relationships, Partnerships and Paradigms for University-Industry Research Collaboration.

II. Summary of Project

The mission of the California Central Coast Research Partnership (C³RP) is to facilitate the exchange of knowledge and skills between the higher education sector and the private sector in San Luis Obispo County, and to encourage the growth of high-tech companies in the region, thereby enhancing economic development and quality of life. The partnership is a long-term plan to create a dynamic and self-supporting university-industry-government partnership that capitalizes on the strengths and mutual interests of the educational and technology-based business sectors. The plan recognizes the key role of higher education in preparing a highly skilled work force and transferring new knowledge to practical uses. The outcomes of this partnership, when fully realized, will be the expansion of current and the creation of new University technology R&D activities; the development of existing technology-based businesses and the creation of new ones; and the generation of opportunities for job training and research and development activities for University and Community College students and faculty in areas of interest to the Department of Defense and national security.

The project will eventually lead to the construction (with private financing) of a technology park on the California Polytechnic State University campus that will provide state-of-the-art space for private technology companies engaged in research and development activities, as well as a business incubator that will provide all of the support services needed by start-up, technology-based companies. At this stage, the project involves planning, analysis, relationship-building and pilot research projects related to development of the long-term partnership and its research foci.

III. Relevance to ONR Objectives

A. Relevant partners.

C³RP represents a coalition of educational institutions, local, state and federal government, and private businesses that have worked together in unprecedented fashion to advance the common goals inherent in the proposed university-industry partnership. The current partners in the project and their contributions include:

California Polytechnic State University

- committed the land for the project, valued at ~\$1.5 million
- provided assistance in financial management of the project

- contributed \$90,000 for a pre-feasibility study by Bechtel Corporation
- committed several hundred thousand dollars of in-kind contributions of senior management time and effort over several years; continues to do so
- invested ~\$800,000 in efforts to raise additional funds for the project

GEO, International (GEOgraphic Network Affiliates, International; a private company)

- has worked *pro bono* with C³RP on communications aspects of the project

CENIC (Corporation for Educational Network Initiatives in California; association of Internet2 universities in CA)

- works with Cal Poly and GEO to further the goals of the IEEAF (see below), goals that will directly benefit C³RP
- CENIC and AARNET, Australia's Academic and Research Network (<http://aarnet.edu.au>) are working on a collaborative effort with the fiber-optic carrier, Southern Cross, to implement a trans-Pacific high-speed network connection (10 Gigabits/sec) that will connect through the Cal Poly campus.

IEEAF (International Educational Equal Access Foundation; established by GEO and CENIC)

- has secured donations of virtual and physical communications assets in at least 37 countries; some of these fiber-optic assets directly benefit this ONR project

City of San Luis Obispo

- in partnership with Cal Poly has developed a carrier-neutral fiberoptic ring around the city.

National Science Foundation

- is working with GEO, IEEAF, CENIC and other universities in the United States to promote the goals of these organizations to develop low-cost fiber-optic networks for the benefit of educational institutions, non-profit organizations and local communities.

Housing and Urban Development

- Has provided funds toward construction of the pilot technology park building.

Efforts are ongoing to secure new partners, including:

- Major corporations
- Small technology-based businesses
- Economic Development Administration

B. Strategic location.

Technological developments in San Luis Obispo related to the intersection of major undersea and terrestrial fiber-optic cable networks on the central coast of California have provided an exceptional opportunity to focus the research partnership initially on the emerging technology area of global telecommunications. Linking the research partnership to this burgeoning field has enabled us to recruit many of the important partners listed above and will provide the strong affiliation between the educational and private sectors that is the foundation for success in university-related technology parks. It will also open new opportunities for federally supported research and development projects.

C. Relevant R&D focus.

Global telecommunications, particularly wireless, "over the horizon" communications, is fundamental to many current and developing defense strategies, including the ability to respond effectively to various forms of terrorist activities (including biological and chemical warfare), and in situations that require large-scale humanitarian assistance and disaster relief – areas which have become far more critical in the wake of the September 11, 2001 terrorist attack on American soil. It is also fundamental to the development of the decision-support systems that underlie and are key to these strategies. Cal Poly's Collaborative Agent Design (CAD) Research Center is the architect and lead developer of one of the first such systems: IMMACCS (Integrated Marine Multi-Agent Command and Control System), with JPL, SPAWAR Systems Center and the Stennis Space Center (NRL) as the other principal team members. Because of this, Cal Poly and the CAD Research Center have taken the lead in the continued development of complex decision-support systems. The C³RP project has provided and will continue to provide support for the CAD Research Center to continue, and expand, its work on on-going projects like those completed for the MCWL, such as IMMACS, and the joint MCWL-ONR ELB (Expanded Littoral Battlefield), ACTD (Advanced Concept Technical Demonstration) project.

The scope of the CADRC projects, however, is much broader than simply the continuation of current projects of the kind described above. Command and control technology is developing rapidly and will have nearly universal applications. The basis of this technology is the ability to store "information" rather than "data", a concept that is fundamental to the capacity to utilize that information to support complex decision-making. IMMACS is one of the first of such systems to use this concept, and has led the field, but the bringing together of commercial and University research and development through C³RP will lead to expansion of applications and technological advances in this arena.

In addition to telecommunications, many other research areas have been targeted for development through C³RP. These have been selected because Cal Poly has demonstrated or developing strengths in these areas. They include:

Agricultural and environmental biotechnology	Telecommunications technologies
Aerospace technologies	Photonics
Rendering, animation and modeling	Graphic communication technologies
Software engineering	Nano- and micro-technology
GIS and GPS applications in agriculture, biology, architecture and engineering	Computer engineering (small systems, peripherals, custom applications)
Network hardware and software technology	Surveillance, logistics, command & control support systems
Data processing	Image analysis
Remote sensing	Bio-engineering
Polymers and coatings	Robotics
Electrooptics	Magnetic levitation (transportation)
Power generation and distribution	Risk assessment and prediction of fire terrorism
Biological risk assessment and detection	Environmental hazard assessment and detection
Protection of the nation's food and water supplies	Seismic research
Transportation disaster management and control	

The majority of these research areas mesh with strategic initiatives identified by the Office of Naval Research. Research and advanced development projects in these strategic areas are being developed, often in collaboration with industry partners identified through C³RP and recruited to join the partnership.

D. University-industry-government partnership.

The primary focus of this initiative is to forge a strong link between private sector R&D and University applied research to speed the development of new knowledge and the transfer of technology to the public and private sectors. San Luis Obispo has become a draw for technology businesses (with a heavy concentration of software development companies) from both the LA Basin and Silicon Valley. For example, SRI (Stanford Research Institute), International operates a "software center of excellence" in the city. Branches of major corporations are also located nearby, for example, Sun Microsystems, Veritas, and Sunbay Software. Lockheed-Martin has a research and development group in nearby Santa Maria. Two local companies manufactured critical components for the Mars rovers and other companies, e.g. California Fine Wire, are suppliers to the military. Also located on the Central Coast are branches of two major biotechnology companies: Promega Biosciences and Santa Cruz Biotechnology.

E. University strengths.

Cal Poly is a State university that has achieved national distinction as a polytechnic university, with engineering and computer science programs ranked among the very best undergraduate programs in the country. Its strengths have led it to orchestrate the research partnership effort and the consortium of partners described herein. Cal Poly also has affiliations with CSA (California Space Alliance) and with Vandenberg Air Force Base, where it has offered an M.S. in Aerospace Engineering by distance learning. The high bandwidth that will be associated with the eventual physical site selected for the partnership will allow Cal Poly to offer many more academic programs by distance learning to remote locations. In particular, through possible collaborative agreements at cable-head locations around the world (including Asia and Europe) our programs can be made available to military personnel stationed almost anywhere in the world. This could

be tied into training programs for ONR and, if desirable, to training directly related to research projects.

In summary, the California Central Coast Research Partnership has taken advantage of a confluence of factors, including existing and potential relationships, fortuitous and unique technological and economic developments in the region, the particular strengths and expertise of the CAD Research Center, and a meshing of the research and development interests of the University, the Office of Naval Research, and the private sector. C³RP is the vehicle for fully realizing the benefits of the common goals and synergies of the partners and their respective resources.

IV. Summary of Results During the Period of Performance

A. General.

This project was originally funded through an award from ONR in FY '02, covering the period September '01 through December '02. Accomplishments during this first award period were described in a detailed report to ONR in March '03. A second award began in June '02 and ended in December '03. Accomplishments during this second award period were described in a detailed report to ONR in March '04. The current award began March 15, 2004 and ended July 14, 2005. Accomplishments during the period of this award are summarized below. Detailed reports are presented later in this document.

An overview of accomplishments to date on the project follows:

- Research carried out by the **CADRC (Cooperative Agent Design Research Center)**, of particular interest to ONR and the Marine Corps, was again funded. A detailed report on this project, Knowledge Management Using Semantic Web Languages and Technologies, is provided later on in this document.
- **New research** has been developed and some research has been continued, including several with industry collaboration. They include topics highly relevant to defense and national security, such as nanotechnology, haptics, image analysis, materials, energy efficiency, communications, network technologies, remote sensing, malaria, biofouling and corrosion, and underwater optical sensing. Detailed reports of the results of these projects are presented in Section IV. B. of this report.
- Support for these research projects has resulted in **significant follow-on funding** from government and private sponsors. Since July 1, 2003, C3RP-supported faculty have received more than \$14 million in follow-on funding.
- A **new technology** was developed that uses fiberoptics for undersea optical sensing.

- **New research facilities** were developed, including an anechoic chamber for studies of radio frequency communications and antennae, and a floating platform for studying marine coatings that are ecologically benign and prevent biofouling and corrosion.
- Significant enhancements have been made in **information technology infrastructure**:
 - **Internet2** connectivity was initially applied for, approved, and acquired for the campus in November 2001, to support current and future research efforts. Internet2 membership and connectivity has continued this year
 - CENIC (see above) and AARNET, Australia's Academic and Research Network (<http://aarnet.edu.au>) continue to work on a collaborative effort with the private sector, to implement a **trans-Pacific high-speed network connection (10 Gigabits/sec)**. The California-based landing site will be in San Luis Obispo County and will connect into CENIC's high-speed network at its network point of presence located on the Cal Poly campus. Cal Poly's geographic location, its ability to act as a "hardened" facility to support critical network backbone equipment, as well as the existing fiber-optic infrastructure built out in partnership with the City of San Luis Obispo, has positioned Cal Poly to be the access point for the high-speed network corridor to Australia's research environments and potentially other Eastern Pacific Rim research networks. **This project is being developed without use of ONR funds.**
 - A **grid computing network** was established to support specific research projects that require high-end computing capability previously unavailable on campus. The grid will be used to support such projects on a rotating, demand-driven basis. It will access other major and similar resources (e.g. the San Diego Supercomputing Center) through Internet2-networked capacity.
- **Several pilot projects** were funded to explore **new uses of Internet2** for research and education. Three presentations on the results of these projects were competitively selected and presented at the program of the Spring 2005 Internet2 conference. The projects explored such topics as operating research instrumentation remotely over I2; I2 videoconferencing; virtual-team collaboration over I2; redundant peer-to-peer file systems; utilizing Internet2 to integrate multimedia repositories in an adaptive learning environment; and real-time searching on Internet2. Detailed reports on these projects are provided later on in this report.
- A team of faculty from several colleges produced a Handbook of Guidelines on the incorporation of the latest sustainable practices, materials and technologies into research and industrial buildings.
- A **database of technology-based companies** that are potential partners in the project and research collaborators has been updated and expanded.

- **Relationships** have been established with new technology companies that are potential research collaborators, including: Alltech, Inc., Applied Biotechnology Institute, Battelle Science and Technology International, DuPont, Siemens, Florida Environmental Research Institute, GeoScan Technologies, InfoGard Laboratories, and Orbis, Corp.
- The **web site for the project** (www.c3rp.org), which presents C³RP as an interface between Cal Poly and business/industry for the purpose of facilitating R&D relationships, has been maintained and updated.
- A **research brochure**, highlighting the applied research strengths, facilities and resources of Cal Poly, is nearly complete. It will report results of ongoing representative projects and will be a tool for attracting industry partners to collaborate in the applied research efforts being supported through C3RP.
- Efforts continue to develop industry partners in the **biotechnology sector** for the purpose of developing research and training activities in this field. To this end we continue to work with the Central Coast Biotechnology Center in Ventura, CA, with two local community colleges, and with several biotech companies, including Amgen, Baxter, Fziomed, Genentech, Promega BioSciences, Hardy Diagnostics, and Santa Cruz Biotechnology.
- The project's leaders have continued to work with other private and government (including HUD and EDA) partners to advance the project and to attract research collaborators and support.

B. Detailed Research Reports

Following are detailed reports of the technical results of research projects carried out this year. They are presented in the following order:

1. Results of CADRC research
2. Results of research projects
3. Results of Internet2 pilot projects

Knowledge Management Using Semantic Web Languages and Technologies

Project Investigators:

Jens G. Pohl
Executive Director
Collaborative Agent Design Research Center

Steve Gollery
Software Engineer
Collaborative Agent Design Research Center

IV.B.1: Results of CADRC Research

Knowledge Management Using Semantic Web Languages and Technologies

Steven Gollery
Collaborative Agent Design Research Center (CADRC)
Cal Poly, San Luis Obispo, California
6/30/2005

1. Executive Overview

Each organization of more than a few persons generates a number of documents containing information about the activities of the organization. The sum of these documents provides a kind of organizational memory that can be used both in evaluations of past performance and as the basis of future planning based on previous experience.

Unfortunately, the nature of these documents mitigates against the reuse of information for purposes other than those for which each document was originally intended. To locate all the information about some aspect of the organization, it frequently becomes necessary for human beings to search a mass of documents to manually extract and collate all text related to the problem at hand. It would be advantageous if a software system could be used to find all relevant information and assemble it into a single document for input to the planning or evaluation process. But the current document-centric approach to information organization limits the functionality and utility of such a software system.

The Semantic Web Knowledge Management research project being undertaken by the Collaborative Agent Design Research Center (CADRC) at the California Polytechnic State University (Cal Poly), San Luis Obispo postulates that a more useful organizational memory can be created by separating the information from the structure imposed when that information is embedded in specific documents. We propose a system that allows users to create informational units rather than documents. Document structure is specified by objects outside the units themselves, enabling the reuse of information in multiple documents while maintaining the referential integrity of each organizational unit.

Project researchers in the CADRC Center are working towards the production of a test-bed system to explore various approaches to information entry and retrieval. To support such a system, they have defined a preliminary information structure known as an ontology using the semantic web language OWL (OWL 2004, Antoniou and Harmelen 2004). Tests on the use of this ontology as the basis of the system are ongoing.

This report of research completed under C3RP funding during FY04-05 discusses the information needs and representational approach for a knowledge management system using semantic web technologies.

2. Introduction

The Semantic Web Knowledge Management project is intended to demonstrate the use of semantic web languages, concepts and technologies in the design and implementation of a knowledge repository for the support of the decision-making process. Initially, we are focusing on concepts and functionality related to an organization involved in software development, using the kinds of information that are generated in the course of development projects in our Center at Cal Poly as a test case. However, we expect that the ontology and supporting tools are relevant to

other organizations as well.

During the software development process, large amounts of information and knowledge are recorded in individual documents. Collectively, these documents form an organizational memory that can be used as part of making decisions for individual projects and for the entire organization. The knowledge management project explores the potential value of storing information in a single common repository in a form that can support the creation of tools that provide access based on an explicit representation of the semantics of each individual piece of information.

The remainder of this report is a discussion of the different sections of the ontology and what sort of functionality each section is intended to support. The ontology itself is divided into two parts. One part contains concepts and relationships that can be used to describe an organization and its projects. This part is fairly straightforward. The other area covered by the ontology represents the information itself, from several points of view. These two areas are covered individually. Following the knowledge management section, the report covers the association of topics with various parts of the knowledge management ontology, and the use of external ontologies.

As the two parts of the ontology have evolved, it has become apparent that there is ambiguity over which part should contain a given concept. For instance, it seems fairly clear that a project team is part of an organization. Each team is responsible for one or more projects, and each project has a list of requirements. Each requirement is a piece of knowledge about the project. The question then becomes: Are requirements part of the organization ontology, or are they part of the knowledge management ontology?

Currently, requirements are modeled as part of the organization because of their close association with a project. But it would be equally reasonable to include requirements in the knowledge management area. This and similar questions are likely to be revisited in the future.

3. The Organization Ontology

The Organization ontology (Figure 1) represents concepts and relationships for describing organizations. This is currently a minimalist view: it includes just enough to allow the definition of the part of an organization that deals with Projects, Requirements, Tasks, and other related information. A complete ontology for organizations would naturally be much larger. Note: in the rest of this document, where it is necessary for elements of the Organization ontology to be distinguished from elements of other ontologies, the Organization elements will be identified using the prefix "ORG."

The Organization ontology uses parts of several ontologies designed by other sources. There is more about the use of outside ontologies later in this report. One of the most important external contributions for the organization ontology is "Friend of a Friend", or FOAF. FOAF is a very popular ontology that is referenced in many other sources. We use it here as the basis for many of our people-related classes and properties.

The Agent class is the base for several important classes. It refers to anything that can act, and so includes both Person and Organization. `ORG:Agent` inherits from `FOAF:Agent`, and adds properties such as "is responsible for" (zero or more Tasks), "is involved with" (zero or more Projects), and "administers" (zero or more Projects).

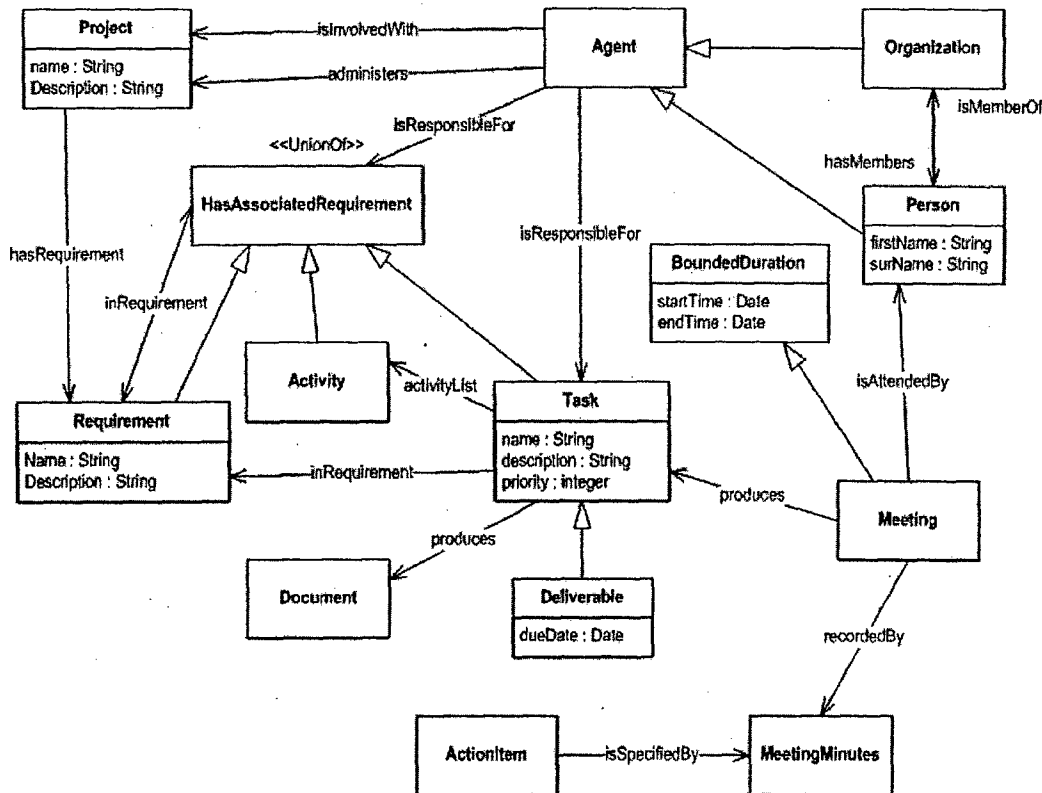


Figure 1: Classes and properties for describing an organization (partial)

Person is a subclass of both `ORG:Agent` and `FOAF:Person` (which is itself a subclass of `FOAF:Agent`, among others). To the properties inherited from `Agent`, the `Person` class adds a first name and a surname, and an “attends” property whose value is zero or more instances of `Meeting`. A `Person` is also a member of zero or more `Organizations`.

`Organization` is a subclass of `ORG:Agent` and of `FOAF:Organization`. An `Organization` has a name and a list of members (instances of `Agent`).

`Project` is a subclass of `FOAF:Project`. Each project has a name, and may have a description, a sponsor, and a list of `Agents` that are involved in the project. Projects also potentially have an “is described by” property whose value is an instance of `Document`, and may have a `DecisionDocument` associated with it. However, these last two are subject to review: it may be that these concepts are covered by classes and relationships in the knowledge management ontology (Figure 2).

A `Project` also has a list of `Requirements`. This is currently an unordered list. A `Project` may have an “is bound by” property whose value is an instance of `Contract`.

`BoundedDuration` is the base class for all classes that have a start time and an end time.

`Meeting` is a subclass of `BoundedDuration`. Each instance of `Meeting` “is attended by” a list of `Person` objects and “produces” zero or more `Tasks`. It is likely that `Meeting` will be extended further, either here or in the Knowledge Management ontology. The intent of `Meeting` is to provide a target for the `MeetingMinutes` document type, so that minutes can be entered into the system as fragments, to later be assembled for presentation, either stand-alone or as part of a decision document.

Requirement is a subclass of BoundedDuration. A Requirement has a name and a description, and a lists of Activities, Tasks, and other Requirements. This list is ordered, since some of the elements will have dependencies. Each Requirement is associated with exactly one Project.

Task is a subclass of BoundedDuration. A Task is “defined at” a Meeting, “produces” a Document, “is bound to” a Contract, has a description, a date issued, a priority, and a name. Each Task also has a list of Requirements of which the task is a part. Additionally, a Task may have an ordered list of Activities directly defined for it. Finally, a Task may of course also inherit Activities from the Requirements to which it belongs.

An Activity has a name and a description. Activities apply to all tasks that are defined within the same Requirement, and are inherited by sub-Requirements.

ActionItem “is specified by” MeetingMinutes. This class is currently under evaluation while we are investigating whether it is needed? If so, what does it need as properties?

4. The Knowledge Management Ontology

The key assumption of the knowledge management (*km*) ontology (Figure 2) is that the information in a document is more fundamental than the document itself, and that storing information separately from the document structure will allow information to be used in multiple contexts. To that end, the knowledge management ontology is divided into three areas: Fragments; Assemblies; and, DocumentTypes. Each of these areas is discussed below.

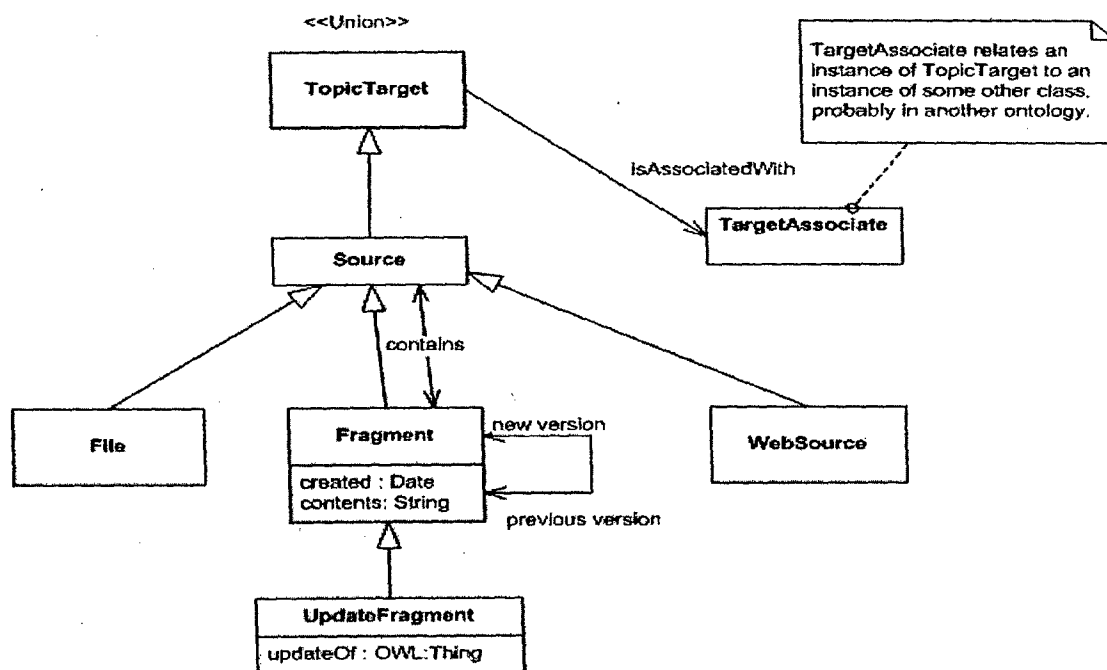


Figure 2: Partial ontology for representing textual information units.

4.1 Fragments

Fragments are the most fundamental elements of the ontology. Each fragment is intended to contain a reasonably self-sufficient piece of knowledge or information. For instance, a report on

the current status of a requirement could be considered as a single fragment.

The structure of a Fragment is very simple. Each Fragment has a "contents" property whose value is a string of arbitrary length. Each Fragment also has a "created" property whose value is a Date. This allows systems to organize fragments chronologically for presentation if a user has that need.

Each Fragment also has a "previous version" and a "next version" property that point to other instances of Fragment. This provides for a simplistic form of version control.

Currently, Fragment is a subclass of Source. Each instance of Source may contain multiple Fragments, each of which in turn may be contained by many instances of Source. It should be noted that this was an early idea of how to handle the concepts now fleshed out more fully in the Assembly area (below). It is unknown whether it will be useful to maintain the "contains" relationship in the future.

Fragment also has one subclass, UpdateFragment, which allows users to enter some new information relating to another object. This might allow, for instance, an update to some information originally gleaned from knowledge acquisition and therefore differs from "new version" because an update is an addition to existing information, while a new version replaces the old version. Also, an UpdateFragment can update anything, while the "version" properties always associate two Fragment instances.

The Fragment concept is very simple, but it is expected that the bulk of the knowledge repository will be made up of Fragment instances.

In addition to Fragment, Source has two other subclasses: File; and, WebSource. These exist for two purposes. First, to allow users to associate topics with resources that are external to the repository structure, and second, to enable Reference objects (see below) to refer to external resources, as in citing another document.

4.2 Assemblies

One of the uses of Fragments is to provide the contents of one or more documents. To accomplish this, the ontology defines the concept of an Assembly. Each Assembly structures a set of Fragments into a single document. An Assembly is a generic means of representing the organization of information for some specific purpose (Figure 3).

Assemblies provide the ability to define a specific order for a collection of Fragments. Each Assembly includes an ordered list of Part instances. Each Part is associated with a Fragment or some other type of object that can be included in a visual presentation. A document, then, is a set of Fragments organized according to an Assembly.

Each Part instance is contained by one or more Assemblies. Part currently has four subclasses: FragmentPart; Reference; ReferenceList; and, ObjectInsert. This is not intended as a comprehensive list of all potential types of document sections, but represents simply a convenient starting point.

A FragmentPart "refers to" an instance of Fragment. This is likely to be the most often-used class in an Assembly. When a FragmentPart is encountered in the "contains" list of an Assembly, the contents of the Fragment are inserted into the output document at that point. A Fragment may be referred to by many FragmentParts, allowing the same information to be included in many documents without requiring users to rewrite or to copy-and-paste.

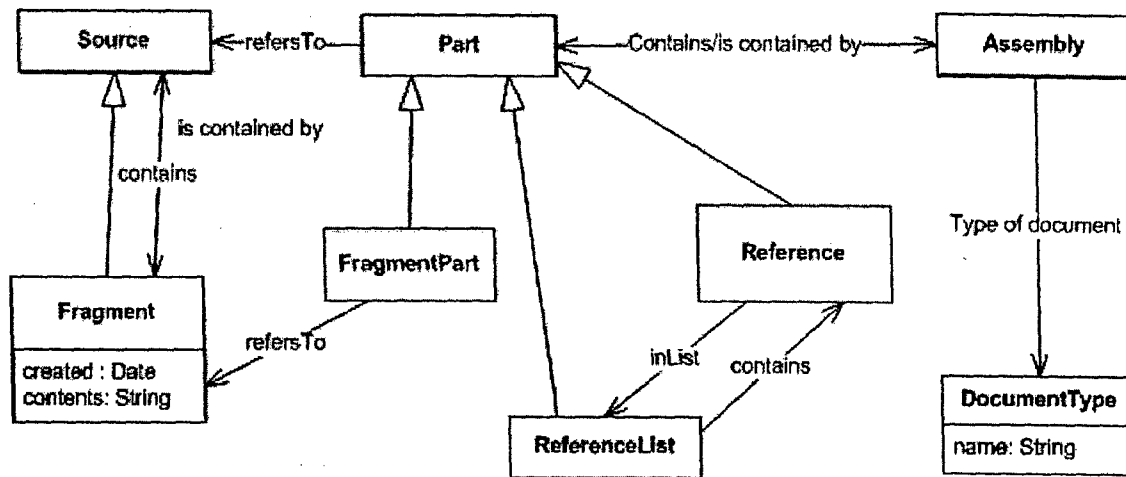


Figure 3: Classes and properties for describing the assembly of fragments and other sources into a document instance

Reference and ReferenceList are used together. An Assembly may contain a ReferenceList. Each ReferenceList contains an ordered list of Reference objects. Each Reference object has exactly one value for the “refers to” property. This value must be an instance of Source, which means that it can be a Fragment, a File, a WebSource, or an UpdateFragment. The expectation is that References will most often be associated with a File or a WebSource.

ObjectInsert is intended to allow the inclusion of values from some object outside the knowledge management ontology in a document. The specific use-case is the presentation of the definition of a requirement, along with the current status of that requirement. As noted earlier, the concept of a Requirement is part of the Organization ontology, while status reports would be one or more Fragments. In order to display an object of an arbitrary class, it is necessary for an ObjectInsert to contain two pieces of information. First, the ObjectInsert must have a property whose value is the object to display. This requirement is filled by the “refersTo” property inherited from the Part class. Second, each ObjectInsert needs a property that describes what properties of the “refersTo” object should be displayed.

This information is contained in the value of the “viewLens” property. That value is an instance of <http://www.w3.org/2004/09/fresnel#Lens>. The Fresnel ontology is imported from the Haystack project (<http://haystack.lcs.mit.edu/>). Since Fresnel is also used as part of the DocumentType section of the knowledge management ontology, it will be discussed in more detail below.

Together, the classes of Assembly, Part, ObjectInsert, Reference, and ReferenceList provide a basis for defining the contents of a specific individual document. However, it is recognized that constructing a document by repeatedly instantiating these classes is too tedious to be practical. What is needed is some way to define a general structure for a type of document and then allow the system to construct the assembly based on that structure, possibly with some assistance from a user. The concepts for the document type definition are discussed in the next section.

4.3 DocumentType

Each instance of DocumentType and its associated classes defines the structure for a category of documents. For example, a project team may define the elements of its decision document as a set of objects and properties based on classes in this section of the ontology. The DocumentType is intended to support tools that automatically create an assembly of Fragments for presentation, or that construct a user interface that enables user interaction to support the creation of documents. This part of the ontology is still under consideration; this section is based on current ideas and is subject to change.

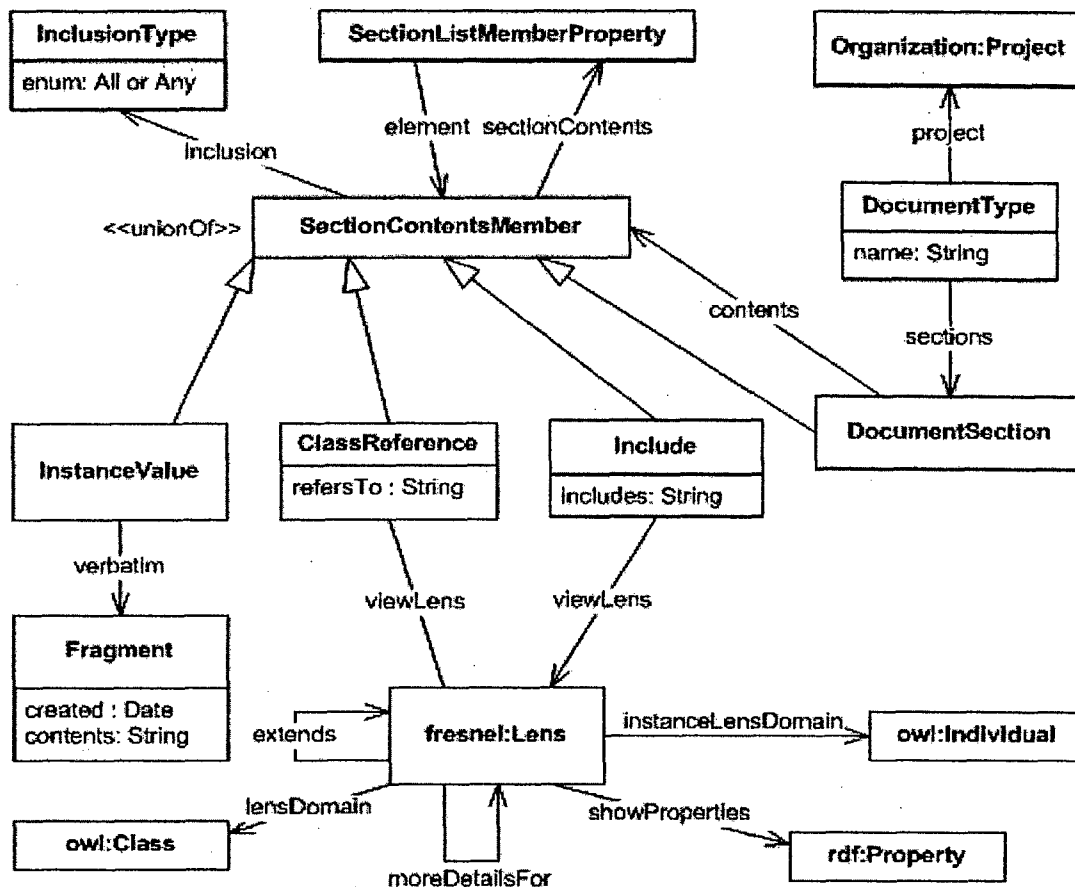


Figure 4: Classes and properties to describe types of documents

Each DocumentType has a name and zero or more associations with an org:Project (i.e., a class imported from the Organization ontology). This allows each project to potentially have its own structure for documents without requiring the invention of unique yet meaningful names for document types that have similar purposes but different requirements for multiple projects.

The structure of each DocumentType is defined by the "sections" property, which is an ordered list of DocumentSection objects. The elements of the "section" list are instances of SectionContentsMember, which is a class that is the union of several other classes: DocumentSection; Include; ClassReference; and, InstanceValue. Together, these four classes

provide the means to describe each type of section that a document can have. Each of these classes is discussed in greater detail below.

Each instance of `SectionContentsMember` has a `"sectionContents"` property which is an ordered list of `SectionListMember` objects. This list contains objects defining the contents of the section. Each `SectionListMember` has an `"element"` property whose value is another instance of `SectionContentsMember`. This means that each section of a document type definition potentially consists of a list of other sections. In practice, these lists are likely to contain one member in most cases, but conceptually this structure allows a document type to have nested sections. `SectionListMember` has another important property: `"sectionProperty,"` which relates the section to a property of the object whose values are being displayed in the containing section.

As an example that will hopefully clarify the need for this property, consider the case of a list of requirements, each of which has a list of tasks, activities, and sub-requirements. A document type structure that defines how to organize a list of requirements into a document needs to be able to state that the presentation of a given requirement includes a section that displays the list of tasks. To allow this, it is necessary for the document type definition to refer to the property that relates a requirement object to the list of objects that it contains. The `"sectionProperty"` property fulfills this need.

It should be noted that the current definition of `"sectionProperty"` states that its range is `rdf:Property`. This means that the ontology as a whole is in `OWL:Full`, the most general form of `OWL`. `OWL:Full` ontologies are theoretically undecidable, and as a result many reasoners will not process them correctly, if at all. This may become an issue in the future. If so, then this decision will need to be reconsidered.

A `DocumentSection` has an ordered list of instances of `SectionContentsMember`. Each `DocumentSection` defines the structure of one section of the document, where the meaning of `"section"` is determined on a per-document type basis.

`SectionContentsMember` has four subclasses: `InstanceValue`; `ClassReference`; `Include`; and, `DocumentSection`. A `DocumentSection` can include other `DocumentSections`, allowing reuse of structures in multiple document type definitions.

Each instance of `InstanceValue` has a `"verbatim"` property whose value is an instance of `Fragment`. This `Fragment` will be inserted into every Assembly generated from this instance of `DocumentType`. This could be used for introductory material such as the description of a project, for example, or for some boilerplate text.

`Include` provides the ability to insert an instance of some class into a document at a given point. `Include` has one property, `"includes"`, which is the URI of the class. In an automatically generated assembly, an instance (or all instances) of this class would be inserted. For a tool that incorporates user interaction, the presence of an `Include` instance in the `DocumentType` would signal the need to display a list of available instances of that class, possibly along with a form to create a new instance.

`ClassReference` is very similar to `Include`, except that `ClassReference` also allows the addition of a `Fragment` to update the object. `ClassReference` would be used, for instance, to display a `Task` (part of the Organization ontology) along with the current status of the `Task`.

Both `Include` and `ClassReference` are not yet complete. In many cases, there will be a

need to specify more information about the properties and values of an object that should be displayed. An appropriate approach for representing information is still under consideration.

SectionContentsMember also includes an optional “inclusion” property which, if present, will have one or two values: Any; or, All. The intent of “inclusion” is to define how many instances of a class should be inserted into the document. If the inclusion type is “All”, then every existing instance should be included. When the type is “Any”, there is a choice in which the user must participate. An example of “All” would be in the preparation of a document that lists the current status of the project: in such a document, every instance of Requirement must be included. “Any”, on the other hand, might be used in a document for a weekly meeting where the status of only some requirements has been updated.

5. Topics, TopicTargets, and External Ontologies

In addition to the construction of documents and the representation of information in a manner that allows automated repurposing, the knowledge management ontology also includes the ability to add indications of the topic of Fragments, Parts, and Assemblies. This will enable semantically-based searches in addition to traditional text-based searches, which in turn will provide the ability to generate ad-hoc documents without the need for the creation of a DocumentType structure.

Source, Part, and Assembly are all subclasses of TopicTarget. More specifically, TopicTarget is the union of the three classes, meaning that every instance of TopicTarget is also an instance of one of these classes. (Generally, OWL classes can overlap, but in this case Source, Part, and Assembly are declared to be disjoint with each other, meaning that they do not share objects.)

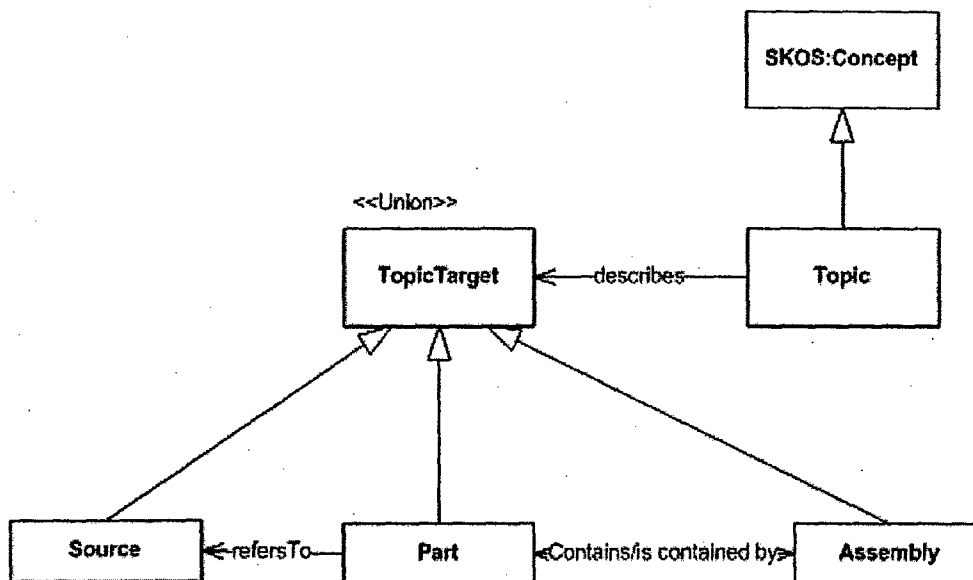


Figure 5: Classes and properties to annotate information objects with topics

A TopicTarget “is described by” one or more Topics. (“describes” is the inverse property of “is described by”.) Topic is a subclass of the SKOS class Concept. SKOS (Simple Knowledge Organization Scheme, <http://www.w3.org/2004/02/skos/>) is an existing ontology that is used by the knowledge management ontology (*km*). One of the useful facilities of OWL is the ease with which external ontologies may be integrated within new ontologies, potentially allowing existing tools to be used in processing parts of the new ontology. A later section of this document discusses the external ontologies utilized by the Organization and Knowledge Management ontologies.

SKOS defines a number of relationships between Concept instances. For our purposes, the most useful are likely to be SKOS:narrower and SKOS:broader, which allows the definition of subclass/superclass relationships between instances of Concept, and SKOS:relatedTo, which is a general relationship from which more specific non-hierarchical relationships may be derived.

As users enter new fragments into the repository, they will have the opportunity to add Topic instances to each fragment. These Topics may be selected from a list of existing topics or the user may enter a new topic. For new topics, the system will work with the user to determine if the topic has any relationship to existing topics. In this way, an ontology of topics will be constructed based on continuing interaction with the users of the system. Some automated processing may also be possible, based on statistical analysis of the text and the use of existing taxonomies such as WordNet (Fellbaum 1998).

Because the list of topics is created as new information is added to the system instead of relying on a pre-defined ontology, the process is related to the concept of a “folksonomy”: a word coined by information architect Tom Vander Wals (<http://vanderwals.net>) to refer to vocabularies that arise from the efforts of groups of people informally describing information resources. Folksonomies are generally associated with systems that allow on-line communities to add “tags” (i.e., which are essentially keyword descriptions) to various kinds of web resources. Among the better-known of such sites are del.icio.us, Technorati (www.technorati.com), and Flickr (www.flickr.com), which focus on annotating web sites, web logs, and online photographic collections, respectively.

Tag vocabularies are built one word at a time as users decide for themselves the best way to describe a resource. This practice leverages the fact that people in a specific field or area of interest tend to use similar terminologies in talking about their subject. A tagging system externalizes these vocabularies and makes them available for use in retrieving information. However, tagging systems tend to result in “flat” vocabularies where tags (or “concepts”) are not related to each other, but only to the web pages, photographs, or other resources that the tags describe. Without associations between terms, flat vocabularies are restricted to information retrieval based solely on the exact matches of key words.

The SKOS ontology retains the attractive property of a vocabulary emerging from the interaction of groups of people instead of limiting users to a predefined set of terms. At the same time, SKOS allows systems to go beyond a flat vocabulary by adding the ability for users to construct hierarchies of concepts as in a true taxonomy and to create new kinds of relationships as appropriate for specific domains. The addition of hierarchical relationships allows search and retrieval engines to understand, for instance, that a search for “mammal” should also return resources tagged with “elephant” and “mouse,” even though those resources are not tagged specifically with “mammal.”

Through the use of the Topic and SKOS ontologies, we hope to be able to provide tools to permit the retrieval of relevant information for ad hoc queries over the current state of the repository as

well as for the construction of new documents.

6. External Ontologies Included in Project

One of the benefits of using semantic web languages to define ontologies is the ease with which the ontology designer can make use of existing ontologies. This benefit is increased due to the common practice of making ontologies publicly available for use in other projects.

For this project, there are three major external ontologies that supply important concepts and relationships. There are also other ontologies involved, but their influence is indirect or circumstantial.

- **FOAF:** Friend of A Friend (<http://xmlns.com/foaf/0.1/>) provides the base concepts of Person and Organization. FOAF is a widely-used ontology and it is possible that in the future some existing tools for processing FOAF information may be useful in the knowledge management system.
- **SKOS:** Simple Knowledge Organization System (<http://www.w3.org/2004/02/skos/>) provides the description of a Concept that is central to the idea of annotated documents, fragments, and other objects with topics describing their subject matter. In the *km* project ontology, *skos:Concept* is subclassed as *km:Topic*. Other aspects of SKOS are discussed in the previous section.

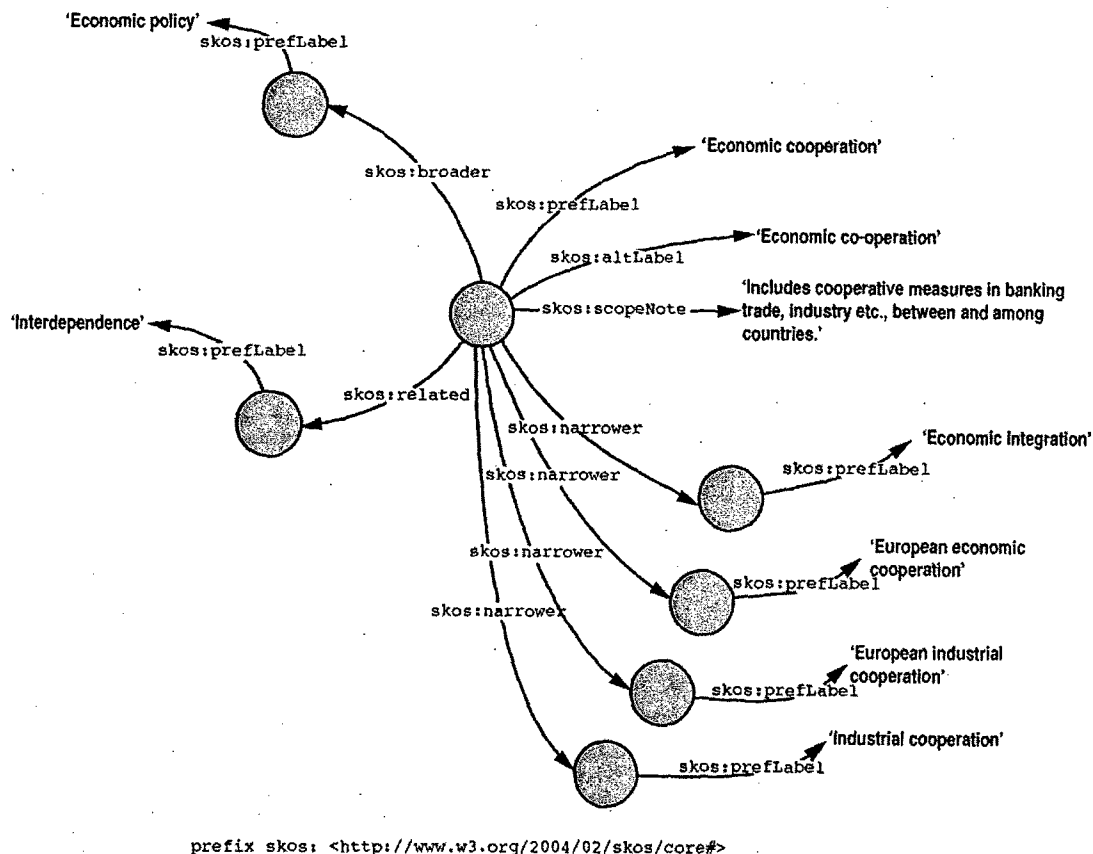


Figure 6: SKOS example
(from <http://www.w3.org/TR/2005/WD-swbp-skos-core-guide-20050510/>)

- **Fresnel Lens:** (<http://www.w3.org/2004/09/fresnel#>) Fresnel is a set of related ontologies whose classes and properties are intended to allow the description of documents built from values associated with objects (refer documentation at: <http://simile.mit.edu/repository/fresnel/trunk/docs/manual/FresnelVocabulary.htm>). There are two primary divisions in Fresnel: Lens, which defines views on objects; and, Style, which provides concepts related to the presentation of information defined using instances of Lens and related classes, and their properties.

The *km* ontology makes heavy use of Fresnel Lens in describing document type definitions. There is a possibility that the Style section of Fresnel may become the basis for future document presentation tools and user-interface elements.

There are several other ontologies that are partially included in the knowledge management system due to the fact that they are referenced by one of the three explicitly imported ontologies. Two of the more important are:

- **Dublin Core (dc):** (<http://purl.org/dc/terms/> and <http://purl.org/dc/elements/1.1/>, with documentation at: <http://dublincore.org/>) Dublin Core defines metadata elements such as dc:title, dc:subject, dc:author, and so on, that enable descriptions of information about resources such as documents and web pages.
- **PIM/Contact:** (<http://www.w3.org/2000/10/swap/pim/contact#>) We have not been able to locate a great deal of documentation on PIM Contact. FOAF derives several of its classes, such as FOAF:Person, from classes in Contact, which links the Organization part of this project's ontology indirectly to Contact. The purpose of PIM Contact is to represent all of the objects and relationships that might be involved in defining all of the ways that a person can be contacted: email, phone (business, fax, and home), location (several types), and so on.

The connection between FOAF and PIM/Contact exposes one potential pitfall in reusing existing ontologies. In Contact, a "SocialEntity" can be related to an instance of the "_EmailAddress" class using the "emailAddress" property. In FOAF, in contrast, the "mbox" property relates an "Agent" to a "Resource." There is no explicit relationship between contact:SocialEntity and FOAF:Agent. The same information (i.e., the email address of a person or organization) is represented in two different ways and the importing ontology (FOAF) does not include an attempt to reconcile these differences. This can lead to some apparent inconsistencies in the ontology definition, as the next section discusses.

7. Issues of Working with External Ontologies

As described in the previous section, the Knowledge Management and Organization ontologies utilize several ontologies developed by other organizations. There are several positive aspects to using externally developed ontologies. For instance, the public nature of such ontologies increases the possibility that logical flaws have been removed through wider inspection, much as open source software may have fewer bugs than closed source software, simply because more people have examined the code. Also, in some cases, it may be possible for a system to incorporate existing ontology-specific tools and libraries, reducing development costs and increasing reliability. However, there are also drawbacks to using externally-developed ontologies. This section lists some issues that have arisen during development of the knowledge management system.

Overlapping Features: Some of the existing ontologies have overlapping features. In addition to the email address example mentioned above, FOAF and Contact have several other classes and properties that represent the same concepts, but have incompatible definitions. Both FOAF and Contact, for instance, define a Person class (FOAF:Person is a subclass of contact:Person) and they both define "firstName" properties for instances of their own Person class. The FOAF "firstName" property has no defined relationship to the Contact "firstName" property. This sort of condition makes it difficult to know how to handle these properties. For the purposes of the Organization ontology, the approach is to simply ignore features of external ontologies that are overlapping, conflicting, or simply outside the needs of the proposed system. There is a concern, however, that this approach may cause problems in the future in the event that there are opportunities for communication with other systems that may use these external ontologies to support their own functionality.

Different Representations: Many of the existing ontologies are expressed in RDF (and RDFS) instead of OWL. This can result in a need for extra processing, especially in the absence of an inference engine. For example: RDF includes a Property class that can be used to specify associations between two objects, or between an object and an instance of a data type, such as a string or an integer. OWL specializes `rdf:Property` into `owl:ObjectProperty` (i.e., when the value of the property is an object) and `owl:DatatypeProperty` (i.e., when the value is a simple data type). If an `rdf:Property` has a range specified, an OWL-aware reasoner may be able to infer that the property's type is either `owl:ObjectProperty` or `owl:DatatypeProperty`, which in turn allows the property to be processed by code and rules aimed at the OWL property types. In the absence of a reasoner, this inference must be performed explicitly in order for the system to treat an instance of `rdf:Property` as an instance of one of the OWL property types.

Inferencing Obstacles: Ontologies, such as FOAF, need to be edited in order to be used with an inference engine. FOAF imports the OWL and RDF ontologies, and this creates errors when fed to a reasoner that already includes the semantics of these languages. Other ontologies include definitions that cause different problems for a reasoner. The Fresnel Lens ontology (<http://simile.mit.edu/repository/fresnel/trunk/ontologies/lens-core.rdfs.n3>) includes the description of two resources that are instances of `rdf:resource`, which, although legal in an RDF ontology, causes errors when loaded as an OWL ontology. (In fact, the Lens ontology defines these as instances of "rdf:Resource," which is incorrect due to the capitalization of "Resource." After correction, we see the error due to instantiation of `RDF:resource`.) Many of the ontologies included in this project have similar issues, some of which require that the ontologies be altered before they can be used.

Additionally, there is a further problem specific to the Fresnel ontology. The Fresnel ontology is in fact composed of four ontologies, namely: `lens`; `lens extended`; `style core`; and, `style extended`. Each of these ontologies is defined in its own file, but all use the same URL (i.e., <http://www.w3.org/2004/09/fresnel#>). This is legal for OWL and RDF, since there is nothing in the specification of either language that requires an ontology to be defined in a single file. However, from a practical point of view this arrangement is problematic because the OWL library that this project uses locates ontology representations by URL: either directly, by assuming that the URL is a location where a program can find the ontology; or, indirectly through a mapping between the URL and the local file location. In the case of Fresnel, neither of these approaches works, since there is nothing located at the given URL and it is impossible to

map a single URL to four different files. Fortunately, at this early stage of our project the knowledge management ontology uses only concepts from the lens ontology part of Fresnel, which is contained in a single file. This is perhaps an illustration of how easy it can be to build dependencies into an ontology. In this case, dividing the ontology into four separate files creates no issues for the project using Fresnel (Haystack, <http://haystack.csail.mit.edu/>), but this decision creates problems when trying to use the ontology in other environments, creating an interoperability issue.

8. Future Work

The semantic web knowledge management ontology is sufficiently complete to serve as the basis for a set of project management and decision support tools. The first generation of such tools falls into several categories. The level of effort required to implement this list of tools is far greater than is possible to complete in a single year. Therefore, the list should be read as potential functionality for some future date, not necessarily within the next year.

1. ***Creation of instances of organization-related classes and relationships:*** These include projects, personnel, requirements, tasks, activities, and events. The implementation of the user-interface in this area has begun, and needs to be completed.
2. ***User-interface facilities:*** Development of a user-interface for constructing fragments based on initial document structure definitions. As an example, meeting minutes may have a standard structure, with variations for specific projects or even specific meeting types. Those structures will be defined as document types within the ontology. There is then a need for tools to create user interfaces for given document structures. These will probably be a combination of generic elements that apply to any document structure instance, with some specialized elements for parts of an individual document structure. The tools that are needed here fall into two areas: first, the "engine" that translates document structure definitions into user interface elements; and second, developer tools for defining special case elements as necessary.
3. ***Definition of document type structures:*** Initially, work on the two categories listed above can proceed based on hand-built models. But these structure definitions are too complex to be constructed directly. To be successful, the system must enable users who know nothing about the details of the ontology to define their own document types. This will require experimentation to determine what tools might be usable in this area.
4. ***Support for multiple drafts of a document:*** When the system has brought together many fragments into an assembly based on a document type structure definition, it is likely that the result will not be a completely polished document. Users will probably need to edit the results. But the system needs to maintain links between the various versions of each fragment. When other documents include the same fragment, every version of that fragment should be available to the user.
5. ***What-You-See-Is-What-You-Get (WYSIWYG) support:*** The final output of an instance of a document type should be acceptably formatted. The system needs to

include tools to allow the user to describe the visual presentation of the material and to associate that description with the document type structure for later use.

6. ***Searching based on semantic annotations:*** This is the original impetus for the system, although laying down the infrastructure has become the focus of work to this point.
7. ***Ad hoc document creation:*** While many work products can be described in generic format, many documents will be created only once. Creating these documents should not require the user to first create a document type structure definition, particularly since such definitions are likely to be complex. Instead, there must be some simpler interface for users to define what they want to include in a document and build the contents based on that definition.
8. ***Storable, sharable queries:*** In constructing reports, it should be possible to create queries to assemble all the relevant parts of the document contained in the repository. By making these queries persistent, another user will be able to see the same report by executing the stored queries.

References

- Fellbaum C. (1998); 'WordNet: An Electronic Lexical Database'; MIT Press, Cambridge, Massachusetts.
- Antoniou G. and F. van Harmelen (2004); 'A Semantic Web Primer'; MIT Press, Cambridge, Massachusetts.
- OWL (2004); OWL Web Site: <http://www.w3.org/2004/OWL/>

Molecular Sensors and Defenses Against Ultraviolet Radiation

Project Investigator:

Nikki L. Adams

Assistant Professor

Department of Biological Sciences, California Polytechnic State University

IV.B.2: Results of Research Projects

A. ABSTRACT

Many organisms are exposed to damaging levels of ultraviolet radiation (UVR, 290-400 nm). The overall goals of this study were to identify molecular targets of UV-induced damage and to characterize and quantify natural sunscreens (mycosporine-like amino acids, MAAs) in local marine organisms. More specifically, the first aim addressed in this study was to identify molecular targets (markers) of UVR-induced damage that lead to perturbations in cell division using sea urchin embryos as a model system. We examined effects of UVR on molecules that control cell division, such as the cyclin dependent kinases including Cdc2 (cdk1) and document that phosphorylation (potential activity) is affected negatively by UVR. In addition, we used sequence data and western blotting to determine that both Cdc25 and Chk1, which work upstream of and control activity of Cdc2, are likely to be present in sea urchin embryos. Second, we complemented these studies by investigating natural sunscreens, MAAs, in marine algae to screen for novel (undiscovered) MAAs and to determine which species might be suitable for future studies investigating the protective role of MAAs. We found that all 12 species of red macroalgae contain a variable suite of known MAAs. This research may benefit marine science and the biotechnology industry by identifying molecular markers of UV- damage that can be used to assess amounts of damage occurring in nature and provide a means for testing the effectiveness of natural and commercial sunscreens.

B. BACKGROUND AND GOALS OF RESEARCH

Depletion of stratospheric ozone has increased the amount of solar ultraviolet radiation (UVR, 290-400 nm, specifically UVB, 290-320 nm) reaching the Earth's surface, making it increasingly important to understand effects of UVR on organisms (Madronich et al., 1998). Solar radiation is the primary driving force for most processes in the ocean (Whitehead and De Mora, 2000). Nevertheless, UVR harms aquatic organisms such as embryonic stages of marine invertebrates that float at the ocean's surface or live in shallow water (Adams and Shick, 1996; 2001; Gleason and Wellington, 1996; Häder et al., 1998; Karentz and Bosch, 2001). Damaging levels of solar UVR can penetrate to at least 20 m in highly transparent water, 20-30 m in Antarctic waters (Smith et al. 1992), and to several meters in organically rich coastal seawater (Smith and Baker, 1979; Booth and Morrow, 1997; Adams et al., 2001). Assessment of UVR's impact on life histories at the ecological and cellular levels is particularly important because factors influencing early development will determine adult population characteristics.

UVR causes direct damage to DNA, proteins, and membrane lipids and indirect damage by forming reactive oxygen species (ROS) (Tyrrell, 1991). UV-irradiation of cells causes dosage-dependent delays in cell division and developmental abnormalities. One of the earliest model systems for study of this phenomenon at the cellular level was sea urchin eggs and embryos (Adams and Shick 1996; 2001; Rustad, 1971). These abnormalities may be viewed microscopically, but it is important to understand their cellular and molecular origin by identifying the molecular targets of UVR. In addition, among the non-chordate deuterostomes, the sea urchins are the primary target for research in genomics because they are the only non-chordate deuterostomes that serve as a major research model (Davidson et al., 2004).

In all eukaryotes that have been studied, the sequential formation, activation, and deactivation of a series of structurally regulated serine/threonine protein kinases regulate progression of cells through the cell cycle (Morgan, 1997). These enzymes consist of a

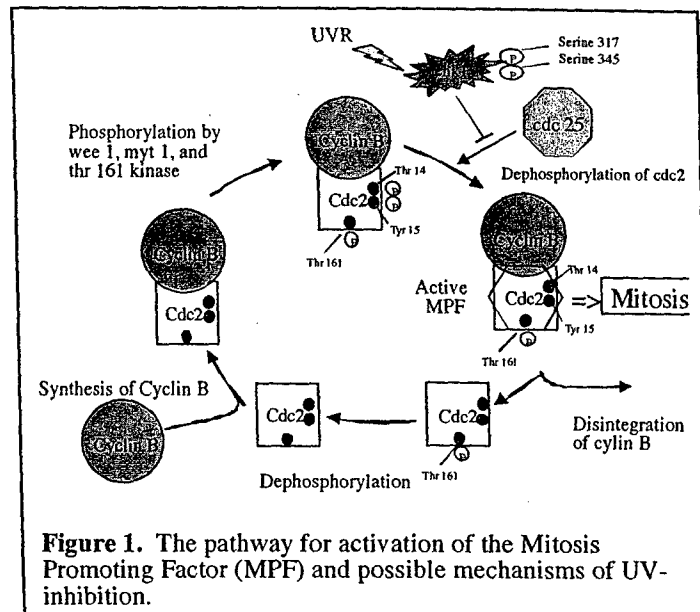
regulatory subunit, a cyclin, and a catalytic subunit, Cdc2, a cyclin dependent kinase (cdk), which combine to form Mitosis-Promoting Factors (MPFs). Post-translational modification and inhibitory proteins regulate activity of MPFs (Fig.1). This complex is the key regulator of cell cycle checkpoints known as the G2/M (mitosis) transition (Murray and Kirschner, 1991).

Upstream kinases (add phosphates) and phosphatases (remove phosphates) regulate MPF activity (Fig. 1). Upon activation of sea urchin eggs, protein synthesis begins and cyclin B is synthesized. Cdc2 is present in eggs and binds to the newly synthesized cyclin, to form an inactive MPF. Once the MPF is formed, two proteins, Myt 1 and Wee1, phosphorylate Cdc2 at two inhibitory sites, Tyr 15 and Thr 14. Then, Thr 161 kinase, phosphorylates Cdc2 at an activating site, Thr 161 (Coleman and Dunphy, 1994; Suprywicz et al., 2000). Accumulation of the repressed form of MPF to a threshold level creates precise control over entry into mitosis. Cdc25 (a phosphatase) is responsible for removing the inhibitory phosphates at Thr 14 and Tyr 15 activating MPF and propelling the cell into mitosis (Peng et al., 1997). If any of these events are delayed, mitosis is stalled (Fig. 1). This pathway is highly conserved among organisms and cell types, including echinoderm embryos (Meijer et al., 1989; Okano-Uchida et al., 1998; Suprywicz et al., 2000).

Dephosphorylation of Cdc2 at Tyr 15 and of Cdc25 at Ser 216 is inhibited by UVR in human keratinocytes (Gabrielli et al., 1997; Herzinger et al., 1995) or general damage to DNA (Furnari et al., 1997; Sanchez et al., 1997). In addition, Cdc25 is inhibited via phosphorylation at Ser 216 by Chk1 kinase. In mammalian cells, UV-irradiation and genotoxic stress activate Chk1, by phosphorylation of Ser 317 and 345 (Zhao et al., 2001). Examination of Chk1 phosphorylation may provide the most direct marker of UV-induced mitotic delays documenting molecular damage by UVR. The evidence in mammalian somatic cells, which demonstrate that Chk1 is activated and Cdc25 and Cdc2 activity are inhibited by UV-exposure, indicate that this is likely to be the case in sea urchin embryos. Our preliminary evidence support this hypothesis and indicate that further investigation of effects of UVR on this pathway in sea urchin embryos may allow us to more fully understand the mechanism of UV-induced cleavage delays.

Our previous experiments indicate dephosphorylation of Cdc2 at Tyr 15 is delayed in sea urchin zygotes that are exposed to artificial UVR. Once mitosis has progressed, Cdc2 becomes dephosphorylated at Thr 161 and is ready for another round of cell division. Thr 161 is phosphorylated similarly in embryos of both treatments, but that its dephosphorylation is delayed in UV-irradiated embryos, what we would expect if cell mitosis had been delayed. The delay in dephosphorylation of Cdc2 correlates precisely with the delays in cell division in these batches of embryos (Adams, in preparation, See original proposal).

Shallow-dwelling organisms have natural defenses and behaviors that may reduce exposure to solar UVR, particularly during periods of peak irradiance (Adams, 2001; Pennington



& Emlet, 1986). Phototrophic organisms that rely directly on sunlight, or planktonic and sessile organisms that cannot avoid solar UV-exposure remain exposed to potentially damaging levels of solar UVR (Jerlov, 1950; Smith & Baker, 1979). Fortunately, they may receive protection by accumulating mycosporine-like amino acids (MAAs) that absorb UVR and may dissipate its energy harmlessly (Dunlap & Shick, 1998; Dunlap & Chalker, 1986; Shick et al., 2000).

MAAs are a suite of water soluble compounds with absorption maxima ranging from 309 to 360 nm. They have overlapping absorption ranges that extend across much of the spectrum of UVR, creating effective broad-spectral sunscreens (Dunlap & Shick, 1998). They are ubiquitous among marine organisms and they protect sea urchin embryos against UV-induced delays in cell division and developmental abnormalities (Adams and Shick, 1996; 2001). It is still unclear, however, which molecular targets are affected by UVR in sea urchin embryos leading to cleavage delay and developmental abnormalities and which targets are protected by MAAs.

MAA concentration varies among tissues, often being highest in the tissues most exposed to UVR (Chioccare et al., 1986; Dunlap et al., 1989; Shick et al., 1992; Adams & Shick, 1996; 2001). MAA concentrations in corals and macroalgae are positively correlated with natural levels of UVR (Dunlap & Shick, 1998; Franklin et al., 1999; Karsten et al., 1998), so that organisms may regulate concentrations of UV-absorbing compounds in proportion to the amount of UVR they experience in their environment (Dunlap et al., 1986; Gleason, 1993; Shick et al., 1996; 1999). Red macroalgae have been studied extensively and shown to specifically regulate their concentrations of MAAs in relationship to UV-exposure (Franklin et al., 1999; Karsten et al., 1998). Thus, they have the potential to serve as bio-sensors of UV-exposure. Red algae studied to date contain a wide-array of MAAs and have also been used in experiments demonstrating dietary accumulation of MAAs from algae in marine invertebrates (Carroll and Shick, 2000; Adams and Shick 1996; 2001).

The synthesis of MAAs is restricted to bacteria, cyanobacteria, fungi, and algae by the shikimic acid pathway in these organisms (Favre-Bonvin et al., 1987; Shick et al., 1999). Marine consumers such as sea urchins and nudibranchs are unable to synthesize the compounds themselves and acquire MAAs from their diets of algae (Adams & Shick, 1996; Carefoot et al., 1998; Carroll & Shick, 1996). Adult sea urchins, *Strongylocentrotus droebachiensis*, sequester MAAs in their eggs, but not sperm (Adams & Shick, 1996). *S. droebachiensis* presumably feeding on a mixed diet in nature produces eggs having intermediate concentrations of MAAs (Adams & Shick 2001; Carroll & Shick, 1996). MAAs do not appear to be accumulated in mammalian cells through the diet, however, they can be absorbed by human skin cells and have the potential to serve as topical sunscreens (Mason et al., 1998).

MAAs protect marine invertebrates and phytoplankton against UV-induced damage (Adams and Shick 1996 & 2001; Neale et al., 1998). MAAs in the eggs of *S. droebachiensis* protects them in part from UV-induced delays in cleavage (Adams and Shick, 1996) and abnormalities during later development (Adams & Shick, 2001). Fortification of eggs with MAAs may decrease cellular damage and developmental abnormalities, but the mechanism of protection remains unknown.

To address these aims, we examined how solar UVR affects phosphorylation of Cdc2 and whether Cdc25 and Chk1 exist in purple sea urchins, *S. purpuratus*, and whether they are affected by UVR. In addition, we screened 12 species of red algae for MAAs. Results presented constitute on ongoing study that will build on the results from this first year of investigation.

C. PROGRESS OF RESEARCH

Aim 1. Identify molecular targets of UV-induced delays in cell division in sea urchin embryos, *Strongylocentrotus purpuratus*. We measured the levels of UVR that sea urchin eggs and embryos experience in the field (data not shown). Then, we examined potential targets and mechanisms of UV-induced damage in the laboratory and field to establish molecular markers of damage. One of the most prominent effects of UVR on cells is disruption of the cell cycle that can lead to skin cancers, and thus obvious candidates for markers of UVR-induced delay are the cell cycle regulatory proteins, including cyclin dependent kinases (cdks) such as Cdc2, Cdc25, and Chk1 kinase. Chk1 is an especially exciting target (potential sensor of damage) because it can inhibit proteins that control mitosis and it has been shown to play an important role in UV-induced damage, embryonic development and tumor suppression in other cell types.

Aim 1-A. Effects of solar UVR on phosphorylation/Activity of Cdc2. We had previously demonstrated that Cdc2 activity (as indicated by dephosphorylation at Tyr 15) is delayed by artificial UV-irradiation. We have built upon these results and confirmed that cell division and Cdc2 dephosphorylation at (Tyr 15) is delayed in embryos from eggs exposed to natural solar UVR (Fig. 3).

Materials and Methods

Collection of gametes and exposure experiments

Ripe adult *S. purpuratus* were collected from the central coast of California and held in a recirculating seawater system at Cal Poly. Sea urchins were induced to spawn gametes using intracoelomic injection of 0.5 M KCl. Eggs were washed with filtered seawater and a 20% suspension of eggs was prepared. Eggs were exposed to natural sunlight under the following conditions: 1) PAR (photosynthetically active radiation, 400-700nm) and protected from UVR by covering them with UV-opaque Plexiglas G (50% transmission at 400nm) or 2) exposed to PAR + UVR using UV-transparent Plexiglas UF-3 (50% transmission at 295nm). This latter filter provided the same amount of PAR light to the embryos as in the control. The suspensions were exposed to direct sunlight in front of the Marine Science building of the California Polytechnic State for 20 mins. During this time, the samples were constantly stirred to allow for maximum exposure of each egg in the solutions. Simultaneously, UVR was measured using an International Light IL1400A radiometer, and model SEL033 UVA and SEL UVB sensors with peak sensitivities at 350 and 295 nm respectively.

Preparation of protein lysates

Immediately after irradiation, the egg samples were each diluted to a 10% solution and subsequently incubated with 100mM amino triazole (ATAZ) to prevent polymerization of the fertilization membrane for 10 mins prior to fertilization. A sample of each egg suspension was centrifuged at 1000 rpm for 1 minute and the seawater decanted. Eggs were lysed using a buffer containing 0.1% Triton X-100, 20mM HEPES, 150mM NaCl, 60mM Na 2-glycerophosphate, 15mM disodium EGTA, 0.5mM sodium vanadate, 10 μ M PIC, 1 μ M PMSF, 1mM sodium fluoride and by passage through a 27-gauge hypodermic needle. The lysate was then centrifuged at 20,000 rpm at 4°C for 20 mins. Supernatants were collected, aliquoted, and snap frozen using liquid nitrogen and stored at -80°C for later biochemical analysis.

The remaining unfertilized eggs (both control and UV-exposed) were fertilized using a 1:50,000 dilution of sperm. Fertilization was confirmed and only samples that achieved $\geq 90\%$

fertilization were used for analysis. Samples were taken at 15 mins, 70 mins, 90 mins, 110 mins and 130 mins after fertilization. They were subsequently processed in the same manner as the egg samples.

Analysis of UV-induced cleavage delay

Subsamples of embryos from the same cultures were fixed in a 1% formalin solution to preserve them for later analysis. These samples were taken at 80 mins post-fertilization and again every ten mins until 100% of the embryos had reached the first cell cleavage, generally around 200 mins after fertilization. At least 200 embryos were counted to determine the percentage of embryos that had cleaved, completed the first cell division, for each of the time points. Graphs of percent cleavage versus time after fertilization yielded the times as which 50% of the embryos had cleaved in both the control and the UV irradiated embryos (Fig. 2a). These values were then converted into total percent cleavage delay (%CD) (equation below) to adjust for variations among batches and to allow for comparisons among different experiments. Total percentage cleavage delay was used as an indicator of the amount of damage the UV irradiated embryos received compared to the control embryos.

$$\%CD = \frac{(\text{Time for 50\% of UV embryos to divide}) - (\text{Time for 50\% of Control embryos to divide})}{\text{Time for 50\% of Control embryos to divide}}$$

Protein Identification and Analysis

Protein concentrations of each sample (UV and control) were determined using the Pierce bicinchoninic acid (BCA) method with absorbance at 562nm. Equal amounts (25 μ g) of protein were loaded into each lane of a 10% polyacrylamide gel (BIO-RAD). Proteins were separated utilizing SDS polyacrylamide gel electrophoresis (PAGE) with BIORAD Mini-PROTEAN 3 electrophoresis module. Simultaneously, positive and negative controls for pCdc2 (Tyr 15, Cell Signaling) were run as well as a molecular weight ladder (BIO-RAD). Proteins were then transferred onto nitrocellulose using a BIO-RAD Mini Trans-Blot Electrophoretic Transfer Cell. Blots were blocked in 5% bovine serum albumin (BSA) or 5% nonfat milk in wash buffer (20mM Tris, 150 mM NaCl, pH 7.6, 0.1% Tween 20). One blot was then incubated using a 1:1000 dilution of primary Cdc2 antibody (Cell Signaling) in 5% BSA blocking buffer. Simultaneously, the other blot was incubated using a 1:750 dilution of phospho-Cdc2 antibody (Cell Signaling) in 5% dry milk buffer. Subsequently, the blots were washed and then incubated using a 1:10,000 dilution of HRP conjugated secondary goat-anti-rabbit antibody (BD Transduction Laboratories). A final series of washes was applied to both blots before incubating enhanced chemiluminescence (ECL) reagents (Pierce SuperSignal West Dura Extended Duration Substrate) to detect anti-body-labeled proteins. The blots were imaged using Quantity One software and a BIO-RAD Fluor-S imager in the Cal Poly Undergraduate Biotechnology Laboratory. Band densities were compared among similar time points in the "Cdc2" and "pCdc2" blots using Quantity One software. Relative concentrations of phosphorylated Tyr 15-Cdc2 and total Cdc2 proteins were then compared at each time point after fertilization. Percentage relative phosphorylation was calculated by first dividing the relative density of pCdc2 band with the relative Cdc2 density at the same time point to get relative phosphorylation and then dividing that number with by the highest relative phosphorylation in the blot. Percentage relative phosphorylation was determined to standardize the signal and to help us to compare delays in dephosphorylation (Tyr 15) among blots/experiments.

Statistical analysis

We compared UV doses among experiences using a one-way ANOVA with Tukey's post-hoc analysis (Statview 5.0.1, SAS Institute). Because there were significant differences in the doses of UVA and the doses of UVB among experiments, we did not perform statistical analysis examining affects of UVR on Cdc2 phosphorylation. We will repeat these experiments this next year in an attempt to get more consistent UV exposures.

Results

The UVA and UVB irradiance measurements (mW/cm^2) and their respective doses (J/cm^2) are shown for each experiment in Table 1. There was a significant difference among both UVA and UVB doses among experiments ($P=0.0014$ and $P=0.0003$ respectively). UVA levels were significantly higher on 5/25/04 than both other dates ($P < 0.05$), which were not significantly different from each other. UVB levels were significantly lower on 4/0/04 than both other dates ($P < 0.05$), which were not significantly different from each other.

Table 1. Average light measurements taken during each exposure experiment. These values are irradiance (mW/cm^2) and total dose (J/cm^2). Three measurements were taken simultaneously during exposure experiments (immediately before, midway through, and immediately after) and those values were averaged. UVR measurements were taken under the UV-transparent Plexiglas UF-3 filter.

Experiment	UVA	UVB
04/09/04	2.69mW/cm ²	.003 mW/cm ²
	3.23J/cm ²	.0038J/cm ²
05/25/04	3.59mW/cm ²	.0045mW/cm ²
	4.31J/cm ²	.0054J/cm ²
06/22/04	2.97mW/cm ²	.0045mW/cm ²
	3.56J/cm ²	.0054J/cm ²

Figure 2a depicts a typical graph of the percentage of embryos cleavage vs. time since fertilization for control and UV-irradiated embryos of the same batch. Embryos exposed to UVR experienced a delay in the first cell division of up to 35 mins, with an average delay (\pm SD) of 29 (\pm 14) mins. The average percentage delay (\pm SD) for the three experiments was 19.9 (\pm 12.1)%.

Relative Cdc2 phosphorylation (Tyr 15) was calculated by first dividing the relative densities of the p-Cdc2 bands in the western blot with the relative densities of Cdc2 bands from the same sample. The sample with the largest relative pCdc2:Cdc2 density for each experiment was deemed "100%". The values of the other samples (UV-irradiated and noon-irradiated; 0, 15, 70, 90, 110, 130 mins post-fertilization) were then divided by that largest value to calculate relative phosphorylation percentages for each sample from an exposure experiment (Fig. 2b).

Relative phosphorylation of Cdc2 (Tyr 15) appears to be equal within treatment but increases in both treatments until ~ 90 mins post-fertilization. By 110 mins, phosphorylation of Cdc2 (Tyr 215) of the control embryos decreased relative to previously levels and compared to UV-irradiated embryos. These results are consistent with our previous results using artificial UV-exposures, however there is much more variance in the amount of phosphorylation of Cdc2 (Tyr 15) in this experiment as might be expected due to greater variability in UV doses. Nevertheless, this study provides more realistic evidence of how natural UVR may be affecting embryos and the activity of Cdc2 in the field. Although statistical analysis has not been performed on these

data, there appear to be dramatic differences in percentage relative phosphorylation at the 110- and 130-minute time points.

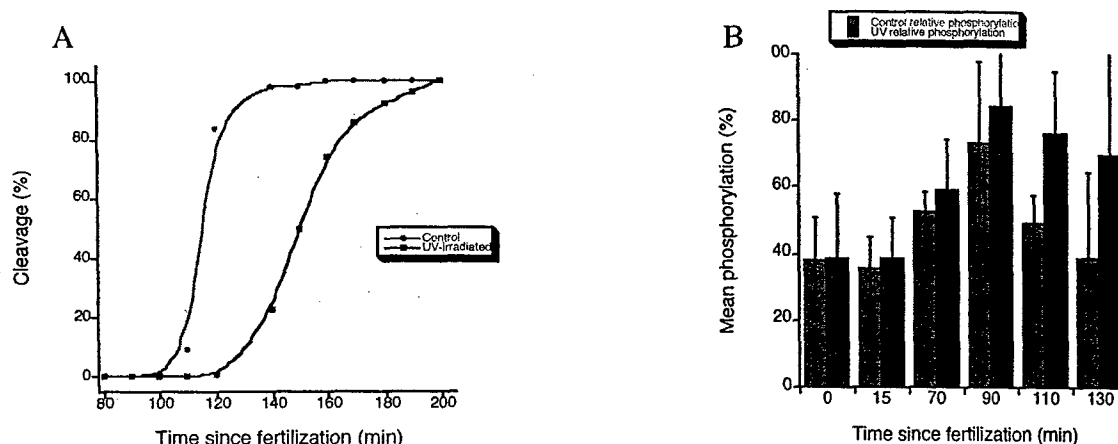


Figure 2. A. Cleavage delay data for embryos of *S. purpuratus* eggs exposed to solar UVR on 05/25/04. Mean time to 50% cleavage shows a delay of 35 mins in embryos whose eggs were exposed to solar UVR for 20 mins. B. Mean values (\pm S.D.) of relative percent phosphorylated Cdc2 in sea urchin embryos at specific time points post fertilization ($n=3$). Note: normal division occurs at ~110 mins.

Conclusions

Cleavage delay data indicate that UV-exposure causes a delay in division of *S. purpuratus* embryos whose eggs were exposed to natural solar radiation. With an average delay in the first mitotic event of 29 (± 14) mins it can be suggested that UVR has the potential to substantially impede the development of sea urchin embryos, quite possibly leading to significant ecological impacts if an entire population is experiencing similar dosages of UVR. In addition, the biochemical data obtained from these three UVR experiments appear to suggest that UV-exposure causes a delay in dephosphorylation of the MPF inhibitory Tyr 15 of Cdc2. These results may explain the UV-induced cleavage delays and developmental stage-sensitivity of sea urchin embryos observed by Rustad (1960).

Because the UV exposures were not identical among these experiments we did not perform statistical analysis on the Cdc2 data. Nevertheless, based on the relative phosphorylation of Cdc2 obtained from embryos of UV-irradiated eggs, there appears to be substantially less pCdc2 (Tyr 15) in non-irradiated embryos when compared with UV-irradiated embryos at the 110- and 130-minute time points. At these time points, we would expect Cdc2 to be active and the cells to be dividing, but dephosphorylation appears to be delayed in UV-irradiated cells.

In more recent preliminary experiments, we have examined effects of UVR on phosphorylation in UV-irradiated embryos (instead of irradiated eggs) because our previous results had shown that embryos are more sensitive to UVR than eggs. These results appear to be similar to all of our previous results for p-Cdc2.

Aim 1-B. Effects of solar radiation on development *in situ*. In a side project, we have also demonstrated that biologically effective solar UVR penetrates into surface waters (to at least 1 m) at our Center for Coastal Marine Sciences in San Luis Obispo Bay to cause delays in division of sea urchin embryos (data not shown, similar to Fig. 3a). These results demonstrate that current levels of UVR *in situ* in surface coastal waters can cause developmental delays in sea

urchin embryos and that we can successfully perform experiments with natural sunlight to examine the molecular targets of UV-induced delays in division. Eventually, we will perform experiments *in situ* similar to those discussed in Aim 1-A at the CCMS.

Aim 1-C. The presence of Cdc25 in sea urchin embryos. Active Cdc25 removes the inhibitory phosphate at Tyr 15 from Cdc2. Therefore, we have examined whether Cdc25 is present in sea urchin embryos.

Materials and Methods

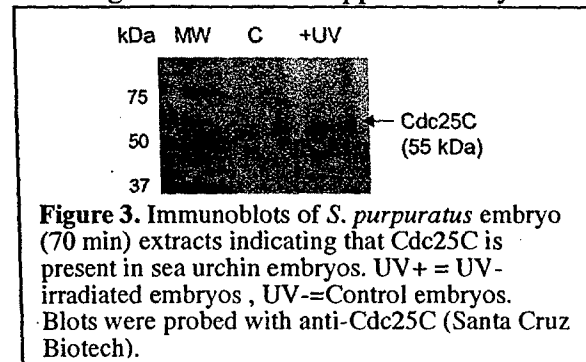
Methods for collection of gametes and culture of embryos and preparations of embryo lysates were the same as described above (Section A). Cultures of sea urchin embryos from the same batch were then examined. Proteins were separated using SDS PAGE and then transferred onto a nitrocellulose membrane and relative levels of Cdc25C was determined by immunoblot analysis using a Cdc25 antibody generated against human Cdc25C (Santa Cruz Biotechnology, Inc.). In addition, we tested one other antibody for Cdc25C and two antibodies for Cdc25B, but had very limited success with these antibodies.

Results

The Cdc25C antibody from Santa Cruz Biotech recognized a band at approximately 55 kDa in sea urchin embryo lysates. A similar band at the same molecular weight was also recognized in Hela cell lysates (data not shown).

Discussion

These results indicate that Cdc25C is present in sea urchin embryos and that we may begin our investigations into whether Cdc25C is affected by UVR. We are currently testing four commercially available antibodies for phospho-specific Cdc25C (p-Cdc25, Ser 216). Using these antibodies, we will examine whether UV-irradiation of sea urchin embryos phosphorylates Cdc25C at Ser 216 (see Adams renewal proposal 2005). We predict that Cdc25C, which is a phosphatase that removes Tyr 14 from Cdc2 will be inactivated in sea urchin embryos (phosphorylated at Ser 216) by UV-exposure.



Aim 1-D. Examination of Chk1 in sea urchin embryos. Chk1 is a kinase that controls activity of Cdc25. Sequence homology in the Chk1 kinase domain suggests overall structural conservation across species. The transduction pathways for DNA damage and replication checkpoints are composed of a shared group of conserved proteins that may also act as the sensors (Rhind and Russell, 2000). These homologs (identified in all eukaryotes) share a similar N-terminal kinase domain (residues 1-265) as well as scattered homology throughout the C-termini (Chen et al., 2000). Therefore, one of our first steps was to examine the current sequences published for the sea urchin, *S. purpuratus*, genome (url) to search for evidence about whether Chk1 exists in sea urchins. In addition, we examined whether Chk1 protein exists in sea urchin eggs and embryos. These data will be the first documentation of Chk1 in sea urchins.

Materials and Methods

To better understand whether Chk1 is present in *S. purpuratus*, the National Center for Biotechnology Information (NCBI) GenBank was searched for Chk1 homologs in other organisms. A Chk1 homolog (*Schizosaccharomyces pombe*) CHEK1 was found in *Homo sapiens*. This homolog is found on chromosome 11; maps 11q24-q24 and is a protein-coding gene (NCBI Entrez Gene). A related sequence AF016582, which encodes mRNA was used for additional work because it is more conserved across species due to the removal of exons from the sequence. This sequence was then "blasted" via tblastx against the sea urchin genome (NCBI, AAGJ000000000). Tblastx converts a nucleotide query sequence into protein sequences in all six reading frames and then compares this to an NCBI nucleotide database, which has been translated on all six reading frames. <http://www.ncbi.nlm.nih.gov/blast/html/blastcgihelp.html> - protein databases

In addition, adult *S. purpuratus* were collected and gametes handled as described in Aim 1A. Eggs were exposed to UVR (290-400 nm) in the laboratory using Q Panel UV-340 lamps that simulate the solar spectrum of UVR (Adams et al., 2001; Shick et al., 1999). Eggs were fertilized and embryos were exposed to PAR (visible light, 400-700nm) and protected from UVR by covering them with UV-opaque acrylic or exposed to PAR + UVR using UV-transparent acrylic covers as described in Aim 1 A. Lysates were prepared and protein assays were performed as described in Aim 1-A. Proteins in lysates were separated by loading 50 µg total protein onto 12% acrylamide gels for SDS PAGE. Proteins were transferred and blots probed using general techniques described in Aim 1-A.

We tested four antibodies for Chk1 (Cell Signaling, Santa Cruz Biotechnologies) at multiple concentrations. Only one antibody for total Chk1 (Ser 296) gave us consistent results (Fig. 4). In addition, we tested three antibodies for p-Chk1 (Ser 345, Cell Signaling, Santa Cruz Biotechnologies) and two antibodies for p-Chk1 (Ser 317, Cell Signaling & Novus). Densitometry was performed as described in Aim 1-A.

In addition, we compared the density for the Chk1 band between Control and UV-irradiated embryos for three batches of eggs and exposure experiments to determine whether UVR-is likely to be affecting Chk1. Statistical analysis has not been performed on these data at this point because we believe we need to optimize our Chk1 detection capabilities further.

Results

Three sequences with low e values were obtained and evaluated (NCBI sequences CD291492, CD311509, and DN577951) for homology with the human Chk1 protein sequence by alignment of the sequences. E values are the statistical significance threshold for reporting matches against database sequences. Low e values mean that there is little chance that the match is expected to be found merely by chance. The associated DNA sequences for CD291492, CD311509 and DN577951 were obtained from NCBI and entered into DNA Strider. An attempt was made to align the DNA sequences with the DNA sequence of AF016582.

Two areas of homology within the kinase domain of Chk1 were found. Homology within the kinase domain of the Chk1 protein of *Homo sapiens* (hs), *Mus musculus* (mm), *Xenopus laevis* (xl), *Drosophila melanogaster* (dm), *Caenorhabditis elegans* (ce), *Saccharomyces cerevisiae* (sc) *Schizosaccharomyces pombe* (sp) are shown in Figure 4. The sea urchin sequences that were homologous to the human Chk1 sequence are shown in this alignment.

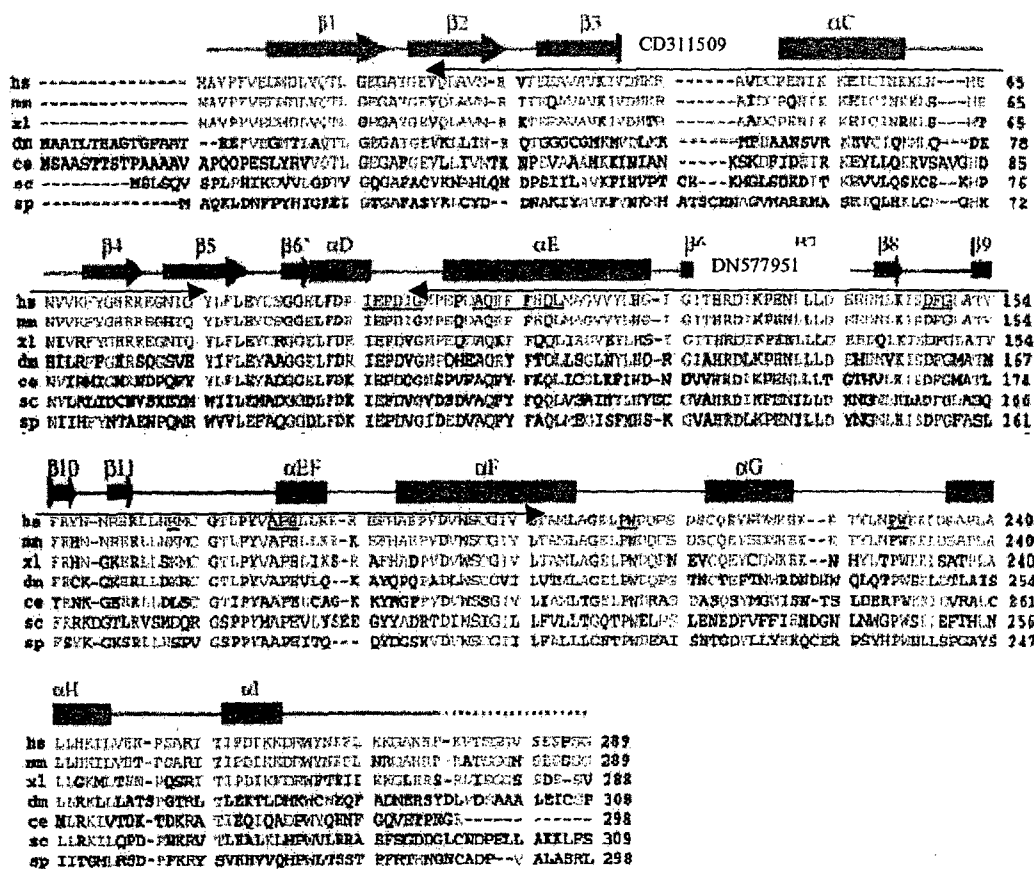


Figure 4. Sequence Homology of *S. purpuratus* sequences CD311509 and DN577951 with Chk1 kinase domains of *Homo sapiens* (hs), *Mus musculus* (mm), *Xenopus laevis* (xl), *Drosophila melanogaster* (dm), *Caenorhabditis elegans* (ce), *Saccharomyces cerevisiae* (sc) and *Schizosaccharomyces pombe* (sp). Black arrows indicate alignment of the sea urchin sequences.

http://www.sciencedirect.com/science?_ob=MIimg&_imagekey=B6WSN-4195FF1

Further, the antibody generated against human Chk1 at Ser 296 (Cell Signaling) recognizes proteins in sea urchin lysates (Fig 5). These results were quantified for three batches of embryos and for control and UV-irradiated embryos (Fig. 5). Multiple bands appear on these blots (data not shown) indicating that our conditions require more further optimization. Nevertheless, it is clear that there is a band at ~56 kDa as would be expected for Chk1.

Although the relative density of bands for Chk1 appeared to vary among dates and possibly between Controls and UV-irradiated embryos on at least one date, there is no consistent trend (Fig. 6). Nevertheless, these results are quite preliminary and we are currently working to optimize our detection capabilities for Chk1 (see below).

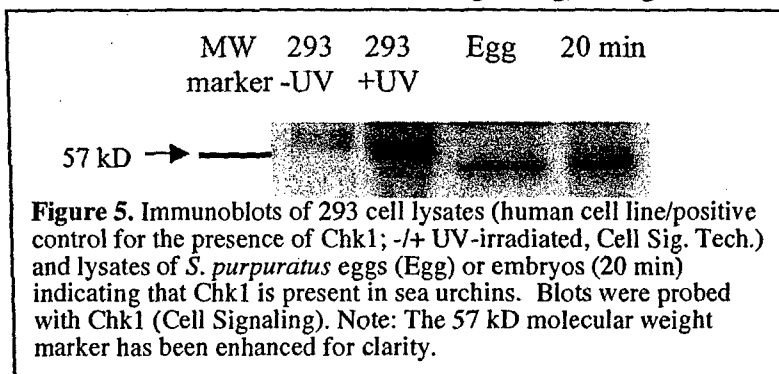


Figure 5. Immunoblots of 293 cell lysates (human cell line/positive control for the presence of Chk1; +/- UV-irradiated, Cell Sig. Tech.) and lysates of *S. purpuratus* eggs (Egg) or embryos (20 min) indicating that Chk1 is present in sea urchins. Blots were probed with Chk1 (Cell Signaling). Note: The 57 kD molecular weight marker has been enhanced for clarity.

To date, none of the antibodies for phospho-specific Chk1 reliably detected Chk1 in lysates of sea urchin embryos (data not shown). The antibody for p-Chk1 (Ser 317) by Novus was promising, recognizing proteins in lysates from the sea urchin embryos, but we did not get adequate results for the positive and negative controls to verify that this antibody was accurately detecting p-Chk1 in UV-irradiated human cell lines where we believe it should exist.

Discussion

The general conservation of cell cycle proteins throughout evolution and the identification of Chk1 homologs in organisms as diverse as fission yeast and humans make Chk1 a logical protein to be present in *S. purpuratus*. Sequence alignment of sea urchin sequences the identified kinase domain of the Chk1 protein of humans, mice, frogs, fruit flies, round worms and yeast were manually found for amino acids

168 through 527 and amino acids 525 through 821 as shown in Figure 4. This indicates that the *S. purpuratus* genome includes a kinase domain similar to those identified as Chk1 kinase domains in these organisms. Chk1 is therefore likely to be present in the *S. purpuratus* genome and have a similar function to that found in the homologs of other organisms.

The sea urchin genome is currently being annotated, and will be available soon for use. Once this task is accomplished, the use of the genome for gene identification will be greatly enhanced. Due to the high level of conservation of cell cycle proteins, Chk1 is probably transcribed and available as maternal mRNA in sea urchin embryos. If the gene sequence for Chk1 can be elucidated, then cloning of the gene will be possible. Further cloning of the gene (planned for 2005-2006) will allow further investigation into the presence and activity of the Chk1 protein, and lead to a better understanding of its function in the UV-induced cellular response in the purple sea urchin.

Similarly, our direct attempts to find Chk1 in sea urchin lysates indicate that Chk1 may be present in sea urchin eggs and embryos (Fig. 5). In addition, our preliminary data indicate that the overall concentration of Chk1 is not affected by UVR. We would not necessarily expect a change in Chk1 concentration, but instead posttranslational modification by way of Chk1 at Ser 317 or 345, which typically occurs upon UV-irradiation of cells.

Due to lack of reliable identification of a phospho-specific antibody for use in sea urchin lysates, we were not able to determine whether we can test whether UVR affects phosphorylation of Chk1 in sea urchin embryos yet. We are currently optimizing our western blotting conditions for identifying Chk1 in sea urchin lysates and testing whether phospho-specific antibodies that recognize Chk1 phosphorylated at Ser 317, Ser 345 and Ser 296 (indicating genotoxic stress) detect these forms of Chk1 in UV-irradiated sea urchin eggs and embryos.

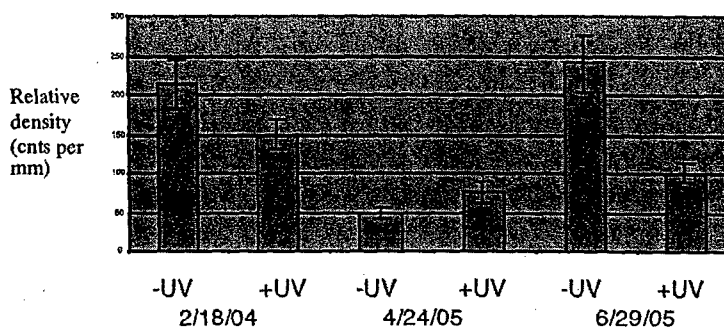


Figure 6. *Strongylocentrotus purpuratus*. Relative density of Chk1 in counts/mm² \pm S.D. embryos at 120 minutes post fertilization That had been protected from (-UV) or exposed to UVR (+UV). Exposure experiments performed 2/18/04, 4/24/05 and 6/29/05. Total Chk1 antibody, Cell Signaling 1:750 dilution.

In addition, we plan to immunoprecipitate Chk1 to concentrate it away from other proteins to enhance its signal. Currently, we must run 50 μ g of total protein on our gels, which is twice as much as we must load for detection of other proteins and which increases our background noise on these gels. An enhanced signal and the isolation of Chk1 on these gels and subsequent blots will also allow us to probe these blots with general antibodies for phosphorylated serines, which may allow us to detect changes in Chk1 phosphorylation if the other phosphospecific antibodies do not work. We are also currently optimizing our detection capabilities with our newly acquired Amersham/GE Typhoon-Trio laser imager.

Aim 1-Overall Conclusion

These results taken together are bringing us closer to understanding how UVR affects molecules that control the cell cycle in sea urchin embryos and potentially in other cells. Our future work may allow us to assess the entire molecular pathway between UV-induced genotoxic stress and effects of UVR on the molecules that control entry into mitosis. In addition, this may allow us to develop molecular markers to detect UVR-induced damage in multiple marine organisms.

Aim 2. Identification and quantification of MAAs in local red algae. We identified and quantified MAAs from 12 species of red macro algae from the Central Coast of California in an attempt to catalog the types of MAAs available in these species and screen for novel MAAs.

Materials and Methods

MAAs were extracted and analyzed from 12 species of red algae collected from intertidal zones in San Luis Obispo County, CA. MAAs were extracted from algae using three serial extractions of 100% methanol. MAAs were separated by reverse-phase HPLC, identified, and quantified by examining the absorption maximum of each peak and using quantitative standards prepared by Dr. W. C. Dunlap (Australian Institute of Marine Science, Townsville). Peak separation was achieved using reversed phase analysis on a Phenosphere C8 (Phenomenex) column in a mobile phase composed of 55% aqueous methanol and 0.1% acetic acid using a Hewlett Packard 1100 HPLC and a flow rate of 0.8 ml/min. Detection was achieved using a Hewlett Packard diode array detector.

Results

MAAs were detected in all samples of algae tested. All species of algae contain shinorine, one of the most common MAAs in algae. Palythine was the next most abundant MAAs in many species of algae. Only trace amounts of porphyra-334 were found in *Rhodomenia pacifica*. In addition, only small amount of asterina-330 and usijurine were found in two species of algae (Table 2).

Table 2. Concentrations of mycosporine-like amino acids (nmol/mg dry wt.) in tissues of algae collected from Shell Beach, CA 2004. (N=number of replicates, n.d. = not detectable).

Species	N	Concentration of MAAs (nmol/mg dry wt. \pm S.D.)					Total
		Shinorine	Porphyra-334	Palythine	Asterina 330	Usijurine	
<i>Mastocarpus papillatus</i>	8	2.42 \pm 0.88	n.d.	n.d.	n.d.	n.d.	2.42 \pm 0.88
<i>Mazzaella splendens</i>	3	0.99 \pm 0.02	n.d.	3.11 \pm 0.18	0.178 \pm 0.01	0.12 \pm 0.01	4.31 \pm 0.21
<i>Mazzaella leptorynchos</i>	6	1.61 \pm 0.18	n.d.	1.53 \pm 0.23	n.d.	n.d.	3.20 \pm 0.43
<i>Mazzaella affinis</i>	3	0.33 \pm 0.03	n.d.	0.41 \pm 0.05	n.d.	n.d.	0.74 \pm 0.64
<i>Mazzaella parksii</i>	3	0.62 \pm 0.17	n.d.	n.d.	n.d.	n.d.	0.62 \pm 0.17
<i>Rhodomenia pacifica</i>	5	0.87 \pm 0.9	0.02 \pm 0.01	1.25 \pm 0.41	n.d.	n.d.	2.04 \pm 0.58
<i>Rhodomenia rhizoides</i>	3	1.22 \pm 0.17	n.d.	n.d.	n.d.	n.d.	1.22 \pm 0.17
<i>Rhodomenia californica</i>	3	1.25 \pm 0.23	n.d.	n.d.	n.d.	n.d.	1.25 \pm 0.23
<i>Rhodomenia arborescens</i>	3	0.71 \pm 0.08	n.d.	n.d.	n.d.	n.d.	0.71 \pm 0.08
<i>Prionitis lanceolata</i>	3	1.31 \pm 0.16	n.d.	2.07 \pm 0.31	n.d.	n.d.	3.38 \pm 0.47
<i>Endocladia muricata</i>	3	2.19 \pm 0.16	n.d.	n.d.	n.d.	n.d.	2.19 \pm 0.16
<i>Chondracanthus canaliculatus</i>	3	0.51 \pm 0.06	n.d.	1.09 \pm 0.10	0.13 \pm 0.01	0.05 \pm 0.01	1.79 \pm 0.17

Discussion

These results indicate that the complement of MAAs in local red algae are fairly simple to analyze and are consistent with other species of red algae from other geographic regions (Carroll and Shick, 1996; Adams et al., 2001; Karsten et al., 1998). Unfortunately, no new MAAs were discovered in these samples. Nevertheless, one rare and exciting MAA, usijurine, appeared in two species of the algae. Usijurine is quite unstable and may allow us to examine what molecular differences among MAAs affect stability.

Identification and quantification of MAAs in local algae allowed us to create a catalog of the MAAs contained in local species of red algae for future studies on dietary accumulation and protection by MAAs. In addition, these results provide a foundation for future work examining the role of MAAs as nature sunscreens and biosensors.

The relatively simple MAA content of these algae facilitates future experiments evaluating MAAs as biosensors and using the algae as a source of MAAs for dietary accumulation studies because it is much more direct to track changes or accumulation of one or two MAAs in a system. We will continue to screen local red algae from other collections sites and to build on this work. This year we will screen local purple sea urchins, *Strongylocentrotus purpuratus* ovaries and eggs for MAAs.

D. USE OF FUNDS

Funds were used to purchase materials and supplies, pay for travel to one scientific meeting, provide release time for the PI, and provide assistantships for one graduate and three undergraduate students. All of these students have presented their results at local scientific meetings in posters or oral presentations, such as the Cal Poly Science and Mathematics Student Research Conference. In addition, results of the Chk1 work will be presented in a poster at the December Meeting for the American Society of Cell Biologists. We intend to publish results from this work in refereed journals with students as co-authors on these papers. In addition, funding of this proposal provided seed money to generate preliminary data to acquire funding from the National Science Foundation, Integrative Animal Biology Program ("Molecular mechanism of UV-induced cleavage delays in sea urchin embryos") to Nikki Adams.

REFERENCES

- Adams, NL (2001) UV radiation evokes negative phototaxis and covering behavior in the sea urchin *Strongylocentrotus droebachiensis*. *Mar Ecol Prog Ser* 213: 87-95.
- Adams, NL & Shick, JM (1996). Mycosporine-like amino acids provide protection against ultraviolet radiation in eggs of the green sea urchin, *Strongylocentrotus droebachiensis*. *Photochem. and Photobiol.* 64: 149-58.
- Adams, NL and Shick, JM (2001). Mycosporine-like amino acids prevent UVB-induced abnormalities during early development of the green sea urchin *Strongylocentrotus droebachiensis*. *Mar. Biol* 138: 267-280.
- Adams, NL, Shick, JM, and Dunlap, WC (2001). Selective accumulation of mycosporine-like amino acids in ovaries of the green sea urchin, *Strongylocentrotus droebachiensis*, is not affected by UVR. *Mar. Biol.* 138: 281-294.
- Booth CR, & Morrow JH (1997) The penetration of UV into natural waters. *Photochem Photobiol* 65: 254-257
- Chen, P.; Luo, C.; Deng, Y.; Ryan, K.; Register, J.; Margosiak, S.; Tempczyk-Russell, A.; Nguyen, B.; Myers, P.; Lundgren, K.; Kan, C.; O'Connor, P. (2000) The 1.7-angstrom crystal structure of human cell cycle checkpoint kinase Chk1: implications for Chk1 regulation. *Cell* 100: 681-692.
- Coleman, TR & Dunphy, WG (1994). Cdc2 regulatory factors. *Curr. Opin Cell Biol.* 6: 877-882.
- Dunlap WC, Shick JM (1998) Ultraviolet-radiation-absorbing mycosporine-like amino acids in coral reef organisms: A biochemical and environmental perspective. *J Phycol* 34: 418-430
- Franklin LA, Yaklovena I, Karsten U, Lüning K (1999) Synthesis of mycosporine-like amino acids in *Chondrus crispus* (Florideophyceae) and the consequences for sensitivity to ultraviolet B radiation. *J Phycol* 35: 682-693
- Gabrielli, B, Clark, J, McCormack, A, & Ellem, K (1997). Ultraviolet light-induced G2 phase cell cycle checkpoint blocks Cdc25-dependent progression into mitosis. *Oncogene*, 15: 749-58.
- Gleason DF., & Wellington, GM. (1996). Variation in UVB sensitivity of planula larvae of the coral *Agaricia agaricoides* along a depth gradient. *Mar. Biol.*, 123: 693-703.
- Häder D-P, Kumar HD, Smith RC, & Worrest RC (1998) Effects on aquatic ecosystems. In: van der Leun JC, Tang X, and Tevini M (eds), *Environmental Effects of Ozone Depletion: 1998 Assessment*, United Nations Environment Programme Report, pp 53-68
- Herzinger, T, Funk, J, Hillmer, K, Eick, D, Wolf, D, & Kind, P (1995). UVB irradiation-induced G2 cell cycle arrest in human keratinocytes by inhibitory phosphorylation of the Cdc2 cell cycle kinase. *Oncogene* 11: 2151-56.
- Karentz, D. & Bosch, I (2001) Ozone-related increases in UV radiation. *Amer. Zool.* 41: 3-16.
- Karsten U, Franklin LA, Lüning K, Wiencke C (1998) Natural ultraviolet and photosynthetically active radiation induce formation of mycosporine-like amino acids in the marine macroalga *Chondrus crispus* (Rhodophyta). *Planta* 205: 257-62
- Madronich, S, McKenzie, R, Bjorn, L, & Caldwell, (1998). Changes in biologically active ultraviolet radiation reaching the Earth's surface. In *Environmental Effects of Ozone Depletion: 1998 Assessment* (Ed. by J. C. van der Leun, X. Tang, and M. Tevini), pp. 5-19. United Nations Environment Programme Report.
- Mason DS, Schafer F, Shick JM, & Dunlap WC (1998) Ultraviolet radiation-absorbing mycosporine-like amino acids (MAAs) are acquired from their diet by medaka fish (*Oryzias latipes*) but not by SKH-1 hairless mice. *Comp Biochem Physiol* 120A: 587-598
- Meijer, L, Arion, D, Golsteyn, R, Pines, J, Brizuela, L, Hunt, T. & Beach, D (1989). Cyclin is a component of the sea urchin egg M-phase specific H1 kinase. *EMBO J.* 8:2275-2282.
- Morgan, D (1997). Cyclin-dependent kinases *Ann. rev. Cell Dev. Biol.* 13: 261-91.
- Murray A & Kirschner M (1991). What controls the cell cycle?. *Sci. Amer.* 264: 56-63.
- Okano-Uchida, T, Sekiai, T, Lee, KS, Okumura, E, Tachibana, K & Kishimoto, T (1998). *In vivo* regulation of cyclin A/Cdc2 and cyclin B/Cdc2 through meiotic and early cleavage cycles in starfish. *Dev. Biol.* 197: 39-53.
- Peng, C-Y, Graves, PR, Thoma, R, Wu, Z, Shaw, A, & Piwnicka-Worms, H (1997). Mitotic and G2 checkpoint control: regulation of 14-3-3 protein binding by phosphorylation of Cdc25c on ser-216. *Science* 277:1501-05.
- Rhind, N., and Russell, P. (1998) Mitotic DNA damage and replication checkpoints in yeast. *Curr. Opin. Cell Biol.* 10: 749-58.
- Rusted, R (1971). Radiation response during the mitotic cycle of the sea urchin egg. In *Developmental Aspects of the Cell Cycle* (Ed. by I. Cameron, G. Padilla, & A. Zimmerman). pp. 127-159. Academic Press, New York.
- Sanchez, R., Wong, C, Thoma, R, Richman, R, Wu, Z, Piwnicka-Worms, H, & Elledge, SJ (1997) Conservation of the Chk1 checkpoint in mammals: linkage of DNA damage to cdk regulation through Cdc25. *Science* 277:1497-501.
- Shick, JM, Romaine-Lioud, S, Ferrier-Pages, C, and Gattuso, J-P (1999). Ultraviolet-B radiation stimulates shikimate pathway-dependent accumulation of mycosporine-like amino acids in the coral *Stylophora pistillata* despite decreases in its population of symbiotic dinoflagellates. *Limnol. Oceanog.* 44: 1667-1682.
- Smith RC, Prezlin BB, Baker KS, Bidigare RR, Boucher NP, Coley T, Karentz D, MacIntyre S, Matlick HA, Menzies D, Ondrusek M, Wan Z, Water KJ (1992) Ozone depletion: ultraviolet radiation and phytoplankton biology in natural waters. *Science* 255: 252-259
- Smith, RC & Baker, K (1979). Penetration of UV-B and biologically effective dose-rates in natural waters. *Photochem. Photobiol.* 29: 311-323.
- Tevini M (1993) Molecular biological effects of ultraviolet radiation. In: Tevini M (ed), *UV-B Radiation and ozone depletion: Effects on Humans, Animals, Plants, Microorganisms, and Materials*. Lewis Publishers, Boca Raton, FL. pp 1-16
- Zhao, H and H. Piwnicka-Worms (2001). ATR-mediated checkpoint pathways regulate phosphorylation and activation of human Chk1. *Mol Cell. Biol.* 21, 4129-4139.

**Antenna Bandwidth Improvement and
Emissions and Mounting Structure Studies**

Project Investigator:

Dean Arakaki
Assistant Professor
Electrical Engineering Department

C³RP Final Report, August 2005

The primary objectives of the 2004-2005 C³RP project have been to:

- Develop accurate computer models of microstrip patch antennas verified through measurements taken in the Cal Poly Anechoic Chamber
- Develop new patch antenna geometries for wider bandwidth operation
- Develop and apply high-impedance (EBG: electronic bandgap) ground planes for the reduction/elimination of surface waves that cause interferometer nulls in radiation patterns
- Develop an Electromagnetic Compatibility (EMC) chamber and establish testing capabilities
- Characterize the EMC chamber and accompanying instrumentation; carry out conducted emissions testing on actual systems

The development of accurate simulation models for patch antennas has been established on a four-element microstrip patch antenna planar array, shown in Fig. 1 below.

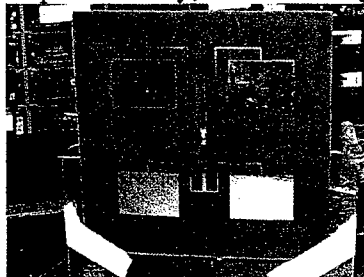


Fig. 1 Four-Patch Microstrip Array

This array was modeled using the Sonnet application (antenna simulation software) and fabricated on an FR-4 substrate printed circuit board. The array was also tested for both radiation pattern and SWR (standing wave ratio) response as a function of frequency (1.5GHz to 3.0GHz) in the Cal Poly Antenna Anechoic Chamber. The computer-predicted radiation pattern, modeled by the Method of Moments (MoM) technique, is compared to the measured pattern taken at the 2.62GHz frequency in Fig 2 below.

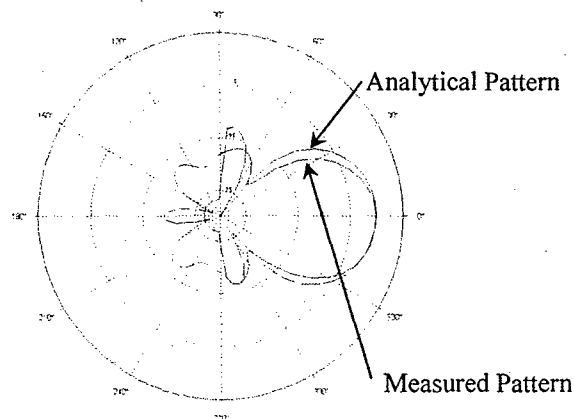


Fig. 2 E-Plane Radiation Patterns at 2.62GHz
Comparison for Four-Patch Microstrip Array: Measured vs. Analytical

The predicted pattern has a first-null beamwidth of 110° , while the measured pattern has a 100° value, which yields a higher gain for the measured pattern compared to the analytical version. Since the analytical pattern assumes an infinite ground plane, this pattern should have a narrower beamwidth; thus, the comparison is opposite from what is expected. Possible explanations for this discrepancy include calibration errors in the test setup and relatively high reflection levels in the anechoic chamber.

The input matching characteristics were also computed for the four-patch array, shown in Fig. 3 below.

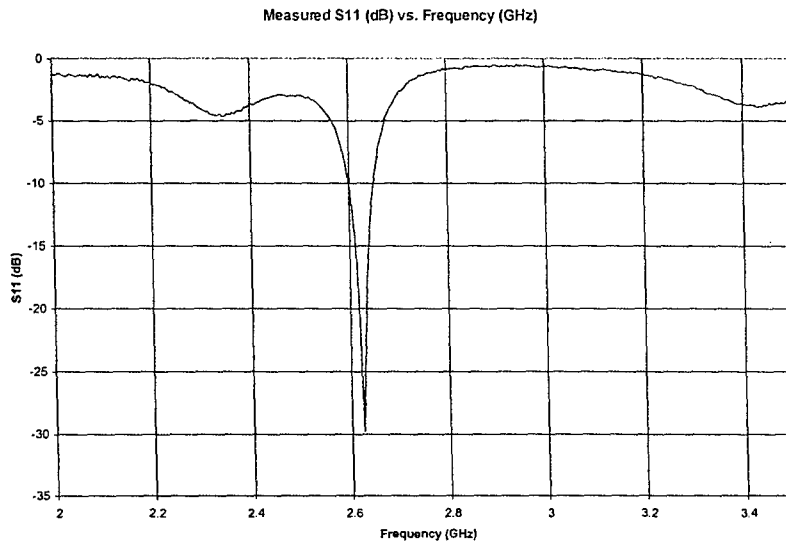


Fig. 3 Input Matching Characteristics for Four-Patch Microstrip Array
|S₁₁| (dB) vs. Frequency (GHz)

Note that the array is matched at 2.62GHz, while the intended frequency is 2.50GHz. This was caused by the tolerance in the dielectric constant value obtained from the manufacturer's datasheet for FR-4 material. A dielectric constant of 4.90 was assumed from the datasheet, while the actual ϵ_r value is between 4.05 and 4.20. Substituting the corrected value into the Sonnet and optimizing for the new material constant will yield a design with a resonant frequency closer to the intended 2.50GHz value.

New wideband designs have been developed for microstrip patch antennas. Current designs yield bandwidths in the 10% to 15% range. New antenna geometries, developed through a highly refined combination of previously-used techniques, have resulted in simulated bandwidths of 25% to 30%. We are currently identifying fabrication companies to construct the design. Upon successful construction of the new design, simulation results will be compared to radiation pattern and SWR measurements in the Anechoic Chamber.

Circular-E probe fed antenna on a microwave substrate

Fig. 4 shows the HFSS model for a probe fed circular E shaped antenna. Unlike the antenna described in [1], the antenna below is printed directly on a microwave substrate (Rogers RT/duriod 5880). Since the probe is contained within a microwave substrate rather than unsupported, the structure becomes durable and of practical use.

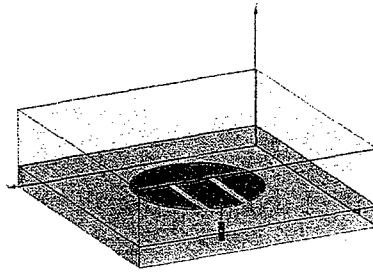


Fig 4: Model of Probe Feed - Circular E-Shaped Antenna

Fig. 5 shows the VSWR of the above model as a function of frequency at 0.1GHz resolution. Placing the antenna directly on the substrate dramatically decreased its performance. Not only did the antenna operate at a much higher frequency range, but also the bandwidth was decreased. This is due to the increase in the substrate permittivity. As relative permittivity increases, the electrical thickness of the substrate decreases. This creates a resonant frequency at a higher frequency.

The following bandwidths were calculated by defining the frequency range where VSWR values are less than two. The antenna described in [1] operates between 1.538GHz and 1.998GHz, which corresponds to a bandwidth of 26.0%. The simulated antenna operates at the higher range of 9.95GHz to 10.43GHz, which corresponds to a bandwidth of 4.7%. The frequency of operation of the simulated antenna is slightly wider than that of the antenna from [1], but since the frequency is much higher, the bandwidth is significantly less. Increasing the physical thickness of the dielectric could lower the frequency, but this makes fabrication unpractical using Rogers RT Duroid 5880 standard board thicknesses.

An L-shaped capacitive feed can increase the bandwidth of microstrip antennas [2]. It creates an improved match by offsetting the inductance added by the length of the probe feed. Incorporating an L-shaped probe feed into this design might help increase the bandwidth.

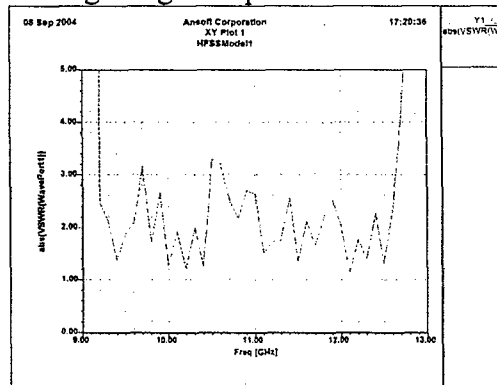


Fig. 5: VSWR of Circular E shaped - probe fed antenna

Circular-E antenna with L-shaped probe feed

To improve the bandwidth of the previously simulated antenna, an L-shaped probe was used rather than the standard coaxial probe. The L-shaped probe is coupled to the antenna but makes no physical contact. Besides the feed, all materials and dimensions are identical to the antenna discussed above.

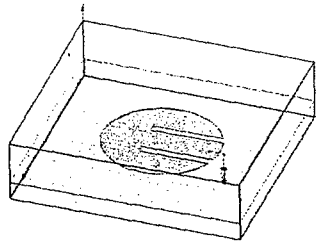


Fig. 6: L-shaped probe fed - Circular E antenna

Fig. 7 shows the VSWR vs. frequency for the above antenna model: the performance was improved significantly by the addition of the L-shaped probe. Once again, the following bandwidths were calculated by defining the frequency range where VSWR is less than two. By examining Figure 4, it can be seen that this antenna has two major frequency ranges of operation: 7.6GHz to 9.6GHz, (bandwidth of 23.3%) and 12.25GHz to 14.05GHz (bandwidth of 13.7%).

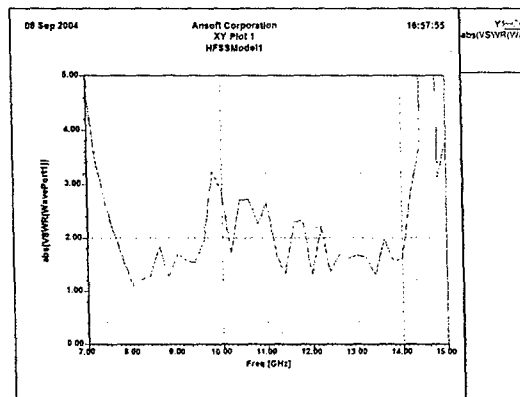


Fig. 7: Circular E shaped antenna with an L-shaped probe feed

Although there is significant improvement in the bandwidth using the L-shaped probe feed, it is difficult to embed a bent probe directly into a microwave substrate. The antenna can be more easily fabricated if the microwave substrate below the horizontal section of the probe feed is replaced by foam. Another option is to replace the horizontal section of the probe feed with a section of microstrip. This creates a common stacked antenna design, which can be fabricated.

Circular-E antenna with a modified L-shaped probe feed

To create this design, the horizontal arm of the L-shaped probe feed was replaced by a length of microstrip line. The HFSS model of the antenna is shown in Fig. 8.

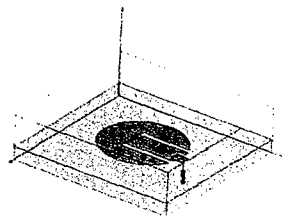


Fig. 8: Model of modified L-shaped probe fed patch antenna

As shown Fig. 8, the coaxial probe is set back from the edge of the patch antenna. The microstrip patch used on the feed is 11mm long, but only 9mm of it is under the actual radiating patch. The VSWR of this design is shown in Fig 9. The antenna operates between 10.3GHz and 12.76GHz, giving it a bandwidth of 21.3%. The bandwidth using this feed is 2% lower than with the standard L-shaped probe feed. This is due to increased reflections at the input caused by a less perfect match and/or feed point.

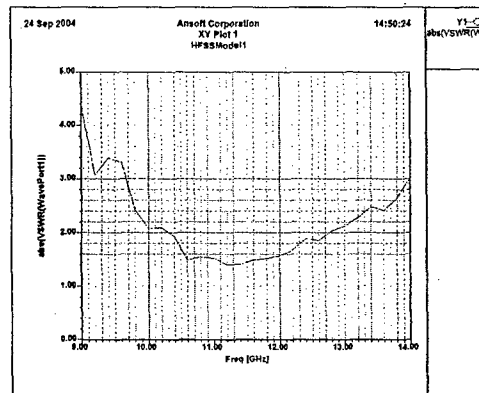


Fig. 9: VSWR of a circular-E antenna using the modified L-shaped probe feed

It is possible to create an improved match by fine-tuning the dimensions of the probe feed. The simplest way to do this is through a parametric study. Before adjusting the probe feed, the width of the substrate was adjusted to fit standard board sizes available from Rogers Corporation. The current design has 10.5mm of dielectric below the microstrip feed and 1.5mm above it. These dimensions must be adjusted so the antenna can be fabricated with the standard panel dimensions shown in Table 1.

Rogers Corporation: Standard Dimensions of RT/duroid 5870 and 5880	
Thickness (mm)	Panel Size (mm)
0.127	457 x 305
0.254	457 x 610
0.381	457 x 915
0.508	457 x 1224
0.787	
1.575	
3.175	

Table 1: Rogers Corporation Standard Dimensions

To achieve dimensions close to the models presented, it is necessary to use two panels. Both are 457mm x 305mm, but one board is 3.175mm in thickness, while the other is 1.575mm. By stacking three pieces of the 3.175mm board with one piece of the 1.575 board, we achieve a thickness of 11.1mm under the probe. One more 1.575mm board is used above the probe. Since all simulations were done on a substrate size of 150mm x 150mm, two additional antennas could be created with the two panels mentioned previously. Simulations were done to see the effect of this change on the antenna performance. The new VSWR response is shown in Fig. 10.

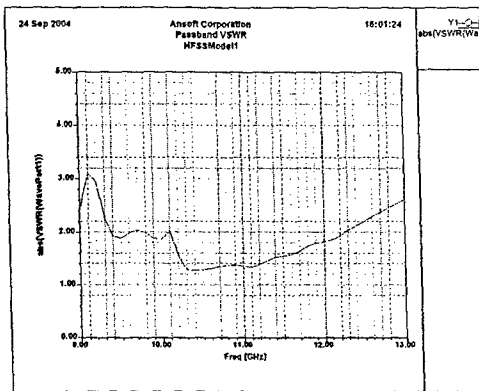


Fig. 10: VSWR of antenna using standard panel sizes of RT/duroid 5870 and 5880

The antenna meets the $VSWR = 2$ specification between 10.1GHz and 12.26GHz and achieves a bandwidth of 19.32%. The drop in bandwidth could be due to less coupling between the feed and the patch due to increased distance between them. Now that the design can be fabricated using available material and techniques, the dimensions can be optimized to obtain improved results.

Although the antenna can be fabricated as described above, costs could be prohibitive. It is preferable to use thicker boards so each layer (above and below the feed line) consists of a single layer. This cannot be done using Rogers standard board thicknesses; however, Cumings standard thicknesses are much greater. Cumings standard thicknesses are shown in Table 2 below.

Cumings: Standard Dielectric Board Sizes	
Thickness (mm)	Panel Size (mm)
3.2	30.48 x 30.48
6.4	
9.5	
12.7	
15.9	
19.1	
25.4	
38.1	
50.8	
63.5	
76.2	

Table 2: Cumings standard dielectric sizes

Since HFSS does not have Cumings dielectric materials stored in its library, it was created using datasheet values. A model was then created. The dielectric below the feed is 9.5 mm and above, it is 3.2 mm. The thickness above the feed is nearly twice the previous value. This will decrease the coupling between the feed and patch and decrease the antenna bandwidth. The VSWR of this model is shown below along with its 3D radiation pattern at 11 GHz.

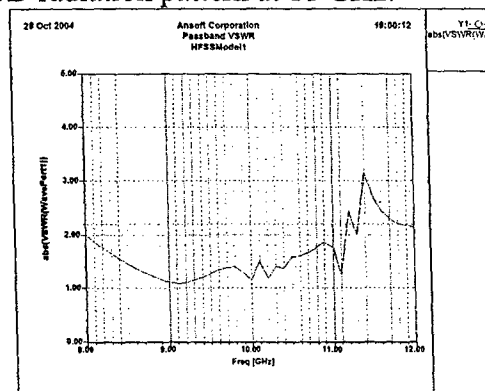


Fig. 11: VSWR Using Cumings Dielectric Standard Thickness Values

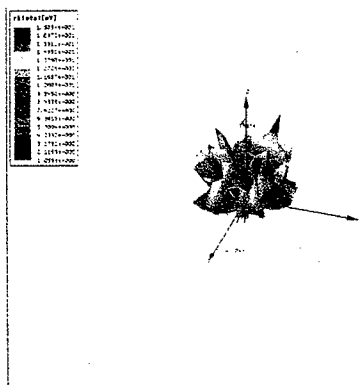


Fig. 12: 3D Radiation Pattern Using Cuming Dielectric at 11 GHz

Fig. 11 shows that the antenna meets VSWR requirements between 8 and 11.15 GHz, yielding a bandwidth of 32.9%. This value was obtained through the parametric study shown below. The bandwidth decreased by 4%. The new dielectric also affected the radiation pattern. Compared to the radiation pattern of Fig. 9, the new pattern is less uniform and generally lower in magnitude. Thus, there are directions in which the antenna does not radiate effectively.

A model that uses standard board dimensions and potentially improved results can be created using sections of Rogers 5880 and Cumings dielectric substrates. By using a 1.575 mm thick section of Rogers 5880 above the feed and a 9.5 mm thick section of Cumings dielectric below it, the results should be more similar to those shown below.

Parametric study on the circular E capacitive fed antenna; microstrip feed dimensions

Optimizing the feed can improve the impedance match at the input, thereby increasing the antenna bandwidth. To design the microstrip feed in a way similar to the original L-probe feed, the width was decreased from 9mm to 5mm. The VSWR response is shown in Fig. 13.

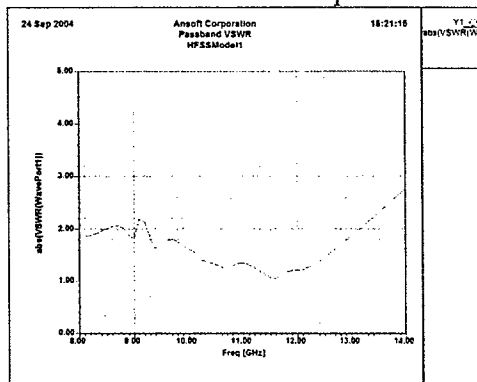


Fig. 13: VSWR of Circular E antenna with a 5mm wide microstrip feed

Decreasing the width of the microstrip patch dramatically increased the antenna's bandwidth to 34.93% due to an improved input impedance match. Since the input center conductor of the coaxial cable is 1mm in diameter, decreasing the width of the microstrip patch will make fabrication difficult. Adjusting the feed length from its original value of 11mm may yield further performance enhancements. Table 3 shows the results of this study.

	Capacitive Feed Length (mm)		
	11	16	21
Bandwidth	34.93%	36.82%	32.26%
Center Frequency (GHz)	11.195	11.215	11.685
Peak Directivity	5.3366	6.7808	4.9276
Peak Gain	4.9482	7.102	5.2588
Radiated Power (W)	0.90672	1.0415	1.064
Radiation Efficiency	0.92724	1.0474	1.0672

Table 3: Results of changing the feed length

As Table 3 demonstrates, the best results were achieved at a feed length of 16mm, which resulted in a bandwidth of 36.82%. Further lengthening of the feed decreases the antenna bandwidth.

By changing the slot lengths, it is possible to increase the bandwidth. This occurs because the current must flow around the slot to create the low resonant frequency while the radius of the patch determines the high frequency resonance. The results of this study are shown in Table 4.

Capacitive Feed Length: 15 mm

	Slot Length (mm)		
	43	48	53
Bandwidth	36.97%	36.82%	34.98%
Center Frequency (GHz)	11.225	11.215	11.065
Peak Directivity	5.9936	6.7808	5.5405
Peak Gain	6.3748	7.102	5.8379
Radiated Power (W)	1.0535	1.0415	1.0507
Radiation Efficiency	1.0636	1.0474	1.0537

Table 4: Optimized Slot Lengths

As shown in Table 4, decreasing the slot length resulted in a negligible increase in the bandwidth, while the peak directivity and peak gain decreased. A slot length of 48mm was chosen in the final design effect on directivity and gain.

Final Antenna Design Results:

The VSWR response for the final design is shown in Fig. 14. It meets VSWR requirements between 9.15GHz and 13.28GHz, yielding a bandwidth of 36.82%. Fig. 15 shows the 3D radiation pattern at 11 GHz. All of the following radiation patterns are plotted in dB.

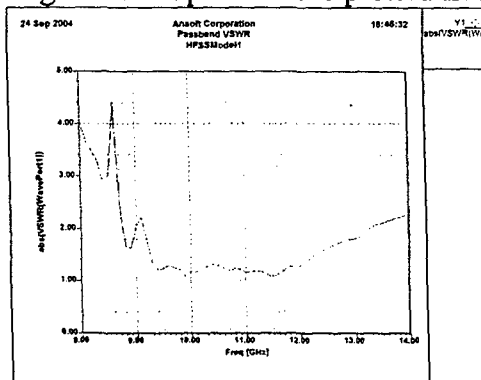


Fig. 14: VSWR of Final Design (feed: 5mm x 16mm, slot length: 48mm)

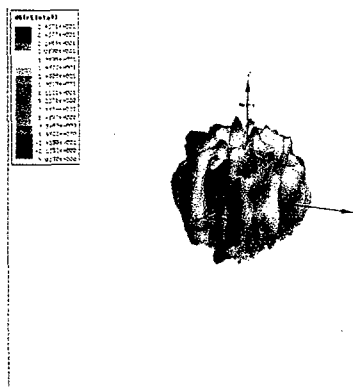


Fig. 15: 3D radiation pattern of the final design

Figure 16 is an E-plane cut of the radiation pattern at 11 GHz.

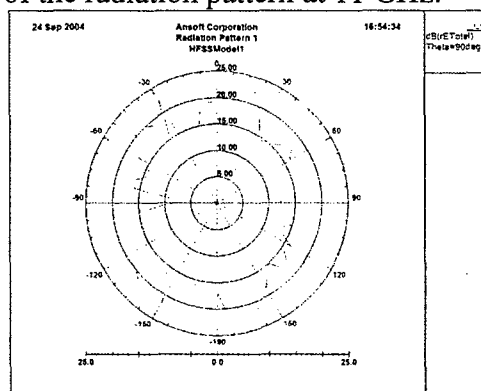


Fig. 16: $\theta = 90^\circ$ Radiation Pattern

The third project has been modeled (using a rectangular probe-fed patch antenna) and shown to reduce effective surface waves as evident from the substantial reduction of interferometer nulls produced by patch antennas mounted on standard substrate geometries. The Electronic Bandgap ground plane is pictured in Fig. 17 below.

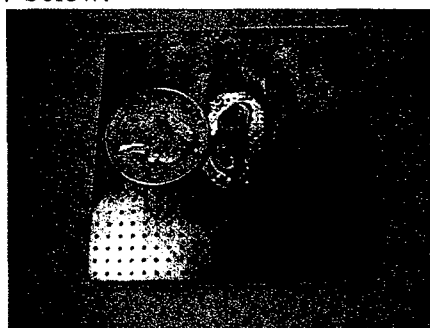


Fig. 17: Electronic Bandgap Ground Plane for Suppressing Surface Waves

Matching characteristics (SWR) have been measured over the range 9GHz to 11GHz and matches to within 0.5 of the simulated response throughout the band. The radiation patterns will be measured in the Cal Poly Anechoic Chamber within the next few weeks.

Evidence of the significant reduction of surface waves striking the edges of the ground plane and causing pattern ripple can be seen in Fig. 18: solid vs. EBG ground plane backed circularly-polarized patch antennas.

θ -cut, $\phi = 0^\circ$ Radiation Pattern Compared (Vertical Polarization)

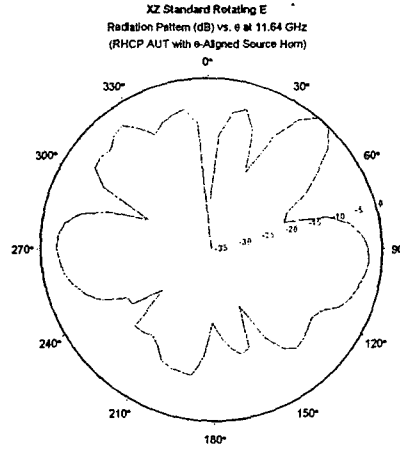


Fig. 18: CP Microstrip Patch on Solid Ground Plane

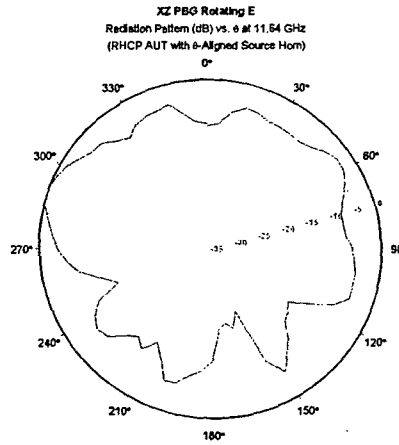


Fig. 19: CP Microstrip Patch on EBG Ground Plane for Suppressing Surface Waves

Note that the circularly-polarized patch antenna mounted on the EBG ground has a significantly smoother radiation pattern compared to the same patch on the solid ground plane. Further refinements to the EBG model are being developed to finalize the design and build several prototypes to test in the Cal Poly Anechoic Chamber.

The standard patch antenna has a minimum axial ratio of 0.132 dB and a 3dB axial ratio BW of 20MHz. Axial ratio is calculated using the polarization ellipse and the following relations:

$$\gamma = \tan^{-1} \left(\frac{|E_2|}{|E_1|} \right) \quad (1)$$

$$\varepsilon = \frac{1}{2} \sin^{-1} (\sin 2\gamma \sin \delta) \quad (2)$$

where δ is the phase angle of the vertical with respect to the horizontal component of the electric field. Axial ratio (AR) is calculated using

$$AR_{dB} = 20 \log[\cot(\epsilon)] \quad (3)$$

An Electromagnetic Compatibility (EMC) screen room was donated to Cal Poly by Power Standards, Inc (Emeryville, CA) and assembled in the ARDFA building, room 112 (see Fig. 20).

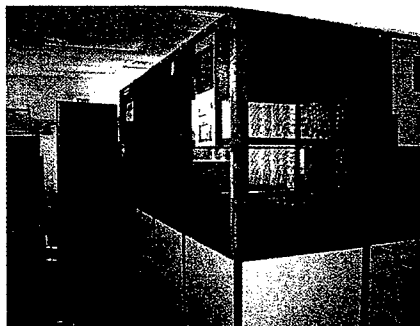


Fig. 20: Cal Poly EMC Screen Room in Building 04, Room 112

Through C³RP funds, an RF signal generator, spectrum analyzer, quasi-peak detector, LISN (line impedance stabilization network: FCC-LISN-50-16-2-01) and two power supply units were purchased to enable conducted emissions measurements from the power supply units (see Fig. 21).

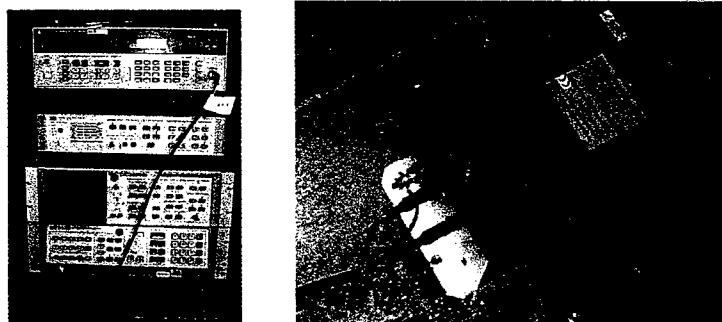


Fig. 21: EMC Screen Room Instrumentation: RF Signal Generator, Spectrum Analyzer, Quasi-Peak Detector, LISN (right-hand side)

Software to coordinate the operation of the spectrum analyzer and to compute the emissions spectrum was acquired from CKC Laboratories (Fremont, CA), see Fig. 22.

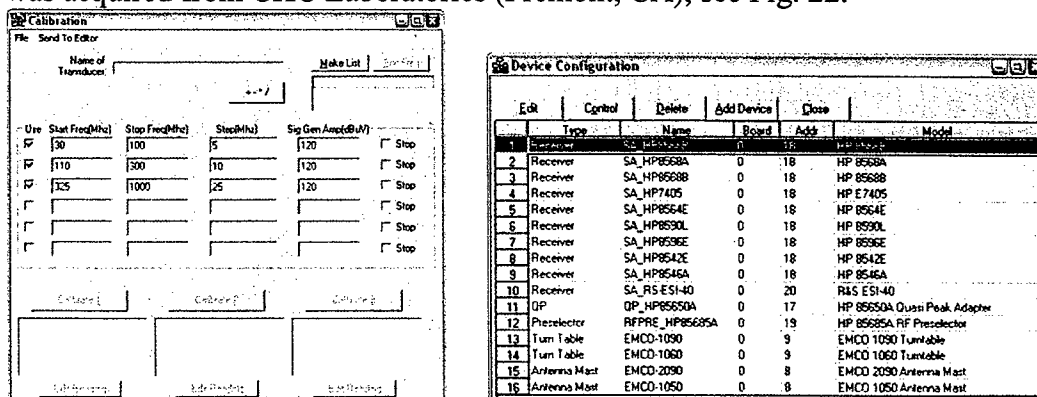


Fig. 22: Screen Shots of CKC EMC Software

To verify system operation, one of the two power supply units was tested 'as is,' while the EMI filter was removed from the other unit (see Fig. 23).

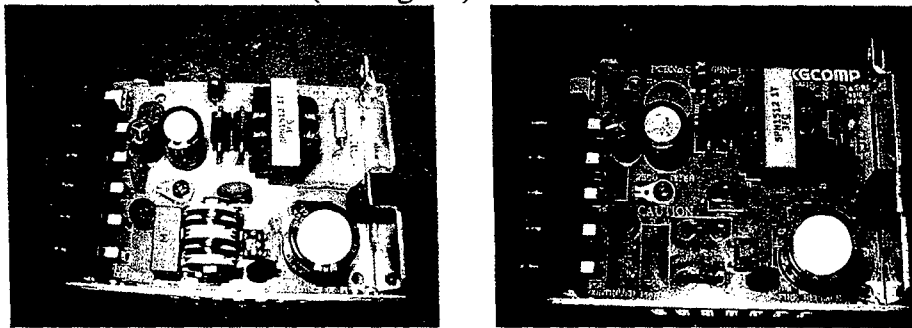


Fig. 23: Power Supply Units: With and Without EMI Filter

Both noise spectrum outputs were compared to the FCC, Part 15, Class B, quasi-peak specification, and the unit with the EMI filter in place was found to emit noise levels below the FCC spec. As expected, the unit with the EMI filter removed did meet the FCC requirement. This test validated all components in the system and also the function of the EMI filter in the power supply unit.

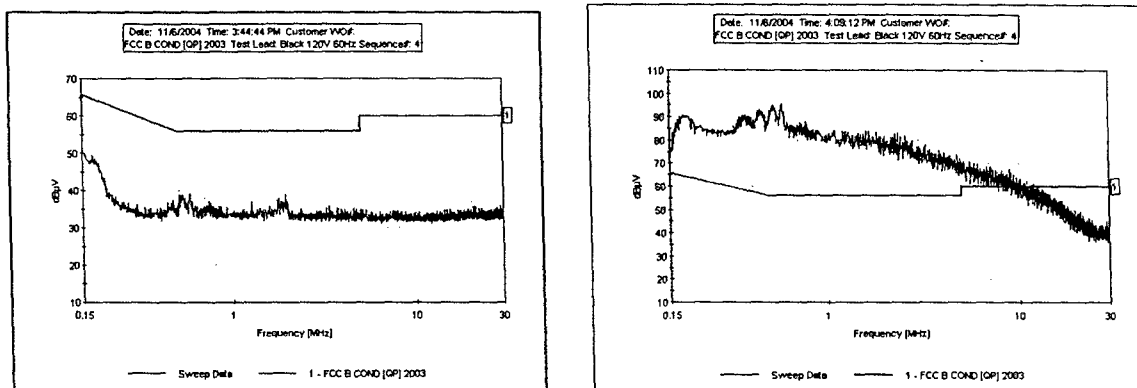


Fig. 24: Switching Power Supply Emissions (black = measured, blue = FCC spec):
With and Without EMI Filter

References:

- [1] W. Hsu, K. Wong, "A Wideband Circular Patch Antenna," *Microwave and Optical Technology Letters*, Vol 25, No. 5, pp.327-328, June 5, 2001.
- [2] A. Shackelford, K. Fong, K.M. Luk, "Design of Small-Size Wide-Bandwidth Microstrip-Patch Antennas," *IEEE Antennas and Propagation Magazine*, Vol.45, No.1, February 2003.

Appendix

Conference Paper Submitted to 2005 Antenna Measurement Techniques Association (AMTA) Conference, Newport, RI.

Title: Conducted Emissions Testing For Electromagnetic Compatibility, System Verification: (separate file)

CONDUCTED EMISSIONS TESTING FOR ELECTROMAGNETIC COMPATIBILITY (SYSTEM VERIFICATION AND SETUP)

Maximilian Moy
Systems Integration – Owego, Lockheed-Martin
1801 State Route 17C
Owego, NY 13827-3998

Dean Arakaki
Electrical Engineering Department, California State Polytechnic University
San Luis Obispo, CA 93407

ABSTRACT

Operating frequencies in the gigahertz range is creating an increased need for electromagnetic compatibility (EMC) testing. In the United States, FCC regulations require conformance to radiated and conducted emissions specifications. An EMC laboratory was established at Cal Poly San Luis Obispo (screen room, test instrumentation, and software) and an experiment was developed to explore conducted emissions effects. This paper will describe the test configuration, explain the calibration procedure needed to acquire accurate measurements, and illustrate measurement techniques applied to two example systems. In addition, the data collection process is illustrated through software donated by CKC Laboratories (EMC specialists). To verify the functionality of the laboratory and to assess measurement accuracy, two 12V/15W switching power supplies are characterized for conducted emissions performance; one as supplied by the vendor (KGCMP) and a second unit with the EMC filters removed. The noise spectrum for both units are plotted against frequency and compared to FCC specifications. The unaltered unit is shown to be in compliance, thus verifying the accuracy of the test procedure and instrumentation.

Keywords: Facility Descriptions, Data Acquisition, Commercial Products, Measurement Systems, Standards

1.0 Introduction

This paper describes a system level design for performing university-level EMC testing for conducted emissions in compliance with FCC part 15 standards [1].

ANSI C63.4-2001 [2] was the primary guide used for the design of the system. Electromagnetic compatibility references [3, 4] also aided in the completion of this project.

An EMC laboratory was established at California Polytechnic State University, hereafter referred to as "Cal Poly." The eventual goal is to provide EMC instruction to students and prepare them for real-world problems faced in industry today.

2.0 Conducted Emissions and Measurement

Conducted emissions is the radio frequency noise present in the physical wiring or traces of an electrical system. This noise is generated by switching transistors or harmonic resonances within a circuit. This results in unwanted common mode and differential mode currents within a system. Detailed analysis indicating their existence can be found in [3, 4].

A Line Impedance Stabilization Network (LISN) performs conducted emissions measurements. A LISN provide two functions [3], to isolate the test system within its boundaries and to provide a measurement point. The operator selects the frequency range, which is usually governed by the standard being used. For this system, FCC part 15 [1] was used.

3.0 System Setup

The equipment was selected based on the information provided in [3, 4] and recommendations at CKC Laboratories and Montrose Compliance. All equipment was purchased through the C³RP Cal Poly initiative.

Due to the existence of an anechoic chamber and a high power FM antenna, the EMC system was enclosed in a copper mesh screen room.

For observation of RF signals present in the system, an HP 8568B Spectrum Analyzer (SA) with the HP 85650A quasi peak adaptor was used. The adaptor is needed to screen out high amplitude noise that occurs at intermittent intervals.

For automated control of the SA, a desktop computer was used with a GPIB interface. CKC Laboratories donated the interface software.

For SA burnout protection, an ARA Transient Limiter was used. An ARA High-Pass Filter was included in the system to suppress frequencies outside the operating range.

The LISN used in the system is a Fischer Custom Communications 16A, twin line LISN. The operating frequency is 150kHz to 100MHz, well within the FCC part 15 standards.

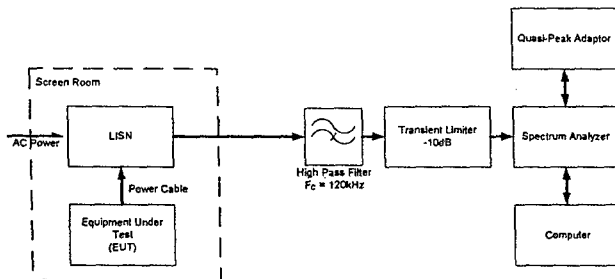


Figure 1 System Block Diagram

The equipment configuration internal to the screen room, such as bench placement, LISN placement and spacing, was based on ANSI C63.4 standards [2].

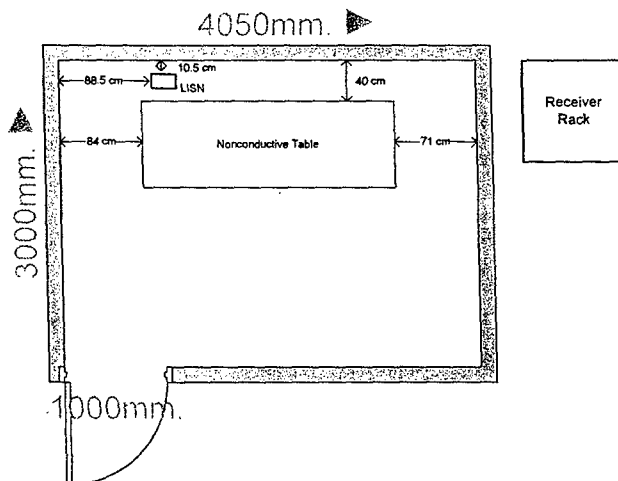


Figure 2 Room Layout

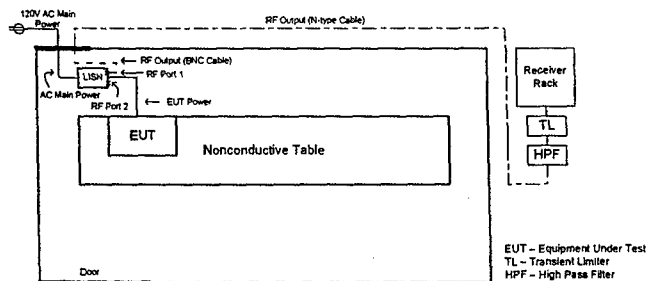


Figure 3 Wiring Diagram

The data sheets supplied with the equipment indicate that the devices are operating within specification needed in this system. At the Cal Poly laboratory, the devices were subjected to a frequency sweep from 150kHz to 30MHz at 107dBμV (0dBm) to ensure proper operation upon the delivery of items. In addition, all cables and connectors were measured for loss. For safety precautions, the earth grounding of the screen room and the earth ground connections to the LISN were tested and verified to be electrically conductive.

4.0 System Verification

For verification of system operation, the noise floor of the system was measured. The pink line (in Figures 4 and 5) represents the FCC Class B voltage limit.

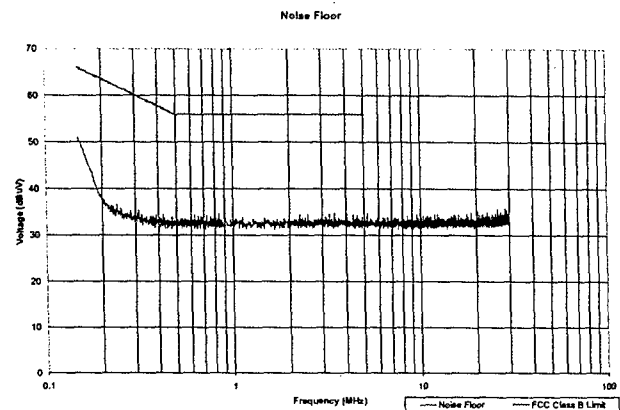


Figure 4 System Noise Floor Plot

The trace represents the noise floor of the system, which was approximately 32dBμV.

As outlined in the ANSI standards [2] a complete computer system was setup and measured. One measurement was made of the monitor and another with the computer itself. Both measurements conformed to FCC class B standards [1].

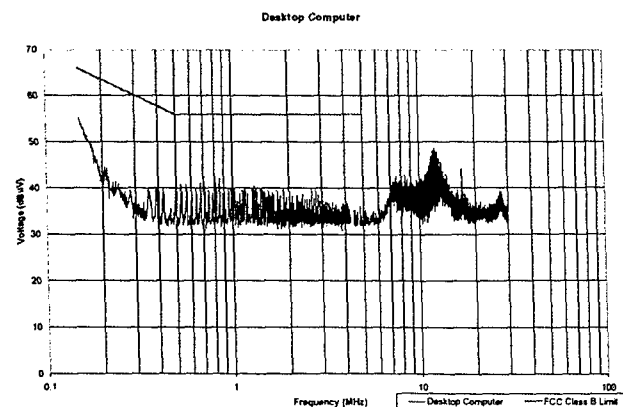


Figure 5 Desktop Computer Emissions

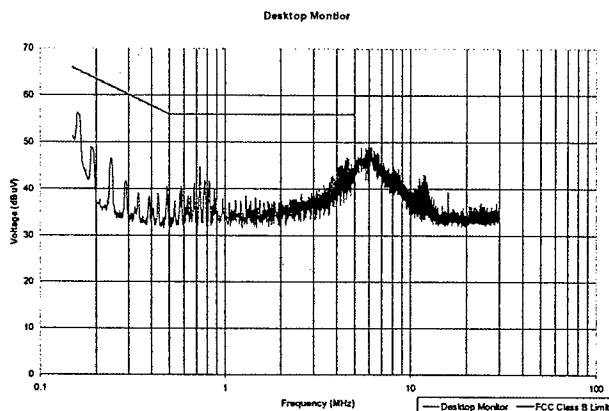


Figure 6 Desktop Monitor Emissions

5.0 EMC Experiment/Study with Switching Power Supplies

To further test the performance and functionality of the system and to provide a basic laboratory experiment for students, a commercial power supply was measured with its electromagnetic interference (EMI) filters removed. The power supply contained a common mode choke and a differential mode current bypass capacitor. The power supplies are manufactured by KGCOMP and are rated at 12V/15W.

Measurements were made with both filters removed, only the chokes installed, only the bypass capacitor installed, and with both filters installed. In addition, the system noise floor was measured.

The power supply was placed in the screen room in accordance with ANSI standards [2] which require a minimum height from the floor and distance from the walls, and routing of the power cables.

Using the CKC Laboratories software, the parameters were configured for a FCC class B device. Following procedures outlined in the ANSI standards [2], both the black "Hot" and white "Neutral" lines were measured. The voltage measurements were compared against each other and against the FCC standards for a Class B device.

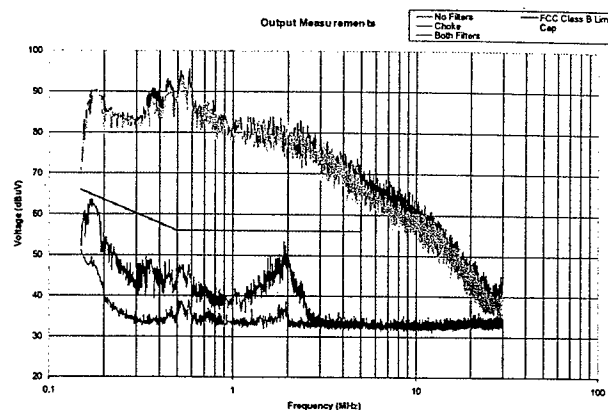


Figure 7 Output Plots

The blue trace is the measurement with no filter elements installed. The device does not meet FCC Class B specifications: amplitude peaks exceed the 40dB over the limit. The green trace represents the emissions performance with only the bypass capacitor of the EMI filter installed. Only a slight improvement (less than 5dB) can be seen. Upon insertion of the EMI chokes (red trace), the voltage amplitude greatly diminished and now meets FCC specifications. Finally, the purple trace indicates system performance with the entire EMI filter in place. These filters reduce the power supply EMI emission levels near the noise floor of the system.

6.0 Summary

The goal of providing a conducted emissions laboratory at Cal Poly was achieved with these tests. At a systems level, all elements of the system operated as predicted. The system showed compliance to FCC class B consumer goods. Further investigation of the EMI measured in these experiments are beyond the scope of this paper and is left to future students taking the EMC courses to study. The author hopes this EMC laboratory will be the stepping-stone into bringing EMC studies to Cal Poly.

8. REFERENCES

- [1] Federal Communications Commission. FCC Rules and Regulations Part 15. Washington DC, FCC, 2003
- [2] American National Standards Institute. ANSI C63.4 2001 American National Standard for Methods of Measurement of Radio-Noise Emissions from Low-Voltage Electrical and Electronic Equipment in the Range of 9kHz to 40GHz. New York, IEEE, 2001
- [3] Montrose, Mark and Nakauchi, Edward. Testing for EMC Compliance Approaches and Techniques. New York, IEEE Press/John Wiley and Sons, Inc., 2004.

[4] Paul, Clayton. Introduction to Electromagnetic Compatibility. New York, John Wiley and Sons, Inc., 1992

9. ACKNOWLEDGMENTS

The authors wish to thank the Office of Naval Research through Cal Poly's C³RP research initiative for the acquisition of all EMC instrumentation. They would also like to thank CKC Laboratories for their donation and personal support to this project. The authors would also like to personally thank Mark Montrose of Montrose Compliance, Bryan Kellogg of Rantec, Steve Behm and Christine Nicklas of CKC labs, and Dr. Taufik of Cal Poly for advice and support of this project.

**Development of multi-marker genetic testing protocols for fresh versus
cryopreserved bovine embryos.**

Project Investigators:

**Jonathon L. Beckett
Associate Professor
Animal Science Department**

**Deborah M. Beckett
Lecturer
Animal Science Department**

Abstract

In order to ensure a consistent supply of safe, affordable and high-quality animal based food products, producers of domestic livestock strive to improve genetic influences in their herds. This requires identification, and propagation of animals that demonstrate desirable characteristics. Increasing the genetic potential of sires has taken place for more than 50 years through artificial insemination. With high-performing females, the collection of embryos gives producers the potential to increase selection pressure. However, the most significant potential gains will be achieved through genetic testing. Recent identification of genetic markers for traits of interest has lead to commercially available tests for traits of interest. Successful efforts to combine the reproductive biotechnologies with genomic techniques enable scientists to identify embryos carrying increased genetic potential for certain traits. An example of genetic testing is the predetermination of the sex of offspring by taking a biopsy of cells from a multicell embryo, and testing for the presence of Y-linked markers. Many attempts at sexing semen and identification of sex in preimplantation embryos have been mildly successful. However, recent advances in gene amplification enable investigators to use sex-specific probes to determine sex in only 1 cell removed from embryos. The biopsy method has had variable success in fresh embryos. However, manipulation of cryopreserved embryos reduces viability of the embryos (Bredbacka, 1998). Therefore, novel approaches to improve pregnancy rates may result in effective reproductive rates. Recent research at Cal Poly has demonstrated that success in biopsy procedures followed by genetic testing for a single trait is possible. The proposed research sought to identify a method for multiple marker selection of embryos. The markers of interest were sex, and κ -casein as an example of an important production marker. DNA from collected cells collected from embryo biopsies were amplified using three different whole genome amplification protocols. Of the three methods, the multiple strand displacement amplification method provided the most consistent coverage of genomic DNA, and yield template that was useful as template for polymerase chain reaction (PCR) and presence of alleles for the two traits was identified. Secondly, the success of the procedure was compared between fresh and cryopreserved embryos. The embryo survival of biopsied fresh embryos was 65%, comparable to nonbiopsied embryos. However, the embryos that were biopsied, then frozen and thawed, offered survival of only 25%. Overall, the results of the study are very supportive of the feasibility of applying marker assisted selection to bovine embryo biopsies. This will result in much greater efficiency of selection, and promote greater incorporation of DNA technology into livestock production.

Statement of the problem

Breakthroughs in basic research and development of new technologies provide the tools necessary to promote massive change. Unfortunately, one of the limiting factors in incorporating these new technologies into production practices is finding individuals or companies who can apply the technologies to advance production. Whether it is agricultural genetics or human pharmaceuticals, achieving a competitive advantage will depend on selecting technology partners who provide quality solutions. Incorporation of the recent technologies in agriculture to (a) promote the efficiency by which food can be produced, (b) enhance food safety and (c) increase food quality is vital to fully capitalize on the tremendous advances in biotechnology.

Advances in animal production can be attributed to one of two factors: (1) genetics, and (2) the environment allowing those genetics to be expressed. Regardless of the extreme efforts

producers expend to improve the environment, they will continue to be limited by slow genetic improvement in the domestic livestock species. Long-term improvements in any phenotype require improvements in the genetic capacities of the animals contributing to the food, fiber or entertainment industries associated with animals. Indeed, the extent to which genetics can improve production is obvious in the dairy industry. Single trait selection for increased milk production has resulted in an approximate 300% improvement in per cow milk production during the last 30 years. These improvements have not been observed in the beef industry.

Genetic improvement can be explained by the equation:

$$\frac{(\text{accuracy})(\text{intensity})(\text{variation})}{\text{Generation interval}}$$

The factor that generally restricts genetic improvement is selection intensity. This can be described as the number of animals available for selection to the next generation. In all species allowing artificial insemination, selection intensity on the male side has been dramatically improved with the advent of artificial insemination. However, selection intensity on the females in a herd has virtually not changed. Only 50% of offspring are available for selection to the next generation. Until the gender of offspring can be predetermined, selection intensity on the female side will continue to be the limiting factor in genetic improvement. A method to accurately sex bovine embryos will be highly valuable to a producer who can increase the number of females from which to choose for breeding the following year. With one year of sex selection, a producer could increase the genetic improvement in the herd dramatically.

Embryo Biopsy

Recently, techniques have been developed in which cells in the fertilized embryos have been removed and tested for genetic sex (Bredbacka et al., 1995). This biopsy procedure allows researchers to capture the complete essence of an animal's genetic composition with a single cell. Sex-specific probes have been developed that identify X- or Y- chromosomes, specifically. This enables investigators to test the sexual identity contained in the DNA of a single cell. This can be accomplished by amplifying the genes responsible for encoding sex using polymerase chain reaction (PCR) technology. The biopsy procedure itself is invasive, obtrusive and requires inordinate training. However, the success rates are rewarding, resulting in a high degree of identification of offspring sex. There is approximately a 10-15% decrease in viability due to biopsy (Van Vliet et al., 1989). The methods have been established in laboratory animal species. Although some investigators are attempting to apply these techniques to domestic livestock species, the survival rate of biopsied embryos, particularly those previously frozen for storage (50% survival rate for biopsy with cryopreservation), and the accuracy of the results limits reproductive rates such that application in bovine embryos is not yet feasible. In sexing embryos, recent methods have been established that are so sensitive that less manipulation of the embryo is necessary, thereby increasing potential viability.

Embryo sexing

Various methods of predetermining sex of offspring have been tested. Initial attempts focused on differentiating sperm cells containing Y-chromosomes from sperm cells containing X chromosomes. This was met with limited success. Any intervention to differentiate the sperm

cells decreased motility and survivability of the sperm cells. In addition, the sequestration of either sex sperm cells was mildly successful, at best. As transfer of embryos from donor cows to recipient cows became more accepted in the cattle industry, researchers began focusing on identification of sex of the embryos prior to transfer. Initial attempts at cytogenetic analysis were unsuccessful and impractical. Other techniques included the use of male specific antibodies to recognize male embryos and X-linked enzymes to identify female embryos (Herr and Reed, 1991). These efforts, although moderately successful, were unable to provide satisfactory results for adoption by producers.

Previous research in our laboratory has characterized the advantages and disadvantages of two available methods to sex an embryo biopsy: Ampli-Y non-electrophoretic PCR, and PCR with electrophoresis. Both of these methods have been used with highly variable results in the bovine industry.

Production markers

There are currently four commercially available genetic marker tests in the beef industry. Both address the quality of product. Of the four, three were identified through private ventures, and the primer sequences are proprietary. Currently, in order to determine the genotype of a mating, producers must allow a cow to carry a pregnancy, and test the offspring once it is born. This is at great expense, both in terms of capital investment and as opportunity lost by having a cow carry a calf that does not have a desirable genotype. By testing an embryo through preimplantation genetic diagnosis, producers can select embryos based on their genotype. Embryos with undesirable genotypes will be discarded, thereby improving the productivity of the industry.

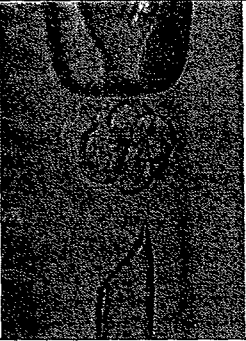
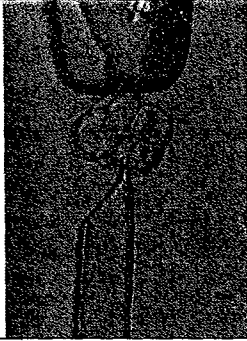
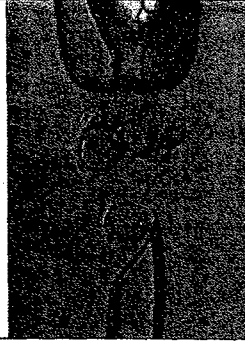
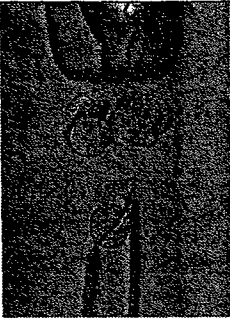
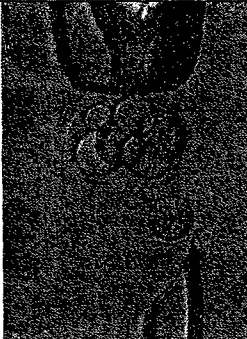
Study Objectives

The objectives of this study were two fold: (1) determine the viability of biopsied fresh versus cryopreserved bovine embryos, and (2) develop an effective protocol for multiple marker genotype selection that is commercially feasible. These objectives were accomplished by superovulating and flushing donor cows, cryopreserving half of the embryos from each flush. Each embryo – fresh or cryopreserved – was biopsied and DNA extracts for testing. The embryos were placed in recipient cows to test true survivability to parturition. Secondly, three separate methods of whole genome amplification were tested on embryo biopsy lysates to determine efficacy in replicating genomic DNA such that the amplified template would be useful for testing for the presence of production markers, i.e. k-casein, μ -calpain and sex.

I Embryo Biopsy

A. Methodology

Embryos were biopsied fresh immediately after a day 6 flush from 5 donor cows. Embryos from each donor cow were equally divided between the two treatment groups (fresh transfer and frozen-thawed transfer). From the 5 flushes, 20 embryos were transferred fresh into recipients immediately following biopsy. An additional 20 embryos were biopsied, frozen for 3-24 hours in liquid nitrogen, then thawed and transferred to assess the survival of embryos enduring multiple insults.

		
The embryo is held by suction while a biopsy needle is brought into range.	The embryo biopsy pipet is inserted and gentle suction is applied to dislodge 1-2 blastomeres.	A blastomere is removed which contains an entire copy of the animal's DNA.
		
The biopsy has been completed successfully.	The biopsied embryo is intact after the biopsy is completed. This will be repeated for all embryos.	

The method used for embryo cryopreservation was a standard ethylene glycol freezing procedure that has proven to be successful for non-insulted, intact embryos.

1. Improvements over prior procedures

In previous studies, it appeared as though the pipettes selected for the biopsy procedures minimized damage to the embryo, but caused damage to the blastomeres such that they would rupture, leading to the loss of genomic DNA. Larger pipettes were used to lessen the damage to the blastomeres. The pipettes were custom made (Humagen, Norfolk, VA) with an inner diameter of 35 microns and an outer diameter of 45 microns. They also had a bevel and a spike to allow easy entry through the zona pellucida. This also allowed for the use of a single pipette instead two pipettes which are often used in other labs. The use of a single pipet allows for a quicker biopsy procedure and less manipulation of the delicate embryo, both increasing embryo viability. Occasionally, embryos will naturally extrude blastomeres which may or may not contain a full complement of DNA. Removing the extruded blastomeres, rather than damaging the embryo with a biopsy needle, offers the advantage of allowing the embryo proper to remain undamaged, thereby increasing embryo viability. However, extruded blastomeres were only used as the source of DNA when there were multiple extruded blastomeres because they don't always have a complete set of DNA. Removing 3-4 blastomeres virtually ensures that a full complement of DNA will be realized. If the embryo was completely intact (no extruded blastomeres), a small portion of the embryo was aspirated into the biopsy pipet. The pipet was

slowly removed from the zona pellucida. As the embryo piece was stretched the zona pellucida would pinch off the biopsy. Occasionally, additional shaking of the pipet or rubbing on the dish was needed to free the biopsy from the embryo. The degree of difficulty was recorded for each biopsy on a scale of 1-5 (easiest-hardest).

B. Results

Of the fresh transfers, 13 of the 20 recipients (65%) were confirmed pregnant via ultrasound palpation at 56 days. This compares very favorably with transfers of nonbiopsied embryos. However, only 5 of the 20 (25%) recipients receiving embryos that were frozen after biopsy were confirmed pregnant. By visual appraisal, the embryos were in good to excellent condition after biopsy, and it was expected that the embryos would survive the cryopreservation at a rate only slightly less than those embryos transferred fresh. Indeed, the 65% success observed in the current study confirms the procedure is adequate. However, the low pregnancy rate in the recipients receiving cryopreserved suggests that manipulated embryos may present challenges to the procedure. One potential problem could be the hole in the zona pellucida created during the biopsy procedure allowed the cryoprotectant to reach the embryo at a rate more rapid than usual. The ethylene glycol component of the cryoprotectant is lethal to embryonic cells if exposed for too long.

B. Future Work

Adjustments to the cryopreservation procedures must be explored. The primary factors include (1) adjusting the equilibration time that the embryos are in the ethylene glycol, and (2) using a glycerol freezing procedure. This procedure is less toxic, but yields lower results in intact, non-biopsied embryos.

II Whole Genome Amplification

Introduction

Unfortunately, the amount of DNA available in 1-4 cells from an embryo biopsy is insufficient to employ as a template for a number of PCR reactions. There are currently three recognized methods to amplify the entire genome of a mammalian DNA sample: Primer Extension Preamplification (PEP), Improved Primer Extension Preamplification (iPEP) and Multiple Displacement Amplification (MDA). The extent to which these methods amplify genomic DNA from very low initial DNA volume and concentration were evaluated, both for ease of use and consistency in their amplification.

Primer Extension Preamplification

Originally used to amplify the DNA in a single haploid sperm cell, the PEP procedure was first developed by Zhang and coworkers (1992) in an effort to develop an effective method of WGA. PEP amplifies segments of genomic DNA using a random 15-mer primer allowing for simultaneous binding to multiple loci. The short segment primers can result in extensive coverage of genomic DNA (gDNA). Two major problems with PEP are (1) Taq polymerase not lasting long enough to fully amplify the genomic template, and (2) preferential amplification of one allele (Zhang et al., 1992; Dietmaier et al., 1999). Completeness of coverage is dependent on the gDNA sequence composition, and persistence of the Taq polymerase. These variables have led to disparity in results for different laboratories which calls into question the value of the procedure for embryo genotype characterization. This bias is of significant concern when using

PEP product as template for polymorphic loci testing in the pre-implantation genetic diagnosis of embryos.

Improved Primer Extension PCR

In order to mitigate the potential problems with PEP, modifications to the procedure were implemented in a new protocol, IPEP. The original PEP protocol was changed in two ways (Dietmaier et al., 1999): First, after the 55°C elongation step, a supplemental elongation step at 68°C for 30 seconds was added to give the polymerase additional time to extend the nascent strand. Secondly, a combination of polymerases was used in lieu of Taq polymerase alone. The Expand High Fidelity™ kit (Boehringer, Mannheim, Germany) was utilized which combines Taq polymerase and *Pwo* I, a high fidelity proofreading enzyme with 3'-5' proofreading capabilities. This substitution improved the quality of the newly transcribed template increasing the usefulness of the IPEP product as template for subsequent PCR reactions.

Studies have shown IPEP to be superior to PEP in terms of template representation when looking at several single nucleotide polymorphisms (SNP). Varying by three modifications, IPEP has been shown to be superior to PEP advancing it over PEP as a preferred method of WGA (Hartmann et al., 1998).

Multiple Strand Displacement

Multiple strand displacement amplification is a highly efficient method of DNA replication based on the rolling circle amplification (RCA) originally developed for amplifying large circular DNA templates such as bacteriophage and plasmid DNA (Dean et al., 2002). Using bacteriophage Φ 29 polymerase, the strand displacement method of RCA was soon discovered as an efficient process to amplify the linear double stranded DNA of eukaryotic organisms for the purpose of WGA.

The main advantage of MDA in comparison to PEP and IPEP is it requires no thermocycling. After a single denaturation step to separate the double stranded genomic DNA, there are no subsequent denaturation cycles. The MDA protocol also combines annealing and extension into one step at a low temperature of 30°C which is the optimal temperature at which the random hexamer primer binds. The random hexamer primer has a 5' thiophosphate modification which prevents 5'-3' exonuclease activity.

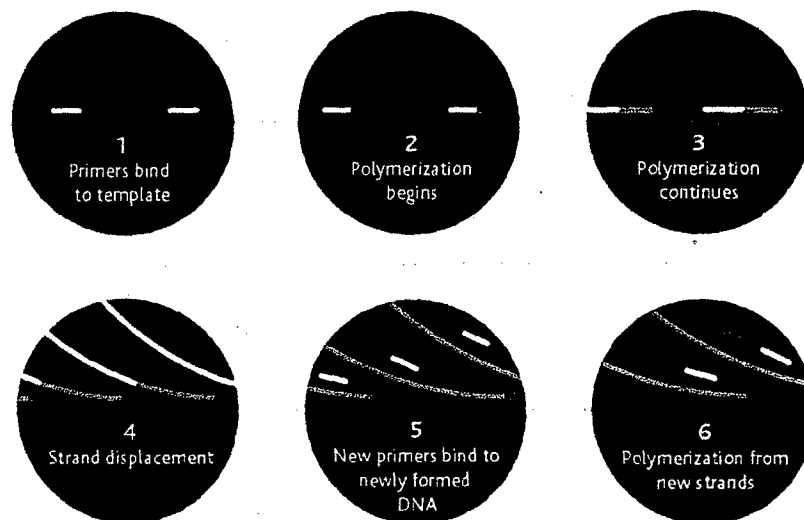


Figure 1. Series showing Multiple strand displacement. 1. Primers bind. 2/3. Polymerization as new strands are synthesized. 4. Strands are displaced by newly synthesized strands. 5. New primers bind to newly formed strands of DNA. 6. Synthesis of new strands from previously displaced strands. Reprinted from Amersham Biosciences manual for Genomiphi.™

Without the 5' modification, enzymatic digestion of the random hexamer would occur when the polymerase of an upstream growing chain collided with an already bound downstream primer (Figure 1). An upstream strand which collides into a modified primer can also continue growth due to displacement of the downstream strand. The displaced regions then act as templates which allow for primer binding, strand elongation and more displacement. This "hyperbranching" is a highly efficient process which yielding newly synthesized DNA.

The efficiency of MDA compared to PCR-based WGA's (PEP, IPEP) is significantly increased due to the high processing provided by the bacteriophage $\Phi 29$ polymerase. Statistically, the $\Phi 29$ polymerase error rates (5×10^{-67}) are appreciably lower than that of Taq polymerase (5×10^{-6} ; Mamone, 2003). The $\Phi 29$ polymerase is also unique in that it amplifies 10 kb fragments, has proofreading capabilities (Dean et al., 2002; Patki and Nelson, 2002; Handyside et al., 2004) and is active at relatively low temperatures (30°C).

Estimation of genome coverage by MDA is as high as 99.82% (Paez et al., 2004). Further, to determine the success of MDA in terms of genome representation, the number of SNP's successfully detected by MDA was compared to that detected of unamplified samples. The success rate of MDA to effectively identify SNP's was determined to be 92.06% vs. 92.93% for the unamplified sample (Paez et al., 2004). Research suggests that the use of isothermal WGA will be the universal first step in marking a new era for procedures such as preimplantation genetic diagnosis which require large amounts of DNA from minute starting quantities (Handyside et al., 2004).

A. Methodology

A comparative analysis of three methods of whole genome application was performed on lysates from embryo biopsies. Previously cryopreserved bovine (*Bos taurus*) embryos were used for all experiments and embryo biopsy. Embryos were flushed 6 days post-ovulation and cryopreserved. Straws were removed from liquid nitrogen and held in air for one minute, then

placed in a 37°C water bath for one minute. Straws were wiped clean and cut on each end with scissors. The cotton end of the straw was then placed into a 0.10 ml syringe and the plunger pushed to expel the wash drops and the embryo into a Petri dish. Each embryo was placed in a 0.5 ml drop of 1M sucrose for 8 minutes. After 8 minutes, each embryo was placed into a separate PBS/10% DNA-free FBS drop for 8 minutes to hydrate the embryo. At this point, the embryo was graded by the researcher and prepared for biopsy if deemed viable.

A biopsy dish was prepared by making 10 µl drops of PBS with 10% DNA-free BSA for each embryo and adding a mineral oil overlay. After an embryo was added to each drop, the dish was placed under an Eppendorf® (Brinkmann) micromanipulator and 1-5 blastomeres were removed from each embryo with a 35-micron biopsy needle (Humagen, Norfolk, VA). To prevent cross contamination of DNA from biopsies, the biopsy needle was rinsed repeatedly with PBS between embryos and all contents expelled into a separate wash drop. The biopsies were placed in a 0.5 ml reaction tube with 5 µl of PBS. Approximately 15 µl of proteinase K (.20 mg/ml, in 90% 1X tris, 10% proteinase K) were added and heated to 56°C for one hour for cell lysis. Inactivation of proteinase K was achieved at 96°C for ten minutes. Lysed biopsies were then stored at -20°C.

Methodology for conducting each of the WGA procedures is fully described in Moton-Redding (2005).

B. Results

The original procedure, PEP, and its improvement, iPEP, both resulted in inconsistent and inconclusive results. This is likely due to bias during the initial stages of amplification and/or lack of consistent amplification throughout the genome. However, the most recent method of whole genome amplification, multiple displacement amplification (MDA), has been used successfully in forensic fingerprinting and other tests in which the amount of initial template is limiting.

Of the three methods of whole genome amplification, PEP and iPEP provided inconsistent product. The inability to reliably amplify markers off the WGA template from PEP and iPEP rendered them unusable to uniquely increase DNA. The MDA, on the other hand, appeared to amplify the template consistently throughout the genome. Seven random Bovine DNA markers were tested on undiluted MDA product, and all amplified significantly. In addition, the time required for the MDA procedure was tested. Amplification for less than 12 hours yielded insufficient product. However, amplification appeared to plateau at 16 hours (see Table 1, and Figure 2).

Table 1. Spectrophotometry readings from different amplification times of MDA samples. MDA sample incubated at 0 hours indicates cell lysate.

MDA sample incubation times (hours)	Dilution	OD @ 260	Ratio OD @ 260/280	Approximate DNA conc. (µg/µl)
16	1/100	0.4158	1.3200	2019
12	1/100	0.37601	1.4173	1880
6	1/10	0.7777	1.6069	889
0	1/10	0.0178	0.9128	9

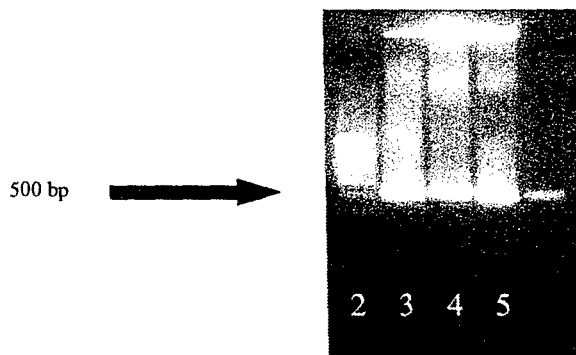


Figure 2. MDA product representing different incubation times. 16 hours of incubation (**lane 2**); 12 hours of incubation (**lane 3**); 6 hours of incubation (**lane 4**); unamplified cell lysate (**lane 5**). Amplicons are consistent with Kappa casein primers (443 bp) which were used to demonstrate efficiency and brightness of banding. 100 bp Bioline (MA) Hyperladder IV™ (**lane 1**).

Looking at the performance of the K-casein locus, almost all WGA systems amplified with complete success (see Figure 3). Only a single amplification failure occurred for all 14 reactions amplifying the κ -casein locus and it was with the IPEP as template. While all WGA systems did perform well, the significant amount of DNA streaking in the MDA lanes is evidence that the MDA is producing more product than the PEP or IPEP. In

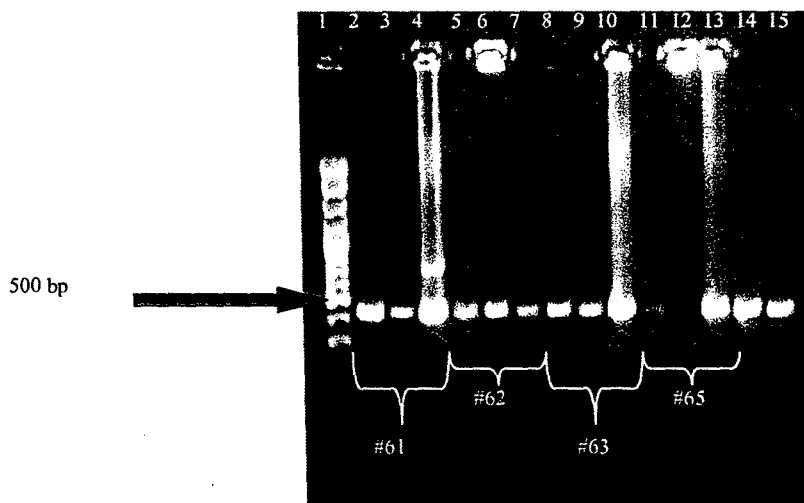


Figure 3. Amplification of the Kappa casein region using PEP, IPEP and MDA as template. Arrows indicate Kappa casein amplicon as follows: Purple: PEP (**lanes 2, 5, 8, 11**); Blue: IPEP (**lanes 3, 6, 9, 12**); Red: MDA (**lanes 4, 7, 10, 13**). Amplification failure resulted using IPEP template (**lane 12**). With the exception of **lane 7** all lanes using MDA exhibited significant streaking associated with high amounts MDA product. Blood DNA (**lanes 14, 15**). Braces at bottom indicate lysate embryo number. Fisher Scientific (NJ) 100 bp ladder (**lane 1**).

addition, the MDA demonstrates streaking with only 1 μ l template opposed to 5 μ l for both the PEP and the IPEP reactions.

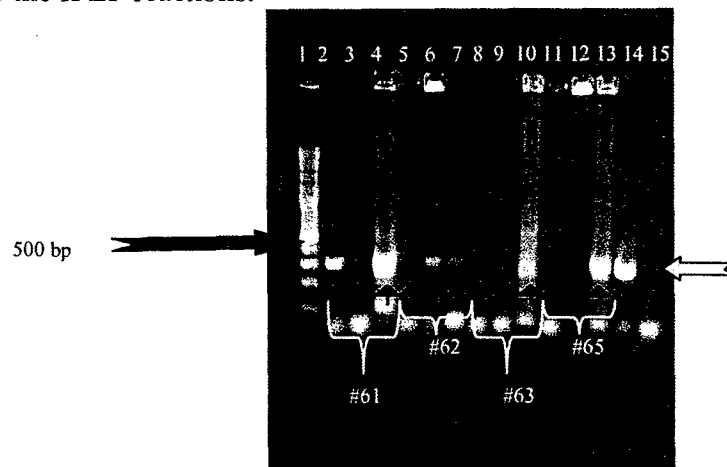


Figure 4. Amplification of the Sex locus using PEP, IPEP and MDA as template for known male samples. Arrows indicate Sex locus amplicon as follows: Purple: PEP (lane 2) ; Blue: IPEP (lane 6, 8); Red: MDA (lanes 4, 7, 10, 13). Amplification failure resulted using PEP and IPEP templates (lanes 3, 5, 9, 11, 12). Successful amplification of sex locus using MDA template was demonstrated in all lanes. Male blood DNA (lane 14) and female blood DNA (lane 15). Gray arrow indicates a questionable amplicon representing a male in the female blood DNA lane. This could be due to contamination. Braces at bottom indicate lysate embryo number. Fisher Scientific (NJ) 100 bp ladder (lane 1).

While the PEP and IPEP both performed relatively well in a side by side comparison with the κ -casein locus, amplification of the Sex locus was only marginally successful for PEP and IPEP (Figure 4). When amplifying the Sex locus off known male WGA product from the same embryos under the same conditions, failure of PEP and IPEP to produce amplification occurred frequently. Further, while some lanes produced a questionable band indicating the possibility of a male, so did the female blood DNA control. While PEP and IPEP did perform poorly when used as template for the Sex locus, the MDA produced amplicons in every attempt. Amplification results from the Kappa casein and the Sex locus both suggest the MDA is a much more reliable method of amplification than the other WGA's tested.

C. Future Work

MDA product must be tested with a greater number of markers to ensure that the entire genome is amplified uniquely. Several sex determination markers were tested, with varying results. It is critical that a control be included in the results. Unfortunately, several of the markers do not have internal controls, thereby leading to improper conclusions. If there is insufficient DNA template, the test yields a female result by default. This is a potential problem when utilizing DNA from embryo biopsies. However, when sufficient DNA template is available, the primers available for the various sex determination genes are excellent. The sex determination test that offers the greatest opportunity is the ZFX/ZFY test from the University of Wisconsin. Primers for the nested PCR reaction are being redesigned such that the test will run in a single reaction, and will have an internal control.

Implications

These results are very supportive of the potential to apply the marker-assisted selection to bovine embryo biopsies, without suffering a significant suppression in embryo survivability. As more

markers are identified (disease resistance, fertility, product quality, etc.), there will be greater opportunity to decrease production costs, improve product quality and enhance animal health and resistance to diseases. These improvements will be realized a full year earlier in each production system by using DNA genotyped embryos. Indeed, the research described is one of the early steps in developing a new reproduction strategy for producers in which top cows will be superovulated and flushed to equally top bulls, and embryos will be biopsied, genotyped for multiple traits, and cryopreserved. The embryos meeting certain genotype requirements would then be available for placement into recipient cows, sold, or possibly discarded if they do not hold the genetic complement desired.

References

- Bredbacka P. 1998. Recent developments in embryo sexing and its field application. *Reproduction, Nutrition, and Development* 38:605-613.
- Bredbacka P, A. Kankaanpaa, and J. Peippo. 1995. PCR-Sexing of bovine embryos: A simplified protocol. *Theriogenology* 44:167-176.
- Dean, F.B., S. Hosono, L. Fang, W. Lui, F Faruqi, P. Bray-Ward, Z. Sun, Q. Zong, Y. Du, J. Du, M. Driscoll, W. Song, S. Kingsmore, M. Egholm, and R. Lasken. 2002. Comprehensive human genome amplification using multiple strand displacement. *Proc Nat Acad Science*, 99: 8, 5261-5266.
- Dietmaier, W, A. Hartmann, S. Wallinger, E. Heinmoller, T. Kerner, E. Endi, K.W. Jauch, F. Hofstadter, and J. Ruschoff. 1999. Multiple mutation analysis in single tumor cells with improved whole genome amplification. *American Journal of Pathology*, 154, 83-95.
- Handyside, A., M.D.Robinson, R.J. Simpson, M.B. Omar, M.A. Shaw, J.G. Grudzinskas, and A. Rutherford. 2004. Isothermal whole genome amplification from single and small numbers of cells: A new era for pre-implantation genetic diagnosis of inherited disease. *Molecular Human Reproduction*, 10: 10, 767-772.
- Hartmann, A., W. Dietmaier, S. Wallinger, E. Heinmoeller, F. Hofstaedter, and J. Rueschoff. 1998. Improved PEP-PCR: Evaluation of reliability for microsatellite and sequencing analyses of multiple genetic loci from microdissected single few or tumor cells. *Cancer Prevention and Detection*, 22: supplemental.
- Herr C.M. and K.C. Reed. 1991. Micromanipulation of bovine embryos for sex-determination. *Theriogenology* 35:45-54
- Mamone, T.J. 2003. A method for representatively amplifying genomic DNA. *Genom/Proteom Tech.* 21-24.
- Moton-Redding, N. 2005. Investigation and validation of whole genome amplification processes using DNA from bovine blastocyst biopsies. Masters Thesis, Cal Poly State University.

- Paez, J.G., M. Lin, R. Beroukhi, J.C. Lee, X. Zhao, D.J. Richter, S. Gabriel, P. Herman, H. Sasaki, D. Altshuler, C. Li, M. Meyerson, and W.R. Sellers. 2004. Genome coverage and sequence fidelity of Φ 29 polymerase-based multiple strand displacement whole genome amplification. *Nucleic Acids Research*. **32**:09, e71.
- Patki, A. and J. Nelson. 2002. An alternative method for preparing templates for DNA sequencing. *Genom/Proteom Tech*. **2**:5, 28-31.
- Van Vliet R.A., A.M. Verrinder Gibbons, and J.S. Walton. 1989. Livestock embryo sexing: A review of current methods with emphasis on Y-specific DNA probes. *Theriogenology* **32**:421-438.
- Zhang, L., X. Cui, K. Schmitt, R. Hubert, W. Navidi, and N. Arnheim. 1992. Whole genome amplification from a single cell: Implications for genetic analysis. *Proc. Natl. Acad. Sci. USA*. **89**, 5847-5851.

**Real-time underwater monitoring of sunlight penetration into
the ocean water at Avila Bay, California.**

Project Investigator:

Dr. T.J. Bensky
Assistant Professor
Physics Department
Cal Poly State University
San Luis Obispo, CA 93407

Report Summary

This final report describes the current results of a study on sunlight penetration into the ocean water at Avila Bay, Ca. As implemented, a series of 10 fiber optic cables are deployed at fixed and incremental depths below the ocean surface. The submersed end of each fiber points upward, collecting a sunlight sample at its respective depth. The fibers deliver the light sample to a spectrometer on the pier surface, which determines the spectral content of the light between 400 and 1200 nm. Continuous and real-time optical properties of the ocean water are derived from this data. Funding for this project was used for supplies and summer stipends for the PI and three undergraduate students.

Introduction and Project Significance

The initial reason for studying sunlight penetration in the ocean water was to optically track phytoplankton activity at Avila Bay, CA, an effort which is ongoing. Phytoplankton are known to absorb strongly at 440 nm, so it is hoped that tracking intensity fluctuations of this wavelength in the ocean, phytoplankton activity could be deduced. Work on this hypothesis is ongoing, and many other research possibilities from this work have become apparent. The location of this project, at Avila Bay, Ca (city: Avila Beach, Ca, 93424, USA see <http://maps.google.com/maps?oi=map&q=Avila+Beach,+CA>) was chosen since Cal Poly operates a pier/research facility in this Bay, about 20 minutes from campus. The pier extends 1 km due-South from the coast allowing for easy access to a 10 m column of open ocean water. The existing apparatus, currently deployed at this pier, can obtain a real-time optical map of a vertical column of ocean water. The "optical map" here is knowledge of discrete wavelength intensities, between 400 and 700 nm, at multiple depths below the ocean surface. The real-time sensing of this project means the wavelength range is continuously sampled by computer, and is able to visit multiple depths in seconds. A project website, including links to "live" data and images is available at <http://atom.physics.calpoly.edu/Marine/FiberArray/>.

Apart from phytoplankton monitoring, work is also being done on:

- **Harmful Algal Blooms.** "Red tides" and harmful algal blooms (HABs) are consequences of phytoplankton colonies with out-of-control growth. Potent neuro-toxins released by some species can affect the sea-based food-chain. As of June 5, 2005, a HAB has halted the shellfish industry in the New England coasts. Red tides, which occur often during the summer months in Avila Bay, will be monitored and detected using this apparatus. Optically, the reddish sea-color indicates strong reflection of the ocean of red-wavelengths (650 nm and higher), meaning the same wavelengths will appear at decreased intensities for transmitted light. This work will attempt to correlate visual ocean appearance before, during and after HAB conditions, by monitoring transmitted sunlight into the ocean. It is hoped an optical signature of a pending HAB will be found.
- **Attenuation Coefficients.** The extinction rate with depth of a given wavelength is still a fundamental optical parameter of the ocean. Compiling an ongoing database of such coefficients can lead to a better understanding of the degradation of a light signal as it travels under the ocean surface. This has importance in the areas of underwater photography, or underwater light detection (instances where light signals must travel through the ocean water, on route to a detector). *The Navy would be interested in ongoing measurements of attenuation coefficients to supplement LIDAR measurements performed over ocean water.*
- **Trends in sediment transport.** Near-coastal waters, such as those at our monitoring point, often appear brown and muddy, as large particulates are being circulated with the ocean waters. Large

particulates would represent a significant decrease in transmitted light intensity across all wavelengths. Large particulates scatter down-welling light out of the beam in equal proportions at all wavelengths. This can be monitored with our apparatus, in the form of random deviations from exponential attenuation across all wavelengths, as random concentrations of particulates move into and out of the down-welling light beam. Such sediment transport can result in the formation of Nepheloid layers, which are areas of concentrated particles, parallel to the ocean surface. Such layers frequently yield false signals in LIDAR-based bathymetric studies. *The Navy might be interested in some form of characterization of these layers to correct LIDAR measurements.*

With the apparatus successfully deployed and operations, the above describe work is currently ongoing.

Work Progress Summary

The work completed on this project between 6/2004 and 6/2005 is detailed here. Note that this work was completed by PI T. Bensky in the Physics Department and **three undergraduate physics majors: Dov Rohan, Grant Gallagher, and Darren Fraser.** Darren and Dov will both derive their senior project work from this project, which is required for graduation from Cal Poly.

The core submersible apparatus is shown here.

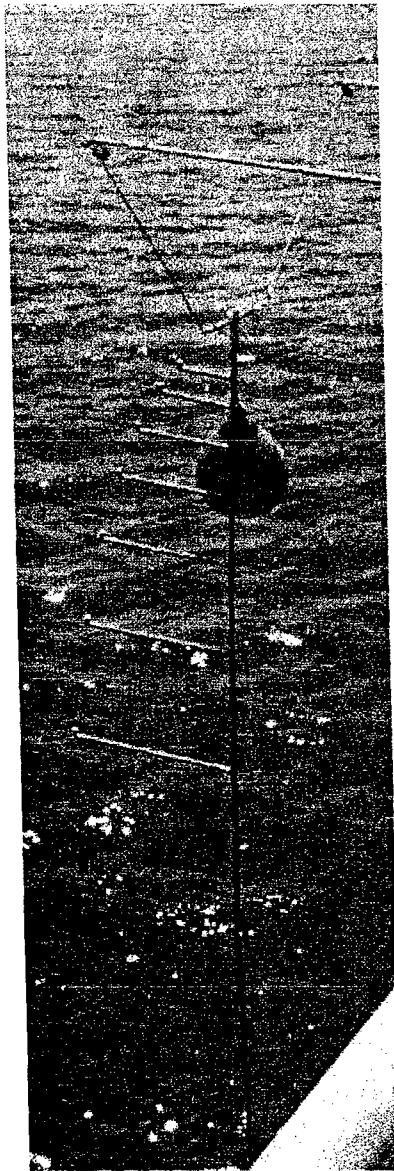


Figure 1: The core apparatus shown during a launch into the ocean

The structure is 25-feet in length, and was made entirely from 1-inch-diameter copper pipe. The structure consists of two primary parts. The first is the core-support structure, consisting of a 25-foot vertical section of pipe. At the top is a perpendicular cross-piece about 4 feet long, whose ends are attached to ropes, securely binding the apparatus to the pier itself. When submersed, the entire structure floats under the buoy (see Figure 1), to hold it at a constant depth relative to the approximate 6-foot tides at Avila Bay. The two attachment ropes are kept taut, preventing the apparatus from rotating. A lead weight is attached to the deep-end of the apparatus, to help in stabilizing the apparatus in a vertical orientation. Attached to the pier itself, and parallel to the ocean surface are two 20-foot sections of 3/4-inch galvanized pipe. These are used to support and hold the floating apparatus at a fixed distance from the pier, in order to avoid shadows cast by the pier and to avoid the structure becoming entangled with the pier substructure. At exponentially increasing lengths along the 25-foot vertical section are "arms" of increasing length, which hold the fiber optic cables in an upward pointing orientation to collect light samples. The fibers are

routed inside of the copper pipe.

Fiber routing. A total of 13, 1000 micro-meter diameter fiber optic cables were cut to approximately 145 feet. This length includes 25 feet from the pier surface to the ocean surface, plus length for a fiber to extend to a maximum depth of approximately 30 feet. The remaining 90-foot length was needed to route the fibers into a storage-shed on the pier, which houses the computer and data acquisition instruments. The fibers were all cut to an identical length to remove any ambiguity that might arise concerning the attenuation of light as it passes through different lengths of cable. The fibers emerging from the copper structure were all woven into 3/4-inch clear, thick-walled Tygon tubing. This keeps the individual fibers from becoming entangled, and provides a strong layer of protection as the fibers run from the apparatus, up to the pier, then along the pier surface and into the storage shed for data acquisition. In all, 10 fibers are pointed up, one points down at the deepest point (to capture ocean-bottom reflection data), there is a redundant upward fiber for later cross-checking of light intensity, and a final fiber pointing straight up at the sky (in the air), to capture total incident light intensity upon the ocean surface.

Data Acquisition. Once inside the storage-shed, the 13 fibers are connected to a 16-to-1 fiber optic multiplexer, shown in Figure 2. The multiplexer allows for automatic selection of any one of the 13 fibers to feed the input line to the light spectrometer (shown in Figure 2 on top of the multiplexer). The spectrometer analyzes the incoming light and decomposes it into intensity of light received at a particular wavelength, between 200 and 1200 nm, in increments of 1 nm.

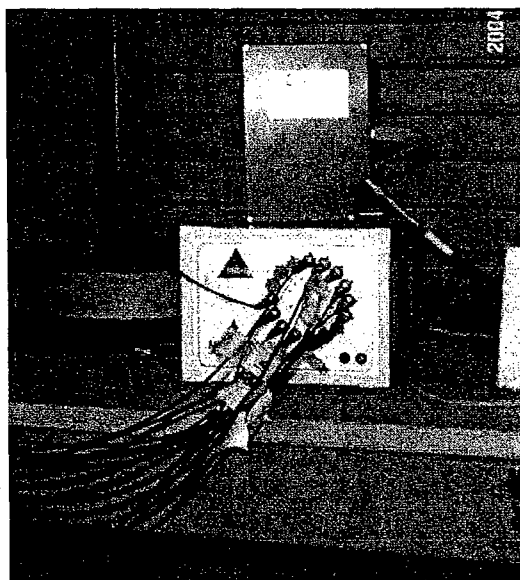


Figure 2: The 16-to-1 fiber optic multiplexer, accepting input from 13 incoming fibers.

Automated Data Acquisition. With the fibers connected to the multiplexer-spectrometer pair, data acquisition can begin. Custom software written in the C++ language by T. Bensky does the following. First it selects fiber N, where N is a number between 1 and 13, representing which fiber is to be read. The multiplexer is controlled by sending ASCII commands to it via the serial port. With an appropriate fiber selected, the software instructs the spectrometer to read and process the incoming light signal. The spectrometer is USB-based, and custom drivers had to be written to acquire the intensity versus wavelength data from the spectrometer, in the automated fashion desired. The spectra is saved to the hard drive and the process is repeated for the next fiber. All 13

fibers are sampled and read in approximately 20 seconds, and entire process is repeated every 15 minutes. A raw data plot generated by the software after a typical fiber-sampling session is shown in Figure 3. Each curve in this Figure represents the light spectra read from each fiber. The differing amplitudes of each curve are part of the science under investigation. The software normalizes all curves to be equal in amplitude before the apparatus is submersed. The C++ software is up to approximately 1,000 lines of C++ code (and growing).

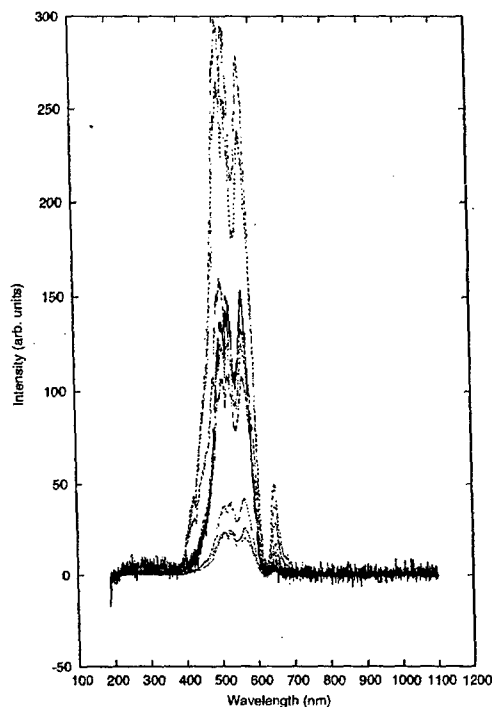


Figure 3: A sample data overview. Each curve represents the spectra obtained from an individual fiber.

Computer/server configuration. A “recycled” 266 MHz PC with 64 Megabytes of RAM running the Linux operating system is the core data acquisition computer. The decision was made to go with Linux for stability and adaptability to older PCs. Also, software costs needed to be kept to an absolute minimum. Since custom software was needed, the many programming tools Linux offers could be used, and it was desired that the computer be networked and run its own web server so data and up-to-the-minute status information could be retrieved. The server has been configured in this way, and is the one actually serving up the “live” data feeds at the site <http://benskypier.marine.calpoly.edu>. The live, networked computer also permits software modifications and data retrieval from the Cal Poly campus, eliminating the need to physically go to the pier to access the acquired data.

Our evaluation of this project at this point in time is that the entire system is stable and operational. A sense of the device's operation, including its response to the harsh ocean conditions (fouling) and the type of data that is collected is becoming clear, as is what science this apparatus will deliver. During the summer/academic year 2005, a careful and systematic delve into data observation and analysis is planned.

Near-term work

The priority phenomena for the next few months is to optically classify the build up, existence, then decay of a "red tide" or "harmful algal bloom" (HAB), as mentioned in the introduction. This happens frequently during the summer months in Avila Bay, and this project is on track to optically capture these events.

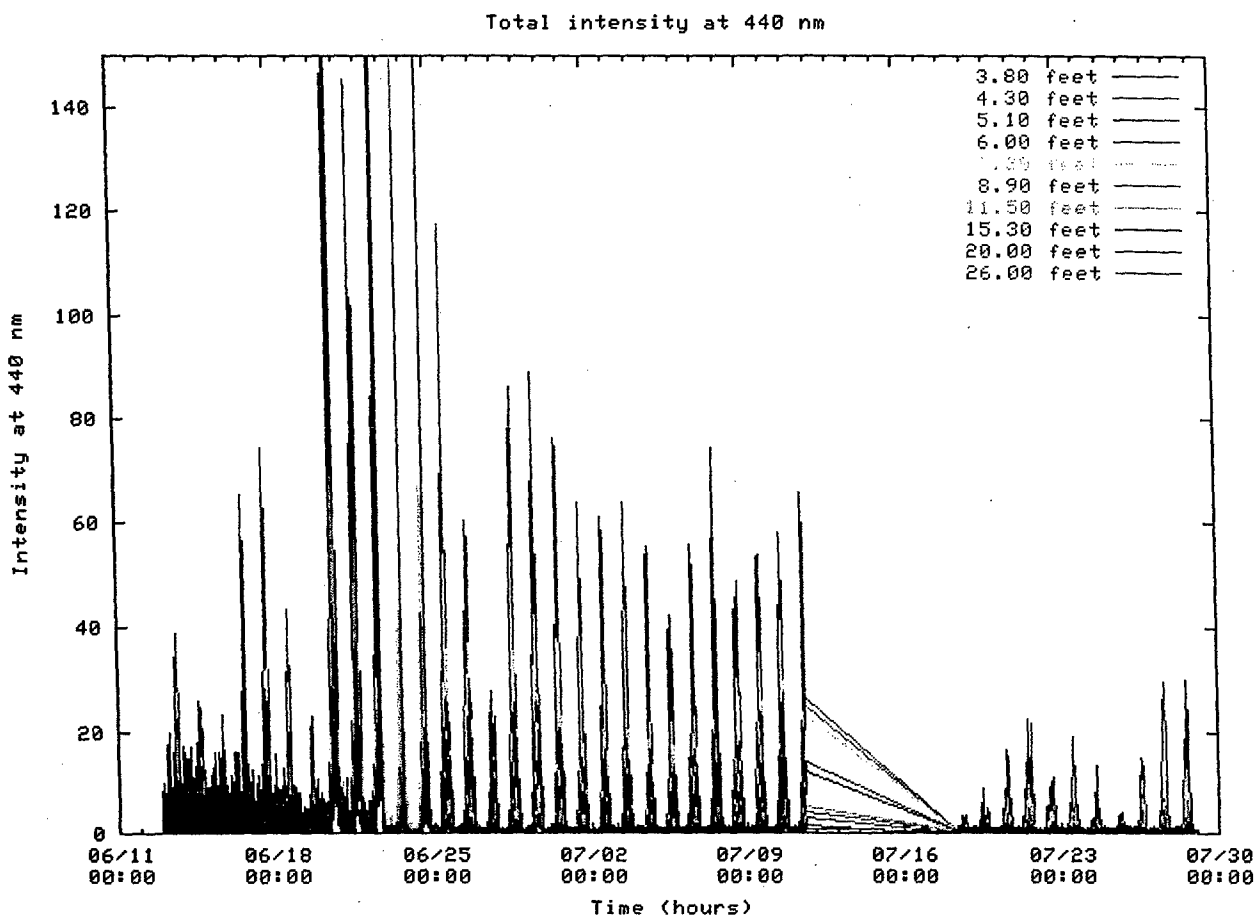
Bottom reflection monitoring. *The Navy expends considerable effort in ocean bathymetric measurements.* Their measurements involve reflecting high-powered laser pulses from the bottom of the ocean, in order to map the under-sea terrain. The signal to noise ratio in these measurements depends crucially on the amount of light reflected from the ocean floor. Using this apparatus, the ratio between the signals obtained from the downward- and upward-looking fibers will allow for continuous monitoring of light intensity reflected from the ocean floor.

Attenuation Coefficients. Attenuation coefficients across the visible spectrum are natural parameters to extract from the acquired data, as discussed. *The Navy is interested in such parameter for reasons involving underwater visualization, as in photography or other types of sub-surface imaging.* }

Chlorophyll fluorescence. The stimulated fluorescence of Chlorophyll discussed in above, in addition to rote tracking of sunlight absorption at 440 nm, will allow for both active and passive monitoring of phytoplankton activity.

Wavelength history. A measurement we have dubbed "wavelength history" will serve as a unique long-term optical look at the ocean. By this, it is meant that the intensity of an individual wavelength, can be viewed, as a function of time and depth. For example, the ocean usually appears green, indicating that green wavelengths (near 532 nm) are not readily absorbed by the ocean water. Tracking the intensity of this wavelength as a function of time would serve as a overall "green-ness" ocean color indicator.

As an example, the device has been instructed to track the light intensity at 440 nm. This wavelength is important because phytoplankton in the ocean water absorb strongly at this wavelength. It is our hypothesis here that tracking this wavelength might yield clues as to the concentration of phytoplankton at various depths in the sampled water column. A 1.5-month-long data set is shown in Figure 4.



Thu Jul 28 21:54:32 2005
Figure 4: Intensity of 440 nm light as a function of depth.

This graph extends from 2005-06-11 to 2005-07-30. The peaks come at 24-hour intervals and occur approximately at noon each day. Data from 6/25 and onward is considered reliable. The gap near 7/16 was due to a power outage at the pier. From this data we observe that between 6/25 and 7/09, the intensity of 440 nm was most intense at 4.3 feet below the water. This corresponds to a month of strong winds over much of the day, mixing the water. The data from 7/16 and onward corresponds to a period of much calmer days with less water mixing due to the wind. Work is underway to correlate with and water mixing and penetration of 440 nm light and how that might lead to observation of phytoplankton activity.

Total light field. By computing the area under each curve in a basic data sample shown in Figure 3, the "total light field" at a given depth can be determined. Intuitively, one might expect a very simple trend: a maximum of light at the shallowest fiber and a minimum of light at the deepest fiber, with the total light field decreasing between the two. *We have never observed this trend to be true.* Figure 5 shows the integrated light field derived from Figure 3.

Frequently, the light field at the shallowest fiber is systematically less than that at neighboring and deeper fibers. In this case, the water is "brightest" nearly 10 feet under the surface. Our initial hypothesis is that lensing due to the water is playing a role. This will be investigated further, which would be of interest to anyone involved with collecting light under the ocean (underwater imaging, cameras, etc.).

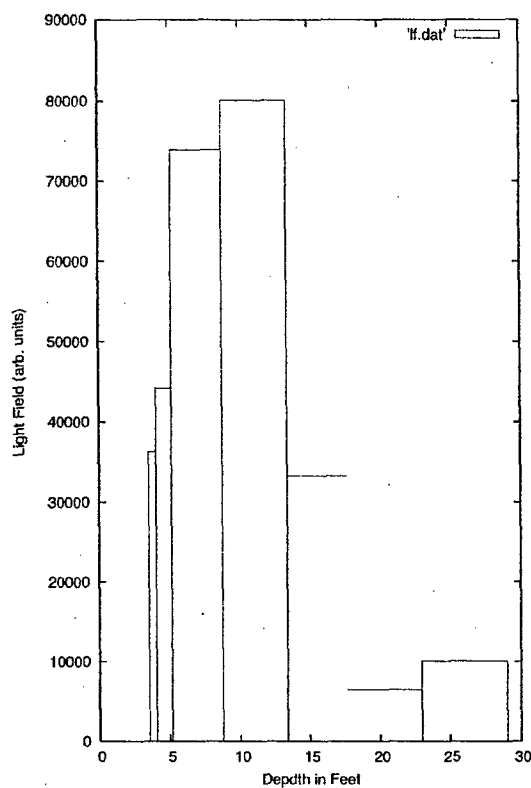
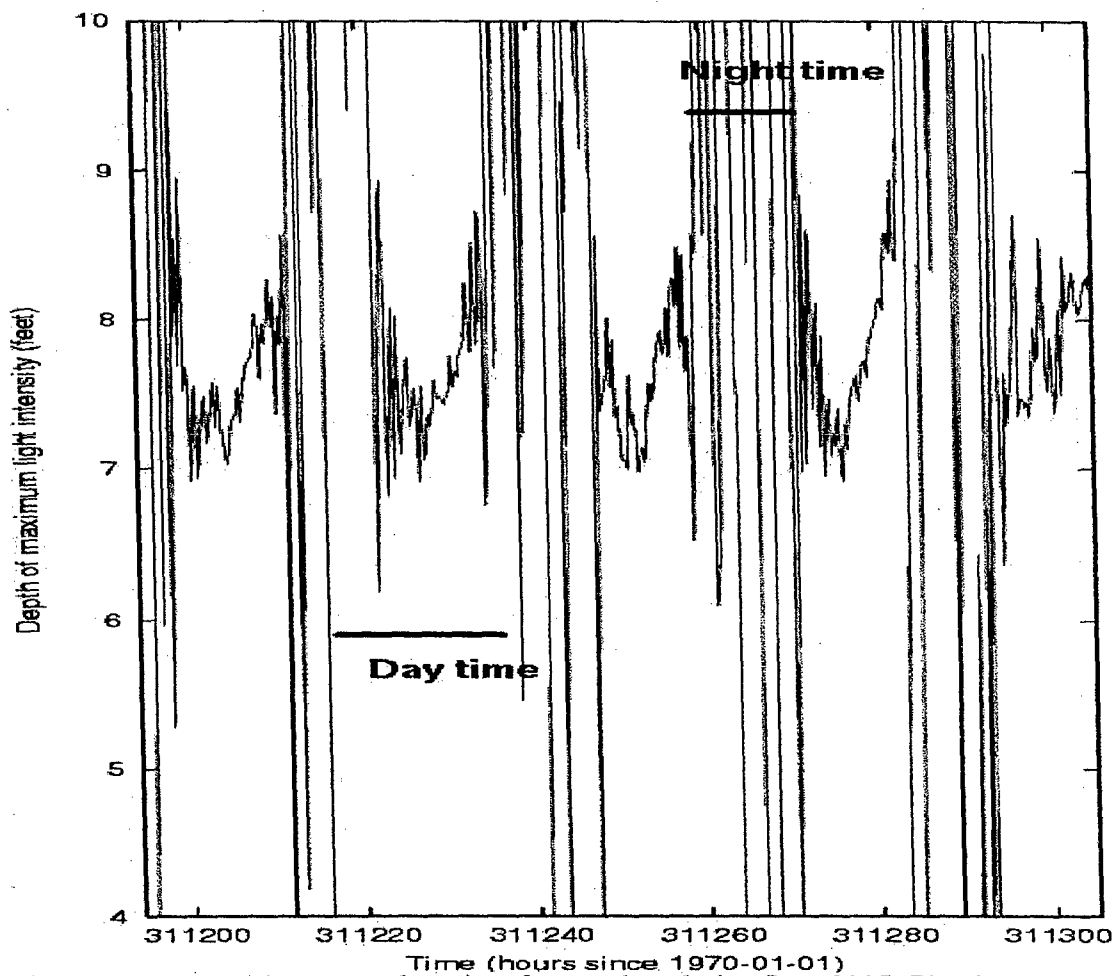


Figure 5: Total light field as a function of depth, as derived from Figure 3, by integrating under each curve in Figure 3.

We are also able to take the “average depth” of Figure 5, revealing the average depth at which most light intensity appears to exist. Visually, this average would answer the following question: at what depth would one draw a vertical line on Figure 5 that was at “center of mass” of the bars? This is performed at each acquisition run. A sample plot is shown in here in Figure 6.



This data was extracted from a random time frame taken during June 2005. The tick marks on the x-axis are time, in increments of 20 hours. The large groups of spikes that extend vertically off of the top and bottom of the graph are to be disregarded. They were taken by the software during night-time hours, where there is no clearly defined average depth where a maximum amount of light appears. Between these groups of large spikes are distinct curves, appearing somewhat consistent from day to day. The maximum brightness appears at 8 feet below the surface, rising quickly to nearly 7 feet, before retreating back to 8 feet before darkness sets in once again. Although this represents an overall shift of only one foot, the trend is clearly systematic; there may very well be fine-scale trends in downwelling light penetration through the ocean. Analysis of this effect is on going.

Summary of Technical Challenges Overcome

At the onset of this project, it wasn't entirely clear how to deploy any such instrument from the Cal Poly pier at Avila Bay. Problems involving corrosion, bad weather, equipment theft, deployment, retrieval, maintenance procedures, and extreme instrument fouling have all plagued this effort. As of this writing however, these problems have been largely overcome. The entire instrument design and implementation is now operating in a stable manner, and since February 2005, has been deployed for increasing longer periods of time. As of August 1st 2005, the instrument has completed 73 days of continuous deployment and operation. Careful monitoring of incoming data, as initially proposed, is ongoing. The PI intends on seeking additional funding for this work for three primary reasons:

I. Project maintenance and longevity. The harshness of the marine environment on a submersed instrument requires higher levels of maintenance than for work done in a controlled (indoor) laboratory environment.

II. Optical monitoring enhancement. Two limitations of this instrument have become apparent during this work.

1. The apparatus passively monitors sun-light penetration into the ocean. Through a minor modification, the device could actively retrieve optical properties of the ocean by stimulating and collecting under-sea fluorescent signals.
2. The second is a limitation due to the quality of the fibers currently in use. If higher quality optical fibers could be added to the system, a valuable "cross-check" could be applied to incoming data.

III. Undergraduate Student Research Stipends. Undergraduate students appear to be very enthusiastic about working on oceanographic research projects the pier. The work is very active, has a good mix of laboratory and out-of-doors work, and they seem to relate well to the purpose of studying the ocean with an emphasis on physics and optics.

Conclusions

In sum, we have deployed a "home-built" instrument that allows for the study of sun-light penetration into the ocean water. There is an abundance of data incoming from this device and we are only beginning a systematic study it. Several preliminary trends have already been identified.

Human Sensing

Project Investigators:

Charles Birdsong
Assistant Professor
Mechanical Engineering Department

Peter Schuster
Assistant Professor
Mechanical Engineering Department

C3RP Final Project Report

Human Sensing

Charles Birdsong

Peter Schuster

Mechanical Engineering Department
Cal Poly State University

Abstract

This report summarizes the work completed in the first year of this long term research effort funded by the C3RP. In this work the focus was on developing a sensor system that meets the broad description of a human sensor while also meeting the specific applications of pre-crash detection, pedestrian safety and military sensing. The work consisted of a literature search, sensor acquisition, sensor testing, and algorithm development. The project was very successful meeting the stated objectives. Three sensors were identified as good candidates: ultrasonic, RADAR and LIDAR. Commercially available samples of each were acquired, instrumented and tested. Algorithms were developed to read the sensor raw data and compute telemetry data.

An additional objective of this project was to foster learning and research at Cal Poly. This was accomplished by involving students from many different levels and backgrounds. The project resulted in two technical papers submitted for publication, many industry contacts, equipment donations, several proposals for external funding and support for students and faculty.

Introduction

Improving vehicle occupant safety has been an increasingly important area of study since the mid 1960's. Initially this work was centered on controlling post impact occupant dynamics through the use of structural modifications, crush zones, seatbelts, and airbags. These methods have been successful however there is still potential for improvement. The next leap forward in occupant safety is pre-crash sensing. Figure 1 demonstrates some possible safety benefits of pre-crash sensing. Current vehicles do not have any means of anticipating a crash. In the short time frame (approximately 10-20 milliseconds) after a crash is detected by mechanical or electronic sensors the options for deploying safety technologies is limited. Currently airbags are deployed approximately 10 - 20 ms after impact and must be inflated rapidly so that they are in place to protect the passenger. If the crash could be anticipated, then additional time would be available to deploy new safety technologies (e.g. audible alarms, seatbelt pre-tensioners, automatic door locking, seat stiffeners, seat position control, automatic window closing, slower airbag inflation rates, and automated braking). The result would be increased vehicle crash survival rates. In addition, pre-crash detection will reduce the incidence of unnecessary airbag deployment. Studies show that unnecessary airbag deployment can cause greater injuries than a minor crash would cause (Jones 2002).

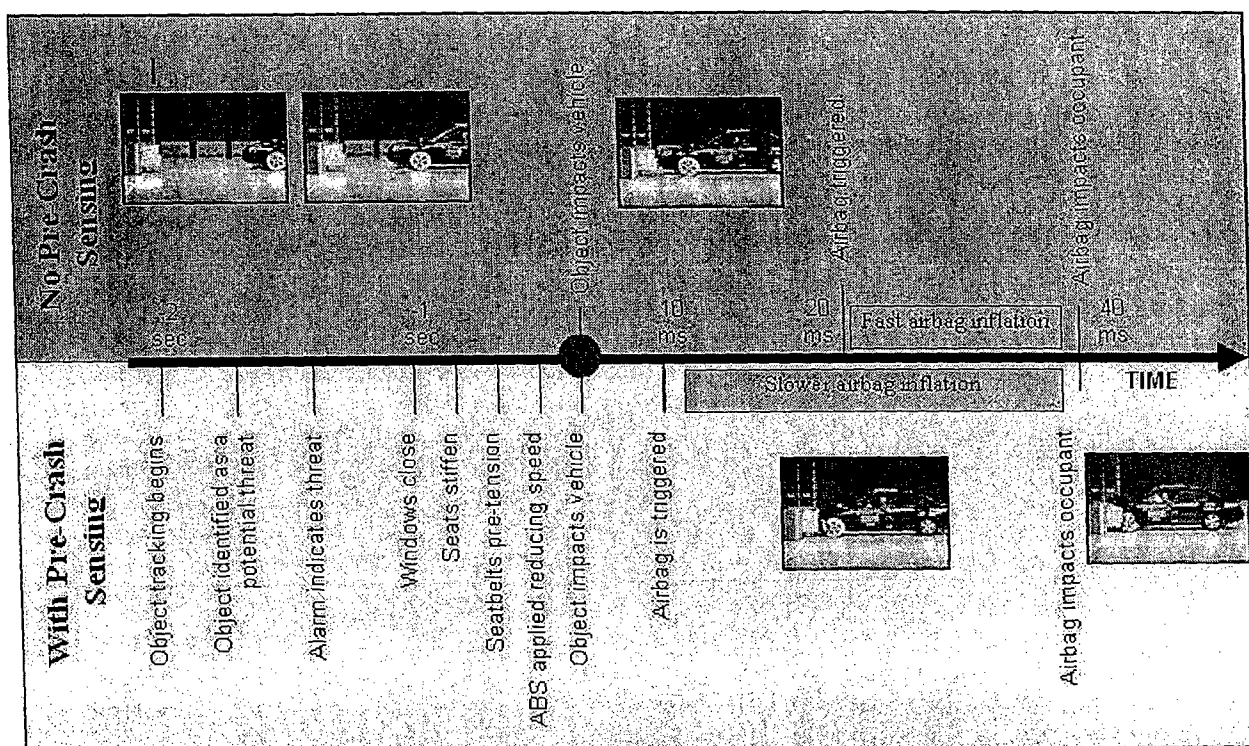


Figure 1: Timelines for collisions with and without pre-crash sensing

External sensors are now being adopted into passenger vehicles—reducing the costs and enlarging consumer acceptance. Ultrasonic sensors are used today as parking aids on vehicles with large blind spots, infrared sensors have been used to aid vision at night and radars are used in adaptive cruise control (ACC) systems to maintain safe following distance when cruise control

is active. These sensors are used in a passive sense and not used to actively avoid or aid in a crash event. However it has been proposed that they could be integrated with intelligent real-time algorithms to do so.

Another related topic is pedestrian safety. Passive pedestrian safety technologies are currently being implemented on vehicles throughout Europe and Japan. New technologies such as softer bumpers, energy-absorbing hoods/fenders, and crushable wiper spindles offer some reduction of pedestrian injuries should an accident occur. However, these new technologies will only achieve a slight reduction in pedestrian injuries and fatalities, even though they are costly and require extensive compromises in vehicle packaging and reductions in other areas of vehicle performance to implement. Significant reductions in injuries and fatalities will require the implementation of dynamic or active systems such as external airbags and accident avoidance technologies (e.g. pre-crash braking). Pre-crash sensing is a prerequisite for implementing these more advanced countermeasures, and is therefore a critical technology for delivering any significant improvement in pedestrian safety. In fact, the development of a robust, reliable, cost effective sensing system is a key prerequisite for delivery of most advanced safety countermeasures.

The area of personnel sensing is also of interest in military traditional battle settings, urban battle scenarios, terrorist tracking and identification and police surveillance. There is some crossover interest in remote sensing for weather and geological mapping. The Office of Naval Research is interested in Electro-Optical (EO)/Infrared (IR) Sensor Processing and defines this subject as: "Detect, classify/identify, and localize/geolocate air, sea-surface, and ground targets by improving the performance of the signal and image processing techniques associated with electro-optical (EO) and infrared (IR) sensors (passive and active) that operate from the visible through longwave infrared bands."

In this work the focus was on developing a sensor system that meets the broad description of a human sensor while also meeting the specific applications of pre-crash detection, pedestrian safety and military sensing.

Summary of Work Completed

This section describes in detail the activities completed during the year funded by C3RP.

Literature review

A literature review was conducted to find previous work and understand the state of the art. It was found that this area of work is new and there is good potential for contribution to the academic understanding of the topic and for external funding by industry and or private and government agencies.

A short list of relevant publications collected follows.

Table 1: Relevant SAE (Society of Automotive Engineers) Papers

Title	Authors	SAE Paper No.	Date
The computation of airbag deployment times with the help of pre-crash information	Marc Theisen Sybille Eisele Michael Rolleke	2002-01-0192	03-04-2002
Crash sensors for inflatable occupant restraint systems	E. Pujdowski	720420	05-22-1972
A complete frontal crash sensor system	David Breed W. Thomas Sanders Vittorio Castelli	930650	03-01-1993
Investigation of sensor requirements and expected benefits of predictive crash sensing	William R. Swihart Albert F. Lawrence	950347	02-27-1995
Crash sensor basic requirements	Trevor O. Jones Oliver T. McCarter	720419	05-22-1972
Tradeoffs and testing for frontal crash sensing systems	Tony Gioutsos Ed Gillis	932911	10-25-1993
Comparative analysis of crash sensors	Trevor O. Jones Oliver T. McCarter Robert N. Oglesby	720035	01-10-1972
Application of radar for automotive crash avoidance	Christopher L. Lichtenberg	870496	02-23-1987
The role of vision sensors in future intelligent vehicles	Lisa Hamilton Lawrence Humm Michele Daniels Huan Yen	2001-01-2517	08-20-2001
Predictive safety systems - steps toward collision mitigation	Peter M. Knoll Bernd-Josef Schaefer Hans Guettler Michael Bunse Rainer Kallenbach	2004-01-1111	03-08-2004
Sensing in the ultimately safe vehicle	Randy Frank	2004-21-0055	10-18-2004
An ultrasonic proximity system for automobile collision avoidance	Kert L. Cartwright Gopi R. Jindal	920393	02-24-1992
Application of ultrasonic technology to obstacle detection	James R. Cherry	952617	11-13-1995
Collision warning		1-105-3-86	03-01-1997
Analysis of lane change crash avoidance	José L. Bascuñana	951895	08-07-1995
Obstacle state estimation for imminent crash prediction and countermeasure deployment decision-making	Kwaku O. Prakah-Asante Mike K. Rao Gary S. Strumolo	2003-01-2261	06-23-2003

Gavrila, D.M. "Sensor-Based Pedestrian Protection," *IEEE Intelligent Systems*, Vol. 16, No. 6, November/December 2001.

Jones, Robert C., 2002, "Technologies for Static Airbag Suppression Systems", 6th International Symposium and Exhibition on Sophisticated Car Occupant Safety Systems, Karlsruhe, December 2-4, 2002.

Lyons, C. T. and Taskin, I., 2000, "A low-cost MMIC based radar sensor for frontal, side or rear automotive anticipatory pre-crash sensing applications," *IEEE Intelligent Vehicles Symposium*, The Ritz-Carlton Hotel, Dearborn, MI, USA.

National Highway Traffic Safety Administration, "Traffic Safety Facts 2003," <http://www-nrd.nhtsa.dot.gov/pdf/nrd-30/NCSA/TSFAnn/2003HTMLTSF/TSF2003.HTM>, 2005.

Spies, Hohenwart, D., 2002, "What is Achievable Today and in the Near Future? - Overview on Technologies: Radar, Video, IR," 6th International Symposium and Exhibition on Sophisticated Car Occupant Safety Systems, Karlsruhe, December 2-4, 2002.

Zhao and C. Thorpe, Carnegie Mellon University's NavLab , "Stereo- and Neural Network-Based Pedestrian Detection," IEEE Trans. Intelligent Transportation Systems, vol. 1, no. 3, Nov. 2000, pp. 148-154.

Industry Contacts

In addition to collecting data on sensors, contact was initiated with a number of automotive safety and sensor equipment companies. A list of the most important contacts is provided.

- Ford
 - Birdsong visited Srini Sundararajan at Ford Research Laboratory to discuss the topic of human sensing for pedestrian safety and pre-crash detection. Srini also sponsored a Ford University Research Program grant by Schuster and Birdsong.
- Delphi
 - Based on Ford suggestions, contact was initiated with Michael Ray
 - Donated an active cruise control radar and a backup assist radar
- BGM Engineering Inc
 - Small business in Michigan developing automotive safety-related technologies.
 - Joe Mazur provided input on the topic of bi-static radar
 - This contact lead to a NSF STTR proposal between BGM, Schuster and Birdsong to develop bi-static sensor for pre-crash sensing.
- Innovative Survivability Technologies (IST)
 - Small business in Goleta, California, developing military survivability technology.
 - Birdsong and Schuster met with the company president and other executives to discuss cooperation with Cal Poly on related topics.
 - Plan to jointly submit a U.S. Army proposal for technology development.

Proposal submitted to Ford Motor Company

Schuster and Birdsong submitted a proposal to the Ford University Research Program (URP) titled, "Development and assessment of cost effective pedestrian pre-crash sensing and discrimination system." This program requires matching funds from a specific department within Ford. The proposal was sponsored by Ford Research Laboratory's Active Safety Department. The URP was significantly scaled back this year and the proposal was not funded.

Proposal submitted to National Science Foundation

Building on the work completed in this project, Schuster and Birdsong prepared and submitted a National Science Foundation Small Business Technology Transfer (STTR) project proposal with BGM Engineering. This proposal was titled, "Integrating a Bi-Static Radar into a Vehicle Pre-Crash Sensing System," and focuses on the baseline testing and algorithm development required to determine the viability of reduced-cost bi-static radar for this application. The proposal is under review.

Sensor review and comparison

A literature review identified a large array of possible sensors to be evaluated for use in this application. The table below summarizes the various sensors considered.

Table 2: Comparison Matrix of Current Sensor Technologies

	Ultrasonic	LIDAR	RADAR	Bi-Static RADAR	Vision	Active Infrared	Passive Infrared
Cost	Low	High	High	Medium	Low	Low	Low
Computation Overhead	Low	High	Medium	Medium	High	Low	Low
Range	3m	5m to 150m	1m to 150m	7m	Line of sight		
Operating Conditions		Clear visibility to 150m	Normal to heavy rain or snow	Normal to heavy rain or snow	Clear visibility		
Commercially Available	Yes	Yes	Yes	No	Yes	Yes	Yes
Industry Acceptance	High	None	Some	None	None	None	None
Accuracy	$\pm 0.05\text{m}$	$\pm 0.3\text{m}$	$\pm 1.0\text{m}$		NA		
Update Frequency	40Hz	400Hz	10Hz		<30Hz		
Potential for Object Discrimination	Low	Some	Low	Low	High	None	Low
Detection Capabilities	Distance	Distance, speed, geometry	Distance, speed, power	Distance	Distance, speed, geometry, object class data	Presence	Presence
Target Size	Basketball		Motorcycles and larger		Varies with distance		

The primary goal of this system is to detect objects and gather telemetry information from them. A secondary goal is to collect classification data about the objects that have been identified as a threat. While there is any number of sensor combinations, sensors must be selected based not only on performance but also cost, availability, acceptance and maturity. To this end the following three sensors were selected as good candidates for further investigation: Radar, Ultrasonic, and LIDAR.

The radar was chosen because it gathers the most telemetry information under the widest range of environmental conditions at the highest frequency. Radars are one of the most expensive sensors available; however, since they are an integral part of ACC systems that are now becoming popular on commercial and luxury vehicles the incremental cost of adding this to the system is lowered.

The scanning laser or LIDAR is selected to be a complement to the radar. While current systems do not sample as fast as the radar they provide additional information. They provide some

indication of object geometry and can be used to predict how the vehicle will deform during the impact. When used in combination with the radar the system should be able to determine when there is a fault and indicate this to the vehicle operator. There is the possibility of object discrimination based on the type of signal from each sensor. Figure 5 shows one possible coverage region for a scanning LIDAR. Note that a scanning LIDAR could be designed to have an arbitrary coverage angle.

The ultrasonic sensor was selected since these sensors are in common use on vehicles today, they are inexpensive, and they cover an area directly in front of the vehicle that is not commonly covered by other available sensors. The region that they do cover is possibly the most important as it is where the data has the highest degree of validity and the prediction of an impact is most reliable. Figure 6 shows the portion of the region of interest covered by Ultrasonic sensors.

Sensor acquisition

Initially effort was made to develop industry contacts and attempt to get sensors donated in exchange for access to the technical reports and test results. This was successful for the RADAR systems from Delphi. Other sensors were purchased from the C3RP equipment budget. The following sensors were acquired for evaluation:

Table 3: Sensors Acquired for Testing

Sensor	Source	Cost
Active Cruise Control RADAR	Delphi	Donation (~\$2000)
Backup Assist RADAR	Delphi	Donation (~\$1000)
Laser Range Finder	MDL (Measurement Devices, Ltd)	\$2000
Ultrasonic Range Finder	Hobby Engineering	\$50
Backup Ultrasonic Sensor	???	???
Ultrasonic Range Finder	Home Depot	\$50
String Potentiometer	Space Age Controls	\$500

Sensor characterization

A major component of this project was developing a uniform lab test protocol for evaluating a sensor's performance. This was critical since published data on sensors reports performance only in specific tests, often not relevant to the task of pre-crash detection. This section describes the procedures for testing the various sensor sub-systems associated with the pre-crash sensing system. Note that because of the method of sensor fusion used on this project some of the sensors will fail certain parts of the test. This is by design, as it is the system as a whole that—after integrating the data all of the data from the various external sensors—makes decisions about object location and threat level.

Terms Defined

Clean background: A clean background refers to the environment in which a test takes place. This is not intended to represent a real world test environment, but rather a background that introduces no signal when an object of interest is not present. This will vary for each sensor sub-system, and should be noted with any data collected for that sensor.

Barrier Object: This is target that is intended to represent the barriers that divide the directions of traffic on freeways. This object is defined as a metal divider mounted on wooden stakes.

Pedestrian Object: This is a test target that is intended to represent a human. This is a randomly selected member of the team.

Point Object: This is a test target that is intended to represent a light post, fire hydrant, or similar object. It shall be defined as a four foot long 6" steel pipe mounted vertically.

Vehicle Object: This is a test target that is intended to represent other vehicles that the system might see. This shall be a bumper mounted such that its base is no less than 16" from the ground and its top is no more than 30" from the ground.

1 Static Tests

These tests determine the sensor sub-systems ability to detect object the object of interest with and without background objects.

1.1 Single Object Tests

1.1.1 In Lane Test

Test Targets: vehicle, pedestrian and point

Place the target directly in front of the sensor, if there are more than one sensors then place the target at the location that would represent the mid-point of the front of the vehicle, at a distance of 0.25m. Increase the distance from the sensor to the target in increments of 0.25m until there is no reading from the sensor or until the object is 30m away, taking reading from the sensor at each location.

For targets other than the vehicle and barrier repeat the above procedure with the target placed 0.3m and 0.6m to the right of the centerline of the vehicle, if the sensor is not expected to give symmetric results also repeat with the target placed 0.3m and 0.6m to the left of the centerline of the vehicle.

1.1.2 Out of Lane Test

Test Targets: vehicle, pedestrian and point

This test is only to be performed if the sensor system in question has a range and sensing angle such that it would detect objects outside the lane of travel. In the U.S., automobile travel lanes are between 3.05m and 3.35m wide.

Again using a clean background place the target 3.1m to the right of the vehicle centerline at a distance of 0.25m, or the minimum distance for which there is signal, from the plane that extends out from the front of the vehicle. Increase the distance from the baseline in increments of 0.25m until the target is 30m from the baseline or there is no signal from the sensor.

1.2 Multiple Object Tests

These tests are intended to determine the sensor's ability to differentiate between the target and other objects.

1.2.1 Fixed Targets

Test Targets: vehicle and pedestrian

Clutter Targets: barrier and point

For this test use a clean background and simulate real world clutter using one of the clutter targets. Place the test target at the mid-point of the vehicle at a distance of 0.25m from the front of the vehicle. Place the clutter target 1.75m to the right of the simulated vehicle at a distance of 2m from the front of the vehicle. Increase the distance between the test target and the vehicle until it reaches 30m or there is no reading from the sensor. For test targets other than the vehicle repeat for test target locations 0.3m and 0.6m to the right and left of the centerline of the vehicle. If the sensor is not expected to give symmetric results repeat with the clutter object placed on the left side of the vehicle.

1.2.2 Moving Targets

Test Targets: vehicle and pedestrian

Clutter Targets: vehicle and pedestrian

For this test use a clean background and simulate real world clutter using one of the clutter targets. Place the test target at the mid-point of the vehicle at a distance of 0.25m from the front of the vehicle. Place the clutter target 3.2m to the right of the simulated vehicle at a distance of 2m from the front of the vehicle. Increase the distance between the test target and the vehicle until it reaches 30m or there is no reading from the sensor. For test targets other than the vehicle repeat for test target locations 0.3m and 0.6m to the right and left of the centerline of the vehicle.

Repeat with the clutter target at a distance of 4m and 6m. If the sensor is not expected to give symmetric results repeat with the clutter object placed on the left side of the vehicle.

2 Shake Table Tests

These testes are intended to give an indication of sensor performance when the vehicle it is mounted to vibrates.

2.1 Single object tests

2.1.1 In Lane Test

Test Targets: vehicle, pedestrian and point

Set the sensor portion of the sensor sub-system on a shake table whose displacement is driven by a sine wave.

Place the target directly in front of the sensor, if there are more than one sensors then place the target at the location that would represent the mid-point of the front of the vehicle, at a distance of 0.25m. Increase the distance from the sensor to the target in increments of 0.25m until there is no reading from the sensor or until the object is 30m away, taking data from the sensor at each location. At each location determine the maximum displace at which the sensor reading is deviates by no more than 5% of it's nominal reading or 15cm peak displacement.

For targets other than the vehicle and barrier repeat the above procedure with the target placed 0.3m and 0.6m to the right of the centerline of the vehicle, if the sensor is not expected to give symmetric results also repeat with the target placed 0.3m and 0.6m to the left of the centerline of the vehicle.

2.1.2 Out of Lane Test

Test Targets: vehicle, pedestrian and point

Set the sensor portion of the sensor sub-system on a shake table whose displacement is driven by a sine wave.

This test is only to be performed if the sensor system in question has a range and sensing angle such that it would detect objects outside the lane of travel, in the United States automobile travel lanes are between 3.05m and 3.35m wide.

Again using a clean background place the target 3.1m to the right of the vehicle centerline at a distance of 0.25m, or the minimum distance for which there is signal, from the plane that extends out from the front of the vehicle. Increase the distance from the baseline in increments of 0.25m until the target is 30m from the baseline or there is no signal from the sensor, taking data from the sensor at each location. At each location determine the maximum displacement at which the sensor reading is deviates by no more than 5% of its nominal reading or 15cm peak displacement.

2.2 Multiple Object Tests

These tests are intended to determine the sensor's ability to differentiate between the target and other objects.

2.2.1 Fixed Targets

Test Targets: vehicle and pedestrian

Clutter Targets: barrier and point

Set the sensor portion of the sensor sub-system on a shake table whose displacement is driven by a sine wave.

For this test use a clean background and simulate real world clutter using one of the clutter targets. Place the test target at the mid-point of the vehicle at a distance of 0.25m from the front of the vehicle. Place the clutter target 1.75m to the right of the simulated vehicle at a distance of 2m from the front of the vehicle. Increase the distance between the test target and the vehicle until it reaches 30m or there is no reading from the sensor, taking data from the sensor at each location. At each location determine the maximum displacement at which the sensor reading is deviates by no more than 5% of its nominal reading or 15cm peak displacement. For test targets other than the vehicle repeat for test target locations 0.3m and 0.6m to the right and left of the centerline of the vehicle. If the sensor is not expected to give symmetric results repeat with the clutter object placed on the left side of the vehicle.

2.2.2 Moving Targets

Test Targets: vehicle and pedestrian

Clutter Targets: vehicle and pedestrian

Set the sensor portion of the sensor sub-system on a shake table whose displacement is driven by a sine wave.

For this test use a clean background and simulate real world clutter using one of the clutter targets. Place the test target at the mid-point of the vehicle at a distance of 0.25m from the front

of the vehicle. Place the clutter target 3.2m to the right of the simulated vehicle at a distance of 2m from the front of the vehicle. Increase the distance between the test target and the vehicle until it reaches 30m or there is no reading from the sensor, taking data from the sensor at each location. At each location determine the maximum displacement at which the sensor reading is deviates by no more than 5% of its nominal reading or 15cm peak displacement. For test targets other than the vehicle repeat for test target locations 0.3m and 0.6m to the right and left of the centerline of the vehicle.

Repeat with the clutter target at a distance of 4m and 6m. If the sensor is not expected to give symmetric results repeat with the clutter object placed on the left side of the vehicle.

Technical Paper Publications

The following two papers have been submitted to Society of Automotive Engineers.

"Evaluation of Cost Effective Sensor Combinations for a Vehicle Pre-crash Detection System," John Carlin, Charles Birdsong, Peter Schuster, William Thompson, Daniel Kawano [*Paper under review*]

The future of vehicle safety will benefit greatly from pre-crash detection – the ability of a motor vehicle to predict the occurrence of an accident before it occurs. There are many different sensor technologies currently available for pre-crash detection. However no single sensor technology has demonstrated enough information gathering capability within the cost constraints of vehicle manufacturers to be used as a stand alone device. A proposed solution consists of combining information from multiple sensors in an intelligent computer algorithm to determine accurate pre-crash information. In this paper, a list of sensors currently available on motor vehicles and those that show promise for future development is presented. These sensors are then evaluated based on cost, information gathering capability and other factors. Cost sensitivity is lower in large commercial vehicles than in personal vehicles due to their higher initial cost and longer life span making them a good candidate for early adoption of such a system. This work forms the basis for ongoing research in developing an integrated object detection and avoidance pre-crash detection system.

"Test Methods and Results for Sensors in a Pre-Crash Detection System," Charles Birdsong, Peter Schuster, John Carlin, Daniel Kawano, William Thompson [*abstract accepted*]

Automobile safety can be improved by anticipating a crash before it occurs and thereby providing additional time to deploy safety technologies. This requires an accurate, fast and robust pre-crash sensor that measures telemetry, discriminates between classes of objects over a range of conditions, has sufficient range and area of coverage surrounding the vehicle. The sensor must be combined with an algorithm that integrates data to identify threat levels. No one sensor provides adequate information to meet these diverse and demanding requirements. However the requirements can be met with an optimal combination of multiple types of sensors. Previous work considered criteria for evaluating various sensors to find an optimal combination. This work presents test methods and results for a

set of sensors proposed for use in a pre-crash detection system. The test methods include static and dynamic telemetry testing to identify the range, accuracy, reliability and operating conditions for each sensor. Each sensor is evaluated for its ability to discriminate between classes of objects. The tests are applied to ultrasonic, laser range finder and radar sensors. These sensors were selected because they provide the maximum information, cover a broad range and region and are commercially viable in passenger vehicles.

Initial sensor algorithms developed

Algorithm development is an important component of this work. The following work was completed in the first year. This area of research is expected to be the main focus in the next phase of work after the individual sensors have been evaluated:

Bi-Static Radar

Preliminary algorithms were developed for bi-static RADAR. This effort included simulation of prediction at different impact (or near miss) speeds. Three scenarios were examined at 20mph (~8.9 m/s) and 40mph (~17.9 m/s):

1. Impact with the front center of the vehicle
2. Impact with the front of the vehicle 0.25m inside the right fender
3. Near miss 0.25m outside the right front fender of the vehicle

A similar study consisted of the "Predicted Distance vs. Bi-static Distance" as this analysis shows that the predicted distance is a function of position and direction of travel and not of actual speed. Another simulation was performed of an object crossing in front of the vehicle at 1m, 2m, and 3m. Also the effect of noise was analyzed.

Ultrasonic

Several algorithms were developed to process data from an ultrasonic range finder. The algorithms focused on maximizing the accuracy and response time. Fixed and variable sampling rates were studied. Also filtering was studied to reduce measurement noise.

Multi-Disciplinary Project Based Learning

One of the objectives of this project was to foster learning and research at Cal Poly. This was accomplished by involving students from different levels and backgrounds. An electrical engineering graduate student was the center of the student team. He provided knowledge and skills in electronics and programming. In addition, two mechanical engineering seniors and one mechanical engineering sophomore worked on the project.

The following two senior projects were generated from this project.

- "Feasibility of using low-cost ultrasonic sensors for vehicle pre-crash sensing," Daniel Kawano
- "Testing vehicle for pre-crash sensors," William Thompson

In addition the project objectives and status was presented at the following seminars:

- Cal Poly Student Section of Society for Automotive Engineers, winter 2005

- Cal Poly Student Section of American Society for Mechanical Engineers, winter 2005
- Cal Poly Graduate Seminar, winter 2005

Recommendations for Future Work

The goals of the next phase of this project include:

- Complete sensor characterization
- Sensor fusion
- Develop algorithms
- Address object discrimination
- Interdisciplinary teamwork
- Publish work in SAE conference

Sensor Characterization: We have completed characterization of the infrared and ultrasonic sensors. Characterization of the radar and laser sensors is ongoing. This work requires initiating communication with the sensors through CAN Bus and RS232 communication, developing software to control and read the data and conducting laboratory tests to quantify the performance relative to the application of human sensing and pre-crash detection. All the necessary hardware has been acquired. The development is suitable for undergraduate students.

- Infrared: completed
- Ultrasonic: completed
- Radar: in progress
- Laser: in progress

Sensor Fusion: The next task consists of combining the information from different sensor hardware and software into one system where the data can be combined in an optimum way. This will require software development in a programming environment such as Labview. The key factors will be synchronizing the signals so that all data can be used to accurately determine target telemetry. Maximizing the sampling rate of the system is another important priority. Each sensor has a different sampling rate making the fusion a challenge.

Develop Algorithms: Once all the sensor data streams are integrated we will develop algorithms that combine the data to predict a crash and perform object discrimination. The objectives of the algorithm development are to provide the maximum quantity of information as early as possible in a possible crash scenario. In addition the system must not produce false positive signals so attention must be given to rejecting noise and tuning the system to meet the objectives.

Object Discrimination: In addition to object detection a goal of the project is to discriminate between inanimate objects and humans to meet the needs of protecting pedestrians. Some of the sensors provide signals in addition to telemetry that can be used for this purpose. Work must be done to develop an independent algorithm that combines the discrimination signals to meet this goal.

Interdisciplinary Teamwork: This project requires mechanical, electrical and computer science skills. We anticipate more of a focus in the area of computer science in the next phase of work

due to the needs for algorithm development. There is also potential to coordinate and cooperate with the DARPA Challenge team as they have similar objectives as this project.

Publications: We anticipate publishing a second paper related to this work, at the SAE World Congress. Our literature review shows that few papers have been published in this area. It is our conclusion that much of this work is being done by private industry without publication to protect proprietary development. This creates an opportunity to break ground in the academic development of this technology. Our first paper described the objectives of the human sensing project and pre-crash detection and compared individual sensors. The second paper will describe our experimental results for each individual sensor and propose an algorithm for sensor fusion. We anticipate publishing a third paper after the entire system is integrated and optimized.

Test Methods and Results for Sensors in a Pre-Crash Detection System

Charles Birdsong, Ph.D., Peter Schuster, Ph.D., John Carlin, Daniel Kawano, William Thompson
California Polytechnic State University, San Luis Obispo, California

Abstract

Automobile safety can be improved by anticipating a crash before it occurs and thereby providing additional time to deploy safety technologies. This requires an accurate, fast and robust pre-crash sensor that measures telemetry, discriminates between classes of objects over a range of conditions, has sufficient range and area of coverage surrounding the vehicle. The sensor must be combined with an algorithm that integrates data to identify threat levels. No one sensor provides adequate information to meet these diverse and demanding requirements. However the requirements can be met with an optimal combination of multiple types of sensors. Previous work considered criteria for evaluating various sensors to find an optimal combination. This work presents test methods and results for a set of sensors proposed for use in a pre-crash detection system. The test methods include static and dynamic telemetry testing to identify the range, accuracy, reliability and operating conditions for each sensor. Each sensor is evaluated for its ability to discriminate between classes of objects. The tests are applied to ultrasonic, laser range finder and radar sensors. These sensors were selected because they provide the maximum information, cover a broad range and region and are commercially viable in passenger vehicles.

Outline

I. Introduction

II. Test Methods

A. Static Tests

1. Range
2. Accuracy
3. Reliability
4. Environmental Factors
5. Vibration

B. Dynamic Tests

1. Accuracy
2. Sensitivity to Direction
3. Near Miss

C. Object Discrimination

III. Test Results

A. Ultrasonic

B. LIDAR

C. RADAR

IV. Future Work

V. Conclusions

Evaluation of Cost Effective Sensor Combinations for a Vehicle Precrash Detection System

John Carlin, Charles Birdsong, Ph.D., Peter Schuster, Ph.D., William Thompson, Daniel Kawano

California Polytechnic University, San Luis Obispo

Copyright © 2005 SAE International

ABSTRACT

The future of vehicle safety will benefit greatly from precrash detection – the ability of a motor vehicle to predict the occurrence of an accident before it occurs. There are many different sensor technologies currently available for pre-crash detection. However no single sensor technology has demonstrated enough information gathering capability within the cost constraints of vehicle manufacturers to be used as a stand alone device. A proposed solution consists of combining information from multiple sensors in an intelligent computer algorithm to determine accurate precrash information. In this paper, a list of sensors currently available on motor vehicles and those that show promise for future development is presented. These sensors are then evaluated based on cost, information gathering capability and other factors. Cost sensitivity is lower in large commercial vehicles

than in personal vehicles due to their higher initial cost and longer life span making them a good candidate for early adoption of such a system. This work forms the basis for ongoing research in developing an integrated object detection and avoidance precrash detection system.

INTRODUCTION

Improving occupant safety has been an increasingly important area of study since the mid 1960's. Initially this work was centered on controlling post impact occupant dynamics through the use of structural modifications, seatbelts, and airbags. The idea of using external sensors to improve vehicle safety is similarly not a new one 1, 2. Ultrasonic sensors are commonly used today as parking aids on vehicles with large blind spots and

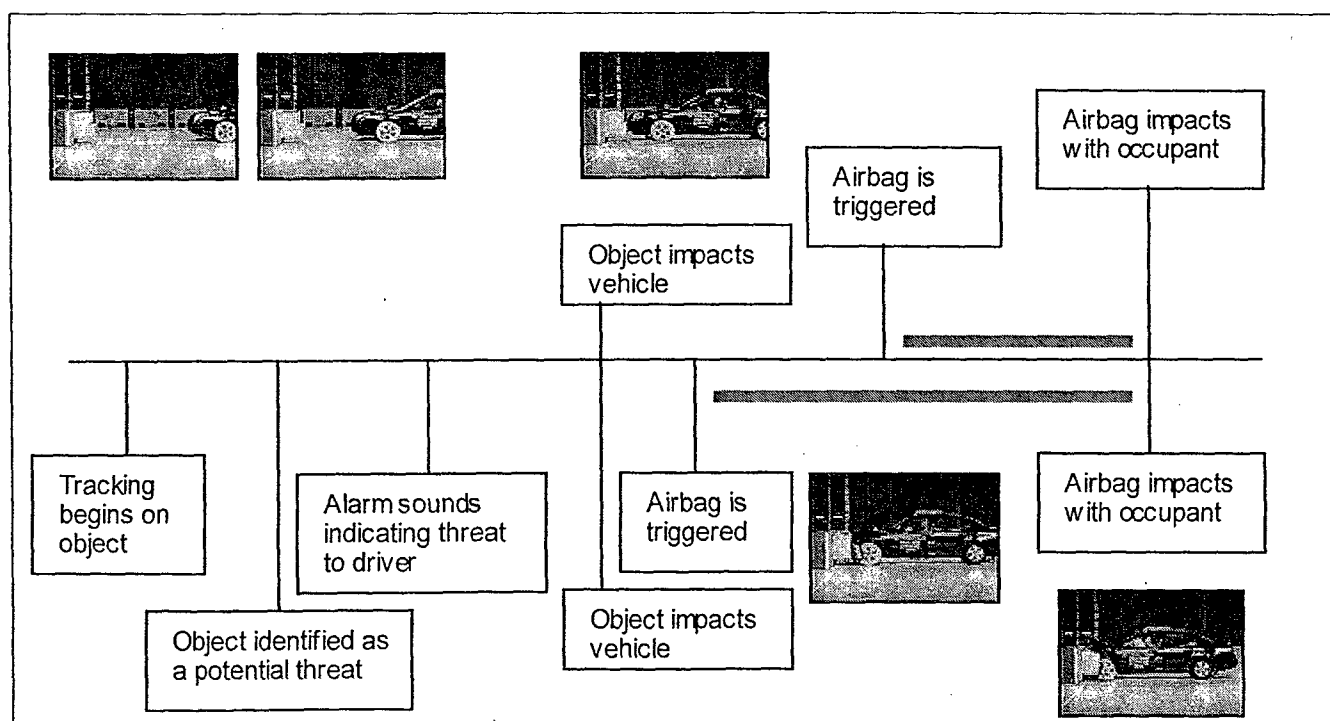


Figure 1 – Timelines for collisions with and without precrash sensing

radars are used in adaptive cruise control (ACC) systems to maintain safe following distance when cruise control is active.

We will identify a possible set of requirements for precrash sensing and survey the current state of the art for a variety of sensor technologies. In comparing the sensor technologies we compare not only the capabilities of the various sensors but also the cost and overhead of including such a sensor on a vehicle as this is an important part of system acceptance. Furthermore a possible group of sensors is presented that is expected to meet these requirements.

It is anticipated the initial implementation of a precrash sensing system will be on less cost-sensitive vehicles such as luxury cars and large commercial vehicles. In particular, commercial vehicles have a higher initial cost, longer life span, and greater liability from accident occurrence. This makes them good candidates for early adoption of such a system.

Improving occupant safety beyond existing standards requires more information than is currently gathered by automobiles during an impact. Currently when an accident occurs the airbag sensors trigger the airbags within 10ms of the impact. The initial goal of a pre-crash system would be to bias the decision made by the impact sensors allowing for triggering based on expected impact severity. Coupled with seat belt pre-tensioning the number and severity of occupant injuries could be greatly reduced. Figure 1 shows an example impact where the precrash system triggers the airbags early, reducing the pressure required for inflation, and thereby reducing the contact force with the occupant.

The ability to predict accidents beyond the immediate event horizon has a number of other advantages. According to 1 in 49% of accidents the brakes are not used at all. By predicting that a collision is imminent a system could activate the brakes prior to the collision reducing the severity of the impact. Furthermore the airbags could be triggered prior to impact further reducing the force of inflation and the risk of deployment related injuries.

REQUIREMENTS OF A FRONTAL PRECRASH

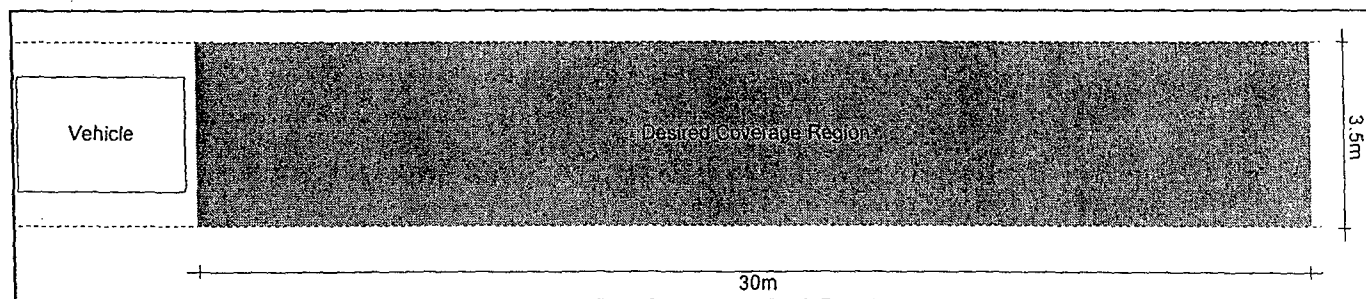


Figure 2 - Coverage Region of Suggested System

SYSTEM

To aid in evaluating how sensor technologies fit into the picture of precrash sensing it is important to establish what the system as a whole must be able to do. The system must not produce false positives and have a low occurrence of false negatives to provide value. Furthermore the system should be able to determine when it will not be effective due to road or weather conditions and inform other portions of the vehicle electronics and the driver that the system is not providing a benefit.

The system must be able to respond to threats in a timely manner. There are two different facets of system response time that, while related, need to be discussed separately. First there is the issue of how long the system takes to begin tracking a threat once it has entered the forward path of the vehicle. This response time will be dependant on the technical limitations of sensor covering the area in which the threat exists. The second type of system response time is related to the time required for the system to tag the object as a likely threat and notify the driver or take protective measures. This is a more difficult issue to address because while it is in part reliant on the technical limitations of system components the major factor is the accuracy of the collision prediction model used.

Defining the coverage region is a somewhat arbitrary task without specifically defining the vehicle and conducting an exhaustive survey of when driver warnings and other preventative measures are best performed. However one must be defined as a starting place. To this end it seems reasonable to gather data about objects in the same lane of travel as the vehicle. The distance from the front of the vehicle that should be covered should be far enough to detect objects traveling at high speed, but not so far as to provide information about objects for which predictions are dubious at best. To meet these requirements the minimum region of coverage for the system is defined to be an area 3.5m wide and 30m long in front of the vehicle as shown in Figure 2. This is based on travel lane width in the United States and the distance traveled by a vehicle going 60mph in 1 second.

A precrash sensing system must also be able to differentiate objects that are not threats to the vehicle from those that are. Table 1 gives a list to object types that should be identified and some example objects for each type.

Type of object	Example object
Large high mass	Tree, other vehicle
Large low mass	?

Medium high mass	Motor cycle, cow
Medium low mass	Pedestrian
Small high mass	Road barrier

Table 1 – Possible threat objects

Finally there are several constraints on the system. Most of them are typical for automotive electronics such as temperature, humidity, and vibration. The incremental cost of such a system is a serious constraint and as a result the chosen sensors should be integrated into other, pre-existing applications such as Active Cruise Control (ACC). Finally sensors must be placed on vehicles in such a way that the coverage of the sensor is not severely limited due to occlusion.

POSSIBLE SENSORS

As a first step toward an integrated precrash sensing system this study will initially focus on sensors that provide telemetric data rather than classification data regarding the object of interest. In identifying possible sensors for this task it is important to understand a variety of issues including the coverage zone that each sensor is capable of providing information for, the type of information provided by each of the sensors, and cost of the sensor. Table 2 gives a summary of these factors for each of the technologies covered in this survey for typical

	Ultrasonic	LIDAR	RADAR	Bi-Static	Vision	AIR	PIR
Cost	Low	High	High	Medium	Low	Low	Low
Computation Overhead	Low	High	Medium	Medium	High	Low	Low
Range			1m to 150m				
Operating Conditions			Normal to heavy rain or snow				
Commercially Available	Yes	Yes	Yes	No	Yes	Yes	Yes
Industry Acceptance	High	None	Some	None	None	None	None
Accuracy			±1.0m				
Update Frequency	40Hz		10Hz				
Potential for Object Discrimination	Low	Some	Low	Low	High	None	Low
Detection Capabilities	Distance	Distance, speed, geometry	Distance, speed, power	Distance	Distance, speed, geometry, object class data	Presence	Presence
Target Size			Motorcycles and larger				

Table 2 - Comparison Matrix of Current Sensor Technologies

state of the art sensors of each type.

ULTRASONIC SENSORS

Ultrasonic sensors have the advantage that they are already integrated into the front and rear bumpers of many vehicles for backup and parking assist. The low cost of ultrasonic sensors means they can be placed on the vehicle in such a manner as to cover any region of interest adjacent to the vehicle.

Backup and parking aid ultrasonic sensors work by sending out a high frequency pulse and measuring the time until the echo is received. Using this method of operation they have no ability to determine the target angle or speed.

Individually a typical ultrasonic sensor has an aperture of roughly 45° and has a maximum range of 10m, so in practice three or four sensors are combined to cover either the front or rear bumper of the vehicle. This arrangement is made out of expedience rather than any technical limitation of the sensors themselves. Next generation sensors could use a single transmitter and combine the receivers in a phased array fashion to provide location information in a manner not dissimilar from the way many submarine sonar systems work.

LASER

Laser Imaging Detection and Ranging (LIDAR) sensors work in a manner similar to the ultrasonic sensors. The primary difference is that because of the small beam

diffraction of the lasers involved, a fixed laser will not cover more than a small point directly in front of the laser. To overcome this deficiency a mirror or prism can be used to scan the beam over various angles. This means that the update rate of a LIDAR is inversely proportional to the angle of coverage.

LIDAR systems can measure distance with high accuracy. Additionally they can be made to measure object speed based on the Doppler shift of the return signal. Combined with the correct computer algorithm these systems can also provide information regarding target geometry in the scanning 6.

Because of the point source nature of a LIDAR system they generally do not have wide coverage cones. This means that close to the vehicle the LIDAR will have blind spots as shown in Figure 7.

Because LIDAR systems rely on the ability of light to travel through whatever medium is between the source and the target their capabilities are dependant of the presence of airborne particulates. Military systems have been designed with enough power to overcome all but the most dense clouds of particulate, but such systems can easily damage the human eye and would be inappropriate for use on civilian vehicles.

RADAR

Classically RADio Detection And Ranging (RADAR) has been the province of aircraft and air traffic control systems. More recently Doppler based systems have

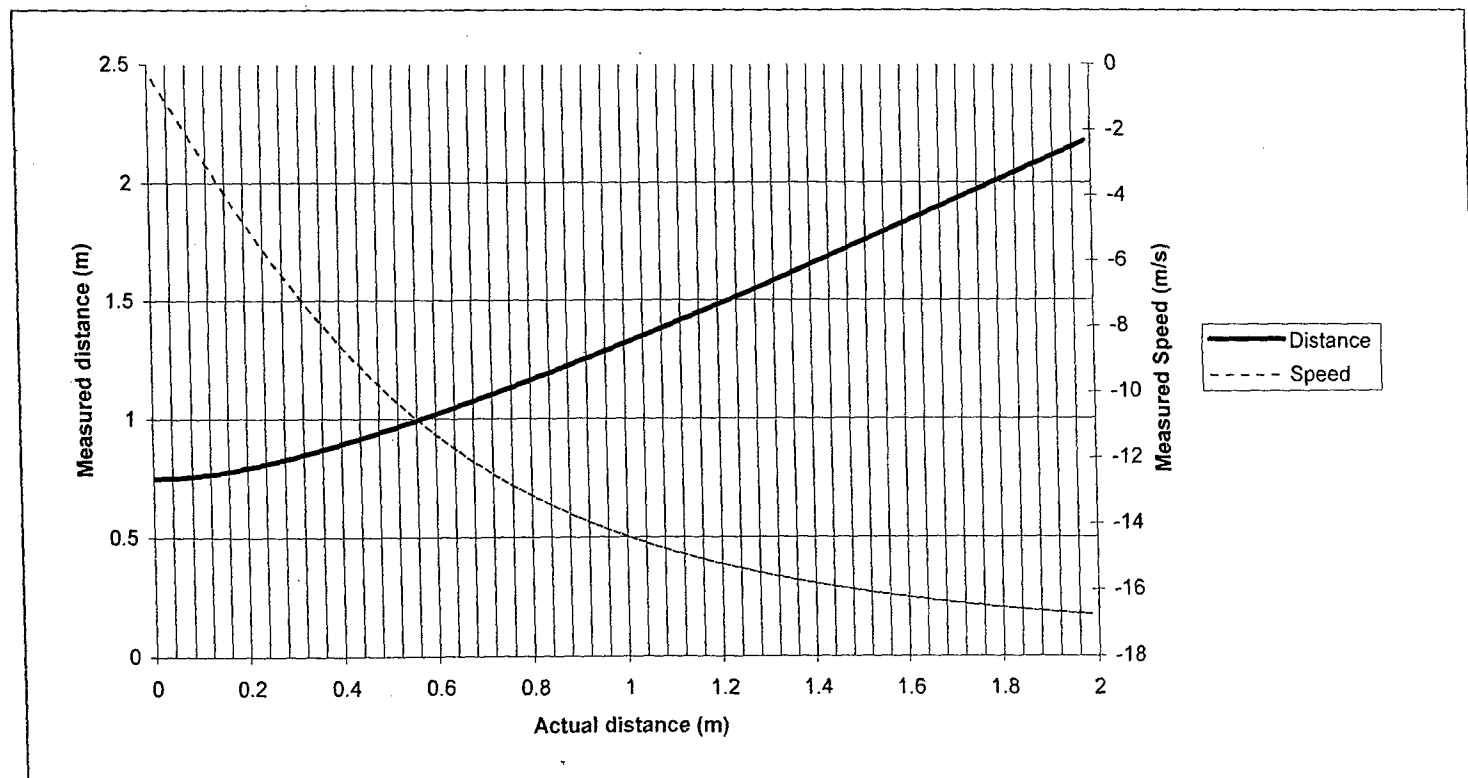


Figure 3 - Measured Distance and Speed vs. Actual distance from Vehicle Front for bi-static radar for Object with 40mph collision

been used in traffic speed enforcement and other civilian applications. Currently radars are being used as an aid for cruise control systems to reduce driver interaction. It is these Active Cruise Control (ACC) radars that maybe adapted for use in pre-crash sensing.

Radars have the capability to measure both object location and speed. ACC radars are capable of covering most of the region of interest for pre crash sensing. Like the LIDAR systems they have trouble detecting objects adjacent to the vehicle, however they are not as limited as LIDAR in the width of the coverage cone.

Radars can operate under nearly all practical driving conditions, although airborne particulates such as rain or snow will reduce the effective range.

BI-STATIC RADAR

Bi-static radars operate in much the same way as conventional (mono-static) radars. The difference is that the transmitter and receiver are not collocated. This means that the distance returned by such a system is actually the distance from a point halfway between the transmitter and receiver. Due to the complexity involved in simultaneously controlling both the receiver and transmitter, scanning bi-static radars are uncommon, so most systems only return the distance to the nearest object. Because of the nature of the system each distance represents an ellipse rather than a circle with the transmitter and receiver being the foci of the ellipse. As a result, an object traveling on a straight path with constant speed will appear to have acceleration. Figure 3 shows an example of this with simulated objects on an impact path with the front of the vehicle at 40mph.

Bi-static radars are currently in development for use as close-in sensors to predict side impacts. Such systems work by collecting distance, speed, and acceleration information from a target. Then, using statistical means, they determine the probability that the target will impact the vehicle. Currently proposed systems place the transmitter at either the A-pillar or the C-pillar of a occupant vehicle and the receiver at the other pillar. By placing the transmitters on opposite pillars the same number of antenna could be used to cover not only the sides but also the front and rear of the vehicle. This type of system could replace Ultrasonic sensors in precrash sensing and as parking aids.

The coverage region of a bi-static radar is naturally elliptical in nature. The possible range of a bi-static

radar exceeds what is needed by precrash sensing. In operation bi-static RADAR use the same fundamental principals as conventional RADAR and have the same range of environmental conditions.

VISION

When discussing vision systems we are really discussing three different types of systems: visible light, passive infrared vision (PIRV), and active infrared vision (AIRV). Vision - primarily visible light - systems have been

presented in the literature, 3 and 1, as means of solving many of the problems related to pre-crash sensing. This is in no small part due to the

fact that vision systems are what humans use as our primary sensor for vehicle control. In fact vision sensors are the only sensor presented that would be able to cover the entire region of interest effectively while collecting control related information at the same time.

Vision sensors also collect data far beyond the telemetry data collected by most other sensors presented in this survey. Figure 4 shows an example of this. Based on this image we can tell that the road being traveled on is about to make a right turn, it is relatively flat, there are two lanes of travel, and most importantly there are no objects in the probable path of travel that present a danger to the vehicle.

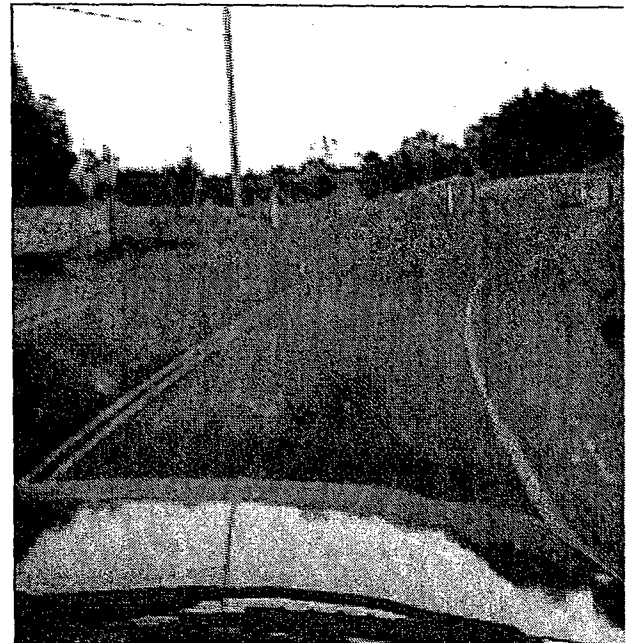


Figure 4 - Typical road scene

The biggest drawback of vision systems of any type is not the sensors themselves but rather the computational overhead associated with extracting the information that most human drivers can gather from a scene almost instinctively. Figure 5 shows lane makers detected using the Hough transform, a well understand algorithm for finding lines in images. This process alone is no trivial task 7; and this is just a small piece of the information that could be extracted from the scene.

Additionally, vision sensors themselves do not provide any telemetry data about objects in the scene. This data has be to gathered either with a separate sensor or inferred from a second vision sensor using stereovision triangulation.

Unlike the human eye, CMOS or CCD vision sensors do not automatically adjust to scene light and contrast. They must be tied to a system that correctly estimates the amount of light present and adjusts the gain of the sensor appropriately. This must happen rapidly and accurately as light conditions can change dramatically during either sunset or sunrise.

The final drawback to vision based systems, especially visible light systems, is that their performance degrades rapidly in the presence of airborne particulates such as dust or precipitation. This problem is made worse by the fact that the conditions under which these sensors provide the least benefit are those in which the drivers need for such a system are the greatest.

NON-VISION PASSIVE INFRARED (PIR)

PIR sensors are commonly used in motion detectors for alarm systems as well as in automatic doors. These systems are robust and have low maintenance.

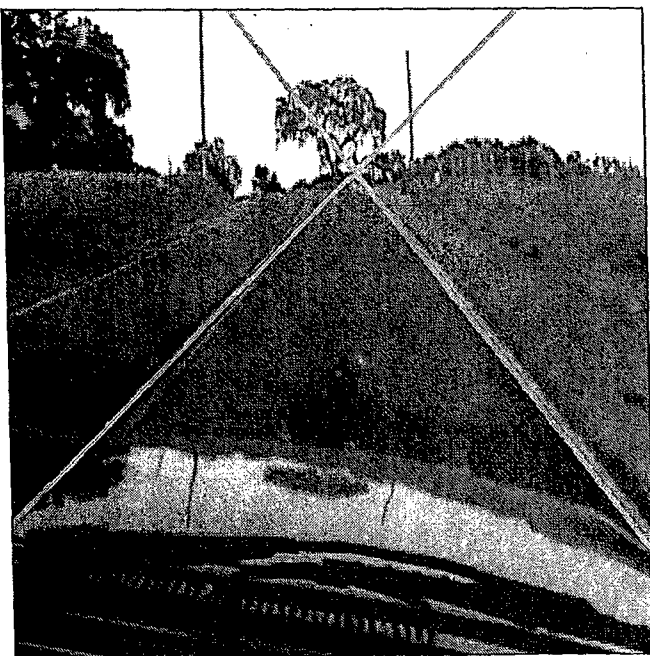


Figure 5 – Road scene with lane markers identified

However they are inappropriate for use in pre-crash sensing since they rely on a known ambient null condition on which to base decisions regarding the presence of objects. For example at sunrise or sunset the sun produces far in excess of enough IR to trip such a system. While this condition can be accounted for in a fixed system it is likely to have problems on a platform that moves.

NON-VISION ACTIVE INFRARED (AIR)

AIR systems are used in many industrial and commercial applications to determine the presence of objects, including people. Direct AIR systems work with an emitter and detector that placed at separate locations and aimed such that light from the emitter travels to the detector. Such systems detect objects when the detector no longer receives a signal from the emitter. Reflected systems work in much the same way except that they rely on a reflective surface to bounce the light from the emitter to the detector. Such a system relies on the emitter producing enough light to illuminate the target object so that it reflects more IR light than is present in the background.

AIR systems do not use time of flight measurements to collect distance information, but rather relay on the presence or absence of a return signal to determine if an object is present. Some systems exist that use the strength of the return signal to determine distance, however the distance measurements are only valid for objects whose reflectivity characteristics match the calibration object.

The primary limit to the range of an AIR system is the power and cost of the emitter. Focusing lenses on both the transmitter and receiver can be used to increase the range of the system as the cost of reducing the aperture.

As a result of their wide use and acceptance of AIR systems might seem to be a perfect fit for precrash sensing. The drawback of these types of sensors is that they only provide presence information. Considering that AIR systems are only slightly less expensive than ultrasonic systems and they only provide presence information rather than presence and distance they do not appear to be cost effective.

SUGGESTED SENSOR SYSTEMS

The primary goal of this system is to detect objects and gather telemetry information from them. A secondary goal is to collect classification data about the objects that have been identified as a threat. While there are any number of sensor combinations, sensors must be selected based not only on performance but also cost, availability, acceptance and maturity. To this end the following three sensors have been selected for further investigation: Radar, Ultrasonic, and LIDAR. This

range of environmental conditions at the highest rate of speed. Radars are one of the most expensive sensors available; however, since they are an integral part of ACC systems that are now becoming popular on commercial and luxury vehicles the incremental cost of adding this to the system is lowered. Figure 6 shows the relationship between the desired coverage region and the region covered by an ACC radar.

The scanning laser or LIDAR is selected to be a complement to the radar. While current systems are not as fast as the radar they provide us with additional

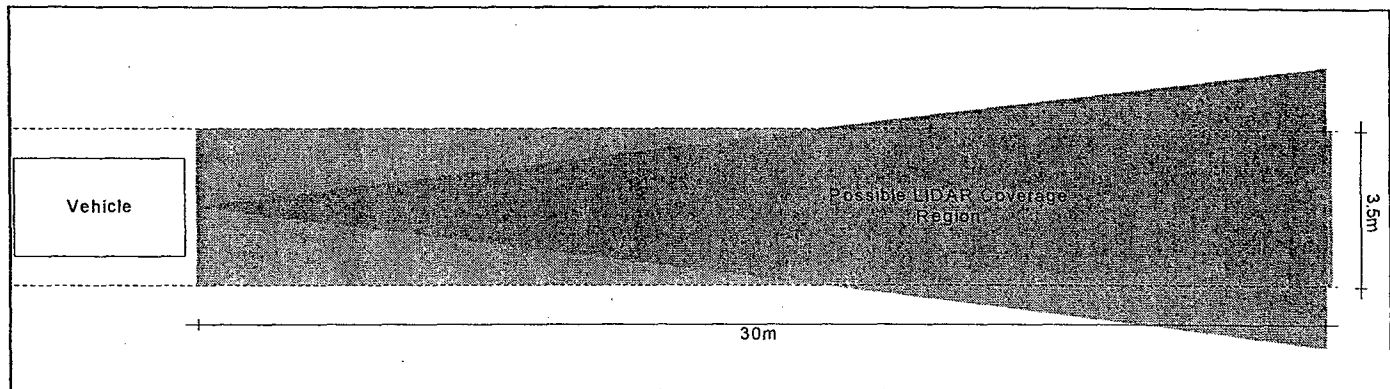


Figure 7 - LIDAR coverage region overlaid on suggested coverage region

means that the entire region of interest, except that right in front of the vehicle, is covered by two of the three sensors. There are no doubt combinations with higher performance or lower cost. Given that the cost and capabilities of each of the sensor technologies is constantly changing it is important to bear in mind that in the future there may be different and better combinations.

The radar was chosen for the simple reason that it gathers the most telemetry information under the widest

information: First, the ability to provide some indication of object geometry is important and can be used to predict how the vehicle will deform during the impact. Second when used in combination with the radar the system should be able to determine when there is a fault and indicate this to the driver. Thirdly there is the possibility of object discrimination based on the type of signal from each sensor. **Figure 7** shows one possible coverage region for a scanning LIDAR, note that a LIDAR could be designed to have an arbitrary aperture.

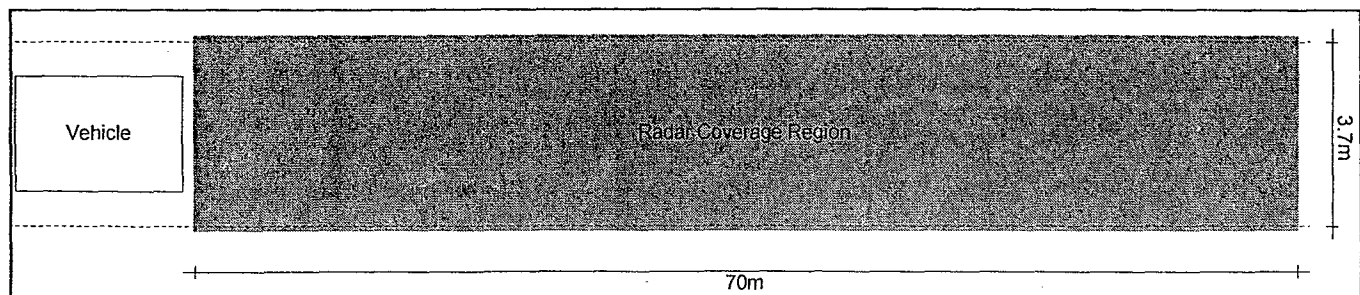


Figure 6 - Radar coverage region.

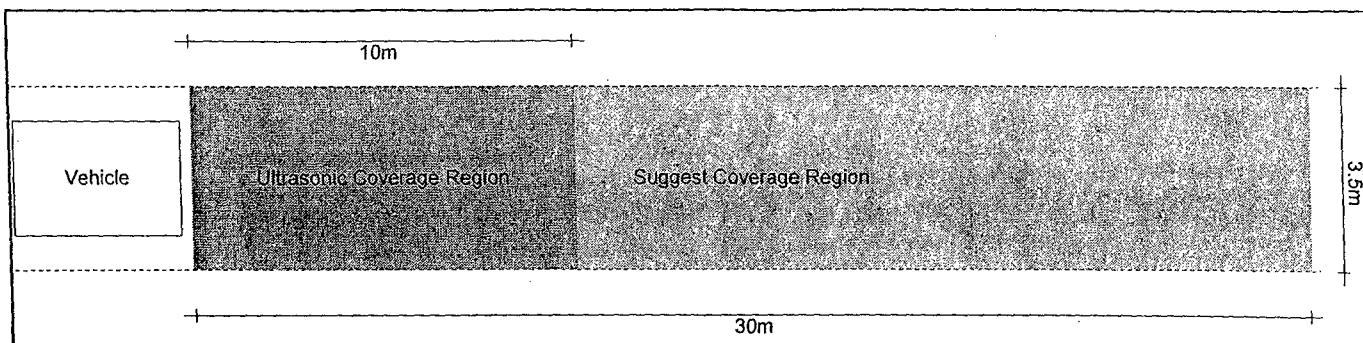


Figure 8 - Ultrasonic coverage region as compared to system coverage region

Ultrasonic sensors were selected as they are already common on vehicles today, they are inexpensive, and they cover an area directly in front of the vehicle that is not commonly covered by other available sensors. The region that they do cover is possibly the most important as it is where the data has the highest degree of validity and the prediction of an impact is most reliable. Figure 8 shows the portion of the region of interest covered by Ultrasonic sensors.

SYSTEM FUNCTIONALITY

The proposed system would work by first identifying the presence of an object using the RADAR. The object is then tracked using both the RADAR and the LIDAR so long as it is in the region of interest. At this point the system would begin to make predictions regarding the likely hood that the object will collide with the vehicle and at what closing velocity. As the object gets close enough the Ultrasonic sensor tracks it and the system alerts the vehicles active safety systems of the likelihood of an imminent impact, along with information regarding the possible seriousness of the impact.

FUTURE WORK

While all of the above sensors are specified by their manufactures, for most of them there is sparse information regarding their performance relative to precrash sensing. A uniform test procedure needs to be established and the sensors need to be individually tested against a variety of objects under simulated environmental conditions. This is the next step of our research plan.

This paper has addressed the needs of precrash sensing as they relate to vehicles approaching objects in the path of travel. An important extension to this is expanding the coverage region so that a precrash system could potentially predict object approaching from the sides such as at an intersection.

Finally an algorithm must be developed that relates telemetric data of an object to the probability of impact. This involves not only generating significant simulations, but also real world testing to ensure that the simulations are representative.

CONCLUSION

A survey comparing the cost and capabilities of current state of the art sensor technologies has been present for use in intelligent vehicle design. A possible set of requirements for a precrash sensing system has been laid out. A framework for integrating several sensors together to meet these requirements has been presented.

ACKNOWLEDGMENTS

This research was funded by grant from the Office of Naval Research (ONR) through the California Central Coast Research Partnership (C3RP). We would like to thank Delphi for providing us with two radar systems for our use and evaluation.

REFERENCES

1. Knoll, Peter, Schaefer, Bernd-Josef, Guettler, Hans, Bunse, Michael, & Kallenbach, Rainer, *Predictive Safety Systems - Steps Towards Collision Mitigation*, SAE 2004 World Congress & Exhibition, March 2004, Detroit, MI, USA, Session
2. Breed, David, Sanders, W. Thomas, & Castelli, Vittorio, *A Complete Frontal Crash Sensor System - 1*, SAE S.A.E. transactions. 102, no. 6, (1993): 900
3. Hamilton, Lisa, Humm, Lawrence, Daniels, & Yen Huan, *The Role of Vision Sensors in Future Intelligent Vehicles*, S.A.E. transactions. 110, Part 7 (2001): 613-617
4. Cherry, James, *Applications of Ultrasonic Technology for Obstacle Detection*,
5. Cartwright, Kert & Jindal, Gopi, *An Ultrasonic Proximity System for Automobile Collision Avoidance*,
6. Beraldin, J.-A., Rioux, M., Livingstone, F.R., King, L., *Development of a Real-Time Laser Scanning System for Object Recognition, Inspection, and Robot Control*, SPIE Proceedings, Telemanipulator Technology and Space Telerobotics. Boston, Massachusetts, USA. September 7-10, 1993. Vol. 2057, pp. 451-461

7. Chen, Ling, Chen, Hongjian, Pan, Yi, Chen, Yixin, A *Fast Efficient Parallel Hough Transform Algorithm on LARPBS*, The Journal of Supercomputing 29, no. 2 (2004), pp 185-195

Feasibility of Using a Low Cost Ultrasonic Sensor for Vehicle Pre-Crash Sensing

by

Daniel Takashi Kawano

**Mechanical Engineering Department
California Polytechnic State University**

San Luis Obispo

2005

Statement of Disclaimer

Since this project is a result of a class assignment, it has been graded and accepted as fulfillment of the course requirements. Acceptance does not imply technical accuracy or reliability. Any use of information in this report is done at the risk of the user. These risks may include catastrophic failure of the device or infringement of patent or copyright laws. California Polytechnic State University at San Luis Obispo and its staff cannot be held liable for any use or misuse of the project.

Table of Contents

Acknowledgments.....	v
List of Tables	vi
List of Figures	viii
Nomenclature.....	xii
Abstract.....	xiv
Chapter	
1 Introduction.....	1
1.1 Background of the Project	1
1.2 Objective of the Project	2
1.3 Problem Definition.....	2
2 Survey of the State-of-the-Art	4
3 Design Development.....	7
3.1 Design Requirements	7
3.2 Analysis.....	9
3.3 Conceptual Design Alternatives	14
4 Description of the Design	16
4.1 The Design	16
4.2 Initial Testing Demonstrating Proof-of-Principle.....	18
5 Static-Static Testing.....	27
5.1 Testing Procedure	27
5.2 Results of the Testing.....	28
5.3 Conclusions from the Testing	32
6 Sonic Cone Testing.....	34
6.1 Testing Procedure	34
6.2 Results of the Testing.....	36
6.3 Conclusions from the Testing	37

7	Clutter Testing	39
7.1	Testing Procedure	39
7.2	Results of the Testing.....	40
7.3	Conclusions from the Testing.....	42
8	Static-Dynamic Testing	44
8.1	Testing Procedure	44
8.2	Results of the Testing.....	47
8.3	Conclusions from the Testing.....	52
9	Final Conclusions and Recommendations	53
9.1	Other Considerations	53
9.2	Summary of the Conclusions and Recommendations	55
	Appendix A Detailed Schematics and Parts List	57
	A.1 Detailed Sensing System Schematics	57
	A.2 Addition of the String Potentiometer.....	63
	A.3 Parts List	68
	Appendix B Supporting Derivations.....	69
	B.1 Displacement and Average Velocity	69
	B.2 Equation of Motion for a Ball Falling through Air.....	81
	B.3 EES Code for Solving the Equation of Motion for a Ball Falling through Air	84
	References.....	85

Acknowledgments

I would like to thank the following individuals for their assistance and contributions to this senior project as part of the Cal Poly Human Sensing Project:

Dr. Charles Birdsong

John Carlin

Dr. John Ridgely

Dr. Peter Schuster

Will Thompson

List of Tables

Table 1	Decision matrix for determining whether to use an off-the-shelf ultrasonic sensor or to construct one	15
Table 2	Decision matrix for determining the most effective method for acquiring data.....	15
Table 3	Actual distance between the file cabinet and sensor compared to data from the sensor.....	19
Table 4	Distance and average velocity calculated from the first 12 time intervals for the sensor and the positioner moving away from the sensor.....	23
Table 5	Distance and average velocity calculated from the first 12 time intervals for the sensor and the positioner moving toward the sensor.....	23
Table 6	Distance data for a box from the ultrasonic sensor as compared to the measured distance for the static-static testing.....	29
Table 7	Distance data for a ball from the ultrasonic sensor as compared to the measured distance for the static-static testing.....	30
Table 8	Distance data for a round metal column of 0.205 m diameter from the ultrasonic sensor as compared to the measured distance for the static-static testing.....	30
Table 9	Distance data for a vehicle rear bumper from the ultrasonic sensor as compared to the measured distance for the static-static testing.....	31
Table 10	Distance data for a pedestrian from the ultrasonic sensor as compared to the measured distance for the static-static testing.....	31
Table 11	Number of data samples from the sensor as a function of vehicle or target speed	33
Table 12	Distance data from the ultrasonic sensor as compared to the measured distance between it and the midpoint of a box placed at various distances from and along the centerline	36
Table 13	Measured distance to the edge of a vehicle front bumper as compared to distance data from the sensor with a pole used as a clutter object.....	42

Figure 17	Absolute deviation as a function of displacement for various target objects used in the static-static testing	32
Figure 18	Depiction of the sonic cone testing setup	34
Figure 19	Experimental setup for the sonic cone testing	35
Figure 20	Depiction of the possible displacement range detected by the sensor for the sonic cone testing	35
Figure 21	Depiction of the ultrasonic sensor's sonic cone.....	37
Figure 22	Experimental setup for the vehicle-pole clutter test	39
Figure 23	Vehicle-pole clutter test setup.....	40
Figure 24	Experimental setup for the vehicle-vehicle clutter test.....	41
Figure 25	Vehicle-vehicle clutter test setup.....	41
Figure 26	Experimental setup for the static-dynamic testing.....	45
Figure 27	Close-up of the string pot.....	45
Figure 28	Ultrasonic sensing system with the string pot included.....	46
Figure 29	Static-dynamic testing setup	46
Figure 30	Close-up of the static-dynamic testing setup	47
Figure 31	Displacement of a box away from the ultrasonic sensor as a function of time as compared to the displacement measured by the string pot	48
Figure 32	Displacement of a column away from the ultrasonic sensor as a function of time as compared to the displacement measured by the string pot	48
Figure 33	First test for the displacement of a pole away from the ultrasonic sensor as a function of time as compared to the displacement measured by the string pot	49
Figure 34	Second test for the displacement of a pole away from the ultrasonic sensor as a function of time as compared to the displacement measured by the string pot	49

Figure 35	Third test for the displacement of a pole away from the ultrasonic sensor as a function of time as compared to the displacement measured by the string pot	50
Figure 36	Displacement of a vehicle rear bumper away from the ultrasonic sensor as a function of time as compared to the displacement measured by the string pot	50
Figure 37	Displacement of a pedestrian away from the ultrasonic sensor as a function of time as compared to the displacement measured by the string pot	51
Figure 38	Absolute deviation as a function of displacement for various target objects used in the static-dynamic testing.....	51
Figure 39	CAD drawing of the ultrasonic sensor.....	57
Figure 40	Color-coded wires from the sensor hooked up to the I/O connector block.....	58
Figure 41	LabVIEW™ algorithm used to generate an input pulse and acquire data from the ultrasonic sensor	60
Figure 42	Prompting the user to choose a location to save collected data to.....	59
Figure 43	Generating an input pulse for the sensor based on time information provided by the user on the front panel	61
Figure 44	Front panel where input pulse characteristics are specified by the user and collected data is displayed.....	61
Figure 45	Measuring the return pulse width, calculating the relative displacement, and displaying the information for the user	62
Figure 46	Measuring the elapsed time per run and displaying the information on the front panel	62
Figure 47	Creating an array of data and saving it to file.....	63
Figure 48	Additional color-coded wires from the string pot hooked up to the I/O block	64
Figure 49	String pot attached to a DC power supply	65
Figure 50	Modified LabVIEW™ algorithm with data acquisition from the string pot	66

Figure 51	Establishing an analog voltage input channel and reading the voltage data from the string pot.....	67
Figure 52	Displaying and saving the distance information from the string pot.....	67
Figure 53	Oscilloscope screen capture of an ultrasonic sensor's output and received signals after having gone through additional computation in the sensor circuitry	69
Figure 54	Diagram showing how the distance between the sensor and an object, Δx , is determined	70
Figure 55	Sensitivity of the distance between the sensor and an object with respect to temperature, relative to a nominal operating temperature of 20°C.....	76
Figure 56	Sensitivity of the distance between the sensor and an object with respect to humidity, relative to a nominal operating temperature and relative humidity of 20°C and 30%, respectively	78
Figure 57	Multiple output and received signals	79
Figure 58	Relative velocity between the sensor and an object moving toward each other	80
Figure 59	Free-body and mass-acceleration diagrams of a sphere falling through air	82

Nomenclature

Variables

A	frontal area of a sphere, m^2
c	speed of sound, m/sec
C_D	drag coefficient
d	degrees of freedom of air molecules
D	diameter of a sphere, m
F	force acting on an object, N
g	gravitational acceleration, m/sec^2
H	humidity, kPa
∂H	variation in humidity, kPa
k	ratio of specific heats
k^*	ratio of specific heats corrected for temperature and humidity
m	mass, kg
M	molecular weight, $\frac{kg}{kmol}$
M^*	molecular weight corrected for temperature and humidity, $\frac{kg}{kmol}$
ν	kinematic viscosity, m^2/sec
P	air pressure, kPa
R	gas constant for air, $\frac{kJ}{kmol \cdot K}$
\bar{R}	universal gas constant, $\frac{kJ}{kmol \cdot K}$
Re	Reynolds number
ρ	density, kg/m^3
S	sensitivity
t	time, sec
T	air temperature, K
∂T	variation in air temperature, $^{\circ}C$
Δt	time it takes for the sensor output signal to reach an object, sec
v, \bar{v}	velocity, m/sec
x	position of a falling sphere, m
\dot{x}	velocity of a falling sphere, m/sec
\ddot{x}	acceleration of a falling sphere, m/sec^2
Δx	distance between the ultrasonic sensor and an object, m
$\partial(\Delta x)$	variation in the distance between the sensor and an object, m
y	fraction of molecules in moist air that are water
ϕ	relative humidity, %
$\partial \phi$	variation in relative humidity, %

Subscripts

1	state 1 of the sensor and object
2	state 2 of the sensor and object
air	property of air
Ar	argon
atm	atmospheric
D	based on the diameter of a sphere
delay	delay between the output and return signals from the sensor
delay,1	delay for state 1
delay,2	delay for state 2
drag	related to the drag acting on an object
g	saturated water vapor
NOP	evaluated at the nominal operating point
N_2	nitrogen
o1	output signal for state 1
o2	output signal for state 2
O_2	oxygen
object	object detected by the sensor
object/sensor	object relative to the sensor
r1	return signal for state 1
r2	return signal for state 2
ref	reference value
sensor	ultrasonic sensor
T	evaluated at temperature T
v	water vapor
w	water
$\Delta x / H$	distance between the sensor and object with respect to humidity
$\Delta x / T$	distance between the sensor and object with respect to temperature

Abstract

Passenger safety in a vehicle can be greatly enhanced by predicting imminent crashes through the use of on-board “smart” sensors. Unfortunately, many of the sensors currently integrated into commercial vehicles are either expensive or are not being applied toward higher-speed pre-crash sensing. Ultrasonic sensors are a low cost alternative to current devices with the potential of application in high-speed pre-crash sensing systems. An ultrasonic sensor can be used to measure the displacement and relative velocity between it and a target object by measuring the time delay between the output and received signals. Since testing of an ultrasonic sensor was the main focus of this project, an off-the-shelf sensor was purchased instead of designing and constructing a device by hand. Furthermore, LabVIEW™ was the chosen method of data acquisition because of its ease of use and user-friendly interface, as compared to other hardware and software such as an oscilloscope and a microcontroller. A LabVIEW™ algorithm was created to read time delay data from the Devantech SRF04 Ultrasonic Range Finder and convert it to a measured displacement. Extensive testing of the sensor (including static, sonic cone, clutter, and dynamic) for a variety of target objects (such as boxes, columns, pedestrians, vehicles, etc.) revealed that the sensor accurately measures the relative displacement between it and the target within the manufacturer’s published range of 3.0 m and sonic cone. It was also found that it may be possible to detect objects at distances greater than 3.0 m, but further testing should be conducted to confirm this. Furthermore, additional testing should be done with more diverse geometries and orientations of the target objects, as well as various placements and orientations of the sensor. Several

issues concerning the data collection algorithm, including a slower than expected data sampling rate, a gradual slowdown in the sampling rate, and implementation of a data filter, should be addressed and resolved. Overall, the ultrasonic sensor performed well and would be a good candidate for use in a vehicle pre-crash sensing system up to a speed of about 20 mph.

Chapter 1

Introduction

1.1 Background of the Project

Ultrasonic sensors are used extensively in industry in applications where conventional optical sensors fail. According to Migatron Corp. [1], some of these applications include liquid level control, thickness gauging, and high speed counting on assembly lines. An ultrasonic sensor can detect an object's presence simply by receiving an echo of the pulse the sensor sent out. An ultrasonic sensor can also be used to determine the distance between it and an object by measuring the time delay between the output and received signals. This simple idea is the basis for this project.

Passenger safety in a vehicle can be greatly enhanced by detecting obstacles and predicting imminent crashes using a variety of "smart" sensors, including radar, vision, and laser devices. Unfortunately, many of these devices are expensive, making it a challenge to manufacture a vehicle with a pre-crash sensing system that is also affordable to the average consumer. Ultrasonic sensors are a low cost alternative with great potential. When integrated into a vehicle body and onboard computer, an ultrasonic sensor can be used to detect the presence of an obstacle, determine how far away it is, and calculate its speed if it is moving. This information can be analyzed to determine if a crash is imminent and, if so, deploy airbags at a rate such that the airbags themselves do not cause harm to the passengers. This information can also be used to employ other passenger safety technologies, including seatbelt tightening to secure a crash victim during impact.

This project is part of a larger research effort, the Cal Poly Human Sensing Project, to investigate low cost alternatives for current vehicle pre-crash sensing systems, including ultrasonic sensors and economical versions of radar, vision, and laser devices.

1.2 Objective of the Project

The objective of this project is fourfold. First, whether a low cost ultrasonic sensor is suitable for accurate distance and velocity measuring will be explored. Second, the effects of environmental conditions, including air temperature and humidity, on the sensor's performance will be examined. Third, extensive testing will be conducted to determine how accurately the sensor measures distance and velocity under a variety of target and road conditions. Lastly, the limitations of the sensor and if any improvements can be made to its performance will be explored. Ultimately, it is desirable to determine whether a low cost ultrasonic sensor is suitable for integration into commercial vehicles to assist in pre-crash sensing.

1.3 Problem Definition

Given a low cost ultrasonic sensor:

1. Determine whether changes in air temperature and humidity will significantly affect its ability to accurately measure relative displacement and velocity.
2. Create a sensing system which accurately determines the distance to and velocity of a target (by initial testing).
3. Perform extensive testing of the system under a variety of conditions including: various target types, placement, and velocity; interference from other objects; and road conditions.

4. Analyze its strengths and limitations, and make recommendations concerning its role in a vehicle pre-crash sensing system.

Chapter 2

Survey of the State-of-the-Art

Ultrasonic sensors have long been used in industrial applications for detecting objects or measuring distances. The success of ultrasonic sensors in industry is based largely on their low cost and ability to detect troublesome objects for conventional optical (vision) sensors. For example, Brian Duval [2] explains in a recent article in *Sensors* that ultrasonic sensors can detect transparent and highly reflective materials that often cause problems with optical sensors. Other benefits of an ultrasonic sensor include long range* and broad area detection. However, the latter is also one of its limitations. As Duval [2] explains, the wide sonic cone emitted by the sensor makes it difficult to detect small targets. Also, there is a higher chance of interference from other objects.

Some materials like foam and extremely rough surfaces absorb or diffuse the emitted sound waves, resulting in a very weak or nonexistent return signal. According to Kert L. Cartwright and Gopi R. Jindal [3] in "An Ultrasonic Proximity System for Automobile Collision Avoidance," porous surfaces are difficult to detect at long distances because most of the ultrasonic energy is absorbed. Also, the more angled a target surface is with respect to the sensor, the less likely it will be detected. Cartwright and Jindal [3] explain that for even a smooth flat surface which reflects sound waves rather well, its ability to be detected diminishes significantly when placed at 45° to a projected pulse.

One method of using ultrasonic sensors to measure distances between objects is accomplished by measuring the time delay between the output and received signals.

* It should be noted that the sensor tested has a maximum range of 3 m. By "long range," Duval refers to sensors with maximum ranges of 3 m and up.

However, the speed of sound is affected by a variety of environmental conditions. According to Dennis A. Bohn [4] in an article of the *Journal of the Audio Engineering Society*, the speed of sound through air is independent of pressure, but temperature can have a significant effect. Less significant is the effect of humidity, but to determine the distance between objects as accurately as possible corrections should be made to account for this.

Currently, ultrasonic sensors are mostly in the experimental phase for vehicle pre-crash sensing systems. As Austin Weber [5] explains in an article of *Assembly Magazine*, Ford unveiled in mid 2003 its Taurus Telematics to Safety (T2S) concept vehicle which included a variety of safety systems. Ultrasonic sensors were installed for park assist, in which the driver is warned of obstacles while in reverse. *Autoworld Malaysia* [6] reported that Ford also unveiled a Windstar T2S with similar features and that the 2004 Mercury Monterey minivan employs both front and rear ultrasonic object sensing. Furthermore, Ford's Freestar minivan uses four ultrasonic sensors installed in the rear bumper for its "Reverse Sensing System," depicted in Figure 1. However, the use of these sensors is currently limited to static measurements of obstacles or operation at very low speeds, such as in park assist. Application of ultrasonic sensors in a vehicle pre-crash sensing system would require that they function effectively at greater vehicle speeds in the range of 35 mph and up.

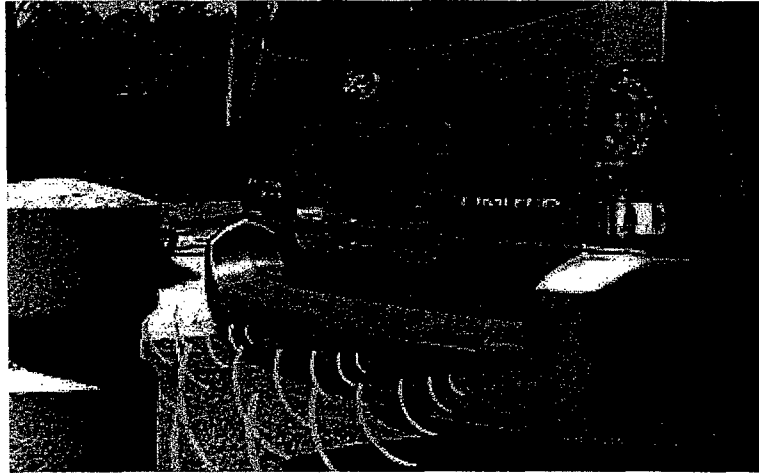


Figure 1. Four ultrasonic sensors in the rear bumper of the Ford Freestar minivan used for detecting objects while in reverse (photo courtesy of Ford [7]).

Chapter 3

Design Development

3.1 Design Requirements

In order to be integrated into a vehicle pre-crash sensing system, the ultrasonic range finder testing system must meet the following basic design requirements:

1. The ultrasonic sensor must be able to accurately determine the distance between it and a target of interest.
2. From collected distance and elapsed time data, the sensor must be able to accurately calculate the relative velocity between it and the target.

To meet the above basic design requirements, the sensor should be capable of detecting a wide range of targets under a variety of road conditions. The types of targets to be tested include the following:

- a. Pedestrians
- b. Vehicles
- c. Point objects such as trees, poles, and miscellaneous small targets
- d. Objects of various geometries and surfaces that the sensor may have difficulty detecting

In addition, the sensor's ability to detect an object is affected by the location of the target, its speed, the presence of clutter, and possibly vibrations due to road conditions. Therefore, the above mentioned targets are to be test under the following sets of sensor-target conditions:

- a. *Static-static* – both the sensor and target are to be kept at a fixed relative displacement. This test will primarily determine how well certain objects are detected over the sensor's specified range of operation.
- b. *Static-dynamic* – keep the target object stationary as the sensor is moved toward it at various speeds, or vice versa. The goal of this test is to determine the range of target speeds for which the sensor can accurately calculate relative velocity.
- c. *Target location* – begin with the target directly in front of the sensor along its centerline and then displace the target to the left and right of the centerline. The primary purpose of this test is to investigate the extent of the sensor's sonic cone and its effect on distance and velocity sensing.
- d. *Clutter* – place obstacles out of the target's way but within the sensor's sonic cone. This test will examine the sensor's ability to distinguish between the target of interest and obstacles within its detection area.

A more detailed testing procedure for each type of test is provided in Chapters 5 through 8.

The chosen method for acquiring data from the ultrasonic sensor is through the use of National Instruments' LabVIEW™ data acquisition software. See Chapter 4, Section 1 for more details.

3.2 Analysis

An ultrasonic sensor can be used to determine the distance between it and an object by measuring the time it takes for its output signal to bounce off the object and return to the sensor, or the time delay, t_{delay} . The basic functions of the ultrasonic sensing system are illustrated in the block diagram of Figure 2. A LabVIEW™ algorithm first generates a TTL level electrical signal corresponding to the desired input to the sensor. The input signal is sent to the sensor's processor chip where it is converted from digital to analog format. The analog electrical signal is then used by the piezoelectric ultrasonic transmitter to generate the desired sound wave. When (or if) the echo is detected by the ultrasonic receiver, it creates a corresponding analog electrical signal that is subsequently converted to TTL format. This return signal is then analyzed in LabVIEW™ and used to calculate the distance between the sensor and the detected object.

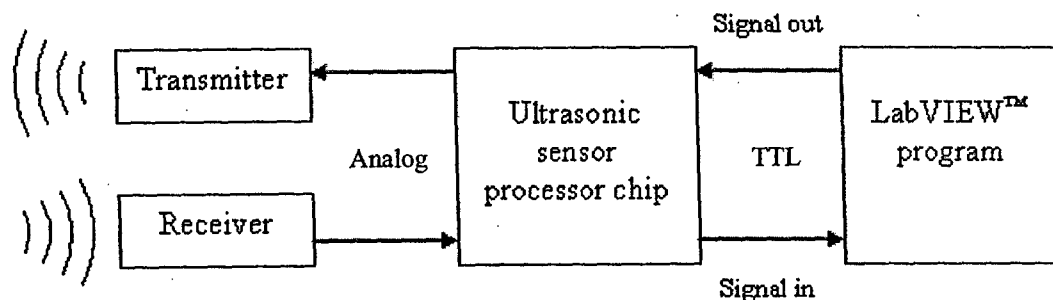


Figure 2. Block diagram depicting the ultrasonic sensing system interface and signals.

When working with TTL, an analog signal is represented by only one of two values: 0V or +5V, typically. For the sensor, 0V would represent no input signal generation and the waiting period for a return signal to be detected. A value of +5V corresponds to an input pulse and detection of an echo (where the length of the return pulse is proportional to the relative displacement between the sensor and object). As a result of converting from analog to TTL format, the input and return signals as viewed by LabVIEW™ or as seen on an oscilloscope appear as rectangular waves, as depicted in Figure 3. According to the manufacturer, the time delay is measured from the falling edge of the output signal to the falling edge of the echo.

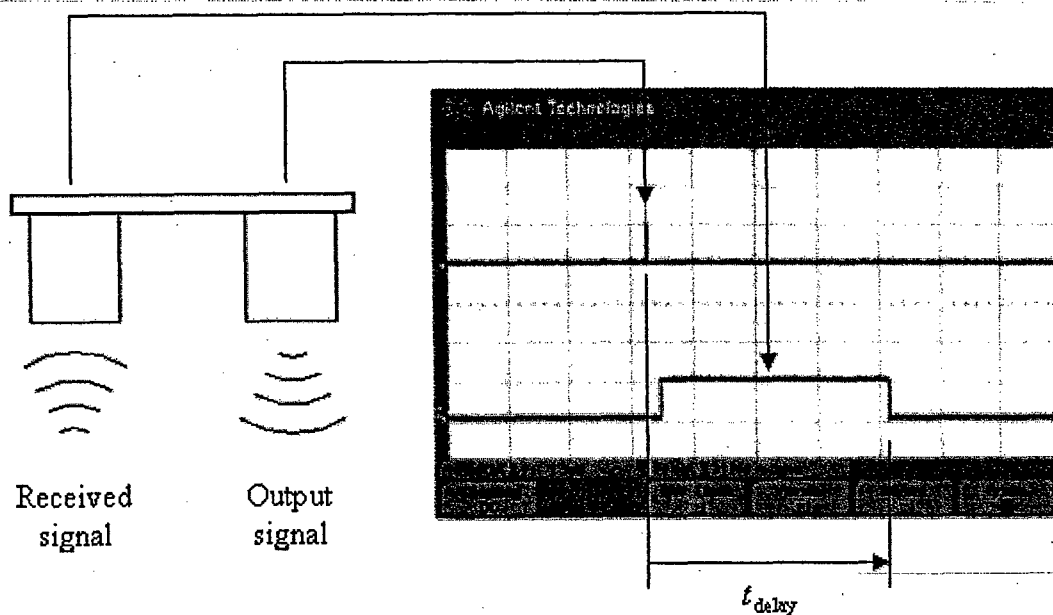


Figure 3. Sensor output and received signals seen by an oscilloscope as rectangular waves because of conversion from analog to TTL format.

Beginning with the definition of velocity,

$$v = \frac{dx}{dt}$$
$$v \approx \frac{\Delta x}{\Delta t}$$

where the velocity, v , is the speed of sound, c , Δx is the distance between the sensor and an object, and Δt is the time it takes the sensor's output signal to reach the object. Note that the time delay between the signals is actually twice the time it takes the sound wave to reach the object. Therefore, rearranging to solve for Δx and substituting Δt with half of the time delay gives

$$\Delta x = \frac{1}{2} c t_{\text{delay}}$$

The speed of sound evaluated at a temperature of $T = 20^{\circ}\text{C}$ is $c = 343.20 \text{ m/sec}$. Therefore, the distance between the sensor and an object is given by

$$\Delta x = (171.60) t_{\text{delay}}$$

where Δx is in m and t_{delay} is in sec. The sensitivity of the calculated distance with respect to changes in air temperature and humidity was analyzed, and the effects of temperature and humidity were found to be negligible. For a detailed analysis, refer to Appendix B, Section 1.

To solve for the velocity of an object of interest, measurements from successive sets of output and return pulses are used, as depicted in Figure 4.

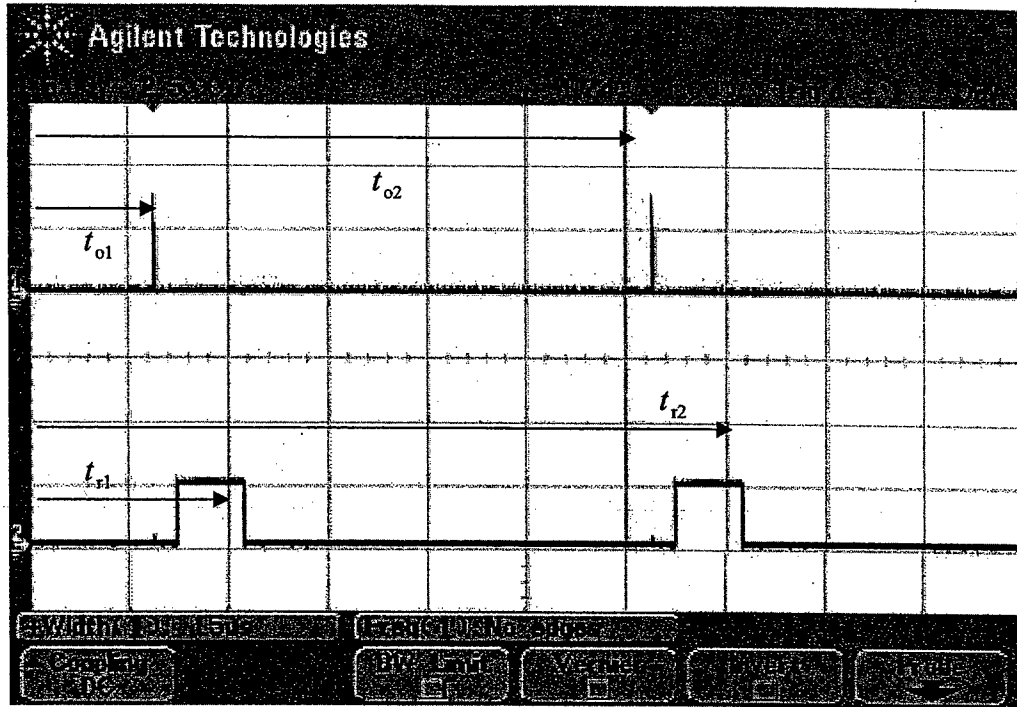


Figure 4. Output and received signals in succession.

To calculate velocity, both the time delays and average times are considered. The average time for the first signal, t_1 , is given by

$$t_1 = t_{o1} + \frac{1}{2}(t_{r1} - t_{o1})$$

$$t_1 = \frac{1}{2}(t_{r1} + t_{o1})$$

Similarly, the average time for the second signal, t_2 , is

$$t_2 = \frac{1}{2}(t_{r2} + t_{o2})$$

The velocity of the object relative to the sensor is expressed as

$$\vec{v}_{\text{object/sensor}} = \vec{v}_{\text{object}} - \vec{v}_{\text{sensor}}$$

Rearranging to solve for the object's velocity gives

$$\vec{v}_{\text{object}} = \vec{v}_{\text{object/sensor}} + \vec{v}_{\text{sensor}}$$

Beginning with the definition of velocity to solve for the velocity of the object relative to the sensor,

$$\begin{aligned}\bar{v}_{\text{object/sensor}} &= \frac{dx}{dt} \\ \bar{v}_{\text{object/sensor}} &\approx \frac{\Delta x}{\Delta t} \\ \bar{v}_{\text{object/sensor}} &= \frac{x_2 - x_1}{t_2 - t_1}\end{aligned}$$

which reduces to

$$\bar{v}_{\text{object/sensor}} = \frac{c(t_{\text{delay},2} - t_{\text{delay},1})}{(t_{o2} + t_{r2}) - (t_{o1} + t_{r1})}$$

Therefore, the absolute velocity of the object is given by

$$\bar{v}_{\text{object}} = \frac{(343.20)(t_{\text{delay},2} - t_{\text{delay},1})}{(t_{o2} + t_{r2}) - (t_{o1} + t_{r1})} + \bar{v}_{\text{sensor}}$$

where all velocities are in m/sec and all times are in sec. See Appendix B, Section 1 for the full derivation.

Note that this expression determines only the object's component of velocity parallel to the sensor's. In other words, if the sensor and object were moving toward each other head-on, the actual absolute velocity of the object would be found. However, if the sensor was moving straight and the object came at the sensor at an angle, only the component of velocity parallel to the sensor's movement would be determined. Although this is not a true representation of the object's velocity, the information is still useful in determining whether the object is too close to the sensor and not slowing down; that is, the information about the relative velocity between the vehicle and a target object is what is important and will ultimately determine whether a crash is imminent or not.

3.3 Conceptual Design Alternatives

Two options were available for this project: either construct an ultrasonic sensor from scratch, or simply purchase a low-cost, general purpose sensor. Each of these options has their advantages and disadvantages. Although designing and building a sensor would allow it to be better suited for the scope of this project (that is, for integration into a vehicle pre-crash sensing system) since it could be tuned as necessary, it would take a considerable amount of time to design, construct, and debug. The alternative is to use a general purpose, off-the-shelf sensor, which would allow for immediate implementation and interfacing with a data acquisition system. The downside to this is that the sensor cannot be tailored to the desired application (actually it could be but the sensor may get damaged in the process). Since the focus of this project is testing of an ultrasonic sensor to determine whether it is a good candidate for use in a vehicle pre-crash sensing system, purchasing a sensor would be the best option.

Although the chosen method for data acquisition is through the use of LabVIEW™, the manufacturer of the ultrasonic sensor provides examples of other possible interfaces, including microcontrollers such as Basic Stamp II and Brainstem®. Furthermore, data could be collected solely using hardware, such as an oscilloscope. However, collecting a continuous stream of data using a scope is cumbersome and time-consuming, whereas the goal is to create a means of collecting and analyzing data quickly and efficiently and in a manner similar to how it would be done in an on-board vehicle sensing system. Also, because of the very short time periods involved in using an ultrasonic sensor (i.e., the output signal and the time delay), a counter with a high resolution is necessary. Thus, digital timers (such as the counters used in LabVIEW™) are an ideal choice over old-

fashioned, low-resolution analog timers. LabVIEW™ was chosen because of its immediate availability, compatibility with common data acquisition devices, and user-friendly programming interface.

Decision matrices are presented in Tables 1 and 2 for determining what type of sensor to use (off-the-shelf or hand-built) and how to acquire data, respectively. Each criterion is evaluated with a score from 1 (worst) to 10 (best).

Table 1. Decision matrix for determining whether to use an off-the-shelf ultrasonic sensor or to construct one.

Criterion	Weight	Hand-Built Sensor	Off-the-Shelf Sensor
Cost	2	7	5
Expected Performance	4	6	9
Implementation Time	3	3	9
Ability to Optimize	1	10	1
	Total	57	74

Table 2. Decision matrix for determining the most effective method for acquiring data.

Criterion	Weight	LabVIEW™	Hardware Instruments	Microcontrollers
Implementation Time	1	7	8	5
Ease of Data Collection	4	9	7	7
Speed of Data Collection	3	9	4	7
Ability to Incorporate Various Interfaces	2	9	5	7
	Total	88	58	68

Chapter 4

Description of the Design

4.1 The Design

The ultrasonic sensing system consists of four main components:

1. The Devantech SRF04 ultrasonic range finder distributed by Acroname Inc.
2. A computer running National Instruments' LabVIEW™ 7.1 data acquisition software.
3. A National Instruments' data acquisition (DAQ) card, PCI-6221.
4. A shielded I/O connector block from National Instruments, SCB-68.

As shown in Figure 5, the entire system is mounted on a rolling cart for ease of placement during testing.

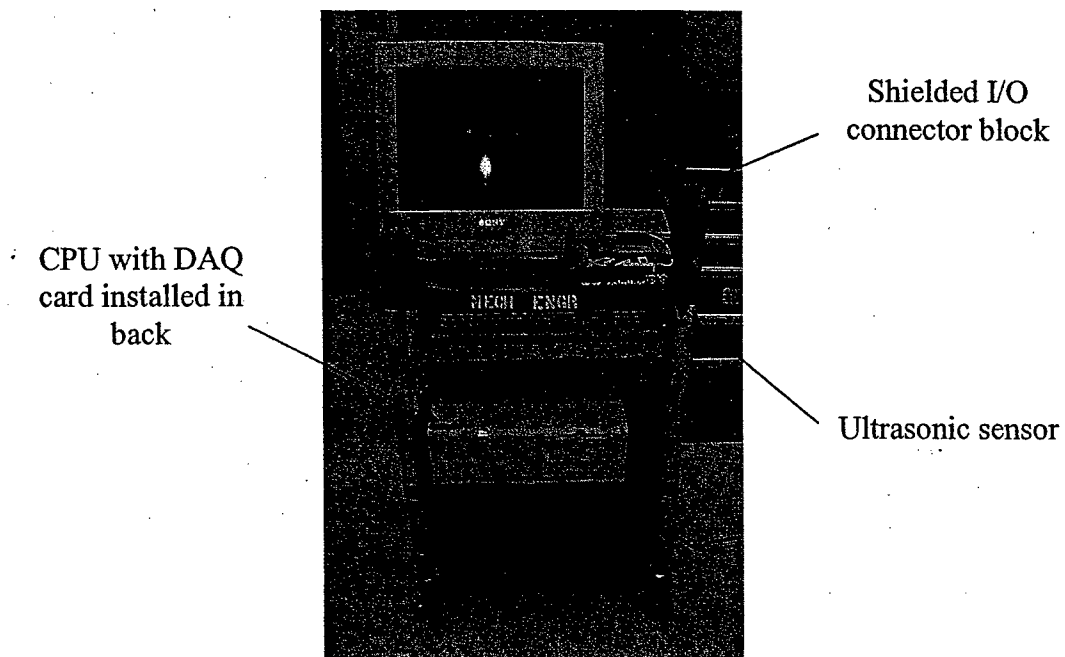


Figure 5. Ultrasonic sensing system on a rolling cart for ease of movement.

The DAQ card is installed in the computer's CPU, and the I/O connector block is connected directly to the DAQ card. The sensor is interfaced with the connector block via color-coded wires from the sensor, as depicted in Figure 6.

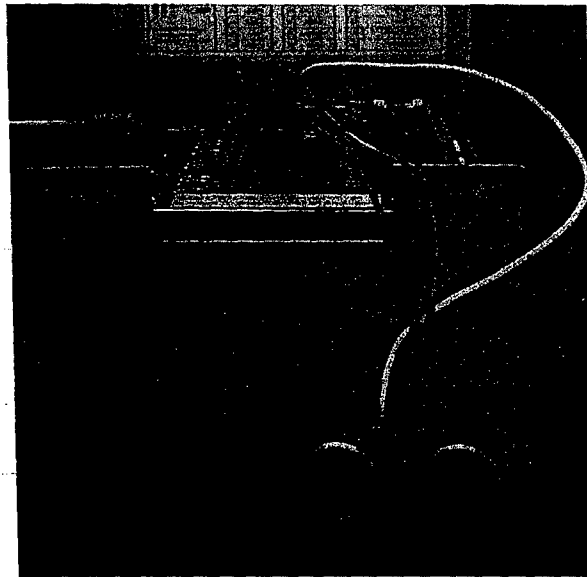


Figure 6. Ultrasonic sensor interfaced with the I/O connector block.

One of the four wires is connected to the block's +5 V power supply, and another is hooked to ground. The remaining two wires correspond to the sensor's input and output terminals, each of which is connected to a separate counter on the block. For more detail on the interfacing, refer to Appendix A, Detailed Schematics and Parts List.

The sensor input and output are controlled and monitored by an algorithm, or *virtual instrument* (VI), created in LabVIEW™. Figure 7 presents an operational block diagram depicting the VI's function.

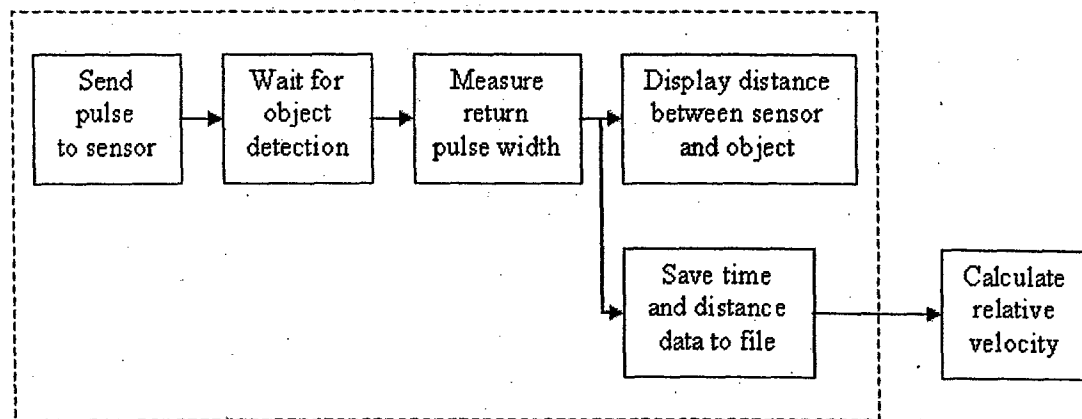


Figure 7. Operational block diagram of the LabVIEW™ algorithm.

The VI instructs one counter to generate a 10 μ sec pulse that is then sent to the sensor. After an object is detected and the echo is received, another counter measures the pulse width of the return signal. The distance between the sensor and the object is calculated and displayed, and then the distance, elapsed time, and return pulse width data is saved to a file. The file can then be opened in Excel™ where the data is reduced to give the average relative velocity between the sensor and detected object and the object's absolute velocity. For the actual LabVIEW™ algorithm and a detailed explanation of the various components, see Appendix A. It should be noted that the VI estimates the time delay as the return pulse width, an assumption to be later verified by initial testing.

4.2 Initial Testing Demonstrating Proof-of-Principle

Before proceeding to extensive testing based on the design requirements outlined in the previous chapter, initial testing of the sensing system was conducted to verify its accuracy. Three tests were performed, the first of which checked the system's ability to measure distance effectively. Figure 8 shows the experimental setup in the Donald E. Bently Center for Engineering Innovation, building 13-127.

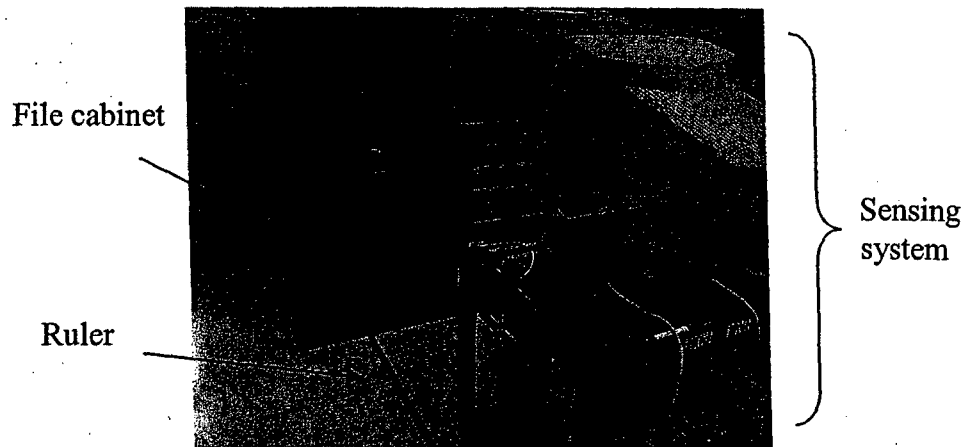


Figure 8. Experimental setup used to test the sensing system's ability to measure distance.

The system was placed facing a large cabinet at 0.25 m increments up to 3.00 m. The distance displayed by the VI was compared to the measured distance from the base of the cabinet to the ultrasonic transducers, located at half the depth of their protective cylindrical casings (refer to Appendix A for a CAD drawing of the sensor). The results of the experiment are presented in Table 3.

Table 3. Actual distance between the file cabinet and sensor compared to data from the sensor.

Run	Measured Distance (m)	Sensed Distance (m)	Deviation (m)
1	0.250	0.251	0.001
2	0.500	0.499	-0.001
3	0.750	0.748	-0.002
4	1.000	0.995	-0.005
5	1.250	1.247	-0.003
6	1.500	1.495	-0.005
7	1.750	1.742	-0.008
8	2.000	1.987	-0.013
9	2.250	2.252	0.002
10	2.500	2.480	-0.020
11	2.750	2.740	-0.010
12	3.000	2.995	-0.005

The results indicate that the system does a very good job at measuring the distance between the sensor and file cabinet, and therefore the assumption that the time delay can be approximated by the return pulse width is a valid one.

The second test checked to see if the system could determine relative velocity effectively. To do this, an object with a known position-versus-time curve was needed, and the pneumatic positioning device in the Parker Hannifin Control Systems Laboratory, building 13-102, was used for this purpose. The experimental setup is shown in Figure 9.

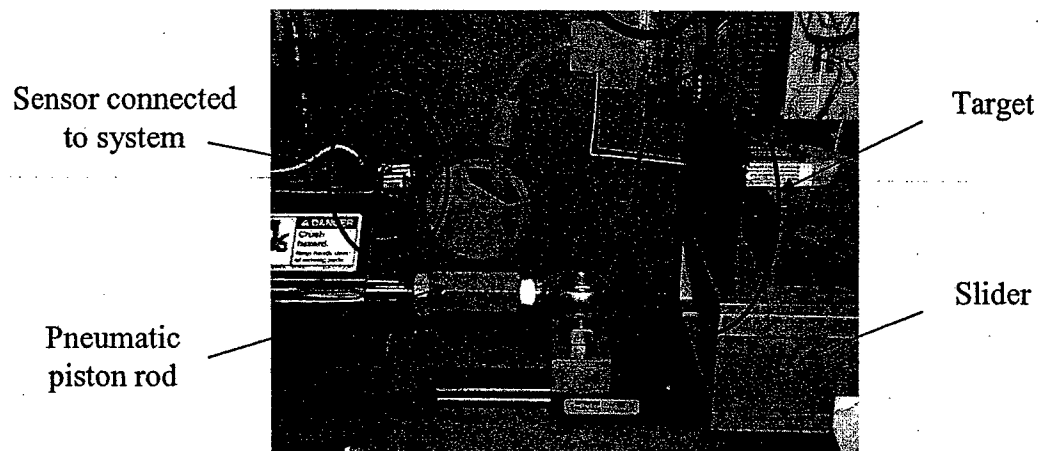


Figure 9. Experimental setup used to test the sensing system's ability to determine relative velocity.

The pneumatic positioning system consists of a sliding piston rod and a fixed resistive strip that together act as a *linear voltage differential transducer*, or LVDT. As the piston moves, a sliding contact on the other end of the rod moves along the resistive strip, generating an output voltage that varies linearly with the piston position (hence it being a LVDT). The LVDT is a LWG 225 model linear potentiometer provided by Novotechnik Inc., and it has a resolution of less than 0.01 mm. The system's data acquisition program records, saves, and displays the position of the piston rod as a

function of time. For more information on the pneumatic positioning system, refer to the ME 422 Laboratory Manual [12].

The sensor was placed facing the positioning device's slider, attached to which was a target for the sensor to detect. When the pneumatic device was actuated causing the slider to move, the pneumatic system's data collection program as well as the ultrasonic system recorded slider displacement and time data. Figures 10 and 11 display the results of the test, with data from the ultrasonic sensor plotted as square markers.

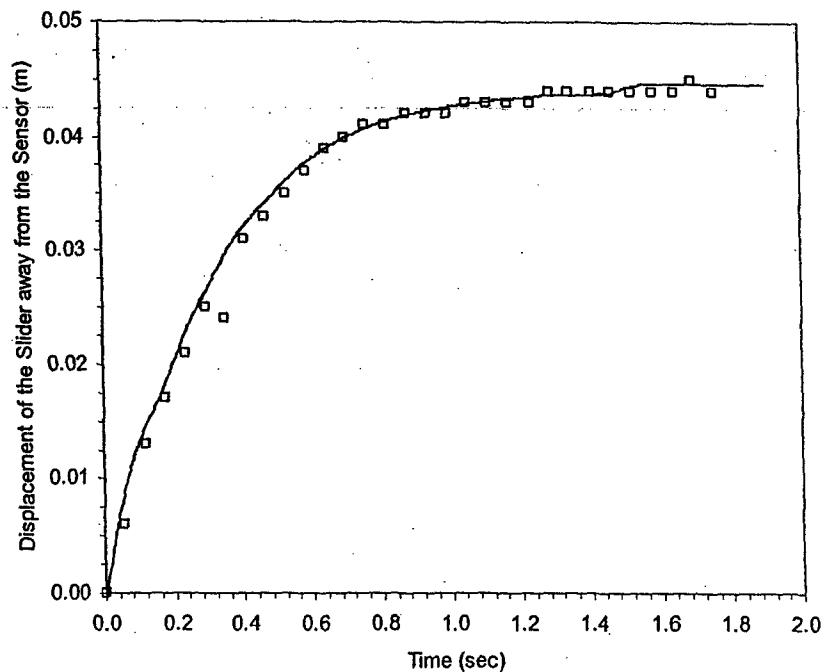


Figure 10. Slider displacement away from the sensor over time as measured by both the pneumatic and ultrasonic systems.

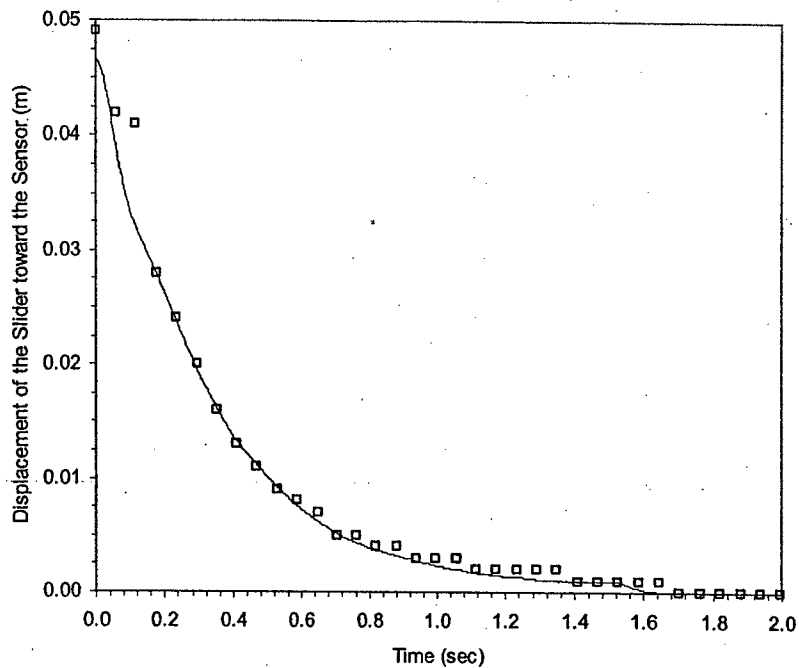


Figure 11. Slider displacement toward the sensor over time as measured by both the pneumatic and ultrasonic systems.

The figures show that the position-versus-time curves generated by the data retrieved from the sensor correlate well with the actual motion of the pneumatic positioner for displacements away from and toward the sensor. The figures also demonstrate that the number of data points collected allow for an accurate estimate of the actual position-versus-time profile using straight-line approximations between the data points, the slopes of which represent the average relative velocities. Tables 4 and 5 list the straight-line approximated average velocities and displacements for the sensor and positioner, corresponding to the first 12 time intervals recorded by the sensing system.

Table 4. Distance and average velocity calculated from the first 12 time intervals for the sensor and the positioner moving away from the sensor.

Pneumatic Positioner		Ultrasonic Sensor		Deviations	
Distance (m)	Average Velocity (m/sec)	Distance (m)	Average Velocity (m/sec)	Distance (m)	Average Velocity (m/sec)
0.0086	0.108	0.0060	0.157	-0.0026	0.049
0.0143	0.114	0.0130	0.092	-0.0013	-0.022
0.0181	0.072	0.0170	0.068	-0.0011	-0.004
0.0225	0.068	0.0210	0.075	-0.0015	0.007
0.0262	0.068	0.0250	0.061	-0.0012	-0.007
0.0295	-0.017	0.0240	0.057	-0.0055	0.074
0.0322	0.118	0.0310	0.043	-0.0012	-0.075
0.0343	0.034	0.0330	0.035	-0.0013	0.001
0.0363	0.034	0.0350	0.033	-0.0013	-0.001
0.0377	0.034	0.0370	0.026	-0.0007	-0.008
0.0389	0.034	0.0390	0.021	0.0001	-0.013
0.0399	0.017	0.0410	0.016	0.0011	-0.001

Table 5. Distance and average velocity calculated from the first 12 time intervals for the sensor and the positioner moving toward the sensor.

Pneumatic Positioner		Ultrasonic Sensor		Deviations	
Distance (m)	Average Velocity (m/sec)	Distance (m)	Average Velocity (m/sec)	Distance (m)	Average Velocity (m/sec)
0.0386	-0.135	0.042	-0.118	0.0034	0.017
0.0316	-0.11	0.041	-0.018	0.0094	0.092
0.0279	-0.068	0.028	-0.22	0.0001	-0.152
0.0241	-0.072	0.024	-0.069	-0.0001	0.003
0.0197	-0.073	0.02	-0.067	0.0003	0.006
0.0163	-0.057	0.016	-0.069	-0.0003	-0.012
0.0133	-0.049	0.013	-0.051	-0.0003	-0.002
0.0111	-0.035	0.011	-0.034	-0.0001	0.001
0.0091	-0.034	0.009	-0.033	-0.0001	0.001
0.0075	-0.028	0.008	-0.018	0.0005	0.010
0.0061	-0.023	0.007	-0.017	0.0009	0.006
0.0053	-0.019	0.005	-0.035	-0.0003	-0.016

The tables show that the average relative velocities calculated using straight-line approximations for the pneumatic positioner and sensor correlate well. The only exceptions are two skewed values near the top of the tables, caused by a measured displacement in the sensor data that was off a bit from the actual distance. A filter could be used to eliminate such outliers, one of which is a Kalman filter that is discussed in Chapter 9, Final Conclusions and Recommendations. Nevertheless, the data suggests that the sensor can be used effectively to determine average relative velocity and the absolute velocity of an object from collected distance and time data for small displacements and average velocities.

However, of greater importance is the performance of the sensor in situations where the sensor and/or target object are moving at higher speeds. To evaluate the sensor's ability to measure relative displacement under such circumstances, a third test involving a falling basketball was performed, as illustrated in Figure 12, where "T" denotes the transmitter side of the sensor and "R" denotes the receiver side.

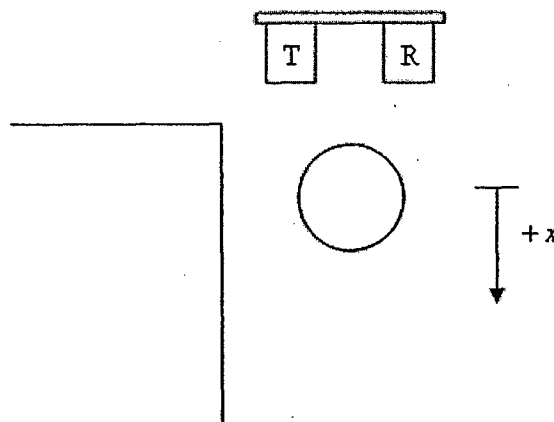


Figure 12. Experimental setup for the basketball drop test used to evaluate the sensor's performance with objects moving at higher speeds.

The ultrasonic sensing system was brought up to the second floor of building 13, and the sensor was positioned over the ledge of the walkway, pointing down toward the courtyard below. A basketball was held about 5 cm in front of the sensor and then let go, and the sensor measured the displacement of the basketball away from the sensor as it fell to the courtyard. This procedure was repeated several times, and the results of the testing are presented in Figures 13 and 14 alongside the theoretical displacement curve solved from the differential equation describing the falling basketball's motion. For a full derivation of the equation of motion, see Appendix B, Section 2.

As shown in Figure 13, compared to the theoretical motion, the sensor does a fairly accurate and consistent job determining the relative displacement between it and the falling basketball up to about 2.0 m. However, once the ball is greater than about 2.0 m from the sensor, the sensor no longer detects the ball and returns an erroneous value of about 5.5 m, as shown in Figure 14. Despite this, the results indicate that the sensor can effectively determine the distance between it and a target when either or both are traveling at higher speeds.

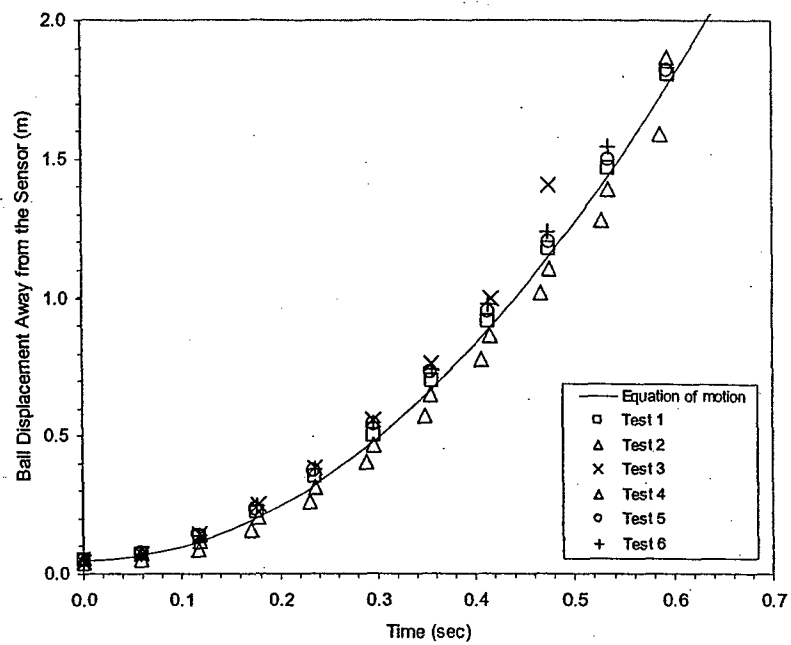


Figure 13. Collected data for the displacement of a basketball falling away from the sensor as compared to the solution to the equation of motion.

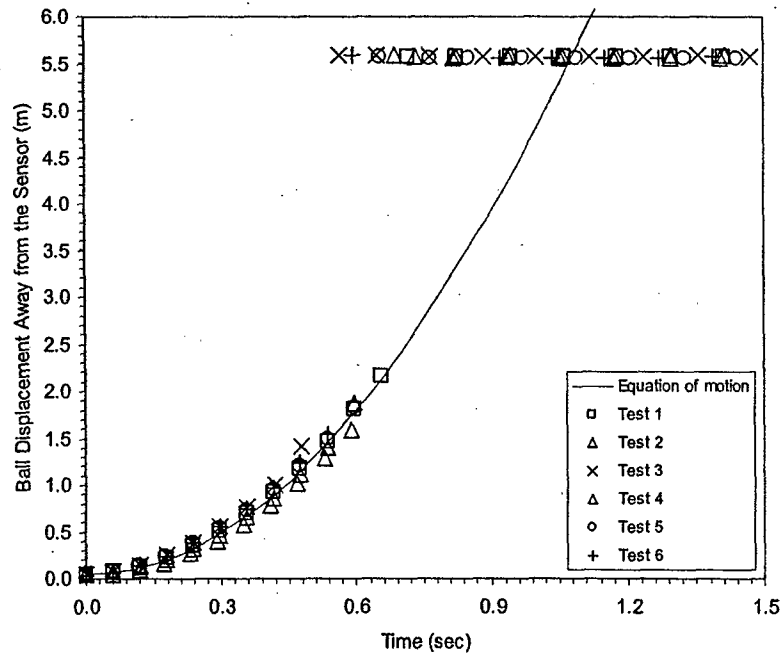


Figure 14. Depiction of the sensor's detection cutoff point of about 2.0 m.

Chapter 5

Static-Static Testing

5.1 Testing Procedure

After completing initial testing of the ultrasonic sensor, four major tests were conducted to evaluate the sensor's performance under a variety of conditions, including objects of various geometries and locations relative to the sensor. The first of these tests was the static-static testing.

In this round of testing, the sensor was held fixed as the center of the target object was moved away from the sensor in 0.25 m increments along the centerline of the sensor, as depicted in Figure 15. The test was conducted using a variety of target objects, including a box, a basketball, a round metal column (of 0.205 m diameter), a vehicle rear bumper, and a pedestrian. The experimental setup with a box as the target is shown in Figure 16. Distance data was collected until the target object was out of range.

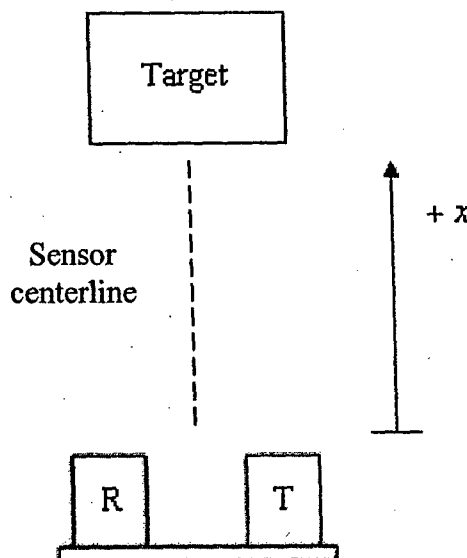


Figure 15. Experimental setup for the static-static testing.



Figure 16. Static-static testing setup with a box as a target object.

5.2 Results of the Testing

For the most part, the sensor returned a stream of distance data that correlated well with the actual relative displacement. However, on occasion the sensor returned erroneous values, and when the average of the distance data was taken it became skewed considerably due to these outliers. As a result, all distance data within the sensor manufacturer's published range was manually filtered to eliminate these outliers.

Furthermore, if the stream of distance data jumped wildly from accurate to false readings, and vice versa, then the average *accurate* reading was presented in parentheses to denote a reading from the sensor with marginal accuracy. Also, a double dash (--) means that no data was collected for the corresponding distance, which implies that the target object was out-of-range.

The results from the static-static round of testing are presented in the following tables, with results from using a box, a basketball, a column, a vehicle rear bumper, and a pedestrian as target objects in Tables 6, 7, 8, 9, and 10, respectively.

As shown in Table 6, the sensor does an effective job at detecting the relative displacement between it and a box, even up to 6.0 m – a distance of twice the manufacturer's published range! With the basketball, column, vehicle bumper, and pedestrian as target objects, the sensor performed about the same, with reliable object detection getting cut off at about 4.0 m of relative displacement. Even though the sensor did not perform as well when sensing these objects, it was still able to sense them outside of the published range. The results of the testing are summarized in a deviation-vs.-displacement curve in Figure 17.

Table 6. Distance data for a box from the ultrasonic sensor as compared to the measured distance for the static-static testing.

Measured Distance (m)	Distance from Sensor Data (m)	Deviation (m)	Measured Distance (m)	Distance from Sensor Data (m)	Deviation (m)
0.25	0.26	0.01	3.25	3.26	0.01
0.50	0.49	-0.01	3.50	3.52	0.02
0.75	0.76	0.01	3.75	3.75	0.00
1.00	1.00	0.00	4.00	4.06	0.06
1.25	1.26	0.01	4.25	4.30	0.05
1.50	1.52	0.02	4.50	4.55	0.05
1.75	1.77	0.02	4.75	4.80	0.05
2.00	2.01	0.01	5.00	5.06	0.06
2.25	2.27	0.02	5.25	5.30	0.05
2.50	2.51	0.01	5.50	5.56	0.06
2.75	2.76	0.01	5.75	5.82	0.07
3.00	3.02	0.02	6.00	6.04	0.04

Table 7. Distance data for a ball from the ultrasonic sensor as compared to the measured distance for the static-static testing.

Measured Distance (m)	Distance from Sensor Data (m)	Deviation (m)	Measured Distance (m)	Distance from Sensor Data (m)	Deviation (m)
0.25	0.26	0.01	2.50	2.60	0.10
0.50	0.51	0.01	2.75	2.81	0.06
0.75	0.76	0.01	3.00	3.05	0.05
1.00	1.01	0.01	3.25	3.29	0.04
1.25	1.26	0.01	3.50	3.61	0.11
1.50	1.51	0.01	3.75	3.85	0.10
1.75	1.79	0.04	4.00	4.07	0.07
2.00	2.02	0.02	4.25	(4.31)	(0.06)
2.25	2.27	0.02	4.50	5.97	1.47

Table 8. Distance data for a round metal column of 0.205 m diameter from the ultrasonic sensor as compared to the measured distance for the static-static testing.

Measured Distance (m)	Distance from Sensor Data (m)	Deviation (m)	Measured Distance (m)	Distance from Sensor Data (m)	Deviation (m)
0.25	0.26	0.01	2.75	2.77	0.02
0.50	0.52	0.02	3.00	3.03	0.03
0.75	0.76	0.01	3.25	3.28	0.03
1.00	1.01	0.01	3.50	3.53	0.03
1.25	1.27	0.02	3.75	3.81	0.06
1.50	1.51	0.01	4.00	4.04	0.04
1.75	1.76	0.01	4.25	(4.29)	(0.04)
2.00	2.01	0.01	4.50	(4.54)	(0.04)
2.25	2.27	0.02	4.75	6.04	1.29
2.50	2.52	0.02	5.00	--	--

Table 9. Distance data for a vehicle rear bumper from the ultrasonic sensor as compared to the measured distance for the static-static testing.

Measured Distance (m)	Distance from Sensor Data (m)	Deviation (m)	Measured Distance (m)	Distance from Sensor Data (m)	Deviation (m)
0.25	0.29	0.04	2.75	2.81	0.06
0.50	0.53	0.03	3.00	3.09	0.09
0.75	0.77	0.02	3.25	3.36	0.11
1.00	1.01	0.01	3.50	3.63	0.13
1.25	1.25	0.00	3.75	3.88	0.13
1.50	1.56	0.06	4.00	4.14	0.14
1.75	1.75	0.00	4.25	4.45	0.20
2.00	2.00	0.00	4.50	4.71	0.21
2.25	2.26	0.01	4.75	(4.97)	(0.22)
2.50	2.53	0.03	5.00	5.95	0.95

Table 10. Distance data for a pedestrian from the ultrasonic sensor as compared to the measured distance for the static-static testing.

Measured Distance (m)	Distance from Sensor Data (m)	Deviation (m)	Measured Distance (m)	Distance from Sensor Data (m)	Deviation (m)
0.25	0.38	0.13	2.75	2.82	0.07
0.50	0.58	0.08	3.00	3.10	0.10
0.75	0.81	0.06	3.25	3.36	0.11
1.00	1.08	0.08	3.50	3.66	0.16
1.25	1.34	0.09	3.75	3.84	0.09
1.50	1.59	0.09	4.00	4.11	0.11
1.75	1.84	0.09	4.25	4.33	0.08
2.00	2.04	0.04	4.50	(4.59)	(0.09)
2.25	2.32	0.07	4.75	(4.82)	(0.07)
2.50	2.58	0.08	5.00	--	--

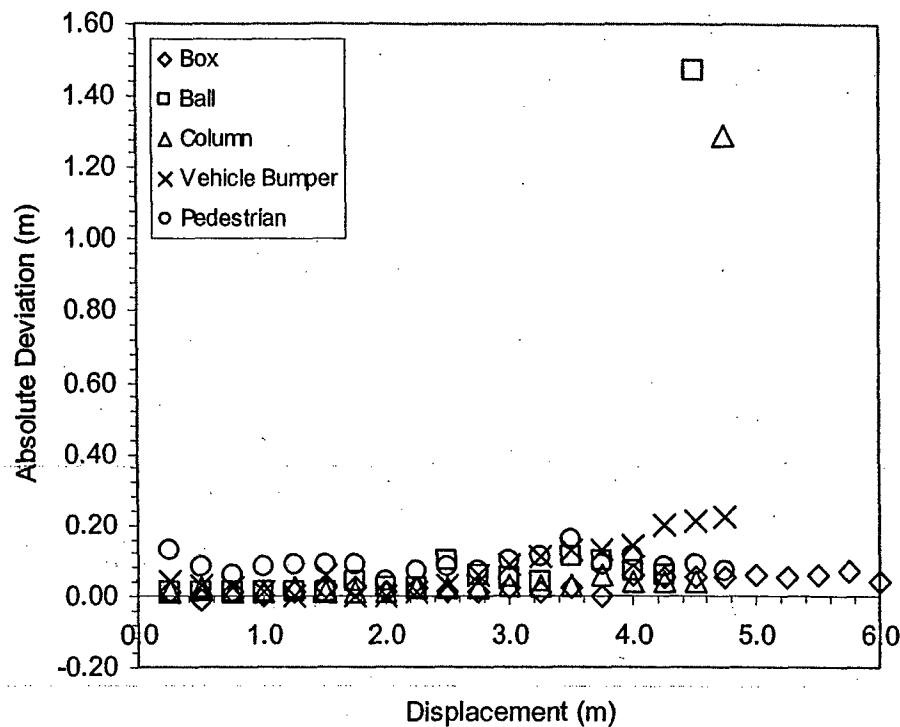


Figure 17. Absolute deviation as a function of displacement for various target objects used in the static-static testing.

5.3 Conclusions from the Testing

It was surprising to find that the ultrasonic sensor could reliably detect objects at distances outside of the range published by the manufacturer. Although realistically most potential threats to a vehicle will not be directly in front of the onboard ultrasonic sensors, the results of the static-static testing reveal that the sensors could possibly detect these threats at greater distances than previously believed possible. This is a great advantage in that it allows for more time to assess the magnitude of the threat and to employ pre-crash safety maneuvers. Furthermore, a greater range of detection would enable the sensor to be operated at higher vehicle or target speeds than previously believed possible since a target object could be detected over a longer range in the same amount of time (i.e., it could move at faster speeds and still be detected). As shown in

Table 11, the sensor's sampling rate (based on an operating frequency of 34 Hz) decreases as the vehicle or target speed increases, where the minimum amount of data points required to accurately represent a target's movement is at least about 10. Thus, within the manufacturer's published range of 3 m, the sensor can effectively detect a moving target up to about 20 mph. If further testing shows that the sensor can detect objects out to 6 m, then it may be possible for the sensor to be operated at 45 mph.

Table 11. Number of data samples from the sensor as a function of vehicle or target speed.

Speed (mph)	Number of Samples over 3 m	Number of Samples over 6 m
5	45.63	91.27
10	22.82	45.63
15	15.21	30.42
20	11.41	22.82
25	9.13	18.25
30	7.61	15.21
35	6.52	13.04
40	5.70	11.41
45	5.07	10.14
50	4.56	9.13

Chapter 6

Sonic Cone Testing

6.1 Testing Procedure

Starting with a box placed 0.25 m out along the sensor's centerline and 1.0 m to the left of the centerline, the box was then moved at 0.25 m increments until it was 1.0 m to the right. Next, the box was placed another 0.25 m along the sensor's centerline, and the box was moved from left to right. This process was repeated until the box was 3.0 m along the centerline from the sensor. The experimental setup is illustrated in Figure 18 and shown in Figure 19. As the target is displaced away from the centerline, the sensor actually detects the near edge of the box instead of the center, as depicted in Figure 20. The collected distance data from the sensor was compared to this possible range. A diagram depicting the sensor's sonic cone was then constructed from the results.

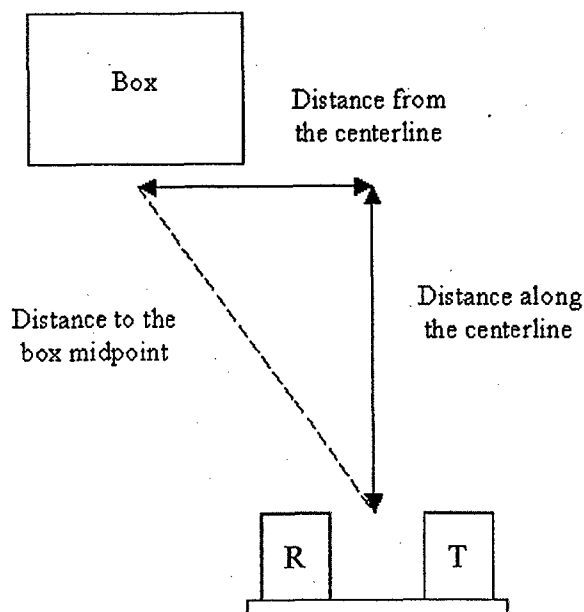


Figure 18. Depiction of the sonic cone testing setup.

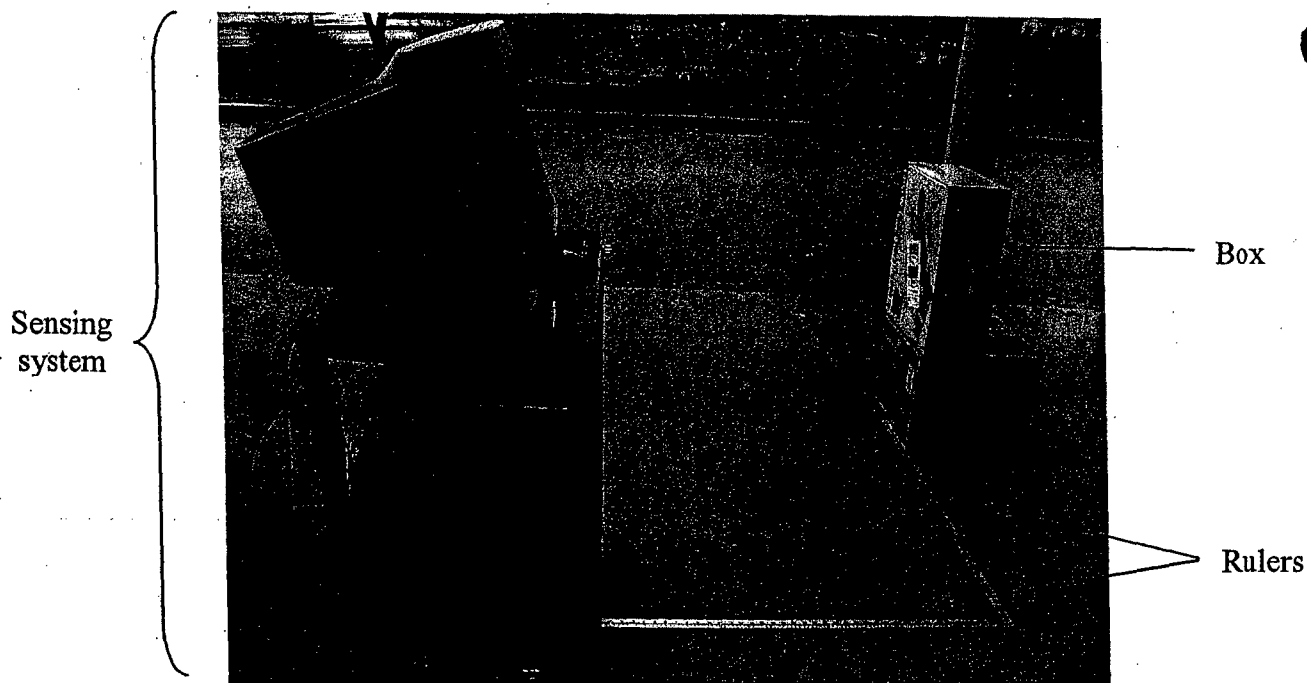


Figure 19. Experimental setup for the sonic cone testing.

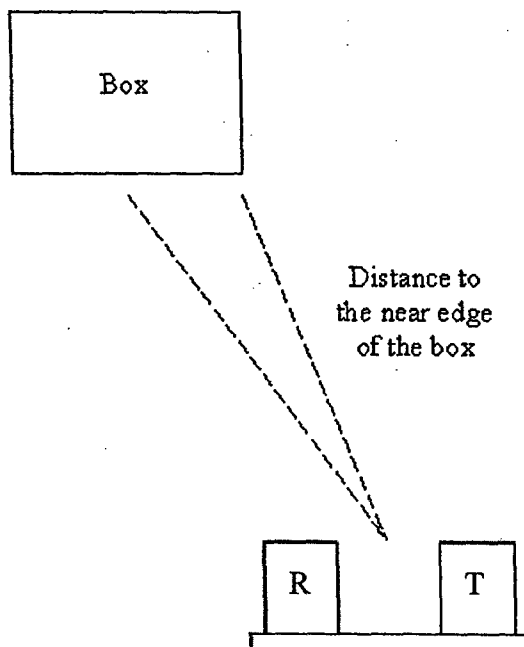


Figure 20. Depiction of the possible displacement range detected by the sensor for the sonic cone testing.

6.2 Results of the Testing

The results of the sonic cone testing are shown in Table 12, and a diagram depicting the sonic cone derived from the collected data is presented in Figure 21. Results presented in parentheses indicate values close to but outside the actual possible range, as illustrated in Figure 20. Results in square brackets correspond to erroneous values returned by the sensor, such as when no object was detected.

As shown in Table 12 and Figure 21, the data suggests that the sonic cone is asymmetrical about the sensor centerline, with about a 20° coverage area on the right with respect to the centerline and a 15° coverage area to the left with some areas of marginally accurate detection. Overall, the sensor performed well in detecting the target object, and the experimental sonic cone is similar to that published by the manufacturer.

Table 12. Distance data from the ultrasonic sensor as compared to the measured distance between it and the midpoint of a box placed at various distances from and along the centerline.

Distance along the Centerline	Distance from the Centerline								
	Left				Center	Right			
	1.0 m	0.75 m	0.50 m	0.25 m	0 m	0.25 m	0.50 m	0.75 m	1.0 m
0.25 m	[5.95]	[5.95]	[5.95]	[5.95]	0.26	[5.95]	[5.95]	[5.95]	[5.95]
0.50 m	[5.95]	[5.95]	[5.93]	0.53	0.50	0.55	[5.94]	[5.95]	[5.95]
0.75 m	[5.93]	[5.93]	1.97	0.79	0.76	0.77	[5.93]	[5.93]	[5.93]
1.00 m	[5.92]	[5.91]	1.10	1.02	1.00	1.01	1.08	[5.92]	[5.92]
1.25 m	[5.92]	[5.92]	1.32	1.26	1.24	1.24	1.31	[5.91]	[5.91]
1.50 m	[5.92]	1.69	1.60	1.55	1.54	1.50	(1.68)	[5.91]	[5.91]
1.75 m	[5.91]	1.86	1.77	1.75	1.77	1.76	1.81	[5.91]	[5.91]
2.00 m	[5.92]	2.13	2.07	2.04	2.02	2.02	2.05	(2.98)	[5.91]
2.25 m	[5.91]	2.38	2.32	2.28	2.27	2.26	2.33	(2.76)	(2.96)
2.50 m	[5.91]	[5.36]	2.56	2.53	2.52	2.51	2.54	[3.86]	[3.36]
2.75 m	[5.91]	(2.98)	2.82	(2.79)	2.77	2.76	2.79	(2.95)	(3.05)
3.00 m	[5.91]	[5.91]	3.07	(3.05)	3.03	3.03	(3.14)	(3.18)	(3.25)

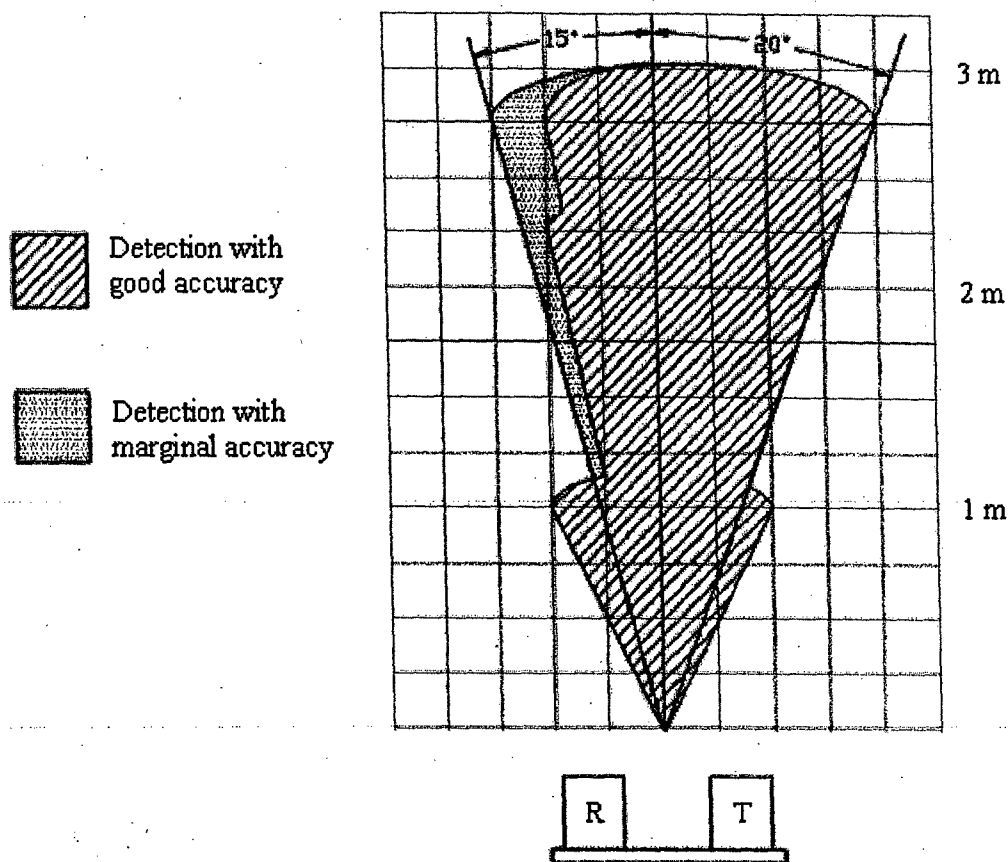


Figure 21. Depiction of the ultrasonic sensor's sonic cone.

6.3 Conclusions from the Testing

The sonic cone asymmetry was not a big surprise, with greater coverage area on the transmitter side of the sensor. This makes sense since an object further out toward the receiver side of the sensor would encounter less of the projected sound wave from the transmitter, whereas the opposite is true on the transmitter side. As suggested by the limited coverage closer to the sensor, application in a vehicle pre-crash sensing system would require the use of multiple sensors for complete coverage of the vehicle's frontal area.

Although the testing only went out to 3.0 m from the sensor, the static-static testing results suggest that it may also be useful to know what the sonic cone would look like if the test object were placed at even greater distances. Furthermore, it may be worthwhile to perform another round of testing with the sensor placed vertically instead of horizontally (as was previously done) to determine whether the orientation of the sensor has an effect on the sonic cone.

Chapter 7 Clutter Testing

7.1 Testing Procedure

Clutter testing was conducted to evaluate the sensor's ability to distinguish between the target of interest and a clutter object within the sensor's sonic cone. In terms of a vehicle pre-crash sensing system, the objective of this test is to determine how well the on-board sensor can distinguish between a potential threat and clutter, like high-volume traffic. Two clutter tests were performed, the first involving a vehicle and a column (pole) acting as clutter. A metal column (of 0.205 m diameter) was located about 1.0 m to the left of the vehicle's left edge at a distance of about 1.80 m along the centerline of the sensor, as depicted in Figure 22 and shown in Figure 23. The left edge of the vehicle front bumper was placed along the sensor's centerline and moved away from the sensor up to 3.0 m in increments of 0.25 m. The measured distance to the vehicle bumper and the collected data from the sensor were compared and analyzed to determine the sensor's vehicle detection cutoff point.

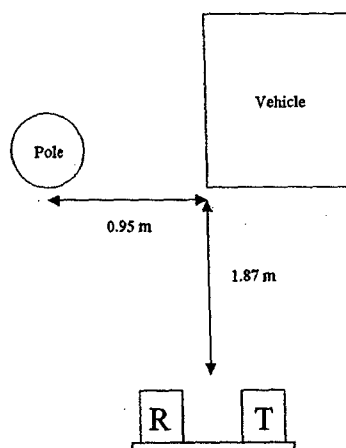


Figure 22. Experimental setup for the vehicle-pole clutter test.

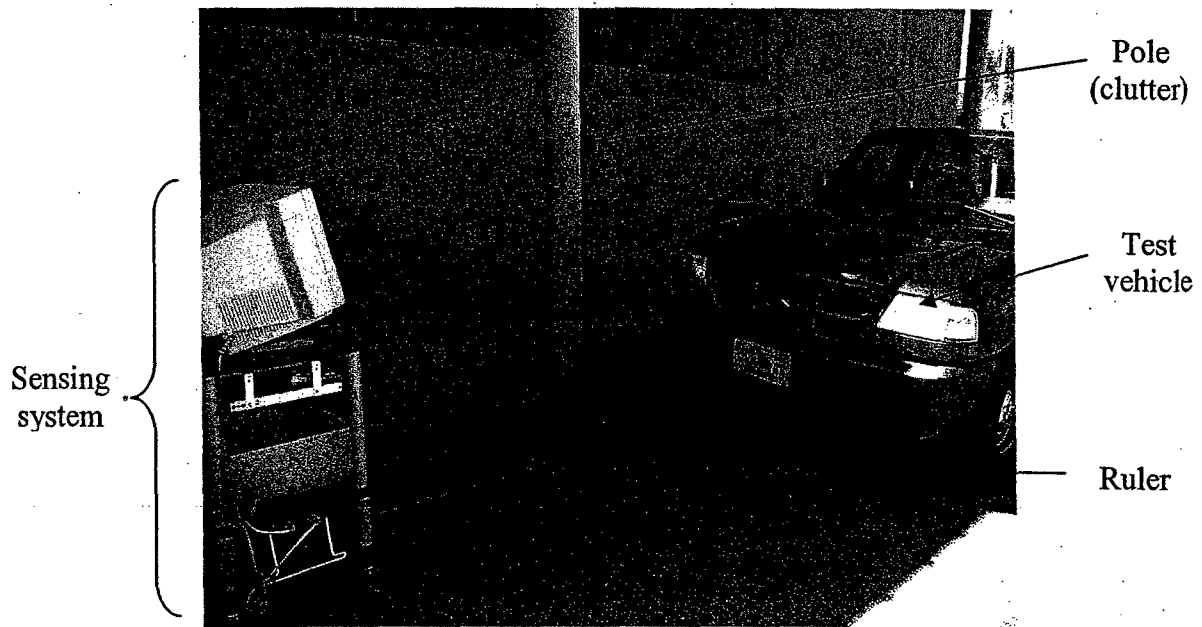


Figure 23. Vehicle-pole clutter test setup.

The second clutter test involved another vehicle as a clutter object instead of a pole, with the vehicle to be detected by the sensor on the right and the clutter object on the left, as depicted in Figure 24 and shown in Figure 25. The clutter vehicle was held fixed as the right edge of the test vehicle's front bumper was moved away from the sensor in 0.25 m increments along the sensor's centerline up to 3.0 m. The target detection cutoff point was then determined from the measured and sensed distance data.

7.2 Results of the Testing

The clutter testing results are tabulated in Tables 13 and 14. It is clear from the data in Table 13 where the transition occurs, or when the sensor stops detecting the target vehicle and begins to detect the clutter object (pole). It is not so clear for the vehicle-vehicle clutter testing, as shown in Table 14. When vehicles were used for both the target and clutter objects, there was quite a bit of scatter in the data from the sensor after the point at which transition should have occurred.

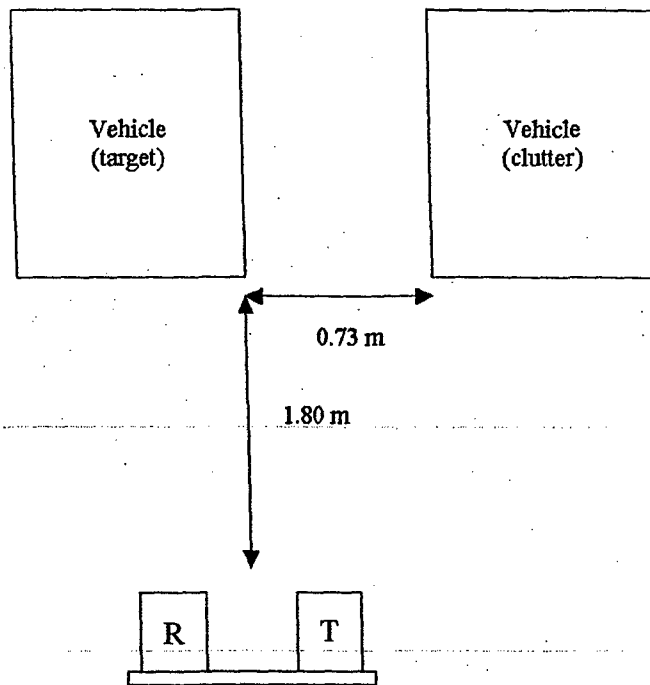


Figure 24. Experimental setup for the vehicle-vehicle clutter test.

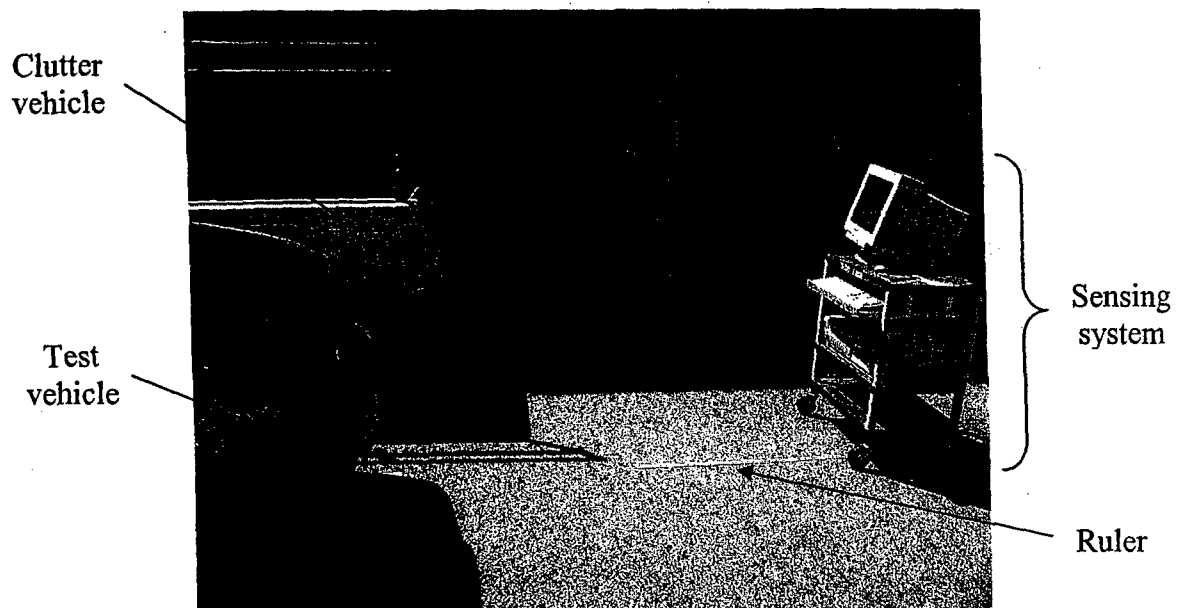


Figure 25. Vehicle-vehicle clutter test setup.

Table 13. Measured distance to the edge of a vehicle front bumper as compared to distance data from the sensor with a pole used as a clutter object.

Measured Distance (m)	Distance from Sensor Data (m)	Deviation (m)	Measured Distance (m)	Distance from Sensor Data (m)	Deviation (m)
0.25	0.31	0.06	1.75	1.74	-0.01
0.50	0.51	0.01	2.00	1.98	-0.02
0.75	0.72	-0.03	2.25	2.15	-0.10
1.00	0.97	-0.03	2.50	2.13	-0.37
1.25	1.25	0.00	2.75	2.13	-0.62
1.50	1.49	-0.01	3.00	2.13	-0.87

Table 14. Measured distance to the edge of a vehicle front bumper as compared to distance data from the sensor with another vehicle used as a clutter object.

Measured Distance (m)	Distance from Sensor Data (m)	Deviation (m)	Measured Distance (m)	Distance from Sensor Data (m)	Deviation (m)
0.25	0.25	0.00	1.75	1.74	-0.01
0.50	0.49	-0.01	2.00	1.99	-0.01
0.75	0.72	-0.03	2.25	2.12	-0.13
1.00	0.99	-0.01	2.50	(2.49)	(-0.01)
1.25	1.22	-0.03	2.75	(2.76)	(0.01)
1.50	1.42	-0.08	3.00	(2.08)	(-0.92)

7.3 Conclusions from the Testing

The results of the clutter testing show that the sensor had a difficult time distinguishing between the target and clutter object when both were vehicle bumpers. When the sensor should have been sensing the clutter vehicle, it would flip-flop between detecting it and the target vehicle. The geometry of the clutter vehicle's rear bumper may have been a factor, causing the projected sound waves to be dispersed. A similar problem was encountered when performing the static-static testing, in which placement of the sensor and the geometry of the vehicle rear bumper affected the measured displacement. Thus, an issue to consider for application in a pre-crash system is where sensors should be mounted in a front bumper relative to another vehicle's rear bumper to

minimize inaccurate readings and to what extent various bumper shapes have on the sensor readings.

Chapter 8

Static-Dynamic Testing

8.1 Testing Procedure

The final round of testing involved moving the sensor away from a test object, or vice versa (whichever was easier to do), a distance of about 2.0 m along its centerline over a time period of roughly 2.0 to 4.0 sec, as depicted in Figure 26. To accurately determine the position of the target relative to the sensor as a function of time, the sensor's LabVIEW™ VI was modified to include distance data from a string potentiometer, or string pot. A close-up of the string pot and a picture of the modified sensing system are shown in Figures 27 and 28, respectively. For more information on the modified VI and the string pot, see Appendix A, Section 2.

As shown in Figure 29, an assistant was needed to hold the end of the string pot cable next to the target object because of the considerable amount of force needed to pull the cable. Also, Figure 30 shows a close-up of the sensor and string pot assembly used for testing. The tests were performed for a variety of test objects, including different sized poles (one with a diameter of 0.205 m, and the other 0.095 m), a box, a vehicle rear bumper, and a pedestrian. The distance data from the sensor was then compared to the data generated by the string pot.

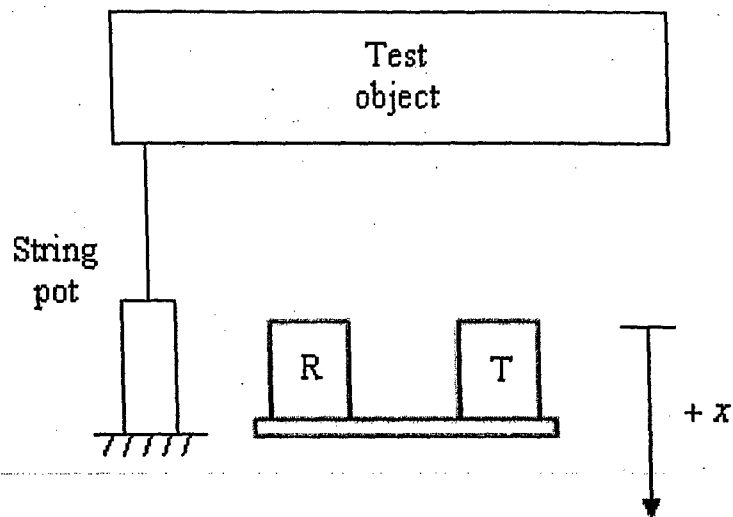


Figure 26. Experimental setup for the static-dynamic testing.

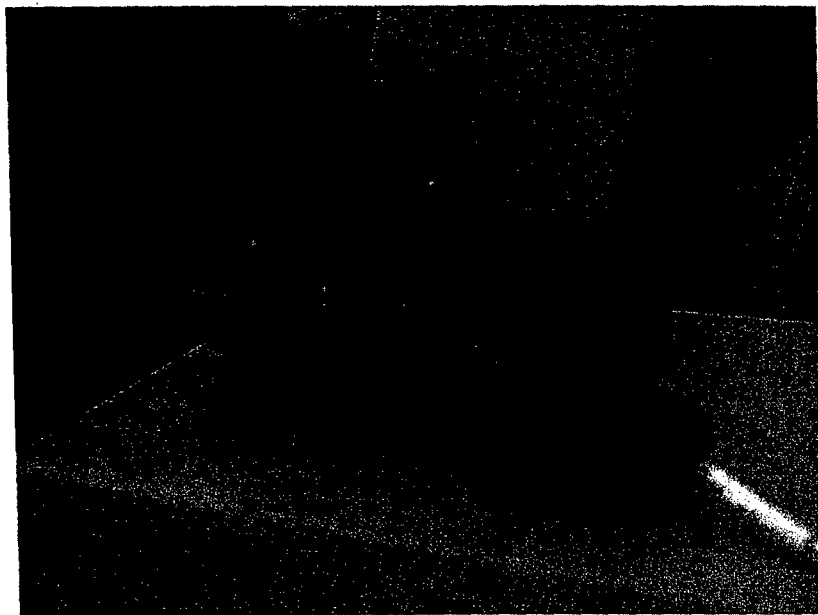


Figure 27. Close-up of the string pot.

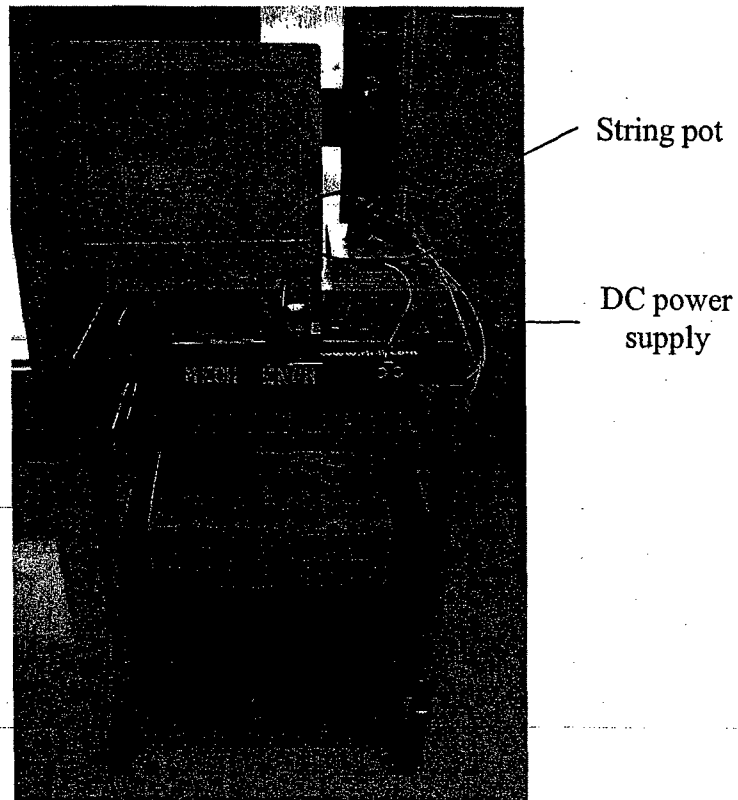


Figure 28. Ultrasonic sensing system with the string pot included.

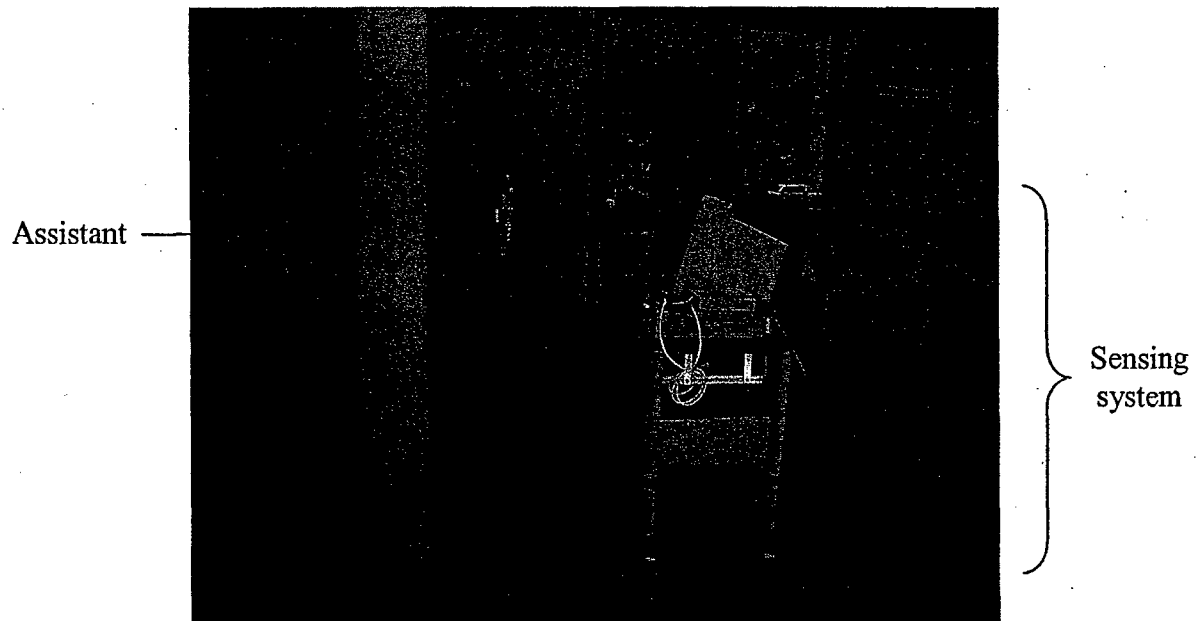


Figure 29. Static-dynamic testing setup.

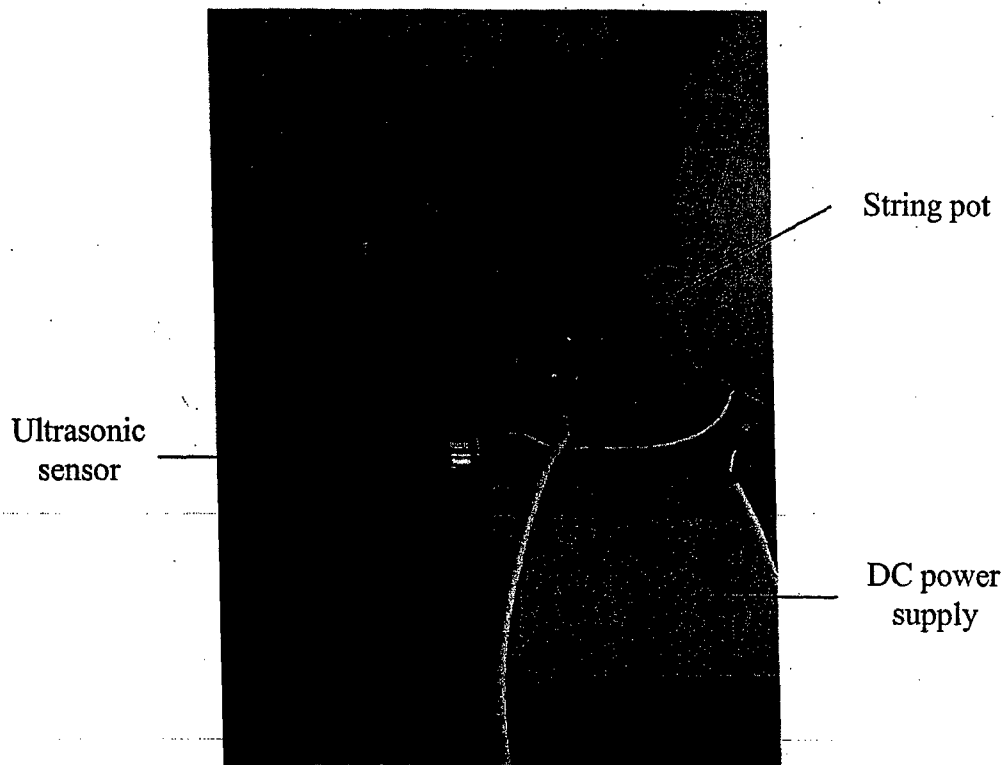


Figure 30. Close-up of the static-dynamic testing setup.

8.2 Results of the Testing

The results for the static-dynamic testing are presented in Figures 31 through 38, in which displacement of the target objects away from the ultrasonic sensor as measured by the string pot and sensor is plotted over time for comparison. As the figures show, overall the sensor accurately measures the displacement of the test object (with occasional scatter), with the exception of the pole (0.095 m in diameter) as a target. Multiple trial runs with the pole as shown in Figures 33 through 35 indicate that the sensor consistently underestimates the displacement of the pole. Also of interest is what happens when the string pot cable reaches its maximum length. Figure 31 clearly indicates when the string pot is maxed out, resulting in a horizontal line at about 2.1 m. In this case, the sensing system was still moving when the string pot reached its

maximum range, and therefore the sensor continued to measure a displacement. The results of the static-dynamic testing are summarized in a deviation-vs.-displacement curve in Figure 38.

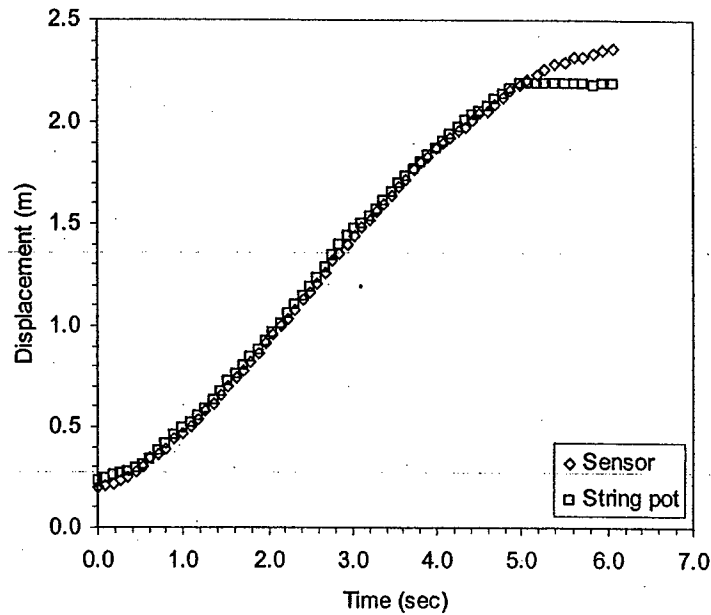


Figure 31. Displacement of a box away from the ultrasonic sensor as a function of time as compared to the displacement measured by the string pot.

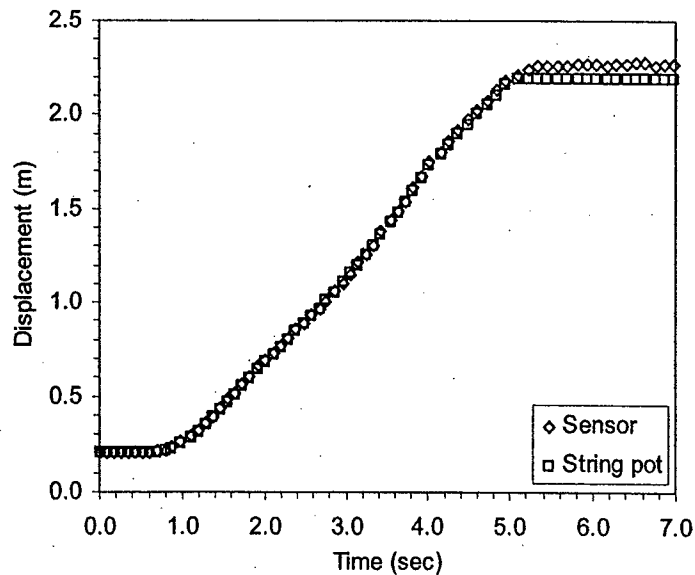


Figure 32. Displacement of a column away from the ultrasonic sensor as a function of time as compared to the displacement measured by the string pot.

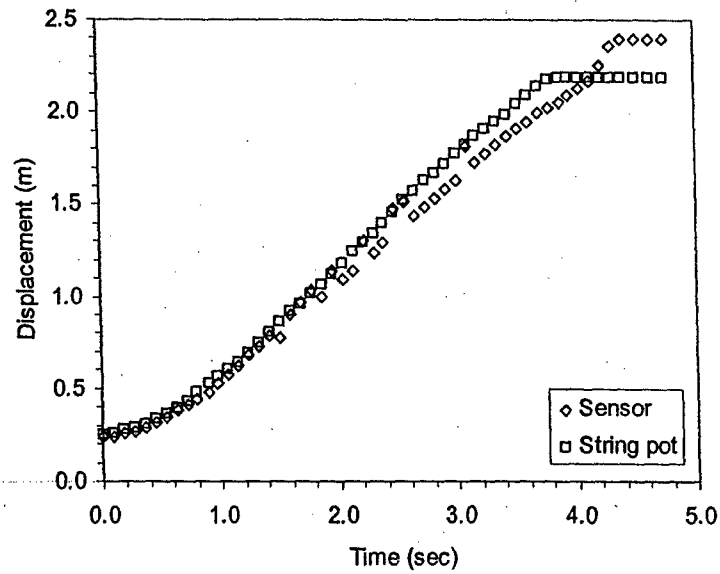


Figure 33. First test for the displacement of a pole away from the ultrasonic sensor as a function of time as compared to the displacement measured by the string pot.

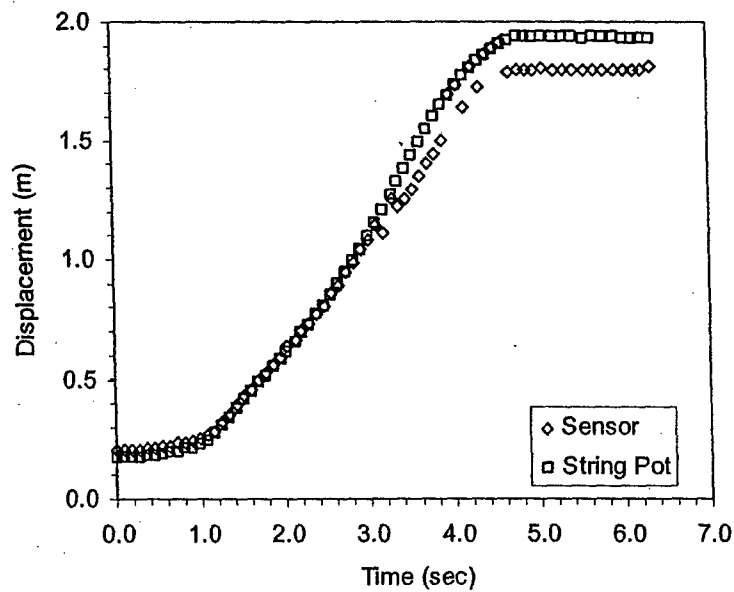


Figure 34. Second test for the displacement of a pole away from the ultrasonic sensor as a function of time as compared to the displacement measured by the string pot.

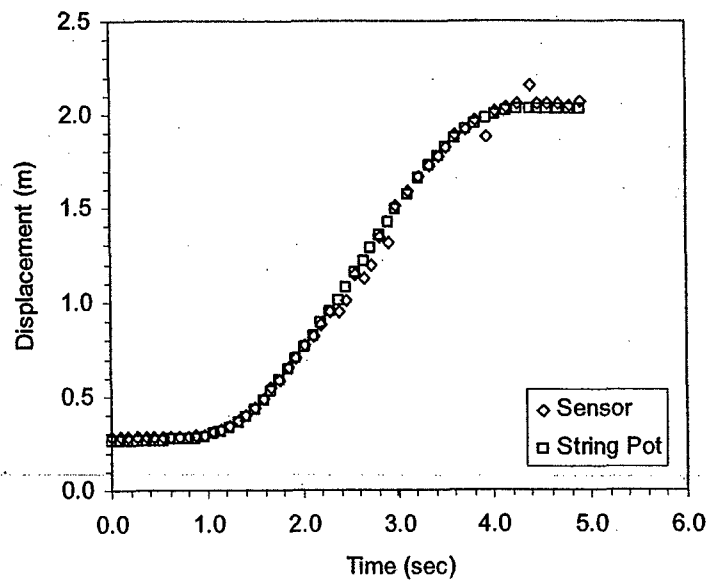


Figure 35. Third test for the displacement of a pole away from the ultrasonic sensor as a function of time as compared to the displacement measured by the string pot.

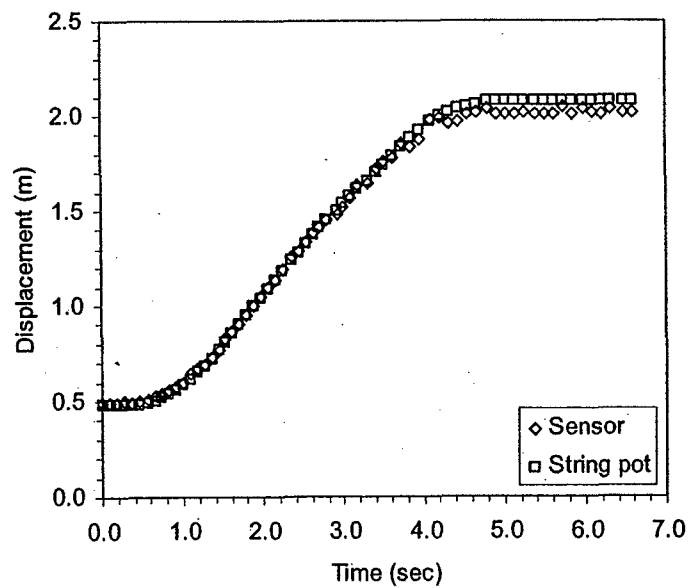


Figure 36. Displacement of a vehicle rear bumper away from the ultrasonic sensor as a function of time as compared to the displacement measured by the string pot.

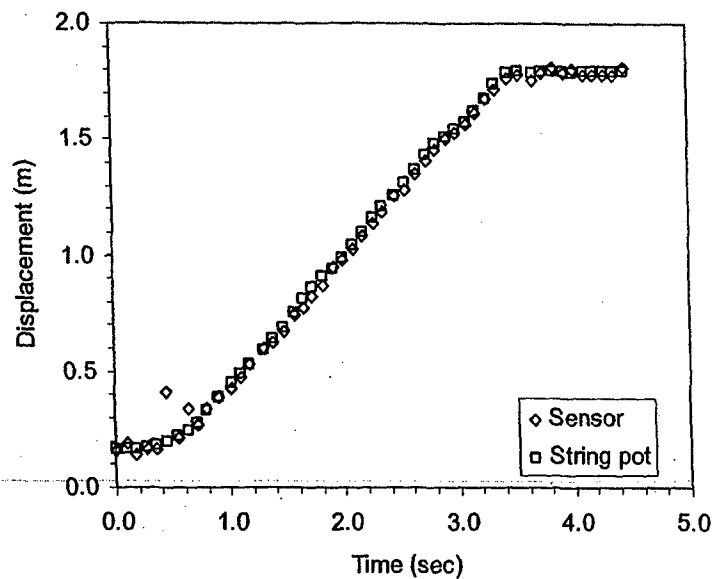


Figure 37. Displacement of a pedestrian away from the ultrasonic sensor as a function of time as compared to the displacement measured by the string pot.

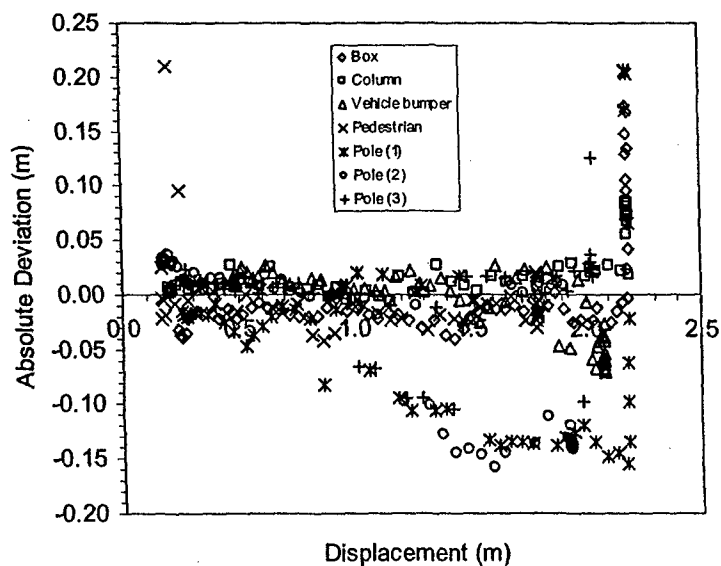


Figure 38. Absolute deviation as a function of displacement for various test objects used in the static-dynamic testing.

8.3 Conclusions from the Testing

The sensor performed very well in the static-dynamic testing except when the target object was a small-diameter pole. The sensor consistently underestimated the pole's displacement, and the reason for this behavior is still unclear. One would expect the sensor to *overestimate* the displacement, not the opposite. Although the underestimate was not a considerable amount, it could lead to problems when pre-crash safety maneuvers are performed (i.e., false signals from the algorithm causing airbags to deploy when not needed). It would be beneficial to conduct this portion of the testing for various diameters between the two extremes used (0.205 m and 0.095 m) to determine at what size pole the readings from the sensor should be questioned.

Also, as indicated in Figure 31, it is possible for the string pot to max out but continue to record movement with the ultrasonic sensor. This problem can be alleviated by securely mounting the string pot to the sensing system since it was being held by hand during testing and could have slipped. Furthermore, several of the runs generated streams of data that had a few outliers. This is especially typical when a pedestrian is used as a target object because skin and clothing may diffuse the transmitted sound waves. These outliers can be eliminated by filtering the collected data. Also, it should be noted that the sensing system (or target) was moved at an uncontrolled speed; that is, although it was desirable to move the sensing system (or target) at a constant velocity for each round of testing, this was nearly impossible to accomplish with the given experimental procedure.

Chapter 9

Final Conclusions and Recommendations

9.1 Other Considerations

In addition to the need for further testing of the ultrasonic sensor, a number of improvements could be made in data collection and interpretation, including revisions to the current data acquisition algorithm and the use of a data filter.

Several issues came up during development and testing of the sensing system algorithm. First, even though the ultrasonic sensor could operate at a frequency of about 34 Hz, the elapsed time per displacement measurement from the LabVIEW™ VI averages about 0.05 sec at best, or a frequency of only 20 Hz. Another algorithm-related issue deals with the considerable slowdown in the frequency of data collection when the system is run for long periods of time. When the algorithm is started, the average time per measurement is about 0.05 sec. After about 10 to 20 sec of operation, a noticeable slowdown in the data collection frequency occurs, gradually worsening until the average time per measurement approaches about 0.2 sec, or 5 Hz. By this point the ultrasonic sensor is rendered useless since it cannot generate a sufficient amount of data at such a low sampling frequency. Lastly, there are a number of revisions that could be made to the current VI to improve sensor performance. For example, instead of setting a data collection frequency, a feedback loop that adjusts the sampling rate could be implemented since objects that are close to the sensor can be detected at higher frequencies and vice versa. Another improvement to consider is to create a buffer in which collected data is temporarily placed until execution of the VI is stopped, at which

point the data is saved to a file. By establishing a buffer, the VI can concentrate entirely on collecting data as quickly as possible. These revisions to the data collection algorithm would greatly enhance the performance of the ultrasonic sensor.

For the most part the ultrasonic sensor returns accurate displacement data, but on occasion there is some scatter. For this reason it may be worthwhile to investigate the use of a filter to eliminate outliers in the collected data. One such filter is a Kalman filter, and the results of Table 15 suggest that it can effectively filter a set of collected data. For more information on how a Kalman filter works, refer to Grewel and Andrews' *Kalman Filter: Theory and Practice Using MATLAB* [8].

Table 15. Kalman filtered and unfiltered distance data.

Unfiltered Distance (m)	Kalman Filtered Distance (m)
0.000	0.000
0.006	0.001
0.013	0.005
0.017	0.012
0.021	0.019
0.025	0.025
0.024	0.027
0.031	0.031
0.033	0.034
0.035	0.036
0.037	0.038
0.039	0.040

Although it is a decent filter, a Kalman filter does have several disadvantages. For one thing, it requires about 5 iterations before it converges, and so the first portion of the filtered data is largely incorrect. However, since the sensor is intended for use over extended periods of time as part of a vehicle pre-crash sensing system, simply ignoring the first 5 data points would have very little effect on the sensor's overall performance.

Also, the Kalman filter requires a fixed time step, whereas the elapsed time per displacement measurement from the sensor fluctuates. This is not so much a problem when the sensor is operated for short periods of time, where the average time per measurement is relatively constant. However, the gradual slowdown that occurs when the sensor is run for a long time is can become a problem. As of now, use of a Kalman filter should be limited to data collected over short periods of sensor operation until the VI can be modified to eliminate the gradual slowdown in data collection.

9.2 Summary of the Conclusions and Recommendations

The following is a summary of the conclusions and recommendations based on the experimental data from the ultrasonic sensor and the algorithm used to collect it:

- The sensor effectively measures the displacement between it and a variety of test objects (including boxes, columns, vehicles, pedestrians, etc.) within the manufacturer's published range of up to 3.0 m under a number of testing conditions (static, sonic cone, clutter, dynamic, etc.). It is also possible to detect objects at distances greater than this range with mixed results.
- Further testing should be conducted using objects with a wider variety of geometries and orientations relative to the sensor, including when these objects are placed further than the published range. Also, the effect of changing the orientation of the sensor (i.e., when placed vertically instead of horizontally) on the accuracy of the collected data should be investigated.
- The current algorithm used to operate and collect data from the ultrasonic sensor should be modified to obtain a faster data sampling rate; eliminate slowdown in the program when operated for long periods of time; establish a buffer to temporarily

store collected data that is saved to file after execution of the algorithm is stopped; and implement a feedback loop to adjust the data sampling rate based on the target object's location.

- Use of a Kalman filter (or another type of filter) should be investigated to eliminate scatter in the collected data and then implemented when the before mentioned revisions to the sensing system algorithm have been achieved.

The above findings suggest that, although further testing and some revisions to the current sensing system are needed, the Devantech SRF04 Ultrasonic Range Finder is a good candidate for a vehicle pre-crash sensing system up to a vehicle or target speed of about 20 mph, with the possibility of an increase in the operating speed.

Appendix A

Detailed Schematics and Parts List

A.1 Detailed Sensing System Schematics

Figure 39 is a CAD drawing provided by Acroname Inc. [9] of the Devantech SRF04 ultrasonic range finder. The CAD drawing is actually of the manufacturer's SRF08 model, but the SRF04 and SRF08 are identical in shape and size.

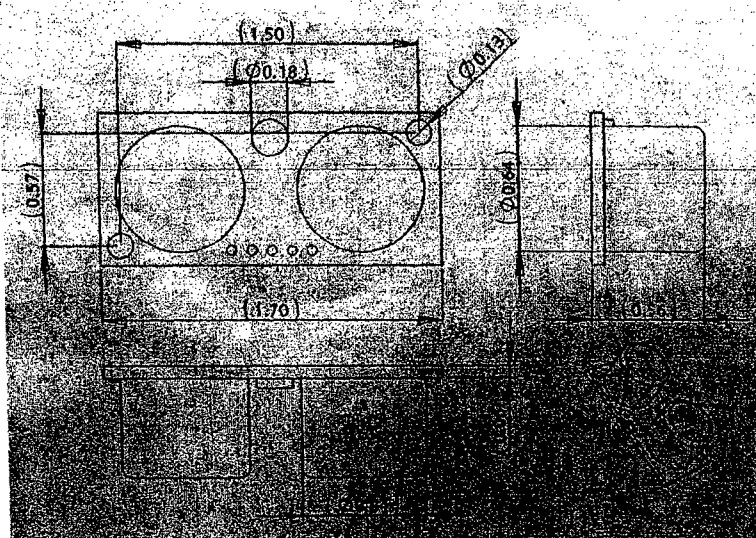


Figure 39. CAD drawing of the ultrasonic sensor.

The sensor consists of a rectangular circuit board from which extend four color-coded wires corresponding to a +5V power input (red), ground (black), an input pulse (blue), and the return signal (white). Mounted on the front of the circuit board are two cylindrical housings protecting the two ultrasonic transducers, one for generating a sound wave from the input pulse and the other for detecting the echo. Among performing many other functions, the sensor's circuitry converts the detected echo into a digital signal from which the pulse width is measured.

The ultrasonic sensor's color-coded wires are interfaced with the I/O connector block as shown in Figure 40.

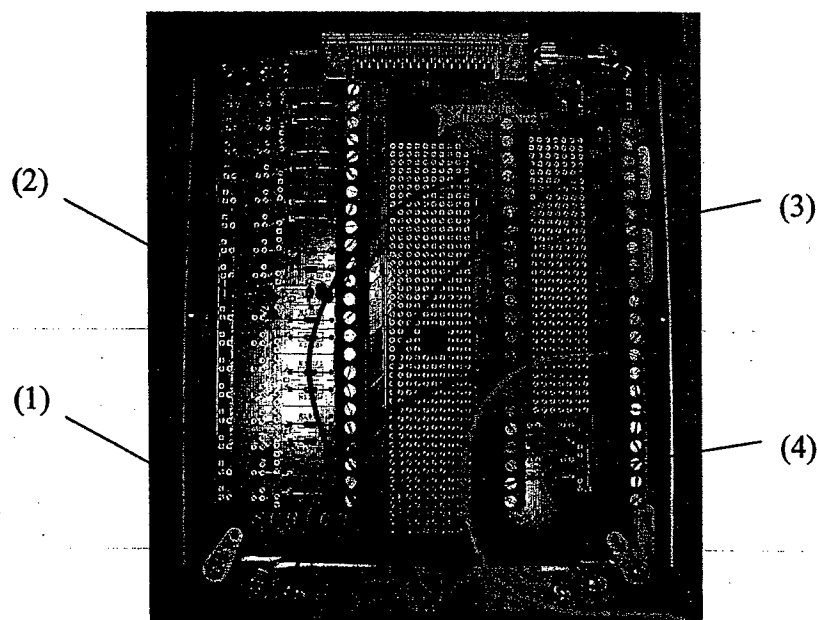


Figure 40. Color-coded wires from the sensor hooked up to the I/O connector block.

Wire 1 (red) corresponds to the sensor's power input and is connected to the I/O block's +5V power terminal (+5V, FUSED), pin 8. Wire 2 (black) is connected to ground (DGND), pin 13, to complete the circuit. It should be noted that the connector block has several DGND terminals; the decision to use pin 13 was arbitrary. Wire 3 (blue) carries the input signal generated by the LabVIEW™ algorithm from the I/O block's counter 0 to the sensor. The wire is connected to pin 2 (GPCTR0_OUT), the counter's output terminal. Finally, wire 4 (white) sends the return pulse from the sensor to counter 1. It is connected to pin 41 (PFI4/GPCTR1_GATE), the counter's input terminal. The connections are summarized in Table 16.

Table 16. Connection guide for interfacing the sensor with the I/O connector block.

Wire (Number)	Pin No.	Signal
Red (1)	8	+5V, FUSED
Black (2)	13	DGND
Blue (3)	2	GPCTR0_OUT
White (4)	41	PFI4/GPCTR1_GATE

The LabVIEW™ algorithm, or *virtual instrument* (VI), created to generate an input pulse and acquire data from the sensor is presented in Figure 41. The following is a step-by-step breakdown of the diagram's main components and functions.

Referring to Figure 42, when the program is executed it asks the user to choose a location where collected data will be saved to.

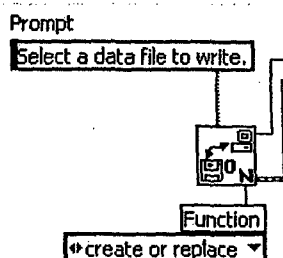


Figure 42. Prompting the user to choose a location to save collected data to.

Figure 43 shows the block diagram responsible for generating a pulse that is sent to the sensor. The first block creates a pulse based on information provided by the user on the front panel (see Figure 44), including the pulse frequency, duty cycle (the pulse width divided by the period), idle state (low or high), and the counter used to generate the pulse. Next is the “DAQmx Timing” block which specifies the mode of pulse generation (continuous) and sets the timing source (“implicit” refers to the counter). The final block initializes the pulse generation.

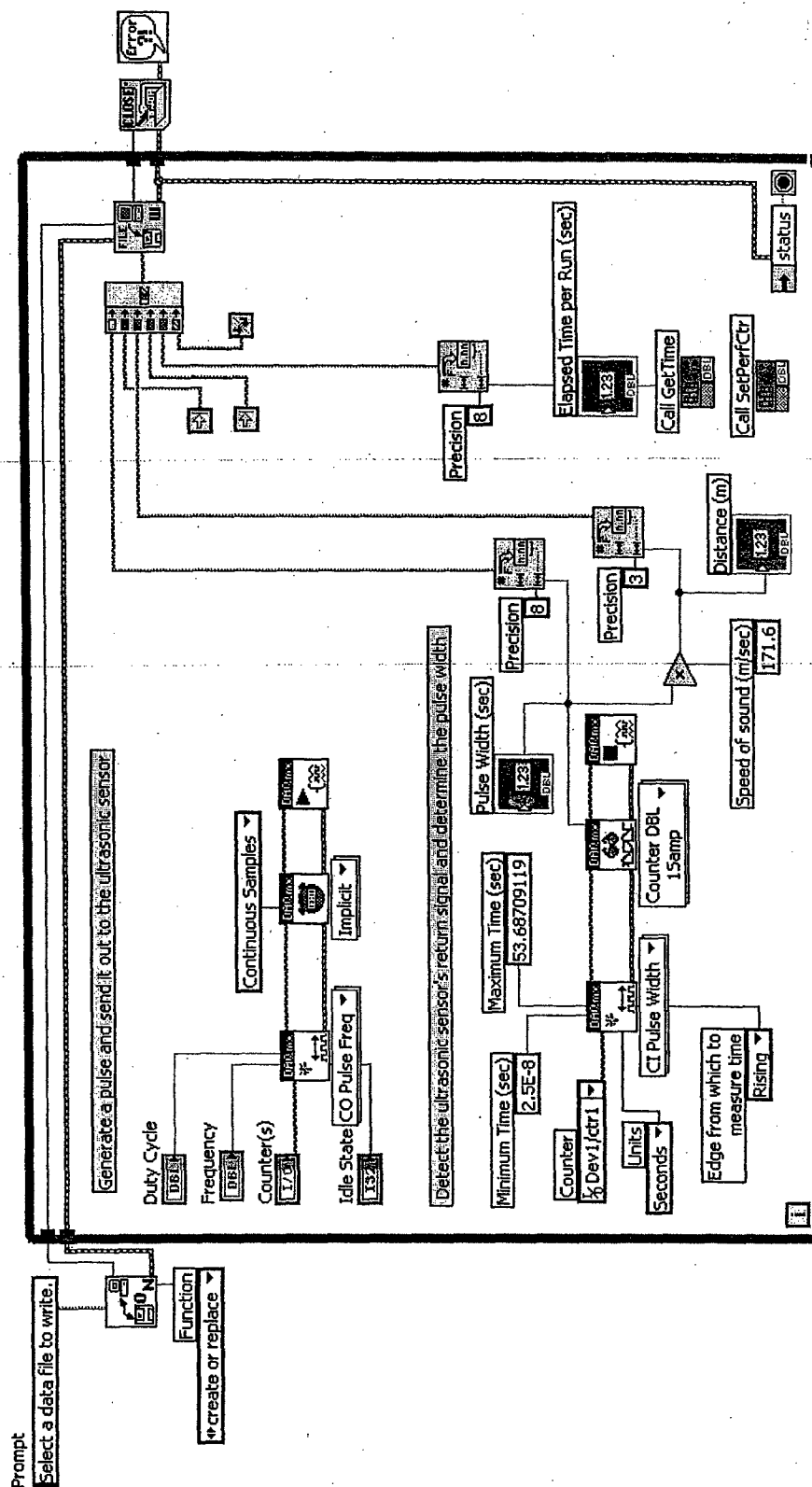


Figure 41. LabVIEW™ algorithm used to generate an input pulse and acquire data from the ultrasonic sensor.

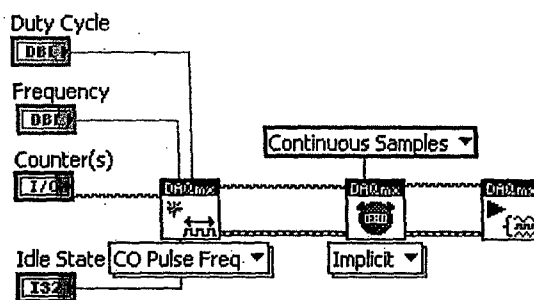


Figure 43. Generating an input pulse for the sensor based on time information provided by the user on the front panel.

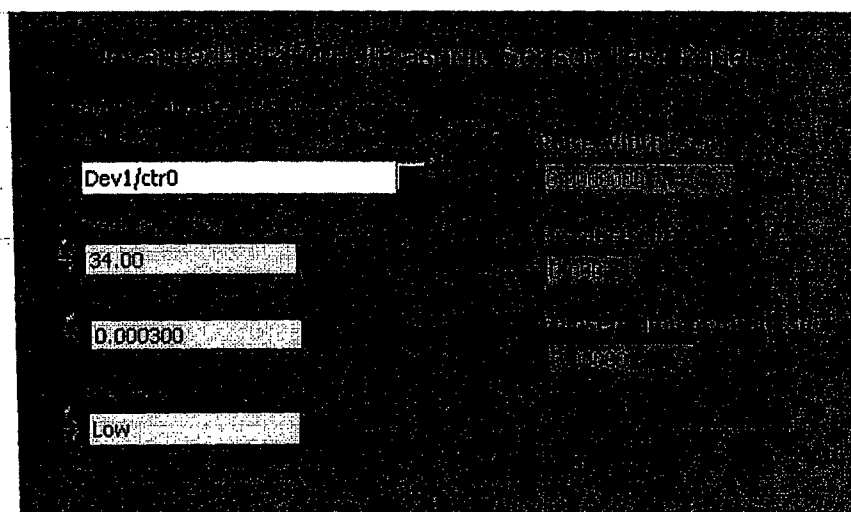


Figure 44. Front panel where input pulse characteristics are specified by the user and collected data is displayed.

The block diagram in Figure 45 measures the return pulse width, calculates the distance between the sensor and the detected object, and then displays the pulse width and distance data on the front panel. The first block specifies which edge of the return signal to start measuring time and the counter used to do so. The second block reads the measured pulse width from the counter, and then the task is stopped. The pulse width is then used to calculate the relative displacement, which is displayed along with the pulse width for the user. Finally, these two numbers are formatted into strings.

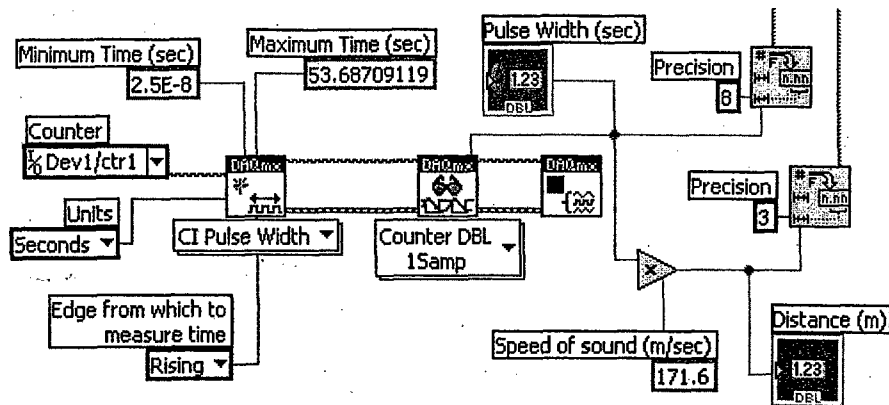


Figure 45. Measuring the return pulse width, calculating the relative displacement, and displaying the information for the user.

Figure 46 shows the diagram used to keep track of the elapsed time per run; that is, it times how long it takes for the system to generate the pulse, send it out, receive a return signal, and measure the pulse width. The “Call GetTime” and “Call SetPerfCtr” blocks measure time by accessing the elapsed time recorded by the computer processor. This time is then displayed on the front panel and formatted into a string.

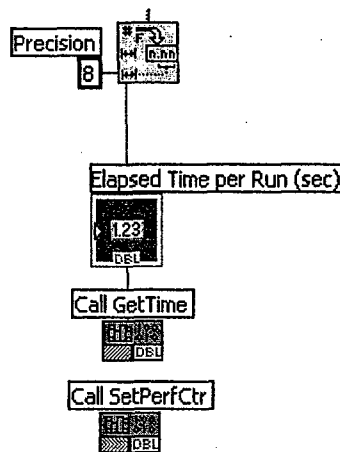


Figure 46. Measuring the elapsed time per run and displaying the information on the front panel.

The block diagram in Figure 47 takes all the strings (return pulse width, distance, and elapsed time) and creates an array, which is then saved to the user-specified file. The file is closed when the user signals the end of data collection. Note that a heavy gray line separates the “Write to File” and “Close File” blocks. This line is part of the “while loop” that encloses the block diagrams in Figures 43, 45, 46, and 47. The “while loop” allows the VI to acquire and record data continuously until told to stop.

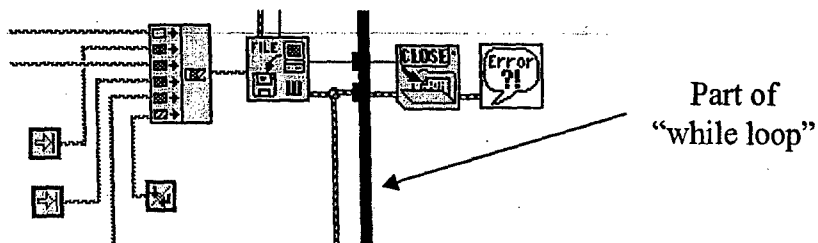


Figure 47. Creating an array of data and saving it to file.

A.2 Addition of the String Potentiometer

To accurately determine the position of the target relative to the sensor as a function of time for the static-dynamic testing, the sensor's LabVIEW™ VI was modified to include distance data from a string potentiometer, or string pot. According to the manufacturer of the device, SpaceAge Control Inc. [10], the string pot consists of a stainless steel cable that is wound on a threaded drum attached to a rotary sensor. When the cable is pulled on, the threaded drum rotates and the rotary sensor generates an electrical signal linearly proportional to the distance the cable is pulled. The string pot generates a signal of 0 to 5 V over a range of about 2.1 m.

The additional connections to the I/O block for the string pot are shown in Figure 48. Wire 1 (white) corresponds to the high output voltage signal from the string pot and is connected to pin 68 (ACH0). Wire 2 (yellow) is the string pot's low output signal and is attached to pin 34 (ACH8). It should be noted that the yellow wire was actually soldered onto a green wire that connects to the string pot.

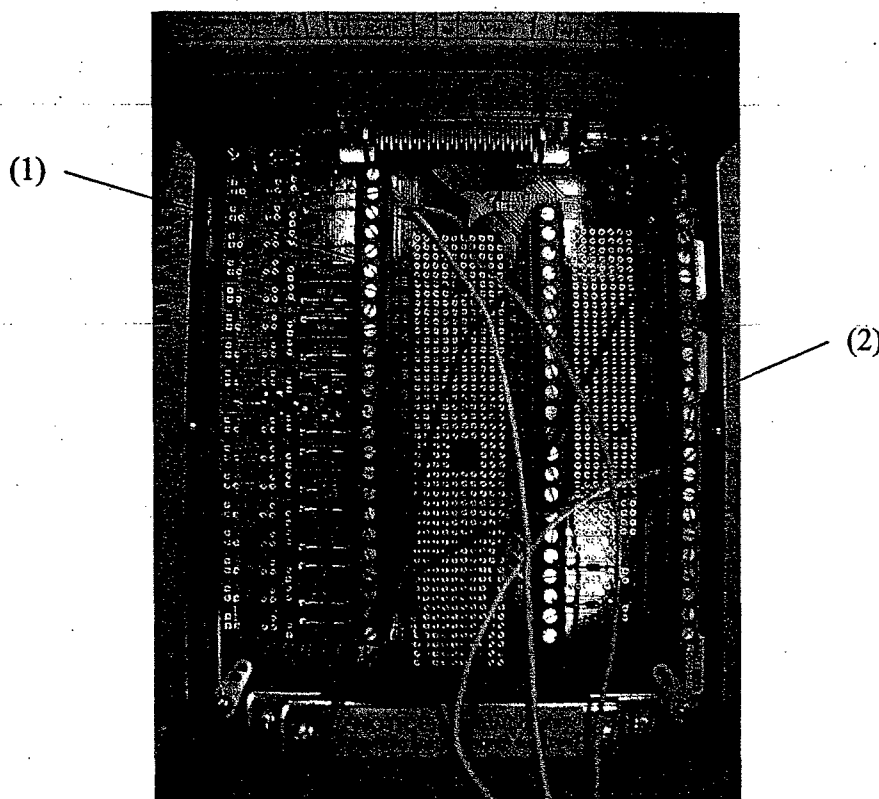


Figure 48. Additional color-coded wires from the string pot hooked up to the I/O block.

The string pot has an additional two wires, red and black, that are connected to a DC power supply, as shown in Figure 49. To be run in differential mode, in which LabVIEW™ takes the difference between the high and low voltage signals from the string pot, the device requires a minimum of 12 V.



Figure 49. String pot attached to a DC power supply.

The connections for the string pot are summarized in Table 17.

Table 17. Connection guide for interfacing the string pot with the I/O connector block.

Wire (Number)	Pin No.	Signal
White (1)	68	ACH0
Yellow (2)	34	ACH8
Red (--)	--	+12 V (Power Supply)
Black (--)	--	-12 V (Power Supply)

The modified LabVIEW™ block diagram with data acquisition from the string pot is shown in Figure 50. Referring to Figure 51, the first block establishes that an analog voltage signal is to be read by analog input channel 0. Also, the mode of data acquisition is set to differential, where the maximum and minimum possible output voltages are ± 5 V. The second block establishes the data acquisition rate and characteristics, including a sample rate of 1000 Hz and whether to continuously sample data (continuous mode) or stop after the specified amount of samples (finite mode). The number of

samples (in this case 10,000) as well as the sample rate can be chosen arbitrarily so long as the algorithm returns a stream of voltage data. If the number of samples and the sample rate are too low, then the program will only return a single value. The third and fourth blocks execute data acquisition on the requested channel and read the data from the string pot, respectively. The last block stops execution and is optional – the algorithm will work properly even without this block.

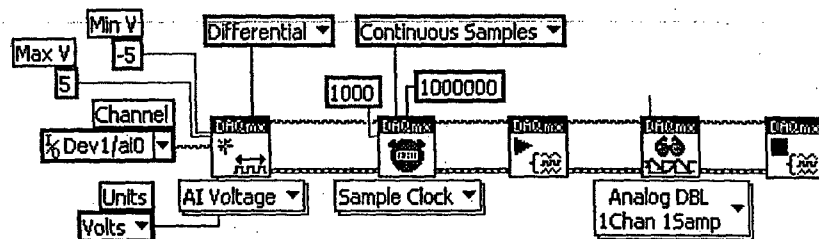


Figure 51. Establishing an analog voltage input channel and reading the voltage data from the string pot.

Figure 52 shows the block diagram for displaying and recording the information from the string pot. The voltage data read from the string pot is converted into a displacement based on the manufacturer's output voltage range of 0 to 5 V and the sensor's calibrated distance range of about 2.17 m. This distance data is then formatted into a string and saved to file along with the other information from the ultrasonic sensor.

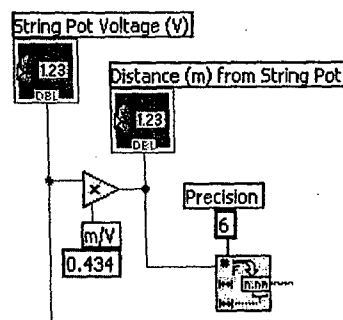


Figure 52. Displaying and saving the distance information from the string pot.

A.3 Parts List

The components of the final design are tabulated in Table 18.

Table 18. Components of the ultrasonic sensing system.

Component	Manufacturer
Devantech SRF04 ultrasonic range finder	Acroname Inc.
Trinitron Multiscan 210GS monitor	Sony
OptiPlex GX110 computer CPU	Dell
Rolling cart	--
PCI-6221 data acquisition card	National Instruments
SCB-68 shielded I/O connector block	National Instruments
String potentiometer	SpaceAge Control Inc.
Adjustable DC power supply	Hewlett-Packard

Appendix B Supporting Derivations

B.1 Displacement and Average Velocity

When connected to an oscilloscope or computer software, an ultrasonic sensor's output and received signals will produce pulses similar to those in Figure 53. These pulses are actually electrical signals corresponding to the pure output and received signals having gone through additional computation in the sensor circuitry. The time delay, t_{delay} , or the difference between the time the output pulse was sent and its echo was received, is used to determine the distance between the sensor and an object.

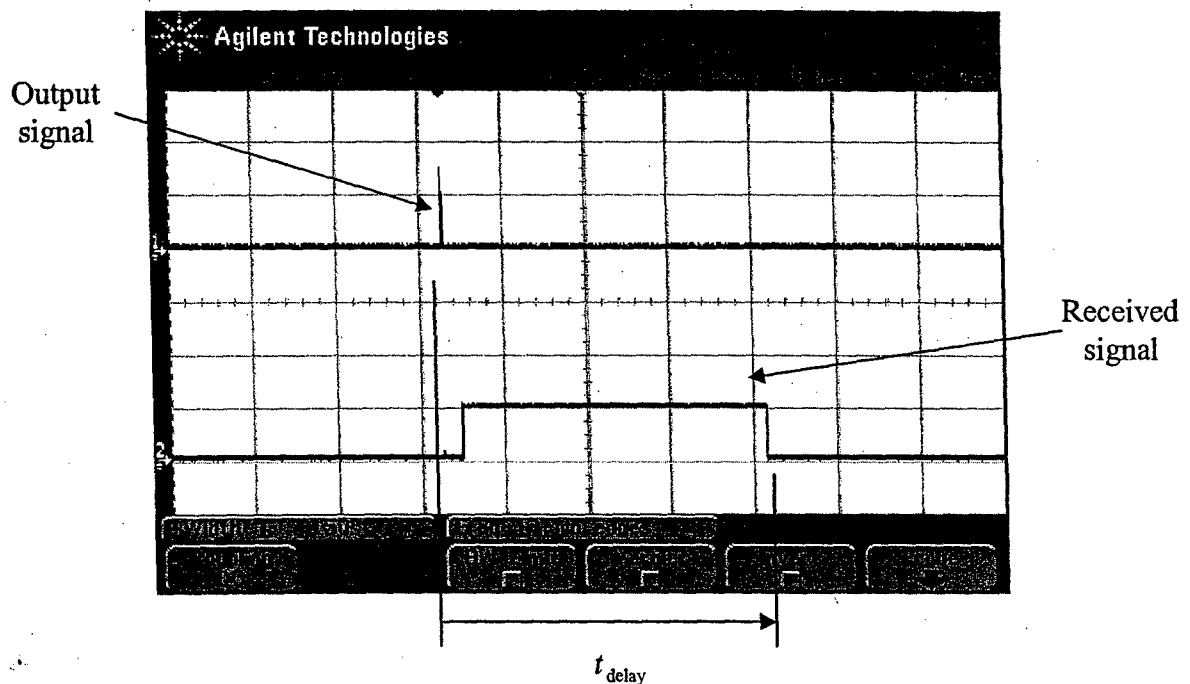


Figure 53. Oscilloscope screen capture of an ultrasonic sensor's output and received signals after having gone through additional computation in the sensor circuitry.

When calculating the distance between the sensor and an object, only half of the measured time delay is used, as shown in Figure 54.

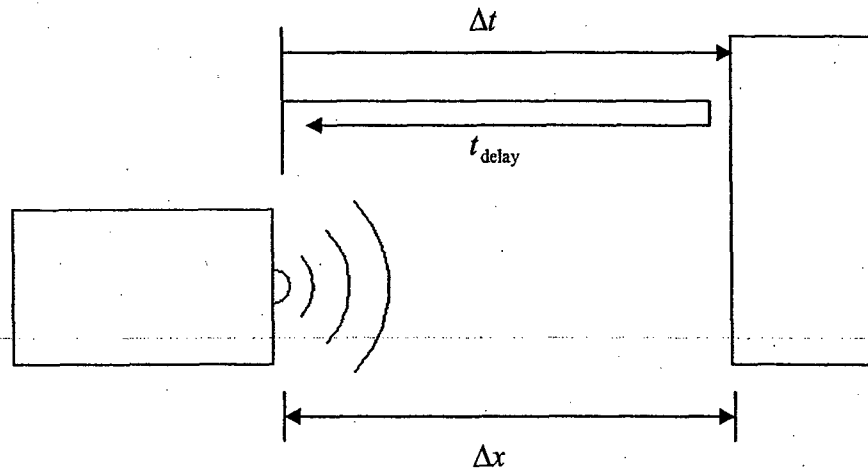


Figure 54. Diagram showing how the distance between the sensor and an object, Δx , is determined.

Beginning with the definition of velocity,

$$v = \frac{dx}{dt}$$

$$v \approx \frac{\Delta x}{\Delta t}$$

Rearranging to solve for the distance between the sensor and an object, Δx , replacing velocity, v , with the speed of sound, c , and substituting Δt with half of the time delay gives

$$\Delta x = \frac{1}{2} c t_{\text{delay}}$$

The speed of sound, c , is governed by the following equation:

$$c = \sqrt{kRT}$$

or

$$c = \sqrt{k \frac{\bar{R}}{M} T}$$

where k is the ratio of specific heats, \bar{R} is the universal gas constant, M is the molecular weight of dry air, and T is the air temperature in absolute scale. According to Bohn [4], the ratio of specific heats can be rewritten as

$$k = \frac{d+2}{d}$$

where d is the degrees of freedom of air molecules. Air can be approximated as a diatomic gas, and diatomic molecules have 5 degrees of freedom. Therefore,

$$k = \frac{7}{5}$$

Bohn [4] explains that the presence of water in air causes the average number of degrees of freedom to increase by a fraction of molecules in moist air that are water, y :

$$k^* = \frac{7+y}{5+y}$$

where $*$ denotes quantities corrected for humidity. Also, the average molecular weight of dry air decreases with added moisture. The composition of dry air according to Yunus A. Cengel and Michael A. Boles [11] in *Thermodynamics: An Engineering Approach*, 4th Ed. is summarized in Table 19.

Table 19. Composition and molecular weight of dry air.

Element	Percentage (%)	Molecular Weight (kg/kmol)
Oxygen (O ₂)	20.9	31.999
Nitrogen (N ₂)	78.1	28.013
Argon (Ar)	0.9	39.948

Thus, the average molecular weight of dry air is

$$\begin{aligned}
 M &= (\% \text{O}_2)M_{\text{O}_2} + (\% \text{N}_2)M_{\text{N}_2} + (\% \text{Ar})M_{\text{Ar}} \\
 M &= 0.209\left(31.999 \frac{\text{kg}}{\text{kmol}}\right) + 0.781\left(28.013 \frac{\text{kg}}{\text{kmol}}\right) + 0.009\left(39.948 \frac{\text{kg}}{\text{kmol}}\right) \\
 M &= 28.925 \frac{\text{kg}}{\text{kmol}}
 \end{aligned}$$

According to Bohn [4], the average molecule weight of moist air, M^* , is given by

$$M^* = M - (M - M_w)y$$

where M_w is the molecular weight of water, or $18.015 \frac{\text{kg}}{\text{kmol}}$. Therefore, the average molecular weight of moist air is

$$\begin{aligned}
 M^* &= 28.925 - (28.925 - 18.015)y \frac{\text{kg}}{\text{kmol}} \\
 M^* &= 28.925 - 10.910y \frac{\text{kg}}{\text{kmol}}
 \end{aligned}$$

Relative humidity, ϕ , is defined as the following:

$$\phi = \frac{P_v}{P_g} \bigg|_T$$

where P_v is the vapor pressure of water at temperature T , and P_g is the saturation pressure of water at the given temperature. The vapor pressure of water is given by

$$P_v = yP_{\text{atm}}$$

where P_{atm} is atmospheric pressure. Combining these two equations gives

$$\begin{aligned}\phi &= \frac{yP_{\text{atm}}}{P_g)_T} \\ yP_{\text{atm}} &= \phi P_g)_T \\ y &= \frac{\phi P_g)_T}{P_{\text{atm}}}\end{aligned}$$

Thus, the ratio of specific heats corrected for humidity and the average molecular weight of moist air are, respectively,

$$k^* = \frac{7 + \frac{\phi P_g)_T}{P_{\text{atm}}}}{5 + \frac{\phi P_g)_T}{P_{\text{atm}}}}$$

and

$$M^* = 28.925 - 10.910 \left(\frac{\phi P_g)_T}{P_{\text{atm}}} \right)$$

The speed of sound corrected for temperature and humidity effects is given by

$$c^* = \sqrt{k^* \frac{\bar{R}}{M^*} T}$$

The previous expression can be written as the following with respect to a reference value for the speed of sound, c_{ref} :

$$\begin{aligned}\frac{c^*}{c_{\text{ref}}} &= \frac{\sqrt{k^* \frac{\bar{R}}{M^*} T}}{\sqrt{k_{\text{ref}} \frac{\bar{R}}{M_{\text{ref}}} T_{\text{ref}}}} \\ c^* &= c_{\text{ref}} \sqrt{\frac{k^*}{k_{\text{ref}}} \frac{M_{\text{ref}}}{M^*} \frac{T}{T_{\text{ref}}}}\end{aligned}$$

Taking the reference to be dry air at 0°C, the speed of sound is

$$c_{\text{ref}} = \sqrt{k_{\text{ref}} \frac{\bar{R}}{M_{\text{ref}}} T_{\text{ref}}}$$

$$c_{\text{ref}} = \sqrt{(1.4) \left(0.2870 \frac{\text{kJ}}{\text{kg} \cdot \text{K}} \right) (273.15 \text{ K})}$$

$$c_{\text{ref}} = 331.29 \text{ m/sec}$$

Thus, the final expression for the speed of sound in m/sec corrected for temperature and humidity is

$$c^* = 331.29 \sqrt{\frac{\left[7 + \frac{\phi P_g}{P_{\text{atm}}} \right]_T}{1.4 \left[5 + \frac{\phi P_g}{P_{\text{atm}}} \right]_T} \frac{28.925}{28.925 - 10.910 \left(\frac{\phi P_g}{P_{\text{atm}}} \right)} \frac{T}{273.15}}$$

Therefore, the distance between the sensor and an object is given by

$$\Delta x = \frac{1}{2} (331.29) t_{\text{delay}} \sqrt{\frac{\left[7 + \frac{\phi P_g}{P_{\text{atm}}} \right]_T}{1.4 \left[5 + \frac{\phi P_g}{P_{\text{atm}}} \right]_T} \frac{28.925}{28.925 - 10.910 \left(\frac{\phi P_g}{P_{\text{atm}}} \right)} \frac{T}{273.15}}$$

where Δx is in m, t_{delay} is in sec, T is in Kelvin, and pressure terms can be in any units as long as they are consistent.

At this point, it would be nice to know how sensitive the calculated distance is to temperature and humidity effects; that is, how much of an effect do temperature and humidity have on the calculated distance over the expected range of use? To answer this question, a sensitivity analysis will be performed, starting with the effects of temperature.

The sensitivity of the calculated distance with respect to temperature, $S_{\Delta x/T}$, is defined as

$$S_{\Delta x/T} = \left. \frac{\partial(\Delta x)}{\partial T} \right|_{\text{NOP}}$$

where NOP stands for the *nominal operating point* of the system. Parameters corresponding to the NOP are arbitrarily chosen, and the values to be used for subsequent sensitivity calculations are summarized in Table 20.

Table 20. Nominal operating point parameters and their values.

Parameter	Value
Temperature, T	20°C (293.15 K)
Relative humidity, ϕ	30%
Saturation pressure of water, $P_g)_T$	2.339 kPa
Atmospheric pressure, P_{atm}	101.3 kPa
Time delay, t_{delay}	5.0 ms

Beginning with the expression for the distance between the sensor and an object, Δx , and rearranging to gather all constants with respect to temperature gives

$$\Delta x = \frac{1}{2} (331.29) t_{\text{delay}} (\sqrt{T}) \sqrt{\frac{\left[7 + \frac{\phi P_g)_T}{P_{\text{atm}}} \right]} \frac{28.925}{1.4 \left[5 + \frac{\phi P_g)_T}{P_{\text{atm}}} \right] 28.925 - 10.910 \left(\frac{\phi P_g)_T}{P_{\text{atm}}} \right) \frac{1}{273.15}}$$

Replacing the constants with C greatly simplifies the equation to

$$\Delta x = C \sqrt{T}$$

Calculating the partial derivative of the distance with respect to temperature yields

$$\begin{aligned} \frac{\partial(\Delta x)}{\partial T} &= \frac{1}{2} C (T)^{-\frac{1}{2}} \\ \frac{\partial(\Delta x)}{\partial T} &= \frac{C}{2\sqrt{T}} \end{aligned}$$

Evaluating the expression at the nominal operating point values summarized in Table 20 gives the sensitivity:

$$S_{\Delta x/T} = \left. \frac{\partial(\Delta x)}{\partial T} \right|_{\text{NOP}}$$

$$S_{\Delta x/T} = 0.001465 \frac{\text{m}}{^{\circ}\text{C}}$$

The effect of temperature on the calculated distance can be presented graphically by plotting the change in distance, $\partial(\Delta x)$, against the change in temperature, ∂T , about the nominal operating point, where the sensitivity, $S_{\Delta x/T}$, represents the slope of the line.

Such a plot is provided in Figure 55.

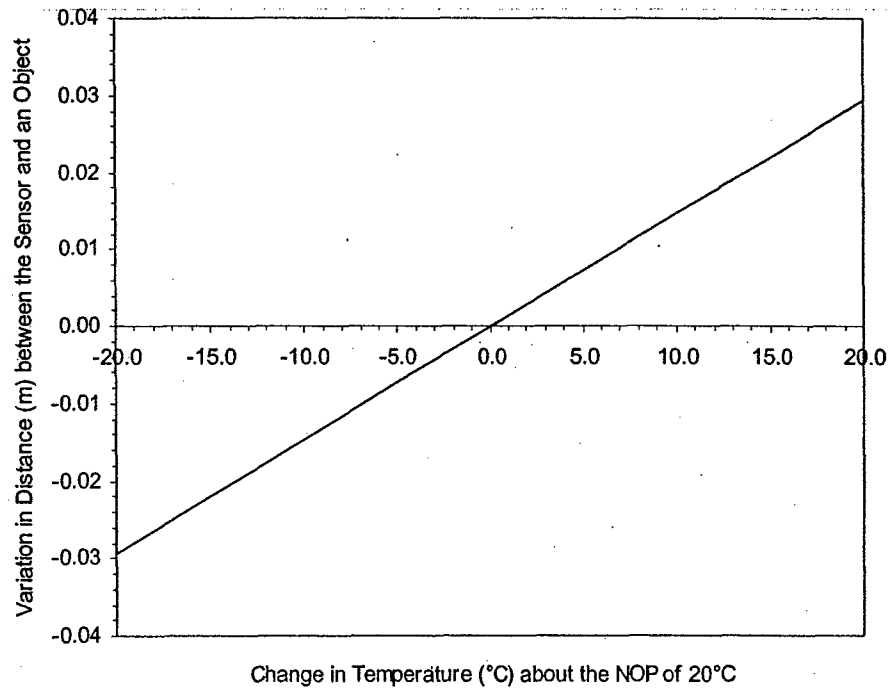


Figure 55. Sensitivity of the distance between the sensor and an object with respect to temperature, relative to a nominal operating temperature of 20°C.

As with temperature, the sensitivity of the calculated distance due to humidity effects is simply the partial derivative of the distance with respect to humidity, evaluated at the nominal operating point:

$$S_{\Delta x/H} = \left. \frac{\partial(\Delta x)}{\partial H} \right|_{\text{NOP}}$$

where the humidity, H , is defined as the product of the relative humidity and the saturation pressure of water at the temperature of interest, or

$$H = \phi P_g)_T$$

Starting with the expression for the distance between the sensor and an object, and rearranging to gather all constants with respect to humidity gives

$$\Delta x = \frac{1}{2} (331.29) t_{\text{delay}} \sqrt{\frac{28.925 P_{\text{atm}} T}{1.4(273.15)}} \cdot \sqrt{\frac{7 P_{\text{atm}} + H}{(5 P_{\text{atm}} + H)(28.925 P_{\text{atm}} - 10.910 H)}}$$

Substituting the constants with C simplifies the equation to

$$\Delta x = C \sqrt{\frac{7 P_{\text{atm}} + H}{(5 P_{\text{atm}} + H)(28.925 P_{\text{atm}} - 10.910 H)}}$$

Taking the partial derivative with respect to H and evaluating it at the nominal operating point gives the sensitivity:

$$S_{\Delta x/H} = 0.001361 \frac{\text{m}}{\text{kPa}}$$

Note that H is varied by changing the humidity ratio. Temperature is held constant, and so the saturation pressure of water is also constant. Therefore, for convenience, Figure 54 shows the variation in distance, $\partial(\Delta x)$, with changes in humidity ratio,

$$\partial \phi = \frac{\partial H}{P_g)_T}, \text{ about the nominal operating point.}$$

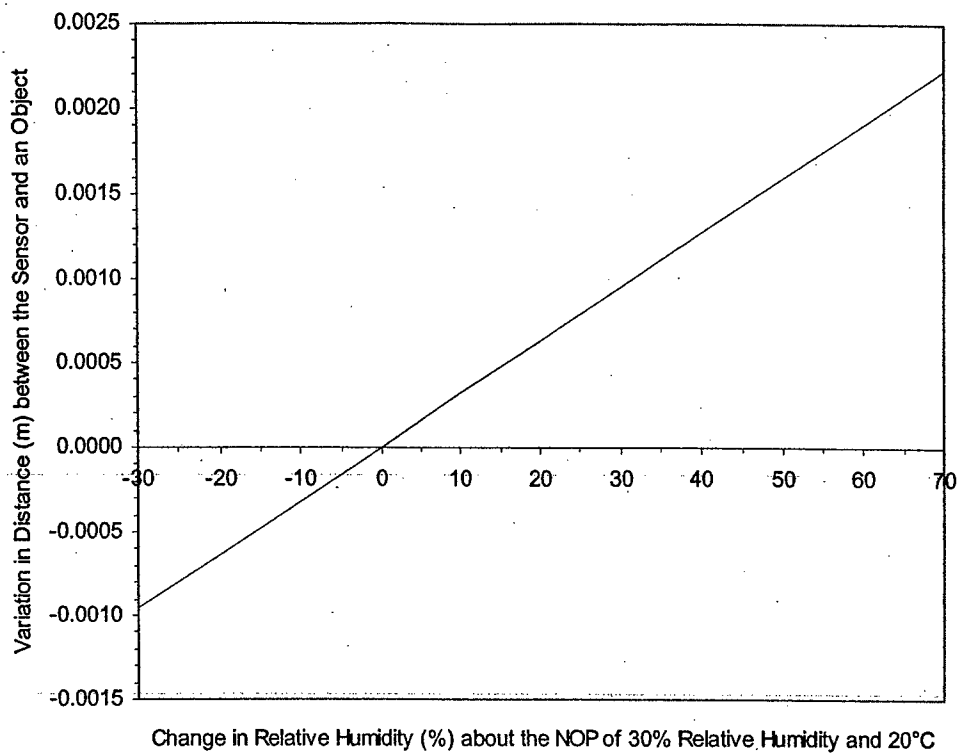


Figure 56. Sensitivity of the distance between the sensor and an object with respect to humidity, relative to a nominal operating temperature and relative humidity of 20°C and 30%, respectively.

As shown in Figures 55 and 56, neither temperature nor humidity has a great effect on the calculated distance between the sensor and an object. Even on a respectably warm day (about 30°C), the error in the distance will only be about 0.02 m, or 2 cm. Likewise, even at 100% relative humidity (a 70% increase with respect to the nominal operating point), the error is even less by about a factor of 10. These findings show that the expression for the distance between the sensor and an object can be greatly simplified in two ways: humidity effects can be ignored, and the speed of sound can be evaluated at a nominal temperature of 20°C with very minimal error in the calculated distance. Thus, the new reference speed of sound is

$$c = \sqrt{k \frac{\bar{R}}{M} T}$$

$$c = \sqrt{(1.4) \left(0.2870 \frac{\text{kJ}}{\text{kg} \cdot \text{K}} \right) (293.15 \text{ K})}$$

$$c = 343.20 \text{ m/sec}$$

Therefore, the distance between the sensor and an object is given by

$$\Delta x = \frac{1}{2} c t_{\text{delay}}$$

$$\Delta x = (171.60) t_{\text{delay}}$$

where Δx is in m and t_{delay} is in sec.

With the distance between the sensor and an object determined, the velocity of the object can now be found. Figure 57 shows two output and received signals in succession.

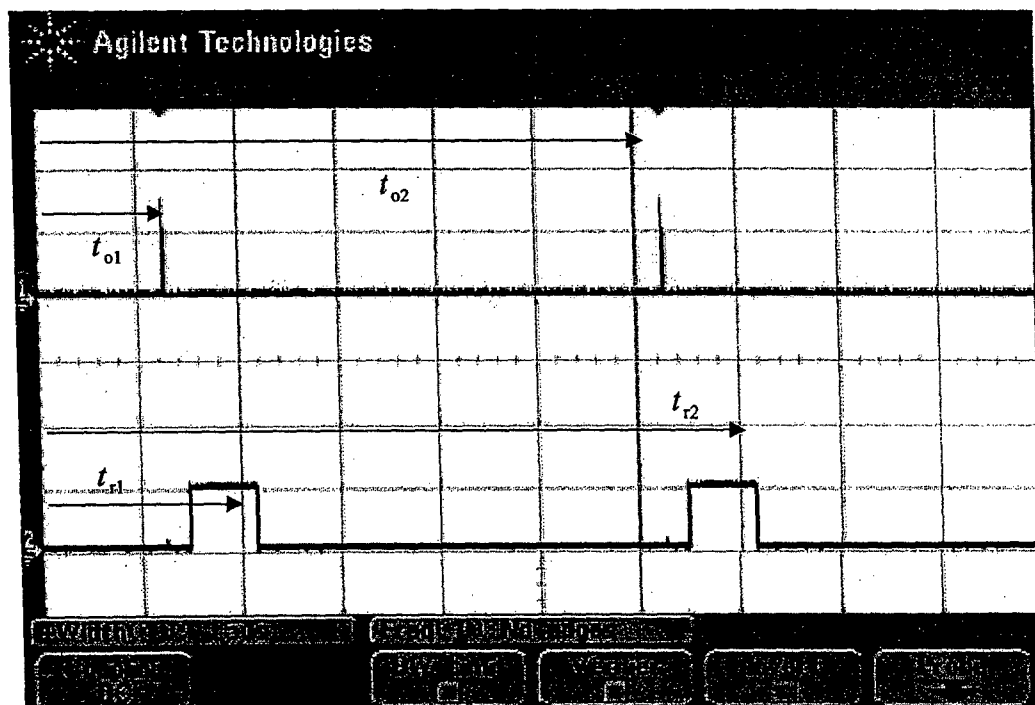


Figure 57. Multiple output and received signals.

To estimate velocity, both the time delays and average times are considered. The average time for the first signal, t_1 , is given by

$$t_1 = t_{o1} + \frac{1}{2}(t_{r1} - t_{o1})$$

$$t_1 = \frac{1}{2}(t_{r1} + t_{o1})$$

Similarly, the average time for the second signal, t_2 , is

$$t_2 = \frac{1}{2}(t_{r2} + t_{o2})$$

Figure 58 demonstrates the relative velocity between the sensor and an object which are moving toward each other. Positive movement is defined as to the right.

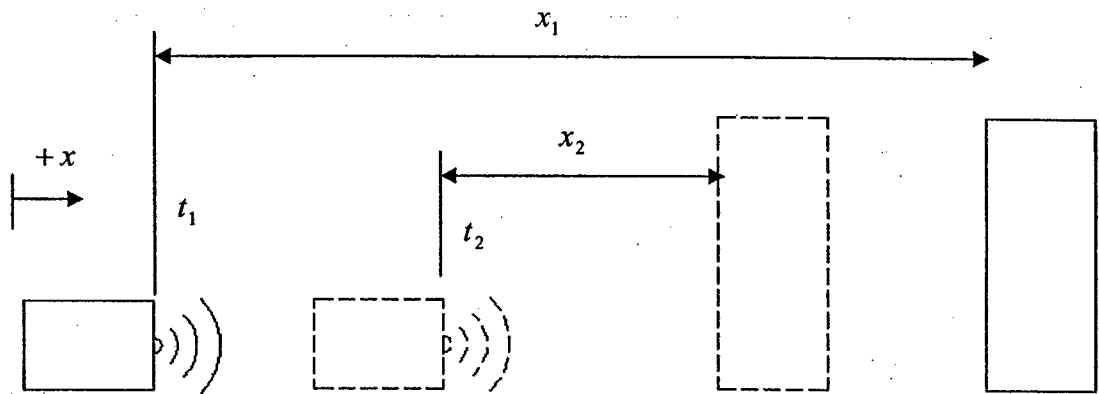


Figure 58. Relative velocity between the sensor and an object moving toward each other.

The velocity of the object relative to the sensor is expressed as

$$\vec{v}_{\text{object/sensor}} = \vec{v}_{\text{object}} - \vec{v}_{\text{sensor}}$$

Rearranging to solve for the object's velocity gives

$$\vec{v}_{\text{object}} = \vec{v}_{\text{object/sensor}} + \vec{v}_{\text{sensor}}$$

Starting from the definition of velocity to solve for the velocity of the object relative to the sensor,

$$\begin{aligned}\bar{v}_{\text{object/sensor}} &= \frac{dx}{dt} \\ \bar{v}_{\text{object/sensor}} &\approx \frac{\Delta x}{\Delta t} \\ \bar{v}_{\text{object/sensor}} &= \frac{x_2 - x_1}{t_2 - t_1}\end{aligned}$$

Thus, the object's relative velocity is

$$\begin{aligned}\bar{v}_{\text{object/sensor}} &= \frac{\frac{1}{2}ct_{\text{delay},2} - \frac{1}{2}ct_{\text{delay},1}}{\frac{1}{2}(t_{o2} + t_{r2}) - \frac{1}{2}(t_{o1} + t_{r1})} \\ \bar{v}_{\text{object/sensor}} &= \frac{c(t_{\text{delay},2} - t_{\text{delay},1})}{(t_{o2} + t_{r2}) - (t_{o1} + t_{r1})}\end{aligned}$$

Therefore, the absolute velocity of the object is found as follows, assuming the velocity of the sensor is known:

$$\bar{v}_{\text{object}} = \frac{(343.20)(t_{\text{delay},2} - t_{\text{delay},1})}{(t_{o2} + t_{r2}) - (t_{o1} + t_{r1})} + \bar{v}_{\text{sensor}}$$

where all velocities are in m/sec and all times are in sec.

B.2 Equation of Motion for a Ball Falling through Air

The free-body diagram of a sphere of diameter D and mass m falling through air is depicted in Figure 59. Considering the effects of air resistance, the aerodynamic drag on the falling sphere can be expressed as

$$F_{\text{drag}} = \frac{1}{2}C_D\rho_{\text{air}}Av^2$$

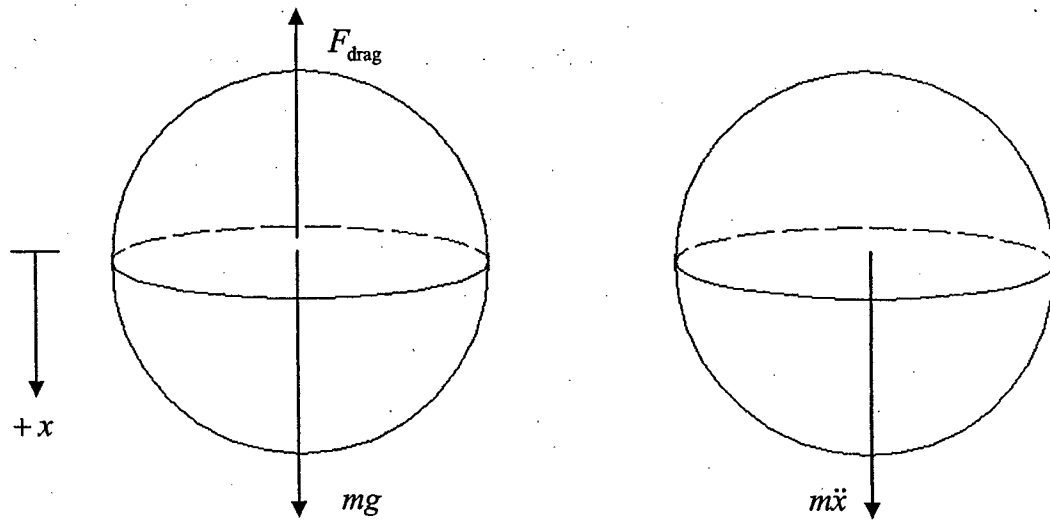


Figure 59. Free-body and mass-acceleration diagrams of a sphere falling through air.

where C_D is the drag coefficient, ρ_{air} is the density of the air, A is the frontal area of the sphere, and v is the velocity. The sphere's drag coefficient is a highly nonlinear function of its Reynolds number, Re_D , which is dependent on the sphere's velocity and diameter and the kinematic viscosity, ν , of the air:

$$C_D = f(\text{Re}_D)$$

$$\text{Re}_D = \frac{vD}{\nu}$$

The sphere's frontal area, A , is simply its projected area, or

$$A = \frac{\pi}{4} D^2$$

Substituting the above expression for the frontal area, the drag force on the sphere can be written as

$$F_{\text{drag}} = \frac{1}{2} C_D \rho_{\text{air}} \left(\frac{\pi}{4} D^2 \right) v^2$$

$$F_{\text{drag}} = \frac{1}{8} C_D \rho_{\text{air}} \pi D^2 v^2$$

From the free-body and mass-acceleration diagrams of Figure 59, the sphere's equation of motion is

$$\begin{aligned}\sum F_x &= m\ddot{x} \\ mg - F_{\text{drag}} &= m\ddot{x}\end{aligned}$$

Substituting the expression for the drag force into the equation yields

$$mg - \frac{1}{8}C_D\rho_{\text{air}}\pi D^2 v^2 = m\ddot{x}$$

Dividing through by the mass of the sphere and rearranging the expression gives

$$\ddot{x} + \frac{C_D\rho_{\text{air}}\pi D^2}{8m}v^2 = g$$

Velocity is simply the derivative of position with respect to time, and therefore the equation of motion can be expressed entirely in terms of position as

$$\ddot{x} + \frac{C_D\rho_{\text{air}}\pi D^2}{8m}(\dot{x})^2 = g$$

Letting the starting position of the falling ball be $x = 0$ and dropping it from rest, the initial conditions for the equation of motion are

$$\begin{aligned}x(0) &= 0 \\ \dot{x}(0) &= 0\end{aligned}$$

The equation of motion is a second-order, nonlinear differential equation with one coefficient that varies nonlinearly with velocity. The solution to the equation of motion was found using Engineering Equation Solver (EES).

B.3. EES Code for Solving the Equation of Motion for a Ball Falling through Air

"Solving the differential equation of motion for a sphere falling through air."
"All units are in SI."

"Constants"

D = 0.2413 [m]

m = 0.585 [kg]

v_o = 1e-3 [m/s]

x_o = 0 [m]

time = 3 [sec]

g = 9.81 [m/s^2]

"sphere diameter"

"mass of sphere"

"initial velocity -- set to value >0 to avoid Re = 0"

"initial position"

"time period for analysis"

"gravitational acceleration"

"Kinematics"

F = m*g

m*a = F - F_d

Area = pi*D^2/4

F_d = Area*C_d*(1/2*rho*v^2)

"weight of sphere"

"force balance"

"frontal area of sphere"

"definition of drag force"

"Calculation of Re"

mu = viscosity(Air, T=25)

rho = density(Air, T=25, P=101.3)

Re = rho*abs(v)*D/mu

C_d = exp(interpolate1('LnRe', 'LnCd', LnRe=Ln(max(.01, Re))))

"Integration"

v = v_o+integral(a,t,0,time)

x = x_o+integral(v,t,0,time)

"velocity at each time step"

"displacement at each time step"

\$integraltable t:0.05, v,x, C_d

\$tabstops 1 in

References

- [1] Migatron Corp. "Ultrasonic Detections and Control Applications." Migatron Corp. <<http://www.migatron.com/applications/apps.htm>>.
- [2] Duval, Brian. "Advances in Analog Distance Sensing." Sensors Online. <<http://www.sensorsmag.com/articles/0904/36/main.shtml>>.
- [3] Cartwright, Kert L. and Gopi R. Jindal. "An Ultrasonic Proximity System for Automobile Collision Avoidance." SAE 1992 International Congress and Exposition (1992): 75-81.
- [4] Bohn, Dennis A. "Environmental Effects on the Speed of Sound." Journal of the Audio Engineering Society 36.4 (1988).
- [5] Weber, Austin. "New Technology Improves Vehicle Safety." Assembly Magazine. <http://www.assemblymag.com/CDA/ArticleInformation/news/news_item/0,6501,98540,00.html>.
- [6] "Future Fords Will Be Safer." Autoworld Malaysia. <<http://www.autoworld.com.my/EMZine/Review/viewpfarticle.asp?awReviewId=1183>>.
- [7] "More Safety & Security Features." Ford Motor Company. <<http://www.fordvehicles.com/freestar/safety/?section=morefeatures>>.
- [8] Andrews, Angus P. and Mohinder S. Grewal. Kalman Filtering: Theory and Practice Using MATLAB. 2nd Ed. Wiley-Interscience. N.p., 2001.
- [9] Acroname Inc. "Dimensions." The Devantech SRF08 Ultrasonic Range Finder. Acroname Inc. Boulder, 2004. pg 12.
- [10] SpaceAge Control Inc. "How Position Transducers Work." SpaceAge Control Inc. <<http://www.spaceagecontrol.com/pthow.htm>>.
- [11] Boles, Michael A. and Yunus A. Cengel. Thermodynamics: An Engineering Approach. 4th Ed. McGraw Hill. New York, 2002. pgs. 703, 824 (Table A-1).
- [12] Owen, Frank C. and John R. Ridgely. Handbook and Reference for the ME422 Laboratory. El Corral Publications, 2004.

Object Detection for Pre-Crash Sensing and Object Avoidance

Dr. Charles Birdsong
Dr. Peter Schuster

Project Goals

◆ Short term goals

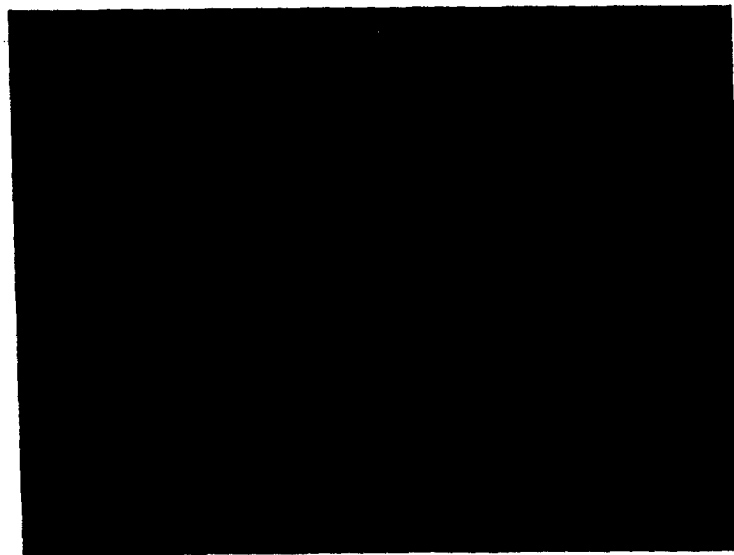
- Improve passenger safety
- Identify sensors that provide classification information

◆ Long term goals

- Extend the system to include object type information and hidden objects

It's not the fall that kills you...

- ◆ it's the sudden STOP!
- ◆ Vehicle Crash Safety
 - Vehicle vs. occupant deceleration is key
- ◆ BUT ...
 - Vehicle deceleration can be controlled
 - Occupant position range is limited
 - Occupant deceleration can be controlled
 - Vehicle 'intrusion' also matters



Near-Term Advantages: Airbags

- ◆ Increased time between air-bag initiation and occupant impact – slower deployment.
- ◆ Improved reliability of deployment decision
 - More likely to deploy air bags during impact
 - Less likely to deploy air bags spuriously

Other Near-Term Advantages

- ◆ Activation of seat belt pretensioners
- ◆ Active anti-submarining passenger seats
- ◆ Active seating (front or rear impacts)
- ◆ Future combination with rear- and side-impact sensors
- ◆ External airbags for pedestrian impacts

Long-Term Advantage: 'Active' Safety Measures

- ◆ Warn driver and other road users
- ◆ Pre-apply or augment braking
- ◆ Auto-steer to avoid object

Needs:

- ◆ Greater detection range
- ◆ Object size determination
- ◆ Object type determination

Sensor Fusion

- ◆ Sensor Fusion is the combination of data from multiple sensors into an information set
- ◆ Information set is generally smaller than sensor set
- ◆ Goal: Whole is greater than the sum of the parts.

Simple Example - Navigation

◆ Using GPS and inertial navigation

- GPS provides location data directly, however data may be inaccurate due to dithering
- Inertial systems provide acceleration data directly, this can be integrated to provide location data

Navigation Example (cont)

$$\hat{S} = \alpha G + \beta I + \psi T \hat{S}^-$$

$$\begin{bmatrix} \hat{p} \\ \hat{v} \\ \hat{a} \end{bmatrix} = \alpha \begin{bmatrix} P_G \\ 0 \\ 0 \end{bmatrix} + \beta \begin{bmatrix} 0 \\ 0 \\ A_I \end{bmatrix} + \psi \begin{bmatrix} 1 & \frac{1}{\Delta t} & \frac{1}{\Delta t^2} \\ 0 & 1 & \frac{1}{\Delta t} \\ 0 & 0 & 1 \end{bmatrix} \begin{bmatrix} \hat{p}^- \\ \hat{v}^- \\ \hat{a}^- \end{bmatrix}$$

Types of Data

◆ Object telemetry

- Position
- Speed

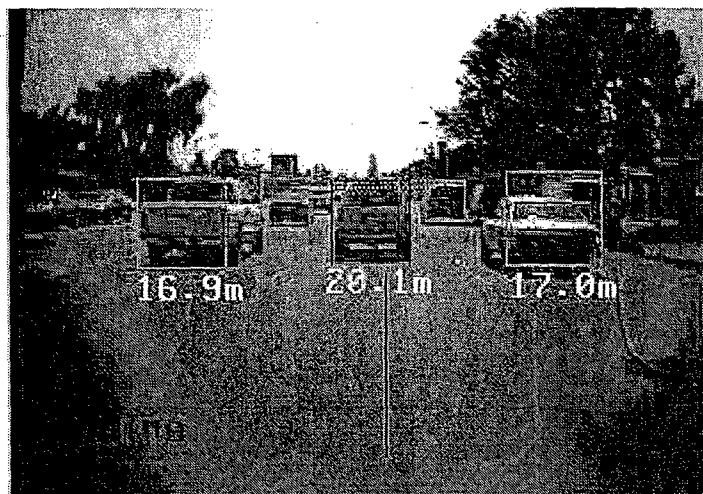
◆ Classification

- Size
- Orientation
- Motion

Sensors for Telemetry Data

- ◆ Laser
- ◆ Radar
- ◆ Ultrasonic

Radar



Radar (cont.)

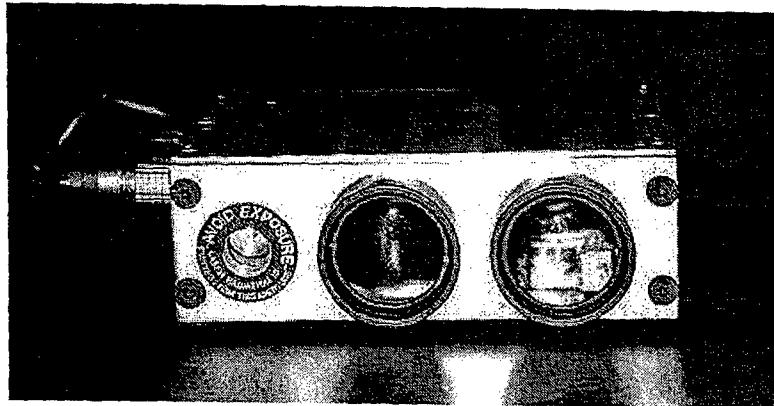
Advantages

- ◆ Long range
- ◆ Multiple target tracking
- ◆ Integrated with other systems (ACC)
- ◆ Already on vehicle

Disadvantages

- ◆ Susceptible to target recombination
- ◆ Expensive

Laser



Laser (cont.)

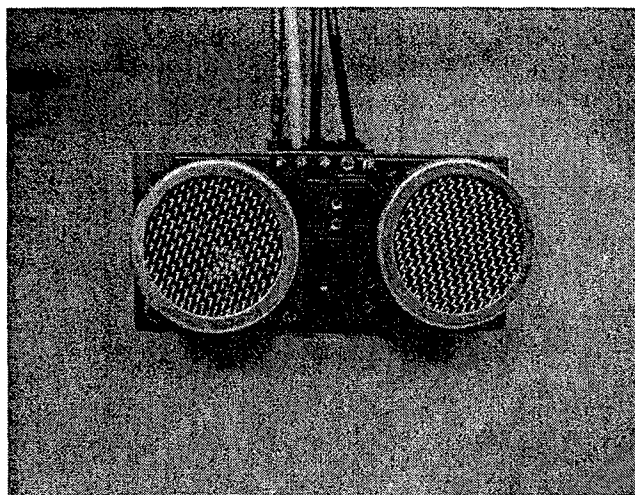
Advantages

- ◆ Long range
- ◆ Accurate
- ◆ Directional

Disadvantages

- ◆ Slow
- ◆ Expensive
- ◆ Subject to weather
- ◆ Directional

Ultrasonic



Ultrasonic (cont.)

Advantages

- ◆ Low Cost
- ◆ Integrated with other systems
- ◆ Already on vehicle
- ◆ Multiple sensors – can triangulate

Disadvantages

- ◆ Short range
- ◆ Non-directional

Future Work

- ◆ Improve determination accuracy
- ◆ Create object classification system
- ◆ Extend the system to cover side impacts
- ◆ Adapt the system for hidden object detection

Nonlinear Analytical Modeling and System Verification Utilizing a
Combined Slide-rock Seismic Response of Wine Barrel Stacks

Project Investigators:

Charles. B. Chadwell

Assistant Professor
Department of Civil and Environmental Engineering
California Polytechnic State University
San Luis Obispo, California

Rakesh Goel

Professor
Department of Civil and Environmental Engineering
California Polytechnic State University
San Luis Obispo, California

Jeremy M. Stanley

Student Researcher
Department of Civil and Environmental Engineering
California Polytechnic State University
San Luis Obispo, California

NONLINEAR ANALYTICAL MODELING AND SYSTEM VERIFICATION UTILIZING A COMBINED SLIDE-ROCK SEISMIC RESPONSE OF WINE BARREL STACKS

C. B. Chadwell¹, R. Goel² and J.M. Stanley³

ABSTRACT

Nearly 90% of California's \$45 billion wine industry operates in high seismic regions, with nearly \$15 billion in wine stored in oak barrels stacked on portable steel racks. Recent laboratory studies and historic earthquake performance of this storage system indicate a need to better understand and analytically model the dynamic behavior of rocking to serve as a basis for earthquake hazard mitigation.

This report illustrates a theoretical framework and simulation model which can be used to investigate the dynamic behavior and expected performance of highly nonlinear models of stacked rigid bodies. The authors performed shake table tests with extensive data acquisition on one high wine barrel stacks in the Parsons Earthquake Engineering Laboratory at Cal Poly, San Luis Obispo. An analytical model was developed and calibrated with the test data using transcendental pulse ground motions of varying amplitude and frequency. Key features of the analytical model include: 1) nonlinear material and geometric springs for rigid body rocking, 2) system nonlinear damping for energy lost in pounding, and 3) coupled Coulomb friction models for relative sliding on various surfaces.

Presented herein are observations and conclusions based on numerical and physical simulations of full scale barrel stack configurations subjected to suites of service and design level earthquake ground motions. The report develops a framework that can be used to better estimate the behavior of highly nonlinear, combined rocking and sliding systems. More directly, it provides a critical tool to analytically approximate losses in the wine industry due to regional earthquakes.

¹Assistant Professor, Dept. of Civil and Environ. Engineering, California Polytechnic State University, San Luis Obispo, CA.

²Professor, Dept. of Civil and Environ. Engineering, California Polytechnic State University, San Luis Obispo, CA.

³Student Researcher, Dept. of Civil and Environ. Engineering, California Polytechnic State University, San Luis Obispo, CA.

Table of Contents

1.0	Introduction.....	1
1.1	History of Modern Wine Barrels.....	1
1.2	California's Wine Industry.....	2
1.3	Previous Performance of Wine Barrel Stacks.....	3
1.4	Previous Research on the Wine Barrel Stacking System.....	5
1.5	Current Research Effort.....	5
2.0	Literature Review.....	7
2.1	Earthquake Rocking Response of Rigid Bodies.....	7
2.2	Rocking of Slender Rigid Bodies Allowed to Uplif.....	7
2.3	Response of Rigid Body Assemblies to Dynamic Excitation.....	8
2.4	Seismic Response of Equipment Anchored to a Base Foundation Allowing Uplift.....	8
2.5	The Rocking Spectrum and the Limitations of Practical Design Methodologies.....	9
3.0	One Barrel Rack Experimental Procedure.....	10
3.1	Component Selection.....	11
3.2	Testing Procedure.....	15
3.3	Ground Motions.....	18
4.0	Analytical Model.....	24
4.1	Background.....	24
4.2	Single Barrel Analytical Model.....	27
5.0	Test Results.....	31
5.1	Transcendental Pulse Motions.....	31
5.1.1	Barrel Sliding Motions.....	33
5.1.2	Effect of the Rack Between the Wine Barrels.....	34
5.1.3	Rocking.....	36
5.1.4	Modeling Results from One Barrel Pulse Tests.....	38
5.2	Earthquake Ground Motions.....	41
5.2.1	Ground Motion Experimentation Tests Results.....	43
5.2.2	Discussion of Ground Motion Experimentation.....	45
6.0	Conclusions and Recommendations.....	47
6.1	Research Summary.....	47
6.2	Conclusions.....	47
7.0	References.....	50

List of Figures

Chapter 1.0	Introduction.....1
Figure 1.1	Wine Barrel Stack Collapse from the San Simeon Earthquake.....4
Chapter 3.0	One Barrel Rack Experiment.....10
Figure 3.0	Four High Two Barrel Stack Ready for Testing.....10
Figure 3.1	Typical Barrel Dimensions.....13
Figure 3.1	Typical 2 Barrel Stack and Rack Configuration.....14
Figure 3.3	Topco WR21.....14
Figure 3.4	Topco Eastern Saddle.....14
Figure 3.5	Typical Test Configuration of a Single Barrel Stack Height.....16
Figure 3.6	Laboratory Setup for the One Barrel Experiment.....17
Figure 3.7	Pictures of the Laboratory Instrumentation.....18
Figure 3.8	Shake Table Acceleration.....19
Figure 3.9	Shake Table Displacement.....20
Figure 3.10	Measured Barrel Acceleration (Rack WR1).....20
Figure 3.11	Measured Barrel Acceleration (Rack WR2).....21
Figure 3.12	Forward Back Ground Motion Acceleration and Displacement.....23
Chapter 4.0	Analytical Model.....24
Figure 4.1	Housner Rocking Block Model.....24
Figure 4.2	Analytical Model.....28
Figure 4.3	Coulomb Friction Model.....29
Figure 4.4	Elastic Gap Element.....29
Chapter 5.0	Test Results.....31
Figure 5.1	Measured Acceleration Time History for 2Hz.....31
Figure 5.2	Measured Acceleration Time History for 4Hz.....32
Figure 5.3	Measured Acceleration Time History for 6Hz.....32
Figure 5.4	Measured Acceleration Time History for 8Hz.....32
Figure 5.5	Barrel Sliding Relative to Table.....33
Figure 5.6	Barrel Sliding and Rack Sliding Relative to Table (2Hz).....34
Figure 5.7	Barrel Sliding and Rack Sliding Relative to Table (6Hz).....35
Figure 5.8	Barrel Sliding and Rack Sliding Relative to Table (8Hz).....35
Figure 5.9	Barrel Sliding and Rack Sliding Relative to Table (4Hz).....36
Figure 5.10	High Mode of Vibration for Rocking Response.....37
Figure 5.11	Predominant Rocking for 2Hz ground motion.....38
Figure 5.12	Damping Variation for the 4Hz Ground Motion, Constant Friction.....39
Figure 5.13	Friction Variation for the 4Hz Ground Motion, Constant Damping.....39
Figure 5.14	Measured verses Simulated Barrel Response for the 2Hz Ground Motions.....40

Figure 5.15	Measured verses Simulated Barrel Response for the 4Hz Ground Motions.....	40
Figure 5.16	Measured verses Simulated Barrel Response for the 6Hz Ground Motions.....	41
Figure 5.17	Ground Motion Characteristics.....	41
Figure 5.18	LA16 Acceleration Time History.....	42
Figure 5.19	LA18 Acceleration Time History.....	42
Figure 5.20	LA19 Acceleration Time History.....	42
Figure 5.21	Acceleration Response Spectra.....	43
Figure 5.22	Simulated Versus Measured Barrel Sliding Response for the LA16 Ground Motion.....	44
Figure 5.23	Simulated Versus Measured Barrel Sliding Response for the LA18 Ground Motion.....	44
Figure 5.24	Simulated Versus Measured Barrel Sliding Response for the LA19 Ground Motion.....	45

1.0 Introduction

The study presented in this report examines the non-linear behavior of portable wine barrel storage systems subjected to seismic ground excitations. The slide, rock and slide-rock phenomena, as studied in other works, have been adopted as part of the reasoning in the analysis. The authors of this paper will systematically examine these response mechanisms with extensive experimentation, and a computer simulation model. The non-linear parameters used in the formulation of the model include, Coulomb Friction, for the interaction of steel, concrete and wood surfaces. Radiation damping will provide a platform to describe the energy loss during cyclic impact. Coefficient of restitution will be verified empirically, and calibrated into the computer model.

1.1 History of Modern Wine Barrels

Originally constructed for carrying of goods by the Northern Europeans the oak wine barrel quickly became the transportation medium for Armenian wines furnished to Babylon in Mesopotamia. Out of happenstance the flavors and aromas of oak nestled in with the wine to produce a product sought by many who enjoyed the beverage. The oak barrel has endured millenniums of use and is now almost exclusively used in the production of fine wines and spirits (Wine Institute, 2005).

Since wine making is an art as well as a science many wine makers go to great extents in selecting the type of oak that will be used in the barrel. These different types of oak influence the flavor of the wine by adding subtle accents specific to the oak variety used in the barrel construction. As the wine stays in the barrel O_2 from the surrounding air is slowly allowed to enter the wine. During this time the wine grows in complexity, while the harsh tannins are smoothed. Many of the wines final qualities can be attributed to the oak barrel (Wine Institute, 2005). However, the oak barrel is not the most economical method of aging the wine. These luxury items range in price anywhere from \$450 to \$700 (Morrow, 2000). Often times oak shavings are used instead, except these wines generally fall into the lower price ranges. Wine makers have attempted to produce quality wines without oak barrels yet popular wine culture tend to disregard this practice. Fine wines

and spirits have evolved around the use of oak barrels and it is highly unlikely that its use will diminish.

1.2 California's Wine Industry

The California wine industry has an annual impact of \$45.4 billion dollars on the state's economy, growing nearly 40 percent from 1998 to 2002, and producing the number one finished agricultural product in the state (Wine Institute, 2005). With all of these wines being produced in California, most of which require extensive long term storage. The portable steel wine barrel rack has been adopted as the most common method for storing oak wine barrels. This very simple rack is constructed from typical steel box sections welded together. A cradle is constructed both on the top and bottom forming a symmetrical rack assemblage. Then, barrels can be stacked one on top of the other, in a very convenient fashion. These stacks are designed for easy transport and relocation for winery operations and storage. They can be stacked very high to utilize the vertical space in a warehouse more efficiently, with barrels stacked upwards of six high being common practice. The racks are equipped with a 7" opening so that a forklift can quickly move these stacks and access the wines more easily (Topco, 2005). Smaller wine operations also utilize the portable steel rack because of its familiarity within the industry. Having an industry standard benefits wine production by providing a large supply of inexpensive storage devices.

The large presence of wine production in California is most noted by the record shipment of 428 million gallons of wine to the U.S. in 2004 (Wine Institute, 2005). California has the fourth largest wine growing region in the world immediately following Italy, France and Spain (Morrow, 2002). Three out of every four bottles consumed in the United States comes from California. As wine culture continues to be popular, and consumption continues to raise production demand, wineries and wine storage practices are at an increasing level of risk. Nearly 90 percent of all winery operations and storage are located in seismic zone 4, UBC criterion; most of the annual 428 million gallons produced annually are contained at these facilities (Morrow, 2002).

The price of convenience has left the wine industry with a highly unstable storage method. Unlike other manufacturing processes wine making requires the harvesting, crushing, and aging of wines before it can be sold. Most wines age anywhere from six months to a year, where aging occurs in the oak barrels. Each year only brings one harvest, unlike other agricultural products that can produce multiple crops. At any give point in the life cycle of a bottle of wine at least one years supply will be stored. This poses serious risk to the economic stability of the winery. Historically these stacking devices have been susceptible to extensive damage during seismic ground excitations. Unfortunately awareness of the limitations of these sacking devices has only recently become a major concern. Previous earthquake damage has indicated that these stacks are highly susceptible to collapse (Morrow, 2000).

1.3 Previous Performance of Wine Barrel Stacks

During the 1989 Loma Prieta Earthquake, minor to moderate damage was realized in a few of the wineries located in the Bay Area and Santa Cruz Mountain Wine Regions. The earthquake occurred on the San Andreas Fault at approximately 5:04pm local time on October 17, 1989. The earthquake epicentered in Los Gatos, just 16km Northeast of Santa Cruz, caused minor to moderate damage to the Rosenblum Cellars, Audubon Cellars, Santa Cruz Mountain Vineyard, David Bruce Winery in Los Gatos, Silver Mountain Wineries in Los Gatos, and Mirassou Winery among others. The approximate losses, both direct and indirect, have been roughly estimated at \$1.5 million dollars (Morrow, 2002).

At the time of the Loma Prieta earthquake, many of the wineries had wine barrel stacking systems that were anchored to the storage facility either to structural walls or foundations. However, from the mid 1980's, many larger wineries have updated their wine barrel stacking system to portable steel frames that are easy to handle, reusable, and versatile. The portable wine barrel stacking devices are not anchored to any structural component in an effort to facilitate ease and speed of handling for the wine makers. The previous system of anchoring wine barrels in stacks to structural systems was responsible for keeping the costs of earthquake damage to acceptable levels. More recent earthquakes

have shown this newer two barrel portable rack system is highly susceptible to collapse under seismic excitation.

After the Napa Valley–Yountville Earthquake of 2000, epicentered in Napa Valley, only few wineries reported any damage at all. This is largely due to the small levels of ground shaking experienced in the region. However, post earthquake reconnaissance reports, coupled with previous experimentation, have suggested that had the earthquake strong shaking lasted slightly longer, or had the ground motion contained slightly higher peak ground accelerations, damage level could have been catastrophic (Morrow, 2000). As is, the portable wine barrel stacking system now used by many San Luis Obispo County wineries are unsafe and may lead to catastrophic financial losses to the local Central Coast economy.



Portable Two
Barrel Wine
Rack

Figure 1.1 - Wine Barrel Stack Collapse from the San Simeon Earthquake

The most recent and significant earthquake in California, the 2003 San Simeon Earthquake, epicentered near Cambria caused significant damage to many of the small local wineries both large and small (EERI, 2004). Upon post earthquake reconnaissance of many San Luis Obispo County wineries by the authors, damage was identified to be distributed heavily among the two barrel rack system (Figure 1). A particular case study presented by Marrow, details a significant loss of wines from Wild Horse Winery. Located in Templeton, California their approximate peak ground acceleration was on the

order of 0.5g. The structure housing this facility reported no structural damage, with minor nonstructural damage. However, due to the nature of these stacks nearly four million dollars in lost wine happened that day. Estimated as 250,000 dollars a second, this moderate quake provides an indication of the highly unpredictable nature of these stacking systems as demonstrated in Figure 1.1.

1.4 Previous Research on the Wine Barrel Portable Stacking System

To date, little research has been performed on the portable wine barrel stacking system subject to seismic excitation. Research results presented by Marrow and Makris (2000) identified 6 failure modes of the wine barrel rack systems from shake table experimentation performed on the University of California, Berkeley shake table. One of the 6 modes identified, Stack Sliding, was one such mode. The Stack Sliding mechanism resulted in no damage to the barrels or barrel stacks and was considered to be the most desirable mechanism. Two of the mechanisms, longitudinal and transverse rocking of the barrel stacks were the next desirable. These mechanisms resulted in a lower likelihood of barrel damage due to energy dissipation through rocking. The so called "rocking mechanism" has been identified as an effective method of earthquake mitigation from many researchers for protection of both structural and nonstructural components (Makris and Black, 2001). The last three mechanisms, transverse walking, rack walking, and top barrel ejection result in a high likelihood of barrel rack system collapse leading to barrel rupture and consequential economic loss. Results from this research suggest that the various modes of failure were dependent on barrel configuration, frequency content of the ground motion, peak ground acceleration, and duration of the strong shaking. While a reasonable pioneering first study, the shortcoming of this research was the absences of data collected and lack of accompanying analytical and theoretical model development.

1.5 Current Research Effort

The research presented in this report is a continuation of the effort, began by Joshua Morrow, to characterize the response and failure mechanisms of the portable wine barrel storage system. In collaboration with Joshua Morrow, the authors of this paper have performed extensive shake table studies, data acquisition, and theoretical modeling of this

system. A Newmark, average acceleration, non-linear, numerical method for multi-degree of freedom systems has been used in the solution to the equations of motion (Chopra 2000). Extensive experimentation on a single barrel stack using transcendental pulse ground motions provided the necessary data for model calibration. The experimental data was fitted to the theoretical model in an attempt to produce an empirical relationship most closely related to physical interpretation. Finally, past earthquake records were used in testing to validate the theoretical model by comparing real data with empirical data from the model.

2.0 Literature Review

2.1 Earthquake Rocking Response of Rigid Bodies

Mohammad Aslam, A.M. ASCE, William G. Godden, M. ASCE and D. Theodore Scalise, Journal of the Structural Division, Feb 1980, pg. 377-392

This study is part of the investigation into the response of radiation shielding systems used in particle accelerators. Because of the way these facilities are constructed, concrete blocks are stacked on top of one another, therefore a rocking rigid body analysis is needed. In their analysis it was indicated that sliding allowed the block to be partly uncoupled with the horizontal component of ground motion. Furthermore, it was suggested that the base coefficient is the control quantity in these situations. Second, if the aspect ratio of the block is greater than $1/\mu$ then the block will not slide under the action of the ground motion. Conclusions of this study indicate the highly non-linear aspect of rigid body rocking. The rocking frequency and response is highly dependant on the boundary conditions. Furthermore block response is further dependant on aspect ratio, block size and coefficient of restitution.

2.2 Rocking of Slender Rigid Bodies Allowed to Uplift

Ioannis N. Psycharis, and Paul C. Jennings, Earthquake Engineering and Structural Dynamics, v.11, pg. 57-76, 1983

Examined in this paper is the rocking response of rigid blocks for the purpose of modeling the uplift that occurs in large buildings during seismic activity. The simple rigid block was analyzed and conclusions were made. The two models used to establish these results came from a simplified Winkler foundation known as the two spring foundation. Winkler's model uses a continuous base of viscous dampers and the general solution is very complex. However, a simplified two spring and two damper model placing dampers and springs at the outer pivot points were examined. Results of the study indicate that the two spring foundation is a simpler approach to the problem, and can be used instead of the Winkler model. The actual numerical results from both methods are in fair agreement.

2.3 Response of Rigid Body Assemblies to Dynamic Excitation

Tibor Winkler, Kimiro Meguro, and Fumio Yamazaki, Earthquake Engineering and Structural Dynamics, v.24, pg. 1389-1408, 1995

This paper examines the behavior of wooden blocks when subjected to harmonic excitations. The mathematical model used in this research is a combination of the work performed by Housner (1963). A series of shaking table experiments revealed various overturning accelerations and compared these results to two analytical methods. The first simplified method disregarded key parameters and as such the results were not in good agreement. The second method incorporated more sliding and friction parameters that resulted in better agreement. The Distinct Element method was analyzed and showed good agreement with the non-linear behavior of the rigid body rocking tests.

2.4 Seismic Response of Equipment Anchored to a Base Foundation

Allowing Uplift

Makris, N., C.J. Black, (2001) "Rocking Response of Equipment Anchored to a Base Foundation". PEER 2001/14, Pacific Earthquake Engineering Research Center, University of California, Berkeley.

Outlined in this paper is the formulation of the rocking response of stored rigid bodies anchored to a foundation. A typical concern is that large devices such as electrical equipment have the ability to rock and possibly topple over during earthquakes. The main focus of the paper is the minimum anchor strength required to support these objects from overturning. Both the service level and ultimate design level earthquakes are examined. Slenderness effects are considered by looking carefully at the plan dimensions verse the footprint of the equipment. Conclusions to the study indicate that there are two distinct capacities to resist uplift. First the anchorage is strong enough to engage the foundation into rocking and second the restrainers fail and the object rocks as a free standing block.

2.5 The Rocking Spectrum and the Limitations of Practical Design Methodologies

Nicos Makris and Dimitriou Konstantinidis, Earthquake Engineering and Structural Dynamics 2003, v.32, pg. 265-289

This paper outlines the fundamental differences between the single degree of freedom (SDOF) oscillator and the rocking response of a rigid block. An attempt is made to prove that the present FEMA 356: Prestandard and Commentary for the seismic rehabilitation of Buildings should disbar the equivalent SDOF oscillator method of determining the response of rocking blocks. The systematic approach outlines the fundamental similarities as well as the differences in the response of the two systems. Assumptions in the paper require an energy loss due to pounding as the block rocks back and forth. The Paper builds on previous works from Housner (1963) and his work on, "The Behavior of Inverted Pendulum Structures during Earthquakes." Further assumptions include; the minimum energy loss during impact depends on the slenderness ratio of the block.

3.0 One Barrel Rack Experiment

In the examination of the response to rocking, sliding, and slide-rock phenomena of the portable wine barrel storage system during seismic excitation, full scale shake table tests

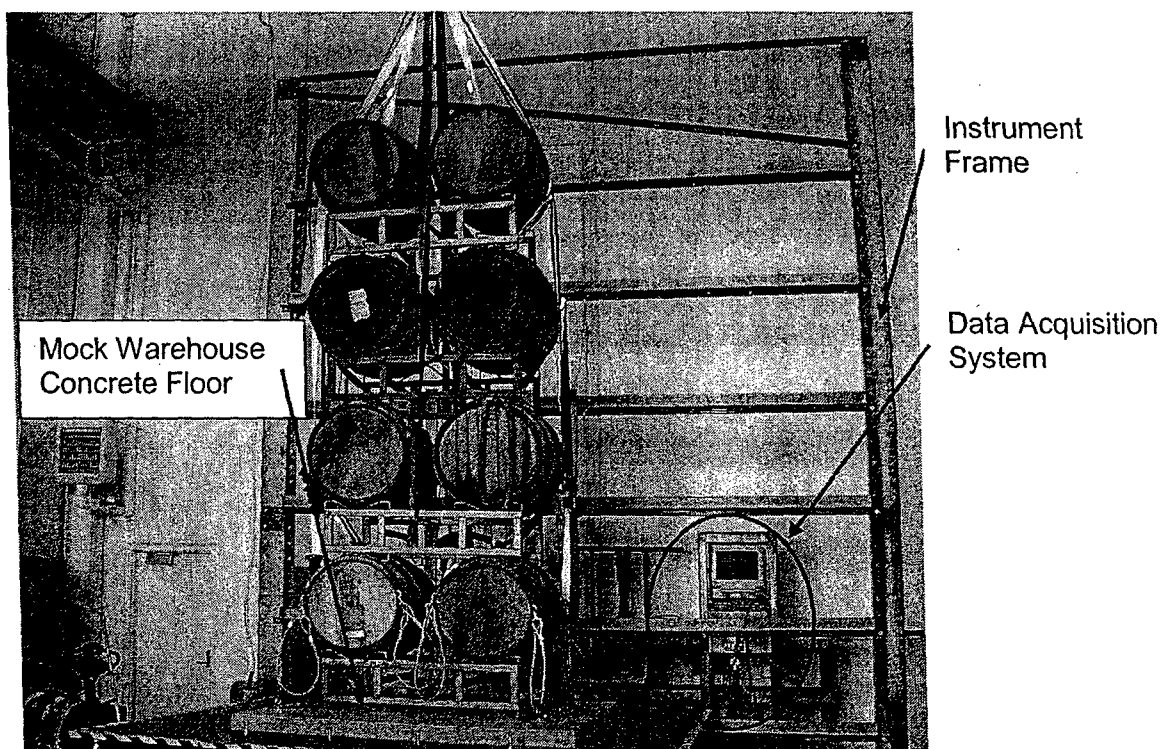


Figure 3.0 – Four High Two Barrel Wine Barrel Stack Ready for Testing

were conducted. The test configuration utilized the typical steel rack and oak barrel stacking method, data acquisition instrumentation, a safety restraint system, and an equipment frame for mounting external measuring devices (Figure 3.0). A concrete slab was designed, constructed and attached to the shake table. The concrete created a surface very similar to a concrete slab system found in most storage facilities. Once in place the slab was anchored to the top surface of the shake table with standard grade bolts. Data acquisition system devices were outfitted to the test specimens in order to collect data later used for model calibration. The barrel-rack stacks were then placed on the concrete surface completing a typical storage scenario, and shake table studies were conducted.

3.1 Component Selection

The Parson's Earthquake testing facility at California Polytechnic State University, San Luis Obispo provided the necessary test platform. Here the shake table operates as a single degree of freedom, one horizontal direction, of motion. The physical surface area of the table is approximately 225 ft² and built of steel. The capacity of the table is 5.25 in peak displacement, 38 in/s² maximum velocity, and a peak acceleration of 10g. The table operates from a central computer, frequency generator and hydraulic actuator. Various input waves can be user defined provided that they remain within the limits of the table capacity. The frequency generator and computer software allow the user a full range of input scenarios. Complete earthquake records, pulse sine/cosine functions, simple sine wave or combination thereof can be used as a test input.

The Parson's Earthquake and dynamic testing facility is equipped to handle large scale testing programs. A 10-ton over head crane supported the movement, and stacking of the barrels. A floor pallet jack provided the necessary ground movement of stacks into and out of the facility. 2" anchor points, monolithically poured, in the warehouse floor system provided a location to mount external equipment, testing apparatus and safety anchorage systems.

The external equipment frame operated as two functions, first as a mounting point for the measuring devices, and second as part of the safety restraining system. The frame was built from two steel I-sections, welded on end to two steel Channel sections. A steel box section was welded as a diagonal brace between the I-section and C-section. These created the upright columns and a mounting surface for the horizontal cross members. L-sections were lag bolted to #2 Douglas Fir-Larch 4 X 6 beams. The I-sections were drilled with a series of 3/4" holes in the flange to provide the horizontal members with a mounting point. These horizontal beams were then bolted to both sides of the vertical I-sections, at various heights to match the expected height of the accompanying barrel stack. The C-section bases were used as the mounting location to the floor of the laboratory with 2" diameter anchor bolts. The preliminary design criteria, for the frame, was to resist a 5 Kip horizontal point load applied to the top of the frame. This criterion

was established to give the frame enough strength to restrain horizontal motion of barrels in the event stack collapse occurred.

To incorporate the equipment frame into the safety restraint system, cables were attached from the frame to the barrels. These cables were made using 3/8" braided steel wire, looped on each end with cable crimps, and then attached to each barrel and corresponding horizontal beam. Since the beams were made from Douglas Fir-Larch, 1/2" lag type eye bolts were mounted to the beams. The eye bolts were doubled at each cable location to allow for an impact load from the barrel to the equipment frame of 1000 lbf. Each barrel was equipped with two cable assemblies mounted on the rim of the barrels near the center proximity. This location best served to minimize interference with the measuring devices and the physical space needed to accompany those devices and their operation. Furthermore, the rim of the barrel includes a steel band originally designed as part of the barrel construction. This provided an excellent attachment point and a heightened strength capacity to ensure that the cable assembly could support the expected loads during stack collapse. Quick style release mechanisms were outfitted to the cable assembly where the cable attaches to the barrel. This measure enables multiple tests to be performed and time efficiency to be maximized.

The vertical restraint of the barrels was accomplished using high grade nylon straps. Each barrel was individually wrapped with a strap. This ensured independent control for each barrel during collapse. Then a system of straps attached each barrel to the over head crane to support the overall stack. Because each barrel was supported from a single overhead point, it was necessary to provide the lateral restraint mentioned above. The safety harnesses and vertical restraints designed for stack collapse did not interfere with the barrel motion yet would engage in the event of large deformation where collapse was eminent.

The second function of the equipment frame is for support of the data acquisition devices. Position transducers (known as potentiometers) were mounted at each level of barrel stack height along the horizontal members. Two position transducers at each level were

used to measure the lateral displacement of each barrel in the stack height. The position transducers were aligned and mounted to the 4 X 6 Beams. The actual height of the string was centered with the mid point of the barrel. The barrels are doubly symmetric, so the strings were attached at the barrel center of mass in the plane of testing.

The concrete surface on the shake table was necessary to establish proper force transfer through friction to the test specimens. The slab was comprised of a normal weight concrete mixture, and reinforcing bars. The concrete mix was poured into a 6ft X 6ft - 3 ½" thick form, and reinforced using a web pattern of #4 reinforcing bars. The slab was professionally finished to a smoothness consistent with a storage warehouse slab on grade to simulate a typical warehouse floor scenario. Pre-aligned holes were placed in the form work to match those of the shake table to allow for proper mounting and securing. Eight grade 3 (½") bolts were used to mount the slab to the shake table to supply enough pre-stressing strength from table to slab for testing.

Barrel Volume	Properties	Dimensions (Inches)	Dimensions (mm)
59 Gallon/ 225 Liter	Stave Thickness	0.987"	24 mm
	Diameter of Head	22.687"	58 mm
	Circumference of Head	71.27"	181 mm
	Diameter of Belly	27.53"	70 mm
	Circumference of Belly	87"	221 mm
	Barrel Height	34.875"	89 mm
	Diameter of Bung Hole	2.0"	50 mm
53 Gallon/ 200 Liter	Stave Thickness	0.937"	24 mm
	Diameter of Head	21.25"	54 mm
	Circumference of Head	66.8"	170 mm
	Diameter of Belly	25.7"	65 mm
	Circumference of Belly	80.625"	205 mm
	Barrel Height	34.875"	89 mm
	Diameter of Bung Hole	2.0"	50 mm
65 Gallon/ 246 Liter	Stave Thickness	0.937"	24 mm
	Diameter of Head	22.687"	58 mm
	Circumference of Head	71.27"	181 mm
	Diameter of Belly	28"	71 mm
	Circumference of Belly	88"	224 mm
	Barrel Height	34.875"	89 mm
	Diameter of Bung Hole	2.0"	50 mm

Figure 3.1 - Typical Barrel dimensions

59 gallon French Bordeaux barrels were used in this study. Each barrel was filled with water in place of wine. The difference in specific gravity is negligible and a correction factor was not used in the model calibration. These barrels are constructed from oak

staves shaped into a bulging cylinder, with hoops around it, a flat circular head at both ends, and at least one hole, generally on the belly, for a bung. Most barrels weigh between 125 lb. and 140 lb. empty and approximately 600 lb. full of wine. 6 to 8 steel hoops are generally spaced along the barrel length. Wineries can specify the placement of the end hoops to either be at the contact point of the rack cradles or to be on either side to allow for a bearing point of metal rack to oak barrel (Morrow 2002). Specific barrel dimensions are given in Figure 3.1.

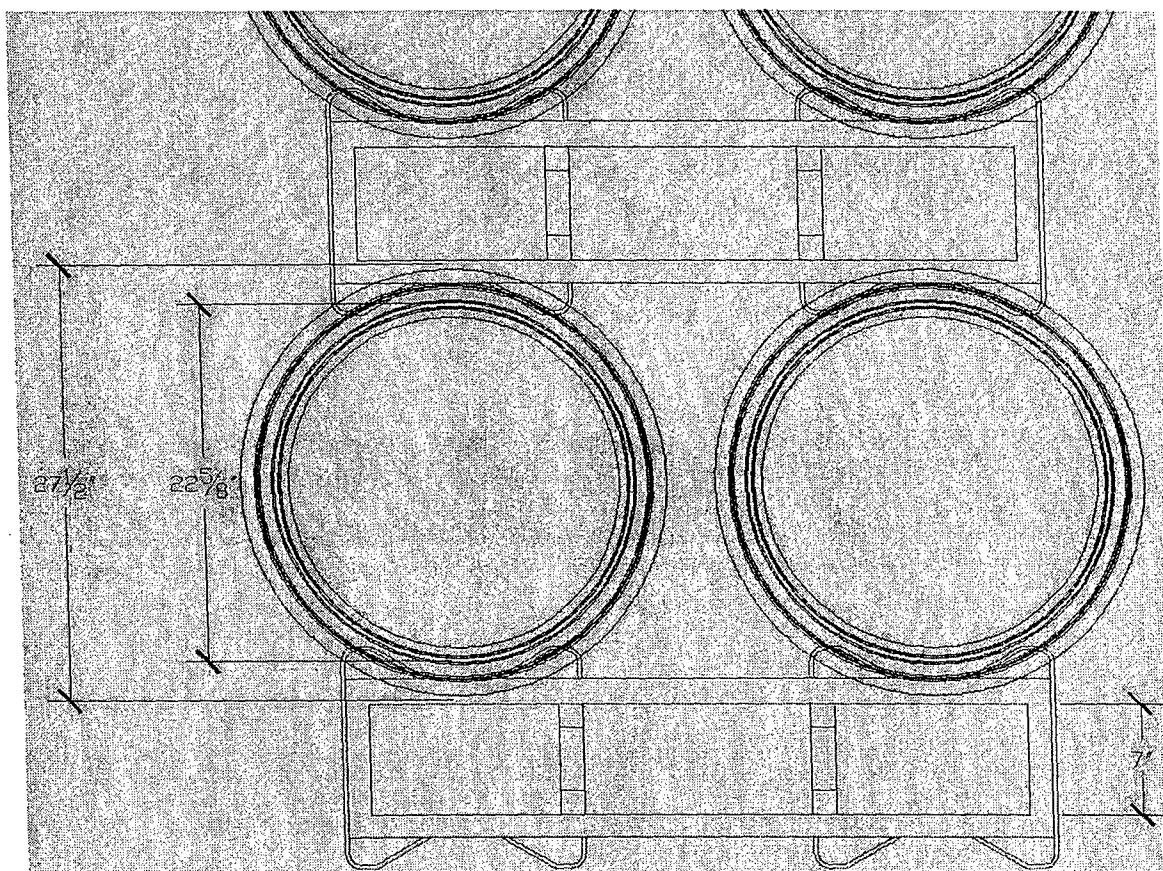


Figure 3.2 - Typical 2 barrel stack and rack configuration.

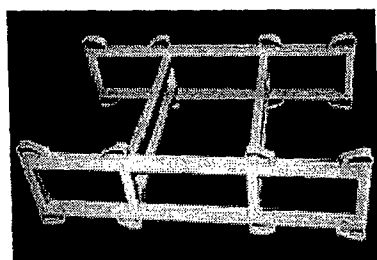


Figure 3.3 - Topco WR2



Figure 3.4 - Topco Eastern Saddle

The steel racks used for the experiment were the two barrel industry standard. Topco, model WR1 and WR2, steel racks were furnished for experimental testing. These racks are an improvement from the previous WR1 model in that they use four cross bars instead of the previous two (Figure 3.3). The newer rack increased the lateral stiffness of the rack assemblage. These racks are constructed using A36 (36 Ksi) 1 1/2" steel box sections. The saddle type used for testing is considered the "Eastern Saddle" and is used most often in industry applications (Figure 3.4). The racks are powder coated from the manufacture to provide superior corrosion resistance and aesthetic appeal. The overall dimensions of the racks are 30-1/2" in length, 44-1/2" in width, and have a 7" opening for fork lift clearance. They can support two wine barrels and stack heights of at least five barrels high. Since wine barrels are offered in various sizes depending on application, these racks can be used with either of the barrel sizes; however, mismatching of barrels in a stack results in uneven stack heights resulting in improper seating and possible instability of the stack.

To collect data for the experiment the National Instruments Data Acquisition system was utilized. Data acquisition included lateral displacement measurements, vertical displacement measurements and lateral acceleration. Each device operates on an individual channel within the operating software. Data points can be collected and saved at a specified frequency. Lower frequency collection would be preferred for a longer duration test and a higher frequency collection would be preferred for shorter duration test. Due to the nature of the test protocol, a high frequency collection frequency was utilized (1000 Hz). The transcendental pulse function ranges from a few tenths of second to a few seconds depending on the frequency.

3.2 Testing Procedure

Two types of tests were run for system verification; first, a series of sine sweeps, and second, a series of transcendental pulse waves. The preliminary data from the sine sweeps indicated the range of frequencies that needed to be looked at when running the pulse wave function.

The instrumentation configuration for the two tests described above included both acceleration and position data. Position transducers were situated such that horizontal displacement measurements could be performed from the stationary equipment frame. Each barrel was equipped with an accelerometer located at the center of mass of the barrel. Four position transducers were mounted from the table surface to the center of mass of the barrel. These four transducers provided the information needed to reduce the data and determine the rocking-sliding behavior. This data was coupled with the data collected from the lateral transducers to determine the relative uplift of the barrel on each end. A final transducer was placed on the table and connected to the rack to determine relative barrel-rack slip, and relative rack-table slip. Figure 3.5 shows the position transducer, P.3, mounted on the equipment frame to measure lateral displacement relative to the stationary equipment frame. The transducers P.1 and P.2 are both mounted to the shake table and collect relative sliding and rocking data. To account for the angle of the transducer P.1, a trigonometric relationship was established and adjusted at each time step.

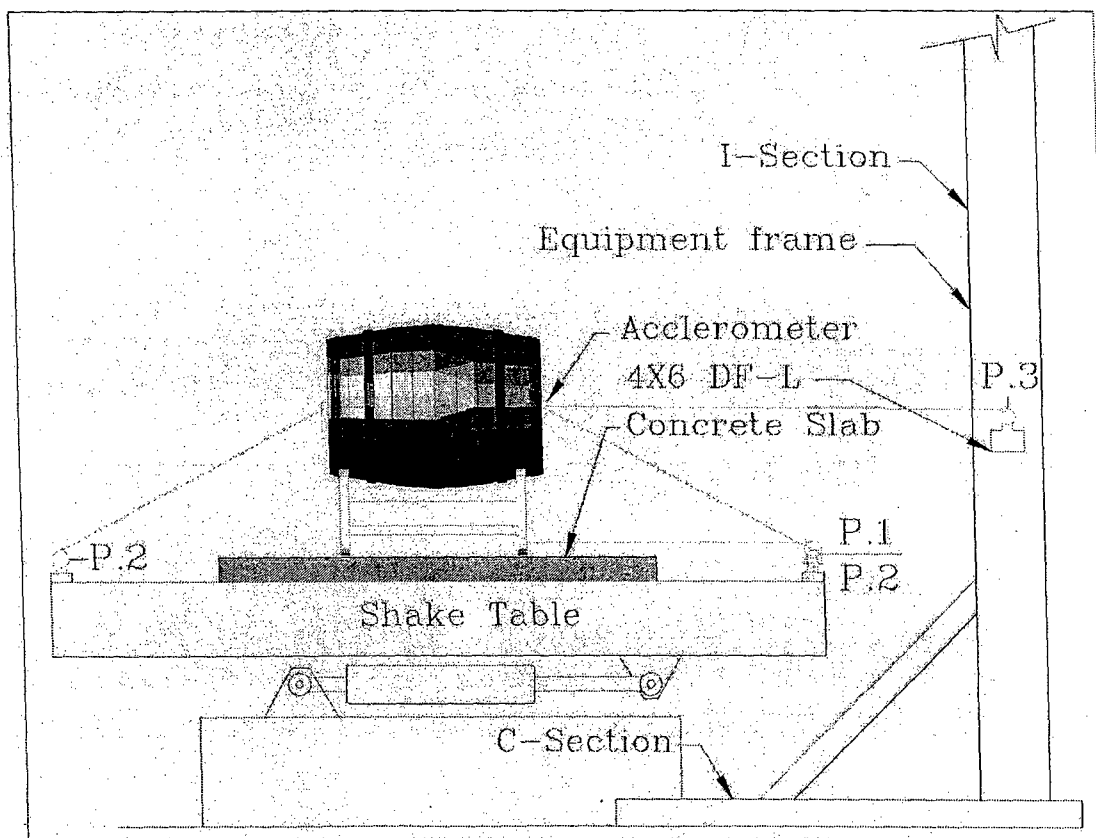


Figure 3.5 - Typical test configuration of a single stack height

The final data collected from the tests came from the table input. During the testing the data acquisition system was linked to the motion of the table. An accelerometer was mounted to the table and calibrated to the actual input from the frequency generator. The position data came from the input to the table from the frequency generator. Again this data was calibrated to the actual displacements of the table using a least squares method and approaching an R-factor (the R-factor is a measure of a curve fit where 1.0 is a perfect fit) of 1.0.

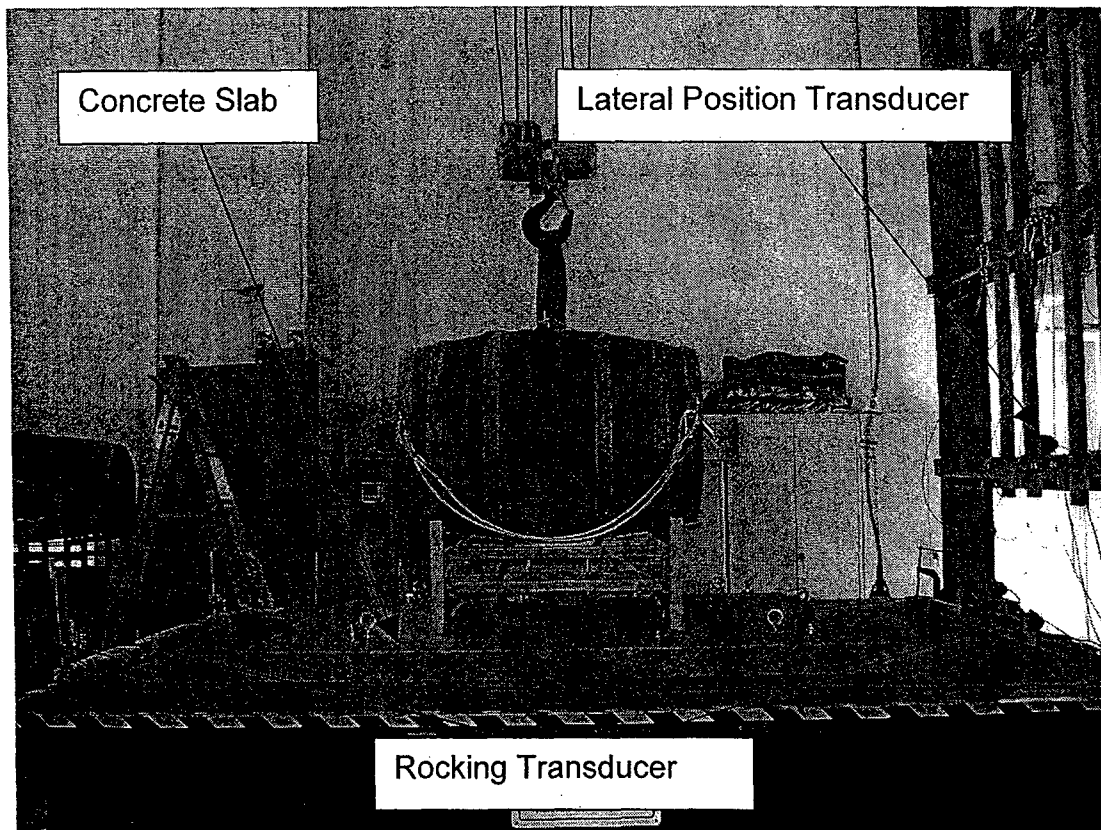


Figure 3.6 – Laboratory setup for the one barrel experiment

The preliminary shake table tests revealed that a range of frequencies exist that contribute to the response of the barrel stacks. Key frequencies were noted from the testing and were used to choose the pulse ground motion input. Another trend was noted from the preliminary testing indicating that the dominant frequency governing either sliding or rocking is dependent on stack height. To establish the key frequencies, sine sweeps at a low acceleration, were performed on the stacks. Using a constant table acceleration of

0.20g, a sweep of sine waves ranging from 2Hz up to 20Hz were input to the shake table to excite the barrel stack. First a series of these tests were performed on the single stack, and second on a two barrel stack. These specific frequencies enabled the formation of the transcendental pulse ground motion records, and corresponding frequency needed. These frequencies establish a basis to isolate rocking verse sliding.

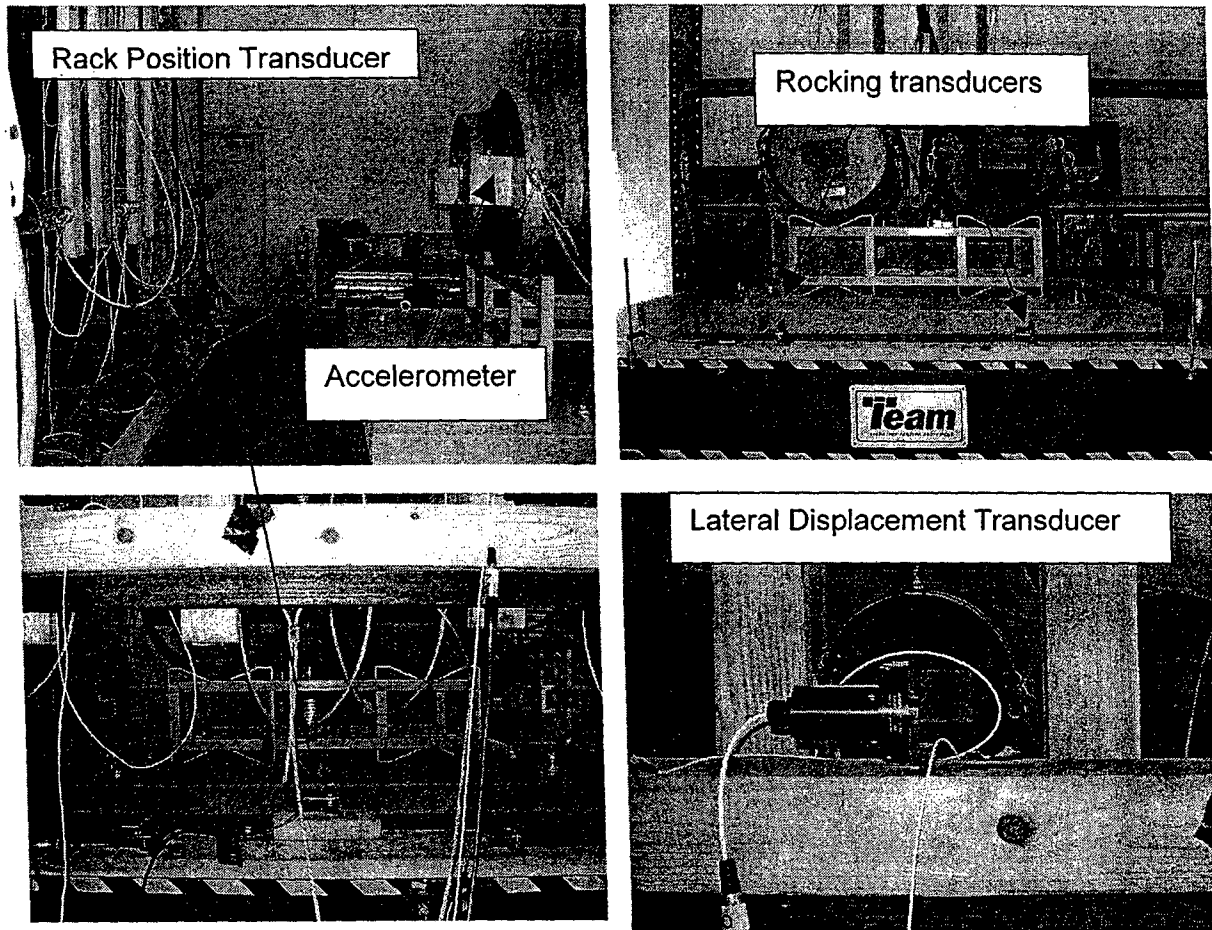


Figure 3.7 – Pictures of Laboratory Instrumentation

3.3 Ground Motions

In the work performed by Housner (1963), his analysis of rocking blocks with rectangular bases and constant material properties have a frequency parameter of $p = \sqrt{3g/4R}$. This frequency parameter is the equivalent to a rigid body rocking period that comes from the solution to the free rocking response of a rigid body.

Where g is the acceleration of gravity and R is the distance from the corner of rocking to the center of mass. If we apply this principle to wine barrel stacks, and assuming the wine barrels and racks are:

- Modeled as a rectangular rigid block.
- Constant material properties throughout.
- Rocking occurs at the corners of the rack.
- The base is considered a rectangular platform.
- At least one corner always maintains contact with the table surface.

Then, the rocking parameter of a single barrel stack modeled as a rigid block would have a rocking period of approximately 3.2 Hz. This result is presuming the rocking frequency is constant, even though tests have indicated otherwise. Using this as a starting point, a sine sweep experiment was conducted on the single barrel stack. Using constant peak shake table acceleration, the frequency of the table was varied from 2 Hz up to 20 Hz. Acceleration data collected from data acquisition, on both barrels and table, were plotted against the table excitation frequencies.

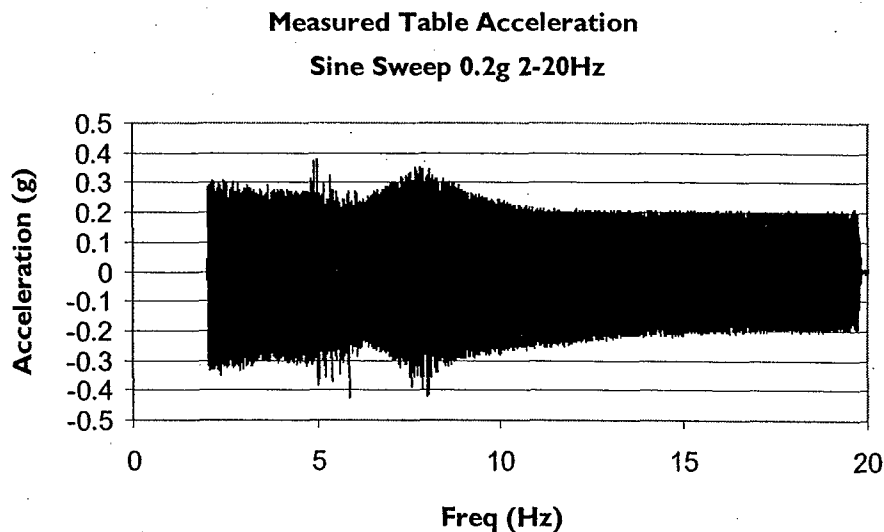


Figure 3.8 - Shake table acceleration measured from data acquisition.

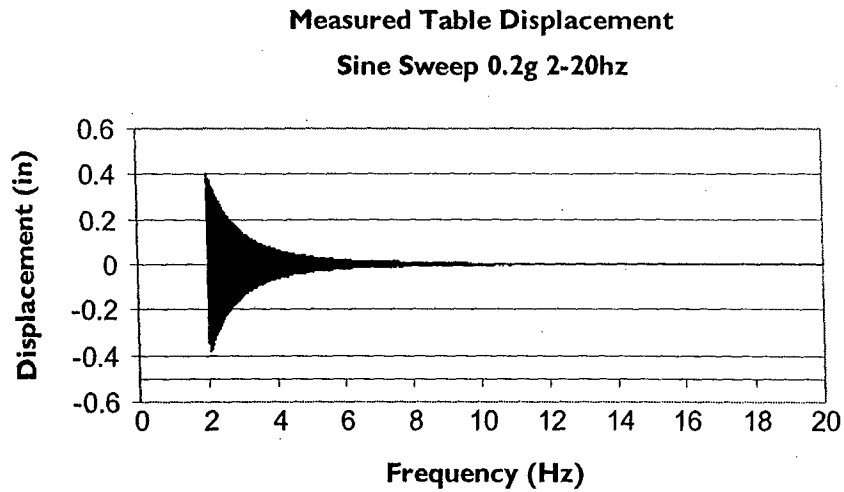


Figure 3.9 - Shake table displacement measured from data acquisition.

Figures 3.8 and 3.9 are plots of the table accelerations verses time and table displacements verses table frequency, respectively. In this system identification experiment, the acceleration is held close to constant at nearly 0.2g. However, the table displacements decay over time. This is necessary to produce a sine wave with constant acceleration. Figures 3.10 and 3.11 are the measured acceleration of the barrel mounted on the WR1 and WR2 racks, respectively. Peak barrel acceleration and corresponding frequency have been highlighted.

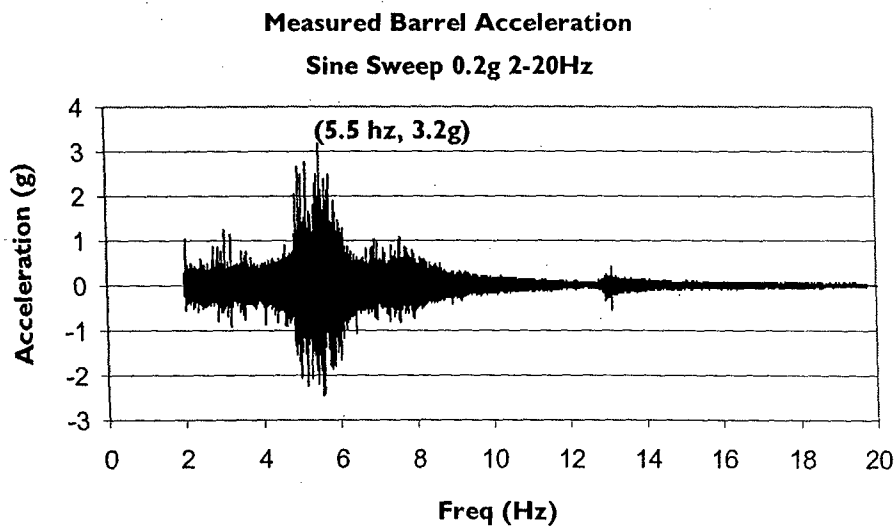


Figure 3.10 - Measured Barrel Acceleration mounted on Rack WR1

Figures 3.10 and 3.11 indicate a different response depending on specific rack model. These tests were repeated and similar results occurred. To avoid rack variation the WR2 rack was chosen for subsequent pulse testing due to its common use in the industry.

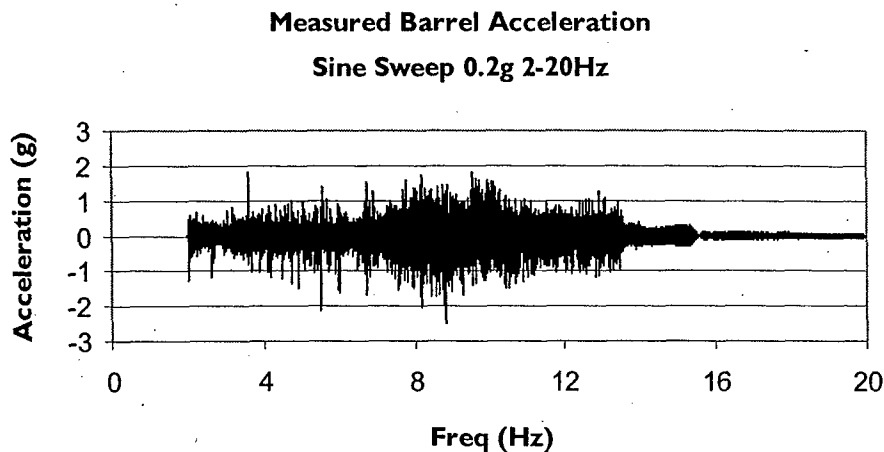


Figure 3.11 - Measured Barrel Acceleration mounted on Rack WR2

With preliminary ranges of frequencies selected from the sine sweep experiment the transcendental pulse functions were selected. These pulse functions were written with 1.0g peak acceleration. The following derivation for the pulse function replicates a fault normal pulse. Morrow (2000) indicated in his study that the fault normal pulse (forward-back type motion) had significantly higher impact on the stacks compared to the fault parallel (forward-stop type motion), so the fault normal pulse was adopted for this test. The table input pulse waves are derived as follows:

$$\begin{aligned} \ddot{u}(t) &= a(t) = A \cos(\omega t) = \frac{\partial v}{\partial t} \\ \dot{u}(t) &= v(t) = \int_0^t A \cos(\omega t) \partial t = A \omega \sin(\omega t) + C_1 \end{aligned} \quad \left. \vphantom{\begin{aligned} \ddot{u}(t) &= a(t) = A \cos(\omega t) = \frac{\partial v}{\partial t} \\ \dot{u}(t) &= v(t) = \int_0^t A \cos(\omega t) \partial t = A \omega \sin(\omega t) + C_1 \end{aligned}} \right\} \text{Initial conditions } \dot{u}(t) = v(0) = 0$$

$$C_1 = 0$$

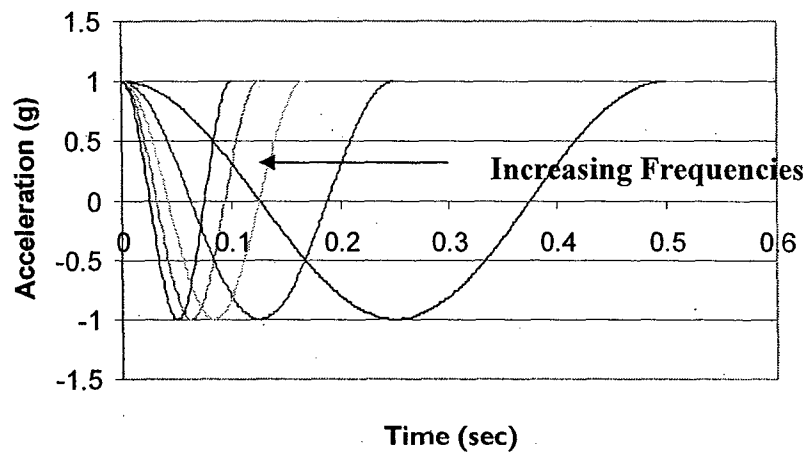
$$\dot{u}(t) = A \omega \sin(\omega t)$$

$$u(t) = \int_0^t A\omega \sin(\omega t) \partial t = -A\omega^2 \cos(\omega t) + C_2 \quad \left. \vphantom{\int_0^t} \right\} \text{Initial conditions } u(0) = 0$$

$$C_2 = A\omega^2 \quad \Rightarrow u(t) = -A\omega^2 \cos(\omega t) + A\omega^2$$

Where, A= acceleration amplitude and ω = circular frequency = $2\pi/T$. To conduct the experimentation, acceleration magnitude and frequency were varied according to the above criteria found from the sine sweeps. 100%, 75%, and 50% gravity tests were performed while selecting frequencies from 2, 4, 6, 8, and 10 Hz. This provided 15 different experiments on a single barrel stack. The acceleration and displacement time histories for the 1g acceleration (100%) at the selected frequencies (2-10 Hz) are given in Figure 3.12.

Acceleration Profile for Pulse Wave Table Input



Displacement Profile for Pulse Wave Table Input

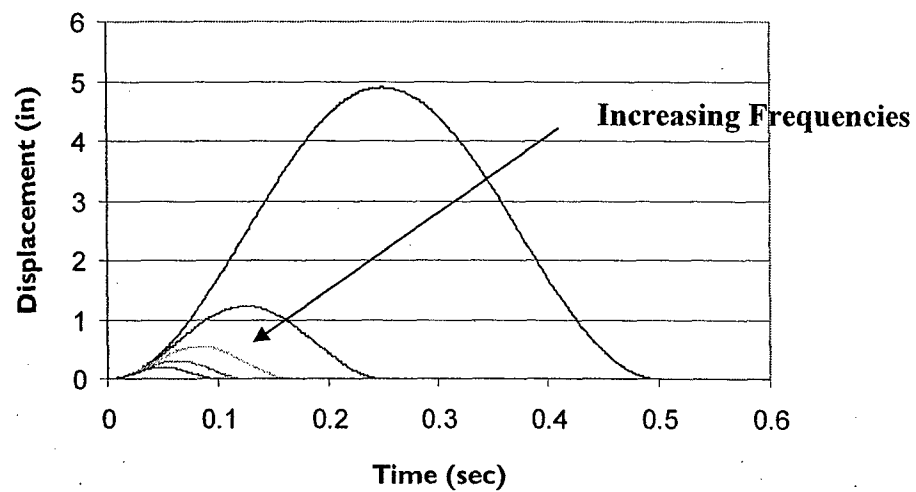


Figure 3.12 – Forward Back Ground Motion Acceleration (top) and Displacement (bottom) Time Histories

4.0 Analytical Model

4.1 Background

Beginning with the work of Housner (1963), who studied the chaotic nature of rocking, a theoretical frame work for rocking was put forth in which many other rocking experiments have been based. By using a half sine pulse excitation he was able to establish a few parameters that seemed to govern the rocking response of rectangular blocks. Mainly the pulse period T_s , amplitude a , $\omega/p > 3$, where $\omega = 2\pi/T_s$ and a parameter p , known well as the frequency parameter, lent itself in the solution to the rocking equation. This parameterizes the aspect ratio of the rocking block, and is given by the frequency parameter p see figure 4.1 for dimensions:

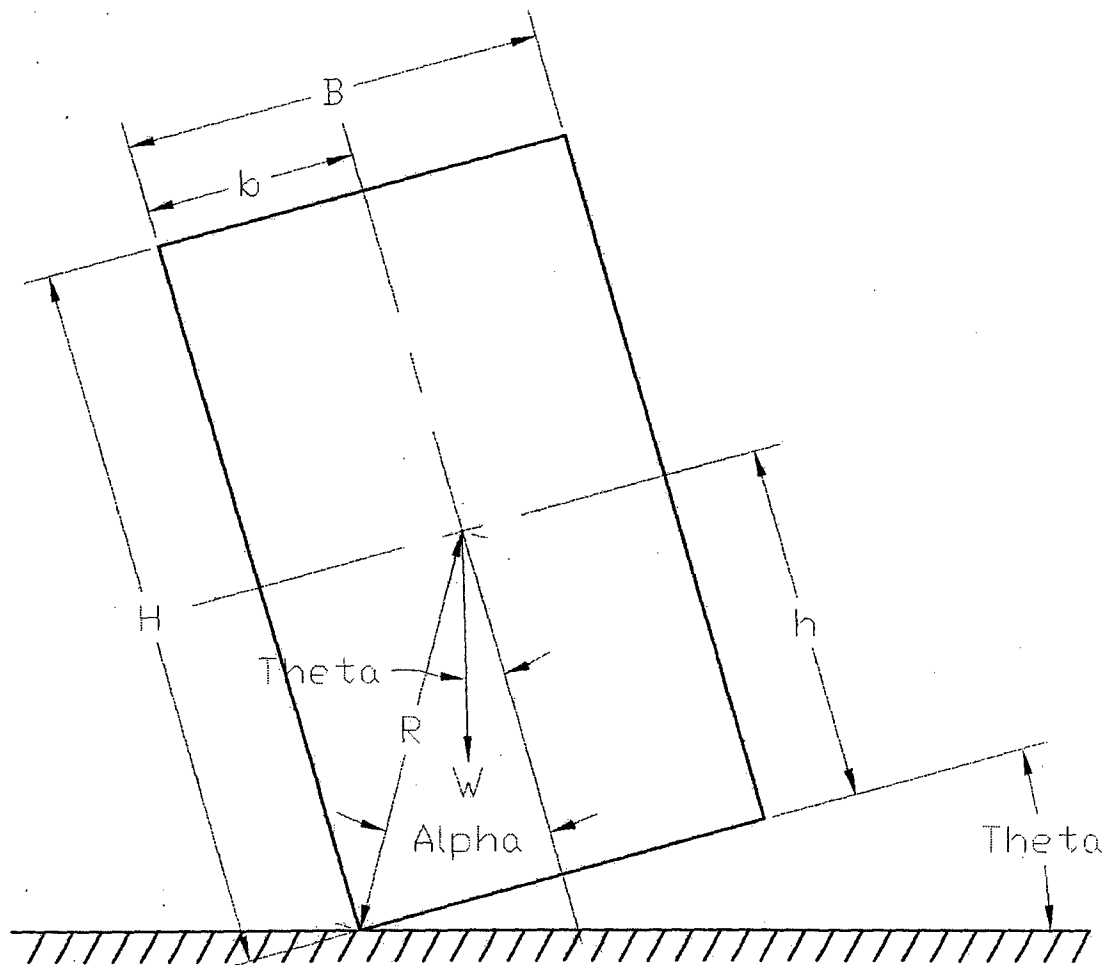


Figure 4.1 - Housner's Rocking Block Model

$$p = \sqrt{\frac{3g}{4R}} \dots\dots\dots (1)$$

From his analysis the block would overturn if:

$$\frac{aT_s}{2} > 2\pi\alpha\sqrt{\frac{Rg}{3}} \dots\dots\dots (2)$$

And:

$$\frac{a}{g} > \frac{B}{H} \dots\dots\dots (3)$$

If both rocking and sliding are present the block will only start rocking if:

$$\mu_s > \frac{B}{H} \dots\dots\dots (4)$$

Where μ_s is the coefficient of static friction. Part of his analysis was to understand the free response of the block given an initial perturbation. In his model the block is assumed to rock about the edges or corners of the block. The equation of motion is described as:

$$I_0 \ddot{\theta} = -WR \sin(\alpha - \theta) \dots\dots\dots (5)$$

Where I_0 is the mass moment of inertia about the edge of the block. R is the distance from the block edge to the center of mass. See the figure 4.1 below, this model shows that as a block is displaced some initial amount and let go it will oscillate about the corners of the block. The block finally comes to rest when the initial energy is completely dissipated. The concept of energy dissipation through radiation damping was used to describe the damping of the block. The solution to the above equation for tall slender blocks is described by:

$$\ddot{\theta} - p^2 \theta = -p^2 \alpha \dots\dots\dots (6)$$

Because for small angles $\sin(\theta) \approx \theta$ therefore the solution to (6) is given by:

$$\theta = \alpha - (\alpha - \theta_0) \cosh(pt) \dots\dots\dots (7)$$

Damping of the block mentioned above is characterized by energy dissipation through impact. After each cycle the block contacts the surface twice. This is a basic assumption in the previous model, and some tests have shown that this is not always the case. In this example the coefficient of restitution can be derived to account for energy loss after each impact. The coefficient of restitution used by Housner for the rigid block is defined as:

$$v = \sqrt{\frac{I_0 \dot{\theta}_{i+1}^2}{I_0 \dot{\theta}_i^2}} = \frac{\dot{\theta}_{i+1}}{\dot{\theta}_i} \dots \dots \dots (8)$$

In this equation $\dot{\theta}_i$ is the angular velocity before impact and $\dot{\theta}_{i+1}$ is the angular velocity after impact. The coefficient of restitution is largely dependent on $\dot{\theta}_i$ and material properties. However, as will be shown later in the work of Mohammad Aslam(1980) the actual nature of rocking cannot be fully justified by using a single pulse wave, but can be a close approximation.

Following the work of Housner, another investigation of rocking response of rigid bodies was conducted by Mohammad Aslam, (1980). His research included a concrete block experiment used to study both pulse wave motion as well as an earthquake simulation of the Pacoima Dam Record from the San Fernando Earthquake of 1971. The equation of motion he used for the rocking block is described as:

$$I_0 \ddot{\theta} - M \ddot{u}(b \sin \theta + h \cos \theta) + M(\ddot{v} + g)(b \cos \theta - h \sin \theta) + S(F_0 + K\Delta_1) \cos \theta + (B - S)(F_0 + K\Delta_2) \cos \theta = 0$$

Where S is the position of the prestressing force; Δ_1 and Δ_2 are the extensions of the prestressing rods. They were assumed linear elastic and connected to the surface on which the block is rocking. This equation of motion was further reduced to indicate that the prestressing rods are not present in a freely rocking block. Substituting the value of $I_0 = \frac{4}{3}MR^2$ and $K=0$ the following equation resulted:

$$\frac{4}{3}R^2 \ddot{\theta} - \ddot{u}(b \sin \theta + h \cos \theta) + (\ddot{v} + g)(b \cos \theta + h \sin \theta) = 0 \dots \dots \dots (9)$$

Assumptions:

- The block rocks without sliding.
- The coefficient of restitution is assumed constant.
- The bottom surface of the block is planar or slightly concave to allow the block to rock about the edges.
- One edge of the block is always in contact with the surface. This assumes that the block does not bounce on impact.

To determine the coefficient of restitution shake table tests were performed on the block. Position instrumentation allowed for continuous measurement of angular displacement. From the results of the test the analytical solution was fitted to the experimental data. Once determined, the coefficient of restitution of the concrete block was used in further studies and simulated ground excitations. In summary, Aslam concluded that frequency is amplitude dependent and dependent on the boundary condition at the base. The rocking response is highly non-linear, and correlation to the model with seismic type input was not achieved.

4.2 Single Barrel Analytical Model

The rigid block model provides a starting point in the development of a model to describe the wine barrel stack. However, this simplified, single degree of freedom idea falls short when applied to a barrel rack assembly. As was seen in the sine sweep test, rocking frequencies were not in agreement with the rigid block model. To account for the many discontinuous surfaces, material properties, and non-homogeneous assembly a multi-degree of freedom system is used. The non-linear nature of the rocking-sliding barrel problem lends itself to the model developed in Figure 4.1. Nine degrees of freedom have been chosen to characterize the response of this single barrel stack. Each degree of freedom is associated with a specific material, pounding, or sliding model to solve the equations of motion. Each degree of freedom listed below will follow with an analytical relationship given in the charts below. From the diagram a few points should be clarified.

- The effective material properties of the frame were determined such that the stiffness of the idealized frame matched the stiffness of the wine barrel rack at Degree-of-Freedom (DOF) 9.
- At the corners, the degrees of freedom that represent rocking, it is assumed that the spring and damper do not act in tension. Thus, in the analysis, when the barrel uplifted, the stiffness of the spring was taken as zero.
- The midpoint (DOF 7 & DOF 8) the spring is a Coulomb friction surface with a constant normal force. The surface can only slide in the direction of the spring. It is not possible to have rotation or uplift.

- At DOF 1, the spring acts only in the lateral direction for Coulomb friction at the surface of the steel rack and concrete interface and the normal force is chosen based on the reaction of the sum of the forces in DOF 2 and DOF 5.
- Rocking is assumed to occur about the corners.
- The rack and barrel are assumed to rock together.

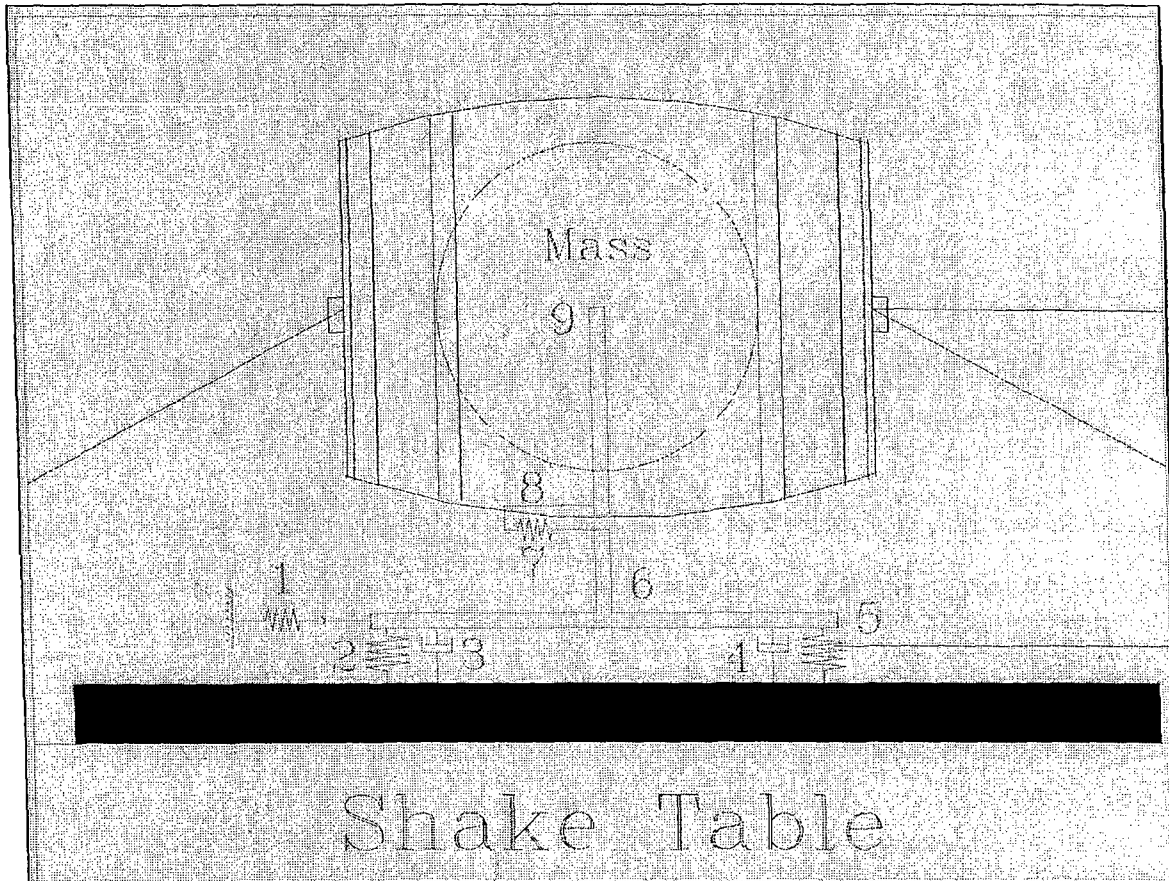


Figure 4.2 - Analytical Model

The mass shown in the picture represents a lumped mass approximation located at the geometric centroid of the barrel.

The Coulomb Friction model is a rigid-plastic model where the force at sliding is the normal force times the friction coefficient. If the frictional force demand exceeds the frictional force capacity, the stiffness is set to zero and the wine barrel rack system is free to slide. If the direction of motion is reversed, the stiffness is again set to rigid and the

restraint is engaged at the displacement where the rack velocity changed direction. The hysteretic model for Coulomb friction is given in Figure 4.3.

At each time step through the analysis, the normal force, N , at sliding is recalculated. If the applied force was greater than the normal force, the spring was set zero stiffness. If the applied force was less than the sliding force, the spring stiffness was set to rigid. A similar model was used between the rack and the barrel with the exception that the normal force was held as a constant.

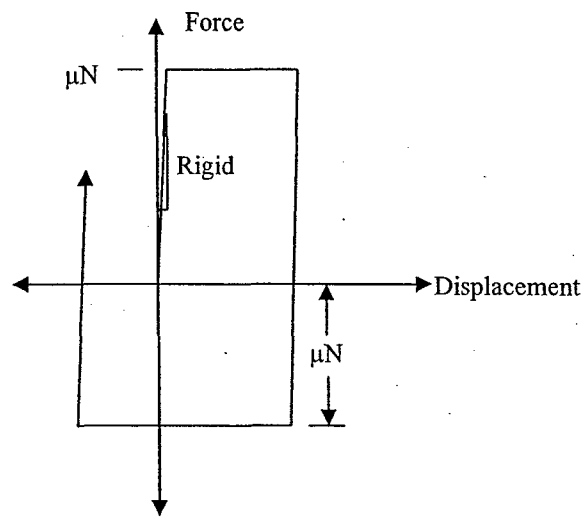


Figure 4.3 - Coulomb Friction Model

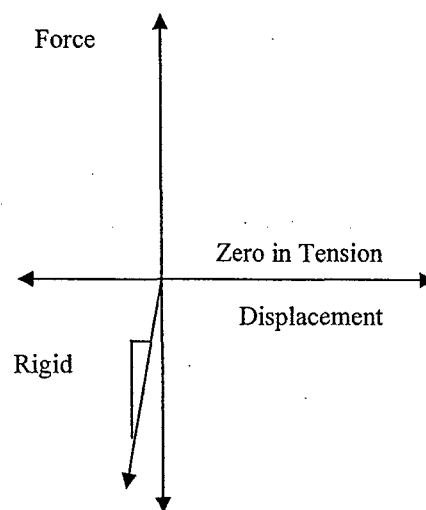


Figure 4.4 - Elastic Gap Element

An Elastic Gap Element was used for the vertical springs at DOF 2 and DOF 4 consistent with the proposed modified Winkler model. The nonlinear force displacement model for the elastic gap element is given in Figure 4.4. The elastic gap element assumes near rigid response when pounding with a zero uplifting response when the spring is put into tension.

The velocity damper consistent with the modified Winkler model was taken as system effective damping. The system damping was varied between 1% and 5% calibrated using Rayleigh Damping (Chopra, 2000) at 1Hz and 5Hz. For preliminary system parameter investigation, this was deemed appropriate. In future modeling, the system damping will be supplemented by velocity dampers at the point of impact.

To form the solution to the model above, a numerical integration method was employed. The governing differential equation for multiple degree of freedom systems is given by the familiar structural dynamics equation in matrix form:

$$M\ddot{U}(t) + C\dot{U}(t) + F_s(U, \dot{U}) = -M\ddot{U}_g(t)$$

Where M and C are the mass and damping matrices, respectively. F_s is the nonlinear system resisting force as a function of the displacement vector (U) and the velocity vector (\dot{U}). The force at any time step is the ground acceleration (table acceleration) times the mass matrix. A Newmark average acceleration method (Chopra, 2000) for multi-degree of freedom systems was employed in the solution of the dynamic equation. The average acceleration method was selected as it is unconditionally stable for any system periods of vibration. The dynamic equation was solved at each time step with an equilibrium correction to account for the nonlinear system behavior using a Newton-Raphson matrix iteration strategy for nonlinear systems (Chopra, 2000).

5.0 Test Results

5.1 Transcendental Pulse Motions

The system identification tests using the sine sweeps indicated that the range of rocking verses sliding for the one barrel high stacks is between 2-10Hz as described in Chapter 3. The shake table was input with a series of pulses to identify specific frequencies associated with rocking, sliding, and a combined rocking/sliding type behavior of the rigid body stacks.

The measured accelerations and velocities of the 1g pulses from accelerometers and displacement transducers are given below for the frequency ranges of 2-8Hz in Figure 5.1-5.4. The data collected from the 10Hz pulses are not included as the displacement transducers used did not have adequate resolution to attain meaningful data in this frequency range.

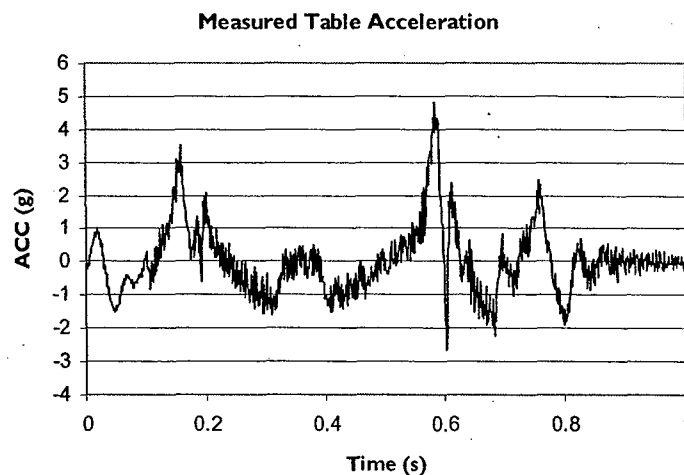


Figure 5.1 - Measured Acceleration Time History for 2Hz Forward Back Pulse

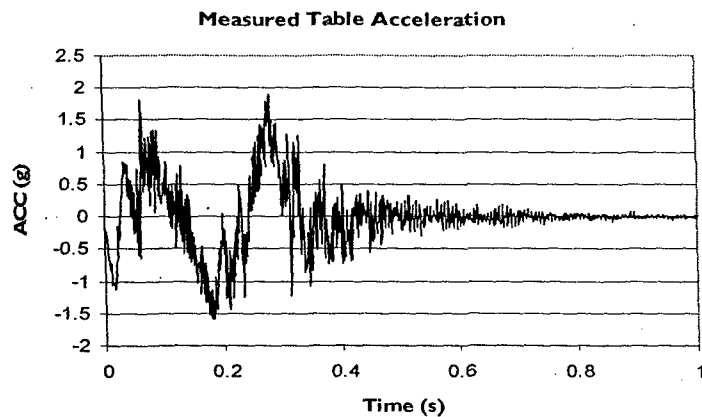


Figure 5.2 - Measured Acceleration Time History for 4Hz Forward Back Pulse

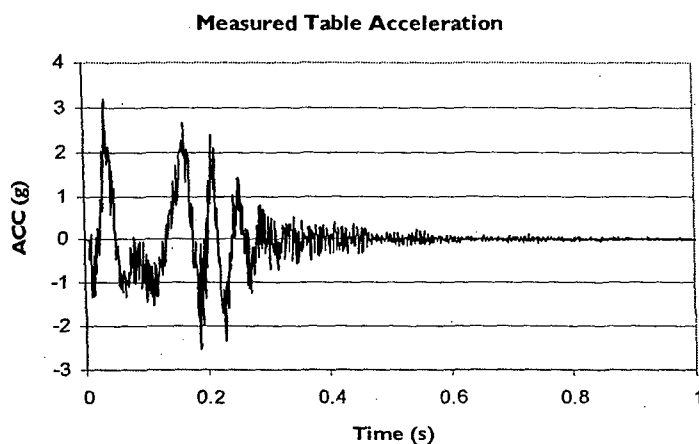


Figure 5.3 - Measured Acceleration Time History for 6Hz Forward Back Pulse

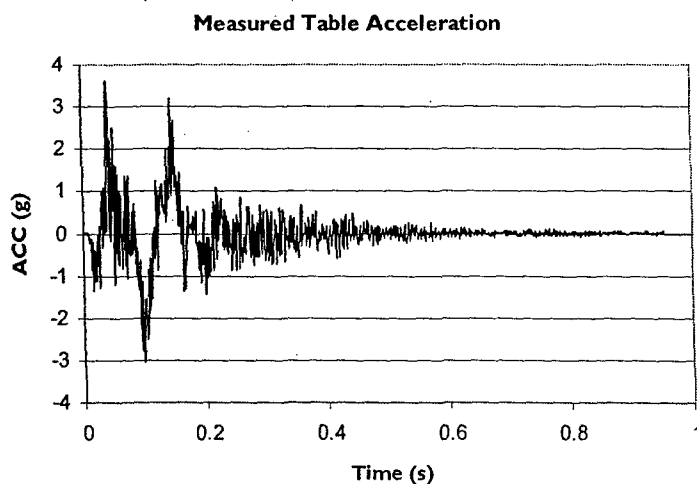


Figure 5.4 - Measured Acceleration Time History for 8Hz Forward Back Pulse

It is of interest to note the difference in measured table accelerations given in Chapter 3 as compared to the actual accelerations recorded during physical simulation. This is due to the nonlinearity of the shake table control system and its inability to replicate an exact input. While the acceleration wave forms are different, the table displacements do reproduce the forward-back type motion desired to replicate the fault normal type ground motion. For input into the nonlinear rocking model, the actual table accelerations, as provided in Figures 5.1-5.4, were used.

5.1.1 Barrel Sliding Motions

Figure 5.5 shows the barrel translations relative to the recorded shake table motions for the 2Hz, 4Hz, 6Hz, and 8Hz ground motion pulses.

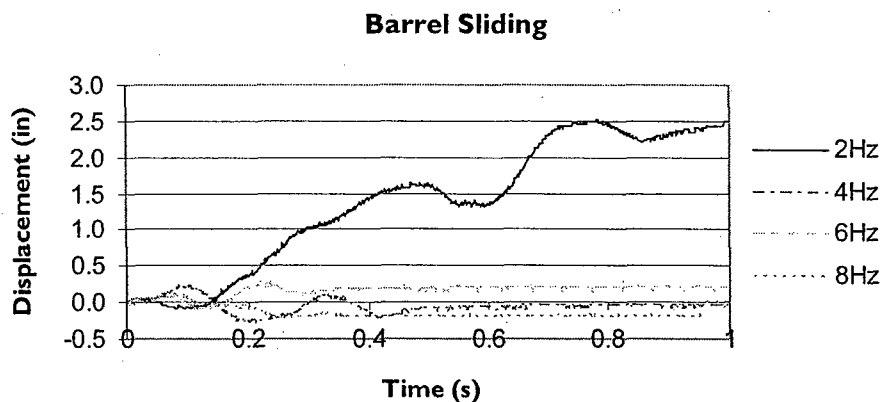


Figure 5.5 - Barrel Sliding Relative to the Shake Table

The test data suggests that sliding is dominant near the lower frequency range. Also, because of the differences between the input and measured accelerations, the 2Hz, 1g ground motion input had roughly 5g occurring at a time of 0.6 seconds. This can be seen in the displacement time history of the barrel by the rapid change in displacements that occur at approximately 0.6 seconds. For the remaining frequencies, little differences were observed in overall behavior with peak relative sliding displacements all found to be under 0.5". This suggests that ground motion with frequency content above 4Hz may have little effect on sliding for the one barrel stack.

5.1.2 Effect of the Rack Between the Wine Barrels

Figure 5.6 shows the absolute table movement, barrel movement relative to the table, and rack movement relative to the table for the 1g, 2Hz ground motion. Figure 5.6 suggests that most of the movement occurs between the rack and the simulated concrete factory floor; however, there is a significant amount of motion (approximately 20-40% of the total barrel sliding) that occurs between the barrel and the rack. It is the excessive barrel sliding within the racks that has been identified as a mechanism contributing to stack collapse (Morrow, 2003).

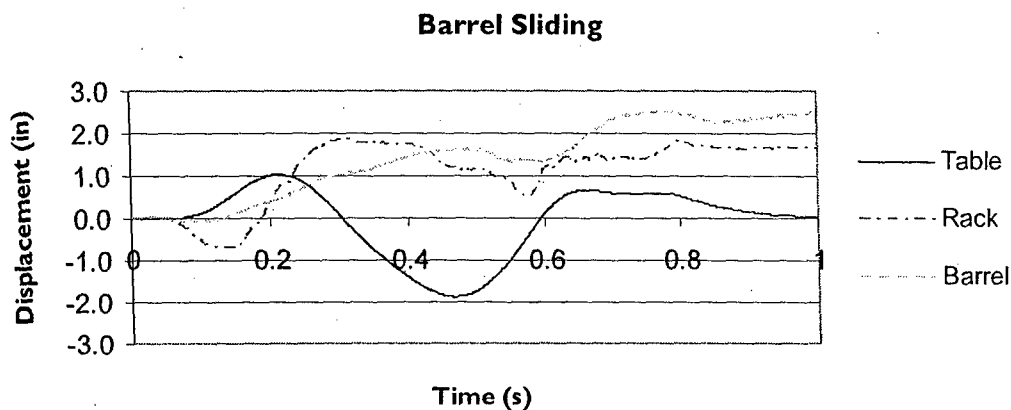


Figure 5.6 - Barrel Sliding and Rack Sliding Relative to the Shake Table for the 1g, 2Hz Motion

As the pulse frequencies increase, the data suggests that the sliding mechanism changes such that the majority of the sliding occurs between the barrel and the rack rather than between the rack and the concrete slab. Figure 5.7 and Figure 5.8 show the relative displacement plots of the 1g, 6Hz and 1g, 8Hz ground motion pulses.

Furthermore, it is observed that both the higher frequency pulses had roughly the same permanent offset but in different directions. This, again, is a likely result of the noise in the measured accelerations as compared to the input ground motions but no conclusions can be drawn.

In consideration of the absolute displacements of the table, the rack, and wine barrel, Figure 5.9 shows that the three objects typically move together in phase. This is consistent for all frequencies tested. This result is not unexpected.

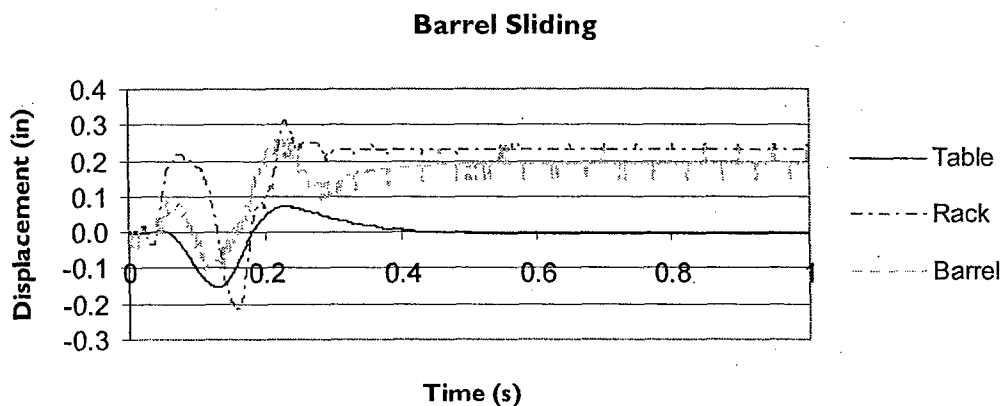


Figure 5.7 - Barrel Sliding and Rack Sliding Relative to the Shake Table for the 1g, 6Hz Motion

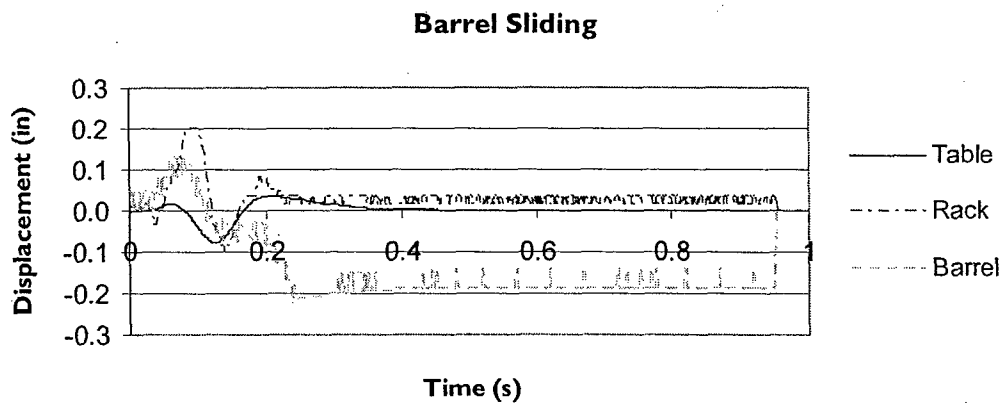


Figure 5.8 - Barrel Sliding and Rack Sliding Relative to the Shake Table for the 1g, 8Hz Motion

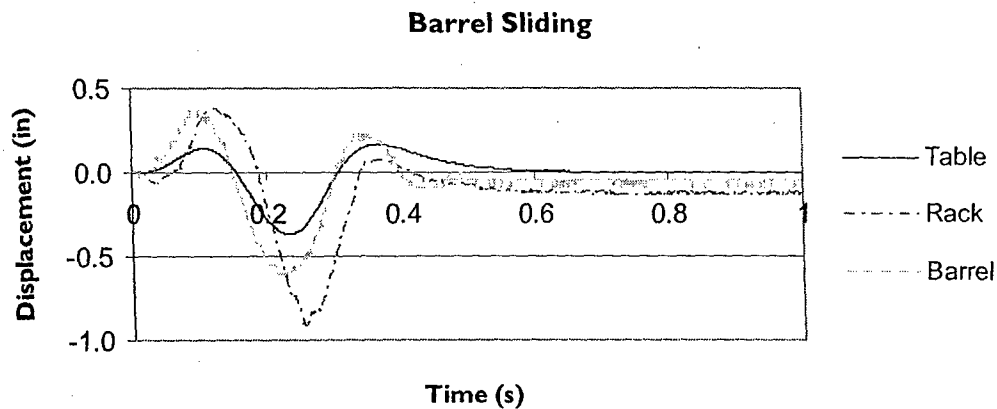


Figure 5.9 - Barrel Sliding and Rack Sliding in Absolute Coordinates for the 1g, 4Hz Motion

However, of particular interest is that the rack shows more movement than both the table and the barrel while moving in phase. This suggests the rack is moving somewhat independently and at larger displacements than either the barrel or the table. This observation was noted in all absolute data sets for all frequencies. To capture this effect in the analytical model, the rack should be included as an independent mass carrying degree of freedom.

5.1.3 Rocking

To capture barrel rocking, displacement transducers were attached directly from the table to the center of mass of the barrels on each barrel end at an angle with the horizontal of approximately 28 degrees. These displacement transducers, due to their angle, captured vertical as well as horizontal displacements. In the data, however, there are errors due to barrel sliding and rotating that could not be accounted for. To minimize the overall errors, the forward and aft displacement measurements were added together (representing the difference), then the vertical projection of the displacements were found. By adding the transducer measurements together, the horizontal displacements cancel leaving only the vertical movement.

Figure 5.10 shows the vertical projected displacements for the two displacement transducers added together for the 1g, 4Hz ground motion record. Data greater than zero

indicates rocking in one direction while data less than zero indicates rocking in the other direction. In addition, a high mode of rocking frequency can be identified at approximately 20Hz (Period = 0.05 seconds). This rocking mode may be the barrel rocking upon the rack independently of the rack rocking atop the simulated concrete warehouse floor slab. This high frequency rocking vibration can clearly be seen in the data from the 1g 4Hz, 6Hz, and 8Hz tests.

Data from the 1g, 2Hz one barrel experiment indicate a longer period of rocking that is not seen in the higher frequency test data (Figure 5.11). This is consistent with visual observation. During the experiments, it was unclear whether rocking had, or had not, occurred. However, during observation of the 1g, 2Hz test it was quite clear that rocking was taking place with the more predominant rocking period being near 10Hz (period = 0.095 sec).

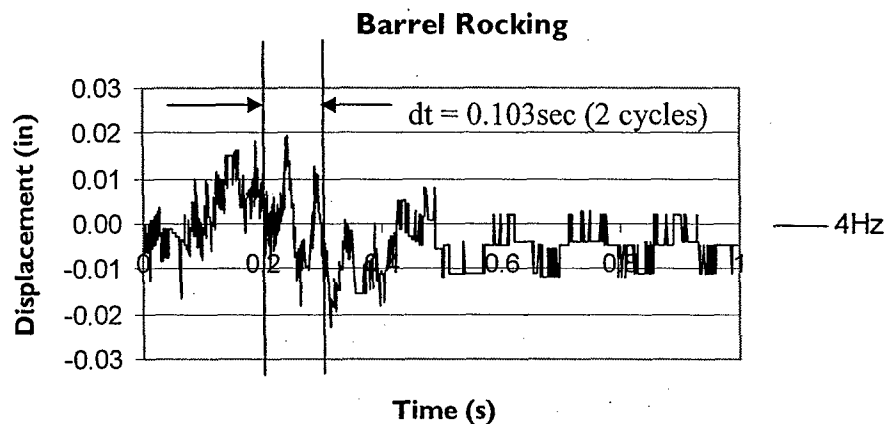


Figure 5.10 - High Mode of Vibration for Rocking Response.

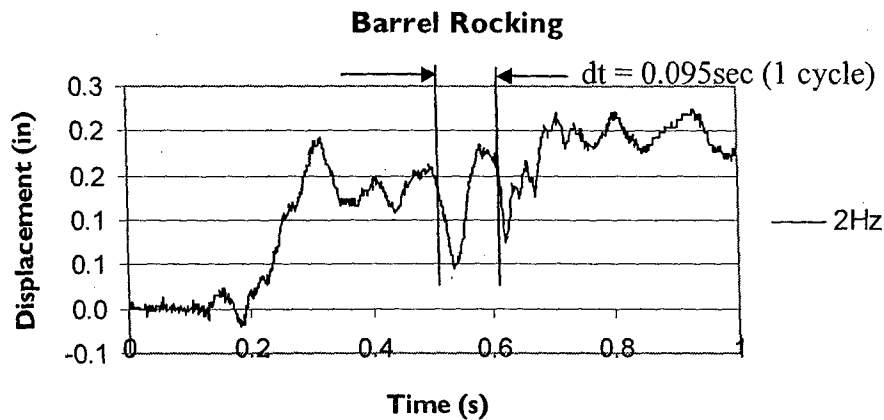


Figure 5.11 - Predominant Rocking for 1g, 2Hz ground motion.

The rocking data for the 1g, 2Hz ground motion test did change from being centered about zero during the period of strong shaking. This is due to the large residual motion of the barrel both relative to the table and relative to the rack. In addition, it was observed that during the experiment, the barrel rotated within the rack as well as about the base. This rotation yields the permanent drifting offset observed in the rocking response. However, the rocking mechanism can still be observed in the data.

5.1.4 Modeling Results from One Barrel Pulse Tests

The parameters in the model were adjusted over a range of overall system damping values, as discussed in Chapter 4, as well as over a range of Coulomb friction coefficients. Analysis was performed over the range of parameters using the 1g, 4Hz ground motion input in an effort to best articulate the simulated and measured barrel displacement data.

In the analysis, the friction coefficient is varied between 5% and 25% while varying the global damping between 1% and 7%. Simulation results suggest general system damping in this range has little effect on analytical results. Figure 5.12 shows the simulation results of predicted barrel displacements with the variation on damping for a typical 15% friction coefficient. This finding was not dependant on the coefficient of friction used.

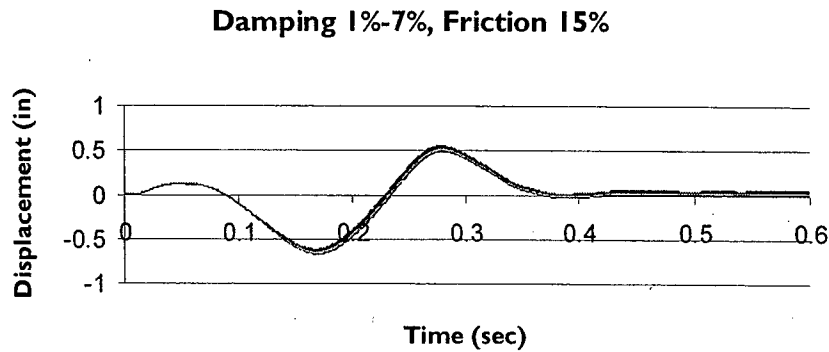


Figure 5.12 - Damping Variation for the 1g, 4Hz Ground Motion, Constant Friction

Model results from the variation on the friction coefficient demonstrate that its effect on overall system response is greater than that of overall system damping. Figure 5.13 shows simulation results from analysis performed with varying friction coefficients between 5%-25% and a constant system damping of 1%. Simulation results suggest, for this case, that increasing the frictional force between the rack and concrete increases the overall permanent offset while decreasing force transmission into the barrel. This reduction in force transmission results in less rack-to-barrel sliding and reduces the risk of stack collapse. From the variation on the parameters considered, a system damping ratio of 2% and a friction coefficient of 5% were chosen to best represent the 1g, 4Hz data set.

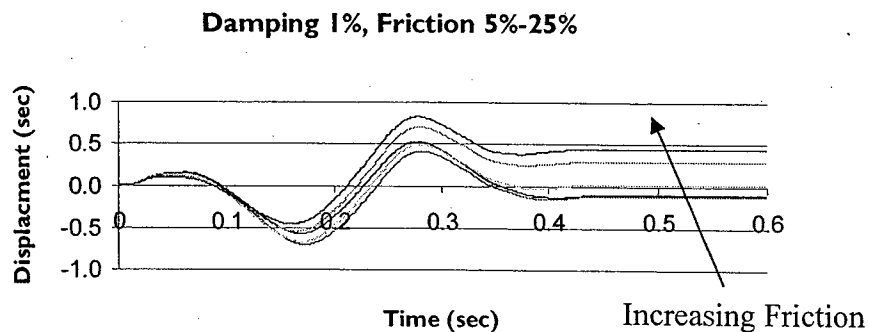


Figure 5.13 - Friction Variation for the 1g, 4Hz Ground Motion, Constant Damping

Figure 5.14, Figure 5.15, and Figure 5.16 show the measured and simulated barrel displacements relative to the table for the 1g, 2Hz, 4Hz, and 6Hz ground motions,

respectively. Simulation results for the 1g, 2Hz ground motion fail to predict the magnitude of the permanent offset, however, the waveforms between the simulated and measured response are similar. Simulation results for the 4Hz do predict offsets and waveforms while the 1g, 6Hz simulation again fails to replicate permanent offsets. During the one barrel forward-back pulse experiments, the barrel stack did rotate in the plane of the shake table. This resulted in the two adjacent barrels having different values for permanent offset. This effect was not considered in the analytical model.

In the simulation of the 1g, 2Hz and 1g, 4Hz records, minor uplift was predicted at a frequency of 10 Hz consistent with observed test data. No uplift was predicted with the 6Hz and 8Hz analytical simulations.

Model versus Measured - 2Hz

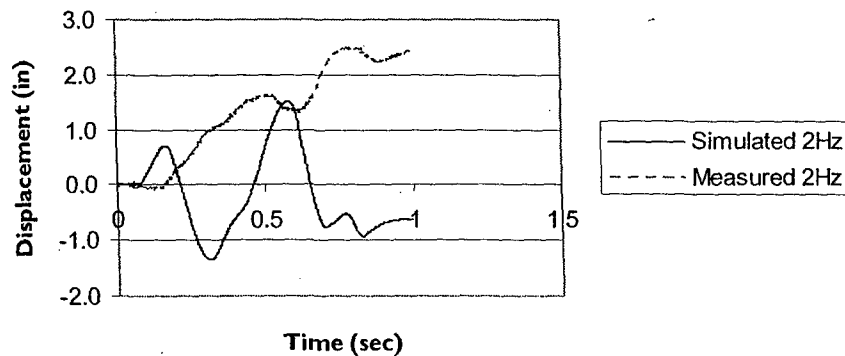


Figure 5.14 - Measured versus Simulated Barrel Response for the 1g, 2Hz Ground Motion

Model versus Measured - 4Hz

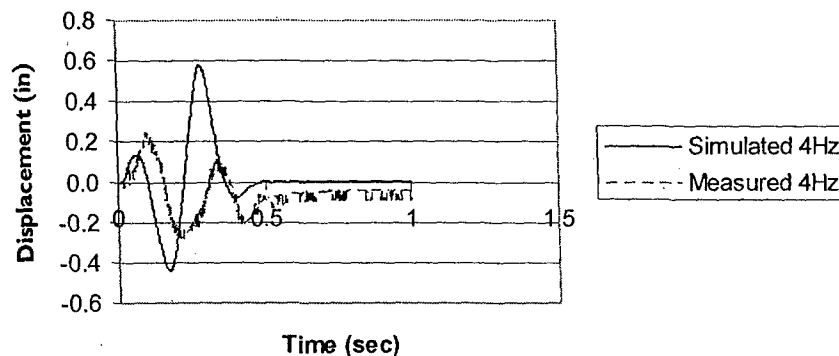


Figure 5.15 - Measured versus Simulated Barrel Response for the 1g, 4Hz Ground Motion

Model verses Measured - 6Hz

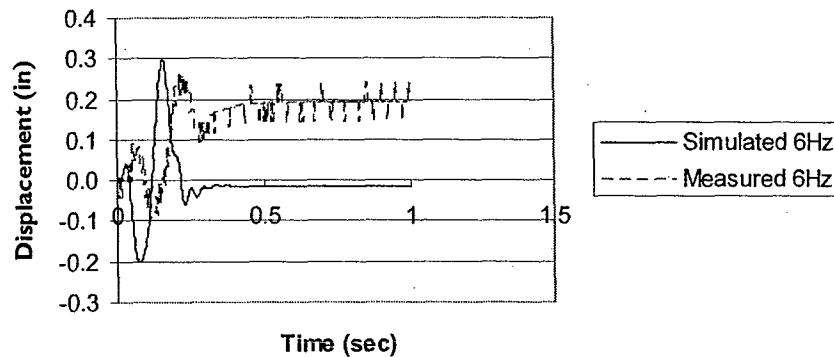


Figure 5.16 - Measured verses Simulated Barrel Response for the 1g, 6Hz Ground Motion

5.2 Earthquake Ground Motions

Three earthquake ground motions were tested on the single barrel stack to investigate the ability of the nonlinear rocking/sliding model to capture the measured uplifts and displacements. The ground motions were chosen for their individual characteristics and frequency content. The ground motion records containing shorter period energy were selected to represent rocking type behavior while the ground motion records containing longer period energy were chosen in an effort to induce sliding in the model. The records selected are classified as design earthquakes that have a 10% probability of occurring over a 50 year period. Details of the ground motions selected (LA16, LA18 and LA19) and their respective acceleration records are provided in Figures 17-20.

Details of Los Angeles Ground Motions Having a Probability of Exceedence of 10% in 50 Years

Name	Record	Earthquake Magnitude	Dist. (km)	Scale Factor	Number of Points	DT (sec)	Duration (sec)	PGA (cm/sec ²)
LA16	Northridge, 1994, Rinaldi RS	6.7	7.5	0.79	2990	0.005	14.945	568.58
LA18	Northridge, 1994, Sylmar	6.7	6.4	0.99	3000	0.02	59.98	801.44
LA19	North Palm Springs, 1986	6	6.7	2.97	3000	0.02	59.98	999.43

Figure 5.17 - Ground Motion Characteristics.

LA16 Acceleration Time History

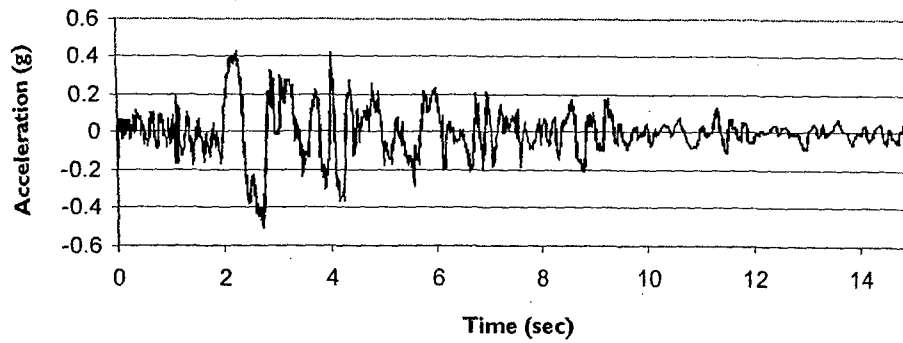


Figure 5.18 - LA16 Acceleration Time History

LA18 Acceleration Time History

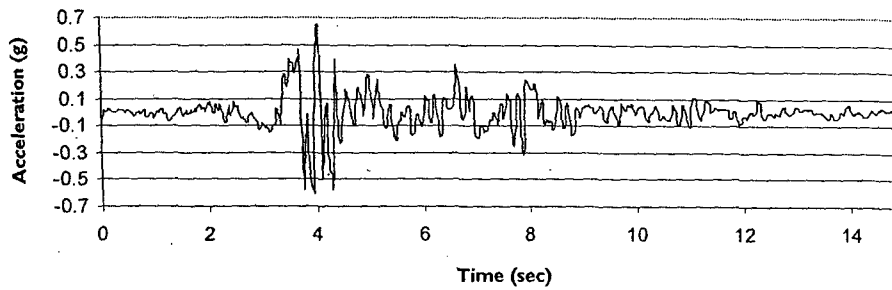


Figure 5.19 - LA18 Acceleration Time History

LA19 Acceleration Time History

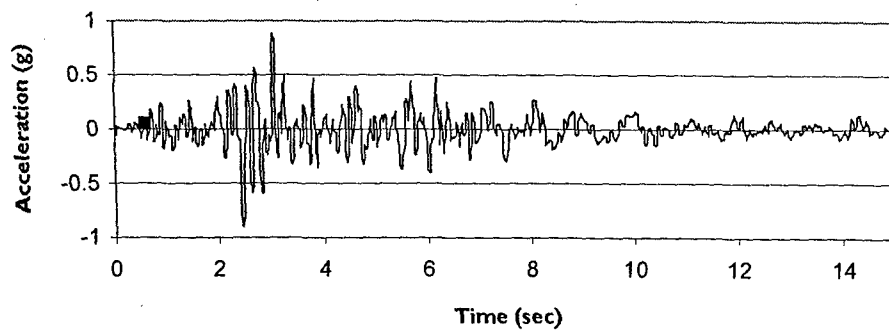


Figure 5.20 - LA19 Acceleration Time History

Figure 5.21 shows the linear response spectrum calculated at 5% of critical damping for the three ground motion records selected. Single barrel tests indicate the system has a rocking period of approximately 0.1 sec. At this period, all three ground motions are in the acceleration controlled region of the spectrum. However, LA16 has a significantly lower acceleration at this rocking period than do the LA18 and LA19 ground motion records. Thus, it is expected that more rocking be observed during the physical simulation of the LA18 and LA19 ground motions. Because all three ground motion records have approximately the same pseudo acceleration coefficient at a period of 0.5 sec (2 Hz), all three records should show equivalent sliding response.

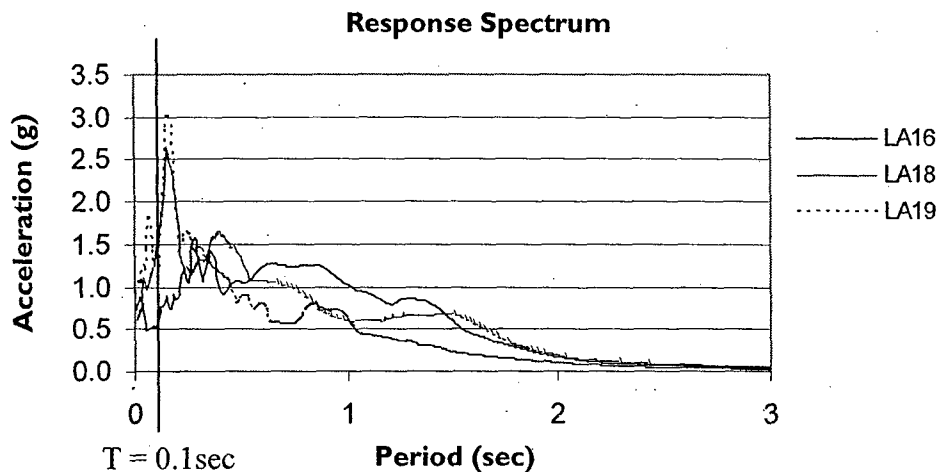


Figure 5.21 - Acceleration Response Spectra

Of interest to note is that the rocking period, as predicted by the Housner is approximately 0.28 seconds (3.5 Hz). This period was not observed as a rocking period in the pulse tests and thus is provided here only for information.

5.2.1 Ground Motion Experimentation Test Results

Comparisons between the simulated and measured barrel sliding is given for the LA16, LA18, and LA19 records in Figures 5.22-5.24, respectively. In all cases the simulations contained approximately the same waveforms as the measured response and captured the peak relative displacement to within 30%. Furthermore, consistent with the forward-back

type pulse ground motion experiments, the model was not able to capture the permanent offset after termination of significant ground shaking. However, the ability to estimate the magnitude of permanent sliding was markedly improved for the earthquake ground motions relative to the forward-back pulse type ground motions.

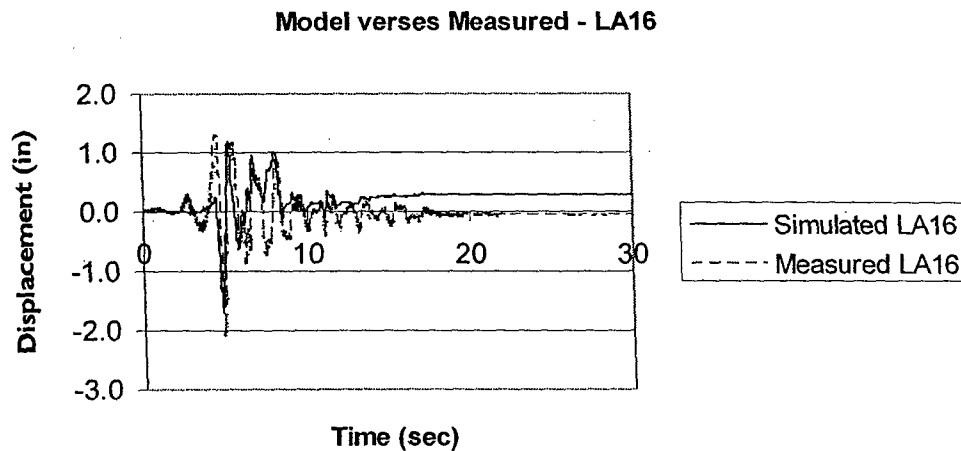


Figure 5.22 - Simulated verses Measured Barrel Sliding Response for the LA16 Ground Motion

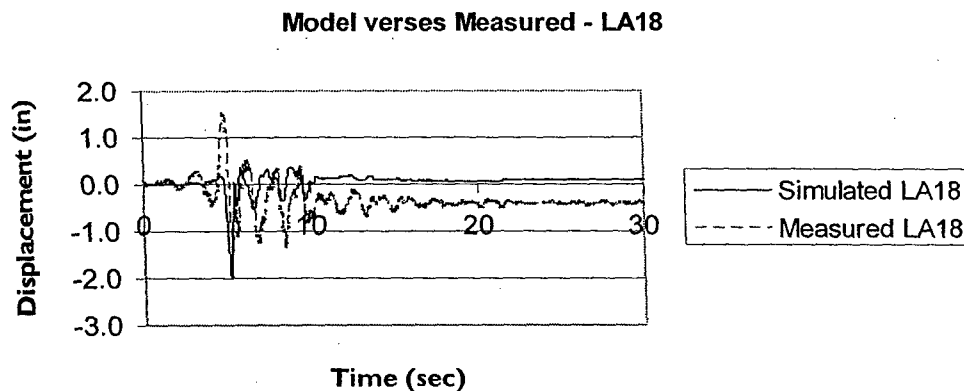


Figure 5.23 - Simulated verses Measured Barrel Sliding Response for the LA18 Ground Motion

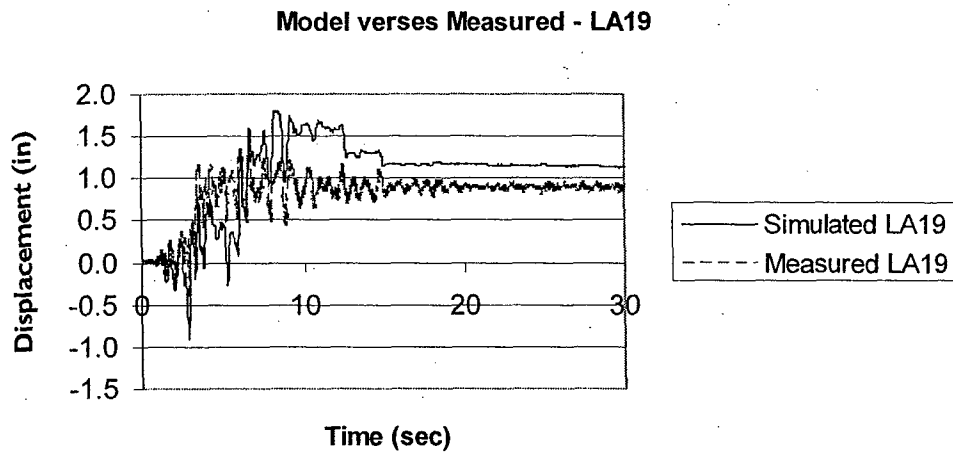


Figure 5.24 - Simulated verses Measured Barrel Sliding Response for the LA19 Ground Motion

It is of interest to note that the largest permanent sliding, both measured and simulated, occurred from response of the LA19 ground motion record. However, the maximum sliding displacements of the three ground motions records range between approximately 1.7 in to 2.1 in. This is consistent with expected results.

From visual and recorded evidence, rocking did occur in both the LA18 and LA19 ground motion records but not from experimentation of the LA16 record. This is again consistent with the expected response. The pseudo acceleration for the LA18 and LA19 ground motion records at the rocking period of 10 Hz is substantially higher than the pseudo acceleration of the LA16 record at 10 Hz. Rocking was not predicted from simulated response of any of the three input ground motions.

5.2.2 Discussion of Ground Motion Experimentation

From the three earthquake simulation tests and test data a few preliminary observations can be made.

- Each set of test data resulted in different combination sliding/rocking responses as expected.

- All ground motion records show significant, but similar, relative sliding. This is consistent with the large barrel sliding type motion found at the sliding period of approximately 2 Hz.
- The LA19 ground motion record is the only record that shows the permanent offset.
- Rocking data indicates significantly more rocking in both the LA18 and LA19 records where rocking was not observed in the LA16 data. This is consistent with the high pseudo acceleration response of the LA18 and LA19 records relative to the LA16 ground motion record.
- The data indicates there are key frequencies, namely a rocking frequency and a sliding frequency, which govern these response mechanisms.
- Overall, the simulated and tested response of the barrels due to the measured input motion was in fair agreement.
- The nonlinear analysis model failed to capture the rocking behavior observed visually, during the experiments, as well as in the data.

7.0 References

- Aslam, M., Godden W. G., Scalise T. D., (1980) "Earthquake Rocking Response of Rigid Bodies", *ASCE Journal of the Structural Division*, V. 106, February, pg. 377-392.
- Chadwell, C. B., G. L. Fenves, S. A. Mahin, (2002) "Cable Stayed Bridge Behavior Under Earthquake Excitation – A Case Study", Earthquake Engineering Research Institute, Proceedings of the 7th National Conference on Earthquake Engineering, Boston, Mass, July 2002.
- Chopra A.K, (2000) "Dynamics of Structures: Theory and Applications to Earthquake Engineering (2nd Ed.)." Prentice Hall: Englewood Cliffs New, NJ, 2000.
- EERI, (2004) "Preliminary Observations on the December 22, 2003, San Simeon Earthquake ", *Earthquake Engineering Research Institute Newsletter*, March 2004, Volume 38, Number 3.
- Housner G.W, (1963) "The Behavior of Inverted Pendulum Structures During Earthquakes" *Bulletine of the Seismological Society of America* 1963; 53(2) pg 404– 417.
- Makris, N., C.J. Black, (2001) "Rocking Response of Equipment Anchored to a Base Foundation". PEER 2001/14, Pacific Earthquake Engineering Research Center, University of California, Berkeley.
- Marrow, J.M., (2000) "2000 M5.2 Yountville/Napa Earthquake Implications for the California Wine Industry", Simpson Gumpertz & Heger, Inc., San Fransisco, CA, <http://www.vingenuity.net/pdf/2000-yountville-quake.pdf>.
- Marrow, J.M., N. Makris (2000) "Experimental Studies on the Earthquake Performance of Wine Barrel Stacks", Earthquake Engineering Research Institute, Proceedings of the 7th National Conference on Earthquake Engineering, Boston, Mass, July 2002.
- Marrow, J.M., (2002) "The Seismic Vulnerability of the California Wine Industry – An Experimental Assessment", 2002 Structural Engineer's Association of California Annual Convention, Santa Barbara, California.
- PEER, (2003) Pacific Earthquake Engineering Research Center, "Open System for Earthquake Engineering Simulation (Opensees)", <http://opensees.berkeley.edu>.
- Psycharis, I. N., Jennings P. C., (1983) "Rocking of Slender Rigid Bodies Allowed to Uplift", *Earthquake Engineering and Structural Dynamics*, V. 11, Pg. 57-76.
- Topco Inc, (2005) "Wine Barrel Rack Specifications", www.topcoproducts.com, 974 Griffin St. Grover Beach, Ca 93433.
- Wine Institute, (2001) "Commercial Wineries", http://www.wineinstitute.org/communications/statistics/commercial_bondedwinery.htm.

Wine Institute, (2003) "2002 California Wine Sales", <http://www.wineinstitute.org/communications/statistics/Sales>.

Wine Institute, (2005), "Industry Back ground and Statistics, <http://www.wineinstitute.org>, 425 Market Street, San Francisco, Ca, April 5, 2005.

Winkler, T., Meguro K., Yamazaki F., (1995) "Response of Rigid Body Assemblies to Dynamic Excitation", Earthquake Engineering and Structural Dynamics, V. 24, Pg. 1389-1408.

**Hydrogen and Residual Stress Effects on the
Performance of NiTi Shape Memory Alloys**

Project Investigators:

Katherine C. Chen
Associate Professor
Materials Engineering, Cal Poly

Eric Kasper
Professor
Civil Engineering, Cal Poly

Garrett Hall
Assistant Professor
Civil Engineering, Cal Poly

Hydrogen and Residual Stress Effects on the Performance of NiTi Shape Memory Alloys

Katherine C. Chen
Final Report, July 2005

The current C3RP project has successfully brought together various Cal Poly faculty and students with Nitinol Devices and Components (NDC) in a strong research collaboration. One full time graduate student in the Materials Engineering department (A. Runciman) is working on her masters thesis on part of the project. She has gone up to the company a few times to prepare samples for later analysis at Cal Poly; and our main NDC contact (A. Pelton) has come down to Cal Poly to conduct some characterization tests in our laboratories. A group of students from the MatE department and Society of Women Engineers (SWE) toured the company in Fremont in the Fall of 2004. In addition, NDC has become more involved with Cal Poly by sponsoring a table at the 2005 SWE Evening with Industry for the first time. This summer, NDC hired 3 Cal Poly Materials Engineering students.

Research project findings have already been written up or presented (abstracts found at end of report). K. Chen presented some of the results at the TMS Annual Meeting in February 2005 in the talk, "Hydrogen Effects on the Phase Stability of NiTi." In May, A. Pelton from NDC presented our collaborative work entitled, "Hydrogen in TiNi: Structural and Diffusional Effect" at the Solid-Solid Phase Transformations in Inorganic Materials 2005 Meeting in Phoenix, AZ. E. Kasper and G. Hall (CE department) visited NDC to discuss some collaborative work with the modeling group at NDC. They ended up writing up a paper on "Numerical Techniques for Modeling Stent Expansion," which is currently under review at the Journal of Biomechanical Engineering.

A new MatE laboratory activity is also being developed for color changes that occur during heat treatment of NiTi. The project objectives met (and some that are continuing) are listed in Table I.

Table I. Objectives of NiTi research proposal met

- examine changes in the NiTi structure due to varying amounts of hydrogen
- correlate structural changes with effects on the transition temperatures
- model NiTi behavior for predictive capabilities of performance
- provide student research projects and learning experiences
- set up capability to perform high-temperature experiments
- isolate and characterize hydrides in the NiTi microstructure (continuing work)
- propose mechanisms in order to optimize processing procedures (continuing work)

Experimental Results

An alternate method for introducing hydrogen into the NiTi samples was developed and optimized to gain more control and reproducibility. Several samples with different amounts of hydrogen were produced at NDC. Refinements to our x-ray diffraction (XRD) characterization techniques were also made. The installment of the high-temperature XRD sample chamber is underway, and will enhance our studies.

Structural changes were indeed observed as the hydrogen content increased. Figure 1 displays the lattice expansion of the B2 NiTi phase. The plateau in the lattice constant at high levels of hydrogen suggests that the solubility limit has been reached and a new phase has formed (most likely a distinct hydride phase). The scatter in the data (within the two lines at low hydrogen content) suggests nontrivial explanations and is being studied in greater detail.

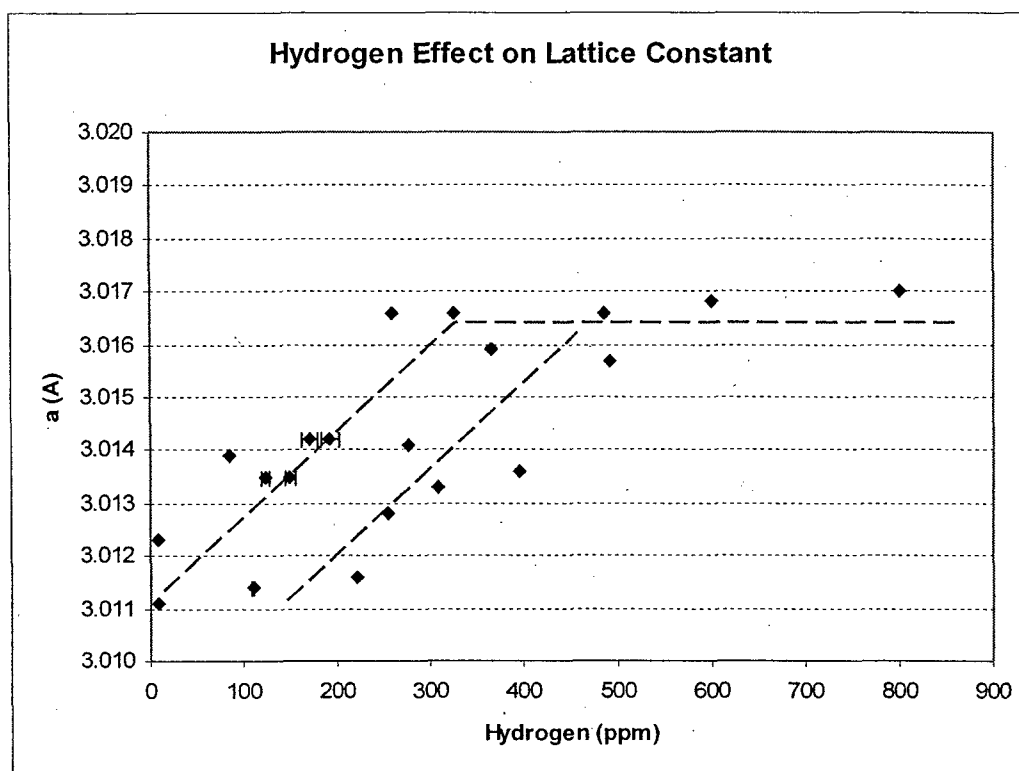


Figure 1. Lattice constant of the B2 NiTi phase as a function of hydrogen shows lattice expansion, which is consistent with theory.

The distinct and new phase was captured with the high-hydrogen content samples with XRD. Figure 2 shows clear peaks due to an apparent hydride phase. Several different crystalline models were tested against the experimental data, and identification of the hydride phase has yet to be determined with certainty. However, previous studies in the literature were also not found to be consistent with our XRD results, thus leading to more intriguing questions about the structure of NiTi-H phases. Scanning Electron Microscopy (SEM) and Differential Scanning Calorimetry (DSC) are being utilized to help characterize the material.

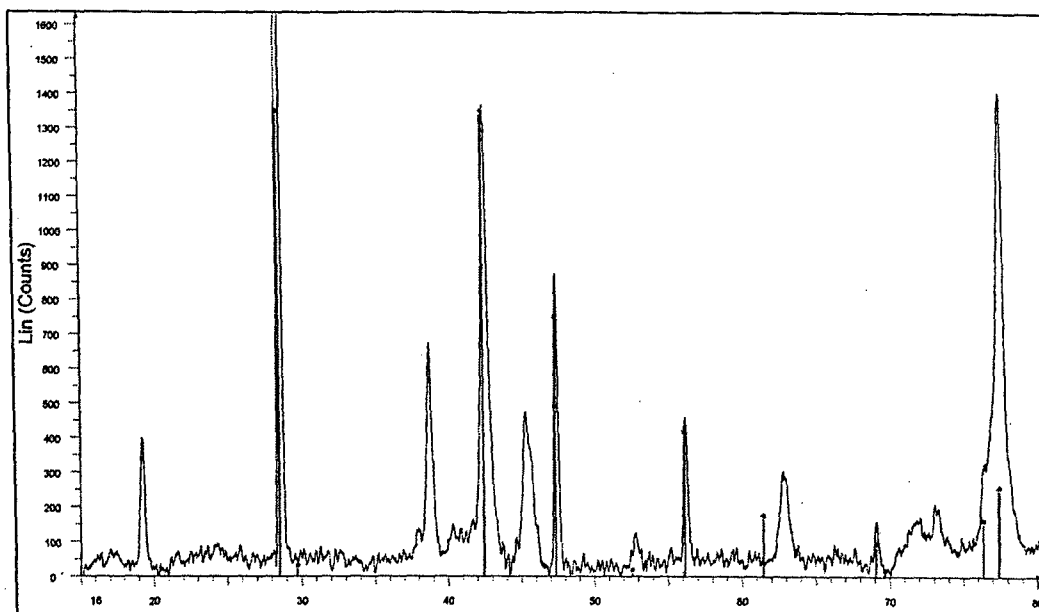


Figure 2. XRD scan of NiTi with 800 wppm H. Peaks in red designate the Si standard, while blue designates B2. The remaining peaks belong to the new, hydride phase.

Abstracts of Presentations and Publications of Results

Hydrogen Effects on the Phase Stability of NiTi – K. Chen, A. Runciman, C. Trepanier, A. Pelton: Presentation at TMS Annual Meeting in San Francisco, CA

Shape memory and superelastic NiTi are finding its way into several commercial products (e.g., endovascular stents, cell phone antennae wire, orthodontic arch wire), as well as potential new applications (such as morphing wings). The A_f (austenite transformation finish) temperature is usually the key property to control, and is very sensitive to processing conditions. During cleaning, etching, or heat treatments, hydrogen can be inadvertently introduced into the NiTi and affect the phase stability and properties. Samples of various amounts of hydrogen in NiTi have been prepared and studied by x-ray diffraction (XRD). With only roughly 80 wppm of H in austenitic NiTi, new XRD peaks appear. Structural effects of hydrogen in martensitic NiTi are also investigated. Hydrogen-induced lattice strains and the appearance of new hydride phases are discussed and correlated against previous diffusion studies.

Hydrogen in TiNi: Structural and Diffusional Effect – A. Pelton, C. Trepanier, X. Gong, A. Runciman, K. Chen: Poster presentation at Solid-Solid Phase Transformations in Inorganic Materials 2005 Meeting in Phoenix, AZ

Austenitic (B2) and martensitic (B19') TiNi samples were charged with hydrogen and analyzed with x-ray diffraction and differential scanning calorimetry. XRD indicates a hydrogen solubility limit on the order of 100 wppm with subsequent formation of a hydride phase. The structure of the hydride is consistent with a tetragonal unit cell with $a = b = 6.36 \text{ \AA}$ and $c = 9.32 \text{ \AA}$, which is based on a $2 \times 2 \times 3$ B2 cell. This paper also discusses hydrogen diffusion through

heat treatments at 400-800°C for 30-3000 seconds. Extensive experimental and analytical computations show that the effective activation energy of hydrogen diffusion under these conditions is approximately 125 kJ/mol for 800 wppm hydrogen and 47.8 kJ/mol for 120 wppm hydrogen.

Numerical Techniques for Modeling Stent Expansion – G. Hall and E. Kasper: Paper submitted to Journal of Biomechanical Engineering

Numerical analysis has become a standard, and in fact required, component of the process in which new biomedical stent devices are designed and approved. Despite this, very little work has been performed comparing the efficiency of various numerical techniques currently available to the analyst. The present paper begins this study by comparing the computational efficiency and results achieved using various methodologies and element technologies in the context of stent deployment simulations. The findings indicate that the methodologies most commonly adopted in the present literature/industrial practice are less than optimal.

Meso-Scale Composites via Solid Freeform Fabrication

Project Investigators:

Robert Crockett
Assistant Professor
Industrial & Manufacturing Engineering Department

David Niebuhr
Assistant Professor
Materials Engineering Department

Meso-Scale Composites via Solid Freeform Fabrication

Robert Crockett, PI
David Niebuhr, Co-Investigator

Project Objectives

The objective of this project was to develop cost effective, advanced manufacturing techniques for creating materials and composites with meso-scale structures (features from 0.1mm – 1mm) through the use of highly complex expendable molds produced using Solid Freeform Fabrication technology. A material system compatible with 3D Printing was developed, in which the waste powder can be removed from the expendable mold by a solvent, and the mold itself can be removed from the final cast object using a second solvent. This “two solvent system” is required in order to produce highly complex, meso-scale composites with geometries which would be impossible to mold or cast by traditional methods. Secondary, yet critical, criteria were that the material system developed be low cost, low-toxicity, and potentially reusable/recyclable, as an expendable mold must be created for each object produced. An additional objective which was not part of the original proposal but which has become a key feature of the resulting system is that the materials and processes be biocompatible for application of project results in the field of biomedical engineering (implants, tissue engineering, etc.).

Major Findings and Results

- Developed low-cost, biocompatible material system (powder/binder/solvents) compatible with 3D Printing (thermal, piezoelectric, and microspray inkjet) and “two solvent” approach to producing complex expendable molds.
- Developed process for producing complex expendable molds with meso-scale features. Demonstrated proof of concept on commercial 3D Printer.
- Evaluated potential near-term applications of complex, meso-scale composites, with a particular focus on biomedical engineering.
- Developed a universal inkjet/powderbed testbed system for continued development of materials and processes.

Results Overview

Three tasks were established to meet the stated objectives of the proposal: *materials development* (Task 1), *process development* (Task 2), and evaluation of near-term *commercial applications* for the resulting materials and processes (Task 3). A key objective of the project was to make the process compatible with existing Solid Freeform Fabrication equipment produced by Z-Corporation (the *Three-Dimensional Printing* process). This objective turned out to be the most challenging component of the project, due to the type of inkjet technology used in the commercial system and the lack of user flexibility in the commercial Z-Corporation control software (see detailed explanation under Task 2). The challenges involved with making the system compatible with existing equipment prompted a mid-project course correction based upon the results at that time: 1) Task 3 and the detailed process characterization from Task 2 would be reduced in scope, 2) the material system would be developed specifically to be biocompatible, and 3) project resources would be used to develop a "universal inkjet testbed", a significantly more flexible system that would allow a wider range of materials to be inkjet along with greater control of process parameters. While this is a slightly different direction from the original stated project objectives, we feel that results are worth the deviation, and have produced a valuable foundation for a wider scope of applications than originally envisioned.

Task 1: Two-Solvent Material System

Develop a material system compatible with the Z-Corporation 3D Printer that allows for two-step solvent removal of expendable molds. A primary solvent is used to remove unbound powder from the mold after building on the machine. The binder protects powder during this step. A second solvent then removes bound powder after casting a polymer into the mold, thus dissolving the mold from around cast object.

Results

- Evaluated multiple material system candidates for binders/carrier solvents compatible with inkjet deposition and the "two solvent" strategy (e.g. must be water proof, but alcohol soluble), including alkali-water soluble binders originally developed for the printing industry, PVA, water-based latex / acrylic paints, and reversible varnishes used for art restoration.
- Selected a system of *powdered milk* for the powder and *isopropyl alcohol-diluted shellac* for the binder – powdered milk is highly water soluble, with low solubility in alcohol, while shellac is water resistant, yet highly soluble in alcohol.
- This system is both biocompatible (in fact, edible!) and low cost.
- Evaluated and modified this system with respect to constraints of the existing 3D Printing system. Key challenges included: 1) adapting the alcohol-based binder system for use in a thermal inkjet (which is designed for aqueous solutions), 2) controlling the rapid evaporation of solvent during the inkjet process to avoid clogging the nozzles, and 3) supplying sufficient shellac to the surface of the powder bed in a solution dilute enough to be printed (e.g. may require multiple printing passes).

Discussion

Components of any candidate material system include a water-soluble powder, a mild-solvent based binder, additives to reduce inkjet nozzle clogging, and a secondary liquid capable of solvating the binder after the final object has been cast. This task was by nature highly linked to Task 2 (process development), and thus was performed iteratively. Early studies and observations indicated some groundrules for material system development:

- 1) In order to make the process time efficient, the binder must be in a carrier solvent that rapidly evaporates. This is especially true if multiple inkjet passes on a single layer are required to deliver a sufficient quantity of binder to the powder. This pointed toward a volatile solvent as the carrier for the binder.
- 2) The powder must be relatively insoluble in the binder solvent, to avoid powder clumping, bleed, etc.
- 3) The two-step solvent process requires that a mild solvent be used for dissolving the unbound powder, with a more chemically active solvent to remove the binder.
- 4) Dissolving unbound powder requires a large quantity of solvent, so the primary solvent should be inexpensive and non-toxic.

These groundrules resulted a research roadmap whereby water would be the first solvent, with a challenge to use as mild and non-toxic a material as possible for the second solvent.

Powder. Evaluation was based on solubility in water and various potential binder solvents (alcohols), bleed, caking, and spreadability (function of particle shape/density/etc). Particle size was not optimized; all particles were sized using a 100 mesh screen, resulting in nominally the same size distribution as the commercial Z-Corporation starch or plaster systems. Other considerations were cost, availability, and toxicity. Powdered milk, table sugar, salt, and cornstarch were evaluated. Powdered milk had best combination of high solubility in water, low solubility in alcohol (a potential binder solvent), and spreadability. While early tests indicated that 100% powdered milk was acceptable, later integrated tests in Task 2 resulted in binder bleed (spreading of binder beyond desired pattern) and clumping of powder. While this system was not optimized, adding ~25-50% cornstarch to the powdered milk appears to stop the binder bleed and clumping without adversely affecting other system properties.

Binder/Carrier Solvent. Both emulsions and solutions were evaluated. The most challenging criteria was that the binder solution be compatible with inkjetting, which requires low viscosity, low solids content, small or no particles, and low "stickiness". Functionally, the binder must hold the powder together in the desired shape, protect the powder from water, and then be "reversible" to dissolve in a second solvent. Cost, availability, and toxicity were again key considerations. Binder formulations were tested using an airbrush, spraying onto templates placed over layers of powder to create simple cross-hatched structures (Figure 1). Multiple layers with layer thickness ranging from ~250 μ m to 1mm were evaluated to determine inter-layer bonding. Strength of the resulting objects was evaluated empirically. Iterative evaluation with solvent formulations and the processing requirements of Task 2 ultimately focused in on



Figure 1. Left: Powderbed testbed. Tray is manually lowered to spread additional layers of powder. Right: Template used with airbrush to deliver binder solutions to powder surface in simple 3D cross-hatch structure.

archival lacquers: “reversible” systems for restoration of paintings. Of this family, shellac appeared to be the most promising. Further tests indicated that, while it was not the strongest at any individual criteria, it was the best candidate from a system perspective. Various saturation levels on the powder surface, and multiple passes of binder spray with moderate drying times between passes were evaluated to achieve a suitable combination of strength of finished part and ability of binder to protect powder in water, yet dissolve in the second solvent. Table 1 is a summary of binder candidates and performance against key criteria. Note that dissolving in a mild solvent was the key challenge. Note also that while shellac was not a top performer in any criteria, it was the only system that achieved all goals.

Second Solvent. Solvents including alcohols (isopropyl, ethanol), various paint thinners (mineral spirits, Citrisolve), and acetone were evaluated. Early on in the project it was recognized that the large volumes of solvent required to dissolve a part favored low-cost and low-toxicity solvents. This turned out to be a key decision, as it allowed for development of a material system that could potentially be used in applications requiring a biocompatible end product. Solvents used for the archival lacquers described in the previous paragraph are extremely mild, and the same solvent can be used as both the binder carrier during inkjetting and as the means to resolute the binder to remove the expendable mold. Isopropyl and ethyl alcohols were the selected solvents. Isopropyl alcohol was selected as the carrier solvent for the binder, as its lower volatility was helpful in reducing inkjet nozzle clogging.

Table 1. Evaluation of binder candidates (+ good, 0 OK, - poor, X unacceptable)

Binder Candidate	Inkjet Compatibility	“Greenbody” Strength	Water Resistance	Dissolve in Mild Solvent
PVA-Based Adhesives	X	+	-	-
Cyanoacrylate (Superglue)	X	+	-	X
Acrylic (Solvent-Based Paint Formulations)	+	0	+	X
Water-Based Acrylic Adhesives	0	+	+	X
Acrylic (Latex Emulsion Paint Formulations)	+	0	+	X
Polyurethane (Water-Based Emulsion for Floor Sealing)	-	0	+	X
Shellac	0	0	0	-

Task 2: Process Development & Characterization

Develop the end-to-end process using the above material system. The resulting process steps of this system are:

- 1. Design bulk object comprised of optimized, meso-scale structures on CAD system, create inverse of resulting CAD model.*
- 2. Print the inverse of the desired structure on a 3D Printing machine using powdered milk as the matrix powder, bound with a diluted shellac/propylene glycol mixture to create an expendable mold.*
- 3. Place the resulting mold in an ultrasonic water bath to remove all unbound (waste) powder from around meso-scale features.*
- 4. Cast a polymer material into the mold.*
- 5. Place the entire system in ethyl or isopropyl alcohol to dissolve the shellac binder and powder, thus removing the mold from around the cast object.*
- 6. Cast a second material into the voids of the resulting part to complete the meso-scale composite.*

Results

- Built a manual 3D Printing system which allowed for controlled thickness layers of powder, with a template placed on top and desired amounts of binder introduced onto the surface via an airbrush.
- As a result of the airbrush trials, determined that the system is quite robust: parts could be constructed using very dilute binder systems, and the results were structurally sound, supported mm-scale detail, and performed satisfactorily in the two-step solvent removal process.
- Produced multiple shellac patterns of a simple, regular lattice structure with 2mm features. Used this part as an expendable pattern to produce a plastic (polyurethane) part.
- Modified the material system to make it compatible with inkjet printing: added nominally 7.5% propylene glycol to reduce evaporation during inkjetting.
- Using the modified material system, small parts could be produced on the 3D Printing machine using single printing passes per layer which resulted in structurally sound objects.
- There is still an unresolved problem with inkjet nozzle clogging – we were only able to build small parts, and results are currently not very reproducible. Although we are trying to make this system compatible with existing 3D Printing systems, a piezoelectric inkjet head or ultrasonic nozzle would be more appropriate for binder deposition.
- “Bleed” of binder after printing is noted. Powder system is currently being optimized to minimize this and increase achievable part resolution (e.g. mixture of starch and powdered milk)

Discussion

The commercial process of *3-D Printing* (Figure 2) is particularly well suited for creating expendable molds with meso-scale features. The process involves spreading a thin layer of powder (starch or plaster), inkjetting a water-based binder onto the surface of the powder in the appropriate 2D pattern, lowering the powder tray, spreading more powder on the surface, and repeating the process to build up an object with the desired geometry. This technique is attractive because it is compatible with virtually any powdered material, and the powder supports overhanging features during the layerwise fabrication process enabling complex, small-scale structures to be produced. The key challenge in developing a material system compatible with commercial equipment (Z-Corporation ZPrinter 310 model) is the type of inkjet technology employed. The ZPrinter uses standard commercial thermal inkjet cartridges (HP10). The thermal inkjet process involves rapidly heating liquid in the nozzle, which expels a droplet as the liquid vaporizes. This system is optimized for water-based solutions. Suspensions of particles, emulsions, or non-aqueous solvents are extremely difficult to inkjet using a thermal process because of firing dynamics and nozzle clogging as solvent vaporizes upon ejection from the nozzles.

An additional but unexpected issue was the lack of user control in the commercial ZPrinter software. Head speed, liquid saturation, multiple passes of the same pattern, and pause time between layers for solvent drying were all critical parameters for this study, yet could not be controlled; these parameters are fixed for ease of use in the highly optimized standard commercial process. While we were partially successful in overcoming these challenges, the difficulties prompted us to stop at the point of a proof-of-principle demonstration with the commercial Z-Corporation equipment. The material system developed in this effort could be optimized for the ZPrinter, but it would likely require company collaboration and more extensive modification of the hardware and software. Instead, we devoted remaining project resources toward development of a custom inkjet testbed that was better suited for early development of materials and processes (see "Hardware" section).

As an iterative part of the material system development, the shellac binder/airbrush delivery system described in Task 1 was optimized. A 100% commercial shellac solution could be successfully airbrushed at moderate air pressure (30 psi), and was near the upper end of the viscosity limit for the airbrush/nozzle combination used in this study. A slow single pass of the airbrush over the powder surface delivered enough shellac to produce weak, but bound, objects.

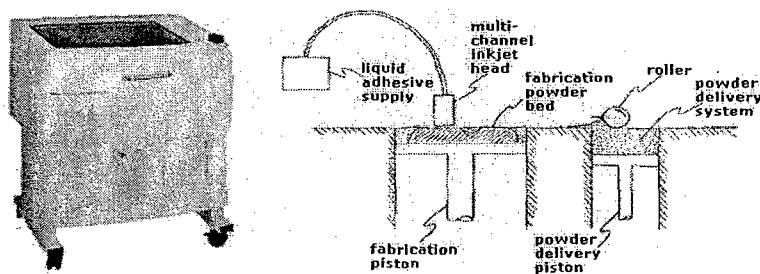


Figure 2. Left: Z-Corporation 3D Printer. Right: 3D Printing Schematic.

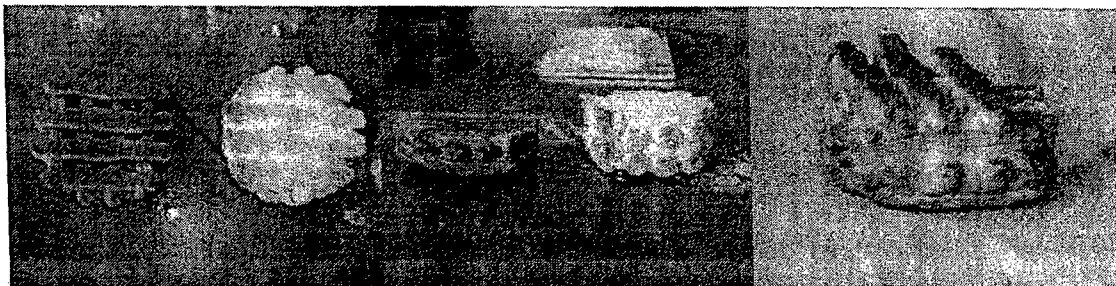


Figure 3. Sample parts produced using airbrush and powder testbed. Left, Center: Samples as they came off the testbed (to right of photos), and after dissolving unbound powder in water. Right: Sample removed from water partway through the dissolving process. Width of bars are 2 mm.

4 passes with ~2 minute dry time between layers produced extremely durable parts. Studies involving dilution of the shellac confirmed that the strength of the final part is a function of the total shellac delivered to the powder surface, regardless of whether it was delivered all at one time or as a series of individual, lower volume passes (e.g. a shellac solution diluted to 25 volume % with isopropyl alcohol, delivered to the surface in 4 passes produced the same results as a single pass of a 100% shellac solution).

Parts were depowdered by submerging in an ultrasonic water bath for 20-30 minutes followed by 1 hour of drying in air at room temperature. This process was repeated 3-4 times until all unbound powder was removed (Figure 3). The process repetition with periodic drying was required to avoid part slumping, which occurs if the part is submerged for an extended period of time. Periodic drying allows the protective shellac, and the interior powder, to regain its initial strength.

The end-to-end process was demonstrated by printing a part representing the inverse of the desired shape (i.e. printing a mold), depowdering as described above, then placing the mold in a tube and casting polyurethane. Once the polyurethane had cured, the polyurethane/mold assembly was submerged in an ultrasonic bath containing isopropyl alcohol. 20-30 minutes of soaking removed the bulk of the mold, resulting in the final plastic part (Figure 4).

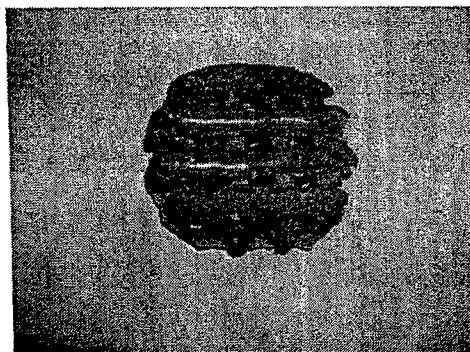


Figure 4. End-to-end process demonstration. Polyurethane object cast into expendable shellac/powder mold and processed using two-step solvent removal system. Width of bars are 2 mm.

Table 2. Optimization of binder solutions for inkjet compatibility

% Isopropyl	% Shellac	% Propylene Glycol	Clog? (Y/N)
95%	5%	0	N
90%	10%	0	Y
90%	5%	5%	N
85%	10%	5%	N
80%	15%	5%	Y
77.5%	15%	7.5%	N
72.5%	20%	7.5%	N

Optimizing the system for compatibility with the thermal inkjet used in the Z-Corporation ZPrinter 310 system proved to be a significant challenge. Inkjet nozzle clogging was reduced, but not fully eliminated, by using a diluted shellac solution and adding a small volume percentage of propylene glycol as a humectant (Table 2 details the optimization process). A mixture of 20% Shellac in 72.5% isopropyl alcohol with the addition of 7.5% propylene glycol provided a formula that was robust (non clogging), yet provided a high enough shellac content to deliver a sufficient amount to the powder surface for binding. This 72.5%, 20%, 7.5% mixture was used for the rest of the time with the HP print head in the ZPrinter 310 machine.

Figure 5 illustrates the results using the above binder formulation to create objects on the ZPrinter 310. Single layer test strips held together quite well, using the "full saturation" setting on the software. While the actual amount of binder delivered to the surface using this setting was not quantified, it appeared visually equivalent to the amount delivered via the airbrush with a similar solution. Multiple passes of the same pattern on a single layer were not possible under the ZPrinter software, which was a major limitation. Additionally, the powdered milk was not dense enough to be spread evenly by the machine's automated roller; when the machine would roll a new layer of powder it would catch on the build area and ruin the previous layer. A mixture of 50% powdered milk and 50% starch solved this problem, and was used for the duration of the experiments.

A significant issue was hanging drops of binder that were consistently observed to be present during machine operation, likely due to the low surface tension of the binder carrier solvent relative to the aqueous solution normally used in ink formulations. This created two problems: 1) the drop would catch the surface of the powder, pulling powder up to the head and clogging the nozzle, and 2) the drop likely contributed to the early failure of the inkjet printhead. Printheads burned out after ~20-30 layers, likely because of the use of alcohol as the operating



Figure 5. Sample parts produced using ZPrinter 310 commercial system. Left: Single layer. Center: part after building, with unbound powder. Right: after dissolving unbound powder. Width of bars are 2mm.

solvent. Using a material system with a non-aqueous carrier solvent and a high solids loading will require a piezoelectric inkjet system (whereby liquid is mechanically forced out of the nozzle by a compressive wave), an ultrasonic nozzle, or a microspray system (described in Hardware section).

As part of this effort, CAD solid models were created to explore mold development issues and illustrate the complex geometry possible via these techniques. Figure 6 shows one example design. Note that the part produced on the machine is the inverse of the final desired shape, as it serves as the mold.

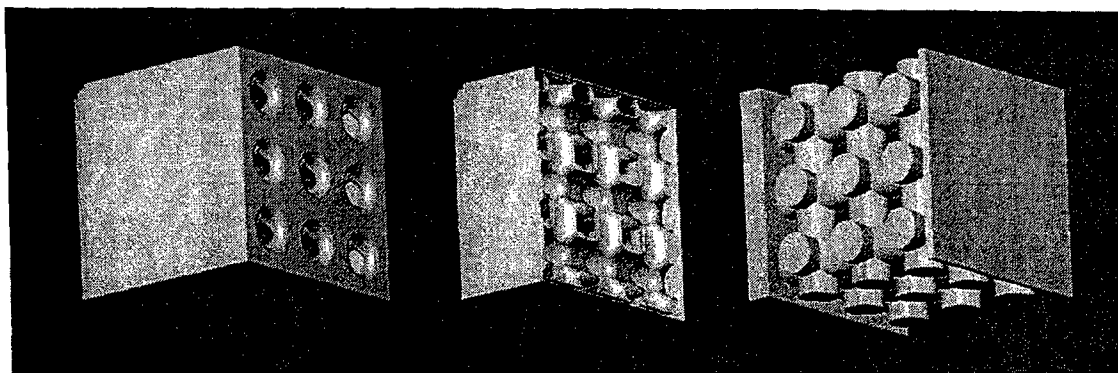


Figure 6. CAD files developed to evaluate capability of the system to create complex parts. Left: CAD model for expendable mold. Center: Cross-section of mold. Right: Shape of resulting object (cast into the expendable mold).

Task 3: Near-Term Commercial Applications

Find appropriate near-term commercial and military applications.

The feasibility of this project was illustrated in the results section. Organic materials were tested that had varying solubility and simple shapes were created. The next step is to determine practical applications for this technology. Several possible engineering devices may benefit from the ability to control both macro and meso-scale, internal and external geometries to a high degree of accuracy and economically. Promising potential applications include:

Hydrogen Storage

The storage of hydrogen is one of the biggest challenges in developing efficient fuel cells. Hydrogen can be compressed or liquefied, both with it challenges. Chemical bonding is the most promising hydrogen storage technique in terms of safety and cost. Metal and liquid hydrides and adsorbed carbon compounds are the principal methods of bonding hydrogen chemically. They are the safest methods as no hydrogen will be released in the event of an accident, but they are also bulky and heavy.ⁱ

Metal hydrides such as FeTi compounds are used to store hydrogen by bonding it to the surface of the material. To ensure that large volumes of hydrogen can be stored it is essential to use small granules of the base material to make a large surface area available. This method follows traditional powder processing of making sub micron powder. Unfortunately, metal hydrides can store only 2-4% of their mass in hydrogen. A newer technology utilizing nanofibers may potentially hold 70% of its mass in hydrogen. The nanofiber array (structure) and geometric development could potentially benefit from our work.ⁱⁱ

Bioactive Filters

Filters utilized to remove pathogens and other airborne contaminants are growing increasingly complex. Efficiency demands as measured by parts per billion and even trillion are not uncommon. Extremely large surface areas in a compact form factor are necessary to achieve this level of filtration. The added challenge is the adaptability of microbes to thrive in filter conditions that may have destroyed them only weeks earlier. Thus, large surface area and complex geometry must be combined to provide a means to flush and inoculate filters. The ability to create large surface areas has been established, but it is unclear on how to combine nano and meso scale into a continuous component. This may be solved using the results of our work as a springboard.

Biomaterials

Bone growth into implants is paramount in developing a mechanically sound joint replacement. The surface area must be carefully controlled to ensure proper growth. For example, nanotubes of titanium oxide have been developed to act as growth sites for hydroxyapatite. The 8 -15 nm feature size has enabled accelerated nucleation and growth of the bonding layer to the titanium implant.ⁱⁱⁱ The small scale has allowed improved growth but the complexity of the structure is limited by the nanotubes inherent shape.

The contact of any biomaterial with blood gives rise to multiple pathophysiologic defensive mechanisms such as activation of the coagulation cascade, platelet adhesion and activation of the complement system and leukocytes.^{iv} This statement illustrates the need for biocompatibility. There are limited materials that are FDA approved for use in the body. Traditional means of forming these materials may not be adequate to produce the shapes required, thus meso scale refinement using several materials normally not co-producible is possible. (For example one can't combine UHMW polyethylene and titanium together into a single casting, forging, etc.)

MEMS Devices

Micro electronic-mechanical systems (MEMS) currently rely on traditional semiconductor fabrication techniques. Silicon though is not the best material for every device as it has low fracture toughness and oxidizes readily at temperatures above 600°C. Considerable research has been conducted in improving range of motion of MEMS devices through a combination of mechanical movement and piezoelectric actuators.^v This again is based on the ability to control the shape and morphology of the materials. Friction also plays a role in performance which can be somewhat controlled by surface roughness and material combinations. It may also be possible to combine materials to create self lubricating composites.

These are only a few examples of the possible applications. Feasibility and implementation would require further study and future work would focus on detailed development of the most promising engineering device. Because the techniques developed in this effort use entirely biocompatible, food-grade materials and are designed to accommodate extremely complex, organic shapes and material / variable density objects, a natural extension of this project would be in biomedical applications. We will continue development of this exploratory work directed toward applications of highly-complex, meso-scale composites in 3 interrelated areas: *bioabsorbable scaffolds for tissue engineering*, creation of *ceramics with variable-density and local property control*, and application of this system in *validation of complex FEA models*.

1) Bioabsorbable Scaffolds for Tissue Engineering

Expendable molds for scaffolds that have predefined 0.1mm-1mm wide internal channels ("macro" features for fluid transfer in a bioreactor) will be created out of powdered milk/shellac binder, manufactured using techniques developed in this project. An aqueous gelatin solution (potentially pre-seeded with cells, depending on the application) will then be cast into the mold. The mold will be dissolved away with an ethanol/water solution and the gelatin scaffold either dried or rehydrated for use in tissue engineering applications.

2) Ceramics and PM with Variable-Density and Local Property Control

Rather than expendable, use techniques developed in this project to create local property control in powder-metallurgy performs or ceramic greenbodies. The goal of this proposed effort is to create mechanically accurate synthetic bone by three-dimensional printing. By adding different amounts of binder containing a combination of colloidal ceramic particles and/or alkoxide compounds onto a powdered ceramic

substrate material, it is possible to selectively add ceramic mass and/or sintering aids (e.g. promote liquid-phase sintering in localized regions) to the resulting ceramic greenbody that will locally alter the properties of the final sintered ceramic. This will enable the creation of post-fired ceramics with areas of higher density, altered mechanical/thermal/electrical properties of the material, etc. This project will develop the materials and manufacturing system to create a variable density ceramic to be used as a knee implant, with regions of low density to promote bone ingrowth, gradually transitioning to fully dense wear surface at the knee contact point.

3) Validation of Complex FEA Models

The manufacturing techniques developed in this project will be applied to the physical validation of highly complex Finite Element Analysis models. FEA of inhomogeneous, anisotropic systems (e.g. bone or complex composites) is a developing field, yet part of the resistance to wider-spread use of these tools is that, because of the complex nature of the materials they are simulating, these models are extremely difficult to validate by controllable, reproducible physical systems. In this project, two-polymer composites, or single-polymer lattices with mesoscale features created by the method developed in previous efforts, will be produced in geometries and with mechanical properties suitable for the validation of inhomogeneous and/or anisotropic FEA models of organic systems such as bone.

Hardware Development

To overcome the limitations of the thermal inkjet and the lack of control flexibility in Z-Corporation commercial software, project resources were used to develop a "universal inkjet testbed" system (Figure 7). A commercial 7-jet microjet spray dot-matrix inkjet (Marsh Unicorn model) is suspended in a stationary position over a 2-axis linear motion table. The powdered system described under Task 1 (Figure 1) is moved underneath the inkjet head in a raster pattern. The entire system is controlled via National Instruments Labview software. A simple graphics program has been implemented in Labview to accept bitmap graphics as the input file, and translate this into both motion control and firing of inkjet nozzles. Binder saturation is controlled by a combination of pressure of the supplied binder solution and speed of the powderedbed beneath the inkjet head.

The microjet spray inkjet, which is designed to print dot-matrix characters onto products on a moving assembly line, has a low inherent resolution, but because the design of the spray nozzles are similar to an airbrush system, this print head allows for a wide range of liquids to be deposited. Seven nozzles are independently controlled to create dot-matrix letters. The commercial control system for this printer has been modified to allow firing control via the Labview system. Initial experiments using the existing printhead control system resulted in parts with nominally 1mm resolution. A near-term activity is to interlace the inkjet nozzle patterns, which should effectively increase the achievable resolution of this system to nominally 100 μ m.

Using this testbed hardware, simple parts have been produced. Because the microjet nozzle is compatible with a wider range of materials, we are currently using a binder solution with increased shellac content: 50% shellac / 45% isopropyl alcohol / 5% propylene glycol at a moderate liquid pressure (28 psi). This system has not been optimized. Preliminary parts produced using five successive inkjet passes and 500 μ m layers hold together, yet are weak and do not fully survive the water depowdering process (Figure 8). We will continue both the hardware development and materials optimization using this system, which can eventually be retrofitted with a piezoelectric inkjet head for increased resolution at a slight reduction of printing robustness.

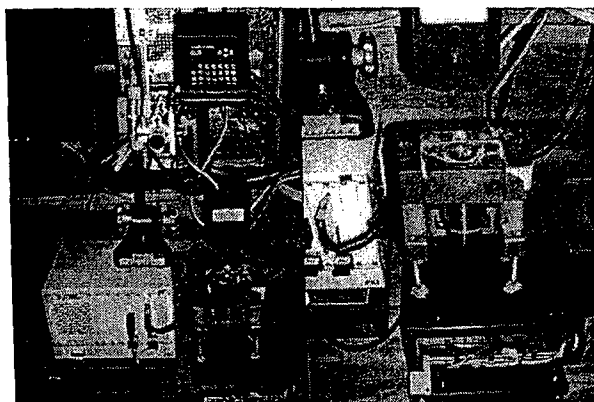


Figure 7. Universal inkjet/powderedbed testbed system.

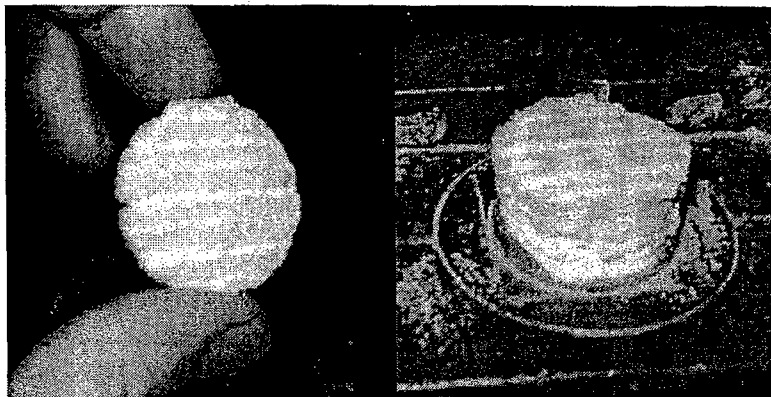


Figure 8. Preliminary results using the newly developed hardware testbed.

Future Efforts and Conclusion

Although the period of performance of this project is over, we do not consider it to be a completed effort. Near term plans are to:

- Increase the resolution of the inkjet testbed and optimize the shellac binder system to support the increased resolution and create durable parts.
- Optimize the techniques for casting of meso-scale features (e.g. pressure, vacuum, low-viscosity casting formulations, etc.)
- Validate the end-to-end creation of polymer objects with meso-scale internal features.

There is also the strong desire to seek follow-on work, as described under Task 3:

- *Bioabsorbable Scaffolds for Tissue Engineering – proposal recently submitted.*
- *Casting Complex Shapes: Human Heart Models – sponsored research project (See Figure 9).*
- *Continued hardware development plus independent work on variable density ceramics/Powder Metallurgy techniques leading to a SBIR proposal with a Los Angeles based startup company.*

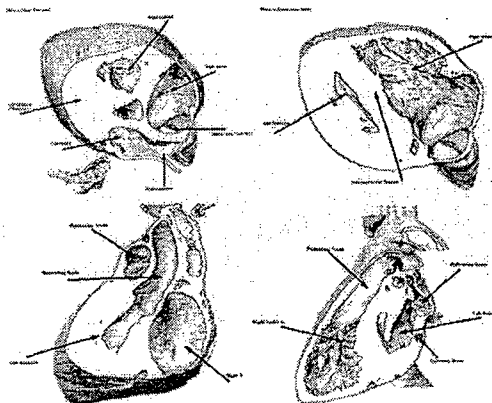


Figure 9. Extremely complex CAD model (human heart) with organic shapes and meso-scale features.

The results of this effort are still quite preliminary, but planned dissemination includes a paper at an upcoming Solid Freeform Fabrication symposium and a key component of a manuscript for a reviewed journal paper on the *engineering and manufacturing of organic shapes*.

While not all of the stated proposal objectives were met, a different direction in the area of biomedical engineering was explored that is extremely promising. The materials and techniques developed in this effort will serve as the foundation for a wider scope of applications than originally envisioned, and we are excited to continue to develop the materials and processes towards applications of complex engineered materials.

TASK 3 REFERENCES

ⁱ <http://www.e-sources.com/hydrogen/storage.html>

ⁱⁱ Chen, X., et al., "Electrochemical hydrogen storage of carbon nanotubes and carbon nanofibers," *International Journal of Hydrogen Energy*, Vol. 29, 2004, pp. 743-748.

ⁱⁱⁱ Seung-Han Oh, et al., "Growth of nano-scale hydroxyapatite using chemically treated titanium oxide nanotubes," *Biomaterials*, Vol 26., January 2005. pp. 4938-4943.

^{iv} Tanzi, M.C., "Bioactive technologies for hemocompatibility," *Expert Review of Medical Devices*. Vol. 2, No. 4, July 2005, pp 473-492.

^v Eniko, T., "Micro-mechanical switch array for meso-scale actuation," *Sensors and Actuators A* Vol. 121, 2005, pp. 282-293.

Development of an HCCI Engine for Combustion Sensing and Control Studies

Project Investigators:

Dr. George J. Delagrammatikas
Assistant Professor
Department of Mechanical Engineering

Dr. Charles Birdsong
Assistant Professor
Department of Mechanical Engineering

Dr. William R. Murray
Associate Professor
Department of Mechanical Engineering

Development of an HCCI Engine for Combustion Sensing and Control Studies

Summary

Homogeneous Charge Compression Ignition (HCCI) is an advanced combustion concept that has the potential to significantly reduce fuel consumption and oxides of nitrogen (NO_x) associated with engine operation. One major challenge that remains is the lack of direct combustion control, which limits an engine's operational regime and promotes excessively high levels of unburned hydrocarbons (HC). Independent and variable intake temperature control has presently been identified as one critical area of research in the engine community. A four-cylinder 1.9L diesel engine was retrofitted with a custom intake manifold system, which included separate runners with integrated air heaters for each cylinder. Since intake air temperature was independently controlled via these non-communicating heaters, cylinder-to-cylinder and cycle-to-cycle variations (CTC's, collectively) were minimized during operation.

Intake charge temperature control proved to be a viable means to affect the quality and operational limits of HCCI combustion. The variations observed between cylinders and cycles support the need for individual cylinder control; a strong correlation between the timing for the onset of HCCI combustion and the intake air temperature was apparent in these initial studies. The temperature to which the intake air must be heated increases with an increase of air/fuel ratio (leaner intake mixtures) and thus, the maximum obtainable IMEP decreases. The coefficient of variation (COV) of indicated mean effective pressure (IMEP) for each cylinder in the stable combustion regime was less than 3% (i.e. nearing production levels). Values of NO_x were obtained at an ultra-low 5 ppm, while HC and carbon monoxide (CO) readings were slightly elevated from a typical baseline engine running in HCCI mode.

The following project was performed under the Office of Naval Research's C3RP program in the Cal Poly Engine Laboratory to address the ongoing challenges of both sensing and controlling combustion quality. This research has led to the successful completion of two graduate theses, one senior project, and an undergraduate research assistantship. Three faculty members in the Mechanical Engineering Department, representing expertise in engine design, advanced controls, and mechatronics, guided these efforts, while one technician was instrumental in the development of the experimental apparatuses. Furthermore, portions of the data acquisition system, the engine control unit, and the dynamometer controller have been integrated within laboratory sections of the internal combustion engine design courses and have been used for additional senior projects. A series of recommendations and future directions are offered at the conclusion of this report.

Introduction

A four-cylinder 1.9L Volkswagen turbocharged direct injection (TDI) engine was converted to operate under HCCI mode. The modifications to the stock configuration included new piston design and fabrication, a redesigned custom intake with integrated heaters and microcontrollers, a port-fuel injection system using 87 octane gasoline, disabling the stock diesel fuel system, the removal of turbomachinery, pressure and temperature sensing instrumentation throughout the experimental test stand, and low- to high-speed data acquisition.

All subsystems were tested individually before a complete system shakedown test was performed. Exploratory experiments and computational analyses were performed concurrently to ensure a thorough understanding of the fundamental operating limits of the engine, CTC

variations, fueling requirements, emissions sensing capabilities, and overall system response to temperature and fuel variations. The engine test stand was designed in a modular fashion such that a variety of additional research goals could be met in the future using the same engine and/or engine family. Potential future projects include gasoline direct injection (GDI), multiple fuel use and fuel switching including diesel and compressed natural gas, blended combustion processes (spark and compression ignition), variable valvetrain actuation, exhaust gas recirculation and heat recovery, and potential application to the Cal Poly Hybrid Vehicle Development Team's Ford Explorer.

HCCI Fundamentals

HCCI is a combustion process that is capable of being both highly efficient and low emitting by combining the auto-ignition characteristics of the compression ignition (CI), or diesel, engine with the premixed air/fuel mixture of the spark ignition (SI), or gasoline, engine. The improvements in thermal efficiencies are produced from the higher compression ratios, while low temperature combustion of locally lean mixtures prevent NO_x emissions from forming.

HCCI can be obtained by either indirect or direct fuel injection. The original intent of this project was to inject gasoline via the stock diesel injectors, though complications arose in locating an appropriate pump system. The decision to design a port fuel injection strategy would have also allowed for potential research collaborations with other institutions.

Because direct injection offers less time for the air/fuel mixture to homogeneously mix, many of the research engines available currently operate with port fuel injection. A small amount of fuel (gasoline as an example) is injected into the cylinder during the intake stroke, and during compression, the fuel and air mixture approaches homogeneity. When the piston reaches the top dead center (TDC) position, the elevated compression ratio promotes simultaneous and uniform combustion throughout the cylinder's combustion chamber, unlike a moving flame front seen in both SI and CI engines. This instantaneous combustion process is commonly modeled using the Constant Volume Ideal Air Standard Cycle, or Otto Cycle, which yields the highest thermal efficiency of any other air standard cycle.

The rapid rates of heat release and pressure rise require that very lean air/fuel mixtures, and thereby power. Loading conditions approaching those of typical gasoline or diesel engine operation would most likely cause structural damage to engine components. Though these power levels are generally low, the efficiencies and NO_x levels produced are still very attractive.

Although the biggest gain in HCCI combustion is the drastically reduced NO_x pollution, there still exist trace amounts of other potentially harmful and federally regulated emissions. Temperatures that were once high enough to form NO_x are now too low to do so, resulting in the freezing reaction of the pollutant to be exhausted on the cylinder's exhaust stroke. Reductions of up to 90-98% are usually seen during HCCI combustion. HCCI has also been reported to produce low smoke and particulate matter (PM) emissions. Though the PM formation mechanism is still not fully understood, one possible explanation is that the absence of fuel-rich regions in the combustion chamber prevents soot formation.

HC and CO emissions, however, are higher than those in a regular diesel engine. One reason for this could be that the low in-cylinder temperatures due to the lean mixtures contribute to decreased post-combustion oxidation rates within the cylinder and increased levels of HC and CO. Mixture preparation is very important in reducing HC emissions because the liquid fuel

deposition on the combustion chamber surfaces results in increased HC emissions. This fuel pooling can also occur in the piston bowl; flat rather than bowl-in-piston designs have been recommended in the open literature to decrease deposition. Furthermore, the higher compression ratios may force greater amounts of HC's into crevice volumes, which prevent combustion from occurring altogether. Upon exhaust, these trapped HC's are expelled from the crevices and/or desorbed from the oil film into the exhaust manifold.

Experimental Apparatus

The following sections address the various subsystems that were developed during the course of this project. Note that preliminary results are provided at the conclusion of this report, which illustrate the research potential of the Cal Poly HCCI engine. For further details on this foundational work, please refer to:

Cheung, Taylor, *Demonstrations of Independent Intake Temperature Control In an Experimental Gasoline HCCI Engine*, Master's Thesis, California Polytechnic State University, San Luis Obispo, CA. 2005

Jacques, Nicholas, *Combustion Stability limits and Cycle-to-Cycle Variations in an Experimental Gasoline HCCI Engine*, Master's Thesis, California Polytechnic State University, San Luis Obispo, CA. 2005

Dietrich, John, *Study of AC Phase Control for Pulse-Width Modulation of HCCI Heaters*, Senior Project, California Polytechnic State University, San Luis Obispo, CA. 2005

Piston Redesign

Higher compression ratios are generally more desirable in an HCCI engine because they contribute to easier autoignition and they require less intake air heating (through internal or external means). The stock diesel engine was received with a nominal 19.5:1 compression ratio, though was measured at 18.4:1 using the following technique. A plastic plate with four cavities of known volume was bolted to the head. Using a graduated burette, colored water was dripped into each cavity through a small through-hole at the 0° position when each piston was moved to its TDC position. The water filled the stock piston bowl and the cavity above the piston (see Figure 1(a)). The cavity volume was then subtracted from the total water volume to find the bowl volume. This procedure was repeated several times for each piston. The plate was then bolted onto the head where the valve crevice volumes were found in a similar fashion (see Figure 1(b)). Finally, compressed gasket volume was approximated to yield total clearance volume for each cylinder. After measuring the stroke and bore (several times and at various locations), the actual compression ratio was determined.

Using this information, the baseline piston (Figure 1(c)) was redesigned to maintain a 16:1 compression ratio (as recommended in the literature), a flat-top piston shape, and the minimum piston topland volume (Figure 1(d)). The fabrication of these pistons was outsourced; the final product is depicted in Figure 1 (e).

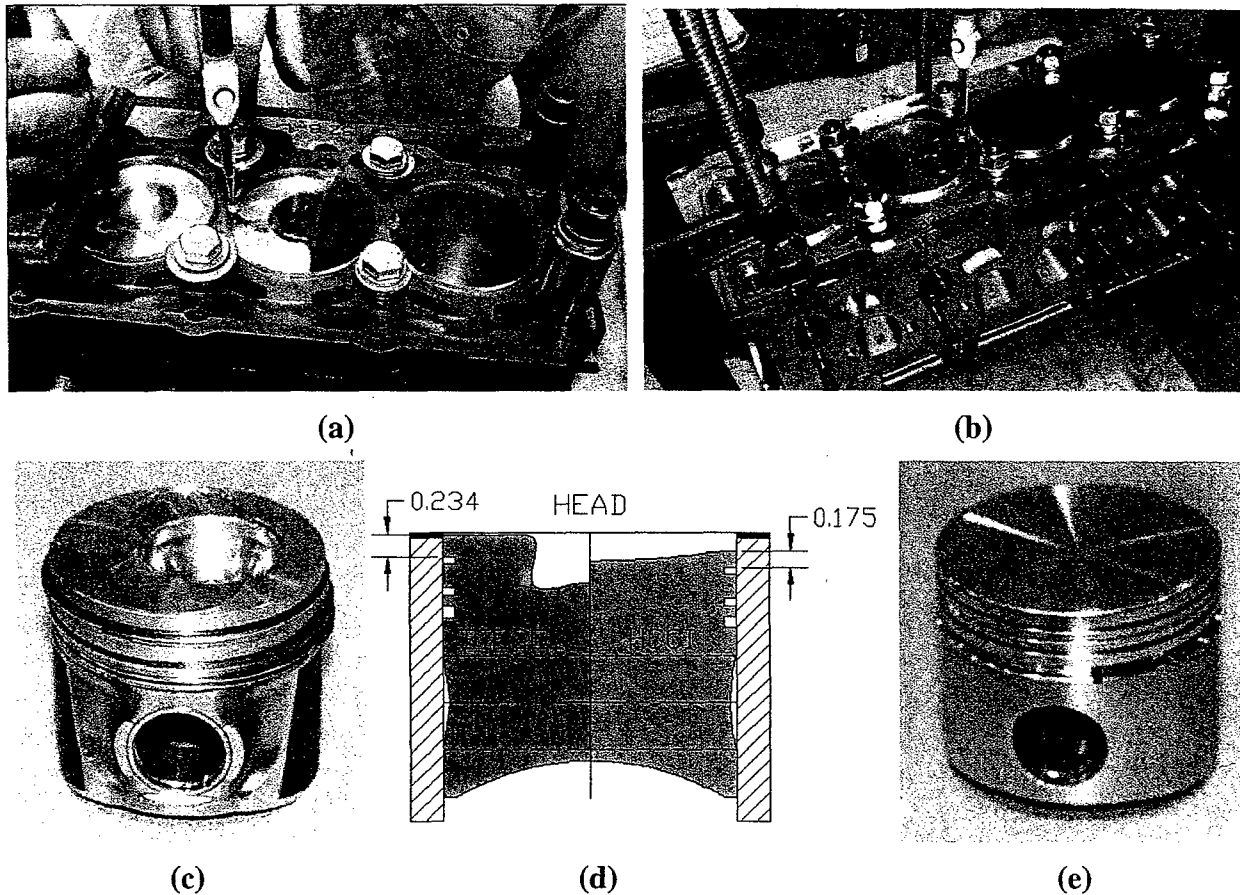


Figure 1: Piston redesign and fabrication process.

Heated Intake Manifold System

The decision to develop an engine with a 16.5:1 compression ratio required that thermal energy be added to the intake air charge such that autoignition would be possible. Four 2-kW air heaters were purchased after computational analyses were performed to determine selection. These heaters were tested in the Thermal Sciences Laboratory using various volumetric flow rates to simulate different engine speeds, and at power levels to simulate varying intake temperature demands. Various thermocouples were also tested to determine the most appropriate combination for the final engine. Figure 2 (a) shows a stock intake heater, the capabilities of which were tested in the Thermal Sciences Lab in the setup provided in Figure 2(b).

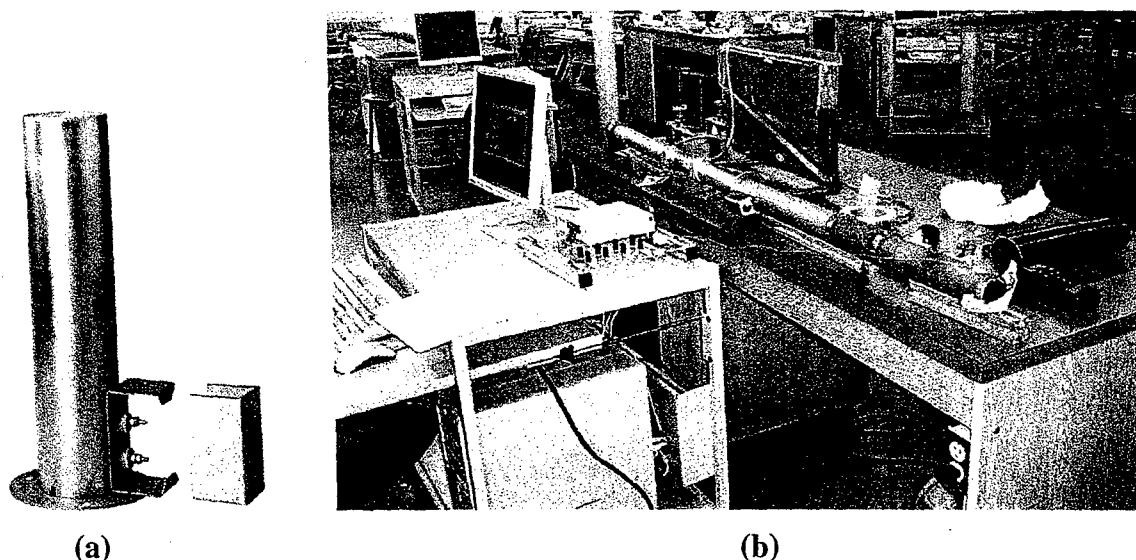


Figure 2: Stock intake heater (a) and experimental setup in Thermal Sciences Lab (b).

The intake heaters were then welded to an aluminum air box shown in Figure 3, which was also integrated with a throttle body. Though not used in this phase of the project, the throttle system was included to study startup enrichment strategies. The remaining components of the intake were four venturis and the modified intake runners, which provided a gradual transition from the larger diameter heaters to the smaller intake port diameters. The unassembled intake is depicted in Figure 3.

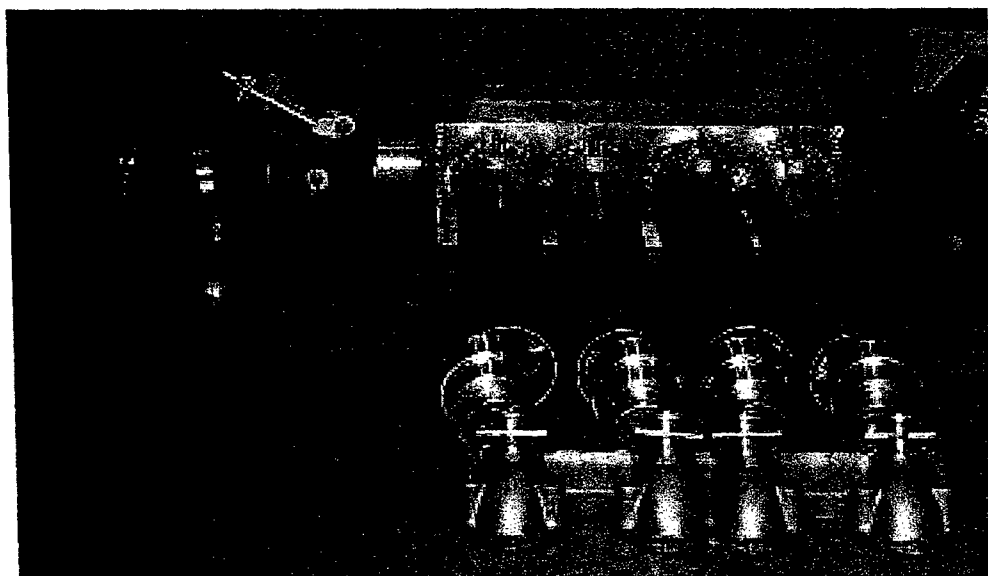
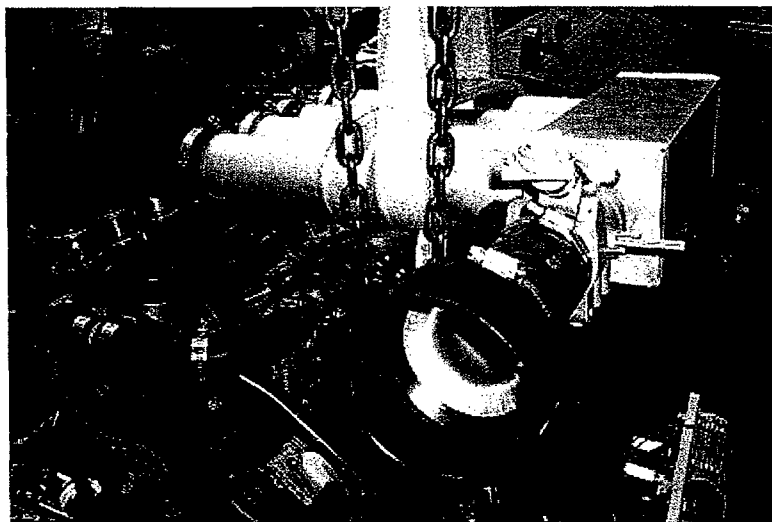


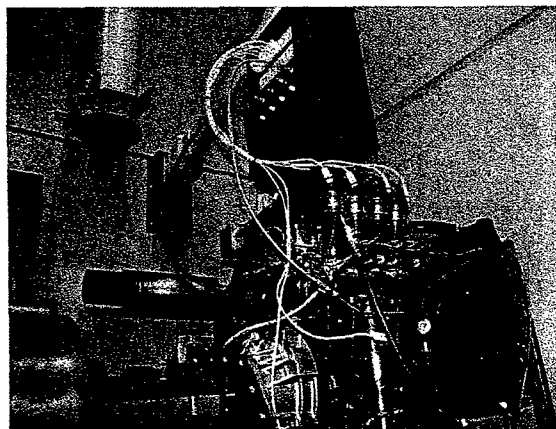
Figure 3: Unassembled intake system.

To address the concern of vibration, high temperature silicon tubes were used to connect the heaters to the four venturi nozzles and then to the modified stock intake. The silicon tubes were chosen to help isolate the heaters from the engine vibrations. The intake assembly is shown during installation on the engine in Figure 4(a), while two views of the assembled engine attached to the DC dynamometer are shown in Figure 4(b) and Figure 4(c). Note that a flexible hose connected the intake to the throttle mechanism to the laminar flow element, or LFE, (shown

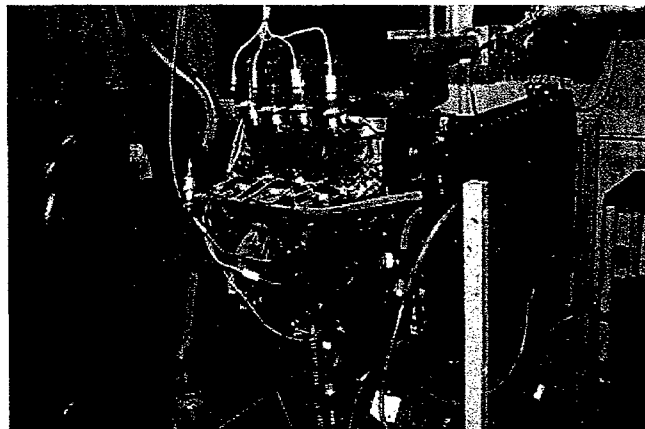
in the background in Figure 4(b) and (c). The LFE was used in conjunction with a lambda sensor (placed in the exhaust) and a fuel balance to determine the actual air fuel ratio the engine was inducting.



(a)



(b)



(c)

Figure 4: Intake system at various stages of assembly.

Note that yellow thermocouple wires are present in each intake and one in the exhaust manifold. All are directed to the data acquisition system outside the test cell through the overhead boom shown in Figure 4(b). Like the fuel system to be discussed in the following section, the control system for the heaters was integrated within the dynamometer subsystem and will therefore be addressed in a later section.

Fuel Injection System

Multi-port fuel injection was the desired method of fuel delivery because of its proximity to the intake port (better transient response) and tighter control over metering. The open literature suggests that individual control of each cylinder is necessary in improving engine operation. Therefore, injectors were located after the heaters to prevent any chance of fuel ignition when passing through the heater elements. In addition, the injectors were located before the head, so

that the fuel would be sprayed onto the intake valve, as seen in Figure 5. The hot valves were aid in the vaporization of the fuel, as well as air/fuel mixture preparation.

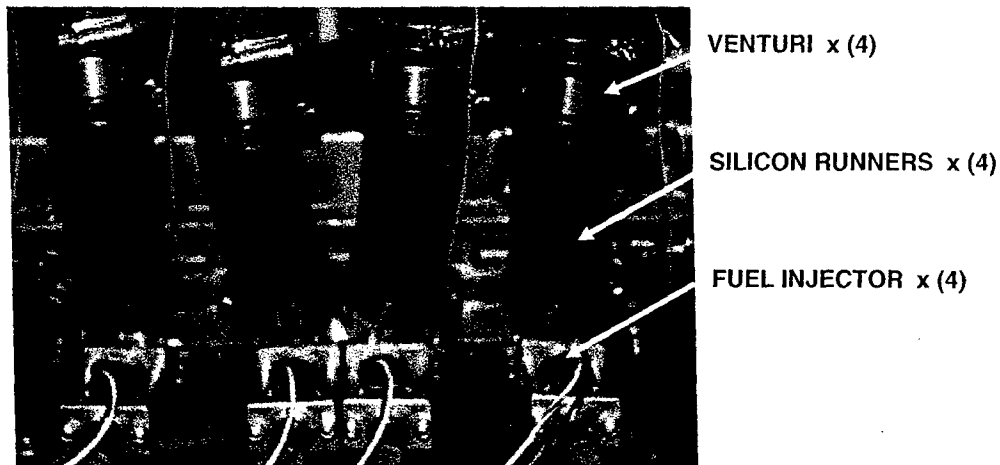


Figure 5: Fuel injector locations

The fuel injectors are connected to the electronic control unit with the red and yellow wires shown in Figure 5. These wires provide the connection for the injector pulse width signal to turn the injectors on and off for prescribed durations.

Data Acquisition and Dynamometer Control Systems

The dynamometer system served as the central hub for data acquisition and subsystem control. The control and data acquisition center is depicted in Figure 6. The test cell, which contains the dynamometer and engine stand, is located through the window seen in Figure 6(a). The following list briefly describes all the numbered systems in this figure.

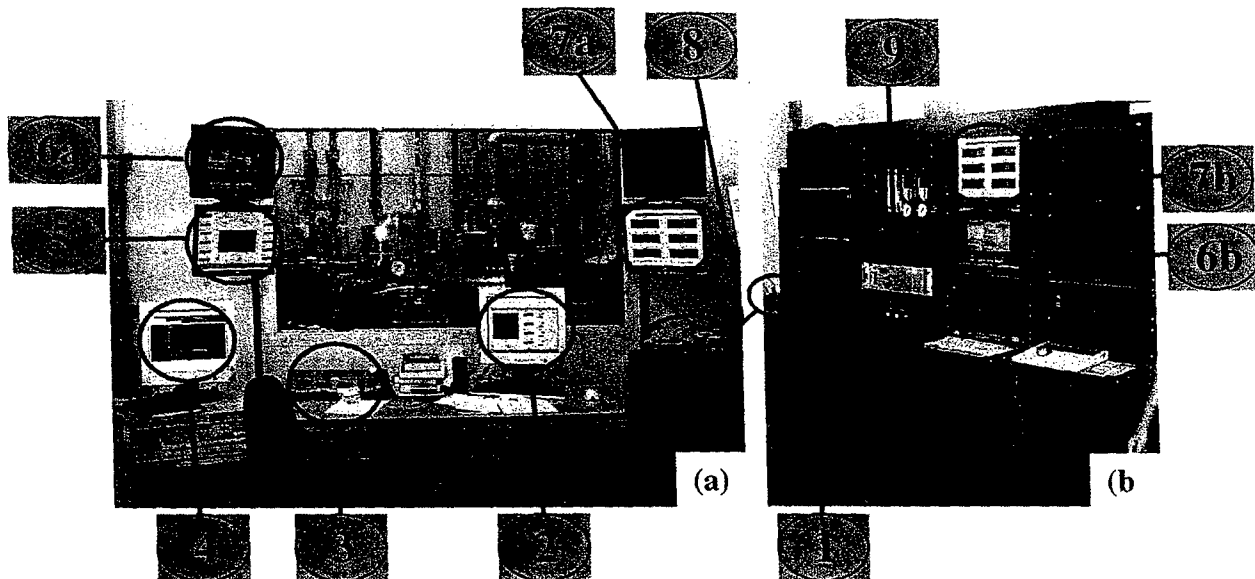


Figure 6: The central dynamometer control system (a) worked in tandem with the fuel balance, emissions analyzers, and fuel controller systems in (b).

Subsystem Description

- 1) Testmate/Cellmate hardware: These control boxes contain the engine test schedules and serve as a data retrieval system.
- 2) The Main Computer: Acquires and retrieves data to/from the Testmate/Cellmate hardware. Digalog Hypercell is the driving program, which is used to direct data appropriately. User inputs to the heater control units are provided to the Hypercell software here. A sample screenshot from the Main Computer is shown in Figure 7.

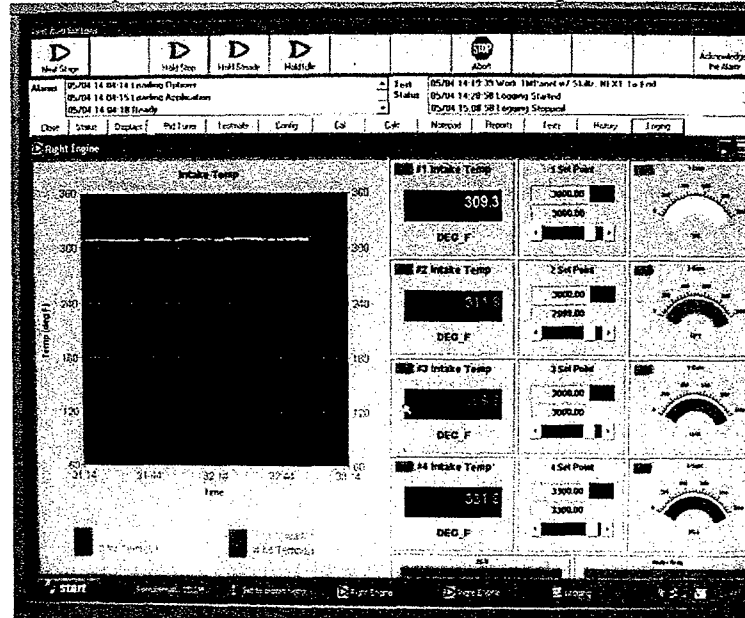


Figure 7: Sample screenshot of the main computer depicting the input temperature request locations and actual air temperature for all cylinder intakes.

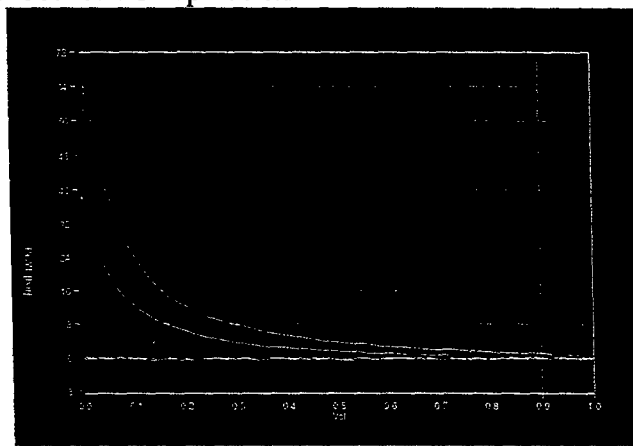
- 3) Digalog Control Panel: Allows the user to vary dynamometer and engine speeds and loads according to a prescribed test schedule saved to the Testmate/Cellmate system. A picture of the control panel is provided in Figure 8.



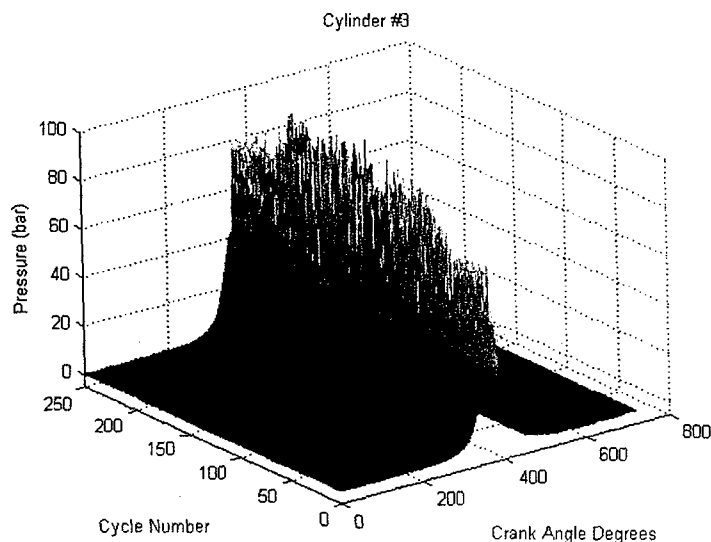
Figure 8: Digalog dynamometer control panel.

- 4) AVL Combustion Analyzer: This system is connected to the in-cylinder pressure transducers that were inserted in each cylinder's glowplug holes. The hardware allows one to collect pressure data on a crankangle basis from each cylinder simultaneously. These data are collected on the corresponding computer and are reduced on a cycle-to-cycle and cylinder-to-cylinder basis. Time- and crank-angle resolved data result.

- a. A screenshot from the AVL computer is shown in Figure 9 (a) for a single cylinder and cycle. Note that the combustion process near TDC is extremely rapid (left-most side of graph). This plot is a typical pressure vs. volume diagram from which IMEP was calculated. The almost-constant volume combustion process suggests thermal efficiencies approaching those of the Otto Cycle.
- b. Data for 50 consecutive cycles were then logged in the AVL database and reduced to yield the plot in Figure 9 (b). In this case, the engine's transient response to a step change in fueling rate was investigated. The engine was operating under HCCI mode for the first 50 cycles, at which point, an increase in fuel mass was imposed using the ECU. The unstable pressure traces that resulted are a clear indication of the onset of knock. At approximately 200 cycles, the fueling rate was returned to its original state. The remaining pressure vs. crankangle traces indicate that the engine required a longer period of time to return to smooth HCCI operation.



(a)



(b)

Figure 9: Pressure data from the AVL Combustion Analyzer in pressure-volume diagram form for a single cylinder and cycle (a) and in cycle-resolved form for one cylinder on a crankangle basis (b).

- 5) Low-speed data acquisition screen: The channels on this output screen are associated with all temperatures and pressures outside the cylinders, engine speed and torque, the LFE flow rate, and fueling rate. A screenshot is shown in Figure 10.

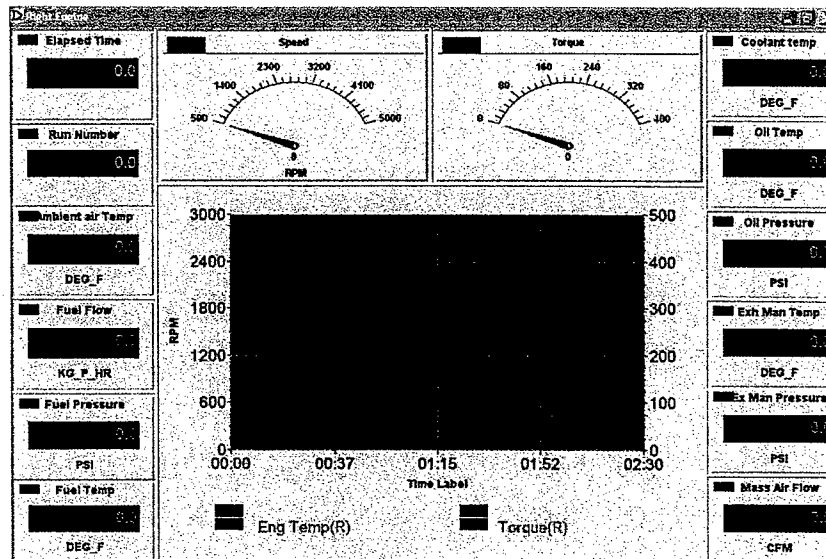


Figure 10: Low speed data acquisition screenshot.

- 6) Electronic Control Unit (ECU) for the fuel injection system. Screen 6(a) is an echoed output from 6(b). The ECU is controlled with the computer in the cabinet in Figure 6(b). The user varies fueling rate to affect the overall air/fuel ratio inducted into the cylinder.

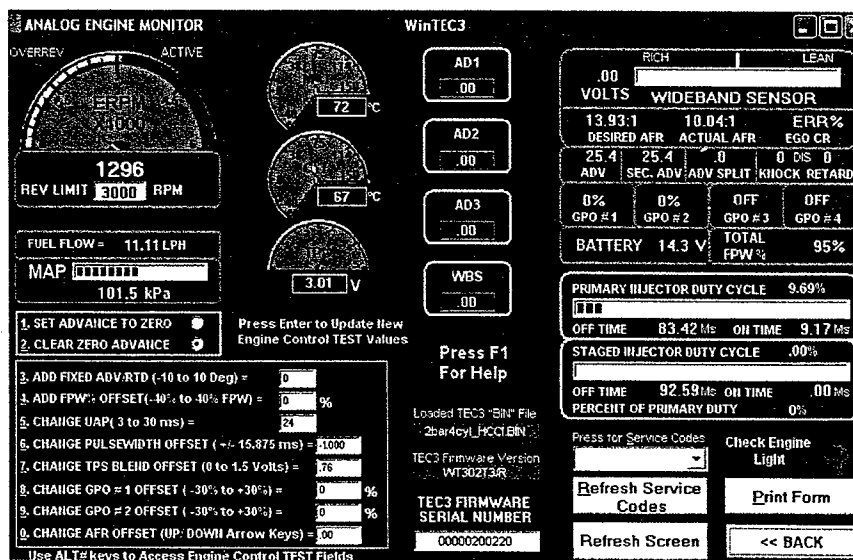


Figure 11: ECU software screen. The UAP, or User Assigned Pulsewidth, was used to vary air/fuel ratio.

- 7) Emissions Analyzers. Screen 7(a) is an echo of 7(b). These readings are of HC, CO, NO_x, O₂, and CO₂ in the exhaust. The oxygen sensor also yields an air/fuel ratio by sampling the products of combustion in the exhaust gas. A screenshot of the readings from the emissions system is given in Figure 12.

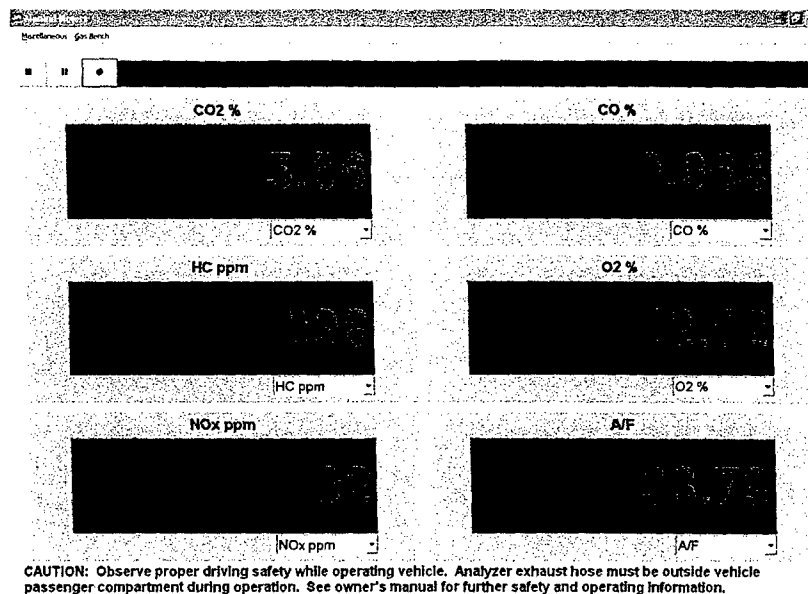


Figure 12: Screenshot of the emissions analysis readings.

- 8) The Heater Control Unit: This hardware is connected to the Testmate/Cellmate systems for data storage. The pulse width modulated (PWM) signal it produces for each heater is controlled by the air temperature request provided to Hypercell by the user on the Main Computer at Screen 1. The hardware and connections are shown in Figure 13.

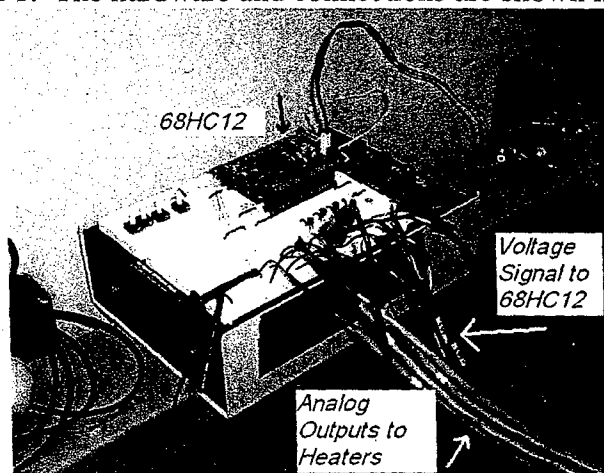


Figure 13: Heater controller apparatus.

- 9) AVL Fuel Balance: This system is connected to the fuel balance inside the test cell that measures fuel consumption by the engine. This reading is also echoed to Screen 5.

Modeling Efforts

The four heater subsystems were modeled in the Matlab/Simulink programming environment. The top level of the model is shown in Figure 14. This model contains the physical heater system along with submodels for the transient response of the heater microcontroller. The energy balance was applied to the system, as shown in the Heater System sublevel in Figure 15. This model was used to gain insights into the responsiveness of the intake air temperature before the engine was ever operated. The proportional, integral, and derivative control factors were

varied in an effort to predict what could be expected in the actual system. The submodels in each block contained empirical correlations and physically-based equations. This simulation was developed as a foundational effort upon which future graduate students could vary correlation factors and improve submodels in an effort to improve the correlation between experimental and model results.

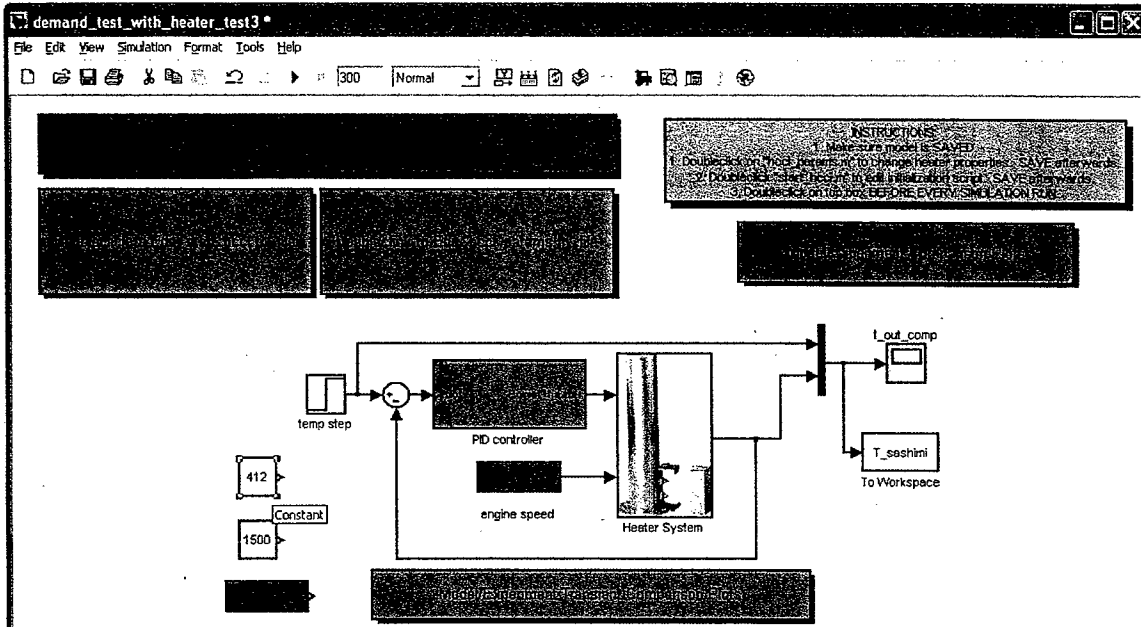


Figure 14: Top level block diagram of the Matlab/Simulink model for the heaters and their controllers.

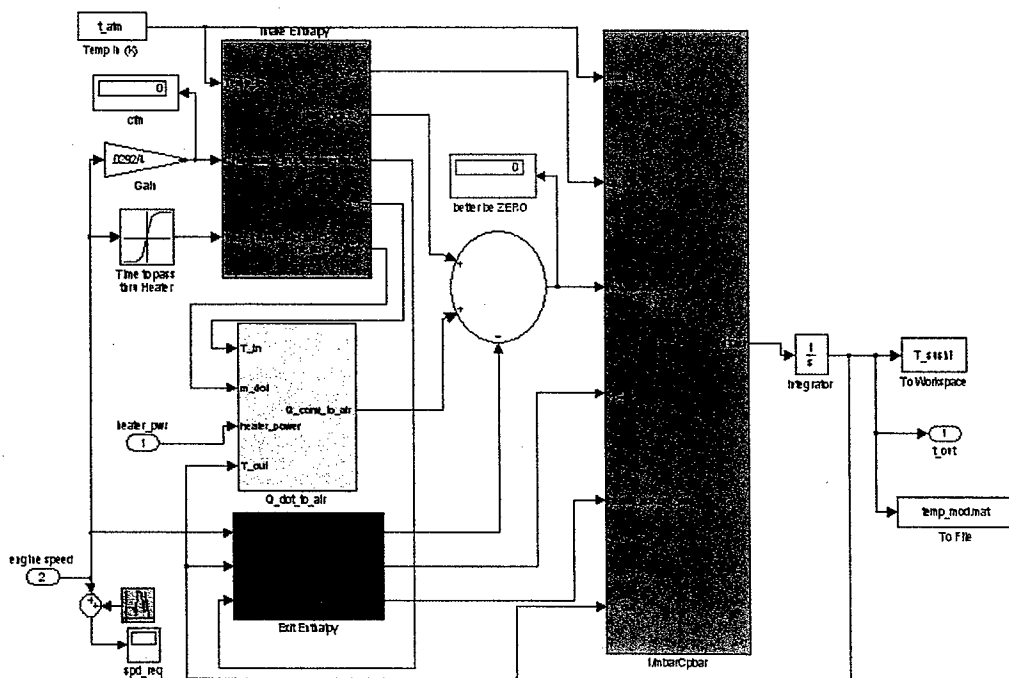


Figure 15: Heater system sublevel indicating the energy balance for each heater.

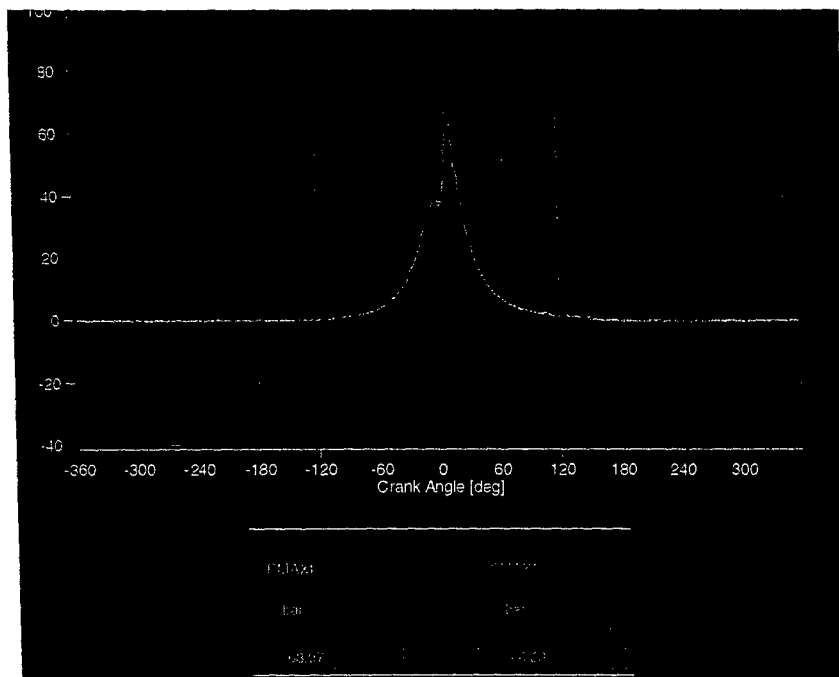
Results and Discussion

As the foundational work for the HCCI engine, it is of particular interest to first determine the operation limits of the engine. Within these limits, the cylinder-to-cylinder and cycle-to-cycle variations are observed to gain a fundamental understanding of how the engine performs. From this information, educated decisions can then be made as to their validity for various avenues of further research and development, in hopes of bringing HCCI combustion closer to being implemented in industry.

Limits of Operation

To determine the limits of operation, an engine speed of 1300 RPM was selected and the air/fuel ratios and intake temperatures were varied. The 1300 RPM engine speed was selected because of the relatively low volumetric flow rate and potentially safer operation. During motoring tests, it was observed that minimal vibrations occurred at this speed, whereas higher engine speeds produced rapid and violent excitation at the engine rails.

Defining the limits of operation can be done by either merely listening for the onset of knock or misfire, or by viewing the in-cylinder pressure trace. Engine knock produces a markedly rough sound as compared to smooth HCCI operation. This rough operation can be viewed on the pressure vs. time diagrams from the AVL combustion analyzer. At certain operational regimes, the combustion event becomes unsteady. That is, combustion does not occur during every consecutive cycle. This phenomenon is called misfire. Examples of smooth operation, misfire, and knock are shown in Figure 16. Note that cylinder firing was synchronized such that these traces could overlay.



(a)

Figure 16 (a): Example of smooth HCCI operation in all four cylinders. Note that, by inspection, the CTC's are minimal because the pressure vs. crankangle overlay.

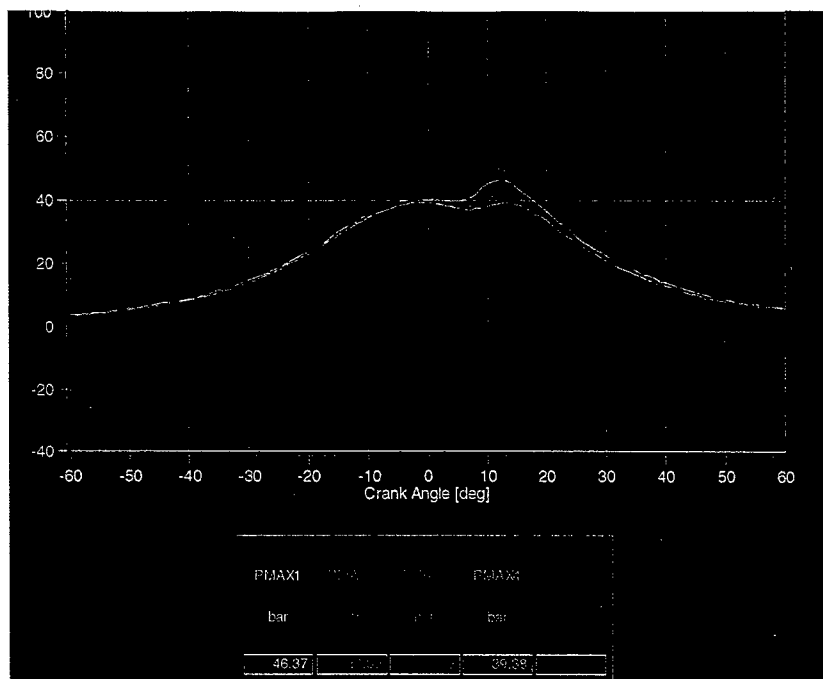


Figure 16 (b): Example of misfire in an HCCI engine.
Note that the time scale has been truncated to show detail around TDC.
For this particular engine cycle, not all cylinders fired.

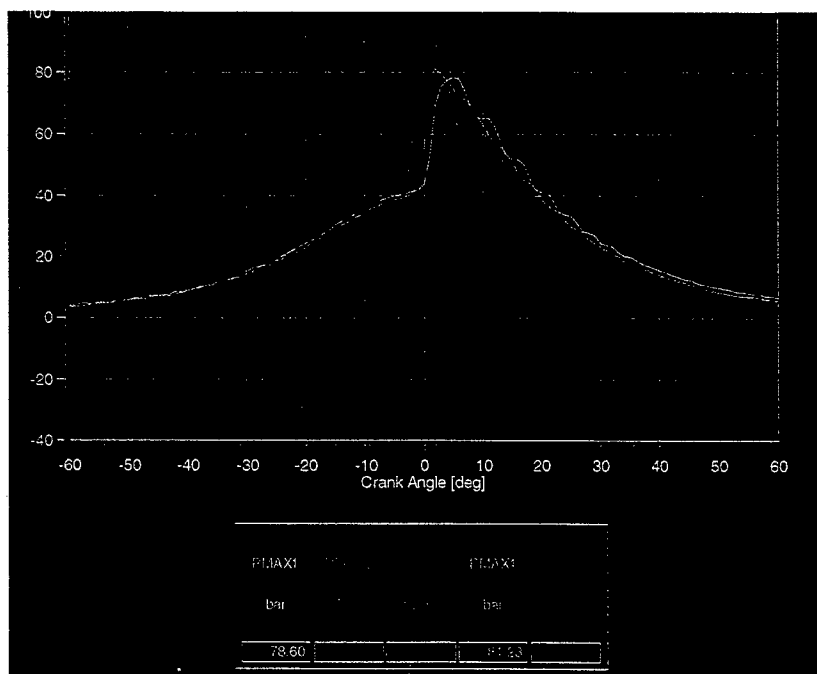


Figure 16 (c): Example of knocking in an HCCI engine. Note the rapid pressure pulsations in each of the cylinders. These pressure waves are undesirable as continued knock damages engine parts.

Various combinations of fueling rate and intake air temperature were provided to the engine at an engine speed of 1300 RPM. The operating map shown in Figure 17.

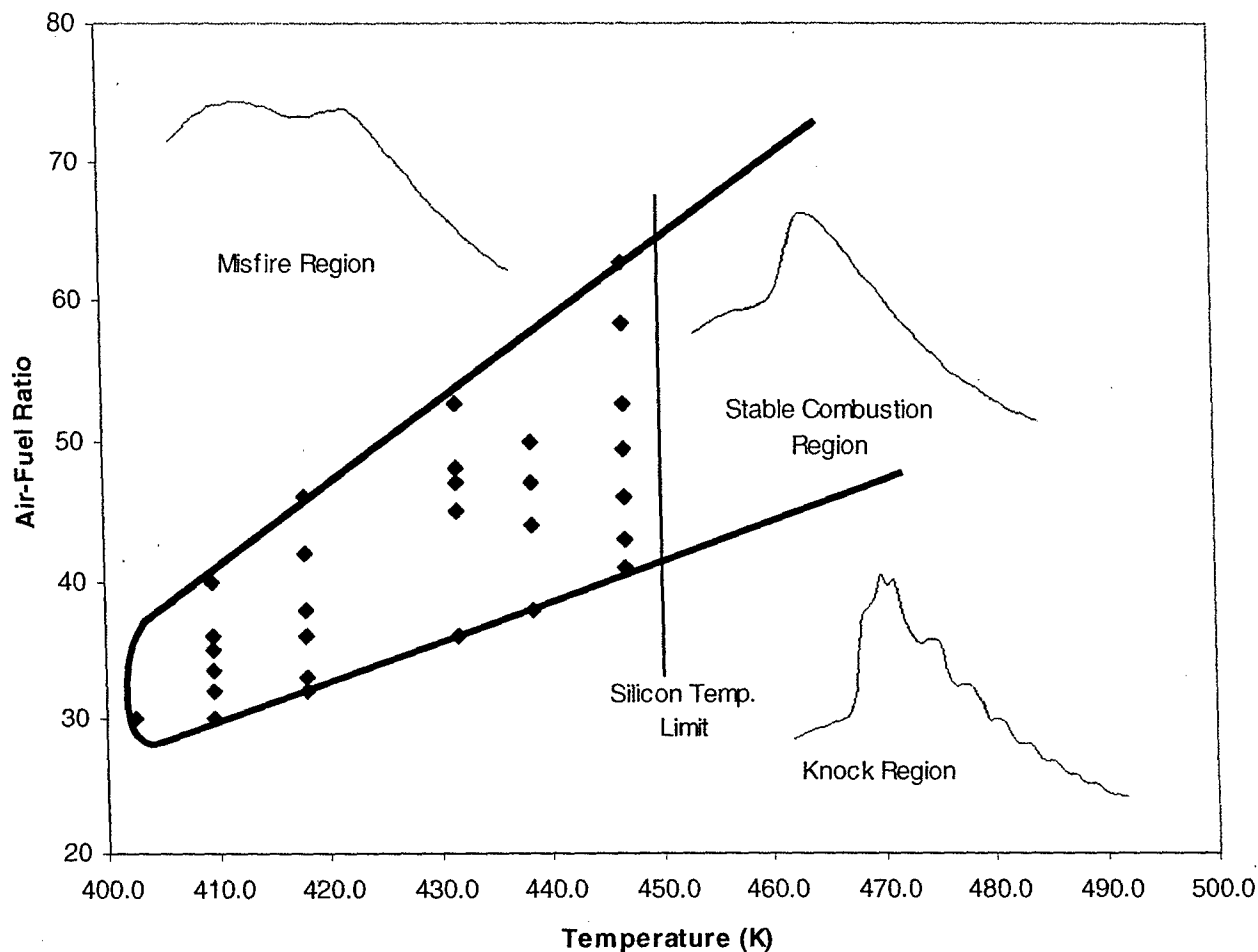


Figure 17: The limits of combustion stability for the Cal Poly HCCI engine.

The area bounded by the thick black line is the region of stable combustion, all values above are misfire and below are knock regions. Just over 400 K (260 °F) is the limit where some cylinders knock while others misfire. To the right of this point, in the stable region, is where the engine produces the most power. The air-fuel ratio is the least is the region, and the most power is going to inherently be produced. This is because the largest amount of fuel is being used and the power is proportional to the amount of fuel reacting. A closer look at each of the three regions of interest is explored on the basis of cylinder-to-cylinder and cycle-to-cycle.

Quantifying CTC Variations

Figure 18 contains two- and three-dimensional illustrations of the three combustion regimes indicated in the engine's operational map. The plots indicating misfire and knock clearly indicate the need for independent, variable intake temperature control. Initial studies in this field have aided in decreasing the cycle-to-cycle and cylinder-to-cylinder variations. These CTC's must first be quantified before comparisons can be drawn.

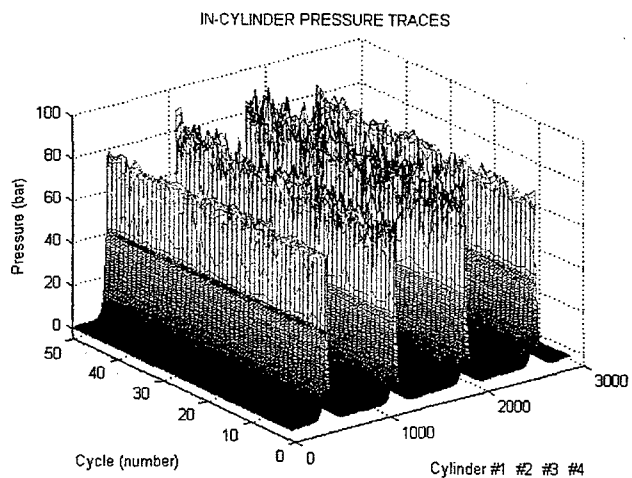
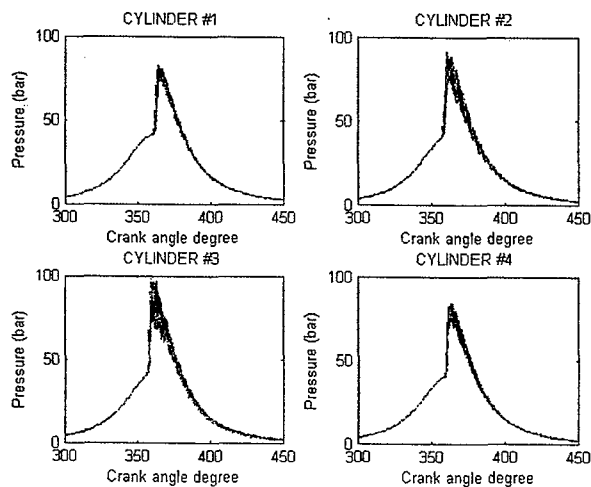
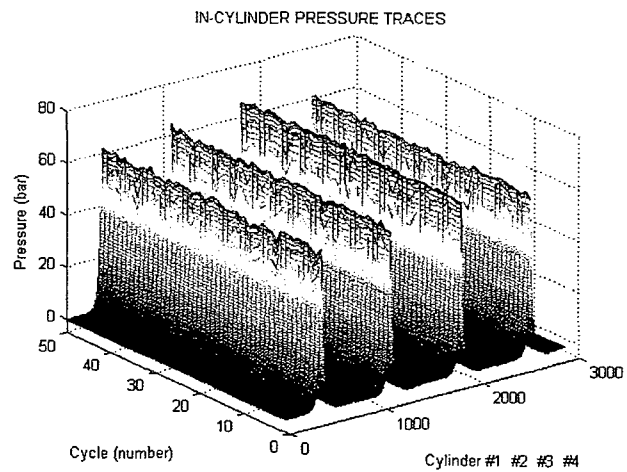
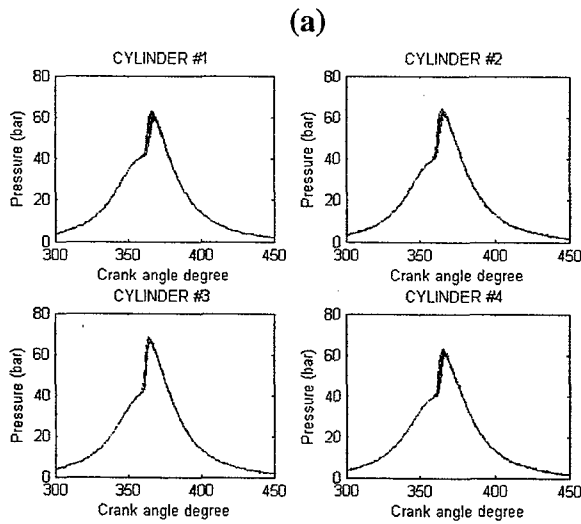
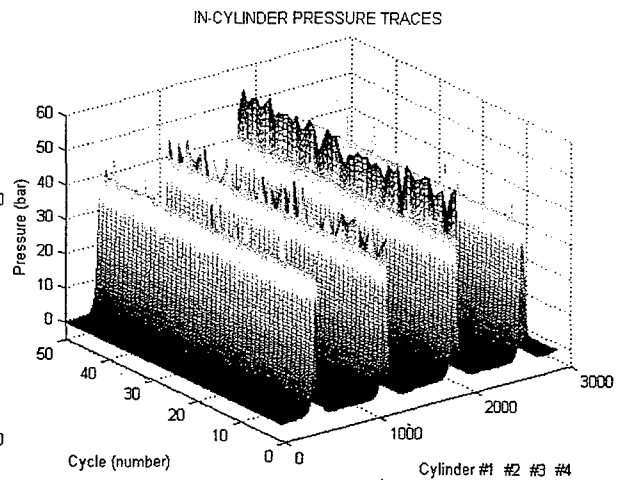
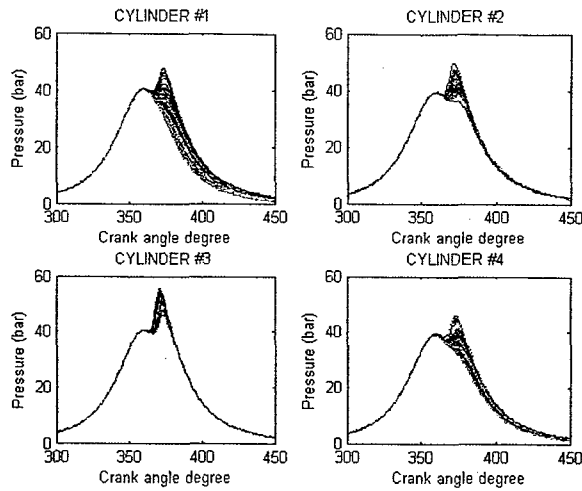


Figure 18: Examples of misfire (a,b), stable operation (c,d), and knock (e,f).

While torque is a valuable measure of a particular engine's ability to do work, it depends on engine size. A more useful relative engine performance measure is obtained by dividing the work per cycle by the cylinder volume displaced per cycle. The parameter so obtained has units of force per unit area and is called the mean effective pressure (mep).

$$mep = \frac{Pn_R}{V_d N}$$

The net indicated mean effective pressure (IMEP) is the work delivered to the piston over the entire four strokes of the cycle per unit displaced volume. The term 'indicated' is a remnant of when indicator gauges were placed inside a cylinder to measure pressure throughout the cycle.

$$IMEP = \frac{\int p dV}{V_d}$$

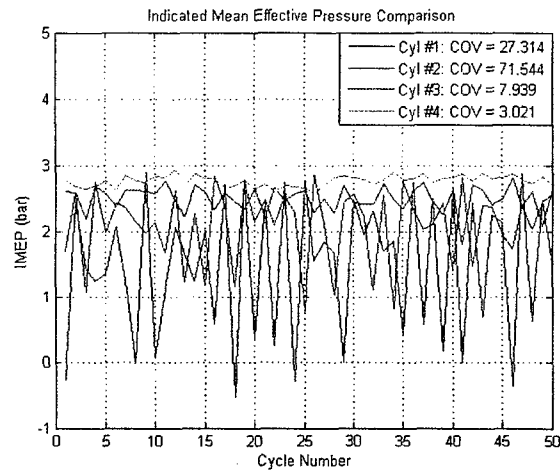
Upon obtaining pressure vs. volume diagrams for all consecutive cycles in each cylinder, these data were then provided to the Matlab environment where the above integration was performed. In addition, the Matlab script determined the standard deviation of the IMEP values for each cycle using the following equation:

$$\sigma_{IMEP} = \sqrt{\frac{n \sum x^2 - (\sum x)^2}{n(n-1)}}$$

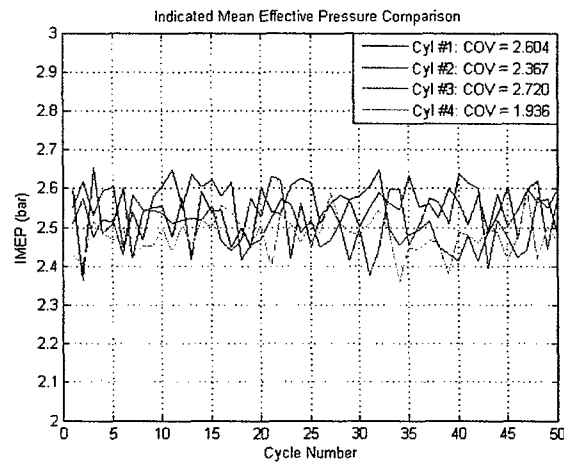
Finally, the COV was determined with:

$$COV = \frac{\sigma_{IMEP}}{mean_{IMEP}} \times 100.$$

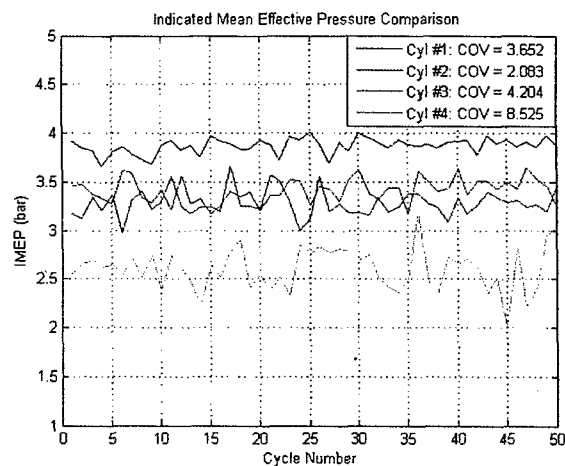
The pressure data illustrated in the previous figures has been reduced using the COV and IMEP Matlab scripts such that COV's for the misfire, stable combustion, and knock regimes can be quantified and compared. Figure 19 depicts the reduced data for these cases, including the COV's for each cylinder and the IMEP at each individual cycle and cylinder.



(a)



(b)



(c)

Figure 19: COV of IMEP for 50 consecutive engine cycles in and engine operating under misfire (a), stable combustion (b), and knock (c).

Regardless of what region the engine is operating a few probable explanations for the variations, could be:

- normal variation in equivalence ratio
- mass air flow fluctuations
- dynamometer speed
- heater fluctuations
- physical dimensions of each cylinder

Emissions

The emissions that are measured are CO, CO₂, HC, O₂, NO_x, air/fuel ratio (A/F), and lambda (λ). Of these emissions the HC, NO_x and the A/F are of particular interest. HCCI combustion produces higher values of HC than a comparable SI engine, thus necessitates reduction. The NO_x is where HCCI has the largest gains, with reductions of approximately 90% of a comparable CI engine. Lastly, the A/F provides feedback as to where the engine is operating. A summary of the typical emissions that were observed are presented in

Table 1: Summary of typical emissions

Run	CO ₂ (%)	CO (%)	O ₂ (%)	HC (ppm)	NO _x (ppm)	A/F Ratio	Lambda
1	4.47	0.096	14.62	405	5	43.5	3.09
2	4.68	0.101	13.57	445	5	40.09	2.84
3	4.65	0.104	13.56	451	5	40.18	2.85
4	4.39	0.106	13.94	435	6	42.37	3.01

All of the values look favorable except for the HC numbers. It is desirable to have lower numbers for HC. There could be a few reasons for this. The HCCI designed pistons have incorporated mechanisms to minimize unburned HC from crevices, so this is ruled out. High HC numbers typical signify that there is not complete combustion or that not all of the fuel is consumed. The especially high levels of fuel consumption may imply that complete vaporization of the fuel mixture does not occur before the onset of combustion. Further studies into this matter are necessary.

Conclusions

The groundwork for a 1.9L gasoline HCCI engine has been completed. Fundamental experiments and analyses of the limits of operation as well as the cylinder-to-cylinder and cycle-to-cycle variations have been performed. The following conclusions can be drawn from the experimental results obtained:

1. Individual intake heating was a viable means to control HCCI combustion. The variations observed support the need for individual cylinder temperature control.
2. There was a strong correlation between HCCI start-of-combustion and intake air temperature.

3. IMEP increases as air temperature and air-fuel ratio decreases, stability limits become increasing narrow in this direction.
4. Limits of operation at 1300 RPM have been defined.
5. The COV of IMEP for each cylinder in the stable combustion region was less than 3%.
6. High values of HC were observed due to inefficient combustion, may be a result of an inhomogeneous air/fuel mixture.
7. NO_x values of 5 ppm were obtained.
8. Fuel conversion efficiency was approximately 16.8%
9. Power produced was 12 bhp (8.95 kW) at 1300 RPM
10. Torque produced was 34 lb-ft (4.7 kg-m) at 1300 RPM

Recommendations for future directions include determining the source of the low fuel conversion efficiency. This might be the reason for the high HC values and reduce them, if not then an investigation to reduce HC is advised. The pistons were designed such that HC would be minimized. To date, this is the lowest topland height being implemented. Theoretically, this should provide the lowest HC values, since crevice volume is one of the major contributors. As discussed, one possible reason for the high HC values is incomplete combustion, due to the intake charge not being fully homogeneous. An investigation into better mixing of the air/fuel mixture is another possibility. There was not much confidence in the fuel flow values that were obtained, due to about 50% fluctuation in readings. Validation of the fuel flow and measuring system is needed or possibly upgrading the system. Utilizing the systems capability to individually control each cylinder will help to improve the already low cycle-to-cycle and cylinder-to-cylinder variations respectively. This will also expand the operating limits of the engine and improve engine power output. As this work was a demonstration and feasibility of the concept, the potential for great advancements in this area has been established.

DEMONSTRATIONS OF INDEPENDENT
INTAKE TEMPERATURE CONTROL IN AN
EXPERIMENTAL GASOLINE HCCI
ENGINE

MAY 2005

AUTHORIZATION FOR REPRODUCTION
OF MASTER'S THESIS

I grant permission for the reproduction of this thesis (or project report in its entirety or any of its parts, without further authorization from me.

Signature

Date

TAYLOR TAILAP CHEUNG
DEPARTMENT OF MECHANICAL ENGINEERING
CALIFORNIA POLYTECHNIC STATE UNIVERSITY
SAN LUIS OBISPO

ii

APPROVAL

TITLE: Demonstrations of Independent Intake Temperature Control in a Gasoline HCCI Engine

AUTHOR: Taylor Tadlap Cheung

DATE SUBMITTED: May 2005

Committee Chair

Signature

Committee Member

Signature

Committee Member

Signature

iii

ABSTRACT

This thesis provides a foundational heater model to be used to individually control the intake air going into each cylinder of Cal Poly State University San Luis Obispo's HCCI engine. The HCCI concept employs operating characteristics from diesel and gasoline combustion, offering potential for higher thermal efficiencies and lower exhaust emissions. HCCI operates with an ultra-lean air/fuel mixture and combusts through auto-ignition.

In order to make HCCI combustion a consumer reality, a number of challenges must first be resolved. Most important is the control over auto-ignition. Because combustion comes from auto-ignition, there is yet of any direct method to precisely manage its timing. There are, however, a number of indirect control methods, and one of the more popular ways is through intake temperature control. HCCI combustion is sensitive to intake air temperature, and monitoring this variable gives more control over stable combustion.

A group of graduate students from the Department of Mechanical Engineering has successfully designed and built an intake system to heat air going to each cylinder. Individual controls for each of the four heaters are implemented, and a linearized PID control strategy is implemented to maintain, with reasonable accuracy, the desired temperature. Individual temperature control allows the user to fine-tune each cylinder and ensure stable operation with different intake temperatures. A Simulink model consisting of one heater is made to compare and validate the experimental setup.

The intake heater with individual temperature control for each cylinder brings HCCI a step closer to reality. Its straightforward design and simplicity makes it a good candidate for continued research and improvements.

iv

ACKNOWLEDGEMENTS

I would like to express my sincere gratitude to my advisor George Delagranmatikas. My thesis was made possible by the support, encouragement, and patience he has given me. More than just my professor, he truly deserves the word "advisor" in that he has also given me direction in achieving my personal and career goals. I am also grateful for the assistance from my co-advisors William Murray and Charles Bitsong. They, along with George, helped me grasp and accomplish my thesis.

I thank the California Central Coast Research Partnership for their gracious support in my thesis. They have broken-down financial barriers and have given me an opportunity to provide future students with a myriad of research opportunities on this engine.

Jim Gerhardt, a major backbone in my thesis, has offered so much technical support with this project. His experience and knowledge has resulted in many forward strides, and the stories and advice he has shared only provide further enlightenment for me.

Nicholas Jacques, not only a great friend, but also a wonderful person to work with, has walked with me side-by-side since our project's beginnings.

My friends and peers here in San Luis Obispo, some having moved on, some still here, all having offered their support in one way or another, I want to thank you as well. My stay in SLO has been short, but it has turned out to be a great one because of all of you. My friends back in the Bay, you have wanted me to move back, and that day has come now.

Finally, I want Mom, Baba, Jennifer, and Vicky to know how much they have meant to me. Thank you for believing in what I am capable of doing.

v

TABLE OF CONTENTS

1. INTRODUCTION	9
1.1 Spark Ignition Combustion: Overview	10
Emissions in SI Combustion	12
1.2 Compression Ignition Combustion: Overview	13
Emissions in CI Combustion	15
1.3 Air-standard Dual Cycle	16
1.4 HCCI Combustion: Overview	17
Emissions in HCCI Combustion	18
1.5 HCCI Research	20
1.6 Current HCCI Trends/Directions	21
GDI HCCI	21
HCCI as Part of a Hybrid Power Source	22
Various Fuels	23
1.7 Cal Poly's HCCI Research Goals	24
Methods of Controlling Auto-Ignition	25
2. HARDWARE AND MODIFICATIONS	30
2.1 VW Engine Specifications	30
2.2 Kimball VW Parts List	31
2.3 Intake Design/Hardware	32
Heater Characterizations (Flow Rates)	37
2.4 Piston Design/Justification	38
2.5 In-cylinder Pressure Transducer Selection	40
2.6 ECU Selection	40
2.7 Thermocouple/Pressure Transducer Selection	41
2.8 Professional Lambda Meter Selection	41
2.9 Throttlebody Selection	44
2.10 Heater Relays Selection	44
2.11 Engine #1 Teardown/Buildup Procedures	45
2.12 Engine #2 Buildup	47
2.13 Engine Setup	51
AVL Encoder mount	51

Pistons	52
Testmate/Cellmate/Hypercell Logistics	53
Cam encoder	57
Boon	58
ECU wiring	59
Radiator and Radiator Fan	59
240V Power Source	60
Coupling Hardware	60
3. VALIDATION FOR MODIFICATIONS AND TESTING PROCEDURES	61
3.1 Volumetric Measurements for Engine Block and Head	61
Procedures	62
3.2 CC After Engine Buildup #1	66
3.3 CC After Engine Buildup #2	67
4. HCCI INTAKE HEATER CONTROL	69
4.1 Heater Characterizations/Energy Balance Equation	69
4.2 Simulink Model and Explanations	71
Other Peripherals	73
Inside the Heater System	77
PID Review	89
PID values	90
4.3 Heater Physical Model	96
Blow-dryet Method	99
HCCI Intake Heater Methods/Troubleshooting	101
5. HCCI ENGINE OPERATION PROCEDURES	111
5.1 Motoring Process	111
5.2 Hypercell Data Logging	113
5.3 Startup	114
6. RESULTS FROM ENGINE OPERATION	118
6.1 Temperature Response to Transient Engine Speed	118
6.2 Adding Fuel for HCCI Combustion	121
7. CONCLUSIONS AND FUTURE RESEARCH DIRECTIONS	125
7.1 Suggestions/Recommendations	125
Software	125

Hardware.....	126
7.2 Wrapping up.....	128
APPENDIX A: TABLE.....	129
APPENDIX B: BIBLIOGRAPHY	133

LIST OF FIGURES

Figure 1.1: Pressure-Volume Diagram for Otto Cycle.....	11
Figure 1.2: Pressure-Volume diagram for a Compression Ignition Cycle.....	14
Figure 1.3: Pressure-Volume Diagram for Dual Cycle.....	16
Figure 1.4: Spontaneous HCCI combustion (spots in chamber representing combustion) [J18]	18
Figure 1.5: NOx emissions vs. engine load for typical HCCI and DI Diesel combustion [J. 19]	19
Figure 1.6: Kopecek et al. HCCI setup: 1. Pulsed Nd: YAG-laser, 2. focusing optics, 3. Volvo TD 100 engine.....	26
Figure 1.7: Side view of engine showing a. active valve train, b. nitrogen/air-feeding pipe, c. exhaust pipe.....	27
Figure 2.1: Aluminum Venturi for Bore Change in Intake.....	33
Figure 2.2: Custom Machined/Welded Intake Port.....	34
Figure 2.3: Plenum Before Heaters (Tubes on Bottom).....	34
Figure 2.4: Laminar Flow Element with K&N Filter.....	35
Figure 2.5: Omegalux 2kW Intake Heater.....	35
Figure 2.6: Preliminary Heater Testing Setup.....	37
Figure 2.7: Preliminary Intake Heater Testing.....	38
Figure 2.8: Original VW TDI "bowl" piston.....	39
Figure 2.9: MoTec Professional Lambda Meter.....	42
Figure 2.10: Lambda TEC3r Conversion Factor.....	44
Figure 2.11: Crydom Heater Relay.....	45
Figure 2.12: 1.9L Bare Block.....	46
Figure 2.13: Lodged Valve and Hole in Piston.....	49
Figure 2.14: VW Special Tool 3418.....	50
Figure 2.15: Same Engine, Different Pistons and Connecting Rods.....	51
Figure 2.16: Encoder Mount.....	52
Figure 2.17: ARIAS piston.....	53
Figure 2.18: Testmate Panel.....	54

Figure 2.19: Cellmate and Testmate Hardware on Top-Left Cabinets.....	56
Figure 2.20: Hypercell Temperature Display Screen (Note Different Set Points)	56
Figure 2.21: Sequential Fuel Injection Cam Encoder.....	58
Figure 2.22: Engine Boom with Thermocouple and Pressure Transducer Lines.....	59
Figure 3.1: Verification of Plexiglas volume.....	62
Figure 3.2: Securing the Plexiglas on the block. Note piston protrusion out of block	63
Figure 3.3: Fluid dripping through hole for block volume measurement.....	64
Figure 3.4: Measurement of head.....	65
Figure 3.5: Stuck bubbles after measurement completion.....	66
Figure 4.1: HCCI Intake Heaters in the form of a closed-loop response.....	72
Figure 4.2: PID Controller.....	73
Figure 4.3: Hcci_params m-file for heater	74
Figure 4.4: Start_hcci speed/temperature file.....	75
Figure 4.5: Behind the "double-click" prior to running simulation.....	76
Figure 4.6: Actual vs. Set point Temperature with Engine Variations.....	77
Figure 4.7: Simulink model representing HCCI engine's intake heater	78
Figure 4.8: Intake Enthalpy Representation.....	79
Figure 4.9: Exit Enthalpy Representation	80
Figure 4.10: Average Mass and Specific Heat Representation.....	81
Figure 4.11: Mass Average Representation	82
Figure 4.12: Specific heat representation.....	82
Figure 4.13: Heater Coil Representation.....	84
Figure 4.14: Heater Wall Temperature Representation.....	85
Figure 4.15: Heater thermal circuit.....	87
Figure 4.16: Model for finding heat transfer coefficient inside heater.....	88
Figure 4.17: Variations in PID and its Effects on Temperature Response	91
Figure 4.18: Heater Response with $k_p=2.5$	92
Figure 4.19: Heater Response with $k_p=5.0$	93

Figure 4.20: Heater Response with $k_p=10.0$	94
Figure 4.21: Theoretical Temperature Maintenance with Engine Speed Variance.....	95
Figure 4.22: Motorola's 68HC12 Microcontroller on Circuit Board	97
Figure 4.23: Flowchart Illustrating Temperature Set Point Data	99
Figure 4.24: Setpoint reads "2799," but is 279.9F.....	101
Figure 4.25: Hypercell PID Screen	102
Figure 4.26: Flow Rate Comparison with Heater Variable during Motoring Process.....	103
Figure 4.27: Preliminary Experimental/Theoretical Heater Comparisons.....	104
Figure 4.28: Fine Tuning of "HCCI_params" to Match Experimental Data	105
Figure 4.29: Final Simulink Model Following Experimental Curve.....	106
Figure 4.30: Complete Hypercell PID Tuner.....	108
Figure 4.31: Similar Temperature at Different Intake Tract Locations.....	110
Figure 5.1: HCCI Control Desk (BCU: Top Left, Engine Parameters: Middle Left, In-Cylinder Pressure: Bottom-Left, Intake Heaters: Center, Emissions: Middle Right, Cellmate and Testmate: Far-Right).....	112
Figure 5.2: Initial Motoring Process before Adding Fuel	115
Figure 5.3: HCCI Misfire Due to Low Temperature of Insufficient Fuel Injection.....	116
Figure 5.4: Cal Poly's Successful HCCI Engine.....	117
Figure 6.1: One Control Feedback to Four Heaters.....	119
Figure 6.2: Temperature Feedback with Four Signals, Four Heaters, Varying Engine Speeds and Temperature Set Points.....	120
Figure 6.3: In-Cylinder Pressure with #3 and #4 Knocking.....	122
Figure 6.4: In-Cylinder Pressure Traces During Stable HCCI Combustion.....	123
Figure 6.5: In-Cylinder Pressure Traces Illustrating Knock in Cylinder #4	124

LIST OF TABLES

1: Volkswagen 19L TDI Engine Specifications.....	129
2: Kimball Parts Purchase List.....	129
3: Engine Speeds and Corresponding Theoretical Flow Rates.....	130
4: Preliminary Heater Calculations for Flow vs. Engine Speed.....	130
5: Engine Buildup #2 Head Measurements.....	130
6: Engine Buildup #2 Block Measurements.....	131
7: Compression Ratios for Engine #2 Buildup.....	131

LIST OF EQUATIONS

Equation 2-1: Ideal gas law.....	36
Equation 2-2: Flow rate conversion.....	36
Equation 2-3: Fuel/Air Equivalence Ratio.....	42
Equation 2-4: Substitution.....	43
Equation 4-1: General energy balance equation.....	69
Equation 4-2: Simplified energy balance equation.....	69
Equation 4-3: Assumption of constant mass with time.....	70
Equation 4-4: Use of chain rule.....	70
Equation 4-5: Rearranging terms.....	70
Equation 4-6: Substituting heater characteristics.....	70
Equation 4-7: Separating tight side to three distinct terms.....	71
Equation 4-8: Conversion from CFM to Mass Flow Rate.....	80
Equation 4-9: Energy Balance of Heater Coil.....	83
Equation 4-10: Heat loss by radiation exchange with inside wall.....	83
Equation 4-11: Heat loss by convection from heater coil.....	84
Equation 4-12: General equation for heater coil energy balance.....	85
Equation 4-13: Heat transfer by convection out of outer wall.....	86
Equation 4-14: Heat transfer by convection out the inner wall.....	86
Equation 4-15: Wall Temperature Representation.....	87
Equation 4-16: Reynolds number.....	88
Equation 4-17: Determination of convection heat transfer coefficient \bar{h}	89

1. INTRODUCTION

From the late nineteenth century until present day, two dominant, four-stroke, combustion methods have found their ways into the majority of today's automobiles. The average family car is most likely powered by a spark ignition (gasoline) engine, while bigger, heavy-duty vehicles are equipped with a compression-ignition (diesel) engine. Over the past century or so, these two concepts have seen many technological advances, but have overall remained the same. Though each has evolved to offer relatively high energy density compared with other types of fuel, they inevitably emit toxic gases into the atmosphere. With more and more people becoming dependent on the automobile, and because the world's oil supply is not a bottomless pit, we must find different ways to either stop or slow-down the oil-draining and polluting process. The Environmental Protection Agency (EPA) sets emissions standards for engine manufacturers to abide by in order to reduce the levels of nitric oxides, hydrocarbons, carbon oxides, and other pollutants deemed harmful to mankind's health or the environment.

Fortunately there currently exist a number of solutions. Hybrid electric vehicles, a common sight today, combines an electric power source to a small conventional gasoline/diesel engine, which helps minimize the need for a big thirsty, high-emitting engine. Some vehicles now offer "cylinder deactivation," where one bank of cylinders is turned off during normal, constant-load operation. However, despite these somewhat beneficial solutions, their pollutants are still present because of their conventional combustion methods. Researchers have therefore tried new methods of combustion to reduce both emissions and fuel consumption: one of them is homogeneous charge compression ignition (HCCI). It is

compared with the Otto and Diesel cycle. However, the cycles to be discussed are not thermodynamic cycles; rather they are representations that allow one to "follow the state of the working fluid as the engine executes a complete operating cycle." ¹

1.1 SPARK IGNITION COMBUSTION: OVERVIEW

The Otto cycle is used to define Spark Ignition Combustion. The order of the strokes is: Intake, Compression, Combustion, and Exhaust. The engine cycle starts off with the intake stroke, where the piston, situated at top-dead-center (TDC), moves away from the top while drawing fresh ambient air along with fuel (gasoline) with the intake valve opened. The intake process changes to compression when the piston approaches bottom-dead-center (BDC). The intake valves closes and the piston now goes back to TDC, thus compressing the gasoline/air mixture. When the piston returns to TDC, the gasoline/air mixture is very vulnerable to combustion, and the compressed mixture aids in creating a more powerful blast. The spark plug fires off and ignites the gasoline, causing an explosion that drives the piston down in the combustion stage. The fuel/air mixture keeps the flame propagating throughout the chamber, and the pressure climbs with constant volume. This pressure pushes the piston past BDC and back up to TDC, into its exhaust stroke. Right before BDC, the exhaust valve opens up and expels the combusted gasoline/fuel mixture out to the atmosphere. At TDC, the exhaust valve closes while the intake valve opens, and the engine cycle is repeated again with the intake stroke. Figure 1.1 illustrates the working fluid as it goes through an Otto cycle process.

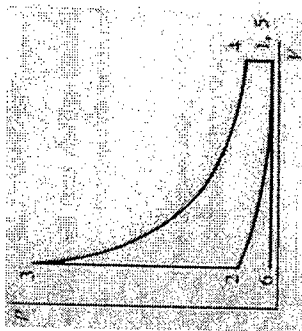


Figure 1.1 Pressure-Volume Diagram for Otto Cycle

The cycle starts off with (1-2), where, at BDC, the piston begins compressing the fuel/air mixture. At (2), TDC, the spark plug sets off a high voltage across its electrodes, and that initiates the flame in the chamber and causes in-cylinder pressure to rise. During (3-4), the piston moves through its expansion stroke, giving work out of the system. At BDC, the exhaust valve opens, and (4-5) illustrates the "blowdown" process where, because the pressure in the cylinder is greater than the ambient, the burned gases are expelled from the chamber. In process (5-6), the piston pushes the exhaust gas out, and in (6-1), the piston pulls a fresh air/fuel mixture back in. The open intake and exhaust valves model the pressures inside the chamber as constant.

One of the biggest problems in an SI engine is abnormal combustion, also known as knock. This is the result from auto ignition of fuel ahead of the flame front created by the spark plug. When the flame is propagating across the chamber, some of the unburned mixture is compressed, which causes pressure, temperature, and density to increase. This increase can create certain chemical reactions which ultimately lead to auto ignition. A high energy release comes out of the auto ignition, which causes high-frequency pressure waves. These

waves are what create the sharp pinging noise called knock. Knock is prevented by the fuel's knock resistance as well as the antiknock characteristics of the engine.

Although many engines nowadays offer enhancements such as variable valve/cam timing, non-existent throttle bodies, or cylinder deactivation, the spark ignition engine still operates on the same basis it has over a century ago.

Emissions in SI Combustion

The SI engine is known to exhaust gases that contain nitric oxide as well as nitrogen dioxide, combined to be known as NO_x [2]. According to Heywood, NO_x is a mixture of nitric oxide NO and nitric dioxide NO_2 that commonly lumped together. NO_x forms primarily when the combustion temperature inside the cylinder chamber reaches over 1700K. Temperatures below this point render NO_x formation negligible. In SI engines, combustion begins at the spark plug, causing a flame front to travel through the cylinder. This flame propagation typically occurs right before top dead center (TDC) of the piston travel. As the flame front propagates through the fuel/air mixture, the temperature and pressure within the cylinder increases, while the cylinder finishes compressing burned and unburned gases. The flame front contains the hottest point of the burning gases and thus concentrates the formation of NO_x . This increase in pressure induces work on the piston to push it back down on the expansion stroke, causing the pressure and temperature to drop. Emissions vary through different engine designs, but generally emit around the same amount of pollution. NO_x levels are around 500-1000ppm. NO is formed usually forms behind the flame-front through nitrogen and oxygen molecule reactions, and its rate is heavily dependent on the combustion temperature.

As with hydrocarbons (HC), the normal range is around 1000-3000ppm. Converted, this corresponds to about 1 to 2% of the fuel flow going into the engine. HC is heavily affected by the air/fuel ratio. With rich mixtures, not enough air will be available to burn-off all the fuel. With very lean mixtures, the HC levels can also rise due to misfire or incomplete combustion. HC is mainly formed on the walls of the cylinders, the crevice volumes between the piston and the walls, absorption of fuel vapor into the cylinder wall's oil layers, and by poor combustion.

Carbon monoxide emissions are the result of rich mixtures and come from the excess fuels. It is controlled through close monitoring of cylinder-to-cylinder variations, and is also prevalent in transient engine operation, where different amounts of fuel are needed.

1.2 COMPRESSION IGNITION COMBUSTION: OVERVIEW

With a four-stroke compression ignition engine, the spark plug is absent because combustion results from fuel injection into air compressed to high pressure. The compression ratio on a Diesel cycle is usually higher, around 12-24:1 versus 8-12:1 for SI engines, to accommodate combustion, and although there are four stages in a four-stroke diesel cycle, the time for the fuel injection is different. During the intake stroke, the piston draws in only ambient air. Because of the lack of a throttle plate as well as drawing only air, the volumetric efficiency is much higher compared to that of an SI engine. In addition, the higher compression ratio results in higher thermal efficiencies. After reaching BDC, the intake valve is closed, and the piston compresses the air inside the chamber towards TDC. While this occurs the air inside the chamber heats up by the Ideal Gas Law PV/mRT . At about 20° before TDC, a high pressure fuel injector sprays the desired amount of fuel into

the chamber. The fuel sprayed is very fine and atomizes into drops within the compressed air. As the liquid fuel evaporates, its vapors mix with the air. After a short delay period, the mixture starts the auto-ignition process and causes combustion, thus pushing the piston back to BDC. The air, fuel, and gases continue mixing, making combustion continue through part of the piston's expansion stroke. At BDC, the exhaust valve opens up and pushes out the combusted mixture. The piston moves back to TDC, pushing out all the exhaust. When the piston arrives at TDC, the exhaust valve closes, and the intake valve opens, allowing fresh air to be drawn in for the next cycle. Figure 1.2 illustrates the processes the working fluid undergoes during this engine cycle.

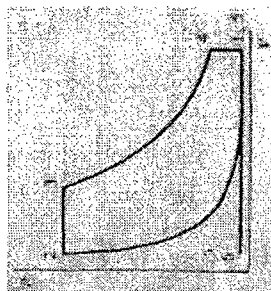


Figure 1.2: Pressure-Volume diagram for a Compression Ignition Cycle

Similar to the SI engine intake process, the cycle begins with work being put into the system from the previous system in the form of compressing only air (1-2). At TDC, heat is put into the system in the form of fuel injection. When that occurs, the piston expands while the flame front continues to burn through the air/fuel mixture. As expansion continues, the piston moves through its stroke, yielding the term "constant pressure" combustion. Work is given out until the piston reaches BDC (4). At (4-5), the exhaust valve opens, allowing the

blowdown process to take place. Exhaust air is displaced (5-6) out to the atmosphere by the piston's exhaust stroke, and process (6-1) illustrates the piston drawing fresh air in for the next cycle.

Since engine power is restricted by the amount of air in the cylinder, most diesel engines (especially large engines) are equipped with turbochargers to increase the density of the inlet air. Thus more fuel, about five percent of the air's mass in the cylinder, can be injected, and more power can be delivered, all while reducing the amount of black smoke in the exhaust [3]. The black smoke, which starts emanating at around 0.7 equivalence ratio, is what contains particulate matter and NO_x . The diesel engine is also somewhat limited by engine speed because the diesel fuel, once injected into the combustion chamber, requires "a short but essential constant amount of time before it starts to burn" [4]. If one sets engine speeds too high, the fuel would never get a chance to initiate its burn process.

Emissions in CI Combustion

Just like an SI engine, the NO_x formed in a CI engine is a result of high combustion temperatures. Overall equivalence ratio also has some effect on NO_x , a higher equivalence ratio (richer mixtures) lead to higher NO_x output.

Hydrocarbons are formed through a variety of operating conditions, and engine-idling/light-load operation produce noticeably higher HC emissions than during full-load operation. When running the engine too rich, HC emissions also increase. Overmixing, a term used for "overcleaning," is an important source for HC. Undermixing, a situation where some of the fuel sprayed from the injection escapes combustion by remaining inside the injector nozzle, also causes high amounts of HC.

15

Particulate matter, consisting mainly of carbon material (soot), result from incomplete fuel hydrocarbon combustion. These amounts are usually around $0.2\text{--}0.6 \text{ g/km}$ [5], and changes composition through temperature increase. The highest particulate concentrations are found in the fuel injection's core region where the equivalence ratios are very high.

1.3 AIR-STANDARD DUAL CYCLE

Though the Otto and Diesel cycle are used to represent SI and CI combustion, respectively, are not the best ways to describe the pressure/volume relations in an actual internal combustion engine. The flame propagation initiated by either the spark plug or fuel injection takes a certain amount of time before it is completed, and during that time the piston travels downward in its expansion stroke with constant pressure. Therefore the Air-Standard Dual, or Limited-Pressure Combustion Cycle is introduced.

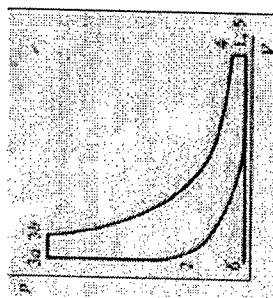


Figure 1.3: Pressure-Volume Diagram for Dual Cycle

For this cycle, the compression process is the same as that for the Otto and Diesel cycle, but the heat addition in this case occurs in two steps. (2-3a) involves constant volume heat

16

addition and contains no work, and (3a-3b) represents the heat added through constant pressure along with work given out. Since combustion occurs at both constant volume and constant pressure, the name "limited pressure" is thus given to this combustion. For process (3b-4), the piston travels the rest of its way to BDC with the help of the built-up pressure inside. (4-5) is the blowdown process, and the exhaust (5-6) and intake (6-1) stroke is the same as the two previous combustion cycles.

1.4 HCCI COMBUSTION: OVERVIEW

Homogeneous Charge Compression Ignition (HCCI) is a combustion process that is capable of being both highly efficient and low emitting. HCCI combines the auto-ignition characteristics of a CI engine with the premixed fuel/air mixture of the SI engine. HCCI has the potential to produce high thermal efficiencies due to higher compression ratios seen in that of diesel engines.

HCCI can be obtained either by indirect or direct fuel injection. The compression ratio is higher than that of gasoline engines; this ensures that auto-ignition is possible. However, too high of a compression ratio can result in knock. Because direct injection offers less time for the air/fuel mixture to homogeneously mix, many of the research engines available currently operate with port fuel injection. A small amount of fuel (gasoline as an example) is injected into the cylinder during the intake stroke, and during compression, the fuel and air reach homogeneity. As mentioned before, combustion occurs from auto-ignition; therefore sparkplugs are non-existent. As the piston hits TDC, combustion occurs simultaneously throughout the cylinder's combustion chamber, unlike those seen in both SI and CI engines

[6]. Figure 1.4 depicts the combustion stage of a single cylinder with port fuel injection and lack of spark plug

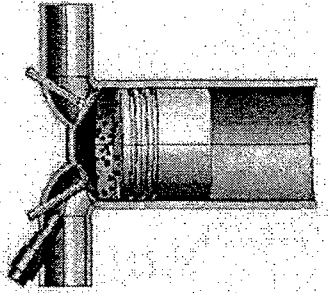


Figure 1.4. Spontaneous HCCI combustion spots in chamber representing combustion) [7]

Emissions in HCCI Combustion

Although the biggest gain in HCCI combustion is the drastically reduced pollution, there still exists trace amounts of emissions.

Temperatures that were once high enough to form NOx are now too low to do so, which results in the freezing reaction of the pollutant to be exhausted on the cylinder's expansion stroke. Reductions of up to 90-98% are usually seen during HCCI combustion (Figure 1.5). NOx is an environmental issue because of the health reasons and the human's body's reaction to it

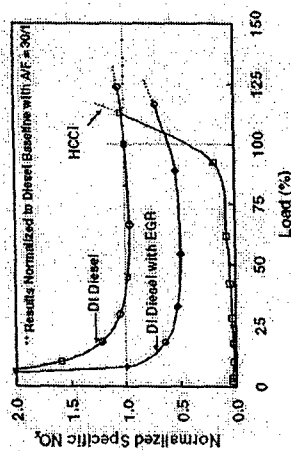


Figure 1.5. *NO_x emissions vs. engine load for typical HCCI and DI Diesel combustion [8]*

According to Stangmaier et al., HCCI also is reported to produce low smoke levels as well as particulate matter emissions. Though the PM formation mechanism is still not fully understood, one possible explanation is that the absence of fuel-rich regions in the combustion chamber discourages soot formation.

However, hydrocarbons (HC) and carbon monoxide (CO) emissions are higher than those in a regular diesel engine. One reason for this could be that the low in-cylinder temperatures due to the lean mixtures contributed to decreased post-combustion oxidation rates within the cylinder and increased levels of HC and CO. Mixture preparation is very important in reducing HC emissions because the liquid fuel deposition on the combustion center surfaces result in increased HC emissions.

In some regards, many claim that HCCI combines the best features of SI and CI engines and is potentially applicable in a wide range of uses. From heavy truck to consumer-scale automotive applications, an HCCI engine could be scaled for use in almost any transportation vehicle. The concept is valid on any piston engine and could be used on

other applications such as stationary power generation or for engines used at a farm to pump water continuously. HCCI is best suited for use in hybrid vehicles because of the lack of demand for the engine to operate over a wide range of speeds or loads compared to a regular vehicle. Implementing HCCI into hybrid vehicles further extend existing benefits of a fuel-efficient vehicle to one that pollutes noticeably less.

However, there currently exist a number of problems that hinder HCCI combustion from finding its way into mainstream society. The problems include packaging, power output, and probably the most important, having full control of when auto-ignition occurs. Since no spark plug exists, not is there direct injection of fuel to initiate the combustion process, there is no sure-fire direct way to control when combustion occurs. There are various indirect ways, and these include water injection, variable valve actuation, inlet air temperature, air/fuel chemistry, as well as compression ratio.

1.5 HCCI RESEARCH

HCCI has made itself a viable solution to today's environmental and health issues. The world is rapidly depriving itself of the fossil fuels used to power today's internal combustion engines. Society has come to rely more and more heavily on the automobile. Since 2001, crude oil prices have doubled [9], and as a result many research institutions are currently finding ways to reduce our world's dependency on crude oil. Along with the recent development of gasoline direct-injection technology, HCCI is becoming a viable source of power for future vehicle applications, especially with running on the hybrid electric mode. HCCI combines the best features of the spark ignition and compressed ignition combustion concept, and these two result in better fuel economy as well as lowered NO_x emissions,

provided that accurate control is made. Until recently, this obstacle hindered HCCI from becoming more approachable, but modern technology and cutting-edge controls have made the combustion more controllable. As different institutions find ways to reliably control the auto-ignition process of HCCI, the concept itself becomes closer to the consumers' hands. Even today, certain institutions have started testing the feasibility of applying HCCI to an automobile.

1.6 CURRENT HCCI TRENDS / DIRECTIONS

GDI HCCI

A small number of institutions have started experimenting with the gasoline direct injection "GDI" concept with HCCI. GDI itself was recently first made public in automobiles by Mitsubishi Japan. Soon other companies started equipping their line of vehicles with GDI engines. GDI technology yields better efficiency when compared to regular ported-injected engines because of the lack of throttle plate, a hindrance to volumetric flow. The fuel injectors are of a high-pressure type, which help further atomize the fuel and yield less "wet spots" in the chamber, proponent to formation of hydrocarbon. Fuel economy is increased through the use of a leaner fuel/air mixture. This, in conjunction with HCCI, has been seen on a few engines, which have yielded positive results.

GDI engines are becoming increasingly common in vehicles OUTSIDE the United States, particularly Japan and Europe, where the sulfur content in fuel is substantially lower. The high sulfur content here in the States renders the high pressure fuel injectors useless by clogging their spray nozzles. There are, however, a few companies who have introduced

variants of the GDI to the American consumer. BMW currently offers GDI on their 6.0L V12 760iL luxury sedan, and Rolls Royce offers the technology in their 6.75L V12 Phantom super car. Isuzu, on a generally lower price spectrum recently introduced a 3.5 liter V6 engine for its Axiom SUV. Audi has also recently introduced their line of FSI direct injection engines that operate with a homogeneous and stratified charge.

Because these trends are still very new, and that Cal Poly is trying to establish itself on firm ground, the idea to utilize GDI technology into the project is delayed perhaps until future research.

HCCI as Part of a Hybrid Power Source

Currently HCCI seems most appropriate in a vehicle as a source of energy. Although HCCI has the potential to be green, its drawbacks include range of operation and low power output. A leaner mixture results in cleaner burning, but at the same time outputs substantially less power. In addition, current technology only allows HCCI to operate in a limited speed range, better when engine speed is constant. With these limitations, it seems most suitable that HCCI be used as a power generator, in farming equipment or even in hybrid vehicles to charge the vehicle's batteries. The engine will operate at constant load and combustion will be more reliable. At the present time, the EPA has their modified VW 1.9L HCCI engine in the process of fitting it to the group's hydraulic hybrid vehicle, currently a rolling chassis [10].

Actually two cutting-edge technologies into one, the hydraulic hybrid uses a hydraulic powertrain and hydraulic propulsion integrated to the vehicle's axle 11. Instead of using batteries and electric motors, the hydraulic tanks and motors store the energy captured from

braking. This technology is currently seeing much development in urban delivery vehicles, where the benefits are most prevalent in stop-and-go driving.

The EPA's HCCI engine contains port fuel injection with Toyota Prius 12-hole gasoline injectors. The original pistons from the existing VW engine were replaced with shallow dish blow pistons yielding 16.5:1 compression ratio. In addition to the stock variable geometry turbocharger, the EPA equipped their engine with a supercharger to help improve transient operation. Through their HCCI setup, the EPA has reported that the engine is flexible enough to operate in a wide range of conditions, provided that the engine has warmed up. As for Cal Poly's HCCI engine, it is desirable to one day fit the unit into the university's Hybrid Vehicle Club's Ford Explorer. To work smoothly as a hybrid powerplant, though, the HCCI engine must overcome the limited steady-state operating range as well as transient operation response.

Various Fuels

Different institutions have experimented with various types of fuels to achieve the most successful HCCI combustion. However, diesel fuel has been rather unfavorable due to its low ignition resistance. Diesel engines, however, seem most suitable because of their robust designs. Therefore researchers have converted various diesel-based engines to operate on fuels ranging from alcohols to CNG to even gasoline, which Cal Poly has done so. Its readily availability makes the fuel easier to obtain, and hopefully one day more consumer-oriented.

However, if desired, and HCCI engine can technically be operated with any type of liquid fuel, provided that the correct combustion ratio is applied to the new fuel [12]. For instance,

if running with n-heptane, then the desirable compression ratio would be 11:1. If running with RON 98, then the compression ratio would have to be increased to a diesel-like 21.5:1.

1.7 CAL POLY'S HCCI RESEARCH GOALS

Cal Poly State University is still relatively new to the HCCI concept and race. Therefore the project must establish a solid foundation, and in this case, it means to get the concept operating in a basic form. HCCI was previously headed by then Professor Brian Higgins shortly after he joined the Cal Poly faculty. Having previous HCCI experience with UC Berkeley, Lawrence Livermore National Labs, as well as Sandia National Laboratory, he brought the idea as well as the basic hardware necessary to get the project started. Two graduate students, Patrick Ferri and Maria Franco, performed their thesis on setting-up and operating in HCCI mode. Unknown reasons resulted in their engine's failure, but a number of useful data points was collected, and therefore Ferri and Franco went on to complete their thesis [13].

When Professor George Delagrammatikas joined the Mechanical Engineering team, in addition to taking over the HCCI project, he took two graduate students, Taylor Cheung and Nicholas Jacques, to proceed towards establishing HCCI again. The two students as well as other project members performed an exhaustive literature study covering all the aspects of HCCI ranging from different engine configurations, test stand setups, hardware specifications, and so forth. Dr. Delagrammatikas at this time also put much effort into finding ways to fund the HCCI project, which included multiple proposals to the California Central Coast Research Partnership (C3RP).

There have been many different methods of initiating the HCCI concept, but Cal Poly's plan was, as mentioned before, to establish a solid foundation. Thus the group decided to obtain HCCI combustion with regular 87-octane gasoline under multi-port injection. Once this engine can reliably run, Dr. Delagrammatikas hopes to incorporate it into the automotive-related courses taught at the university. In addition, future students working on the HCCI engine will have opportunities to update its components like implement the GDI (gasoline direct injection) concept, operate on multiple fuels, as well as rebuild the unit to act as a power generation unit in a road-going vehicle.

Methods of Controlling Auto-Ignition

Besides running on regular port fuel injection, Cal Poly wanted an engine that would offer good control of auto-ignition in the cylinders. As mentioned, one of the biggest issues preventing HCCI from mainstreaming is having direct control of auto-ignition. However, the various modes of indirect control, and these methods include intake air temperature control, variable valve timing, forced induction, fuel injector location, and exhaust gas return, to name a few.

Yamaoka et al. has experimented with different types of fuel injection characteristics in trying to control auto-ignition and combustion in each cylinder every cycle [14]. In their studies, the team compared different spray shapes, pressure conditions, and spray pulse widths. These different variables affected the extent of homogeneity inside the combustion chamber. From their studies, the team concluded that later fuel injection timing between intake and compression stroke amounted to a more inhomogeneous mixture, and that NO_x

25

levels as well as combustion variance increased. Their standpoint was that combustion and auto-ignition was best controlled through precise fuel injection monitoring.

Kopecek et al. [15] has performed research on utilizing "Q-switched" lasers. These lasers deliver a short-pulsed, high-intensity radiation to the region. In addition to generating non-resonant optical breakdown in different gaseous environment, the laser-induced plasmas also offers a number of advantages over the spark plug, like abilities to ignite leaner mixtures and more arbitrary location of ignition location. The team also had their engine equipped with intake heaters to aid HCCI combustion.

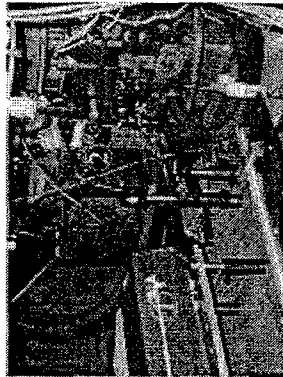


Figure 1.6: Kopecek et al. HCCI setup: 1. Pulsed Nd: YAG-laser; 2. focusing optics; 3. Volvo TD 100 engine

Law et al. [16] from Lotus Engineering has extensively used exhaust gas return (EGR) to yield better operating characteristics during HCCI combustion. Their method in controlling EGR back to the combustion chamber is through "advanced active valve train." The team has devised two exhaust valve control strategies in obtaining desirable HCCI combustion. The two methods differ in the exhaust valve opening/closing timing, but both are regarded

26

as "internal EGR mixing." The first strategy involves closing of the exhaust valve earlier in the exhaust stroke to trap a certain amount of hot exhaust gas, whereas the second strategy opens both intake and exhaust valves during the intake stroke, inducing a hotter air/fuel mixture into the chamber. These strategies, as noted by Lotus, help keep temperatures away from contacting the engine's "cooler" surfaces; thus temperatures remain high all the time.

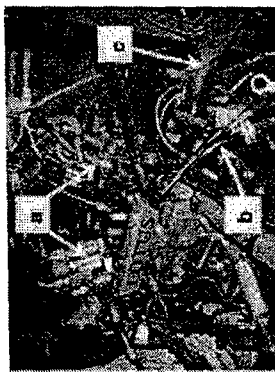


Figure 1.7: Side view of engine showing a. active valve train, b. nitrogen/air-feeding pipes, c. exhaust pipe

The Environmental Protection Agency also has a 1.9L VW TDI engine that is converted to HCCI use [17]. In addition to the stock turbocharger, the team there implemented a supercharger (along with intercooler) to aid in HCCI starting as well as transient operation. Their method of controlling HCCI start of combustion includes adjusting fuel rate, boost level, EGR intake charge, and coolant temperature. For the EPA to deem their engine operation as transient, the inputs must accommodate rapid changes in intake flow rates, boost level, and intake temperature. Through adjusting the intercooler fan speed, the EPA can have some control over the intake temperature.

Christensen, et al. [8], at one point, used a Volvo TD100 turbodiesel engine that ran HCCI on one of the six cylinders. Along with his associates, they implemented inlet air heating with an electrical heater. Water injection was then introduced to slow-down the rate of combustion and control ignition timing. Too fast of a homogeneous combustion rate can generate knock related problems. In addition, the steep pressure increase, along with noisy operation, can wear the engine substantially. From their studies, use of water injection helps retard the ignition timing and combustion rate, but "only in a narrow range." However, hydrocarbons emissions increased because of further lower combustion temperatures. As mentioned, water injection results in poorer combustion quality.

Ferri and Franco maintained, to some degree, control of their HCCI engine by incorporating water injection [19]. Their injectors were 20lb/hr gasoline fuel injectors fed to a common rail, pressurized to operate at 44psi. The water injection system operated on open loop response. Because of an incident involving flooding their engine, Cal Poly's second HCCI engine would utilize a better method of intake temperature control.

Dibble et al. [20,21] has approached the auto-ignition problem with possibly one of the better methods—a preheater that warms the intake air to a desired temperature before heading into the engine. Their engine has been operating in HCCI multi-cylinder mode since October 1999, and though they have performed many tests with various fuels and compression ratios, their intake heater has remained the same through the years. Dibble notes that operating their engine in multi-cylinder mode is quite difficult because of the engine's extreme sensitivity to temperature. "Small differences in temperature from one cylinder to the next can cause a colder cylinder to misfire or a hotter cylinder to ignite very early," the professor explains.

The HCCI team at Cal Poly currently does not have the money to implement advanced valve trains or plasma-induced combustion technologies into their engine to be built. They also do not have the time to try again to see if Ferri's and Franco's water injection system would work again. However, after a lengthy period of research, Dr. Delagrammatikas decided to impose four individual heaters, something no other institution has performed on an HCCI engine. To justify four heaters, the team felt that the idea, which individually heats the air going to each cylinder right before heading into the intake manifold, would give more temperature control over one giant heater on a single tract to the intake manifold, something UC Berkeley's HCCI group currently uses. Plus, a system like this will help extend the longevity of the engine by giving the user/operator more control over knock/misfire. An intricate heater control system like this has not been accomplished by other institutions, so it would be very novel for Cal Poly to introduce it to other HCCI-oriented institutions.

The objective of this thesis is to establish a preliminary framework on Cal Poly's HCCI Engine Intake Temperature Control. The control methods might be crude, but its validity is present once HCCI combustion occurs. Although there are many ways to obtain perfect control of the temperature, the framework provides future researchers to build upon and improve on.

2. HARDWARE AND MODIFICATIONS

Cal Poly's HCCI engine operates with extensive hardware modifications ranging from different suppliers to in-house fabricated parts. Every part on the engine is scrutinized to determine its usefulness in contributing to HCCI operation. Much of the funding for these parts was graciously provided by the C3RP as well as other grants that Dr. Delagrammatikas made possible through proposals.

2.1 VW ENGINE SPECIFICATIONS

Overland Parts, a group specializing in VW and marine diesel engines, has kindly supplied Cal Poly with a newly rebuilt 1.9 TDI turbodiesel long block at a discounted price. The unit donated consisted of the main engine block (with crankshaft), cylinder head and valvetrain, a fuel pump, and oil pan. The original engine's dimensions are as follows in Appendix A1.

Because the engine was originally operating with diesel fuel, the piston crowns were shaped with a bowl so that upon the compression stroke, the fuel inject can concentrate in the confined space (creating a stratified mixture). The compression ratio is listed as 19.5 by VW, but measurements performed by the students reduced that value to 18.34, averaged among the four cylinders. The intake manifold was provided, but would later be modified for the project's goals. The Garrett VNT turbocharger wasn't included, which did not affect the project for Cal Poly's HCCI engine would not utilize the unit. The drive-belts, not included, would be purchased from online VW specialty stores or the local VW dealer when the rebuilding process starts to materialize. In order to account for the possibility of lack of combustion, the fuel injectors were bored-out to accommodate spark plugs to ignite the air/fuel mixture. This ensures combustion in every cycle, even if HCCI does not occur.

2.3 INTAKE DESIGN/HARDWARE

As mentioned, one of the biggest problems with putting HCCI to production is the issue with auto-ignition control. Because HCCI is somewhat similar to knock, many researchers have been trying to find ways to control/predict time of combustion. Various methods of control have been implemented, and so far the solution of pre-heating the intake air has been the most popular and easiest to help control combustion. Examples include the use of a turbocharger to create the heat necessary for combustion. With too much heat though, comes premature ignition (HCCI knock) therefore some institutions (including Cal Poly's previous HCCI group) installed water injection into the intake manifolds. The use of water injection cools intake air should the turbocharger raise the temperature too high.

As mentioned, Cal Poly's current HCCI team has decided to try an "opposite" approach by using a heater for each of the intake ports going to the cylinders. The existing VW intake manifold from the previous HCCI group was chopped and modified until only the openings to the engine head are left. The inside of the manifold is bored using a hand-held grinder to accommodate more air, and the existing water injection holes were replaced with fuel injectors. The heaters' tube diameters were too big to directly attach to the modified intake port. Therefore custom-machined venturis (Figure 2.1) are connected by flexible hose tubing to transition the diameters.

32

The fuel injectors will be located in the intake manifold to allow thorough air/fuel mixing.

The fueling system, originally confirmed to be some sort of GDI, was changed over to port fuel injection (PFI) to maintain simplicity.

Because there is desire for full control of the engine, pressure and temperature information for all areas of the engine is required. In-cylinder pressure transducers are utilized to measure pressure as well as incorporate a combustion sensor. Other pressure transducers/thermocouples are located in the engine oil pan, exhaust and intake manifold, as well as cooling system. Thermocouples are placed in the cooling system, oil pan, fuel line, before and after the intake heaters.

2.2 KIMBALL VW PARTS LIST

As a result of having to completely teardown and rebuild the VW TDI engine, many of the parts holding the different engine assemblies together have to be replaced. VW uses stretch bolts, which are single-use bolts that actually deform plastically—it stretches and will not return to its original length after it has been removed. The stretch bolts are used over the conventional versions so that the head gasket can seal even with different expansion properties from the aluminum head and the iron block. The head gasket used was VW's "three-hole" version, which is the thickest version available. New exhaust and intake gaskets are acquired because the old ones are useless once the manifolds are taken off. Various O-rings and other seals are acquired as necessary. When the Bentley Volkswagen repair manual (Rad Book) [22] specifies to "always replace," no corners are cut. The complete Kimball parts list is shown in Appendix A2.

31

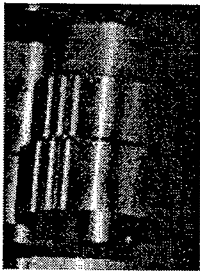


Figure 2.1 Aluminum Venturi for Bore Change in Intake

Baker Precision, a renowned company that specializes in manufacturing and processing of performance plumbing for turbo, coolant, and air intake applications, supplied the flexible hosing to complete the intake. The hoses used with the intake are knitted polyester fabric and reinforced with silicone rubber. Their temperature ratings are from -65°F to 350°F . In addition to providing a joint between the two diameters, the hoses help reduce engine vibrations to the heaters. 90° elbow joints are used to help keep the entire intake assembly more compact. Thus the actual heaters "float" above the engine head assembly. The hoses' lengths were also carefully measured to ensure that each intake track is the same as all others. The custom ports to the manifold are angled away from each other to accommodate the differences in diameter.

33

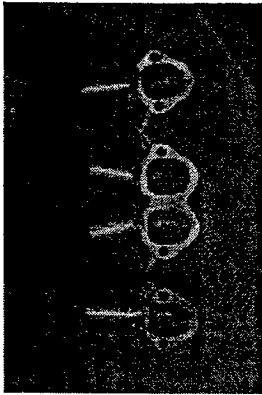


Figure 2.2 Custom Machined/Welded Intake Port

The heaters are then welded to a custom-made plenum to ensure that there is never a choked flow in the intake system.

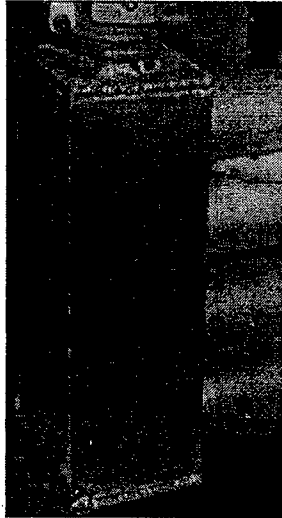


Figure 2.3 Plenum Before Heaters (Tubes on Bottom)

The plenum gets its air from a laminar flow element (LFE), which intakes from ambient atmosphere.

34

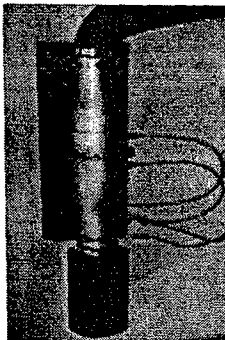


Figure 2.4: Laminar Flow Element with K&N Filter

There was originally speculation about bolting the heaters to the plenum so that replacements (if necessary) could be carried-out easier. Ultimately, the welding took place because of ease of procedure.

The heaters used are purchased from Omegalux®.

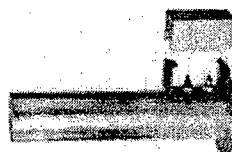


Figure 2.5: Omegalux 2kW Intake Heater

Only to be operated with proper airflow, the heaters provide up to 2-kilowatts of heat on 240VAC while the intake air passes through the heating elements sitting in the 2 3/8" O.D., 12" long aluminum tube. Maximum mass flow rate is 200CFM. When specifying the heater to be used, Jacques performed a number of calculations necessary to properly determine

what heater unit would be most appropriate [23]. In addition to a reasonable price, the heater has to output enough energy to heat intake air to HCCI combustion temperatures. The heater in this case is capable of providing air temperatures up to 600°F, but increase in airflow can quickly hinder rise times. Also, the discovery of only 208VAC meant that the maximum power available from the heaters was reduced to only 1.365kW.

With the volume of each cylinder stroke given at $4.741 \times 10^{-4} \text{ m}^3$, the ideal gas law can be manipulated to find the mass of the air entering the intake in one engine cycle. The pressure is ambient and temperature is the desired 412K.

$$\frac{P_1 V_1}{RT_1} = m \Rightarrow \frac{(95.00 \text{ kPa})(4.741 \times 10^{-4} \text{ m}^3)}{(0.287 \text{ kJ/kgK})(412 \text{ K})} = 0.000381 \text{ kg}$$

Equation 2.1: Ideal gas law

Having found the mass of air through each cycle, the mass flow rate is now desired to correspond with different engine speeds. One must note that an engine cycle includes two revolutions, and that intake of air only occurs in one of the cycles. The method to find the mass flow rate (at 1000RPM) is as follows:

$$m \left(\frac{1000 \text{ rev}}{\text{min}} \right) \left(\frac{1 \text{ min}}{60 \text{ sec}} \right) \left(\frac{1 \text{ cycle}}{2 \text{ rev}} \right) = \dot{m} \Rightarrow 0.003175 \frac{\text{kg}}{\text{sec}}$$

Equation 2.2: Flow rate conversion

In finding the mass flow rates for the anticipated engine operating range, the above formula was used with different theoretical engine speeds to come-up with their respective flow rates Appendix A3.

Heater Characterizations (Flow Rates)

After the heaters were obtained, Cheung, Jacques, and Laszlo performed preliminary flows to observe patterns in heater response.

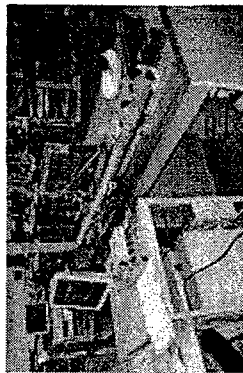


Figure 2.6: Preliminary Heater Testing Setup

The heater tract (Figure 2.6) is set-up to a desired length to accommodate the laminar flow elements length requirements. A manometer is used to measure pressure drop along the miniaturized laminar flow element. The opening to the fan is "throttled" with a cover to provide different flow rates. The team made a chart comparing flow (CFM) to pressure (inches H_2O) using the slope equation printed on the manometer. These values were then used to relate to the engine speed that the HCCI team wanted to see in their operation range. Appendix A4 shows the correlation between mass flow rate (CFM) and pressure (inches H_2O), which is then back-calculated to find the engine speed. Note that these flow values correspond to only one cylinder, and that to get the flow rate of the whole requires multiplying by "4."

By running these preliminary flow tests, the HCCI team now grasps a better feel of the heater's characteristics, such as heater response at different pressure (analogous to RPM),

37

rise and drop time, as well as steady state with various flows. A more comprehensive review of the preliminary testing can be found in Jacques [24]. Figure 2.7 illustrates the heater response from the preliminary tests. The legend shows the different flow rates and how they affect the temperature rise times.

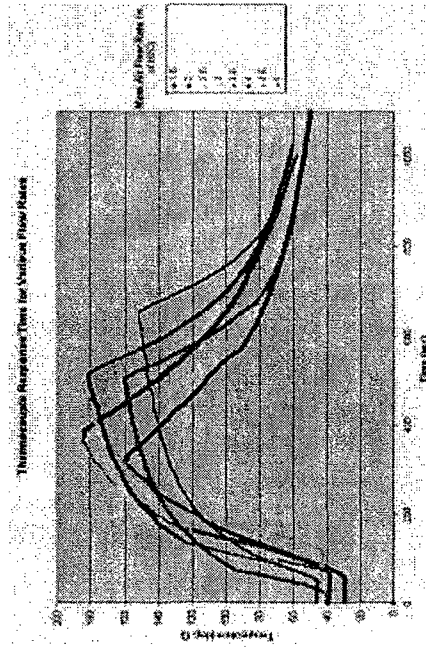


Figure 2.7: Preliminary Intake Heater Testing

It should be noted that with some of the flows, the temperature was not given sufficient time to reach maximum steady-state temperature, but the general curve illustrates how flow rates affect maximum temperature.

2.4 PISTON DESIGN/JUSTIFICATION

The original TDI engine's pistons were contemplated for feasibility in Cal Poly's HCCI application. Although UC Berkeley's Volkswagen HCCI engine operates on propane, they

38

initially retained the original TDI pistons in their engine. This had the Cal Poly students considering going the same direction. However, the diesel piston's "bowl-in-piston" design (Figure 2.8) is rather inappropriate for HCCI combustion. The bowl design is made specifically for diesel combustion, where fuel is sprayed into the bowl to create a stratified mixture. The flame propagation begins inside the bowl and gradually spreads throughout the combustion chamber as the piston continues its expansion stroke.

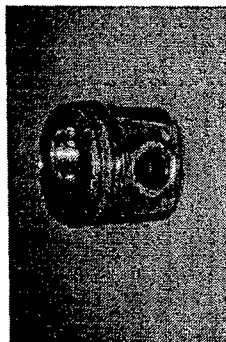


Figure 2.8: Original VW TDI "bowl" piston

With HCCI, combustion is spontaneous throughout the cylinder, so the bowl shape would actually act as an obstacle to homogeneous mixing. In addition, the boundary surfaces pertaining to the bowl in the diesel piston makes it susceptible to piston erosion due to the consequences of knock as well as high pressure changes [25].

With that the diesel pistons had to be replaced with a custom set that were "HCCI-friendly." Cal Poly's researchers desired an HCCI engine that would operate on common 87RON unleaded gasoline, and so the students studied other institutions that used the same fuel on their HCCI engine designs. The piston designs from Sandia National Laboratories as well as The Environmental Protection Agency provided the most influence on Cal Poly's HCCI

piston design. The pistons adopted a "dish" design, as Sandia has called it, which is basically a concave dome on the top of the piston to achieve the desired compression ratio. The design was drawn on SolidWorks CAD program, and the compression ratio was obtained by calculating the volume made from the depth of the dish geometry [26].

Other important piston design considerations included the piston ring land height [27]. Hydrocarbon emissions are formed from unburned gasoline mixtures, and most of this mixture is found in the crevice volumes between the piston and the cylinder chamber wall. To reduce this emission as much as possible, the piston ring land height was raised closer to the top of the piston without sacrificing durability. Finally, the rest of the piston's geometry mimicked that of the existing Volkswagen TDI piston, down to the indentation for the oil spray jets.

2.5 IN-CYLINDER PRESSURE TRANSDUCER SELECTION

Laszlo investigated into Opttran's line of high pressure transducers. Each unit costs about \$800, but they work nicely with AVL's Indimetre 619. The Indimetre relays information to computer software, which then displays real-time pressure data. The sensing element is couple by an optical fiber. The fiber leads to an enclosure that houses all the electronic circuitry. More information about its features and capabilities as well as operational procedures can be viewed in Jacques' thesis.

2.6 ECU SELECTION

The Engines Laboratory at Cal Poly San Luis Obispo houses a number of engines used for class instruction purposes. One of the engines is the Corporate Fuel Research (CFR) engine

used in "ME444: Internal Combustion Engines." The ECU used to relay information to the students is an older model Electromotive Total Engine Control 3 (TEC3). Because of its ease of operability and familiarity with the students and faculty, the new and improved TEC4 was acquired from Electromotive, Inc to control fuel flow into the HCCI engine. As described on the company website [28], the "TEC4 is a PC-programmable engine control system utilizing Windows-based tuning environment." The unit allows the user to operate the engine with throttle body injection, multi-port, or individual throttle bodies. Also new to the unit is the ability to perform on-board data acquisition, which allows the user to record data from up to twenty-five inputs including air/fuel ratios, injector duty cycle and pulse width, RPM, and others.

2.7 THERMOCOUPLE/PRESSURE TRANSDUCER SELECTION

The engine laboratory currently uses the K-type thermocouple from Omega Engineering. These units have been tried and tested and so it would be an unwise as well as time-consuming decision to switch to other types of thermocouples. The pressure transducers selected came from "Invensys Sensor Systems." Cal Poly Mechanical Engineering Department's Jim Gerhardt has had previous experience with these units, so Cheung and Jacques went on to specifying the dimensions and Jim made the order.

2.8 PROFESSIONAL LAMBDA METER SELECTION

The purpose of HCCI is to improve fuel economy and lower emissive pollutants drastically. In order to accomplish this, the amount of fuel ingested has to be extremely low. With a desired fuel/air equivalent ratio F of 0.3, or a relative air/fuel ratio ϕ of 3.33, the TEC4

exhaust gas oxygen sensor simply does not have the range to pickup such low fuel/air mixtures. MoTec's Professional Lambda Meter (PLM) is therefore sought to solve this issue (Figure 2.9).



Figure 2.9: MoTec Professional Lambda Meter

The unit is completely compatible with TEC4's software. In addition, the PLM offers the ability to be programmed to match the user's configurations. However, because of the TEC4's limited air/fuel range, Cheung and Jacques devised a method in which the MoTec's readings were scaled accordingly to match the TEC4's existing calibration. The TEC4 offered a limited Air/Fuel range of 10 - 29.28. According to Cheung and Jacques calculations, Cal Poly's HCCI engine needed an A/F around 48.662. That value is determined as follows:

$$\phi = \frac{F/A_{actual}}{F/A_{rich}}$$

Equation 2.3: Fuel/Air Equivalence Ratio

The F desired is 0.3, and the F/A for stoichiometric operation is 0.085 [29], so the values are substituted and rearranged to solve for the F/A for Cal Poly's actual HCCI operation.

$$(0.3)(0.0685) = F/A_{\text{actual}}$$

Equation 2.4: Substitution

The F/A_{actual} comes out to be 0.02055, but TEC'r operates with A/F_{push} , so taking the inverse of that value yield 48.662, as noted before.

To give a range of λ for the PLM to operate within, the λ limits for HCCI operation are set between 2.70 and 4.00, or a fuel/air ratio of 39.4 to 58.4. But as mentioned before, TEC't operates between 10 and 29.288, and was originally set with a range of 10 - 20. For this reason the PLM has to be modified slightly to accommodate the users' configuration. The users' desired range has to be the same as what TEC't's range is in order to provide the same data output (Figure 2.10). A correction factor of 29.4 will also be needed to inform the user that when TEC't displays a certain exhaust λ value, it is that value plus the correction value that equates the real air/fuel ratio.

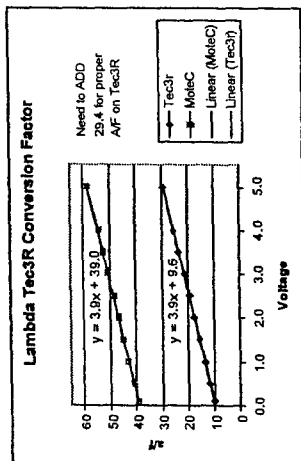


Figure 2.9: Lambda TEC3r Conversion Factor

2.9 THROTTLEBODY SELECTION

The throttle body used in Cal Poly's HCCI engine is the existing Hilborn single throttle body modular unit from Petri's and Franco's engine. The bore is 1 11/16", making it the smallest most restrictive part in the entire intake tract. Initial motoring tests are performed with the throttle plate removed to ensure that the user does not forget to open-wide the throttle. However, the plate is mounted back on in order for the user to have control over the throttling process since the fuel injected is constant. This ensures that a lean air/fuel mixture will always be in the combustion chamber.

2.10 HEATER RELAYS SELECTION

In addition to having a main safety relay that gives or shuts off the intake tube heaters, each of the heaters are outfitted with a Crydom D2410 10A 240V DC solid state relay (Figure 2.11).

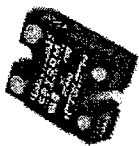


Figure 2.11: Crydom Heater Relay

The relays operate from 0-5V and take this voltage as a signal to either switch the heater power on or off. The relay features "zero-crossing" switching, which is a combination of zero-voltage turn-on and zero-current turn-off. This feature is desirable in that it prevents spikes and noise from being impressed into the power line.

2.11 ENGINE #1 TEARDOWN/ BUILDUP PROCEDURES

In summer of 2004 the HCCI group received the donated engine from Overland Parts and disassembled in order to specify the parts needed to meet project specifications. Through various calculations as well as references to other research institutions with HCCI, the pistons were to be replaced with a new set machined to result in a 16.5:1 compression ratio, r_c . The old intake manifold from the previous HCCI attempt had water injections installed, and so the existing holes would be replaced with fuel injectors instead. Although modified to be port-fuel injection, plans are that once HCCI materializes, the next move would be shifting to GDI HCCI. Parts taken off the engine are organized and separated, and those meant to be only be used once (i.e. stretch bolts) are strictly replaced with new ones.

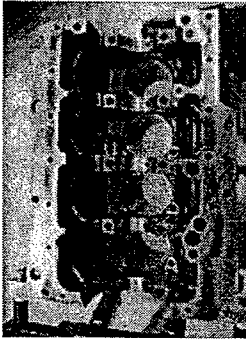


Figure 2.12: 1.9L Bar Block

Everything was separated and organized so that the reusable parts could later be easily located. Since the engine was stock and only refurbished to meet Volkswagen specifications, and that the HCCI concept has yet to touch it, the engine was stripped until only the bare engine block and its pistons and crank were standing by themselves.

In order to determine the correct geometries for the custom HCCI piston, the exact compression ratio had to be determined for the pistons. Volkswagen specified that the original 1.9L TDI engine operates at 19.5:1 compression ratio, but our volumetric measurements on both the engine block and cylinder head (explained in detail later) resulted in 18.34:1 average compression ratio among the four cylinders. The researchers at UC Berkeley's HCCI laboratory also recorded a compression ratio in the same vicinity. Why this value is different than Volkswagen's value remains a question for us.

With guidance from Jim as well as the Red Book and the Haynes Volkswagen repair manual [30] the students (Cheung, Jacques) proceeded to install the piston rings to the pistons, which joined to the connecting rods, which then went into the block to connect with the crankshaft. Fresh engine oil was applied as lubrication to all parts to be joined together. All

tightening torques were from the Red Book, or in some cases when the torque specifications were not available, the Haynes manual.

Once the pistons were installed into the engine, the compression ratio was once again measured to ensure that Cal Poly's HCCI engine would be operating at the desired 16.5:1, but the suppliers had machined the specified pistons with a wrong piston ring land height. As a result, the compression ratio would then be operating at 15.3:1. Therefore one should note that all results gathered from Cal Poly's HCCI engine was with 15.3:1 compression ratio. Though the piston supplier did eventually deliver the correct dimensioned pistons, the wait time had become an issue and the students could not afford the time to teardown and rebuild again.

The engine valve train is installed after completed piston installation. A new head gasket of different thickness (also used in compression ratio calculation) is sandwiched between the block and head via high-torque stretched bolts. Because the timing of the valves is crucial to engine operation, Cheung and Jacques have to be certain of the correct crankshaft position when tightening the camshaft down. Incorrect procedures will result in contact between pistons and valves. The correct method is setting cylinder 1 to top dead center (TDC) and none of the camshaft lobes pushing down on the valve lifters.

2.12 ENGINE #2 BUILDUP

As mentioned previously, setting the cam timing to synchronize with the crankshaft correctly is extremely important. The first engine was built with that in mind, but because of many random checks with the crank rotation, various external parts being added on, and multiple instances of having to take off the timing belt, the engine was ultimately motored with

piston-to-valve contact. Before turning the engine by the dynamometer, Cheung and Jacques had both hand-turned the engine to ensure that all parts were spinning freely. They also took notice of a "popping" sound coming from the combustion chamber—thought to be from valve overlap.

However, because of the slow crank rotation, they were unable to hear the actual contact noises made by the internal hardware. When motoring, the contact sounds were assumed to be characteristic of diesel engines and their "clacking" sounds. The incorrect valve timing also caused the in-cylinder pressure transducer readout to drop in one of the cylinders when the engine speed went above 1800RPM. This was initially thought to be some sort of read error from the software, or that one of the valves was sticking. None of the students expected anything related to incorrect timing.

During the engine's final motoring operation, strange in-cylinder pressure still inclusive, Cheung decided to slowly ramp the engine speed up from the threshold of the erratic pressure readings, 1750rpm. The slow engine speed increase seemed to maintain "correct" pressure values, but just before hitting 1800rpm, the engine suddenly stuttered along with a loud smashing sound. At this point, the engine was now destroyed. Cheung aborted the test, and the engine stumbled to test.

After opening-up the engine and taking the head from the block, one could see that the intake valve had broken loose from its stem and literally "danced" around in the chamber before finally lodging itself into the head. The stem, in turn, punched through the piston, creating a hole for the scraps of metal to contaminate the oil (Figure 2.13). The cylinder walls had a number of scorched marks from the metal bits rubbing against it. Inspection of the other cylinders revealed indentations on the piston crown made by the intake valves.

The only time the piston will hit a valve is when it is at top-dead-center. The only time the piston will hit the intake valve is if the piston came up to TDC too early, or in other words, advanced too much.



Figure 2.11: Lodged Valve and Hole in Piston

To verify this, and to prove that the cam timing was not delayed, the engine cycle is again cited [31]. In a normal operating engine cycle, during the intake stroke, the intake valve opens-up as soon as the piston starts leaving TDC. During the exhaust stroke, the exhaust valve is opened until the piston is at TDC. If the exhaust valve was still open when the piston arrived at TDC, there would be indentations on the piston crowns, which would mean that the valve was late, or delayed, on closing before the piston hit TDC. The same theory goes for the intake valves; because the valves opened-up before the piston left TDC, they were early, or advanced, and in Cal Poly's case, TOO advanced.

After heading up to Overland Parts and graciously receiving another TDI long-block at a discounted price, Cheung and Jacques set forward once again to build another HCCI engine. This time, however, they acquired Volkswagen's "Special Tool 3418" to make certain that the timing would be correct no matter what happened during the installation.

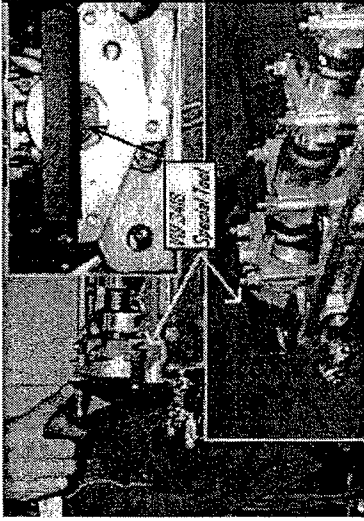


Figure 2.14: VW Special Tool 3418

The original pistons and connecting rods from Engine #2 are oddly different enough so that Cal Poly's second set of pistons, originally designed for Engine #1's connecting rods, do not fit with Engine #2's connecting rods. The pin heights in Engine #2's pistons are different, and since both engines are still operating at 19.5:1 compression ratio, the connecting rod length consequently has to be different as well.

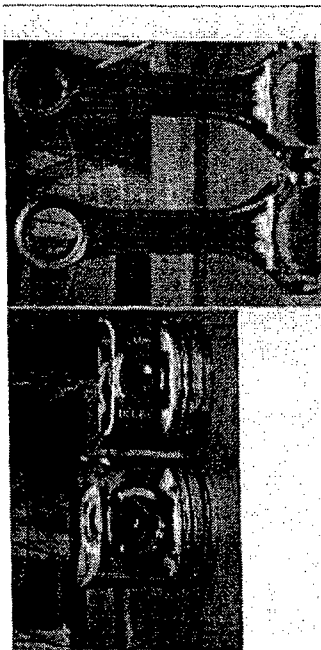


Figure 2.15: Same Engine, Different Pistons and Connecting Rods

As a result, and after thoroughly verifying that the internal hardware is interchangeable among the two engines, the final assembly of Engine #2's internal hardware comprised of Engine #1's connecting rods, connecting rod bearings, and piston pins.

2.13 ENGINE SETUP

Once the engine is built, it is time to add-on the external subsystems as well as the software necessary to monitor and test the HCCI engine. These include the software as well as hardware that is tied into the engine.

AVL Encoder mount

To allow precise measurements of the engine at any point in its crank rotation meant a high-resolution encoder for the HCCI engine. The TECt encoder has a reasonable resolution, but only down to every six degrees [32]. Thus, the high resolution AVL encoder is used instead. At about \$5000 a unit, the AVL encoder is not exactly cheap, but offers just the

tight resolution for the in-cylinder pressure traces. However, this necessitates a custom mount to allow the encoder to attach to the crankshaft. In addition to accommodating the TECt toothed wheel, the encoder mount, designed by Jacques, machined by Laszlo, has to firmly mount to the crankshaft. Figure 2.16 shows the encoder mount with all the attaching hardware. Note the crankshaft axis as reference.

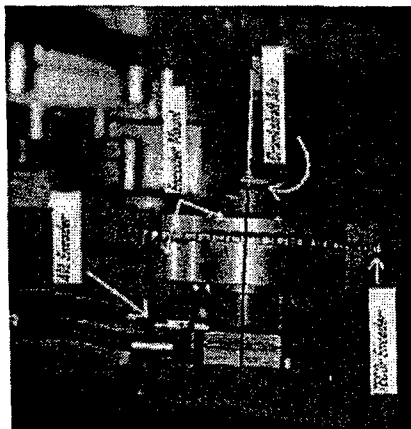


Figure 2.16: Encoder Mount

Pistons

Being that this is now Cheung's and Jacques' second HCCI engine, it is their second experience handling pistons from ARIAS, a renowned piston manufacturer. At that time, no supplier could meet Cal Poly's HCCI piston pin diameter requirement. ARIAS, from the HCCI team's research, seemed like the only manufacturer that would grant their geometry requests. The company's first set of pistons delivered to Cal Poly contained a number of

incorrect geometries, which resulted in a lower-than-desired compression ratio. After the first engine's catastrophic failure, the company's second set was installed into the fresh long-block. At 16.5:1 compression ratio, (confirmed by measurements, detailed later), the HCCI engine is now dimensioned the way it was designed in the first place. Still the same designs with the dished piston crown (Figure 2.17), the units are machined from forged aluminum blanks [33], and contain all the features necessary to fit in the 1.9L TDI engine as well as facilitate HCCI combustion.

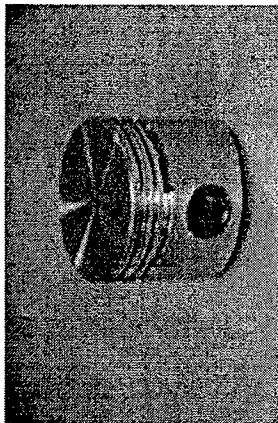


Figure 2.17: ARIAS piston

Testmate/Cellmate/Hypercell Logistics

The engine is built, and a sophisticated unit like this must be controlled by sophisticated computer. Enter Digalog's Cellmate/Testmate/Hypercell group of engine dynamometer system. Ferri's and Franco's HCCI engine was controlled purely manually, without any closed-loop feedback. After receiving funding through the Mechanical Engineering Student Fee Allocation Committee (MESFAC) for Cal Poly's Engine's Laboratory, part of the money was used to acquire a more advanced and updated dynamometer unit. This unit is the one

currently controlling Cal Poly's HCCI engine as well as the Perkins Diesel Engine used for class demonstrations.

Testmate includes the Testmate Panel as well as the hardware sitting in the shelf, and provides the physical power to operate the dynamometer and the engine. The Testmate Panel houses all the functions necessary to get the engine motoring and operating, and various readouts on the panel notify the user of the engine's current operating status.

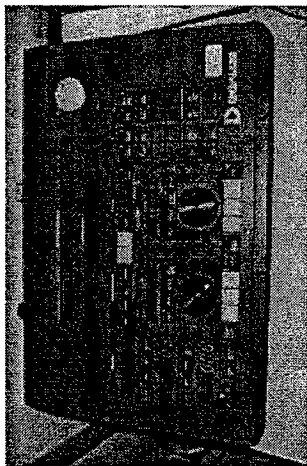


Figure 2.18: Testmate Panel

These include engine torque and power, engine speed, throttle position, dynamometer output percentage, and others. The all-important "Emergency Stop" button sits on the top right, and is used should the engine start to lose control. The "no-load stop" button is used to allow the engine coast from its operating speed to stop without any dynamometer power. The "full-load stop" button halts the engine with full power; this is used for situations like when a hand gets stuck in the belt train. The Testmate hardware relays the information from the Testmate Panel to the Cellmate hardware, which translate the information to the

dynamometer. The dynamometer's output is sent back to Cellmate for feedback, and Cellmate's signal is sent once again to the dynamometer.

Cellmate represents both hardware and software [34]. The two function together to serve as a real-time data acquisition and control system. Cellmate allows the user to concoct tests that run "hands-off." At the same time Cellmate software gathers data specified by the user and stores into its massive hard disk. Cellmate also has the capabilities to control external instruments such as intake heaters in Cal Poly's case, monitor limits, adhere to user set points, and generate displays. Its data can be uploaded and displayed on MS Access.



55

Figure 2.28: Cellmate and Testmate Hardware on Top-Left Cabinets

Hypercell is the software program that runs with Testmate and Cellmate. In it is every piece of information coming from and going to the engine (Figure 2.20). Analog and digital inputs such as intake temperature and dynamometer speed, respectively, are configured in Hypercell through its Configuration Editor. The heater and its control system are also set through the Configuration Editor's PID section. Cal Poly's HCCI manual engine test is also made through Hypercell. The HCCI engine's display screen is built through Hypercell.

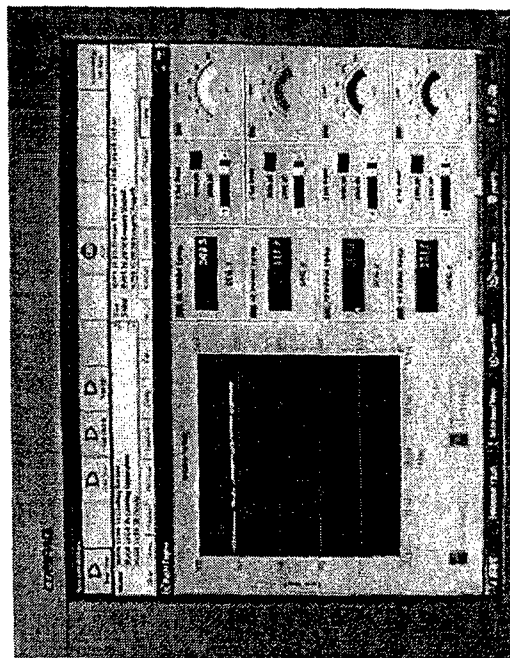


Figure 2.20: Hypercell Temperature Display Screen (Note Different Set Points)

In a sense, Hypercell is the link between the user and Cellmate, for Cellmate computes the tests made and sends that information to the engine and its external subsystems. Although

56

Hypercell is a very powerful program, it is definitely not without any software glitches, as Cheung and Jacques have discovered. Many of the bugs in Hypercell are minimal, but their constant occurrences accumulate to the point where Cheung and Jacques were wasting a large portion of their time figuring out Digalog's mistakes. A simple, yet time consuming occurrence was figuring out the temperature set points for the intake heater controls. After a long iterative process, Cheung discovered that Digalog forgot to include a decimal " " point in the display screen's readouts, and that the temperatures on the display screen had to be divided by "10" to obtain the true values. Hypercell's PID tuning program is also somewhat questionable, and although Cheung and Jacques got the intake heaters to respond somewhat appropriately, this area could definitely see more improvement and fine-tuning. Digalog, owned by the AVL group, is also currently under massive consideration to end its line of product because of the company's internal competition issues. With that in mind, the Mechanical Engineering Department wonders where they will get the technical support if an unsolvable problem arises in the future.

Cam encoder

One of the features available on the TECt was the capability to perform sequential fuel injection. To facilitate this, a cam encoder [35] is mounted onto the path of the timing belt. As quoted from the TECt manual, "a once-per-engine-cycle synchronization, or 'sync,' pulse must be received by the ECU." Mounted on the now-disconnected diesel fuel pump, the single-notched trigger wheel sends off a signal to the magnetic Electromotive sensor every engine cycle, thus firing-off the fuel injectors sequentially.

57

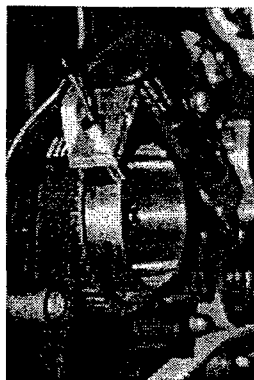


Figure 2.21 Sequential Fuel Injection Cam Encoder

Boom

The test cell's wall-mounted boom is the central location for all the information coming from the engine to go to (besides TECt and in-cylinder pressure transducers). The information from the thermocouples and pressure transducers are then sent from the boom back to Cellmate and its associated software. Such data collected from the boom include oil pressure and temperature, coolant temperature, and heater temperature going into all four cylinders.

58

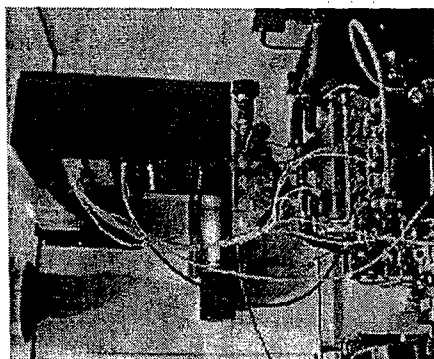


Figure 2.22: Engine Boom with Thermocouple and Pressure Transducer Lines

ECU wiring

The TEGr was wired per Electromotive's Installation and Calibration Manual. The unit itself is bolted onto a separate stand mounted onto the concrete floor. The ECU is accessed by the wall-mounted computers (Figure 2.19).

Radiator and Radiator Fan

There was initially speculation on having closed-loop control with the cooling system. The control would be that when the water temperature reached a threshold, the system would then start circulating itself. The rationale for this is to speed up engine temperature so that HCCI combustion would be obtained sooner. Due to time, manpower, as well as financial budget, the controls for the cooling system was ditched in favor of a simple radiator-

59

mounted fan wired to a manual switch. The fan would be switched on prior to operating the engine.

240V Power Source

One of the biggest issues with the heaters, besides controlling them, was finding the adequate power to turn them on. The Engines Laboratory, however, had 208V circulating the area, and so that became the heater's power source. Although definitely operating at full capacity, the heaters are operating at 1.365kW maximum power as opposed to its 2kW rating.

Coupling Hardware

Between the dynamometer and the engine lie the coupler and its associated hardware. Martin Sprocket & Gear, INC provides the connection necessary for the dynamometer to turn the engine, and vice versa. The coupling sleeves and hubs are oversized to take-on the high-pressure changes experienced from HCCI combustion. The hubs are held in-place by set screws, but are extremely susceptible to becoming loose during low (300-500RPM) motoring speeds. Even with two screws lined-up in each hole, the hubs have been known to loosen itself from either the dynamometer or engine shaft. Therefore it is important that the coupling be inspected prior to each test.

60

3. FOR MODIFICATIONS AND TESTING VALIDATION PROCEDURES

Validations for the hardware selection are made before laying down the drill or making the hardware purchase. Otherwise Cal Poly is selecting parts blindly. Since this is the first time for Cheung and Jacques to work with many of the hardware, ranging from the diesel engine to the engine control systems, the procedures and justifications must be set in stone in order for future students embarking on the project to follow to.

3.1 VOLUMETRIC MEASUREMENTS FOR ENGINE BLOCK AND HEAD

In order to determine the exact compression ratio Cal Poly's TDI engine was originally operating at, Cheung performed numerous volumetric measurements to confirm new HCCI piston's design. The original engine's compression ratio was determined from the volume taken from the engine block V_b , the engine head V_h , and the gasket V_g which was sandwiched by the two. The displaced volume from the block is what gives the engine its "1.9L" designation. With that, the compression ratio was calculated by taking the summation of the volumes from the engine block, the head, and the gasket. The piston sits at TDC in order to obtain the crevice volume. The head is plugged with the in-cylinder pressure transducer as well as the existing fuel injector. The gasket volume is taken with its original "crushed" thickness.

61

Procedures

To measure the volume displaced by either the block or the head, Cheung used the "Plexiglas Method," shown in Figure 3.1.

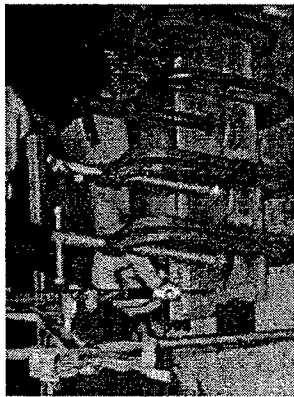


Figure 3.1 Verification of Plexiglas volume

A sturdy piece of Plexiglas has four cylindrical volumes milled out. It is then applied with grease to form a seal with the larger Plexiglas backing. Seen here, Laszlo performs volumetric measurement of the Plexiglas volumes. A burette is used to record the volume dispensed to each cavity. A small hole is drilled to provide an opening for the fluid (colored water) to fill the cavity. This gives a reference volume to note when measuring the head and block. One should also note that the Plexiglas cavity is necessary because at TDC, the piston actually sticks out of the engine block. This is made to ensure the advertised 19.5:1 compression ratio.

After determining the volumes from its cylindrical bores, the Plexiglas is then laid over the engine block, with original pistons still intact at TDC. Because the 1.9L engine does not

62

contain any markings denoting TDC, a dial indicator is placed on the top of the block to find the highest point of the piston. A decent coat of grease is applied to the walls of the combustion chamber. This not only reduces the amount of rust formed, but also restricts the water from leaking past the compression and oil rings. Bolt holes are drilled on the Plexiglas so they can be securely fastened onto the block or head (Figure 3.2).

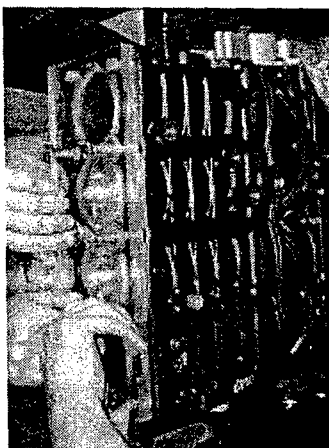


Figure 3.2: Securing the Plexiglas on the block. Note piston protrusion out of block.

The burette assembly is then carefully placed on the Plexiglas and positioned so that the water drips into the cylinder. To reduce the amount of air bubbles trapped in the enclosure, the engine is tilted back a slight amount so that the water fills the entire volume. Coincidentally, the procedure is performed with the block mounted on the engine stand, which offers a degree of tilt (Figure 3.3).



Figure 3.3: Fluid dripping through hole for block volume measurement

Unfortunately, one can not expect a perfect measurement from each trial. Many times the walls of the combustion chamber are not completely coated, and that causes the water to leak, ruining the measurements. There is no way to correct the situation but to remove the Plexiglas, drain the fluid, blow the cylinder clean, and apply more grease. Applying too much grease to the walls, however, can also alter the measurements because now the grease robs the crevice volumes away.

The engine head, with its valve seats, fuel injector and pressure transducer intrusion, and valve geometry, also contributes to the overall compression ratio. To prepare it, the surfaces to be exposed to the measurements are wiped down clean and made sure that no fluid is hiding in the cuts. The Plexiglas is attached to the head using old stretch bolts. Again, grease is applied to the Plexiglas to ensure a seal with the head (Figure 3.4).

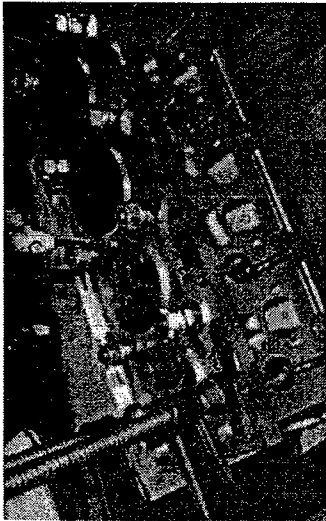


Figure 3.4: Measurement of head

The head volume is trickier to measure since many times bubbles surface AFTER having completed recording the volume displaced (Figure 3.5). One would think the solution would be to just drip more water, but usually the bubbles become stuck and will not surface to the hole opening. Therefore while the water is dipping into the cavity, it is wise to tap out any hidden air pockets that might still be residing.

65



Figure 3.5: Stuck bubbles after measurement completion

3.2 CC AFTER ENGINE BUILDUP #1

As mentioned, Cal Poly's HCCI engine piston supplier, ARIAS, for some reason, supplied Cheung and Jacques with incorrectly dimensioned pistons. This was verified by both simple reverse engineering and also by performing volumetric measurements once installed into the engine block. The measurements provided the necessary values in calculating the clearance volume. The clearance volume is calculated by summing the volume from the engine block, head, and gasket.

$$V_C = V_B + V_H + V_G$$

Equation 3.1: Clearance Volume

The clearance volume is added to the cylinder's displaced volume. The equation for displaced volume is as follows:

66

$$V_D = \frac{\pi B^2 L}{4}$$

Equation 3.2: Displaced volume in a cylinder

where "B" is the cylinder bore and "L" is the stroke. With the displaced and clearance volume equations on hand, one can calculate the compression ratio by the following equation:

$$r_c = \frac{V_D + V_C}{V_C}$$

Equation 3.3: Compression Ratio

After organizing and calculating the data obtained for this engine, the lowest compression ratio seen was 15.29:1, and the highest was 15.55:1. Close examination prior to engine buildup revealed the top piston ringland height being too low, thus robbing compression ratio. If this dimension was machined incorrect, it could possibly be that the dished geometry on the piston crown could be milled-out incorrectly as well.

3.3 CC AFTER ENGINE BUILDUP #2

Since all four pistons from Cheung's and Jacque's first engine were damaged beyond repair, it was appropriate to install ARIAS' second set of pistons. Due to some miscommunication, Cal Poly ended up with two sets of pistons for the price of one, along with no further questions/concerns from both the buyer and seller. The procedures in obtaining volumetric measurements were identical to the first engine except for the modification of fuel injectors instead of spark plugs into the head. The ionization control, something Dr.

67

Delagrammatikas have initially wanted, was to be put-off until further research, and so Cheung and Jacques made the switch back to plugging the holes using the fuel injectors. The head gasket smashed height was carried over from the first engine's measurements, and the measurements for both the engine block and head are tabulated in Appendix A. Using the data from Cylinder #1, the compression ratio is calculated as follows:

$$r_c = \frac{V_D + V_C}{V_C} = \frac{\frac{\pi B^2 L}{4} + (V_B + V_H + V_G)}{(V_B + V_H + V_G)} = \frac{\frac{\pi (7.951 \text{ cm})^2 (5.55 \text{ cm})}{4} + (23.3 - 0.3 + 8.19)}{(23.3 - 0.3 + 8.19)} = \frac{474.053 + 31.19}{31.19} = 16.20$$

Equation 3.4: Calculation of Compression Ratio

Applying this method to the other three cylinders yields compression ratios within the vicinity—a good sign, considering that the first set of pistons gave less than desirable values. The compression ratios for Engine #2 are in Appendix A7. Though they still are slightly lower than the desired 16.5:1 compression, this error could be attributed to a number of factors, including human error, bubbles in various crevices not completely filled, or grease that robbed certain volumes.

68

4. HCCI INTAKE HEATER CONTROL

The tube heaters used for heating the intake air is basically a giant resistor, much like a normal household blowdryer, without the fan. To model it, however, requires application of the energy rate balance [36].

4.1 HEATER CHARACTERIZATIONS/ENERGY BALANCE EQUATION

The overall equation for energy rate balance is:

$$\frac{dE_{cv}}{dt} = \dot{Q}_{cv} - \dot{W}_{cv} + \sum_i \dot{m}_i \left(h_i + \frac{V_i^2}{2} + gz_i \right) - \sum_e \dot{m}_e \left(h_e + \frac{V_e^2}{2} + gz_e \right)$$

Equation 4.1: General energy balance equation

In the case of Cal Poly's HCCI engine's heaters, the work in the control volume is eliminated, as is the potential and kinetic energy. The heater coil represents the heat input, and the inlet and exiting air intake takes care of the intake and exit enthalpy. Rewriting the energy balance equation simplifies to:

$$\frac{dU_{cv}}{dt} = \dot{Q}_{cv} + \dot{m}_{cv}(h_i - h_e)$$

Equation 4.2: Simplified energy balance equation

Because the mass of air going through the heaters remains the same, the energy rate term on the left side of the equation is now expressed as:

$$\frac{dU_{cv}}{dt} = \frac{d(m_{cv} u)}{dt} = m_{cv} \frac{du}{dt}$$

Equation 4.3: Assumption of constant mass with time

Water is also assumed to be incompressible, which results in specific energy depending on temperature only. The use of the chain rule rewrites Equation 4.3 as

$$\frac{du}{dt} = \frac{du}{dT} \frac{dT}{dt} = c \frac{dT}{dt}$$

Equation 4.4: Use of chain rule

where c is the specific heat and dT/dt is the change in air temperature out of the heater with respect to time. Rearranging the energy balance yields:

$$\frac{dU_{cv}}{dt} = \bar{m}_{cv} c \frac{dT}{dt}$$

Equation 4.5: Rearranging terms

As for Calpoly's case, the term on the right side of Equation 4.5 represents the change in temperature after going through the intake heater. In applying the heater's characteristics, the right term is now expanded to:

$$\bar{m} c \frac{dT}{dt} = m_{cv} c (T_1 - T_2) + \dot{Q}_{cv}$$

Equation 4.6: Substituting heater characteristics

where, on the left side, $\bar{m} c$ is the mass and specific heat at constant pressure during the change in air temperature. On the right side, m_{cv} is the mass of the air inside the control

volume (heater tube), T_i is the ambient air temperature, T_j is the temperature of the air out of the heater, and $\dot{Q}_{dot_{cv}}$ is the heater power input. Further expansion of Equation 4.6's right side brings three distinctive areas affecting the output temperature.

$$\overline{m}c \frac{dT_j}{dt} = m_o c T_1 - m_o c T_j + \dot{Q}_o$$

Equation 4.7: Separating right side to three distinct terms

The right side is now represented by the intake air's intake and exit enthalpy, by $m_o c T_1$ and $m_o c T_j$, respectively. The heater, $\dot{Q}_{dot_{cv}}$, undergoes heat transfer through its walls as well as through the heater coils; thus it is modeled extensively, which will be scrutinized in more detail in the Simulink model. Solving for the change in output temperature with respect to time yields:

$$\frac{dT_j}{dt} = \frac{m_o c T_1 - m_o c T_j + \dot{Q}_o}{\overline{m}c}$$

Equation 4.8: Change in Output Temperature With Respect to Time

4.2 SIMULINK MODEL AND EXPLANATIONS

In order to provide validation and to have a reliable form of prediction of the HCCI engine's intake temperatures, a theoretical model must be made. Therefore Simulink is used to model the energy balance equation derived previously. When put into the form of a closed-loop response, the equation is the plant and the controller is in the form of a proportional, integral, and derivative (PID) controller (Figure 4.1).

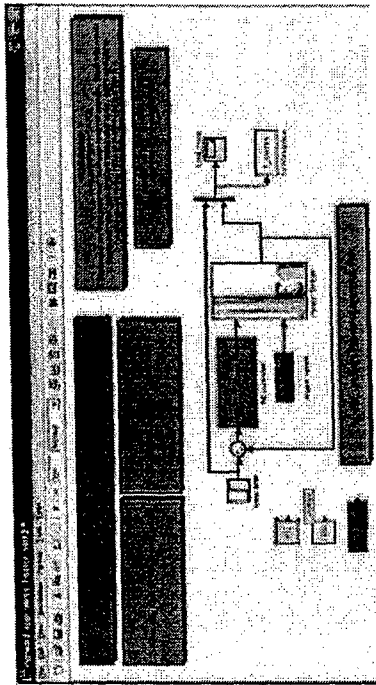


Figure 4.1 HCCI Intake Heaters in the form of a closed-loop response

The heater system is given engine speed and temperature inputs, and the temperature transient response is illustrated on the scope. The output values are also redirected to the Matlab workspace as "T_sashimi," which can later be transferred to EXCEL or other spreadsheet programs for further comparisons. The PID controller is the unit that sends the appropriate signal from the microcontroller to the plant (the heater) to turn on/off at a certain duty cycle until the desired temperature is obtained. During that time, an error is looped back into the PID controller, which in turn recalculates a more appropriate value at achieving the desired output. The PID controller is shown in Figure 4.2

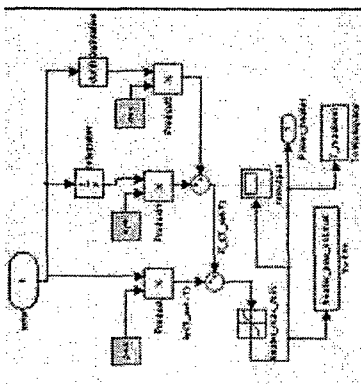


Figure 4.2: PID Controller

Other Peripherals

Besides the closed loop, Dr. Delagrammatikas and Cheung made various Matlab files to enhance running the simulation. One such file was the "*hcccl_params*" file, which held all the heater's variables of the heater, ranging from thermal emissivity of the heater coils to the outer surface area of the heater's aluminum tube (figure 4.3). This file is both accessible from the heater model window and also conventionally from the Matlab prompt.

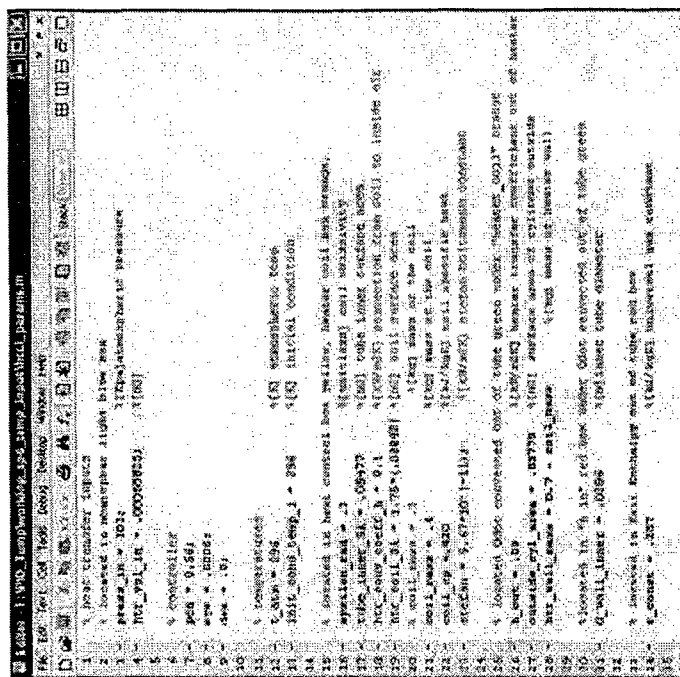


Figure 4.3: *Hcci_params m-file for heater*

By housing all the variables into a single *.m file, the user can better keep track of what values are altered. In addition, having all the variables in a single window greatly improves organization. The variables are grouped under their respective color-coded subsystems. The values for each of the variables are mostly found in the heat transfer text, the

thermodynamics text, hand-calculations, or by comparison with experimental heater testing temperature curves.

The button next to “ncci_params” runs a small program that opens up two “mat” files. One file holds various temperature set points (temp_des), while the other has various engine speed set points (spd_des).

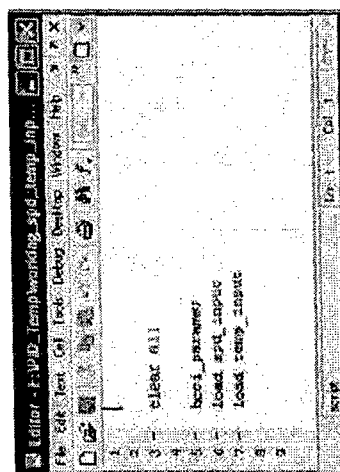


Figure 4.4: Start hcci speed/temperature file

By implementing this file (Figure 4.4) to the model, the user can see how the model responds to different temperature and engine speed set points imposed. For instance, the “temp_des” file would have a list of temperatures set points that initially started at 400K, and then ramped up to 425K, and finally came back down to the original set point. The “spd_des” file would have a range of engine speeds from 900-2000RPM. Running the model with speed and temperature fluctuation tests the transient response of the Simulink model.

52

As per the instructions posted in the Simulink model, the user must double-click the large green button on the top left. This button runs a small Matlab program that clears all previous simulations, leaving the user with a new simulation to start. Figure 4.5 shows the open function made by Dr. Delegrammatikas which clears all previous simulations.

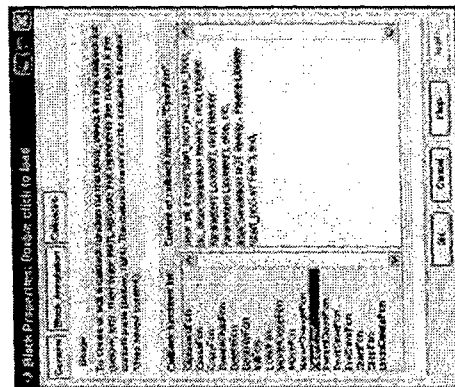


Figure 4.5: Behind the “double-click” prior to running simulation

The heater model's output response is scored, and a "mux" is used to compare the set point to actual output. For instance, a step function containing the two temperature set points as well as engine speed fluctuation is implemented to the model, and the output (figure 4.6) illustrates the effects from engine speed with respect to maintaining the temperature.

will illustrate the effects from engine speed with respect to maintaining the temperature.

76

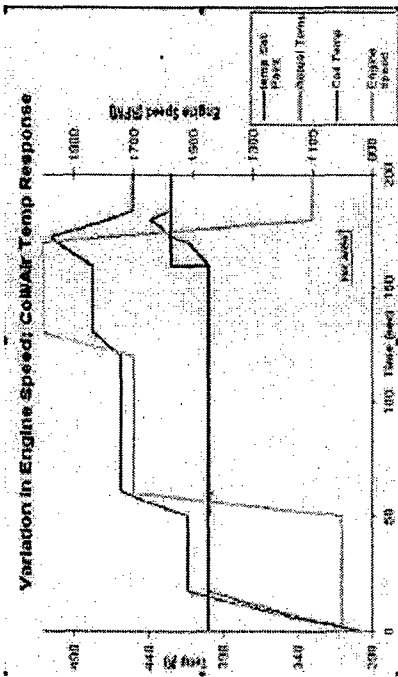


Figure 4.6: Actual vs. Set point Temperature with Engine Variations

Having these two variables allow the user/operator to better observe the temperature response when the engine increases or decreases. For instance, when the engine speed decreases, the reduction in mass flow rate allows the intake air temperature to momentarily rise until the controller takes over and manages the temperature back to acceptable levels.

Inside the Heater System

Each term of the energy balance is implemented in its own subsystem, and the balance revolves around the summation. A display connected to the summation ensures the user that the energy balance is working correctly when the readout is "zero."

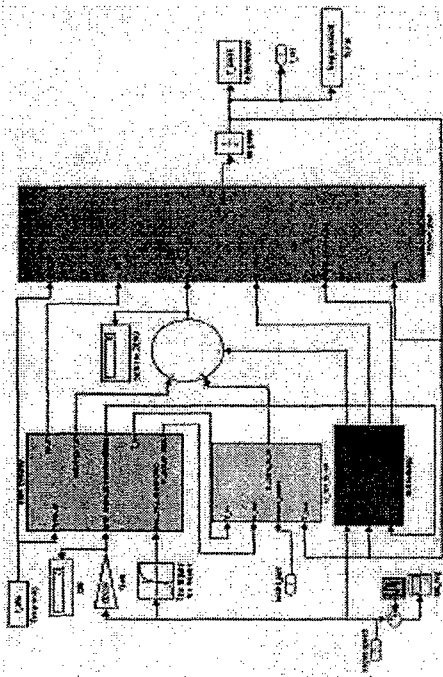


Figure 4.7: Simulink model representing HCCI engine's intake heater

Opening the plant (Figure 4.1) brings-up the energy balance equation. The intake enthalpy is represented by the subsystem on the top left (darker blue), the heater power is in the middle (yellow), and the exit enthalpy on the bottom (red). The temperature coming into the model is set in the "hcci_params" file. To connect engine speed to a CFM reading, Cheung and Jacques performed a motoring process where the engine was turned to a range of speeds; the CFM readings from Hypertcell were then recorded and tabulated to EXCEL. From there a slope was obtained. Dividing by "4" is necessary because the Simulink model represents only one heater while the CFM reading from Hypertcell takes all four cylinders into account. The time it takes for the air to travel through the length of the tube varies as the engine speed changes; thus a look-up table is made and calculated values for the respective engine speeds are inputted. This is necessary because the table now models the air mass changing

with respect to the average temperature in the heater due to expansion. For reference, a scope for the fluctuating engine speed is shown to allow the user engine speed information.

These three terms go to the oval-shaped summation, and the "net_system_Q" is taken to the tall light blue subsystem on the right. This subsystem calculates the average mass and specific heat, and is divided to obtain the temperature out of the heater. The output is then routed back into the model for to find a rolling average for the exit enthalpy, the heater, and calculation of the mass average for the next iteration.

The intake enthalpy box is represented by Figure 4.8.

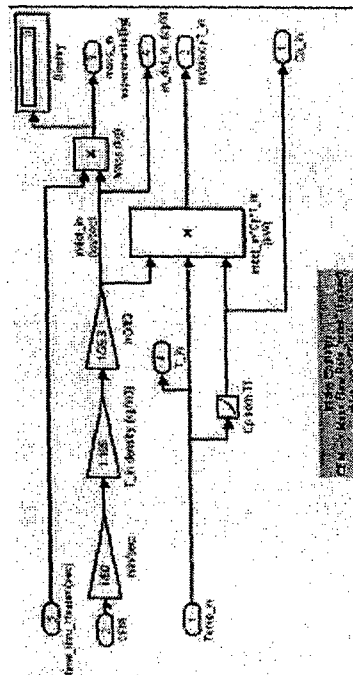


Figure 4.8: Intake Enthalpy Representation

The mass of the air going into the air stream is taken from the "CFM" reading from Hypercell, and conversion from ft³/min to mass flow rate are as follows:

$$\left(\frac{\text{ft}^3}{\text{min}} \right) \left(\frac{\text{min}}{\text{sec}} \right) \left(\frac{1.185 \text{ kg}}{\text{m}^3} \right) \left(\frac{\text{m}^3}{35.3 \text{ ft}^3} \right) = \frac{\text{kg}}{\text{sec}}$$

Equation 4.8: Conversion from CFM to Mass Flow Rate

The mass flow rate is also multiplied by the time it takes for a volume of air to travel the length of the heater tube. The product, the "mass_in_experimental(kg)" is directed to the "exit enthalpy" box for mass flow rate calculations. The "m_dot_in(kg/s)" output goes to the heater subsystem. "m_dot_incpT_in" the energy going to the heater control volume, goes directly to the energy balance equation, and "Cp_in" calculated from a lookup table, is outputted and taken to calculate the average mass/specific heat subsystem.

The exit enthalpy system is represented by Figure 4.9:

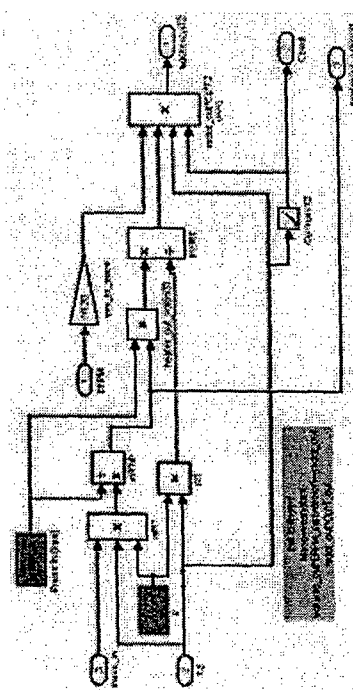


Figure 4.9: Exit Enthalpy Representation

The exit enthalpy takes some of the information from the intake enthalpy in order to accurately calculate the energy coming out the system. "press_in" and "r_const" are both

from the "hccL_params" file, and they are used, along with "mass_in," from the intake enthalpy subsystem, to calculate the new, expanded (due to heat) volume coming out the heater tube. That volume is put back into the ideal gas law to find the mass flow rate. Along with the specific heat and "T," the energy is calculated. "Cpout" and "heaterout_vol(sm³)" are outputted and used to calculate the average mass and specific heat.

Opening the subsystem that calculates the average mass and specific heat reveals the following (Figure 4.10):

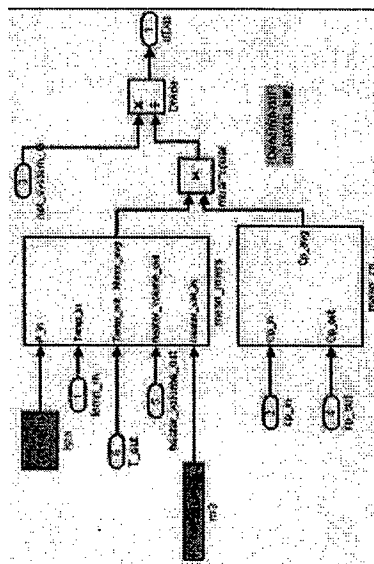


Figure 4.10: Average Mass and Specific Heat Representation

As noted before, the average air mass and specific heat must be taken with respect to each temperature increment because it therefore provides more accuracy over using just the mass/specific heat from the intake air. All the inputs on the left side of the two subsystems contribute to calculating the averages coming out on the right side. The averages are used to

as the denominator (Equation 4.8) to solve for the temperature change with respect to time. The constants in magenta are variables from the parameters file. The mass average is calculated through the following subsystem shown in Figure 4.11:

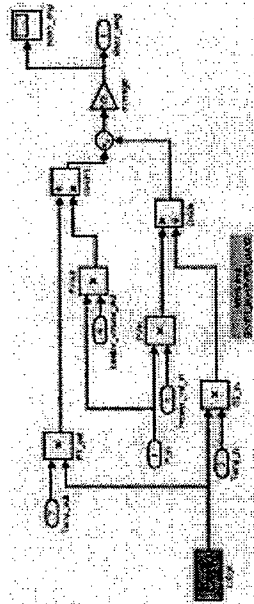


Figure 4.11: Mass Average Representation

The average air mass, "mass_avg," taken from the air temperature coming in and going out the heater, is the result of taking the average of two ideal gas laws calculations. The average specific heat, its subsystem displayed in Equation 4.10, is calculated likewise (Figure 4.12).

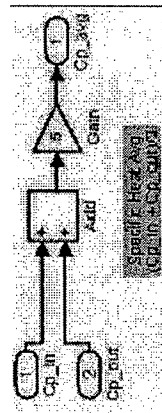


Figure 4.12: Specific heat representation

Armed with the average mass and specific heat, one is ready to find the change in temperature, but not without full explanation of the heater coil and its properties.

The heater coil is twelve inches long, and it runs a spiral configuration throughout the length of the aluminum tube. Because of only 208VAC available, the maximum output from the heaters is 1.365kW. There exists heat transfer in the form of convection and radiation, both coming from the heater coil. The energy balance associated with the heater coil itself is:

$$-(\dot{Q}_{rad} + \dot{Q}_{conv}) + I^2 R = 0$$

Equation 4.10: Energy Balance of Heater Coil

where " \dot{Q}_{rad} " is the heat transfer through radiation, " \dot{Q}_{conv} " is the heat transfer through convection, and " $I^2 R$ " is the heater power input. An example is given from the heat transfer textbook [37] that models an uninsulated pipe passing through ambient atmosphere. The example continues to solve for the heat loss from the pipe. In Cal Poly's HCCI heater model, the textbook example can be used almost identically to model the coil; the heat transfer through radiation is written as:

$$\sigma \epsilon A_s (T_c^4 - T_a^4)$$

Equation 4.11: Heat loss by radiation exchange with inside wall

where " σ " is the Stefan-Boltzmann constant ($\sigma = 5.67 \times 10^{-8} \text{ W/m}^2 \text{ K}^4$), " ϵ " is the emissivity, which provides a measure of how efficiently a surface emits energy relative to a blackbody, and " A_s " is the inner surface area of the heater tube. Because the heater walls are also going to have an effect on the intake air, the heat transfer for that hardware must be accounted for. Therefore, using Equation 4.5, another energy balance is made. The heat transfer from the heater coil to the air is convection, and the appropriate equation for that is:

$$\bar{h} A_s (T_c - T_a)$$

Equation 4.12: Heat loss by convection from heater coil

where " \bar{h} " is the convection heat transfer coefficient, " A_s " is the heater coil surface area, " T_c " is the coil temperature, and " T_a ". The heater coils are naturally going to be hotter than the flowing air, and the air movement provides the convective heat transfer.

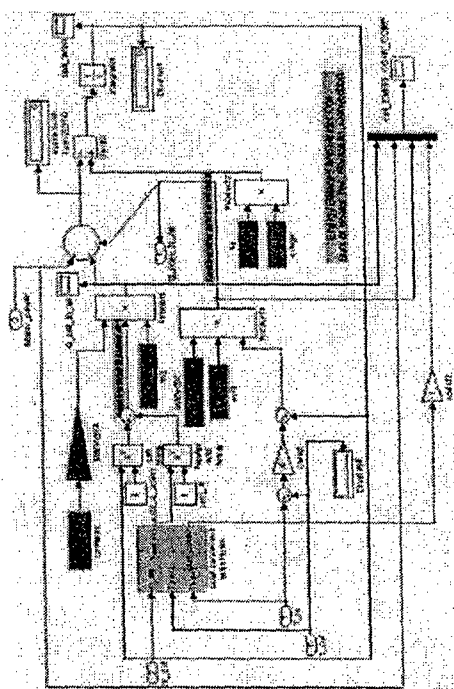


Figure 4.11: Heater Coil Representation

Initially, the heater wall temperature was assumed to be the same as the average temperature of the air flowing in and out, respectively. Running this assumption with the Simulink model, though, made the output as well as the transient response seem a bit skewed, with actual temperature meeting the set point almost instantaneously. Because having the wall temperature equal to the average air temperature inside the tube is a huge unknown

assumption, Cheung and Jacques decided to improve model's heaters wall temperature representation.

To obtain a more precise wall temperature, the convective heat transfer inside AND outside the heater wall is calculated. Equation 4.13 provides the general foundation on how the wall temperature will be calculated. The wall temperature is calculated by the following:

$$\sum \dot{E} = \sum \dot{Q}_{conv} + \sum \dot{Q}_{rad} = mc_p \frac{dT}{dt}$$

Equation 4.13: General equation for heater coil energy balance

For Cal Poly's case, however, heat transfer through radiation from the wall is neglected because it is assumed to be minimal. The overall model for the heater transfer associated with the heater wall is shown in Figure 4.14.

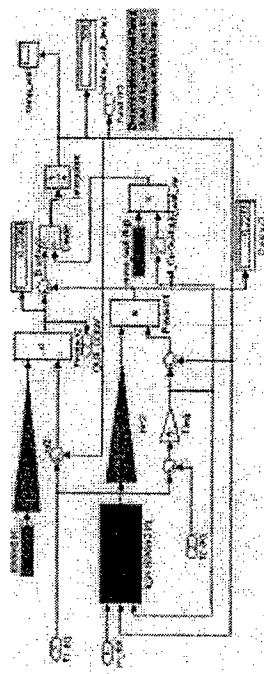


Figure 4.14: Heater Wall Temperature Representation

The top portion of the model (magenta) shows the conductive heat transfer through the outer heater wall. The equation representing the convective heat transfer out the outer wall

$$h_{out} A_{OD} (T_{s,out} - T_{wall})$$

Equation 4.14: Heat transfer by convection out of outer wall

where " h_{out} " is the convection heat transfer coefficient outside the tube (set in the Madab parameters file), " A_{OD} " is the heater tube's outer surface area, " $T_{s,out}$ " is the ambient atmospheric temperature, and " T_{wall} " is the heater wall temperature. Because Cheung assumes that the ambient air outside the heater is still, the heat transfer coefficient could be modeled as a conduction coefficient. Finding the heat transfer through the inner heater wall is much more complicated because of the constantly changing convection heat transfer coefficient. The coefficient was initially assumed to be constant, but because the mass air flow is variable and the wall temperature is changing with respect to time, a more accurate representation must be made. Its equation is represented as:

$$h_{in} A_{ID} \left[\left(\frac{T_1 + T_2}{2} \right) - T_{s,i} \right]$$

Equation 4.15: Heat transfer by convection out the inner wall

where " h_{in} " is the in-tube heat transfer coefficient, " A_{ID} " is the tube's inner surface area, " T_1 " and " T_2 " is the temperature coming in and going out the heater, respectively. As can be seen in Equation 4.14 and Equation 4.15, the wall temperature is subtracted from the air temperature in the tube because, if looking at a thermal circuit, the wall is farthest away from the energy-emitting coil, which consequently receives the least energy, besides the outside ambient air.

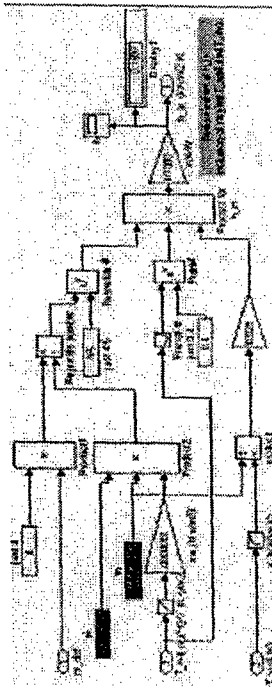


Figure 4.E: Model for finding heat transfer coefficient inside heater

The accompanying equation for Figure 4.16 is first determined by finding the Reynolds number. The Reynolds obtained is either laminar or turbulent; its value is obtained by the following equation:

$$Re_D = \frac{4\dot{m}}{\pi D \mu}$$

Equation 4.17: Reynolds number

Through sample calculations, the Reynolds number is determined to be turbulent for all flows associated with the engine speed range of Cal Poly's HCCI engine. The Nusselt number correlation for a turbulent, fully developed flow, which provides a measure of the convection heat transfer at the surface, can be manipulated to solve for the heat transfer coefficient " h_h " and is derived in Equation 4.18:

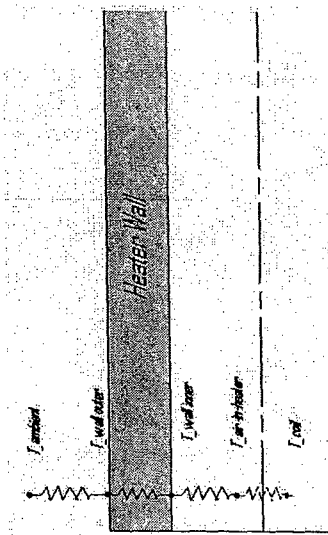


Figure 4.E: Heater thermal circuit

Combined, Equation 4.13 is now rewritten as:

$$h_{ext} A_{ext} (T_{\infty, ext} - T_{wall}) + h_{in} A_{in} \left[\left(\frac{T_1 + T_2}{2} \right) - T_w \right] = mc_p \frac{dT}{dt}$$

Equation 4.E: Wall Temperature Representation

As mentioned, the heat transfer coefficient inside the tube is variable, and is therefore found using the following model:

$$h_i = \left(\frac{k}{D_i} \right) 0.023 \text{Re}_D^{\frac{1}{2}} \text{Pr}^{\frac{1}{4}}$$

Equation 4.8: Determination of convection heat transfer coefficient [38]

The Prandtl number " Pr " is a function of temperature, and its values are therefore put into a lookup table [9]. The coil's thermal conductivity " k " is also picked-up from the heat transfer text, and is incorporated into a lookup table. " D_i " is the heater wall's inner diameter.

PID Review

In a closed-loop response, there exists a plant, which is the system to be controlled, and the controller, which provides excitation for the plant and overall behavior for the system. An input is given (the temperature step in this case). The input goes through the controller with its respective PID values and a signal is given to control the plant, with a new output as obtained. Of course, without anytuning to the controller, one can expect some sort of error signal. This signal, known as "steady-state error," is the difference between the input and output of the system as time goes to infinity. The steady-state error is looped back to the controller, which then recalculates a new signal to be sent to the plant.

To tune the PID controller, one can adjust each of the three variables. First the user should try with the " k_p " or proportional value. This value, when tuned correctly, reduces rise time. In other words, the time to reach a certain temperature at a fixed engine speed would be reduced when a certain " k_p " is applied. Although it helps improve transient response, it does eliminate steady-state error. As the error becomes smaller, the corrective action from the " k_p " values reduces [40]. To take out the steady-state error, the integral control " k_i " is

89

used. Although it helps reduce the error, the side effects created include vulnerability to instability, increased overshoot, as well as a generally decreased settling time. In that case, the third and final variable, the derivative control " k_d ," is used to further reduce overshoot and settling time.

PID values

Most control systems are made possible to operate with just proportional gain. As with Cal Poly's intake heater system, determining the correct values was done by a series of engineering iterative processes where each value was introduced in small increments until the desired output resulted. One could have obtained the PID values through a derivation process, but that would prove to be too time costly. Furthermore, the Simulink model is what allows the user to obtain PID values in the first place without the need for derivation; he/she can tweak the various values to his/her liking.

In determining the PID values for Cal Poly's HCCI engine, Cheung refers to the Sun paper [41] for the most appropriate approach to get the heaters working appropriately. Through Sun's iterative process, and also by observing the output temperature response, a " k_p " value of just 1.0, inputted into the Simulink model, was sufficient to obtain the desired heater response. From Figure 4.17, the set point is notated in black, and when the simulation begins, the desired temperature is 400K, the lower limit of HCCI combustion. At 160 seconds there is a step change and the desired temperature is now 425K, the upper limit of HCCI combustion. Varying " k_p " yields very similar results in terms of heater response. The steady state error is within two or three degrees (Kelvin). By increasing the " k_p " to "10.0," steady-state error is eliminated.

90

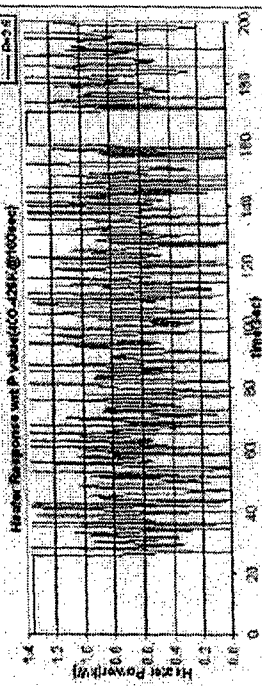


Figure 4.18: Heater Response with $k_p=2.5$

Because a " k_p " of 2.5 results in a steady-state error, a higher " k_p " value is given to see what the effects are. As predicted, the steady error is reduced (Figure 4.17), but now the heater response seems to fluctuate more intensely. By changing " k_p " to 5.0, the heater now responds more erratically. Figure 4.19 illustrates how the heater now seems to have a more "aggressive" effect with the new " k_p " value. Though steady-state error is reduced, the heater output fluctuation leaves one to desire something more quelled and not constantly saturated at its power limits.

92

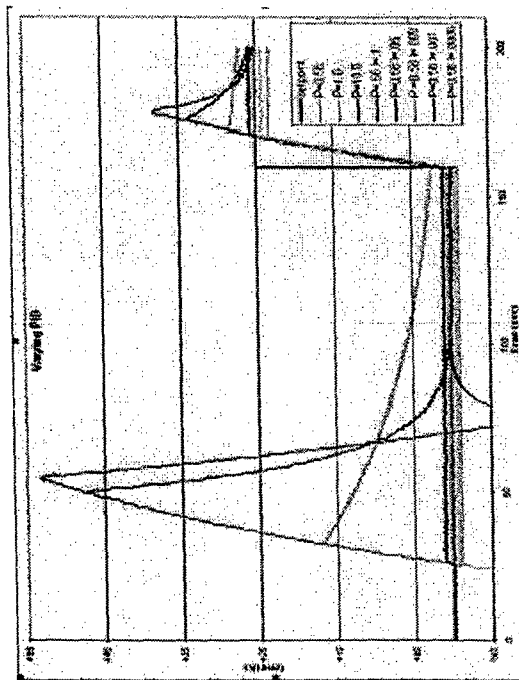


Figure 4.17: Variations in PID and its Effects on Temperature Response

However, the Simulink model is also equipped with a scope for the heater response. There is a significant change in how the heater operates during the process of determining " k_p ". At low " k_p " values such as "2.5," the heater operation seems to settle on an average power output between 0.3-1.1kW, and rarely saturates itself in the upper or lower limits (Figure 4.18).

91

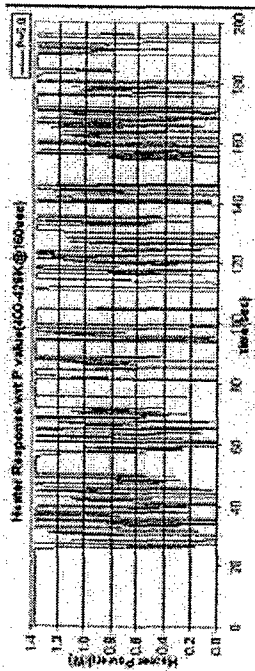


Figure 4.20: Heater Response with $k_p=5.0$

To prove that a higher " k_p " value is not the solution in eliminating steady-state error, the Simulink model was given $k_p=10.0$, to see if the heater response might have reached a threshold of some sort or have settled back down to an average operating range. From Figure 4.17, the heater response now practically eliminates steady error, but one look at Figure 4.20 makes one wonder if the heater is even possible at operating with such power output fluctuations.

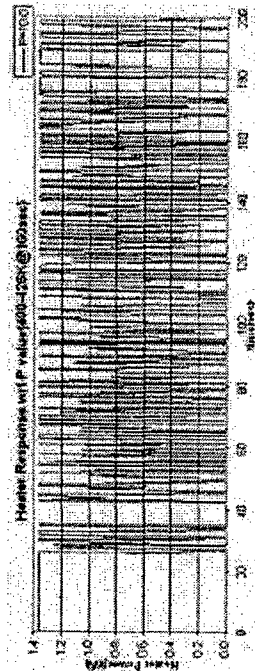


Figure 4.21: Heater Response with $k_p=10.0$

With that in mind, Cheung resorts back to a " k_p " value of 0.56 resulting in a "better" heater output response. He next starts to tinker with $k_i=0.1$, and after running the simulation, the temperature overshoots over fifty degrees Kelvin beyond the set point. Coming back to the set point, the actual temperature undershoots by about ten degrees and finally reaches steady-state, all in about one hundred seconds. Referring to the Sun paper, the procedure for rectifying these situations includes lowering the " k_i " value until desired. Therefore the heater response slowly becomes more favorable with a lower integral gain. Back in Figure 4.17, different " k_i " values results in smaller overshoots, until the values used are $k_p=0.56$, and $k_i=0.0006$. The integral gain is a very small value that one wonders if the system is able to run physically (actual heater) with only a proportional gain value.

One more test to validate the Simulink heater model is to implement different engine speeds while trying to maintain the set point temperature. Figure 4.21 illustrates how, even with fluctuating engine speeds, the Simulink model still theoretically tries to maintain the set point temperature. During the times of increased or decreased engine speed, one will notice a slight decrease or increase in temperature; this is due to the change in mass flow rate as well

not truly represent the actual heater's characteristics. It does, however, provide a general model of what to expect when obtaining experimental data. The model illustrates the aggressiveness in the Simulink model. As the engine speed (baby blue line) rises, the coil temperature (green line) works hard to keep the actual temperature (magenta line) veered away as little as possible from the set point. Towards the end of the simulation, a drop in engine speed noticeable rises the actual air temperature, at which the coil temperature would then lower to maintain the air temperature.

4.3 HEATER PHYSICAL MODEL

Along with the heaters, there also needs to be a controller of some sort that can provide the appropriate switching to set and maintain temperatures. Hypercell's PID Tuner outputs either voltages or current, and these signals connect to a Motorola 68HC12 microcontroller. The microcontroller, mounted to a powered circuit board (Figure 4.22), is then programmed to output pulsed-width-modulation (PWM) for a certain duty cycle rating. That PWM is used to switch the heaters either on/off.

as the aggressiveness in the PID tuning. As the engine speed increases, there is a slight steady-state error, but Cheung deemed that this value was negligible. One also wonders how the temperature reaches the set point and suddenly levels itself out rather than asymptotically approach it. Credit could be given to the heater's power and also to Simulink's aggressiveness. After consulting Dr. Birdsong, he affirmed that the model is reputable as a comparison to the experimental data to be seen.

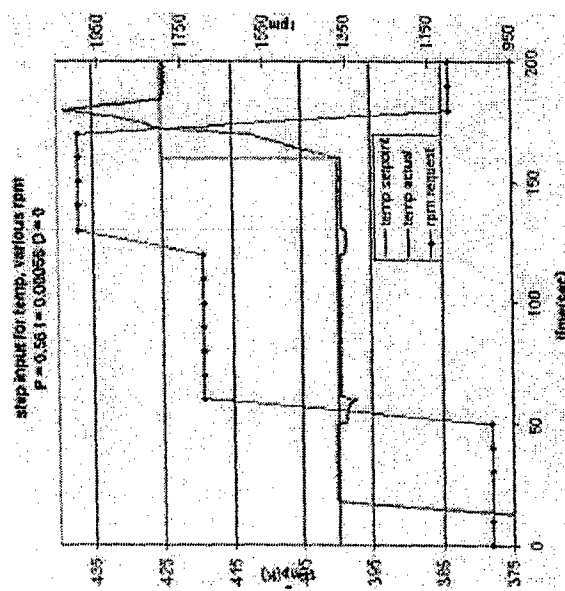


Figure 4.21 Theoretical Temperature Maintenance with Engine Speed Variance

One should take with a grain of salt that though the Simulink heater model presented in this work is very meticulous with respect to the actual HCCI heater's characteristics, it still does

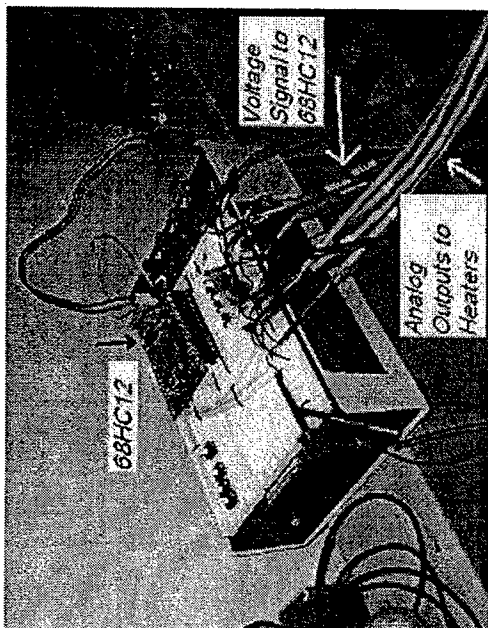


Figure 4.22. Motorola's 68HC12 Microcontroller on Circuit Board

Cheung and Jacques worked with Dietrich on designing the heaters. For Dietrich, this part of the HCCI project represented his Cal Poly Mechanical Engineering Senior Project. Cheung and Jacques gave Dietrich the demands the HCCI engine required, and Dietrich, along with Dr. Murray, worked together on the controls.

To obtain the fastest heater response, Cheung and Jacques wanted the heater control to update at least once per engine cycle (two revolutions). Given that the power from the wall outlet operates at 60Hz, a quick conversion yields:

$$60\text{Hz} \rightarrow \left(\frac{60\text{cycles}}{\text{sec}} \right) \left(\frac{60\text{sec}}{1\text{min}} \right) = 3600\text{ dutycycles/min}$$

Equation 4.19. Number of Heater Updates/Min with Wall Power Frequency

There are two revolutions in each engine cycle, and a quick multiplication yields 7200RPM/min as the maximum engine speed while still obtaining "one heater update per engine cycle." However, due to switching considerations (explained in Dietrich's report), the optimum time to update was every 0.1 seconds, where the updates would synchronize with the wall AC signal and not accidentally cause any voltage impulse. During this update period, there are six AC signals, and these signals govern the number of duty cycles, also six. The methodology and software associated with the microcontroller is explained in Dietrich's report [42].

At 1500RPM a random speed, each engine cycle is 0.08, which is less than the proposed update time. It is possible to lower the PWM update rate to half the time (0.05sec), but doing so would allow only three duty cycles, a very poor resolution to work with. The HCCI team has not tried the original (0.1sec update) model yet, so the microcontroller is given its first test. The following flow chart illustrates what happens to the set point data from start to finish [43]:

and opening it (pressing the button) shuts-down the coil heaters. Instead of trying to use button, Cheung and Jacques reversed-engineered the blow-dryer's internals and its heater switch was soon tied to the Crydom relays, which was connected to Cellmate, which lead to the microcontroller. Since the HCCI engine's intake heaters basically operate on/off, the heater settings on the blow-dryer can be neglected. The relays control whether or not the heaters are turned on/off. The fan is wired to the plug; therefore the fan is always on whenever the plug is in the socket. A thermocouple is taped to the blow-dryer's outlet, and is connected back to the boom, as all the other sensors are connected. Its information is thus displayed in Hypercell's display screen. The blow-dryer's control is set in Hypercell's PID tuner.

When the PID tuner is initiated, the set point temperature is inputted, and the display screen illustrates the temperature. However the heater would not maintain any temperatures close to the set point; instead the blow-dryer's coil heater took the air through a series of unrepeatable temperature patterns. Sometimes the heaters would somewhat cooperate and maintain a temperature, but the occurrence is everything but reliable. Cheung and Jacques tried repeatedly to make temperatures match by changing PID values iteratively, but the blow-dryer exhausted nothing but fluctuating temperatures.

The blow-dryer proved to be useful for preliminary tests, even if the results were less than desirable. However the HCCI engine was now ready to be motored and it seemed more applicable to run heater tests on the actual intake heaters rather than the blow-dryer.

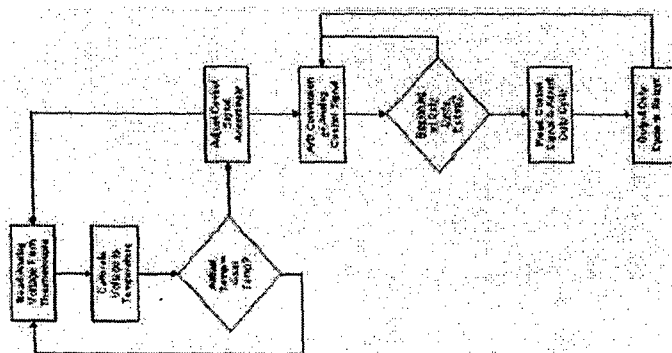


Figure 4.23 Flowchart Illustrating Temperature Set Point Data

Blow-dryer Method

Since using the large, expensive heaters for preliminary testing would be inefficient, Dr. Murray sacrificed his blow-dryer for the HCCI team to use. The blow-dryer contains a manually operated button that allows the user to turn the heater coils off completely. There are also settings for different heater power settings. The heater switch is normally closed,

HCCI Intake Heater Methods/Troubleshooting

Before mentioning anything else, Cheung and Jacques literally made breakthrough by discovering, after almost a month, how to input temperature set points into Hypercell "correctly." As mentioned previously, Hypercell is definitely not without faults, and one of them included the temperature readouts in the software's PID Tuner. The two students spent countless hours inputting temperatures containing three digits, thinking that the inputs were in the "100s," yet the last digit represented the "tenths" place (Figure 4.24).

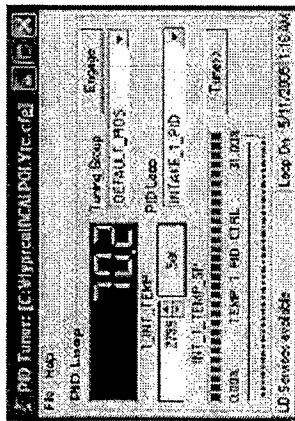


Figure 4.24: Setpoint reads "279.9," but is 279.9F

Unfortunately, someone at Digalog forgot to insert the decimal point, and that sparked all the confusion. This lack of information made setting-up Hypercell's PIDs (Figure 4.25) almost easier, even if Cheung was referring to Hypercell's rather poorly written owner's manual. The manual failed to mention or point-out the important procedures in creating the PIDs. Such instances included the all-important "hcci.ini" file, where, without modifying it rendered the PID Tuner useless. Technical support from Digalog was initially helpful, where the company's service technicians took the time to dissect the HCCI team's problems.

However, seeing that the technical support was continuing without any type of compensation, Digalog gradually hinted at applying for a "work order" where their representatives would, at a significant rate, help troubleshoot the problems. One could continue on with the numerous problems Cheung and Jacques came across during their long familiarization period with the Hypercell program, but there exists other troubleshooting to solve.

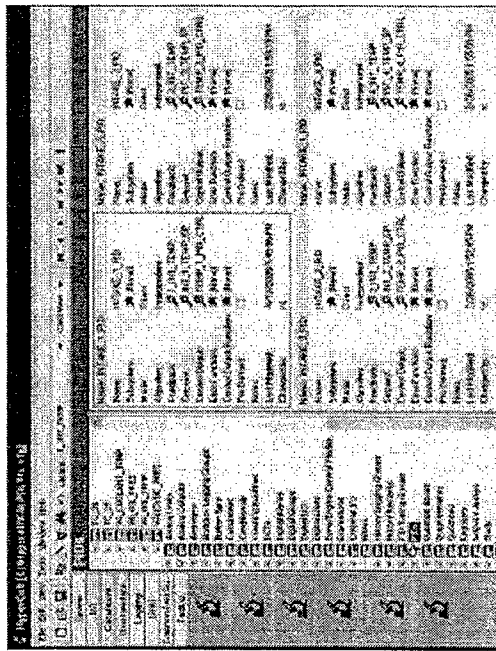


Figure 4.25: Hypercell PID Screen

Even though the heaters are physically connected to the engine, the whole intake system can be disconnected and tested without having to turn the engine. Therefore the fan used back in the heater's fan preliminary tests was used to supply the air flow to the heaters. Before

The HCCI team can better tune the heater control system had a smaller range for the PID values to control intake air temperature now that they are armed with the engine's actual flow values. Before trying to match temperature set points, Cheung and Jacques decided to see how the Simulink's model would compare to the experimental data in terms of attaining maximum steady-state temperature.

Having separating the intake system from the test of the engine, the fan was now "throttled" to different mass flow rates to see what kinds of curves the heaters would generate and how they would compare to the Simulink model. Figure 4.27 shows some preliminary Simulink curves compared with the intake heaters. Both models were set to operate with the same engine speed and maximum temperature.

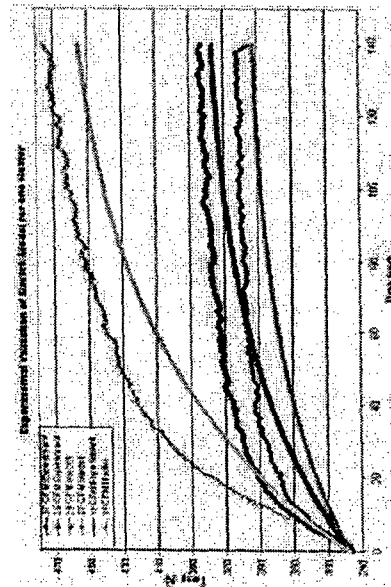


Figure 4.27: Preliminary Experimental/Theoretical Heater Comparisons

The figure illustrates 11, 25, and 37 CFM, which roughly translates to 1570, 3570, and 5280RPM, respectively. The most usable value is probably 11CFM, but the fan's crude

getting all four heaters to work. Cheung and Jacques used to duct tape to cover three of the heaters so they could fine-tune one heater and apply those changes to the other three later on. From previous motoring runs, the team observed engine speed with respect to mass flow rate, measured in CFM. The heaters were then turned on to some maintainable temperature and the mass flow rate was observed again. As predicted, because heat expands air, the mass flow reading dropped from a less dense volume entering the engine. Seen in Figure 4.26, the two charts compare how heat affects the density.

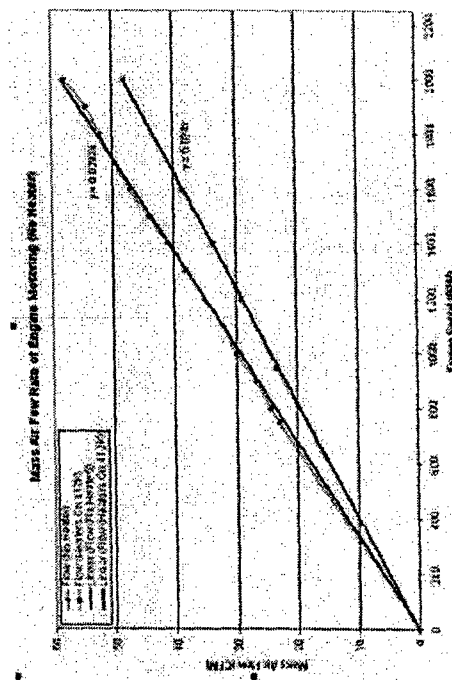


Figure 4.26: Flow Rate Comparison with Heater Variable during Motoring Process

The chart also helped with the "throttling process," While Jacques watches the CFM reading on Hypercell's display screen, Cheung adjusts the fan opening as necessary to mimic the engine speed. One will notice that the chart now focuses on a much smaller engine operating range instead of wide range back towards project's beginnings.

"throttling" process led Cheung and Jacques to experiment with a wider range of flows. When comparing the two models for the first time, one can see that the curves are somewhat similar, although not accurate enough to be representable, yet. Simulink's model seemed to need a bit of "tuning" before it could accurately represent the experimental data. In fact, Figure 4.27's model contained one of the earlier Simulink heater model versions. Through more comparisons between the two models, various details such as more realistic heat transfer coefficients, and calculated (instead of conjectured) heater wall temperatures became implemented to the theoretical model. Figure 4.28 shows how, at 11CFM, the Simulink model responds similar enough to warrant validity against the experimental data.

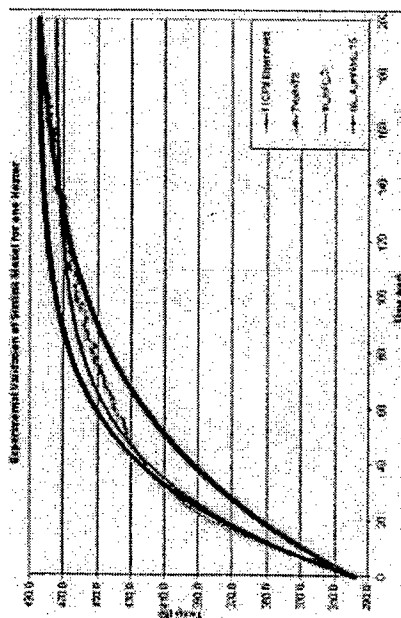


Figure 4.28: Fine Tuning of "HCCI_params" to Match Experimental Data

The magenta curve seems to overlay nicely with the experimental data towards the curves end, but seems to fall under during the transition to steady-state temperature. The green line locks onto the experimental data during the curve's first part, but seems to reach steady-state

at a lower temperature. By changing some more variables like the specific heat as well as the heater coil's emissivity, the blue line, although not perfect, duplicates the experimental data close enough to gain approval of the Simulink model.

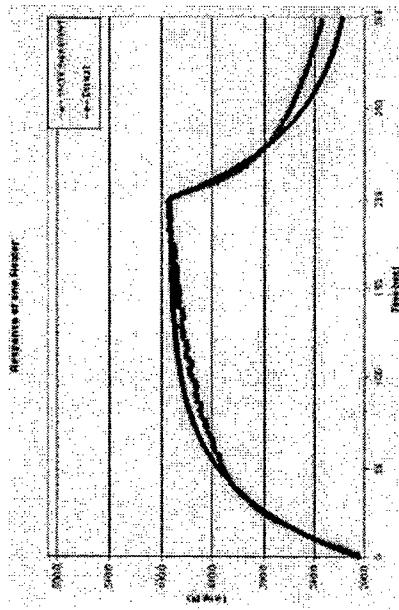


Figure 4.29: Final Simulink Model Following Experimental Curve

Now that the Simulink model is working nicely, heater control troubleshooting resumes. Figure 4.28 and Figure 4.29 illustrated curve-matching with respect to maximum and not transient temperature response between the two systems. This is because the PID Tuner still did not hold a temperature with confidence at that time. Cheung and Jacques then suggested to Dietrich that, instead of trying to reduce update rate, he should try to implement more duty cycles into the microcontroller. The unit was still operating with six duty cycles, and the HCCI team felt that this resolution was much too low to maintain a temperature. Given a temperature set point, the microcontroller will try its best to monitor the heaters, but if provided with such low resolution, the heater will never be operating at a

desired power level. Instead it would fluctuate between two levels, both not really matched to the set point, and ultimately become unstable, as observed by the team.

The initial issue with an update rate that is longer than each engine cycle was dismissed. After testing the heaters for some time, Cheung and Jacques gained a better understanding of the temperature rise and drop time. If the update time was reduced, the duty cycle would drop from six to three settings, thus substantially hurting heater control. Update would certainly be quicker, but the heaters' transient responses do not require such fast updates. A new temperature set point would require at least a few engine cycles before one sees any change in temperature due to the heater's physical properties.

With that in mind, Dietrich's solution was to implement more duty cycles: first to 15, but ultimately to 30. After that, the heater response drastically improved. Not perfect, but this set the foundation for future HCCI intake temperature control development. The PID tuner, as complicated as it can be with its multiple 'initiate' buttons, was set with just a proportional gain and left alone from there on.

During this time Cheung and Jacques also noticed that the heater system responded nicely when only a proportional gain was given to the PID Tuner.

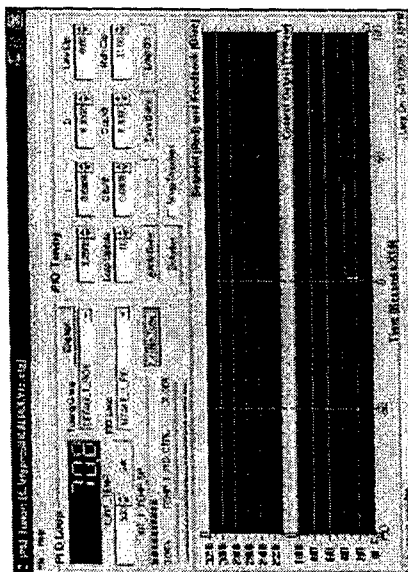


Figure 4.30: Complete Hypercell PID Tuner

Recall that Simulink's model yielded $k_p=0.056$ and $k_i=0.0006$ (Figure 4.17). However, when just the proportional gain was applied to Hypercell, the microcontroller would not send a strong enough signal to the heaters. Thus the temperatures never approached the set point. Therefore Cheung started experimenting with higher gains, and that made a positive effect. Finally, a 9.25 proportional gain net some decent temperatures with the set points in the HCCI operating range. While working the PID Tuner, at a fixed engine speed, a certain proportional value will pull-off a temperature where both the set point and actual temperature coincide. At set points below this temperature, the actual temperature had a positive steady-state error, and negative steady-state errors when the set point was larger than the "magic" temperature. With "9.25" and at 1300RPM, the temperature where both models met was somewhere around 290°F, or 416.5°K, which gave a nice HCCI temperature. " k_p " was now set.

When trying to introduce the theoretical integral gain, Hypercell would go unstable and the heaters would take the intake temperature to interstellar levels, come back below the set point, and repeat, creating a sinusoidal curve when plotted against time. After many iterative attempts, any sort of integral value would succumb to instability. The HCCI team was out of any solutions, and time was starting to seriously take a toll. Therefore, to minimize as many variables as possible, and to continue moving forward the control system, the PID Tuner was thus left with only the proportional gain.

There was speculation about a thermal lag occurring in the intake system, causing the PID Tuner to become unstable. To go about this solution, the intake tract for one of the cylinders was inserted with three thermocouples at different locations:

1. right after the intake heater lodged in the silicon tubes,
2. in the original venturi location
3. at the end of the intake tract right before entering the intake ports

The control thermocouple in this case was the one located at the end of the heater because the thermocouple there would take the air temperature as soon as it comes out the heater—basically no thermal lag.

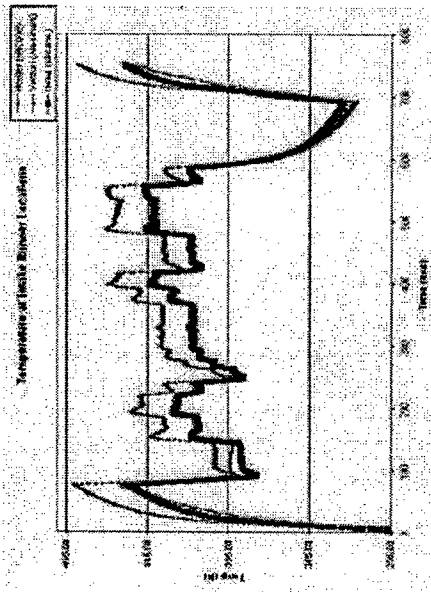


Figure 4.31: Similar Temperature at Different Intake Tract Locations

Figure 4.31 graphs the same temperature response for all three thermocouple locations. More importantly, the temperatures for the heater and port locations were almost identical, which answers the question that the thermocouple at either the end of the heater or before the intake yields the same temperature readings. The higher temperatures found in the aluminum venturi location can perhaps be attributed to radiation heat transfer as well as the bore change. By the ideal gas law, with a constant volume, as the pressure goes down, the temperature would have to increase in order to maintain the same state properties.

With the thermocouple location solved, the PID values confirmed, and the intake temperatures hovering in the set point range, the intake system is now assembled back into the engine for final testing.

5. HCCI ENGINE OPERATION PROCEDURES

5.1 MOTORING PROCESS

Before turning the engine for the first time by the dynamometer, the area has to be clear of any debris or loose rags that might have accumulated from buildup or repairs. The engine oil level is checked, as is the coolant level. The setscrews that hold the coupling flanges in place are scrutinized to ensure they don't cause any slippage that could shear the coupling sleeves. Previous experience shows that any misalignment in the coupling flanges easily ruins the coupling sleeve, so the pillars for the engine are inspected for sturdiness as well as levelness. The cover for the coupling assembly is then covered and bolted down. The battery for the ECU as well as the intake heater main relays is then plugged, and the ventilation as well as the exhaust fan is turned on.

Back at the control desk, the order for turning on the appropriate equipment must be observed closely; otherwise the system might not boot-up correctly.

111



Figure 5.1 HCCI Control Desk (ECU): Top Left, Engine Parameters; Middle Left, Intake Heaters; Bottom-Left, Intake Heaters; Center, Emissions; Middle Right, Cellmate and Testmate; Far-Right)

The dynamometer power supply is first switched on. The operator then turns on the Testmate Panel by flipping the switch on the back of the unit. While Testmate starts up, flipping the switches in the back turns on the Cellmate and Testmate unit. Cellmate contains a hard disk light that stops flashing after completing its booting process. At that time the Testmate Panel LCD screens display "0.0" for both the engine and dynamometer readout. The operator then opens up the Hypercell software on the desktop computer. The main menu bar shows up and the engine is now ready to be motored.

112

5.2 HYPERCELL DATA LOGGING

Because the operator will usually want to log data when the engine is being motored or operating in HCCI mode, Hypercell offers the option of logging data to Cellmate, which can then be uploaded to MS Access. This option is configured before a new test is initialized. The "history" button on the main menu bar opens the history options, which includes location of file to be uploaded, which test number to be uploaded, and what types of data points to be uploaded. The operator will usually want to upload just the data for the test to be run. First, a new history file is created from the "File" menu. This *.his file is used to upload data to MS Access. Next, the operator goes to "Cellmate Status" to confirm what test number is to be saved. "Cellmate Status" displays the test number just completed, and what test is next. Having this information, the operator then goes to "History Options" to specify which test to save. Failure to do so will prompt Hypercell to automatically save the data from all its previous tests.

Now that the History is set, the operator has to set the logging methods, and clicking on "Logging" initiates the options. The logging box appears, and the operator specifies the time for the logging sequence to last. The duration between each logging point is also set, and as a redundant measure, the number of points during this logging session is inputted as well.

After the engine test has been completed, the operator goes back to the "History" box to upload the *.his file from Cellmate to the computer. He/she points to "File," and clicks on "Start," which initiates the uploading process. Upon completion, the progress box will show that all the data for the preceding test is finished uploading to the location specified earlier. The operator now has to close the "History" in order to access the history file. In MS Access, the *.his file is now opened and converted to the appropriate Access file. However,

the software bond between Hypercell and Access contains some glitches yet to be combed out, and the only way to obtain the information from Cellmate is to go through the repetitious warnings and notifications given by Access. Once, however, the operator successfully opens the newly-acquired file, the test data is located in the "RUNXXXXXXDATA" group in the Access file.

5.3 STARTUP

In order to operate the engine in HCCI mode, the motoring process is first achieved. For Cal Poly's HCCI engine, Cheung and Jacques first listened to how the engine sounded at various speeds, and from that they determined 1300RPM to be the smoothest in terms of noise, resonance, and vibrations. When the engine is motored initially, it is brought-up to 950RPM to ensure that everything is running smoothly. The heaters were then turned on and brought to the set point. As the actual temperature asymptote, the engine was fed more revolutions until it reached 1300RPM. From there, the heaters were given a few moments to adjust the air temperatures accordingly.

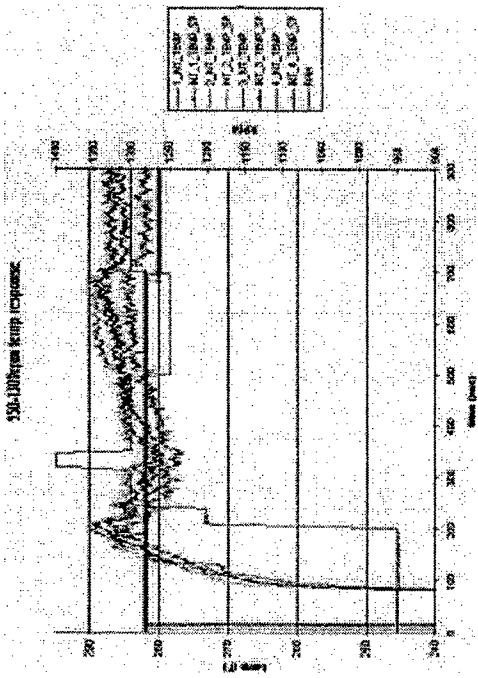


Figure 5.2: Initial Motoring Process before Adding Fuel

Figure 5.2 illustrates the temperature response prior to adding fuel. The intake temperature in cylinder #4 seems to remain lower than the other three, and this could be attributed to its outer location in the engine. Once the temperatures were set, and that fuel was ready to be tipped into the engine, Cheung turned on the TEC'r power through Hypercell's display. The ECU is given a few moments to set itself up, and when that was completed, Jacques initiated the fuel-injecting process by setting the ECU's "user-adjusted pulsewidth" (UAP). Being that this was Cheung, Jacques, Laszlo, and not to mention Dr. Delagrammatikas's first time starting an HCCI engine, the four didn't exactly know what to expect. Temperatures were stable in the HCCI regions, and the fuel injected was calculated correctly. Nothing was happening, and everything was "correct" in the eyes of the team. Dr. Delagrammatikas then

decided to add more fuel to initiate combustion. Like a carbureted engine, the fuel has to be primed a small amount to initiate combustion. Jacques adjusted the UAP to inject more fuel, and Cheung increased the intake temperature across the cylinders from 280°F to 312°F. Jacques kept adding some more fuel, and suddenly the team heard some low, "popping" sounds. From the pressure transducer display, the engine was misfiring (Figure 5.3), which led Dr. Delagrammatikas to enthusiastically point out the engine's willingness to go into HCCI mode.

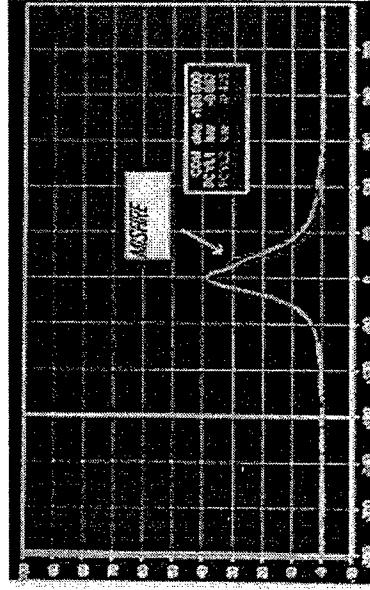


Figure 5.3: HCCI Misfire Due to Low Temperature of Insufficient Fuel Injection

Misfire occurs when combustion happens later in the expansion stroke, at a lesser pressure. This leads to lower thermal efficiencies and extremely low power outputs. The reason behind combustion occurring at a lower pressure is due to the chemical kinetics and mixture properties inside the combustion chamber, which was not part of the study this time. Jacques continue to increase the pulsewidth a bit more, and after giving the chambers some

time to "get a feel of HCCI," the pressure spikes started to come to life, and at that moment Cal Poly had just successfully started up their own HCCI engine.



Figure 5.4: Cal Poly's Successful HCCI Engine

6. RESULTS FROM ENGINE OPERATION

Even when Cal Poly's engine is being motored without any fuel, the heaters can still be operated to see their effectiveness/response at various temperature set points. However, the true test comes when all other factors such as engine combustion heat and air pulsing from the intake cycles play an effect on the heater control system.

6.1 TEMPERATURE RESPONSE TO TRANSIENT ENGINE SPEED

With the engine motoring, the intake system is now tested with just one signal coming from the microcontroller to all four heaters. Using cylinder #1 as the control signal, Cheung goes through various temperature set points and observes the transient response. An oscilloscope is connected as well to monitor duty cycle rating. From Figure 6.1, the initial temperature set points are set at 200, 240, and 280°F. Since these values are lower than the 290°F or so coinciding temperature mentioned previously, one can expect the actual values to be higher. Getting to 280°F brings the actual temperatures quite close to the set point, but there needs to be an explanation as to why there are differences among the four intakes.

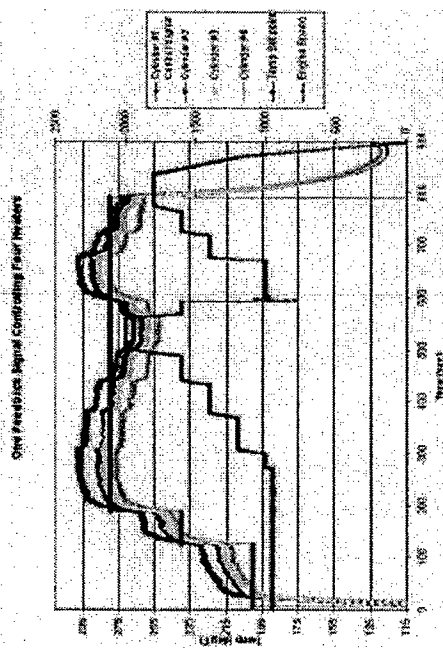


Figure 6.1 One Control Feedback to Four Heaters

In addition, adding some engine speed variation brings some interesting results as well. The oscilloscope displays a noticeable duty cycle increase from its display screen. However, the PID Tuner seems not to have the aggressiveness to accommodate the higher mass flow rates taken by the engine, and as a result the actual temperatures do not maintain the set point. There also is some unexplainable temperature variation across the intake ports. The HCCI team initially thought that the intake system needed some time to heat-up its aluminum walls, silicone tubing, and attain steady-state, but even after 800sec (13+ minutes), the temperature among the four intakes remained in the same order.

That issue is quickly solved by implementing three more signals from the microcontroller to the other heaters. The result is control of four heaters on an individual basis. Figure 6.2 shows the much improved transient temperature response among the four heaters. The

straight lines are the set points, and their offsets between one another illustrate the user changing the temperatures one-by-one. Though there is a small lag between the new set points, this proves to be of very little influence on overall temperature behavior.

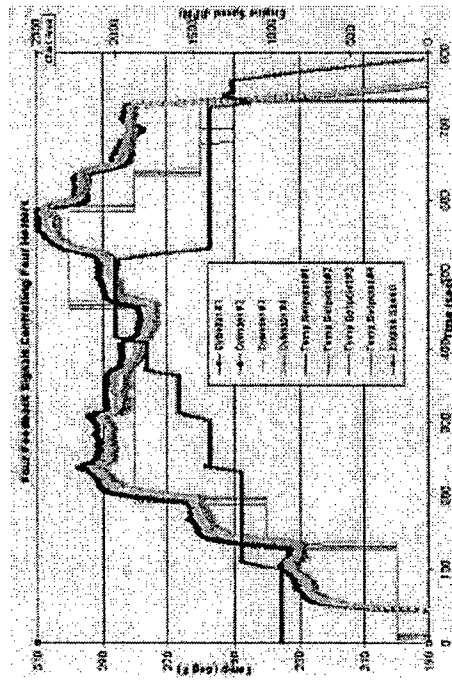


Figure 6.2 Temperature Feedback with Four Signals, Four Heaters, Varying Engine Speeds and Temperature Set Points

As presented before with the "one signal" example, higher engine speeds reveal the PID Tuner's lack of aggressiveness in maintaining the desired temperature. However, because HCCI combustion occurs over a wide range of temperatures, one can set the PID Tuner to a higher set point to compensate for these causes to the heaters less-than-perfect response, which is what Cheung did during the HCCI engine tests.

6.2 ADDING FUEL FOR HCCI COMBUSTION

When operating the engine HCCI mode, Jacques added the necessary fuel to maintain proper combustion, while Cheung varied the intake temperatures until the air/fuel ratio, alwilde monitoring the reading on the MoTec PLM making sure it was around 23:1, the desired HCCI relative air/fuel ratio.

From the very beginning of the HCCI project, the goal of four intake heaters was to have individual control of the air temperature going into the cylinders. The temperature range for HCCI combustion is broad, but this is true only when the proper air temperatures and air/fuel ratios are combined. Jacques performed a preliminary study mapping-out the engine, and Cheung used individual heater control to maintain the desired set points during those tests. During that time all four cylinders were outputting around 280°F (411°K) when cylinder #3 showed visual and audible signs of knock, with cylinder #4 operating at the rich limit of HCCI. Figure 6.3 shows the red pressure spikes in cylinder #3 and #4, signifying knocking inside the combustion chamber, more so in cylinder #3.

121

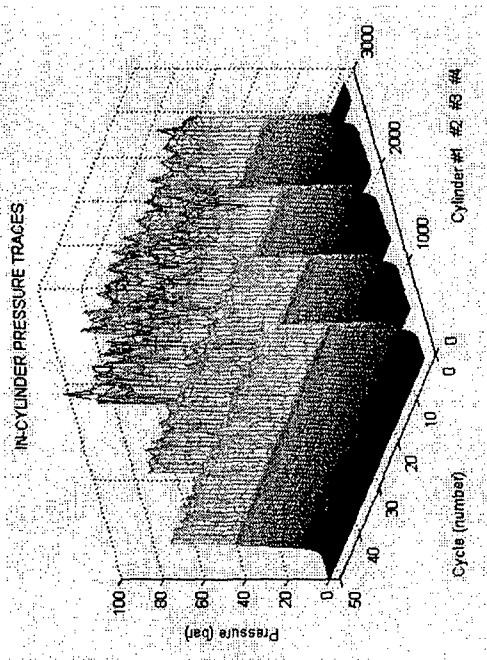


Figure 6.3: In-Cylinder Pressure with #3 and #4 Knocking

A common cause of knock in HCCI combustion is either too much fuel or air temperatures that are too hot. Too much of both initiates combustion at various points in the chamber before and after the piston reaches TDC, which basically defeats the HCCI concept.

Since cylinder #1 and #2 were already running smoothly in their current state, reducing the amount of fuel would result in misfire. Therefore Cheung decreased the intake temperatures in cylinder #3 to around 260°F (400°K), which was in the lower operating region. Within the time it took to lower the intake temperature, the knocking quickly, but not instantaneously, went away. To confirm this, the knocking noise disappeared and out came a much quieter engine operation noise. The in-cylinder pressure (Figure 6.4) traces also illustrated the "signature" HCCI combustion pressure spike.

122

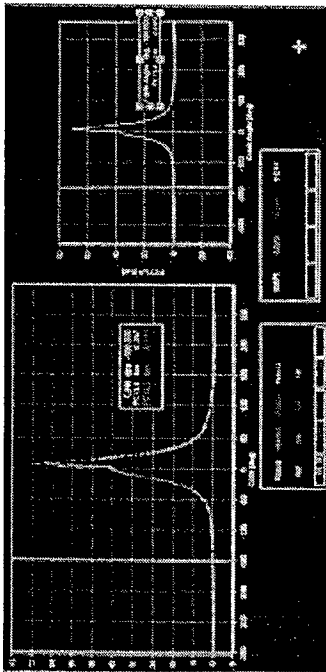


Figure 6.4 In-Cylinder Pressure Traces During Stable HCCI Combustion

Figure 6 further illustrates that by changing the temperature in cylinder #3 to one that is more suitable, knock (represented by the red spikes) is now eliminated. Cylinder #4, untouched, is still operating in the knock threshold region, which confirms the validity of individual heater control in Cal Poly's HCCI engine.

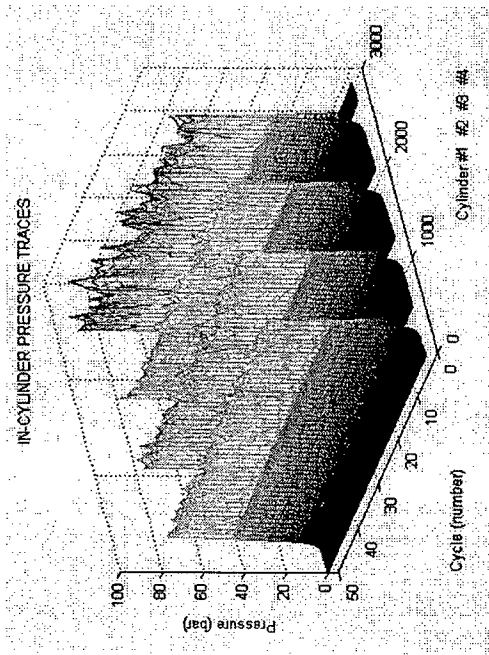


Figure 6.5 In-Cylinder Pressure Traces Illustrating Knock in Cylinder #4

Conclusions and future research directions

The HCCI engine at Cal Poly State University San Luis Obispo sees a great future ahead of it. Mostly free of bugs and running in HCCI mode with confidence, the research performed on this engine has barely even scratched the surface. What was not available previously to control combustion because of old technology is not an excuse anymore today. With its promising benefits, positive results obtained by other researchers, plus the massive research to be carried by this engine, one hopes that HCCI will one day find its way into mainstream society. As mentioned, the focus of HCCI combustion the ultra-low emissions that come out the exhaust; and in the combustion realm, there is probably nothing else that comes close to it.

6.3 SUGGESTIONS / RECOMMENDATIONS

Though Cheung and Jacques have learned the tricks of the trade in operating the software pertaining to the HCCI engine, it would be much more desirable if these glitches were taken out. In the course of the project, the HCCI team spent too much time figuring these small mistakes that the software companies never took out. Being that this engine is only a foundation for many discoveries and changes to come, some of the hardware would benefit from future improvements as well.

Software

Hypercell provided the most headaches with, as mentioned before, with its temperature set point displays, as well as its "hcci.ini" file. In addition to spelling mistakes on their display interface, their logging program was quite confusing to operate, and seemed to ask for repetitive information when configuring the logging files. Hypercell is also very sensitive

125

with its startup procedure. The Cellmate and Testmate units located in the cabinets have to be turned on before the software is executed. The Testmate panel has to be switched on before the Cellmate and Testmate units are turned on. The data file uploaded from Cellmate to MS Access could be a lot smoother since the current transfer process, although successful, is very tedious and contains many interfacing errors. Finally, the Hypercell manual could definitely see more improvements in terms of comprehension as well as elaboration.

The microcontroller currently works good enough to bring the temperatures to the set point vicinities, but it still needs further development. The addition of more duty cycles reduced the PWM update time considerably, and that resulted in lag while attaining set points. It would be nice if the microcontroller had the best of both worlds: higher resolution duty cycles and a fast update rate.

The TEC'r ECU performed as promised, but during the file configuration stages the unit seemed to have malfunctioned and would not inject fuel as programmed to. A call to the helpful staff at Electromotive revealed that the program sometimes has a tendency to act up. Their suggestion was that when these occurrences happen, it would be wise to just start a new configuration file.

Hardware

Many of the modifications on the engine were their first iterations and so their design and implementation were more on the preliminary level. This included the cam sensor, which after observation, illustrated a noticeable amount of eccentricity while the engine was turning over. The encoder mount is also something in need of improvements. It gets the job done

126

in holding both encoders in place, but the mounting process is extremely tedious and awkward, and its design is rather clumsy.

The plenum before the intake heaters could also be better designed for accuracy. After observing various automobile plenums, the one for the HCCI engine could also benefit from a tapered design to flow the same amount of flow throughout all four cylinders. The silicone tubes should also be replaced with another set that can withstand hotter temperatures. The engine mapping process is currently limited by the 350°F limit imposed on the tube.

In the future, the HCCI engine would like to see itself in the bay of a hybrid-electric vehicle. In order to see that as a reality, something needs to be done to accommodate the intake heaters and their power requirement. It would literally be impossible to supply 8kW of power into an automobile; if it did indeed happen the vehicle's offset would outweigh the benefits it was designed for in the first place. Perhaps another method of heating the intake air without the thirst for such large amounts of energy would solve the problem. Still, much research with the current heater setup is needed before moving on to another method.

To maximize the amount of recoverable energy usage, EGR should one day be introduced, in addition to the intake heater concept, to heat the air going to the cylinders. That way the heaters will not have to demand so much power.

Fuel mixing, not investigated yet, would be a good idea to promote even better fuel economy and combustion properties. Various institutions have performed research on that area, and Cal Poly could use those ideas to branch-off into new research areas.

The fuel flow meter has not been mentioned, but it is used to monitor the fuel flow into the engine. The unit is quite old, dating back to the mid 80s, and its accuracy is questionable.

6.4 WRAPPING UP

Cal Poly has come a long way since its first underpinnings with the HCCI concept. It started as a rather crude design with a stringent budget-restricted modification engine, and has since undergone intensive research and development in an extremely short amount of time. Even with first engine's fiasco, the HCCI team (after a slight emotional breakdown) came back up to build-up another engine. Within two months that second engine was successfully operating in HCCI mode. Being the first institution in Central California to embrace an HCCI engine is no small feat by any means, and the students involved with this project sure could not have completed it without their advisors' and peers' encouragements and motivations.

One wonders what the future of combustion brings, and although SI and CI engines seem irreplaceable at the time being, one day society will have the opportunity to fit another type of combustion into their garages, farming fields, power source, and so forth. Cal Poly has made a large step forward by illustrating the capabilities of individual intake temperature control for each cylinder, and this preliminary framework provides the foundation for others to build and improve on.

APPENDIX A: TABLE

Stroke	95.50mm
Connecting Rod Length	144.00mm
Compression Ratio	18.34 (measured)
Firing Order	1-3-4-2
Engine Block/Head	Cast Iron/Aluminum
Piston Geometry	Bowl
Intake Valve Open (1mm lift)	16 CAD ATDC
Intake Valve Close (1mm lift)	25 CAD ABDC
Exhaust Valve Open (1mm lift)	28 CAD BBDC
Exhaust Valve Close (1mm lift)	19 CAD BTDC

1: Volkswagen 1.9L TDI Engine Specifications

QTY	PART NO.	DESCRIPTION
1	N-905-969-02	IDLER BOLT
10	N-901-300-01	MAIN BEARING END CAP BOLTS
8	028-105-425-C	CONNECTING ROD BOLT
6	N-906-650-01	FLY WHEEL BOLT
1	1038-105-229	CRANK SPROCKET SCREW
10	068-103-384-A	HEAD BOLT
1	1038-103-383-K	HEAD GASKET (3 HOLE)
2	028-129-717-D	INTAKE GASKET
4	028-129-589-B	EXHAUST MANIFOLD GASKET
8	N-101-333-01	CIRCLIP
1	044-121-113	THERMOSTAT
1	06B-121-687	COOLANT LINE O-RING
1	1038-121-119-B	COOLANT CONNECTOR O-RING
1	1038-121-119	WATER PUMP O-RING
1	1037-121-688	COOLANT CONNECTOR O-RING
1	1038-103-085-E	FRONT SEALING FLANGE SEAL
1	N-908-132-01	OIL PAN BOLT SEAL

2: Kimball Parts Purchase List

RPM	Theoretical mass flow rate (kg/sec)
1000	0.00317
1500	0.00476
2000	0.00635
2500	0.00794
3000	0.00952
3500	0.01111
4000	0.0127

3: Engine Speeds and Corresponding Theoretical Flow Rates

Engine Spd (RPM)	1000	1500	2000	2500	3000	3500	4000	4500	5000
mdot total (kg/s)	0.0133	0.0199	0.0266	0.0332	0.0399	0.0465	0.0531	0.0598	0.0664
mdot 1 cyl (kg/s)	0.0033	0.0050	0.0066	0.0083	0.0100	0.0116	0.0133	0.0149	0.0166
mdot (CFM)	5.0535	7.5802	10.1069	12.6336	15.1604	17.6871	20.2138	22.7406	25.2673

4: Preliminary Heater Calculations for Flow vs. Engine Speed

Cyl #	Trial 1 (ml)	Trial 2 (ml)	Avg (ml)	Plexiglas Vol (ml)	Difference (ml)
1	36.2	36.2	36.2	35.9	0.3
2	34.9	35.1	35.0	34.9	0.1
3	34.3	34.2	34.2	34	0.3
4	33.2	33.2	33.2	33.4	-0.2

0.125 avg

5: Engine Buildup #2 Head Measurements

Cyl #	Trial 1 (ml)	Trial 2 (ml)	Trial 3 (ml)	Avg (ml)	Plexiglas Vol (ml)	Difference (ml)
1	59.8	58.6	n/a	59.2	35.9	23.3
2	57.7	58	57.8	57.8	34.9	22.9
3	n/a	57.1	56.8	57	34	23
4	56	56	n/a	56	33.4	22.8

22.95 avg

6: Engine Buildup #2 Block Measurements

Cyl #	CR
1	16.2
2	16.3
3	16.34
4	16.3

16.285 avg

7: Compression Ratios for Engine #2 Buildup

APPENDIX B: BIBLIOGRAPHY

- 1 Heywood, John B., *Internal Combustion Engine Fundamentals*, McGraw Hill, INC., 1988.
- 2 Heywood.
- 3 Heywood.
- 4 C. Csere. "The Steering Column: The gasoline engine still has a few tricks left." *Car and Driver*, June 2005. Hachette Filipacchi Media. 2005
- 5 Heywood.
- 6 R. H. Stanglmaier, C. E. Roberts. "Homogeneous Charge Compression ignition (HCCI): Benefits, Compromises, and Future Engine Applications." SAE1999-01-3682.
- 7 R. Ogink. "Homogeneous Charge Compression Ignition (HCCI) Combustion." *Mechanical and Vehicular Engineering—Chalmers Institute of Technology*. <http://www.tfd.chalmers.se/~ogink/hcci_described.html>. 27 April 2005.
- 8 Stanglmaier, Roberts.
- 9 M. Williams. "The End of Oil?" *M.I.T.'s Technology Review*, February 2005
- 10 Sun, Thomas, Gray.
- 11 "EPA building hydraulic hybrid urban delivery vehicle." *Power Electronics Technology*. PRIMEDIA Business Magazines & Media Inc. 2005. <http://powerelectronics.com/autoelectronics/epa_building_vehicle/>. 10 May 2005.
- 12 M. Christensen, A. Hultqvist, B. Johansson. Demonstrating the Multi Fuel Capability of a "Homogeneous Charge Compression Ignition Engine with Variable Compression Ratio." *Lund Institute of Technology*. SAE 1999-01-3679
- 13 P. M. Ferri, M. L. Franco. "Ignition Control in a Homogeneous Charge Compression Ignition Engine." *California Polytechnic State University, San Luis Obispo, CA*. September 2004.
- 14 S. Yamaoka, H. Kakuya, S. Nakagawa, T. Nogi. "A Study of Controlling the Auto-Ignition and Combustion in a Gasoline HCCI Engine." *Hitachi Research Laboratory, Hitachi, Ltd*. SAE 2004-01-0942.
- 15 H. Kopecek, E. Wintner, M. Lackner, F. Winter, A. Hultqvist. "Laser-Stimulated Ignition in a Homogeneous Charge Compression Ignition Engine." SAE 2004-01-0937.
- 16 D. Law, J. Allen, R. Chen. "On the mechanism of Controlled Auto Ignition." SAE 2002-01-0421.
- 17 R. Sun, R. Thomas, C. L. Gray Jr. "An HCCI Engine: Power Plant for a Hybrid Vehicle." SAE2004-1-0933.
- 18 M. Christensen, B. Johansson. "Homogeneous Charge Compression Injection with Water Injection." *Lund Institute of Technology*. SAE 1999-01-0182.
- 19 Ferri, Franco.
- 20 J. Martinez-Frias, S. M. Aceves, D. Flowers, J. R. Smith, R. Dibble. "HCCI Engine Control by Thermal Management." SAE 2000-01-2869.
- 21 R. Dibble, M. Au, J. Girard, S. M. Aceves, D. L. Flowers, J. Martinez-Frias, J. R. Smith. "Current Research in HCCI Combustion at UC Berkeley and LLNL." SAE 2001-01-2511.
- 22 Volkswagen Jetta, Golf, GTI Service Manual, 1999-2003. Bentley Publishers, Cambridge, Mass. 2003
- 23 N. Jacques. "Groundwork Assessment of Cycle-to-Cycle Variation in a 1.9L Gasoline HCCI Engine." June 2005
- 24 Jacques
- 25 Ferri, Franco.
- 26 Jacques
- 27 M. Christensen, B. Johansson, A. Hultqvist. "The Effect of Piston Topland Geometry on Emissions of Unburned Hydrocarbons from a Homogeneous Charge Compression Ignition (HCCI) Engine." SAE 2001-01-1893.
- 28 Electromotive, Inc. patented Direct Ignition and Total Engine Control. <<http://getfuelinjected.com/>>. 10 May 2005.
- 29 Heywood
- 30 G. Parise, M. Coombs, S. Drayton, J. H. Haynes. "VW Golf & Jetta Automotive Repair Manual." Haynes Publishing Group. Somerset, England. 1997
- 31 Heywood.

- 32 Electromotive Engine Controls. TEC³ Installation and Calibration Manual, Version 1.9. Electromotive, 2002.
- 33 ARIAS Pistons website. <<http://www.arias Pistons.com/custompistons.html>>. 8 May 2005.
- 34 Cellmate® CM/3i User Manual. Hardware Section. Digalog. 2001.
- 35 TEC³ Installation and Calibration Manual.
- 36 Moran, Michael J. Fundamentals of Engineering Thermodynamics, 4th Edition, John Wiley & Sons, INC., 2000.
- 37 F. P. Incropera, D. P. DeWitt. Introduction to Heat Transfer, Fourth Edition. John Wiley & Sons, INC., 2002.
- 38 Incropera, Dewitt. Equation 8.60^c.
- 39 Incropera, Dewitt. Table A.4, Appendix A.
- 40 Engineering Note: Tuning the PID Coefficients. Sun Electronic Systems, Inc.
- 41 Engineering Note.
- 42 J. Dietrich. Senior report.
- 43 J. Dietrich.

EXPERIMENTAL ASSESSMENT OF CYCLE-
TO-CYCLE VARIATIONS IN A GASOLINE
1.9L HCCI ENGINE
(DRAFT)

A Thesis presented to the faculty California Polytechnic
State University, San Luis Obispo

In partial fulfillment of the requirements for the degree
masters of science in Mechanical Engineering

By
Nicholas Jacques
June 2005

AUTHORIZATION FOR REPRODUCTION OF
THESIS

I grant permission for the reproduction of this thesis in its
entirety or any of its parts, without further authorization from
me.

Nicholas Jacques

Date

APPROVAL PAGE

TITLE: Groundwork and Assessment of Cycle-to-Cycle Variation of a Gasoline 1.9L HCCI Engine
AUTHOR: Nicholas Jacques
DATE SUBMITTED: June 2005

Dr. George Delagrammatikas
Advisor

Signature

Dr. William Murray
Committee Member

Signature

Dr. Charles Birdsong
Committee Member

Signature

ABSTRACT

Homogenous Charge Compression Ignition (HCCI) has a high potential to significantly reduce fuel consumption, nitric oxides (NO_x). Some major challenges associated with HCCI are no direct control of combustion, extending its operation range and high level of unburned hydrocarbons (HC).

A four-cylinder 1.9L Volkswagen turbocharged direct injection (TDI) engine has been converted to run in HCCI mode. The modifications to the stock configuration included new piston design, custom intake, port-fuel injection, removal of the turbocharger, and instrumentation for data collection. The rest of the engine's stock configuration is retained. The direct injectors are disconnected, but remain to keep the combustion chamber sealed. Four individually controlled heaters are incorporated in the custom intake with fuel added downstream of the heaters.

Fundamental experiments and analyses of the limits of operation as well as the cylinder-to-cylinder and cycle-to-cycle variations have been performed. Individual intake heating is a viable means to control HCCI combustion. The variations observed support the need for individual cylinder control. A strong correlation is seen between the timing for the onset of HCCI combustion and the intake air temperature. The temperature to which the intake air must be heated increases with an increase of air/fuel ratio and the maximum obtainable IMEP decreases. The COV of IMEP for each cylinder in the stable combustion regime is less than 3. Low values of NO_x were obtained at 5 ppm.

ACKNOWLEDGEMENTS

<Insert Acknowledgements>

TABLE OF CONTENTS

1. INTRODUCTION.....	19
1.1 Reciprocating Internal Combustion Engines.....	19
1.2 Spark-ignition engine.....	20
1.3 Compression-ignition engine.....	22
1.4 Analysis of SI engine.....	23
1.5 Analysis of CI engine.....	24
1.6 Homogeneous Charge Compression Ignition Engine.....	25
1.7 HCCI emissions.....	29
HC.....	30
NO _x	31
CO.....	31
1.8 HCCI Cycle-to-cycle variations.....	31
2. GENERAL ANALYSIS OF ENGINES.....	35
2.1 Engine design and operating parameters.....	35
Indicated work per cycle.....	36
Mean effective pressure.....	37
Coefficient of variation.....	37
Fuel/air equivalence ratio ϕ	38
Specific fuel consumption.....	38
3. ENGINE SETUP.....	39
3.1 Piston design.....	40
Piston geometry.....	40
Compression ring location.....	41
Material.....	44
3.2 Intake design.....	44
Engine standard air analysis.....	45
Heater sizing.....	47
Heater characterization.....	50
Intake.....	53
Multi-port fuel injection.....	54
3.3 Engine assembly.....	55
Compression ratio and volumetric measurements.....	58
4. TEST BED.....	61
4.1 Dynamometer control and Data acquisition.....	61
Recording Data.....	65

4.2 In-cylinder pressure traces.....	66
4.3 Fuel control ECU.....	70
ECU Software Configuration.....	72
4.4 Fuel injectors.....	81
4.5 Heater control.....	82
4.6 Emissions.....	83
5. HCCI ENGINE OPERATION PROCEDURE.....	85
Inside Test Cell.....	85
Outside Test Cell.....	85
Controls.....	85
Testmate Controller Panel.....	86
Main Computer.....	86
Performing a Test.....	86
To shut Down.....	86
Test Cell.....	87
6. DATA COLLECTED RESULTS.....	89
6.1 Limits of operation.....	89
6.2 Cylinder-to-Cylinder variations.....	92
Misfire.....	92
Stable Combustion.....	93
Knock.....	94
p-v diagrams.....	94
6.3 Cycle-to-cycle variations.....	96
Misfire.....	96
Stable combustion.....	98
Knock.....	99
6.4 Coefficient of variance of IMEP.....	101
Misfire.....	102
Stable combustion.....	102
Knock.....	103
6.5 Emissions.....	104
7. CONCLUSIONS.....	107
REFERENCES.....	109

LIST OF FIGURES

Figure 1-1 Four-stroke engine cycle [1]	20
Figure 1-2 Sequence of events of a SI engine [1]	21
Figure 1-3 Sequence of events in a CI engine [1]	22
Figure 1-4 p-v diagram of the air-standard Otto cycle	24
Figure 1-5 p-v diagram of the air-standard diesel cycle	24
Figure 1-6 HCCI potential emission gains []	30
Figure 1-7 Different chemiluminescence images at 3 CADATD	33
Figure 1-8 Example of 3D plot of cylinder pressure []	33
Figure 2-1 p-v diagram of actual HCCI combustion	36
Figure 3-1 Piston design as described above ($h_{cr} = 3mm$) [85]	42
Figure 3-2 Solid model of HCCI model piston and actual piston	43
Figure 3-3 Diesel and HCCI piston comparison	43
Figure 3-4 Simplified thermal circuit of a heater	48
Figure 3-5 Power require for one heater	50
Figure 3-6 Experimental setup of heater characterization	51
Figure 3-7 Screen shot of heater experiment	52
Figure 3-8 Heater characterization results	52
Figure 3-9 HCCI intake components	53
Figure 3-10 Installing the HCCI intake on the engine	54
Figure 3-11 Fuel injector locations	55
Figure 3-12 Bottom view of the engine block	56
Figure 3-13 Bottom view of the engine block with the crank and main bearings	57
Figure 3-14 The internals of the engine starting at the top left intake and exhaust lifters, pistons with rings, wrist pins, connection rods, bearings, on the right the pistons assembled	57
Figure 3-15 Bottom and side view of the oil pump installed	57
Figure 3-16 Volumetric measurement of the head	58

List of Figures

Figure 3-17 Right: front view of the engine and Left: is the rear view of the engine	59
Figure 3-18 Installing the engine onto the dynamometer rails	59
Figure 3-19 Complete engine installed	60
Figure 4-1 Block diagram of HCCI test bed	61
Figure 4-2 Testmate panel: dynamometer or engine speed and load control	62
Figure 4-3 Screen shot of Hypercell environment	63
Figure 4-4 Screen shot of configuration file	64
Figure 4-5 HCCI engine displays	64
Figure 4-6 AVL parameter setting window	66
Figure 4-7 Pressure transducer calibration screen	67
Figure 4-8 Indicom determines TDC in this screen	67
Figure 4-9 Pressure vs. CAD window before taking a reading	68
Figure 4-10 Example of the HCCI engine motoring	69
Figure 4-11 p-v diagram of the HCCI engine motoring	69
Figure 4-12 Window for loading stored pressure traces	70
Figure 4-13 WinTEC3 main menu	72
Figure 4-14 WinTEC3 calibration screen	73
Figure 4-15 WinTEC3 basic engine fuel parameters	73
Figure 4-16 Cylinder trim adjustments	74
Figure 4-17 Fuel enrichment parameter	74
Figure 4-18 Starting enrichments settings	75
Figure 4-19 MAI sensor and temperature adjustment turned off	75
Figure 4-20 Warm-up settings and graph	76
Figure 4-21 Deceleration deactivation window	76
Figure 4-22 Setting wide band lambda operation	77
Figure 4-23 TEC'r calibration of the wide band lambda sensor	77
Figure 4-24 Lambda TEC'r Conversion Factor	78

List of Equations

Figure 4-25 TPS limit settings.....	78
Figure 4-26 Volumetric efficiency table in terms of msec.....	79
Figure 4-27 Volumetric efficiency table in terms of % duty cycle.....	79
Figure 4-28 Adjusting fuel input of HCCI engine.....	80
Figure 4-29 Engine monitoring screen.....	80
Figure 4-30 Screen shot to the AEA.....	83
Figure 4-31 Emissions display.....	84
Figure 6-1 Example of misfire.....	90
Figure 6-2 Example of stable HCCI combustion.....	90
Figure 6-3 Example of HCCI combustion with knock.....	90
Figure 6-4 HCCI limits of operation.....	91
Figure 6-5 HCCI combustion.....	92
Figure 6-6 All cylinders misfiring on the same engine cycle.....	93
Figure 6-7 Stable HCCI combustion for all cylinders.....	93
Figure 6-8 All cylinders knocking on the same engine cycle.....	94
Figure 6-9 p-v diagram of misfire.....	95
Figure 6-10 p-v diagram of HCCI combustion.....	95
Figure 6-11 p-v diagram of when engine is knocking.....	95
Figure 6-12 Stable combustion to knock and back to stable combustion.....	96
Figure 6-13 Example of misfire for 50 cycles for each cylinder.....	97
Figure 6-14 Example of misfire in 3D for 50 engine cycles.....	98
Figure 6-15 Example of stable combustion for 50 cycles for each cylinder.....	99
Figure 6-16 Example of stable combustion in 3D for 50 engine cycles.....	99
Figure 6-17 Example of knock for 50 cycles for each cylinder.....	100
Figure 6-18 Example of knock in 3D for 50 engine cycles.....	101

List of Figures

Figure 6-19 IMEP of HCCI operating in the misfire regime for 50 engine cycles.....	102
Figure 6-20 IMEP of HCCI operating in the stable combustion regime for 50 engine cycles.....	103
Figure 6-21 IMEP of HCCI operating in the knock regime for 50 engine cycles.....	103

LIST OF TABLES

Table 1-1 Evaluation of control strategies []	29
Table 3-1 VW 1.9L TDI engine specifications	39
Table 3-2 Dealer part numbers need to rebuild the HCCI engine...	56
Table 3-3 HCCI compression ratio	58
Table 4-1 Digalog Data Acquisition Sensors	62
Table 4-2 List of ECU sensors	70
Table 6-1 Summary of typical emissions	104

LIST OF EQUATIONS

$r_c \odot \frac{V_c}{V_e}$ Equation 2-1.....	35
$T \odot Fb$ Equation 2-2.....	36
$P \odot 2\pi NT$ Equation 2-3.....	36
$W_{e,i} \odot \odot pdV$ Equation 2-4.....	36
$P_i \odot \frac{W_e N}{n_k}$ Equation 2-5.....	37
$mep \odot \frac{P_{u_R}}{V_d N}$ Equation 2-6.....	37
$IMEP \odot \frac{pdV}{V_d}$ Equation 2-7.....	37
$COV \odot \frac{\sigma_{IMEP}}{MEP_{IMEP}} \lambda 100$ Equation 2-8.....	37
$\sigma_{IMEP} \odot \sqrt{\frac{n_s x^2 \int_h x^2}{n(n-1)}}$ Equation 2-9.....	38
$\dot{A}/F \odot \frac{\dot{m}_s}{\dot{m}_f}$ Equation 2-10.....	38
$F/A \odot \frac{\dot{m}_L}{\dot{m}_s}$ Equation 2-11.....	38
$\phi \odot \frac{F/A_{actual}}{F/A_i}$ Equation 2-12.....	38
$\lambda \odot \phi^{\frac{1}{n}} \odot \frac{\dot{A}/F}{\dot{A}/F_i}$ Equation 2-13.....	38
$sfc(g/kWh) \odot \frac{\dot{m}_f(g/h)}{P(kWh)}$ Equation 2-14.....	39

List of Equations

$\eta_f \odot \frac{W_e}{m_f Q_{UV}} \odot \frac{(Pm_R/N)}{(m_f m_R/N) Q_{UV}} \odot \frac{P}{m_f Q_{UV}} \odot \frac{1}{sfc Q_{UV}}$ Equation 2-15.....	39
$\frac{v_1}{v_2} \odot r_c$ Equation 3-1.....	45
$s_2 \odot s_1$ Equation 3-2.....	45
$W_{e,i} \odot W_e \odot W_e$ Equation 3-3.....	45
$W_e \odot U_i [U_i \odot m(u_i [u_i])$ Equation 3-4.....	45
$v_3 \odot v_2$ Equation 3-5.....	46
$u_3 [u_i \odot 0$ Equation 3-6.....	46
$\frac{v_4}{v_3} \odot r_c$ Equation 3-7.....	46
$s_4 \odot s_3$ Equation 3-8.....	46
$W_e \odot U_i [U_i \odot m(u_i [u_i])$ Equation 3-9.....	46
$\eta_{f,i} \odot \frac{W_{e,i}}{m_f Q_{UV}}$ Equation 3-10.....	46
$W_e \odot mc_c(T_i [T_i])$ Equation 3-11.....	46
$W_e \odot mc_c(T_i [T_i])$ Equation 3-12 check this with ME 444 notes.....	46
$\eta_{f,i} \odot \frac{m[(u_i [u_i]) f(u_i [u_i])]}{m_f Q_{UV}}$ Equation 3-13.....	46
$\eta_{f,i} \odot \frac{(T_i [T_i]) f(T_i [T_i])}{T_i [T_i]} \odot \frac{T_i [T_i]}{T_i [T_i]}$ Equation 3-14.....	46
$\frac{T_2}{T_1} \odot \frac{V_1}{V_2} \odot \frac{V_1}{V_2} \odot r_c^n$ Equation 3-15.....	46
$\gamma \odot \frac{c_p}{c_v}$ Equation 3-16.....	46
$T_m \odot \frac{T_{cylinder}}{r_c^2}$ Equation 3-17.....	47

List of Equations

$q'' @ q_o \int q_i$ Equation 3-1848
$q'' A_i @ q_o \int q_i$ Equation 3-1948
$q'' (2\pi r_i L) @ \frac{\ln \frac{r_o}{r_i}}{2\pi k_{cd}} \int \frac{T_i}{h_i} \frac{1}{h_o 2\pi r_o L}$ Equation 3-2048
$q'' @ \frac{T_i}{k_{cd}} \int \frac{1}{h_i} \frac{1}{h_o 2\pi r_o L}$ Equation 3-2148
$Nu \phi \frac{hL}{k_i}$ Equation 3-2249
$Re D @ \frac{4\dot{m}_{air}}{\pi D \mu_{air}}$ Equation 3-2349
$Nu @ 0.023 Re D^{\frac{1}{4}} Pr^{\frac{1}{4}}$ Equation 3-2449
$h_i @ \frac{k_{air}}{D_i} 0.023 Re D^{\frac{1}{4}} Pr^{\frac{1}{4}}$ Equation 3-2549
$T_i @ \frac{q-j}{k_{cd}} \int \frac{1}{h_i} \frac{1}{h_o 2\pi r_o L}$ Equation 3-2650
Equation 4-171
$PW @ \frac{7}{5} \frac{V_{max}}{5} \left\{ UAP \& POT \right\} \frac{1}{\%}$ Equation 4-272
$m_f @ \frac{m_a}{\lambda} \frac{1}{h_f}$ Equation 4-381
$PV @ mRT @ \rho @ \frac{m}{V} @ \frac{P}{RT}$ Equation 4-482

List of Equations

$\dot{m}_s @ \frac{7.75 ft^3}{min} \int \frac{1 min}{860 sec} \int \frac{35.3 m^3}{ft^3} \int \frac{0.85 kg}{m^3}$ Equation 4-582
$m_s @ \frac{0.00316 kg}{sec} \int \frac{60 sec}{1 min} \int \frac{2 revs}{1 cycle} \int \frac{1 min}{81300 revs} \int \frac{2.205 lbs}{kg}$ Equation 4-682
$t @ (1.32 \times 10^6 lbs) \int \frac{hr}{813 lbs} \int \frac{60 min}{1 hr} \int \frac{60 sec}{1000 msec} \int \frac{1000 msec}{1 sec}$ Equation 4-782

1. INTRODUCTION

Improving fuel economy and reducing emissions are two major challenges of any engine design due to the fixed amount of petroleum resources, and ever increasing stringent government emission regulations, as well as the desire for improved air quality. Today's society is highly dependent on engines for its functionality, and thus deems necessary the focus of this study as one possible solution. Current engine combustion methods have their associated limitations that are inherent to the technology, and suggest another method for combustion. Homogenous Charge Compression Ignition (HCCI) has a high potential to significantly reduce fuel consumption, nitric oxides (NO_x) and particulate matter (PM). As with any technology there are compromises, and HCCI is no different. Some major challenges associated with HCCI are no direct control of combustion, extending its operation range and high level of unburned hydrocarbons (HC). The focus of this work is to establish a framework such that HCCI fundamentals can be studied, and allow for various avenues of interest to address the above challenges with practical solutions. Cycle-to-cycle variations, coefficient of variance (COV) and operation limits are addressed in this groundwork project. This project is made possible by a California Central Coast Research Partnership (C3RP) grant from the Office of Naval Research.

1.1 RECIPROCATING INTERNAL COMBUSTION ENGINES

Reciprocating internal combustion engines produce mechanical power from chemical energy of a fuel. The mixture of a fuel and air are the working fluids that are utilized to produce mechanical power by burning a fuel which results in the energy releases of the fuel [1]. The work transfers from the working fluids to the mechanical components of the engine to provide the desired power. Two traditional methods of burning or ignited the fuel of a reciprocating internal combustion engine is by spark-ignition (SI) and compression-ignition (CI) respectively. Due to the simplicity, ruggedness and high power/weight ratio, these two types of engine have found wide application in transportation and power generation [1].

A reciprocating engine involves a piston moving back and forth in a cylinder and transmits power through a connecting rod and crank mechanism to a drive shaft. Reciprocating engines operate on what is known as either a two-stroke or a four-stroke cycle. This paper only deals four-stroke engines. A four-stroke engine requires four strokes to complete one engine cycle, which

consists of two crankshaft revolutions. This is common between SI and CI engines. Figure 1-1 shows each of the four strokes and is described below per Heywood.

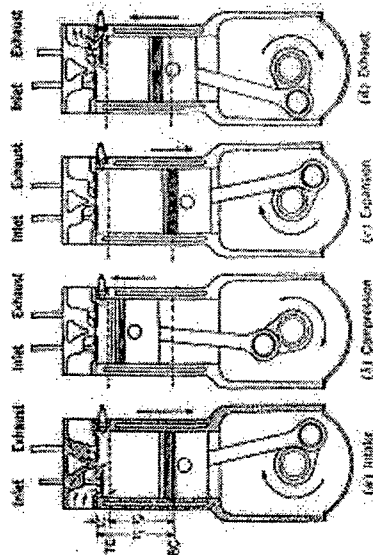


Figure 1-1 Four-stroke engine cycle [1]

- Intake stroke: starts with the piston at top dead center (TDC) and ends with the piston at bottom dead center (BDC). This draws in fresh mixture into the cylinder.
- Compression stroke: starts when both valves are closed and the piston starts back up to TDC. The mixture inside the cylinder is compressed, and toward the end of the stroke, combustion is initiated.
- Power stroke: or expansion stroke starts with the piston at TDC and ends at BDC as the high-temperature, high-pressure, gases push the piston down and force the crank to rotate.
- Exhaust stroke: starts when the piston is at BDC and the exhaust valve opens to initiate the exhaust process pressure where the remaining burned gases exit the cylinder. As the piston approached TDC the inlet valve opens. Just after TDC the exhaust valve closes and cycle starts again [1].

1.2 SPARK-IGNITION ENGINE

Spark-ignition engine or Otto, petrol, gasoline engine operate on a four piston stroke engine cycle as described. In SI engines the

The conventional (stoichiometric charge) SI engine fitted with a three-way catalyst can be seen as a very clean engine compared to a diesel engine. But it suffers from poor part load efficiency [2].

1.3 COMPRESSION-IGNITION ENGINE

In compression-ignition engines, air alone is inducted into the cylinder. The fuel in most applications is injected directly into the engine cylinder just before combustion process is desired to start. Load control is achieved by varying the amount of fuel injected each cycle. The air flow at a given engine speed is essentially unchanged, and there are no throttling losses like an SI engine at part throttle. The compression ratio of a CI engine is typically higher than typical SI engine values. The valve timing is used is similar to SI engines. Air at close to atmospheric pressure is inducted during the intake stroke and then compressed. At about 20° before TDC, fuel injection into the engine cylinder commences. The liquid fuel jet atomizes into drops and the liquid fuel evaporates, and then mixes with the air to within combustible proportions. The air temperature and pressure are above the fuel's ignition point. Therefore after a short delay period, spontaneous ignition or auto ignition of parts of the non-uniform fuel air mixture initiates the combustion process, and the cylinder pressure rises above the non-firing engine level [1]. The flame spreads rapidly through that portion of the injected fuel which has already mixed with sufficient air to burn. As the expansion process progresses, mixing between fuel, air, and burning gases continues, accompanied by further combustion. The exhaust process is similar to that of the four-stroke SI engine. At the end of the exhaust stroke, the cycle starts again [1]. The events can be seen in Figure 1-3.

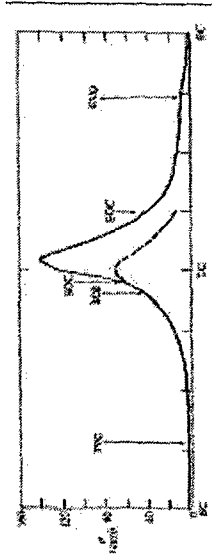


Figure 1-3 Sequence of events in a CI engine [1]

air and fuel are usually mixed together in the intake system prior to entry to the engine cylinder, using a fuel-injection system. The air flow rate is measured directly, and the injection valves are activated by injection pulses whose duration is determined by the electronic control unit (ECU) to provide the desired amount of fuel per cylinder per cycle [1].

During the intake stroke the air/fuel mixture is inducted into the cylinder with the residual burned gases remaining from the previous cycle. Between 10 and 40 crank angle degrees before TDC and an electrical discharge across the spark plug starts the combustion process [1]. A high voltage across the plug electrodes develops a turbulent flame from the spark discharge. The flame propagates across the mixture of air/fuel, and residual gas in the cylinder, and is extinguished at the combustion chamber wall. As the air/fuel mixture burns the cylinder pressure in Figure 1-2 (solid line) rises above the level due to compression alone (dashed line). The latter curve is called the motored cylinder pressure, and the pressure trace obtained from a motored or non-firing engine [1].

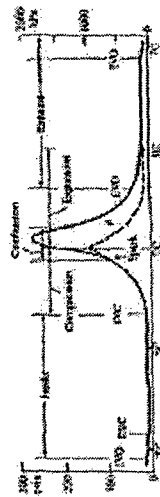


Figure 1-2 Sequence of events of a SI engine [1]

There is an optimum spark timing which, for a given mass of fuel and air inside the cylinder, gives maximum torque. More advanced (earlier) timing or retarded (later) timing than this optimum gives lower output.

About two-thirds of the way through the expansion stroke, the exhaust valve starts to open. The cylinder pressure is greater than the exhaust manifold pressure and a blow down process occurs. The burned gases flow through the valve into the exhaust port and manifold until the cylinder pressure and exhaust pressure equilibrate. The piston then displaces the burned gases from the cylinder into the manifold during the exhaust stroke [1].

CI or diesel engines are widely used in heavy-duty vehicles and in other commercial applications, due to its high efficiency and durability. In the diesel engine soot is formed in the fuel rich regions and NO_x in the hot stoichiometric regions. Due to these mechanisms, it is difficult to reduce both NO_x and soot simultaneously through combustion improvement [2].

1.4 ANALYSIS OF SI ENGINE

The standard Otto cycle or constant volume cycle is an ideal cycle that assumes the heat addition occurs instantaneously while the piston is at TDC. This idealized cycle is a good approximation of a SI engine. The Otto cycle is shown on the pressure versus volume (p-v) diagram of Figure 1-4. The cycle consists of four internally reversible processes in series. The process 1-2 is an isentropic compression of the air as the piston moves from BDC to TDC. The process from 2-3 is a constant volume heat transfer to the air from an external source while the piston is at TDC. This process is intended to represent the ignition of the air/fuel mixture and the subsequent rapid burning. Process 3-4 is an isentropic expansion or power stroke. The cycle is completed by the constant volume process 4-1 in which heat is rejected from the air while the piston is at BDC [1].

On the p-v diagram area 1-2-a-b-1 represents the work done per unit mass in the expansion process. The enclosed area can be interpreted as the net work output or the net heat added [3].

The air-standard Otto cycle consists of two processes in which there is work but no heat transfer, processes 1-2 and 3-4 and two processes in which there is heat transfer but no work, processes 2-3 and 4-1. Expressions from these energy transfers are obtained by reducing the closed system energy balance assuming that changes in kinetic and potential energy can be ignored [3].

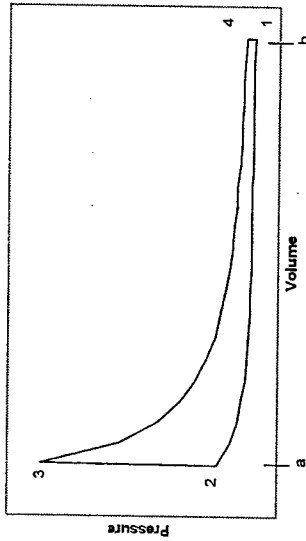


Figure 1-4 p-v diagram of the air-standard Otto cycle

1.5 ANALYSIS OF CI ENGINE

The air-standard diesel or constant pressure cycle is an ideal cycle that assumes the heat addition occurs during a constant-pressure process that starts with the piston at TDC. The diesel cycle is shown in Figure 1-5.

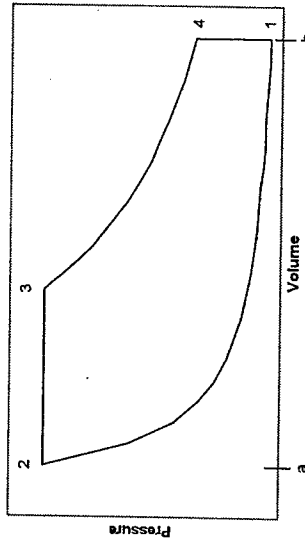


Figure 1-5 p-v diagram of the air-standard diesel cycle

The cycle consists of four internally reversible processes in series. The first process from state 1 to state 2 is the same as the Otto cycle, an isentropic compression. Heat is not transferred to the working fluid at constant volume as in the

Otto cycle. However, in the diesel cycle heat is transferred to the working fluid at constant pressure. Process 2-3 also makes up the first part of the power stroke. The isentropic expansion from state 3 to state 4 is the remainder of the power stroke. The isentropic expansion from state 3 to state 4 is the remainder of the power stroke. As in the Otto cycle, the cycle is completed by the constant-volume process 4-1 in which heat is rejected from the air while the piston is at bottom dead center. This process replaces the exhaust and intake processes of the actual engine [3].

Since the air-standard diesel is composed of internally reversible processes, area on the p-v diagram can be interpreted as heat and work. The area 1-2-a-b-1 is the heat rejected per unit of mass during the compression process. Area 2-3-4-b-a-2 is the work done per unit of mass as the piston moves from TDC to BDC. The enclosed area is the net work output, which equals the net heat added [3].

The most critical assumption in determining how useful these ideal cycles are as indicators of engine performance is the form assumed for the combustion process. The real engine combustion process occupies a finite crank angle period and the spark or fuel-injection timing may be retarded from its optimum advance to closer to TDC. The constant-pressure cycle would correspond to slow and late combustion [1].

1.6 HOMOGENEOUS CHARGE COMPRESSION IGNITION ENGINE

Homogeneous charge compression ignition is a combustion process that has been identified many years ago and has the potential to be highly efficient and low emissions. HCCI combines the ignition characteristics of a compression ignition engine with the premixed air/fuel of the spark ignition engine. HCCI has the potential to produce high thermal efficiencies due to the higher compression ratio and lack of throttling losses seen in that of a SI engine. Combustion occurs simultaneously throughout the cylinder, unlike a flame propagation seen in regular SI and CI engines. This rapid heat release of the combination with the lean fuel mixture, results in a low emission of NO_x and particulate matter without any after-treatment to the exhaust.

In some regards, HCCI combines the best features of SI and CI engines and is applicable to a wide range of uses with many different types of fuels. From heavy trucks to consumer-scale

automotive applications, an HCCI engine could be scaled for use in almost any transportation vehicle. HCCI is applicable to any piston engine and could be used outside the transportation sector such as a power generation engine or an engine used at a farm to pump water. HCCI is best suited for use in hybrid vehicles because the demand for the engine to operate over a range of speeds and loads is very limited compared to a regular vehicle [4]. The use of HCCI in hybrid vehicles could extend the existing benefits of a highly fuel-efficient vehicle with relatively lower emissions.

It is widely agreed that the combustion process in this type of engine occurs by multi-point auto-ignition within the cylinder, caused by compression heating, and that the mixture subsequently reacts by auto-ignition with no flame propagation [5] [6] [7] [8]. It is widely accepted that HCCI combustion is dominated by chemical kinetic with no requirement for flame propagation [9].

HCCI combustion is achieved by controlling the temperature, pressure, and composition of the fuel and air mixture so that it spontaneously ignites in the engine. This control system is fundamentally more challenging than using a spark plug or fuel injector to determine ignition timing as used in SI and CI engines, respectively. The recent advent of electronic engine controls has enabled consideration of HCCI combustion for application to commercial engines.

Studies on HCCI have been performed on two stroke engines [10] 11 12 13 14 [15] showing that HCCI combustion has great potential to reduce cycle to cycle variations and make engine operation smoother. Regarding the great problem with HC emissions from two stroke engines, it is reported that switching to HCCI operation will drastically reduce HC [2]. However, most recent studies on HCCI have been focusing on four stroke engines [16] 17 18 19 20 21 22 23 24 25 26 27 28 29 30 31 32 33 34 35 36 37 38 [39]. In 1983 Njati and Foster were the first to show that it was also possible to achieve HCCI in a four stroke engine [40]. Then the first to test HCCI on a real production engine was Stockinger et al. in 1992 [41].

Disadvantages of HCCI are high unburned hydrocarbons (HC), carbon monoxide (CO), high peak pressures, high rates of heat release, reduced operating range, reduced power per displacement, and difficulty in starting and controlling the engine. The major problem is controlling the ignition timing over a wide load and speed range, since there is no direct control over the ignition

timing as there is in an SI and CI engine. There are many parameters that affect the ignition timing in an HCCI engine. The strongest ones are the inlet temperature and the compression ratio. Another drawback compared to the SI engine and CI engine is higher emissions of unburned HC [2]. In an HCCI engine the fuel is injected into the preheated air in the intake manifold to create a homogeneous charge. During the compression stroke the charge is further heated to attain auto-ignition close to TDC. With HCCI, there is no direct control of the onset of combustion, as the ignition process relies on a spontaneous auto-ignition. The ignition timing can only be controlled indirectly [2].

HCCI control possibilities are variable compression ratio, variable valve timing, operation with multiple fuels, and thermal control. Thermal control is inexpensive to implement and relatively easy to control in a laboratory setting. It has been demonstrated that almost any liquid fuel can be used in a HCCI engine with variable compression ratio [2], including hydrogen, carbon monoxide and diethyl ether (DME) [42]. A fully variable valve train (FVVT) together with an early exhaust valve closing strategy has been demonstrated with HCCI [43]. Many investigators have used dual-fuels to control the mixture and auto-ignition temperature [44] 45 46 47 48 49 [50]. Inlet temperature is a sensitive parameter in controlling the HCCI combustion [36]-[38]. HCCI combustion is a process dominated by chemical kinetics of the fuel-air mixture. The hottest part of the mixture ignites first, and compresses the rest of the charge, which then ignites after a short time lag [51]. The fact that HCCI combustion is not very sensitive to turbulence makes it likely that a thorough, accurate method of analysis of HCCI combustion can be developed. In principle, this comprehensive tool could be obtained by combining a fluid mechanics code with a detailed chemical kinetics code. In this approach, the fluid mechanics code would calculate the temperature distribution within the cylinder, and the chemical kinetics code would calculate chemical heat release as a function of pressure, temperature and composition [51]. The predictions from the analysis have been compared to recent experimental results. The analysis does an excellent job at predicting maximum pressure, burn duration, indicated efficiency and combustion efficiency. These are predicted within 10% or better [51]. A computer simulation of the HCCI engine has been developed for ignition and performance studies. The simulation couples models for mass, species and energy within a zero-dimensional framework [52]. Multi-zone combustion model for an engine cycle simulation code of a gasoline HCCI engine have also been developed [53]. This simulation is used for engine

performance and emissions studies, especially under turbocharged conditions. The simulation couples models for mass, species, and energy within a quasi-dimensional framework [54]. Detailed chemical kinetics is implemented into an engine CFD code to simulate HCCI combustion. Computed cylinder pressures and heat release rates were compared to experimental measurements [55]. Moreover, a single cylinder engine experiments and chemical kinetic modeling have been performed to study the effect of variations in fuel, equivalence ratio, and intake charge temperature on the start of combustion and the heat release rate [56].

Spectrometry and chemiluminescence imaging has been applied to study the homogeneous charge compression ignition combustion process [5]. In-cylinder crank-angle resolved imaging of fuel was obtained using planar laser induced fluorescence (PLIF) in a HCCI engine. The results show that heterogeneous combustion with large spatial and temporal variation, even with a homogeneously premixed charge occurred. It is therefore concluded that the charge inhomogeneity has a modest effect on the combustion process [57]. Attempts have been made to extend the upper load limit for HCCI, by supercharging in combination with exhaust gas recirculation (EGR) [58]. The load limit for HCCI can be extended when supercharging is applied in combination with EGR, without increasing the maximum cylinder pressure [58].

A mode change (SI-HCCI-SI) in a multi cylinder engine has been successfully demonstrated. For the first couple of cycles after a mode change, optimization is needed in order to avoid combustion cycles that deviate too much from the steady state combustion. With the proper setting of the control parameters, no problems with mode changes are encountered [59]. The HCCI operating range can be increased with both mechanical supercharging and turbocharging. The maximum load and brake efficiency are higher with turbocharging than with mechanical supercharging, due to the high parasitic losses with supercharging [60]. The brake efficiency is higher for the turbocharged HCCI than with the natural aspirated SI in the entire operating range for HCCI. The difference in brake efficiency decreases with load and is almost negligible at the maximum turbocharged HCCI load [60].

HCCI combustion can be successfully realized with direct injection of gasoline (GDI) using a passenger car GDI injector mounted in a heavy-duty diesel engine. It was determined that air swirl is playing an important role when it comes to mixture formation, combustion and emissions formation in a directly

injected HCCI combustion system [61]. A direct injection gasoline system was applied to a heavy-duty diesel-type engine to study the effects of charge stratification on the performance of premixed compression ignited combustion [62] [63].

In summary, the published literature has explored a wide array of control strategies. Each method has its own advantages and some less than desirable issues. These strategies are summed up in Table 1-1.

Table 1-1 Evaluation of control strategies [64]

Strategy	Advantage	Issue
VCR	wide range	no available device
hot residuals	low CR ~10:1	small range, low γ
EGR	low cost	small range, low γ
intake heating	wide range	thermal inertia
dual fuel	wide range	special fuels
fuel reformer	single fuel	small range
act. chem. spec.	promote AI	not demonstrated
DI tuning	fast control	small range, NOx, PM
SC	low CO at idle	high load NOx
water injection	higher load	engine corrosion
boost pressure	higher load	peak cyl. pressure

1.7 HCCI EMISSIONS

All of the above control strategies are attempts to gain engine operation while utilizing the HCCI technology emission gains. The emissions of concern are unburned hydrocarbons, nitric oxides, carbon monoxide, and particulate matter. Figure 1-6 is an example of the gains possible with HCCI in terms of PM and NOx. The state-of-the-art diesel technology is from the year 2000. With PM filters or traps as well as selective catalytic reduction methods the emissions can be reduced to meet Euro 4 emission standard of 2005. The green area is the regime in which HCCI engine can operate in, and this is a large improvement over the 2000 diesel engines.

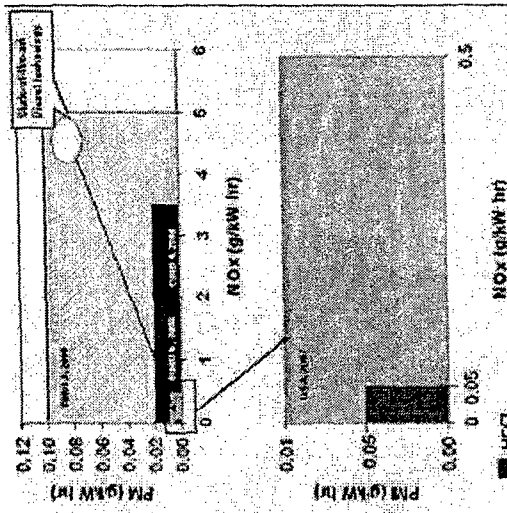


Figure 1-6 HCCI potential emission gains [65]

HC

A serious problem with HCCI is high emissions of unburned hydrocarbons. High HC emissions mean poor combustion quality, which reduces the overall engine efficiency [2]. The low homogeneous combustion temperature related with HCCI prevents NOx formation, but the combustion temperature becomes too low to fully oxidize the fuel completely. The low combustion temperature leads to incomplete combustion, which results in high emissions of unburned hydrocarbons. For highly diluted mixtures the quenching distance is expected to be quite long. With increased compression ratio, there is less time for combustion at constant volume and crevice effects become a larger contributor. The main source for HC can be summarized in the following [66]:

- 1 Bulk quenching
- 1 Wall quenching
- 1 Crevice volumes

Crevice and boundary layers generally remain too cold to react, and result in substantial hydrocarbon and carbon monoxide emissions [51]. Low crevice volume and hot wall engines have

resulted in lower HC emissions [32]. The use of EGR also reduces the specific HC emissions [24].

NO_x

NO_x is a combination of nitric oxide NO and nitric dioxide NO₂ that are commonly lumped together. The formation of NO_x is due primarily to the combustion temperature of the cylinder reaching well over 1700 K (the temperatures below this value render NO_x formation as negligible [1]). In SI engines combustion begins at the spark plug causing a flame front to propagate through the cylinder. As the flame front propagates through the premixed air/fuel mixture the temperature and pressure within the cylinder increases while the cylinder concurrently continues to compress burned and unburned gases. The flame front is at the hottest point of the burning gases and thus provides an ideal location for NO_x formation to take place. This increase in pressure induces work on the piston to push it back down on the expansion stroke, causing the gas temperatures to drop. This results in the freezing reaction of NO_x to be exhausted on the expansion stroke [1]. NO_x is an environmental issue because of health reasons and the human body's reaction to it.

With homogeneous combustion of a premixed mixture, the temperature is expected to be the same in the entire combustion chamber, except near the walls. This in combination with very lean mixtures gives a low maximum temperature during the cycle. NO_x formation is very sensitive to the temperature history during the cycle. At temperatures over 1800 K (2780 °F), the NO_x formation rate increases rapidly with increased temperature. The fast combustion related with HCCI also gives less time for NO_x formation [66].

CO

Carbon monoxide is a result of incomplete oxidation of the fuel. The amount of CO is very dependent on the combustion temperature. Higher combustion temperature results in less CO. Close to the rich limit for HCCI and/or with early combustion phasing very little CO is generated. But close to the lean limit and/or with late combustion phasing substantial amounts of CO can be generated [66].

1.8 HCCI CYCLE-TO-CYCLE VARIATIONS

With HCCI, cycle-to-cycle variations of combustion are very small, since combustion initiation takes place at many points at

the same time. The whole mixture burns almost homogeneously. In this way unstable flame propagation is avoided [2] [67]. Whereas in SI engines, large cycle-to-cycle variations occur since the early flame development varies considerably due to mixture inhomogeneities near the vicinity of the spark plug [68]. In SI engines, large cycle-to-cycle variations occur since early flame development varies significantly. Another factor that leads to reduction in cycle-to-cycle variations of HCCI is how the increased air/fuel mixing results in variation of the peak cylinder pressure [69]. However, too lean of a mixture will lead to incomplete combustion or misfire. The cycle-to-cycle variation of the HCCI combustion process is still significant [70]. Especially the structure of the combustion carries a large variation although the variation in pressure is modest. Some measure of the cycle-to-cycle variation in averaged intensity has been studied. The standard deviation of the averaged intensity at every CAD is considered to represent the cyclic variation satisfactorily [70].

Figure 1-7 suggests that the appearance of multiple combustion cycles is attributed to two major parameters, start of combustion and combustion duration. The large variations at the head and tail of the heat release are contributed to start and end of combustion. Since the rate of heat release is generally very high and thus small variations in start of combustion give large variations in intensities, this explains the large variations at the start and end of combustion. Furthermore, the peak intensity is very high which dampens the normalized deviations at mid heat release [70].



Figure 1-7 Different chemiluminescence images at 3 CAD/ATD

Variations between the cylinders such as individual cylinder intake temperature, compression ratio, wall temperature, contribute to the variation in IMEP [71]. The key to further improving performance of the engine is controlling individual cylinder combustion timing. Minimizing phasing differences between the cylinders is likely necessary to achieve higher BMEP [71]. Cycle-to-cycle variation of in-cylinder pressure is caused by the shifts in the auto-ignition timing of the air-fuel mixture. Measurements of crank angle resolved unburned hydrocarbons show that a much higher level of unburned HC is produced by a late burning HCCI cycle compared to an early one [72].

The cycle-to-cycle variation of in-cylinder pressure over the range of crank angle degree (CAD) of one engine cycle compared to numerous engine cycles is shown in Figure 1-8. The pressure traces in Figure 1-8 are from a single cylinder with variable valve timing.

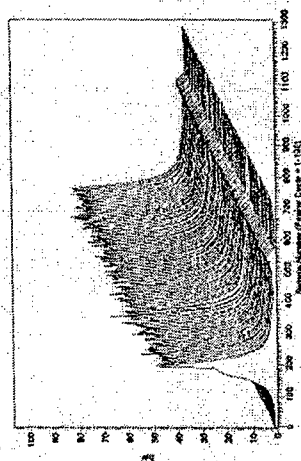


Figure 1-8 Example of 3D plot of cylinder pressure [73]

2. GENERAL ANALYSIS OF ENGINES

A detailed study of the performance of a reciprocating internal combustion engine will take into account many features. These will include the combustion process occurring within the cylinder and the effects of irreversibility associated with friction and with pressure and temperature gradients. Heat transfer between the gases in the cylinder and the cylinder walls and the work required to charge the cylinder and exhaust the products of combustion also would be considered. To simplify the analysis a procedure of air-standard analysis is employed. Where a fixed amount of air modeled as an ideal gas is the working fluid. The combustion process is replaced by a heat transfer from an external source. There are not exhaust and intake processes as in an actual engine. The cycle is completed by a constant-volume heat transfer process taking place while the piston is at BDC. Lastly all processes are internally reversible [1].

Although an air-standard analysis simplifies the study of internal combustion engines considerably, values for the mean effective pressure (MEP) and operating temperatures and pressures calculated on this basis may depart significantly from those of actual engines. Still, insight concerning actual performance can result with such an approach. Looking at the Otto, and diesel cycles, which differ only in the way the heat addition process which replaces the combustion in the actual cycle modeled [1].

An internal combustion engine is not a heat engine in the thermodynamic definition of the term. It is best analyzed as an open system which exchanges heat and work with its surrounding environment. This involves reactants, fuel and air, flow into the system, and products, exhaust gases, and flow out of the system [1]. This approach will be shown in the preliminary heater sizing section after some terms, parameters and measures have been defined.

2.1 ENGINE DESIGN AND OPERATING PARAMETERS

Basic geometric relationships commonly used to characterize engine operation are as follows. Compression ratio r_c :

$$r_c = \frac{V_d + V_c}{V_c} \quad \text{Equation 2-1}$$

Where V_d is the displaced or swept volume and V_c is the clearance volume.

Torque is force (F) times distance (b):

$$T @ Fb \quad \text{Equation 2-2}$$

The power (P) delivered by an engine is the product of torque and angular speed:

$$P @ 2\pi NT \quad \text{Equation 2-3}$$

where N is the crankshaft rotational speed.

Torque is a measure of an engine's ability to do work and power is the rate at which work is done.

Indicated work per cycle

Pressure data for the gas in the cylinder over the operating cycle of the engine can be used to calculate the work transfer from the gas to the piston. The cylinder pressure and corresponding cylinder volume throughout the engine cycle can be plotted on a pressure-volume (p-v) diagram. The indicated work per cycle is obtained by integrating around the curve to obtain the area enclosed on the diagram. In Figure 2-1 is an example of an actual p-v diagram.

$$W_{ei} @ \oint p dV \quad \text{Equation 2-4}$$

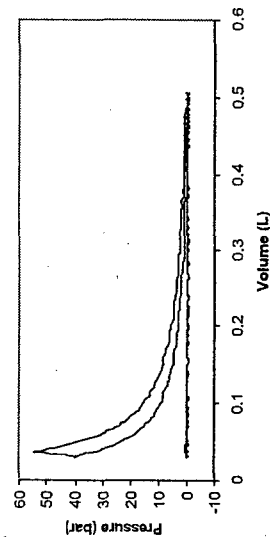


Figure 2-1 p-v diagram of actual HCCI combustion

Gross indicated work per cycle is the work delivered to the piston over the compression and expansion strokes only. Where as Net indicated work per cycle is the work delivered to the piston over the entire four-stroke cycle [1].

Power per cylinder is related to the indicated work per cycle by

$$\sigma_{MEP} \propto \sqrt{\frac{n^2 \int_0^x x^2}{n(n-1)}} \quad \text{Equation 2-9}$$

Fuel/air equivalence ratio ϕ

To define equivalence ratio a few variables need to be defined as well. Stoichiometric combustion occurs when there is just enough oxygen for conversion of all the fuel into completely oxidized products [1].

The air mass flow rate and the fuel mass flow rate are used to define operating conditions for an engine.

Air/fuel ratio:

$$\frac{A}{F} \propto \frac{\dot{m}_a}{\dot{m}_f} \quad \text{Equation 2-10}$$

Fuel/air ratio:

$$\frac{F}{A} \propto \frac{\dot{m}_f}{\dot{m}_a} \quad \text{Equation 2-11}$$

The equivalence ratio describes a value of the chemically correct fuel-to-air ratio for a fuel with respect to a stoichiometric ratio of fuel-to-air. As stated above when all of the products of a chemical reaction are completely oxidized. Therefore, if the actual fuel-to-air ratio is equal to the stoichiometric ratio then ϕ is equal to 1.

$$\phi \propto \frac{\frac{F}{A}}{\frac{F}{A}_{stoich}} \quad \text{Equation 2-12}$$

Lambda is the inverse of the equivalence ratio ϕ . Lambda is the chemically correct air-to-fuel ratio for a fuel, over stoichiometric ratio of air-to-fuel.

$$\lambda \propto \phi^{-1} \propto \frac{\frac{A}{F}}{\frac{A}{F}_{stoich}} \quad \text{Equation 2-13}$$

For fuel-lean mixtures: $\phi < 1$, $\lambda > 1$

For stoichiometric mixtures: $\phi = 1$, $\lambda = 1$

For fuel-rich mixtures: $\phi > 1$, $\lambda < 1$

Specific fuel consumption

Specific fuel consumption is (sfc) is the fuel consumption as a measure of mass flow per unit power output. It measures how efficiently an engine is using the fuel supplied to produce work.

$$P_i \propto \frac{W_{c,i} N}{n_k} \quad \text{Equation 2-5}$$

where n_k is the number of crank revolutions for each power stroke per cylinder. For a four-stroke engine n_k equals 2. This power is the indicated power or the rate of work transfer from the gas within the cylinder to the piston.

Mean effective pressure

While torque is a valuable measure of a particular engine's ability to do work, it depends on engine size. A more useful relative engine performance measure is obtained by dividing the work per cycle by the cylinder volume displaced per cycle. The parameter so obtained has units of force per unit area and is called the mean effective pressure (mep) [1].

$$mep \propto \frac{P_{m,i} N}{V_d} \quad \text{Equation 2-6}$$

The maximum brake mean effective pressure (bmep) of good engine designs is well established. The actual bmep that a given engine develops can be compared with this norm, and the effectiveness with which the engine designer has used the engine's displaced volume can be assessed [1]. Also, for design calculations, the engine displacement required to provide a given torque or power, at a specified speed, can be estimated by assuming appropriate values for bmep for that particular application [1]. The net indicated mean effective pressure (IMEP) is the work delivered to the piston over the entire four strokes of the cycle per unit displaced volume [1].

$$IMEP \propto \frac{pdV}{V_d} \quad \text{Equation 2-7}$$

Coefficient of variation

An important measure of cyclic variability is the coefficient of variation (COV) of the indicated mean effective pressure. It is the standard deviation in IMEP divided by the mean IMEP. It defines the cyclic variability in indicated work per cycle, and it has been found that vehicle drivability problems usually result when COV exceeds 10 percent [1].

$$COV \propto \frac{\sigma_{IMEP}}{\text{mean}_{IMEP}} \times 100 \quad \text{Equation 2-8}$$

where

$$sfc(g/kWh) @ \frac{\dot{m}_f(g/h)}{P(kW)} @ 608.3 sfc(lbm/hp \cdot h) \text{ Equation 2-14}$$

Since sfc has units, a dimensionless parameter that relates the desired engine output to the required input of fuel has a more fundamental value. The ratio of the work produced per cycle to the amount of fuel energy supplied per cycle that can be released in the combustion process is commonly used for this purpose [1]. It is a measure of the engine's efficiency. The fuel energy supplied which can be released by combustion is given by the mass of fuel supplied to the engine per cycle times the heating value of the fuel. The heating value of a fuel is Q_{HV} which defines its energy content [1]. This measure of an engine's efficiency, which is the fuel conversion efficiency given by

$$\eta_f @ \frac{W_e}{\dot{m}_f Q_{HV}} @ \frac{(P \eta_n / N)}{(\dot{m}_f \eta_n / N) Q_{HV}} @ \frac{P}{\dot{m}_f Q_{HV}} @ \frac{1}{sfc Q_{HV}} \text{ Equation 2-15}$$

3. ENGINE SETUP

A 1.9L Volkswagen (VW) turbo direct injection (TDI) diesel engine was selected as the platform for HCCI combustion. The four cylinder VW engine has a 19.5:1 compression ratio, and thus a robust mechanical structure which will be able to withstand the demands of an experimental engine. The stock specifications of the engine are shown in Table 3-1. Moreover the VW TDI engine has been used to obtain HCCI combustion [4] [71].

Table 3-1 VW 1.9L TDI engine specifications

Displacement	1.896 L (115.701 in ³)
Bore	79.55 mm (3.13 in)
Stroke	95.50 mm (3.76 in)
Connecting Rod Length	144.00 mm (5.70 in)
Compression Ratio	18.34 (measured)
Firing Order	1-3-4-2
Engine Block	Cast Iron
Head	Aluminum
Piston Geometry	Bowl-in-piston
Intake Valve Open (1mm lift)	16 CAD ATDC

Intake Valve Close (1mm lift)	25 CAD ABDC
Exhaust Valve Open (1mm lift)	28 CAD BBDC
Exhaust Valve Close (1mm lift)	19 CAD BTDC

The VW engine will be converted to a HCCI engine by removal of the turbocharger, preheating the intake charge, gasoline multi-port fuel injection. This will require changing the compression ratio to 16.5:1, and manufacturing a custom intake manifold. With the modifications stated above, and a few other minor modification for sensor placement the engine has retained the stock configuration. The details of the compression ratio change involved a new piston design which will be discussed in the next section. The custom intake manifold is discussed in the section after the pistons respectively.

3.1 PISTON DESIGN

It is suggested by the literature that the stock diesel piston design is unfavorable for HCCI combustion. The stock diesel combustion chamber design promotes significant heat transfer, high swirl, unfavorable surface to volume ratio, very small clearance between much of the piston top and the head at TDC, and contributes to the high HC values [71]. The stock pistons have boundary layers that promote hot spots within the combustion chamber, which is another negative.

The design constraints for the pistons are to use the stock block, head, and wrist pins, intake and exhaust valves cannot hit pistons and the type of fuel to be used is gasoline. The goals of the piston design are to reduce the compression ratio from 19.5:1 to 16.5:1 which will be explained shortly. Minimize HC emissions, and minimize surface to volume ratio for heat transfer effects.

Piston geometry

Studies have been performed with HCCI and the variation of fuels on a variable compression ratio engine [2] [74], and the recommendation is that when using gasoline as the fuel for HCCI a compression ratio of 16.5:1 results in an optimum power output and combustion efficiency [2] [75]. Therefore, the compression ratio of 16.5:1 was selected with a shallow bowl in piston to minimize surface to volume heat transfer effects.

Compression ring location

HCCI combustion produces more unburned hydrocarbons than desired. Crevices between the cylinder wall and the piston may provide a means to reduce the HC. Emissions of unburned hydrocarbons from diesel engines are generally very small, and the responsible mechanisms do not have much in common with premixed combustion. Regarding emissions of unburned hydrocarbons, most literature on SI engines agrees upon six significant sources [76] summarizes the following significant mechanisms of unburned hydrocarbons:

1. Combustion chamber crevice effects
2. Lube oil absorption/desorption
3. Deposits on the combustion chamber wall
4. Flame quenching, both at the wall and in the bulk
5. Exhaust valve leakage
6. Incomplete combustion

The major contributors are the top-land crevice effect, the lube oil layer absorption/desorption and deposits [77] 78 79 80 81 [82]. It has been shown, with lube free engines, that some 25-35% of the unburned hydrocarbons can be discounted [83]. The top-land crevice is considered to be the largest contributor, and Wentworth [84] has reported that 47-74% of the unburned hydrocarbons can be reduced with a top-land free engine.

To reduce the unburned HC with respect to top-land crevices either minimizing crevice volume or make sure entrance is wide enough to allow flame penetration. The HCCI combustion reaction is very temperature sensitive and therefore controlling temperature in the crevice is too difficult [85]. Saika and Korenatus found that flames can propagate into crevice twice as wide as the surface quench distance [86].

A multi-zone model predicts that HC and CO emissions can be considerably reduced by increasing the wall temperature to 600 K (620 °F) or by building an engine with no crevices. An engine with a 600 K wall and no crevices has near zero HC and CO emissions [87]. This model has been validated by comparison with experimental results recently obtained by [85]. The distance from the top ring to the piston upper face was reduced to 5 mm (0.197 in), and it is quite apparent that HC and CO emission were reduced by the reduction of top-land-crevice volume [32].

In another investigation showed that most of the unburned HC descend from the crevices [85]. Increasing the top-land width to some degree lead to an increase in HC, by opening up the top-land, the HC emissions were in some cases reduced by over 50% [85]. The

reduction of HC with wide top-land geometry was most often accompanied by an increase in CO, reducing the gain in combustion efficiency [85].

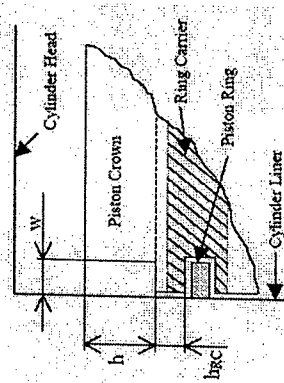


Figure 3-1 Piston design as described above ($h_{HC} = 3\text{mm}$) [85]

Given the previous investigations on piston ring location and the resulting HC and CO emissions can be summarized as such. Either make the crevice large enough for the combustion flame to penetrate the crevice or minimize the crevice to minimize the volume of unburned gases. The geometry for wide crevice and temperature control for the crevice is difficult. A large crevice design which allows for flame penetration increases CO, which is not desirable. Therefore, minimize crevice volume by reducing top-land width to the lowest dimension without scuffing and minimize height while protecting the compression (top) ring.

The HCCI piston design has a top-land height 0.125 in (3.175 mm) and a width of 0.004 in (0.1016 mm). The width is the minimum recommendation from the piston manufacture for 4032 high silicon alloy pistons. The material selection is discussed in the next section. A solid model of the final piston design is shown in Figure 3-2 next to the actual piston. A comparison of the stock diesel and the HCCI pistons are shown Figure 3-3 best shows the top-land dimensions.

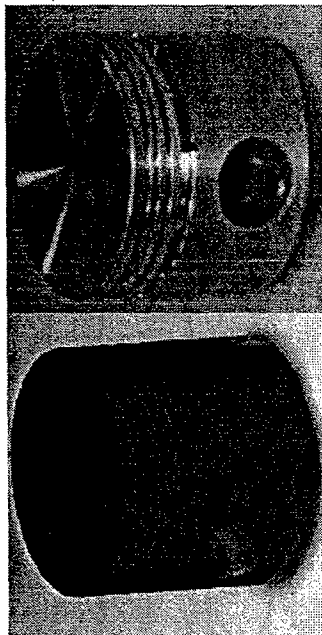


Figure 3-2 Solid model of HCCI model piston and actual piston

In Figure 3-3 notice how the deck height of HCCI piston is shorter than the diesel. This was done to remove the crevice that is created when the piston is at TDC with the diesel design, and allow the combustion flame to penetrate this area. This was a compromise between the heat transfers to surface volume ratio. For detailed schematics of both the diesel and HCCI pistons see Appendix A.

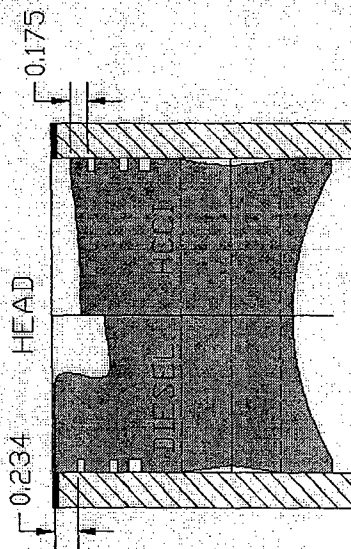


Figure 3-3 Diesel and HCCI piston comparison

Material

The types of materials available for forged pistons are 4032 SAE high silicon aluminum alloy and 2618 high or low silicon aluminum alloy. The 4032 SAE high silicon alloy is durable and lighter than 2618 alloy and is normally used for naturally aspirated engines [88]. The 2618 SAE high or low silicon aluminum alloy is designed for the rigors of forced inducted, marine, and nitrous applications. The 2618 alloy is heavier than 4032 alloy, has poor lubricity qualities, and expands more [88]. The melting point is the same for 4032 and 2618 alloys. The more silicon improves high heat strength and reduces coefficient of expansion.

Hypereutectic pistons or 390 SAE and 332 SAE materials is considered as well. These types of pistons have high heat strength, better endurance, no scuffing, lighter weight, and tighter bore clearances. They should never be used with nitrous, supercharged or turbocharged engines. However, hypereutectic pistons are still a cast piston, very hard and therefore brittle, and unforgiving with knock detonation, and not best suited for HCCI applications [89].

Provided the above information it was determined to have the HCCI pistons made of 4032 high silicon aluminum alloy. The 2618 alloy was not selected due to its poor lubricating qualities, but more so for the fact that it expands more. The expansion would then require larger tolerances, and this makes for larger crevices which produce more emissions. The hypereutectic pistons were not selected due to the sensitivity of knock detonation, which HCCI can be described as controlled knock. Another reason is the cost of getting a casting made for one set of pistons is not feasible.

One last component was considered in the HCCI piston design, and that is the idea of coatings of the pistons and the cylinder walls. Where experimental and theoretical study of the effect of thermal barriers and catalytic coatings in a HCCI engine have been conducted [77]. The effect of the coatings has been examined by engine testing and simple heat transfer analysis. It can be concluded that the thermal boundary layers effected by the coating and that catalytic coatings prove to have a negative effect on unburned hydrocarbon emissions through catalytic flame quenching [77].

3.2 INTAKE DESIGN

The other major modification to the stock VW engine was the intake manifold. It was determined that using heat to obtain HCCI

combustion is method of choice in this work, provided current resources. It is stated in the literature that specific intake manifold temperature and the combustion timing for each cylinder can vary widely. At the lowest temperatures one cylinder can be firing very well while another may be not firing at all due to variation between the cylinders [71]. Given this information, individual heater control is how the implementation of preheating the intake air will be done to obtain HCCI combustion. The next sections discuss the approach to design a new intake.

Engine standard air analysis

After it was determined that individual intake heaters would be used to control HCCI combustion, the type of heater and size needed to be determined. The response time of the heater needs to be able to adjust with changes of the environment, which are slow relative to the more important operating changes of the engine. The amount of heat needed to heat up the intake air is a function of the compression ratio of the engine and the type of fuel being used. These are the main points that will determine the heater size. To determine the heater size an analysis of the engine is required first, as the goal is to obtain HCCI combustion near TDC in the engine.

The first and second laws of thermodynamics are applied to the cylinder contents and the following relationships are obtained:

$$\frac{V_1}{V_2} \otimes \gamma_c \quad \text{Equation 3-1}$$

where V_1 is equal to the sum of V_d and V_c as described above and V_2 is equal to V_c . Since the process is adiabatic and reversible

$$s_1 \otimes s_2 \quad \text{Equation 3-2}$$

$W_{c,i}$, the indicated work per cycle is the sum of the compression stroke work and the expansion stroke work:

$$W_{c,i} \otimes W_c \int W_e \quad \text{Equation 3-3}$$

where the compression work is

$$W_c \otimes U_1 \int U_2 \otimes m(u_1, u_2) \quad \text{Equation 3-4}$$

the subscript numbers are associated with the states in Figure 1-4 of the Otto cycle discussed above. The combustion process for constant-volume cycle:

$$V_3 \otimes V_2 \quad \text{Equation 3-5}$$

$$u_3 \int u_2 \otimes 0 \quad \text{Equation 3-6}$$

the expansion stroke for constant volume cycle:

$$\frac{V_4}{V_3} \otimes \gamma_c \quad \text{Equation 3-7}$$

$$s_4 \otimes s_3 \quad \text{Equation 3-8}$$

and the expansion work is

$$W_e \otimes U_3 \int U_4 \otimes m(u_3, u_4) \quad \text{Equation 3-9}$$

the indicated fuel conversion efficiency

$$\eta_{f,i} \otimes \frac{W_{c,i}}{m_f Q_{LHV}} \quad \text{Equation 3-10}$$

If the working fluid in this ideal cycle is assumed to be an ideal gas, with c_v and c_p constant throughout the engine operating cycle, the equations above can be simplified. The compression work from $W_c \otimes U_1 \int U_2 \otimes m(u_1, u_2)$ Equation 3-4 which becomes

$$W_c \otimes mc_v (T_1 \int T_2) \quad \text{Equation 3-11}$$

the expansion work becomes

$$W_e \otimes mc_v (T_3 \int T_4) \quad \text{Equation 3-12 check this with ME 444 notes}$$

The indicated fuel conversion efficiency is found by substitution into $W_{c,i} \otimes W_e \int W_e$ Equation 3-3 for constant volume cycle:

$$\eta_{f,i} \otimes \frac{m(u_3, u_4) \int (u_2, u_1)}{m_f Q_{LHV}} \quad \text{Equation 3-13}$$

Then the relation for indicated fuel conversion efficiency becomes

$$\eta_{f,i} \otimes \frac{(T_3 \int T_4) \int (T_2 \int T_1)}{T_3 \int T_4} \otimes 1 \int \frac{T_1}{T_2} \int \frac{T_2}{T_3} \quad \text{Equation 3-14}$$

Since 1-2 and 3-4 are isentropic processes between the same volumes, V_1 and V_2 then

$$\frac{T_1}{T_2} \otimes \left(\frac{V_2}{V_1} \right)^{\gamma_c} \otimes \left(\frac{V_1}{V_2} \right)^{\gamma_c} \quad \text{Equation 3-15}$$

where

$$\gamma_c \otimes \frac{c_p}{c_v} \quad \text{Equation 3-16}$$

So, now set T_1 equal to the intake air temperature after the heater and T_2 equal to the temperature in the cylinder near TDC.

For HCCI combustion to occur with 87-octane gasoline a temperature of approximately 1100 K (1520 °F) is required.

$$T_{in} @ \frac{T_{cylinder}}{r_c^{\gamma}} \quad \text{Equation 3-17}$$

Gamma (γ), is assumed to be 1.35 (unit less) [1]. Given that the compression is 16.5:1, all values are known and T_m equals 412 K (282 °F). With the known intake temperature needed prior to going into the combustion chamber for HCCI combustion to occur. The ΔT , or change in temperature needed from the atmosphere can be used to size the heaters. This sizing will also, need to account for the various mass air flow rates that the engine with induct through the heaters for a range of engine speeds.

A heater with a cross frame coil heating element for minimum resistance to the air flow was chosen. The coil heating element has an improved response time due to the relatively low thermal inertia of the coils. The nickel-chrome heating element can operate up to 200 CFM with temperatures of 600°F (589 K). This heater comes with various power-rated models. The 2 kilowatt (kW) model is selected to see if it can meet the power requirements of the engine to properly heat the intake air for HCCI combustion.

Heater sizing

With a preliminary heater selected the physical geometry, material, and power of the heater is known, and flow rate of the air. An energy balance is determined on the heater with the following assumptions: steady-state conditions, fully developed flow, one-dimensional conduction. All of the properties of the air and aluminum heater cylinder-wall are known. A thermal circuit is shown in Figure 3-4.

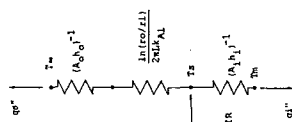


Figure 3-4 Simplified thermal circuit of a heater

Taking the energy balance of the heater,

$$q'' @ q_o \int q_i \quad \text{Equation 3-18}$$

$$q'' A_i @ q_o \int q_i \quad \text{Equation 3-19}$$

$$q'' (2\pi L) @ \frac{T_i [T_i - T_m] \frac{1}{h_i} \frac{1}{2\pi L} - \frac{T_m [T_m - T_a] \frac{1}{h_o} \frac{1}{2\pi L}}{\ln \left(\frac{r_o}{r_i} \right) \frac{1}{2\pi L k}} \quad \text{Equation 3-20}$$

which can be reduced to

$$q'' @ \frac{T_i [T_i - T_m] \frac{1}{h_i} \frac{1}{2\pi L} - \frac{T_m [T_m - T_a] \frac{1}{h_o} \frac{1}{2\pi L}}{\ln \left(\frac{r_o}{r_i} \right) \frac{1}{2\pi L k}} \quad \text{Equation 3-21}$$

where q'' is the heat flux in terms of W/m^2 , T_m is the temperature of the heat source in terms of K, T_i is the ambient air temperature in terms of K, T_m is the temperature of the medium which is the heated air once again in terms of K, r_i and r_o are the inner and out radii respectively in terms of m, h_i and h_o are the inner and outer heat transfer coefficients respectively in terms of $W/m^2 K$, and lastly k_i is the thermal conductivity of aluminum in terms of $W/m K$.

All values are known except for h_i and T_i , which is what is being solved for. To find h_i the following is done. The Nusselt Number is a dimensionless temperature gradient at the surface, and it provides a measure of the convection heat transfer occurring at the surface [90].

$$Nu \phi \frac{hL}{k_f} \quad \text{Equation 3-22}$$

where L is equal to D_i the inner diameter of the heater, k_f is the thermal conductivity of the fluid in this case the air being heated.

To determine if the flow is turbulent or laminar the Reynolds number needs to be found. Reynolds number is a dimensionless ratio of the inertia and viscous forces [90].

$$Re D \phi \frac{4\dot{m}_{air}}{\pi D \mu_{air}} \quad \text{Equation 3-23}$$

If $Re D$ is greater than or equal to 10,000 then the flow is turbulent and fully developed or it is considered to be laminar. Plugging in the values result in turbulent flow over the range of mass air flow that will be seen at any given engine speed. Moreover, due to the cross coil inside of the heater cylinder wall, one would assume turbulent flow purely on the geometry. The following equation is used for the Nusselt Number [90].

$$Nu \phi 0.023 Re D^{0.8} Pr^{0.4} \quad \text{Equation 3-24}$$

where Pr is the Prandtl Number, a dimensionless ratio of the momentum and thermal diffusivities [90].

Setting $Nu \phi \frac{hL}{k_f}$ Equation 3-22 and $Nu \phi 0.023 Re D^{0.8} Pr^{0.4}$ Equation 3-24

equal and solving for h , the following equation is obtained.

$$h_i \phi \frac{k_{air}}{D_i} 0.023 Re D_i^{0.8} Pr^{0.4} \quad \text{Equation 3-25}$$

With all of the variables solved for or know from

$$q'' \phi \frac{T_i (T_i - T_m) \left(\frac{r_i}{k_{air} \ln \frac{r_o}{r_i}} \right) \left(\frac{r_i}{h_o r_o} \right)}{1} \quad \text{Equation 3-21 it can be rearranged to}$$

solve for T_i , the resulting equation is show below.

$$q'' \phi \frac{T_i (T_i - T_m) \left(\frac{r_i}{k_{air} \ln \frac{r_o}{r_i}} \right) \left(\frac{r_i}{h_o r_o} \right)}{1} = \frac{T_i (T_i - T_m) \left(\frac{r_i}{k_{air} \ln \frac{r_o}{r_i}} \right) \left(\frac{r_i}{h_o r_o} \right)}{1} \quad \text{Equation 3-26}$$

The above equations were input into Microsoft Excel spreadsheet over the range of engines speeds expected from the engine.

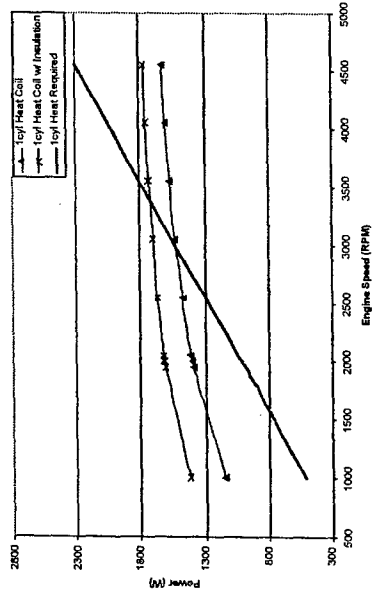


Figure 3-5 Power require for one heater

As shown in Figure 3-5, the required power needed to get T_m which is equal to T_m to the desired value of 412 K (282 °F). This is needed for the 87-octane fuel to auto-ignite at or near TDC. The heater has more than enough power available until approximately 3000 RPM. If a fiberglass insulation tape is added then the maximum speed would be around 3500 RPM. These values are deemed satisfactory given that the maximum stock diesel engine speed is around 4500 RPM. Therefore, four of the 2kW coil heaters are needed for the engine. This means that each intake runner will have its own heater, and a custom intake will need to accommodate the each of the heaters.

Heater Characterization

An Experiment was developed to see the response time of a heater at various mass air flow rates. This was accomplished by

connecting a blower to the heater via a black flexible hose. The air flow was throttled into the blower to simulate the various flow rates of the engine. A monometer is connected to a laminar flow element (LFE) to measure the pressure drop, which is proportional to a flow reading. The heater uses a 240 VAC power source. Then a type K thermocouple was placed before and after the heater to measure the rise in temperature. Below is a picture of the experimental setup in Figure 3-6.

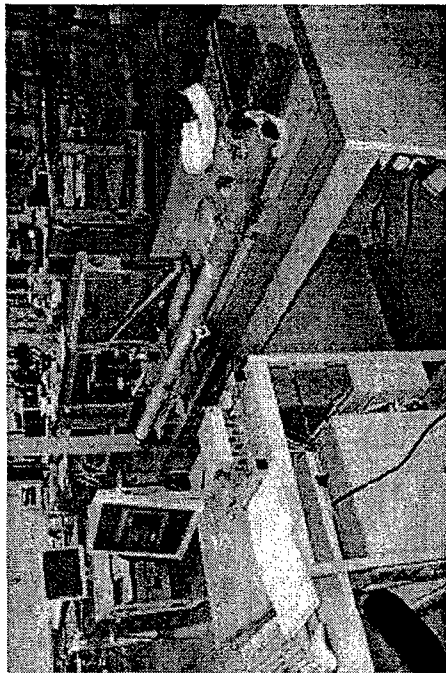


Figure 3-6 Experimental setup of heater characterization

This experiment was performed in the Thermal Sciences Laboratory, where the data was collect with National Instrument data acquisition board operating Lab View software. A screen shot of the user interface of the software is shown in Figure 3-7.

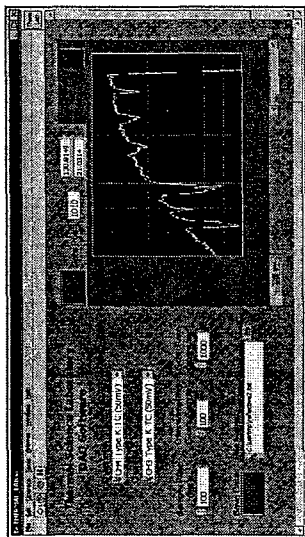


Figure 3-7 Screen shot of heater experiment

After compiling the data, the change in temperature over time for various mass air flow rates is plotted and shown in Figure 3-8.

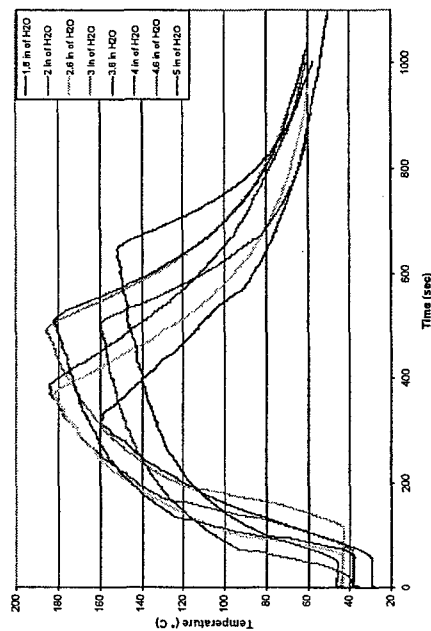


Figure 3-8 Heater characterization results

It is determined that the heaters have a reasonable response time for this application. It is noted, that once the heaters were installed in the test cell, the power source that was available

for the heaters resulted in only 200 VAC. This is due to the fact that the build only has 208 VAC, as this is a function of how the electricity is pulled from the transformer. Lastly there is a voltage drop over the power relays. This lack of electrical power reduces the 2 kW heater to a 1.365 kW heater. This is going to limit the engine operating range on the high end.

Intake

Once it was determined that four heaters were necessary for HCCI combustion to occur, the stock intake needed to be modified to accommodate the heaters. A solid model was developed to evaluate various designs. The design needed to incorporate a Hilborn throttle body, the four heaters, and keep the stock runner locations to properly mount to the head of the engine. Another concern was to isolate the heaters from as much of the vibration as possible. This was done to help preserve the lifetime of the heating elements, so that they would not prematurely fail or fracture due to the heat cycling, the vibration, and then be ingested into the combustion chamber.

A plenum was manufactured to accommodate the proper spacing such that the centerline of the individual runners aligned with the sock head dimensions. The Hilborn throttle body was connected to the plenum. Since, the diameter of the heaters is larger than the stock intake, four-venturi where manufactured to reduce the runner diameters. Lastly, the stock manifold was modified by placing fuel injectors into each runner and cutting the sock plenum off and placing four individual tubes. Each of the above components are shown in Figure 3-9

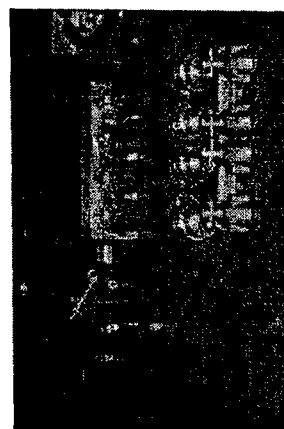


Figure 3-9 HCCI intake components

53

To address the concern of vibration high temperature silicon tubes were used to connect between the heaters the four-venturi and the modified stock intake. The blue silicon tubes will help to dampen the vibrations and isolate the heaters from the engine vibrations. The intake assembly is shown being installed on the engine in Figure 3-10.



Figure 3-10 Installing the HCCI intake on the engine

Some other design criteria of the intake that were included were low air flow resistance, good distribution of air and fuel between cylinders. The design tried to maximize the benefits of pressure wave pulsations to gain ramming effects and basically tune the intake such that the most amount of air could be inducted. However, due to the large diameter of the heaters and the low engine speeds, the intake runners would have to be over 40 in. (101.6 cm) long and this is not reasonable for packaging.

Multi-port fuel injection

Multi-port fuel injection is the desired method of providing fuel. The literature to date suggests that individual control of each cylinder is needed. This will allow for individual fuel control for each cylinder. The injector locations needed to be placed after the heaters to prevent any chance of the fuel igniting as it goes through the heater elements. Therefore, the injectors were located right before the head, so that the fuel is sprayed right onto the intake valve. This can be seen in Figure 3-11.

54

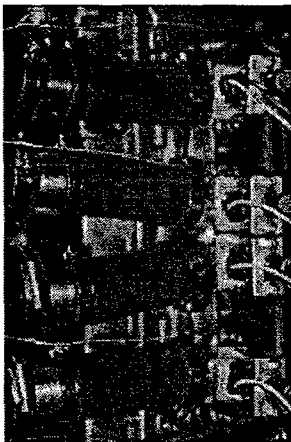


Figure 3-11 Fuel injector locations

The fuel injectors are identified by the red and yellow wiring which connect to the end of the injectors. These wires provide the connection for the injector pulse width signal to turn the injectors on and off.

Other modifications were made to the engine. This included the removal of the brake vacuum pump which was replaced with an aluminum plate and sealant. A thermocouple probe was drilled into the oil plug. A pressure transducer line was taped into the engines pressurized side of the lubricating oil system. Lastly, encoder wheel mounts for the crank and cam were manufactured and associated magnetic sensors for each respectively. These will be seen in the engine assembly photos in the next section.

3.3 ENGINE ASSEMBLY

In order to convert the diesel engine to HCCI engine new pistons were needed for this conversion. This required that the entire diesel engine be disassembled down to just the block, so that the HCCI pistons could be installed, and thus converting the engine along with the new intake design, control strategy, and the other modifications mentioned above. This section shows a series of pictures at various points during the assembly of the HCCI engine and mentions the compression ratio validation.

Numerous parts have to be replaced whenever the engine is rebuilt. This includes stretch-bolts that are used through out the engine. As their name suggests they stretch when the torque specification is applied them and can only be used once. A list

of all the parts needed to rebuild the engine including the stretch bolts are listed in Table 3-2.

Table 3-2 Dealer part numbers need to rebuild the HCCI engine

QTY	PART NO.	DESCRIPTION
1	N-905-969-02	IDLER BOLT
10	N-901-300-01	MAIN BEARING END CAP BOLT
8	028-105-425-C	CONNECTING ROD BOLT
6	N-906-650-01	FLY WHEEL BOLT
1	038-105-229	CRANK SPROCKET SCREW
10	068-103-384-A	HEAD BOLT
1	038-103-383-K	HEAD GASKET (3 HOLE)
2	028-129-717-D	INTAKE GASKET
4	028-129-389-B	EXHAUST MANIFOLD GASKET
8	N-101-333-01	CIRCLIP
1	044-121-113	THERMOSTAT
1	06B-121-687	COOLANT LINE O-RING
1	038-121-119-B	COOLANT CONNECTOR O-RING
1	038-121-119	WATER PUMP O-RING
1	037-121-688	COOLANT CONNECTOR O-RING
1	038-103-085-E	FRONT SEALING FLANGE SEAL
1	N-908-132-01	OIL PAN BOLT SEAL

In Figure 3-12 is the engine block on an engine stand looking from the bottom or oil pan side of the block.

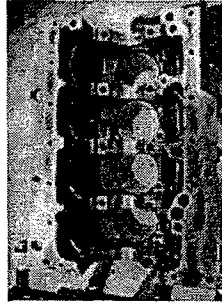


Figure 3-12 Bottom view of the engine block

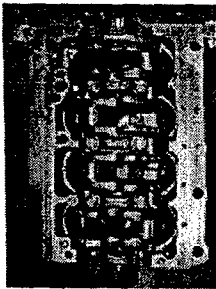


Figure 3-13 Bottom view of the engine block with the crank and main bearings



Figure 3-14 The internals of the engine starting at the top left intake and exhaust lifters, pistons with rings, wrist pins, connection rods, bearings, on the right the pistons assembled



Figure 3-15 Bottom and side view of the oil pump installed

Before the rest of the engine assembly could continue the compression ratio of the HCCI engine needed to be determined. The engine assembly will continue after this quick digression.

Compression ratio and volumetric measurements

An easy way to determine the compression ratio of the engine is to take volumetric measurements of the head and block. This is done by measuring the displacement volume of fluid from a known volume. Figure 3-16 shows an example of measuring the volume of the head. A piece of clear Plexiglas was machined to measure both the head and the block. Water with red dye was used to help visualize accurate measurements.

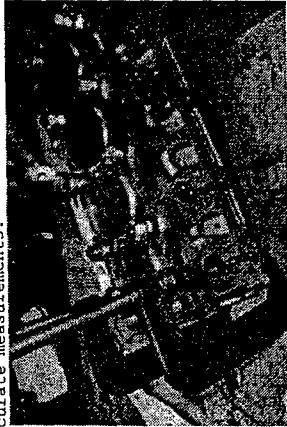


Figure 3-16 Volumetric measurement of the head

After measuring the head and block a number of times the HCCI compression ratio for each cylinder the averages are determined. These values are summarized in Table 3-3.

Table 3-3 HCCI compression ratio

Cylinder (#)	1	2	3	4	Average	Percent Error (%)
Compression ratio	16.21	16.21	16.36	16.41	16.3	1.2

The compression ratio is lower than the desired compression ratio of 16.5:1. However, the average is only 1.2 % lower than the desired valve. This is not a big problem, but the air temperature after the heaters will need to slightly higher than the originally design temperature due to the lower compression ratio.

With the all of the volumetric measurements completed the rest of the engine assembly can be continued. This includes installing the head onto the engine block and then all of the peripherals including the timing belt. The number one piston needs to be at

TDC and then the VW special tool 3418 must be placed at the back of the cam. The special tool slides into a groove on the back of the cam and then rests on the top of the head. This properly locks the cam such that the number one cylinder valves are at TDC. The special tool was kept in place during the rest of the assembly to insure that the timing between the crank and cam was correct. The special tool is shown in Figure 3-17 on the right.

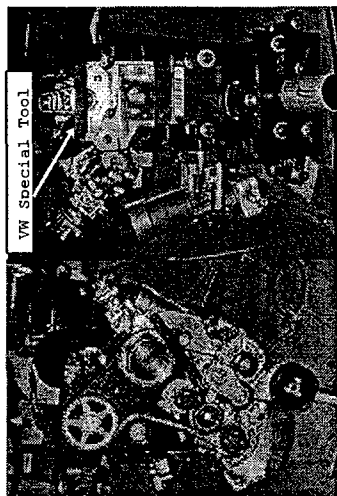


Figure 3-17 Right: front view of the engine and Left: is the rear view of the engine

The rest of the engine components to be installed necessitate that the engine be on the dynamometer. Therefore, the engine is removed from the engine stand by an overhead crane and placed on the rails of the dynamometer. This is shown in Figure 3-18.

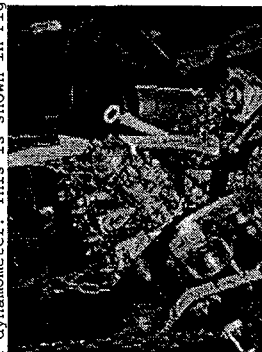


Figure 3-18 Installing the engine onto the dynamometer rails



Figure 3-19 Complete engine installed

In Figure 3-19 the engine is completely assembled. This includes connecting the exhaust, the radiator, sensors for data collection, ECU electronics and sensors, and fuel rail.

Table 4-1 Digalog Data Acquisition Sensors

Sensors connected to Digalog
Tatmoshere
Tintake 1
Tintake 2
Tintake 3
Tintake 4
Toil
Tcoolant
Texhaust
Poill
Pexhaust
Mass air flow

The list in Table 4-1 includes all of the parameters of interest, except for the in-cylinder pressures which are monitored by another system which will be discussed in a later section.

The user interface for the Testmate which controls the dynamometer or engine load and speed is shown in Figure 4-2. Whenever pressing any of the buttons in order for the action to occur the button must be pressed twice. This is to keep a button from accidentally being pressed.

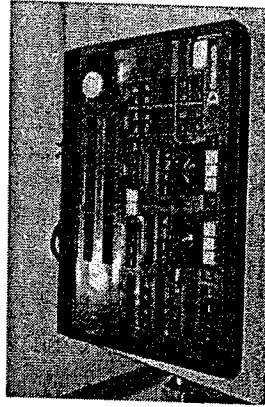


Figure 4-2 Testmate panel: dynamometer or engine speed and load control

The software that allows all of the above components to communicate is developed in a program called Hypercell. In Hypercell a configuration file is defined, and within this file

62

4. TEST BED

Multiple systems are integrated together mechanically, electronically and the associated software with each system. To help reduce the integration a block diagram is developed this is shown in Figure 4-1.

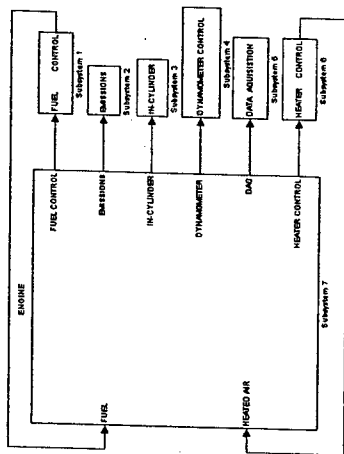


Figure 4-1 Block diagram of HCCI test bed

This helped to reduce the system it into manageable sub systems. Here the hardware and the software of each sub system will be discussed. For a detailed schematic of the test bed see Appendix B.

4.1 DYNAMOMETER CONTROL AND DATA ACQUISITION

The dynamometer and data acquisition subsystem consists of an electric motor, Digalog Cellmate, Testmate panel, Testmate, all of the sensors monitoring the engine, and a PC computer. The electric motor is a 300 HP motor that can either drive the engine by motoring it or it absorbs the energy produced by the engine. The Cellmate is the main controller of the system it is where the programs are operated and saved, it also where the data is stored. The Testmate panel is the interface between a user and the Testmate. The Testmate is the actual controller of the electric motor or the dynamometer controller. Depending on if the dynamometer is in motoring or in absorb mode the Testmate panel is then controlling the electric motor or the engine being tested. The parameters being monitored by the Dialog system and the associated sensor are listed in Table 4-1.

61

all of the sensors locations are determined. A screen shot is shown in Figure 4-3.

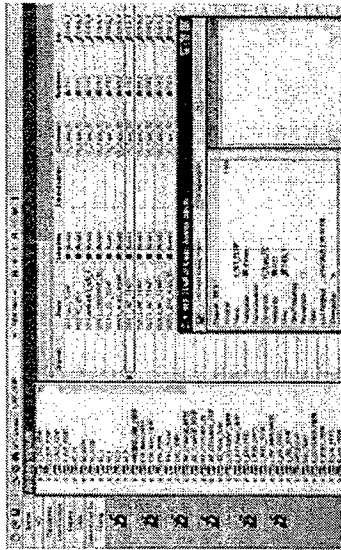


Figure 4-3 Screen shot of Hypercell environment

The Hypercell environment has on the left an explorer tree where one can select all of the various sections within the configuration file. In Figure 4-3 the explorer tree is in the analog inputs section. All of the analog inputs are shown. Then to right in the white and light green striped area are the actual locations of each analog channels and the label of that channel. One can double click on a channel, here 1_INT_TEMP, is selected. This is the intake temperature of the cylinder number 1. Within the blue box is where 1_INT_TEMP is defined, the kind of conversion K_Type tc, which is a type-K thermocouple, and the units are defined in terms of degrees Fahrenheit.

Within Hypercell is where all of the sensors are calibrated in a calibration file. A screen shot of the calibration file is shown in Figure 4-4. Here the user calibrates the sensor and defines what type of engineering units that the signal should be stored in when logged as well as displayed in real time.

Displays are created to allow the user to see engine parameters in real time. The displays also can have inputs for set point values or buttons to turn on and off relays. Two displays are made for the HCCI engine.

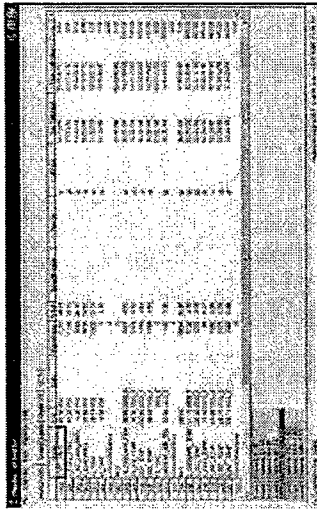


Figure 4-4 Screen shot of configuration file

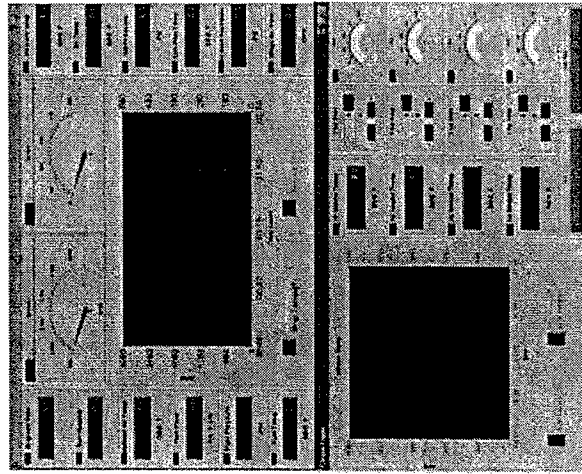


Figure 4-5 HCCI engine displays

The top screen as shown here monitors basic engine parameters like oil and coolant temperature and others, and has a gauge for engine speed and torque. In the middle of the screen is a timeline chart that displays how engine torque, engine temperature, and engine speed, all change with time. The lower screen is used mostly for controlling the heaters. This allows the user to input set points for each of the cylinders, giving individual control of each cylinder. There is a timeline chart in the middle of the screen similar to the one on the top screen. However this monitors just the intake runner temperatures respectively. The gains being sent to each of the heaters is shown by the gauges on the right side of the screen. Finally, at the bottom of the screen is the buttons to turn on the relay for the Electronic Control Unit (ECU) and the power relay for the heaters.

There is a bug in the software regarding the temperature set points. The set point has to have a zero at the end of the actual temperature desired. For example if the desired is 310 then 3100 has to be entered.

Recording Data

To record data Hypercell uses a function called logging. Before data can be logged, a history file must be configured and then a test conducted. To configure the history file the test run number of interest needs to be stated and the type of data points. The history file defines the location to store the data and is used by Microsoft Access to upload the data from the Cellmate. If the test run number is not defined then all of the past runs will be up loaded. From Access the data can then be post processed for graphs and analysis.

With the history file configured, the logging needs to be defined as well. This includes defining the logging sequence, the time duration between points, and the number of points to be stored. This completes the data logging process and once a test is started one simply clicks on the start button. Once a test is completed to retrieve the data is done by going to the history file to upload the data. The history file is then closed and Access is opened. With Access open, the history file is then converted. There is some incompatibility between Hypercell and Access. However, the data will upload and is found the run data group (example RUN000124DATA). From this data group the data is placed in a spreadsheet format.

4.2 IN-CYLINDER PRESSURE TRACES

This subsystem includes a PC computer, AVL 619 Indimeter, AVL encoder, four Optirand AutosI-S in-cylinder pressure transducers, and a 12 volt DC power supply for the pressure transducers. The PC computer operates AVL software called Indicom. This program allows the user to configure a user interface to view the pressure traces in real time. Calibration of the pressure transducer is done here as well. The encoder has to be aligned at TDC with the number one cylinder, this is also done here. The AVL 619 Indimeter is a high speed data acquisition system that records pressure with respect to crank angle degree. An actual p-v diagram of the engine is created in real time. The Indimeter stores multiple engine cycles and can play them back, calculate averages, and puts the data in a form for exporting that other programs can read.

Figure 4-6 shows where all of the hardware is defined and the parameters needed to properly operate the system. This included inputting all of the engine specifications and geometry. The AVL 619 Indimeter is capable of reading different encoders, so the correct one must be defined. If the incorrect one is defined the system will still operate however some of the pressure traces will be erratic while others will look correct. The HCCI system has an AVL 365-0.10 deg (1800 pulses, both edges). The number of channels to be recorded must be specified.

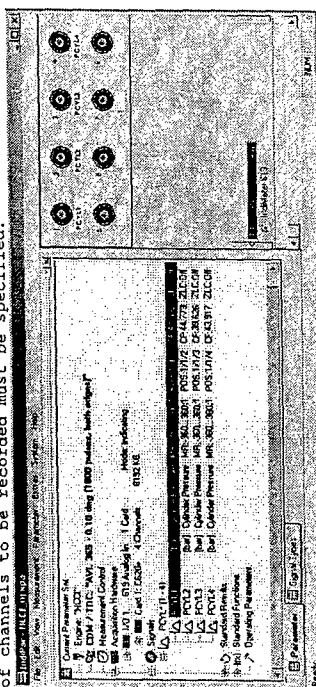


Figure 4-6 AVL parameter setting window

Each of the channels then needs to be defined as a cylinder pressure type and calibrated. The calibration is accomplished by entering the pressure transducers response in term of bar/V. The calibration offset is going to zero the signal. These two values

are sufficient to properly define the channel and no Zero Level Correction is needed. Each of the channels needs to be calibrated to the specific pressure transducer for that channel.

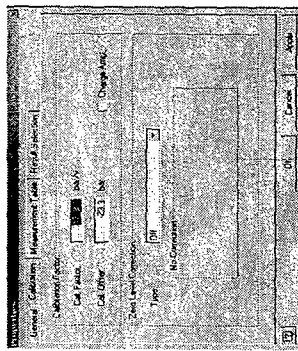


Figure 4-7 Pressure transducer calibration screen

After each of the pressure transducers channels are calibrated then TDC can be determined. The Indicom software can determine this location by motoring the engine with no fuel and clicking on the TDC Determination button in lower right hand corner of the screen shot shown in Figure 4-8.

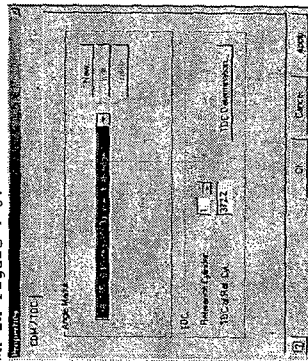


Figure 4-8 Indicom determines TDC in this screen

In this screen shot the correct encoder angle marks must be selected that corresponds to the encoder defined in the previous window. After the engine is motoring Indicom calculates TDC based on the pressure, and as shown in Figure 4-8 the TDC reference is

cylinder one at 372.2 crank angle degrees (CAD). This value is in terms of how the encoder is mounted in relation to TDC. Indicom takes this into account and then displays the pressure traces at TDC or 0 CAD.

Once all of the parameters are defined a display is made to show the information of interest in real time. Various tabs are created, but the ones of most interest are the plot of pressure versus crank angle degree and the p-v diagram. Figure 4-9 shows the screen set to the pressure vs. CAD tab. At the bottom of the screen there are red dots and warnings that pressure 1 to 4 can not be found. This is fine, once the engine start turning the AVL system will find the pressure traces and begin taking readings.

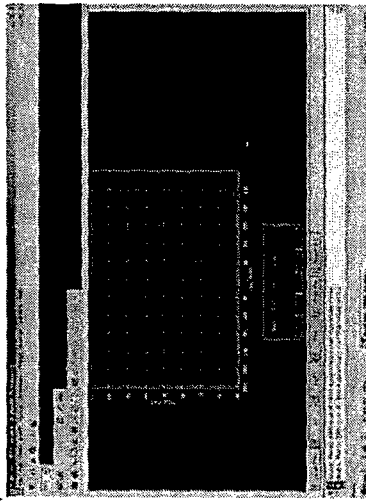


Figure 4-9 Pressure vs. CAD window before taking a reading

An example of the pressure vs. CAD trace is shown in Figure 4-10. This shows in real time what the pressure, in terms of bar, is for each of the four cylinders respectively. The maximum pressure for each is displayed at the bottom of the figure.

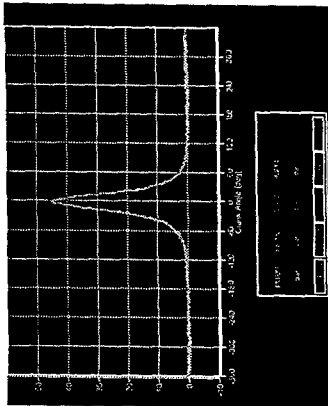


Figure 4-10 Example of the HCCI engine motoring

The p-v diagram that accompanies Figure 4-10 is shown in Figure 4-11. The engine is not producing any power because once the pressure trace reaches its maximum value, which is due to the compression ratio of the engine, it then returns basically on the same path since there is no combustion as the volume increases.

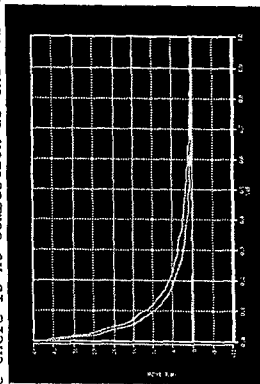


Figure 4-11 p-v diagram of the HCCI engine motoring

The Indicom software allows the user to specify how many engine cycles that are desired to be recorded. This data can then be saved in what is called an IFile. This information is then played again on a cycle-by-cycle duration. This basically represents the data in sequence as if the actual engine was operating again in the exact the same way. To load a previous data set of engine cycles the window shown in Figure 4-12 is opened. Select the IFile of interest and drag it over the window into the window

entitled Select some tests. This will load the stored data into Indicom display for viewing and analysis.

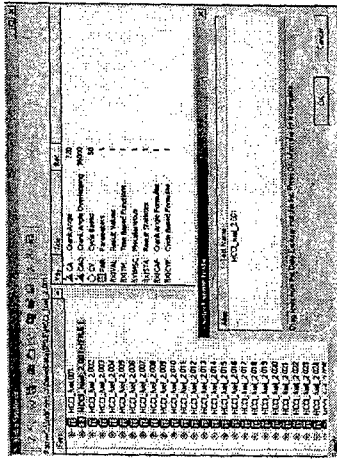


Figure 4-12 Window for loading stored pressure traces

4.3 FUEL CONTROL ECU

To control the fuel an electronic control unit (ECU) manufactured by Electromotive Inc, was selected. One of the major reasons for choosing this unit is its capabilities to use a wide band lambda sensor for closed loop control of the fueling, to possibly be used for future work. Since HCCI combustion is such a lean process it requires the wide band range to be able to detect lambda as defined above. Another reason but of lesser importance is that other engines in the laboratory use a similar system, and this will help to keep the laboratory equipment uniform.

The ECU uses a number of sensors to determine how much fuel to inject on any given engine cycle, a list of these sensor is shown in Table 4-2.

Table 4-2 List of ECU sensors

TEC [®] Sensors
Crank Position magnetic sensor
Cam position magnetic sensor
Coolant temperature sensor (CLT)
Manifold Air Temperature sensor (MAT)
Manifold Air Pressure sensor (MAP)
Throttle Position Sensor (TPS)

Wide Band Lambda sensor (WBL)

All of the sensors listed in Table 4-2 needed to be located on the engine as well as wired.

The ECU only needs a manifold absolute pressure (MAP) sensor signal for the load, and crank sensor signal for engine speed and location for the engine to operate [91]. With these two signals an ignition curve and fuel control is established. The ECU is normally used to control SI engines however the HCCI engine does not have any sparkplugs so the ignition curve is ignored. Normally a signal is sent to direct firing units (DFU) which provide the voltage necessary to create a spark with a sparkplug. During testing the DFU were connected and an arc was created between the terminals. The manufacturer stated that this would not damage the DFU. However, the DFU were disconnected for safety, from being shocked or electrocuted.

A fundamental fuel curve is established by two parameters UAP and POT. UAP is the user adjustable pulse width of the fuel injector, and POT is the pulse width offset time [91]. The fundamental fuel curve only works on a thermodynamically linear engine, which would have a linear torque curve that is a flat horizontal line from idle to redline [91]. This is not how real engines work, but only theoretical, so to compensate for the non-linear fuel consumption a volumetric efficiency (VE) table is used by the ECU. The VE is based on RPM and MAP readings from a look up table which linearly interpolates 256 points for smooth transition from points within the table [91], such that the fuel injector pulse width is adjusted for various loads and engine speeds.

There are fuel compensations or fuel enrichment setting including starting, cold weather, engine accelerations and decelerations. These adjustments add and subtract fuel from the fuel injector pulse width (PW) by the following equation [91].

$$PW @ \frac{7V_{map}}{85} \left(\frac{VE_{ABSOLUTE}}{8} \right) \left(\frac{PPS}{100} \right) \left(\frac{KLT\%}{100} \right) \left(\frac{MAT\%}{100} \right) \left(\frac{EGO\%}{100} \right) \left(\frac{POT}{100} \right) BTO$$

Equation 4-1

Since, this is the first attempt to operate a HCCI engine by this unit, and there are catastrophic consequences if too much fuel is injected to the engine, all of the enrichments have been set to zero to give the user direct control of the fuel.

By setting all of the fuel gains to zero in Equation 4-1 it reduces to

$$PW @ \frac{7V_{map}}{85} \left(\frac{VE_{ABSOLUTE}}{8} \right) \left(\frac{PPS}{100} \right) \left(\frac{KLT\%}{100} \right) \left(\frac{MAT\%}{100} \right) \left(\frac{EGO\%}{100} \right) \left(\frac{POT}{100} \right) BTO$$

UAP and POT will be used to adjust the fuel control. These parameters can be changed on the fly, meaning that while the engine is operating their values can be change in real time and take effect.

ECU Software Configuration

The TEC[®] has its own software called WinTEC3 where one configures the TEC[®], and then uses the same software to calibrate the engine to operate optimally. WinTEC3 comes with several baseline calibration files which are used as a starting point, but must be given a unique name since the default baseline calibration files can not be overwritten. A view of the main menu window is shown in Figure 4-13.

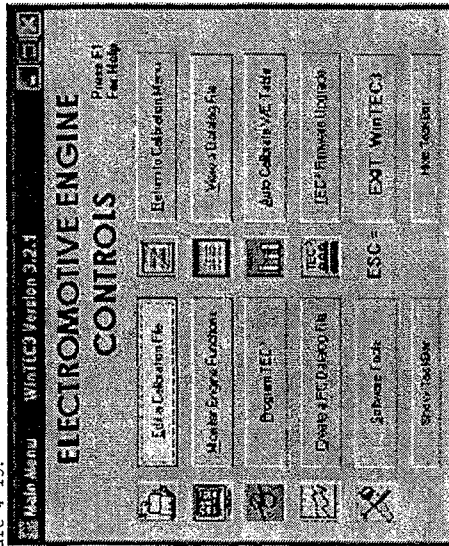


Figure 4-13 WinTEC3 main menu

From the main menu window one clicks on the Edit a Calibration file shown in upper left corner. This button will open a calibration file or .bin file. This is the file that programs the ECU and is executed during engine operation. Once a .bin file has

It turns out that even though the TEC^{3r} can read a wide band lambda sensor, it can only go up to an air/fuel ratio of 29.6 and this is right at the limit of where HCCI combustion stops occurring. To overcome this, the signal coming from the sensor was scaled such that it would be in the range that the TEC^{3r} will read. The value that TEC^{3r} displays is not the actual air/fuel ratio but can be adjusted by adding 29.4 to the TEC^{3r} value. A graph is provided in Figure 4-24.

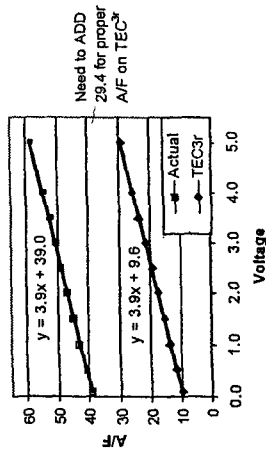


Figure 4-24 Lambda TEC^{3r} Conversion Factor

The last component to be configured is the TPS sensor. The rest of the sensors do not need to be calibrated, however the TPS does. This is simply done by having the throttle completely close and recording the voltage and then opening the throttle to full throttle or wide open and then again recording the voltage. The recorded voltage values are then input in the window shown in Figure 4-25. This provides the ECU with the operating limits of the TPS and thus knows how where the throttle is with respect to its range.

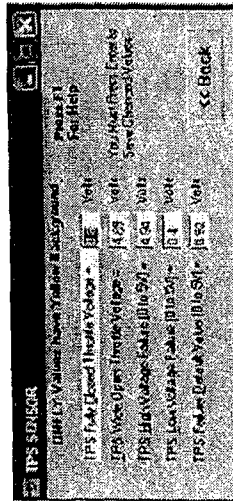


Figure 4-25 TPS limit settings

As mentioned above, the TEC^{3r} has the ability to receive a signal from a wideband lambda sensor, and can ultimately be used for closed loop control of the fuel. The scope of this work is to set up and the engine so that future research can be entertained in this area. The TEC^{3r} normal or default setting is to use an exhaust gas oxygen sensor (EGO). The EGO sensor is not capable of detecting lambda or the air/fuel ratio because HCCI combustion is really lean. The air/fuel ratio for HCCI is around 30 to 60. To use a wide band lambda sensor one of the analog/digital channels of the TEC^{3r} must be used, specifically channel 4. This is shown in Figure 4-22.

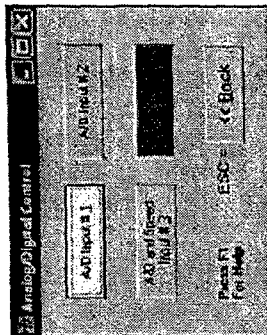


Figure 4-22 Setting wide band lambda operation

Since TEC^{3r} works with verity of wide band lambda sensors the TEC^{3r} needs to be calibrated to interrupt the signal correctly, and this is done in the window shown in Figure 4-23.

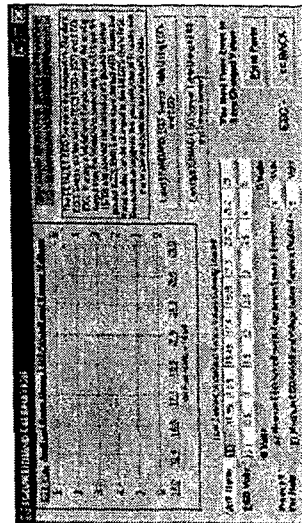


Figure 4-23 TEC^{3r} calibration of the wide band lambda sensor

With all the parameters addressed for the HCCI engine as far as the TEC[®] is concerned. A volumetric efficiency table is produced and this is shown in Figure 4-26. The TEC[®] system was installed with a 2 bar or 208 kPa MAP sensor for flexibility if a turbocharger is needed in future applications. The numbers in the table represent the PW time in terms of msec. At the bottom of the table at 13 kPa the values are in red. This is because the desired time for the injectors to be on is less than the minimum time that the injector can respond. This is not a problem as the time that the injector can respond. This is not a problem as the HCCI engines is not using a turbocharger at this time and not expected to be operating at 13 kPa, but rather around 101 kPa.

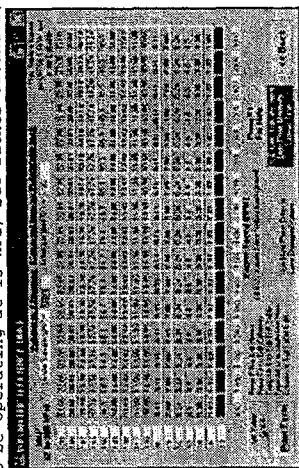


Figure 4-26 Volumetric efficiency table in terms of msec

In Figure 4-27 the same information is displayed as in Figure 4-26, but this time the table values are in terms of percent duty cycle.

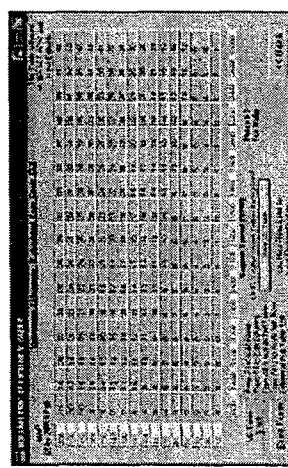


Figure 4-27 Volumetric efficiency table in terms of % duty cycle

Moreover, here are two screen shots of the WinTEC3 software when the engine is operating. In Figure 4-28 is where the fuel is adjusted by changing the UAP value which is highlighted by the smaller yellow box. Then in Figure 4-29 is the engine monitoring view, which is basically a digital dashboard that displays all of the engines functions.

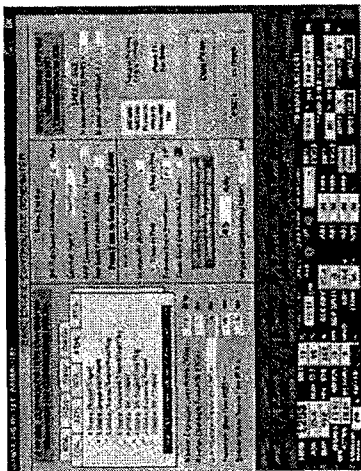


Figure 4-28 Adjusting fuel input of HCCI engine

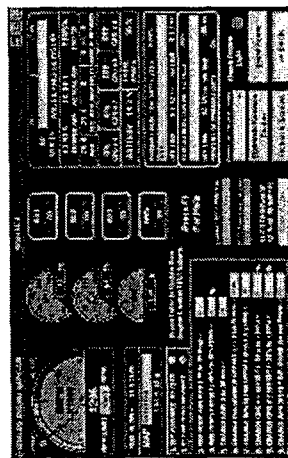


Figure 4-29 Engine monitoring screen

With the ECU configured correctly, the next section will discuss how the fuel injectors are sized and why the WinTEC3 wizard was not used and the alternate approach taken.

feedback to the Cellmate. Cellmate operating the HCCI Hypercell program then calculates the difference between the set point and the value from the feedback, the thermocouple, and adjusts the gains as needed. The HCCI engine display allows the user to input set points for each of the heaters individually. For more information on this section of the HCCI engine please see Cheung 2005 thesis.

4.6 EMISSIONS

To record emissions data an Autologic Autogas Emission Analyzer (AEA) was utilized. This unit conducts diagnostics using a gas analyzer to provide readings of carbon monoxide (CO), carbon dioxide (CO₂), hydrocarbon (HC), oxygen (O₂), nitric oxides (NO_x) including nitric oxide and nitric dioxide, and air/fuel ratio or lambda (λ). The AEA stores the data in a file that can be found through Access. This file provides the data, such that it can be imported into a spreadsheet environment for analysis and graphs. To operate the AEA one simply clicks on the Gas button and goes to Manual Meters which is shown in Figure 4-30.

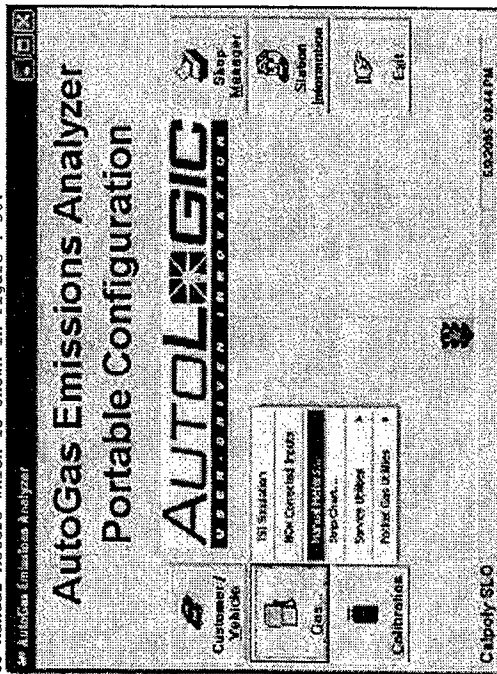


Figure 4-30 Screen shot to the AEA

83

The AEA typical has to calibrate upon turning on, during this time a window will appear stating that zero in progress. The calibration is done automatically. There are two ways to view the data one is in a stripe chart mode and the other is a numeric display. The numeric display is shown in Figure 4-31. To start recording data simply click on the button in the upper left corner with a circle in the middle of it. At times during a test the pump may turn off. If this happens the display will state in red letters Pump Off. To turn the pump back on click on Gas Bench and an option to turn on the pump can be selected.

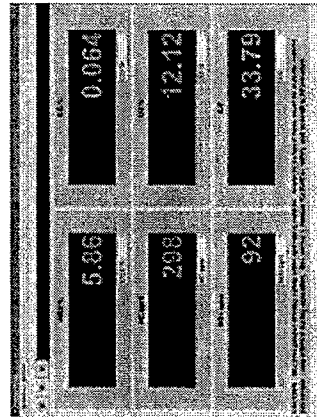


Figure 4-31 Emissions display

84

5. HCCI ENGINE OPERATION PROCEDURE

To operate the HCCI engine it is best to have three persons present. One person to control the fuel and emissions, another to operate the dynamometer and heaters, and finally one to monitor and save data on the in-cylinder pressure traces. There are many subsystems which have to be turned on and properly set before starting the engine. The following list gives an incremental description of the procedure, and concludes with a shut down procedure.

Inside Test Cell

1. Connect battery charger to 12 Vdc battery
2. Connect battery to 12 Vdc connector on G.E. Dyno frame
3. Select gasoline on Fuel Selector Valve on North wall
4. Turn on gasoline Fuel Pump North wall
5. Turn on Exhaust Fan Switch 14, 15, 16 on South wall
6. Turn on Radiator Fan Switch on West Radiator support
7. Turn on AVL Indimeter 619 near window East wall
8. Turn on 12 Vdc power supply for in-cylinder pressure transducers under AVL Indimeter
9. Check engine oil
10. Check engine coolant

Outside Test Cell

11. Connect gasoline to quick disconnect
12. Turn on Main Drive Cabinet (normal condition "POWER ON" lit)
13. Turn on Fuel Balance in rack (2 switches on rear)
14. Turn on Computer with AVL software on cart and open Inidcom file HCCI.nj

Controls

15. Turn on Main Computer at desk
16. Turn on Testmate Control Panel on desk (switch on left rear)
17. Turn on Cellmate and Testmate boxes are in rack (switches in the back)
18. Turn on Left computer in rack and open WinTEC3 file 2bar4cyl_HCCI and AutoGas Emissions Analyzer
19. Connect a charged 9 Vdc battery to microcontroller and turn on the main board (red switch)

Testmate Controller Panel

20. Turn on Panel Enable button (double press for all buttons)
21. Check the following:
 - a. Aux Power ON
 - b. Reverse OFF
 - c. Motor ON
 - d. Absorb ON
 - e. Ignition OFF
 - f. Fuel ON
 - g. Starter OFF
 - h. Throttle Power ON

Main Computer

22. Open Hypercell
23. Open Displays HCCI_A and HCCI_B
24. Open a History file
25. Select Manual Test
26. Define Logging Data Points
27. Click Run Test (the Testmate Controller Panel is now activated)

Performing a Test

28. Motor engine to 1000 RPM
29. Click on Heater Relay button on Display
30. Set Intake temperatures to 3500 then reduce to 3100
31. Wait for engine to warm up
32. Start In-cylinder pressure traces
33. Turn on ECU from Display
34. WinTEC3 Basic Engine Parameters window increase UAP from 23 to approx. 26 by 1 ms increments or until engine starts combustion then reduce UAP back to 24
35. Once engine starts combustng TURN OFF Motor on Testmate Panel
36. Click on button with circle in AutoGas Emissions Analyzer to start recording data
37. Click on Logging in Hypercell to start recording data

To shut Down

1. Turn off ECU on Display
2. Turn off Heater Relay on Display
3. Wait for Intake temperatures to cool
4. Spin engine speed to 0 on Testmate Panel
5. Shut down computers
6. Turn off Testmate Control Panel

Chapter 5

7. Turn off Drive Cabinet
8. Disconnect 9 Vdc battery and turn off board (red switch)

Test Cell

9. Turn off Fuel Pump
10. Turn off Radiator Fan
11. Disconnect 12 Vdc battery
12. Turn off Exhaust Fans
13. Turn off 12 Vdc power supply
14. Turn off AVL Indimeter 619

6. DATA COLLECTED RESULTS

As the foundational work for the HCCI engine it is of particular interest to determine the operation limits of the engine. With in these limits the cylinder-to-cylinder and cycle-to-cycle variations are observed to gain a fundamental understanding of how the engine performs. From this information educated decisions can then be assessed as to their validity for various avenues of further research and development, in hopes of bringing HCCI combustion closer to being implemented in industry.

The HCCI engine operates at 1300 RPM and produces 12.5 hp (9.3 kW). The torque at the same engine speed is 34 lb-ft (4.7 kg-m).

6.1 LIMITS OF OPERATION

To determine the limits of operation an engine speed of 1300 RPM is selected and the air/fuel ratios along with intake temperature are varied. The 1300 RPM engine speed is selected because of the relative low engine speed. During motoring tests it is observed that minimal vibrations occurred at this speed, whereas at other engine speeds the dynamometer rails' natural frequencies are excited.

Defining the limits of operation can be done by two methods. The first being, the sound of the engine, there is a distinct difference in sound when the engine is knocking. When the engine is operating in a stable combustion regime the engine sound is fairly smooth. A less noticeable sound distinction is made when the engine is operating in the misfire region. A more precise method is looking at the in-cylinder pressure traces.

In the misfire region of operation there is the one gradual pressure increase and another pressure rise of similar magnitude this is shown in Figure 6-1. When Stable combustion occurs there is the initial pressure increase and then a very rapid increase and a much higher magnitude than the misfire peaks. This is best seen in Figure 6-2. Then lastly, the knock region may have similar shape as stable combustion, but the magnitude can be much greater and there will be what looks like noise on the pressure trace and this can be seen in Figure 6-3. Knock as defined by the text is the objective source of noise that is transmitted through the engine structure when essentially spontaneous ignition of a portion of the mixture [1].

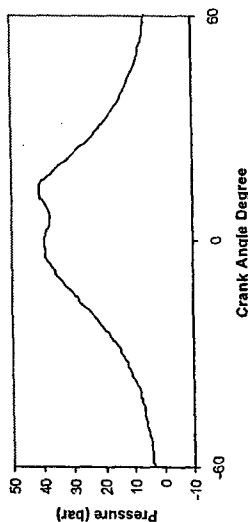


Figure 6-1 Example of misfire

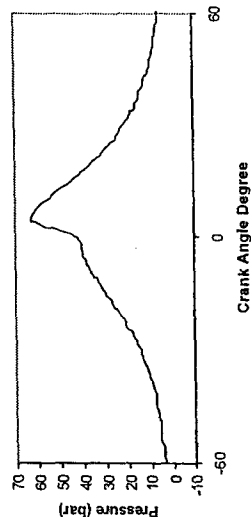


Figure 6-2 Example of stable HCCI combustion

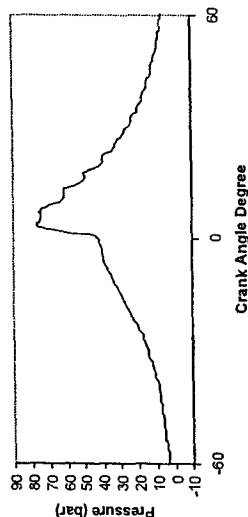


Figure 6-3 Example of HCCI combustion with knock

With each region clearly defined the engine was held at a constant 1300 RPM engine speed. Then at a given temperature the fuel is increased until knock occurred, and then the fuel is

decreased until misfire occurred respectively. Once the limits are determined for a given temperature, then the temperature was increased and the process repeated. Temperature is increased until the intake temperature reaches the limit of the silicon tubes, this limiting factor is due to the high temperatures. The results of this experiment are shown in Figure 6-4.

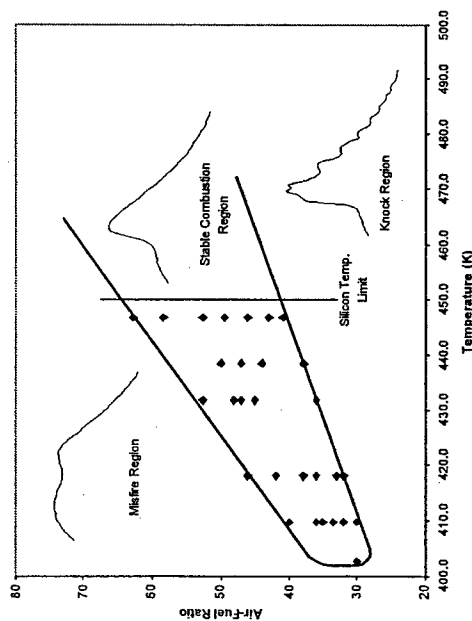


Figure 6-4 HCCI limits of operation

The area bounded by the thick black line is the region of stable combustion and all values above are misfire and below are knock regions. Just of over 400 K (260 °F) is the limit where some cylinders are knocking while others are misfiring. Right before this limit is where the engine produces the most power. This is due to the fact that the largest amount of fuel is being used here by the low air/fuel ratio. This being the case, maybe the silicon temperature limit is not a big issue, because the higher temperatures require less fuel to have stable combustion. Thus, by operating the engine with less fuel then there is going to be less power output naturally, in an already low power output engine.

A closer look at each of the three regions of interest is explored on the basis of cylinder-to-cylinder and cycle-to-cycle.

6.2 CYLINDER-TO-CYLINDER VARIATIONS

When looking at cylinder-to-cylinder variations the Indicom environment is well suited for this, because it overlays each of the four cylinder pressure trace for a given cycle on top of each other. This makes it easy to see where a cylinder pressure trace differs and which cylinder. The maximum pressure of each cylinder is also displayed. In this section each of the three regions will be addressed, but first shown in Figure 6-5 is the first plot that was obtained to confirm that HCCI combustion occurred, and proved the project successful.

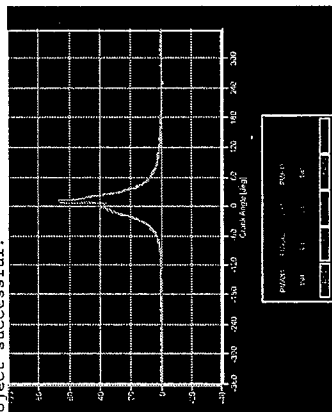


Figure 6-5 HCCI combustion

Misfire

A good example of how on a given engine cycle each of the cylinders can vary greatly is shown in Figure 6-6. Here Cylinder number 3 is on the verge of complete combustion and yet the rest of the cylinders have a decreasing maximum pressure. The maximum pressure is occurring well after top dead center (ATDC) for each of the cylinders around 12 degrees ATDC. The range between the maximum pressures is 10.77 bars, with number 3 being the greatest and number 4 the lowest.

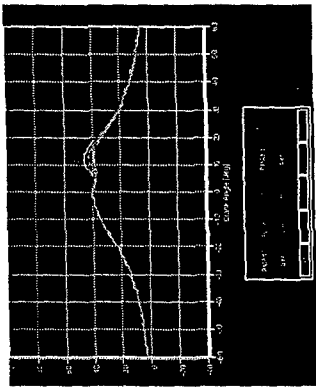


Figure 6-6 All cylinders misfiring on the same engine cycle

Stable Combustion

Figure 6-7 shows stable combustion for all of the cylinders. Cylinder number 3 again has a higher maximum pressure than the rest of the other cylinders. Cylinder 3 is starting to almost look like knock. The maximum pressures for each cylinder occurs at approximately 5 degrees ATDC, with cylinder 3 happening sooner. The range of the maximum pressures is 6.71 bar. Excluding cylinder 3 the range is only 1.83 bar between the rest of the cylinders.

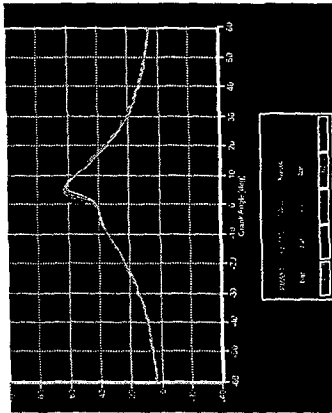


Figure 6-7 Stable HCCI combustion for all cylinders

Knock

Figure 6-8 shows the region of knock for all of the cylinders. Notice how noisy the signal for each of the cylinders looks. There are pressure spikes throughout the pressure curve for each cylinder. This is a damaging region for the engine to be operating in. Cylinder 3 is following along with the rest of the cylinder unlike the two previous examples. It is difficult to determine where the maximum pressure occurs for each cylinder. However, range of the maximum pressures is 9.4 bar.

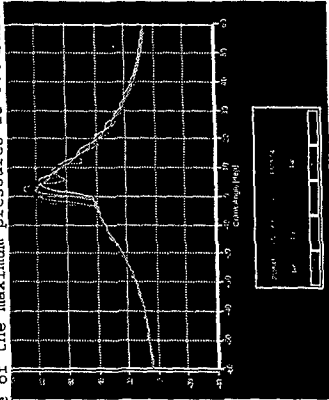


Figure 6-8 All cylinders knocking on the same engine cycle

P-v diagrams

The P-v diagram that is associated with the engine cycle for each operating region is shown in the following figures for comparison. This leads into the cycle-to-cycle variations. In Figure 6-9, misfire, notice how small the area is that is enclosed by the yellow line. This is to be expected since the cylinders are not fully combusting and when combustion does occur there is a large combustion lag or time delay. In Figure 6-10, stable combustion, the area enclosed by the yellow line is larger than the misfire case. Thus producing more work. The peak pressure is higher and the combustion is nearly reached the ideal of the Otto cycle of instantaneous combustion. In Figure 6-11, knocking, enclosed area looks to be slightly smaller than the stable combustion case. The maximum pressure is quite larger than the two previous cases.

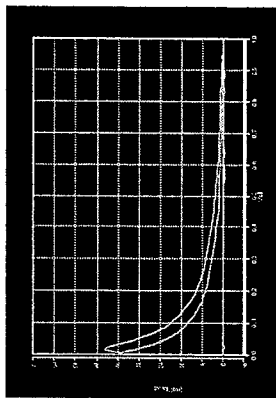


Figure 6-9 p-v diagram of misfire

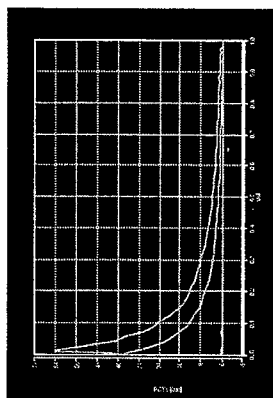


Figure 6-10 p-v diagram of HCCI combustion

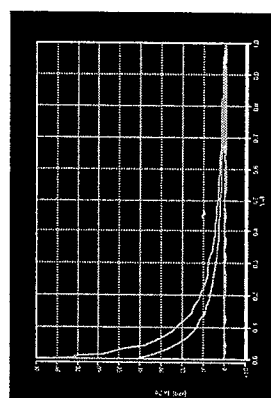


Figure 6-11 p-v diagram of when engine is knocking

6.3 CYCLE-TO-CYCLE VARIATIONS

A convenient way to view cycle-to-cycle variations is in 3-D plots. In these plots one can see how pressure changes from cycle-to-cycle. Figure 6-12 is an example of such a plot: from cylinder number 3. A Matlab program was developed to produce the 3-D plots, this program can be seen in Appendix C. Looking at the first 50 cycle or so the combustion is nice and stable and then a change is induced by increasing the fuel and then knock occurs as was shown in the limits of operation section. Around 200 cycles the fuel is reduced back to a stable operating region. It is clear how more erratic the knock region is compared to the stable region.

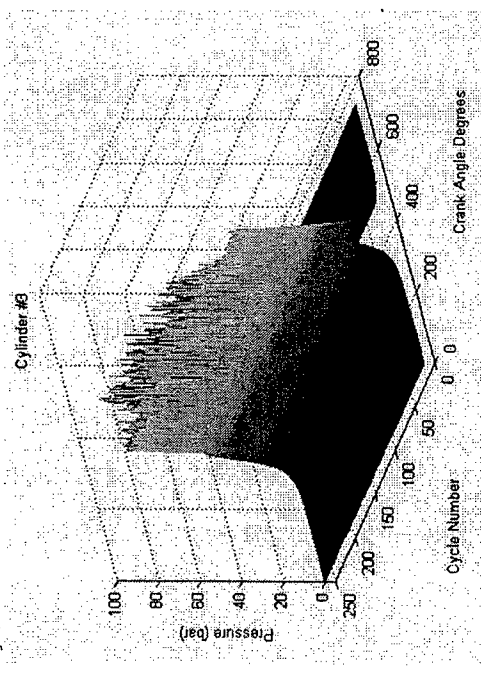


Figure 6-12 Stable combustion to knock and back to stable combustion

Misfire

Looking at the misfire region for each of the cylinders and how they differ from each other for one engine cycle was shown in the last section. The plots in this section are a comparison of multiple engine cycles for the same cylinder. This is not to be confused with the last section.

Figure 6-13 shows each cylinder individually for a continuous 50 cycles of misfire. Cylinder 1 in the upper left has a large variation from motoring pressures to poor HCCI combustion. Cylinder 2 in the upper right has misfire for all 50 cycles and maybe some HCCI combustion. Cylinder 3 in the lower left has some misfire, but looks to have mostly HCCI combustion. Once again cylinder 3 is out of sink with the other cylinders. Lastly in the lower right is cylinder 4 which looks to behave similar to cylinder 1. The same information that is plotted in Figure 6-13 is represented in a 3-D plot in Figure 6-14 for more clarification.

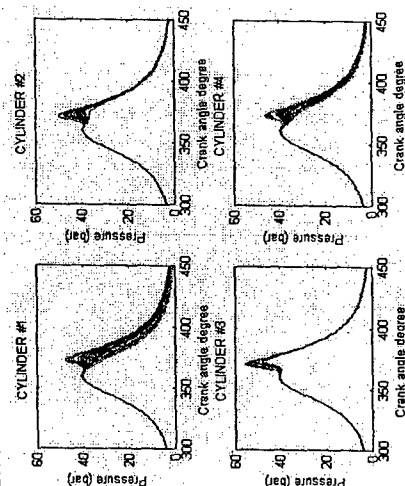


Figure 6-13 Example of misfire for 50 cycles for each cylinder

It can clearly be seen from Figure 6-14 that cylinder 3 is in fact combusting, whereas the rest of the cylinders are misfiring with an occasional pressure spike. Cylinders 1 and 4 have the least amount of pressure spikes.

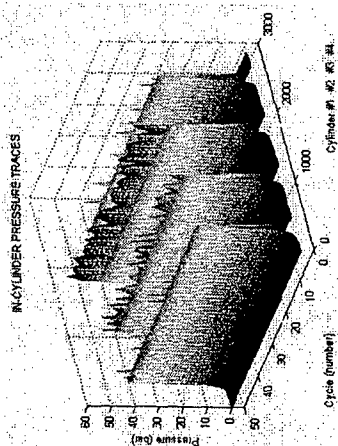


Figure 6-14 Example of misfire in 3D for 50 engine cycles

Stable combustion

Figure 6-15 shows each cylinder individually for a continuous 50 cycles of stable combustion. All cylinders are producing stable combustion. Cylinder 1 in the upper left of Figure 6-15 looks to have the largest variation of when combustion occurs. This is observed by the thickness of multiple lines just before maximum pressure. Cylinder 2 in the upper right and cylinder 4 in the lower right have very similar responses. Cylinder 3 in the lower left has the most repeatable combustion time. This is seen by the 50 cycles overlapping each other very closely, resulting in a thin plot line. The same information that is plotted in Figure 6-15 is represented in a 3-D plot in Figure 6-16 for another perspective.

From Figure 6-16 it can be seen that cylinder 3 has a slightly higher maximum pressure over the 50 cycles than the other cylinders. However, overall the combustion between the cylinders and the cycles is very even and smooth relatively speaking.

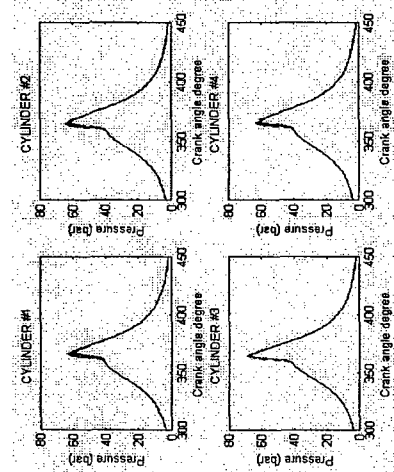


Figure 6-15 Example of stable combustion for 50 cycles for each cylinder

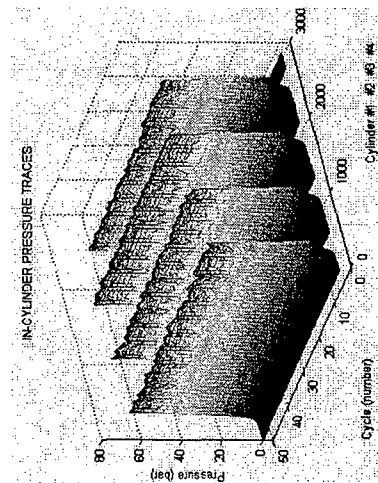


Figure 6-16 Example of stable combustion in 3D for 50 engine cycles

Knock

Figure 6-17 shows each cylinder individually for a continuous 50 cycles where knock is occurring. All cylinders are producing

knock. Cylinder 2 and 3 in Figure 6-17 look to have the largest variation of when combustion occurs, and the highest maximum pressure. This is observed by the thickness of multiple lines just after maximum pressure. Cylinder 3 in the lower left seems to be the worst here in terms of variation. Cylinders 1 and 4 have very similar traces. The pattern between cylinders 2 and 3 and then cylinders 1 and 4 could be due to heat transfer effects. HCCI combustion is sensitive to temperature and cylinders 1 and 4 are inherently on the front and back of the engine respectively. The same information that is plotted in Figure 6-17 is represented in a 3-D plot in Figure 6-18 for another perspective that shows cylinders 2 and 3 have more intense variations than cylinders 1 and 4.

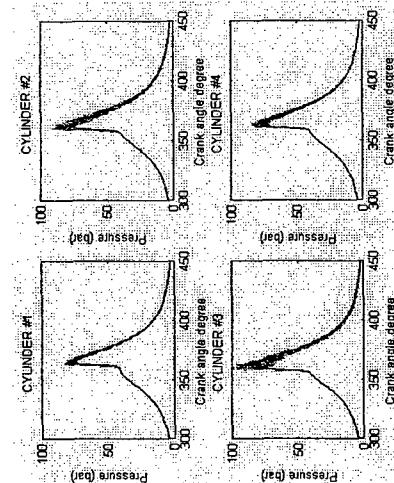


Figure 6-17 Example of knock for 50 cycles for each cylinder

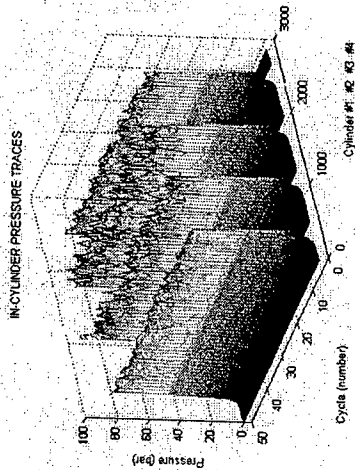


Figure 6-18 Example of knock in 3D for 50 engine cycles

All of the plots from this section have given some good insight into the cylinder-to-cylinder and more so to cycle-to-cycle variations. This insight is purely observational to trends. To quantify these variations a unit of measure is needed. This measure is the coefficient of variance (COV) of the indicated mean effective pressure (IMEP) as defined above. This is the topic of discussion in the next section.

6.4 COEFFICIENT OF VARIANCE OF IMEP

An important measure of cyclic variability is the coefficient of variation (COV) of indicated mean effective pressure. It is given by

$$IMEP @ \frac{\sigma_{IMEP}}{V_d} \quad \text{Equation 2-7}$$

$$COV @ \frac{\sigma_{IMEP}}{mean_{IMEP}} \times 100 \quad \text{Equation 2-8}$$

In order to calculate the work or integral of $p dV$ by the displaced volume the data is imported into a Matlab program that determines the IMEP for each cycle. This program can be seen in Appendix C. To validate the program the area of a simple known shape was imported and checked to see if the calculated area from the program equaled the known area. Then the standard deviation and mean of IMEP are also calculated by the same program.

Chapter 6

Moreover the program plots the IMEP for each cylinder per each cycle and the COV for the 50 cycles.

Misfire

Starting with the misfire condition, the results of the Matlab program are shown in Figure 6-19. The IMEP for cylinders 1 and 2 are have large fluctuations with a COV of 27.314 and 71.544 respectively. This is unacceptable, but then again this is in the misfire region where the engine is hardly even operating.

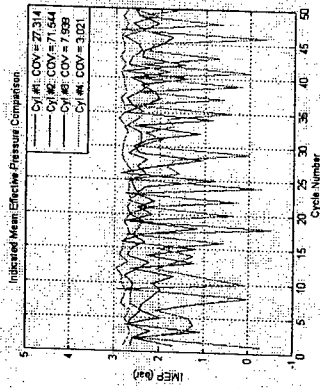


Figure 6-19 IMEP of HCCI operating in the misfire regime for 50 engine cycles

Stable combustion

Here is the real interest of the COV of the IMEP. The engine is producing between 2.4 and 2.6 bar for all cylinders. Cylinder 4 has the lowest COV of 1.936 and cylinder 3 has the largest COV of 2.720. This matches with the rest of the data for cylinder 3, as it has been typical out of sink with the other cylinders. These values of COV are nice and low. The IMEP is on par with engines of similar configuration and size in the literature.

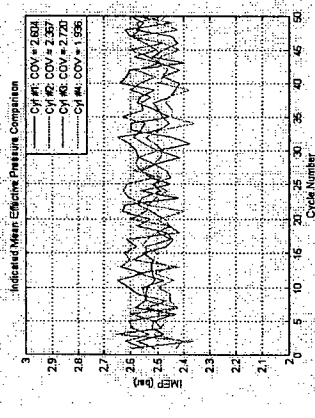


Figure 6-20 IMEP of HCCI operating in the stable combustion regime for 50 engine cycles

Knock

When operating in the knock region the largest IMEP values occur. However, this is at the expense of causing physical damage to the engine. Cylinder 2 has the highest IMEP just under 4 bar and the lowest COV of 2.083. Cylinder 4 had the largest COV of 8.525 and the lowest IMEP.

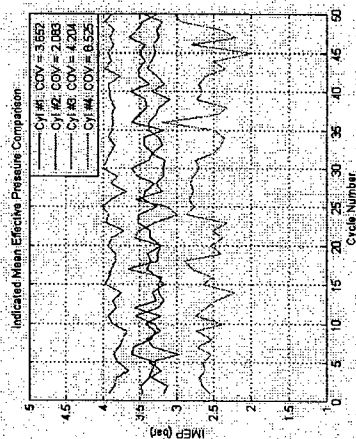


Figure 6-21 IMEP of HCCI operating in the knock regime for 50 engine cycles

Regardless of what region the engine is operating a few probable explanations for the variations, could be the normal variation in equivalence ratio, mass air flow fluctuations, dynamometer speed, heater fluctuations, and physical dimensions of each cylinder.

6.5 EMISSIONS

The emissions that are measured are carbon monoxide (CO), carbon dioxide (CO₂), hydrocarbon (HC), oxygen (O₂), nitric oxides (NO_x), air/fuel ratio (A/F), and lambda (λ). Of these emissions the HC, NO_x and the A/F are of particular interest. HCCI combustion produces higher values of HC than a comparable SI engine, thus necessitates reduction. The NO_x is where HCCI has the largest gains, with reductions of approximately 90% of a comparable CI engine. Lastly, the A/F provides feedback as to where the engine is operating. A summary of the typical emissions that were observed are presented in Table 6-1.

Table 6-1 Summary of typical emissions

Run	CO ₂ (%)	CO (%)	O ₂ (%)	HC (ppm)	NO _x (ppm)	A/F Ratio	Lambda
1	4.47	0.096	14.62	405	5	43.5	3.09
2	4.68	0.101	13.57	445	5	40.09	2.84
3	4.65	0.104	13.56	451	5	40.18	2.85
4	4.39	0.106	13.94	435	6	42.37	3.01

All of the values look really good except for the HC numbers. It is desirable to have lower numbers for HC. There could be a few reasons for this. The HCCI designed pistons have incorporated mechanisms to minimize unburned HC from crevices, so this is ruled out. High HC numbers typical signify that there is not complete combustion or that not all of the fuel is consumed. Given this a look into how efficient the fuel is being utilized is explored by finding the specific fuel consumption (sfc) as defined above by

$$sfc(g/kWh) @ \frac{\dot{m}_f(g/h)}{P(kW)} @ 608.3 sfc(lbm/hp1h) \text{ Equation 2-14}$$

The WinTEC3 measured the mass fuel rate to be 10 lbm/h, and the horse power was 12.5. Plugging in these values gives a sfc of 486.64 (g/kW h). Taking the sfc value and plugging it into

$$\eta_f @ \frac{W_e}{\dot{m}_f Q_{LHV}} @ \frac{(P_{net}/N)}{(\dot{m}_f \dot{V}_R/N) Q_{LHV}} @ \frac{P}{\dot{m}_f Q_{LHV}} @ \frac{1}{sfc Q_{LHV}} \text{ Equation 2-15}$$

gives a combustion efficiency of 16.8%. This is not good. An engine that is configured similarly to this engine had efficiency around 30% for the same amount of power and torque [4]. Using the 30% efficiency value from the literature then gives a sfc value of 275 (g/kW h), which is approximately half of the value seen in this study. Therefore, this supports the idea that not all of the fuel is being consumed, and thus the high HC values. The air-fuel mixture might not be as homogeneous as needed to have reasonable combustion efficiency. This idea is also supported by the literature in that inhomogeneous mixture will lead to increased emissions of HC, and CO [2].

7. CONCLUSIONS

The groundwork for a 1.9L gasoline HCCI engine has been completed. Fundamental experiments and analyses of the limits of operation as well as the cylinder-to-cylinder and cycle-to-cycle variations have been performed. The following conclusions can be drawn from the experimental results obtained.

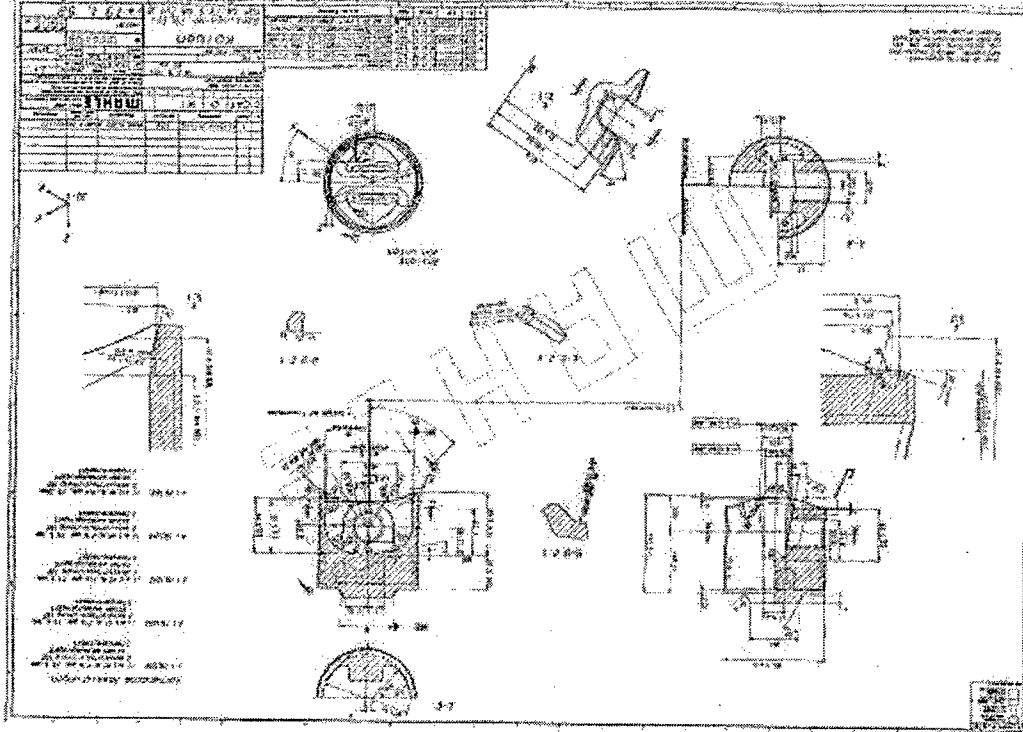
1. Individual intake heating is a viable means to control HCCI combustion. The variations observed support the need for individual cylinder control.
2. A strong correlation is seen between the timing for the onset of HCCI combustion and the intake air temperature.
3. The temperature to which the intake air must be heated increases with an increase of air/fuel ratio and the maximum obtainable IMEP decreases.
4. Limits of operation at 1300 RPM have been defined.
5. The COV of IMEP for each cylinder in the stable combustion region is less than 3.
6. High values of HC are observed due to inefficient combustion. This inefficient combustion may be a result of an inhomogeneous air/fuel mixture.
7. Low values of NO_x were obtained to be 5 ppm.

REFERENCES

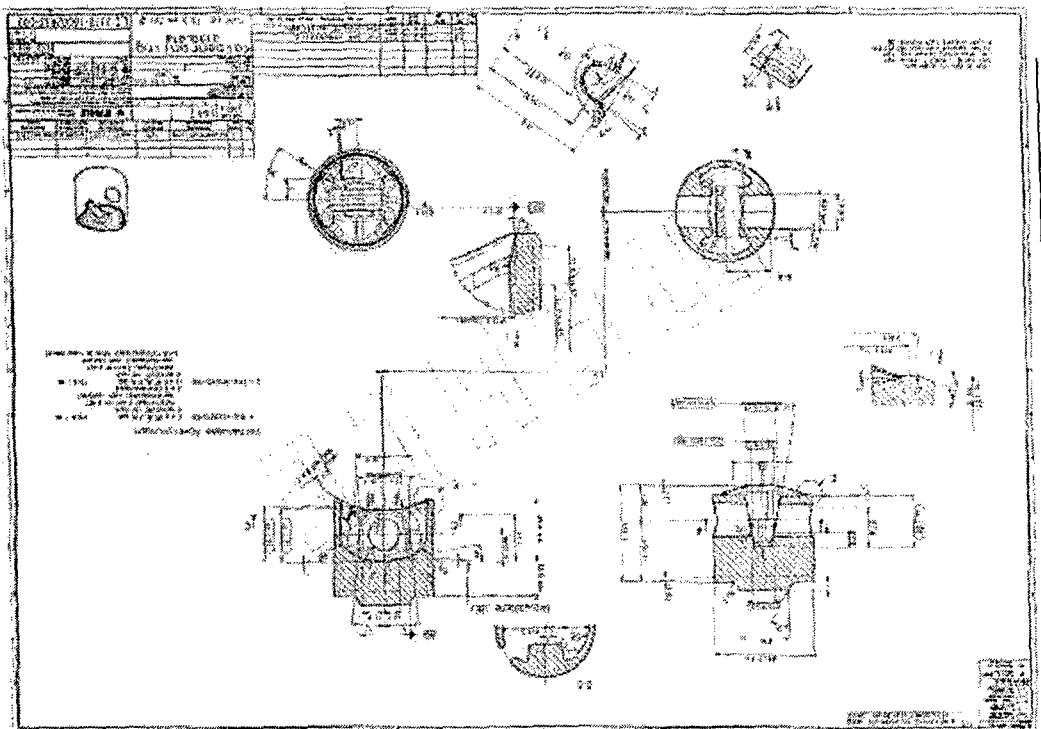
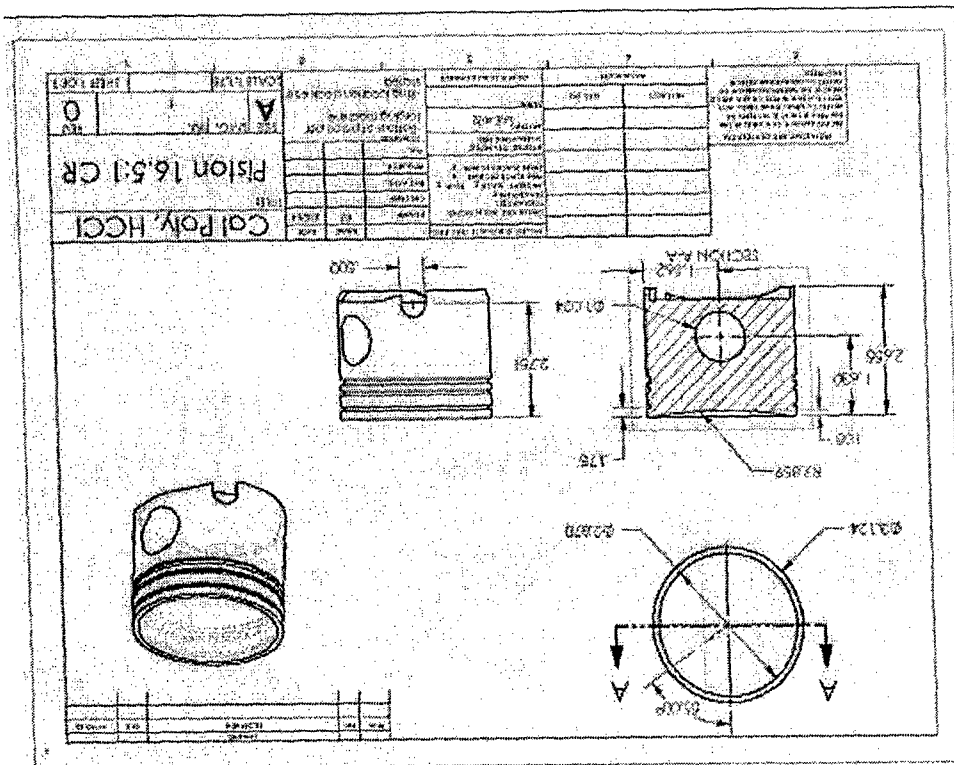
- 1 Heywood, John B., Internal Combustion Engine Fundamentals, McGraw Hill, INC., 1988
- 2 Christensen, M., Hultqvist, A., Johansson, B., "Demonstrating the Multi-Fuel Capability of a Homogeneous Charge Compression Ignition Engine With Variable Compression Ratio" SAE Paper 1999-01-3679
- 3 Moran, Michael J., Shapiro, Howard N., Fundamentals of Engineering Thermodynamics, 4th ed., John Wiley & Sons, INC., 1999
- 4 Sun, R., Thomas, R., and Gray, C. L.: "An HCCI Engine: Power Plant for a Hybrid Vehicle" SAE Paper 2004-01-0933
- 5 A. Hultqvist, M. Christensen, B. Johansson, A. Franke, M. Richter, M. Alden: "A study of the Homogeneous Charge Compression Ignition Combustion Process by Chemiluminescence Imaging", SAE 1999-01-3680
- 6 M. Christensen, B. Johansson, A. Hultqvist: "The Effect of Piston Topland Geometry on Emissions of Unburned Hydrocarbons from a Homogeneous Charge Compression Ignition (HCCI) Engine", SAE 2001-01-1893
- 7 S. Kong, C. Mariott, C. Rutland, R. Reitz: "Experiments and CFD Modeling of Direct Injection Gasoline HCCI Engine Combustion", SAE 2002-01-1925
- 8 S. Aceves, D. Flowers, J. Martinez-Frias, R. Smith, C. Westbrook, W. Pitz, R. Dibble, F. Wright, C. Akinyemi, R. Hessel: "A sequential fluid-mechanic chemical-kinetic model of propane HCCI combustion" SAE 2001-01-1027
- 9 E W Kaiser, J Yang, T Culp, N Xu, M M Maricq, "Homogeneous charge compression ignition engine-out emissions-does flame propagation occur in homogeneous charge compression ignition?", Int. J Engine Research, Vol. 3, No. 4, JER 02802, IMechE 2002
- 10 N. Lida: "Combustion Analysis of Methanol-Fueled Active Thermo-Atmosphere Combustion (ATAC) Engine Using a Spectroscopic Observation" SAE 940684
- 11 M. Noguchi, Y. Tanaka, T. Tanaka, Y. Takeuchi: "A Study on Gasoline Engine Combustion by Observation of Intermediate Reactive Products during Combustion" SAE 790840
- 12 N. Lida: "Combustion Analysis of Methanol-Fueled Active Thermo-Atmosphere Combustion (ATAC) Engine Using a Spectroscopic Observation" SAE 940684
- 13 Y. Ishibashi, M. Asai: "Improving the Exhaust Emissions of Two-Stroke Engines by Applying the Activated Radical Combustion", SAE 960742
- 14 P. Duret, S. Venturi: "Automotive Calibration of the IAPAC Fluid Dynamically Controlled Two-Stroke Combustion Process", SAE 960363
- 15 Automotive Engineering, January issue 1997
- 16 P. Najt, D.E. Foster: "Compression-Ignited Homogeneous Charge Combustion", SAE 892064
- 17 R.H. Thring: "Homogeneous-Charge Compression Ignition (HCCI) Engines", SAE 992068
- 18 T. Aoyama, Y. Hattori, J. Mizuta, Y. Sato: "An Experimental Study on Premixed-Charge Compression Ignition Gasoline Engine", SAE 960081
- 19 T.W. Ryan, T.J. Callahan: "Homogeneous Charge Compression Ignition of Diesel Fuel", SAE 961160
- 20 T. Hashizume, T. Miyamoto, H. Akagawa, K. Tsujimura: "Combustion and Emission Characteristics of Multiple Stage Diesel Combustion", SAE 980505
- 21 H. Suzuki, N. Koike, M. Odaka: "Combustion Control Method of Homogeneous Charge Diesel Engines", SAE 980509
- 22 T. Seko, E. Kuroda: "Methanol Lean Burn in an Auto-Ignition Engine", SAE 980531
- 23 A. Harada, N. Shimazaki, S. Sasaki, T. Miyamoto, H. Akagawa, K. Tsujimura: "The Effects of Mixture Formation on Premixed Lean Diesel Combustion", SAE 980533
- 24 M. Christensen, B. Johansson: "Influence of Mixture Quality on Homogeneous Charge Compression Ignition", SAE 982454
- 25 P. Amneus, D. Nilsson, F. Mauss, M. Christensen, B. Johansson: "Homogeneous Charge Compression Ignition Engine: Experiments and Detailed Kinetic Calculations", Comodia 98, Kyoto, Japan
- 26 H. Ogawa, I. Chenyu, S. Tosaka, Y. Fujiwara, N. Miyamoto: "Combustion Mechanism Analyses with In-chamber Gas Composition Measurements in a Pre-mixed Lean Compression Ignition Engine", Comodia 98, Kyoto, Japan
- 27 M. Furutani, Y. Ohta, M. Kono, M. Hasegawa: "An Ultra Lean Premixed Compression-Ignition Engine Concept and its Characteristics", Comodia 98, Kyoto, Japan
- 28 T. Miyamoto, A. K. Hayashi, A. Harada, S. Sasaki, H. Akagawa, K. Tsujimura: "Numerical simulation of Premixed Lean Diesel Combustion in a DI Engine", Comodia 98, Kyoto, Japan
- 29 R. Takatsuto, T. Igarashi, N. Lida: "Auto Ignition and Combustion of DME and n-Butane/Air Mixtures in Homogeneous Charge Compression Ignition Engine", Comodia 98, Kyoto, Japan
- 30 J. Willan, R. Nieberding, G. Vent, C. Enderle: "The Knocking Syndrome-Its Cure and Its potential", SAE 982483
- 31 N. Shimazaki, H. Akagawa, K. Tsujimura: "An Experimental Study of Premixed Lean Diesel Combustion", SAE 1999-01-0181
- 32 H. Akagawa, et al.: "Approached to Solve Problems of the Premixed Lean Diesel Combustion", SAE 1999-01-0183
- 33 M. Odaka, H. Suzuki, N. Koike, H. Ishii: "Search for Optimizing Control Method of Homogeneous Charge Diesel Combustion", SAE 1999-01-0184

- 34 Y. Iwabuchi, K. Kawai, T. Shoji, Y. Takeda: "Trial of New Concept Diesel Combustion System- Premixed Compression-Ignited Combustion", SAE 1999-01-0185
- 35 G. Andrews, K. Zaidi: "Partial Premixed Diesel Gaseous and Particulate Emissions", SAE 1999-01-0838
- 36 M. Christensen, P. Einewall, B. Johansson: "Homogeneous Charge Compression Ignition (HCCI) Using Iso-octane, Ethanol and Natural Gas- A Comparison to Spark Ignition Operation", SAE 972874
- 37 M. Christensen, B. Johansson, P. Amneus, F. Mauss: "Supercharged Homogeneous Charge Compression Ignition", SAE 980787
- 38 M. Christensen, B. Johansson: "Influence of Mixture Quality on Homogeneous Charge Compression Ignition", SAE 982454
- 39 M. Christensen, B. Johansson: "Homogeneous Charge Compression Ignition with Water Ignition", SAE 1999-01-0182
- 40 P. Najt, D.E. Foster: "Compression-Ignition Homogeneous Charge Combustion", SAE 830264
- 41 Stockinger, H. Schapertons, P. Kuhlmann: "Versuche an einem gemischsugenden Verbrennungsmotor mit Selbstzündung", MTZ, Motortechnisches Zeitschrift 53 (1992) pp 80-85
- 42 T. Shudo, Y. Ono: "HCCI Combustion of Hydrogen, Carbon Monoxide and Dimethyl Ether", SAE 2002-01-01121
- 43 J. Allen D. Law: "Variable Valve Actuated Controlled Auto-Ignition: Speed Load Maps and Strategic Regimes of Operation", SAE 2002-01-0422
- 44 Z. Chen, M. Konno, M. Oguma, T. Yanai: "Experimental study of CI natural-gas/DME homogeneous charge engine", SAE 2000-01-0329
- 45 J. Olsson, O. Erlandsson, B. Johansson: "Experiments and simulation of a six-cylinder homogeneous charge compression ignition (HCCI) engine", SAE 2000-01-2867
- 46 J. Olsson, P. Tunestal, B. Johansson: "Closed-loop control of an HCCI engine", SAE 2001-01-1031
- 47 J. Olsson, P. Tunestal, G. Haraldsson, B. Johansson: "A turbo charged dual fuel HCCI engine", SAE 2001-01-1896
- 48 R. Stanglmaier, T. Ryan, J. Souder: "HCCI operation of a dual-fuel natural gas engine for improved fuel economy and ultra-low gas NOx emissions at low to moderate engine loads", SAE 2001-01-1897
- 49 J. Olsson, P. Tunestal, B. Johansson: "Compression ratio influence on maximum load of a natural gas fueled HCCI engine", SAE 2002-01-0111
- 50 T. Shudo, Y. Ono: "HCCI combustion of hydrogen, carbon monoxide and dimethyl ether", SAE 2002-01-0112
- 51 S. Aceves, D. Flowers, C. Westbrook, R. Smith, W. Rits, R. Dibble, M. Christensen, B. Johansson: "A Multi-Zone Model for Prediction of HCCI Combustion and Emissions", SAE 2000-01-03247
- 52 S.B. Fiveland, D.N. Assanis: "A Four-Stroke Homogeneous Charge Compression Ignition Engine Simulation for Combustion and Performance Studies", SAE 2000-01-0332
- 53 R. Ogink, V. Golovitchev: "Gasoline HCCI Modeling: An Engine Cycle Simulation Code with a Multi-Zone Combustion Model", SAE 2002-01-1745
- 54 S. Fiveland, D. Assanis: "Development and Validation of a Quasi-Dimensional Model for HCCI Engine Performance and Emissions Studies Under Turbocharged Conditions", SAE 2002-01-1757
- 55 S. Kong, C. Marriott, C. Rutland, R. Reitz: "Experiments and CFD Modeling of Direct Injection Gasoline HCCI Engine Combustion", SAE 2002-01-1925
- 56 D. Flowers, S. Aceves, R. Smith, J. Torres, J. Girard, R. Dibble: "HCCI in a CFR Engine: Experiments and Detail Kinetic Modeling", SAE 2000-01-0328
- 57 M. Richter, J. Engstrom, A. Franke, M. Alden, A. Hultqvist, B. Johansson: "The Influence of Charge Inhomogeneity on the HCCI Combustion Process", SAE 2000-01-2868
- 58 M. Christensen, B. Johansson: "Supercharged Homogeneous Charge Compression Ignition (HCCI) with Exhaust Gas Recirculation and Pilot Fuel", SAE 2000-01-1835
- 59 L. Koopmans, H. Strom, S. Lundgren, O. Backlund, I. Denbratt: "Demonstrating a SI-HCCI-SI Mode Change on a Volvo 5-Cylinder Electronic Valve Control Engine", SAE 2003-01-0753
- 60 J. Hyvonen, G. Haraldsson, B. Johansson: "Supercharging HCCI to Extend the Operating Range in a Multi-Cylinder VCR-HCCI Engine", SAE 2003-01-3214
- 61 M. Sjöberg, L. Edling, T. Eliassen, L. Magnusson, H. Angstrom: "GDI HCCI: Effects of Injection Timing and Air Swirl on Fuel Stratification, Combustion and Emissions Formation", SAE 2002-01-0106
- 62 C. Marriott, R. Reitz: "Experimental Investigation of Direct Injection-Gasoline for Premixed Compression Ignited Combustion Phasing Control", SAE 2002-01-0418
- 63 C. Marriott, S. Kong, R. Reitz: "Investigation of Hydrocarbon Emissions from a Direct Injection-Gasoline Premixed Charge Compression Ignited Engine", SAE 2002-01-0419
- 64 J. Yang, T. Culp, T. Kenney: "Development of a Gasoline Engine System Using HCCI Technology- The Concept and the Test Results", SAE 2002-01-2832
- 65 Auto Technology, Oct 2000 p. 54
- 66 M. Christensen, B. Johansson: "Supercharged Homogeneous Charge Compression Ignition (HCCI) with
- 67 M. Christensen, B. Johansson, P. Amneus, F. Mauss: "Supercharged Homogeneous Charge Compression Ignition" SAE Paper 980787

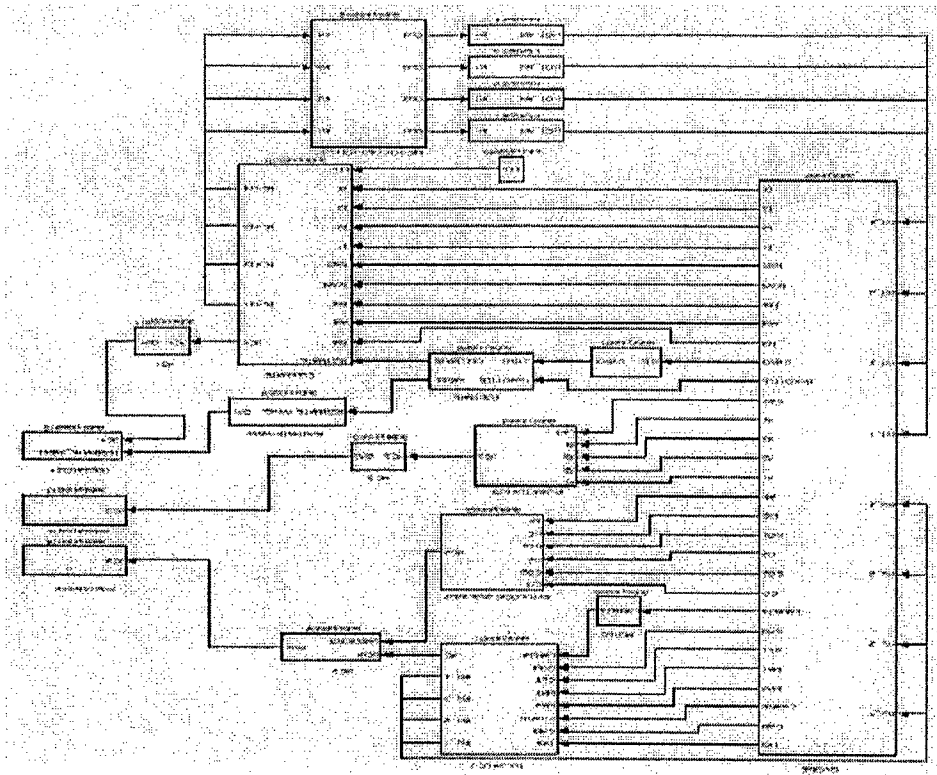
- 68 B. Johansson, H. Meij, M. Alden, G. Juhlin: "Investigations of the Influence of Mixture Preparation on Cyclic Variations in a SI-Engine, Using Laser Induced Fluorescence", SAE 950108
- 69 J. Girard, R. Dibble, D. Flowers, S. Aceves: "An Investigation of the Effect of Fuel-Air Mixture on the Emissions from an HCCI Engine", SAE 2002-01-1758
- 70 A. Hultqvist, M. Christensen, B. Johansson, A. Franke, M. Richter, M. Alden: "A study of the Homogeneous Charge Compression Ignition Combustion Process by Chemiluminescence Imaging", SAE 1999-01-3680
- 71 D. Flowers, S. Aceves, J. Martinez-Frias, J. Smith, M. Ab, J. Girard, R. Dibble: "Operation of a Four-Cylinder 1.9L Propane Fueled Homogeneous Charge Compression Ignition Engine: Basic Operating Characteristics and Cylinder-to-Cylinder Effects", SAE 2001-01-1895
- 72 L. Koopmans, O. Backlund, I. Denbratt: "Cycle to Cycle Variations: Their Influence on Cycle Resolved Gas Temperature and Unburned Hydrocarbons from a Camless Gasoline Compression Ignition Engine", SAE 2002-01-0110
- 73 D. Law, J. Allen, R. Chen: "On the Mechanism of Controlled Auto Ignition", SAE 2002-01-0421
- 74 T. Ryan, T. Callahan, D. Mehta: "HCCI in a Variable Compression Ratio Engine-Effects of Engine Variables", SAE 2004-01-1971
- 75 R. Sun, R. Thomas, C. L. Gray Jr.: "An HCCI Engine: Power Plant for a Hybrid Vehicle", SAE 2004-01-0933
- 76 J. Schramm, S.C. Sorensen: "A model for hydrocarbon emissions from a SI engine", SAE 902169
- 77 A. Hultqvist, M. Christensen, B. Johansson: "The Application of Ceramic and Catalytic Coatings to Reduce the Unburned Hydrocarbon Emissions from a Homogeneous Charge Compression Ignition Engine", SAE 2000-01-1833
- 78 W. Cheng, D. Hamrin, J. B. Heywood: "An overview of hydrocarbon emissions mechanisms in spark ignition engines", SAE 932708
- 79 J. Schramm, S.C. Sorensen: "A model for hydrocarbon emissions from a SI engine", SAE 902169
- 80 J.C. Dent, P.A. Lakshminarayanan: "A model for absorption and desorption of fuel vapor by cylinder lubricating oil films and its contribution to hydrocarbon emissions", SAE 830652
- 81 K. Korematsu: "Effect of fuel absorbed in oil films on unburned hydrocarbon emissions from spark ignited engines", JSME Int. J., 1990 p. 604-614
- 82 E.W. Kaiser et al: "Storage and partial oxidation of unburned hydrocarbons on spark ignition engines: effect of compression ratio and spark timing", Combustion Sci. and Tech., 1984, 36(3-4), 171-180
- 83 S. Ishizawa, Y. Tagaki: "A study of hydrocarbon emissions from spark ignition engines", JSME Int. J., 1987, 30(260), 310-317
- 84 J.T. Wentworth: "The piston crevice volume effect on exhaust hydrocarbon emissions", Combustion Sci. and Tech., 1971 4(1-2), 97-100.
- 85 M. Christensen, B. Johansson, A. Hultqvist: "The Effect of Piston Topland Geometry on Emissions of Unburned Hydrocarbons from a Homogeneous Charge Compression Ignition (HCCI) Engine", SAE 2001-01-1893
- 86 T. Saika, K. Korematsu: "Flame propagation into the ring crevice of a spark ignition engine", SAE 861528
- 87 T. Ryan, T. Callahan, D. Mehta: "HCCI in a Variable Compression Ratio Engine-Effects of Engine Variables", SAE 2004-01-1971
- 88 Arias Pistons, <http://www.arias Pistons.com/>, August 22, 2004
- 89 United Engine & Machine Co., <http://www.kb-silvolite.com/>, August 22, 2004
- 90 Incropera, Frank P., David P. Dewitt: Introduction to heat transfer, 4th ed., Wiley 2002
- 91 Electromotive Engine Controls: "TEC3r Installation and Calibration Manual", Version 1.9 2002



APPENDIX A



APPENDIX B



APPENDIX C

```

*****
% This program takes values from a data.txt file, which is the raw
% pressure values from AVL indimeter. HCCI.rj.xpa, then produces a
% 3D surface of in-cylinder pressure vs crank angle and cycle number
% with all cylinders and individually. A 2-D plot of pressure vs CAD
% for each cylinder is produced with the number of cycles
% overlaying each other.
%
% File name: AVL_plots
%
% *****MUST HAVE: 'data.txt' in the Current Directory*****
%
% Nicholas Jacques, Dr. Delagrammatikas
%
% *****
%
% clear all
%
% *****
% Input Variables
% cdm_max = 2880; % degree max 2880 = 4x720
% cdm_min = 1; % degree min CDM 1
%
% cycle_max = 50; % max cycle, change this value per cycles
% cycle_min = 1; % min cycle 1
%
% load data.txt % uploads raw data from data.txt file
%
% defines variables for each cylinder's set of data
% pcy1 = data(:,1); % sets pcy1 equal to 1st column of data
% pcy2 = data(:,2); % sets pcy2 equal to 2nd column of data
% pcy3 = data(:,3); % sets pcy3 equal to 3rd column of data
% pcy4 = data(:,4); % sets pcy4 equal to 4th column of data
%
% defines variables for each cylinder data such that 720 CAD, number cycles
% map1 = reshape(pcy1,720,cycle_max); % map1 equals cyl1 pressure
% map2 = reshape(pcy2,720,cycle_max); % map2 equals cyl2 pressure
% map3 = reshape(pcy3,720,cycle_max); % map3 equals cyl3 pressure
% map4 = reshape(pcy4,720,cycle_max); % map4 equals cyl4 pressure
%
% *****
%
% Figure 1: 2D plot of cylinders 1 2 3 4 in separate graphs, with number of
% cycles overlaying each other
%
% *****

```

```

figure(1) % defines figure 1
clf % clear figure

subplot(2,2,1) % divides a figure into multiple displays
plot(map1) % plot the variable map1
title('CYLINDER #1 ') % title of figure
xlabel('Crank angle degree') % label for x-axis
ylabel('Pressure (bar)') % label for y-axis
axis([300 450 0 100]) % defines axis parameters

subplot(2,2,2) % divides a figure into multiple displays
plot(map2) % plot the variable map2
title('CYLINDER #2 ') % title of figure
xlabel('Crank angle degree') % label for x-axis
ylabel('Pressure (bar)') % label for y-axis
axis([300 450 0 100]) % defines axis parameters

subplot(2,2,3) % divides a figure into multiple displays
plot(map3) % plot the variable map3
title('CYLINDER #3 ') % title of figure
xlabel('Crank angle degree') % label for x-axis
ylabel('Pressure (bar)') % label for y-axis
axis([300 450 0 100]) % defines axis parameters

subplot(2,2,4) % divides a figure into multiple displays
plot(map4) % plot the variable map4
title('CYLINDER #4 ') % title of figure
xlabel('Crank angle degree') % label for x-axis
ylabel('Pressure (bar)') % label for y-axis
axis([300 450 0 100]) % defines axis parameters

%*****
%
% Figure 2: 3D Plot of cylinders 1 2 3 4 in separate graphs, with number of
% cycles
%
%*****

figure(2) % defines figure 1
clf % clear figure

subplot(2,2,1) % divides a figure into multiple displays
mesh(map1) % creates wireframe parametric surface

subplot(2,2,2) % divides a figure into multiple displays

```

```

mesh(map2) % creates wireframe parametric surface

subplot(2,2,3) % divides a figure into multiple displays
mesh(map3) % creates wireframe parametric surface

subplot(2,2,4) % divides a figure into multiple displays
mesh(map4) % creates wireframe parametric surface
%*****
%
% Figure 3: 3D plot of cylinders 1 2 3 4 together
%
%*****
% Converts raw data into a manageable matrix
%
my_map = [map1,map2,map3,map4]; % set my_map equal to press
cdm_range = [cdm_min:cdm_max] % set the range for crank angle
cycle_range = [cycle_min:cycle_max] % set the range for cycles

figure(3) % defines figure 3
clf % clears figure

mesh(cdm_range,cycle_range,my_map) % creates wireframe parametric surface
hold on % retains the current plot
grid on % adds major grid lines
title('IN-CYLINDER PRESSURE TRACES') % title of figure
xlabel('Cylinder #1 #2 #3 #4') % label for y-axis
ylabel('Cycle (number)') % label for x-axis
zlabel('Pressure (bar)') % label for z-axis

% contour graph displays isolines of matrix
[cs,h] = contour(cdm_range,cycle_range,my_map,30);
axis([0 3000 0 50 -5 100]) % defines axis parameters

```

```

% *****
% This program integrate p-v, and find IMEP and COV for individual
% cylinders and contiguous cycles
%
% File name: imep
%
% *****MUST HAVE: 'find_imep.m' in the Current Directory*****
% 'find_cov.m'
% 'first_plot.m' 'data_runXX.txt'
%
% Nicholas Jacques, Dr. Delagrammatikas
% *****
%
clear all

% 3D plotting routing for single cylinder
plot_me = 2; % 0 = no plots
% 1 = plot cyl # 1
% 2 = plot cyl # 2
% 3 = plot cyl # 3
% 4 = plot cyl # 4

% engine parameters
cmratio = 16.5; % compression ratio
v_clear = 0.0306; % clearance volume, in liters
con_rod = 0.144; % conrod length, m's
stroke = 0.0955; % stroke, m's
bore = 0.0795; % bore, m's
R = con_rod/(0.5*stroke); % defines R
v_disp = ((pi*(bore^2)/4)*stroke)*1000; % calculates displaced volume

% first plot - need to parse using this file
first_plot

% set up crank angle axis
theta = [0:1:719]*(pi/180);

% find volume at each theta
for j = 1:length(theta)
    vol(j) = v_clear * (1 + 5*(cmratio-1)*(R + 1 - cos(theta(j))) - ...
        (R^2 - sin(theta(j)))^2*sin(theta(j)))^(.5));
end

% go through each cycle for each cylinder
% start with cylinder 1, 2, 3, 4

[num,n] = size(pcy1_mesh1);
all_imeps = [];
for ii = 1:4
    if ii == 1
        now_data = pcy1_mesh1;
    elseif ii == 2
        now_data = pcy1_mesh2;
    elseif ii == 3
        now_data = pcy1_mesh3;
    elseif ii == 4
        now_data = pcy1_mesh4;
    end
    for jj = 1:nn
        imep_now(jj) = find_imep(now_data(:,jj), vol, v_disp);
    end
    all_imeps = [all_imeps; imep_now];
end
all_imeps = all_imeps';

[m,n] = size(all_imeps);
for jk = 1:4
    [mean_now, stdev_now, cov_now] = find_cov(all_imeps(:,jk)); % go to find_cov
    all_stdevs(jk) = stdev_now;
    all_means(jk) = mean_now;
    all_covs(jk) = cov_now;
end

% first plot file
% load data text file
load data_run25.txt
my_data = data_run25; % must be the same as the .txt file name

% *****
% keep cylinder convention below
% defines variables for each cylinder's set of data

```



```

pcyl1 = my_data(:,4); % sets pcyl1 equal to 4th column of data
pcyl2 = my_data(:,1); % sets pcyl1 equal to 1st column of data
pcyl3 = my_data(:,2); % sets pcyl1 equal to 2nd column of data
pcyl4 = my_data(:,3); % sets pcyl1 equal to 3rd column of data

rows = length(pcyl4);
cols = rows/720;

% defines rows equal to the length of pcyl4
% defines cols

% defines variables for each cylinder data such that 720 CAD, number cycles
pcyl_mesh1 = reshape(pcyl1,720,cols); % pcyl_mesh1 equals cyl1 pressure
pcyl_mesh2 = reshape(pcyl2,720,cols); % pcyl_mesh2 equals cyl2 pressure
pcyl_mesh3 = reshape(pcyl3,720,cols); % pcyl_mesh3 equals cyl3 pressure
pcyl_mesh4 = reshape(pcyl4,720,cols); % pcyl_mesh4 equals cyl4 pressure

yaxis = [1:1:cols];
thetas = [0:1:719];

% plots the cylinder selected from inep.m for the variable plot_me = X;
if exist('plot_me')
    figure(1)
    clf
    mesh(thetas, yaxis, pcyl_mesh1')
    grid on
    title('Cylinder #1')
    xlabel('Crank Angle Degrees')
    ylabel('Cycle Number')
    zlabel('Pressure (bar)')
    axis([0 800 0 50 -5 100])
elseif plot_me == 2
    figure(2)
    clf
    mesh(thetas, yaxis, pcyl_mesh2')
    grid on
    title('Cylinder #2')
    xlabel('Crank Angle Degrees')
    ylabel('Cycle Number')
    zlabel('Pressure (bar)')
    axis([0 800 0 50 -5 100])
elseif plot_me == 3
    figure(3)
    clf
    mesh(thetas, yaxis, pcyl_mesh3')
    grid on
    xlabel('Crank Angle Degrees')
    ylabel('Cycle Number')
    zlabel('Pressure (bar)')
    axis([0 800 0 50 -5 100])
elseif plot_me == 4
    figure(4)
    clf
    mesh(thetas, yaxis, pcyl_mesh4')
    grid on
    xlabel('Crank Angle Degrees')
    ylabel('Cycle Number')
    zlabel('Pressure (bar)')
    title('Cylinder #4')
    axis([0 800 0 50 -5 100])
end

% plots cylinder 4

function [f] = find_indep(press,vol,v_disp)
% integrate using trapezoidal rule
for i = 1:length(press)
    if i == length(press)
        i = 1;
    end
    pdvs(i) = press(i)*(vol(i+1) - vol(i));
end

% work
work = sum(pdvs);

% inep in bar
f = work/v_disp;

function [my_avg, my_sdev, my_cov] = find_cov(x)
n = length(x);

% find sum of x squared terms
for i = 1:n
    term1(i) = x(i)^2;
end

% find sum of x squared terms
for i = 1:n
    term1(i) = x(i)^2;
end

```

```

figure(1) % defines figure 1
clf % clear figure

subplot(2,2,1) % divides a figure into multiple displays
plot(map1) % plot the variable map1
title('CYLINDER #1 ') % title of figure
xlabel('Crank angle degree') % label for x-axis
ylabel('Pressure (bar)') % label for y-axis
axis([300 450 0 100]) % defines axis parameters

subplot(2,2,2) % divides a figure into multiple displays
plot(map2) % plot the variable map2
title('CYLINDER #2 ') % title of figure
xlabel('Crank angle degree') % label for x-axis
ylabel('Pressure (bar)') % label for y-axis
axis([300 450 0 100]) % defines axis parameters

subplot(2,2,3) % divides a figure into multiple displays
plot(map3) % plot the variable map3
title('CYLINDER #3 ') % title of figure
xlabel('Crank angle degree') % label for x-axis
ylabel('Pressure (bar)') % label for y-axis
axis([300 450 0 100]) % defines axis parameters

subplot(2,2,4) % divides a figure into multiple displays
plot(map4) % plot the variable map4
title('CYLINDER #4 ') % title of figure
xlabel('Crank angle degree') % label for x-axis
ylabel('Pressure (bar)') % label for x-axis
axis([300 450 0 100]) % defines axis parameters

%*****
%
% Figure 2: 3D Plot of cylinders 1 2 3 4 in separate graphs, with number of
% cycles
%
%*****

figure(2) % defines figure 1
clf % clear figure

subplot(2,2,1) % divides a figure into multiple displays
mesh(map1) % creates wireframe parametric surface

subplot(2,2,2) % divides a figure into multiple displays

```

```

mesh(map2) % creates wireframe parametric surface

subplot(2,2,3) % divides a figure into multiple displays
mesh(map3) % creates wireframe parametric surface

subplot(2,2,4) % divides a figure into multiple displays
mesh(map4) % creates wireframe parametric surface
%
%*****
%
% Figure 3: 3D plot of cylinders 1 2 3 4 together
%
%*****
%
% Converts raw data into a manageable matrix
%
my_map = [map1,map2,map3,map4]; % set my_map equal to press
cdm_range = [cdm_min,cdm_max] % set the range for crank angle
cycle_range = [cycle_min,cycle_max] % set the range for cycles

figure(3) % defines figure 3
clf % clears figure

mesh(cdm_range,cycle_range,my_map) % creates wireframe parametric surface
hold on % retains the current plot
grid on % adds major grid lines
title('IN-CYLINDER PRESSURE TRACES') % title of figure
xlabel('Cylinder #1 #2 #3 #4') % label for y-axis
ylabel('Cylinder (number)') % label for x-axis
zlabel('Pressure (bar)') % label for z-axis

% contour graph displays isolines of matrix
[cs,h] = contour(cdm_range,cycle_range,my_map,30);
axis([0 3000 0 50 -5 100]) % defines axis parameters

```

```

%*****
% This program integrate p-v, and find IMEP and COV for individual
% cylinders and contiguous cycles
%
% File name: imep
%
%*****MUST HAVE: 'find_imep.m' in the Current Directory*****
%
% 'find_cov.m'
% 'first_plot.m' 'data_runXX.txt'
%
% Nicholas Jacques, Dr. Delagranmatikas
%
%*****
%
clear all

% 3D plotting routing for single cylinder
plot_me = 2; % 0 = no plots
% 1 = plot cyl # 1
% 2 = plot cyl # 2
% 3 = plot cyl # 3
% 4 = plot cyl # 4

% engine parameters
cmrtio = 16.5; % compression ratio
v_clear = .0306; % clearance volume, in liters
con_rod = 0.144; % conrod length, m's
stroke = 0.0955; % stroke, m's
bore = 0.0795; % bore, m's
R = con_rod/(0.5*stroke); % defines R
v_disp = ((pi*(bore^2)/4)*stroke)*1000; % calculates displaced volume

% first plot - need to parse using this file
first_plot

% set up crank angle axis
theta = [0:1:719]*(pi/180);

% find volume at each theta
for j = 1:length(theta)
    vol(j) = v_clear * (1 + .5*(cmrtio-1)*(R + 1 - cos(theta(j))) - ...
        (R^2 - sin(theta(j))*sin(theta(j)))^(.5)));
end

% go through each cycle for each cylinder
% start with cylinder 1, 2, 3, 4

[run,n] = size(p cyl_mesh1);
all_imeps = [];
for ii = 1:4
    if ii == 1
        now_data = p cyl_mesh1;
    elseif ii == 2
        now_data = p cyl_mesh2;
    elseif ii == 3
        now_data = p cyl_mesh3;
    elseif ii == 4
        now_data = p cyl_mesh4;
    end

    for jj = 1:n
        imep_now(jj) = find_imep(now_data(:,jj), vol, v_disp);
    end

    all_imeps = [all_imeps; imep_now];
end

all_imeps = all_imeps';
[m,n] = size(all_imeps);
for jk = 1:4
    [mean_now, stdev_now, cov_now] = find_cov(all_imeps(:,jk)); % go to find_cov

    all_stdevs(jk) = stdev_now;
    all_means(jk) = mean_now;
    all_covs(jk) = cov_now;
end

% first plot file
% load data text file
load data_run25.txt
my_data = data_run25; % must be the same as the txt file name

% *****
% keep cylinder convention below
% defines variables for each cylinder's set of data

```

```

pcyl1 = my_data(:,4); % sets pcyl1 equal to 4th column of data
pcyl2 = my_data(:,1); % sets pcyl1 equal to 1st column of data
pcyl3 = my_data(:,2); % sets pcyl1 equal to 2nd column of data
pcyl4 = my_data(:,3); % sets pcyl1 equal to 3rd column of data

rows = length(pcyl4);
cols = rows/720;

% defines variables for each cylinder data such that 720 CAD, number cycles
pcyl_mesh1 = reshape(pcyl1,720,cols); % pcyl_mesh1 equals cyl1 pressure
pcyl_mesh2 = reshape(pcyl2,720,cols); % pcyl_mesh2 equals cyl2 pressure
pcyl_mesh3 = reshape(pcyl3,720,cols); % pcyl_mesh3 equals cyl3 pressure
pcyl_mesh4 = reshape(pcyl4,720,cols); % pcyl_mesh4 equals cyl4 pressure

yaxis = [1:1:cols];
thetas = [0:1:719];

% plots the cylinder selected from inep.m for the variable plot_me = X;
if exist('plot_me')
    if plot_me == 1
        figure(1)
        clf
        mesh(thetas, yaxis, pcyl_mesh1')
        grid on
        title('Cylinder #1')
        xlabel('Crank Angle Degrees')
        ylabel('Cycle Number')
        ylabel('Pressure (bar)')
        axis([0 800 0 50 -5 100])
        % plots cylinder 1
    elseif plot_me == 2
        figure(2)
        clf
        mesh(thetas, yaxis, pcyl_mesh2')
        grid on
        title('Cylinder #2')
        xlabel('Crank Angle Degrees')
        ylabel('Cycle Number')
        ylabel('Pressure (bar)')
        axis([0 800 0 50 -5 100])
        % plots cylinder 2
    elseif plot_me == 3
        figure(3)
        clf
        mesh(thetas, yaxis, pcyl_mesh3')
        % plots cylinder 3
    elseif plot_me == 4
        figure(4)
        clf
        mesh(thetas, yaxis, pcyl_mesh4')
        grid on
        xlabel('Crank Angle Degrees')
        ylabel('Cycle Number')
        ylabel('Pressure (bar)')
        title('Cylinder #4')
        axis([0 800 0 50 -5 100])
        % plots cylinder 4
    else
        disp('No Plotting Will be Performed.') % plot_me = 0, then no plot
    end
end

function [f] = find_inep(press,vol,v_disp)
% integrate using trapezoidal rule
for i = 1:length(press)
    if i == length(press)
        i = 1;
    end
    pdvs(i) = press(i)*(vol(i+1) - vol(i));
end

% work
work = sum(pdvs);
% inep in bar
f = work/v_disp;
function [my_avg, my_stddev, my_cov] = find_cov(x)
n = length(x);
% find sum of x squared terms
for i = 1:n
    terms(i) = x(i)^2;
end

```

```

term1 = sum(term1s);
% find sum of x -squared
term2 = sum(x);
term2 = term2^2;

numerator = n*term1 - term2;
denominator = n*(n-1);
sigma = (numerator/denominator)^(.5);
% defines numerator
% defines denominator
% defines sigma

% find stdev
my_stdev = sigma;

% find mean
my_avg = sum(x)/n;

% find cov
my_cov = (my_stdev/my_avg)*100;

```

Development of an Autonomous Tactical Reconnaissance Platform

Project Investigators:

Dianne J. DeTurris
Associate Professor
Aerospace Engineering Department

and

Sema E. Alptekin
Professor
Industrial and Manufacturing Engineering Department

Abstract

The Autonomous Tactical Reconnaissance Platform (ATRP) is a parafoil with a payload that is instrumented for autonomous flight and remote sensing capabilities. The purpose of this project is to prototype a system that can be used as a personal reconnaissance device. The ATRP has many military and civilian uses that are not adequately addressed by remote sensing systems currently available.

Building on work that occurred in Phases I and II of this effort, major advances were made in the electronics, software, launch mechanisms and the launch vehicle. Repeatable flights were made with an onboard camera streaming continuous data to the ground during flight. The participation of undergraduate students was crucial to the success of this project and they made major contributions in all areas of design, development and test. Results from all three phases of this effort continue to be disseminated in various forums including; journal articles, conference presentations and proceedings, and classroom materials.

1. Introduction

The Autonomous Tactical Reconnaissance Platform (ATRP) is a parafoil that carries a payload instrumented for autonomous flight while performing remote sensing activities. A parafoil is a flying wing made of a flexible material, supported and controlled by an array of strings. The ATRP has many potential military and civilian uses that are not adequately addressed by remote sensing systems currently available. Although the ATRP would provide data similar to that from either Unmanned Air Vehicles (UAVs) or Micro Air Vehicles (MAVs), it has unique capabilities and advantages that separate it from both of these types of air vehicles.

Reconnaissance data from various sources have proven to be crucial to the success of most battle campaigns, particularly in recent years. Today our military employs a number of reconnaissance assets including satellites, manned aircraft, unmanned aircraft and human infiltration. All of these assets can provide vital information to commanders at home and in the field, however they all have drawbacks when it comes to supporting the individual soldier in real-time, hostile environments.

In its military version the ATRP would provide the soldier with a close range, real-time view of the immediate surroundings. Another potential use for the ATRP is to provide an enhanced capability for long-range communications in obstructed or rugged terrain. In a reconnaissance role, this device would be extremely valuable in rugged, urban or jungle terrain and during nighttime operations. An infrared and/or visual sensor aboard the ATRP would pinpoint the enemy location and numbers during such exercises. However, the need for real-time reconnaissance data is not limited to the battlefield.

Non-military uses include providing fire location and egress points for forest fire fighting crews and aiding search and rescue teams in locating lost hikers and victims of avalanche. This device also shows great promise in helping farmers and land management professionals to determine areas of plant stress due to drought, pests, salt intrusion and disease[1,2]. Current collection methods such as satellites and manned aircraft are expensive, geographically imprecise, and

frequently unavailable at critical times in the growing season. The ATRP equipped with a Global Positioning System and the appropriate sensors would overcome all of these obstacles and would allow farmers to perform their own personalized data collection and evaluation. Other life saving and communications scenarios can be implemented for this device when outfitted with the appropriate instrumentation.

The ATRP is designed to provide personnel in the field with a means of expanding their knowledge of the nearby environment in a safe, timely and cost effective manner. The ATRP is launched vertically to low altitude (typically <1000 feet) and then flies a pre-selected course while transmitting sensor data to the user on the ground. During flight, it is under full autonomous control, allowing the user to concentrate on the sensor data (i.e. IR imaging, visual imaging, radio communication and potentially laser designation) being communicated to a hand held receiving device. Prior to launch, the user can select one of several pre-programmed flight patterns for the device to follow and then launch, all in a matter of seconds.

The parafoil design is lightweight, easily compacted and deployed, and very stable in flight. An autonomous, fuzzy logic flight controller pilots the parafoil for the ATRP. After launch and deployment, the autonomous controller executes the pre-selected program of flight maneuvers as it glides in the descent phase. A fuzzy logic control method is employed because of advantages in fault tolerance, graceful response to missing or noisy sensor input and compact memory requirements. The entire system is extremely rugged, capable of surviving hard landings and small arms fire.

The ATRP and its launch mechanism are man-portable, with set-up and launch operations achieved in a matter of seconds. A range of launch mechanisms including rocket, compressed air, artillery shell and tethered flight (flown like a kite) are possible with this device. The ATRP is intended to be an inexpensive, expendable device, suitable for a wide variety of mission scenarios. The technology used in the ATRP is commercial-off-the-shelf (COTS) components, easily acquirable and inexpensive to manufacture.

Key accomplishments achieved in this latest Phase III effort include:

- Multiple demonstrations of real-time telemetry and video data capture from instrumentation aboard the ATRP while in flight.
- Dramatic improvements in all physical hardware components including; a new aerodynamic shell design, parafoil ejection system and incorporation of a new parafoil.
- Regular and extensive use of the Compressed Air Launch Mechanism (CALM), including multiple launches in one day, to test and evaluate design improvements.
- Development of a customized board of electronics with 10 times the computing capability, one fourth the size and greatly expanded sensor instrumentation.
- A major software upgrade incorporating a hierarchical Fuzzy Logic structure to provide accurate autonomous guidance under a broad range of environmental conditions.
- Development and implementation of a unique method to automate the optimization of the controller software.
- Dissemination of results through journal articles (acceptance pending) and conference proceedings, and classroom materials.

- Commercialization efforts including a white paper submittal to DARPA BAA05-22, preliminary contacts with Viecore Corp. for potential partnering opportunities, and exploration as an Agri-business concern.

In Phase III a new, improved electronics suite was developed, built, bench tested and flown. The software was significantly improved to take advantage of the increased sensor capability. The simulation capability, developed in the first two phases was enhanced to include a Genetic Algorithm based optimization routine. The Compressed Air Launch Mechanism (CALM) that was developed at the end of Phase II was significantly improved and was used on a regular basis to test a variety of hardware and software improvements.

A brief review of the development of the CALM device is given in Section 2. Detail on the development of the projectile structural hardware is provided in Section 3. Design and development of electronic hardware is summarized in Section 4. An overview of the development of the Fuzzy Logic Algorithm, the flight simulation and the optimization of the Fuzzy membership functions are provided in Sections 5, 6 and 7, respectively. Flight test results are described in Section 8, followed by conclusions in Section 9.

2. Compressed Air Launch Mechanism

An alternative launch mechanism for the ATRP was designed, built and tested during Phase II. The original impetus behind this effort was to demonstrate the ability to replace the need for rocket motors in situations where they would be uneconomical, dangerous or unavailable. A trade study was performed and the Compressed Air Launch Mechanism (CALM) was determined to be an attractive alternative. In the case of farmers, compressed air would normally be readily available, could be continuously renewed, and would be cheaper than buying multiple rocket motors.

As the project progressed, it became clear that an alternative launch mechanism would also be desirable for accelerating the pace of test flights. Although the PI was successful in negotiating with Camp Roberts to perform test flights there, this still did not equal the convenience of testing on the Cal Poly campus. However, we were constrained by safety considerations from using the large motors necessary to obtain usable altitudes on the Cal Poly campus.

Industrial Engineering student Andre Von Muhlen spearheaded the design and development of the original CALM device. During this Phase III effort the mobility and convenience of the CALM was significantly enhanced by Cal Poly Aerospace Engineering student Dan Macy. The upgraded Phase III CALM is pictured in Figure 1. Two tanks made of PVC pipe hold the compressed air that powers the CALM. A high-speed valve releases air from the tanks into the barrel of the device, propelling the payload to the desired altitude. Testing performed on unguided, lightweight projectiles in Phase II achieved altitudes much greater than the desired 500 feet.

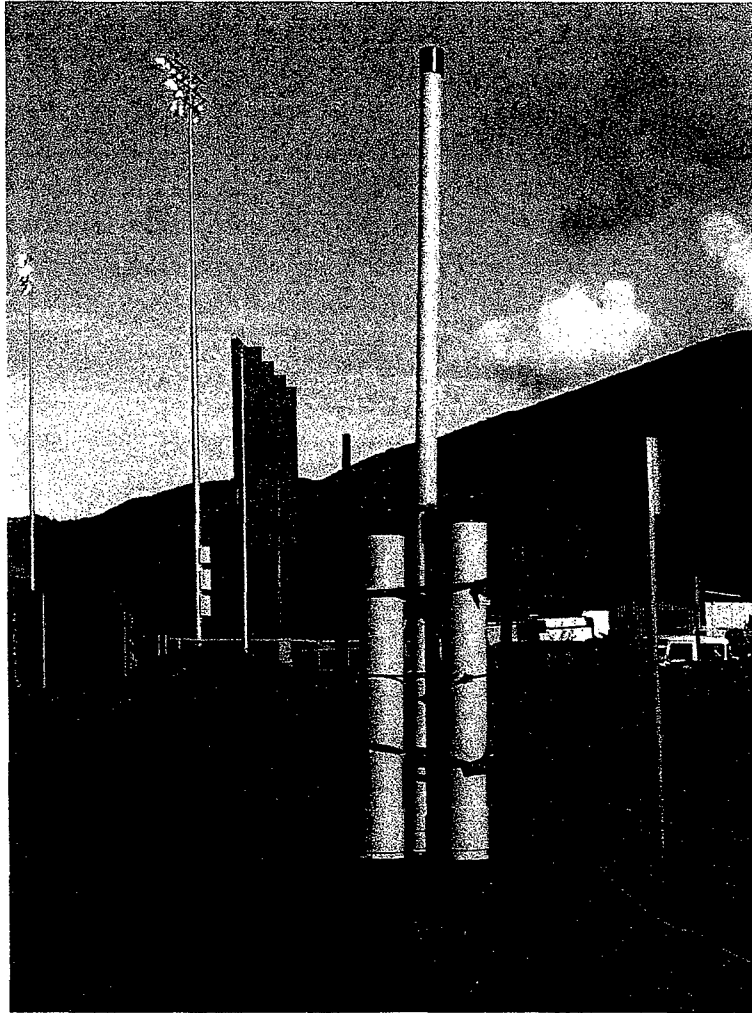


Figure 1 - CALM in Launch Position

Two separate half-scale projectile designs were tested with the CALM device. These prototype vehicles were designed to test aerodynamics of the projectile concepts and to test the launch power of the CALM. The CALM proved to be an invaluable test tool making it possible to achieve the program goals on schedule.

3. Projectile Development and Construction

As the project moved into this Phase III effort, the aerodynamic housing continued to evolve in development efforts. A major impetus in changing the design was the need to accommodate launch from the CALM device. Indeed the term "rocket" was no longer appropriate for the aerodynamic housing, as a rocket motor was no longer used when launched from the CALM.

The switch from rocket launch to compressed gas gun launch was mainly driven by the need to increase the frequency and economics of flight testing. Use of the powerful rocket motors that were required to lift the ATRP to acceptable altitudes is strictly regulated and had to be launched from specially designated areas far from the Cal Poly campus. The nearest available facility,

Camp Roberts, had to reserved well in advance with a great deal of administrative overhead. Additional launch opportunities such as amateur rocket fairs were exploited but were relatively infrequent and occurred much farther from campus.

Although there were many advantages to using the compressed gas CALM device, the change in launch mode imposed a new set of constraints on the projectile design. The 3-inch diameter of the CALM barrel established the maximum allowable diameter for the redesigned projectile. The acceleration or 'g' forces imparted by the CALM during launch also posed a serious challenge to the new vehicle configuration. The maximum force encountered in the rocket launch scenario was on the order 10 g, or 10 time the force of gravity, whereas a projectile launched from the CALM could reach in excess of 80 g's. This requirement to make the electronic and structural components withstand high g loads had the additional benefit of forcing the design to be much more rugged which would prove useful even when modified back to a rocket launched system.

Another critical design criteria imposed by the CALM launch method was the need to minimize the vehicle weight as much as possible. In rocket launch mode, additional weight of the vehicle could be offset by simply employing a more powerful motor. There had always been a concern to keep weight down in order to ensure that the system would be portable, but it was difficult to determine a hard requirement for this issue. The launch capability of the CALM however, sets definite limits on the mass of the projectile that can be launched to the desired altitude range. The weight limitation is dictated primarily by the allowable maximum air pressure in the two CALM storage tanks. In order to achieve altitudes of 500 feet, the projectile weight had to be held to 3 lbs. maximum.

In order to meet these demanding criteria, stronger materials, structural designs and efficient electronics had to be incorporated into the ATRP vehicle. One of the most significant structural changes from previous rocket launch versions was in the design of the stabilizing fins. The projectile needed to have a smooth uninterrupted circumferential segment at the maximum body diameter in order to provide a good seal within the barrel of the CALM device. This requirement led to three alternatives to be initially considered for fin and body design.

A common rocket design, employed in earlier phases of this program, features a long, cylindrical body with fins attached at the base extending outward. A simple modification to this design to make it compatible with launching from the CALM smooth bore barrel would be to encapsulate the fins in a detachable sabot. The sabot, built in halves, would be separated by aerodynamic forces once the projectile had cleared the CALM barrel. This design candidate was rejected because accommodating fins surrounded by a sabot inside the 3 inch diameter CALM barrel would force the projectile body tube to be no more than 1 inch in diameter. A body tube this small was deemed too restrictive to accommodate the space required for all the ATRP system components.

Small demonstration prototypes were developed for two alternative fin designs. One alternative employed a thin rod with attached fins and the other featured retractable fins. Aerospace Engineering student Dan Macy, shown in Figure 2 with the rod and fin design, was responsible

for the construction of both test projectiles. Each projectile had an on-board altimeter to record the maximum altitude achieved and a simple parachute for recovery.

In Figure 3 Dan Macy and Dr. DeTurris are shown packing the parachute for the alternative retractable fin design. The fins were designed to deploy once the projectile had cleared the CALM barrel. The retractable fins worked well in ground tests, however problems were noted in the reliability of the fin deploy mechanism during launch. This design was dropped in favor of the simpler rod and fin model that had no moving parts.

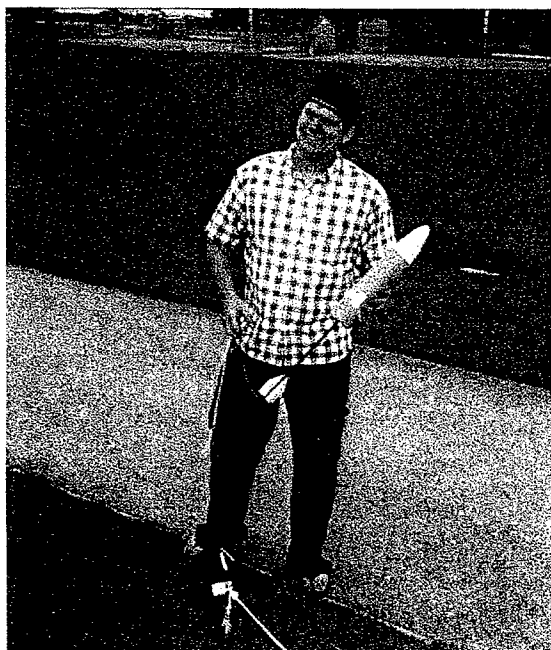


Figure 2 - Dan Macy with the Rod and Fin Prototype



Figure 3 – Dr. DeTurris and Dan Macy with Retractable Fin Prototype

Subsequent full scale vehicle designs were all based on the rod and fin model. In the full scale model, a black powder deploy charge separates the projectile into two components at apogee. The firing of this charge, located at the extreme aft end of the body tube, forces a piston to move rapidly in the forward direction inside the tube. The piston pushes against a stowed parachute and parafoil, which in turn are forced against a nose section comprising the top 1/3 of the body length. The nose section is normally held in position to the rear 2/3 of the body tube by a friction fit coupling. As the ATRP separates at this coupling, the parachute is ejected and remains with the aft body for recovery and re-use.

The parafoil, attached to the nose section, descends under the control of the enclosed electronics. The electronics are mounted on a thin structural plate that runs down the center of the entire length of the nose section. The bottom edge of this plate rests on a bulkhead that seals and protects the nose section from debris as well as providing circumferential support.

The parafoil designs used in the previous two phases of this program were not ideal for the purposes of this project. The first design chosen in Phase I was a parafoil kite which would often deploy incorrectly and required much experimentation to adjust the line lengths to be suitable for free flight as opposed to its tethered flight design. This kite also required a 2-foot long separator bar placed between the left and right hand side support lines. This bar added complexity in the design for stowage and deploy mechanisms.

In Phase II a parafoil designed for a motorized remotely controlled vehicle was discovered and purchased. This parafoil required a much shorter separation bar of about eight inches which could be launched without elaborate deploy mechanisms. This parafoil also had the advantage of being designed for free flight albeit powered flight. Despite these advantages, this second parafoil also had occasional problems with tangles in the lines after deploy and the need for constant tweaking of line lengths for unpowered flight.

In Phase III a parafoil was found that requires no separator bar and is designed for unpowered, free flight. Figure 4 shows the new parafoil with the electronics section in the descent phase of flight. Note in this figure that the separator bar of previous models has been replaced by a rectangular piece of fabric to anchor the support lines. Control lines pass through guide rings attached to this fabric and continue on into the electronics section where they are affixed to servo control arms. As seen in the figure, cloth straps attach the fabric support square to the electronic nose section.

This parafoil was designed for specialty hobbyists for air drop from radio control airplanes. An additional advantage to this parafoil is that it was designed to be folded and deployed in flight just as is required of the ATRP. The only modification required to make it suitable for our purpose was to reinforce the points at which the support lines attached to the parafoil. Very few deploy problems occurred with this parafoil, however future effort may be required to improve the maneuverability and glide ratio of this design.



Figure 4 - New Parafoil and Electronics Section in Flight

4. Electronic Hardware

One of the goals of the Phase III program was to develop a much more capable suite of electronics with expanded sensor, memory and computational capabilities. A micro-controller system was developed with ten times the capability of that provided in the prior work. This micro-controller based system is lightweight, smaller, lower in cost, and has the computing power needed to downlink video in real time. The HandyBoard microcontroller, which served its purpose well through Phases I and II, was replaced by a unit designed and built by Cal Poly Electrical Engineering student, Chris LaFlash. The HandyBoard allowed us to test various software configurations. However, limitations including weight, physical size, power requirements, memory and computational speed were driving the need for a replacement. The new unit has a smaller form factor than the HandyBoard and is designed to fulfill the specific role required by the ATRP (as opposed to the much more general functioning of the HandyBoard). A brief description and role played by the various instruments and electronic components that make up the Phase III controller are described in the following paragraphs.

The U-Blox TIM-LP Global Positioning System (GPS) unit provides absolute location coordinates for the ATRP. This unit provides a position update every 0.25 seconds with a circular error probability (CEP) of 2.5 meters. The GPS receiver is a postage stamp sized board (1 inch square) weighing 3 grams. Successive data readings from the GPS used in conjunction with compass readings provide an estimate of wind speed and asymmetric aerodynamic effects. These estimates are in turn used to correct the desired compass heading to allow the ATRP to fly to the desired destination.

Compass headings are provided by the Precision Navigation Compass Chip Set 11096. The compass is the single most important instrument in the navigation suite. In the event that the GPS system should lose satellite lock, the compass will continue to provide approximate heading information to keep the vehicle on course. Once GPS satellite communication is re-established course heading correction information will be computed and a new desired compass heading is established. The compass also provides a redundant backup capability in determining vehicle turn rates. A rough calculation of turn rate is computed by dividing successive compass measurements by the intervening time interval between those measurements.

An Analog Devices ADXR300 MEMS Gyroscope provides the primary source for turn rate information. The gyroscope is a single chip of negligible weight and size that never the less provides data accuracy well within the requirements necessary for the ATRP mission. Data from this device along with compass heading measurements provide the inputs for the course heading fuzzy logic module. Turn rate information is critical in this module as it helps to prevent overshoot and oscillations in heading control.

Other electronic components in the system include pressure sensors used to identify when deploy altitude has been achieved and a Maxstream Xtend data radio for transmitting instrument telemetry to the ground station. A variety of small servo motors have been used in various ATRP models to provide the control line pulls needed to steer the vehicle. All of the components are firmly soldered, strapped and bolted into place to withstand the 80 g's of force during launch.

The Handy Board, which had provided the 'brains' of the electronics suite in the previous two phases has been replaced by a Rabbit 3000 Microprocessor. This microprocessor runs at 30 MHz (15 times the handy Board), has 512 kb of flash memory and 512 kb of RAM. The board is a mere 1.86 inches wide by 2.65 inches long. The computing power of this unit is more than an order of magnitude greater than that provided by the Handy Board, at much less cost. Control software is developed in a simplified version of the C programming language and is downloaded to the Rabbit board for execution. Figure 5 shows the various components that make up the new electronics package.

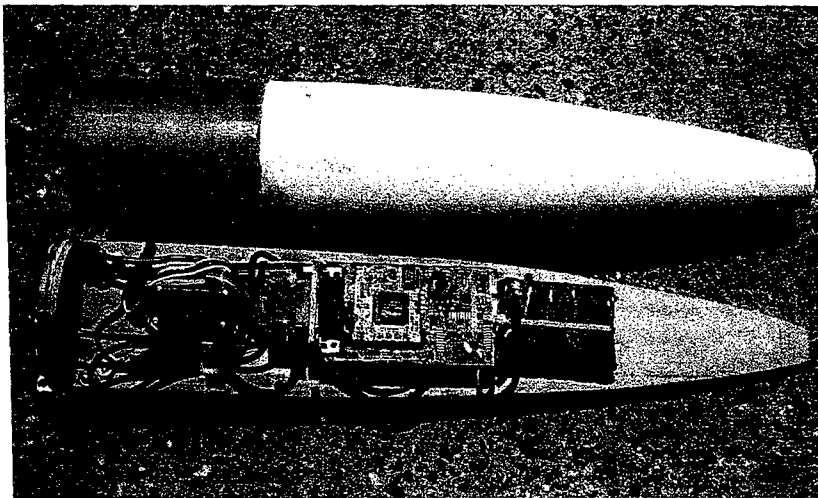


Figure 5 - Phase III Electronics Package

A miniature camera system purchased from BlackwidowAV provides real time video sent by its own separate 200mw transmitter. Video data from the camera is transmitted to a laptop ground unit for real time observation and recording purposes. In an operational scenario, the ground station would be no bigger than a tablet PC, including display and receiver electronics. A still image captured from this camera is shown in Figure 6.

The BlackwidowAV, shown in Figure 7, features; a full color CCD camera with a built-in audio microphone and antenna, a receiver with attached patch antenna, cables for attaching to a display device and a charge converter for the receiver. The electronics that ride on the ATRP, the camera, transmitter and transmit antenna, are incredibly light, having a combined weight of only 1.5 ounces. The camera transmits at the 2.4 GHz and has a range more than sufficient for the purposes of this project. The receiver and receive antenna are also extremely lightweight and are ideal for use in remote locations. Ground tests with this unit have shown excellent performance.



Figure 6 - Image Captured from Onboard Camera

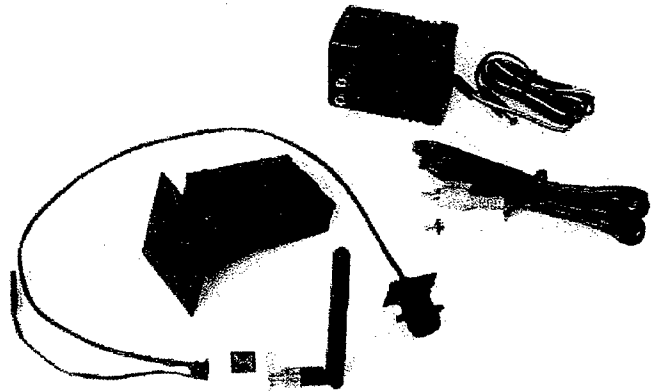


Figure 7 - The Camera, Receiver and Hardware

This unit has flown on many launches from the CALM and has provided excellent quality video in both the ascent and descent phase of the ATRP. The camera system has proven to be remarkably rugged, surviving both the 80 g's of launch and a few rough landings when the parafoil has failed to completely deploy.

5. Comb's Method and the Fuzzy Logic Algorithm

A fuzzy logic control algorithm provides the decision-making strategy for the ATRP. There are a number of other excellent control methodologies available and indeed proportional integral derivative (PID) algorithms of one type or another are used in 90% of current controllers. PID controllers have been enormously successful in a variety of applications and in most cases have proven to be both very efficient and accurate. However, the fuzzy logic controller does have distinct advantages for our particular application. These advantages include robust performance in the presence of noise and signal errors, ease of development, and the capability to provide nonlinear output when required.

One of the disadvantages of a fuzzy logic solution is what is known as "exponential rule explosion". In a fuzzy algorithm, each input parameter has an associated fuzzy membership set as shown in Figure 8. In the typical fuzzy algorithm rules are formed by combining every element in the input membership sets in all possible combinations with the membership set(s) of the output variable(s). An example of rules generated from the input variables "compass heading" and "heading rate of change" and the output variable "heading correction" would be:

If compass heading is "minus big" and heading rate of change is "zero" then heading correction is "plus medium"

If compass heading is "zero" and heading rate of change is "zero" then heading correction is "zero"

If compass heading is "plus big" and heading rate of change is "zero" then heading correction is "minus medium"

•
•
•

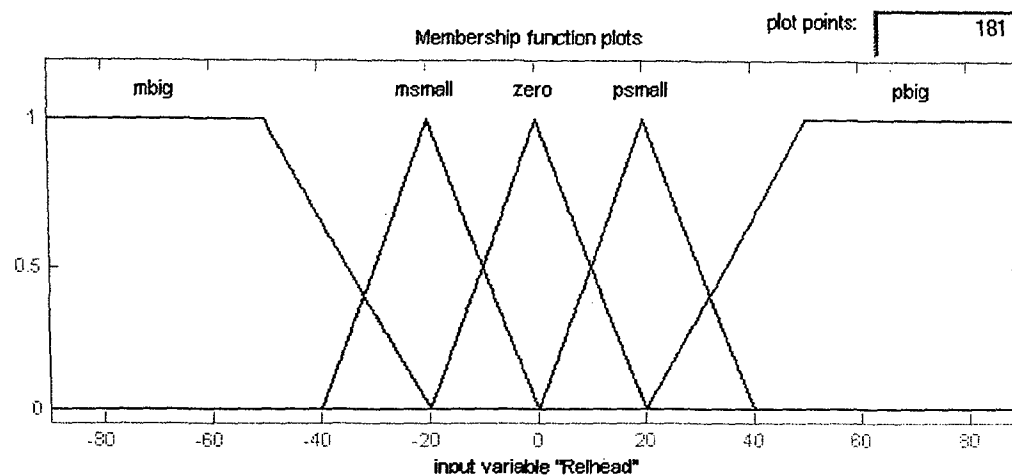


Figure 8 - Membership Set for Compass Heading Input

This system of rules works well for small two input problems, but as the number of inputs and corresponding membership sets increase linearly the number of rules increases exponentially. Combs' method is a relatively obscure technique used to overcome this exponential rule growth problem. For those interested in the details of this method, Cox provides an excellent introduction [11]. The advantage to this technique is that rule growth increases only linearly with the increase in the number of inputs. Therefore a fuzzy system of 5 inputs with 7 membership functions each will have only 35 rules ($5 \times 7 = 35$) rather than the 16,807 (7^5) rules of the conventional technique. Rules formulated in the fashion of the Combs' methodology are constructed as follows:

If compass heading is "minus big" then heading correction is "plus big"

If heading rate of change is "zero" then heading correction is "zero"

If compass heading is "plus big" then heading correction is "minus big"

•
•
•

The main difference between this formulation and that of the traditional method is that in Combs' method every rule has only one antecedent (the part before the *then*) for every consequent (the part after the *then*). At first it may seem counter-intuitive that this simple change results in a dramatic reduction of rules. To illustrate the savings, suppose you have two inputs of five membership functions each (membership functions for the input "compass heading" would be; minus big, minus medium, zero, plus medium, plus big). In order to cover all possible contingencies in the traditional method, every membership function for "compass heading" must be combined with every other membership function in "heading rate of change" to form $5 \times 5 = 25$ rules. In Combs' method every membership function of each input has a single rule to relate it to the output, resulting in $2 \times 5 = 10$ rules.

The breakthrough that Combs has made is to prove that his simpler formulation is equivalent to the traditional method and covers the same solution space as that of the traditional method. This incredible achievement has certain theoretical restrictions that Combs and his collaborators have outlined in a series of published papers [12-15].

In our approach we have violated some of these restrictions, hence our formulation is not strictly equivalent to the traditional method. By performing large numbers of simulation runs, exhausting the input space, we have found no anomalous behavior exhibited using our modified formulation. These simulations have given us confidence that our current approach is sound, however because we are violating the theoretical restrictions, additional testing must always be performed any time the membership functions for the inputs are changed.

The algorithm we have developed is hierarchical in structure. The GPS system allows the ATRP to adjust for absolute position errors introduced by winds, and asymmetric vehicle dynamics. A separate fuzzy logic algorithm uses the current and prior GPS locations to determine the effect of these external forces to generate a heading compensation factor. This compensation factor is then input to the second fuzzy algorithm along with the absolute compass heading and heading rate of change to output a steering command. These two fuzzy algorithms could be combined into one, the modular structure made it easier to develop and modify the algorithm throughout the development process.

There is very little precedent in the literature for using the Combs' reformulation of the fuzzy algorithm in control problems, however we found it worked quite well for our application. Indeed, simulation runs showed excellent performance regardless of which rule formulation was used to test the system. The memory and speed savings of the Combs' method were a key breakthrough for the success of the ATRP project.

There is a large body of research described in the literature on methods to modify membership functions in the optimization process. The technique followed in this application was to define an initial set of triangular membership functions for each variable. A simple scaling function of two independent variables was used for each input to modify the shape and spacing of the membership functions. The scaling function for each input variable has a proportional and an exponent term of the form;

$$F(x) = ax^b \quad (1)$$

The proportional term “a” in equation (1) has the effect of varying the width and spacing of the membership functions evenly over the domain. The term in the exponent “b” produces a nonlinear spacing of membership functions and distorts the straight sides into curved line segments. The combination of the two terms provides good flexibility in modifying the membership functions without incurring a high computational overhead. Figure 9 shows an example of membership functions before and after this scaling function has been applied.

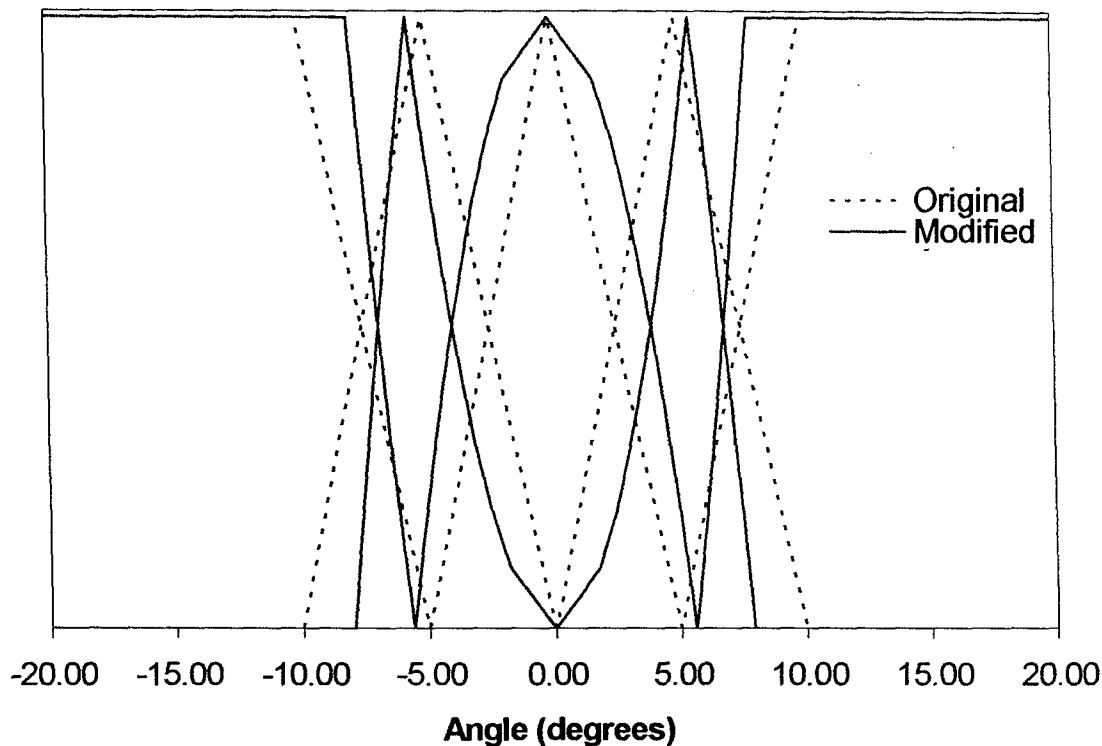


Figure 9 - Membership Functions Before and After Modification ($a = .4$, $b = 2.0$)

The combined effect of the two scaling factors in this example is to widen the membership function centered at 0.0, push the peak of the medium membership functions out wider and pull the outermost membership functions inwards. Different combinations of values of the scaling functions will have widely differing effects on the resulting modified membership functions. There is no provision in this approach for making asymmetric membership functions, however in our own application it is hard to conceive of a scenario where asymmetry would be a desirable trait.

A total of 14 scaling terms for the 7 variables (5 input and 2 output) of the two fuzzy logic modules make up the chromosome for the genetic algorithm optimization. These terms were limited to a range of values between 0.3 and 5.0. Values outside of these limits were found to be well outside the region for any optimal solution.

6. Simulation

The parafoil design is inherently a very simple and stable flight vehicle that does not require a vertical control surface. Turns are initiated by pulling on one of two control lines connected to either side of the parafoil wing. One simplifying assumption made in the simulations was that the parafoil flies at a constant speed with no need for pitch axis control. This assumption is at least valid to a first degree of approximation and was not a limiting factor in optimizing the control algorithm. Figure 10 shows a high-level block diagram of the simulation model.

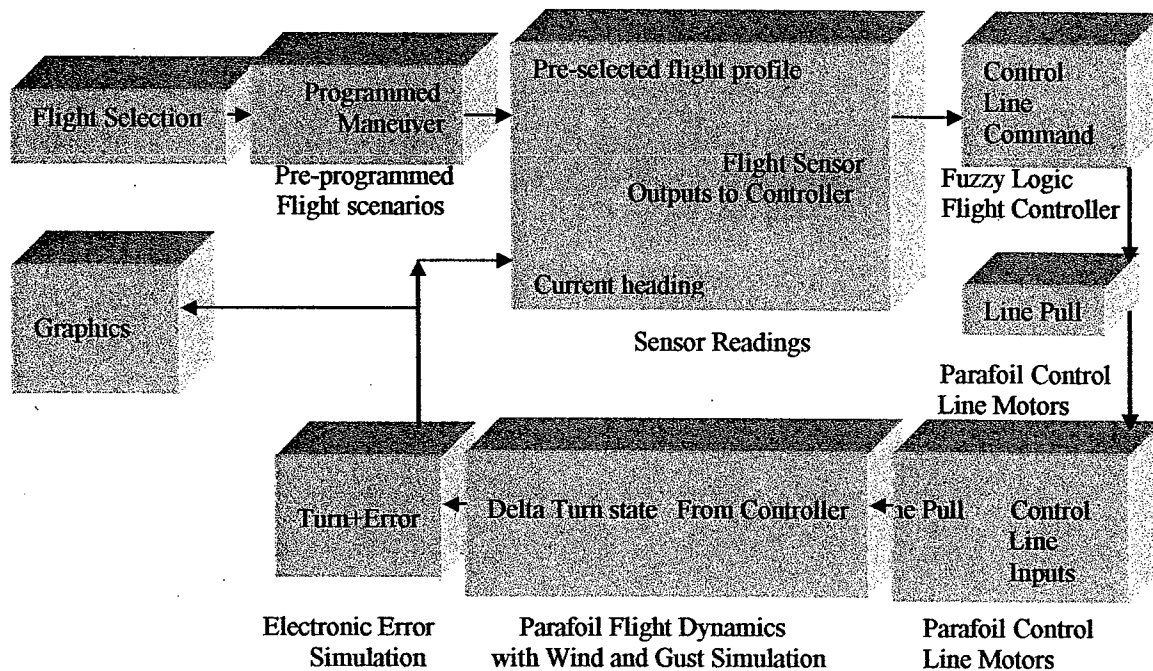


Figure 10 - Block Diagram of Simulation Model

The Matlab/Simulink software environment has been used to run hundreds of simulations of the ATRP system. The main purpose of the simulation runs is to determine the optimum architecture for the fuzzy logic control algorithm. A number of different elements, within the fuzzy algorithm and external environmental conditions, were varied during this optimization process.

Elements subject to optimization within the fuzzy algorithm included; the number and type of inputs, the number, type and value of input membership functions, the number and composition of rules, the number, type and value for the output membership functions, and the defuzzification method employed. Factors that were external to the fuzzy algorithm were modeled to determine how robust the control mechanism would be under non-ideal conditions. These external factors included; wind speed, direction and variability, system noise, instrument errors, initial deploy delay interval, and initial deploy direction of travel.

A number of major improvements have been made to the simulation model since it was first created during the Phase I effort, but the most significant change has been the addition of the GPS modeling capability. The goal of the Phase I effort was to produce an algorithm which would allow the ATRP to follow a pre-programmed course based on compass headings. In

Phase II we developed the capability to follow a course based on pre-programmed, earth coordinate based waypoints. The difference can best be illustrated when wind is introduced into the simulation model as shown in Figures 11 and 12.

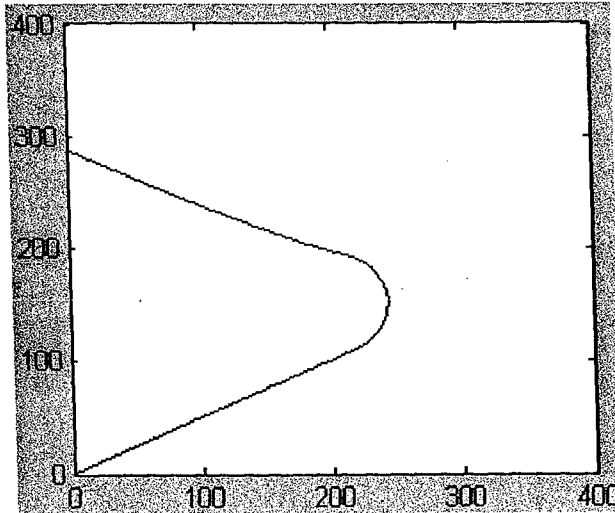


Figure 11 - Ground Track w/o GPS and 5 m/s Cross Wind

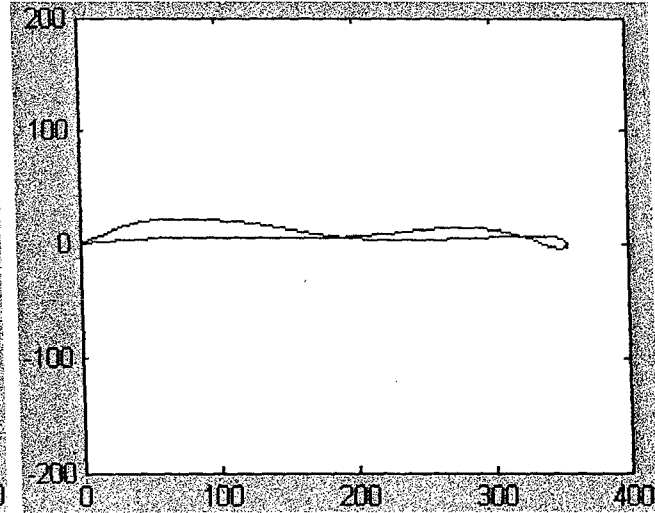


Figure 12 - Ground Track with GPS and 5 m/s Cross Wind

In both figures above, the simulated ATRP starts at the point (0,0) and is programmed to fly due West (along the positive X axis) then turn and head due East (along the negative X axis). Also in both cases, a simulated crosswind blows due North (along the positive Y axis). The difference between the two figures is that a heading correction from the GPS device has been incorporated into the simulation in Figure 12.

Without a GPS correction, the ATRP orients itself to head due West (or East after the turn is executed), but the crosswind carries it toward the North. The GPS unit provides a heading correction once every second to compensate for the wind drift. This feature allows the user to specify specific ground coordinates for the ATRP to cover while it automatically compensates for any wind condition.

7. Optimization

A steady state Genetic Algorithm (SSGA) is used to optimize of the fuzzy logic membership functions. In order to produce a robust control algorithm, the objective function in the optimization process is made dynamic by making random changes to key environmental conditions after each new generation has been produced. A flow diagram of the optimization process is shown in Figure 13. An initial population of solutions is generated by assigning a random value for each variable for each member or 'chromosome' of the pool of candidates. After the SSGA processes of selection, crossover and mutation have been performed, the chromosome for the new offspring is decoded to produce a set of membership functions. These membership functions are incorporated into the fuzzy systems to be used in a simple flight

simulation to determine the fitness of the candidate solution. The process then repeats itself until a satisfactory result is obtained.

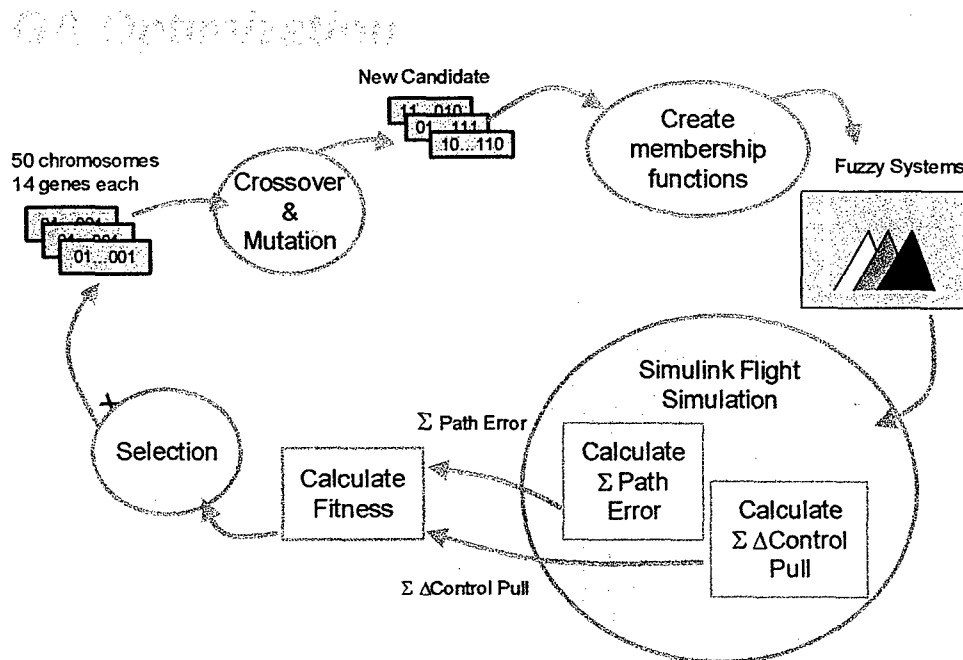


Figure 13 - Block Diagram of GA based optimization

It was not the goal in the development of the optimization algorithm that the most efficient method be developed for tuning the fuzzy membership functions. The goal for this optimization effort was simply to find a spacing and size of membership functions for the inputs and outputs of both fuzzy sub-modules that would satisfy the control algorithm objectives. In the process some interesting techniques were used and a satisfactory outcome was achieved.

A genetic algorithm (GA) was chosen as a convenient method to perform the optimization with a reasonable expectation of success. Genetic algorithms have proven effective in NP hard problems, they are easy to develop and code, and if properly designed they will avoid pitfalls that can trap other optimization techniques. Specifically, a Steady State Genetic Algorithm was chosen for this task as it was expected that this technique would simplify the task of computer code development.

An incremental SSGA is different from a more traditional GA in that only one member of the population of solutions is chosen for replacement at the end of each generation. A generation is defined as completing one full cycle through the process illustrated in Figure 13. There are a number of parameters in the GA process that affect the performance of the optimization that must be set by the designer. The goal for the designer in assigning values to these variables is to establish an efficient balancing act between convergence to a solution and exploring the entire solution space. If convergence occurs too rapidly then the likelihood of finding the global optimum is low. However, if the program is allowed to randomly wander the solution space, then run times can be prohibitively long.

One issue to be determined by the designer is how to select the member of the population to be replaced by the new solution. One obvious choice is to replace the worst performing member, but it has been reported that this can lead to premature convergence on a local optimum. Another choice for replacement is to eliminate the oldest member in the population, but this technique runs the risk of losing the best performing solution. The technique used in this application was to replace the worst performing candidate while maintaining diversity by using a high mutation rate and a dynamic objective function.

There are also a variety of techniques that can be used in determining the parent or parents of the new candidate solution in each generation. Various means of selection include; Fitness Proportionate Selection some form of associated scaling and windowing methods, Roulette Wheel Selection, Rank Selection, and Tournament Selection [28]. In tournament selection, a subset of the population is selected at random and the best candidate from this pool is used for reproduction. A form of tournament selection, with five individuals randomly chosen from the population, was used for this application.

Another choice to be made was whether to pick both parents from the random tournament or to use the best individual in the population as one parent and select the other from the tournament. A comparison of the performance of the two methods is shown in Figure 14. A statistical analysis of a large sample of runs was not performed in making this comparison and so we cannot claim definitively that one method is necessarily better than the other. However, the results shown in the graph are suggestive that that selecting both parents in a random tournament performs better. Further research with a rigorous statistical analysis would be required to make any definitive claims in this regard. This effect is likely due to a need to maintain diversity in the population in order to expedite the search of the entire solution space.

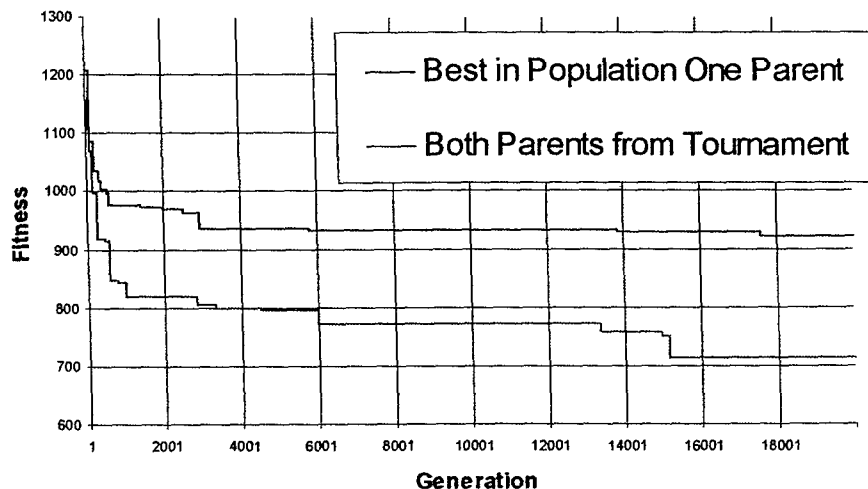


Figure 14 - Comparison of Two Different Selection Schemes

Random tournament selection to obtain both parents was the method used for all runs where the fitness function remained static throughout an optimization run. Eventually the optimization method of using a static fitness function was abandoned and with it the random selection of both parents was abandoned as well. When a dynamic fitness function, as described below, was

incorporated into the optimization routine the elitist strategy of maintaining the best solution in the population as one parent was adopted. The reasoning behind the switch in selection method was based on the assumption that greater continuity in the generation of solutions would be required with a dynamic fitness function. This assumption was not verified and remains as an interesting question for further research.

Another decision to be made in the construction of the SSGA is the type of cross-over to be employed. Cross-over, the exchange of sections of genetic material between parent solutions, can be limited to a single cut and swap operation as in single point cross-over or can occur at multiple locations on the chromosome. A special case of multi point crossover, uniform crossover, was implemented in this application with an equal chance of each bit being contributed by either parent.

The mutation rate was chosen to be extremely high, referred to in the literature as hypermutation, relative to values usually used in most applications with static objective functions. The high mutation rate helps to ensure that the population does not become trapped at a local optima in the solution space. Mutation rates of less than 0.005 are commonly quoted in the literature, whereas a value of 0.4 was used for the majority of the optimization runs in this research.

Using an extraordinarily high mutation rate was expected to provide a more thorough search of the solution space at the cost of greatly increasing the number of iterations required for convergence. A compromise to this expected, though not empirically demonstrated, problem was to perform mutation using a Gaussian rather than uniform distribution. The Gaussian distribution was centered on the previous value taken by the mutated variable to help to lower the probability that a child solution would wander far from the selected parent candidates.

Fitness values for the SSGA were derived from data generated over an entire flight simulation, run in the Matlab/Simulink software environment. The desired flight pattern flown in the simulation, consisting of a straight flight North - 180 degree turn - and straight return towards the South, remained the same throughout an entire optimization run. The fitness of a candidate solution was determined by combining two separate measures of the traits desired for the autonomous controller. One of these desired traits, tracking the desired flight path as closely as possible, was evaluated using equation (2) where the summation is performed over each time step in the flight simulation.

$$P_e = \sum |(P_a - P_i)| \quad (2)$$

Here P_e is the total path error, P_a is the actual path followed and P_i is the ideal path.

There was also a need to minimize the magnitude of pull commands performed by the servo motors. Using the servos as sparingly as possible would save on battery power requirements and was expected to produce a realistically achievable flight profile. This desired trait was captured by summing the change in pull commands at each time step as shown in equation (3).

$$S_t = \alpha \cdot \sum |(S_{ts} - S_{ts-1})| \quad (3)$$

where S_t is a measure of servo use throughout a flight, S_{ts} is the servo position for the current simulation time step, S_{ts-1} is the servo position for the previous time step, and α is a constant used to adjust the relative weight of this trait in the overall minimization function. The sum of equations (2) and (3) provided the fitness measure to be minimized in optimization efforts.

Initially, optimization runs were performed with the environmental variables (crosswind, etc.) fixed in a "worst case" configuration throughout the optimization run. Figure 14 shows the monotonic improvement in fitness expected from this static objective function. It soon became apparent that obtaining a solution by optimizing over a single set of initial conditions would not be sufficiently robust to provide adequate performance over all possible environmental conditions. Maximum wind speed, wind direction, frequency of wind speed change, and initial course heading are the variables that had a significant impact in determining the optimum fuzzy logic membership function values. The approach taken to make the solution more robust was to make the objective function dynamic. The various initial conditions were changed randomly after each generation in the SSGA process.

Figure 15 shows the results of running the SSGA optimization for 3600 generations. A lower fitness score represents a better solution in this minimization problem. The solid black line through the center of the data is a moving average of 144 values. Unlike the results for the static fitness function, this graph exhibits a noisy profile caused by the random choice of initial conditions for the fitness calculation at each generation. During the optimization process the initial environmental conditions for a particular generation may be relatively benign resulting in a good fitness score, whereas the following generation may be faced with a much more difficult set of initial conditions. The resulting plot of successive generations does not show the monotonic improvement as shown by the static fitness case.

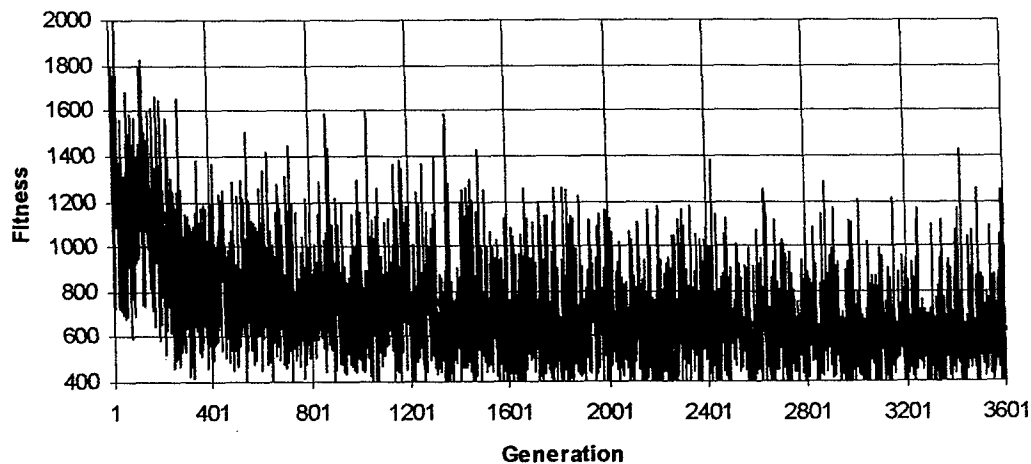


Figure 15 - Most Fit Solution at Each Generation

The trend line shown in Figure 15 shows a rapid initial improvement in the optimization process with a slow tapering improvement in later generations. Figure 16 shows a plot of 6 of the 14 individual genes of the best candidate solutions for each generation of the optimization run. The values for these variables are the dimensionless constants used to adjust the spacing and width of the membership function for the various input parameters as discussed earlier. Note that each

gene starts the run with a wide variation in values, but as the optimization process progresses they tend to form bands of varying widths. Those genes used in the exponent (HPOW, VPOW and CPOW) of the scaling equations tend to form much tighter bands than the proportional terms. Although individual constituents have been limited to bands, it is not clear what value within those bands would provide an overall optimum solution.

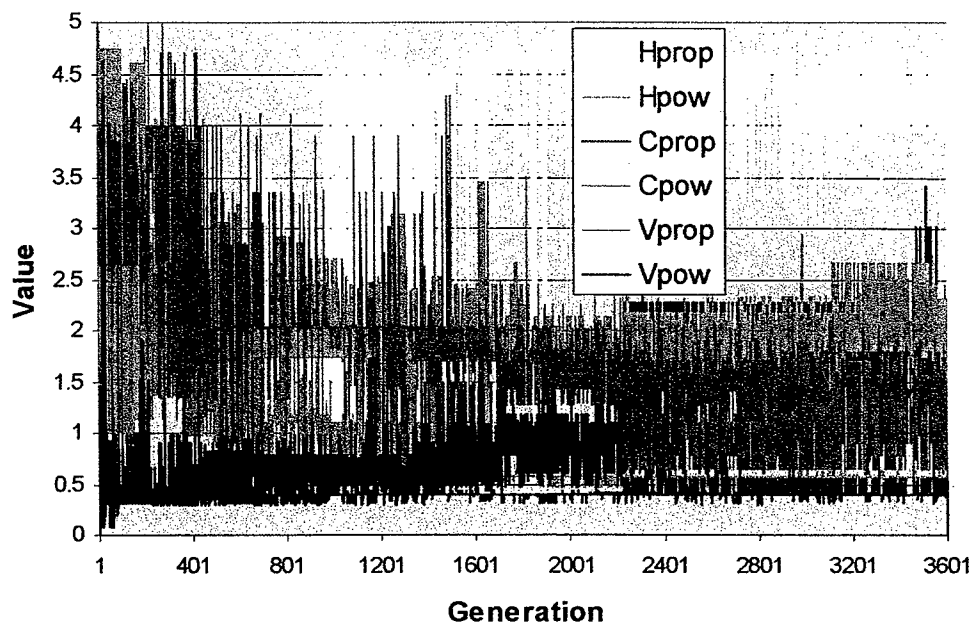


Figure 16 - Control Parameters for Course Heading Fuzzy System

A difficulty arises in that no single solution in the population provides the lowest fitness score for all possible combinations of environmental conditions. A number of methods could have been employed to extract a single solution for each gene and this could be an avenue for future efforts in this area. The relatively simple solution we chose to follow was to continue the optimization run with the mutation parameter reduced to zero. Figures 17 and 18 show the effect that zeroing out the mutation rate has on overall fitness and on the individual genes, respectively.

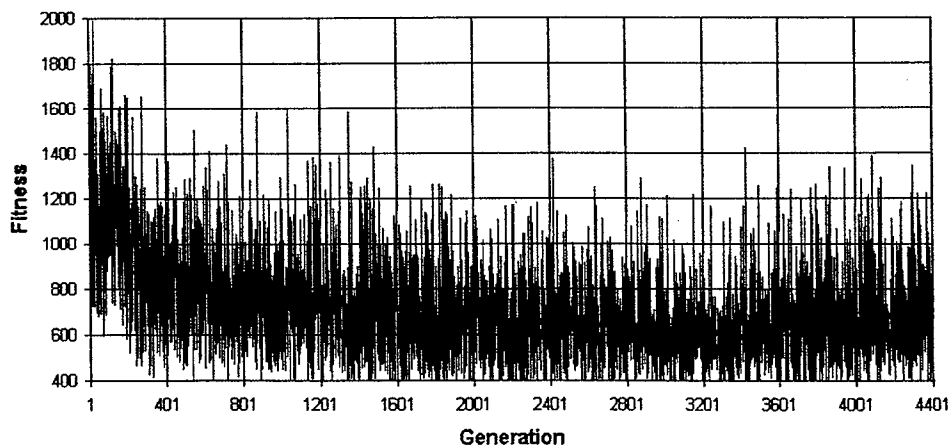


Figure 17 - Fitness with the Mutation Rate Zeroed Out at Generation 3600

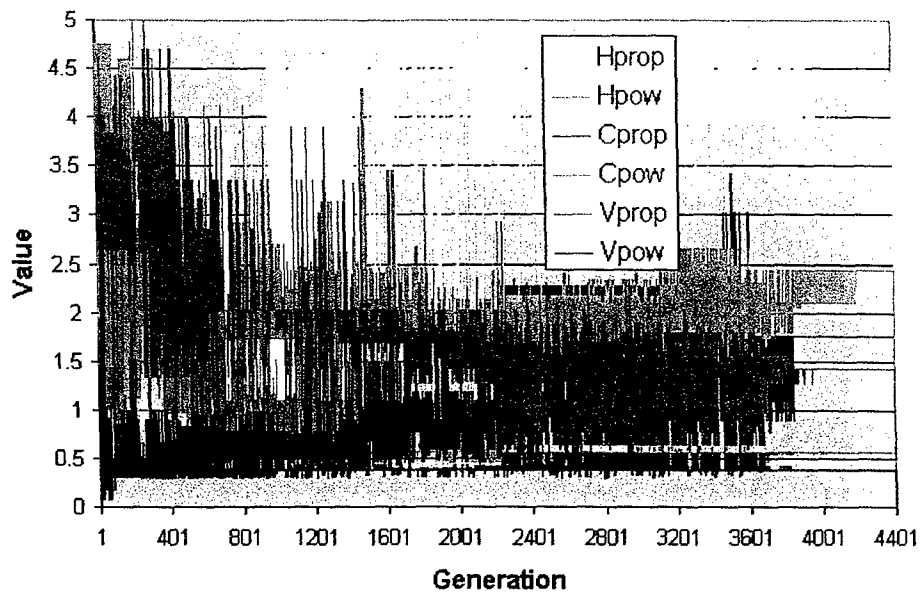


Figure 18 - Constituent Values with Mutation Rate Zeroed Out at Generation 3600

In Figure 18 we see that the optimum values for each of the parameters converge at varying rates to a single value. Moreover, with the mutation rate reduced to zero, these optimum values are shared by every member of the population, meaning that the entire population converges to the same solution. Looking closely at the trend line in Figure 17 it can be seen that this convergence results in a slight worsening of the average fitness over all values of environmental conditions. This effect should not be surprising because at this point in the process the same solution is used for all initial conditions rather than having a variety of candidate solutions in the population available for different initial conditions. The optimization was allowed to continue to run for some time after the population had converged to a single solution in order to ensure that no set of random environmental conditions would produce an unacceptably high fitness value.

Some interesting observations can be made by looking at a plot of the least fit individual in the population in each generation, as shown in Figure 19. Note that once the mutation rate has been zeroed out at generation 3600, the least fit candidates no longer show unacceptably high values. The majority of the high spikes in Figure 19 are extremely unfit individual solutions introduced into the population through mutation. This phenomenon occurs because just as is the case in the natural world, most mutations tend to be inconsequential or harmful rather than helpful. It is the exception to this general tendency that adds to the improvement in candidate fitness.

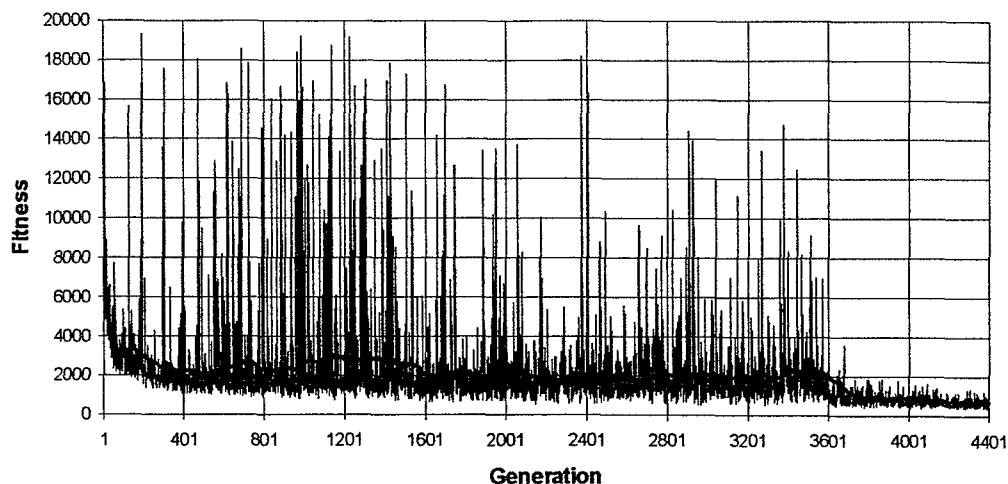


Figure 19 - Least Fit Solution at Each Generation

8. Test Flights

Flight tests in this Phase III effort were performed entirely on the Cal Poly campus using the CALM launch device. These flight tests began very early on in this phase and continued through to the end. Multiple tests were often performed within the same week and turn around within a few hours was demonstrated on more than one occasion. The ability to perform this many tests was a key factor in the success of the project.

Testing performed over roughly the first half of the schedule was primarily devoted to refining the ATRP aerodynamic structure. A simple radio control mechanism was used to guide the parafoil in flight back to the launch area during this development phase. Features such as body length, parafoil deployment techniques, and internal structural elements were refined. Developing the structure to withstand the high acceleration imparted by the CALM was also a major accomplishment during the period. The CALM provided the capability to make many incremental improvements at this time.

It was during this early period too, that CALM launch protocols were further developed. Relationships between air pressure in the CALM storage tanks, vehicle weight and aerodynamics and resultant altitudes achieved were explored. The CALM also underwent one major redesign during this period in order to make it more mobile and easier to set up.

As development continued, more complexity was added to the vehicle until regular flights made with electronics, telemetry and video capture were demonstrated. The optimized autonomous control software was downloaded to the rabbit controller for testing. The BlackwidowAV camera system was installed along with telemetry for transmitting real time video to the ground station laptop. The GPS was loaded and tested in flight. In addition to the video, altimeter data from the rabbit board was also downloaded through telemetry. These "all up" flights were successful and proved the feasibility of the ATRP device. Synchronized, split frame video from the onboard camera and ground based cameras is available on DVD format.

Often multiple flight test objectives of independent systems would be explored on the same flight. Although the bulk of the efforts described above took place in the first part of the Phase III effort, continuous improvement and refinement of virtually all those elements occurred throughout the project.

Flight tests also were useful in determining the limits in capability of the present design. Wind speed is a critical factor in whether the ATRP can successfully complete its mission and our studies have shown that the current design has significant problems in winds of 10 mph or greater. The parafoil glide ratio, glide speed and deploy altitude combine to dictate total flight time of the vehicle. Generally a longer flight time is more desirable, allowing the ATRP to loiter over the area of interest. Loiter time can be extended by increasing deploy altitude and glide ratio or by reducing glide speed. Conversely, increasing glide speed would allow the ATRP to operate in higher wind conditions and cover more ground given that glide ratio and deploy altitude remain the same.

These parafoil aerodynamic issues were addressed in the flight tests by studying the effect of changing the length of the control lines. Shortening the control lines tends to have the effect of increasing both lift in the vertical direction and drag in the forward direction. The combined effect of these forces is to slow the vehicle while maintaining the same glide ratio. At some point, additional shortening of these lines does not result in enough additional lift to compensate for the additional drag and the glide ratio will rapidly degrade. A large number of test flights were partially devoted to optimizing line lengths in order to obtain the best compromise in the tradeoff between flight time and flight speed.

The timing of the deployment of the parafoil also proved to be a critical element in the success of any flight. It was soon discovered that deploying too soon or too late in the projectile trajectory could cause undue strain on the parafoil support lines. It was also noted however that some forward momentum was desirable in order to get the parafoil cells to properly inflate.

9. Conclusions

This Phase III provided a successful conclusion to the development objectives established for the ATRP program. Software for autonomous control was optimized and tested in the onboard electronics suite. Improvements in hardware components included a new parafoil, aerodynamic shell design and parafoil ejection system. The Compressed Air Launch Mechanism was improved to the point that multiple launches could occur in one day. Repeatable flight tests with data transmitted in real time to the ground shows that the system is robust and operating according to design.

Several attempts were made to further develop and exploit this technology through contracts with the Army, Navy, DARPA and private industry. It has been disappointing that to date none of these applications proved successful. There have, however, been a number of gratifying accomplishments in the form of published conference proceedings and pending papers associated with this program. In addition, some encouragement has been received by individuals in the

various government agencies with which we have dealt. We are still hopeful that the right match may be found within government research circles.

The project certainly provided excellent educational experience for the students directly involved in the effort and for use as class materials for the investigators involved. It is assured that even if the ATRP itself does not continue in some form, at least the lessons learned from this project will be expressed in future projects by the individuals involved.

The achievements of the group included ground breaking efforts in both hardware and software design. We would like to thank the representatives from ONR for their support and feedback during reviews of the project. We would also like to especially thank the efforts of Susan Opava for making it possible to achieve our program goals.

References

1. GopalaPillai, S., Tian, L., Beal, J., "Detection of Nitrogen Stress in Corn Using Digital Aerial Imaging", 1998.
2. Johannsen, C.J., "Agricultural Applications of Remote Sensing", 2001.
3. Martin, F. G., "The Handy Board Technical Reference", Gleason Research, 2000.
4. Clark, Kevin, "Sampcode.c"
<http://www.egr.msu.edu/classes/ece482/Teams/99spr/design5/deliverables/code/main.c>
5. Martin, Fred, "Serialio.c" <http://216.239.33.100/search?q=cache:Y3ohOvJ5bI4C:www-isl.ece.arizona.edu/~soccer/Fall2002/ai/serialio.pdf+serialio.c+fred+martin&hl=en&ie=UTF-8>
6. Mulders, Symen "Comm.c" http://clubs.plattsburgh.edu/csc/handy_car/source/comm.c
7. Drushel, Richard F., "Conio.c" <http://handyboard.com/software/contrib/drushel/conio.c>
8. Lang, Kam, "RF Serial Communication for the MIT Handy Board or Motorola 68HC11 MCU"
9. MATLAB, <http://www.mathworks.com>.
10. DeTurris, D., Ervin J. and Alptekin, S., Development of an Autonomous Tactical Reconnaissance Platform, Proceedings of 17th AIAA Aerodynamic Decelerator Systems Technology Conference, May 20-22, 2003, Monterey, California.
11. Cox, E., The Fuzzy Systems Handbook: A Practitioner's Guide to Building, Using, and Maintaining Fuzzy Systems. Boston, MA: Academic, 1994.
12. Combs, William E. and James Andrew, Combinatorial Rule Explosion Eliminated by a Fuzzy Rule Configuration, *IEEE Transactions on Fuzzy Systems*, Vol. 6, No. 1, 1998.
13. Dick, S. and Abraham Kandel, A comment on "Combinatorial Rule Explosion Eliminated by a Fuzzy Rule Configuration" by William E. Combs and James Andrews, *IEEE Transactions on Fuzzy Systems*, Vol. 7, No. 4, pp: 475-477, 1999.
14. Mendel, J. M. and Qilian Liang, Comments on Combinatorial Rule Explosion Eliminated by a Fuzzy Rule Configuration, *IEEE Transactions on Fuzzy Systems*, Vol. 7, No. 3, pp: 369-373, 1999.
15. Weinschenk, J. J., W. E. Combs and R. J. Marks II, Avoidance of Rule Explosion by Mapping Fuzzy Systems to a Union Rule Configuration, *FUZZIEEE*, accepted for publication, 2003.

Bibliography

1. Passino, K.M. and Yurkovitch, S., Fuzzy Control, Addison-Wesley, CA, 1998.
2. Sugeno, M., "Development of an Intelligent Unmanned Helicopter", presentation at the World Automation Congress, May 10-14, 1998, Anchorage, Alaska.
3. Swanson, S., Fuzzy Control of the Shuttle Training Aircraft, Applications of Fuzzy Logic Towards High Machine Intelligence Quotient Systems, Prentice Hall, NJ, 1997, pg. 387.
4. Fournell J. and S. E. Alptekin, "Fuzzy Logic Fly-by-Wire System", Proceedings of World Automation Congress, May 10-14, 1998, Anchorage, Alaska.
5. Ervin J. and S. E. Alptekin, "Fuzzy Logic Control of a Model Airplane", Proceedings of the 1998 IEEE International Conference on Systems, Man, and Cybernetics, October 11-14, 1998, San Diego, California.
6. Alptekin, S.E., Fournell, J. and Ervin, J. "An Investigation of Fuzzy Logic Control of a Complex Mechatronic Device", Proceedings of the 2nd International Conference on Recent Advances in Mechatronics, ICRAM'99, May 24-26, 1999, Istanbul, Turkey.
7. Wind Dance Parafoil Kite <http://www.seattleairgear.com/>
8. Guided Parafoil Air Delivery System-Light, <http://www.fas.org/man/dod-01/sys/ac/equip/gpads-1.htm>
9. Learning and soft computing : support vector machines, neural networks, and fuzzy logic models , Kecman, V. (Vojislav), Cambridge, Mass.: MIT Press, c2001.
10. Advanced fuzzy systems design and applications, Yaochu Jin, Heidelberg ; New York : Physica-Verlag, 2003.
11. Soft computing: integrating evolutionary, neural, and fuzzy systems, Andrea Tettamanzi, Marco Tomassini. Berlin; New York : Springer, c2001.
12. Fuzzy logic techniques for autonomous vehicle navigation, Dimiter Driankov, Alessandro Saffiotti, editors.Heidelberg ; New York : Physica-Verlag, c2001.
13. Intelligent control systems using soft computing methodologies, edited by Ali Zilouchian, Mo Jamshidi. Boca Raton, Fla. : CRC Press, c2001.
14. Soft computing agents: new trends for designing autonomous systems, Vincenzo Loia, Salvatore Sessa, editors.Heidelberg ; New York: Physica-Verlag, c2001.
15. Introduction to neuro-fuzzy systems / Robert Fuller, Heidelberg ; New York: Physica-Verlag, c2000.
16. Soft computing in mechatronics, Kaoru Hirota, Toshio Fukuda (eds.), Published: New York : Physica-Verlag, c1999.
17. Soft computing for intelligent robotic systems, Lakhmi C. Jain, Toshio Fukuda, (eds.), Heidelberg; New York : Physica-Verlag, c1998.

Development of an Autonomous Tactical Reconnaissance Platform

D.J. DeTurris, J.C. Ervin and S.E. Alptekin

Submitted to the

AIAA Journal of Aerospace Computing, Information and Communication

November 2004

Acceptance Pending

Development of an Autonomous Tactical Reconnaissance Platform

Dianne J. DeTurris¹

Cal Poly State University, San Luis Obispo, CA 93407

Jon C. Ervin²

Apogee Research Group, Los Osos, CA 93402

and

Sema E. Alptekin³

University of California at Berkeley, Berkeley, CA 94720-1774

&

Cal Poly State University, San Luis Obispo, CA 93407

In this paper, an application of Fuzzy Logic in the control of an autonomous parafoil surveillance platform is described. A unique methodology (Combs' method) was employed to reduce the common problem of 'exponential rule expansion' encountered in Fuzzy Control Systems. The use of this method also simplified the tuning process of the fuzzy system by requiring the optimization of only the membership functions and not the rule base. Modularity and simplicity of design were further enhanced by adopting a layered fuzzy logic architecture. The fuzzy system was optimized over a wide range of simulated flight conditions, providing a simple yet robust means of controlling the vehicle. Hardware limitations in terms of memory, computational speed and cost were critical factors driving the need for a simple yet robust control algorithm. This autonomous parafoil, developed under a grant from the Office of Naval Research, was designed to follow a predetermined flight pattern from altitudes of 350 meters or more down to the ground. Flight tests of a rocket-launched prototype device and simulation in the Matlab/Simulink software environment have verified that this fuzzy logic control method performs to the required specifications.

I. Introduction

THE reconnaissance vehicle that is the subject of this research study was given the somewhat unwieldy name Autonomous Tactical Reconnaissance Platform or simply ATRP. The main hardware elements of this device consist of a 3.5 square meter parafoil, an electronics payload with a protective aerodynamic housing and a launch system. The ATRP is designed to fill the need for an airborne reconnaissance device that is highly portable, low cost, easy to use, rugged and can be rapidly deployed. It is envisioned that this device would be used as a rapid response reconnaissance vehicle to perform short-range missions including locating enemy mortar positions and scouting in urban and/or rugged terrain. Training requirements for the ATRP are minimal since it is completely autonomous in flight, however a manual override exists for added user flexibility. Design requirements called for a re-usable flight vehicle and electronics that weighed less than 5 lbs. and cost less than \$1,000 in parts.

Conceptually, the ATRP can be launched in a number of ways including; small rocket launch, artillery shell or even tethered flight. Both rocket launch and compressed air guns have been used to launch the device in the current development effort. The vertical launch capability is a distinct advantage in environments where trees or buildings make landing and takeoff impossible for most micro-flyer concepts.

¹ Associate Professor, Aerospace Engineering Department, Bldg. 13, Room 257, Senior Member of AIAA.

² Senior Researcher.

³ Visiting Scholar, Berkeley Initiative in Soft Computing, Electrical Engineering and Computer Science Department, University of California at Berkeley, and Professor, Industrial and Manufacturing Engineering Department, Cal Poly State University, San Luis Obispo, Bldg. 26, Room 100.

Providing a close range, real-time view of the immediate surroundings can also be valuable in a number of civilian applications in the fields of land management and farming. Several researchers have found that aerial data can be of great value to farmers in evaluating the health and maturity of crops in the field [1,2]. Current collection methods such as satellites and manned aircraft are expensive, geographically imprecise, and frequently unavailable at critical times in the growing season. The ATRP, equipped with a Global Positioning System and the appropriate sensors overcomes these obstacles and would allow farmers to perform a more personalized crop evaluation. The ATRP could also aid in search and rescue missions such as in forest fires or avalanche.

In military applications, ATRP is designed to provide personnel in the field with a means of obtaining surveillance data of the near environment in a safe, timely and cost effective manner. The ATRP is launched to low altitude (typically <350 meters) and flies a pre-selected course while transmitting sensor data to the user on the ground. During flight, the device is fully autonomous allowing the user to concentrate on the sensor data (i.e. IR and/or visual imagery) being communicated to a hand held receiving device. The user can select one of several pre-programmed flight patterns and launch the device, all in a matter of seconds.

A parafoil design was chosen for several key advantages over rigid structure alternatives. It is lightweight, easily compacted and deployed, and very stable in flight as shown in the video. A parafoil is also much more rugged than rigid structures and will continue to perform well with minor rips and holes in the fabric canopy. Turns are made by pulling on either a left or right hand control string, making it much simpler to control than rotary or fixed wing craft. The one disadvantage to this design is the lack of a power plant to keep the craft aloft. This limits the user to a total of 5 minutes or less of surveillance time. However, the intended mission for this device is to respond to a known threat or reconnoiter an area soon to be entered and the limited dwell time over the target is not a serious drawback in this scenario. Additional time over the target area can be achieved through recovery and re-launch of the device or launching additional units.

An autonomous, fuzzy logic flight controller was chosen as the means to pilot the parafoil after launch and deploy. The controller executes a pre-selected program of flight maneuvers as it glides in the descent phase, which may include a return to the launch point if user safety permits. A fuzzy logic control method is employed because of advantages it has in fault tolerance and graceful response to missing and/or noisy sensor input. A unique methodology (Combs' method) was employed to reduce the common problem of 'exponential rule expansion' encountered in Fuzzy Control Systems. The use of this method also simplified the tuning process of the fuzzy system by requiring the optimization of only the membership functions and not the rule base. Modularity and simplicity of design were further enhanced by adopting a layered fuzzy logic architecture.

In the next section, we provide a brief background on Fuzzy Control and Combs method. Development of the Fuzzy Logic Architecture for the ATRP application is presented in the third section, followed by a discussion of the simulation and optimization of the control algorithm. In the fourth section, the design and fabrication of a prototype electronics package and current work on an upgraded system are described. The results of flight tests and conclusions are reported in the final two sections.

II. Fuzzy Control

A fuzzy logic control algorithm provides the decision making strategy for the ATRP. Attributes of fuzzy logic that make it appealing for this project are the ability to model nonlinear functions, robustness in the face of imprecise input and ease of code generation. Fuzzy logic algorithms are intuitively easy to understand and allow the user to encapsulate the experience of experts in an efficient manner. Fuzzy logic controllers are seeing much more widespread use in a wide range of industrial and consumer devices (i.e. washing machines, automobiles and microwave ovens). Many of the references cited at the end of this article can give the reader a much more comprehensive insight into fuzzy logic fundamentals [3-13].

Developed by Lotfi Zadeh in the early 1960s, Fuzzy Logic is a paradigm for modeling imprecision often found in engineering applications [14]. Zadeh recognized that, although computers operate in a world of ones and zeros, the real world is more analog in nature [15-16]. While traditional computing approaches require a rigid classification of objects into one category or another, fuzzy logic allows for partial membership of an object into multiple categories. This generalization to crisp logic allows for a more flexible, human like decision process and can be especially effective in systems where a closed form mathematical solution does not exist.

A simple example of this technique can be shown in the determination of a comfortable water temperature in drawing a bath. Typically bath water temperature would not be characterized in a binary fashion as hot or cold, but as a range between hot and cold. Indeed, the notion of what is hot, cold and just right will vary among individuals and environmental circumstances. Although our description of an environment may be imprecise, there is still potentially useful information contained in these descriptions. This information is ignored by traditional methods but can be captured in the fuzzy logic paradigm.

Figure 1 illustrates the three basic steps in the fuzzy logic decision-making process. Crisp inputs, such as a temperature reading of 40.3 degrees C in the bath water example, are presented to the fuzzification block. Inside this block crisp inputs are transformed into their respective fuzzy representation. These fuzzy variables are evaluated by the inference engine using the knowledge base, which typically consists of a number of fuzzy membership functions and rules governing the relationship between input and output variables. The fuzzy output is then put through a defuzzification process to obtain a crisp output.

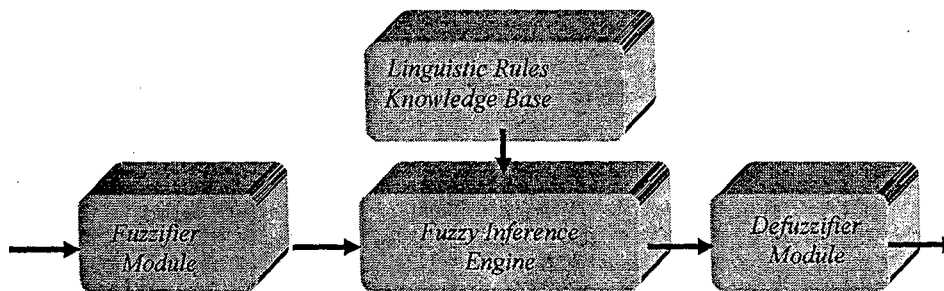


Fig. 1 The basic steps in the fuzzy logic decision-making process.

One of the disadvantages of a fuzzy logic algorithm is what is known as “exponential rule expansion”. In general, each input parameter has a number of associated fuzzy membership functions. In the typical fuzzy algorithm, the rule base is created through all possible combinations of the input fuzzy sets. In the bath water example, two inputs – “Water Temperature” and “Air Temperature”, are combined to form rules as shown in Fig. 2. If these two inputs have three input membership functions (MFs) each, the total number of rules generated are: 3 MFs for variable 1 x 3 MFs for variable 2 = 9 rules (three of which are shown in Fig. 2). This system of rules works well for a small two input problem, but as the number of inputs and/or corresponding membership functions increase linearly, the number of rules increases exponentially. This is a problem that has been encountered by many researchers as their fuzzy logic applications became more complex. Several solutions have been proposed in the recent literature [17-20]. One of the simpler and more promising solutions has been developed by W. Combs. An excellent introduction to Combs’ method is provided in Cox [21].

If bath water is “hot” and air temperature is “cold” then flow is “No Change”
If bath water is “warm” and air temperature is “cold” then flow is “hot”
If bath water is “cold” and air temperature is “cold” then flow is “hot”
 •
 •
 •

Fig. 2 Rules for Two Input Bath Water Temperature Control.

Combs calls the standard fuzzy logic formulation the Intersection Rule Configuration (IRC) because rule antecedents are formed through the intersection of the membership sets of the input variables. In the bath water example, the intersection of bath water is "hot" and air temperature is "cold" in the antecedent implies the consequent flow is "no change". Combs' alternative to the IRC formulation is the Union Rule Configuration (URC). Rules in the URC are formed by the union of implications that have only a single element in the antecedent. URC rules for the bath water example would be formed as shown in Fig. 3.

If bath water is "hot" then flow is "cold"
If bath water is "warm" then flow is "no change"
If air temperature is "cold" then flow is "hot"

•
•
•

Fig. 3 Rules for Two Input Bath Water Temperature Control.

Combs does emphasize that there may not be a simple transformation from a traditional rule base to a URC rule base. The construction of the Combs' URC should be started from scratch with care taken in determining the input variables to use and in designing membership functions for those variables. He does assert that a URC, created with certain restrictions in mind, will model the same solution space to the same degree of accuracy as the traditional IRC. The restrictions on the construction of the rule base and membership functions are not particularly onerous and violating them does not necessarily invalidate a practical implementation of the method. A detailed discussion of these restrictions and a method for dealing with them if required can be found in a series of published commentary and clarification [22-26].

At first it may seem counter-intuitive that this simple change results in a dramatic reduction of rules. The effect of Combs' formulation is that there is one rule for each membership function of each input variable. When a new variable is added, the existing rule base will likely remain the same and only rules for the new membership set need to be added. To illustrate the savings, suppose you have a fuzzy system of 5 inputs with 7 membership functions each, Combs method will have only 35 rules ($5 \times 7 = 35$) rather than the 16,807 (7^5) rules of the conventional technique.

In addition to the advantage of rule reduction, the URC also makes it possible to add inputs incrementally without creating the need for a total reformulation of the rule base. Several authors have performed research in creating a modular, multi-layered fuzzy architecture. One of the benefits of this technique is that it allows the designer to build functionality, as new modules are added, without redesigning the rule base for each of the existing modules. Typically, a higher level, governing module, needs to be completely reformulated to blend the output of the new lower level module with that of other modules at the same level. The URC can simplify this blending process since it makes it possible to add rules to the governing module without the need to reformulate the entire rule base.

The breakthrough that Combs has made has been very beneficial in this current project, where capability has increased incrementally throughout the design process. On the other hand, the theoretical restrictions that Combs has described for his method have not been a significant factor in the performance of the controller. Indeed, in previous research efforts at Cal Poly we have found that these restrictions can be relaxed and still provide good results in practical applications [27-31].

III. Development of the Fuzzy Logic Architecture

The process of developing the fuzzy logic modules was accomplished in stages throughout the life of the project. In the initial phase, a general plan was developed for a modular control system and work was focused on developing the electronic hardware and lower level software control capabilities. Subsequent phases of the project were devoted

to increasing both hardware capability and developing higher functions in the software. The modular structure of the fuzzy system was critical in allowing the project to proceed smoothly with increasing complexity in the overall design.

Due to the compressed schedule of the project, software development and hardware implementation were taking place concurrently. The first fuzzy logic software module developed was designed to provide the vehicle with the ability to follow a desired compass course. At the same time two very different compass models were purchased for testing with the hardware. One compass was very expensive and had the ability to compensate for tilt and nearby magnetic anomalies. The other compass was one-tenth the cost, but much less accurate and lacked any compensation capabilities. Through the analysis it was eventually determined that the fuzzy logic algorithm was robust enough to allow us to use the much cheaper compass with acceptable performance. The cheaper compass also opens up the possibility of using multiple compasses in an operational vehicle, thus increasing redundancy in the design and survivability of the system.

The first step in developing the course-following capability was to determine what inputs the fuzzy logic algorithm would need. Conceivably, it seemed possible that a single input, the angle difference between some predetermined desired heading and the true heading as measured by the compass, would be the only input needed to steer the ATRP to the desired heading. The desired course heading could be achieved simply by generating control commands that would drive this angle difference ($\Delta\theta$), to zero throughout the flight.

It was expected and soon confirmed that $\Delta\theta$ alone was insufficient to provide good course-following capability. Problems of overshoot and oscillation were too extreme to be considered acceptable for the ATRP application. A second input for the fuzzy logic module was produced by differentiating $\Delta\theta$ with respect to time. The addition of this angular velocity input was sufficient to provide the damping needed to bring both overshoot and oscillations within acceptable limits. Figures 4a and 4b provide a simulation comparison of the performance of the control algorithm with one and two inputs, respectively. These figures plot the ground track of a simulated parafoil flight with units given in meters along each axis. In these simulations the controller is directed to fly parallel to the X axis in the positive direction, perform a 180 degree turn and fly parallel to the X axis in the negative direction. The simulation begins with the vehicle flying a heading of 25 degrees above the X axis. Without the angular velocity input (Fig. 4a) the controller begins to oscillate out of control and cannot perform the desired 180 degree turn at all. In Fig. 4b stable flight pattern is shown with the simulated ATRP traveling 450 meters and executing a 180 degree turn to return to the launch area. A third input, angular acceleration, was also considered as a further refinement to the flight controller program. This third term has so far proven to add little value in improving accuracy, but it is maintained in the software as a hedge against possible future usefulness as the system continues to be developed.

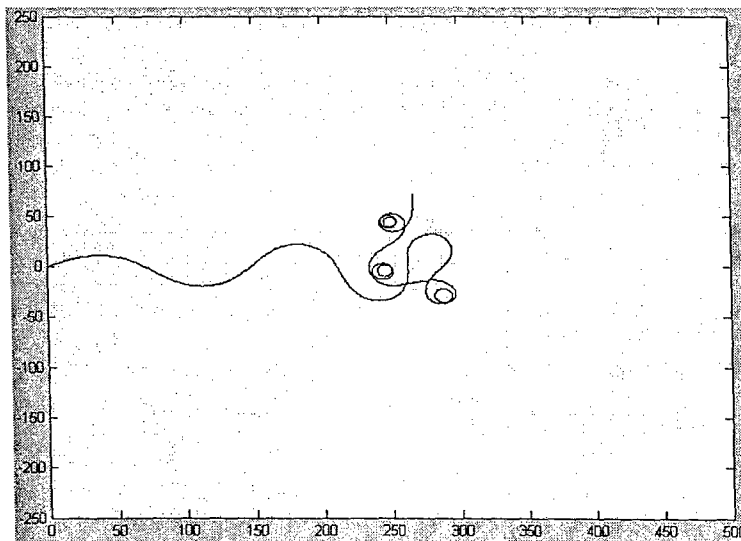


Fig. 4a Standard Fuzzy Control with one input.

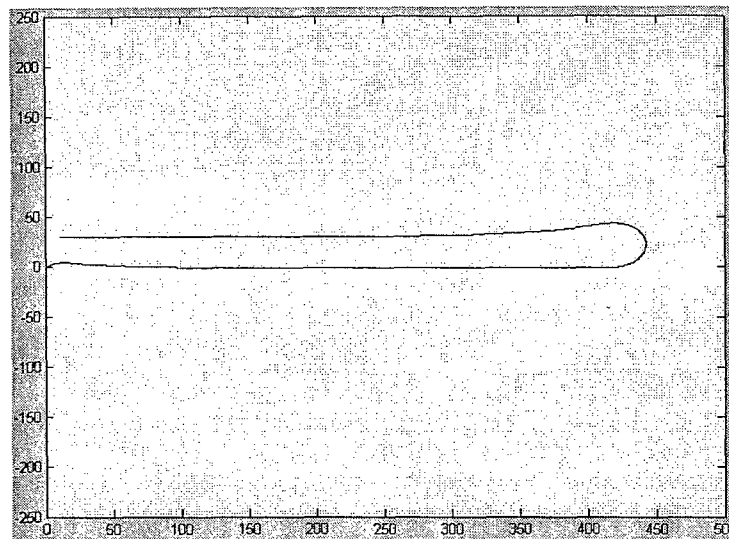


Fig. 4b Standard Fuzzy Control with two inputs.

The next step in the process was to develop membership functions for the three inputs ($\Delta\theta$, angular velocity and angular acceleration) and the one output (control line pull). The magnitude and sign of the output determines the magnitude and direction of the pull on the control lines, which in turn determined the magnitude and direction of turns of the ATRP.

Simple triangle functions were chosen for the membership sets of the three input variables and singletons were used for the output set. These choices were driven primarily by the desire to minimize memory storage and maximize computation speed. Despite the use of such simple shapes for the membership functions, the control surface for this system can still be quite complex. Singleton membership functions are a zero order form of a Takagi-Sugeno-Kang (TSK) fuzzy construct [29]. Defining the output membership functions in this manner simplifies the defuzzification process and further reduces computational requirements.

Combs method was used in the construction of the fuzzy algorithm, thus rules were automatically defined when the number of membership functions was determined. This helped to narrow the optimization task to the design of the input and the output membership functions. Here again the number of membership functions for each input was driven by a desire to keep the number low for computational reasons, while providing sufficient degrees of freedom to obtain acceptable performance. Once the shape and number of the membership functions had been established, the task that remained was to optimize their spacing and width for each fuzzy variable.

Five triangular membership functions were chosen for both $\Delta\theta$, and angular velocity, while only three were used for angular acceleration. In a standard fuzzy logic algorithm, a maximum of $5 \times 5 \times 3 = 75$ rules would have been required to fully define all possible combinations. However, following the principles of Combs method only 13 rules were needed to define the rule base. Figure 5 shows the same simulation run as was performed for Fig. 4b except that the standard fuzzy rules have been replaced with the much fewer Combs method rules. In this example and in an exhaustive series of simulation test runs, Combs method rules were shown to perform equally well as the standard fuzzy rule structure.

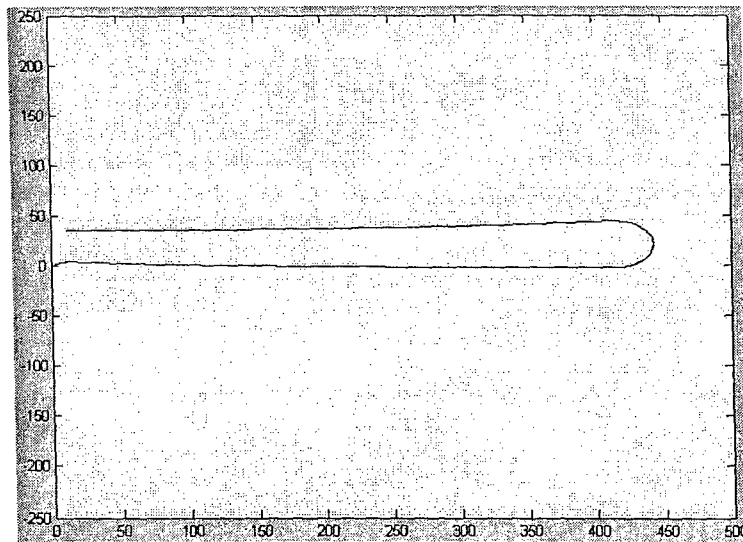


Fig. 5 Combs fuzzy control with two inputs.

The course-heading module described above cannot provide point-to-point navigation in a real world vehicle. Specifically, it will not maintain a desired ground track in the presence of cross winds and asymmetries in the vehicle aerodynamics. Figure 6 shows the effect of a cross wind on the ground track of a vehicle equipped only with the course-heading module. This displacement downwind is similar to what would happen to a boat crossing a stream if it is pointed directly across the current. Just as the boat must be pointed upstream in order to arrive at a point directly across the stream, so to must the parafoil be pointed slightly upwind to arrive at the desired destination. An additional fuzzy logic module had to be constructed as a front end for the course-heading module in order to provide proper navigation in ground based coordinates.

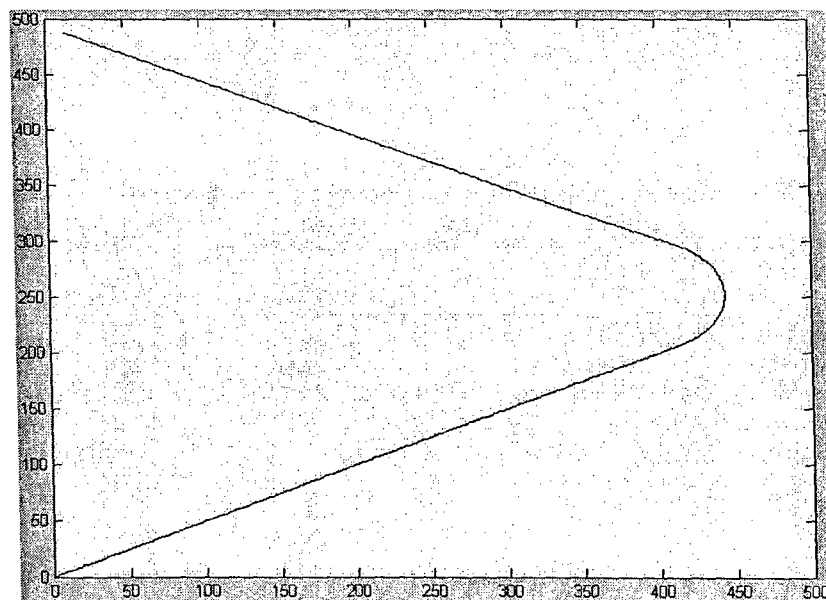


Fig. 6 Combs method with two inputs and 5m/s cross wind.

The purpose of the layered structure of these two modules is somewhat different from that described by other researchers. Raju et al. [30] use a hierarchical structure to reduce the number of rules required by the fuzzy algorithm. Outputs from the intermediate layers of this type of structure may have very little intuitive meaning to the human expert. Tunstel et al. use multiple layers to control so-called primitive behaviors with higher-level composite behaviors [31]. In contrast, here the top layer acts more like a pre-processor for the lower, course-heading layer.

The input to the course correction layer is provided by a Global Positioning Satellite (GPS) system locator unit. When four or more satellites are in view, the GPS unit provides absolute coordinates in longitude and latitude for the vehicle at periodic intervals. The controller uses the current position as provided by the GPS unit along with coordinates of the vehicle start position and destination to calculate a cross range component and angle offset from the ideal path as shown in Fig. 7. These two values along with the derivative with respect to time of the cross range component are used as inputs to the course correction layer.

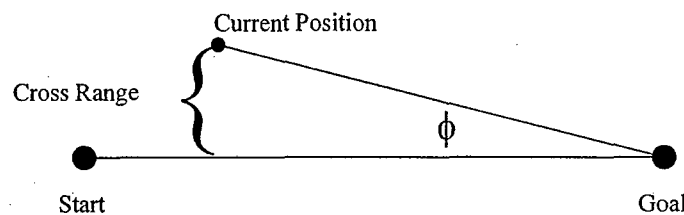


Fig. 7 Inputs for Course Correction module.

The course correction layer has seven membership functions for each of the three input values. A typical set of membership functions for the Cross Range input is shown in Fig. 8. In this figure the domain of the membership functions runs from a value of -100 meters designated "Negative Large" to +100 meters designated "Positive Large". Any input that falls outside of the extreme values is truncated to the maximal value of the domain for purposes of the fuzzy logic computation. Values in between these two extremes are designated "Negative Medium", "Negative Small", "Zero", "Positive Small", and "Positive Medium". The truth value for each membership function is read on the vertical axis as a number from 0 (false) to 1 (true) with the possibility of taking on any value in between these two extremes. A complete rule base in a standard fuzzy system would require 343 rules, however using Combs method only 21 rules are needed. The diagram in Fig. 9 shows the relationship of the two fuzzy systems and how they combine to provide an output command to the control actuators. By dividing the system into modular sub-units, logic problems can be easily traced and capability added with relative ease. The addition of the course correction layer allows the vehicle to fly a desired ground track despite the presence of a cross wind as shown in Fig. 10.

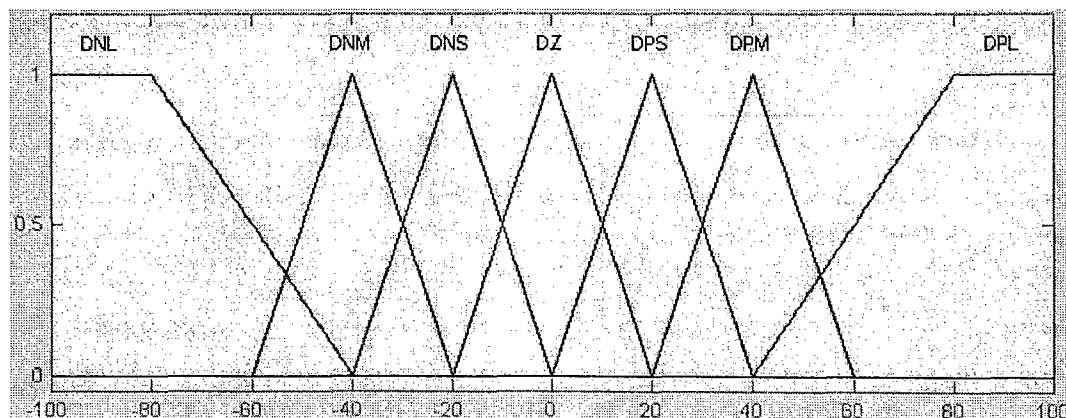


Fig. 8 Membership functions for Cross Range input.

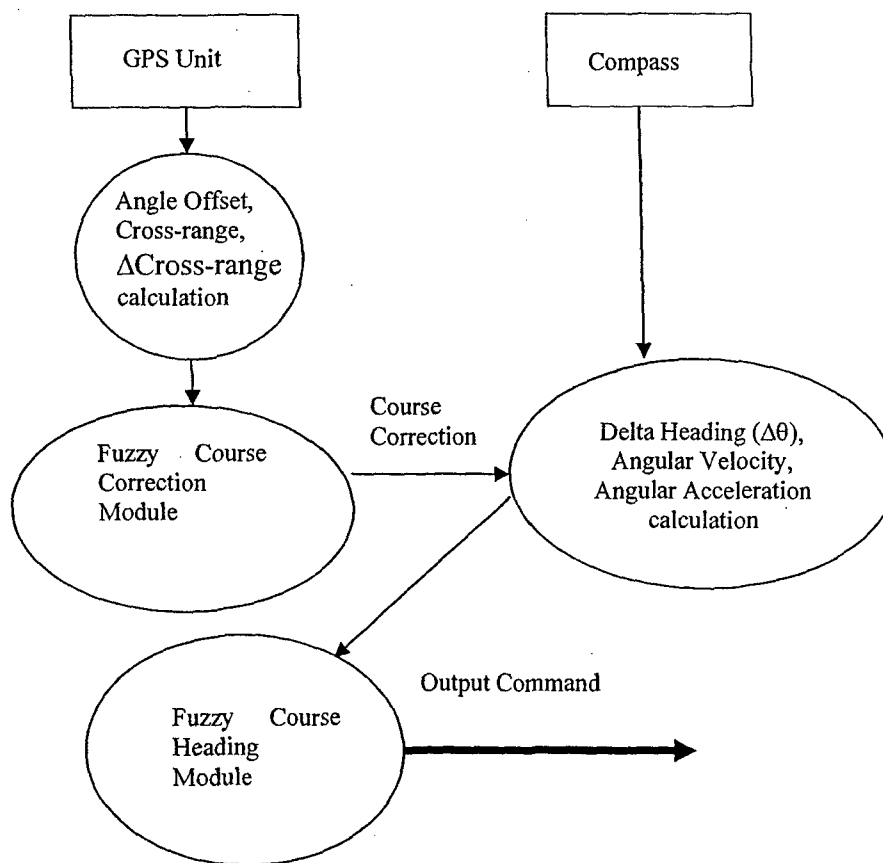


Fig. 9 Fuzzy Layered Structure.

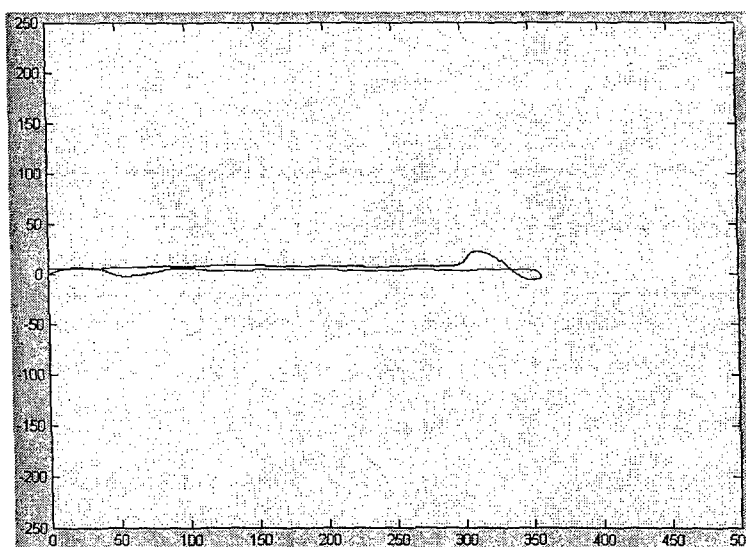


Fig. 10 Combs Method with Two Inputs and 5m/s Cross Wind and GPS Correction.

An alternative guidance scheme to the multi-layered structure employed here would have been to use input from a GPS unit alone to guide the vehicle to its waypoint destinations. Theoretically, this solution seems quite feasible and even less complicated since it eliminates the need for a compass altogether. This GPS option was not seriously pursued for reasons of overall system reliability. The ATRP is designed to be a quick reaction, work anywhere device, including conditions where the skies may be partially obscured by buildings, trees, atmospheric disturbances and signal jamming. In such cases, satellites may be obscured and the GPS device may function only intermittently at best. As it is designed, the vehicle can be guided by the compass alone and will make use of even intermittent input from the GPS unit. The compass also is a much simpler device and is expected to have a much greater mean time between failure (MTBF) rate. The compass is also capable of providing a continuous output that has proven to be essential during high turn rate maneuvers. The high update rate helps the fuzzy controller to minimize turn overshoot and oscillation effects.

The controller response has proven to be quite robust even when electronic noise, instrument inaccuracies and gusting winds are introduced into the simulation. These simulation runs were performed in the Matlab/Simulink software environment while the fuzzy logic modules were developed in the Matlab Fuzzy Logic Toolbox. It is this simulation capability that made it possible to refine the control software and thus drastically reduce the number of test flights necessary for control optimization.

IV. Simulation and Optimization

The parafoil is inherently a very simple and stable flight vehicle. Directional control is provided by pulling on one of two control lines with connections to points on either side of the parafoil wing. Simulation of the flight of the parafoil from first principles is still a daunting task even for such a simple control mechanism. The large number of unknown, and likely unknowable, factors makes an exact simulation impossible. Unknown factors include variations in wind speed and direction, sensor inaccuracies, controller inaccuracies and physical imperfections affecting the aerodynamics of the vehicle. The challenge then becomes one of how to use simulation to design an effective control algorithm with so much uncertainty and inaccuracy in the simulation model.

One factor that helps mitigate the uncertainty in the simulation is the robust nature of the fuzzy logic control mechanism. Parameters within the simulation including wind speed, wind direction, wind gusts, electronic noise, instrument inaccuracy, initial heading, parafoil speed and parafoil turning rate have all been varied over their respective, expected ranges. The fuzzy control algorithm has proven to be capable of performing well over a wide range of values for each of these factors. Thus, the expectation is that although the simulation may be lacking in absolute accuracy, it does cover the range of values that would be encountered by actual flight hardware.

Despite its limitations, the fidelity of the simulation has improved as results of flight tests have been incorporated into the simulation model. Parafoil flight speed, turn rate versus control line pull and lift over drag (L/D) ratio can all be derived from onboard instrumentation and ground based measurements. These refined parameters have then been incorporated into the simulation model, which in turn is used to improve the flight vehicle control algorithm. This cycle of continuous improvement has allowed the development of the prototype vehicle to meet an aggressive series of scheduled milestones.

One simplifying assumption made in the simulations was that the parafoil flies at a constant speed with no need for pitch axis control. This assumption is at least valid to a first degree of approximation and was not a limiting factor in optimizing the control algorithm. The objective of the simulation was not to optimize the aerodynamic qualities of the parafoil platform and therefore only a rough degree verisimilitude was necessary to achieve our goals for the simulation. The goals for the simulation have been to:

- determine the minimum number of sensor inputs to achieve satisfactory, stable control
- determine the most effective sensor inputs for achieving control
- optimize various fuzzy logic components (i.e. membership functions, rule base, etc.) under ideal conditions
- test/re-optimize the algorithm under simulated sensor and environmental sources of imprecision (i.e. sensor electronic noise, wind gust disturbance, wind drift)

Figure 11 shows a block diagram of the various software components used in the simulation and optimization process.

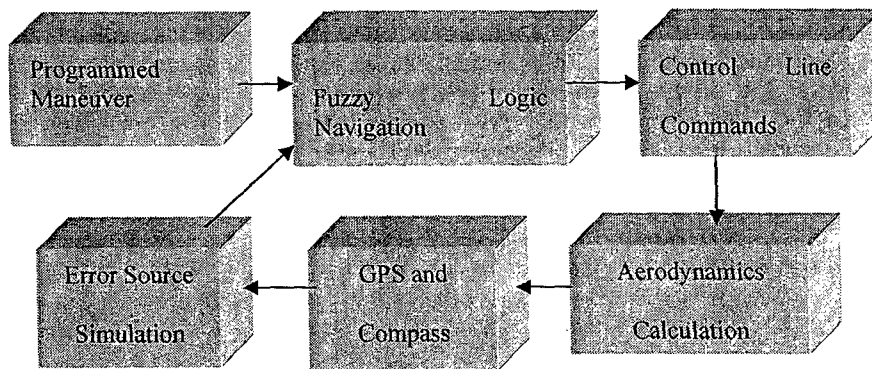


Fig. 11 Simulation Block Diagram.

Following the block diagram in Fig. 11, the simulation begins with the selection of a desired flight path. The difference between the desired and actual heading ($\Delta\theta$) along with the first and second derivatives of this difference are supplied to the course-following fuzzy logic module. Any adjustments from the course correction module are added to $\Delta\theta$ and the controller uses these inputs to produce a control line pull command. The effect of the control line pull command on the aerodynamic performance of the parafoil is computed and an incremental parafoil heading vector is determined. This heading vector is used to update the ground track map and to produce a simulated GPS measurement. Any simulated electronic errors are combined with the heading vector. The current GPS measurement along with the start and goal coordinates are used to compute the inputs for course correction module. The output from the course correction module completes the loop and the simulation runs for the length of an entire simulated mission profile.

Initial optimization runs were performed assuming ideal conditions and in later analysis error sources such as electronic noise, wind gusts, instrument bias errors, and random heading after initial deploy were added. One of the more critical error modes that required evaluation was the effect of compass bias errors on system performance. The effect of this error contributor was the determining factor in the selection between the more accurate TCM2-50 or less expensive Dinsmore compass. Comparison of simulation runs such as those shown in Figures 12a and 12b were used to determine that the Dinsmore compass would provide adequate accuracy for the ATRP project. The figures show the effect of a constant 3 degree bias in the compass reading on the vehicle ground track. A variable error that was dependent on compass heading was also tested in the simulation and proved to be less of a factor than even the constant bias condition. The effect of compass bias error was ameliorated by the GPS driven Fuzzy Course Correction module. Without this module, the bias error would have caused a constant drift in the ground track similar to that shown in Fig. 6 for a cross-wind condition.

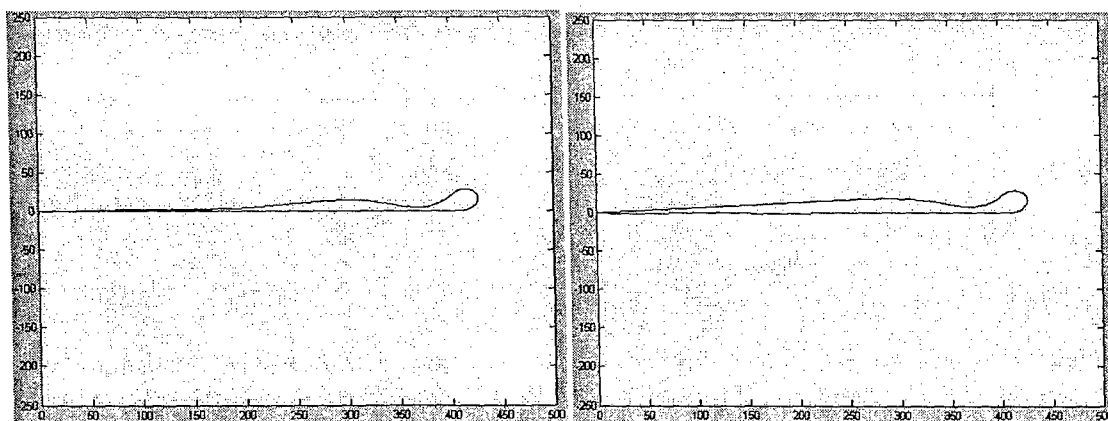


Fig. s 12a & 12b Without and With 3 Degree Compass Error, Respectively.

The shape of the vehicle trajectory in Fig. 12a suggests that additional tuning of the fuzzy logic modules may yield even better results. The simulated vehicle appears to over correct slightly when coming out of the turn, where instead a smoother transition to straight flight would be preferred. Regardless, it is apparent that a bias in the compass reading has a minimal effect on the performance of the system.

Electronic noise was modeled as a simple normal distribution of white noise. Despite the havoc this error mode played with the calculated derivatives of the instrument inputs, the fuzzy modules responded well even when no data smoothing was employed. Simulation runs performed with much higher levels of noise than were observed from bench tests of the instruments still showed excellent vehicle control.

Deployment angle is an error mode that occurs as the result of a random vehicle orientation that occurs during initial deployment from its altitude delivery mechanism. However the vehicle arrives at altitude; either by rocket, compressed air canon, artillery shell or air drop; it is likely to begin its mission at some arbitrary angle to the desired direction of travel. The guidance system must get the vehicle traveling in the desired direction as quickly as possible due to the limited amount of flight time available to the unpowered parafoil. Fortunately the fuzzy controller can be tuned to minimize overshoot and oscillations, thus extending as much as possible the ground surveillance capability of the vehicle.

Unlike cross-wind conditions, wind gusts can act asymmetrically on the vehicle to cause it to make unpredictable turn maneuvers. As an error source, the frequency of gusts is expected to lie somewhere between that of electronic noise and the near constant bias of cross-winds. Gusts were modeled as a sinusoidal function of varying amplitude over the course of a simulation run. Gust magnitudes of up to 50% of vehicle velocity and varying frequencies were simulated and these effects still allowed the vehicle to perform within acceptable limits. Fig. 13 shows a worst case scenario of all of the error sources described above.

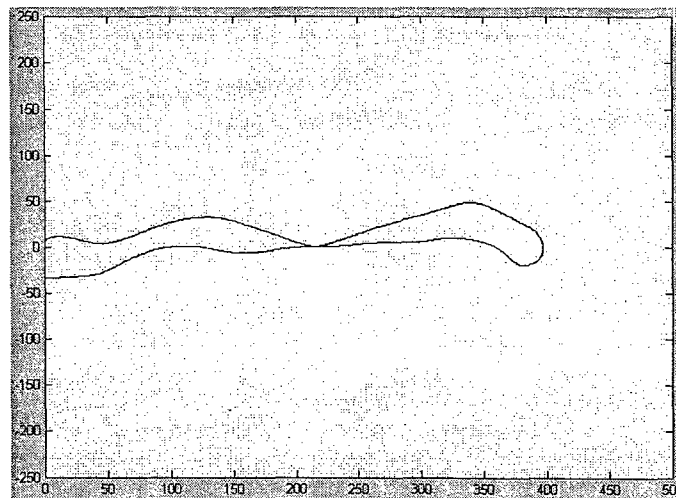


Fig. 13 Worst Case Scenario of Various Error Sources.

Compared to the ideal case shown in Fig. 12a, this trajectory more closely resembles that of a drunken sailor. The main contributing error source is the variability in the strength of wind gusts. However, despite the degradation in performance seen in the figure above, this trajectory would likely be considered "good enough" to accomplish the reconnaissance mission.

The majority of the analysis effort was devoted to evaluating various fuzzy architectures under the non-ideal conditions described above. The membership functions for both fuzzy modules were adjusted to account for these perturbations and the resulting system produced was found to be capable of handling the most extreme conditions applied. All of these adjustments were performed manually and it is expected that this tedious process will be replaced in the future with an automated procedure.

V. Electronics Hardware

The prototype electronics package that was flown on all the early test flights is shown in Fig. 14. The board at the top of this figure holds the TCM2-50 compass manufactured by Precision Navigation Inc. This compass includes a tilt sensor that allows the unit to provide $\pm 1.5^\circ$ accuracy when tilted up to 50° from the horizontal plane. The compass can also be calibrated to compensate for magnetic distortions induced by close proximity to ferrous materials and magnetic fields. In calibration mode, the compass is tilted and rotated through one or more full circles thus allowing the compass to collect magnetic field data in three dimensions. The three dimensional map of the distorting fields is computed and stored in the compass electronics.

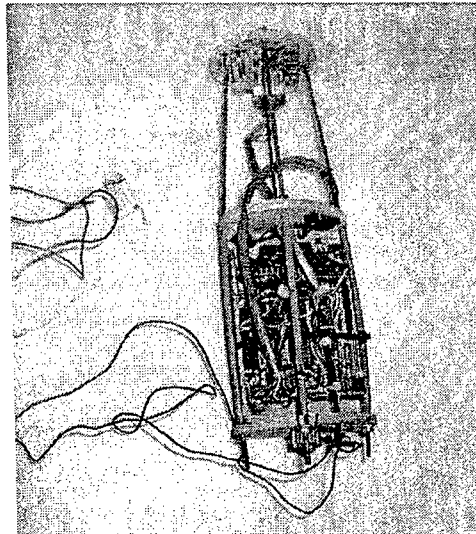


Fig. 14 Prototype Electronics Package.

The TCM2-50 performed very well in bench tests and in flight testing, however the relatively high cost of the unit prompted the search for a replacement. The Dinsmore Analog Sensor 1655 proved to be an adequate replacement for a fraction of the cost. Once a circuit had been developed to broaden the dynamic range, response curves were painstakingly mapped and the accuracy of this unit was brought to within $\pm 3^\circ$. Simulations have shown that this degree of accuracy is sufficient for the fuzzy logic controller to steer the vehicle on the desired flight path.

The electronics shown in the bottom half of the picture consists mainly of a Handy Board microcontroller developed at MIT [32]. The Handy Board has a clock speed of 2MHz and has 32 kilobytes of battery backed RAM for user programming. When combined with the optional Expansion Board as shown, it has a robust array of digital and analog data ports. In addition, the Handy Board has provision for 6 servo motor output ports and an RS232 serial port. This device provided excellent service during the bench testing and prototype flight testing.

This prototype electronics package also included an ADXL 190 accelerometer produced by Analog Devices Inc. This device, capable of measuring acceleration up to 100 g's, provided experimental verification of the g profile of the ATRP in flight. An accelerometer may play an essential role in the final design as a means to determine optimum deployment altitude and as a means of detecting landing touchdown. In the prototype flight tests, deployment was detected and communicated to the Handy Board microcontroller by means of a simple magnetic switch. The two halves of this switch were located on either side of the separation seam.

A vastly improved electronics package is currently under development. This new board has been developed in-house and is faster, smaller, less expensive and suits the specific requirements of the ATRP project. Most importantly, the new electronics suite will be much more energy efficient and require will much smaller batteries. The smaller battery requirement is expected to shave as much as 50% of the weight off of the electronics package as a whole.

The CPU of the new unit is provided by a Rabbit 3000 microprocessor embedded in a Rabbit Model RCM3400 core module. The microprocessor operates at 29.4 MHz which is a 15-fold increase over the Handy Board used in the prototype. The RCM3400 also has 16 times the memory storage than was available in the prototype device. This unit also has more than adequate numbers of input and output ports for interfacing with the variety of sensors that will be incorporated into the advanced electronics suite. Sensors incorporated into the expanded electronics package include;

- a GPS module capable of updates every .25 second
- a pressure sensor for altitude measurements with 3 meter resolution
- a separate pressure sensor for air speed measurement
- a yaw rate gyro capable of measuring slew rates up to 150 deg/sec
- a low cost magneto-inductive sensor for compass measurements
- an accelerometer capable of measuring up to 100 g acceleration

These sensors will provide inputs to an expanded version of the hierarchical fuzzy logic structure described in the preceding sections. An evaluation of each sensors contribution to overall system success will be made through simulation and flight test. Instruments that do not contribute significantly toward mission success and/or survivability at a low cost will not be included in the final vehicle design.

VI. Flight Tests

A series of flight tests were performed to test the rocket design, the deploy mechanism, and to gather information about the aerodynamic characteristics of the parafoil that could be used to optimize the flight controller. The four ft tall, 3 inch diameter rocket was made out of phenolic tubing and used a plastic nosecone and fiberglass fins. The rocket was launched on commercially available solid rocket motors of varying sizes depending on vehicle weight, to allow the rocket to reach apogee at an acceptable test altitude between 500 and 1000 ft. A standard motor burnout delayed ejection charge was used in conjunction with a piston to separate the nose from the rocket body and release the parafoil.

The prototype vehicle shown in Fig. 15 below represents the culmination of a development program that experienced a gradual evolution in design. The parafoil control line separator bar alone, the short aluminum bar running perpendicular to the rocket body, has undergone significant reduction and modification since the construction of the first flight vehicle. In the initial test flights, the parafoil was controlled from the ground by means of a radio control mechanism designed and built for this project. A series of flights under autonomous control were then performed at Camp Roberts Army Training base in California. Early autonomous flights were generally marred by flaws in the parafoil deployment mechanism. However, in the second autonomous flight, despite a late deploy event and tangled support lines, the fuzzy logic controller was able to follow the desired path albeit with significant oscillations.

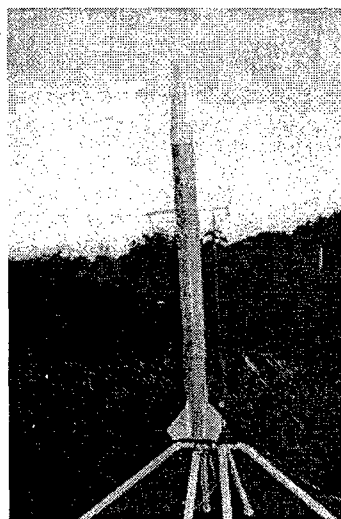


Fig. 25 Improved Parafoil Control Design (note the small control line separator mounted sideways through the rocket).

In the design configuration shown, the separation joint is located 10 centimeters below the parafoil control line separator bar. When separation occurs at apogee the two halves split apart and the aft section releases a simple parachute to drift back to the ground. The forward section contains the parafoil and electronic guidance payload. The parafoil is released from the aft part of the forward section and flies the preprogrammed course with the nose of the rocket pointing down toward the ground. In the next development phase, the vehicle design requirement will be that all parts return as a single unit under autonomous control.

A new launch mechanism, using a compressed-air canon pictured in Fig. 16, has since been developed to allow for cheaper and more frequent flight tests. The electronics package and projectile have been redesigned to withstand the much greater g forces imparted by this device. Initial tests on prototype projectiles, such as the one shown in Fig. 17, have shown that this device is capable of delivering a 0.5 lb payload to altitudes well in excess of 500 feet. Flight testing of functional hardware is scheduled to recommence using this device in the next phase of the project.

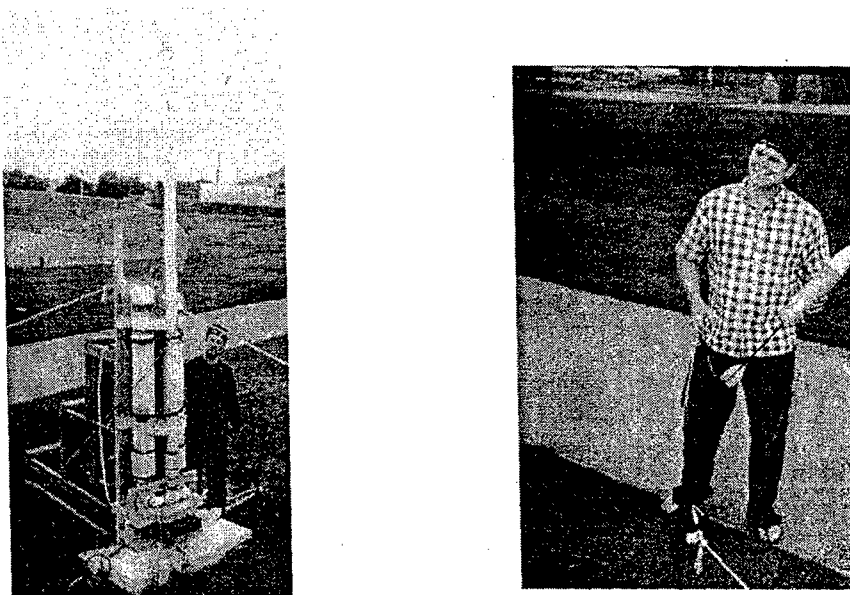


Fig. 36 & 17 Compressed Air Launch Mechanism and Prototype Test Projectile.

VII. Conclusions and Future Work

This project has shown that a fuzzy logic algorithm can provide the means for autonomous control of a parafoil in flight. The fuzzy logic control software was relatively simple to construct and proved to be both robust and forgiving of noisy inputs in simulations and test flights. These attributes made it ideal in an application where a major goal was to keep total product costs and system complexity to a minimum.

Combs method of formulating fuzzy rules proved to be an effective means of minimizing the number of rules, resulting in tremendous savings in memory and execution speed. Although we cannot generalize our results to all fuzzy logic applications, the method seems to hold promise for a number areas where the "curse of rule expansion" has been shown to be a limiting factor. The layered organization of the fuzzy modules made for an easily understood and modifiable architecture. Future development may include adding additional modules to further enhance capability.

The Matlab/Simulink software suite proved to be a powerful tool for developing and simulating the flight system. The Matlab Fuzzy Logic Toolbox was also very helpful in the development of fuzzy membership functions and production rules. The optimization of the membership functions was performed through a tedious, trial and error exercise which will be automated in future work.

Preliminary flight tests served to produce data to improve the fidelity of the simulation, however autonomous tests were often marred by flaws in the deployment mechanism. The flight testing also proved to be relatively expensive and was cumbersome to coordinate and execute. A compressed-air launch mechanism has been designed and tested to alleviate all of these difficulties.

The ATRP has the potential to be superior in terms of cost, ruggedness/durability, ease of use, portability, time to activate and reusability when compared with competing technologies in a variety of mission scenarios. Future improvements will include incorporating the new technologies necessary to field a system ready for operational activity. The size and weight of the prototype system electronics and motor control package can be reduced by using more basic electronic elements in the design, a lighter and more efficient motor and battery and lighter instrument packaging. Other enhancements that will be incorporated are collision avoidance sensors, and a remote sensing device (e.g. IR camera) with telemetry transmitted to a ground station. The remote sensing device will communicate to a handheld wireless device with the user in real-time.

Other potential applications include airdrop guidance, battle damage assessment, and communications enhancement in rugged terrain. Civilian applications include; an aid in search and rescue efforts, evaluating plant health by farmers and land management workers, and as a communications and observation device for forestry fire fighting crews. The ATRP appears to have the potential for improving efficiency in both military and civilian applications with a very favorable cost/benefit ratio.

Acknowledgments

This project is sponsored by the Department of the Navy, Office of Naval Research (N00014-02-1-0754). The authors gratefully acknowledge the Cal Poly Research Dean's office for their support of this effort. We are also grateful for the enthusiasm and effort displayed by the interdisciplinary team of Cal Poly undergraduate and graduate student researchers that have contributed to this project. Special thanks go to Dan Macy, Trevor Foster, André von Muhlen, Tim Reed, and Chris LaFlash.

References

- ¹Gopala Pillai, S., Tian, L., Beal, J., "Aerial imaging to detect field nitrogen deficiency in corn", ASAE paper no. 983030, ASAE St Joseph, MI, 1998.
- ²Johannsen, C.J., Baumgardner, M.F., Willis, P.R., and Carter, P.G., "Advances in Remote Sensing Technologies and their Potential Impact on Agriculture." *1st International Conference on Geospatial Information for Agriculture and Forestry*, Paper 2-1. Vol. I: 6-11, Lake Buena Vista, FL, 1998.
- ³Yager, R.R., and Zadeh, L.A., (Eds.), *An Introduction to Fuzzy Logic Applications in Intelligent Systems*, Kluwer Academic Publishers, Boston, 1992.
- ⁴Zadeh, L.A. and Kacprzyk, J., (Eds.), *Fuzzy Logic for the Management of Uncertainty*, John Wiley & Sons, New York, 1992.
- ⁵Zadeh L.A., "Fuzzy Logic, Neural Networks and Soft Computing", *Communications of the ACM*, 37(3), 1994, pp. 77-84
- ⁶Zadeh L.A., "Soft computing and Fuzzy Logic", *IEEE Software*, 11(1-6), 1994, p. 48-56.
- ⁷Zadeh L.A., "Fuzzy Logic and the Calculi of Fuzzy Rules and Fuzzy Graphs", *International Journal of Multiple-Valued Logic*, 1, 1996, p. 1-39.
- ⁸Zadeh L.A., "From Computing with Numbers to Computing with Words -- From Manipulation of Measurements to Manipulation of Perceptions", *IEEE Transactions on Circuits and Systems*, 45, 1999, pp. 105-119.
- ⁹Sinha, N.K., Gupta, M.M., and Zadeh, L.A., (Eds.), *Outline of Computational Theory of Perceptions Based on Computing with Words, Soft Computing & Intelligent Systems*, 3-22, New York; Academic Press, 2000.
- ¹⁰Jamshidi, M., Titli, A., Zadeh, L. A., and Boverie, S., (Eds.), *Applications of Fuzzy Logic*, Prentice Hall, 1997.
- ¹¹Mendel, J. M., *Uncertain Rule-Based Fuzzy Logic Systems Introduction and New Directions*, Prentice-Hall, Upper Saddle River, NJ, 2001.
- ¹²Passino, K., and Yurkovich, S., *Fuzzy Control*, Addison Wesley Longman, Menlo Park, CA, 1998.
- ¹³Yen, J., Langari, R., and Zadeh, L. A., (Eds.), *Industrial Applications of Fuzzy Logic and Intelligent Systems*, IEEE, 1995.
- ¹⁴Zadeh, L. A., "Fuzzy Sets", *Information and Control*, Vol.8, 1965, p. 338-353.
- ¹⁵Zadeh L.A., "Outline of a new approach to the analysis of complex systems and decision Processes", *IEEE Trans. Man. Cybernetics*, No.3, 1973, pp. 28-44.
- ¹⁶Zadeh L.A., "Fuzzy sets as a basis for a theory of possibility", *Fuzzy Sets and Systems*, Vol.1, 1978, pp. 3-28.
- ¹⁷Cox, E., *The Fuzzy Systems Handbook: A Practitioner's Guide to Building, Using, and Maintaining Fuzzy Systems*, Academic, Boston, MA, 1994.
- ¹⁸Guven, M. K. and Passino, K. M., "Avoiding Exponential Parameter Growth in Fuzzy Systems", *IEEE Transactions on Fuzzy Systems*, Vol. 9, No. 1, 2001, pp: 194-199.

- ¹⁹Wang, L.-X., "Analysis and Design of Hierarchical Fuzzy Systems", *IEEE Transactions on Fuzzy Systems*, Vol. 7, No. 5, 1999, pp: 617-624.
- ²⁰Raju, G.V.S., and Zhou, J., "Adaptive Hierarchical Fuzzy Controller", *IEEE Transactions on Systems, Man, and Cybernetics*, Vol. 23, No. 4, 1993, pp. 973-980.
- ²¹Linkens, D. A. and Nyongesa, H. O., "A Hierarchical Multivariable Fuzzy Controller for Learning with Genetic Algorithms", *International Journal of Control*, Vol. 63, No. 5, 1996, pp. 865-883.
- ²²Combs, W.E., and Andrews, J.E., "Combinatorial Rule Explosion Eliminated by a Fuzzy Rule Configuration", *IEEE Transactions on Fuzzy Systems*, Vol. 6, No. 1, 1998, pp. 1-11.
- ²³Weinschenk, J. J., Marks II, R. J. Combs, W. E., "Layered URC fuzzy systems: a novel link between fuzzy systems and neural networks", *International Joint Conference on Neural Networks*, Portland, Oregon, 2003, pp. 2995-3000.
- ²⁴Weinschenk, J. J., Combs, W. E., Robert J. Marks II, "Avoidance of rule explosion by mapping fuzzy systems to a disjunctive rule configuration", *International Conference on Fuzzy Systems (FUZZ-IEEE)*, St. Louis, MO, 2003.
- ²⁵Dick, S. and Abraham Kandel, "A comment on 'Combinatorial Rule Explosion Eliminated by a Fuzzy Rule Configuration' by William E. Combs and James Andrews", *IEEE Transactions on Fuzzy Systems*, Vol. 7, No. 4, 1999, pp. 475-477.
- ²⁶Mendel, J. M. and Liang, Q., "Comments on Combinatorial Rule Explosion Eliminated by a Fuzzy Rule Configuration", *IEEE Transactions on Fuzzy Systems*, Vol. 7, No. 3, 1999, pp: 369-373.
- ²⁷DeTurris D., Ervin, J., and Alptekin, S. E., "Development of an Autonomous Tactical Reconnaissance Platform", 17th AIAA Aerodynamic Decelerator Systems Technology Conference, Monterey, California, 2003, AIAA-2003-2117.
- ²⁸Gasmi, C. and Alptekin, S. E., "Supplier Selection Using Fuzzy Logic", *WSEAS Transactions*, 2003, pp. 210-215.
- ²⁹Sugeno, M., *Industrial Applications of Fuzzy Control*, Elsevier Science Inc., New York, 1985.
- ³⁰Raju, G.V.S., et al., "Hierarchical Fuzzy Control", *International Journal of Control*, Vol. 54, No. 5, 1991, pp. 1201-1216.
- ³¹Tunstel E., Lippincott, T. and Jamshidi, M., "Behaviour Hierarchy for Autonomous Mobile Robots: Fuzzy-behaviour Modulation and Evolution", *International Journal of Intelligent Automation and Soft Computing*, Vol. 3, No. 1, Special Issue on Autonomous Control Engineering, 1997, pp. 37-50.
- ³²Martin, F. G., "The Handy Board Technical Reference", Gleason Research, 2000.

Optimization of the Fuzzy Logic Controller for an Autonomous UAV

Jon C. Ervin
Apogee Research Group
Los Osos, CA 93402
apogee@alumni.calpoly.edu

Sema E. Alptekin
California Polytechnic State
University
San Luis Obispo, CA 93407, USA
salpteki@calpoly.edu

Dianne J. DeTurris
California Polytechnic State
University
San Luis Obispo, CA 93407, USA
ddeturri@calpoly.edu

Abstract

In this paper, we describe the optimization of membership functions in an application employing a hierarchical Fuzzy Logic Controller. The size of the rule base is made manageable by using a unique formulation, known as Combs method, to help control the problem of 'exponential rule expansion'. The optimization is performed using a steady state genetic algorithm with a dynamic fitness function. The controller being developed is designed to fly a small, autonomous parafoil, suitable for short-range reconnaissance and land survey applications. The optimization process is performed in the Matlab/Simulink software environment and incorporates fuzzy logic modules developed in the Matlab Fuzzy Logic Toolbox. Hardware limitations in terms of memory, computational speed and cost were critical factors driving the need for this simple yet robust control algorithm.

Keywords: Genetic Algorithms, Fuzzy Logic.

1 Introduction

Using Genetic Algorithms (GA) to optimize the performance of a Fuzzy Logic Controller (FLC) has been the focus of a number of research efforts [1-8]. The approach taken in this application combines various techniques explored in previous research efforts. The FLC produced in this research was specifically designed to provide autonomous guidance for a short range, unmanned air vehicle

(UAV). The main hardware elements of the Autonomous Tactical Reconnaissance Platform (ATRP) are a 3.5 square meter parafoil, an electronics payload with a protective aerodynamic housing and a launch system.

In order to keep product costs to a minimum, inexpensive electronic components were used to provide inputs to the controller software. A fuzzy logic control method is employed in the ATRP for its advantages in fault tolerance and graceful response to missing and/or noisy sensor input. One of the major drawbacks to fuzzy control is the exponential growth in the number of rules as the number of input variables increases linearly. A unique methodology (Combs' method) is used to address this problem of 'exponential rule expansion' [9]. The use of Combs' method also simplified the tuning process of the fuzzy system by requiring only the optimization of the membership functions and not the rule base. Modularity and simplicity of design were further enhanced by adopting a hierarchical fuzzy logic architecture.

A steady state Genetic Algorithm (SSGA) is used to optimize of the fuzzy logic membership functions. In order to produce a robust control algorithm, the objective function in the optimization process is made dynamic, with random changes to key environmental conditions occurring after each new generation has been produced. A flow diagram of the optimization process is shown in Fig. 1. After the SSGA processes of selection, crossover and mutation have been performed, the chromosome for the new offspring is decoded to produce a set of membership functions. These membership functions are incorporated into the fuzzy systems to be used in a simple flight simulation to determine the fitness of

the candidate solution. The process then repeats itself until a satisfactory result is obtained.

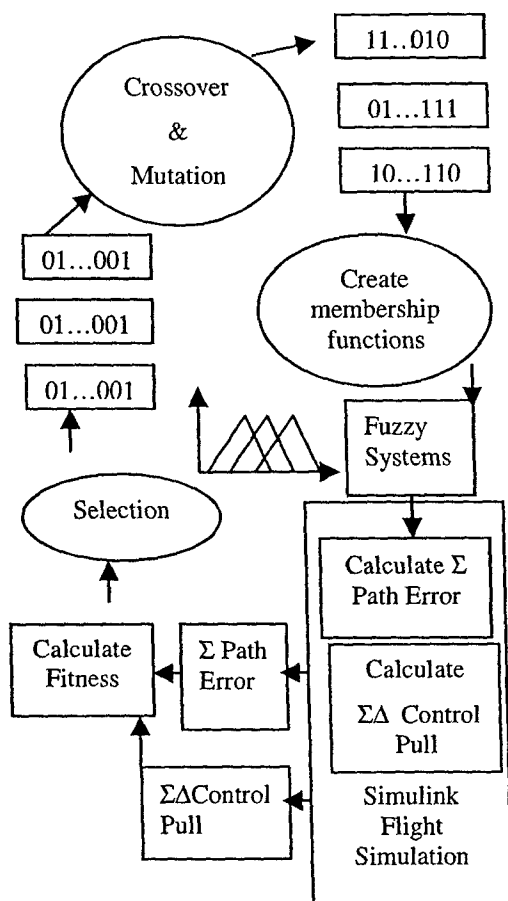


Figure 1. Block Diagram of GA based optimization

The optimization process is performed entirely within the Matlab software environment. The same Matlab/Simulink simulated flight plan with randomized environmental conditions is used to evaluate the fitness of each candidate solution in the GA population.

In Section 2, we provide a brief background on Fuzzy Control and Combs method. Development of the Fuzzy Logic Architecture for the ATRP application is presented in Section 3, followed by a discussion of the simulation and optimization of the control algorithm in Section 4. The hardware implementation of the concept is reported in Section 5 with conclusions and future work discussed in Section 6.

2 Fuzzy Control

A fuzzy logic control algorithm provides the autonomous decision making strategy for the ATRP. Attributes of fuzzy logic that made it appealing for this application are the ability to model nonlinear functions, robustness in the face of imprecise input and ease of code generation. Fuzzy logic algorithms are intuitively easy to understand and allow the user to encapsulate the experience of experts in an efficient manner. References cited at the end of this article can give the reader a much more comprehensive insight into fuzzy logic fundamentals [10-12].

One of the well documented disadvantages of the fuzzy logic algorithm is known as "exponential rule expansion". In general, each input variable has a number of associated fuzzy membership functions. In the simplest approach to building a rule base, a separate rule is formed for each of the possible combinations of the input membership functions. A 2 input - 1 output system with 3 membership functions each would have $3^2 = 9$ rules in this type of rule base. This system of rules works well for a small two input problem, but as the number of inputs and/or corresponding membership functions increases linearly, the number of rules increases exponentially. Usually an attempt is made to reduce the number of rules either by eliminating those rules that would not be encountered in the operating environment or in some way limiting the number of membership functions for each variable.

A method first developed by Combs allows us to avoid the exponential rule growth in favor of a much more manageable linear growth [9]. The main difference between the Combs' formulation and that of the traditional method is that in Combs' method every rule in the rule base has only one antecedent for every consequent. Each membership function of all the input variables is used once in the antecedent of a rule in the rule base. In the 2 input - 1 output example, the number of rules in the rule base is reduced to six versus nine for the traditional method. For a high speed controller, this difference would be trivial but a modest increase in the number of inputs and membership functions can soon lead to a very large rule base and an incredible reduction in rules using Combs method. To illustrate, suppose you have a fuzzy system of 5 inputs with 7 membership functions each, Combs method will have only 35 rules ($5 \times 7 = 35$) rather than the 16,807 (7^5) rules of the conventional technique.

Using Combs' method to construct rules also served to simplify the optimization process discussed in a later section of this paper. The optimization task was further simplified by predetermining the number of membership functions for each input variable. It was necessary to keep the number of membership functions to the barest possible minimum due to memory and speed constraints of the microcontroller. At the same time the demands of the control function required enough membership functions for each input to provide the flexibility needed to achieve good flight performance. A large number of simulation flights were performed, with varying environmental conditions, to empirically determine a reasonable number of membership functions for each variable. If the optimization had proven unable to develop a solution that met requirements then one option to consider would have been to increase the number of membership functions for at least some of the input variables.

There is a large body of research described in the literature on methods to modify membership functions in the optimization process. The technique followed in this application was to define an initial set of triangular membership functions for each variable. A simple scaling function of two independent variables was used for each input to modify the shape and location of the membership functions. The scaling function for each input variable has a proportional and an exponent term of the form;

$$F(x) = a x^b \quad (1)$$

The proportional term "a" in (1) has the effect of varying the width and spacing of the membership functions evenly over the domain. The term in the exponent "b" produces a nonlinear spacing of membership functions and distorts the straight sides into curved line segments. The combination of the two terms provides good flexibility in modifying the membership functions without incurring a high computational overhead. Fig. 2 shows an example of the modification of membership functions that can be achieved with this scaling function.

The combined effect of the two scaling factors in this example is to widen the membership function centered at 0.0, push the peak of the middle membership functions out wider and pull the outermost membership functions inwards. Different combinations of values of the scaling functions will

have widely differing effects on the resulting modified membership functions. There is no provision in this approach for making asymmetric membership functions, however in this application it is hard to conceive of a scenario where asymmetry would be a desirable trait.

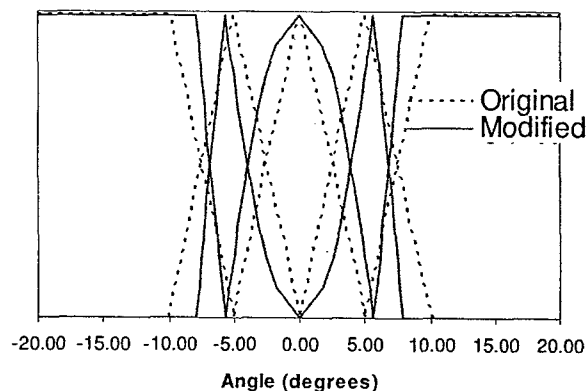


Figure 2. Membership Functions Before and After Modification ($a = .4$, $b = 2.0$)

A total of 14 scaling terms for the 7 variables (5 input and 2 output) of the two fuzzy logic modules make up the chromosome for the genetic algorithm optimization. These terms were limited to a range of values between .3 and 5.0. Values outside of these limits were found to be well outside the region for any optimal solution.

3 The Simulation Model

The flight simulation developed in Matlab/Simulink is used to evaluate candidate solutions passed from the optimization routine. The difference between the desired and actual heading ($\Delta\theta$) along with the first and second derivatives of this difference are supplied to the **Course Following** fuzzy logic module. Any adjustments from the fuzzy **Course Correction** module are added to $\Delta\theta$ and the controller uses these inputs to produce a control line pull command. The effect of the control line pull command on the aerodynamic performance of the parafoil is computed and an incremental parafoil heading vector is determined.

Simulated electronic noise and bias error values are combined with the heading vector. This heading vector is then used to update the ground track map and to produce a simulated GPS measurement. The current GPS measurement along with the start and

goal coordinates are used to compute the inputs for the fuzzy **Course Correction** module. The output from the **Course Correction** module completes the loop and the simulation runs for the length of an entire simulated mission profile

The two fuzzy logic sub-modules of the simulation serve as the brain for the autonomous controller. It is the membership functions for the input and output variables for each of these modules that are the focus of the optimization effort. The simulation parameters of wind strength, frequency of wind gusts, direction of wind and initial deploy heading are randomly altered during an optimization run after each generation has been computed.

4 Optimization Parameter Choices

A genetic algorithm (GA) was chosen as a convenient method to perform the optimization with a reasonable expectation of success. Genetic algorithms have proven effective in NP hard problems, they are easy to develop and code, and if properly designed they will avoid pitfalls that can trap other optimization techniques. Specifically, a Steady State Genetic Algorithm (SSGA) was chosen for this task as it was expected that this technique would simplify the task of computer code development.

An incremental SSGA is different from a more traditional GA in that only one member of the population of solutions is chosen for replacement at the end of each 'generation'. One issue to be determined by the designer is how to select the member to be replaced. One obvious choice is to replace the worst performing member, but it has been reported that this can lead to premature convergence on a local optimum before the entire solution space can be explored. Another choice for replacement is to eliminate the oldest member in the population, but this technique runs the risk of losing the best performing solution. The technique used in this application was to replace the worst performing candidate while maintaining diversity through the application of a high mutation rate and a dynamic objective function.

There are also a variety of techniques that can be used in determining the parent or parents of the new candidate solution in each generation. Various means of selection include; Fitness Proportionate Selection with some form of associated scaling and windowing methods, Roulette Wheel Selection,

Rank Selection, and Tournament Selection [13]. A form of tournament selection, with five individuals randomly chosen from the population, was used for this application. Another choice to be made was whether to pick both parents from the random tournament or to use the best individual in the population as one parent and select the other from the tournament.

Random tournament selection to obtain both parents was the method used for all runs where the fitness function remained static throughout an optimization run. Eventually the optimization method of using a static fitness function was abandoned and with it the random selection of both parents was abandoned as well. When a dynamic fitness function, as described below, was incorporated into the optimization routine the elitist strategy of maintaining the best solution as one parent was adopted. The change in selection method was adopted based on the assumption that greater continuity in the generation of solutions would be required to obtain a feasible solution within a reasonable number of iterations. This assumption was not verified and remains as an interesting question for further research.

Another decision to be made in the construction of the SSGA is the type of cross-over to be employed. Cross-over, the exchange of sections of genetic material between parent solutions, can be limited to a single cut and swap operation as in single point cross-over or can occur at multiple locations on the chromosome. A special case of multi point crossover, uniform crossover, was implemented in this application with an equal chance of each bit being contributed by either parent. The mutation rate of .4, referred to in the literature as hypermutation, was chosen to ensure that the population did not become trapped at a local optima in the solution space.

Using an extraordinarily high mutation rate was expected to provide a more thorough search of the solution space at the cost of greatly increasing the number of iterations required for convergence. A compromise to this expected, though not empirically demonstrated, problem was to perform mutation using a Gaussian rather than uniform distribution.

Fitness values for the SSGA were derived from data generated over an entire flight simulation run in the Matlab/Simulink software environment. One of these desired traits, tracking the desired flight path as closely as possible, was evaluated by calculating the difference between the ideal path and the actual

path at each time step. There was also a desire that the magnitude of pull commands performed by the servo motors be minimized as much as possible. This desired trait was captured by summing the change in pull commands at each time step. The sum of these two error measures provided the fitness measure to be minimized in optimization efforts.

5 Results

Fig. 3 and Fig. 4 show the results of running the SSGA optimization for 4,400 generations.

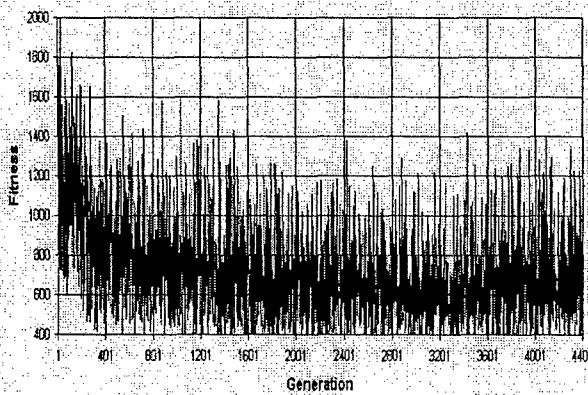


Figure 3. Fitness with the Mutation Rate Zeroed Out at Generation 3600

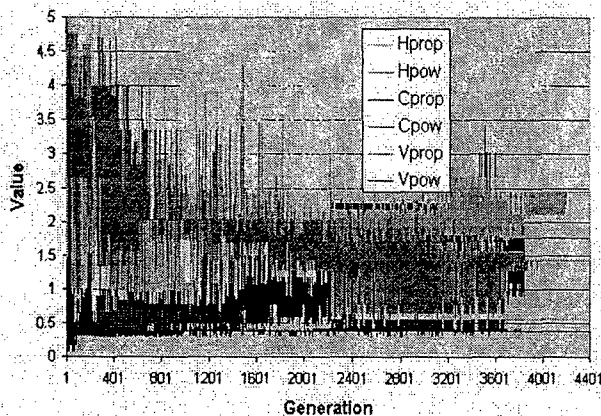


Figure 4. Constituent Values with Mutation Rate Zeroed Out at Generation 3600

The solid black line through the center of the data in figure 3 is a moving average of 144 values. Fig. 3 exhibits a noisy profile caused by the random choice of initial conditions for the simulation performed at

each generation. During the optimization process the initial environmental conditions for a particular generation may be relatively benign resulting in a good fitness score, whereas the following generation may be faced with a much more difficult set of initial conditions.

When the mutation rate is zeroed out at generation 3,600, the values of the individual genes eventually converged to a single value. The effect of this convergence resulted in a slight worsening of the average fitness over all values of environmental conditions. The optimization was allowed to continue to run for some time after convergence had occurred to ensure that no set of conditions would produce an unacceptable fitness value.

Fig. 5 shows the least fit candidates throughout the optimization run. Note that once the mutation rate has been zeroed out at generation 3600, the least fit candidates no longer show unacceptably high values.

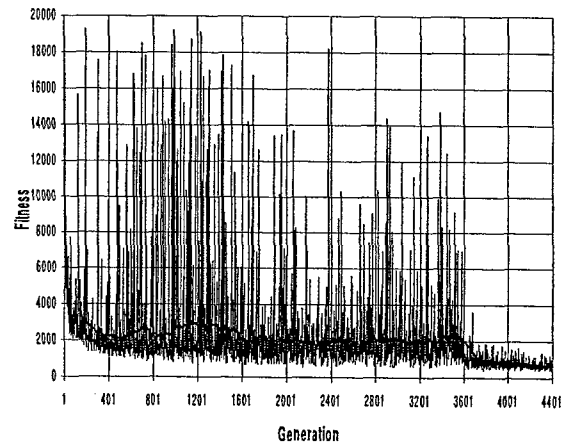


Figure 5. Least Fit Solution at Each Generation

Maximum wind speed, wind direction, frequency of wind speed change, and initial course heading are the variables that had the greatest impact in determining the optimum fuzzy logic membership function values. The various initial conditions were changed randomly after each generation in the SSGA process.

6 Conclusions and Future Work

The optimization of a FLC using a Genetic Algorithm was a crucial element in the development of an autonomous UAV. The combination of using Combs Method to construct rules, using simulation

in the construction of the fitness function and making the fitness function dynamic in the GA optimization proved effective in achieving the desired controller properties.

The Combs method of formulating fuzzy rules proved to be a very effective means of minimizing the number of rules, resulting in tremendous savings in memory and execution speed. Although we cannot generalize our results to all fuzzy logic applications, the method seems to have merit for a number of applications where the "curse of exponential rule expansion" has been shown to be a limiting factor. The hierarchical organization of the fuzzy modules made for an easily understood and modifiable architecture. Future development may include adding additional modules to further enhance capability.

Throughout the optimization process decisions had to be made between several promising alternatives in order to proceed to the next step. A thorough examination of each alternative was not possible, so choices were made based on simplifying assumptions and prior experience.

The probability of mutation was chosen to be very high, reflecting the desire to ensure that the entire domain would be searched for candidate solutions. An interesting trade study could be performed to examine what effect that varying the mutation rate would have on solution convergence. Toward the end of the optimization run, specific scaling values were obtained by forcing the mutation rate to zero. Other methods, such as a least squared error analysis of candidate solutions might be expected to give better results. These are a few of many avenues of research that could be explored with respect to the assumptions and techniques used in this project.

References

- [1] Tunstel E. and Mo Jamshidi, "On Genetic Programming of Fuzzy Rule-Based Systems for Intelligent Control", *International Journal of Intelligent Automation and Soft Computing*, Vol. 2, No. 3, p: 273-284, 1996.
- [2] Cordon, O., F. Herrera, L. Magdalena, and P. Villar, "A Genetic Learning Process for the Scaling Factors, Granularity and Contexts of the Fuzzy Rule-Based System Data Base, World Scientific, 2001.
- [3] Maniadakis, M., S. Hartmut, "A Genetic Algorithm for Structural and Parametric Tuning

of Fuzzy Systems", European Symposium on Intelligent Techniques, ESIT99.

- [4] Hoffman, F., G. Pfister, "Evaluationary Design of a Fuzzy Knowledge Base for a Mobile Robot", *International Journal of Appropriate Reasoning*, 11:1-158, 1994.
- [5] Fukuda, T., N. Kubota, "An Intelligent Robotic System Based on a Fuzzy Approach", *Proceedings of the IEEE*, Vol. 87, No. 9, September 1999.
- [6] Tunstel E., T. Lippincott, and M. Jamshidi, "Behaviour Hierarchy for Autonomous Mobile Robots: Fuzzy-behaviour Modulation and Evolution", *International Journal of Intelligent Automation and Soft Computing*, Vol. 3, No. 1, pp. 37-50, 1997.
- [7] Ghosh A., S. Tsutsui and H. Tanaka, "Function Optimization in Nonstationary Environment using Steady State Genetic Algorithms with Aging of Individuals, IEEE International Conference on Evolutionary Computation'98.
- [8] Cordon O., F. Herrera, Hoffman, and L. Magdalena, *Genetic Fuzzy Systems - Evolutionary and Learning of Fuzzy Knowledge Bases*, World Scientific, 2001.
- [9] Combs, W.E., and J.E. Andrews, "Combinatorial Rule Explosion Eliminated by a Fuzzy Rule Configuration", *IEEE Transactions on Fuzzy Systems*, Vol. 6, No. 1, pp. 1-11, 1998.
- [10] Jamshidi, M., A. Titli, L. A. Zadeh, and S. Boverie, (Eds.), *Applications of Fuzzy Logic*, Prentice Hall, 1997.
- [11] Zadeh, L.A., "Outline of a new approach to the analysis of complex systems and decision processes", *IEEE Trans. on Systems, Man and Cybernetics SMC-3*, 28-44, 1973.
- [12] Cox, E., *The Fuzzy Systems Handbook: A Practitioner's Guide to Building, Using, and Maintaining Fuzzy Systems*, Academic, Boston, MA, 1994.
- [13] Hancock, P., "An Empirical Comparison of Selection Methods in Evolutionary Algorithms", printed in the *Proceedings of the AISB Workshop on Evolutionary Computation*, 1994.

Acknowledgments

This project is sponsored by the Department of the Navy, Office of Naval Research (N00014-01-1-1049 and N00014-02-1-0754). The authors gratefully acknowledge the California Polytechnic State University Research Dean's office for their support of this effort. We are also grateful for the enthusiasm and effort displayed by the interdisciplinary team of Cal Poly undergraduate and graduate student researchers that have contributed to this project. Special thanks go to Dan Macy and Chris LaFlash.

Improving Power Conversion Efficiencies of Polymer Based Solar Cells

Project Investigator:

Robert Echols
Assistant Professor
Physics Department, Cal Poly State University

ABSTRACT

Polymer based solar cells show great promise as a lightweight low cost method to harvest the Sun's abundant energy. However, before these novel solar cells become a viable technology, fundamental advancements in power conversion efficiency (light energy into electrical energy) must be realized. In the past year, we have employed two complimentary approaches; computer simulations and direct experimentation to improve power conversion efficiencies of polymer based solar cells.

We have improved our simulation program to include the electric and temperature dependent mobility characteristics of charge carriers, in addition to incorporating the spectral characteristics of the light source and absorbing polymer. Comparing simulation output from this new computer code with experiments has allowed us to quantify the power conversion losses due to incomplete absorption and internal device inefficiencies (recombination and lack of exciton dissociation). In addition, we developed a simpler numeric model to address the effects of incomplete absorption and polymer band gap on solar cell device performance. We were able to show that the best devices made to date are limited by absorption indicating that nearly all the absorbed photons are making useful electrical power. Under the assumption that all absorbed photons make useful electrical power we probed the effect of lower band gap polymers on device performance to show a near doubling in output power for polymers with band gaps of about 1.4 eV.

The importance of improving absorption highlighted above is being realized experimentally with the use of dye. Using a dyed nanoparticle TiO_2 layer in conjunction with a blended polymer/fullerene derivative layer, we have improved device absorption and power conversion efficiency. While the dyed nanoparticle TiO_2 layer polymer devices (without the fullerene derivative) are currently inferior to the polymer/fullerene derivative devices (one of the best devices being made to date with 3% power conversion efficiencies), the novelty in our work comes from combining the best ideas from both device designs individually into a single device. In the coming year we expect to hone our experimental techniques by focusing on TiO_2 roughness, dye type and annealing times to improve upon our novel design concept. Although still a work in progress, two physics majors working on this aspect of the project took first place in the physical and mathematical science division at the annual Cal State University statewide competition for their research presentation, "Improving Polymer Photovoltaic Device Performance with Annealing, PCBM and Dyed TiO_2 ".

INTRODUCTION

Polymer based solar cells show tremendous potential as a low cost alternative to the traditional silicon based solar cells. In the last decade, device design and material improvements have increased the power conversion efficiencies (η_p) to 5% (for a review see the many articles in [1]). Researchers accomplish 5% power conversion efficiencies using many approaches. Some of the most successful techniques involve bulk heterojunction devices using a blend of polymers [2] (e.g. M3EH-PPV with CN-ether-PPV) or polymer with nanoparticles such as PCBM [3]. The blended materials phase segregate allowing easier transport of electrons and holes in addition to dissociation sites for excitons (bound electron/hole pairs created by the absorption of light). Other approaches modify the Gratzel cell by replacing the problematic liquid electrolyte with a solid state component such as a molecule [4] or polymer [5]. Improving η_p beyond 5% will require lower band gap polymers to capture more photons from the solar spectrum. These lower

band gap polymers are just now becoming available and being investigated [6]. Additional losses include poor charge carrier mobilities, incomplete exciton dissociation, and electron/hole recombination. Our recent numeric work aims to quantify the loss mechanisms in bulk heterojunction polymer based solar cells to further elucidate needed improvements in device design and materials for viable photovoltaics.

In the sections that follow we describe our ideal solar cell model and quantify losses due to incomplete absorption. Our detailed model is introduced and used to investigate losses from exciton dissociation inefficiencies and electron/hole recombination. We finish our computational work by determining optimal band gaps for an ideal cell limited only by inefficient absorption. We conclude with a section on our experimental efforts towards improving polymer conversion efficiencies using a solid state dye-sensitized titanium dioxide layer with PCBM blended polymer serving as an active layer and hole transporter.

SIMULATION MODELS

Ideal Model

To investigate inefficient absorption of polymer based solar cells we have developed the following idealized model. The charge continuity equation governing electrons given by

$$e \frac{dn(x)}{dt} = \frac{dJ_n(x)}{dx} + G(x), \quad (1)$$

lacks a recombination term. We assume that all *absorbed* photons create excitons which dissociate to generate current. The generation term,

$$G(x) = \int e \alpha(\lambda) I(\lambda) e^{-\alpha(\lambda)x} d\lambda, \quad (2)$$

incorporates the polymer blend absorption $\alpha(\lambda)$ at wavelength λ , the photon flux density $I(\lambda)$ per wavelength interval of the AM 1.5 spectrum and x is the distance into the photoactive layer. In steady state, equation (1) is easily integrated giving the current leaving the device,

$$J = \int e I(\lambda) (1 - e^{-\alpha(\lambda)L}) d\lambda, \quad (3)$$

with L being device thickness.

Detailed Model

Our detailed simulation code follows the work described in [7], where the authors model transient and steady-state behavior of space charges in multilayer polymer light emitting diodes. The equations listed below capture the bulk macroscopic properties of the polymer.

$$\frac{dE}{dx} = \frac{e}{\epsilon} (p(x) - n(x)) \quad (4)$$

$$J_n(x) = e\mu_n(x, E)n(x)E(x) + \mu_n(x, E)kT \frac{dn(x)}{dx} \quad (5)$$

$$e \frac{dn(x)}{dt} = \frac{dJ_n(x)}{dx} - r \frac{e}{\varepsilon} (\mu_n + \mu_p)n(x)p(x) + \beta G(x) \quad (6)$$

The microscopic details of charge hopping between polymer chains and charge delocalization along a π -conjugated segment of the polymer backbone are incorporated into the field dependent mobility, $\mu(E(x))$, based on the Poole-Frenkel form,

$$\mu(E(x)) = \mu(0) \exp(\gamma \sqrt{E(x)}). \quad (7)$$

Gauss's law in one dimension (equation (4)), is suitable for determining the electric field, $E(x)$, for the approximately infinite parallel plate geometry of a polymer solar cell. The electric field that is modified by the photon induced charge densities for holes, $p(x)$, and electrons, $n(x)$, must be integrated to satisfy the potential difference across the electrodes, $\Delta V = \int E(x)dx$. The electron current, equation (5), contains drift and diffusion components. Equation (6), expressing conservation of charge for electrons, contains the same generation term used in the ideal model, modified by an exciton dissociation efficiency, β . Excitons are assumed to be dissociating throughout the polymer due to appropriately chosen energy levels for the electron and hole transporting polymers in the blend. The bimolecular recombination contains the Langevin form multiplied by a free parameter, r . Equations for hole current and continuity are analogous to the electron case.

For a given applied voltage, self-consistent solutions of these equations in time leads to steady state distributions of each quantity within the polymer device and the current exiting the device, generating current-voltage (J-V) curves. For photocurrent action spectra, the generation term is not integrated over wavelength. All polymer parameters are taken from experiment [2,8]. The only free parameters are the exciton dissociation efficiency, β , and the recombination parameter, r .

SIMULATION RESULTS

From our ideal model we use equation (3) to determine output electrical power limited only by absorbed photons, open circuit voltage, and fill factor for M3EH-PPV:CN-ether-PPV polymer blends (1:1 by weight) and M3EH-PPV:PCBM polymer/nanoparticle blends (1:4 by weight). Assuming devices with 100 nm length, open circuit voltage=0.6 V and 50% fill factor, the maximum theoretical power conversion efficiency is $\eta_p=5.6\%$ for the polymer blend and $\eta_p=3.5\%$ for the PCBM blend. These results indicate PCBM device designs are nearly optimized with reported power conversion at about 3% [3]. To make dramatic improvements in conversion efficiency for PCBM blends we need polymers with smaller band gaps and higher absorptivities. In contrast, M3EH-PPV:CN-ether-PPV polymer blend experiments yield power conversion efficiencies at or just below 1% depending on electrode configuration [2] indicating additional internal device losses.

To quantify internal losses in the polymer blend we use our detailed model in conjunction with experimental data to determine the exciton dissociation efficiency, β , and the

recombination parameter, r . At low light intensities, typical of photocurrent action spectra conditions, the recombination parameter has no effect on simulation results. We adjust β till the peak in the simulated external quantum efficiency shown in figure 1 matches the experimental value (see also figure 4 in [2]), determining exciton dissociation efficiency to be 0.36. The most notable difference between experiment and simulation occurs below 400 nm with a rise in the experimental quantum efficiency due to absorption in the titanium oxide layer. In the computer code, the titanium oxide layer is only treated as an effective electrode [9], and absorption in this layer is not included. Above 550 nm, the experimental result tails off more quickly than the simulation, possibly due to polymer absorption without exciton generation.

With β set, we determine the recombination parameter by aligning experimental

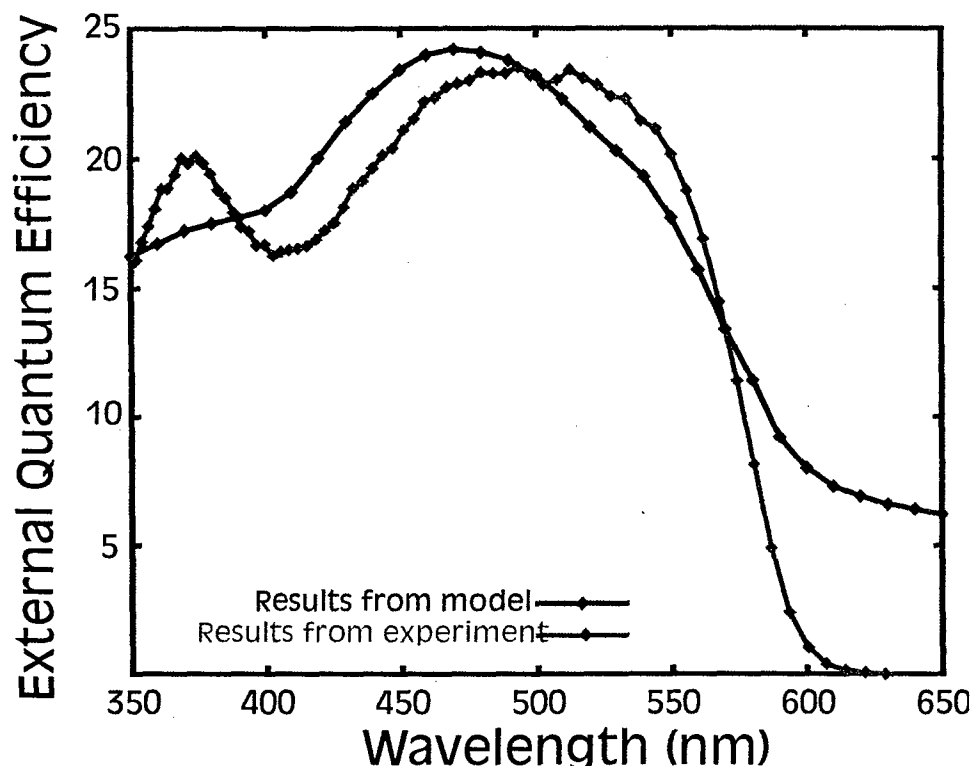


Figure 1. Photocurrent action spectra for M3EH-PPV:CN-ether-PPV polymer blend.

simulation short circuit current densities for a 60 nm cell. In figure 2 we show the effect of varying cell thickness (active polymer layer) on J-V curves (compare with figure 6 in [2]). The authors of [2] report short circuit densities of 17, 26, and 33 A/m² for device thickness corresponding to 85, 60, and 45 nm under approximately 800 W/m² illumination from a xenon bulb. Our computer simulations yield similar values of short circuit current densities, 21, 26, and 29 A/m² for the appropriate thickness mentioned above. As devices are made thinner short circuit densities increase because the internal electric field increases even though the absorbed photons decrease. These devices are evidently limited by poor charge carrier mobility. To make

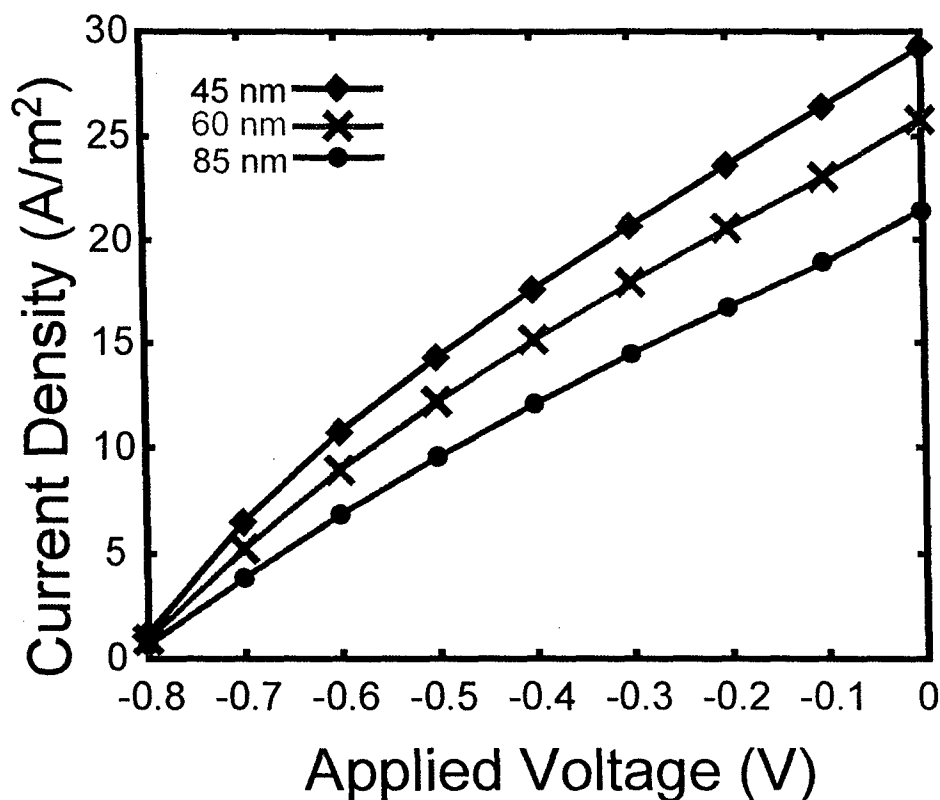


Figure 2. J-V curves for M3EH-PPV:CN-ether-PPV polymer blend with 45, 60, and 85 nm thickness.

short circuit current densities of the modeled 60 nm device match experiment we choose the recombination parameter to be 0.2. Larger values of the recombination parameter give a greater spread in short circuit current between the 85 nm and 45 nm device due to less space charge in the device, resulting in a greater internal field, but the device becomes less efficient overall. Given the uncertainties in spectral mismatch between the AM 1.5 spectra and a xenon bulb, light source calibration, actual device thickness and charge carrier mobility variations, to name a few, our results seem reasonable but need more careful comparison to experiment.

Looking to the future when lower band gap polymers become more available, we use our ideal model to estimate the potential increases in power conversion efficiency. Using a Gaussian absorption spectrum (peak absorption= $1.65 \times 10^7 \text{ m}^{-1}$ and standard deviation=142 nm) we run the ideal code with the peak at different wavelengths to simulate varying band gaps. Our results in figure 3 show a near doubling in output power (assuming devices with 100 nm length, open circuit voltage=0.6 V and 50% fill factor) as the approximate band gap lowers from 2 eV to just below 1.4 eV. While a real polymer blend will likely have more absorption at smaller wavelengths than our symmetrical Gaussian, improving absorption of polymer based solar cells will continue to play an important role in future device designs.

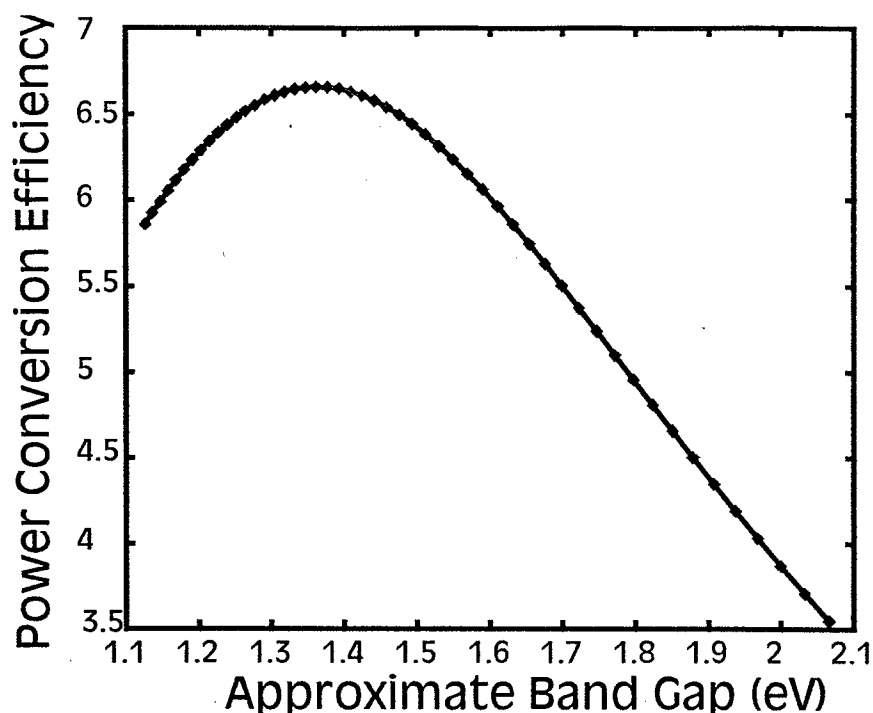


Figure 3. Ideal power conversion efficiency as a function of approximate band gap.

EXPERIMENTAL RESULTS

As discussed above in the simulation results section, polymer:PCBM blended devices are efficiently using absorbed photons to generate electricity. To improve power conversion beyond 3% we need smaller band gap polymers or other techniques to improve absorption. In the absence of commercially available low band gap polymers, we have been experimenting with dye to increase absorption of incoming solar radiation. Our experimental research closely follows the work reported in [5] to create a solid state dye-sensitized titanium dioxide (TiO_2) solar cell with poly(3-octylthiophene) (or P3OT) as a hole transporting layer. However, to improve charge carrier mobility we have blended our P3OT with PCBM and applied the annealing techniques discussed in [10] and [11].

Figure 4 below shows schematically the cell design with the polymer film being either pure P3OT or a blend of PCBM and P3OT (4:1 by weight). The TiO_2 layer is spin

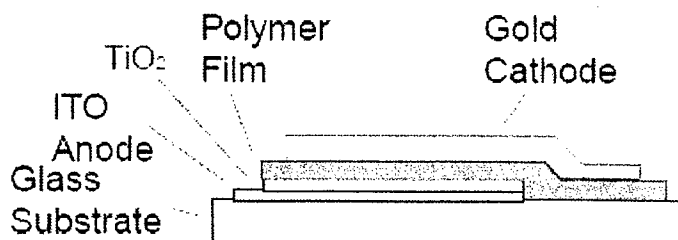


Figure 4. Cell structure for basic TiO_2 heterojunction solar cell.

cast from a solgel solution making a very smooth layer or from a colloidal suspension of titanium dioxide particles (21nm average size nanoparticle) resulting in a ruff surface. To improve absorption, ruthenium dye is applied onto the TiO_2 before application of the polymer film. Our preliminary results indicate dye has little effect on the smooth TiO_2 solgel devices with power conversion efficiencies (η_p) equal to $8.8\text{e-}3\%$. Previous work reported in [5] shows an increase in η_p from $2.8\text{e-}3\%$ to $1.0\text{e-}2\%$ upon addition of dye to a TiO_2 solgel device. By blending our polymer film with PCBM we were able to improve η_p by more than a factor of 10 to 0.11% and upon annealing up to 0.15% .

In contrast to the smooth solgel TiO_2 , a ruff nanoparticle TiO_2 layer provides larger surface area for the dye to bind resulting in improved absorption and power conversion efficiency. For a dyed nanoparticle TiO_2 device using polymer blended with PCBM we find $\eta_p=0.12\%$ compared to a similar device without dye, $\eta_p=8.4\text{e-}3\%$. Unlike the authors of [5], we had much less success with nanoparticle devices not blended with PCBM, $\eta_p=1.2\text{e-}5\%$ rising to $\eta_p=8.8\text{e-}3\%$ with annealing compared to their result of $\eta_p=8.0\text{e-}2$ which rose to $\eta_p=0.15\%$ upon application of dye. We suspect the main difference in our result to be the size of the TiO_2 nanoparticle. The authors in [5] use nanoparticles with an average size of 13nm compared to our 21nm . As seen in figure 5, an atomic force microscope (AFM) picture of the TiO_2 nanoparticle layer shows a large

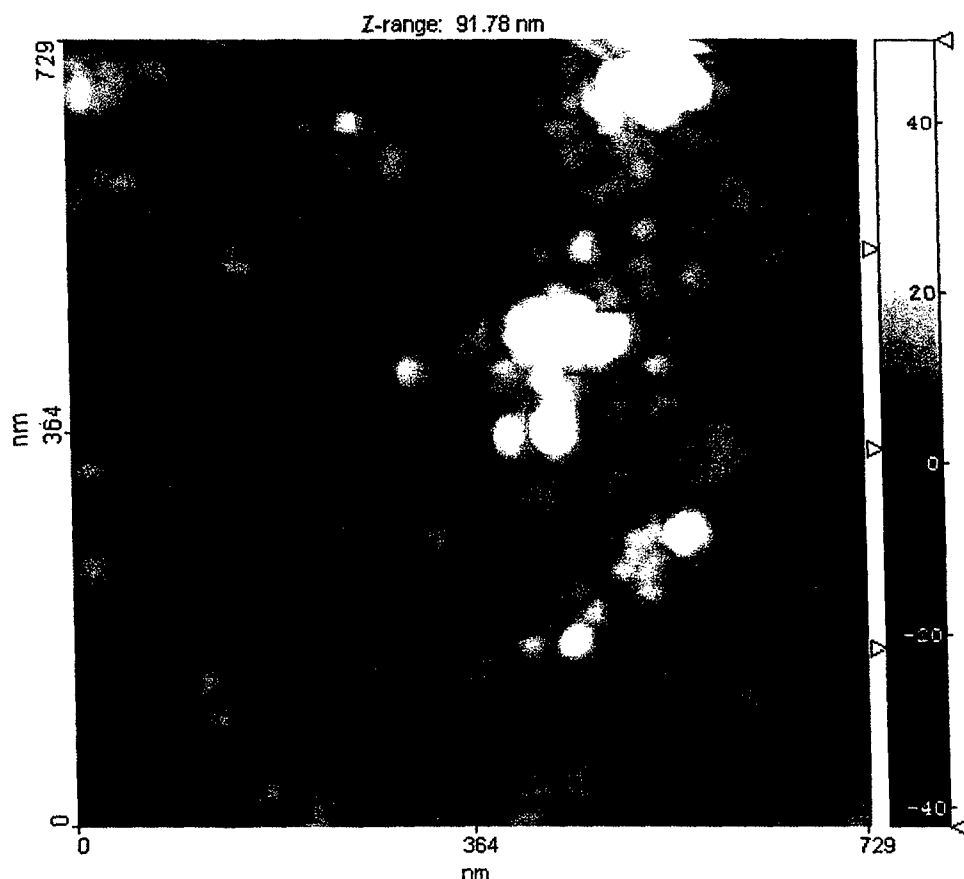


Figure 5. AFM image of TiO_2 nanoparticle surface.

variation in surface height of about 100nm . Such large TiO_2 height variations on the same order of the polymer thickness ($\sim 100\text{nm}$) most likely leads to partial shorts within a device and

reduced efficiencies. We look forward to confirming our suspicion that smaller TiO_2 nanoparticle size leads to smoother films and better performing devices.

In addition to improving upon our novel design with smaller sized TiO_2 nanoparticles, we expect additional improvements by switching to the polymer poly(3-hexylthiophene), using [70]PCBM in place of [60]PCBM, and trying a hydrophobic variant of the ruthenium dye. Use of the polymer poly(3-hexylthiophene) with a slightly lower band gap than poly(3-octylthiophene) and better charge carrier mobility should result in improved power conversion efficiency. The expected device performance advantage of [70]PCBM over [60]PCBM derives from the asymmetrical nature of [70]PCBM leading to increased absorption. Lastly, the hydrophobic ruthenium dye allows greater penetration of the polymer into the TiO_2 layer leading to increased conduction pathways and enhanced performance of the solar cell.

CONCLUSIONS

Our numeric results indicate that substantive increases in power conversion efficiencies of polymer based solar cells will require improvements in exciton dissociation, charge carrier mobility, and most notably higher absorptivities. For the polymer blend (M3EH-PPV:CN-ether-PPV) we have shown power conversion could reach 5.6% in the absence of losses from inefficient exciton dissociation, low charge carrier mobilities and recombination. However, according to our model, a real polymer blend loses an additional 64% from the *ideal* maximum as excitons fail to dissociate, with the rest lost to slow moving charge carriers recombining in the device. In contrast, the *ideal* polymer/nanoparticle blend (M3EH-PPV:PCBM) device yields $\eta_p=3.5\%$, close to experimentally reported values. Dramatic improvements for these devices will require increasing absorption. If smaller band gap polymers are used our ideal model suggests a near doubling in expected output power. To further improve absorption, layered devices with varying band gaps might be effective. We are currently developing models for layered devices with multiple band gaps. Successful models will allow experiments to begin by targeting optimal thickness generated from the simulations. Additional future work includes model comparisons with experimental temperature dependent J-V curves and power output dependence on illumination.

Experimentally we demonstrate potential for dye-sensitized TiO_2 devices with the P3OT:PCBM polymer/nanoparticle blend combining as a hole transporter and active layer. Including PCBM into these devices improves efficiency by more than a factor of 10 for both solgel and nanoparticle TiO_2 . However, our basic nanoparticle TiO_2 device without PCBM performs worse than what is reported in the literature indicating necessary improvements. We hope to remedy our device deficiency by using smaller TiO_2 nanoparticles. In addition, we expect to see devices with enhanced power conversion efficiencies by using [70]PCBM and P3HT to improve absorption, with hydrophilic ruthenium dye for better penetration of the polymer blend into the TiO_2 layer.

REFERENCES

- [1] "Organic Based Photovoltaics", *Mat. Res. Soc. Bull.* **30**, (2005).
- [2] A. J. Breeze, Z. Schlesinger, S. A. Carter, H. Tillmann and H. H. Horhold, "Improving power efficiencies in polymer-polymer blend photovoltaics," *Solar Energy Material and Solar Cells*, **83**, 263 (2004).
- [3] C. J. Brabec, N. S. Sariciftci, and J. C. Hummelen, "Plastic Solar Cells," *Adv. Funct. Mater.* **11**, 15 (2001).
- [4] L. Schmidt-Mende, S. M. Zakeeruddin, and M. Gratzel, "Efficiency improvement in solid-state-dye-sensitized photovoltaics with an amphiphilic Ruthenium-dye," *Appl. Phys. Lett.* **86**, 013504 (2005).
- [5] D. Gebeyehu, C. J. Brabec, F. Padinger, T. Fromherz, S. Spiekermann, N. Vlachopoulos, F. Kienberger, H. Schindler, and N. S. Sariciftci, "Solid state dye-sensitized TiO₂ solar cells with poly(3-octylthiophene) as hole transport layer," *Syn. Met.* **121**, 1549 (2001)
- [6] C. Winder, G. Matt, J. C. Hummelen, R. A. J. Janssen, N. S. Sariciftci, and C. J. Brabec, "Sensitization of low bandgap polymer bulk heterojunction solar cells," *Thin Solid Films* **403-404**, 373 (2002).
- [7] B. Ruhstaller, S. A. Carter, S. Barth, W. Riess, and J. C. Scott, "Transient and steady-state behavior of space charges in multiplayer organic light-emitting diodes," *J. Appl. Phys.* **89**, 4575 (2001).
- [8] Personal communication with A. J. Breeze and Y. Nakazawa.
- [9] A. C. Arango, L. Johnson, H. Horhold, Z. Schlesinger, S. A. Carter, "Efficient Titanium Oxide/Conjugated Polymer Photovoltaics for Solar Energy Conversion," *Adv. Mater.* **22**, 1689 (2000).
- [10] F. Padinger, R. S. Rittberger, and N. S. Sariciftci, "Effects of Postproduction Treatment on Plastic Solar Cells," *Adv. Funct. Mat.* **13**, 85 (2003).
- [11] A. J. Breeze, Z. Schlesinger, S. A. Carter, and P. J. Brock, "Charge transport in TiO₂/MEH-PPV polymer photovoltaics," *Phys. Rev. B* **64**, 5205 (2001).

Exploring the design and fabrication of nanoscale architectures fashioned via layer-by-layer adsorption of polyelectrolytes

Project Investigators:

**Dr. Derek E. Gragson
Associate Professor
Chemistry and Biochemistry**

The research funded by this grant was a continuation of my work in the area of multilayer thin films and nanoscale architectures. The current goal of my efforts is to quantify the amount of water incorporated into multilayer thin films constructed using the layer-by-layer technique and polyelectrolytes. Multilayer structures constructed in this fashion, generally called polyelectrolyte multilayers or PEMUs, have recently been widely studied and explored as devices in a wide variety of applications. Areas of active research and proposed application include drug encapsulation and delivery, control of surface wettability, immunosensing, use in optical devices by incorporating conducting polymers, electroluminescent moieties, and nonlinear optical chromophores, as well as nanoparticle synthesis and stabilization. Crucial to the successful use and further application of polyelectrolyte multilayer films is a detailed and quantitative molecular understanding of the mechanisms governing multilayer film formation including the role water plays in their fabrication.

Undergraduate students under my supervision have largely performed the work presented here and have been involved in each aspect of the work reported. A large portion of the funds requested was used to support my salary as well as the salaries of three undergraduate students. Three students were supported during the summer of 2004 (Max Von Euw, Glenn Eldridge, and Andrew Macaluso) and each worked ~250 hours on the project.

The basic approach has been to compare the data obtained from quartz crystal microbalance (QCM), attenuated total reflection Fourier transform infrared spectroscopy (ATR-FTIR), and atomic force microscopy (AFM) measurements. Each technique offers unique information that complements the others. For example ATR-FTIR and QCM can in principle be used to quantify the amount of water incorporated into PEMUs during deposition of the polyelectrolyte. In these experiments we employ ATR-FTIR to monitor the amount of polyelectrolyte deposited after each deposition cycle and then obtain the surface density per layer of specifically the polyelectrolyte. In similar experiments employing QCM we monitor the total mass of material adsorbed (polyelectrolyte + counter ions + water) after each deposition cycle. Comparison of the QCM data with the ATR-FTIR data should allow us to determine the amount of water and counter ions deposited in each cycle by a simple subtraction. Figures 1 and 2 show representative data of this type of comparison for the PDADMAC/PSS PEMU system. From the

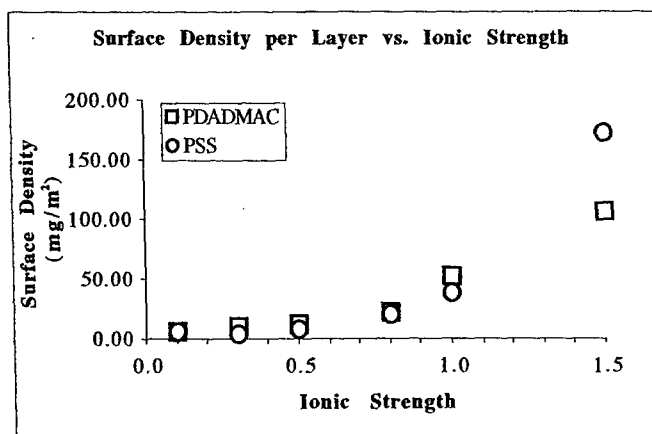


Figure 1: Surface density per layer for PDADMAC/PSS PEMUs plotted as a function of ionic strength as measured by QCM.

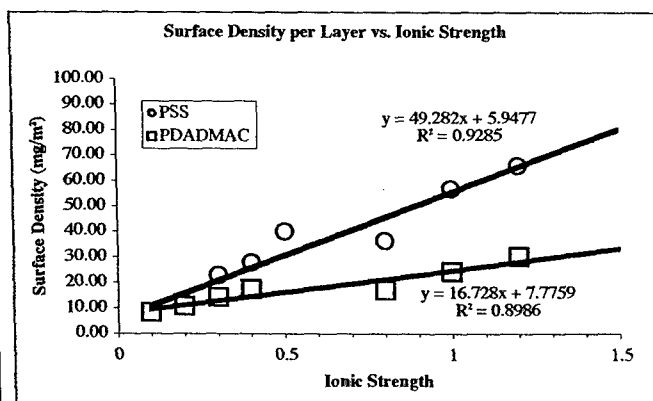


Figure 2: Surface density per layer for PDADMAC/PSS PEMUs plotted as a function of ionic strength as measured by ATR-FTIR.

data in Figures 1 and 2 we can readily identify the effect ionic strength has on PEMU surface density for the PDADMAC/PSS system but we have found it difficult to quantify the amount of water present via a simple subtraction of the two results. We are currently working to resolve this issue and plan to incorporate other techniques, most likely thermal gravimetric analysis (TGA), to help in our quantification of water content.

We have also conducted experiments similar to those summarized in figures 1 and 2 on the PAH/PSS PEMU system. This system differs from the PDADMAC/PSS system in that PAH is a polyamine and its charge density along the polymer chain is pH dependant. We find that for this system the surface charge density per layer is relatively unaffected by ionic strength but that it is greatly affected by pH. Figures 3 and 4 summarize these observations. Max and Glenn presented a poster at the spring National ACS meeting in San Diego in March describing their result on the formation of multilayer films using PAH and PSS as the polyelectrolyte building blocks.

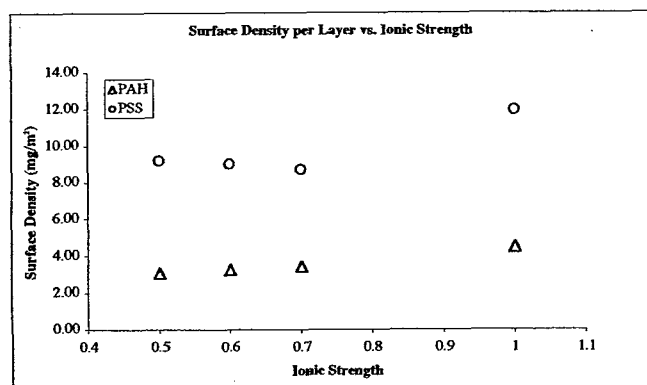


Figure 3: Surface density per layer for PAH/PSS PEMUs plotted as a function of ionic strength as measured by ATR-FTIR

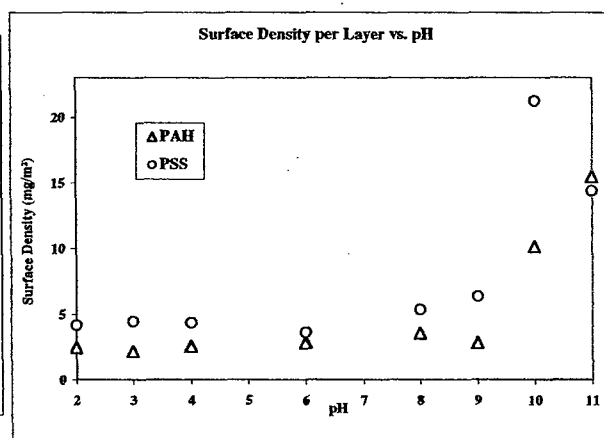


Figure 4: Surface density per layer for PAH/PSS PEMUs plotted as a function of pH as measured by QCM

A second area we began exploring this past summer was the difference in PEMU fabrication technique. Many other research groups employ a simple dipping technique to deposit the polyelectrolytes onto the solid substrate. A few groups have recently begun using a spin coating method that dramatically saves time and possibly produces more uniform films. We wanted to investigate the differences between these two fabrication techniques. Our initial efforts have involved the use of an AFM to characterize the film thickness for each deposition method. Figure 5 shows our preliminary results for the PDADMAC/PSS system. In these experiments

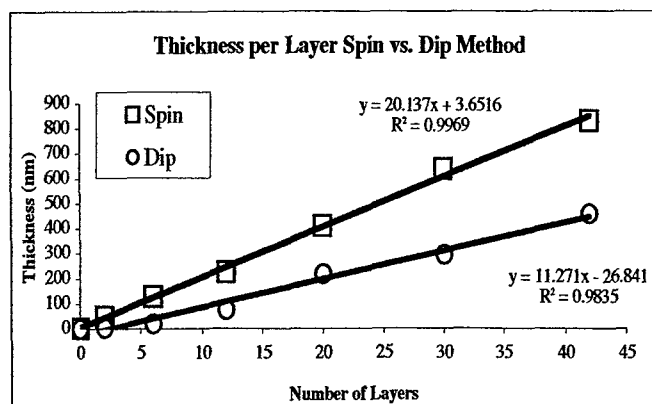


Figure 5: Thickness of PDADMAC/PSS PEMUs plotted as a function of layer as measured by AFM.

PEMUs are formed either by the dip or spin method and dried in an ambient environment. After drying polyelectrolyte is removed from the solid substrate with a razor blade in several regions. Then the PEMUs are imaged with AFM and the difference in height between the bare solid substrate and the PEMU surface is recorded. As we see in Figure 5 both techniques produce films that grow linearly, but the spin coated films show a larger increase in thickness per layer than the dip coated films. The difference in deposited mass is due to the factors that control the adsorbed mass in each method. For the dip method the adsorbed mass is largely determined by thermodynamics and the equilibrium state between adsorbed and non-adsorbed polyelectrolyte. However for the spin-coated films the adsorbed mass is determined by the amount of polyelectrolyte placed on the spinning surface and the kinetics of polyelectrolyte desorption.

Rapid Delivery of Massive Geospatial Data over Internet2

Project Investigators:

Dr. Michael Haungs
Assistant Professor
Department of Computer Science

Dr. Rollin Strohman
Professor Emeritus
Department of BioResource & Agricultural Engineering

Research Project Deliverables/Findings

System Evaluation

The main goal of the project was to study the factors that limit the performance of delivering sections of a massive, geospatial dataset over Internet2. Our dataset was generously provided for study by AirphotoUSA who will also benefit from the results of this study.

Our experiment testbed consisted of six Dell GX270 Pentium 4, 2.8 GHz CPU, with a 533 MHz front-side bus, 512KB L1 cache, and a 1MB L2 cache. They were all running Windows XP SP1 and connected via Gigabit Ethernet. Five of the six machines served as clients that generated requests for 1024x768 jpeg pictures randomly from a set of 40 locations across California. The data server machine was connected to the dataset via a Maxtor 200GB external hard drive (7200RPM, 8MB cache, USB 2.0). Our setup simultaneously looks at web service setups as well as direct network mapped solutions.

Analyzing the results of our tests led to the following findings:

1. CPU utilization was not an issue.
2. With modest resources, could serve 200 simultaneous, highly interactive users.
3. Main memory is the limiting factor. *This suggests that server-side software responsible for parsing client requests should be optimized to have a small memory footprint.*
4. Both a web services and network mapped drive approach are feasible.

Evaluate distribution to all I2 universities

We also wanted to investigate the issues involved with centrally serving AirphotoUSA's dataset from Calpoly to all Internet2 connected universities. We investigated some of the performance issues (see above), but two other important issues to address are user satisfaction (teacher and student) and security.

To explore user satisfaction, we constructed a prototype service that exports a one meter resolution, seamless orthophoto of California. This service was used by two instructors here at Calpoly; Tom Mastin, in his BRAE 345 course and David Yun in his FNR 318 class. The instructors were enthusiastic about the software and data but the students were less so. Two factors affected this response. The students tested the data at the end of the quarter after they had a fair amount of experience with higher resolution local color imagery. The older lower resolution black and white data was not as impressive. There were also problems with the license server that reduced the quality of the experience. Additional tests with students with less image experience and a higher interest in large area coverage would be useful. We are also actively pursuing collaboration with K12.

Because AirphotoUSA's dataset is proprietary, we also investigated ways to prevent illegal access. We looked at data, machine, and user level methods of protection. These methods could be used independently or in tandem. For data level security, AirphotoUSA already provides encryption. In addition to this, we recommend

watermarking the dataset to aid the tracking and identifying of stolen data. To supply machine level security, we rely on firewall technology and AirphotoUSA's license management system. Finally, to supply user authentication, we recommend using Shibboleth. "Shibboleth, a project of Internet2/MACE, is developing architectures, policy structures, practical technologies, and an open source implementation to support inter-institutional sharing of web resources subject to access controls."¹

AirphotoUSA Recommendations

Per our agreement with AirphotoUSA, we compiled a list of recommendations that they can apply to their software to facilitate serving massive, geospatial datasets over Internet2:

1. Modify the license server to accommodate simultaneous requests.
2. Re-engineer the data access DLL:
 - a. To have a smaller working set (relieve memory pressure).
 - b. To operate asynchronously to optimize throughput

Investigation of the use of AirPhotoUSA data in ERDAS Imagine

AirphotoUSA presently allows the reading of their propriety data compression inside ESRI products by use of the MapHandler dll. At the start of this project it was felt that since ERDAS supplied the ESRI raster engine that the same dll would work directly. At the time we focused on this problem, the raster engines for the two products were not the same version. I believe ESRI and ERDAS are still having some compatibility issues. ERDAS has sent a description of possible solutions directly to AirPhotoUSA.

Project Result Dissemination

Hard copies of these presentations and publications are included in the appendix of this report.

Peer-Reviewed Presentations

- Michael Haungs, Brett Cannon, Rollin Strohman, and Paul Weckler, "Rapid Delivery of Massive Geospatial Data over Internet2", Fall 2004 Internet2 Member Meeting, September 27-30, 2004, Austin, TX
- Michael Haungs and Rollin Strohman, "Experiences Delivering Massive Geospatial Datasets for Educational Use", Spring 2005 Internet2 Member Meeting, May 2-4, 2005, Arlington, VA.
- Michael Haungs and Rollin Strohman, "Integrating and Delivering Massive Geospatial Datasets for Educational Use", CENIC 2005, March 7-9, 2005, Marina Del Rey, CA

¹ <http://shibboleth.internet2.edu/about-shibboleth.html>

- Rollin Strohman, Michael Haungs, Tom Mastin, and Paul Weckler, "Rapid Delivery of Massive Geospatial Data over Internet2", ASPRS 2005 Annual Conference, March 7-11, 2005, Baltimore, MA

Invited Talks

- Michael Haungs, "Experiences Delivering Massive Geospatial Datasets for Educational Use", NJIT Internet2 Day, April 22, 2005, Newark, NJ

Rapid Delivery of Massive Geospatial Data over Internet2



Michael Haungs
Brett Cannon
Rollin Strohman
Paul Weckler

Large, Online Datasets Abound

- TerraServer
 - Microsoft/US Geological Survey (USGS)
- Soil Data Mart
 - Natural Resources Conservation Service
 - US Department of Agriculture
- Sloan Digital Sky Survey
 - NASA, Los Alamos National Laboratory, NSF, University of Chicago, Johns Hopkins, Japan Participation Group, many more...

The Challenge

- Build services to connect researchers to these type of datasets
- The service needs to be:
 - Accessible
 - Commodity technology
 - Integrated
 - Export a common interface for multiple datasets
 - User-friendly

Approach 1

- Download data
 - Too much
 - Maintenance
 - Complicated System
 - Updates
 - Keeping data "fresh"
 - Duplicated Effort

Approach 2

- Standardize on an access protocol
 - SOAP, HTML, XML?
 - Samba, NFS?
 - Web Service API
 - OpenGIS?
 - Incentive to collaborate?
 - Open standards not optimized for specific use
 - Availability
 - Load balancing

Approach 3

- Data Warehouse
 - Centralized Solution
 - Storage
 - Maintenance
 - Data Acquisition
 - Scalability
 - Sufficient Bandwidth and processing power

Current Projects

- The National Map (USGS)
- SkyServer (Sloan Digital Sky Survey)
- BioMOBY (NSF)
- NOTEBOOK Project (San Diego Supercomputing Center)

Our Mission

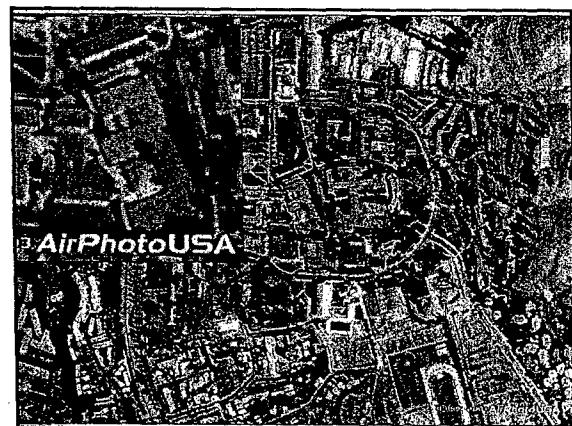
- Build a service to provide massive, remote geospatial datasets for educational use
- Data Warehouse Approach, optimized for:
 - Proprietary dataset
 - Interactive, explorative
 - Internet2

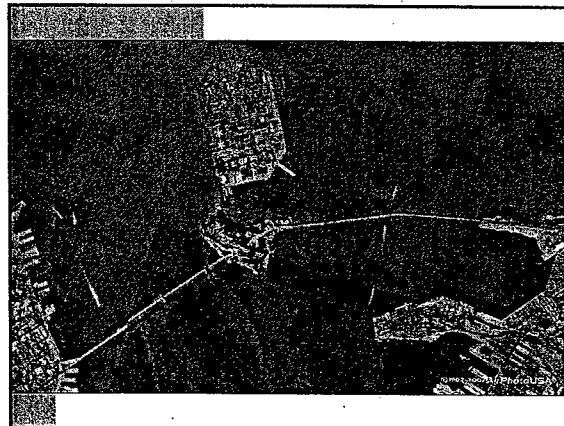
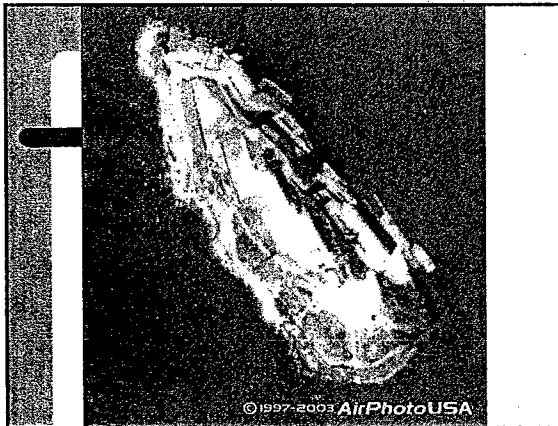
AirPhotoUSA

- Seamless, one-meter resolution aerial orthophotography covering over 3 million square miles of the US
- 20TB (2.5 TB compressed)
- Value added processing
 - Tone changes
 - Overlapping images
- Generously made available by AirPhotoUSA for this study

AirPhotoUSA

- Security
 - Licenses
 - Protecting the dataset
- Limited Customization
 - Do not have access to code





Educational Use

- Pedagogical use differs from scientific
 - Interactivity
 - Limited lab time
 - Require quick, fluid responses
 - Treasure-hunt approach
 - Multiplicity
 - Groups performing similar activities
 - Connectivity

Internet2

- Changes basic assumption of client/server applications
 - Fast machines and slow communication
- Do old optimizations still make sense?
 - Caching? Compression? Remote desktops?
- Other optimizations?
 - Prefetching? Indirection?

Internet2

- CalPoly
 - 1 Gb/s backbone
 - 622 Mb/s pipe to ISP in L.A.
 - ISP connects to Abilene I2 network at 2.2 Gb/s
 - Future
 - Can grow up to 10Gb/s (Abilene Limit)

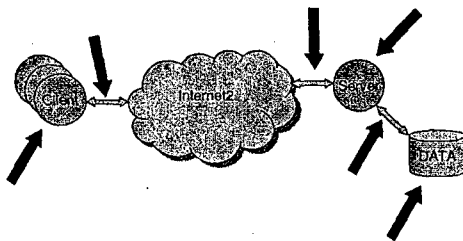
Current work

- Client/Server Organization
 - Separate administrative domains
 - Client independent of server
- Bottleneck Analysis

Client/Server Organization

- Direct access
 - NFS, Samba, TCP/IP session
 - LAN model
- Web services
 - HTTP, SOAP, XML, UDDI, WSDL, OpenGIS
 - Distributed model
- We are looking at both

Bottleneck Analysis



Bottleneck Analysis

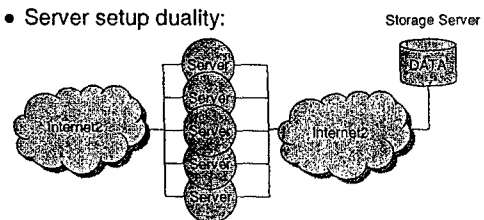
- Measuring
 - CPU Utilization
 - Memory (Paged and non-paged)
 - I/O (Disk bytes and queue length)
 - Network Bandwidth (Bytes/sec)

Performance Metrics

- User-response time
 - What delays are noticeable to the user?

Experiment Setup

- Server setup duality:



Experiment Setup

- Machines
 - Dell GX270
 - Intel Pentium 4 2.8 GHz CPU
 - 512KB L1 cache, 1MB L2 cache
 - 533MHz front-side bus
 - 512MB RAM
 - Gigabit Ethernet Card
 - 75GB ATA/100 IDE Hard drive
 - Windows XP SP1

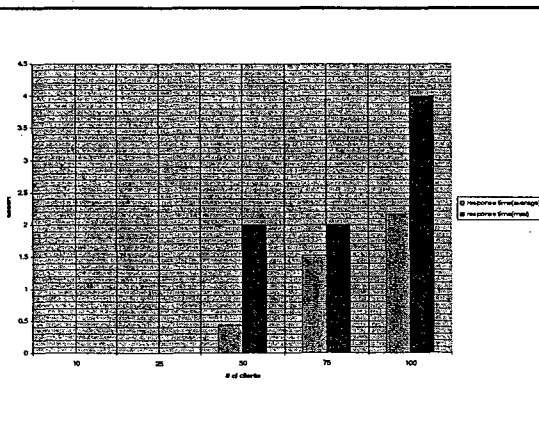
Experiment Setup

- Maxtor 200GB External Hard Drive
 - 7200 RPM
 - 8MB Cache
 - USB 2.0 (up to 480Mbps/sec)

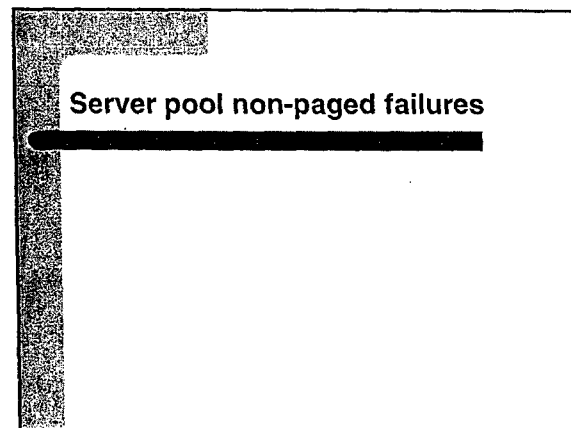
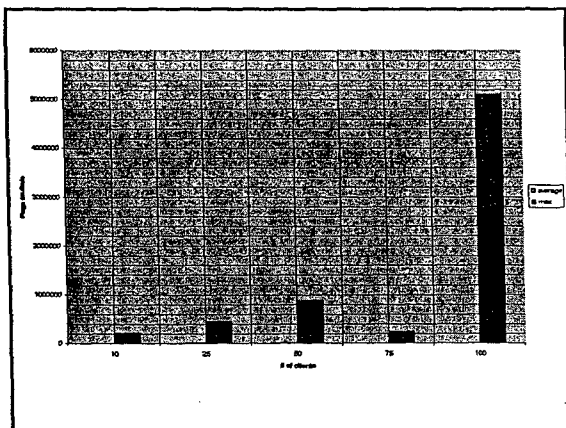
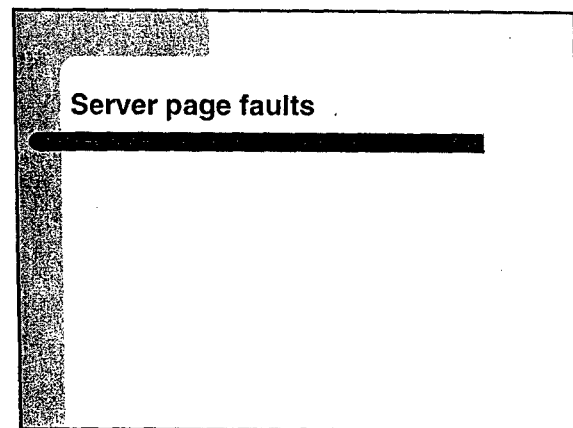
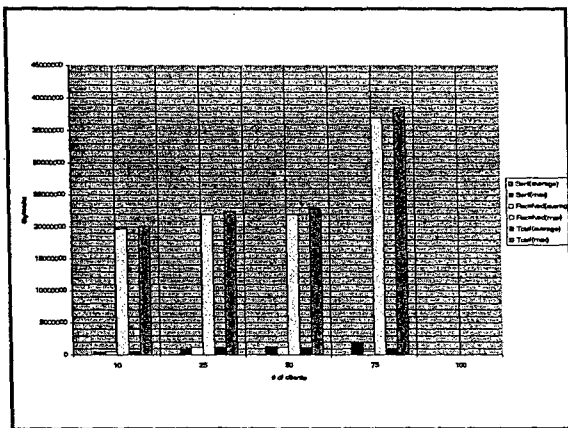
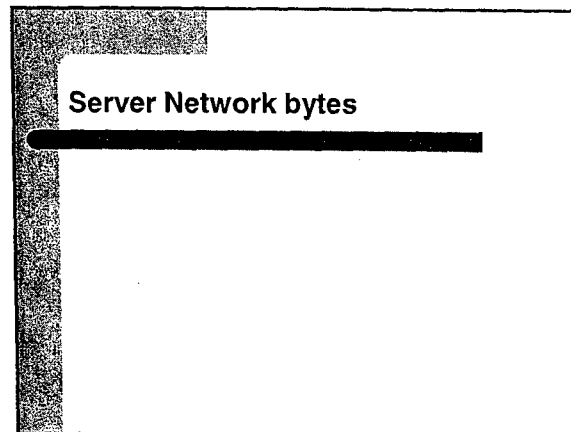
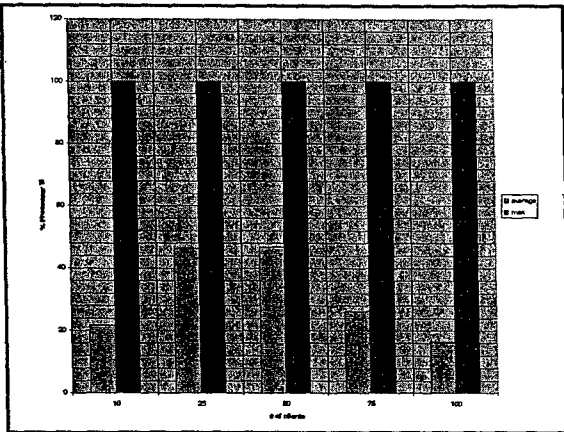
Experiment Setup

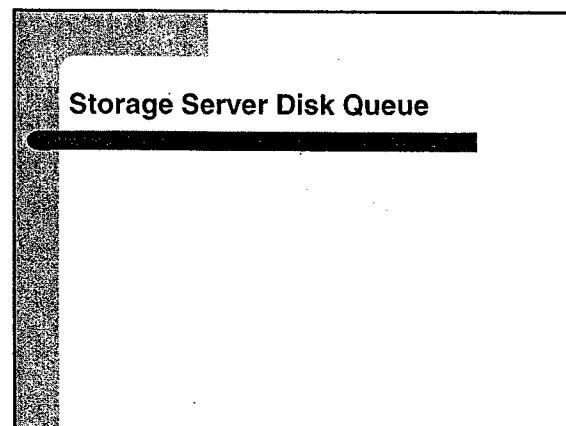
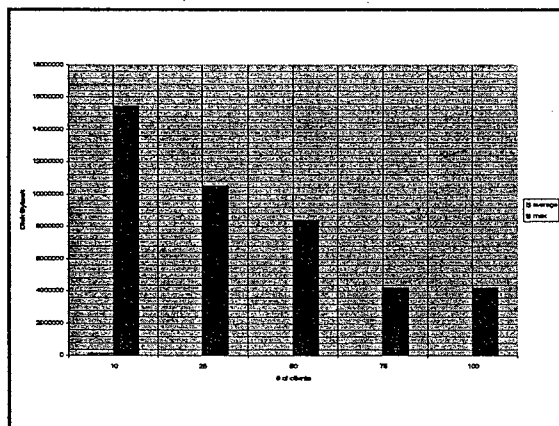
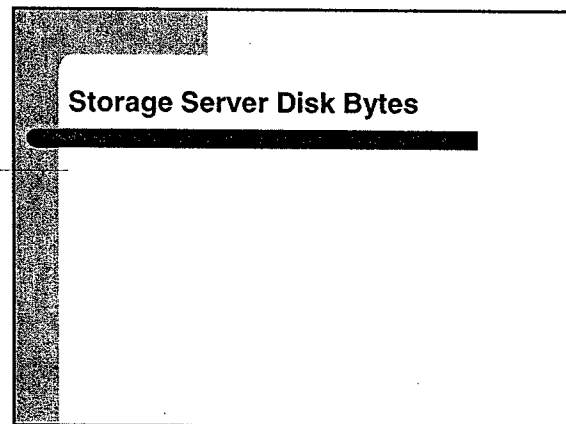
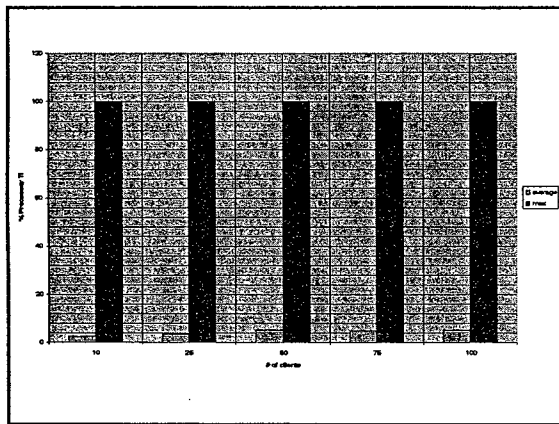
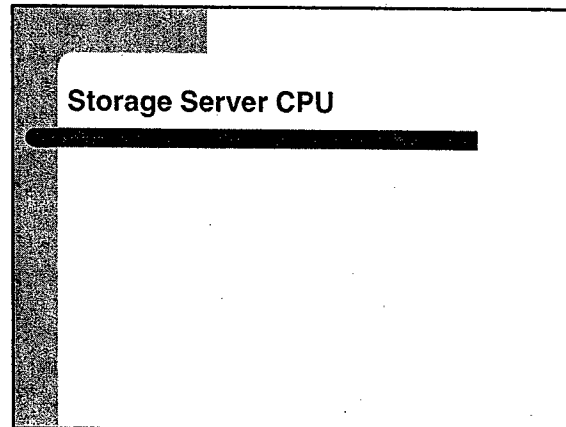
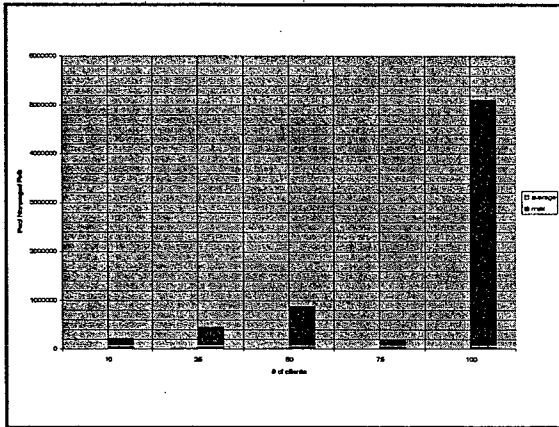
- Requests/Client
 - 40 random points in California
 - Maximum resolution
 - Screen size:
 - Bytes/request:
 - Approximates 4 users/client

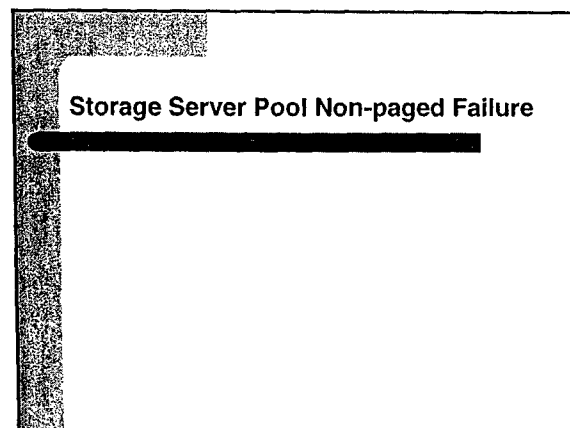
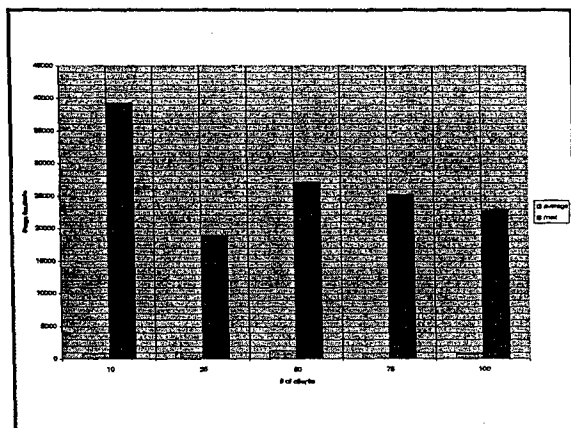
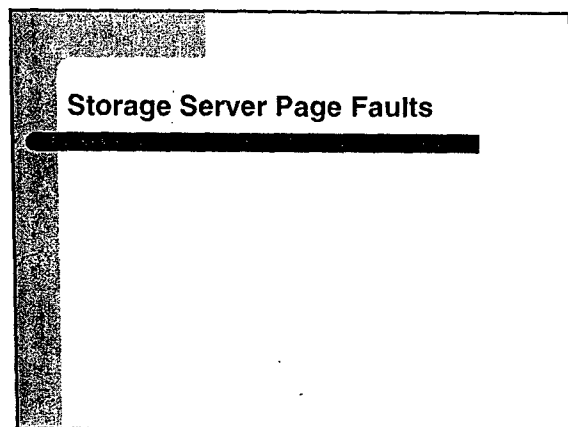
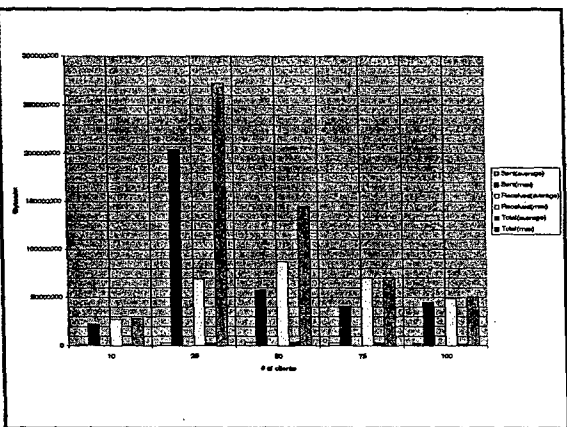
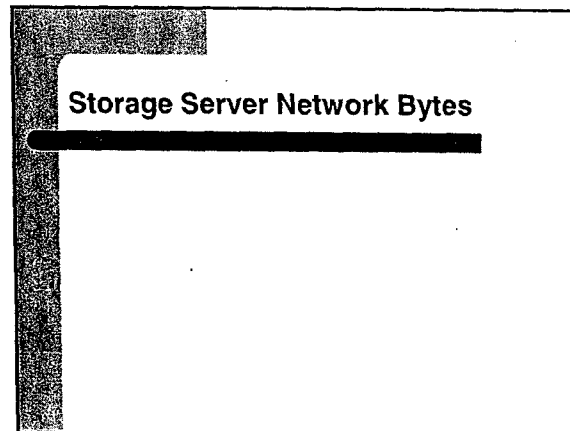
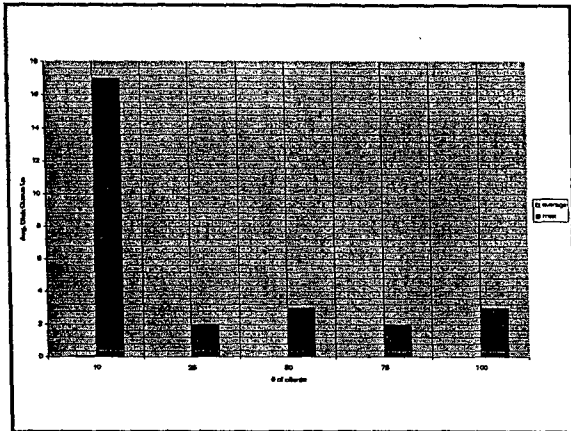
Response times (Server)

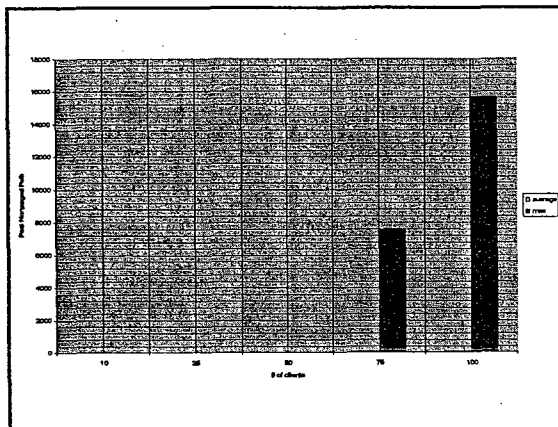


Results:: Server CPU









Analysis

- CPU not an issue
- Network and Disk load
 - Sufficient for 400 simultaneous, highly interactive users
- AirphotoUSA proprietary DLL for accessing data
 - BOTTLENECK for web services scenario
 - Need more RAM or optimize DLL

Recommendations

- AirphotoUSA
 - License server bottleneck
 - Possible race condition
 - Central and serial access
 - Port to Linux (or use Windows 2003 server)
 - Windows XP problems
 - Optimize DLL for web service use
 - Smaller working set, memory footprint

Recommendations

- Client/Server organization
 - Server needs sufficient RAM (> 512MB)
 - Standard 2-tier web service model works
 - Direct attached storage works
 - Currently investigating new ideas
 - Client-side centralized caching to capitalize locally on multiplicity

Future Work

- Prototype Implementation with set of 12 Universities
 - CalPoly, Stephen F. Austin, South Dakota, Oklahoma State
- Virtual Teaming
 - Educator Collaboration
- National Dissemination
 - All Internet2 Universities
 - K/12
 - Group data purchase
- Serving Other Datasets from Calpoly
- New Client/Server Architectures
 - Build them

Conclusion

- If you are interested in any aspect of this project, please contact us at:
 - Michael Haungs, mhaungs@csc.calpoly.edu
 - Rollin Strohman, rstrohma@calpoly.edu

Experiences Delivering Massive Geospatial Datasets for Educational Use



Michael Haungs, Ph.D.
Rollin Strohmman, Ph.D.

Our Mission

- Build a service to provide massive, remote geospatial datasets for educational use over Internet2

Demonstration

Uses

- Virtual Field Trips
 - California Missions
- Wildlife study
 - Monarch butterfly migration paths
- City layout and design
- Base layer in remote GIS
- Seems endless...

Benefits

Approximately 80% of business and government information has some reference to location, but until recently the power of geographic/spatial information and location has been underutilized as a vital resource to improve economic productivity, decision making, and delivery of services. We are an increasingly distributed and mobile society. Our technologies, services, and information resources must be able to leverage location (i.e., my geographic position right now) and the spatial information that helps us visualize and analyze situations geographically.

Open Geospatial Consortium

Issues

- Administration
- Data Quality
- Data Source
- Performance
- Customization
- Educational Use

Administration

- Distributed
 - Every person for themselves

Administration

- Standard Protocols (OGC)
 - WMS, WMF, GML, SFS, ...
 - Tie together existing efforts

Administration

- Federated
 - National Map
- Centralized
 - Google, ESRI, Terraserver
 - Most efficient use of resources

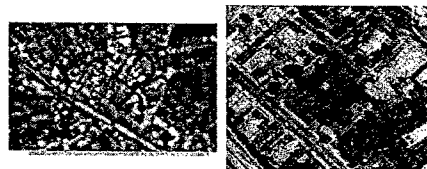
Data Quality

- Uniform coverage
 - 1-meter resolution (minimum)
 - Need for novice users
 - Seamless, tone matched

Google Comparison I



Google Comparison II



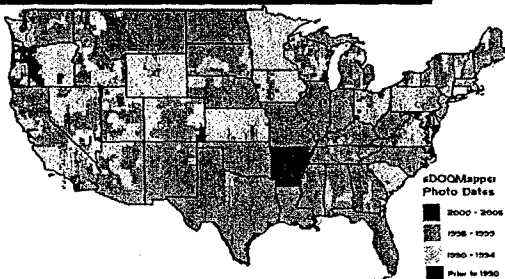
Data Source

- Free Sources
 - USGS, NAIP, AmericaView
 - Adv: License free
 - Dis: Mosaicking, compression, updates, storage
- Proprietary
 - AirphotoUSA, ESRI
 - Adv: Seamless, orthophoto
 - Dis: Security, Flexibility
- Government plans?

AirphotoUSA dataset

- Airphoto USA
 - Seamless, one-meter resolution aerial orthophotography covering over 3 million square miles of the US
 - 20TB (2.5 TB compressed)
 - Generously made available by AirPhotoUSA for our study
 - Viewing software - PhotoMapper
 - Rapid pan and zoom for best user experience

AirphotoUSA dataset



Performance

- Targeting high-bandwidth connections
 - Internet2 Universities
 - Future Kindergarten through 12th grade
 - Network speed will continue to improve

Performance

- CalPoly, San Luis Obispo, CA
 - 1 Gb/s backbone
 - 622 Mb/s pipe to ISP in L.A.
 - ISP connects to Abilene I2 network at 2.2 Gb/s
 - Future
 - Can grow up to 10Gb/s (Abilene Limit)

Performance

- Internet2
 - Changes basic assumption of client/server applications
 - Fast machines and slow communication
 - Do old optimizations still make sense?
 - Caching? Compression? Remote desktops?

Performance

- Internet2
 - Other optimizations?
 - Prefetching? Indirection?
 - Counter example
 - VNC is an example of an application designed for low bandwidth connections

Customization

- End-user requirements
 - K20 Educators
 - Researchers
 - Special Projects

Educational Use

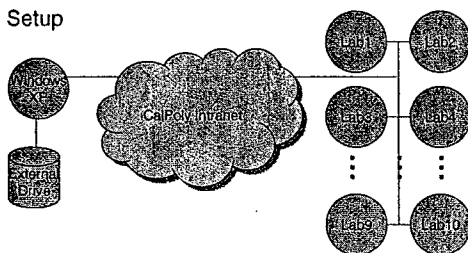
- Interactivity
 - Limited lab time
 - Require quick, fluid responses
 - Treasure-hunt approach
- Multiplicity
 - Groups performing similar activities

Educational Use

- Educator Collaboration
 - Curriculum development
 - Collaboration tools?
- Advertisement
- Training
- Delivery

Pilot Study Preliminary Results

- Setup



Experiment Setup

- Server Machine
 - Dell GX270
 - Intel Pentium 4 2.8 GHz CPU
 - 512KB L1 cache, 1MB L2 cache
 - 533MHz front-side bus
 - 512MB RAM
 - Gigabit Ethernet Card
 - 75GB ATA/100 IDE Hard drive
 - Windows XP SP1

Experiment Setup

- Maxtor 200GB External Hard Drive
 - 7200 RPM
 - 8MB Cache
 - USB 2.0 (up to 480Mbps/sec)

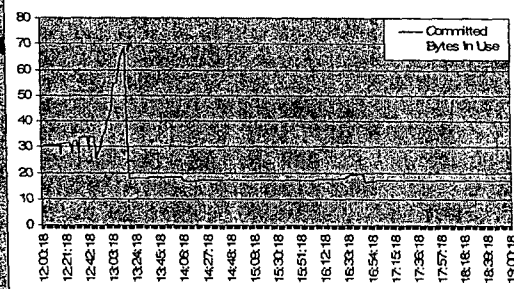
Experiment Setup

- Maxtor 200GB External Hard Drive
 - 7200 RPM
 - 8MB Cache
 - USB 2.0 (up to 480Mbps/sec)

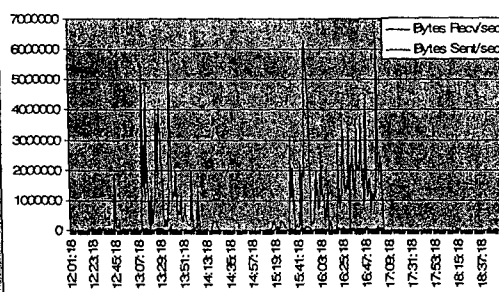
Experiment Setup

- Two Labs
 - 12pm – 1:30pm (Tom Maston, CalPoly)
 - Photomapper Viewer Tutorial
 - 3pm – 6pm (David Yun, City of SLO)
 - Pan and Zoom to:
 - Morro Rock, CalPoly, Own home, San Andreas fault, Disneyland, Golden Gate Bridge, Death Valley.

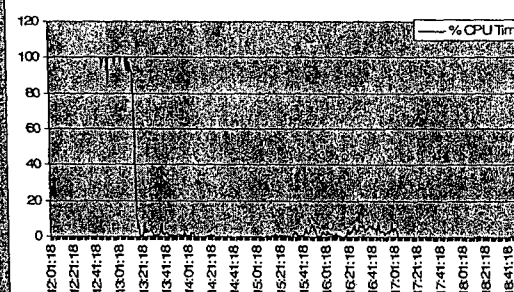
Pilot Study Preliminary Results : Memory

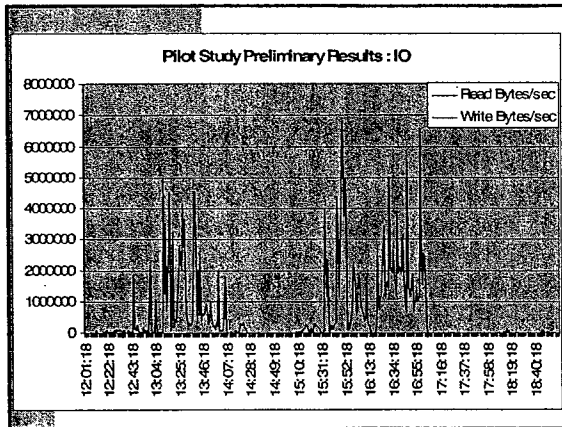


Pilot Study Preliminary Results : Network



Pilot Study Preliminary Results : CPU





Pilot Study Preliminary Results

- Instructor Impressions
 - Enthusiastic about:
 - Performance
 - Dataset
 - Software

Pilot Study Preliminary Results

- Student Impressions
 - Not Impressed....
 - Two factors:
 - Experienced with higher resolution local color imagery
 - Initial license server problems

Pilot Study Preliminary Results

- Exploring color datasets
 - NAIP
- Hybrid approach
 - AirphotoUSA base
 - Incorporate NAIP datasets as become available

Project Status

- We have access to a seamless, orthophoto of entire US
- Conducted an initial feasibility study
 - Bottleneck analysis
 - Testing in CalPoly labs
- Have access to multiple data sources
 - Generate own
 - Pursue proprietary model

Project Status

- End application
 - Pursuing multiple avenues
 - Investigating novel approaches
 - Need input from community
- Educator Collaboration
 - Pedagogical best practices
 - K-12 curriculum development

Future Work

- Prototype Implementation with set of I2 Universities
 - CalPoly, Stephen F. Austin, South Dakota, Oklahoma State
- Virtual Teaming
 - Educator Collaboration
- National Dissemination
 - All Internet2 Universities
 - K/20
 - Group data purchase
- Serving Other Datasets from Calpoly
- New Client/Server Architectures
 - Build them

AmericaView

"Satellite data is expensive, and using the data requires significant investments in software, hardware, and training. It has often been hard for university researchers to use or even access the data, particularly at smaller schools or research facilities. For three decades this has hindered applied research and made it difficult to train the workforce, both current and future."

Conclusion

- If you are interested in any aspect of this project, please contact us at:
 - Michael Haungs, mhaungs@calpoly.edu
 - Rollin Strohman, rstrohma@calpoly.edu
- Questions?

Integrating and Delivering Massive Geospatial Datasets for Educational Use



Michael Haungs, Ph.D.
Rollin Strohman, Ph.D.

Our Mission

- Build a service to provide massive, remote geospatial datasets for educational use

AmericaView

"Satellite data is expensive, and using the data requires significant investments in software, hardware, and training. It has often been hard for university researchers to use or even access the data, particularly at smaller schools or research facilities. For three decades this has hindered applied research and made it difficult to train the workforce, both current and future."

Related Work

- TerraServer
 - Microsoft/US Geological Survey (USGS)
- Soil Data Mart
 - Natural Resources Conservation Service
 - US Department of Agriculture
- Sloan Digital Sky Survey
 - NASA, Los Alamos National Laboratory, NSF, University of Chicago, Johns Hopkins, Japan Participation Group, many more...

Related Work

- The National Map (USGS)
- SkyServer (Sloan Digital Sky Survey)
- BioMOBY (NSF)
- NOTEBOOK Project (San Diego Supercomputing Center)
- GEON (SDSC, Penn State U, UC San Diego, Geological Survey of Canada)

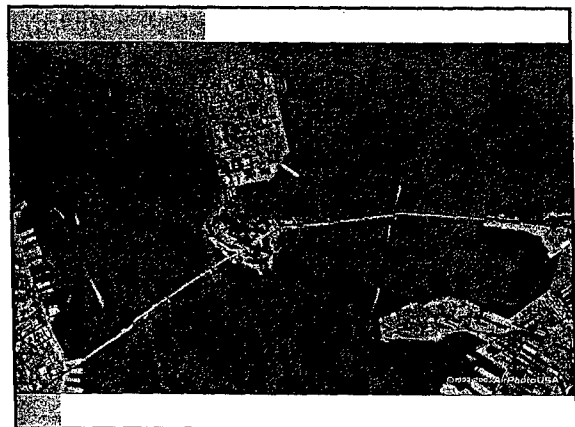
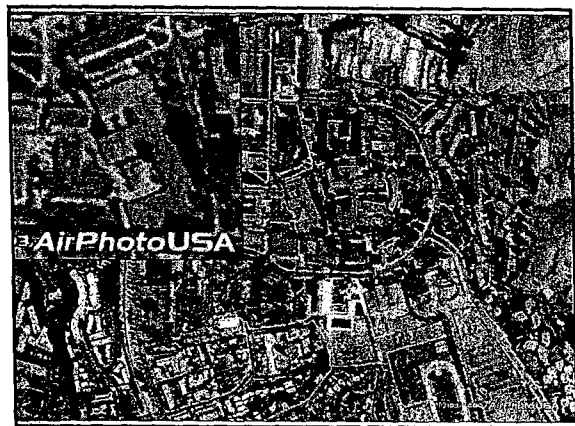
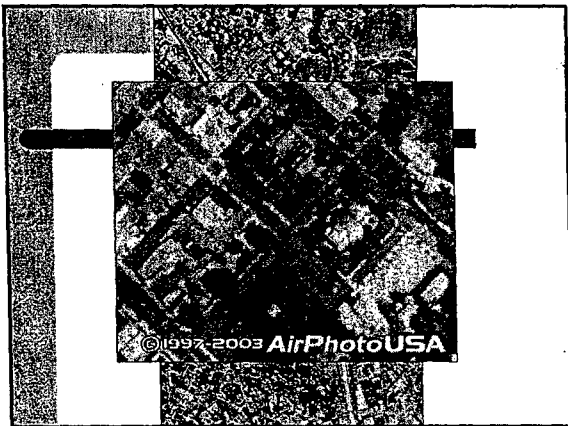
Pedagogical use differs from scientific

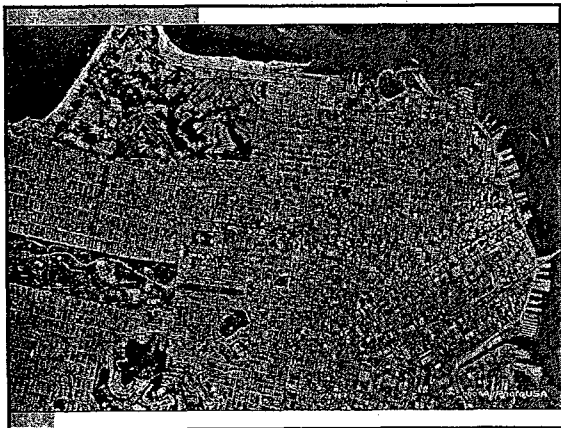
- Interactivity
 - Limited lab time
 - Require quick, fluid responses
 - Treasure-hunt approach
- Multiplicity
 - Groups performing similar activities
- Connectivity
 - High speed networks

MapSurfer

- <http://casil.ucdavis.edu/mapsurfer>

Something like the following...





Movie showing dataset performance

- Receiving computer
 - IBM Thinkpad T23
 - 1 Ghz CPU, 768 MB RAM
 - 100 Base-T network connection
 - Running PhotoMapper and Camtasia Studio
 - Actual performance better than shown



Uses

- California missions (Virtual Field Trips)
- Monarch butterfly migration paths
- National wildlife reserves
- City layout and design
- Geographic Information Systems (GIS)
- Seems endless...

Benefits

- Gets students excited about learning:
 - Geography
 - History
 - Sociology
 - Architecture
 - City Planning
 - Forestry
- Exposure to GIS technology

Issues

- Which dataset should we use?
 - Proprietary? Build and maintain our own?
- How should we build the application?
 - Optimized for educational use
 - Thin client, Thick client, pure data export?
- How should we incorporate such a service into K-20 curriculum?
- What is the method of delivery?

Which dataset should we use?

- One meter resolution
- Proprietary Dataset
 - AirphotoUSA
 - Seamless of entire USA
- Exploring building own seamless orthophoto of California
 - CaliforniaView (<http://gis.ca.gov/casil/usgs.gov/>)
 - AmericaView (<http://www.americaview.org/>)

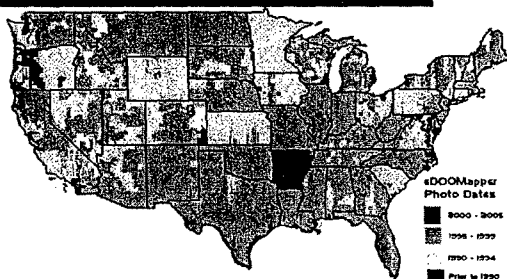
Why 1 meter resolution?

- Intended users have limited photo interpretation experience
- First task is to find your house
 - then investigate your neighborhood
 - learn to interpret top view in process
- Curiosity key to learning process

Using a proprietary dataset

- Airphoto USA
 - Seamless, one-meter resolution aerial orthophotography covering over 3 million square miles of the US
 - 20TB (2.5 TB compressed)
 - Generously made available by AirPhotoUSA for our study
 - Viewing software - PhotoMapper
 - Rapid pan and zoom for best user experience

Using a proprietary dataset



Using a proprietary dataset

- Issues:
 - Security
 - Licenses
 - Protecting the dataset
 - Shibboleth (<http://shibboleth.internet2.edu/>)
 - Limited Customization
 - Do not have access to code
 - Cost

Using a proprietary dataset

- Advantages:
 - We have this now
 - It's very good quality
 - Good compression/performance
 - Should be able to scale to large numbers of users

Building our own dataset

- Steps
 - Acquire Digital Orthophoto Quarter Quads (DOQQ) from free source
 - Mosaicking (Leica Geosystems, ERMapper)
 - Compress to JPEG2000 (ERDAS)
 - Necessary over fast networks?

Building our own dataset

- Issues
 - Computational and Storage resources
 - Maintaining updates
- Advantages
 - Free use

How should we build the application?

- How should we build this application to best fit the needs of K-20 educators?
- Requirements
 - Scalable
 - Flexible
 - Available
 - Interactive
 - Intuitive

How should we build the application?

- Options
 - Web Service
 - Web Application
 - Distributed Application

Web Service

- Request tiles via a standard web services API
- Advantages
 - Flexible
 - Web page
 - GIS Applications
 - Custom Viewers
 - With or without layer support

Web Service

- Disadvantages
 - No client-side support
 - Duplicated effort
 - Requires high level of expertise from client

Web Application

- Client-side
 - Only requires a web browser (thin client)
 - Java plug-in
- Server-side
 - No need to conform to communication standard

Web Application

- Advantages
 - No client-side administration/maintenance required
 - Works well with proprietary data
 - Full control of application
 - Updates automatic
- Disadvantages
 - Extra "connection-time" load
 - Simple client-side application

Distributed Application

- Client-side
 - Provide full featured client to user (Thick Client)
 - Maintained/supported by us
 - Collaborate with a vendor?
- Server-side
 - General vector data repository

Distributed Application

- Advantages
 - Minimal user expertise
 - End-to-end optimizations
 - Load balancing
 - Caching
 - Quality Control
- Disadvantages
 - Resources
 - Cost
 - License software (3rd party vendor)
 - Inflexible

Current Work: Application

- Data Warehouse Approach, optimized for:
 - Proprietary dataset
 - Interactive, explorative
 - Internet2
- Calpoly Farmland GIS project
 - 6000 acres
 - 4000 students
 - ESRI products

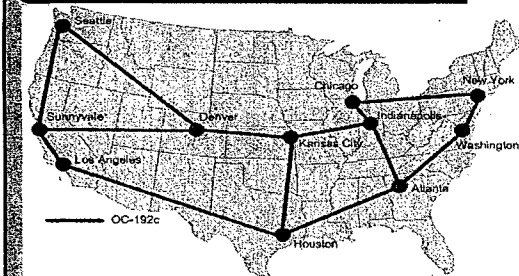
K-20 Curriculum

- K-20 Curriculum
 - What do teachers want?
- Educator Collaboration
 - Curriculum development
 - Collaboration tools?
- Advertisement
- Training
- Delivery

Internet2

- Project Focus
 - Internet2 Universities
 - Future Kindergarten through 12th grade
 - Network speed will continue to improve

Internet2 (Abilene Network)



Internet2

- CalPoly, San Luis Obispo, CA
 - 1 Gb/s backbone
 - 622 Mb/s pipe to ISP in L.A.
 - ISP connects to Abilene I2 network at 2.2 Gb/s
 - Future
 - Can grow up to 10Gb/s (Abilene Limit)

Internet2

- Changes basic assumption of client/server applications
 - Fast machines and slow communication
- Do old optimizations still make sense?
 - Caching? Compression? Remote desktops?
- Other optimizations?
 - Prefetching? Indirection?

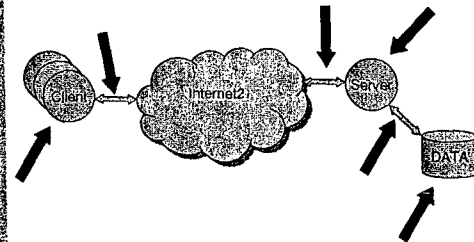
Questions?

- Next: Some results of a study conducted for AirphotoUSA

Initial Study

- Understand existing bottlenecks of hardware and proprietary software for serving AirphotoUSA's geospatial dataset.

Bottleneck Analysis



Bottleneck Analysis

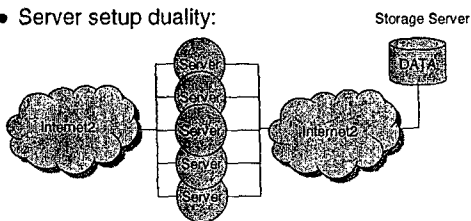
- Measuring
 - CPU Utilization
 - Memory (Paged and non-paged)
 - I/O (Disk bytes and queue length)
 - Network Bandwidth (Bytes/sec)

Performance Metrics

- User-response time
 - What delays are noticeable to the user?

Experiment Setup

- Server setup duality:



Experiment Setup

- Machines
 - Dell GX270
 - Intel Pentium 4 2.8 GHz CPU
 - 512KB L1 cache, 1MB L2 cache
 - 533MHz front-side bus
 - 512MB RAM
 - Gigabit Ethernet Card
 - 75GB ATA/100 IDE Hard drive
 - Windows XP SP1

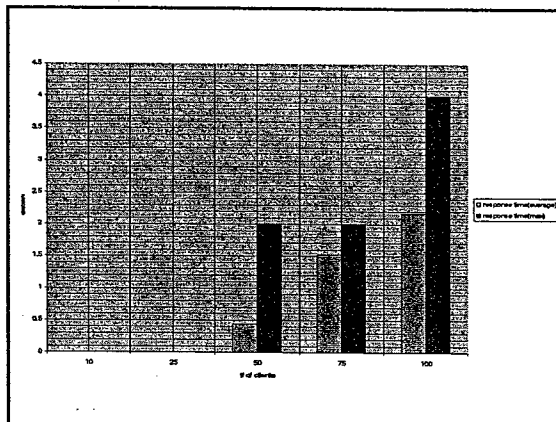
Experiment Setup

- Maxtor 200GB External Hard Drive
 - 7200 RPM
 - 8MB Cache
 - USB 2.0 (up to 480Mbps/sec)

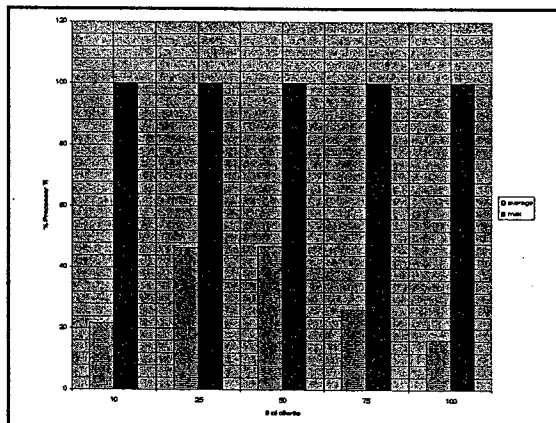
Experiment Setup

- Requests/Client
 - 40 random points in California
 - Maximum resolution
 - Image size: 1024x768, ~1/3 MB
 - Approximates 4 users/client

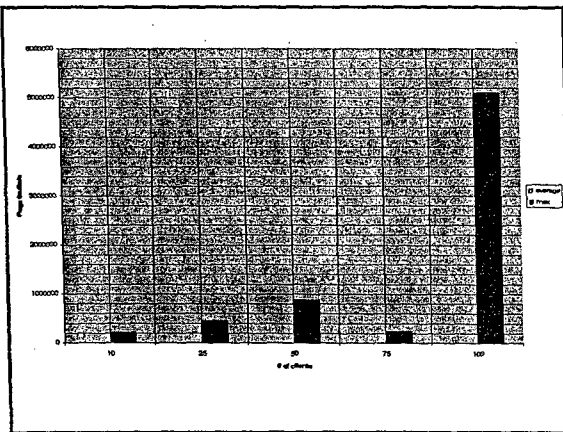
Response times (Server)



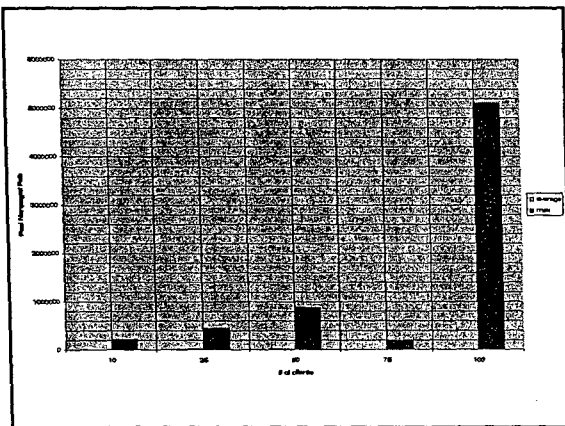
Results:: Server CPU



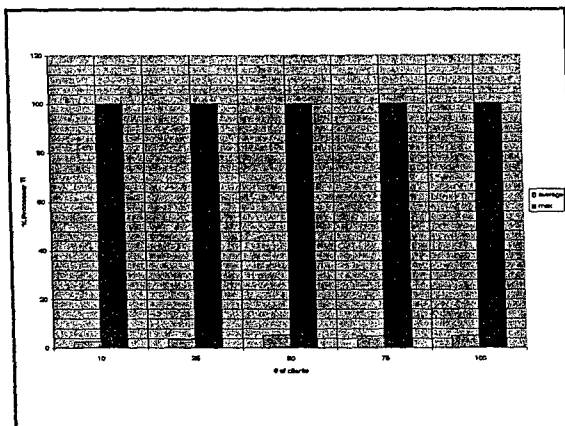
Server page faults



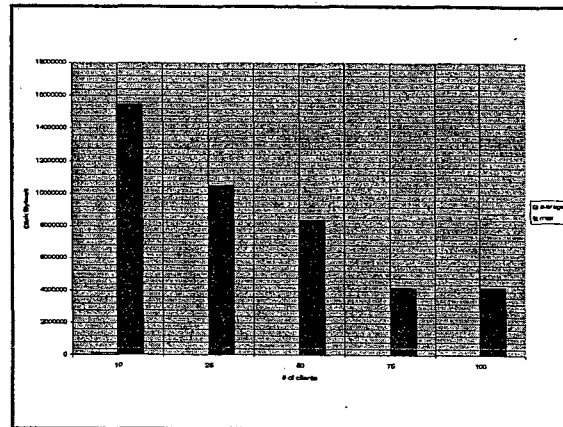
Server pool non-paged failures



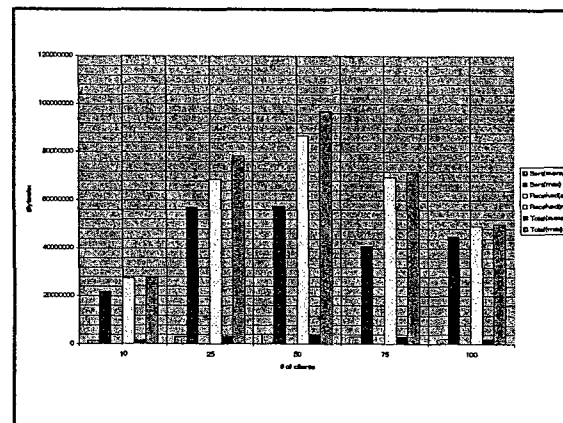
Storage Server CPU



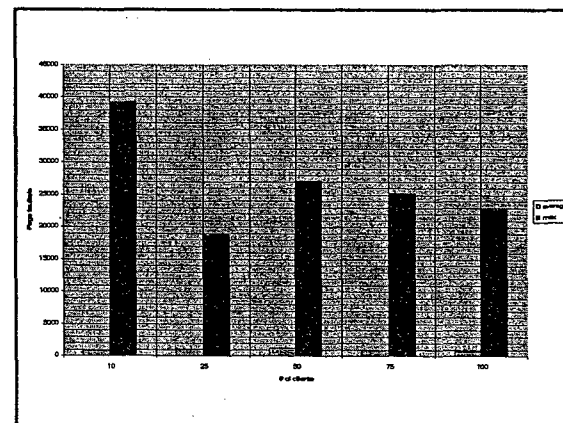
Storage Server Disk Bytes



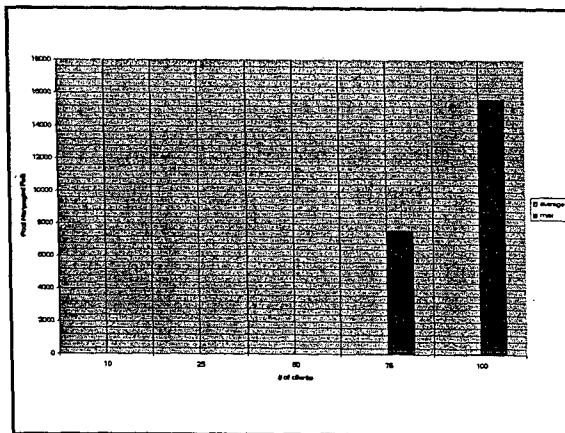
Storage Server Network Bytes



Storage Server Page Faults



Storage Server Pool Non-paged Failure



Bottleneck Analysis Summary

- CPU not an issue
- Network and Disk load
 - Sufficient for 200 simultaneous, highly interactive users
- AirphotoUSA proprietary DLL for accessing data
 - BOTTLENECK for web services scenario

Recommendations

- AirphotoUSA
 - License server bottleneck
 - Possible race condition
 - Central and serial access
 - Port to Linux (or use Windows 2003 server)
 - Windows XP problems
 - Optimize DLL for web service use
 - Smaller working set, memory footprint
 - Asynchronous operation
 - Improve data retrieval

Recommendations

- Client/Server organization
 - (Storage) Server needs sufficient RAM (> 512MB)
 - Server-level OS
 - Network optimization, multiple processes
 - Standard 2-tier web service model works
 - Direct attached storage works
 - Currently investigating new ideas
 - Client-side centralized caching to capitalize locally on multiplicity

Wrap up

- We have access to a seamless, orthophoto of entire US
- Conducted an initial feasibility study
 - Bottleneck analysis
 - Testing in CalPoly labs
- Have access to multiple data sources
 - Generate own
 - Pursue proprietary model

Wrap up

- End application
 - Pursuing multiple avenues
 - Investigating novel approaches
 - Need input from community
- Educator Collaboration
 - Pedagogical best practices
 - K-12 curriculum development

Future Work

- Prototype Implementation with set of 12 Universities
 - CalPoly, Stephen F. Austin, South Dakota, Oklahoma State
- Virtual Teaming
 - Educator Collaboration
- National Dissemination
 - All Internet2 Universities
 - K/20
 - Group data purchase
- Serving Other Datasets from Calpoly
- New Client/Server Architectures
 - Build them

Conclusion

- If you are interested in any aspect of this project, please contact us at:
 - Michael Haungs, mhaungs@calpoly.edu
 - Rollin Strohman, rstrohma@calpoly.edu
- Questions?

RAPID DELIVERY OF MASSIVE GEOSPATIAL DATA OVER INTERNET2

Rollin Strohman, Professor Emeritus, Cal Poly
Michael Haungs, Assistant Professor, Cal Poly

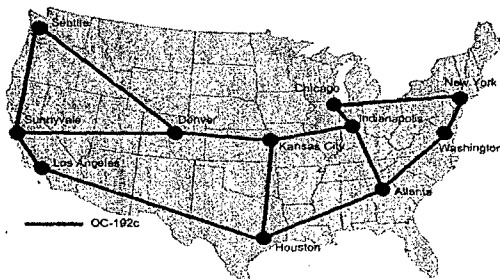
Collaborators

Brent Cannon, Master's Candidate, Cal Poly
Tom Mastin, Instructor, Cal Poly
 California Polytechnic State University (Cal Poly)
 San Luis Obispo, CA 93407
Paul Weckler, Assistant Professor, Oklahoma State
 University, Stillwater, Oklahoma

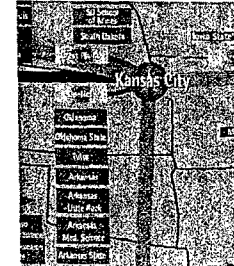
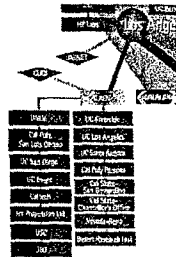
Project Focus

- Internet2 Universities
 - Network speed not an issue (10Gb/second backbone)
- Future Kindergarten through 12th grade
 - Network speed will continue to improve for all

Abilene Network 10Gb/sec



Cal Poly and Oklahoma State 622 Mb/sec connection



Dataset Choice

- Digital Orthophoto Quarter Quads
 - National Digital Orthophoto Program
 - <http://www.ndop.gov/data.html>
 - Characteristics
 - National Coverage
 - 1 meter Black and White Pixel
 - Data age about 7 – 10 years old
 - Best that might be affordable

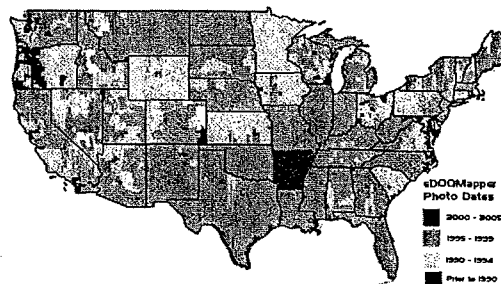
Why 1 meter resolution?

- Intended users have limited photo interpretation experience
- First task is to find your house
 - then investigate your neighborhood
 - learn to interpret top view in process
- Curiosity key to learning process

Collaborating with AirPhotoUSA

- Provided dataset and viewing software for tests
- Viewing Software – PhotoMapper
 - Rapid pan and zoom for best user experience
- Dataset – eDOQMapper
 - Seamless coverage of all USA available
 - Initial tests with California only

eDOQMapper



Movie showing Dataset performance

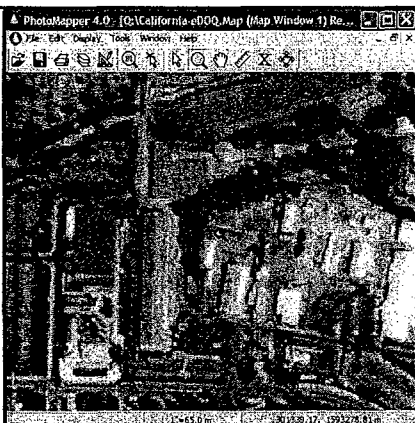
- Receiving computer
 - IBM Thinkpad T23
 - 1 Ghz CPU, 768 MB RAM
 - 100 Base-T network connection
 - Running PhotoMapper and Camtasia Studio
 - Actual performance better than shown

Pan and Zoom
To San Francisco



Use Thumbwheel
to zoom out.

Add vector layers
Highways
Cities
DOQQ



Funding education use

- Education could benefit from a shorter refresh cycle on DOQQ data
- Shibboleth (digital rights management) needed to protect market for private companies) <http://shibboleth.internet2.edu/>
- Federal support needed for AirPhotoUSA data distribution schools
- To justify purchase from AirPhotoUSA we need to look at alternatives.

Other DOQQ Distributions

Two available in ESRI ArcService

- <http://www.esri.com/software/arcwebservices/about/data.html#imagery>
- GlobeXplorer U.S. DOQQ Imagery
 - i-cubed data
 - http://www.i3.com/products/edoqq_doqq.htm
- Pixxures U.S. DOQQ Imagery
 - Mosaic on the fly

Other DOQQ Distributions

- Raw data through AmericaView
A Nationwide Consortium for Remote Sensing Education, Research, and Geospatial Applications
- California data through CaliforniaView
 - <http://casil.ucdavis.edu/casil/usgs.gov/>
- Other sources see
<http://www.ndop.gov/data.html>

AmericaView

- Administered by the USGS under the Land Remote Sensing (LRS) Program and carried out at USGS facilities.
- AmericaViewSM Consortium is comprised of university-led, state-based consortia
- Source of low cost DOQQ's
 - <http://www.americaview.org/About.html#Pop>
 - Click on need for AmericaView

CaliforniaView DOQQ

The screenshot shows the CaliforniaView DOQQ website. It features a header with the California State Information logo and a search bar. Below the header, there is a section titled "California Digital Ortho (Quadrant) Quads DOQQs". This section includes a list of DOQQs with columns for Name, Date Acquired, Size, and Description. The list includes items like "San Francisco Bay Area", "San Jose", "San Diego", etc.

Name	Date Acquired	Size	Description
San Francisco Bay Area	10-04-2000	1.6 TB	
San Jose	10-04-2000	1.6 TB	
San Diego	10-04-2000	1.6 TB	
San Francisco Bay Area	10-04-2000	1.6 TB	
San Jose	10-04-2000	1.6 TB	
San Diego	10-04-2000	1.6 TB	

New software capabilities

- To use low cost data from AmericaView
 - Need automated mosaic production
 - Lots of disk – estimated 5 TB for California alone
 - Students trained in mosaic software operation
- Companies supplying mosaicking software
 - Leica
 - http://gis.leica-geosystems.com/products/lps/documents/lps_data_mosaic.pdf
 - ERMapper
 - http://www.ermapper.com/document/doc.aspx?doc_id=57

Compression

- Mosaic may need compression to reduce size.
- With improved networks that may not be the correct answer.
- JPEG2000 is a new open standard
 - <http://www.jpeg.org/jpeg2000/>

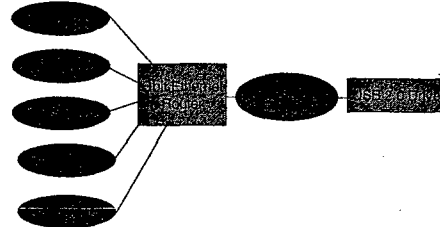
AirphotoUSA Performance tests

Machines

- Dell GX270
 - Intel Pentium 4 2.8 GHz CPU
 - 512KB L1 cache, 1MB L2 cache
 - 533MHz front-side bus
- 512MB RAM
- Gigabit Ethernet Card
- 75GB ATA/100 IDE Hard drive
- Windows XP SP1

AirphotoUSA Performance tests

• Test Configuration (Samba Mount)

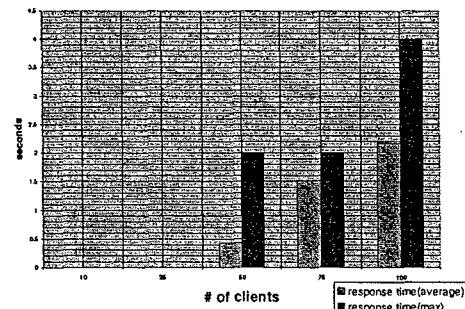


AirphotoUSA Performance tests

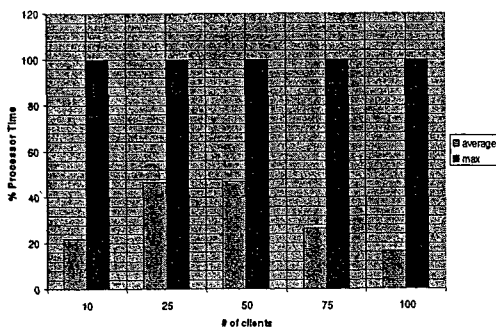
• Test Configuration

- Each test computer simulates 1-10 users
- Each user requests images for random locations in the California

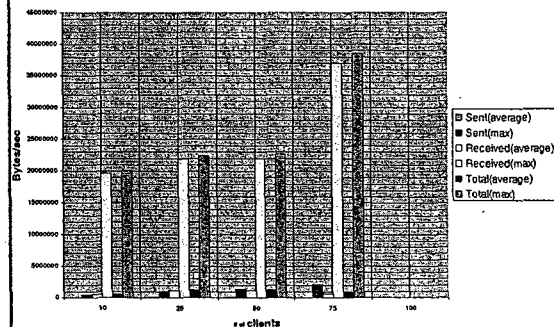
Server response times



Server CPU Utilization



Server Network Bytes



Experiences Delivering Massive Geospatial Datasets for Educational Use



Michael Haungs, Ph.D.
Rollin Strohman, Ph.D.

Our Mission

- Build a service to provide massive, remote geospatial datasets for educational use over Internet2

Demonstration

Uses

- Virtual Field Trips
 - California Missions
- Wildlife study
 - Monarch butterfly migration paths
- City layout and design
- Base layer in remote GIS
- Seems endless...

Benefits

Approximately 80% of business and government information has some reference to location, but until recently the power of geographic or spatial information and location has been underutilized as a vital resource for improving economic productivity, decision making, and delivery of services. We are an increasingly distributed and mobile society. Our technologies, services, and information resources must be able to leverage location (i.e., any geographic position, not just now) and the spatial information that helps us visualize and analyze situations geographically.

Open Geospatial Consortium

Issues

- Administration
- Data Quality
- Data Source
- Performance
- Customization
- Educational Use

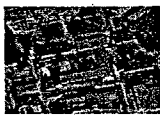
Administration

- Distributed
 - Every person for themselves
- Federated
 - National Map
- Centralized
 - Google, ESRI, Terraserver
 - Most efficient use of resources
- Standard Protocols (OGC)
 - WMS, WMG, GML, SFS, ...
 - Tie together existing efforts

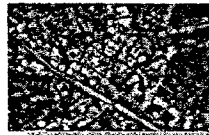
Data Quality

- Uniform coverage
 - 1-meter resolution (minimum)
 - Need for novice users
 - Seamless, tone matched

Google Comparison I



Google Comparison II



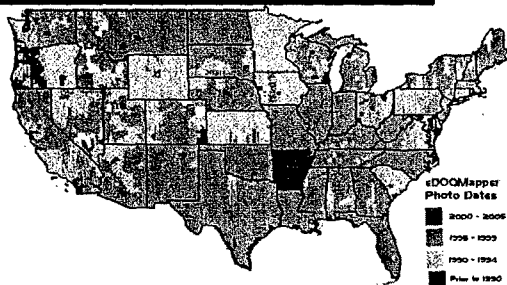
Data Source

- Free Sources
 - USGS, NAIP, AmericaView
 - Adv: License free
 - Dis: Mosaicking, compression, updates, storage
- Proprietary
 - AirphotoUSA, ESRI
 - Adv: Seamless, orthophoto
 - Dis: Security, Flexibility
- Government plans?

AirphotoUSA dataset

- Airphoto USA
 - Seamless, one-meter resolution aerial orthophotography covering over 3 million square miles of the US
 - 20TB (2.5 TB compressed)
 - Generously made available by AirPhotoUSA for our study
 - Viewing software – PhotoMapper
 - Rapid pan and zoom for best user experience

AirphotoUSA dataset



Performance

- Targeting high-bandwidth connections
 - Internet2 Universities
 - Future Kindergarten through 12th grade
 - Network speed will continue to improve

Performance

- CalPoly, San Luis Obispo, CA
 - 1 Gb/s backbone
 - 622 Mb/s pipe to ISP in L.A.
 - ISP connects to Abilene I2 network at 2.2 Gb/s
 - Future
 - Can grow up to 10Gb/s (Abilene Limit)

Performance

- Internet2
 - Changes basic assumption of client/server applications
 - Fast machines and slow communication
 - Do old optimizations still make sense?
 - Caching? Compression? Remote desktops?

Performance

- Internet2
 - Other optimizations?
 - Prefetching? Indirection?
 - Counter example
 - VNC is an example of an application designed for low bandwidth connections

Customization

- End-user requirements
 - K20 Educators
 - Researchers
 - Special Projects

Educational Use

- Interactivity
 - Limited lab time
 - Require quick, fluid responses
 - Treasure-hunt approach
- Multiplicity
 - Groups performing similar activities

Educational Use

- Educator Collaboration
 - Curriculum development
 - Collaboration tools?
- Advertisement
- Training
- Delivery

Project Status

- We have access to a seamless, orthophoto of entire US
- Conducted an initial feasibility study
 - Bottleneck analysis
 - Testing in CalPoly labs
- Have access to multiple data sources
 - Generate own
 - Pursue proprietary model

Project Status

- End application
 - Pursuing multiple avenues
 - Investigating novel approaches
 - Need input from community
- Educator Collaboration
 - Pedagogical best practices
 - K-12 curriculum development

Future Work

- Prototype Implementation with set of 12 Universities
 - CalPoly, Stephen F. Austin, South Dakota, Oklahoma State
- Virtual Teaming
 - Educator Collaboration
- National Dissemination
 - All Internet2 Universities
 - K/20
 - Group data purchase
- Serving Other Datasets from Calpoly
- New Client/Server Architectures
 - Build them

AmericaView

"Satellite data is expensive, and using the data requires significant investments in software, hardware, and training. It has often been hard for university researchers to use or even access the data, particularly at smaller schools or research facilities. For three decades this has hindered applied research and made it difficult to train the workforce, both current and future."

Conclusion

- If you are interested in any aspect of this project, please contact us at:
 - Michael Haungs, mhaungs@calpoly.edu
 - Rollin Strohman, rstrohma@calpoly.edu
- Questions?

Cement Stabilized Recycled Aggregates for Roadway Base

Project Investigators:

Daniel C. Jansen
Assistant Professor
Department of Civil and Environmental Engineering

Ashraf M. Rahim
Assistant Professor
Department of Civil and Environmental Engineering

INTRODUCTION

The U.S. highway system plays a critical role in the movement of military equipment and personnel, particularly in wartime. In the event of a national military or security emergency, heavy equipment, including oversized cargo vehicles and personnel must be deployed expeditiously with personnel from military installations to various seaports and airports. Also, the capability of the highway system to manage massive amounts of traffic in major emergency evacuations is critical to the safety and survival of threatened populations. Reliable and durable base materials for pavements is vital for producing durable quality flexible pavements which will be in operable condition when the emergency occurs and can handle the additional burden at the time of the emergency. Also, in the event of a national catastrophe which results in roadways which need to be reconstructed quickly, base materials which can be placed quickly with minimum labor are also needed.

The general area of this research is in the recycling of materials into roadway construction applications, a growing field which is attracting investors for both research and new product development. The work conducted began as a pilot investigation into whether a newly developed synthetic lightweight aggregate can be used to produce an economically viable and improved pavement base material. The work required the development of laboratory procedures which can be used for future research and proposals. The work was expanded to include an investigation into use of recycled materials into flowable fills, also known as controlled low strength materials.

While recycled materials and industrial by-products are generally perceived to be inferior to virgin materials, in many cases they can produce favorable products either because they provide some special property not obtainable with traditional materials, or they are superior when only poor local materials are available. Additional benefits from using recycled materials and industrial by-products include reducing the consumption of our natural resources, reducing the amount of waste diverted to our shrinking landfill sites, and reducing the costs of construction projects. While the positive environmental impacts of using recycled materials and industrial by-products should be enough to warrant the acceptance of these materials in construction applications, they are generally not generally well received as the suitable performance of the materials is paramount. To this end, these materials must show some additional performance or cost benefit to be readily accepted into use.

OBJECTIVES

The objective of this work was to conduct initial investigations into using recycled or industrial by-products in roadway bases and fills for roadway applications. The work was to demonstrate that the use of selected recycled materials and industrial by-products are not only feasible but can also be beneficial from an engineering standpoint. The work conducted is not intended to be an end unto itself, but to provide data and experience which will be a springboard for the investigators into this field of study. The intentions are to continue to study this field and to obtain funding from other sources including public agencies and private companies.

CEMENT STABILIZED BASES

Background

A typical flexible pavement is shown in Figure 1. The surface and binder courses are asphalt pavement and are usually placed in two separate layers for economical reasons and because hot mix asphalt is too stiff to be placed in a single thick layer. The base and sub-base courses consist of crushed stone, stabilized crushed stone, or soil cement. Finally there is a layer of compacted subgrade just above the natural subgrade. The durability of the surface course is dependent not only on its own quality, but of the quality of the layers below.

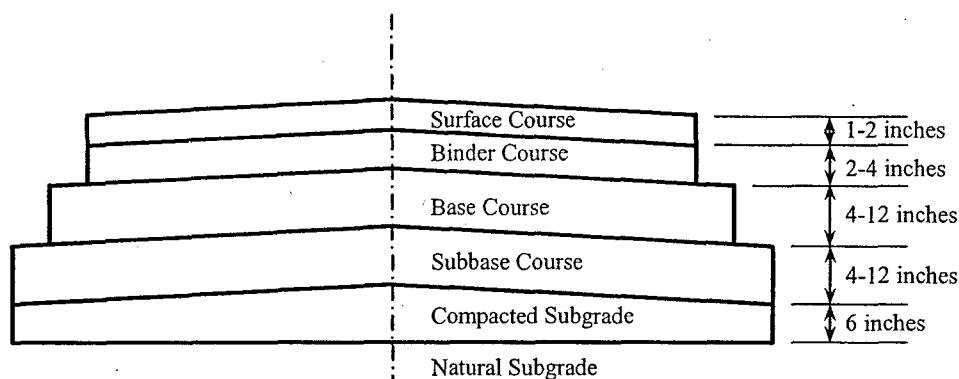


Figure 1: Typical Cross Section of a Conventional Flexible Pavement

Use of crushed stone in the base and sub-base courses, while providing reasonable quality when untreated, requires the mining, crushing, and transportation of the material. Thus it is relatively costly and is dependent on local natural resources. In cases where high traffic loads requires better performing base and sub-bases, quality crushed stone can also be stabilized with portland cement or lime. Stabilized base or sub-base materials are either mixed in place at the job site, or are combined in a mixing plant and transported to the site. These materials are loosely spread and then densified by means of conventional rollers. While this improves the quality of the base and sub-base courses, it also increases the cost. In some states, such as Louisiana, Texas, Mississippi, and parts of California, quality crushed stone is not ubiquitous; therefore, it needs to be either transported long distances, making it more expensive, or lower quality crushed stone is used and stabilized. Furthermore, the *in situ* soil can be stabilized with portland cement to produce soil cement. While soil cement is often the best option, it requires more cement making it more expensive to produce a base material of similar strength as that obtained with a stabilized crushed stone. For cement stabilized crushed stone, typically 5 to 10% by weight of the base will be Portland cement whereas soil cement may require up to 20% cement by weight.

Other options to using crushed stone or the *in situ* soil, include using recycled paving material (asphalt or concrete), blast furnace slag, and bottom ash [1]. When stabilized, these alternatives can produce good quality base and sub-base courses with the added benefits that they replace depleting natural resources and utilize what would ordinarily be waste products which would have to be land filled. Slag is limited in availability to areas near iron ore processing facilities, and recycled paving material is limited to applications where roads are being rebuilt and on site crushing of the material can be difficult producing inconsistent results.

The work conducted investigated the use of two recycled materials for stabilized base course including scrap tire rubber and a new synthetic lightweight aggregate which the PI has been involved with. The properties of the stabilized base materials were compared to those of traditional stabilized crushed aggregates. The objectives of the research was to demonstrate the feasibility of base courses produced with these recycled materials with the hope they can be shown to be economically comparable and their mechanical and durability properties are improvements over stabilized crushed aggregates.

Experimental Procedures

Materials

Synthetic Lightweight Aggregate (SLA)

The synthetic lightweight aggregate (SLA) was developed by the PI, Dr. Jansen while at Tufts University in Massachusetts through collaboration with Professor Robert Malloy from University of Massachusetts, Lowell, and Professor Chris Swan from Tufts University. Professor Malloy is a plastics engineer, and Professor Swan is a geo-environmental engineer. The SLA was manufactured from fly ash and mixed recycled plastic. The two components were selected because of their availability and under utilization.

Fly ash is the fine portion of the coal combustion products (CCP) produced at power generating stations and is typically collected from the flue gases by electrostatic precipitators. In the United States, 128.7 million tons of CCPs are produced each year; 76.5 million tons of which is fly ash [1]. Presently, only 35.4% of the CCPs (34.8% of fly ash) produced annually are recycled in applications including concrete, flowable fill, soil stabilization, and snow and ice control; the remaining material is typically disposed of in landfills. With tighter restrictions on NO_x emissions imposed by the implementation of the 1990 Clean Air Act Amendment [2], less desirable CCPs containing higher levels of unburned carbon, ammonia, and sulfur compounds will result. The annual cost of disposing of CCPs is approximately \$1 billion; a figure that will surely rise as available landfill space diminishes and the amount of harmful constituents in the fly ash increases. Finding possible uses for large quantities of CCPs that can tolerate variance in CCP composition is becoming vital for sustained environmental development.

Annually, the need for plastic recycling becomes more important due to the continuous expansion of the plastics industry; consumption of plastic in the United States is nearly five times greater today than it was in 1970. It is estimated that in the U.S. alone, 40 million tons of plastic were used in product manufacturing in 1998. Unfortunately, the recycling rates for plastics have not kept pace with the increased level of production. As a result, waste plastics packaging and durable products represent a significant portion of the Municipal Solid Waste (MSW) stream [3]. By 2000, 63% of the United States' population had plastics recycling in their MSW collection programs, and from 1986 to 1999, the number of plastic recycling companies increased from 310 to a total of 1677 [4]. 750,000 tons of plastics were recycled in 1999 which accounted for a 23% rate of recycling [4]. However, the capacity to process some types of plastics, accompanied by the low market demand, far exceeds the capabilities of the current industry. Most plastics, specifically all thermoplastics, can be "mechanically" recycled. The recycling infrastructure for both polyethylene terephthalate (PET) and HDPE are fairly well established. The limited rate of recycling for other thermoplastics is more of an economic rather than a technical issue. The cost of segregation, cleaning, transportation and reprocessing the waste plastic limits the reuse of the theoretically recyclable materials [5]. The economics of plastic recycling are greatly improved if the "degree" of separation and cleaning for the waste

plastic is minimized. As a result, once the primary sorting is performed, commingled plastics remain. With different plastic types and colors, there is little or no market for commingled plastics; the different plastics melt at different temperatures and some begin to burn before other melt. Even if all the different plastics are melted, they don't blend properly and form brittle nearly useless product. The work developing the SLA examined the effects of changing composition of the commingled plastic and different sources of fly ash; it was found these parameters had little influence on the mechanical properties of the SLAs [6-8].

Concrete produced using the SLAs showed there was significant decrease in the compressive strength and modulus of elasticity of the concrete in comparison to concrete produced with natural aggregates [6, 8-10]. However, further investigations found the freeze-thaw durability to be greatly improved with the use of SLAs as aggregates [8-10].

Virgin Aggregate

The virgin aggregate used in this study, denoted Aggregate A was primarily crushed rock that was gravel sized. The aggregate was obtained from Hanson Aggregates in Santa Margarita, California. Aggregate D was composed of sand sized particles. The aggregate was collected from Hanson Aggregate in Santa Margarita, California.

Portland Cement

Type II/V Portland cement was used in this testing program. It was obtained from Sawyer Building Supply in Santa Maria, California and produced by Colton Cement.

Experimental Investigation

The main testing program included physical characterization of the SLA and virgin aggregates. Cement stabilized samples were made with varying amounts of cement and different amounts of replacement of the aggregate A with the SLA. The cement stabilized aggregate mixtures were mixed by hand then compacted using the modified proctor compaction method. The samples produced were nominally 4 inches in diameter by 6 inches in length (100 x 150 mm). The amount of water was varied to obtain the optimal amount of compaction. Once the optimal water content was obtained for a particular mixture, it was then held constant. Additional samples were produced and subsequently tested for their unconfined compressive strength and tensile strength (obtained using the splitting tensile strength method).

Results

Physical Properties of the Aggregates

Sieve analyses were performed in accordance with ASTM C136 on both the SLA and the virgin aggregates. The results are shown in Figure 2. Aggregate A was classified as a well-graded gravel (GW) according to the Unified Soil Classification System. The same system classified Aggregate D as a clean well-graded sand (SW). The SLA had mostly gravel sized particles and was more uniformly graded as shown in Figure 2.

Table 1 shows a summary of the other physical properties that were determined for the various aggregates. The bulk specific gravity of each aggregate was determined in accordance with ASTM D2726-04.

The moisture content was determined using ASTM D789 and the absorption capacity was found using ASTM D570. The moisture contents were not as significant to the testing process as the rest of the physical properties, because each of the aggregates were oven dried and allowed to cool for 48 hours prior to use in the mixtures.

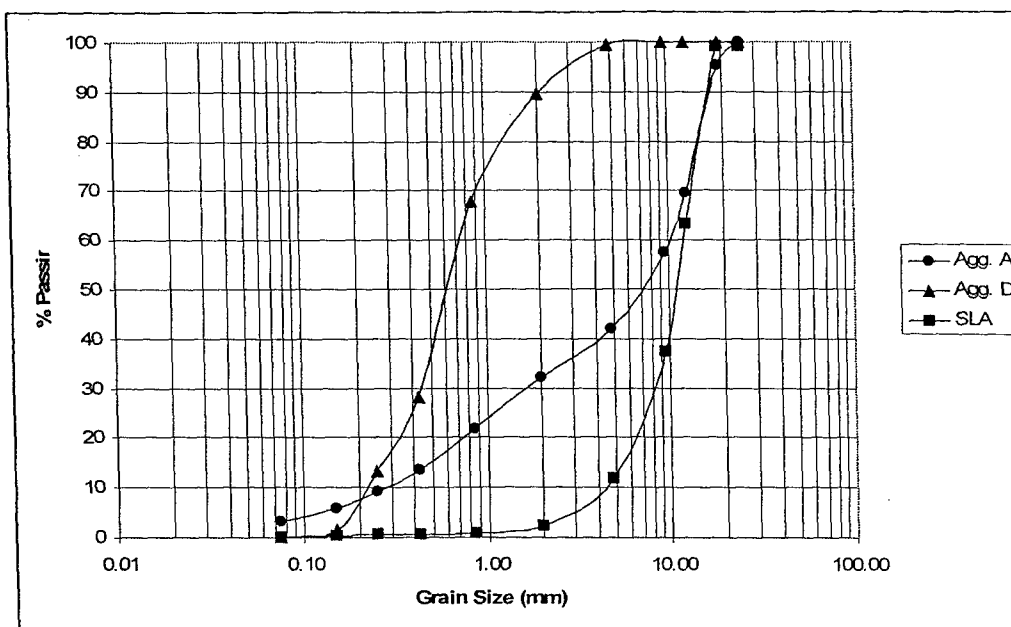


Figure 2: Sieve Analysis for Aggregates

Table 1: Physical Properties of the Aggregates

Aggregate	Bulk Specific Gravity	Moisture Content (%)	Absorption (%)
A	2.70	5.04	ND*
D	2.58	ND*	2.00
S	1.48	0.75	11.75

*Not Determined

Unconfined Compressive Strength Testing

The unconfined compressive strength testing was performed in accordance with ASTM D1633. The results for the compressive strength tests are shown in Figure 3. The notation used lists Agg. A / SLA / Agg. D by volume, so for example the 70/20/10 means the aggregate in the sample consisted of 70% aggregate A, 20 % SLA, and 10% aggregate D by volume. The results show that as the cement content increases, the compressive strength also increases. At 5% cement content, the 100/0/0 and 70/20/10 mixtures are comparable. The same goes for the 100/0/0 and 40/40/20 mixtures at 8% cement content. Around an 8% cement content, the data shows that a 40% SLA mixture becomes preferable to a 100% virgin aggregate mixture.

Splitting Tensile Strength Testing

The splitting tensile strength tests were performed using a procedure identical to that of ASTM 496-96. The results of those tests are shown in Figure 4. It is clear from this test that two major trends are present. The first trend is that the splitting tensile strength increases with increasing cement content. The second is that the strength increases with an increase in the percent of the mixture that is virgin aggregate. It also seems that as the cement content increases so does the difference in strength between the three mixtures, indicating that the cement content more significantly affects the tensile strength in the samples with higher percentages of virgin aggregates.

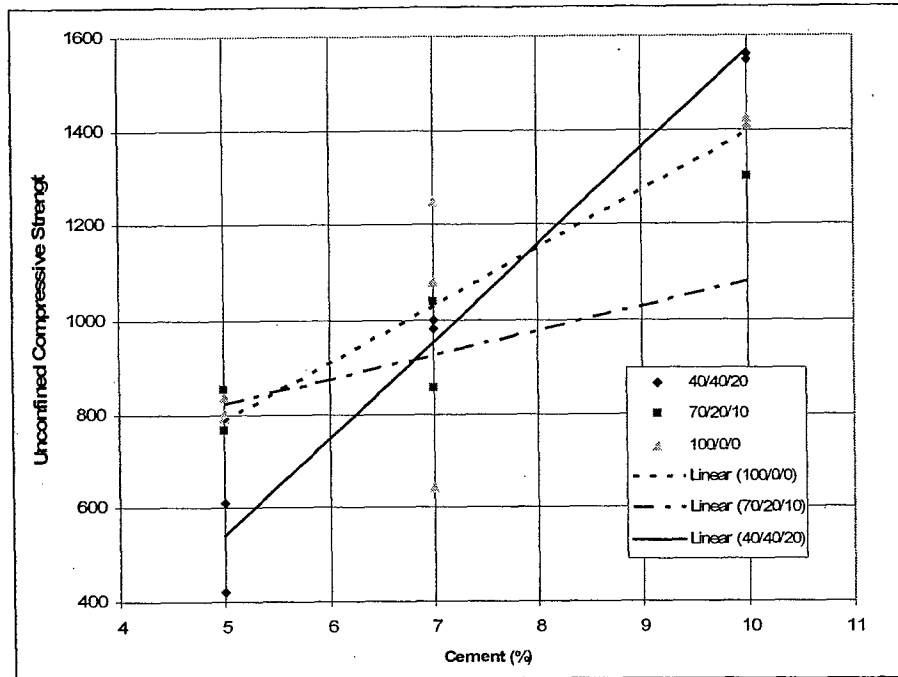


Figure 3: Unconfined Compressive Strength Testing Results

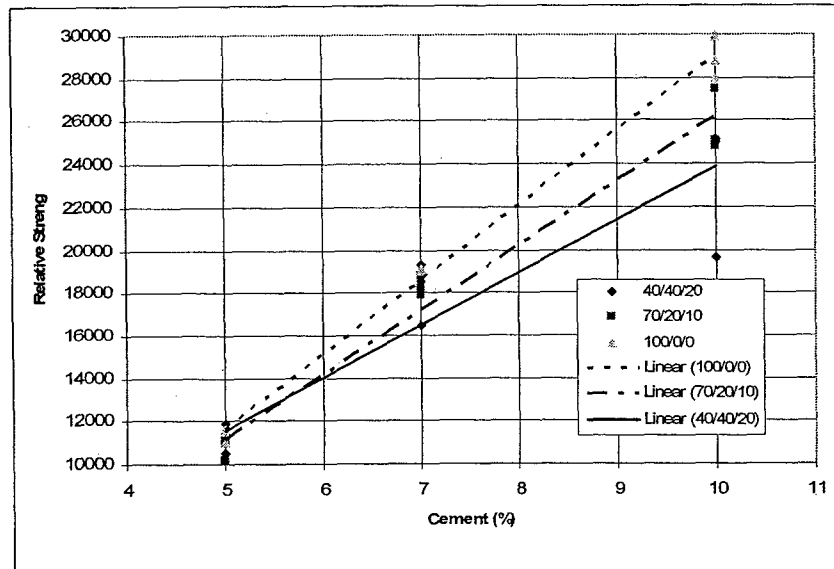


Figure 4: Splitting Tensile Strength Test Results

Conclusions

Three different Agg. A, Agg. S and Agg. D mixtures stabilized with 5, 7, and 10% portland type II/V cement were evaluated for use as road subbase. The minimum unconfined compressive strength for a subbase according to California Test 312 (1978) is 750 psi. The results of this study lead to the following conclusions.

- The unconfined compressive strength of the mixtures increases with an increase in the cement content.

- The rate at which the unconfined compressive strength increases with an increase in the cement content varies based on the SLA content.
- The splitting tensile strength increases with an increase in cement content and virgin aggregate content.
- Mixtures with less than 40% SLA and cement contents higher than 6% all meet the requirement for the unconfined compressive strength of a subbase.
- Having met the strength requirements SLA seems to be a viable subbase material when stabilized with the proper amount of cement.

CONTROLLED LOW STRENGTH MATERIAL (FLOWABLE FILL)

Background

Controlled low-strength materials (CLSM), also known as flowable fills, are defined by the American Concrete Institute (ACI) as self-compacting cementitious materials primarily used as backfill in place of compacted fill. CLSM's consist of small amounts of Portland cement, water, and sand. In some cases, coarse aggregates or large volumes of fly ash are used. CLSM's are designed to have an unconfined compressive strength of 8 MPa (1200 psi) or less. In most cases, CLSM's are designed with the intent of future excavation in mind, which requires an unconfined compressive strength of 2 MPa (300 psi) or less, and 1 MPa (150 psi) or lower is preferable for excavatability. CLSMs are also often referred to as flowable fills, controlled-density fills, soil-cement slurries, or two-sack slurries.

Uses

The most common use for a CLSM is as a backfill material. Since they do not require compaction and can be designed to behave as a fluid (hence the term "flowable fill"), they are ideal for use in confined spaces where access is limited and compacting would be difficult. They can be poured or pumped into a narrow trench and the material quickly fills into any voids, making them ideal for backfilling around pipes and other obstacles. CLSMs also make excellent bedding material for electrical and phone conduits. The fact that they can be used in place of compacted fill means that repair work can be done with smaller trenches and less extensive excavation around the affected area, resulting in lower costs and more efficient scheduling.

Other uses for CLSMs include foundation supports, pavement bases, sub-bases, and subgrades. The required compressive strength will vary depending upon the application. For areas with weaker soils, the use of a CLSM sub-base for the foundation can effectively distribute the load of the structure over a greater area of the soil, resulting in a higher factor of safety for the structure. CLSMs can also be used to provide a greater bearing capacity for a footing or building foundation, which decreases the required thickness of the slab.

Advantages

Most CLSMs gain strength very quickly, with some having a total set time of under an hour. Some can even be walked on after just 25-30 minutes and can support the placement of a wearing surface, such as concrete or asphalt, after about an hour. When such CLSMs are used for road repairs, this reduces the traffic-bearing repair time to only 4 hours. This is a significant improvement over using compacted fill, which requires much longer closure time before the road can be driven on again.

CLSMs also require very little time to prepare and can easily be mixed in large quantities on short-notice. Most ready-mix suppliers will accept orders for CLSMs for almost any application required and mixes can be prepared to easily meet most design requirements for strength and flowability.

While the cost of using CLSMs may have higher material costs than using the original soil for compacted fill, the labor involved with compacted fill makes the use of CLSMs far less expensive.

Use of non-standard materials

The aggregates used in a CLSM mixture can come from a wide variety of materials. Some alternative aggregate materials being tested include foundry sand, pea gravel, coal bottom ash, and limestone screenings, but many options exist. Aggregates should be selected based on the desired properties of a specific CLSM mixture. The individual properties of the aggregate material, such as grain size, angularity, and cohesiveness, can greatly affect the physical properties of the mixture. Since CLSMs are designed to have a low compressive strength, it is not necessary to use high-quality aggregate material that would normally be required for high performance concrete mixtures. This opens up the possibility to consider many materials for use as an aggregate that would not normally be considered, such as recyclable materials, quarry by-products, and construction by-products. Such materials can be both useful and highly economical. However, any non-standard material should be tested prior to being used in any CLSM mixture to determine its acceptability and applicability to the design.

Objectives

The most important issue of CLSM is the ability to predict and control long term strength development. Fluid-state properties such as flowability, volume stability (bleeding), and initial setting time are also important properties for the usability of CLSMs and can influence strength development. The properties of CLSMs are largely a function of the distribution of ingredients. The goal of these experiments were to develop a proper mix design for CLSM in place of compacted soil. To find the ideal mix, 6 batches were produced using sand, water, and varied fly ash and cement contents. The second objective was to examine the use of limestone and granite screenings as partial or complete replacement of the sand. Screenings are waste materials produced in crushing stone in the production of aggregates. Millions of tons of screenings are produced in the U.S. each year and storage and disposal is an issue. Screenings can be further divided into crusher fines and filter cake depending on the separation process at the aggregate crushing facility. To meet the second objective, limestone and granite crusher fines (LCF and GCF) and granite filter cake (GFC) are all used in flowable fills.

Test Methods

Flow Consistency

The test method for determining the flowability of each CLSM mixture was consistent with ASTM D 6103. The test was performed using an open-ended 3" x 6" cylinder mold on a flat, level surface. A sampling was taken from a fresh mixture of CLSM and poured into the top end of the cylinder mold. The surface was then leveled off using a metal straightedge and any spillage was removed away from the cylinder. Immediately after filling and leveling-off the cylinder, it was then raised with one quick, steady motion to allow the CLSM to slump uniformly onto the flat surface. The spread diameter of the slump was measured and recorded and the

sample was returned to the rest of the mixture. This process was then repeated, adding more water to the mix in between each test until the desired flow consistency was achieved. The purpose of this test is to determine the water required for each different mix design to achieve the desired flowability. For this study, the goal was to achieve a flow consistency that would produce a slump of approximately 10 inches in diameter using a 3" x 6" cylinder. A flow test as performed is shown in Figure 5.

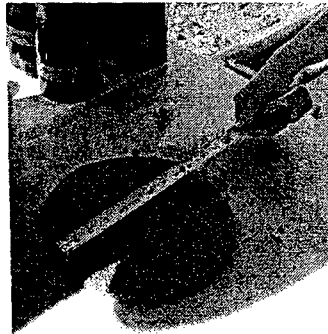


Figure 5: Testing for Flow

Penetration Testing (Short-Term Strength)

The early age strength for each CLSM mixture was determined using a pocket penetrometer. This test is designed to monitor the early-strength development of the CLSM within the first few hours of setting. For each different mixture, a sample was poured into a mold and set aside for testing. Measurements were taken at 30-minute intervals during the first three hours of setting time. The measurements recorded were calculated using the pressure required to plunge a 1-inch diameter circular foot a depth of $\frac{1}{4}$ inch into the surface of the sample. Testing for the short-term strength is shown in Figure 6.



Figure 6: Short Term Compression Testing and a Pocket Penetrometer

Compression Strength Testing

Testing of the unconfined compressive strength of each mixture was performed in accordance with ASTM D 4832. The samples were prepared by pouring the CLSM into 4" x 8" cylindrical molds and allowing the mixture to set for four days, upon which time the samples were placed into a curing room for the remainder of the 28-day testing period. The curing room

used met the requirements of ASTM Method C 192. Samples were removed from the curing room and then tested after 7, 14, 21, and 28 days for testing. At each testing age, three cylinders from each mixture were removed from the curing room, plaster caps were applied to the ends of the cylinders, and tested using a Geotest S5480 model testing machine.

Mixtures Investigated

Materials

A single source of Type II Portland cement, a Class F fly ash, sand, and three types of screenings were used in the investigations. The three screenings used were obtained from two local quarries and included limestone crusher fines (LCF), granite crusher fines (GCF), and granite filter cake (GFC). The crusher fines were similar to sand although consistently finer than what would be allowed in sand for the use in concrete. The granite filter cake all passed a #100 sieve (150 μ m) with a majority passing the #200 sieve (75 μ m).

Mixture Proportions

Four series of tests were performed. Seven reference mixes (REF), based on traditional mix designs for CLSMs, were produced to give baseline comparisons for the mixes with crusher fines. Three series of mixes were produced using the crusher fines: six mixes using limestone crusher fines (LCF), six mixes using granite crusher fines (GCF), and five mixes using granite filter cake (GFC). The mixture proportions are shown in Tables 2 through 5. The naming scheme for the mixtures is type of crusher fines used as replacement of sand, pounds of cement and fly ash per cubic yard of CLSM, and the percent of normal sand replaced by the crusher fines. For example, mix GFC 200/25/10.4 is the granite filter cake series with 200 lbs of cement per cubic yard, 25 lbs of fly ash per cubic yard, and 10.4% of the aggregates is filter cake, by weight.

Table 2: Reference Mixture Proportions

	REF 50/600/0	REF 100/0/0	REF 100/300/0	REF 100/600/0	REF 200/0/0	REF 200/600/0	REF 300/0/0
Cement (lbs/yd ³)	48	84	98	109	189	222	321
Fly Ash (lbs/yd ³)	572	0	293	652	0	665	0
Sand (lbs/yd ³)	2119	2486	2450	2257	2602	2195	2609
Water (lbs/yd ³)	588	687	567	479	609	461	564
Total Weight (lbs/yd ³)	3327	3257	3407	3496	3399	3544	3494

Table 3: Mixture Proportions with Limestone Crusher Fines (LCF)

	LCF 50/600/100	LCF 100/0/100	LCF 100/600/100	LCF 200/0/100	LCF 200/600/100	LCF 300/0/100
Cement (lbs/yd ³)	3510	100	100	200	200	300
Fly Ash (lbs/yd ³)	6129	0	600	0	600	0
Limestone Crusher Fines (lbs/yd ³)	7614	3075	2150	2851	2050	2525
Sand (lbs/yd ³)	0	0	0	0	0	0
Water (lbs/yd ³)	11556	451	550	500	550	600
Total Weight (lbs/yd ³)	3450	3626	3400	3551	3400	3425

Table 4: Mixture Proportions with Granite Crusher Fines (GCF)

	GCF 100/0/33	GCF 100/0/66	GCF 100/0/100	GCF 200/0/33	GCF 200/0/66	GCF 200/0/100
Cement (lbs/yd ³)	100	100	100	200	200	200
Fly Ash (lbs/yd ³)	0	0	0	0	0	0
Granite Crusher Fines (lbs/yd ³)	1014	2059	2998	939	1909	2848
Sand (lbs/yd ³)	2097	1033	0	1944	957	0
Water (lbs/yd ³)	208	696	710	601	586	1085
Total Weight (lbs/yd ³)	3419	3888	3808	3684	3652	4133

Table 5: Mixture Proportions with Granite Filter Cake (GFC)

	GFC 100/100/7.8	GFC 100/75/8.7	GFC 100/50/9.6	GFC 200/25/10.4	GFC 200/0/11.2
Cement (lbs/yd ³)	100	100	100	200	200
Fly Ash (lbs/yd ³)	100	75	50	25	0
Granite Filter Cake (lbs/yd ³)	222	249	277	305	332
Sand (lbs/yd ³)	2621	2621	2621	2621	2621
Water (lbs/yd ³)	607	572	578	570	650
Total Weight (lbs/yd ³)	3650	3617	3626	3721	3803

Results and Conclusions

Short-Term Strength Gain

A benefit of using CLSM is the quick strength gain allowing loads within a few hours. Strength gain is measured as the time require for CLSM to go from the plastic state to a hardened state so it can be paved over an put into service.

As can be seen from Figure 7, the initial strength gain of CLSMs can vary significantly. It can be seen that the REF 200/0/ mixture gained strength the quickest while the 50/600 mixture barely gained any strength over the 4 hours. Cement content plays an important role with strength gain; by doubling the cement content, strength at four hours increases by 90%. Conversely, the presence of fly ash slows down strength gain, as seen by comparing mixtures REF 200/0/0 and REF 200/600/0. Pozzolanic materials such as fly ash chemically react with calcium hydroxide to form compounds processing cementitious properties; however, this reaction rate is slow, whereas, cement can hydrate with water alone. Generally, cement increase strength gain and fly ash lowers strength gain. The trends discerned from this data are 1) that strength gain initiates faster with higher cement contents and 2) incorporation of fly ash delays the initial strength gain.

When the sand is entirely replaced with limestone crusher fines, as shown in Figure 8, the amount of time to set is approximately the same for the same cement and fly ash contents. Similarly, with the use of granite crusher fines, shown in Figure 9, no discernable trends can be seen as the amount of sand replaced by granite crusher fines is increased.

In the granite filter cake (GFC) series shown in Figure 10, the reference series comparison is REF 100/300/0; initially 200 lbs of fly ash is replaced with granite filter cake (GFC 100/100/7.8). Fly ash and granite filter cake are both extremely fine materials which help control bleeding when large amounts of water are used with small cement contents. As more of the fly ash is replaced with granite filter cake, the initial setting actually occurs at an earlier time, a significant advantage with CLSMs.

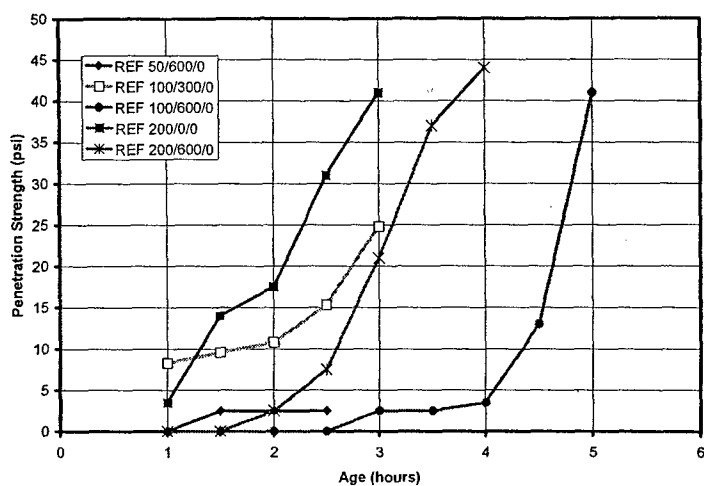


Figure 7: Early Age Strength Gain for Reference Mixtures (REF)

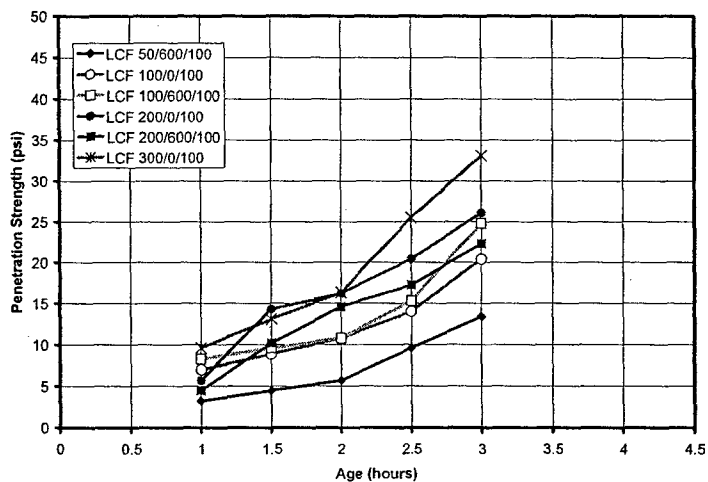


Figure 8: Early Age Strength Gain for Mixtures with Limestone Crusher Fines (LCF)

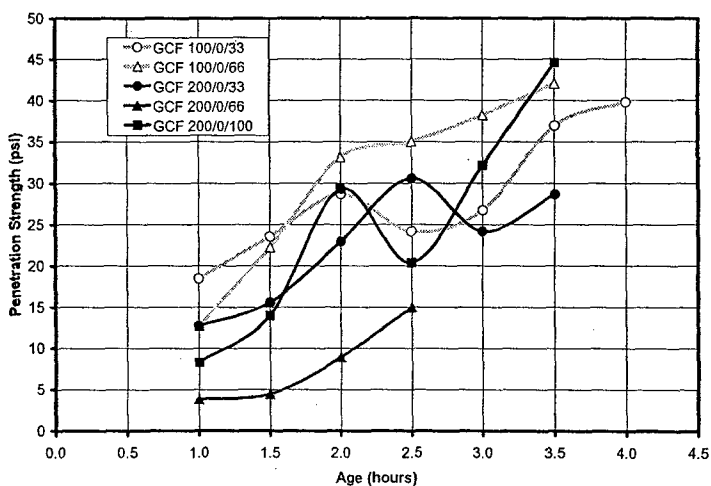


Figure 9: Early Age Strength Gain for Mixtures with Granite Crusher Fines (GCF)

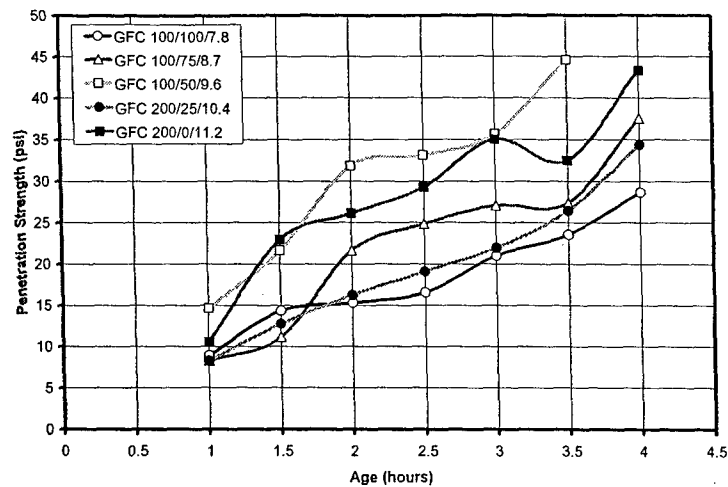


Figure 10: Early Age Strength Gain for Mixtures with Granite Filter Cake (GFC)

Unconfined Compressive Strength Test Results

As stated earlier, for excavability, the long-term compressive strength should remain under 300 psi with the strength ideally being below 150 psi. From the compression results of the reference series shown in Figure 11, mixes REF 100/600/0, REF 200/600/0, and REF 300/0/0 all exceeded the 300 psi limit, and only mixes REF 100/0/0 and REF 100/300/0 remained under the 150 psi limit. The general trends that were observed include significant increases in strength with the use of higher cement contents, and the use of 300 lbs of cement per cubic yard being too much. Increasing the amount of fly ash also increased the long-term strength. Although 300 lbs of fly ash only increased the strength slightly, use of 600 lbs of fly ash per cubic yard increased the strength significantly, in fact making the CLSM too strong for use with all but 50 lbs of cement per cubic yard.

By comparing the results in Figures 11 and 12, the replacement of sand with limestone crusher fines decreased the strengths of the stronger CLSM mixes significantly while it may slightly increase the long-term strength of the lower strength CLSM mixes. This is a significant advantage since it could provide a method for controlling the long-term compressive strength of CLSMs even at higher cement or fly ash contents. It should be noted that some of the limestone crusher fine mixes still exceeded the 300 psi threshold, although not by as much as when standard sand was utilized.

The strengths increase consistently as more of the sand is replaced with granite crusher fines as shown in Figure 13 and comparing with the results in Figure 11. This is not necessarily in contradiction to the results obtained with the limestone crusher fines as the mixes used with the granite crusher fines had no fly ash and only 100 or 200 lbs of cement per cubic yard making them all of the lower strength variety.

As seen in Figure 14, the use of granite filter cake as replacement of fly ash consistently decreased the long-term compressive strength of the CLSMs. It should be noted that in comparing REF 100/300/0 to GFC 100/100/300 mixes, the GFC mix is approximately the same as the REF mix with the exception that the GFC mix replaces 200 pounds of fly ash with granite

filter cake and shows a significantly higher strength which goes against the general trend observed in Figure 14.

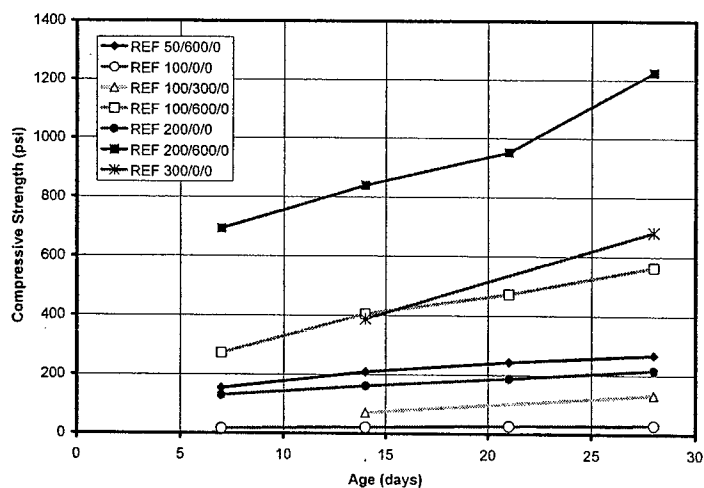


Figure 11: Unconfined Compressive Strengths of Reference Series (REF)

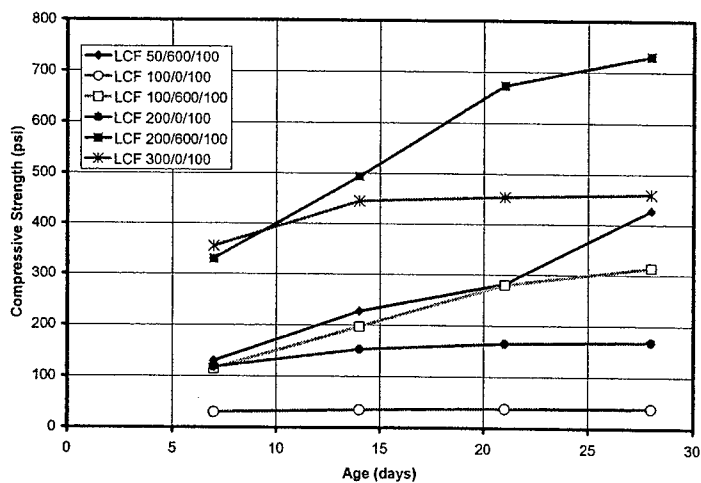


Figure 12: Unconfined Compressive Strengths of Limestone Crusher Fines Series (LCF)

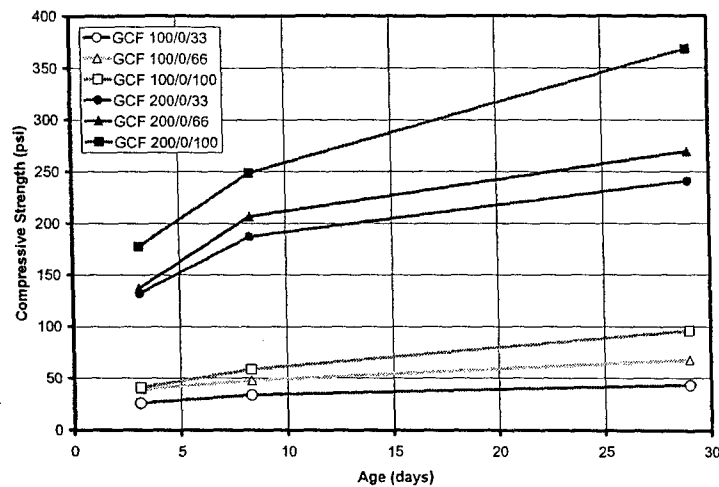


Figure 13: Unconfined Compressive Strengths of Granite Crusher Fines Series (GCF)

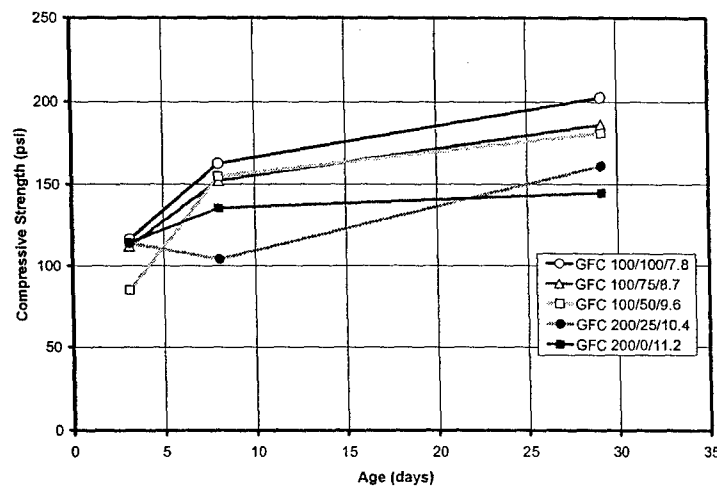


Figure 14: Unconfined Compressive Strengths of Granite Filter Cake Series (GFC)

Conclusions

This work represents the findings of a laboratory investigation into the feasibility of using screening from the production of aggregates in controlled low strength materials. The findings can be summarized as:

- Mixtures with cement contents of 100 to 200 pounds per cubic yard with moderate amounts (about 300 lbs per cubic yard) of fly ash were ideal.
- Fly ash decreases early short-term strength and cement increases long-term strength gain.
- Replacing the normal sand with limestone crusher fines had little or no impact on the short-term strength gain while moderating the long-term strength gain of higher strength CLSM mixtures.
- Using increased amounts of granite crusher fines as replacement of normal sand increased the long-term strength gain of mixes with 100 to 200 pounds of cement, although only moderately. Similar to limestone crusher fines, the short-term strengths were unaffected.

- Replacing fly ash with granite filter cake improves the CLSM by both reducing the setting time while keeping the long-term strength lower. At the same time, bleeding was kept to a minimum.

OUTCOMES

The work presented were initial investigations into using recycled or industrial by-products in roadway bases and fills under roadways. The work demonstrated that the use of selected recycled materials and industrial by-products are not only feasible but can also be beneficial from an engineering standpoint. To this end, the PI and Co-PI have submitted two proposals to continue this work. The first proposal, "The Use of Waste Tires in Flowable Fill-Laboratory Assessment" submitted to the *National Council on Highway Research Program* for \$62,123, was rejected. The second proposal, "Improving Excavatable Flowable Backfill with Recycled Materials" submitted to Caltrans for \$100,650 has been accepted and work will begin October 2005. Based on work performed for the literature review, the PI made the presentation "Reuse of Plastics in Concrete" at the American Concrete Institute's Spring Convention, New York, NY, April 17-21, 2005.

REFERENCES

- [1] American Coal Ash Association, "ACAA Releases Coal Combustion Products Production and Use Figures," [http://www.acaa-usa.org/PDF/aaaa_2002_ccp_svy\(11-25-03\).pdf](http://www.acaa-usa.org/PDF/aaaa_2002_ccp_svy(11-25-03).pdf), accessed Dec. 14, 2003.
- [2] Environmental Protection Agency, "Nitrogen Oxides (NO_x) Reduction under Phase II of the Acid Rain Program (Group 1 and Group 2 Boilers)," <http://epa.gov/airmarkets/arp/nox/phase2.html>, accessed Dec. 10, 2003.
- [3] "Resin Report", *Modern Plastics*, V. 76, No. , 1999, 72pp.
- [4] Plastics Resource, "State of Plastics Recycling," Nov. 2000. <http://www.plasticsresource.com>, accessed Dec. 14, 2003.
- [5] Ehrig, R.J., Eds, *Plastic Recycling*, Hanser Publishers, New York, NY, 1989.
- [6] Jansen, D.C.; Kiggins, M.L.; Swan, C.; Malloy, R.A.; Kashi, M.G.; Chan, R. A.; Chouman, J.; Javdekar, C.; Reiad, A.; Rogers, B.; Siegal, C.; Subbhiya, R.; and Weingram, J., "Lightweight Fly Ash / Plastic Aggregates in Concrete," Transportation Research Board 2001 Meeting, Washington, D.C., January 2001, CD-ROM Publication, paper number TRB-01-3128, 29 pages.
- [7] Malloy, R.A., Desai, N., Wilson, C., Swan, S., Jansen, D., Kashi, M., "High Carbon Fly Ash / Mixed Thermoplastic Aggregate for Use in Lightweight Concrete," *Society of Plastics Engineering*, Annual Technical Conference, Dallas, TX, May 2001, Vol. 47, pp. 2743-2751.
- [8] Jansen, D.C.; Kiggins, M.L.; Swan, C.; Malloy, R.A.; Kashi, M.G.; Chan, R. A.; Chouman, J.; Javdekar, C.; Siegal, C.; and Weingram, J., "Lightweight Fly Ash / Plastic Aggregates in Concrete," Transportation Research Board, Journal of the Transportation Research Board, Materials and Construction: Concrete 2001, No. 1775, Paper 01-3128, pp. 44-52.
- [9] Kiggins, M.L., "Synthetic (Fly Ash/Plastic) Lightweight Aggregates in Concrete," M.S. Thesis, Tufts University, 2001, 298 pp.
- [10] Weingram, J., "Shrinkage and Durability of Concrete Containing Plastic-Fly Ash Aggregates," M.S. Thesis, Tufts University, 2003, 175 pp.

Reuse of Plastics in Concrete

by

Daniel C. Jansen

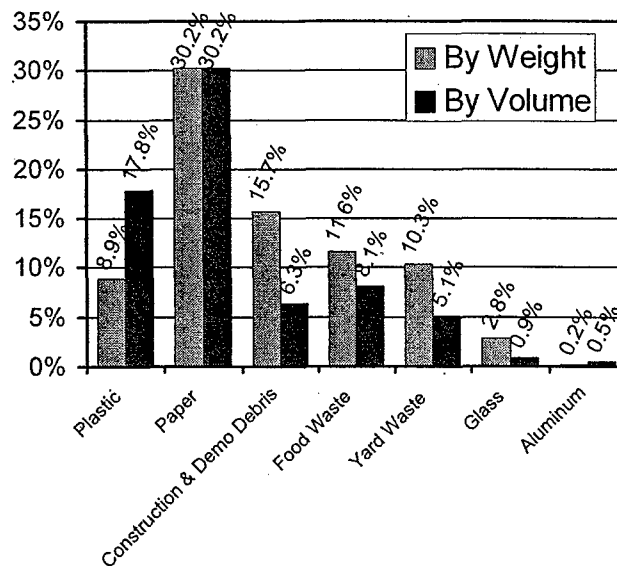
Presented at
the American Concrete Institute's Spring Convention
New York, NY

April 17-21, 2005

Reuse of Plastics in Concrete

Daniel C. Jansen
Cal Poly State University
San Luis Obispo, CA

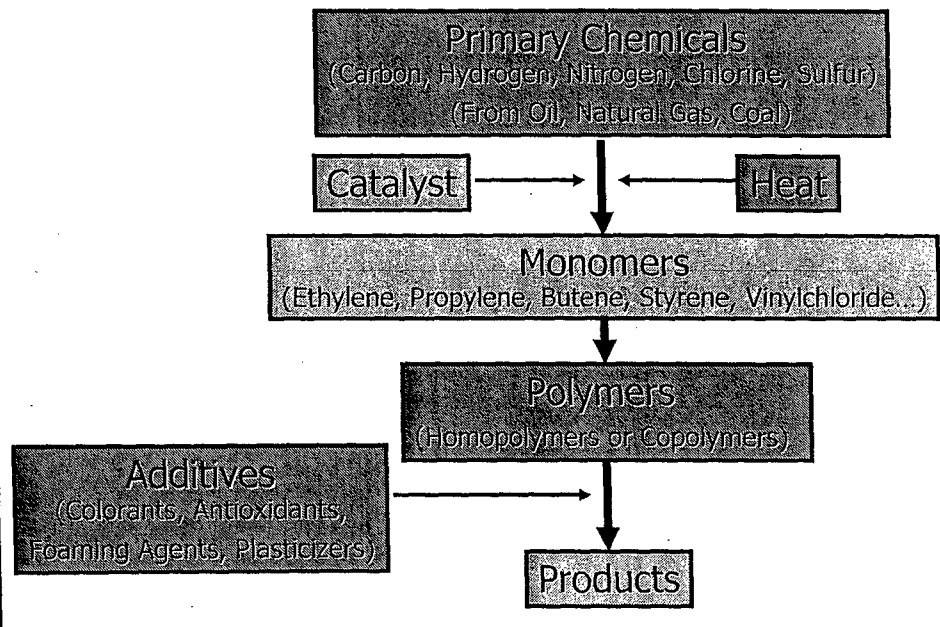
Municipal Solid Waste in U.S.



Outline

- Overview of Plastics
 - Plastic Types
 - Recycling of Plastics
 - Issues with Recycling of Plastics
- Reuse of Plastics in Concrete
 - Properties
 - Example
 - The Future
- Conclusions

Plastic Production









Characterization

- Thermosetting
 - Hardening is irreversible
 - Examples:
 - Polyurathane
 - Unsaturated Polyesters
 - Epoxies
- Thermoplastics
 - Can be reheated and remolded
 - Degradation does occur
 - Examples:
 - High Density Polyethylene
 - Polystyrene
 - Polypropylene

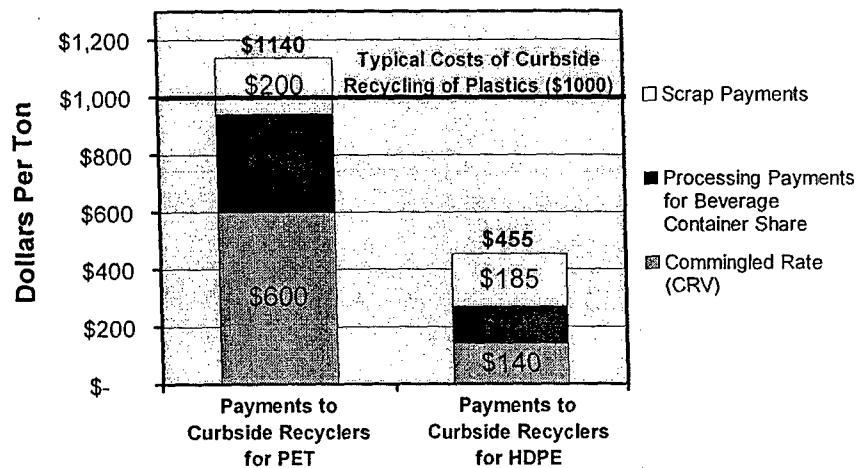
Recycled Plastics

		PET (PETE) - Polyethylene Terephthalate Beverage Containers
		HDPE - High Density Polyethylene Milk Containers, Laundry Detergent Bottles, Plastic Bags
		V - Vinyl / Polyvinyl Chloride Vegetable Oil Container, Pipes
		LDPE - Low Density Polyethylene Flexible Film Bags, Flexible Lids, Plastic Bags

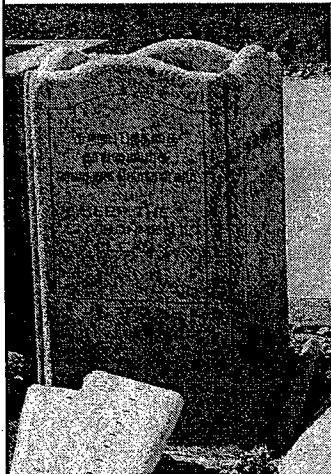
Recycled Plastics

		PP - Polypropylene Jar Lids, Container Closures, Battery Cases, Box Liners
		PS - Polystyrene Fast Food Foam Boxes, Foam Cups, CD Cases
		O - Other Automobile Parts, Computer Cases

Plastic Recycling Costs and Values



Recycling of Plastics



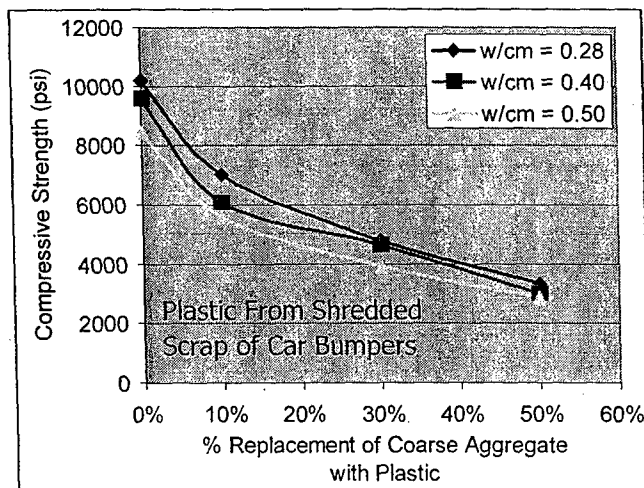
- Plastics are manually separated by type
 - Types #1 (PET) and #2 (HDPE)
 - Are easily sorted
 - Are easily recycled into new products
 - Remaining is commingled plastic "#3 - #7":
 - 30% #1
 - 30% #2
 - Incompatible thermoplastics – no practical value as feed material for new products

State of Plastic Recycling

- Plastics Still Pose a Waste Management Problem:
 - In landfills, plastics constitute
 - 8.9% by weight
 - 17.8% by volume
 - 2nd largest category (paper is 1st)
 - Plastic production is increasing faster than plastics recycling

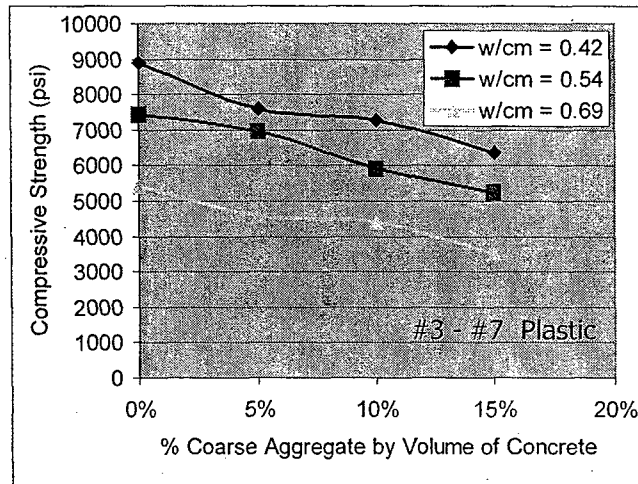
Properties of Concrete Containing Plastics

Concrete Compressive Strength



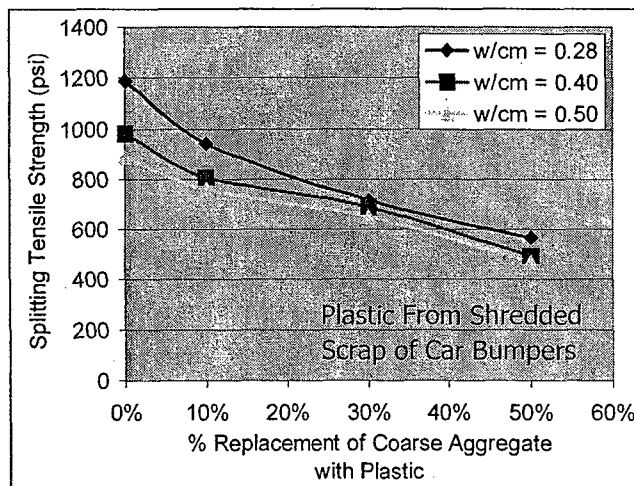
From: Al-Manaseer, A. A., and Dalal, T. R., "Concrete Containing Plastic Aggregates," *Concrete International*, V. 19, No. 8, Aug. 1997, pp. 47-52.

Concrete Compressive Strength



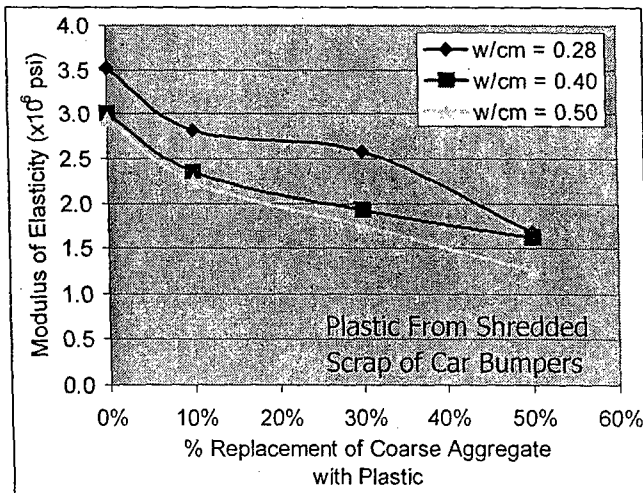
From: Ghaly, A. M., "Compression and Deformation Performance of Concrete Containing Postconsumer Plastics," *Journal of Civil Engineering Materials*, V. 16, No. 4, Aug. 2004, pp. 289-296.

Concrete Splitting Tensile Strength



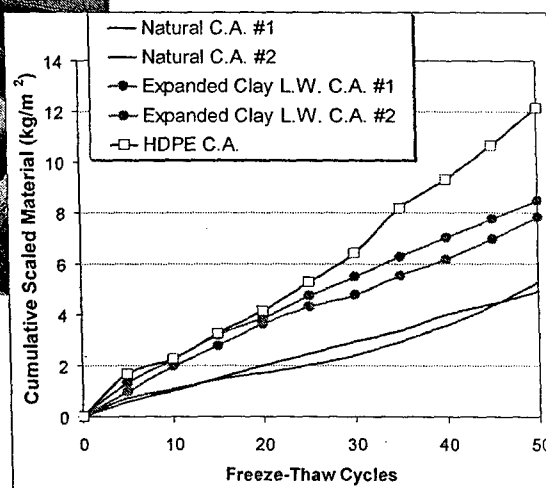
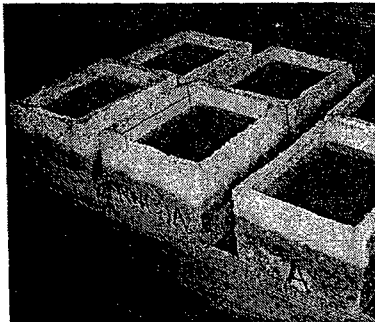
From: Al-Manaseer, A. A., and Dalal, T. R., "Concrete Containing Plastic Aggregates," *Concrete International*, V. 19, No. 8, Aug. 1997, pp. 47-52.

Modulus of Elasticity of Concrete



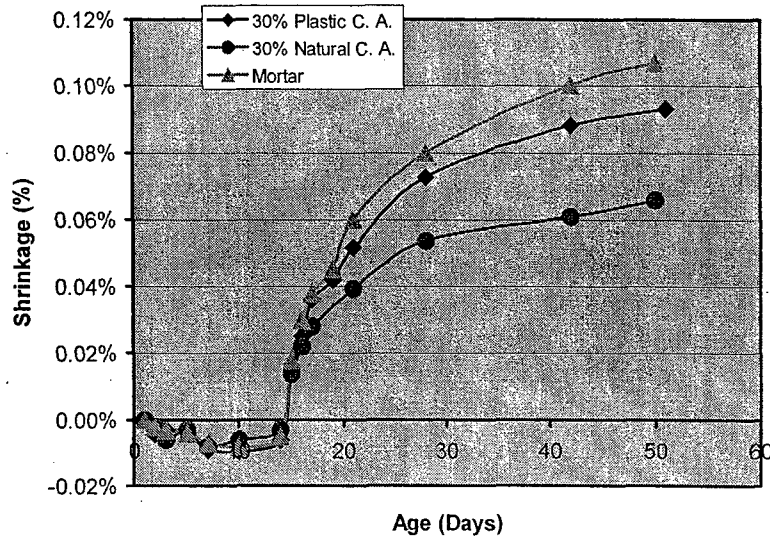
From: Al-Manaseer, A. A., and Dalal, T. R., "Concrete Containing Plastic Aggregates," *Concrete International*, V. 19, No. 8, Aug. 1997, pp. 47-52.

Salt Scaling Durability



Coarse Aggregate 35% by Total Concrete Volume

Shrinkage



Small Fiber Contents

- Small Amounts of Plastic (0.5% to 5%) in Fiber, Flake, or Strip Form Result in:
 - small decreases in compressive and tensile strengths¹⁻³
 - reduced flexural toughness¹
 - reduced crack widths in ring test^{2,3}
 - small² or significant³ increase in impact resistance
 - small increase in permeability (RCPT test)²
 - significant decrease in abrasion resistance³

1. Cavey, J. K.; Krizek, R. J.; Sobhan, K.; Baker, W. H., "Waste Fibers in Cement Stabilized Recycled Aggregate Base Course Material," *Transportation Research Record*, V. 1496, 1995, pp. 97-106.
 2. Soroushian, P.; Eldarwish, A. I.; Tili, A.; Ostowari, K., "Experimental Investigation of the Optimized Use of Plastic Flakes in Normal-Weight Concrete," *Magazine of Concrete Research*, V. 51, No. 1, 1999, pp. 27-33.
 3. Soroushian, P.; Plasencia, J.; Ravanbakhsh, S., "Assessment of Reinforcing Effects of Recycled Plastic and Paper in Concrete," *ACI Materials Journal*, V. 100, No. 3, pp. 203-207.

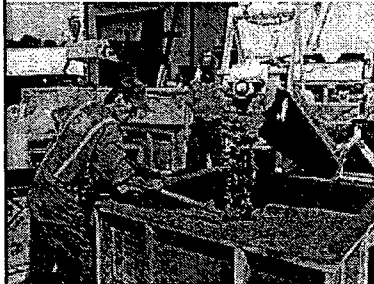
Are there any positives?

Case: Canigliaro Industries



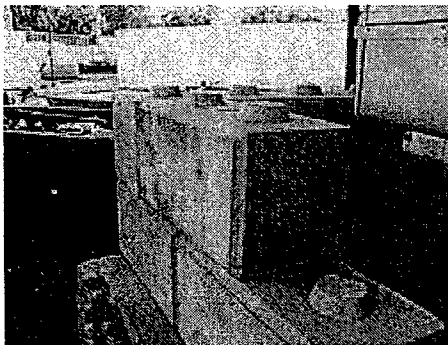
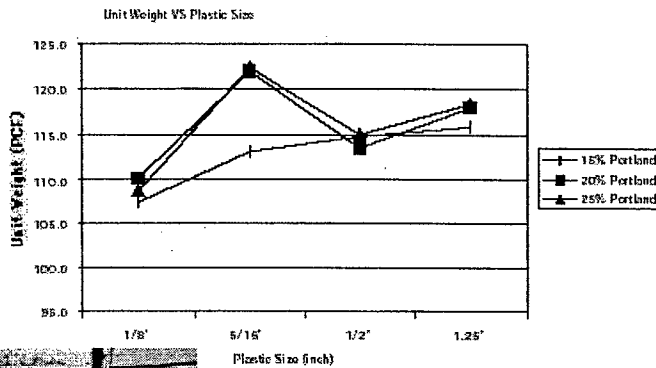
Framingham, MA

Plas-Crete



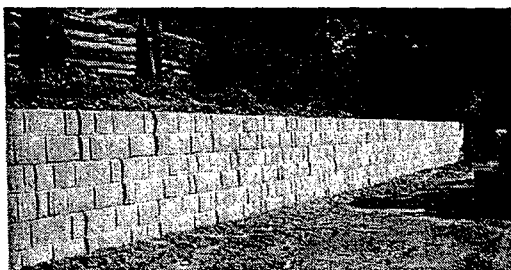
Hooper, F., "PLAS-CRETE: A Lightweight, Portland Cement Concrete Product Manufactured From Discarded Mixed No. 3-7 Plastics," Chelsea Center for Recycling and Economic Development, Report #42, 2002.

Max. Plastic		Cement	Plastic/
Batch	Content	Sand	Particle
No.	(%)	Ratio	Size
1	15	3:2	1/8"
2	15	3:2	5/16"
3	15	3:2	1/2"
4	15	3:2	1.25"
5	20	3:2	1/8"
6	20	3:2	5/16"
7	20	3:2	1/2"
8	20	3:2	1.25"
9	25	3:2	1/8"
10	25	3:2	5/16"
11	25	3:2	1/2"
12	25	3:2	1.25"

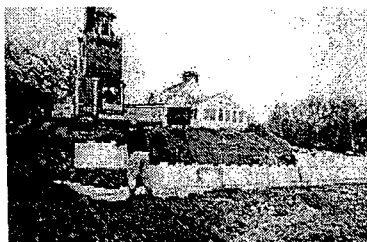
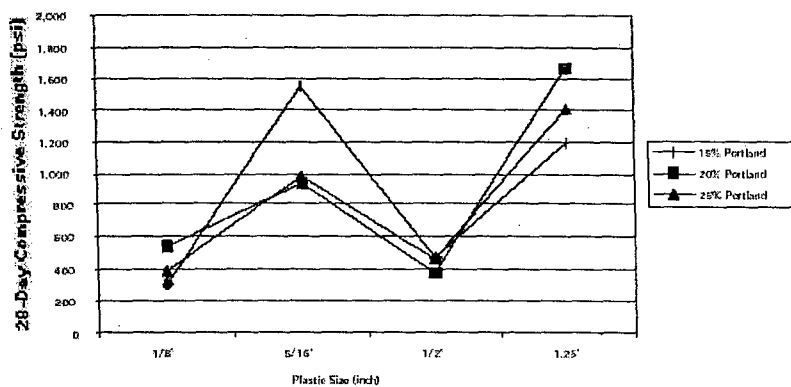


Uses commingled plastic

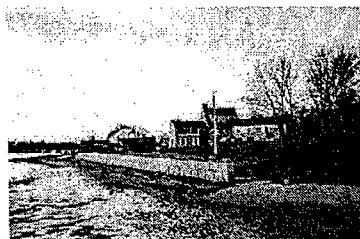
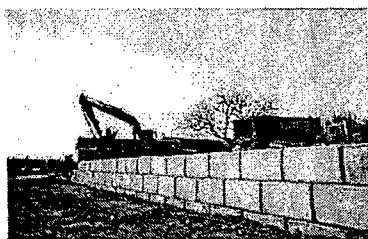
Hooper, F., "PLAS-CRETE: A Lightweight, Portland Cement Concrete Product Manufactured From Discarded Mixed No. 3-7 Plastics," Chelsea Center for Recycling and Economic Development, Report #42, 2002.



Hooper, F., "PLAS-CRETE: A Lightweight, Portland Cement Concrete Product Manufactured From Discarded Mixed No. 3-7 Plastics," Chelsea Center for Recycling and Economic Development, Report #42, 2002.



Currently selling 250 blocks per week using 31 tons of plastic.

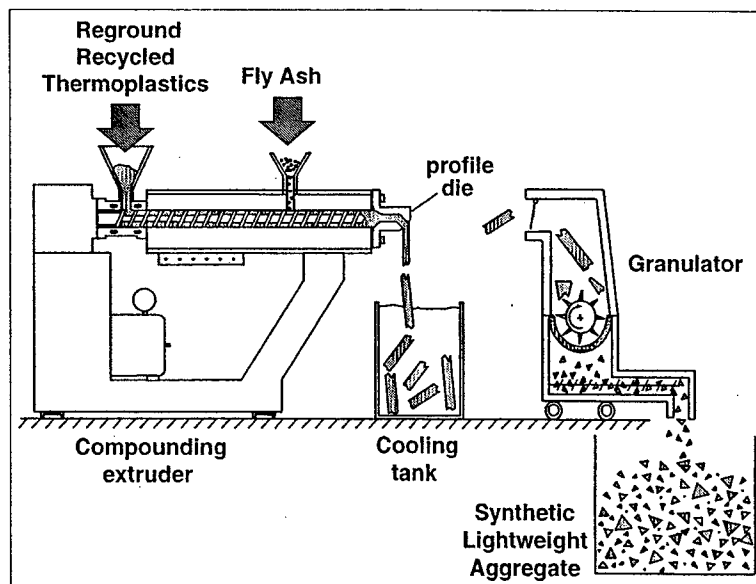


Future Directions

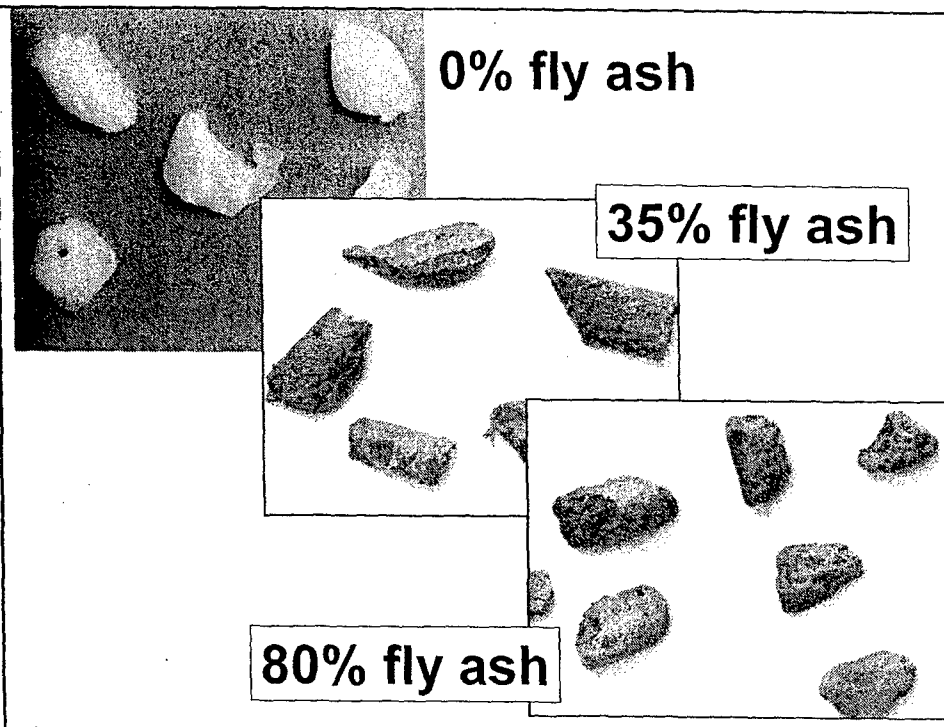
- Need more innovation if properties of concrete containing plastic are to be improved
 - Chemical Treatment¹
 - Bleach
 - Bleach + NaOH
 - Thermal Mixing with Fly Ash (SLA)²

1. Naik, T. R.; Singh, S. S.; Huber, C. O.; Brodersen, B. S., "Use of Post-Consumer Waste Plastics in Cement-Based Composites," *Cement and Concrete Research*, V. 26, No. 10, pp. 1489-1492.
2. Jansen, D. C.; Kiggins, M. L.; Swan, C.; Malloy, R. A.; Kashi, M. G.; Chan, R. A.; Javdekar, C.; Siegal, C.; Weingram, J., "Lightweight Fly Ash-Plastic Aggregates in Concrete," *Transportation Research Record, Materials and Construction: Concrete* 2001, No. 1775, pp. 44-52.

Production of SLAs



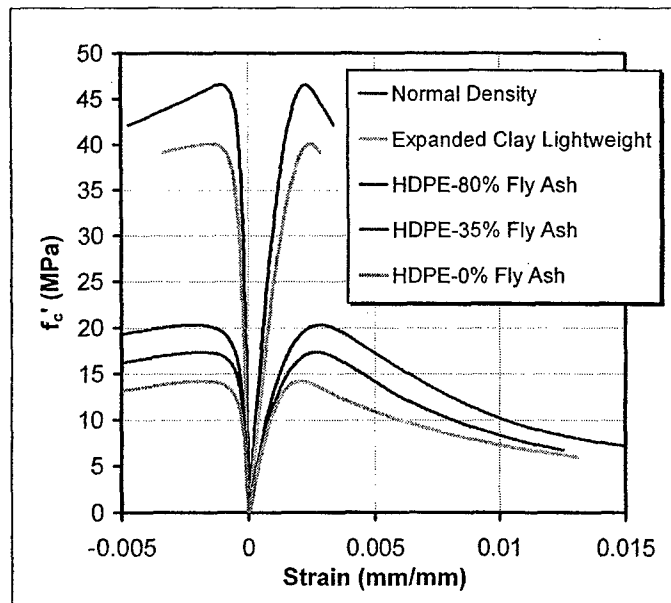
Production of SLAs



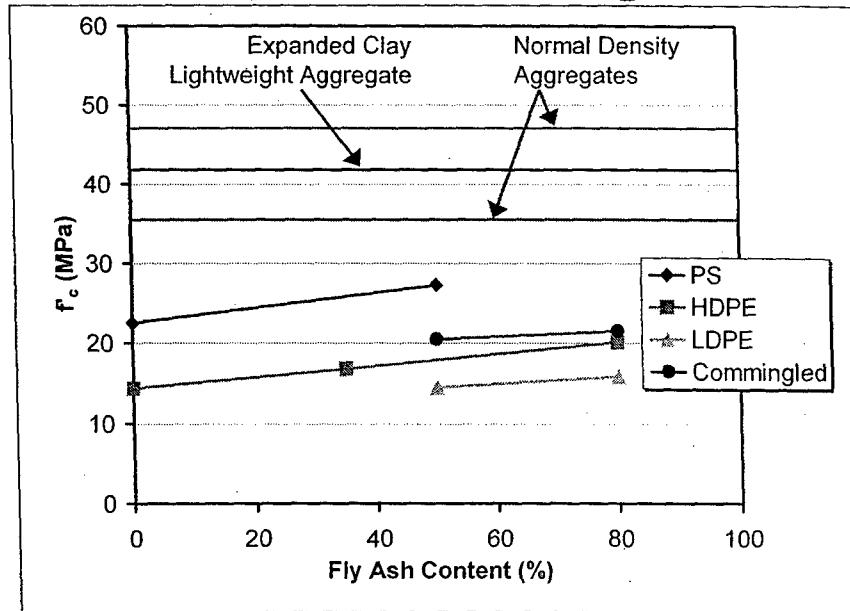
Concrete Mixes

- W/C of 0.35, 0.42, and 0.50
- Volume Fraction of Coarse Aggregates = 0.33
- Natural Sand Used
- Compared with natural coarse aggregates and expanded clay lightweight aggregates

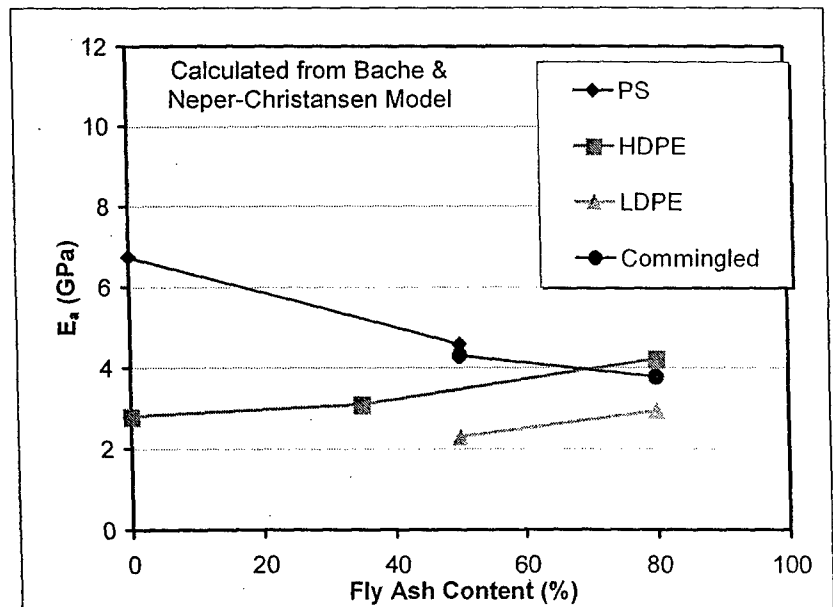
Compressive Behavior



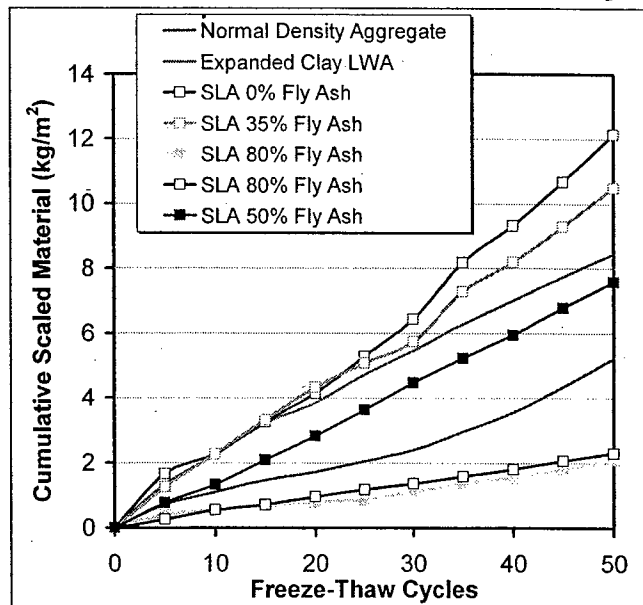
Compressive Strengths



Aggregate Modulus of Elasticity



Salt Scaling Durability



Conclusions

- There is a great need for finding alternative applications for recycled plastics:
 - Commingled (#3-#7)
 - Films
 - Thermosetting plastics
- Using plastics in raw form generally degrade all properties of concrete
 - Use of plastics in raw form in concrete is still economically beneficial
- There is a need for innovative processing of plastics to improve their performance in concrete.

Acknowledgements

This work was sponsored by the Department of the Navy, Office of Naval Research, under Award # N00014-04-1-0436

The Effect of Probiotics on the Species Distribution of *Bifidobacterium* and *Lactobacillus* in Healthy Subjects Undergoing Antibiotic Therapy

Project Investigators:

Christopher L. Kitts
Associate Professor

Biological Sciences/Cal Poly State University/Environmental Biotechnology Institute

Executive Summary

Antibiotic therapy is known to disrupt the intestinal microbial community, sometimes with unpleasant (diarrhea) or even dangerous (*Clostridium difficile* colitis) consequences. Oral consumption of live, beneficial bacteria (probiotics) has been suggested as a means to normalize intestinal communities after antibiotic use. Strains of *Bifidobacterium* and *Lactobacillus* are commonly used. Physiologic effects of probiotics are not clearly understood, but the significance can be inferred by observing changes in the fecal flora after probiotic consumption.

The goal of this study was to evaluate the effect of *Bifidobacterium* and *Lactobacillus* probiotics in volunteers administered antibiotics. Half the subjects were given a mixture of probiotic bacteria, while the other half were given a placebo. Fecal samples were collected 7 times during the 48-day study. The antibiotic Augmentin was administered from days 14 to 21 and the probiotic/placebo from days 14 to 34. DNA was extracted from the fecal samples and amplified with *Bifidobacterium* and *Lactobacillus* specific PCR primers. Species distribution for each genus was analyzed by Terminal Restriction Fragment Length Polymorphism (TRFLP) analysis of the PCR products. This analysis did not show significant, Augmentin-induced changes in the *Bifidobacterium* community, but probiotic feeding did moderate the effect of antibiotic treatment on the *Lactobacillus* community. Additionally, TRF could not specifically detect the administered probiotic strains of *Bifidobacterium* and *Lactobacillus* due to overlapping TRF signals from native strains.

Introduction

The gut represents the largest mucosal surface in the body and the microbial community present can have a large effect on immune function. This community consists of a large number of different species, although only a few account for most of the bacteria present. It is believed that a healthy intestinal flora can protect against certain types of infection and studies have shown that a healthy intestinal flora is a good barrier against potentially pathogenic microorganisms [1]. Antibiotics are known to disrupt this normal intestinal flora. They can cause disturbance in normal bowel function, disruption of mucosal integrity, and symptoms including diarrhea, bloating, flatulence, and intestinal pain [2].

It has been hypothesized that probiotics, live microbial feed supplements that can benefit a host by improving its intestinal microbial balance [3], can facilitate gut normalization after antibiotic treatment. They can produce a variety of health benefits including reduction in the intensity and duration of diarrheal illness, improvement in immune system function, alleviation of lactose intolerance, anticarcinogenic effects, and antihypertensive effects [4, 5]. Probiotics, primarily *Lactobacillus* and *Bifidobacterium* species, are found in many dairy foods and supplements, including over 80% of commercially available yogurt. However, when fed to healthy subjects, probiotics only modestly affect fecal flora and the strains used do not tend to be permanent colonizers.

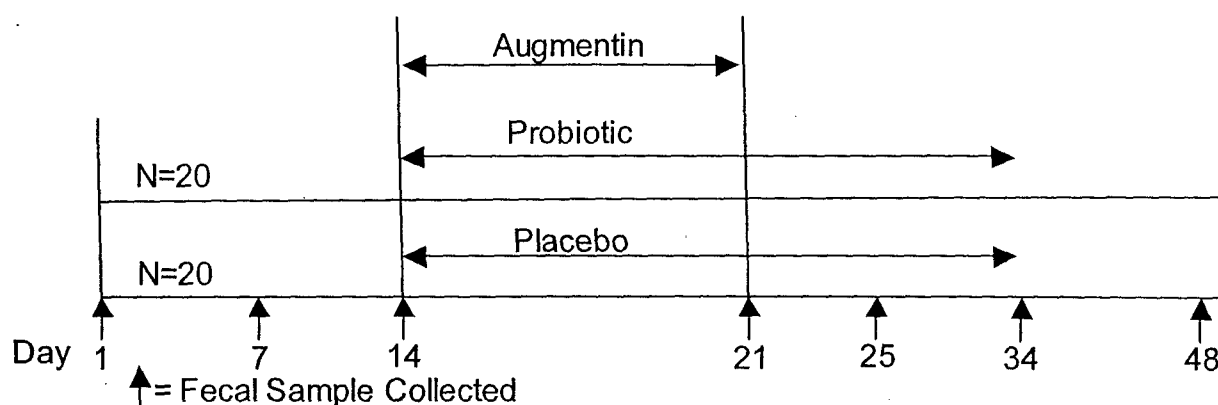
Lactobacilli and Bifidobacteria represent only a fraction of the normal healthy intestinal community. However, changes in their population structure could potentially have important health effects. TRFLP analysis is a rapid way of estimating population structure and because PCR primers specific to *Lactobacillus* and *Bifidobacterium* groups are available, TRFLP was used to follow changes in *Lactobacillus* and *Bifidobacterium* populations

Materials and Methods

Study Design

Healthy individuals were recruited who agreed to be on antibiotics for one week for study purposes only. Each subject received a one-week course of the antibiotic Augmentin (GlaxoSmithKline, Brentford London), a mixture of amoxicillin and clavulanic acid, 875 mg orally twice a day. This antibiotic was selected because of a high rate of antibiotic-associated diarrhea. Patients were then randomized (1:1) to either the placebo or the probiotic test product consisting of a capsule containing a dried bacterial preparation of probiotic bacteria in the genera, *Lactobacillus* and *Bifidobacterium*. The following strains and amounts were fed: *Bifidobacterium bifidum* Bb-02 (5×10^8), *Bifidobacterium lactis* Bl-04 (5×10^9), *Bifidobacterium lactis* Bi-07 (5×10^9), *Lactobacillus acidophilus* NCFM (5×10^9), and *Lactobacillus paracasei* Lpc-37 (5×10^9). The total dose of probiotic was 2×10^{10} bid (4×10^{10} daily). The other group received a placebo consisting of the same filler used in the bacterial preparation, maltodextran, without the bacteria. The study was conducted over 48 days. Three baseline (no treatment) fecal samples were obtained at days 1, 7, and 14, followed by the 7-day course of Augmentin. Fecal samples were then collected on days 21, 25, 34, and 48. Probiotic/Placebo treatment began on day 14 and continued until day 34 (Fig. 1).

Fig. 1. Schematic of the Antibiotic-Probiotic experimental design.



Forty subjects recruited with enrollment criteria permitting only patients over eighteen without significant acute or chronic illnesses. Permitted medications included those that were constant throughout the study and only if they had no established or suspected impact on gut flora. Individuals were excluded if they were pregnant, breastfeeding, had a penicillin allergy, a history of gastrointestinal illness or had been on any antibiotics in the preceding four weeks. Fermented foods or any probiotic preparations were prohibited for four weeks before entry into the study and throughout the duration of the protocol.

Isolation of bacterial DNA

Fecal samples were obtained for TRF analysis by adding approximately 1 gram of feces to a 2 mL screw-cap tube and freezing at -80°C until shipment. Samples were then extracted in triplicate using the MoBio Ultraclean® soil DNA kit following manufacture's protocol with the addition of 5 additional washes with S4. Success of each extraction was determined by measuring DNA concentration in the extraction product with a Spectramax spectrophotometer.

PCR Amplification

PCR was performed using primers homologous to highly conserved regions on the 16S rRNA gene. For *Bifidobacterium* sp., the reverse primer was Bifid-R (5'-ggT gTT CTT CCC gAT ATg CTA CA-3') [6], and the fluorescently labeled forward primer was Bif164-F (5'-ggg Tgg TAAT gCC ggATg-3') [7]. 50 μL reactions were carried out using 5 μL of 10x Buffer, 3 μL of 10 mM dNTP, 2 μL 20 $\mu\text{g mL}^{-1}$ BSA, 7 μL 25 mM MgCl_2 , 1 μL of each primer, and 0.3 μL 5 U μL^{-1} TaqGold®. Reaction temperatures and times were 92°C for 10 min; 30 cycles of 94°C for 20 sec, 57.4°C for 20 sec, and 72°C for 30 sec; and a final extension of 72°C for 10 min.

For *Lactobacillus* sp., the reverse primer was Lab677 (5'CACCgTACACATgg Ag-3') [8], and the fluorescently labeled forward primer was Ba2F (5' gCY TAA CAC ATg CAA gTC gA-3') – a universal Bacterial primer [9]. The 50 μL reactions were carried out using 5 μL of 10x Buffer, 3 μL of 10 mM dNTP, 2 μL 20 $\mu\text{g mL}^{-1}$ BSA, 7 μL 25 mM MgCl_2 , 1 μL of each primer, and 0.3 μL 5 U μL^{-1} TaqGold®. Reaction temperatures and times were 92°C for 10 min; 30 cycles of 94°C for 20 sec, 56°C for 20 sec, and 68°C for 40 sec; and a final extension of 72°C for 10 min.

All reactions were performed in triplicate and then combined using a MoBio Ultraclean® PCR Cleanup Kit following manufacture's protocol. Amounts of amplified PCR product DNA in each sample were determined using a fluorometer.

Enzyme Digest and TRF Pattern Generation

An enzyme digest was performed on each cleaned PCR product using New England Biolabs restriction endonucleases *HhaI* (*Bifidobacterium*) and *HaeIII* (*Lactobacillus*). Each 40 μ L *HhaI* digestion used 75 ng of DNA, 1 U of enzyme, 0.4 μ L of BSA, and 4 μ L of buffer. The samples were digested for 4 hours at 37°C and inactivated for 20 min at 65°C. Each 40 μ L *HaeIII* digestion used 75 ng of DNA, 1 U of enzyme, and 4 mL of buffer. The samples were digested for 4 h at 37°C and inactivated for 20 min at 80°C. Digestion products were ethanol precipitated and resuspended in 20 μ L of formamide and 0.25 μ L of CEQ 600 base pair standard. Terminal restriction fragment profiles were obtained using CEQ 8800 DNA Analysis system (Beckman Coulter, Fullerton, CA). TRF peaks were identified by matching to TRFs generated using sequences from the Ribosomal Database Project and GenBank.

Data Preparation and Statistical Analysis

Terminal Restriction Fragment (TRF) length in nucleotides, and TRF peak area were exported from the CEQ 8800 into Excel (Microsoft, Seattle, WA). To standardize the data for comparison between samples, the area under each TRF peak was normalized to total amount of DNA analyzed and expressed as parts per million (ppm). Peaks with an area of less than 10,000 ppm (<1% of the total for that sample) were excluded from analysis to reduce noise.

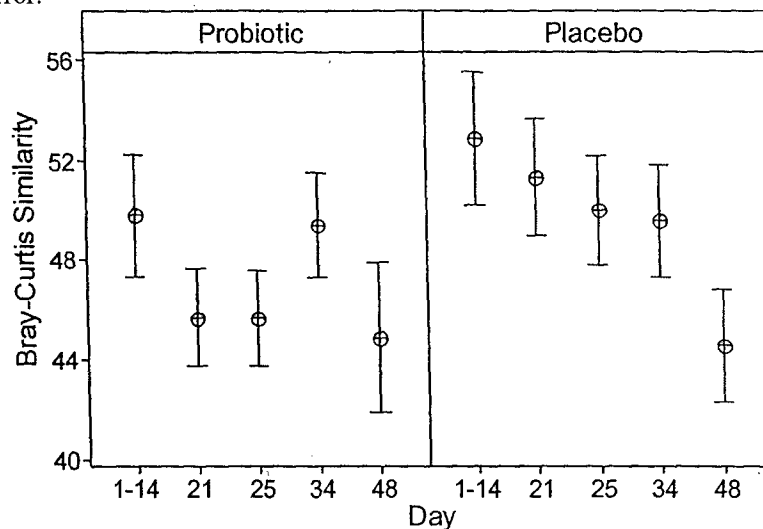
Normalized TRF data sets were transformed by taking the square root of the area under each TRF peak to de-emphasize large TRF peaks while still taking relative abundance into account [10]. Transformed data were analyzed using Bray-Curtis similarity [11] using Minitab (Minitab Inc., State College PA) and Excel.

Results

Bifidobacterium

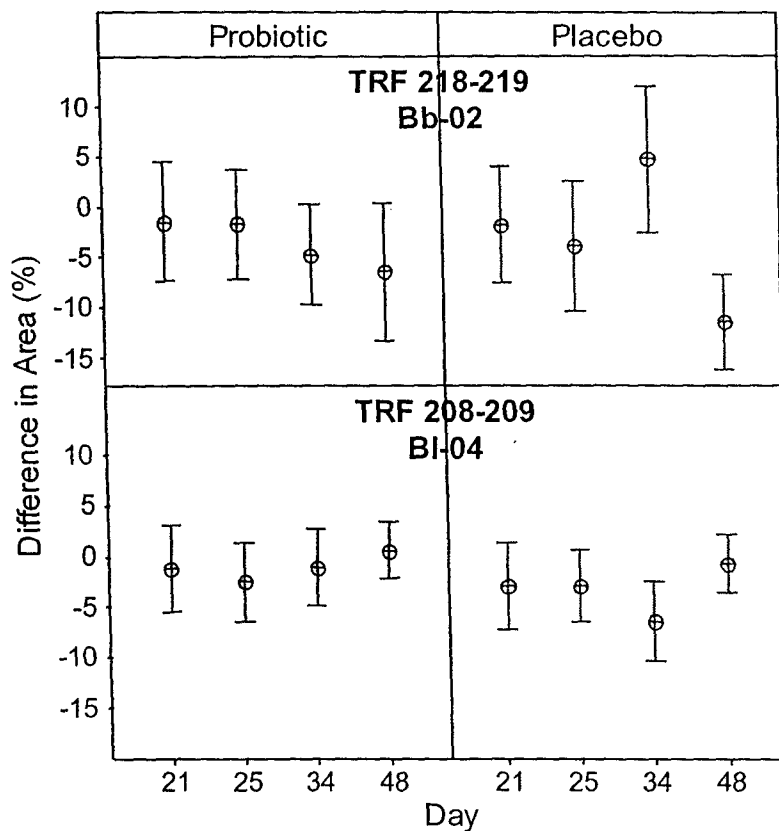
256 samples, from 36 subjects (18 in each treatment group) fit the criteria necessary to provide meaningful data on the effects of probiotics on fecal Bifidobacterial communities. Antibiotic effect was determined by calculating Bray-Curtis similarities to baseline (days 1-14) for day 21 individually for each subject (Fig. 2). Within baseline similarity compared to similarity of day 21 to baseline resulted in no significant difference in either treatment group (T-test, probiotic, $p = 0.189$; placebo, $p = 0.663$). There appeared to be a trend of return to baseline by day 34 in the probiotic group, but not in the placebo treatment group (Fig. 2). However, this trend could not be statistically significant because there was not a significant antibiotic effect.

Fig. 2. Average Bray-Curtis similarity from baseline (days 1-14) for each day after treatment. Error bars represent one standard error.



The three different strains of probiotic *Bifidobacteria* fed to the subjects (probiotic treatment group) were tracked in the TRF patterns. There was no apparent trend for either *Bifidobacterium bifidum* Bb-02 (TRFs 218-219) or *Bifidobacterium lactis* BI-04 (TRFs 208-209) (Fig. 3), in fact, there appeared to be no change from baseline values. *Bifidobacterium lactis* Bi-07 (TRF 106) was not found in any subject, before or after probiotic treatment.

Fig. 3. Difference in TRF peak area from baseline (days 1-14) for each day after treatment.

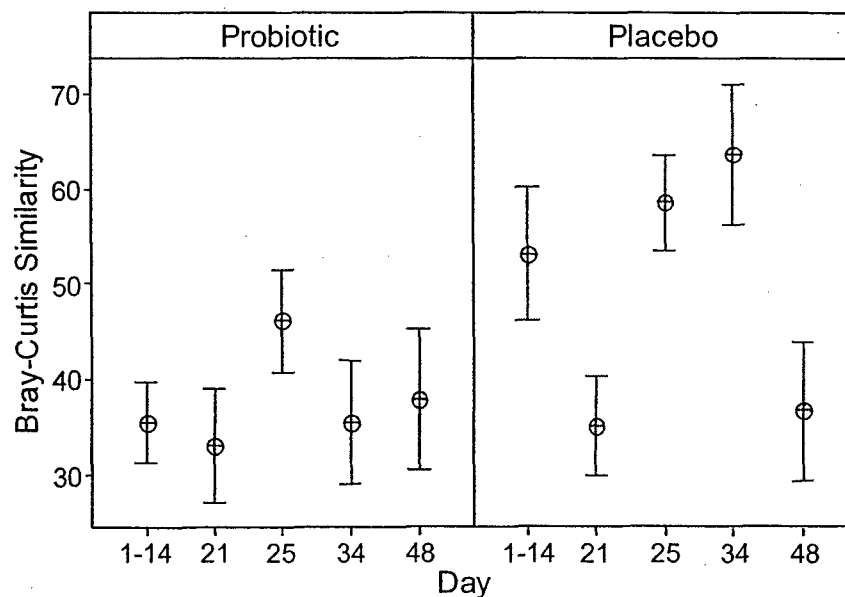


Lactobacillus

There were very low numbers of *Lactobacillus* present in most of the fecal samples. *Lactobacilli* were only detected by PCR in about 40% of the samples. The other 60% of the fecal samples either had *Lactobacillus* numbers that were below the detection limit for the PCR primers or had PCR inhibitors present that inhibited amplification of *Lactobacillus* DNA.

Antibiotic effect was determined by calculating Bray-Curtis similarities to baseline (days 1-14) for day 21 individually for each subject with data for at least two baseline samples and at least one after treatment sample (Fig. 5). Therefore, 7 subjects from the probiotic treatment group and 6 subjects from the placebo group were included in the analysis. T-tests of within baseline (days 1-14) similarity to similarity of day 21 to baseline resulted in a significant effect in the placebo group ($p = 0.047$) and no effect in the probiotic group ($p = 0.751$). Therefore, probiotics did not appear to significantly affect *Lactobacillus* community structure (Fig. 5) but may have stabilized the *Lactobacillus* community against an antibiotic challenge.

Figure 5. Average Bray-Curtis similarity from baseline (days 1-14) for each day after treatment. Error bars represent one standard error.



Discussion

Overall results from the *Lactobacillus* and *Bifidobacterium* specific primers were mixed. Probiotic strains could not be accurately tracked, most likely because of too many overlapping TRF's from native flora. For *Bifidobacteria*, an antibiotic effect on community structure was observed, but was not statistically significant. A probiotic effect was also observed, but was not significant. Therefore, the probiotic strains did not appear to significantly alter community structure but, may have stabilized the *Bifidobacterium* community against an antibiotic challenge. For *Lactobacilli*, cell numbers were often below the PCR detection limit, but in the PCR positive samples, it appeared as if community structure was significantly altered by antibiotic therapy in the placebo group, but not the probiotic group. Once again, probiotic treatment may have stabilized the *Lactobacillus* community against an antibiotic challenge.

References

- [1] Fuller, R. (1991) Probiotics in human medicine. *Gut*. 32, 439-442. Bergogne-Berezin, E. (2000) Treatment and prevention of antibiotic associated diarrhea. *Int. J. Antimicrob.* 16, 521-6.
- [3] Fuller, R. (1989) Probiotics in man and animals. *J. Appl. Bacteriol.* 66, 365-378.
- [4] Gill, H.S. and Guarner, F (2004) Probiotics and human health: a clinical perspective. *Postgrad. Med. J.* 80, 516-526.
- [5] Sanders, M.E. (1999) Probiotics. *Food Technol.* 53, 67-77. Matsuki, T., Watanabe, K., Fujimoto, J., Miyamoto, Y., Takada, T., Matsumoto, K., Oyaizu, H., and Tanaka, R. (2002) Development of 16s rRNA-Gene-Targeted Group-Specific Primers for the Detection and Identification of Predominant Bacteria in Human Feces. *Appl. Environ. Microbiol.* 68, 5445-5451.
- [7] Satokari, R., Vaughan, E., Akkermans, A., Saarela, M., and de Vos, W. (2001) Bifidobacterial Diversity in Human Feces Detected by Genus-Specific PCR and Denaturing Gradient Gel Electrophoresis. *Appl. Environ. Microbiol.* 67, 504-513.
- [8] Heilig, H., Zoetendal, E., Vaughan, E., Marteau, P., Akkermans, A., and de Vos, W. (2002) Molecular Diversity of *Lactobacillus* spp. and Other Lactic Acid Bacteria in the Human Intestine as Determined by Specific Amplification of 16S Ribosomal DNA. *Appl. Environ. Microbiol.* 68, 114-123.
- [9] Kaplan, C.W., Astaire, J.C., Sanders, M.E., Reddy, B.S. and Kitts, C.L. (2001) 16S ribosomal DNA terminal restriction fragment pattern analysis of bacterial communities in feces of rats fed *Lactobacillus acidophilus* NCFM. *Appl. Environ. Microbiol.* 67, 1935-1939.
- [10] Blackwood, C.B., Marsh, T., Kim, S., and Paul, E.A. (2003) Terminal restriction fragment length polymorphism data analysis for quantitative comparison of microbial communities. *Appl. Environ. Microbiol.* 69, 926-932.
- [11] Rees, G.N., Baldwin, D.S., Watson, G.O., Perryman, S., and Nielson, D.L. (2004) Ordination and significance testing of microbial community composition derived from terminal restriction fragment length polymorphisms: application of multivariate statistics. *Ant. Van Leeuw.* 86, 339-347.

Note: This research was co-sponsored by Danisco, Inc. The Danisco funding was used to study the effect of antibiotics and probiotics on the total bacterial consortium, rather than the specific primer sets used for the work reported here.

The Effect of Probiotics on the Species Distribution of *Bifidobacterium* and *Lactobacillus* in Healthy Subjects Undergoing Antibiotic Therapy

A.L. Engelbrektsen¹, H. D. Nguyen¹, D. Y. Lung¹, J. R. Korzenik², M.E. Sanders³, G. Leyser⁴, T.R. Klaenhammer⁵, C. L. Kitts¹

Environmental Biotechnology Institute, San Luis Obispo, CA

²Massachusetts General Hospital, Harvard Medical School, Boston, MA

³Dairy and Food Culture Technologies, Centennial, CO

⁴Danisco, Madison, WI

⁵North Carolina State University, Raleigh, NC

Antibiotic therapy is known to disrupt the intestinal microfloral community, sometimes with unpleasant (diarrhea) or even dangerous (*Clostridium difficile* colitis) consequences. Oral consumption of live, beneficial bacteria (probiotics) has been suggested as a means to normalize intestinal communities after antibiotic use. Strains of *Lactobacillus acidophilus* and *Lactobacillus* are commonly used as probiotics. Physiologic effects of probiotics are not clearly understood, but the significance can be inferred by observing changes in the fecal flora after probiotic

The goal of this study was to evaluate the effect of the combination of rifampin and rifabutin on the growth of *B. subtilis* and *L. acidophilus* in the presence of probiotic bacteria and Lactobacillus products in volunteers. The subjects were given a 14-day course of rifampin and rifabutin, followed by a 14-day course of probiotic bacteria. Half the subjects were given a placebo. Fecal samples were collected 7 times during the study. The antibiotic, rifampin, was administered on days 14 to 21 and the probiotic placebo from days 14 to 21. DNA was extracted from the fecal samples and amplified with *Bifidobacterium* and *Lactobacillus* specific PCR primers. Specific distribution for each genus was analyzed by terminal restriction fragment (TRF) length polymorphism (RFLP) analysis of the PCR products and standard culturing techniques. The results of the study showed that rifampin-induced changes in the *Bifidobacterium* community kept overall *Bifidobacterium* numbers higher. In contrast, TRF culture analysis demonstrated that probiotic feeding moderated the effect of antibiotic treatment on the *Lactobacillus* community. Culture analysis showed no significant change in *L. acidophilus* numbers with treatment. Additionally, TRF signals could not consistently detect the administered

The gut represents the largest mucosal surface in the body and the microbial community present can have a large effect on immune function. This community consists of a mixture of different species, although only a few are believed to account for most of the bacteria present. It is hypothesized that a healthy intestinal flora can protect against certain types of infection and studies have shown that a healthy intestinal flora is a good barrier against potentially pathogenic bacteria [1, 2].

Antibiotics are known to disrupt this normal intestinal flora. They can cause disturbance in normal bowel function, disruption of mucosal integrity, and symptoms including diarrhoea, bloating, flatulence, and intestinal pain (Bergoppe et al. 2000).

It has been hypothesized that probiotics can facilitate gut normalization after antibiotic treatment. Probiotics are defined as live microorganisms that, when administered in adequate amounts, confer a health benefit on the host [3].

889). They can produce a variety of health benefits including reduction in the intensity and duration of diarrheal episodes, improvement in immune system function, and lactose intolerance, anticarcinogenic effects, and immunomodulatory/persuasive effects (Sanders, 1999; Gill and Guerner, 2004). Probiotics, primarily *Lactobacillus* and *Bifidobacterium* species, are found in many dairy foods and supplements, including over 80% of commercially available products. However, when fed to healthy subjects, probiotics only modestly affect fecal flora and the strains used do not appear to be permanent colonizers. *Lactobacillus* and *Bifidobacterium* are thought to represent only a fraction of the normal fecal flora. The use of probiotics to improve the health of the population structure could potentially have important health effects.

This study involved two groups of individuals who both received a one-week course of the antibiotic Augmentin (amoxicillin and clavulanic acid). One of the groups also took a probiotic test product consisting of a capsule containing a dried bacterial preparation of probiotic bacteria in the genera, *Lactobacillus* and *Bifidobacterium* as follows.

Bifidobacterium bifidum Bb-02 (x10⁹)
Bifidobacterium lactis B-04 (x10¹⁰)
Bifidobacterium lactis B-04 (x10¹⁰)
Lactobacillus acidophilus NCFM (x10⁹)
Lactobacillus acidophilus NCFM (x10⁹)
Lactobacillus paracasei Lpc37 (x10⁹)
Total GDN x10¹⁰ (40 mg daily)
Total GDN x10¹⁰ (40 mg daily)

The other group received a placebo. The subjects were assigned to placebo (no treatment) fecal samples were obtained at days 1, 7, and 14. All subjects (Placebo treatment) began on day 14 and continued until day 34. TRF analysis is a new way of estimating population structure and relative abundance of *Bifidobacterium* and *Lactobacterium* groups in fecal samples.

Figure 1 is a timeline diagram illustrating the study design. It shows two parallel horizontal timelines for two groups of 20 subjects each (N=20). The top timeline (N=20) shows a sequence of treatments: Augmentin (14 days), followed by a 14-day gap, then Probiotic (14 days), and finally Placebo (14 days). The bottom timeline (N=20) shows a sequence of treatments: Placebo (14 days), followed by a 14-day gap, then Probiotic (14 days), and finally Augmentin (14 days). Both timelines end with a 'Feed Sample Collected' at day 48. Arrows indicate the duration of each treatment period.

References

* Bergegne-Betzheim E, 2000. Treatment and prevention of antibiotic associated diarrhea. *Int J Antimicrob* 16:324-8.

1. Feller R, 1989. Antibiotics in man and animals. *J Appl Bacteriol* 66:365-378.

2. Feller R, 1991. Probiotics in human medicine. *Gut* 32:439-442.

3. Gill H.S. and Guarnier F. Probiotics and human health: a clinical perspective. *Postgrad Med J* 2004; 80:516-526.

4. Sanders M.E. 1989. Probiotics. *Food Technol* 53:67-77.

Figure 1. Average Bay-Curt similarity from baseline (days 1-14) for each day after treatment. Error bars represent one standard error.

Day	Placebo (Mean)	Placebo (SE)	Phobic (Mean)	Phobic (SE)
1	18.5	1.5	18.5	1.5
2	20.5	1.5	16.5	1.5
3	22.5	1.5	14.5	1.5
4	24.5	1.5	12.5	1.5
5	26.5	1.5	10.5	1.5
6	28.5	1.5	8.5	1.5
7	30.5	1.5	6.5	1.5
8	32.5	1.5	4.5	1.5
9	34.5	1.5	2.5	1.5
10	36.5	1.5	0.5	1.5
11	38.5	1.5	-1.5	1.5
12	40.5	1.5	-3.5	1.5
13	42.5	1.5	-5.5	1.5
14	44.5	1.5	-7.5	1.5

- Antibiotic Effect
 - T-test of within baseline (days 1-14) similarity to similarity of day 21 to baseline
 - No effect in the probiotic group ($p=0.189$)
 - No effect in the placebo group ($p=0.663$)
- Probiotic Effect
 - Trend of return to baseline in the probiotic group by day 34
 - No apparent return to baseline in the placebo group

Figure 3. Difference in TFR points at end baseline (days 1-10) for each day after treatment

Day	Placebo	TRF 234-216
1	-10	10
2	-10	10
3	-10	10
4	-10	10
5	-10	10
6	-10	10
7	-10	10
8	-10	10
9	-10	10
10	-10	10

• Average basal
 subtracted from
 day subsequent
 • Significant
 • Significant
 placebo

tracking of fed probiotic peaks
 • No apparent trend for *Bifidobacterium bifidum* BB-02 (TRF 218-9)
 • No apparent trend for *Bifidobacterium lactis* BB-04 (TRF 208-9)

Day	BLANK (log CFU)	BLANK+25 (log CFU)
0	~2.5	~2.5
12	~3.0	~2.0
24	~3.5	~1.8
36	~4.0	~1.6
48	~4.5	~1.5

counts for each subject were the counts for that subject on each antibiotic treatment.

ference between probiotic and control (ANOVA, $p=0.030$).

Figure 3. Average Bray-Curtis similarity (non-baited) (days 1-10) for *Phaeobacillus* and *Phaeocystis* after treatment. Error bars represent one standard error.

- Antibiotic Effect
- T-test of within baseline (days 1-14) similarity to similarity of day 21 to baseline
- No effect in the probiotic group ($p=0.751$)
- Significant effect in the placebo group ($p=0.047$)
- Probiotic Effect
- Antibiotic treatment did not effect *Lactobacillus* community structure

Figure 8 Mean±SD of difference from baseline (days 1–14) for the mean (horizontal line) and SD (vertical line) of the mean SD representation for a standard error.

Day	Prophetic (Mean Difference)	Pseudo (Mean Difference)
1	0.8	0.8
21	0.6	0.6
48	0.2	0.2

Average baseline counts for each subject were subtracted from the counts for that subject on each day subsequent to antibiotic treatment.

- No significant difference between probiotic and placebo group (ANOVA, $p=0.772$)

Figure 1 is a bar chart showing the effect of probiotic and placebo on log colony forming units (CFU) for all patients and for patients with major histocytotoxicity. The y-axis is 'Log CFU' ranging from 0 to 10. The x-axis is 'Day' with markers at 1, 2, 3, 4, 5, 6, 7, 8, 9, 10, 11, 12, 13, 14, 15, 16, 17, 18, 19, 20, 21. The chart is divided into two sections: 'Probiotic' (left) and 'Placebo' (right). Each section shows two data series: 'All patients' (solid circles) and 'Major histocytotoxicity' (open circles). Error bars represent one standard error.

Day	Treatment	Group	Log CFU (approx.)
1	Probiotic	All patients	4.5
2		All patients	4.5
3		All patients	4.5
4		All patients	4.5
5	Probiotic	All patients	4.5
6		All patients	4.5
7		All patients	4.5
8		All patients	4.5
9	Probiotic	All patients	4.5
10		All patients	4.5
11		All patients	4.5
12		All patients	4.5
13	Probiotic	All patients	4.5
14		All patients	4.5
15		All patients	4.5
16		All patients	4.5
17	Probiotic	All patients	4.5
18		All patients	4.5
19		All patients	4.5
20		All patients	4.5
21	Probiotic	All patients	4.5
22		All patients	4.5
23		All patients	4.5
24		All patients	4.5
1	Placebo	All patients	4.5
2		All patients	4.5
3		All patients	4.5
4		All patients	4.5
5	Placebo	All patients	4.5
6		All patients	4.5
7		All patients	4.5
8		All patients	4.5
9	Placebo	All patients	4.5
10		All patients	4.5
11		All patients	4.5
12		All patients	4.5
13	Placebo	All patients	4.5
14		All patients	4.5
15		All patients	4.5
16		All patients	4.5
17	Placebo	All patients	4.5
18		All patients	4.5
19		All patients	4.5
20		All patients	4.5
21	Placebo	All patients	4.5
22		All patients	4.5
23		All patients	4.5
24		All patients	4.5

c Effect
parent trend when data were averaged
ss all subjects

- General
 - Could not accurately track the strains
 - Too many overlapping TFs
 - No trends could be seen by p/p or data averaged across all substrates
- *Bifidobacterium*
 - Probiotic strains kept overall but did not significantly alter structure
 - An antibiotic effect on co-culture structure was observed but not significant
- The probiotic group appeared baseline by day 34, the placebo did not
- Counts were significantly different between the placebo group (decreased)

- Numbers were so low that the PCR detection limit was exceeded
- Only 40% of the samples detected *Lactobacillus*
- Overall numbers were not affected by treatment, but community structure was
- Antibiotic treatment significantly affected community structure in the probiotic group, but not in the probiotic group without antibiotic
- Count data showed no antibiotic effect

H.D. Nguyen¹, D.Y. Lung¹, A.L. Engelbrektson¹, J.R. Korzenik², M.E. Sanders³, G. Leyer⁴, C.L. Kitts¹
¹Environmental Biotechnology Institute, California Polytechnic State University, San Luis Obispo, CA, USA
²Gastroenterology Intestinal Unit, Massachusetts General Hospital, Harvard Medical School, Boston, MA
³Dairy and Food Culture Technologies, Centennial, CO, USA
⁴Danisco



DANISCO

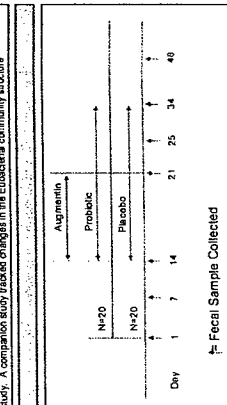
Background: Antibiotic therapy is known to disrupt the beneficial microbial community, sometimes with unpleasant or even dangerous consequences. Oral consumption of live, beneficial bacteria probiotics consisting of strains of *Bifidobacterium* and *Lactobacillus* has been suggested as a means to normalize intestinal communities after antibiotic use. Physiological effects of probiotics are not clearly understood, but the significance of probiotics can be studied by observing changes in the local flora after probiotic consumption. The goal of this study was to evaluate the effect of *Bifidobacterium* and *Lactobacillus* probiotics in volunteers administered antibiotics. Half the subjects were given a measure of antibiotic during the 48 days study. The antibiotic, Augmentin[®], was administered from days 14 to 21 and the probiotic, Danisco, from days 14 to 34.

Methods: DNA was isolated from the fecal samples and amplified with *Bifidobacterium* and *Lactobacillus* specific primers. Species identification for each genus was analyzed by Terminal Restriction Fragment (TRF) Length Polymorphism analysis of the PCR products. Augmentin[®] was administered to half the subjects and the other half received a placebo. Preliminary analyses of TRF signals from the subjects did not show consistent alteration of the *Bifidobacterium* community due to probiotic feeding. In contrast, probiotic feeding appeared to moderate the effect of antibiotic treatment on the *Lactobacillus* community.

Conclusions: TRF signals could not consistently detect the administered probiotic strains of *Bifidobacterium* and *Lactobacillus* from feces at subject's feces. The effect of probiotic feeding will become clearer after the data from the remaining subjects in the study are analyzed.

Probiotics: primarily *Lactobacillus* and *Bifidobacterium* species are found in some dairy foods and supplements in the USA. These two genera are normal components of the healthy human intestinal microbiota. The physiological effects of probiotics are not established, and clinical uses of them are still under investigation, but it is anticipated that probiotics may assist in the normal communities within the gut. A major effect of antibiotic treatment is the disruption of the native gut community that may lead to a loss of probiotic species. The purpose of this study was to evaluate the effect of probiotics on the local flora of people taking an antibiotic. One of the objectives was to determine the impact of probiotic therapy during and after antibiotic therapy on local bacterial communities. The antibiotic administered in this study was Augmentin[®] (amoxicillin and clavulanic acid) and the test product was a capsule containing a dried bacterial preparation of probiotic strains of *Lactobacillus* and *Bifidobacterium*, as follows:
Bifidobacterium bifidum B-442 (5x10⁹)
Bifidobacterium lactis B-307 (5x10⁹)
Lactobacillus acidophilus NCFM (5x10⁹)
Lactobacillus paracasei Lb81 (5x10⁹)
Total dose: 2x10¹⁰ cfu (4x10¹⁰ cfu/day)

Although these organisms represent a fraction of the total intestinal community, changes in the population structure of these organisms could have important health effects. TRF analysis is a rapid way of estimating population structure, because PCR is specific to *Bifidobacterium* and *Lactobacillus* and *Bifidobacterium* groups are positive for probiotics that occur during the study. A comparison study looked at changes in the *Bifidobacterium* community structure.



> Does the antibiotic, Augmentin, administered during the course of one week have an effect on the *Lactobacillus* and *Bifidobacterium* communities?
 > Does the administered probiotic alter the effect of Augmentin?
 > Could the administered probiotic be detected using TRF analysis?

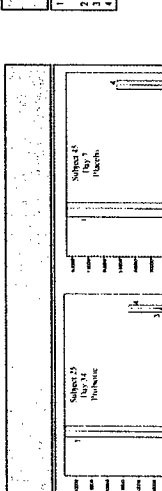
Extraction of bacterial DNA
 Colony counts were performed on the fecal samples and stored at -80°C until analyzed. Samples were extracted and purified using the QIAzol Lysis Reagent and QIAzol Lysis Reagent. Samples were extracted and purified using the QIAzol Lysis Reagent and QIAzol Lysis Reagent. Samples were extracted and purified using the QIAzol Lysis Reagent and QIAzol Lysis Reagent.

PCR Amplification
 The extracted DNA was amplified using the primers designed for the *Bifidobacterium* and *Lactobacillus* species. The PCR products were analyzed using the TRF analysis. The TRF analysis was performed using the TRF analysis. The TRF analysis was performed using the TRF analysis.

Data Analysis
 The TRF signals were analyzed using the TRF analysis. The TRF signals were analyzed using the TRF analysis. The TRF signals were analyzed using the TRF analysis. The TRF signals were analyzed using the TRF analysis.

Results
 The TRF signals were analyzed using the TRF analysis. The TRF signals were analyzed using the TRF analysis. The TRF signals were analyzed using the TRF analysis. The TRF signals were analyzed using the TRF analysis.

Conclusions
 The TRF signals were analyzed using the TRF analysis. The TRF signals were analyzed using the TRF analysis. The TRF signals were analyzed using the TRF analysis. The TRF signals were analyzed using the TRF analysis.

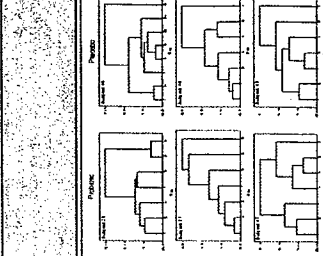


TRF signal analysis
 The TRF signal analysis was performed using the TRF analysis. The TRF signal analysis was performed using the TRF analysis. The TRF signal analysis was performed using the TRF analysis. The TRF signal analysis was performed using the TRF analysis.

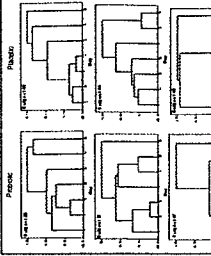
TRF signal analysis
 The TRF signal analysis was performed using the TRF analysis. The TRF signal analysis was performed using the TRF analysis. The TRF signal analysis was performed using the TRF analysis. The TRF signal analysis was performed using the TRF analysis.

TRF signal analysis
 The TRF signal analysis was performed using the TRF analysis. The TRF signal analysis was performed using the TRF analysis. The TRF signal analysis was performed using the TRF analysis. The TRF signal analysis was performed using the TRF analysis.

TRF signal analysis
 The TRF signal analysis was performed using the TRF analysis. The TRF signal analysis was performed using the TRF analysis. The TRF signal analysis was performed using the TRF analysis. The TRF signal analysis was performed using the TRF analysis.



TRF signal analysis
 The TRF signal analysis was performed using the TRF analysis. The TRF signal analysis was performed using the TRF analysis. The TRF signal analysis was performed using the TRF analysis. The TRF signal analysis was performed using the TRF analysis.



TRF signal analysis
 The TRF signal analysis was performed using the TRF analysis. The TRF signal analysis was performed using the TRF analysis. The TRF signal analysis was performed using the TRF analysis. The TRF signal analysis was performed using the TRF analysis.

Nonlinear Constitutive Equations for Cartilage Growth Analysis

Project Investigators:

Stephen M. Klisch
Associate Professor
Mechanical Engineering

Andrew Davol
Associate Professor
Mechanical Engineering

Excerpt from initial proposal:

"The long-term goal of the proposed research is to develop and use analytical and experimental methods to quantitatively characterize the complex relationship between stimuli, cellular metabolism, tissue growth, and biomechanical function for cartilaginous tissues. *The specific aims are to develop a nonlinear stress constitutive equation for the solid matrix of cartilage using the methods of continuum mechanics and to use this equation in a cartilage growth mixture model to solve equilibrium growth boundary-value problems related to tissue engineering experiments to predict how tissue composition, geometry, and pre-stresses evolve during in vitro growth.* An expected outcome of the research is the development of more accurate cartilage growth models that may be used in the successful design of tissue engineered cartilage constructs for the repair of cartilage defects."

Specific Aims:

Aim 1. Developing a nonlinear stress vs. strain constitutive equation for the cartilage solid matrix.

Aim 2. Developing an analytical solution to the growth boundary-value problem for idealized growth conditions.

We have met the specific aims as evidenced by the following published conference abstracts:

1. Klisch, SM, Asanbaeva A, Davol A, Sah RL. Cartilage growth mixture model: finite strain theory, constitutive equations, and boundary-value problem solutions. *Proceedings of the International Plasticity Meeting*, 2005.
2. Klisch SM, Holtrichter SE, Sah RL, Davol A. A bimodular second order orthotropic stress constitutive equation for cartilage. *Transactions of the ASME: Advances in Bioengineering*, 2004.

The accepted conference abstract:

3. Klisch, SM, Sah, RL, Davol, A. A bimodular theory for finite deformations: comparison of orthotropic second-order and exponential stress constitutive equations for articular cartilage. *First International Conference on Mechanics of Biomaterials*, 2005.

And the accepted *invited* manuscript for a special issue on cartilage in a peer-reviewed journal:

4. Klisch, SM. A bimodular theory for finite deformations: comparison of orthotropic second-order and exponential stress constitutive equations for articular cartilage. *Biomechanics and Modeling in Mechanobiology*, accepted.

Summary

Under this grant, a second-order bimodular theory for finite deformations of elastic orthotropic materials has been developed that allows the mechanical properties of the tissue to differ in tension and compression. In its most general form this model requires 61 independent material constants to fully describe the behavior. An initial study (Klisch et al. 2004) was performed only retaining three of the second-order terms. In that study tensile and confined compression data were used in a nonlinear regression scheme to determine the 18 independent material constants that remained in the equation for pure stretch deformations. The bimodular second-order orthotropic stress-strain equation successfully described the assumed nonlinear tensile and confined compressive responses in three orthogonal directions as seen in Figure 1. However, the predicted infinitesimal material constants did not correspond to a positive-definite stiffness matrix as evidenced by the negative value for E_3 , shown in Table 1.

Table 1, Material constants corresponding to the infinitesimal theory; H_A =aggregate modulus (MPa), E =Young's modulus (MPa), ν =Poisson's ratio.

H_{A1+}	1.73	H_{A1-}	0.17	ν_{12+}	0.50	ν_{12-}	0.08
H_{A2+}	2.76	H_{A2-}	0.17	ν_{13+}	0.73	ν_{13-}	0.27
H_{A3+}	0.68	H_{A3-}	0.10	ν_{21+}	1.10	ν_{21-}	0.12
E_{1+}	1.44	E_{1-}	0.09	ν_{23+}	0.24	ν_{23-}	0.09
E_{2+}	2.39	E_{2-}	0.11	ν_{31+}	1.63	ν_{31-}	0.43
E_{3+}	0.28	E_{3-}	-0.02	ν_{32+}	0.24	ν_{32-}	0.08

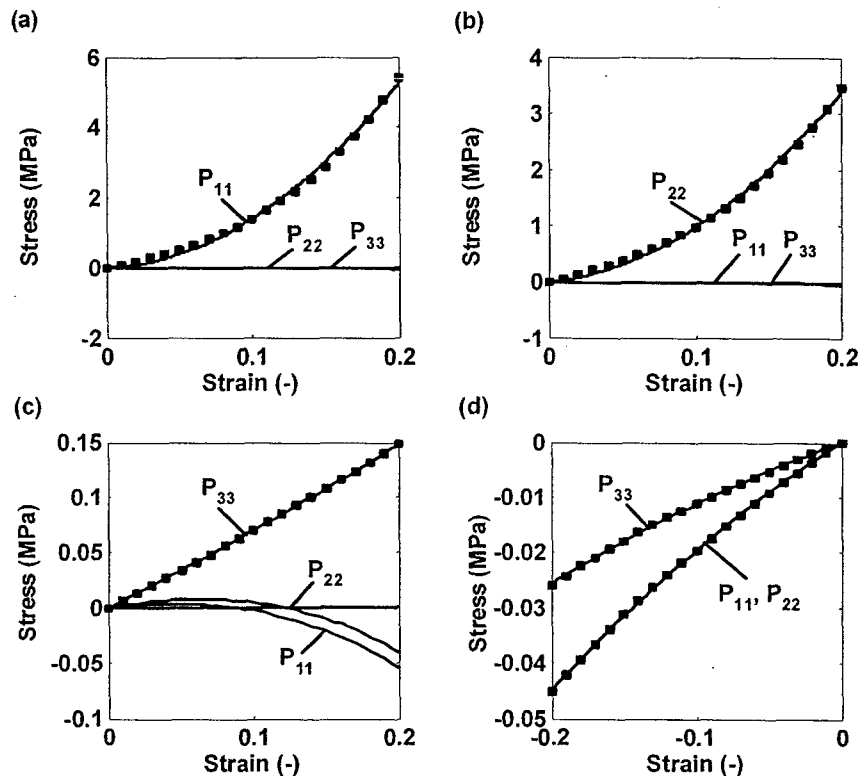


Figure 1, Experimental (▪) and theoretical (—) results for simple tension in the 1-dir (a), 2-dir (b), 3-dir (c) and confined compression (d).

Several other reduced forms of the model have been proposed (Klisch, Sah, Davol, 2005; Klisch, accepted). A set of constraining assumptions on the strain energy function used in this model reduce the number of independent material constants down to 14. Stability considerations at the origin where the behavior “jumps” between tension and compression along with preliminary results for confined compression tests resulted in three more constants being eliminated. Final models with 6, 7, 8, and 9 independent constants respectively were implemented in a nonlinear regression analysis and fit to a hypothetical experimental dataset for adult human cartilage to show the efficacy of these reduced models. These results are shown in Figures 2 through 5. The data set contained information for confined compression and uniaxial tension tests. When compared to a seven parameter exponential model, all of the second-order modes gave better correlation to the data. These results suggest that utilizing a second-order bimodular approach may be promising for some applications with cartilaginous tissues.

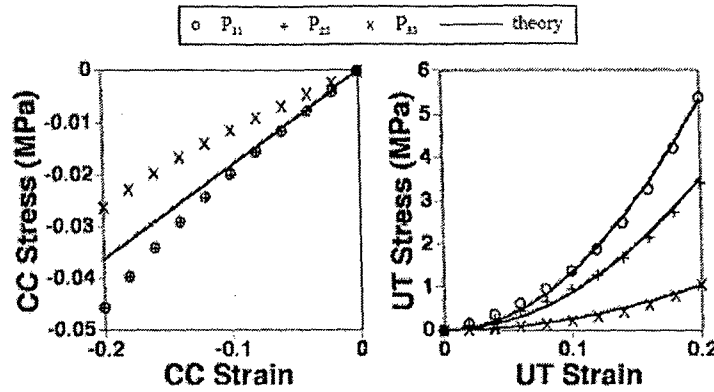


Figure 2, 6-parameter second-order model predictions for the confined compression (CC) response and the uniaxial tension (UT) response. The theoretical CC curves are linear and equal in the 1, 2, and 3 directions.

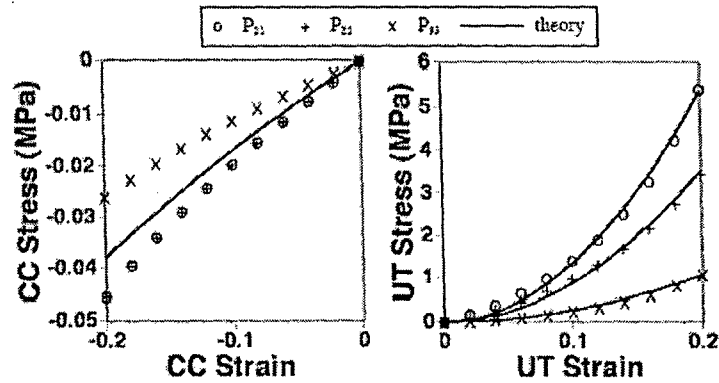


Figure 3, 7-parameter second-order model predictions for the confined compression (CC) response and the uniaxial tension (UT) response. The theoretical CC curves are nonlinear and equal in the 1, 2, and 3 directions.

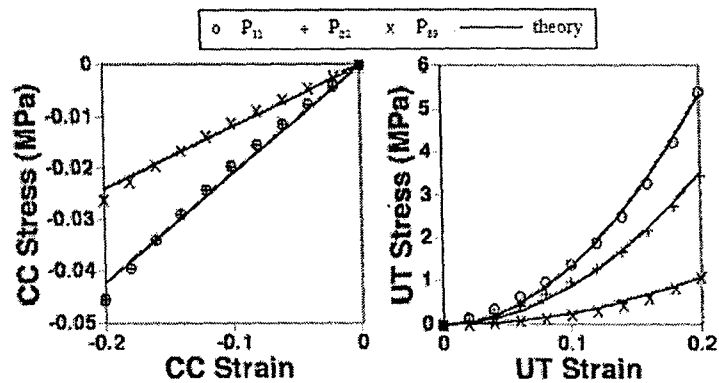


Figure 4, 8-parameter second-order model predictions for the confined compression (CC) response and the uniaxial tension (UT) response. The theoretical CC curves are linear.

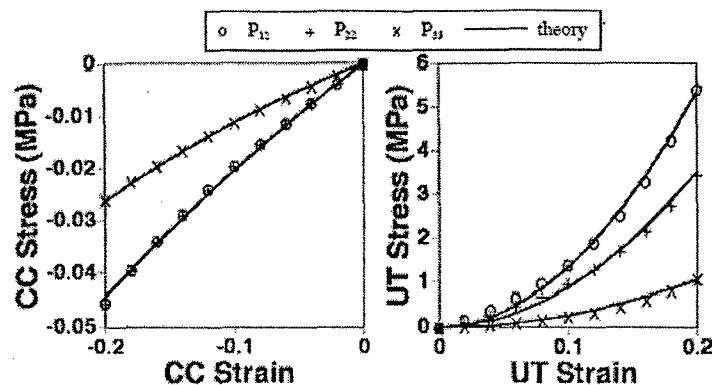


Figure 5, 9-parameter second-order model predictions for the confined compression (CC) response and the uniaxial tension (UT) response. The theoretical CC curves are nonlinear.

Boundary-value problems have been solved to illustrate how the model may be used to describe the evolution of tissue geometry, composition, and mechanical response during *in vitro* growth of cartilage explants (Klisch, Asanbaeva, Davol, Sah, 2005). The models were correlated to growth experiments performed at UCSD. Specimens were separated into three groups: REF group specimens were tested immediately; FBS group specimens were incubated for 13 days in medium supplemented with 20% fetal bovine serum; and CABC group specimens were pre-treated with chondroitinase ABC to deplete proteoglycan concentration by >90% before incubation using the same protocol as the FBS group. Experimental data included measures of tissue composition and geometry before and after incubation and an averaged tensile modulus. An additional BV-problem was solved corresponding to the CABC group with increased remodeling that produces a stiffer collagen network (CABC+R). The results suggest (Figure 6) that collagen remodeling in the current model is needed to predict the experimentally observed increase in tensile integrity. Ultimately, a refined cartilage growth mixture model may be used as a predictive tool in the design of tissue engineered constructs that fulfill geometric and biomechanical requirements for the successful repair of cartilage defects.

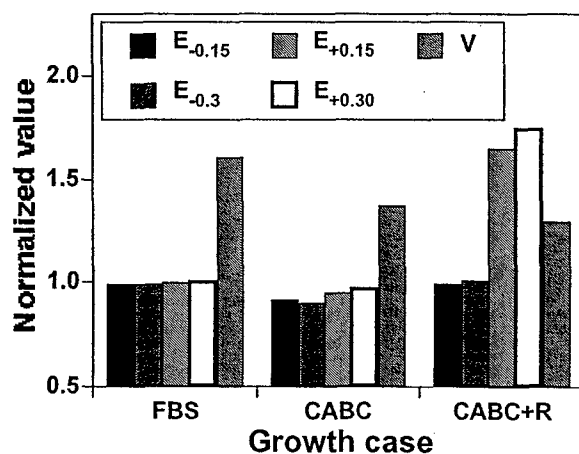


Figure 6, Predictions for ST/UCC moduli and volume normalized by REF values.

CARTILAGE GROWTH MIXTURE MODEL: FINITE STRAIN THEORY, CONSTITUTIVE EQUATIONS, AND BOUNDARY-VALUE PROBLEM SOLUTIONS

Stephen M. Klisch^{*}, Anya Asanbaeva^{**}, Robert L. Sah^{**}, Andrew Davol^{*}

^{*} Department of Mechanical Engineering, California Polytechnic State University,
San Luis Obispo, CA 93407, sklisch@calpoly.edu, adavol@calpoly.edu

^{**} Department of Bioengineering, University of California at San Diego, 9500 Gilman
Drive, La Jolla, CA 92093-0412, asanbaeva@ucsd.edu, rsah@ucsd.edu

ABSTRACT: A cartilage growth mixture model (CGMM), that includes the nonlinear and asymmetric tensile-compressive response of the cartilage solid matrix to finite strains, is presented. Boundary-value problems are solved to illustrate how the model may be used to describe the evolution of tissue geometry, composition, and mechanical response during *in vitro* growth of cartilage explants.

INTRODUCTION: The two primary components of cartilage, proteoglycan (PG) and type II collagen (COL), have distinct mechanical and growth response functions. We developed a CGMM (Klisch et al. [2000, 2003a, 2003b]) that allows an arbitrary number of tissue constituents to differentially grow in response to mechanical stimuli. Substantial challenges must be overcome before the CGMM may be used as a predictive tool for tissue engineering applications. The objective of this work is to develop the framework for refining and validating the model with specific *in vitro* growth protocols.

PROCEDURES, RESULTS AND DISCUSSION: We focus on the two constituents of the cartilage solid matrix (SM) that are the major contributors to its mechanical properties: PG and COL. Equilibrium growth boundary-value (BV) problems are considered, as the time scales of typical *in vivo* and *in vitro* mechanical loading and growth responses differ by several orders of magnitude. The PG and COL are assumed to be bound to the extracellular matrix so that their deformation gradient tensors \mathbf{F}^p and \mathbf{F}^c are equal to the SM deformation gradient tensor \mathbf{F}^s . Volumetric growth is defined relative to a SM stress-free reference configuration κ_r using a decomposition of \mathbf{F}^p and \mathbf{F}^c into elastic ($\mathbf{F}_e^p, \mathbf{F}_e^c$) and growth ($\mathbf{F}_g^p, \mathbf{F}_g^c$) tensors (Fig. 1):

$$\mathbf{F}^s = \mathbf{F}_e^p \mathbf{F}_g^p = \mathbf{F}_e^c \mathbf{F}_g^c. \quad (1)$$

The solid matrix stress \mathbf{T}^s is equal to the sum of the PG and COL stresses:

$$\mathbf{T}^s = \mathbf{T}^p + \mathbf{T}^c; \quad (2)$$

due to the internal constraint introduced by Eqn. (1) the equilibrium equations reduce to those for the SM:

$$\text{div} \mathbf{T}^s = \mathbf{0}. \quad (3)$$

Stress constitutive equations for the PG and COL constituents are defined relative to reference configurations (κ^p, κ^c) by assuming that growth occurs at constant stress and

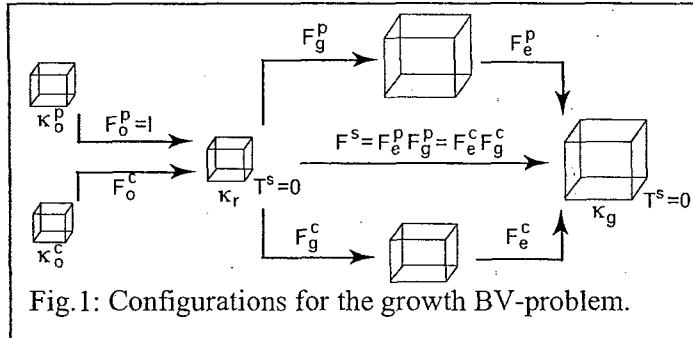
density; i.e., the stress depends only on the elastic tensors ($\mathbf{F}_e^p, \mathbf{F}_e^c$). Here, we take κ_r^p to coincide with κ_r and assume

$$\mathbf{T}_{\kappa_r}^p = -(\alpha_1(\det \mathbf{F}_e^p)^{-1} + \alpha_2(\det \mathbf{F}_e^p)^{-2})\mathbf{I}, \quad (4)$$

where the material constants (α_1, α_2) can be estimated from tissue composition as outlined in Klisch et al. [2003b]. For COL, we recently derived a general theory for bimodular anisotropic elastic materials; here we use an equation that is second order in the Biot strain \mathbf{E} defined relative to a stress-free COL configuration κ_s^c :

$$\begin{aligned} \mathbf{T}_{\kappa_s^c}^c = \mathbf{R}[\{ \lambda_1 \mathbf{E}_{11} + \gamma_1 (\mathbf{E}_{11})^2 \} \mathbf{E}_1 \otimes \mathbf{E}_1 + \{ \lambda_2 \mathbf{E}_{22} + \gamma_2 (\mathbf{E}_{22})^2 \} \mathbf{E}_2 \otimes \mathbf{E}_2 \\ + \{ \lambda_3 \mathbf{E}_{33} + \gamma_3 (\mathbf{E}_{33})^2 \} \mathbf{E}_3 \otimes \mathbf{E}_3 + \lambda (\mathbf{E}_{22} + \mathbf{E}_{33}) \mathbf{E}_1 \otimes \mathbf{E}_1 \\ + \lambda (\mathbf{E}_{11} + \mathbf{E}_{33}) \mathbf{E}_2 \otimes \mathbf{E}_2 + \lambda (\mathbf{E}_{11} + \mathbf{E}_{22}) \mathbf{E}_3 \otimes \mathbf{E}_3 + 2\mu \mathbf{E}] \mathbf{R}^T \end{aligned} \quad (5)$$

where \mathbf{R} is the COL rotation tensor and the second order constants ($\gamma_1, \gamma_2, \gamma_3$) may jump across surfaces of discontinuity; e.g., $\gamma_1 = \gamma_{1+}$ if $\mathbf{E}_{11} > 0$ and $\gamma_1 = \gamma_{1-}$ if $\mathbf{E}_{11} < 0$. The COL stress equation relative to κ_r is obtained by evaluating (5) at $\mathbf{E} = \mathbf{E}_s^c + \mathbf{E}_e^c + \mathbf{E}_e^c$ where \mathbf{E}_s^c is the COL residual strain between κ_s^c and κ_r and \mathbf{E}_e^c is the COL elastic strain relative to κ_r . Data from the literature was used to estimate the material constants ($\alpha_1, \alpha_2, \lambda_a, \lambda, \mu$) and \mathbf{E}_s^c (assumed to be spherical). Upon assuming $\gamma_{1+} = \gamma_{2+} = \gamma_{3+} = \gamma$ and $\gamma_{1-} = \gamma_{2-} = \gamma_{3-} = 0$, γ was calculated so that the SM stress was zero in κ_r .



Articular cartilage explants were harvested from the patellofemoral groove of newborn (1-3 weeks) bovine calves at a depth of ~0.4-0.7 mm below the articular surface. Specimens were separated into three groups: REF group specimens were tested immediately; FBS group specimens were

incubated for 13 days in medium supplemented with 20% fetal bovine serum; and CABC group specimens were pre-treated with chondroitinase ABC to deplete PG concentration by >90% before subsequent incubation using the same protocol as the FBS group (Asanbaeva et al. [2004]). Experimental data included measures of tissue composition and geometry before and after incubation and an averaged tensile modulus.

The percentage mass increase for the PG and COL constituents were calculated for the FBS and CABC groups relative to the REF group and used to estimate isotropic growth tensors of the form $\mathbf{F}_g^\alpha = g^\alpha \mathbf{I}$, where $\det \mathbf{F}_g^\alpha = (g^\alpha)^3$ describes the percentage mass increase. Then, the corresponding equilibrium growth BV-problems (FBS, CABC) were formulated by specifying the growth tensors in (1) and solved for the SM deformation gradient tensors that satisfy Eqns. (1-5) and which determine the grown configurations κ_g . An additional BV-problem was solved corresponding to the CABC group with γ

increased by 100% to reflect a remodeling that produces a stiffer COL network (CABC+R). The SM stress response in simple tension (ST) and unconfined compression (UCC) was solved numerically relative to κ_r (REF) and κ_g (FBS, CABC, CABC+R).

The model describes the asymmetric and nonlinear nature of the SM stress response in ST and UCC (Fig. 2). Model results for the FBS and CABC+R BV-problems (Fig. 3) agreed qualitatively with the experimental data (Asanbaeva et al. [2004]); the FBS group experienced reduced moduli and the greatest volume increase while the CABC+R group experienced increased moduli and the least volume increase. Model results for the CABC BV-problem contrasted with the experimental data as the predicted moduli were reduced.

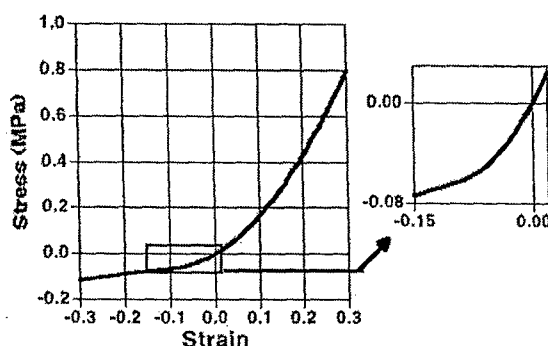


Fig.2: ST/UCC response of the SM relative to the REF configuration.

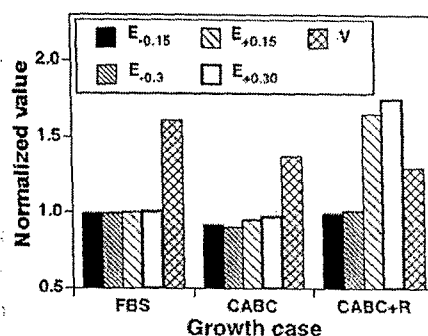


Fig.3: Predictions for ST/UCC moduli (E) at four strain levels (± 0.15 , ± 0.30) and volume (V) normalized by REF values.

CONCLUSIONS: The results suggest that COL remodeling in the current model is needed to predict the experimentally observed increase in tensile integrity. Ongoing studies are aimed at obtaining more accurate stress constitutive equations for these *in vitro* growth protocols to refine and validate the model. Ultimately, a refined CGMM may be used as a predictive tool in the design of tissue engineered constructs that fulfill geometric and biomechanical requirements for the successful repair of cartilage defects.

ACKNOWLEDGEMENTS: NSF, NIH, NASA, Office of Naval Research.

REFERENCES:

- Asanbaeva A. et al., 2004, "Mechanisms of Cartilage Growth: Alteration of Function and Composition In Vitro by Deposition of Collagen and Proteoglycan Matrix Components", *Trans Orthop Res Soc* 29:554.
- Klisch S.M., Sah R.L., Hoger A., 2000, "A Growth Mixture Theory for Cartilage", *Proc. of the ASME Symposium on Mechanics in Biology*.
- Klisch S.M., Hoger, A., 2003a, "Volumetric Growth of Thermoelastic Materials and Mixtures", *Math. Mech. Solids*, **8**, 377-402.
- Klisch S.M. et al., 2003b, "A Growth Mixture Theory for Cartilage with Application to Growth-related Experiments on Cartilage Explants", *J. Biomech. Engng.* **125**, 169-179.

IMECE2004-59475

A BIMODULAR SECOND-ORDER ORTHOTROPIC STRESS CONSTITUTIVE EQUATION FOR CARTILAGE

Stephen M. Klisch¹, Suzanne E. Holtrichter¹, Robert L. Sah², Andrew Davol¹

(1) Mechanical Engineering Department
California Polytechnic State University
San Luis Obispo, CA

(2) Department of Bioengineering
University of California, San Diego
La Jolla, CA

INTRODUCTION

The design of tissue-engineered constructs grown *in vitro* is a promising treatment strategy for degenerated cartilaginous tissues. Cartilaginous tissues such as articular cartilage and the annulus fibrosus are collagen fiber-reinforced composites that exhibit orthotropic behavior and highly asymmetric tensile-compressive responses. They also experience finite deformations *in vivo*. Successful integration with surrounding tissue upon implantation likely will require cartilage constructs to have similar structural and functional properties as native tissue. Reliable stress constitutive equations that accurately characterize the tissue's mechanical properties must be developed to achieve this aim. Recent studies have successfully implemented bimodular theories for infinitesimal strains (Soltz et al., 2000; Wang et al., 2003); those models were based on the theory of Curnier et al. (1995).

The objective of this work was to develop a more accurate cartilage stress constitutive equation for finite strains. Specifically, the first aim was to derive an orthotropic bimodular stress-strain equation with three surfaces of discontinuity. The second aim was to assess the ability of the equation to simultaneously describe the nonlinear tensile and compressive responses in three orthogonal directions for the superficial region of articular cartilage.

METHODS

Theory

First, a second-order orthotropic stress constitutive equation was derived using the first Piola-Kirchhoff stress tensor \mathbf{P} and the Biot strain tensor \mathbf{E} , based on the approach of Hoger (1999). That equation was expressed in terms of the structural tensors, $\mathbf{A} = \mathbf{a} \otimes \mathbf{a}$, $\mathbf{B} = \mathbf{b} \otimes \mathbf{b}$, and $\mathbf{C} = \mathbf{c} \otimes \mathbf{c}$ where $(\mathbf{a}, \mathbf{b}, \mathbf{c})$ are mutually orthogonal unit vectors that define the orthotropic planes of reflectional symmetry. Then, a bimodular

equation was derived subject to the two continuity conditions that are necessary and sufficient for the stress-strain equation to be continuous across a surface of discontinuity. Using three surfaces of discontinuity normal to the unit vectors $(\mathbf{a}, \mathbf{b}, \mathbf{c})$, the continuity conditions were used to identify the material constants that may be discontinuous across each surface. The resulting equation had 61 material constants. In this study, we retained only three of the second-order terms. For pure stretches, the equation reduced to:

$$\begin{aligned} \mathbf{P} = & \lambda_{aa}[E_{11}](\mathbf{A} \cdot \mathbf{E})\mathbf{A} + \lambda_{bb}[E_{22}](\mathbf{B} \cdot \mathbf{E})\mathbf{B} + \lambda_{cc}[E_{33}](\mathbf{C} \cdot \mathbf{E})\mathbf{C} \\ & + \lambda_{ab}[(\mathbf{A} \cdot \mathbf{E})\mathbf{B} + (\mathbf{B} \cdot \mathbf{E})\mathbf{A}] + \lambda_{bc}[(\mathbf{B} \cdot \mathbf{E})\mathbf{C} + (\mathbf{C} \cdot \mathbf{E})\mathbf{B}] \\ & + \lambda_{ac}[(\mathbf{A} \cdot \mathbf{E})\mathbf{C} + (\mathbf{C} \cdot \mathbf{E})\mathbf{A}] + \mu_a(\mathbf{A} \cdot \mathbf{E})\mathbf{A} \\ & + \mu_b(\mathbf{B} \cdot \mathbf{E})\mathbf{B} + \mu_c(\mathbf{C} \cdot \mathbf{E})\mathbf{C} + \gamma_{a1}[E_{11}](\mathbf{A} \cdot \mathbf{E})^2\mathbf{A} \\ & + \gamma_{b1}[E_{22}](\mathbf{B} \cdot \mathbf{E})^2\mathbf{B} + \gamma_{c1}[E_{33}](\mathbf{C} \cdot \mathbf{E})^2\mathbf{C} \end{aligned} \quad (1)$$

where the following notation has been used: $\lambda_{aa}[E_{11}] = \lambda_{aa+}$ if

$E_{11} > 0$ and $\lambda_{aa}[E_{11}] = \lambda_{aa-}$ if $E_{11} < 0$. There are 18 material

constants in (1): λ_{aa+} , λ_{aa-} , λ_{bb+} , λ_{bb-} , λ_{cc+} , λ_{cc-} , λ_{ab} , λ_{ac} , λ_{bc} , μ_a ,

μ_b , μ_c , γ_{a1+} , γ_{a1-} , γ_{b1+} , γ_{b1-} , γ_{c1+} , and γ_{c1-} .

Analysis

To describe tissue anisotropy, three directions were considered: parallel to the split line direction (1); perpendicular to the split-line direction (2); and perpendicular to the surface (3). Tensile responses in the 1 and 2 and confined compressive responses in the 3 directions for human humeral head cartilage were taken from Huang et al. (1999). Tensile responses in the 3 and confined compressive responses in the 1 and 2 directions were estimated by scaling bovine data from Wang et al. (2003) and Korhonen et al. (2001). Exponential functions and infinitesimal material constants reported in Huang et al. (1999)

were used to identify stress-strain values at 2% strain increments and to make initial guesses for the material constants. Since critical strain levels exist for second order theories, functional strain levels for the nonlinear regression were considered to be from 0 to 20% for this study. Assumed values for the Poisson's functions were based on the papers mentioned above. A simultaneous nonlinear regression algorithm was performed in Mathematica (Wolfram, V5.0) using the approach developed by Klisch and Lotz (1999).

RESULTS

The theoretical predictions for the stress-strain responses in tension and compression for all three loading directions were nearly indistinguishable from the experimental curves (Fig. 1). The predicted stress-strain curves corresponding to the traction-free boundary conditions were nearly zero for simple tension in the 1 and 2 directions, but reached approximately 30% of the loading stress for simple tension in the 3 direction. The compressive Young's modulus E_3 (Table 1) was slightly negative resulting in a stiffness matrix for infinitesimal deformations that was not positive-definite.

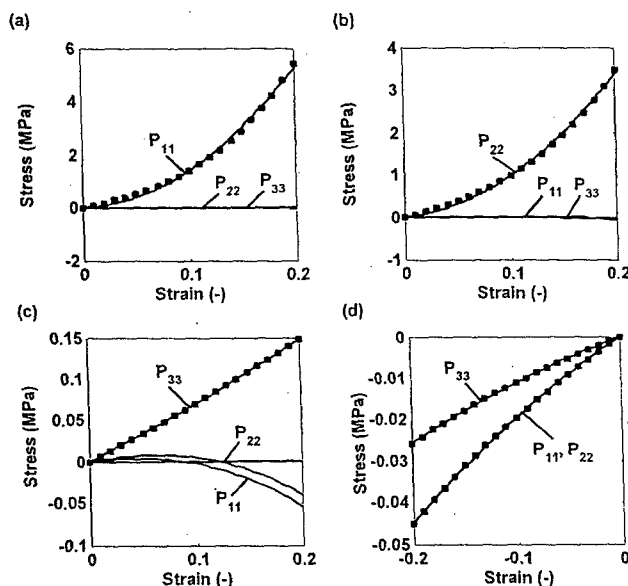


Fig. 1 Experimental (•) and theoretical (—) results for simple tension in the 1-dir (a), 2-dir (b), 3-dir (c) and confined compression (d).

DISCUSSION

The bimodular second-order orthotropic stress-strain equation successfully described the assumed nonlinear tensile and confined compressive responses in three orthogonal directions for the superficial region of articular cartilage. However, the predicted infinitesimal material constants did not correspond to a positive-definite stiffness matrix. One solution to ensure positive-definiteness may be to include unconfined compression data in the nonlinear regression.

An advantage of using a bimodular theory is its apparent success in modeling the highly asymmetric tensile-compressive response. An advantage of using a second-order theory is that an exact stress constitutive equation is derived with material constants that have a clear physical interpretation. For example, the λ_{aa} , λ_{bb} , and λ_{cc} constants reflect the differences in the collagen microstructural orientation while terms that were neglected in the present study reflect microstructural interactions (e.g., collagen crosslinking) between fibers.

The results of this study suggest that the proposed theory may be used to accurately describe the orthotropic stress-strain response of cartilaginous tissues for finite strains. This approach may prove critical for many applications, including the accurate assessment of the mechanical properties of both native tissue and tissue engineered constructs grown *in vitro* for the repair of *in vivo* defects.

Table 1 Material constants corresponding to the infinitesimal theory; H_A =aggregate modulus (MPa), E =Young's modulus (MPa), ν =Poisson's ratio.

H_{A1+}	1.73	H_{A1-}	0.17	ν_{12+}	0.50	ν_{12-}	0.08
H_{A2+}	2.76	H_{A2-}	0.17	ν_{13+}	0.73	ν_{13-}	0.27
H_{A3+}	0.68	H_{A3-}	0.10	ν_{21+}	1.10	ν_{21-}	0.12
E_{1+}	1.44	E_{1-}	0.09	ν_{23+}	0.24	ν_{23-}	0.09
E_{2+}	2.39	E_{2-}	0.11	ν_{31+}	1.63	ν_{31-}	0.43
E_{3+}	0.28	E_{3-}	-0.02	ν_{32+}	0.24	ν_{32-}	0.08

ACKNOWLEDGMENTS

Funding was received from NSF CMS-0245709 and the Department Office of Naval Research N00014-04-1-0436.

REFERENCES

- [1] Soltz, M.A., and Ateshian, G.A., 2000, "A conewise linear elasticity mixture model for the analysis of tension-compression nonlinearity in articular cartilage," *J. Biomech. Eng.*, **122**, pp. 576-586.
- [2] Wang, C.B., et al., 2003, "Optical determination of anisotropic material properties of bovine articular cartilage in compression," *J. Biomech.*, **36**, pp. 339-353.
- [3] Curnier, A., He, Q. C., and Zysset, P., 1995, "Conewise linear elastic materials," *J. Elas.*, **37**, pp. 1-38.
- [4] Hoger, A., 1999, "A second order constitutive theory for hyperelastic materials," *Int. J. Sols. Struct.*, **36**, pp. 847-868.
- [5] Huang, C.-Y., et al., 1999, "Anisotropy, inhomogeneity, and tension-compression nonlinearity of human glenohumeral cartilage in finite deformation," *ORS Trans.*, **24**, pp. 95.
- [6] Korhonen, R.K., et al., 2001, "Effect of ionic environment on the compression-tension nonlinearity of articular cartilage in the direction perpendicular to articular surface," *ORS Trans.*, **26**, pp. 439.
- [7] Klisch, S.M., Lotz, J.C., 1999, "Application of a fiber-reinforced continuum theory to multiple deformations of the annulus fibrosus," *J. Biomech.*, **32**, pp. 1027-1036.

A bimodular theory for finite deformations: comparison of orthotropic second-order and exponential stress constitutive equations for articular cartilage

S.M. Klisch¹, R.L. Sah², A. Davol¹

¹*Mechanical Engineering Department, California Polytechnic State University, San Luis Obispo, CA*

²*Department of Bioengineering, University of California, San Diego, La Jolla, CA*
sklisch@calpoly.edu

Articular cartilage exhibits anisotropic behavior with a highly asymmetric tensile-compressive response due to the distinct mechanical properties of its molecular constituents, primarily proteoglycans and collagens. Accurate stress constitutive equations for articular cartilage may be used in finite element models of in vivo joints to improve our understanding of cartilage degeneration and failure and in finite element models of cartilage tissue engineering experiments to improve our understanding of the mechanotransduction process. Motivated by the difficulty of developing accurate stress constitutive equations valid for finite deformations for cartilage, a bimodular theory for finite deformations of elastic materials is developed for the cartilage solid matrix. As an alternative to traditional exponential type equations, an orthotropic stress constitutive equation that is second-order in terms of the Biot strain tensor is derived. Several reduced forms of the bimodular second-order equation, with 6-9 parameters, and a bimodular exponential equation, with 7 parameters, were fit to an experimental dataset that captures the highly asymmetric and anisotropic mechanical response of cartilage. All of the second-order equations provided a better fit than the exponential equation, suggesting that the bimodular second-order equation may be appealing for some applications. Finally, we show how a microstructurally-based stress constitutive equation for the proteoglycan constituent can be integrated with the bimodular stress constitutive equation for the solid matrix in order to provide an even more accurate description of experimentally observed mechanical behavior in tension and compression.

Keywords: Cartilage, orthotropic, bimodular, finite deformations, elastic.

Klisch, "A bimodular theory for finite deformations ..."

A BIMODULAR THEORY FOR FINITE DEFORMATIONS: COMPARISON OF
ORTHOTROPIC SECOND-ORDER AND EXPONENTIAL STRESS CONSTITUTIVE
EQUATIONS FOR ARTICULAR CARTILAGE

5 Stephen M. Klisch

Department of Mechanical Engineering, California Polytechnic State University,
San Luis Obispo, CA

For submission to *Biomechanics and Modeling in Mechanobiology*

10 March 31, 2005

Address all correspondence to:

Stephen M. Klisch, Ph.D.
15 Associate Professor
Mechanical Engineering Department
California Polytechnic State University
San Luis Obispo, CA 93407
(805) 756-1308; FAX (805) 756-1137
20 sklisch@calpoly.edu

Abstract

Cartilaginous tissues, such as articular cartilage and the annulus fibrosus, exhibit orthotropic behavior with highly asymmetric tensile-compressive responses. Due to this complex behavior, it is difficult to develop accurate stress constitutive equations that are
5 valid for finite deformations. Therefore, we have developed a bimodular theory for finite deformations of elastic materials that allows the mechanical properties of the tissue to differ in tension and compression. In this paper, we derive an orthotropic stress constitutive equation that is second-order in terms of the Biot strain tensor as an alternative to traditional exponential type equations. Several reduced forms of the
10 bimodular second-order equation, with 6-9 parameters, and a bimodular exponential equation, with 7 parameters, were fit to an experimental dataset that captures the highly asymmetric and orthotropic mechanical response of cartilage. All of the second-order equations provided a better fit than the exponential equation, suggesting that the bimodular second-order equation may be appealing for some applications with
15 cartilaginous tissues.

Introduction

The work in this paper is motivated by the difficulty of, and the need for, developing accurate stress constitutive equations for fiber-reinforced cartilaginous tissues. Cartilage is composed of chondrocytes embedded in an extracellular matrix consisting primarily of
20 proteoglycans, a crosslinked collagen network, and water. The proteoglycans are negatively charged molecules that mainly resist compressive stresses (Lai et al. 1991; Bassar et al. 1998) while the collagen network primarily resists tensile and shear stresses

(Venn and Maroudas 1977; Mow and Ratcliffe 1997). Due to this molecular structure, articular cartilage typically exhibits a mechanical response with marked anisotropy and tension-compression asymmetry (Woo et al. 1976; Woo et al. 1979; Akizuki et al. 1986; Soltz and Ateshian 2000; Laasanen et al. 2003; Wang et al. 2003), and likely experiences
5 finite, multi-dimensional strains due to typical *in vitro* and *in vivo* loads. Although MRI measurements of *in situ* and *in vivo* joints have predicted that cartilage is subject to average strains of less than 10% under physiologic loading conditions (Herberhold et al. 1999; Eckstein et al. 2000), local strains may be much higher due to nonhomogeneous mechanical properties that depend on both anatomic location (Laasanen et al. 2003) and
10 depth from the articular surface (Schinagl et al. 1997; Wang et al. 2001). For physiologic loading conditions, FEM contact analyses (Donzelli et al. 1999; Krishnan et al. 2003) suggest that *in situ* cartilage may experience local strains up to 26%, suggesting that the tissue is in the nonlinear range of its stress-strain relationship (Huang et al. 1999).

Due to the complex mechanical behaviour of cartilaginous tissues, the development
15 of accurate finite deformation models of the equilibrium elastic response has been difficult. Lotz and colleagues developed an orthotropic finite deformation model for the annulus fibrosus using an exponential strain energy function; however, maximum errors between theoretical and experimental stresses in uniaxial tension were approximately 100% (Klisch and Lotz 1999; Wagner and Lotz 2004). For articular cartilage, there has
20 not been a finite deformation model presented that accurately describes its orthotropic response for multiple experimental protocols in a specimen-specific manner. However, an elastic stress constitutive equation for finite deformations has been used in more complex models, including multiphasic models with isotropic (Holmes and Mow 1990; Kwan et

al. 1990; Ateshian et al. 1997) and transversely isotropic (Almeida and Spilker 1997) material symmetry.

For infinitesimal strains, Ateshian and colleagues (Soltz and Ateshian 2000; Wang et al. 2003) have employed elastic and biphasic models with a bimodular stress
5 constitutive equation that allows for different mechanical properties in tension and compression. Their model can describe the mechanical response in unconfined compression in three orthogonal directions while providing reasonable predictions for other protocols (Wang et al. 2003). Those models were based on a bimodular theory for
10 infinitesimal strains (Curnier et al. 1995) in which the material constants may be discontinuous (or jump) across a surface of discontinuity in strain space, provided that stress continuity conditions are satisfied at the surface. Recently, several exponential models for finite deformations that allow for different mechanical properties in tension and compression have been used for the arterial wall (Holzapfel et al. 2004) and the
annulus fibrosus (Baer et al. 2004). However, those models have not employed a general
15 theory that ensures stress continuity across the surface of discontinuity. One reason that an exponential strain energy function is often used may be due to its ability to model the highly asymmetric tension-compression response without invoking the bimodular feature (Almeida and Spilker 1997; Klisch and Lotz 1999; Wagner and Lotz 2004).

Our long-term goal is to develop an accurate stress-strain equation that can
20 simultaneously describe the equilibrium elastic response in tension, confined and unconfined compression, and torsional shear. Accurate stress constitutive equations for articular cartilage may be used in finite element models of *in vivo* joints to improve our understanding of cartilage degeneration (Donzelli et al. 1999; Krishnan et al. 2003) and

in microstructural finite element models to improve our understanding of the mechanotransduction process (Guilak and Mow 2000). In this study, we hypothesized that a bimodular second-order stress constitutive equation can be used to accurately model the anisotropic and asymmetric tensile-compressive response of cartilaginous tissues.¹ The specific objectives are to: 1) derive a general bimodular theory for finite deformations; 2) derive a bimodular second-order stress constitutive equation for orthotropic materials; and 3) to compare the predictive capability of several bimodular second-order models with a bimodular exponential model using experimental data gathered from the literature. In the Discussion, we present ongoing aims that relate to the integration of the derived phenomenological model with microstructurally based models and cartilage growth theories.

Background

The deformation gradient tensor \mathbf{F} is uniquely decomposed by the polar decomposition theorem as

$$\mathbf{F} = \mathbf{R}\mathbf{U} \quad (1)$$

where \mathbf{R} is a proper-orthogonal tensor and the right stretch tensor \mathbf{U} is a symmetric positive-definite tensor. The Biot strain tensor \mathbf{E} and right Cauchy-Green deformation tensor \mathbf{C} are defined as

$$\mathbf{E} = \mathbf{U} - \mathbf{I}, \quad \mathbf{C} = \mathbf{F}^T \mathbf{F}, \quad (2)$$

where the superscript T signifies the transpose operator. The Cauchy and first Piola-Kirchhoff stress tensors (denoted as \mathbf{T} and \mathbf{P} , respectively) are related by

¹ For the bimodular models proposed here, several advantageous features are presented in the Discussion.

$$\mathbf{J}\mathbf{T} = \mathbf{P}\mathbf{F}^T, \quad (3)$$

where \mathbf{J} is the determinant of \mathbf{F} . The stress constitutive equations for a Green-elastic material may be expressed as

$$\mathbf{P} = 2\mathbf{F} \frac{\partial W}{\partial \mathbf{C}} = 2\mathbf{F} \sum_{i=1}^n \frac{\partial W}{\partial I_i} \frac{\partial I_i}{\partial \mathbf{C}}, \quad (4)$$

- 5 where W is a scalar strain energy function that depends on a set of invariants of \mathbf{C} , $I_C = \{I_i(\mathbf{C}); i = 1, n\}$, corresponding to the material symmetry group:

$$W = \hat{W}(\mathbf{C}) = \tilde{W}(I_1(\mathbf{C}), I_2(\mathbf{C}), \dots, I_n(\mathbf{C})) \equiv \tilde{W}(I_C). \quad (5)$$

For the second-order theory, an alternative form of the stress constitutive equation for a Green elastic material is used:

$$10 \quad \mathbf{T} = \mathbf{R}\hat{\mathbf{T}}(\mathbf{U})\mathbf{R}^T = \mathbf{R}\tilde{\mathbf{T}}(\mathbf{E})\mathbf{R}^T, \quad \mathbf{P} = \mathbf{R}\hat{\mathbf{P}}(\mathbf{U}) = \mathbf{R}\tilde{\mathbf{P}}(\mathbf{E}), \quad (6)$$

where the functions $\hat{\mathbf{T}}(\mathbf{U})$ and $\hat{\mathbf{P}}(\mathbf{U})$ are derived from W :

$$W = \hat{W}(\mathbf{U}) = \tilde{W}(I_1(\mathbf{U}), I_2(\mathbf{U}), \dots, I_n(\mathbf{U})) \equiv \tilde{W}(I_U) \quad (7)$$

and $I_U = \{I_i(\mathbf{U}); i = 1, n\}$ is the set of basic polynomial invariants of \mathbf{U} corresponding to the material symmetry group. The notation I_I will be used to signify that the set

- 15 $\{I_i(\mathbf{U}); i = 1, n\}$ is to be evaluated at $\mathbf{U}=\mathbf{I}$ (i.e., in the reference configuration).

For isotropic elastic materials, various second-order theories for Green-elastic materials have been proposed using different strain tensors (Murnaghan 1937; Murnaghan 1951; Rivlin 1953; Hoger 1999) which differ depending on which strain tensor is used (Ogden 1984). In this paper, the Biot strain tensor is used in the second-
20 order equations for two reasons. First, it has a clear physical interpretation; the eigenvalues of the Biot strain tensor represent the principal extensions. Second, the results of (Van Dyke and Hoger 2000) suggested that the second-order stress equations

using the Biot strain tensor, as compared to other strain measures, provided a better approximation of the exact solutions to a group of boundary-value problems using specific nonlinear elastic materials. For an arbitrary material symmetry group, general stress constitutive equations that are second-order in terms of the Biot strain tensor have been presented (Hoger 1999). That approach used functions $\hat{\mathbf{T}}(\mathbf{U})$ and $\hat{\mathbf{P}}(\mathbf{U})$ derived from $\hat{\mathbf{W}}(\mathbf{U})$ and the truncated series expansion for the gradient of $\hat{\mathbf{W}}(\mathbf{U})$.² The resulting second-order stress equations are

$$\begin{aligned}\mathbf{T} &= \mathbf{R}\{\Psi_1[\mathbf{E}] + \text{sym}(\mathbf{E}\Psi_1[\mathbf{E}]) - (\text{tr}\mathbf{E})\Psi_1[\mathbf{E}] + (1/2)\Psi_2[\mathbf{E},\mathbf{E}]\}\mathbf{R}^T, \\ \mathbf{P} &= \mathbf{R}\{\Psi_1[\mathbf{E}] + \text{skw}(\mathbf{E}\Psi_1[\mathbf{E}]) + (1/2)\Psi_2[\mathbf{E},\mathbf{E}]\},\end{aligned}\quad (8)$$

where $\text{tr}(\cdot)$ is the trace operator, $\text{sym}(\cdot)$ and $\text{skw}(\cdot)$ are the symmetric and skew parts of a tensor, and

$$\begin{aligned}\Psi_1[\mathbf{E}] &= \mathbf{D} \frac{\partial \hat{\mathbf{W}}}{\partial \mathbf{U}}(\mathbf{I})[\mathbf{E}] = \frac{\partial^2 \mathbf{W}}{\partial I_k \partial I_j}(\mathbf{I}_I) \frac{\partial I_j}{\partial \mathbf{U}}(\mathbf{I}) \left\{ \frac{\partial I_k}{\partial \mathbf{U}}(\mathbf{I}) \cdot \mathbf{E} \right\} + \frac{\partial \mathbf{W}}{\partial I_j}(\mathbf{I}_I) \frac{\partial^2 I_j}{\partial \mathbf{U}^2}(\mathbf{I})[\mathbf{E}], \\ \Psi_2[\mathbf{E},\mathbf{E}] &= \mathbf{D}^2 \frac{\partial \hat{\mathbf{W}}}{\partial \mathbf{U}}(\mathbf{I})[\mathbf{E},\mathbf{E}] = \frac{\partial^3 \mathbf{W}}{\partial I_p \partial I_k \partial I_j}(\mathbf{I}_I) \left\{ \frac{\partial I_p}{\partial \mathbf{U}}(\mathbf{I}) \cdot \mathbf{E} \right\} \left\{ \frac{\partial I_k}{\partial \mathbf{U}}(\mathbf{I}) \cdot \mathbf{E} \right\} \frac{\partial I_j}{\partial \mathbf{U}}(\mathbf{I}) \\ &\quad + 2 \frac{\partial^2 \mathbf{W}}{\partial I_k \partial I_j}(\mathbf{I}_I) \left\{ \frac{\partial^2 I_j}{\partial \mathbf{U}^2}(\mathbf{I})[\mathbf{E}] \right\} \left\{ \frac{\partial I_k}{\partial \mathbf{U}}(\mathbf{I}) \cdot \mathbf{E} \right\} + \frac{\partial^2 \mathbf{W}}{\partial I_k \partial I_j}(\mathbf{I}_I) \frac{\partial I_j}{\partial \mathbf{U}}(\mathbf{I}) \left\{ \mathbf{E} \cdot \frac{\partial^2 I_k}{\partial \mathbf{U}^2}(\mathbf{I})[\mathbf{E}] \right\} \\ &\quad + \left\{ \frac{\partial \mathbf{W}}{\partial I_j}(\mathbf{I}_I) \right\} \mathbf{D} \left\{ \frac{\partial^2 I_j}{\partial \mathbf{U}^2}(\mathbf{I})[\mathbf{E}] \right\} [\mathbf{E}].\end{aligned}\quad (9)$$

Explicit equations for $\Psi_1[\mathbf{E}]$ and $\Psi_2[\mathbf{E},\mathbf{E}]$ were obtained for isotropic and transversely isotropic materials in (Hoger 1999). The formulas presented in Appendix A define, and are used to calculate, the derivatives that appear in (8-9).

² See equations 2.27-2.28 and 3.3 in (Hoger 1999).

Methods

In this section, we derive the equations for $\Psi_1[\mathbf{E}]$ and $\Psi_2[\mathbf{E}, \mathbf{E}]$ for orthotropic materials in order to obtain the second-order stress constitutive equation. Then, we propose a general theory for bimodular elastic materials and derive equations for
5 bimodular second-order orthotropic materials. Finally, we study the ability of bimodular second-order and exponential models in describing the mechanical response of cartilaginous tissues in uniaxial tension and confined compression.

Second-order orthotropic materials

For orthotropic materials, we assume that the material symmetry group includes
10 reflections about three planes defined by a set of three basis vectors ($\mathbf{E}_1, \mathbf{E}_2, \mathbf{E}_3$). Structural tensors ($\mathbf{M}_1, \mathbf{M}_2, \mathbf{M}_3$) are defined as

$$\mathbf{M}_1 = \mathbf{E}_1 \otimes \mathbf{E}_1, \quad \mathbf{M}_2 = \mathbf{E}_2 \otimes \mathbf{E}_2, \quad \mathbf{M}_3 = \mathbf{E}_3 \otimes \mathbf{E}_3, \quad (10)$$

where \otimes is the tensor dyadic product. We use the set of invariants

$$\begin{aligned} \{I_i(\mathbf{U})\} &= \{\mathbf{M}_1 \cdot \mathbf{U}, \mathbf{M}_1 \cdot \mathbf{U}^2, \mathbf{M}_2 \cdot \mathbf{U}, \mathbf{M}_2 \cdot \mathbf{U}^2, \mathbf{M}_3 \cdot \mathbf{U}, \mathbf{M}_3 \cdot \mathbf{U}^2, \mathbf{I} \cdot \mathbf{U}^3\} \\ &= \{I_1, I_2, I_3, I_4, I_5, I_6, I_7\}. \end{aligned} \quad (11)$$

15 A straightforward calculation leads to

$$\left\{ \frac{\partial I_i}{\partial \mathbf{U}}(\mathbf{U}) \right\} = \{\mathbf{M}_1, \mathbf{M}_1 \mathbf{U} + \mathbf{U} \mathbf{M}_1, \mathbf{M}_2, \mathbf{M}_2 \mathbf{U} + \mathbf{U} \mathbf{M}_2, \mathbf{M}_3, \mathbf{M}_3 \mathbf{U} + \mathbf{U} \mathbf{M}_3, 3\mathbf{U}^2\}; \quad (12)$$

consequently,

$$\left\{ \frac{\partial I_i}{\partial \mathbf{U}}(\mathbf{I}) \right\} = \{\mathbf{M}_1, 2\mathbf{M}_1, \mathbf{M}_2, 2\mathbf{M}_2, \mathbf{M}_3, 2\mathbf{M}_3, 3\mathbf{I}\}. \quad (13)$$

Using (A3) and (12) leads to

$$\begin{aligned} 20 \quad \left\{ \frac{\partial^2 I_i}{\partial \mathbf{U}^2}(\mathbf{I})[\mathbf{E}] \right\} &= \left\{ \mathbf{D} \frac{\partial I_i}{\partial \mathbf{U}}(\mathbf{I})[\mathbf{E}] \right\} \\ &= \{\mathbf{0}, \mathbf{M}_1 \mathbf{E} + \mathbf{E} \mathbf{M}_1, \mathbf{0}, \mathbf{M}_2 \mathbf{E} + \mathbf{E} \mathbf{M}_2, \mathbf{0}, \mathbf{M}_3 \mathbf{E} + \mathbf{E} \mathbf{M}_3, 6\mathbf{E}\}. \end{aligned} \quad (14)$$

Using (A6-A8) and (12) leads to

$$\left\{ D \left[\frac{\partial^2 I_i}{\partial U^2} (\mathbf{I}) [\mathbf{E}] \right] \right\} \{\mathbf{E}\} = \frac{\partial^2 (\partial I_i / \partial U_{pq})}{\partial U_{kl} \partial U_{mn}} (\mathbf{I}) E_{kl} E_{mn} \mathbf{e}_p \otimes \mathbf{e}_q = \{\mathbf{0}, \mathbf{0}, \mathbf{0}, \mathbf{0}, \mathbf{0}, \mathbf{0}, 6\mathbf{E}^2\}. \quad (15)$$

Using (13-15) in (9) we obtain

$$\begin{aligned} \Psi_1[\mathbf{E}] = & \lambda_{11} E_{11} \mathbf{M}_1 + \lambda_{22} E_{22} \mathbf{M}_2 + \lambda_{33} E_{33} \mathbf{M}_3 \\ & + \lambda_{12} [E_{11} \mathbf{M}_2 + E_{22} \mathbf{M}_1] + \lambda_{23} [E_{22} \mathbf{M}_3 + E_{33} \mathbf{M}_2] + \lambda_{13} [E_{11} \mathbf{M}_3 + E_{33} \mathbf{M}_1] \\ & + \mu_1 (\mathbf{M}_1 \mathbf{E} + \mathbf{E} \mathbf{M}_1) + \mu_2 (\mathbf{M}_2 \mathbf{E} + \mathbf{E} \mathbf{M}_2) + \mu_3 (\mathbf{M}_3 \mathbf{E} + \mathbf{E} \mathbf{M}_3) \end{aligned} \quad (16)$$

5 and

$$\begin{aligned} (1/2) \Psi_2[\mathbf{E}, \mathbf{E}] = & \alpha_1 \mathbf{E}^2 + \alpha_2 (\mathbf{I} \cdot \mathbf{E}^2) \mathbf{I} + 2\alpha_2 (\mathbf{I} \cdot \mathbf{E}) \mathbf{E} \\ & + (\mathbf{I} \cdot \mathbf{E}^2) \{\alpha_3 \mathbf{M}_1 + \alpha_4 \mathbf{M}_2 + \alpha_5 \mathbf{M}_3\} \\ & + (\mathbf{I} \cdot \mathbf{E}) \{\alpha_6 (\mathbf{M}_1 \mathbf{E} + \mathbf{E} \mathbf{M}_1) + \alpha_7 (\mathbf{M}_2 \mathbf{E} + \mathbf{E} \mathbf{M}_2) + \alpha_8 (\mathbf{M}_3 \mathbf{E} + \mathbf{E} \mathbf{M}_3)\} \\ & + E_{11} \{\alpha_9 (\mathbf{M}_1 \mathbf{E} + \mathbf{E} \mathbf{M}_1) + \alpha_{10} (\mathbf{M}_2 \mathbf{E} + \mathbf{E} \mathbf{M}_2) + \alpha_{11} (\mathbf{M}_3 \mathbf{E} + \mathbf{E} \mathbf{M}_3)\} \\ & + E_{22} \{\alpha_{12} (\mathbf{M}_1 \mathbf{E} + \mathbf{E} \mathbf{M}_1) + \alpha_{13} (\mathbf{M}_2 \mathbf{E} + \mathbf{E} \mathbf{M}_2) + \alpha_{14} (\mathbf{M}_3 \mathbf{E} + \mathbf{E} \mathbf{M}_3)\} \\ & + E_{33} \{\alpha_{15} (\mathbf{M}_1 \mathbf{E} + \mathbf{E} \mathbf{M}_1) + \alpha_{16} (\mathbf{M}_2 \mathbf{E} + \mathbf{E} \mathbf{M}_2) + \alpha_{17} (\mathbf{M}_3 \mathbf{E} + \mathbf{E} \mathbf{M}_3)\} \\ & + 2\{\alpha_3 E_{11} + \alpha_4 E_{22} + \alpha_5 E_{33}\} \mathbf{E} \\ & + [\{\alpha_6 \mathbf{M}_1 + \alpha_7 \mathbf{M}_2 + \alpha_8 \mathbf{M}_3\} \cdot \mathbf{E}^2] \mathbf{I} + [\{\alpha_9 \mathbf{M}_1 + \alpha_{10} \mathbf{M}_2 + \alpha_{11} \mathbf{M}_3\} \cdot \mathbf{E}^2] \mathbf{M}_1 \\ & + [\{\alpha_{12} \mathbf{M}_1 + \alpha_{13} \mathbf{M}_2 + \alpha_{14} \mathbf{M}_3\} \cdot \mathbf{E}^2] \mathbf{M}_2 + [\{\alpha_{15} \mathbf{M}_1 + \alpha_{16} \mathbf{M}_2 + \alpha_{17} \mathbf{M}_3\} \cdot \mathbf{E}^2] \mathbf{M}_3 \\ & + \gamma_1 (E_{11})^2 \mathbf{M}_1 + \gamma_2 (E_{22})^2 \mathbf{M}_2 + \gamma_3 (E_{33})^2 \mathbf{M}_3 \\ & + \gamma_{12} E_{11} \{E_{11} \mathbf{M}_2 + 2E_{22} \mathbf{M}_1\} + \gamma_{13} E_{11} \{E_{11} \mathbf{M}_3 + 2E_{33} \mathbf{M}_1\} \\ & + \gamma_{14} E_{11} \{E_{11} \mathbf{I} + 2(\mathbf{I} \cdot \mathbf{E}) \mathbf{M}_1\} + \gamma_{21} E_{22} \{2E_{11} \mathbf{M}_2 + E_{22} \mathbf{M}_1\} \\ & + \gamma_{23} E_{22} \{E_{22} \mathbf{M}_3 + 2E_{33} \mathbf{M}_2\} + \gamma_{24} E_{22} \{E_{22} \mathbf{I} + 2(\mathbf{I} \cdot \mathbf{E}) \mathbf{M}_2\} \\ & + \gamma_{31} E_{33} \{2E_{11} \mathbf{M}_3 + E_{33} \mathbf{M}_1\} + \gamma_{32} E_{33} \{2E_{22} \mathbf{M}_3 + E_{33} \mathbf{M}_2\} \\ & + \gamma_{34} E_{33} \{E_{33} \mathbf{I} + 2(\mathbf{I} \cdot \mathbf{E}) \mathbf{M}_3\} + \beta_1 (\mathbf{I} \cdot \mathbf{E}) \{2E_{11} \mathbf{I} + (\mathbf{I} \cdot \mathbf{E}) \mathbf{M}_1\} \\ & + \beta_2 (\mathbf{I} \cdot \mathbf{E}) \{2E_{22} \mathbf{I} + (\mathbf{I} \cdot \mathbf{E}) \mathbf{M}_2\} + \beta_3 (\mathbf{I} \cdot \mathbf{E}) \{2E_{33} \mathbf{I} + (\mathbf{I} \cdot \mathbf{E}) \mathbf{M}_3\} \\ & + \beta_4 \{2E_{11} E_{22} \mathbf{M}_3 + 2E_{22} E_{33} \mathbf{M}_1 + 2E_{11} E_{33} \mathbf{M}_2\} \\ & + \beta_5 \{2E_{11} E_{22} \mathbf{I} + 2E_{11} (\mathbf{I} \cdot \mathbf{E}) \mathbf{M}_2 + 2E_{22} (\mathbf{I} \cdot \mathbf{E}) \mathbf{M}_1\} \\ & + \beta_6 \{2E_{11} E_{33} \mathbf{I} + 2E_{11} (\mathbf{I} \cdot \mathbf{E}) \mathbf{M}_3 + 2E_{33} (\mathbf{I} \cdot \mathbf{E}) \mathbf{M}_1\} \\ & + \beta_7 \{2E_{22} E_{33} \mathbf{I} + 2E_{22} (\mathbf{I} \cdot \mathbf{E}) \mathbf{M}_3 + 2E_{33} (\mathbf{I} \cdot \mathbf{E}) \mathbf{M}_2\} \\ & + \beta_8 (\mathbf{I} \cdot \mathbf{E})^2 \mathbf{I} \end{aligned} \quad (17)$$

where the 46 material constants are defined in appendix B as functions of the partial derivatives of W . Combined with (8), these results produce the orthotropic stress constitutive equation that is second-order in the Biot strain tensor.

Bimodular elastic materials

- 5 Curnier et al. (Curnier et al. 1995) developed a bimodular theory for linear elastic materials in terms of the second Piola-Kirchhoff stress and Lagrange strain tensors. Here, a bimodular theory for finite deformations is posed in terms of the right stretch tensor \mathbf{U} or, equivalently, the Biot strain tensor \mathbf{E} . Here, the elasticity tensors associated with $\hat{\mathbf{P}}(\mathbf{U})$ and $\tilde{\mathbf{P}}(\mathbf{E})$ (defined in (6)₂) are defined as

$$10 \quad P_U = \frac{\partial \hat{\mathbf{P}}(\mathbf{U})}{\partial \mathbf{U}}, \quad P_E = \frac{\partial \tilde{\mathbf{P}}(\mathbf{E})}{\partial \mathbf{E}}, \quad (18)$$

where it can be shown that $P_U(\mathbf{E} + \mathbf{I}) = P_E(\mathbf{E})$. We require the existence of a stress free reference configuration; i.e., $\hat{\mathbf{P}}(\mathbf{I}) = \tilde{\mathbf{P}}(\mathbf{0}) = \mathbf{0}$. A scalar valued function of \mathbf{U} or \mathbf{E} that identifies a surface of discontinuity in the 6-dimensional strain space is defined as

$$g_U(\mathbf{U}) = \mathbf{0}, \quad g_E(\mathbf{E}) = g_U(\mathbf{E} + \mathbf{I}) = \mathbf{0}, \quad (19)$$

- 15 where it can be shown that

$$\frac{\partial g_U}{\partial \mathbf{U}}(\mathbf{E} + \mathbf{I}) = \frac{\partial g_E}{\partial \mathbf{E}}(\mathbf{E}). \quad (20)$$

Due to the surface of discontinuity, the stress constitutive equation and, consequently, the elasticity tensor may be different on either side of the surface of discontinuity; here we define

$$20 \quad \tilde{\mathbf{P}}(\mathbf{E}) = \begin{cases} \tilde{\mathbf{P}}_+(\mathbf{E}) & \text{if } g_E(\mathbf{E}) > 0 \\ \tilde{\mathbf{P}}_-(\mathbf{E}) & \text{if } g_E(\mathbf{E}) < 0 \end{cases}, \quad P_E = \begin{cases} P_{E+} & \text{if } g_E(\mathbf{E}) > 0 \\ P_{E-} & \text{if } g_E(\mathbf{E}) < 0 \end{cases}. \quad (21)$$

In (Curnier et al. 1995), a theorem was proved that establishes necessary and sufficient conditions for the stress-strain equation to be continuous across the surface of discontinuity. Here, that theorem is slightly modified, because the major symmetry of the elasticity tensor for linear elastic materials was invoked in (Curnier et al. 1995) whereas
 5 the elasticity tensor for finitely elastic materials need not possess major symmetry. By not invoking that symmetry assumption, a minor modification of the proof presented in (Curnier et al. 1995) leads to the following necessary and sufficient conditions for the stress-strain equation to be continuous across the surface of discontinuity:

$$\tilde{\mathbf{P}}(\mathbf{E}) = \tilde{\mathbf{P}}_+(\mathbf{E}) = \tilde{\mathbf{P}}_-(\mathbf{E}), \quad [[P_E]] = P_{E+} - P_{E-} = s(\mathbf{E})\mathbf{M}(\mathbf{E}) \otimes \frac{\partial g_E}{\partial \mathbf{E}}, \quad (22)$$

10 for all \mathbf{E} such that $g_E(\mathbf{E}) = 0$, where $s(\mathbf{E})$ is a scalar valued function and $\mathbf{M}(\mathbf{E})$ is a second order tensor.³ Due to material symmetry, the surface of discontinuity must satisfy

$$g_E(\mathbf{E}) = \tilde{g}_U(\mathbf{I}_U) \Big|_{\mathbf{U} = \mathbf{E} - \mathbf{I}}. \quad (23)$$

The development in (18-23) can be easily modified if one prefers to work with the Cauchy stress. The functions $\hat{\mathbf{T}}(\mathbf{U})$ and $\tilde{\mathbf{T}}(\mathbf{E})$ replace $\hat{\mathbf{P}}(\mathbf{U})$ and $\tilde{\mathbf{P}}(\mathbf{E})$, where elasticity

15 tensors are similar to (18); e.g. $T_E = \partial \tilde{\mathbf{T}}(\mathbf{E}) / \partial \mathbf{E}$.

Bimodular second-order orthotropic materials

For a second-order elastic material, not all surfaces that satisfy the material symmetry restriction (23) will satisfy the continuity conditions (22). In order to model tension-compression asymmetry along the three directions defining orthotropy, we use three

20 surfaces of discontinuity:

$$g_1 = \mathbf{M}_1 \cdot \mathbf{E} = E_{11} = 0, \quad g_2 = \mathbf{M}_2 \cdot \mathbf{E} = E_{22} = 0, \quad g_3 = \mathbf{M}_3 \cdot \mathbf{E} = E_{33} = 0. \quad (24)$$

³ See Lemma 3.2 in (Curnier et al. 1995).

Consider the surface $g_1=0$. Inspection of the stress constitutive equation for \mathbf{P} (obtained from (8)₂, and (16-17)) reveals that the first continuity condition (22)₁ (i.e., $\tilde{\mathbf{P}}_+(\mathbf{E}) = \tilde{\mathbf{P}}_-(\mathbf{E})$ for all \mathbf{E} such that $E_{11}=0$) requires that the only material constants that may jump across this surface are the set $\{\lambda_{11}, \gamma_1, \gamma_{12}, \gamma_{13}, \gamma_{14}\}$. We adopt the notation

$$5 \quad [[\lambda_{11}]] = \lambda_{11+} - \lambda_{11-}, \quad \lambda_{11}[E_{11}] = \begin{cases} \lambda_{11+} & \text{if } E_{11} > 0 \\ \lambda_{11-} & \text{if } E_{11} < 0 \end{cases} \quad (25)$$

The terms in $\tilde{\mathbf{P}}(\mathbf{E})$ that involve the jump constants are highlighted as follows:

$$\begin{aligned} \tilde{\mathbf{P}}(\mathbf{E}) = & \dots + \lambda_{11}E_{11}\mathbf{M}_1 + (1/2)\{\lambda_{11}E_{11}(\mathbf{E}\mathbf{M}_1 - \mathbf{M}_1\mathbf{E})\} + \gamma_1(E_{11})^2\mathbf{M}_1 \\ & + \gamma_{12}E_{11}\{\mathbf{E}_{11}\mathbf{M}_2 + 2\mathbf{E}_{22}\mathbf{M}_1\} + \gamma_{13}E_{11}\{\mathbf{E}_{11}\mathbf{M}_3 + 2\mathbf{E}_{33}\mathbf{M}_1\} \\ & + \gamma_{14}E_{11}\{\mathbf{E}_{11}\mathbf{I} + 2(\mathbf{I} \cdot \mathbf{E})\mathbf{M}_1\} + \dots \end{aligned} \quad (26)$$

Using (26) and calculating the jump in the elasticity tensor P_E using (18)₂ we obtain, switching to indicial notation,

$$\begin{aligned} 10 \quad [[P_E]] = & [[\partial \tilde{P}_{AB} / \partial E_{KL}]] = [[\lambda_{11}]]\{\delta_{1A}\delta_{1B}\delta_{1K}\delta_{1L} + (1/2)[E_{12}(\delta_{2A}\delta_{1B} - \delta_{1A}\delta_{2B}) \\ & + E_{13}(\delta_{3A}\delta_{1B} - \delta_{1A}\delta_{3B})]\delta_{1K}\delta_{1L}\} + 2[[\gamma_{12}]]E_{22}\delta_{1A}\delta_{1B}\delta_{1K}\delta_{1L} \\ & + 2[[\gamma_{13}]]E_{33}\delta_{1A}\delta_{1B}\delta_{1K}\delta_{1L} + 2[[\gamma_{14}]](E_{22} + E_{33})\delta_{1A}\delta_{1B}\delta_{1K}\delta_{1L} \end{aligned} \quad (27)$$

where the condition $E_{11}=0$ at the interface was used. Furthermore,

$$\frac{\partial g_1}{\partial E_{KL}} = \frac{\partial E_{11}}{\partial E_{KL}} = \delta_{1K}\delta_{1L}, \quad (28)$$

so that the second continuity condition (22)₂ becomes

$$[[P_E]] = s(\mathbf{E})\mathbf{M}_{AB}\delta_{1K}\delta_{1L}. \quad (29)$$

- 15 Comparison of (27) and (29) reveals that the second continuity condition may be satisfied. Therefore, a bimodular second order material with a surface of discontinuity defined by $g_1=E_{11}=0$ may be represented by replacing the set of material constants $\{\lambda_{11}, \gamma_1, \gamma_{12}, \gamma_{13}, \gamma_{14}\}$ by $\{\lambda_{11}[E_{11}], \gamma_1[E_{11}], \gamma_{12}[E_{11}], \gamma_{13}[E_{11}], \gamma_{14}[E_{11}]\}$. Using a similar analysis, or by interchanging indices appropriately, a bimodular material with additional

surfaces of discontinuity $g_2=E_{22}=0$ and $g_3=E_{33}=0$ may have the set of discontinuous material constants $\{\lambda_{22}, \gamma_2, \gamma_{21}, \gamma_{23}, \gamma_{24}\}$ and $\{\lambda_{33}, \gamma_3, \gamma_{31}, \gamma_{32}, \gamma_{34}\}$, respectively. Consequently, the most general bimodular second-order stress equations has a total of 61 independent material constants. A similar analysis using the Cauchy stress reveals that the same material constants can jump across these surfaces of discontinuity. The resulting equation is too long to present here; instead, we propose a reduced form since it is not feasible to use a 61-parameter model.

To obtain a reduced model, we make the following assumptions regarding the dependence of the strain energy function W (7) with respect to the invariants I_i (11): (i) W is independent of $\{I_2, I_4, I_6\}$; (ii) W is a polynomial function of terms that are uncoupled with respect to the invariants $\{I_1, I_3, I_5, I_7\}$; (iii) W is at most a quadratic function of the invariant I_7 .⁴ Consequently, upon setting $W_2=0$, $W_4=0$, $W_6=0$, $W_{ij}=0$ ($i \neq j$), and $W_{777}=0$ in the material constant definitions in Appendix B, most of the second-order constants vanish and $\mu_1 = \mu_2 = \mu_3 = \alpha_1 = \mu$, $\lambda_{12} = \lambda_{13} = \lambda_{23} = \alpha_2 = \lambda$. The resulting bimodular equation has 14 parameters. Preliminary analysis suggested that material stability is difficult to ensure if the first-order terms jump, because 8 stiffness matrices must be positive-definite; see (Wang et al. 2003; Klisch et al. 2004). Furthermore, preliminary results for models that included the second-order terms associated with λ and μ exhibited a non-convex mechanical response in CC; these terms were also neglected.⁵ Thus, we consider the reduced model

⁴ These restrictions can be relaxed somewhat as (8) signifies that only the corresponding derivatives of W as evaluated in the reference configuration must vanish.

⁵ Consequently, the equation studied is no longer an exact second-order approximation.

$$\begin{aligned}
 \mathbf{P} = \tilde{\mathbf{R}}\mathbf{P}(\mathbf{E}) = & \mathbf{R}\{\lambda_{11}E_{11}\mathbf{M}_1 + \lambda_{22}E_{22}\mathbf{M}_2 + \lambda_{33}E_{33}\mathbf{M}_3 \\
 & + \lambda[(E_{22} + E_{33})\mathbf{M}_1 + (E_{11} + E_{33})\mathbf{M}_2 + (E_{11} + E_{22})\mathbf{M}_3] + 2\mu\mathbf{E} \\
 & + (1/2)\lambda_{11}E_{11}(\mathbf{E}\mathbf{M}_1 - \mathbf{M}_1\mathbf{E}) + (1/2)\lambda_{22}E_{22}(\mathbf{E}\mathbf{M}_2 - \mathbf{M}_2\mathbf{E}) \\
 & + (1/2)\lambda_{33}E_{33}(\mathbf{E}\mathbf{M}_3 - \mathbf{M}_3\mathbf{E}) + (1/2)\lambda[(E_{22} + E_{33})(\mathbf{E}\mathbf{M}_1 - \mathbf{M}_1\mathbf{E}) \\
 & + (E_{11} + E_{33})(\mathbf{E}\mathbf{M}_2 - \mathbf{M}_2\mathbf{E}) + (E_{11} + E_{22})(\mathbf{E}\mathbf{M}_3 - \mathbf{M}_3\mathbf{E})] \\
 & + \gamma_1E_{11}^2\mathbf{M}_1 + \gamma_2E_{22}^2\mathbf{M}_2 + \gamma_3E_{33}^2\mathbf{M}_3\}
 \end{aligned} \tag{30}$$

which results in a maximum of 11 parameters. It is important to emphasize that in (30), only the second-order material constants may jump. Consequently, the elasticity tensor (in addition to the strain energy function and stress-strain equation) is continuous across

5 the surfaces of discontinuity whereas the gradient of the elasticity tensor may jump. Finally, for pure stretch deformations, (30) simplifies to

$$\begin{aligned}
 \mathbf{P} = \tilde{\mathbf{P}}(\mathbf{E}) = & \lambda_{11}E_{11}\mathbf{M}_1 + \lambda_{22}E_{22}\mathbf{M}_2 + \lambda_{33}E_{33}\mathbf{M}_3 \\
 & + \lambda[(E_{22} + E_{33})\mathbf{M}_1 + (E_{11} + E_{33})\mathbf{M}_2 + (E_{11} + E_{22})\mathbf{M}_3] + 2\mu\mathbf{E} \\
 & + \gamma_1E_{11}^2\mathbf{M}_1 + \gamma_2E_{22}^2\mathbf{M}_2 + \gamma_3E_{33}^2\mathbf{M}_3.
 \end{aligned} \tag{31}$$

A bimodular exponential orthotropic material

To compare the predictive capability of (31) with current exponential models, we
10 considered a strain energy function of the form (5):

$$W = \tilde{W}(I_C) = \frac{a_1}{2}[I_7 - (I_7)^{-1}]^2 + \sum_{i=1}^3 \frac{b_i}{2c_i} [e^{c_i(I_i-1)^2} - 1], \tag{32}$$

with seven parameters ($a_1, b_1, c_1, b_2, c_2, b_3, c_3$) where, for convenience, we have ordered the invariants of \mathbf{C} as

$$\begin{aligned}
 \{I_i(\mathbf{C})\} = & \{\mathbf{M}_1 \cdot \mathbf{C}, \mathbf{M}_2 \cdot \mathbf{C}, \mathbf{M}_3 \cdot \mathbf{C}, \mathbf{M}_1 \cdot \mathbf{C}^2, \mathbf{M}_2 \cdot \mathbf{C}^2, \mathbf{M}_3 \cdot \mathbf{C}^2, \det \mathbf{C}\} \\
 \equiv & \{I_1, I_2, I_3, I_4, I_5, I_6, I_7\}.
 \end{aligned} \tag{33}$$

15 The isotropic part of (32) (i.e., the term dependent on I_7) was based on the orthotropic model of (Wagner and Lotz 2004) while the anisotropic part of (32) was based on (Holzapfel et al. 2004). Recently, exponential strain energy functions of the type (32)

have been employed that are "bimodular" (Baer et al. 2004; Holzapfel et al. 2004). In those studies the anisotropy is attributed to the presence of collagen fibers that are hypothesized to support only tensile stresses. To be consistent with those studies, it suffices to investigate whether the constants b_1 , b_2 , and b_3 can jump across surfaces of discontinuity defined by $I_1=1$, $I_2=1$, and $I_3=1$, respectively. First, (4) is used to calculate \mathbf{P} , which can then be expressed as $\mathbf{P} = \mathbf{R}\tilde{\mathbf{P}}(\mathbf{E})$. Then, using the methods outlined above, it can be confirmed that the continuity conditions (22) can be satisfied while allowing the constants b_1 , b_2 , and b_3 to jump across the surfaces $I_1=1$, $I_2=1$, and $I_3=1$, respectively. Thus, to employ the exponential model (32) and to be consistent with (Baer et al. 2004; Holzapfel et al. 2004) we take $b_1=0$, $b_2=0$, and $b_3=0$ when $I_1<1$, $I_2<1$, and $I_3<1$, respectively, resulting in a 7-parameter model.

Material stability conditions

An advantage of using the reduced form (30) is that necessary and sufficient conditions for material stability are straightforward to derive and apply. Here, we follow the definition and interpretation of incremental stability for the conjugate pair of Biot stress and Biot strain as presented in (Ogden 1984). The Biot stress tensor $\mathbf{T}^{(1)}$ is defined as

$$\mathbf{T}^{(1)} = (1/2)(\mathbf{P}^T \mathbf{R} + \mathbf{R}^T \mathbf{P}). \quad (34)$$

Here, $\mathbf{T}^{(1)}$ corresponds to the symmetric part of $\tilde{\mathbf{P}}(\mathbf{E})$ defined by (30); consequently, $\mathbf{T}^{(1)}(\mathbf{E})$ is equivalent to $\tilde{\mathbf{P}}(\mathbf{E})$ for pure stretches as given in (31). By using (31) to calculate the elasticity tensor P_E and additively decomposing it as $P_E = P_{E1} + P_{E2}$ such

that P_{E1} contains the first order terms and P_{E2} contains the second order terms, the stability criterion becomes⁶

$$\text{tr}\{(P_{E1}\dot{\mathbf{E}})\dot{\mathbf{E}}\} + \text{tr}\{(P_{E2}\dot{\mathbf{E}})\dot{\mathbf{E}}\} > 0 \text{ for all } \dot{\mathbf{E}} \neq 0. \quad (35)$$

To obtain necessary conditions, first consider stability at zero strain. Then, $P_{E2}=\mathbf{0}$ and (35) reduces to $\text{tr}\{(P_{E1}\dot{\mathbf{E}})\dot{\mathbf{E}}\} > 0$ for all $\dot{\mathbf{E}} \neq 0$, leading to the condition that P_{E1} must be positive-definite; i.e., the first order material constants λ_{11} , λ_{22} , λ_{33} , λ , and μ must correspond to a positive-definite stiffness matrix. Then, noting that for a fixed $\dot{\mathbf{E}}$ the numerical value of $\text{tr}\{(P_{E1}\dot{\mathbf{E}})\dot{\mathbf{E}}\}$ is finite and positive, consideration of a strain state \mathbf{E} with arbitrarily large magnitude leads to the condition that $\text{tr}\{(P_{E2}\dot{\mathbf{E}})\dot{\mathbf{E}}\} > 0$ for all $\dot{\mathbf{E}} \neq 0$, where $\text{tr}\{(P_{E2}\dot{\mathbf{E}})\dot{\mathbf{E}}\} > 0$ is

$$2\gamma_1 E_{11}(\dot{E}_{11})^2 + 2\gamma_2 E_{22}(\dot{E}_{22})^2 + 2\gamma_3 E_{33}(\dot{E}_{33})^2 > 0. \quad (36)$$

This inequality then leads to the necessary conditions that $\gamma_{1+}>0$, $\gamma_{2+}>0$, $\gamma_{3+}>0$, $\gamma_{1-}<0$, $\gamma_{2-}<0$, $\gamma_{3-}<0$. Sufficiency follows easily.

Stability restrictions are difficult to obtain and verify when using an exponential strain energy function such as (32). In (Wagner and Lotz 2004), it was noted that $a_1>0$ is necessary for having a positive definite strain energy function. In (Holzapfel et al. 2004), it was argued that $b_1>0$ is a sufficient condition for strong ellipticity. Thus, these relations are sufficient for incremental stability.

Experimental data

We constructed a hypothetical experimental dataset (Table 1) that may approximate the mechanical response of adult human cartilage in the surface region, which typically

⁶ See eqn. (6.2.211) and footnote on pg. 407 of (Ogden 1984), where this inequality is interpreted as stability "under tractions which follow the material, i.e. rotate with the local rotation \mathbf{R} ."

exhibits the strongest anisotropy. The data corresponded to uniaxial tension (UT) and confined compression (CC) experiments along three directions: 1 - parallel to the split-line, 2 - perpendicular to the split line and parallel to the surface, and 3 - perpendicular to the surface. To develop the UT data sets, a two-parameter exponential function was used
5 to generate data from 0-20% strain in 2% increments. For UT in the 1 and 2 directions, the parameters were adopted from (Huang et al. 1999; Huang et al. 2005). For UT in the 3 direction, the parameters from the UT1 equation were scaled down using a ratio of the infinitesimal Young's moduli reported in (Chahine et al. 2004) for bovine cartilage. Poisson's ratios were assumed to be the same in all three UT experiments, and to be
10 linearly increasing functions of axial strain. The Poisson's ratio at 0% UT strain was assumed to correspond to the Poisson's ratio for infinitesimal deformations in unconfined compression since the stress-strain equation is continuous through the origin, and was chosen using theoretical predictions with bovine tissue (Wang et al. 2003). The Poisson's ratio at 16% strain was specified using the data reported in (Huang et al. 1999). To
15 develop the CC data sets, a two-parameter exponential function (Ateshian et al. 1997) was used to generate data from 0-20% strain in 2% increments; the parameters were based on results of (Huang et al. 1999; Huang et al. 2005). It was assumed that the CC response was the same in the 1 and 2 directions.

Regression analysis

20 A simultaneous nonlinear regression algorithm was performed in Mathematica (Wolfram, V5.0) based on an approach developed by (Klisch and Lotz 1999), in which the Levenberg-Marquardt method is used to minimize the chi-squared merit function. Four second-order models were studied, with 6, 7, 8, and 9 parameters (Table 2), and one

exponential model was studied, with 7 parameters. The assumed Poisson's functions were used to prescribe the off-axis strains for UT. Then, a composite function representing a total of 12 equations was derived: 3 axial stress-axial strain equations in CC, 3 axial stress-axial strain equations in UT, and 6 transverse stress-axial strain equations in UT (corresponding to the traction-free boundary conditions). Initial values are required as a starting point for the set of material constants in the regression analysis. When employing the second-order models, the first-order parameters were set to values corresponding to the infinitesimal material constants and the second-order parameters were set equal to zero. When employing the exponential model, initial values were based on those reported in (Holzapfel et al. 2004; Wagner and Lotz 2004).

Preliminary analyses with the second-order models studied revealed non-convexity in the stress-strain response that was accompanied by a violation of the stability criteria. Since the stability restrictions could not be imposed a priori with the numerical algorithm, we formulated a consistent strategy that achieved admissible solutions for each of the models. First, the material constant γ_{1-} was set to a constant value of -0.2 MPa in the 7-PAR and 9-PAR models, corresponding to a value obtained in preliminary analyses in which the second order models were applied to the CC data alone (Klisch et al. 2004). Second, the material constant λ was decreased by increments of 0.1 MPa until a positive-definite elasticity tensor was achieved. The exponential model converged to a set of parameters that satisfied the stability restrictions. After the nonlinear regression analysis was performed, the second-order model parameters were used to derive the exact solutions to the CC and UT boundary-value problems, while the exponential model

parameters were used to obtain exact and numerical solutions to the CC and UT boundary-value problems, respectively.

Results

The numerical values for the material constants for the second-order models are presented in Table 3; the numerical values for the exponential model were $(a_1, b_1, c_1, b_2, c_2, b_3, c_3) = (0.01, 2.66, 3.47, 1.90, 2.88, 0.44, 4.54; \text{MPa})$. Quantitatively, all second-order models provided a better fit than the exponential model, as the χ^2 values were 105.16, 105.15, 105.16, and 105.16 for the 6-, 7-, 8- and 9-PAR second-order models, respectively, and 105.34 for the exponential model.⁷ Qualitatively, the theoretical predictions of the UT responses were the same for all models, while the theoretical predictions of the CC response and Poisson's ratios were different (Figs. 2-5 and Table 4). In particular, for the second-order models the CC response was linear for the 6- and 8-PAR models because $\gamma_{1-} = \gamma_{2-} = \gamma_{3-} = 0$, nonlinear for the 7- and 9-PAR models because $\gamma_{1-} = \gamma_{2-} = \gamma_{3-} < 0$, equal in all 3 directions for the 6- and 7-PAR models because $\lambda_{11} = \lambda_{22} = \lambda_{33}$, and not equal in all 3 directions for the 8- and 9-PAR models because $\lambda_{11} \neq \lambda_{22} \neq \lambda_{33}$. Similarly, the nature of the Poisson's functions varied between the second order-models (Table 4). The Poisson's functions were linear for the 6- and 8-PAR models because $\gamma_{1-} = \gamma_{2-} = \gamma_{3-} = 0$, nonlinear for the 7- and 9-PAR models because $\gamma_{1-} = \gamma_{2-} = \gamma_{3-} < 0$, equal in all 3 directions for the 6- and 7-PAR models because $\lambda_{11} = \lambda_{22} = \lambda_{33}$, and not equal in all 3 directions for the 8- and 9-PAR models because $\lambda_{11} \neq \lambda_{22} \neq \lambda_{33}$. For the exponential model, the CC responses were nonlinear and equal in

⁷ A lower chi-squared number represents a lower error between the data and the fit.

all 3 directions while the Poisson's functions were nonlinear and equal in all 3 directions (Figure 5 and Table 4).

Discussion

In this paper, a bimodular theory for finite deformations was developed with the
5 aim of accurately modeling the orthotropic and asymmetric mechanical response of
cartilage. The general bimodular orthotropic stress constitutive equation that is second-
order in Biot strain, subject to three surfaces of discontinuity, was found to have 61
material constants. Reduced models with 6-9 parameters were proposed and their ability
to describe experimental data representative of cartilage was assessed. The success of the
10 bimodular second-order models, as compared to the bimodular exponential model,
suggests that they may be appealing for some applications.

Previous nonlinear orthotropic models for biological tissues have adopted an
exponential strain energy function. Lotz and colleagues proposed several exponential
strain energy functions for the annulus fibrosus with the aim of obtaining a fit of
15 experimental data to within one standard deviation of the mean response. In particular, a
9-parameter model was used to fit 2 UT and 2 CC experiments (Klisch and Lotz 1999)
and a 6-parameter model was used to fit 3 UT, 2 CC, 1 unconfined compression, and 1
biaxial tension experiment (Wagner and Lotz 2004). Other models for the annulus
fibrosus include a 3-parameter exponential model that was fit to 2 UT experiments
20 (Eberlein et al. 2001) and a 6-parameter exponential model with material constants
specified to be consistent with published material properties (Baer et al. 2004). For
arterial tissue, a 3-parameter exponential model was used to fit a biaxial tension
experiment and then predict the response in combined extension and inflation (Holzapfel

et al. 2004). In all of these previous models, the exponential strain energy functions have been successful at either describing data from individual experiments very accurately or at describing data from multiple experiments in an "averaged" sense. However, they have not been shown to achieve a high level of accuracy in describing data from multiple
5 experiments in a specimen-specific manner.

For articular cartilage, a stress constitutive equation for finite deformations that can accurately describe the orthotropic and asymmetric mechanical response for multiple experimental protocols has not been proposed. However, bimodular models have been used. As mentioned before, Ateshian and colleagues (Soltz and Ateshian 2000; Wang et
10 al. 2003) used a bimodular model for infinitesimal strains. Also, the orthotropic model proposed for arterial tissue (Holzapfel et al. 2004) and the transversely isotropic model proposed for the intervertebral disc (Baer et al. 2004) allowed for different mechanical properties in tension and compression; however, those models did not address the issue of stress continuity across a surface of discontinuity in strain space. Other bimodular models
15 include fiber-reinforced cartilage FEMs in which cable elements, which only support stress under tension, are used to model collagen fibers (Li et al. 1999; Soulhat et al. 1999; Korhonen et al. 2003; Li and Herzog 2004; Wilson et al. 2004).

The bimodular second-order stress constitutive equation has several advantageous features. First, the use of a second-order equation removes the uncertainty regarding the
20 form of the strain energy function for orthotropic materials; as the number of terms and, consequently, the number of material constants is known. However, there is still uncertainty as to which terms need to be retained in order to accurately model the mechanical response. Second, a systematic procedure for establishing initial guesses for

the material constants in a nonlinear regression analysis may be used. Specifically, the first-order constants may be initially set to values obtained using an analysis with infinitesimal strains while the second-order constants may be initially set to zero. Third, the material constants in the second-order equation are straightforward to interpret. From a mathematical perspective, some constants correspond to the infinitesimal theory while other constants represent nonlinear (i.e., second-order) effects. Also, the constants do have a physical interpretation; for example, the material constants (λ_{11} , λ_{22} , λ_{33} , γ_1 , γ_2 , γ_3) may reflect the microstructural properties of collagen fibers (e.g., orientation and crosslink density) that give rise to direction-dependent tensile properties, while other second-order constants not used here may reflect interaction terms among collagen fibers oriented in different directions. Fourth, the stability criteria for the reduced models are fairly easy to implement. Since the first-order constants may not jump, one stiffness matrix must be checked for positive definiteness, as compared to a maximum of 8 if these constants are allowed to jump. In a preliminary study (Klisch et al. 2004), we found that ensuring positive definiteness of 8 stiffness matrices may be overly challenging; see also the discussion in (Wang et al. 2003). A justification for not allowing the first-order constants to jump is that the experimental stress-strain response is continuous through the origin in strain space, as demonstrated for annulus fibrosus (Wagner and Lotz 2004) and articular cartilage (Chahine et al. 2004).

A limitation of the present study is the uncertainty regarding the theoretical Poisson's ratios that are presented in Table 4. For example, in (Huang et al. 1999) the Poisson's ratios measured at 16% strain for UT in the 1 and 2 directions were 1.31 and 1.33, respectively, whereas the 6PAR model here resulted in constant Poisson's ratios of

0.493. In contrast to earlier studies with exponential strain energy functions in (Klisch and Lotz 1999) and (Wagner and Lotz 2004), in this study an exact solution to UT can be obtained for the second-order models. The stress-strain curves for the exact solutions were nearly identical to those obtained in the nonlinear regression; consequently, the uncertainty in the Poisson's ratios do not seem to affect the models' ability to model uniaxial tension. However, errors may be introduced when extrapolating to biaxial stress states. Another limitation is that the data used did not correspond to a complete set of UT and CC experimental data for a specific source of articular cartilage (i.e., anatomic site, species, age, etc.); however, it did describe a highly orthotropic and asymmetric mechanical response that is typical of cartilage. To address these limitations, a current aim of ours is to collect unconfined compression data (which is equivalent to a biaxial tension experiment) as well as CC, UT, and torsional shear data for a specific source of articular cartilage in order to further refine the bimodular second-order model.

It is important to note that the present approach is phenomenological. Microstructural models have the advantage that they offer a structure-function relationship that relates the tissue's microstructure to macroscopically observed mechanical properties. For example, experiments with healthy and osteoarthritic cartilage explants have shown that osteoarthritis is accompanied by an increase in tissue hydration and a decrease in proteoglycans (Maroudas 1976), leading to the hypothesis that increased collagen damage is the primary mechanism for swelling (Basser et al. 1998). That hypothesis is based on a stress balance assumption: in equilibrium, the collagen tensile stress balances the swelling pressure produced by the fixed charge density (Maroudas 1976; Bank et al. 1997). The fiber-reinforced FEMs are microstructural

models that employ the stress-balance hypothesis; indeed, the results of one study led to the claim that modeling the tension-compression nonlinearity using separate elements for the collagen and proteoglycan constituents is needed to accurately model the mechanical behavior of normal and degraded cartilage (Korhonen et al. 2003). However, 5 microstructural models typically aim to describe the general features of the tissue's mechanical response (at least in the realm of large strains) and not to accurately fit data from multiple experimental protocols performed on the same specimen.

Phenomenological models have a role in developing accurate biomechanical models. Our approach has been to first develop a phenomenological model, since we 10 believe that phenomenological models may result in more accuracy⁸, and then to incorporate microstructural considerations. We have recently decomposed the solid matrix stress constitutive equation into proteoglycan and collagen stress equations. In particular, in (Bingham et al. 2005) a microstructural model first proposed in (Basser et al. 1998) and further developed in (Klisch et al. 2003) was used to develop a 15 proteoglycan stress equation with material constants that depend on the masses of the tissue constituents (i.e., proteoglycans, collagens, and water) while the 6-PAR bimodular model presented here is used for the collagen stress equation.

Stress-strain equations for cartilage that can accurately model nonlinearity, anisotropy, and tension-compression asymmetry have practical applications. They may 20 be used in FEMs of *in vivo* joints; the results of (Donzelli et al. 1999; Krishnan et al. 2003) suggest that more accurate stress constitutive equations for large deformations may lead to an improved understanding of cartilage degeneration and failure. Also, they may

⁸ For example, see the discussion on molecular and phenomenological models of rubber elasticity presented in Chapter 7 of (Ogden 1984).

lead to an improved understanding of the mechanotransduction process at the microstructural level. For example, FEMs that include the mechanical properties of the extracellular matrix have been used to estimate the mechanical microenvironment of the cell in both the intervertebral disc (Baer et al. 2004) and articular cartilage (Guilak and
5 Mow 2000).

In recent years, we have developed several cartilage growth mixture models in which the collagen and proteoglycan constituents may grow in a differential manner (Klisch et al. 2000; Klisch et al. 2001; Klisch et al. 2003; Klisch and Hoger 2003; Klisch et al. 2005), with the goal of quantifying *in vitro* growth of cartilage explants and tissue
10 engineered constructs. In typical *in vitro* growth studies, the finite deformation theory is needed because large elastic deformations can be expected to occur (Chen et al. 2003), and because finite deformation models are needed to describe how mechanical properties evolve during growth. For example, in (Klisch et al. 2003) it was shown how nonlinear stress-strain equations can predict the evolution of mechanical properties during growth.
15 Accurate stress constitutive equations are a critical need for conducting a robust validation test of the cartilage growth models by comparing theoretical predictions of the growth tensors with direct experimental measures of growth.

Acknowledgements

I would like to thank Mrs. Suzanne Holtrichter for assistance in developing the program
20 used in the regression analysis. Funding was received from an NSF RUI grant and the Office of Naval Research, Department of Navy.

Appendix A

The formulas presented here⁹ are to be used to evaluate derivatives of the basic polynomial invariants needed to derive the second-order stress constitutive equation for orthotropic materials. Let $\mathbf{Z} = \hat{\mathbf{Z}}(\mathbf{X})$ be a tensor-valued function of a tensor \mathbf{X} . Then \mathbf{Z} is
 5 differentiable at \mathbf{X} if there exists a linear mapping $D\hat{\mathbf{Z}}(\mathbf{X})$ (i.e., the derivative of \mathbf{Z} at \mathbf{X}) such that

$$\hat{\mathbf{Z}}(\mathbf{X} + \mathbf{Y}) = \hat{\mathbf{Z}}(\mathbf{X}) + D\hat{\mathbf{Z}}(\mathbf{X})[\mathbf{Y}] + o(\mathbf{Y}) \text{ as } \mathbf{Y} \rightarrow \mathbf{0}, \quad (\text{A1})$$

where, introducing the norm operator $|\cdot|$,

$$\tilde{\mathbf{Z}}(\mathbf{Y}) = o(\mathbf{Y}) \text{ if } \lim_{\mathbf{Y} \rightarrow \mathbf{0}} \frac{|\tilde{\mathbf{Z}}(\mathbf{X})|}{|\mathbf{X}|} = 0. \quad (\text{A2})$$

10 If \mathbf{Z} is differentiable at \mathbf{X} , then the following standard results can be used to calculate the derivative:

$$D\hat{\mathbf{Z}}(\mathbf{X})[\mathbf{Y}] = \left. \frac{d}{d\varepsilon} \hat{\mathbf{Z}}(\mathbf{X} + \varepsilon \mathbf{Y}) \right|_{\varepsilon=0}, \quad (\text{A3})$$

and

$$D\hat{\mathbf{Z}}(\mathbf{X}) = \frac{\partial \hat{Z}_{ij}}{\partial X_{kl}}(\mathbf{X}) \mathbf{e}_i \otimes \mathbf{e}_j \otimes \mathbf{e}_k \otimes \mathbf{e}_l, \quad (\text{A4})$$

15 such that

$$D\hat{\mathbf{Z}}(\mathbf{X})[\mathbf{Y}] = \frac{\partial \hat{Z}_{ij}}{\partial X_{kl}}(\mathbf{X}) Y_{kl} \mathbf{e}_i \otimes \mathbf{e}_j. \quad (\text{A5})$$

The second derivative of \mathbf{Z} , if it exists, is the derivative of $D\hat{\mathbf{Z}}(\mathbf{X})$:

$$D^2\hat{\mathbf{Z}}(\mathbf{X})[\mathbf{Y}, \mathbf{Y}] = D\{D\hat{\mathbf{Z}}(\mathbf{X})[\mathbf{Y}]\}[\mathbf{Y}]. \quad (\text{A6})$$

⁹ See, e.g., (Gurtin 1984).

The following standard results can be used to calculate the second derivative:

$$D^2\hat{Z}(\mathbf{X}) = \frac{\partial^2 \hat{Z}_{ij}}{\partial X_{kl} \partial X_{mn}}(\mathbf{X}) \mathbf{e}_i \otimes \mathbf{e}_j \otimes \mathbf{e}_k \otimes \mathbf{e}_l \otimes \mathbf{e}_m \otimes \mathbf{e}_n, \quad (\text{A7})$$

such that

$$D^2\hat{Z}(\mathbf{X})[\mathbf{Y}, \mathbf{Y}] = \frac{\partial^2 \hat{Z}_{ij}}{\partial X_{kl} \partial X_{mn}}(\mathbf{X}) Y_{kl} Y_{mn} \mathbf{e}_i \otimes \mathbf{e}_j. \quad (\text{A8})$$

5 Appendix B

The material constants in the orthotropic second-order constitutive equation (15-16) are defined as follows, where the subscripts refer to the partial derivative of W with respect to the corresponding invariant $I_i(\mathbf{U})$.

$$\begin{aligned} \lambda_{11} &= W_{11} + 4W_{12} + 4W_{22} + 6W_{17} + 12W_{27} + 9W_{77}, \\ \lambda_{22} &= W_{33} + 4W_{34} + 4W_{44} + 6W_{37} + 12W_{47} + 9W_{77}, \\ \lambda_{33} &= W_{55} + 4W_{56} + 4W_{66} + 6W_{57} + 12W_{67} + 9W_{77}, \\ \lambda_{12} &= 3W_{17} + 6W_{27} + 9W_{77} + W_{13} + 2W_{23} + 3W_{73} + 2W_{14} + 4W_{24} + 6W_{74}, \\ \lambda_{13} &= 3W_{17} + 6W_{27} + 9W_{77} + W_{15} + 2W_{25} + 3W_{75} + 2W_{16} + 4W_{26} + 6W_{76}, \\ \lambda_{23} &= 3W_{37} + 6W_{47} + 9W_{77} + W_{35} + 2W_{45} + 3W_{75} + 2W_{36} + 4W_{46} + 6W_{76}, \\ \mu_1 &= W_2 + 3W_7, \quad \mu_2 = W_4 + 3W_7, \quad \mu_3 = W_6 + 3W_7, \\ \alpha_1 &= 3W_7, \quad \alpha_2 = 9W_{77}, \\ \alpha_3 &= 3W_{71} + 6W_{72}, \quad \alpha_4 = 3W_{73} + 6W_{74}, \quad \alpha_5 = 3W_{75} + 6W_{76}, \\ \alpha_6 &= 3W_{72}, \quad \alpha_7 = 3W_{74}, \quad \alpha_8 = 3W_{76}, \\ \alpha_9 &= W_{12} + 2W_{22}, \quad \alpha_{10} = W_{14} + 2W_{24}, \quad \alpha_{11} = W_{16} + 2W_{26}, \\ \alpha_{12} &= W_{32} + 2W_{42}, \quad \alpha_{13} = W_{34} + 2W_{44}, \quad \alpha_{14} = W_{36} + 2W_{46}, \\ \alpha_{15} &= W_{52} + 2W_{62}, \quad \alpha_{16} = W_{54} + 2W_{64}, \quad \alpha_{17} = W_{56} + 2W_{66}, \\ \gamma_1 &= 2W_{111} + 12W_{112} + 24W_{122} + 16W_{222}, \\ \gamma_{12} &= 2W_{113} + 4W_{114} + 8W_{123} + 16W_{124} + 8W_{223} + 16W_{224}, \\ \gamma_{13} &= 2W_{115} + 4W_{116} + 8W_{125} + 16W_{126} + 8W_{225} + 16W_{226}, \\ \gamma_{14} &= 6W_{117} + 24W_{127} + 24W_{227}, \end{aligned}$$

$$\gamma_2 = 2W_{333} + 12W_{334} + 24W_{344} + 16W_{444},$$

$$\gamma_{21} = 2W_{133} + 8W_{134} + 8W_{144} + 4W_{233} + 16W_{234} + 16W_{244},$$

$$\gamma_{23} = 2W_{335} + 4W_{336} + 8W_{345} + 16W_{346} + 8W_{445} + 16W_{446},$$

$$\gamma_{24} = 6W_{337} + 24W_{347} + 24W_{447},$$

$$\gamma_3 = 2W_{555} + 12W_{556} + 24W_{566} + 16W_{666},$$

$$\gamma_{31} = 2W_{155} + 8W_{156} + 8W_{166} + 4W_{255} + 16W_{256} + 16W_{266},$$

$$\gamma_{32} = 2W_{355} + 8W_{356} + 8W_{366} + 4W_{455} + 16W_{456} + 16W_{466},$$

$$\gamma_{34} = 6W_{557} + 24W_{567} + 24W_{667},$$

$$\beta_1 = 18W_{177} + 36W_{277}, \quad \beta_2 = 18W_{377} + 36W_{477}, \quad \beta_3 = 18W_{577} + 36W_{677},$$

$$\beta_4 = 2W_{135} + 4W_{136} + 4W_{145} + 8W_{146} + 4W_{235} + 8W_{236} + 8W_{245} + 16W_{246},$$

$$\beta_5 = 6W_{137} + 12W_{147} + 12W_{237} + 24W_{247},$$

$$\beta_6 = 6W_{157} + 12W_{167} + 12W_{257} + 24W_{267},$$

$$\beta_7 = 6W_{357} + 12W_{367} + 12W_{457} + 24W_{467},$$

$$\beta_8 = 18W_{777}$$

REFERENCES

- [1] Akizuki S, Mow VC, Muller F, Pita JC, Howell DS, Manicourt DH (1986) Tensile properties of human knee joint cartilage: I. Influence of ionic conditions, weight bearing, and fibrillation on the tensile modulus. *J Orthop Res* 4: 379-392
- 5 [2] Almeida ES, Spilker RL (1997) Mixed and penalty finite element models for the nonlinear behavior of biphasic soft tissues in finite deformation. Part i-alternative formulations. *Comput Methods Biomech Biomed Engin* 1: 25-46
- [3] Ateshian GA, Warden WH, Kim JJ, Grelsamer RP, Mow VC (1997) Finite deformation biphasic material properties of bovine articular cartilage from confined
- 10 [4] Baer AE, Laursen TA, Guilak F, Setton LA (2004) The micromechanical environment of intervertebral disc cells determined by a finite deformation, anisotropic, and biphasic finite element model. *J Biomech Eng* 125: 1-11
- [5] Bank RA, Krikken M, Beekman B, Stoop R, Maroudas A, Lafeber FPJG, Te
- 15 [6] Koppele JM (1997) A simplified measurement of degraded collagen in tissues: Application in healthy, fibrillated and osteoarthritic cartilage. *Matrix Biol* 16: 233-243
- [7] Bassar PJ, Schneiderman R, Bank RA, Wachtel E, Maroudas A (1998) Mechanical properties of the collagen network in human articular cartilage as measured by osmotic stress technique. *Arch Biochem Biophys* 351: 207-219
- 20 [8] Bingham M, Davol A, Sah RL, Klisch SM (2005) A nonlinear finite element model of cartilage growth under in vitro dynamic compression ASME Summer Bioengineering Conference, in review
- [9] Chahine NO, Wang CC, Hung CT, Ateshian GA (2004) Anisotropic strain-dependent material properties of bovine articular cartilage in the transitional range from tension to
- 25 [10] compression. *J Biomech* 37: 1251-1261
- [11] Chen AC, Williamson AK, Hee CK, Mendolsohn ES, Masuda K, Thonar EJ-MA, Sah RL (2003) Correlated variation in compressive properties and glycosaminoglycan concentration during *in vitro* cartilage growth. *Trans Orthop Res Soc* 28: 657
- [12] Curnier A, He QC, Zysset P (1995) Conewise linear elastic materials. *J Elast* 37: 1-
- 30 [13] 38
- [14] Donzelli PS, Spilker RL, Ateshian GA, Mow VC (1999) Contact analysis of biphasic transversely isotropic cartilage layers and correlations with tissue failure. *J Biomech* 32: 1037-1047
- [15] Eberlein R, Holzapfel GA, Schulze-Bauer CA (2001) An anisotropic constitutive model for annulus tissue and enhanced finite element analyses of intact lumbar disc
- 35 [16] bodies. *Comput Methods Biomech Biomed Eng* 4: 209-230
- [17] Eckstein F, Lemberger B, Stammberger T, Englmeier KH, Reiser M (2000) Patellar cartilage deformation in vivo after static versus dynamic loading. *J Biomech* 33: 819-825
- [18] Guilak F, Mow VC (2000) The mechanical environment of the chondrocyte: A
- 40 [19] biphasic finite element model of cell-matrix interactions in articular cartilage. *J Biomech* 33: 1663-1673
- [20] Gurtin M (1984) Introduction to continuum mechanics. Academic Press, New York

- [16] Herberhold C, Faber S, Stammberger T, Steinlechner M, Putz R, Englmeier KH, Reiser M, Eckstein F (1999) In situ measurement of articular cartilage deformation in intact femoropatellar joints under static loading. *J Biomech* 32: 1287-1295
- [17] Hoger A (1999) A second order constitutive theory for hyperelastic materials. *Int J Solids Struct* 36: 847-868
- [18] Holmes MH, Mow VC (1990) The nonlinear characteristics of soft gels and hydrated connective tissue in ultrafiltration. *J Biomech* 23: 1145-1156
- [19] Holzapfel GA, Gasser TC, Ogden RW (2004) Comparison of a multi-layer structural model for arterial walls with a fung-type model, and issues of material stability. *J Biomech Eng* 126: 264-275
- [20] Huang CY, Stankiewicz A, Ateshian GA, Flatow EL, Bigliani LU, Mow VC (1999) Anisotropy, inhomogeneity, and tension-compression nonlinearity of human glenohumeral cartilage in finite deformation *Trans Orthop Res Soc*
- [21] Huang CY, Stankiewicz A, Ateshian GA, Mow VC (2005) Anisotropy, inhomogeneity, and tension-compression nonlinearity of human glenohumeral cartilage in finite deformation. *J Biomech* 38: 799-809
- [22] Klisch SM, Lotz JC (1999) Application of a fiber-reinforced continuum theory to multiple deformations of the annulus fibrosus. *J Biomech* 32: 1027-1036
- [23] Klisch SM, Sah RL, Hoger A (2000) A growth mixture theory for cartilage. In: Casey J, Bao G (ed) *Mechanics in biology AMB 242 & BED 46 ASME*
- [24] Klisch SM, Van Dyke T, Hoger A (2001) A theory of volumetric growth for compressible elastic materials. *Math Mech Solids* 6: 551-575
- [25] Klisch SM, Chen SS, Sah RL, Hoger A (2003) A growth mixture theory for cartilage with applications to growth-related experiments on cartilage explants. *J Biomech Eng* 125: 169-179
- [26] Klisch SM, Hoger A (2003) Volumetric growth of thermoelastic materials and mixtures. *Math Mech Solids* 8: 377-402
- [27] Klisch SM, Holtrichter SE, Sah RL, Davol A (2004) A bimodular second-order orthotropic stress constitutive equation for cartilage *Proceedings of IMECE*
- [28] Klisch SM, Sah RL, Hoger A (2005) A cartilage growth mixture model for infinitesimal strains: Solutions of boundary-value problems related to in vitro growth experiments. *Biomechan Model Mechanobiol* In press
- [29] Korhonen RK, Laasanen MS, Toyras J, Lappalainen R, Helminen HJ, Jurvelin JS (2003) Fibril reinforced poroelastic model predicts specifically mechanical behavior of normal, proteoglycan depleted and collagen degraded articular cartilage. *J Biomech* 36: 1373-1379
- [30] Krishnan R, Park S, Eckstein F, Ateshian GA (2003) Inhomogeneous cartilage properties enhance superficial interstitial fluid support and frictional properties, but do not provide a homogeneous state of stress. *J Biomech Eng* 125: 569-577
- [31] Kwan MK, Lai WM, Mow VC (1990) A finite deformation theory for cartilage and other soft hydrated connective tissues--i. Equilibrium results. *J Biomech* 23: 145-155
- [32] Laasanen M, Toyras J, Korhonen R, Rieppo J, Saarakkala S, Nieminen M, Hirvonen J, Jurvelin JS (2003) Biomechanical properties of knee articular cartilage. *Biorheology* 40: 133-140

- [33] Lai WM, Hou JS, Mow VC (1991) A triphasic theory for the swelling and deformation behaviors of articular cartilage. *J Biomech Eng* 113: 245-258
- [34] Li L, Soulhat J, Buschmann mD, Shirazi-Adl A (1999) Nonlinear analysis of cartilage in unconfined ramp compression using a fibril reinforced poroelastic model. *Clin Biomech* 14: 673-682
- 5 [35] Li LP, Herzog W (2004) Strain-rate dependence of cartilage stiffness in unconfined compression: The role of fibril reinforcement versus tissue volume change in fluid pressurization. *J Biomech* 37: 375-382
- [36] Maroudas A (1976) Balance between swelling pressure and collagen tension in normal and degenerate cartilage. *Nature* 260: 808-809
- 10 [37] Mow VC, Ratcliffe A (1997) Structure and function of articular cartilage and meniscus. In: Mow VC, Hayes WC (ed) *Basic orthopaedic biomechanics* Raven Press, New York
- [38] Murnaghan FD (1937) Finite deformation of an elastic solid. *Am J Math* 59: 235-260
- 15 [39] Murnaghan FD (1951) *Finite deformation of an elastic solid*. Dover, New York
- [40] Ogden RW (1984) *Non-linear elastic deformations*. Dover, Mineola, New York
- [41] Rivlin RS (1953) The solution of problems in second order elasticity theory. *J Rat Mech Anal* 2: 53-81
- 20 [42] Schinagl RM, Gurskis D, Chen AC, Sah RL (1997) Depth-dependent confined compression modulus of full-thickness bovine articular cartilage. *J Orthop Res* 15: 499-506
- [43] Soltz MA, Ateshian GA (2000) A conewise linear elasticity mixture model for the analysis of tension-compression nonlinearity in articular cartilage. *J Biomech Eng* 122: 576-586
- 25 [44] Soulhat J, Buschmann MD, Shirazi-Adl A (1999) A fibril-network-reinforced biphasic model of cartilage in unconfined compression. *J Biomech Eng* 121: 340-347
- [45] Van Dyke T, Hoger A (2000) A comparison of second-order constitutive theories for hyperelastic materials. *Int J Solids Struct* 37: 5873-5917
- 30 [46] Venn MF, Maroudas A (1977) Chemical composition and swelling of normal and osteoarthritic femoral head cartilage. I. Chemical composition. *Ann Rheum Dis* 36: 121-129
- [47] Wagner DR, Lotz JC (2004) Theoretical model and experimental results for the nonlinear elastic behavior of human annulus fibrosus. *J Orthop Res* 22: 901-909
- 35 [48] Wang CC, Chahine NO, Hung CT, Ateshian GA (2003) Optical determination of anisotropic material properties of bovine articular cartilage in compression. *J Biomech* 36: 339-353
- [49] Wang CC-B, Hung CT, Mow VC (2001) An analysis of the effects of depth-dependent aggregate modulus on articular cartilage stress-relaxation behavior in compression. *J Biomech* 34: 75-84
- 40 [50] Wilson W, van Donkelaar CC, van Rietbergen B, Ito K, Huiskes R (2004) Stresses in the local collagen network of articular cartilage: A poroviscoelastic fibril-reinforced finite element study. *J Biomech* 37: 357-366
- [51] Woo SL-Y, Akeson WH, Jemmott GF (1976) Measurements of nonhomogeneous directional mechanical properties of articular cartilage in tension. *J Biomech* 9: 785-791
- 45

Klisch, "A bimodular theory for finite deformations ..."

[52] Woo SL-Y, Lubock P, Gomez MA, Jemmott GF, Kuei SC, Akeson WH (1979)
Large deformation nonhomogeneous and directional properties of articular cartilage in
uniaxial tension. J Biomech 12: 437-446

5

Table 1: Values of Young's modulus E , Poisson's ratio ν , and aggregate modulus H_A at 0% and 16% strain levels in the 1,2, and 3 directions for the experimental dataset used (E and H_A in MPa).

5

PARAMETER	DIRECTION		
	1	2	3
E_0	7.8	5.9	1.2
$E_{0.16}$	42.8	26.3	9.0
ν_0	0.05	0.05	0.05
$\nu_{0.16}$	1.33	1.33	1.33
H_{A0}	0.18	0.18	0.10
$H_{A0.16}$	0.26	0.26	0.15

Table 2: Material parameters in the second-order models studied. + indicates that the material constant was an independent parameter.

10

PARAMETER	MODEL			
	6-PAR	7-PAR	8-PAR	9-PAR
λ_{11}	+	+	+	+
λ_{22}	$= \lambda_{11}$	$= \lambda_{11}$	+	+
λ_{33}	$= \lambda_{11}$	$= \lambda_{11}$	+	+
λ	+	+	+	+
μ	+	+	+	+
γ_{1+}	+	+	+	+
γ_{2+}	+	+	+	+
γ_{3+}	+	+	+	+
γ_{1-}	$= 0$	+	$= 0$	+
γ_{2-}	$= 0$	$= \gamma_{1-}$	$= 0$	$= \gamma_{1-}$
γ_{3-}	$= 0$	$= \gamma_{1-}$	$= 0$	$= \gamma_{1-}$

Table 3: Numerical values (MPa) for the material parameters of the second-order models obtained from regression analysis.

PARAMETER	MODEL			
	6-PAR	7-PAR	8-PAR	9-PAR
λ_{11}	0.087	0.071	0.113	0.098
λ_{22}	0.087	0.071	0.145	0.130
λ_{33}	0.087	0.071	0.003	-0.013
λ	0.170	0.140	0.120	0.080
μ	0.044	0.036	0.044	0.036
γ_{1+}	134.0	134.1	133.8	133.9
γ_{2+}	88.0	88.1	87.7	87.7
γ_{3+}	26.4	26.4	26.9	26.9
γ_{1-}	0	-0.2	0	-0.2
γ_{2-}	0	-0.2	0	-0.2
γ_{3-}	0	-0.2	0	-0.2

5

Table 4: Average values of Poisson's ratios ν_{ij} (i =loading direction, j =direction of transverse strain component) predicted for the models (calculated at 20% strain). Poisson's ratios were constant for the 6-PAR and 8-PAR models but not for the other models. Note that a constant Poisson's ratio corresponds to a linear Poisson's function.

10

PARAMETER	MODEL				
	6-PAR	7-PAR	8-PAR	9-PAR	EXP
ν_{12}	0.493	0.464	-0.512	0.074	0.436
ν_{13}	0.493	0.464	1.993	0.811	0.436
ν_{21}	0.493	0.464	-0.894	0.093	0.436
ν_{23}	0.493	0.464	2.498	0.798	0.436
ν_{31}	0.493	0.464	0.418	0.326	0.436
ν_{32}	0.493	0.464	0.300	0.254	0.436

15

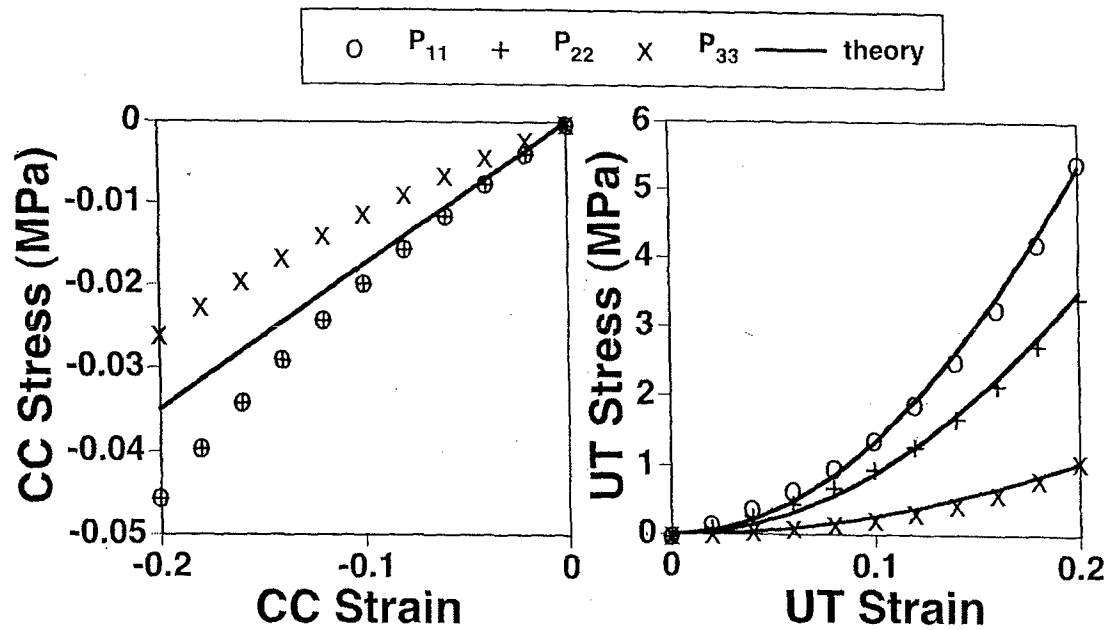


Fig.1. Theoretical predictions for confined compression (CC) response and uniaxial tension (UT) response using the 6-parameter model. The theoretical CC responses are

5 linear and equal in the 1, 2, and 3 directions.

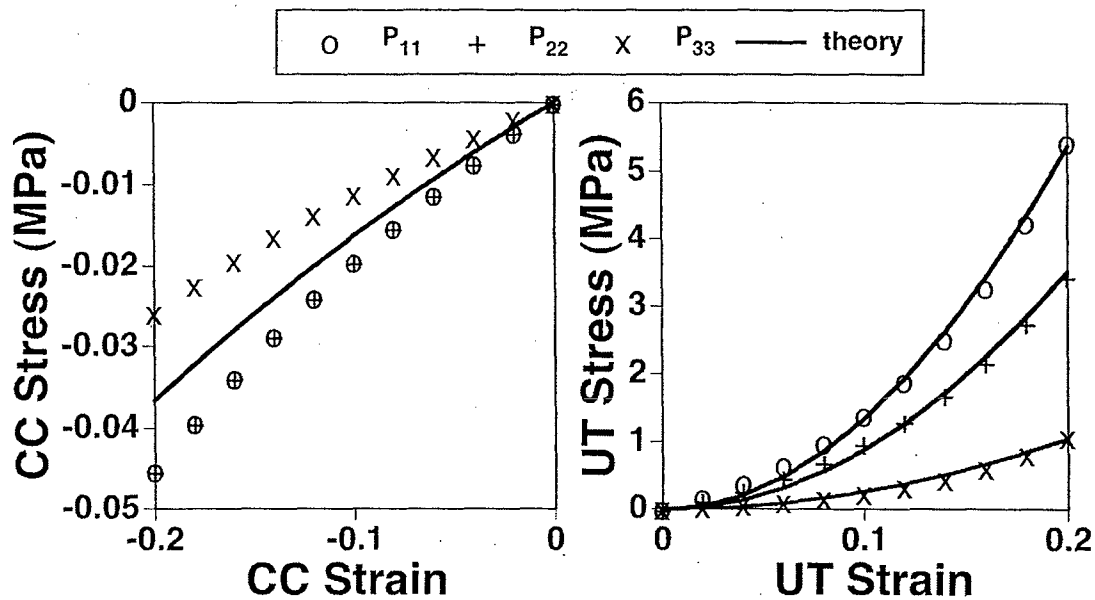


Fig.2. Theoretical predictions for confined compression (CC) response and uniaxial tension (UT) response using the 7-parameter model. The theoretical CC responses are nonlinear and equal in the 1, 2, and 3 directions.

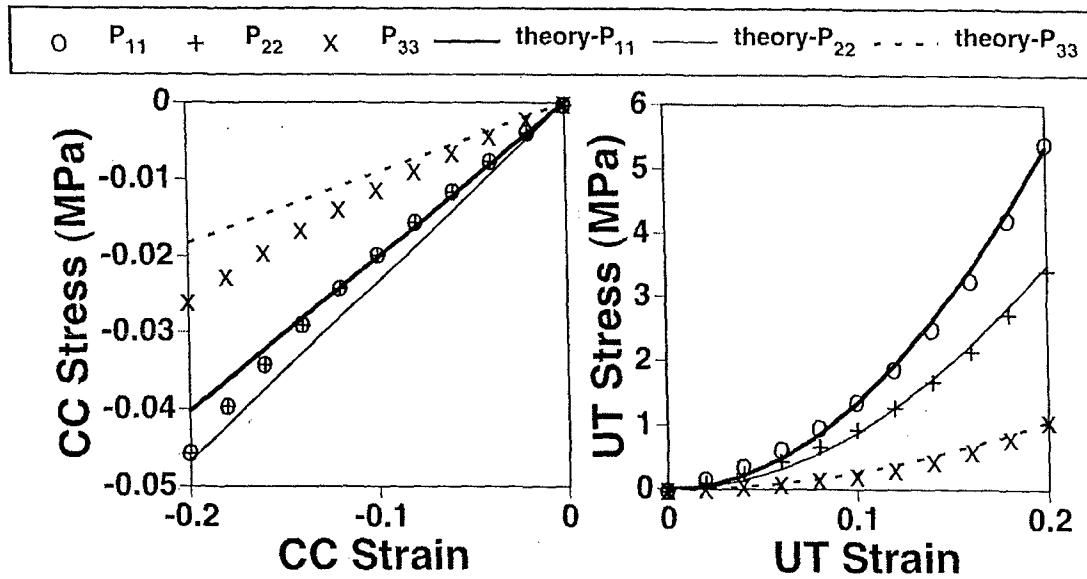


Fig.3. Theoretical predictions for confined compression (CC) response and uniaxial tension (UT) response using the 8-parameter model. The theoretical CC responses are

5 linear.

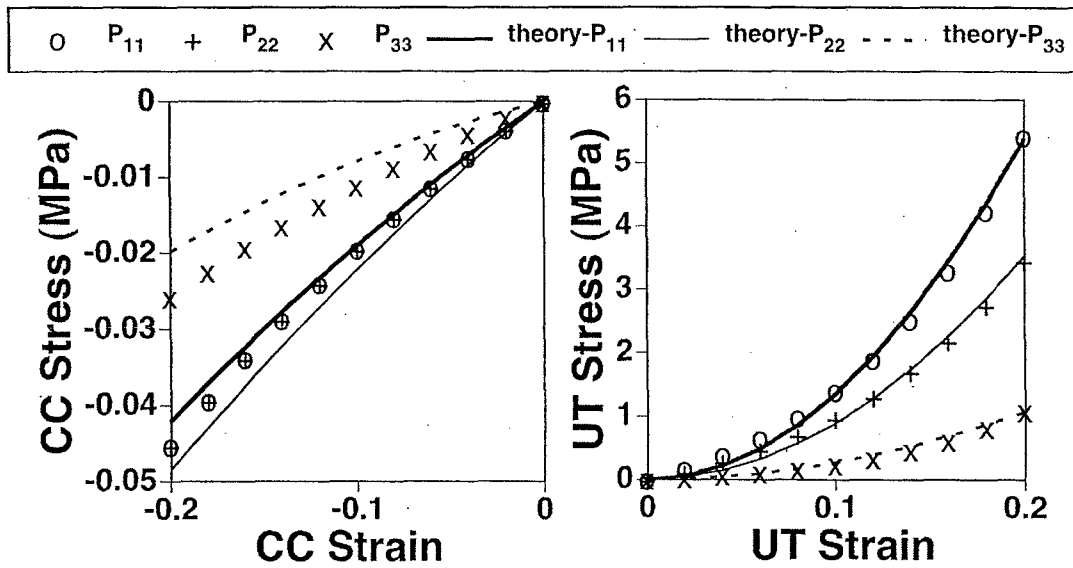


Fig.4. Theoretical predictions for confined compression (CC) response and uniaxial tension (UT) response using the 9-parameter model. The theoretical CC responses are

5 nonlinear.

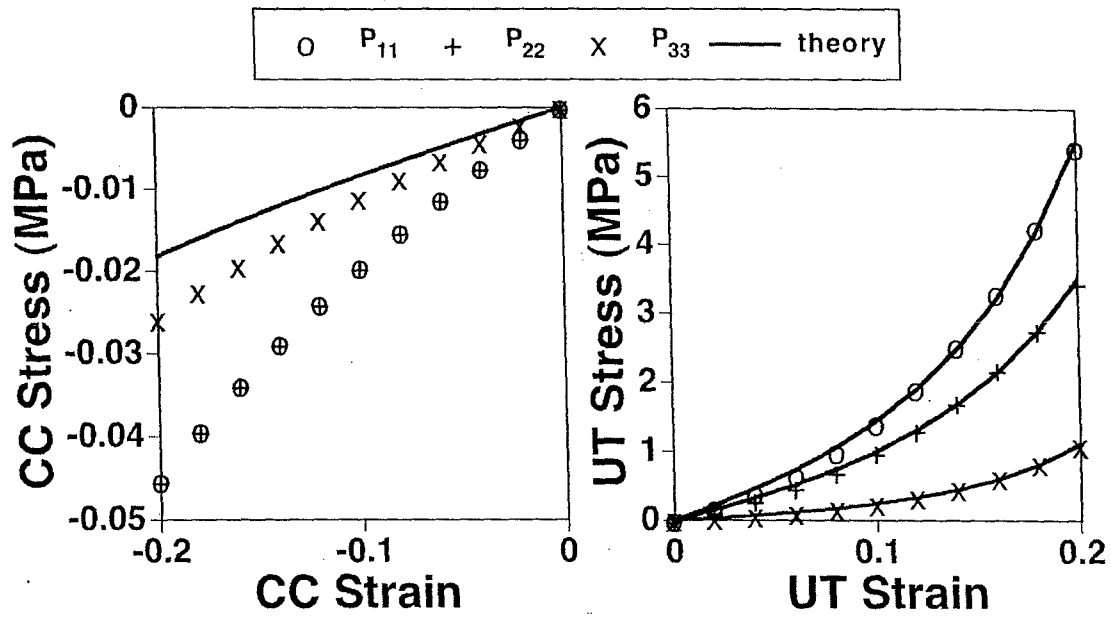


Fig.5. Theoretical predictions for confined compression (CC) response and uniaxial tension (UT) response using the exponential model. The theoretical CC responses are

5 nonlinear and equal in the 1, 2, and 3 directions.

**Production of transgenic quail expressing phytase to increase nutrient availability and
reduce environmental impact**

Office of Naval Research Award # N00014-04-1-0436

Project Investigators:

Elizabeth A. Koutsos
Assistant Professor
Animal Science Department
California Polytechnic State University San Luis Obispo CA USA

Daniel G. Peterson
Assistant Professor
Animal Science Department
California Polytechnic State University San Luis Obispo CA USA

The PI and Co-PI obtained funding from the Department of the Navy, Office of Naval Research (Award # N00014-04-1-0436) to assess and validate methods for the development of transgenic quail producing a bacterial-derived phytase enzyme in the upper digestive tract as a model for such application in commercial poultry. We have made substantial progress in this endeavor. As the project timeline ends, we have achieved virtually all of our stated objectives, with the exception of the small-scale P digestion trial. Since we are at the transfection stage of our experiments, we expect to have chicks hatched for the digestibility trials in the upcoming months, at which point we will complete the final objective of this project.

Our efforts so far have led to the cloning of a proventriculus-specific gene promoter, the preprogastrin (PPG) promoter, (G. Guenther, E. Koutsos and D. Peterson, 2005; GenBank accession #AY939854). This project has also led to the cloning and characterization of a novel form of the AppA phytase gene from *E.coli*. Using these cloned DNA fragments, as well as a green fluorescent protein marker gene we have designed and created a transgene construct for generation of transgenic quail expressing the phytase enzyme specifically in the upper digestive tract (**Figure 1**). The PPG gene promoter is intended to limit the expression of the phytase transgene to the proventriculus, while the T7 promoter that controls GFP will lead to expression in all cells and allow for a simple visual assessment of transgene incorporation into cells.

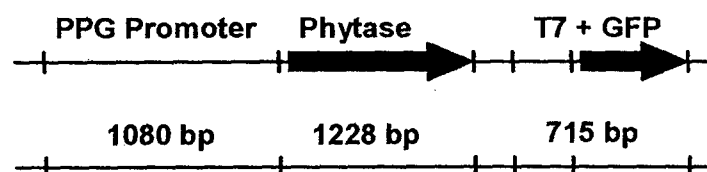


Figure 1. Phytase transgene construct. The cloned preprogastrin gene promoter is located upstream of the cloned AppA phytase gene and is intended to limit the expression of the phytase gene to the proventriculus. The GFP gene is under the control of the T7 promoter which will promote expression in all cell types and will allow for easy assessment of transgene integration into cells.

The phytase enzyme isolated from the Cal Poly quail population has been characterized for optimal pH (**Figure 2**), temperature (**Figure 3**) and thermostability (**Figure 4**) using a yeast recombinant expression system. This work was performed in collaboration with Dr. Chad Stahl Iowa State University and a manuscript is in preparation. Interestingly, compared to the form of enzyme most commonly used in industry, the gene sequence for our phytase enzyme leads to three amino acid substitutions, and enzyme characterization suggests differences in thermostability and optimal temperature and pH, which might result in different functional characteristics of this enzyme.

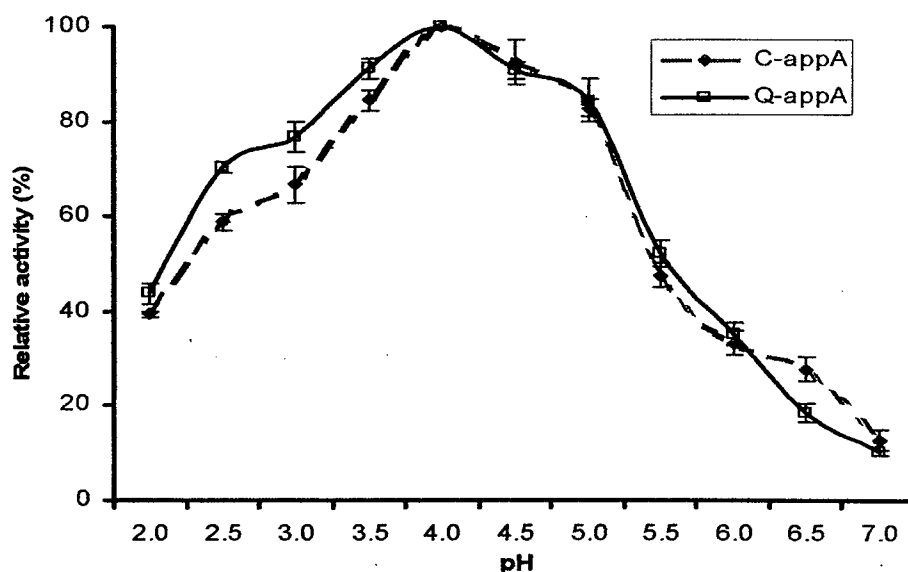


Fig. 2. The pH profiles of the recombinant C-appA and Q-appA phytases expressed in *Pichia pastoris*. Values, presented as percentages of their respective maximal activity at pH 4.0, are mean \pm SD of three assays with the partially purified enzymes. An asterisk indicates a significant difference ($P < 0.05$) between C-appA and Q-appA phytases at pH 2.5, 3.0 and 6.5.

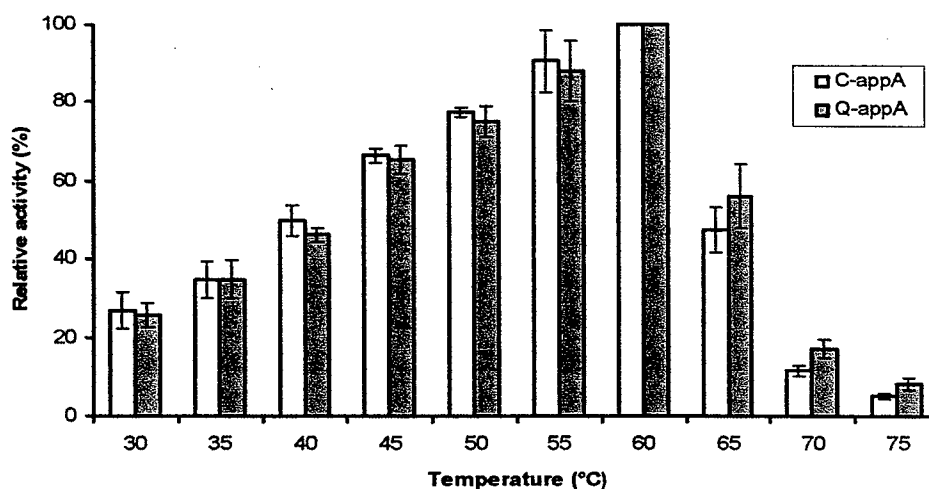


Fig. 3. Optimal temperature of the recombinant C-appA and Q-appA phytases expressed in *Pichia pastoris*. Phytase activity was determined by the release of Pi from sodium phytate at pH 4.0 at varying temperatures. Values, presented as percentages of their respective maximal activity at 60°C, are means \pm SD of three assays with the partially purified phytases. An asterisk indicates a significant difference ($P < 0.05$) between C-appA and Q-appA at 65, 70 and 75°C.

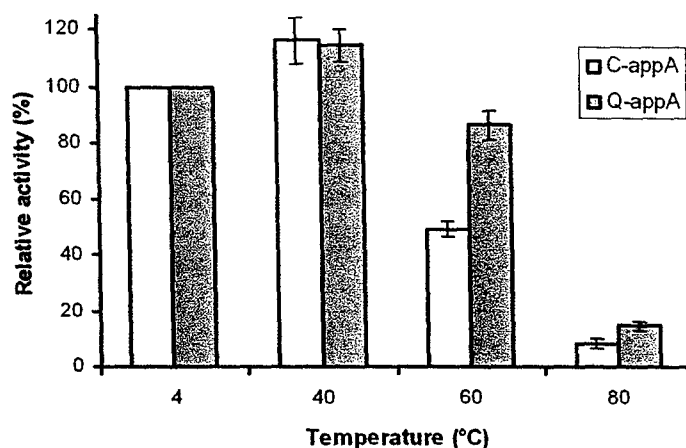


Fig. 4. The thermostability of the recombinant C-appA and Q-appA phytases expressed in *Pichia pastoris*. Both phytases were incubated in 0.2 M sodium citrate, pH 4.0, for 10 min at 40, 60 and 80°C, and the residual phytase activity was determined after the incubation. Values, presented as percentages of their respective activity of the same enzyme stored on ice (4°C), are means \pm SD of three assays with the partially purified phytases. An asterisk indicates a significant difference ($P < 0.01$) between the two enzymes.

In regards to methodologies for transfection of quail, we have developed a method to isolate and selectively culture primordial germ cells (PGC) from birds (**Figure 5**). PGC contribute to the developed bird's reproductive system, including their germline cells. Transfection of PGC and successful genomic integration of the transgene, followed by incorporation into a developing embryo, will allow for the germline inclusion of the transgene in those animals. We are currently validating transgene incorporation into PGC, and the repopulation of a developing embryo with these genetically modified cells. Additionally, we are comparing this method of transgene introduction (i.e. PGC incorporation) with the direct transfection of developing embryos *in ovo*, for which methods have been developed and are being validated in our labs through the support of this grant.



Figure 5. Staining of quail primordial germ cell (PGC) with fluorescent-labeled lectin. The left panel shows a quail PGC and a non-PGC; the right panel shows these cells visualized after staining with a PGC specific fluorescent marker to identify these cells.

As stated above, this project has thus far led to the discovery of a unique form of the chicken preprogastrin gene promoter that we have made publicly available through the GenBank database (Guenther et al., 2005; accession # AY939854) with an undergraduate student as lead author. We have also cloned a unique form of the bacterial phytase gene from *E. coli* derived from the Cal Poly quail population, and a publication describing this enzyme is in preparation (C. Stahl, G. Guenther and D. Peterson, manuscript in preparation). We will also attend a Transgenic Animal Research Conference in August, 2005 where one of our undergraduate students will present our progress in this endeavor. These research endeavors will provide valuable methodology for development of transgenic avian species, which may have broad applications in regards to nutrition and animal production as well as disease resistance and other novel applications. Additionally, the development of a commercial poultry species which expresses phytase can significantly impact P excretion and subsequent P contamination that would otherwise lead to eutrophication and degradation of water systems and aquatic environments.

Transgenic Animal Research Conference V

Lake Tahoe, CA

Aug 14-18, 2005

Abstract:


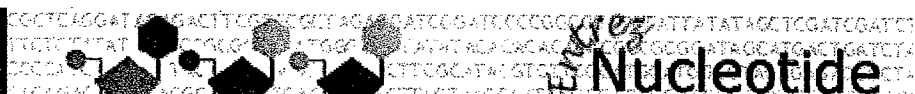
Development of methods for the production of transgenic quail expressing an *E. Coli* phytase gene

G.G. Guenther^{*1}, L. M. Hylle¹, C. H. Stahl², E.A. Koutsos¹ & D.G. Peterson¹

¹ Dept. of Animal Science, California Polytechnic State University, San Luis Obispo, CA

² Dept. of Animal Science, Iowa State University, Ames, Iowa

Excess phosphorus (P) in manure is a major environmental pollutant associated with poultry and swine production and is directly related to eutrophication, which results in the death of aquatic organisms and loss of biodiversity. Phytate accounts for 50-80% of plant phosphorus and this phytate-bound P is unavailable to simple-stomached animals. As a result, this P is not utilized by the animal and is therefore excreted. Phytases are enzymes that cleave inorganic phosphate from phytic acid, thereby improving its bioavailability to simple-stomached animals. Strategies intended to limit levels of P excretion in production animals have included dietary supplementation of phytase, as well as the use of transgenic crops with reduced phytate levels. Additionally, the recent production of transgenic pigs which express recombinant phytase in the digestive tract have been shown to increase phytate-P availability and therefore reduce P excretion. We have developed a phytase transgene construct for production of transgenic quail as a model system for application to commercial poultry. We have isolated and cloned the chicken preprogastrin promoter (PPGP) which is designed to limit the expression of a recombinant phytase to the proventriculus where it will be secreted into the upper GI tract. The PPGP was cloned from genomic DNA isolated from the Cal Poly chicken population, and the phytase gene was cloned from an *E. coli* isolated from the Cal Poly quail population. The phytase gene sequence is distinct from other *AppA* phytases previously reported, and codes for a functional phytase enzyme. Expression of this new phytase in a yeast system has yielded a functional protein with enzymatic properties highly suited for use in a recombinant poultry system. We have developed a protocol for the isolation and culture of quail primordial germ cells (PGC) from 5.5 day old embryos for transfection and repopulation of a developing embryo with PGCs harboring the transgene construct. A green fluorescent protein gene controlled by the T7 promoter was included in the construct to allow for the simple assessment of transgene incorporation in cells, developing embryos, and tissues of the adult animals.

[PubMed](#)
[Nucleotide](#)
[Protein](#)
[Genome](#)
[Structure](#)
[PMC](#)
[Taxonomy](#)
[OMIM](#)
[Books](#)

Search for

Range: from to
☐ Reverse complemented strand
 Features: ☐ SNP ☐ CDD

☒ MGC
 ☐ HPRD
 ☐ STS

☐ 1: [AY939854](#). Reports *Gallus gallus* pre...[gi:60687488]

[Links](#)

LOCUS AY939854 1080 bp DNA linear VRT 15-MAR-2005
 DEFINITION *Gallus gallus* preprogastrin gene, promoter and 5' UTR.
 ACCESSION AY939854
 VERSION AY939854.1 GI:60687488
 KEYWORDS .

SOURCE *Gallus gallus* (chicken)
 ORGANISM *Gallus gallus*
 Eukaryota; Metazoa; Chordata; Craniata; Vertebrata; Euteleostomi;
 Archosauria; Aves; Neognathae; Galliformes; Phasianidae;
 Phasianinae; *Gallus*.

REFERENCE 1 (bases 1 to 1080)
 AUTHORS Guenther,G.G., Koutsos,E.A. and Peterson,D.G.
 TITLE *Gallus gallus* preprogastrin gene promoter variant
 JOURNAL Unpublished

REFERENCE 2 (bases 1 to 1080)
 AUTHORS Guenther,G.G., Koutsos,E.A. and Peterson,D.G.
 TITLE Direct Submission
 JOURNAL Submitted (19-FEB-2005) Animal Science, California Polytechnic
 State University, 1 Grand Ave., San Luis Obispo, CA 93407, USA

FEATURES Location/Qualifiers
 source 1..1080
 /organism="Gallus gallus"
 /mol_type="genomic DNA"
 /db_xref="taxon:9031"
 promoter <1..981
 mRNA 982..>1080
 /product="preprogastrin"
 5'UTR 982..>1080

ORIGIN

```

1 tgggtcaata caagaggaac tgtggctctg tgagataaca gcagcctcag tgcgtgctcct
61 ctgagcacag agaggggggt gagccgcccc gggagcaccg cagtgtgggg gtggtacaga
121 gagaggtaca actctgtgcc tatgtgtaat acagctctgc ttcataagccc tgtgcagccg
181 tatgtctcatt ctctgtggct gtacagttcg gctgtgcctt tctgtgaacc ttcaaagacg
241 gacacagcac ccygtgcagc tgagccatcc tcacaccccc ttctatgcag cactgtctgt
301 ctctacagaa acactgtgca tgtgcatctg tgtctgctgg ggggtgtgtg gcacatatac
361 aggcaacaaa gtacatccat ctgtgcatag atacayatwg acttacatct gtgtatatag
421 acgtacactt acatatgtat atacataata tacattatct gtgtacctac atctctgcct
481 ctatatgayt gtgtaagtgt atacatrcat gtacacagtc cacacacacg tttgtgtcca
541 gcatcacagc gtgttttatg ttggatgggg cccagcagct gctgcagcct ccagggtgcc
601 catggacccc ctgcccccat gtccctgggtg ggggcacaga gctgtgttct gctgtggggg
661 ggctcagaac agagtgcagt tgtgtgttaa gagatgtgtg tatatatgta tgtataccta
721 cgtacacacg catgtgtatg gatgggtgtg tatggatata tgtgtgcaca gatgtgcgta
781 tatggatatg ggcacctatg gatagatatg tgtatgcatg tatgtgtgtg tgcataacca
841 tggatgcgcg tgtctgcgtg tgcgtggctg catgtatgtg tgtgtggggc gacgtgtgcg
  
```

901 tccatccccg cgtacctccg cgtccccgaac accgcagcag tcggagccgc cccggggcgg
961 agcgcagcgc gggcgccctc aaaagtgcgg acggagcgca gggagaggtg cggagcccc
1021 ggagcagcag cgtgaggtga ggaggacgt ggggggggga tgtggggaac acctgggagg

//

[Disclaimer](#) | [Write to the Help Desk](#)
[NCBI](#) | [NLM](#) | [NIH](#)

Feb 9 2005 14:51:10

**Mechanistic study of the cyclin-dependent kinase PfPK5/Pfcyc-1 from
the malarial parasite, *Plasmodia falciparum***

Project Investigators:

Lisa M. Lindert
Assistant Professor
Department of Chemistry and Biochemistry
California Polytechnic State University,
San Luis Obispo

Mechanistic study of the cyclin-dependent kinase PfPK5/Pfcyc-1 from the malarial parasite, *Plasmodia falciparum*

Principle Investigator: Lisa M. Lindert, Assistant Professor, Cal Poly, San Luis Obispo

Knowledge of the differences between the cyclin-dependent kinases in humans and the malarial parasite *P. falciparum* is crucial to the design of drugs that can specifically target plasmodial CDKs to halt parasite replication. The overall goal of this project is to contribute to this knowledge by investigating the catalytic mechanism of the malarial CDK *P. falciparum* protein kinase 5 (PfPK5) and its associated cyclin subunit *P. falciparum* cyclin 1 (Pfcyc-1). PfPK5/Pfcyc-1 is similar to the well-studied human CDK2/cyclin A. Thus, this study provides the information necessary to directly compare a human and a plasmodial CDK. Kinetic studies determine the dynamics of how an enzyme binds its substrates and produces products in real time, parameters that are important to understanding enzyme function. The three objectives for this project were to: purify large quantities of recombinant PfPK5/Pfcyc-1 for assays of enzymatic activity, determine the steady-state kinetic mechanism of PfPK5 with respect to ATP and a synthetic peptide and to involve undergraduates in basic biochemical research with a practical application.

Our progress toward these goals over the past year has been significant. Since the funding of this grant I have had a total of four undergraduate students working on this project at various stages and levels. During the summer months of 2004 there were three undergraduate students, funded by this grant, in my lab working on the project. During the academic year another student joined the effort and prior to the funding of this project two other undergraduates worked to produce preliminary findings to support the writing of the proposal. Thus, a total of six undergraduates have received advanced training in biochemical laboratory techniques and have directly contributed to the success of this project. Two of these students have graduated and are employed at a biotech company in Camarillo, CA.

There has been significant progress toward the research goals of this project. During the summer months of 2004 students worked to refine the protocol we had developed for purification of the PfPK5 and cyc-1 proteins as recombinant GST-fusions in *E. coli* (Figure 1). The protein was produced in sufficient quantities to allow enzymatic analysis with respect to a small protein histone H1. We have completed our first aim and show below that we can successfully purify recombinant PfPK5/cyc-1 from *E. coli* cell lysates and assay its activity with respect to ATP and histone H1. This procedure is very amenable to student preparation and three different students have successfully performed the purification.

Our initial goal as stated above was to use a synthetic peptide as a substrate, but initial trials were performed with this small protein because it is more cost-effective and was shown to be a better substrate than a synthetic peptide for CDK2/cyclin A(4). It has the advantage of being a cost-effective substrate for initial analysis, but because it is a protein purified from an animal (bovine) source, its sequence cannot be modified. Using histone H1 as a substrate we found that the K_m for ATP in the presence of saturating quantities of PfPK5 was 59 μM , which is a concentration that has been found to be a consistent value across the large group of Ser/Thr protein kinases(1). The K_m for histone H1 was less consistent and difficult to determine, a problem that can occur when a protein substrate with many potential phosphorylation sites is employed in enzymatic assays. Our results suggest that the K_m for this substrate is approximately 100 μM .

Currently we are working with toward the second aim. Our progress in assaying the activity of PfPK5/cyc-1 with respect to a synthetic peptide has not progressed as expected. Our initial work began using the synthetic peptide with the amino acid sequence PKTPKKAKKL. The PKTPKKAKKL peptide has a similar sequence to histone H1 and was used extensively in the characterization of CDK2/cyclinA(2, 3). Our original hypothesis was that this peptide would be phosphorylated by PfPK5/cyc-1 with a different kinetic mechanism from CDK2/cyclin A. Our data supports this hypothesis, however the differences are so dramatic it may not be experimentally possible to characterize them. It appears that the K_m for this peptide is in the high micromolar range or perhaps low millimolar range, making it unamenable for kinetic study. We would not be able to obtain soluble concentrations of peptide high enough to saturate the enzyme with this substrate and perform analysis of ATP binding. Although this result has frustrated our research efforts in characterizing the kinetic mechanism of PfPK5/cyc-1 it is a significant finding. The human enzyme, CDK2/cyclinA uses this synthetic peptide efficiently and has a K_m for PKTPKKAKKL in the low micromolar range (12 μ M) (2). Therefore, although we cannot strictly characterize the magnitude of the difference between the human and malarial enzymes, we have found that they bind to substrates with vastly different affinity. This suggests a difference in substrate specificity previously unrecognized for these enzymes. Our next step is to look at the sequence carefully and make a series of peptides with varying sequence to probe the specificity of PfPK5/cyc-1.

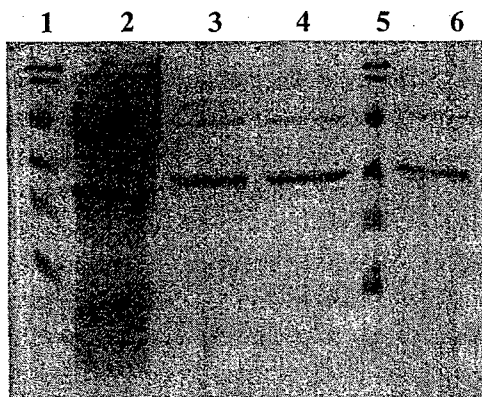


Figure 1: SDS-PAGE analysis of PfPK5/cyc-1 purification from bacterial cell lysates. Lanes 1 and 5 contain protein standards. The sizes of the bands from top to bottom are 103,77,50,34.3,28.8, 20.7 kDa. Lane 1 is the bacterial cell lysate sample containing GST-PfPK5 and GSP-cyc1. Lanes 3, 4 and 6 contain fractions eluted following protease cleavage of the PfPK5/cyc-1 complex from the glutathione agarose column. PfPK5 and cyc-1 are very similar in size HPLC analysis of the purified protein confirmed the presence of a protein with the expected size of the PfPK5/cyc-1 heterodimer, 79.5 kDa (data not shown).

References:

1. Adams, J. A. 2001. Kinetic and catalytic mechanisms of protein kinases. *Chem Rev* **101**:2271-90.
2. Hagopian, J. C., M. P. Kirtley, L. M. Stevenson, R. M. Gergis, A. A. Russo, N. P. Pavletich, S. M. Parsons, and J. Lew. 2001. Kinetic basis for activation of CDK2/cyclin A by phosphorylation. *J Biol Chem* **276**:275-80.
3. Stevenson, L. M., M. S. Deal, J. C. Hagopian, and J. Lew. 2002. Activation mechanism of CDK2: role of cyclin binding versus phosphorylation. *Biochemistry* **41**:8528-34.
4. Stevenson-Lindert, L. M., P. Fowler, and J. Lew. 2003. Substrate specificity of CDK2-cyclin A. What is optimal? *J Biol Chem* **278**:50956-60.

Registration of Color Images in Non-Rigid Environments

Project Investigator:

Dr. Jose Macedo
Associate Professor
Industrial & Manufacturing Engineering Department

Abstract

The project developed and tested methods to register images of objects obtained over time for the purpose of detecting if any change has occurred. Two specific applications of this technology were explored in this project. These are: skin cancer screening and surveillance for detection of improvised explosive devices (IEDs) and landmines. Registration in this context means identifying corresponding features in two or more images from the same scene and estimating some mapping function between these images. Typically the purpose of registration is to enhance the information provided by a single image. The objective in this project is to identify aspects of the scene that may have undergone geometric changes over time, and measure the magnitude of those changes. The techniques developed build on methods published during the last two years in the computer vision and medical literature. The algorithms developed were prototyped and tested using Matlab computer software available at CalPoly. Testing included synthetic images as well as images obtained using a laboratory setting.

Introduction to Image Registration

Image registration is in general the process of overlaying two or more images of the same scene. These images may have been obtained at different times, and/or from different viewpoints, and/or by different types of sensors. It geometrically aligns two images for the purpose of integrating the information from multiple sources, or detecting change.

Image registration is widely used in: remote sensing for environmental monitoring, medicine (combining X-ray, MRI, CT) for monitoring tumor growth, treatment verification, planning surgery or radiation therapy, and computer vision for industrial inspection and quality control.

Applications of image registration can be divided into four main groups depending on the conditions of the image acquisition:

1) Images obtained from *different viewpoints*.

Images of the same scene are acquired from different viewpoints. The objectives can be to obtain an improved 2D view, or to obtain a 3D representation of the object in the scene, or to estimate relative camera positions.

2) Images obtained at *different times*.

Images of the same scene are acquired at different times. The objectives can be to detect and evaluate changes in the scene which may appear between consecutive image acquisitions. Examples of applications: Surveillance for security monitoring or detecting land mines. Medical imaging to monitor healing therapy, or monitor tumor evolution. Remote sensing to monitor global land usage, or landscape planning.

3) Images obtained with *different sensors*.

Images of the same scene are acquired with various sensors of different types. The objectives may be to integrate the information obtained from different sources to gain more detailed scene representation. Examples of applications: Surveillance for security monitoring by combining radar with infrared imaging. Medical diagnostic or surgery planning applications that may combine information from multiple sensors such as: magnetic resonance image (MRI), ultrasound and X rays.

4) Scene to *model* registration.

Images of a scene and a model of the scene are registered. The model can be a computer representation of the scene, for instance in manufacturing it can be a computer model of a part being manufactured, or in medicine it can be an 'average' patient or specimen, or in remote sensing it could be a map, etc. The objective is to localize the model in the acquired image and compare image to model to detect possible deviations.

Most registration methods consist of the following four steps (see Figure 1, from Zitova 2003):

- a) **Feature selection.** Salient and distinctive objects (regions of high contrast, edges, contours, line intersections, corners, etc.) are detected.
- b) **Feature matching.** The correspondence between features detected in both images is established. Techniques include use of various feature descriptors, statistical similarity measures, and spatial relationships among the features.
- c) **Estimate transform model.** The type and parameters of the mapping functions that align both images are estimated. The parameters of the mapping functions are estimated using the established feature correspondence.
- d) **Image transformation and integration.** The sensed image is transformed by means of the mapping functions.

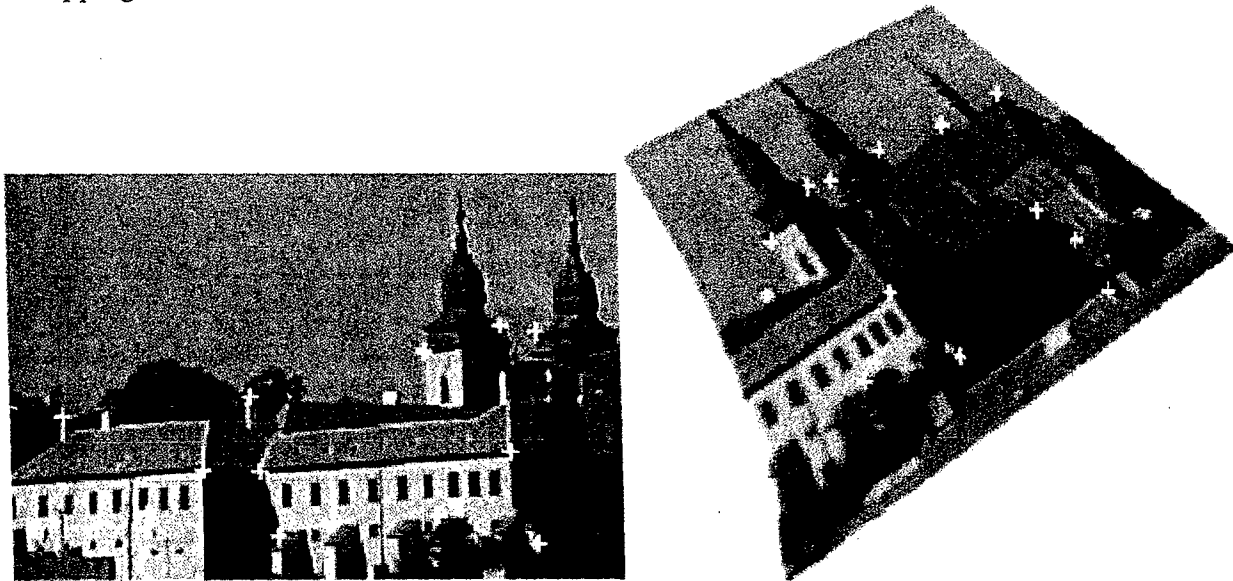


Figure 1 (a). Steps in Registration Process - Feature Selection [from Zitova 2003]

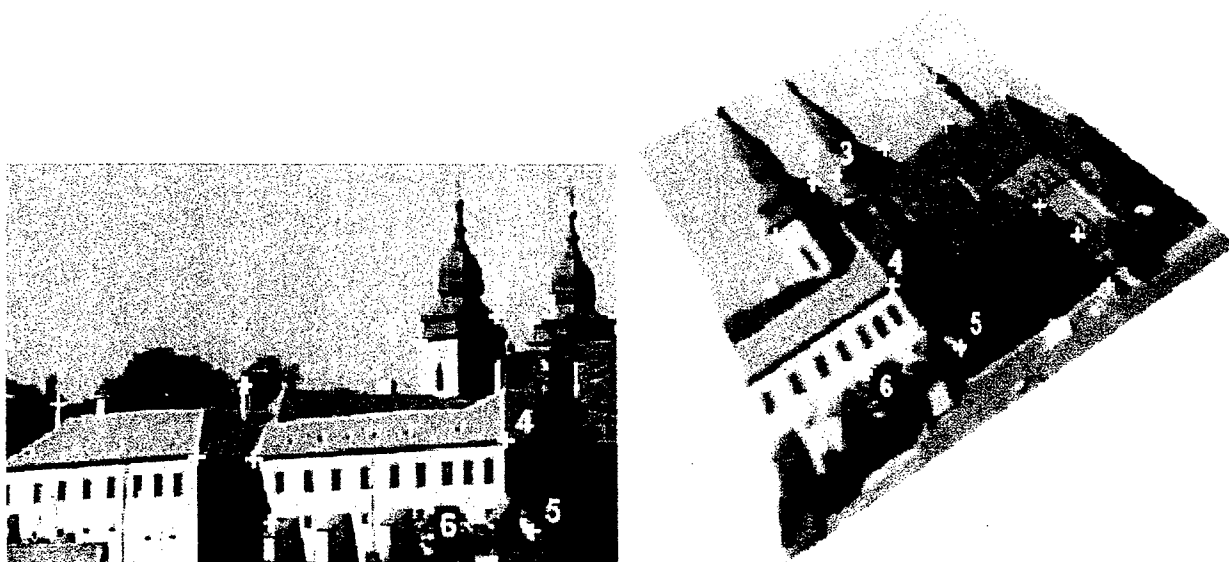


Figure 1 (b). Steps in Registration Process - Feature Matching [from Zitova 2003]

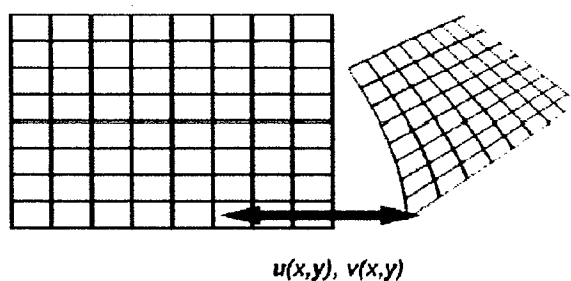


Figure 1 (c). Steps in Registration Process - Estimate Transform Model [from Zitova 2003]



Figure 1 (d). Steps in Registration Process - Image Transformation and Integration [from Zitova 2003]

Many industrial applications, mobile robot navigation and space exploration rely on registering sequences of images for rigid environments. The geometry in these scenes remains unchanged over time. These conditions have led to development of efficient algorithms for navigation of an orbiter around asteroid Eros in 2000 [Johnson] and navigation and obstacle avoidance of the Mars rovers missions in 2003-2004 (see Figure 2)

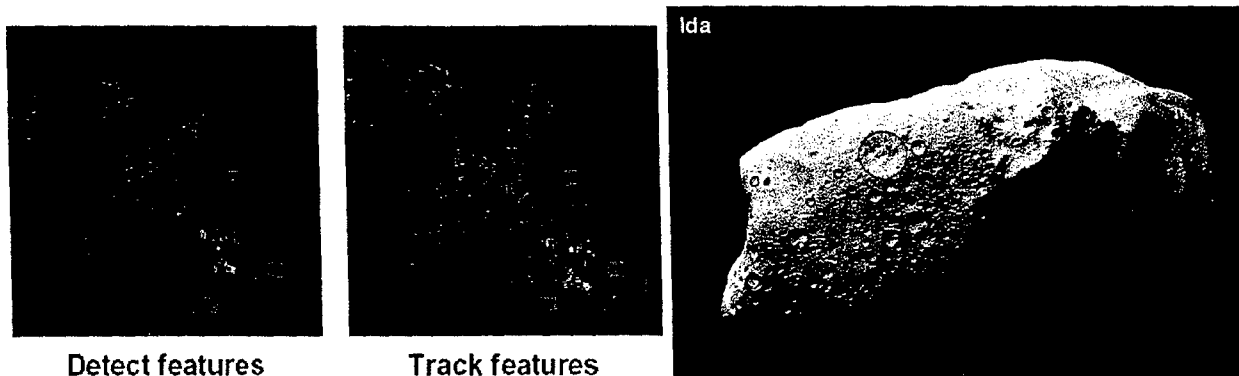


Figure 2. Registration of Rigid Body Images (from Johnson – JPL NASA)

In most medical applications the assumption of rigid bodies has to be relaxed and the scene is treated as having some degree of non-rigidity (or elasticity), particularly when images are obtained at different times.

Improvised Explosive Devices (IEDs) and Landmine detection.

In this project we are interested in developing an image registration methodology for fast and accurate change detection to locate buried landmines and improvised explosive devices (IEDs). The intent is to help alleviate the problem of roadside bombs claiming lives in situations like present day Iraq. Figures 3 and 4 show advancing ground forces along a main supply route in Iraq. Figure 5 through 10 show various IEDs found in Iraq. Figures 11 -12 show the aftermath of IEDs in Iraq.



Figure 3. Scenario example, roads in Iraq



Figure 4. Scenario example, roads in Iraq



Figure 5. IED encased in concrete

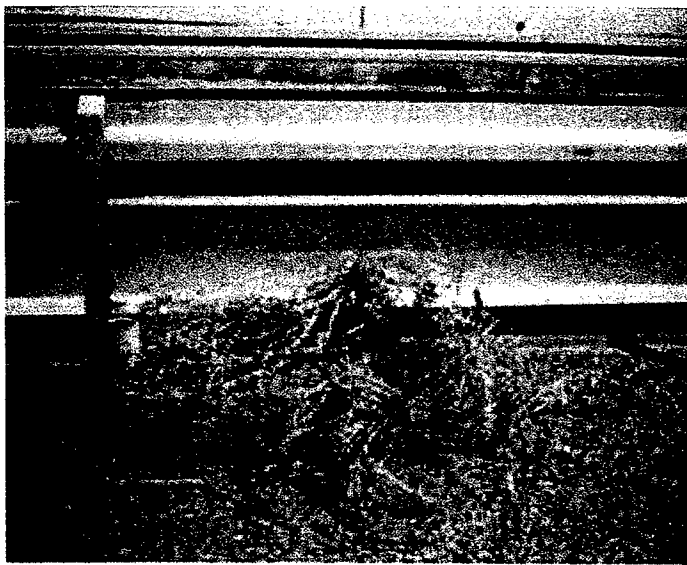


Figure 6. IED hidden in grass



Figure 7. IED hidden under rocks, side view



Figure 8. IED hidden under rocks, top view



Figure 9. IED hidden in bag



Figure 10. IED hidden in bag



Figure 11. IED aftermath



Figure 12. IED aftermath in Iraq

Figure 13 shows a weathered landmine found in Croatia, and Figure 14 shows training exercises to use equipment to detect landmines in the border between Chile and Bolivia.

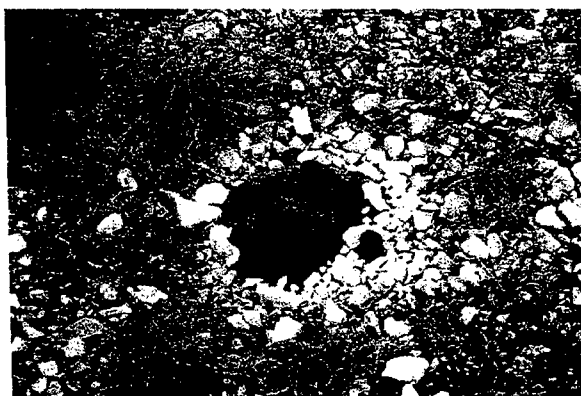


Figure 13. Weathered landmine in Croatia



Figure 14. Landmine Detection Training

The methodology assumes that sequences of aerial images of the road or terrain can be obtained at periodic time intervals. We speculate that by registering and comparing high resolution images obtained before and after IEDs or landmines are placed on the ground, it will be possible to identify and locate them. Corresponding images of the same terrain from consecutive sequences can be processed to detect if the terrain has changed or been disturbed. The image processing methodology requires registering corresponding images by identifying matching natural landmarks in both images, then calculating and performing scale and perspective transformations in order that both images can be superimposed and compared. Change detection algorithms need to be fast, sensitive and have low false alarm rates.

Figure 15 illustrates a possible deployment scenario in which images from unmanned aerial vehicles (UAV) are used for change detection of IEDs along supply routes. Corresponding images obtained earlier (ie. the prior day) can be compared to images obtained ahead of the advancing ground forces. In this scenario, location information about positive detections is communicated to advancing ground forces.

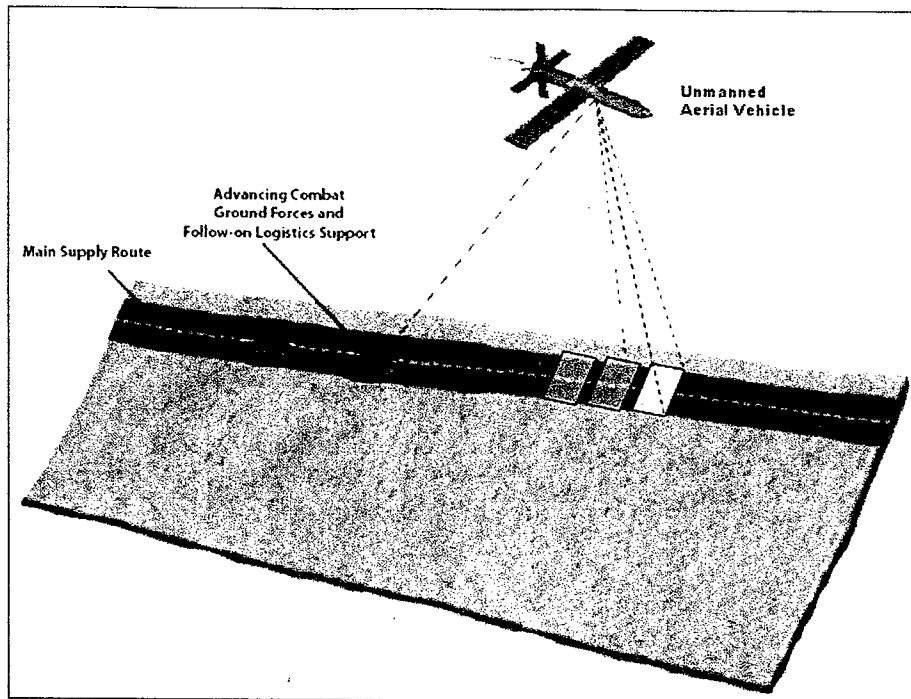


Figure 15. Illustration of Deployment Scenario – Change Detection of IEDs along Supply Route

Methodology and Results for IED and Landmine detection by image registration.

A methodology was developed to register and compare images to detect landmines. The image processing methodology registers corresponding images by identifying matching natural landmarks in both images. The program calculates and performs scale and perspective transformations so that both images can be superimposed and compared. A change detection algorithm is then applied to detect potential IEDs and landmines with low false alarms due to changes in illumination or other small natural changes. This methodology was tested in a laboratory setting using a medium size Cartesian robot to manipulate a CCD camera. A sand and rock box was placed within the robot workspace volume. Figure 16 shows the laboratory setup. Several cylindrical disks of controlled sizes and aspect ratios, shown in Figure 17, were used to simulate landmines.

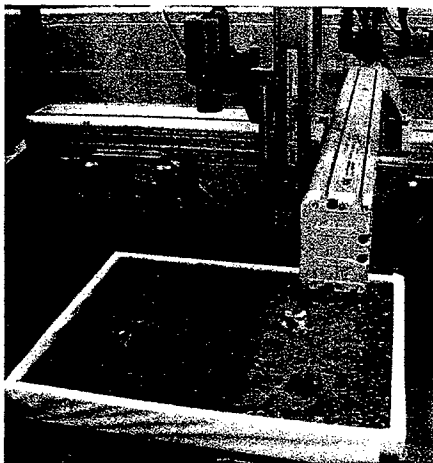


Figure 16. Laboratory Setup

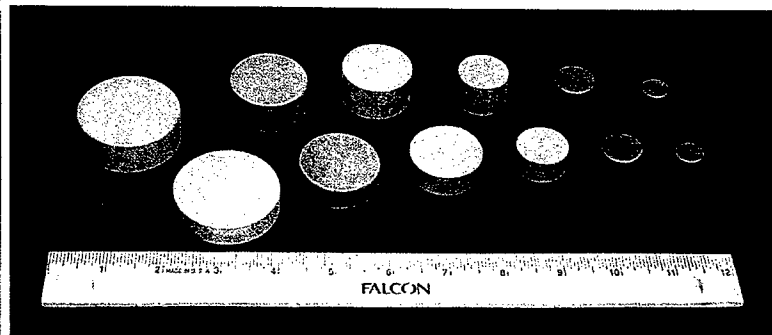


Figure 17. Simulated Mines

Several image sequences were obtained before and after burying the simulated landmines. The factors controlled during image acquisition were: resolution of the camera, angle of the camera with respect to a vertical, size of the simulated landmines, horizontal distance between camera positions, and amount of illumination. Figures 18 and 19 show matching sample images obtained by the CCD camera before and after the landmines were buried. Figure 20 shows the location where landmines are buried in Figure 18. Extreme care was observed in burying the simulated landmines so that the terrain does not look as if it had been disturbed.

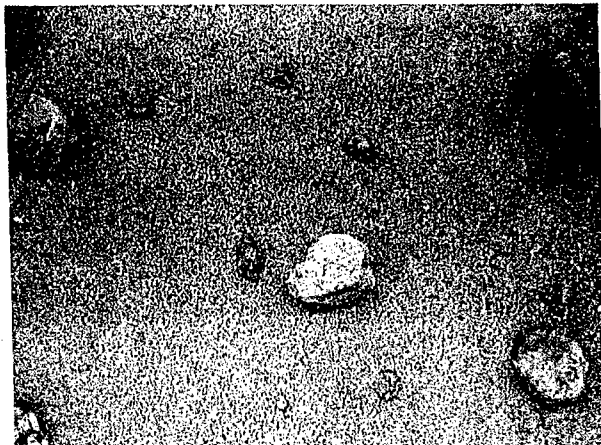


Figure 18. Terrain Before Mines were Buried

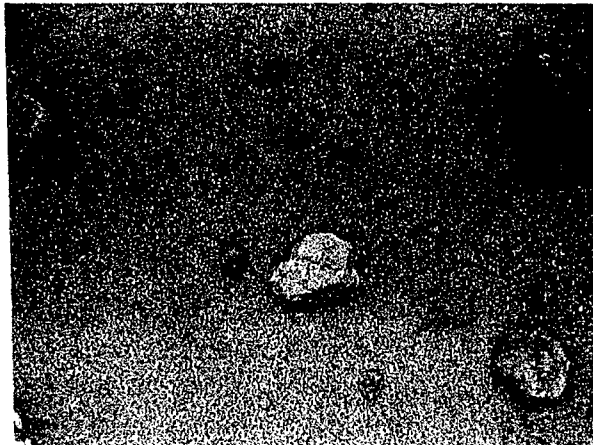


Figure 19. Terrain After Mines were Buried

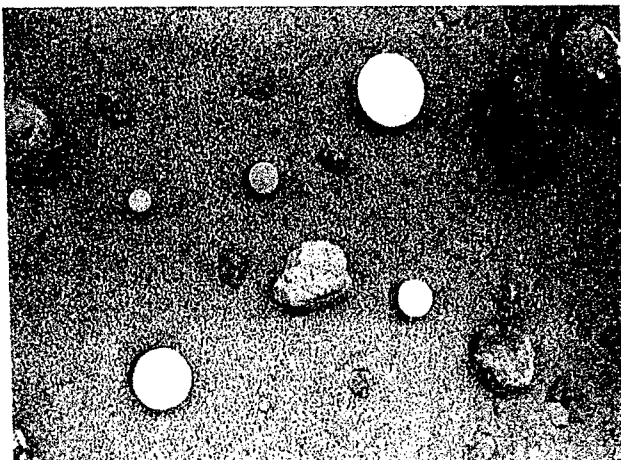


Figure 20. Terrain with Mines at Bury Locations

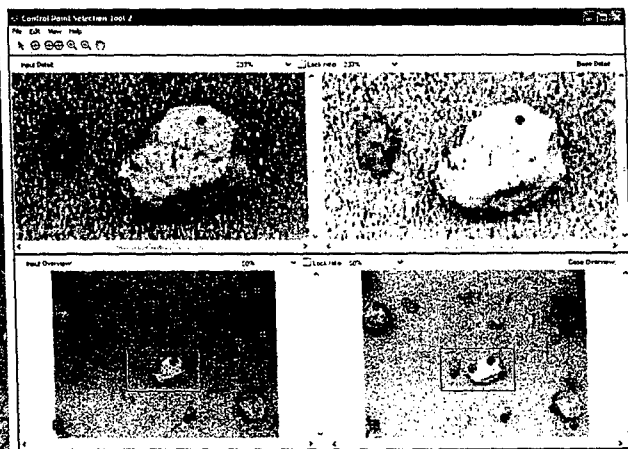


Figure 21. Registration Points on Corresponding Images

The image registration process developed is as follows: **Image acquisition.** Images are acquired at periodic time intervals. The images are recorded for future use. **Feature selection.** Identify natural landmarks on two corresponding images. Salient and distinctive objects (regions of high contrast, edges, contours, line intersections, corners, etc.) are detected. **Feature matching.** Find correspondence between two sets of natural landmarks. Figure 21 shows several matched features corresponding to Figures 18 and 19. **Estimate transform model.** The type and parameters of the mapping functions that align both images are estimated. The parameters of the mapping functions are estimated using the established feature correspondence. **Image transformation and integration.** The sensed image is transformed by means of the mapping functions. Both images (new or sensed image, and prior or base image) can be overlaid.

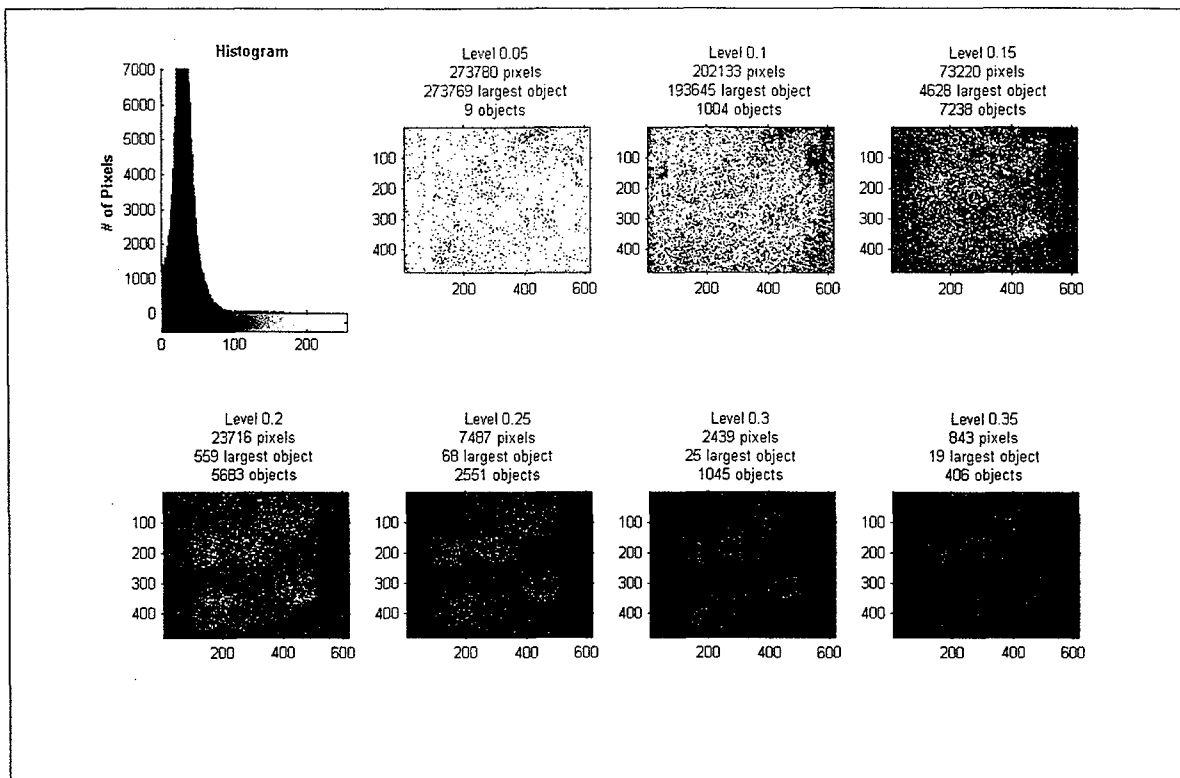


Figure 22. Analysis of Registered Images

The change detection methodology developed is as follows: **Histogram equalization.** The sensed image is corrected for variations in light intensity with respect to the base image. **Differentiation.** Subtract the sensed image (after being transformed and equalized) from the base (prior) image. Significant differences (changes) should show as higher intensity levels in the resulting image. **Histogram of difference.** Calculate the histogram of the difference of registered images. **Progressive threshold.** Calculate several (six to ten) threshold levels at equally spaced areas under the histogram curve. Use these threshold levels to produce corresponding binary images. Figure 22 shows the result of this analysis. **Cluster identification.** For each of the binary images, progressively use a square Region of Interest (ROI) to evaluate if the ROI is part of a positive cluster. The size of the ROI should be designed to fit the largest IED to be detected (depends on the sensor resolution). A cluster is detected if the percent of positive pixels in the ROI exceeds the percent of positive pixels in the whole image by a controlled sensitivity margin. This margin should be used as a parameter to determine the Receiver Operating Characteristic (ROC) curve. Adjacent positively detected regions should be aggregated into a larger positive region.

The factors controlled during image processing were: the number of registration points used, the size of the clustering region of interest, and the sensitivity margin for positive identification.

The results obtained with this methodology are very encouraging. The methodology was able to detect all landmines when the image registration produced a good match. Figures 23 and 24 illustrate the results of applying this methodology to the images in Figures 18 and 19. The probability of false alarm was significantly reduced when the camera orientation was always vertical and maintained the same orientation when the two registered images were acquired.

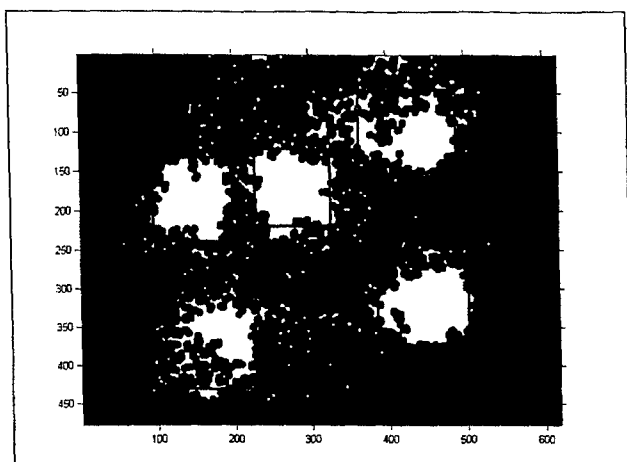


Figure 23. Detected Clusters.

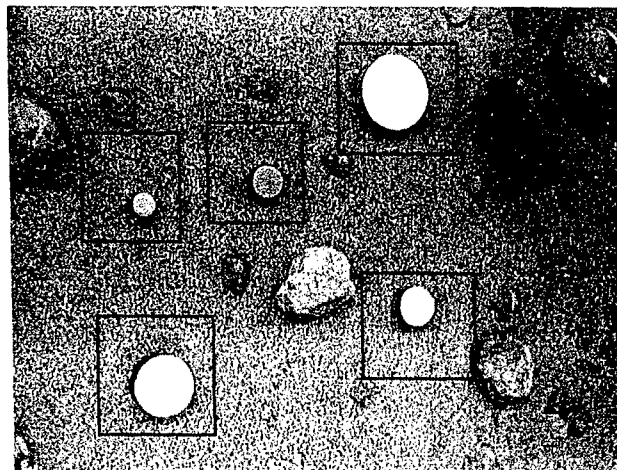


Figure 24. Mapping Detected Clusters on Image.

Future Work for IED and Landmine detection by image registration.

Several issues need to be researched and resolved before this methodology could be used as intended. First, the image registration process requires manual intervention. This process should be automated to be of practical use. In the area of automatic landmark identification, Karl Rohr [Rohr 1997] has used differential operators to identify points with high degree of intensity variation. We will adapt the technique developed by K. Rohr [Rohr 1997] for detecting point. Matching landmarks from two images will be accomplished using Johnson's version [Johnson 1999] of the iterative closest point (ICP) algorithm originally developed by Zhang [Zhang 1994].

Also, we would like to conduct tests to quantify probability of detection and false alarm using levels of camera resolution likely to be deployed in the field. The tradeoff between probability of detection and false alarm rate will be displayed using standard receiver operating characteristic (ROC) curves.

The following are extensions of the current work that we would like to conduct:

(1) Automate the image registration process.

The image registration process used requires manual intervention. This process needs to be automated to be of practical use. We would like to explore techniques to automatically identify natural landmarks that are most suitable to be identified in subsequent images, and also to provide precise image registration. We will determine processing speed and computing requirements.

(2) Improve the change detection algorithm.

The probability of false alarm increases as the camera position and orientation diverge for the two registered images, as well as when the lighting conditions change significantly. We would like to explore techniques to make the analysis and detection less sensitive to these sources of variability between image sequences. We would like to conduct laboratory experiments to test the effect of illumination changes and lower camera resolution that are more realistic for field tests. We will analyze and present results using receiver operating characteristic curves to compare discrimination between real and false detection. We will determine processing speed and computing requirements.

(3) Explore other imaging technologies

We would like to explore the capability of other sensor technologies, such as Ladar or infrared imaging, to provide an improved solution to the land mine detection problem by image registration of sequences of aerial images. Registration using Ladar is likely to be a 3-dimensional problem, as opposed to the 2-dimensional case in our approach. We will seek collaboration in this regard from researchers at JPL-NASA.

(4) Planning for static and fly-over field tests.

We would like to initiate planning of field tests that would provide images in more realistic environments. We would like to explore options, possibilities and costs associated with conducting these tests.

(5) Systems requirements analysis.

We would like to initiate a systems requirements analysis of likely implementation scenarios, so that future development meets realistic conditions and constraints. This would include determining various implementation issues such as: the image resolution required for specific dimensions of detectable objects, lens selection and number of frames per second to be acquired as function of flight altitude and velocity, and image location resolution by integrating a GPS stamp on image sequences.

An abstract has been submitted to the American Institute of Aeronautics and Astronautics (AIAA) Space Conference in Long Beach, August 31 to September 1, 2005 (sponsored by Raytheon). Pending acceptance, the paper will be presented at the AIAA Space 2005 Conference next August. The paper will describe the methodology, testing environment, tests conducted and results obtained. Kevin Lim, a masters degree student in Industrial Engineering is completing his M.S. thesis working on this project. He is expected to finish in Fall of 2005.

Skin Cancer Screening using Image Registration and Change Detection

The advice from the medical community to individuals who have high risk of developing skin cancer is to monitor changes in their mole size, color, and shape. It is a challenge to do this type of screening visually, and some individuals resort to taking pictures to keep records to monitor changes over time. The photographs are then matched and compared visually to the skin lesions. This research project is intended to automate this process by using computer image processing techniques to register and compare images of the same individual obtained at repeated time intervals. We speculate that by automatically registering and comparing images of skin lesions, early detection of moles or lesions undergoing growth can be achieved more consistently than relying on patient's or physician's memory or by visual inspection alone.

Pilot Study and Results for Skin Cancer Screening.

A methodology was developed to compare registered images to detect possible changes, and measure them when changes were detected. Development and testing was conducted on synthetic images. The images below illustrate the case of using this technique for screening skin cancer. The methodology should be able to detect mole growth as shown in Figure 26 relative to Figure 25. Figures 27 through 30 show the detected growth and measure its change as a percentage.

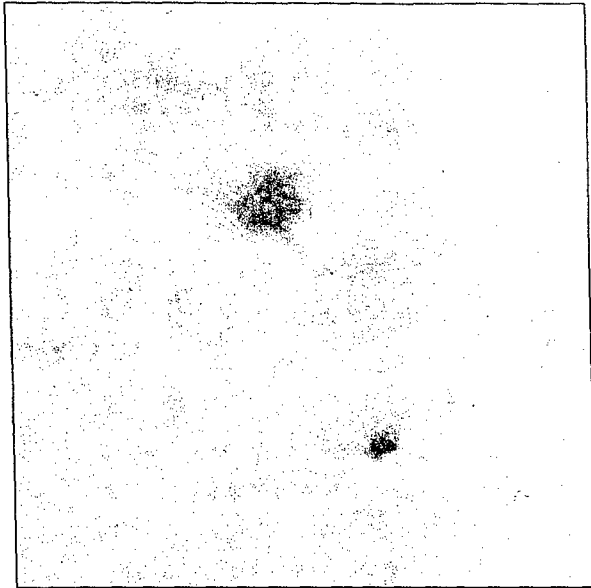


Figure 25. First (Base) Image

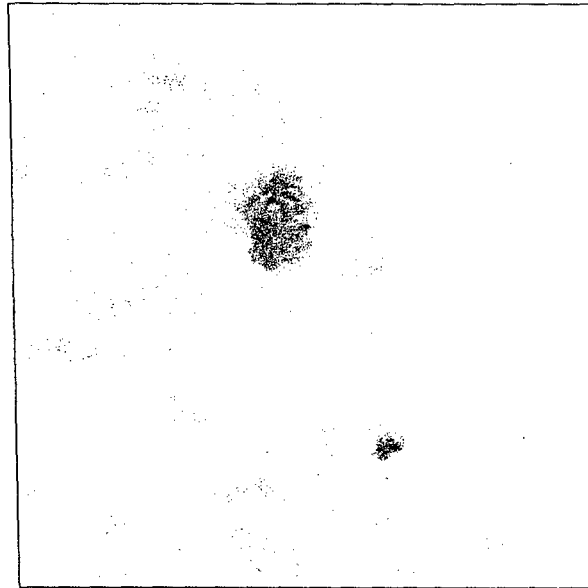


Figure 26. Second Image After Mole Growth

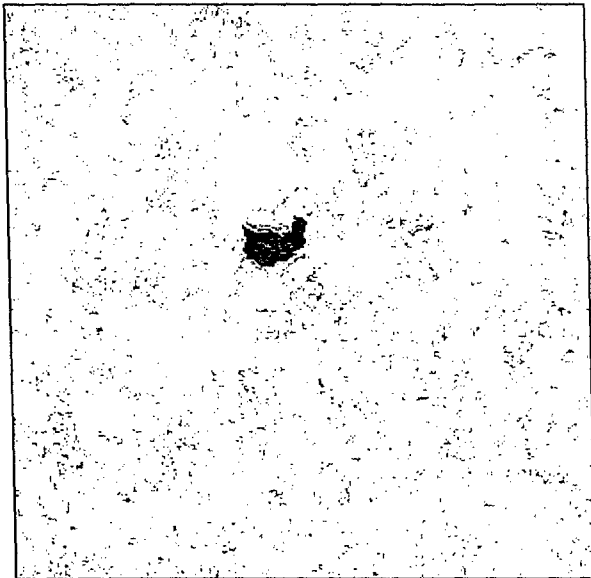


Figure 27. Difference in Registered Images

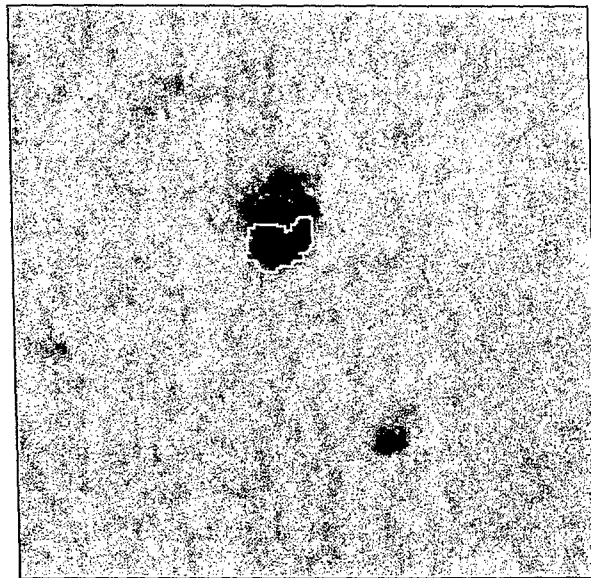


Figure 28. Overlaid Boundary of Growth

In the area of image registration for skin cancer screening, there are some recent journal publications that are relevant to this project. Bruce McGregor developed an algorithm to register images of pigmented skin lesions [McGregor 1998]. The work by Andrea Sboner [Sboner 2003] expands on classification of melanoma images, Philippe Schmid-Saugeon [Schmid-Saugeon 2003] published an article on computer-aided diagnostics of skin cancer. Joe Stanley [Stanley 2003] wrote of using fuzzy logic methods to discriminate images of melanoma from benign lesions.

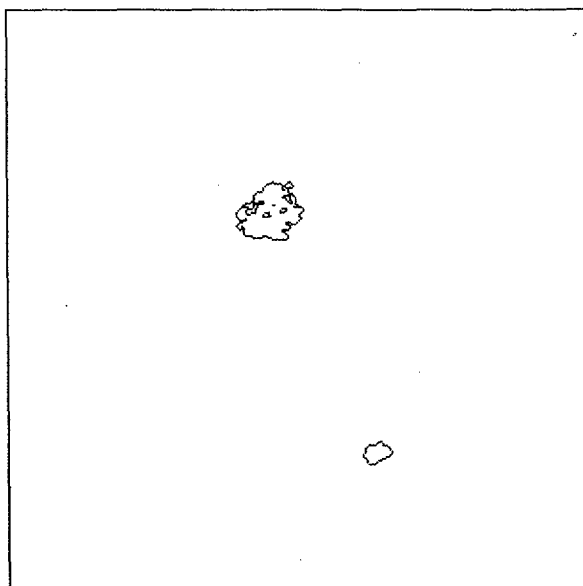


Figure 29. Boundary of Original Mole
Area : 929 pixels

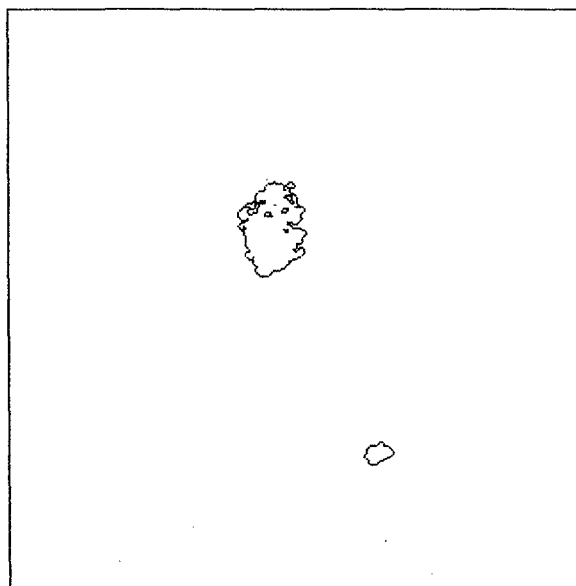


Figure 30. Boundary of Mole After Growth
Area : 1433 pixels, percent growth: 54.2%

Future Work for Skin cancer Screening by Image Registration.

The following are extensions of the current work that we would like to conduct:

(1) Team with dermatologists.

We would like to develop a team and establish collaboration with dermatologists interested in this research project. During Summer 2005, we will conduct visits to possible collaborators in dermatology departments at UCLA, UCSD and the Sloan-Kettering Cancer Center in New York. The objective will be to bring expertise into this project from the medical field, and initiate relationships for collaboration and preparation of future proposal for external funding.

(2) Automate the image registration process.

The image registration process currently being used requires manual intervention. This process would benefit from increased use of automation to be of greater practical value. We would like to replicate the techniques developed by McGregor [McGregor 1998] and Rönning [Rönning 1998] to automatically register skin images and explore improving their accuracy and ease of use.

(3) Develop a body map for image acquisition.

In order for this methodology to work efficiently it is proposed that a simple and effective method to map images acquired from various parts of the body be developed. The MD Anderson Cancer Center at the University of Texas currently uses a paper chart. It is proposed that a computerized schematic be developed to map digital images of the human body.

(4) Test methodology with human subjects.

During Fall 2005 and Winter 2006, we would like to collect images using volunteer human subjects at Cal Poly. A proposal has been submitted to the Cal Poly Committee for use of

Human Subjects. In this study, we will photograph only the parts of the body that are normally exposed to the sun, specifically, arms, neck and face. Subjects will be asked to come twice, at 3 to 6-months intervals to take a second set of photographs. The two sets of photographs will be used to test the image processing methodology to detect changes in skin mole size or color. We may have expenses related to remuneration of human subjects, and of medical support to review the images for possible abnormalities. Issues still needing resolution are body mapping (item 3 above), illumination techniques that provide quality images, and image system calibration so that changes in mole size can be reported not only in pixels but also in inches or millimeters.

References

Benameur, Said, et al, "3D/2D registration and segmentation of scoliotic vertebrae using statistical models" *Computerized Medical Imaging and Graphics*, Elsevier, 27 (2003) 321–337

Hasler, David, et al, "Outlier Modeling in Image Matching", *IEEE Transactions On Pattern Analysis And Machine Intelligence*, Vol. 25, No. 3, March 2003

Johnson, Andrew E. and Matthies, Larry H., "Precise Image-Based Motion Estimation for Autonomous Small Body Exploration", *5th International Symposium on Artificial Intelligence, Robotics and Automation in Space*, 1999 (iSAIRAS'99), pp. 627-634.

Macedo, J and Hernandez, F. (Honeywell), "Computer Vision Inspection of Die Cast Valve Seats", *Third Bolivarian Mechanical Engineering Conference (COBIM III)*, July 22-24, 2003, Lima, Peru.

Macedo, J., Manduchi, R. (JPL), and Matthies, L. (JPL), "Ladar-based Discrimination of Grass from Obstacles for Autonomous Navigation," *Proceedings of the International Symposium on Experimental Robotics (ISER-2000) Conference*, December 10-13, 2000, Honolulu, Hawaii.

Matthies, L. (JPL-NASA), Macedo, J. and Manduchi, R. (JPL), "Statistical Pattern Recognition of Ladar Data for Discrimination of Grass from Obstacles in Autonomous Navigation," *Proceedings of SPIE – Unmanned Ground Vehicle Technology III*, April 16-17, 2001, Orlando, Florida.

Matthies, L., Bergh, C. Castano, A (JPL-NASA), Macedo, J., Manduchi, R. (UCSC), "Obstacle Detection in Foliage with Ladar and Radar", *Proceedings of the 11th International Symposium of Robotics Research (ISRR)*, October 19-22, 2003, Sienna, Italy.

Maintz, J. B. and Viergever, M. A., "A Survey of Medical Image Registration" *Medical Image Analysis*, Oxford University Press, (1998) volume 2, number 1, pp 1–37

McGregor, Bruce, "Automatic Registration of Images of Pigmented Skin Lesions", *Pattern Recognition*, Pergamon, Vol. 31, No. 6, pp. 805–817, 1998

Pluim, Josien P.W., and Fitzpatrick, J. Michael, editorial page, *IEEE Transactions On Medical Imaging*, Vol. 22, No. 11, November 2003.

Rohr, Karl, "On 3D Differential Operators for Detecting Point Landmarks", *Image and Vision Computing*, Elsevier, 15 (1997) pp. 219-233.

Sboner, Andrea, et al, "A Multiple Classifier System for Early Melanoma Diagnosis", *Artificial Intelligence in Medicine*, Elsevier, 27 (2003) pp. 29-44.

Schmid-Saugeon, Philippe, et al, "Towards a computer-aided diagnosis system for pigmented skin lesions", *Computerized Medical Imaging and Graphics*, Elsevier, 27 (2003) pp. 65-78.

Stanley, R. Joe, et al, "A Fuzzy-Based Histogram Analysis Technique For Skin Lesion Discrimination In Dermatology Clinical Images", *Computerized Medical Imaging and Graphics*, Elsevier, 27 (2003) pp. 387-396.

Zhang, Z., "Iterative point matching for registration of free-form curves and surfaces", *International Journal on Computer Vision*, 13 (2) (1994) pp. 119-152.

Zitova, Barbara, and Flusser, Jan, "Image registration methods: a survey", *Image and Vision Computing*, Elsevier, 21 (2003) 977-1000

Adaptive Change Detection Methodology for Buried Mine and IED Detection from Space

Jose A. Macedo* and Kevin Lim†

California Polytechnic State University, San Luis Obispo, California, 93407

The paper describes an image processing methodology developed to detect buried improvised explosive devices (IEDs) and landmines. The methodology assumes that sequences of aerial images of the same terrain, for instance a dirt road, can be obtained at periodic intervals of time. Corresponding images of the same terrain from two consecutive sequences can be processed to detect if the terrain has changed or been disturbed and may contain buried landmines. The image processing methodology requires registering corresponding images by identifying matching natural landmarks in both images, then calculating and performing scale and perspective transformations so that both images can be superimposed and compared. An adaptive methodology to compare registered images was developed in order to avoid false alarms due to changes in illumination or other small natural changes. The methodology was tested in a laboratory setting using a medium size Cartesian robot to manipulate a charge-coupled device (CCD) camera. A sand and rock box was placed within the robot workspace volume. Several cylindrical disks of controlled sizes and aspect ratios were used to simulate landmines. Several image sequences were obtained before and after burying the simulated landmines. Extreme care was observed in burying the simulated landmines so that the terrain does not look as if it had been disturbed. The results obtained with this methodology are good. The paper will describe the methodology, testing environment, tests conducted and results obtained.

I. Introduction

Image registration is the process of overlaying two or more images of the same scene. These images may have been obtained at different times, and/or from different viewpoints, and/or by different types of sensors. The two images are then geometrically aligned to integrate the information from multiple sources and in this case to detect change.

In this project we are interested in developing a fast and accurate image registration and change detection methodology to locate buried landmines and improvised explosive devices (IEDs). This application is of great importance considering the current military situation in Iraq, where many casualties are due to roadside bombs. The intent is to help alleviate the problem of roadside bombs claiming lives in situations like present day Iraq. Figure 1 show advancing ground forces along a main supply route in Iraq. Figure 2 through 4 show various IEDs disguised as debris along the roadside in Iraq. Recent reports indicate that IEDs are being buried making them more difficult to detect. Figure 5 shows a weathered landmine found in Croatia, and Figure 6 shows training exercises to use equipment to detect landmines in the border between Chile and Bolivia. These images suggest that we need a methodology to detect recently buried objects that range in size between a few inches to a few feet.

The methodology in this paper assumes that sequences of aerial images of the road or terrain can be obtained at periodic time intervals. By registering and comparing high resolution images obtained before and after IEDs or landmines are placed on the ground, it will be possible to identify and locate them. Corresponding images of the same terrain from consecutive sequences can be processed to determine if the terrain has changed or been disturbed. Change detection algorithms need to be fast, sensitive and have low false alarm rates.

* Associate Professor, Industrial and Manufacturing Engineering Department.

† Graduate Student, Industrial and Manufacturing Engineering Department.

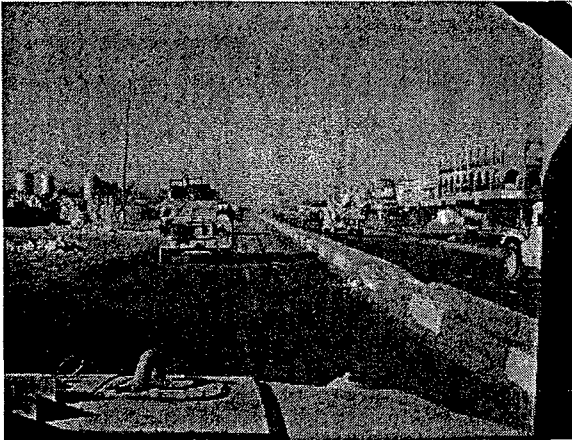


Figure 1. Scenario example, roads in Iraq



Figure 2. IED encased in concrete



Figure 3. IED hidden under rocks, side view



Figure 4. IED hidden in bag

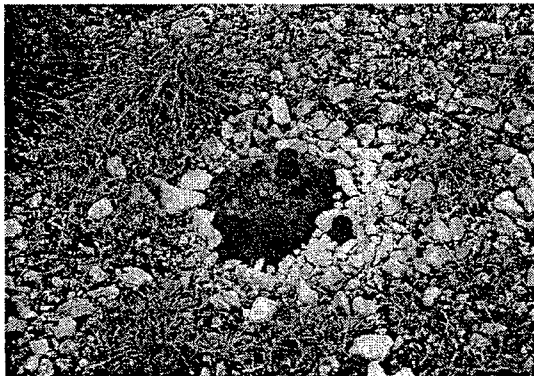


Figure 5. Weathered landmine in Croatia



Figure 6. Landmine Detection Training

The solution approached assumes that sequences of aerial images of the road or terrain can be obtained at periodic time intervals. We speculate that by registering and comparing high resolution images obtained before and after IEDs or landmines are placed on the ground, it will be possible to identify and locate them. Corresponding images of the same terrain from consecutive sequences can be processed to detect if the terrain has changed or been disturbed. The image processing methodology requires registering corresponding images by identifying matching natural landmarks in both images, then calculating and performing scale and perspective transformations in order that both images can be superimposed and compared.

Figure 7 illustrates a possible deployment scenario in which images from unmanned aerial vehicles (UAV) are used for change detection of IEDs along supply routes. Corresponding images obtained earlier (ie. the prior hour, day or week) can be compared to images obtained ahead of the advancing ground forces. In this scenario, location information about positive detections is communicated to advancing ground forces.

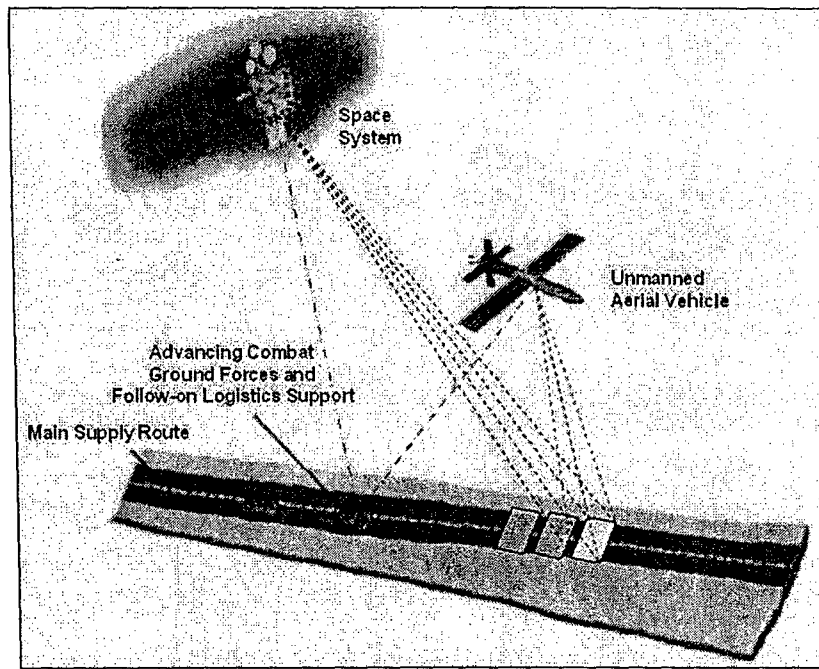


Figure 7. Illustration of Deployment Scenario –
Change Detection of IEDs along Supply Route

II. Methodology

The image processing methodology registers corresponding images by identifying matching natural landmarks in both images. The program calculates and performs scale and perspective transformations so that both images can be superimposed and compared. A change detection algorithm is then applied to detect potential IEDs and landmines with low false alarms due to changes in illumination or other small natural changes.

The image registration process developed is as follows: **Image acquisition.** Images are acquired at periodic time intervals. The images are recorded for future use. **Feature selection.** Identify natural landmarks on two corresponding images. Salient and distinctive objects (regions of high contrast, edges, contours, line intersections, corners, etc.) are detected. **Feature matching.** Find correspondence between two sets of natural landmarks. **Estimate transform model.** The type and parameters of the mapping functions that align both images are estimated. The parameters of the mapping functions are estimated using the established feature correspondence. **Image transformation and integration.** The sensed image is transformed by means of the mapping functions. Both images (new or sensed image and prior or base image) can be overlaid.

The change detection methodology developed is as follows: **Histogram equalization.** The sensed image is corrected for variations in light intensity with respect to the base image. **Differentiation.** The sensed image (after being transformed and equalized) is subtracted from the base (prior) image. Significant differences (changes) should show as higher intensity levels in the resulting image. **Histogram of difference.** Calculate the histogram of the difference of registered images. **Progressive threshold.** Calculate six threshold levels using the mean and standard deviation of the histogram. These threshold levels are used to produce corresponding binary images. **Cluster identification.** For each of the binary images, a series of morphological operators are used to find connected objects. A square Region of Interest (ROI) is used to evaluate the size and density of connected objects and to decide if they are a detected cluster. The size and density decision variables will depend on the size of IEDs to be detected and the imaging resolution.

III. Laboratory Experiments

This methodology was tested in a laboratory setting using a medium size Cartesian robot to manipulate a CCD camera. A sand and rock box was placed within the robot workspace volume. Figure 8 shows the laboratory setup. Several cylindrical disks of controlled sizes and aspect ratios, shown in Figure 9, were used to simulate landmines.

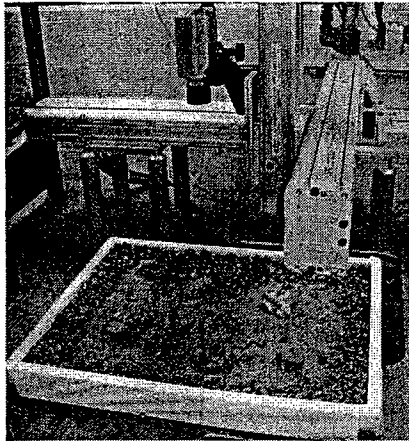


Figure 8. Laboratory Setup

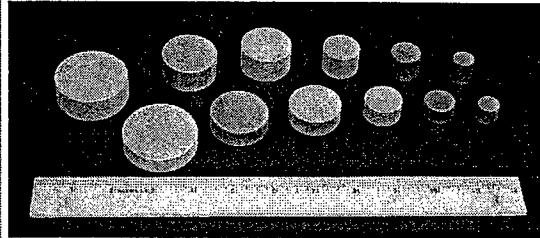


Figure 9. Simulated Mines

Details on the equipment used are as follows. The two cameras used in the experiments were SONY DFW-V500 (640 x480), and SONY XCD-X710CR (1024x768). This paper describes only results obtained with the SONY XCD-X710CR. Both cameras were used with an 8.5-mm lens. The dimensions of the sand and rock box were 18 in by 25 in. The camera was at a distance of 28 inches from the sand box. The diameters of the cylindrical disks used in the experiments were: 0.55 in (14 mm), 0.78 in (20 mm), 1.0 in (25 mm), 1.5 in (38 mm), and 1.93 in (49 mm). The height of the disks used in this paper was 0.5 in (13 mm).

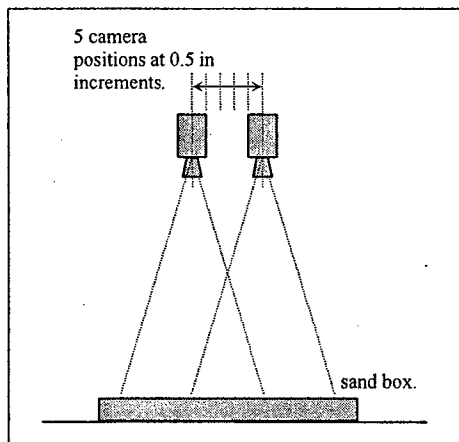


Figure 10. Five Camera Positions

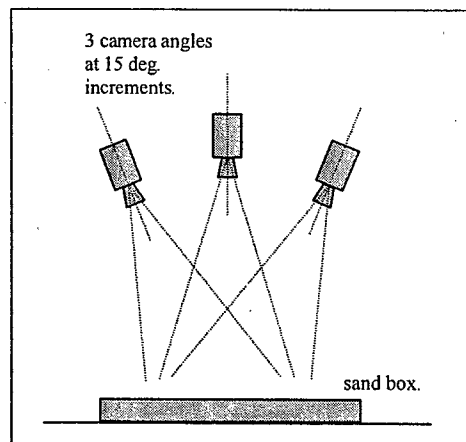


Figure 11. Three Camera Orientations

The camera position and orientation was controlled in two modes as follows. The first mode was displacement only, as shown in Figure 10, where the camera remained perpendicular to the sand box, and five images were obtained at 0.5 in increments. The second mode was rotation and displacement, as shown in Figure 11, where three camera orientations at 15 degree intervals were used, and the camera position was displaced as needed to observe the same area in the sand box. Preliminary image processing and data analysis using images obtained using rotation of the cameras (as in Figure 11), result in large number of false detections. An actual field platform such as an unmanned aerial vehicle (UAV) or space system will not be subjected to significant rotation, so this problem is not an issue. Therefore, this paper describes results obtained with the displacement only mode of

controlling the camera movements (as shown in Figure 10). Other factors controlled during image acquisition were: amount of illumination and location of the light sources. We used dimmer controls to introduce small variations in the amount of illumination during our experiments, and our methodology proved robust to these changes. Changes in the location of the light source produced shifting shadow patterns that resulted in large number of false detections. Later in this paper, in the section "plans for future work," we discuss an approach that we propose to eliminate this problem. This paper describes results obtained with light sources at fixed locations.

Images were obtained at each of the five camera positions (as in Figure 10) both before and after burying the simulated landmines. All five simulated landmines were buried at the same time at various random locations within the sand box. An additional image was obtained to show the location where the simulated mines were going to be buried. Extreme care was observed in burying the simulated landmines so that the terrain does not look as if it had been disturbed. The process was repeated four times, for a total of 40 paired images plus 4 additional images showing the bury locations. Figures 12 and 13 show matching sample images obtained before and after the landmines were buried. Figure 14 shows the location where landmines are buried in Figure 13. Images in Figures 12 through 14 were obtained with the SONY DFW-V500 with a resolution of 640 x480 pixels.



Figure 12. Terrain Before Mines were Buried

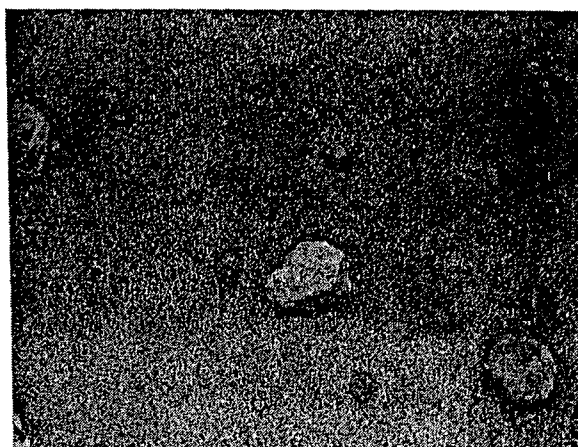


Figure 13. Terrain After Mines were Buried

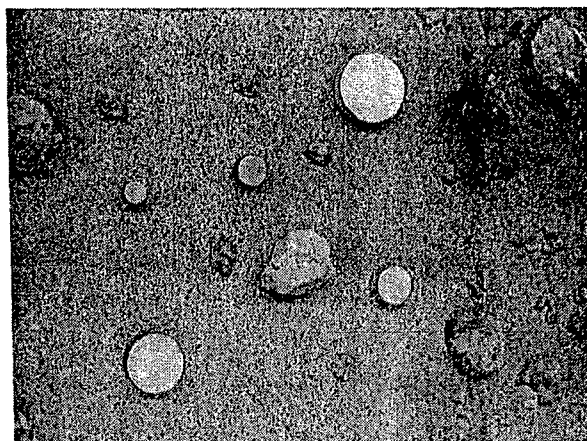


Figure 14. Terrain with Mines at Bury Locations
(Set 1, Camera Resolution 640 x480)

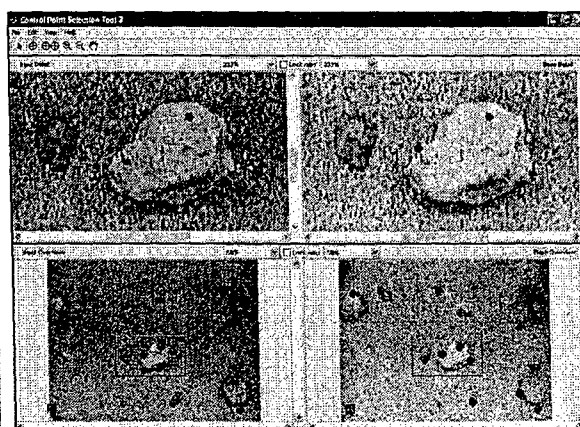


Figure 15. Registration Points on Corresponding
Images

When the image processing methodology described earlier in Section II is applied to the images in Figures 12 and 13, the first step is to register both images by identifying and matching natural landmarks. Figure 15 shows an example in which 18 matching natural landmarks were identified on both images and used as registration points. We also investigated the effect of the number of registration points used on the probability of detection and false alarms.

After the images are registered, the change detection methodology is applied. Figure 16 shows an analysis of the image that is produced by subtracting the registered images. This image difference is viewed at a progression of seven threshold levels. In Figure 16, the lower left frame illustrates the five clusters of white dots that are located where the simulated mines were buried. The methodology identifies these clusters by using morphological operators.

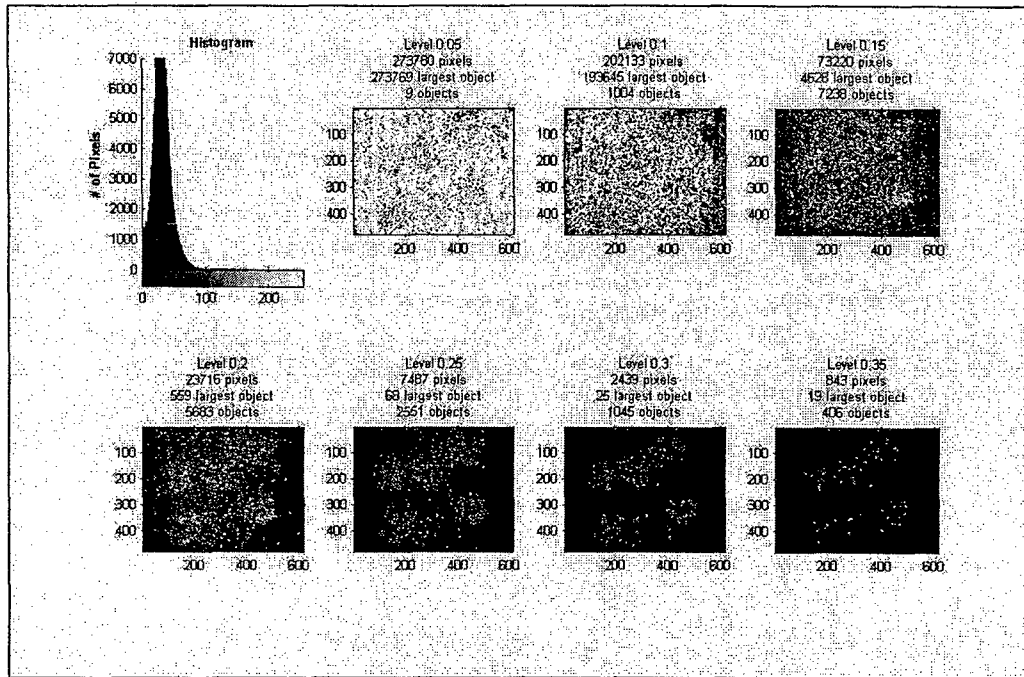


Figure 16. Analysis of Registered Images at Various Threshold Levels

Figure 17 shows the clusters detected when applying the change detection process. Figure 18 again shows the location where the simulated mines were buried. Rectangular red overlays have been manually placed on each of the detected cluster in Figure 17 and on each of the mine locations in Figure 18. The size of the clusters are not necessarily correlated to the size of the mines. Burying the simulated mines disturbed a region larger than the diameter of the mines.

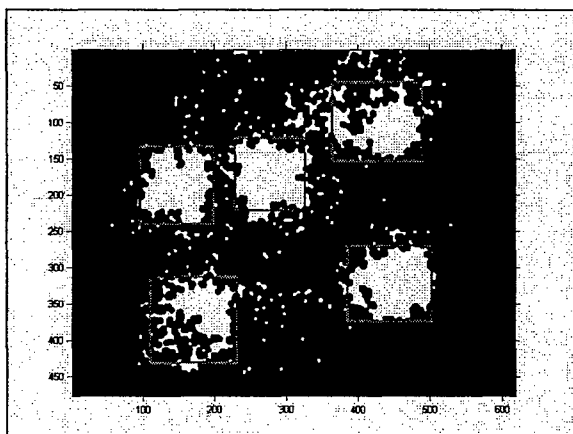


Figure 17. Detected Clusters.

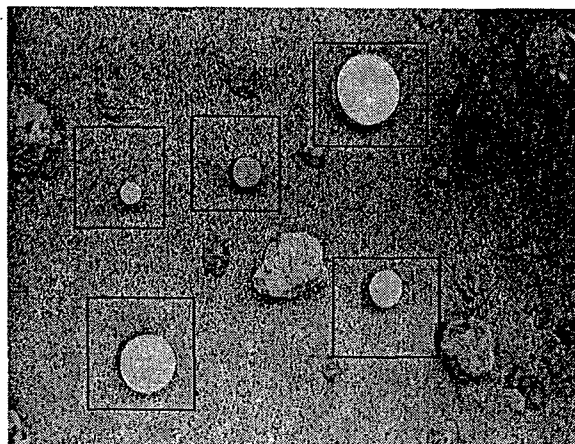


Figure 18. Mapping Detected Clusters on Image.

IV. Results

The results obtained with this methodology are very encouraging. This methodology was able to detect all landmines when the image registration produced a good match. In this section we demonstrate results obtained with images obtained the SONY XCD-X710CR with a resolution of 1024x768 pixels. Figures 19 and 20 show matching sample images obtained before and after the landmines were buried. Figure 21 shows the location where landmines are buried in Figure 20.

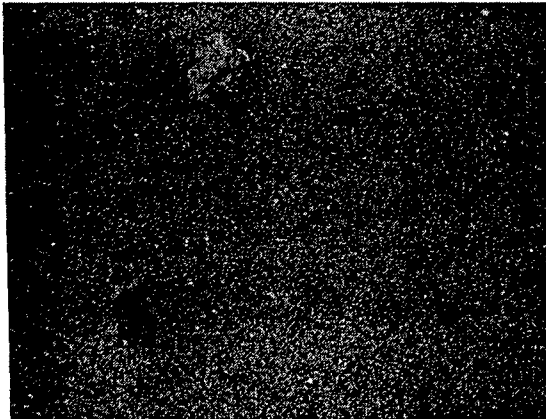


Figure 19. Terrain Before Mines were Buried

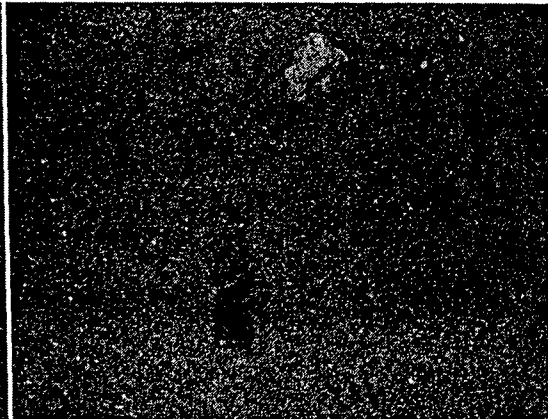


Figure 20. Terrain After Mines were Buried

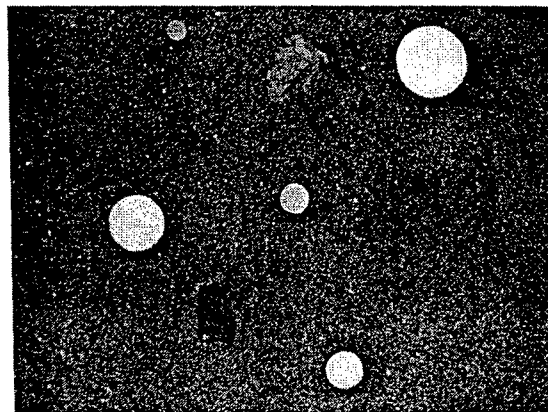


Figure 21. Terrain with Mines at Bury Locations

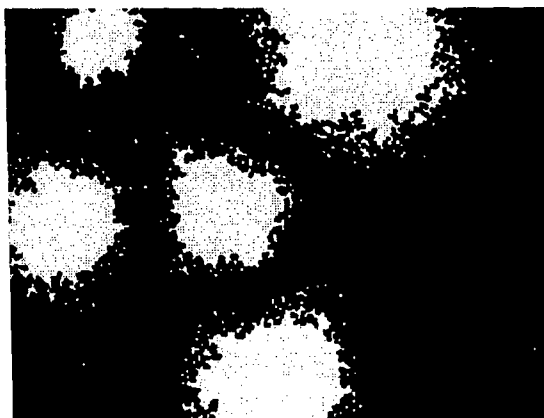


Figure 22. Best Case of Cluster Detection
(Camera Shift = 0, 20 Reg. Pts.)

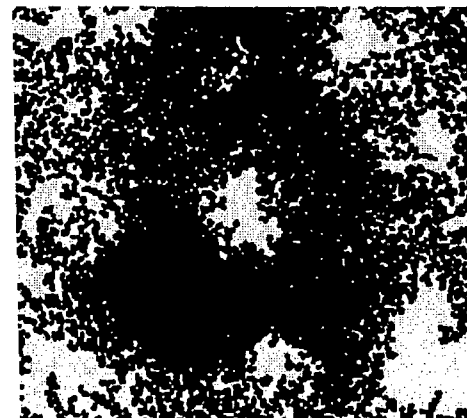


Figure 23. Worst Case of Cluster Detection
(Camera Shift = 25, 5 Reg. Pts.)

A. The Effect of Shifting Camera Position.

The registration and analysis was repeated using shifts of 0.5, 1.0, 1.5, 2.0, and 2.5 inches in camera position between images obtained before and after burying the mines. Figures 24 to 29 show the deterioration in the cluster detection as the camera displacement shifts from 0 to 2.5 inches. The first false alarm appears at 27 in Figure 28 in which a rock is detected as a change in the lower-right corner. This is typical of other images analyzed, so we can say that with this setup, the detection method works well for up to 1.5 inches of camera displacement.

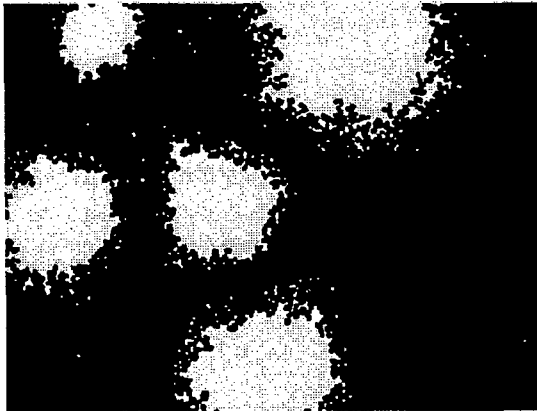


Figure 24. Camera Shift = 0 in, 15 Reg. Pts.

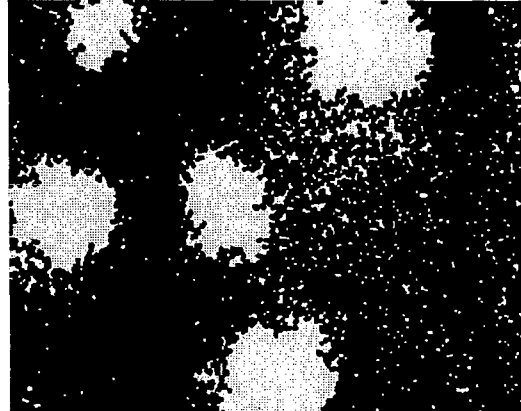


Figure 25. Camera Shift = 0.5 in, 15 Reg. Pts.

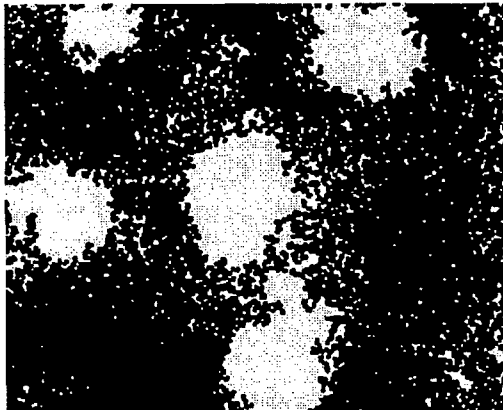


Figure 26. Camera Shift = 1.0 in, 15 Reg. Pts.

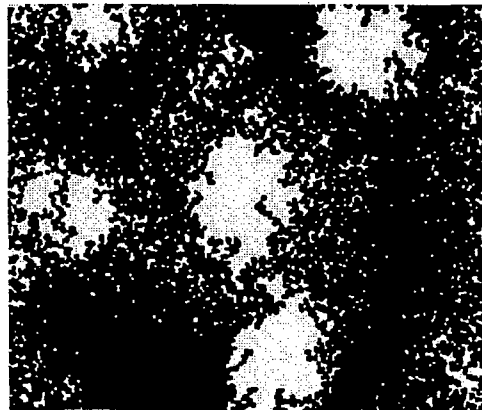


Figure 27. Camera Shift = 1.5 in, 15 Reg. Pts.

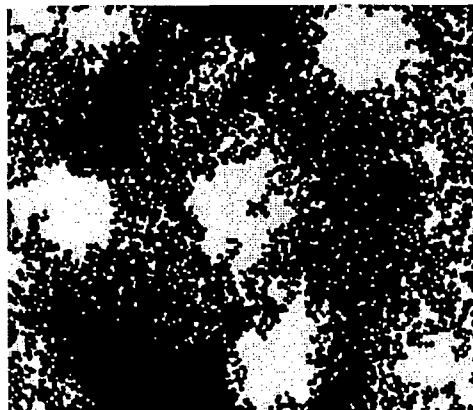


Figure 28. Camera Shift = 2.0 in, 15 Reg. Pts.

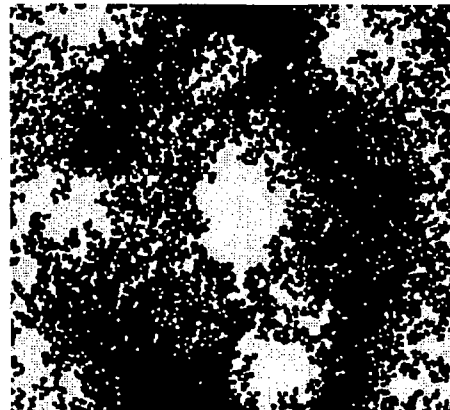


Figure 29. Camera Shift = 2.5 in, 15 Reg. Pts.

B. The Effect of Number of Registration Points.

The registration and analysis was repeated using 5, 10, 15, and 20 registration points on each image. Figures 30 through 33 show change detection clusters detected using a fixed camera position (zero shift) and 5, 10, 15 and 20 registration points. Results show that using 5 registration points is insufficient to produce a good match and be able to detect change. Increasing the number of registration points to 10 showed significant improvement and produced good results. Selecting 10, 15, or 20 registration points did not showed a significant difference.

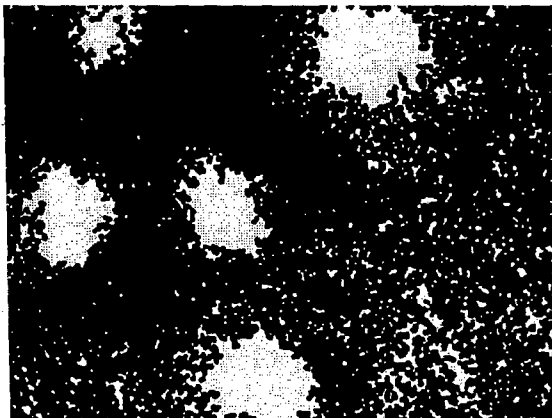


Figure 30. Camera Shift = 0 in, 5 Reg. Pts.

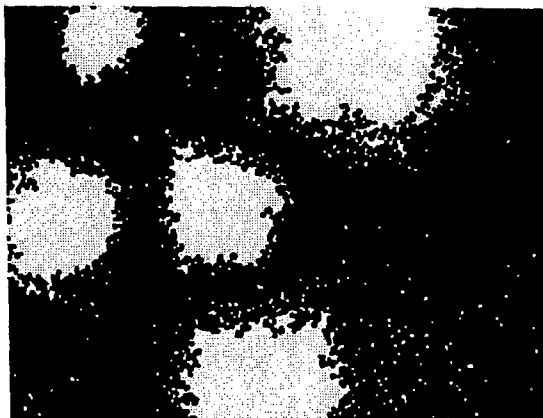


Figure 31. Camera Shift = 0 in, 10 Reg. Pts.

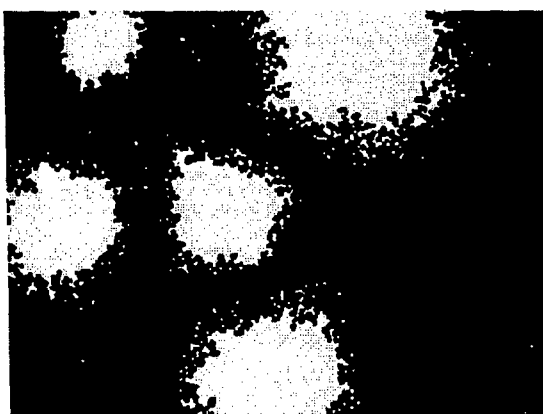


Figure 32. Camera Shift = 0 in, 15 Reg. Pts.

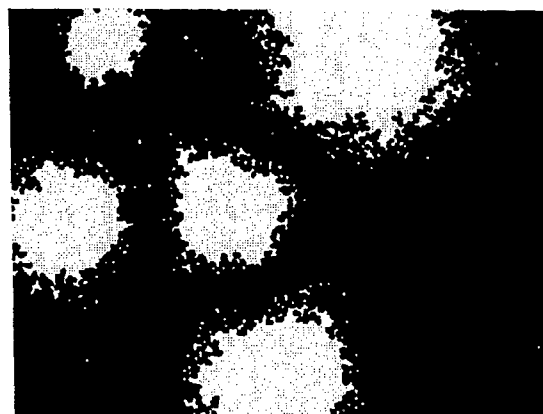


Figure 33. Camera Shift = 0 in, 20 Reg. Pts.

C. The Effect of Threshold Level

The registration and analysis was repeated for four threshold levels defined as $\mu + k\sigma$, where μ and σ are the mean and standard deviation of the image histogram, and k is a constant. The values of k were equal to 1.0, 1.2, 1.4 and 1.6. The best results were obtained for $k = 1.0$, or a threshold level of $\mu + \sigma$.

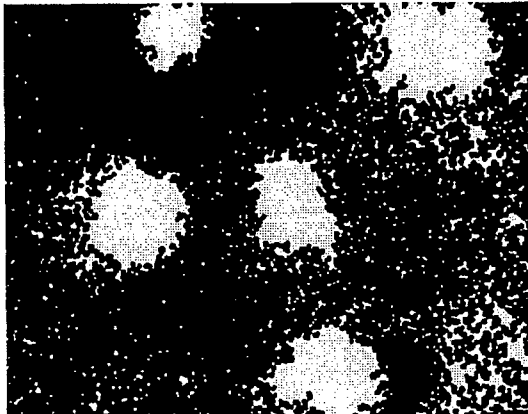


Figure 34. Thresh= 1.0, Shift= 0.5 in, 10 Reg. Pts.

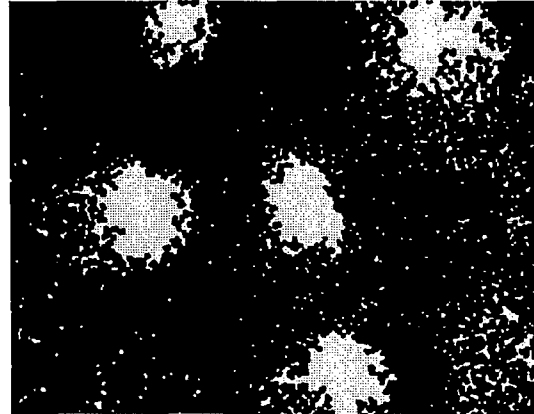


Figure 35. Thresh= 1.2, Shift= 0.5 in, 10 Reg. Pts.

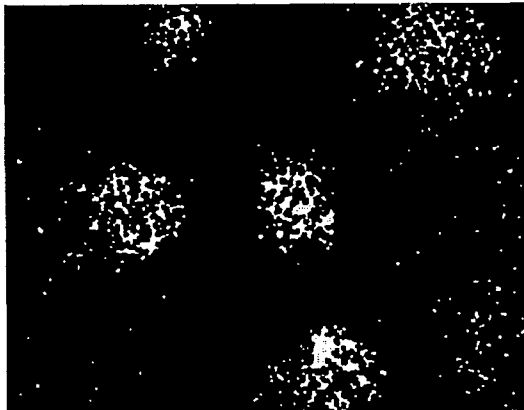


Figure 36. Thresh= 1.4, Shift= 0.5 in, 10 Reg. Pts.

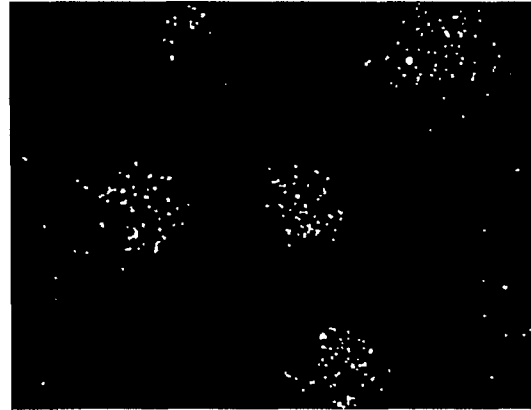


Figure 37. Thresh= 1.6, Shift= 0.5 in, 10 Reg. Pts.

V. Analysis

This section will quantify performance of the method by estimating the probability of correctly detecting a simulated landmine and the probability of false alarms.

We estimated the probability of detecting a simulated mine as the fraction of the number of detected pixels in a circular area of diameter defined by the largest detection made on that mine. For example, Figure 38 shows the circle that overlays the largest detected cluster for mine 2. We know that there was a mine in that location -that produced that much detectable change. To estimate the detection probability for the same mine under other processing parameters, we overlaid the same circle (diameter and location) on the new processed image. The fraction of detected area inside the circle is an estimate of the probability of detecting that mine with those processing parameters. For example the process in Figure 40 has a higher probability (0.893) of detecting the mine than the process in Figure 41. The process in Figure 41 has a low probability (0.113) of detecting the mine. We estimated these probabilities for each combination of mine size, camera displacement, number of registration points, and threshold level.

The probability of false detection (false alarm) was estimated for each frame as the ratio of detected pixels in the frame to total pixels after removing the areas corresponding to mines. For example Figure 39 shows the removal of the area corresponding to mine 2.

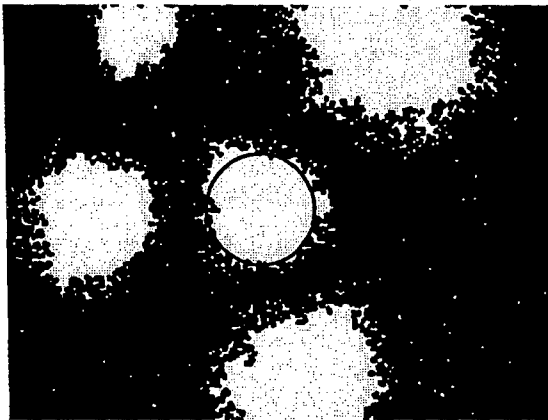


Figure 38. Circle for Largest Detection of Mine 2

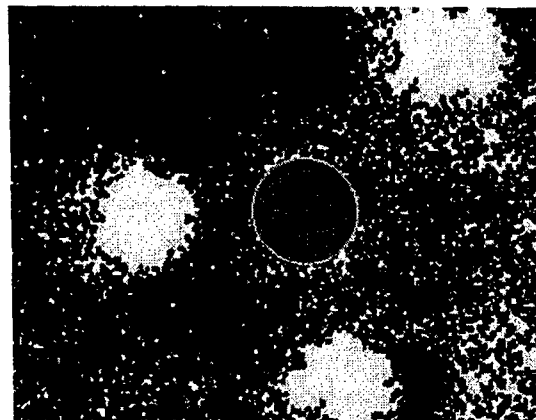


Figure 39. Mask Possible Detection Area of Mine 2

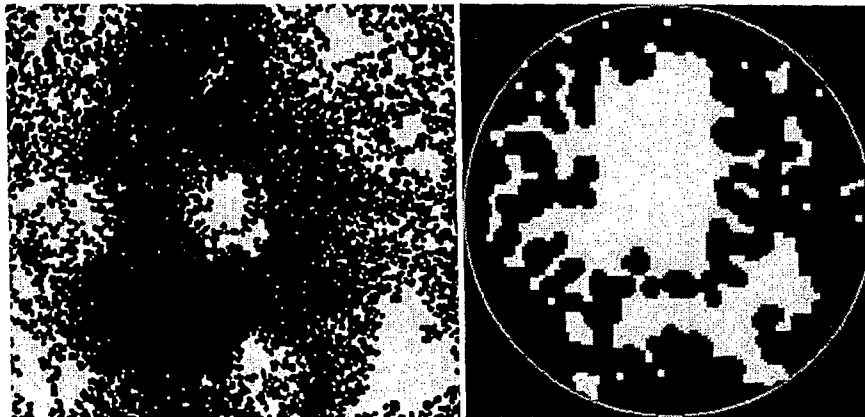


Figure 40. Probability of Detecting Mine 2 = 0.893

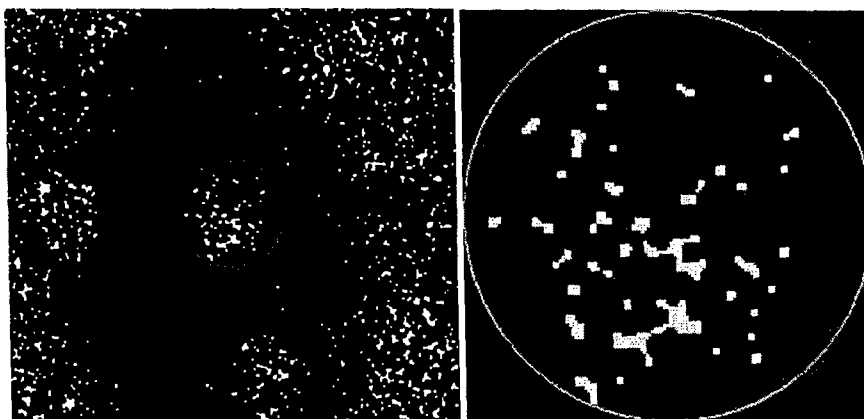


Figure 41. Probability of Detecting Mine 2 = 0.113

The probabilities of detection and probabilities of false alarm were grouped by camera shift, and plotted as Receiver Operating Characteristic (ROC) Curves. Figure 42 shows the ROC Curves for various camera shifts. A 45 degree line has been added for reference. These curves confirm that as the camera shift increases, the performance of detection degrades, but in all cases remains above the 45 degree reference line.

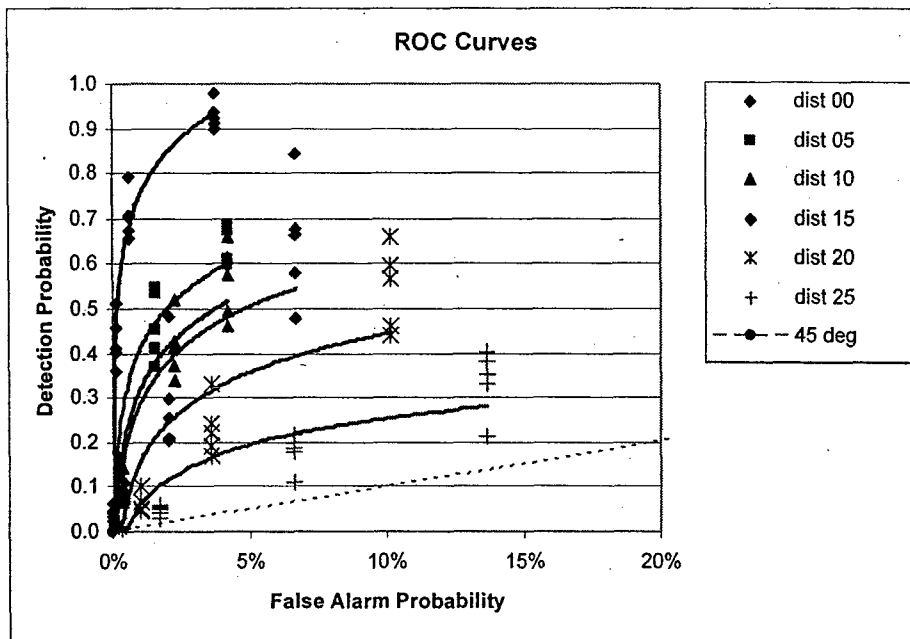


Figure 42. Receiver Operating Characteristic Curves

VI. Implications for Space Systems

It would be incorrect to extrapolate results obtained in a controlled laboratory environment to a field system and expect that the performance will follow. Some calculations, however, can be useful in planning future field tests. For example, the smallest simulated mine in the lab was 14 mm in diameter. When imaged with the SONY XCD-X710CR (resolution of 1024x768 pixels) from a distance of 28 inches, the mine's diameter was equivalent to 37 pixels across. This seems to be a large number of pixels, and is perhaps unnecessary. It may be possible to reduce the number of pixels provided lab tests with lower resolution confirm that doing so does not affect the robustness of the research methods or the efficacy in detecting change. In the case of field test, to detect an object that is 6 ft in diameter, with 37 pixels across, we would require a resolution of 2 inches. At that resolution, if a camera with 1024 x 768 pixels is used, we would be able to observe an area of 120 ft by 160 ft in a single frame.

The detection performance in the lab degraded when the lateral shift of the camera was greater than 2 inches. That is between 13% and 16% of the length and width of the observed area in the sand box (11 by 15 in). In the case of a field test, if we assume that the observed area is 120 ft by 160 ft, we would need to capture images within 16 ft accuracy or every 16 ft.

VII. Plans for Future Work

The following are extensions of the current work.

Investigate change detection performance as function of image resolution. Image resolution obtained with high-flying aircraft or space systems may be such that the size of objects of interest may be comparable or smaller than image resolution. We want to investigate the performance of change detection methods as the size of objects to detect is near or even smaller than image resolution.

Automate the image registration process. The image registration process used requires manual intervention. This process needs to be automated to be of practical use. We would like to explore techniques to automatically identify natural landmarks that are most suitable to be identified in subsequent images, and also to provide precise image registration. A methodology was developed by Karl Rohr⁶ for automatic landmark identification. This method uses differential operators to identify points with high degree of intensity variation. We plan to adapt the technique developed by K. Rohr⁶ for detecting registration points. Matching landmarks from two images will be accomplished using Johnson's² version of the iterative closest point (ICP) algorithm originally developed by Zhang⁷. We will determine processing speed and computing requirements.

Improve the change detection algorithm. The probability of false alarm increases as the camera position diverges for the two registered images, as well as when the light source position change significantly. We plan to explore using a laser detection and ranging (LADAR) sensor in addition to CCD cameras to make the change detection less sensitive to changes in light source position between image sequences.

Explore other imaging technologies. We plan to explore the capability of other sensor technologies, such as infrared imaging and LADAR, to provide an improved solution to the landmine detection problem by image registration of sequences of aerial images.

Planning for static and fly-over field tests. We plan to conduct field tests that would provide images in more realistic environments.

Systems requirements analysis. We plan to conduct a systems requirements analysis of likely implementation scenarios, so that future development meets realistic conditions and constraints. This would include determining various implementation issues such as: the image resolution required for specific dimensions of detectable objects, lens selection and number of frames per second to be acquired as function of flight altitude and velocity, and image location resolution by integrating a GPS stamp on image sequences.

VIII. Conclusions

This paper described an image processing methodology developed to detect buried improvised explosive devices (IEDs) and landmines. The methodology assumes that sequences of aerial images of the same terrain, for instance a dirt road, can be obtained at periodic intervals of time. Corresponding images of the same terrain from two consecutive sequences can be processed to detect if the terrain has changed or been disturbed and may contain buried landmines. The methodology was tested in a laboratory and produced very good results when the conditions were most favorable.

Several issues need to be researched and resolved before this methodology could be used as intended. The image registration process requires manual intervention. This process should be automated to be of practical use. Also, shadows generate false alarms when the light source changes location. It may be possible to use LADAR to discriminate shadows from actual changes. Finally, we would like to conduct field tests to quantify probability of detection and false alarm using images obtained under realistic conditions.

Acknowledgments

This work was sponsored by the Department of the Navy, Office of Naval Research, under Award # N00014-04-1-0436.

References

- ¹Radke, R., et al, "Image Change Detection Algorithms: A Systematic Survey", *IEEE Transactions On Image Processing*, Vol. 14, No. 3, March 2005, pp. 294-307.
- ²Johnson, Andrew E. and Matthies, Larry H., "Precise Image-Based Motion Estimation for Autonomous Small Body Exploration", *5th International Symposium on Artificial Intelligence, Robotics and Automation in Space*, 1999 (iSAIRAS'99), pp. 627-634.
- ³Macedo, J., Manduchi, R. (JPL), and Matthies, L. (JPL), "Ladar-based Discrimination of Grass from Obstacles for Autonomous Navigation," *Proceedings of the International Symposium on Experimental Robotics (ISER-2000) Conference*, December 10-13, 2000, Honolulu, Hawaii.
- ⁴Matthies, L. (JPL-NASA), Macedo, J. and Manduchi, R. (JPL), "Statistical Pattern Recognition of Ladar Data for Discrimination of Grass from Obstacles in Autonomous Navigation," *Proceedings of SPIE - Unmanned Ground Vehicle Technology III*, April 16-17, 2001, Orlando, Florida.
- ⁵Matthies, L., Bergh, C. Castano, A (JPL-NASA), Macedo, J., Manduchi, R. (UCSC), "Obstacle Detection in Foliage with Ladar and Radar", *Proceedings of the 11th International Symposium of Robotics Research (ISRR)*, October 19-22, 2003, Sienna, Italy.
- ⁶Rohr, Karl, "On 3D Differential Operators for Detecting Point Landmarks", *Image and Vision Computing*, Elsevier, 15 (1997) pp. 219-233.
- ⁷Zhang, Z., "Iterative point matching for registration of free-form curves and surfaces", *International Journal on Computer Vision*, 13 (2) (1994) pp. 119-152.
- ⁸Zitova, Barbara, and Flusser, Jan, "Image registration methods: a survey", *Image and Vision Computing*, Elsevier, 21 (2003) 977-1000.

**Understanding the Adversity of Perchlorate Contamination in Water by Permeation
Studies through
Reverse Osmosis (RO)/ Nanofiltration (NF) Membranes**

Project Investigator:

Parna Mukherjee
Assistant Professor
Civil and Environmental Engineering Department

Abstract

Contamination of groundwater by perchlorate (ClO_4^-) is a widespread problem in California, Nevada and Utah. ClO_4^- is of concern because it has potential human health effects at extremely low concentrations. The thyroid gland in human beings requires iodide (I^-) for its normal functioning. When ClO_4^- is present in water, ClO_4^- competitively inhibits I^- accumulation by the thyroid gland and hence disrupts the endocrine system. The permeation of I^- through the biological cell membrane into thyroid gland is analogous to the permeation of electrolytes through semi-permeable polymer membranes like Reverse Osmosis (RO) and Nanofiltration (NF). The rate of permeation of competing ions (here ClO_4^- and I^-) through RO and NF membranes can be predicted from their ion exchange selectivity.

In this study, the ion exchange separation factors of various ion exchange resins were used to determine the relative permeability of iodide with respect to perchlorate. Strong base anion exchange resins, Purolite A400, A860, A850 and A500 were used in these experiments. The separation factor for perchlorate with respect to iodide ($\alpha_{\text{ClO}_4^-/\text{I}^-}$) was experimentally determined two ways in this study:

- batch isotherm technique
 - o $\text{ClO}_4^-/\text{I}^-$ isotherm
 - o $\text{ClO}_4^-/\text{Cl}^-$ and I^-/Cl^- isotherm
- elution time of ions from ion chromatogram

Table A1 shows the average values of separation factor for perchlorate with respect to iodide ($\alpha_{\text{ClO}_4^-/\text{I}^-}$) as obtained by these various methods.

Table A1 Separation Factors for perchlorate with respect to iodide ($\alpha_{\text{ClO}_4^-/\text{I}^-}$) for various strong base anion exchange resins

Resin Used	Matrix Type	$\alpha_{\text{ClO}_4^-/\text{I}^-}$
Purolite A 400	Polystyrene Gel	6.36 to 4.10
Purolite A 500	Polystyrene Macroporous	3.7 to 3.28
Purolite A 850	Polyacrylic Gel	3.98 to 3.68
Purolite A 860	Polyacrylic Macroporous	3.19 to 1.69

All of the resins were shown to have a $\alpha_{\text{ClO}_4^-/\text{I}^-}$ greater than 1, which indicates that ClO_4^- is more selective than I^- , which in turn means that ClO_4^- permeates preferentially through RO and NF membranes. This proves that ClO_4^- has lower hydrated ionic radii than I^- and hence explains the preferential uptake of ClO_4^- over I^- through the biological membrane into the thyroid gland.

Results

1.1 Capacity

The absolute capacity for both chloride and iodide forms were analyzed because of their different selectivities to perchlorate. Different selectivities create different exchanges of co-ions, which is what absolute capacity quantifies.

1.1.1 A400 Resin

Table 1 shows the data generated by the A400 chloride form capacity. The concentrations of perchlorate and chloride in solution were analyzed for each round. The ion exchange absolute capacities of the resins were determined by saturating the resins with perchlorate and analyzing the aqueous solution. The aqueous solution concentrations converted to milliequivalents were used along with initial concentrations to calculate the amount of perchlorate adsorbed on the resin. Columns 9 and 10 show the accumulative total of ions on resin or in solution after each round. This number divided by the initial amount of resin is used to determine the capacity in meq/g.

Table 1: Absolute Capacity Calculations for A400 Resin in Chloride Form

Round	Cl ⁻ (mg/L) in sol at equi	Cl ⁻ (meq/L) in sol at equi	ClO ₄ ⁻ (mg/L) in sol at equi	ClO ₄ ⁻ (meq/L) in solution at equi	Cl ⁻ (meq) in solution (round)	ClO ₄ ⁻ (meq) in solution at equi	ClO ₄ ⁻ on Resin (round) (meq)	ClO ₄ ⁻ on Resin (total) (meq)	Cl ⁻ (meq) in solution (total)	ClO ₄ ⁻ Capacity of resin (meq/g)	Cl ⁻ Capacity of resin (meq/g)
1	222.25	6.27	278.27	2.80	0.63	0.28	0.74	0.74	0.63	3.61	3.07
2	28.73	0.81	788.03	7.92	0.08	0.79	0.23	0.96	0.71	4.72	3.47
3	19.49	0.55	686.89	6.90	0.06	0.69	0.33	1.29	0.76	6.32	3.74

For A400 in iodide form Table 2 was created.

Table 2: Absolute Capacity Calculations for A400 Resin in Iodide Form

Round	I ⁻ (mg/L) in sol at equi	I ⁻ (meq/L) in sol at equi	ClO ₄ ⁻ (mg/L) in sol at equi	ClO ₄ ⁻ (meq/L) in solution at equi	I ⁻ (meq) in solution (round)	ClO ₄ ⁻ (meq) in solution at equi	ClO ₄ ⁻ on Resin (round) (meq)	ClO ₄ ⁻ on Resin (total) (meq)	I ⁻ (meq) in solution (total)	ClO ₄ ⁻ Capacity of resin (meq/g)	I ⁻ Capacity of resin (meq/g)
1	428.57	3.38	123.24	1.24	0.34	0.12	0.31	0.31	0.34	1.62	1.74
2	181.08	1.43	290.56	2.92	0.14	0.29	0.15	0.46	0.48	2.38	2.48
3	40.09	0.32	401.66	4.04	0.03	0.40	0.03	0.49	0.51	2.55	2.64
4	10.43	0.08	429.87	4.32	0.01	0.43	0.01	0.50	0.52	2.59	2.69

The capacity from both sides should be similar. For A400 chloride form the numbers aren't very close. The capacity used for these isotherms was from the chloride side. According to experiments, the capacity determined and used in isotherm analysis for

A400 perchlorate chloride and iodide chloride isotherms is 3.74 meq/g, this is the last number in the last row of the table. For consistency, the capacity from the ClO_4^- side was applied to all of the other isotherm calculations as both calculations were close. The capacity used in experiments from the following tables is the last number in the second to last row. The iodide capacity of the A400 resin is 2.59 meq/g used in the A400 perchlorate iodide isotherm.

1.1.2 A860 Resin

The results for A860 in chloride form are shown in Table 3.

Table 3: Absolute Capacity Calculations for A860 Resin in Chloride Form

Round	Cl^- (mg/L) in sol at equi	Cl^- (meq/L) in sol at equi	ClO_4^- (mg/L) in sol at equi	ClO_4^- (meq/L) in solution at equi	Cl^- (meq) in solution (round)	ClO_4^- (meq) in solution at equi	ClO_4^- on Resin (round) (meq)	ClO_4^- on Resin (total) (meq)	Cl^- (meq) in solution (total)	ClO_4^- Capacity of resin, (meq/g)	Cl^- Capacity of resin (meq/g)
1	161.79	4.56	68.77	0.69	0.46	0.07	0.35	0.35	0.46	1.58	2.07
2	79.59	2.24	156.70	1.57	0.22	0.16	0.26	0.61	0.68	2.77	3.08
3	32.39	0.91	305.82	3.07	0.09	0.31	0.11	0.72	0.77	3.28	3.50
4	8.13	0.23	382.30	3.84	0.02	0.38	0.04	0.76	0.80	3.43	3.60

According to experiments, the capacity used for chloride form in the A860 perchlorate chloride and iodide chloride isotherms is 3.43 meq/g.

Capacity results for A860 in iodide form are presented below in Table 4.

Table 4: Absolute Capacity Calculations for A860 Resin in Iodide Form

Round	I^- (mg/L) in sol at equi	I^- (meq/L) in sol at equi	ClO_4^- (mg/L) in sol at equi	ClO_4^- (meq/L) in solution at equi	I^- (meq) in solution (round)	ClO_4^- (meq) in solution at equi	ClO_4^- on Resin (round) (meq)	ClO_4^- on Resin (total) (meq)	I^- (meq) in solution (total)	ClO_4^- Capacity of resin (meq/g)	I^- Capacity of resin (meq/g)
1	402.27	3.17	173.83	1.75	0.32	0.17	0.26	0.26	0.32	1.30	1.56
2	181.35	1.43	270.35	2.72	0.14	0.27	0.17	0.43	0.46	2.12	2.26
3	79.98	0.63	354.74	3.57	0.06	0.36	0.08	0.51	0.52	2.52	2.57
4	33.89	0.27	410.52	4.13	0.03	0.41	0.03	0.54	0.55	2.64	2.71

Through experimentation a capacity of 2.64 meq/g was determined for use in the A860 perchlorate iodide isotherms.

1.1.3 A850 Resin

The results for A850 in chloride form are shown in Table 5.

Table 5: Absolute Capacity Calculations for A850 Resin in Chloride Form

Round	Cl ⁻ (mg/L) in sol at equi	Cl ⁻ (meq/L) in sol at equi	ClO ₄ ⁻ (mg/L) in sol at equi	ClO ₄ ⁻ (meq/L) in solution at equi	Cl ⁻ (meq) in solution (round)	ClO ₄ ⁻ (meq) in solution at equi	ClO ₄ ⁻ on Resin (round) (meq)	ClO ₄ ⁻ on Resin (total) (meq)	Cl ⁻ (meq) in solution (total)	ClO ₄ ⁻ Capacity of resin (meq/g)	Cl ⁻ Capacity of resin (meq/g)
1	84.7015	2.39	5.79	0.06	0.24	0.01	0.37	0.37	0.24	1.78	1.16
2	21.4	0.60	4.129	0.04	0.06	0.00	0.37	0.74	0.30	3.57	1.45

According to experiments, the capacity used for chloride form in the A850 perchlorate chloride and iodide chloride isotherms is 3.57 meq/g.

Table 6: Absolute Capacity Calculations for A850 Resin in Iodide Form

Round	I ⁻ (mg/L) in sol at equi	I ⁻ (meq/L) in sol at equi	ClO ₄ ⁻ (mg/L) in sol at equi	ClO ₄ ⁻ (meq/L) in solution at equi	I ⁻ (meq) in solution (round)	ClO ₄ ⁻ (meq) in solution at equi	ClO ₄ ⁻ on Resin (round) (meq)	ClO ₄ ⁻ on Resin (total) (meq)	I ⁻ (meq) in solution (total)	ClO ₄ ⁻ Capacity of resin (meq/g)	I ⁻ Capacity of resin (meq/g)
1	391.87	3.09	168.08	1.69	0.31	0.17	0.27	0.27	0.31	1.45	1.67
2	154.77	1.22	281.86	2.83	0.12	0.28	0.15	0.42	0.43	2.29	2.32
3	67.08	0.53	370.65	3.73	0.05	0.37	0.07	0.49	0.48	2.64	2.61
4	23.38	0.18	404.84	4.07	0.02	0.41	0.03	0.52	0.50	2.81	2.71

Table 6 above displays the capacity of 2.81 meq/g for A850 in iodide form used in the A850 perchlorate iodide isotherm.

1.1.4 A500 Resin

The A500 resin iodide absolute capacity was previously determined as 4.16 meq/g (Schieberl, 2005). The perchlorate iodide isotherm with A500 resin experiment in this research only needed the capacity of iodide form for calculations. The absolute capacity in chloride form for the A500 resin was not necessary and therefore not used.

1.1.5 Comparison of Resin Capacities

Table 7: Absolute Capacity Results

Resin	Type	Experimental Capacity (Cl form), meq/g	Experimental Capacity (I form), meq/g
A-400	Gel	3.74	2.59
A-860	Macroporous	3.43	2.64
A-850	Gel	3.57	2.81
A-500	Macroporous		4.16*

The experimental capacities found for the resin in chloride form are higher than the iodide form. The gel chloride resins have a slightly higher capacity than the macroporous chloride resins. The iodide capacities also are higher for gel than macroporous resins except for A500. The experimental capacity for the A500 resin in chloride form was not used because only a perchlorate iodide isotherm was run. This was to make a comparison with the analysis and procedure from a previous work.

1.2 Iodide Chloride Isotherms

Iodide chloride isotherms were created using data for resin in chloride form with an iodide solution. The chloride form capacities of the resins are used to determine the initial milliequivalents of chloride on the resin phase. The chloride capacity of the resins, the weights of resin, volumes of solution, the initial concentration of iodide, the final solution of iodide and final solution of chloride have to be obtained from each sample. Isotherm Tables provides the data for each of the isotherms presented in Sections 1.2, 1.3 and 1.4.

The iodide chloride isotherm is the first step in determining an average $\alpha_{\text{ClO}_4/\text{I}}$.

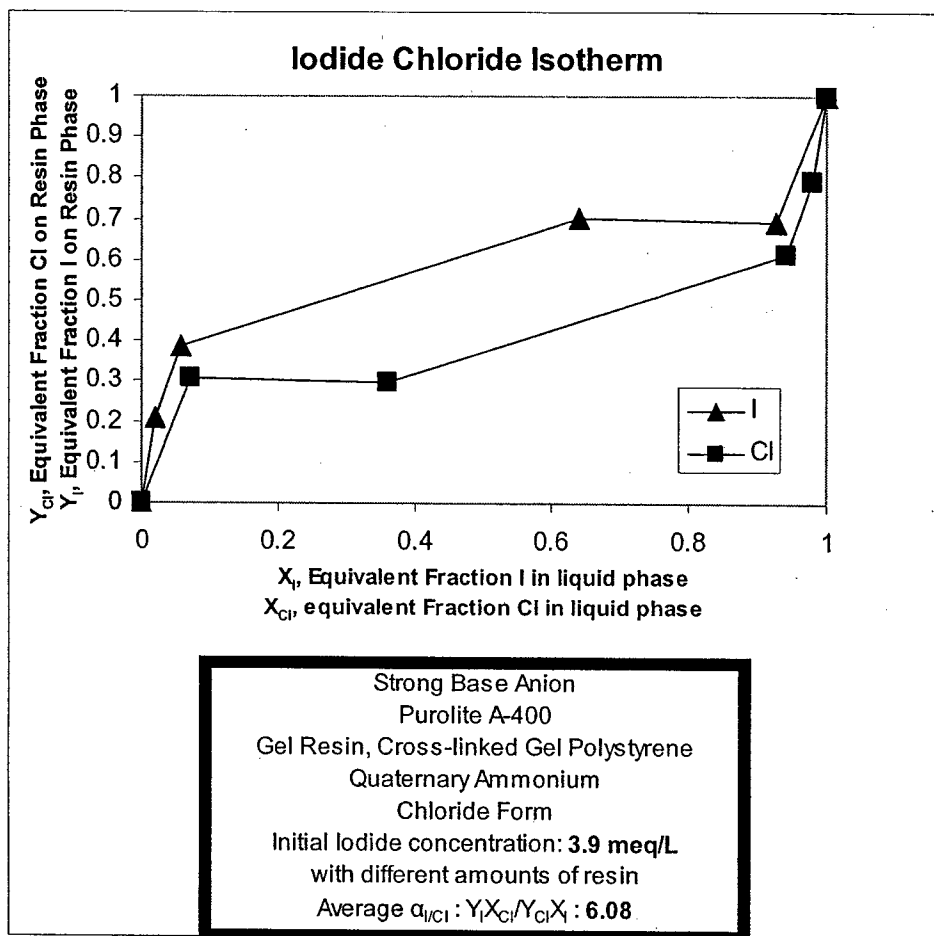


Figure 1: Iodide Chloride Isotherm with Resin A400

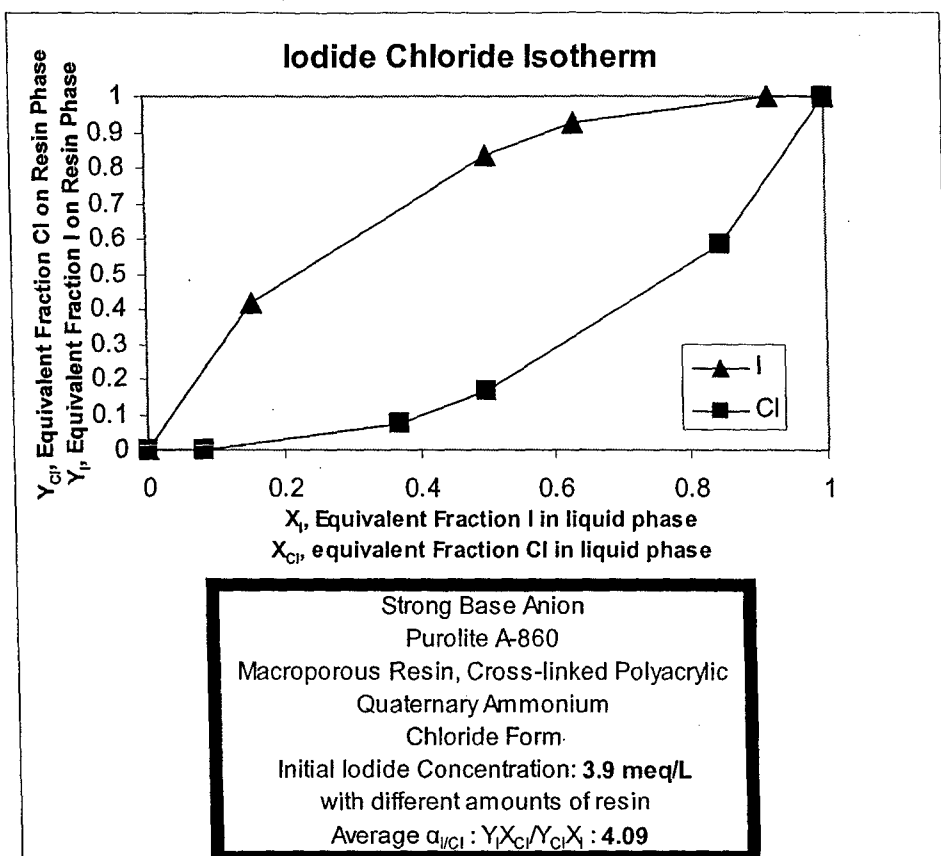


Figure 2: Iodide Chloride Isotherm with Resin A860

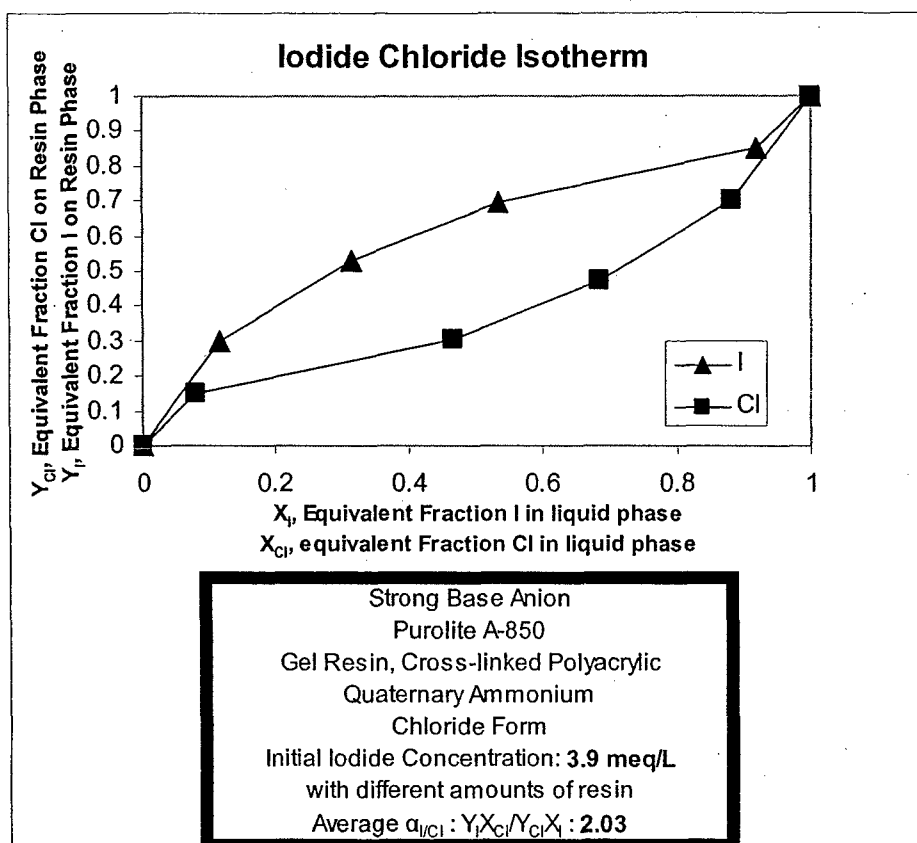


Figure 3: Iodide Chloride Isotherm with Resin A850

Figures 1 through 3 show the iodide chloride isotherms obtained for the data for the A400, A860 and A850 resins. No iodide chloride isotherm was created for A500 because previous research had created this isotherm. The separation factor of perchlorate with respect to iodide for A500 resin is only found directly through this research so iodide chloride and perchlorate isotherms for A500 resin were not created.

1.3 Perchlorate Chloride Isotherms

Perchlorate chloride isotherms were determined with a perchlorate solution and resin in chloride form. The chloride capacities, volumes of solution and weights of the resins were also used. This is the second step in determining $\alpha_{ClO_4/I}$.

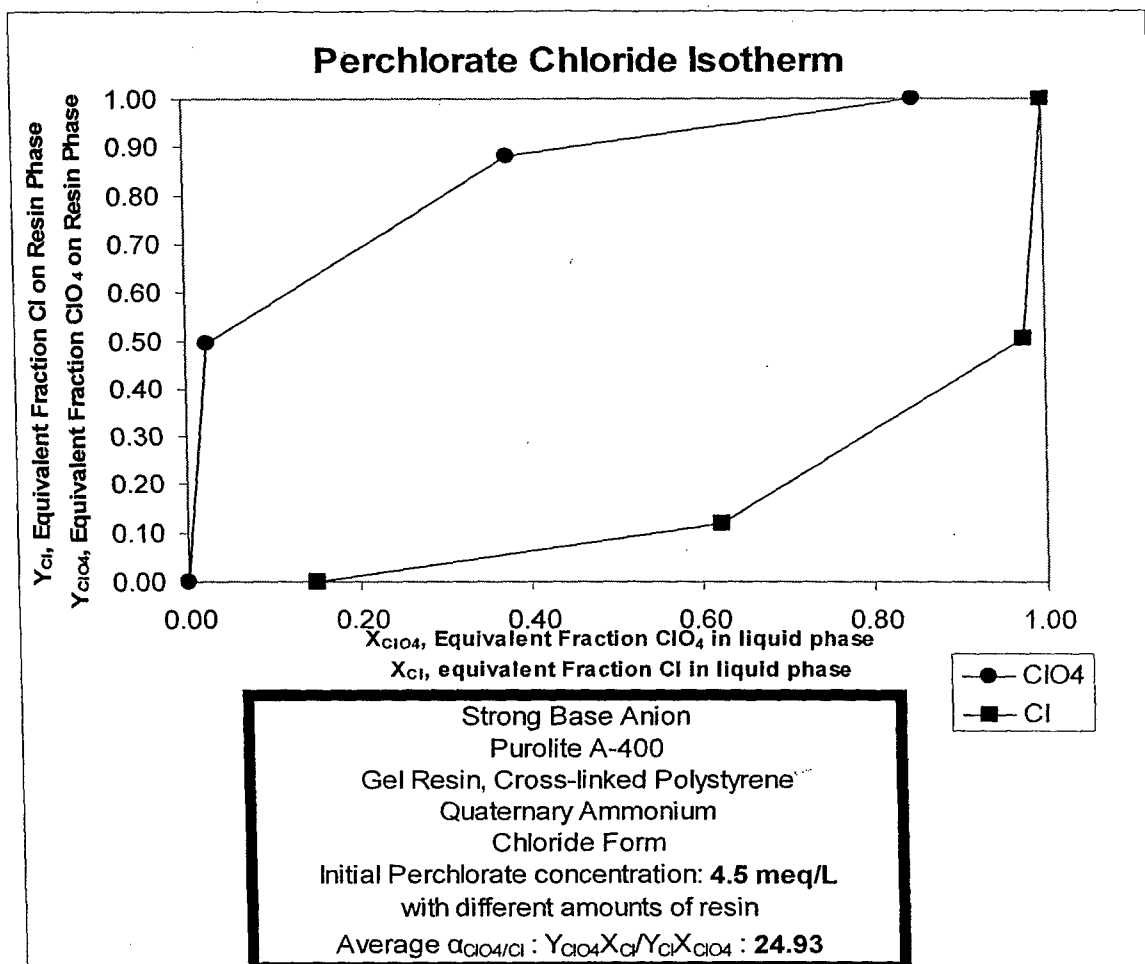


Figure 4: Perchlorate Chloride Isotherm with Resin A400

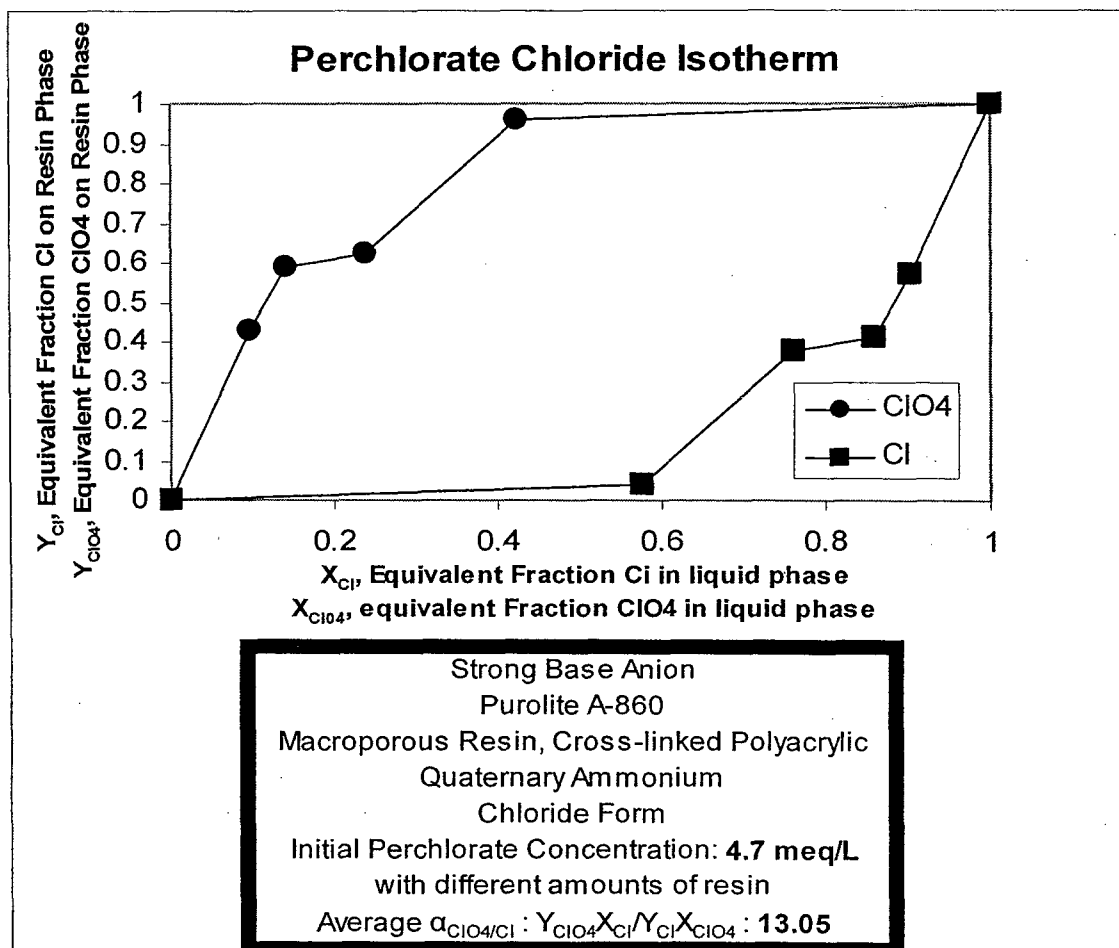


Figure 5: Perchlorate Chloride Isotherm with Resin A860

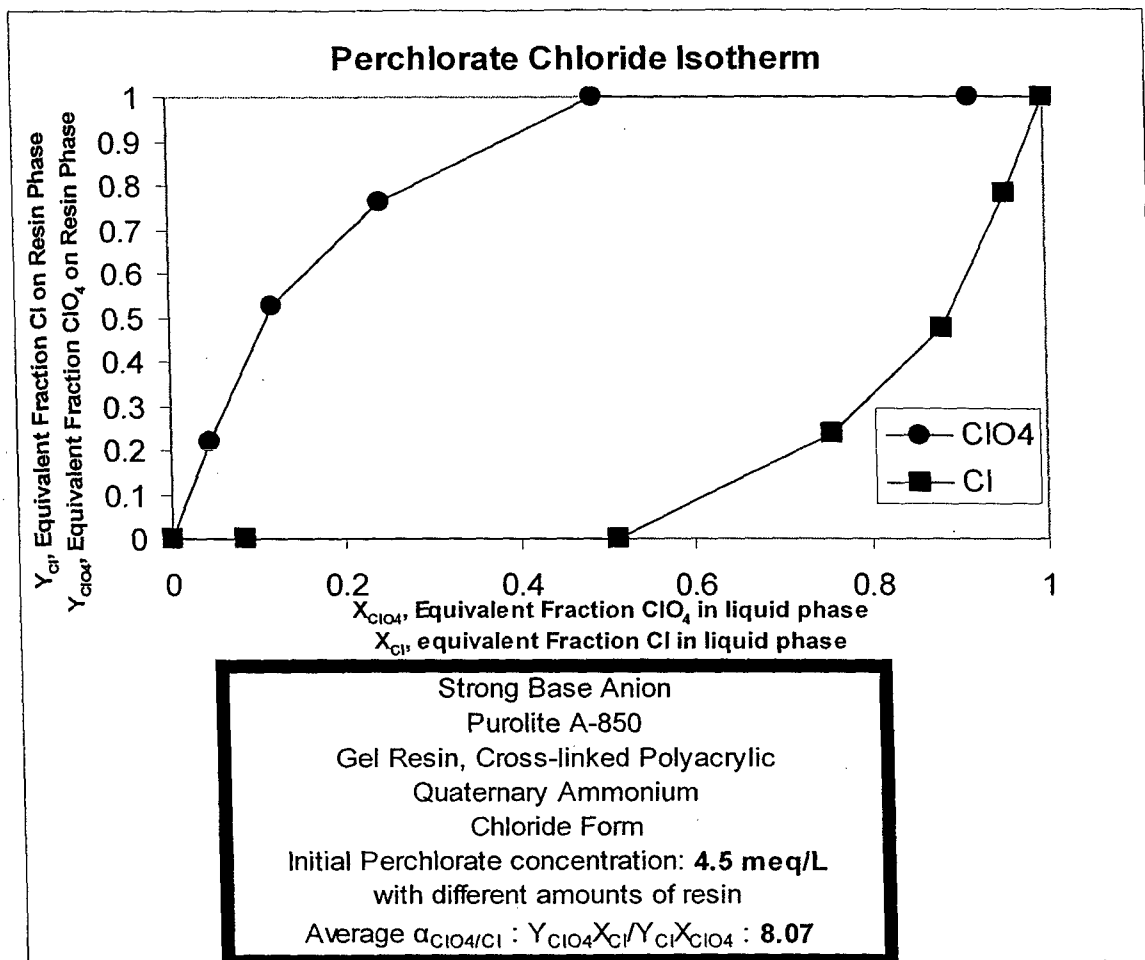


Figure 6: Perchlorate Chloride Isotherm with Resin A850

Figures 4 through 6 show the isotherms created to determine the average separation factors of perchlorate with respect to chloride of A400, A860 and A850 resins. These separation factors along with the separation factors of iodide with respect to chloride will be used to determine the separation factor of perchlorate with respect to iodide indirectly. These results are shown in Section 1.5.

1.4 Perchlorate/Iodide Isotherms

Perchlorate iodide isotherms directly calculate $\alpha_{\text{ClO}_4/\text{I}}$ using a perchlorate solution and resin in iodide form. Just like with the other isotherms, the weights of the resins, and volumes of the solution are measured. The iodide ion exchange capacity is used along with initial and final perchlorate concentrations and final iodide concentration to create the isotherms. Figures 8 and 9 prove the separation factor does not vary much with a change in concentration under homovalent conditions where separation factor is equal to selectivity. This confirms the reproducibility of the calculated separation factor and analysis method. Figure 11 shows comparison of the analysis in this thesis to previous research. Figures 7, 9, and 10 show the isotherms that created an average separation factor of perchlorate and iodide for direct calculation.

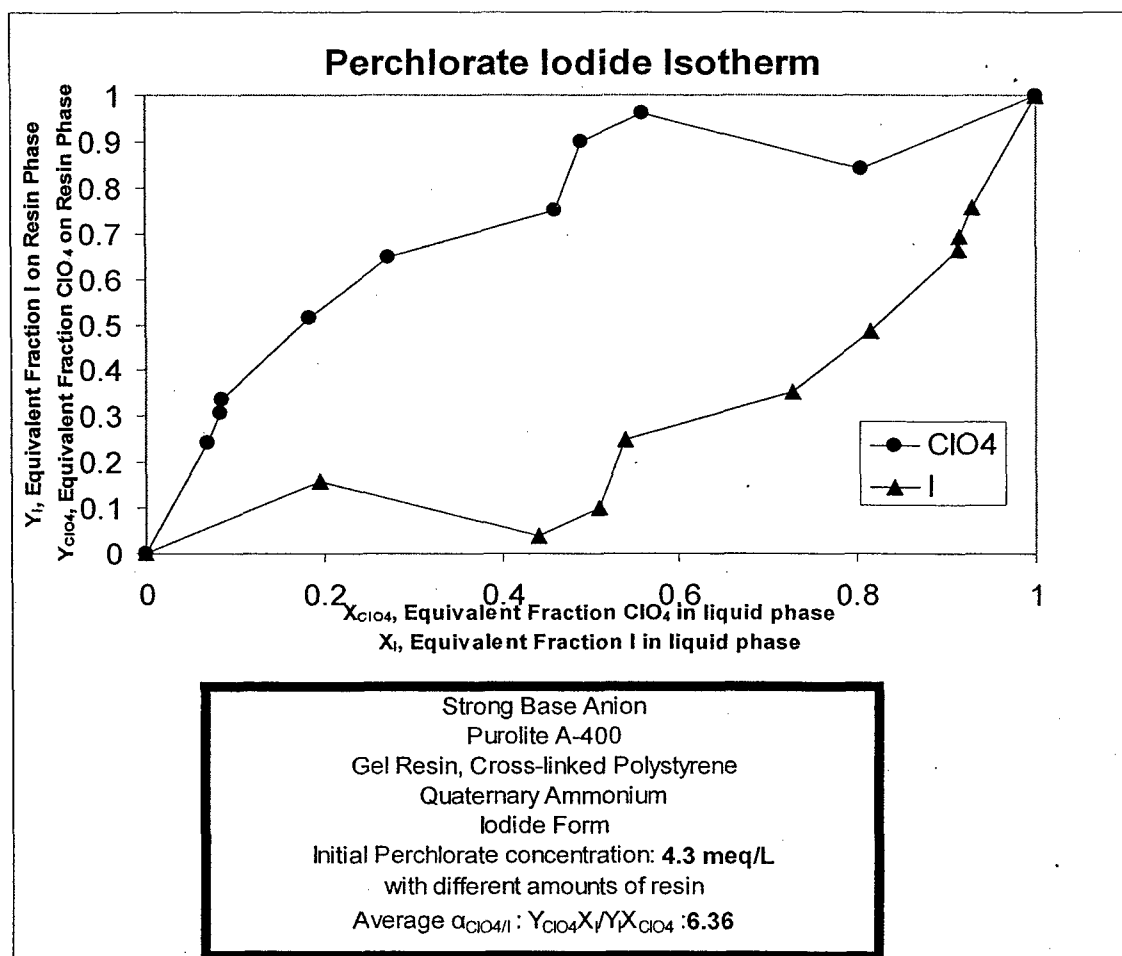


Figure 7: Perchlorate Iodide Isotherm with Resin A400

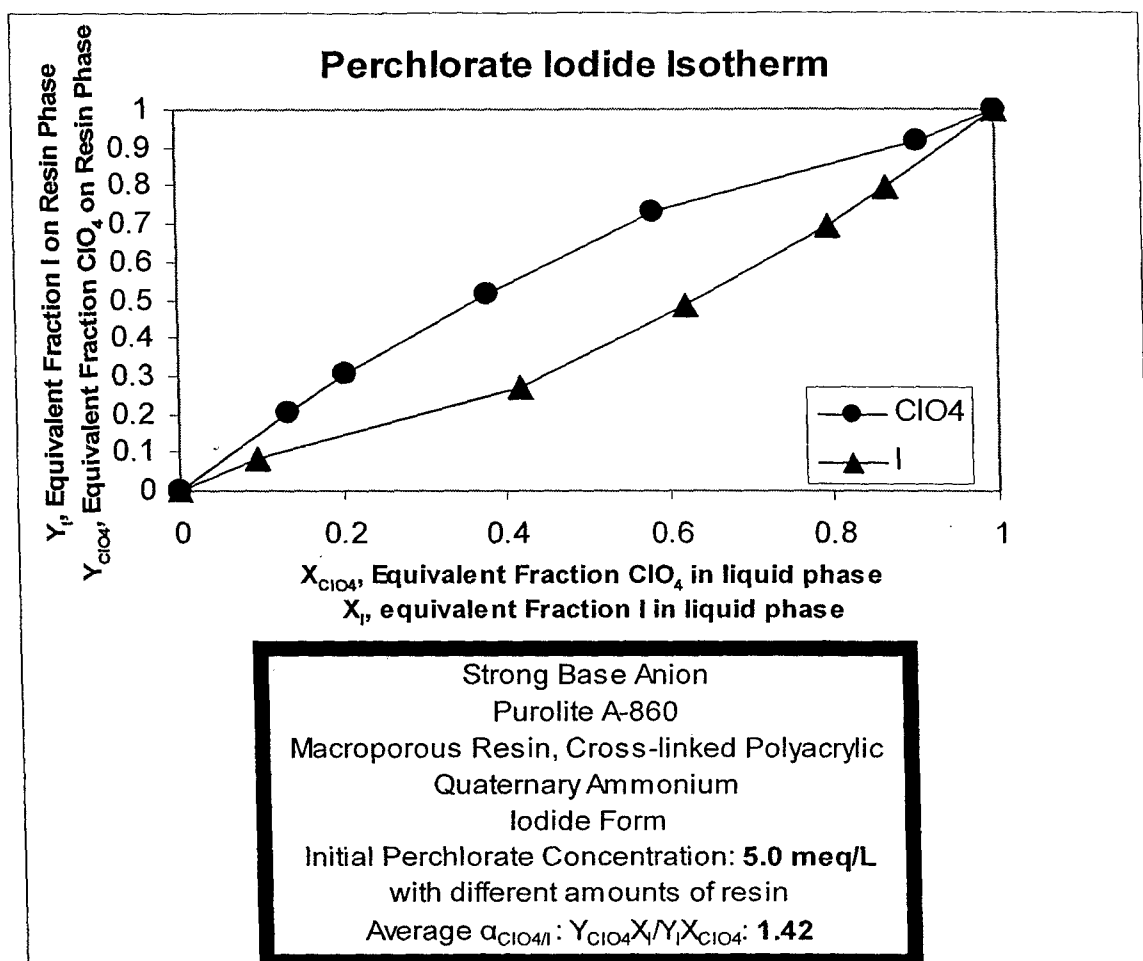


Figure 8: Perchlorate Iodide Isotherm with Resin A860 (1)

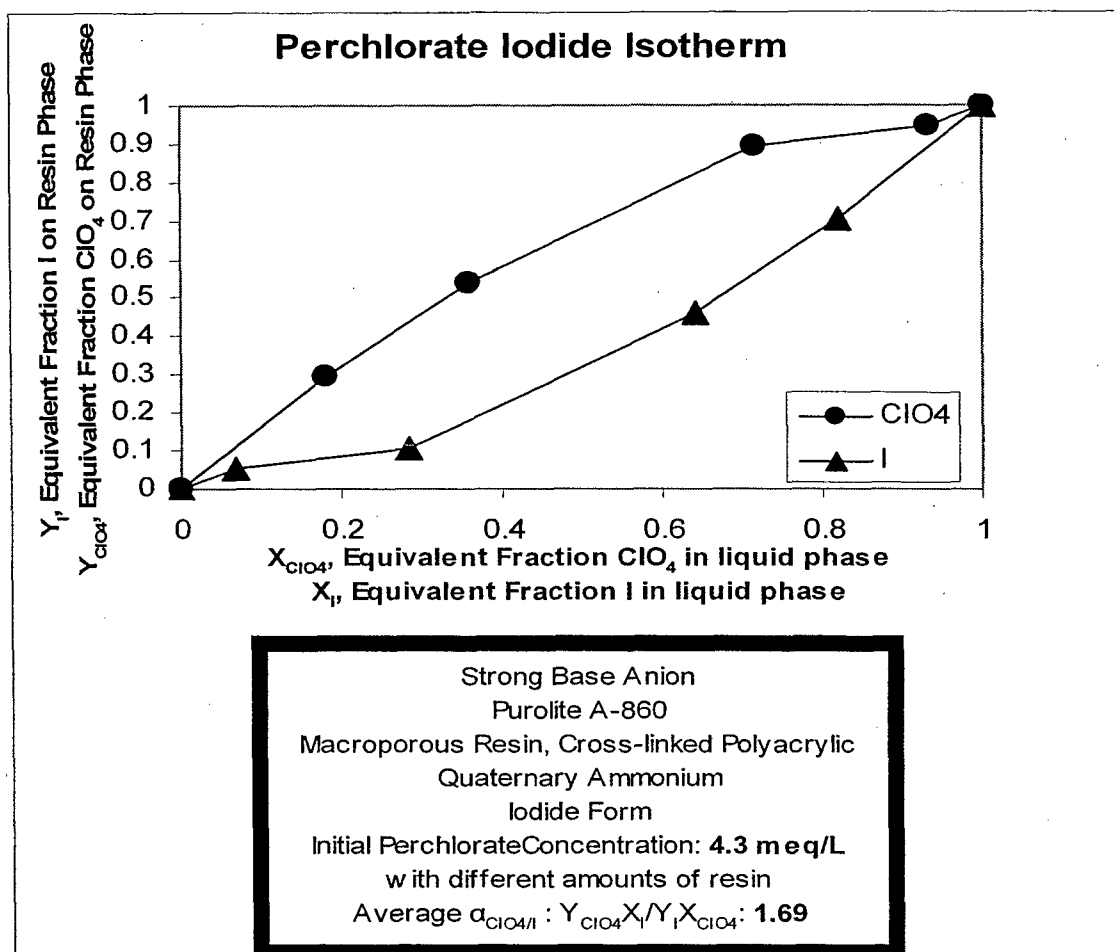


Figure 9: Perchlorate Iodide Isotherm with Resin A860 (2)

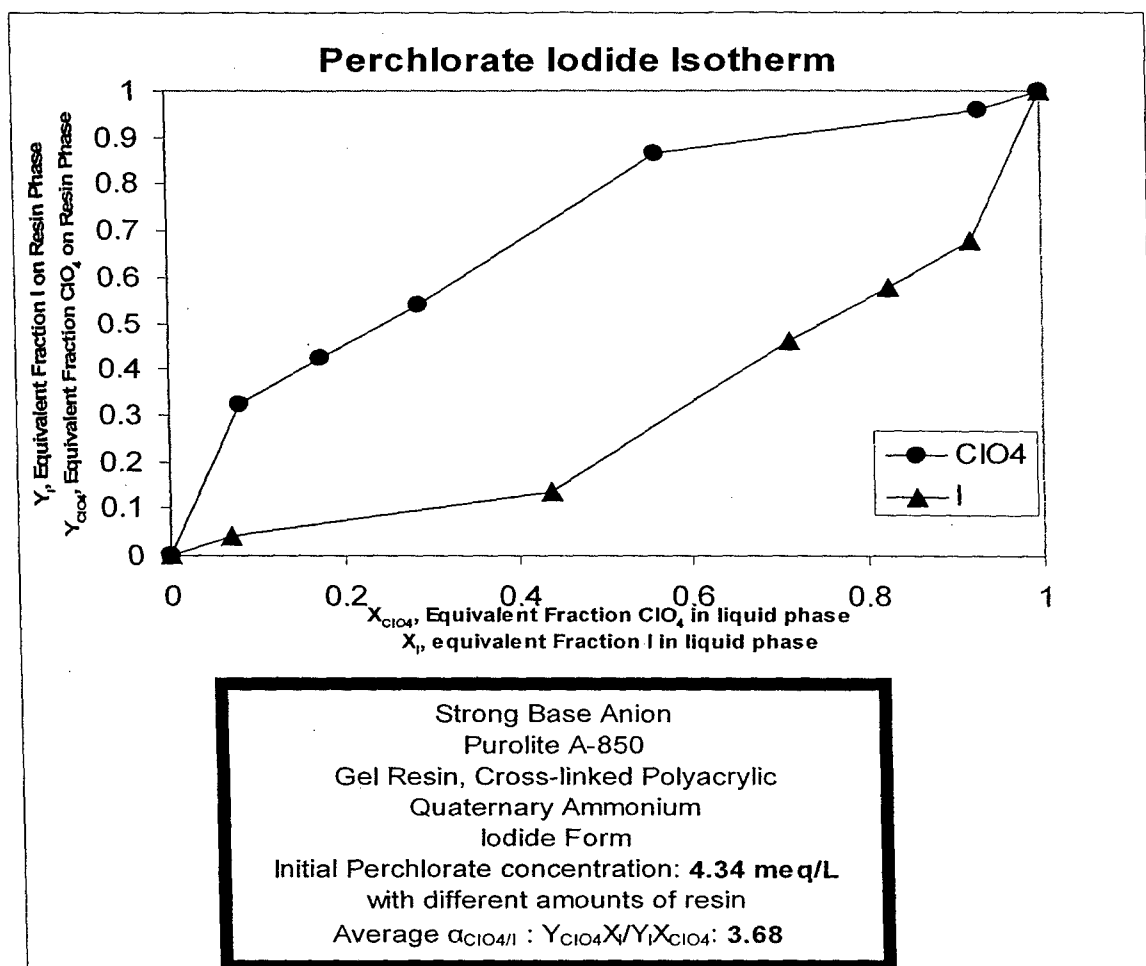


Figure 10: Perchlorate Iodide Isotherm with Resin A850

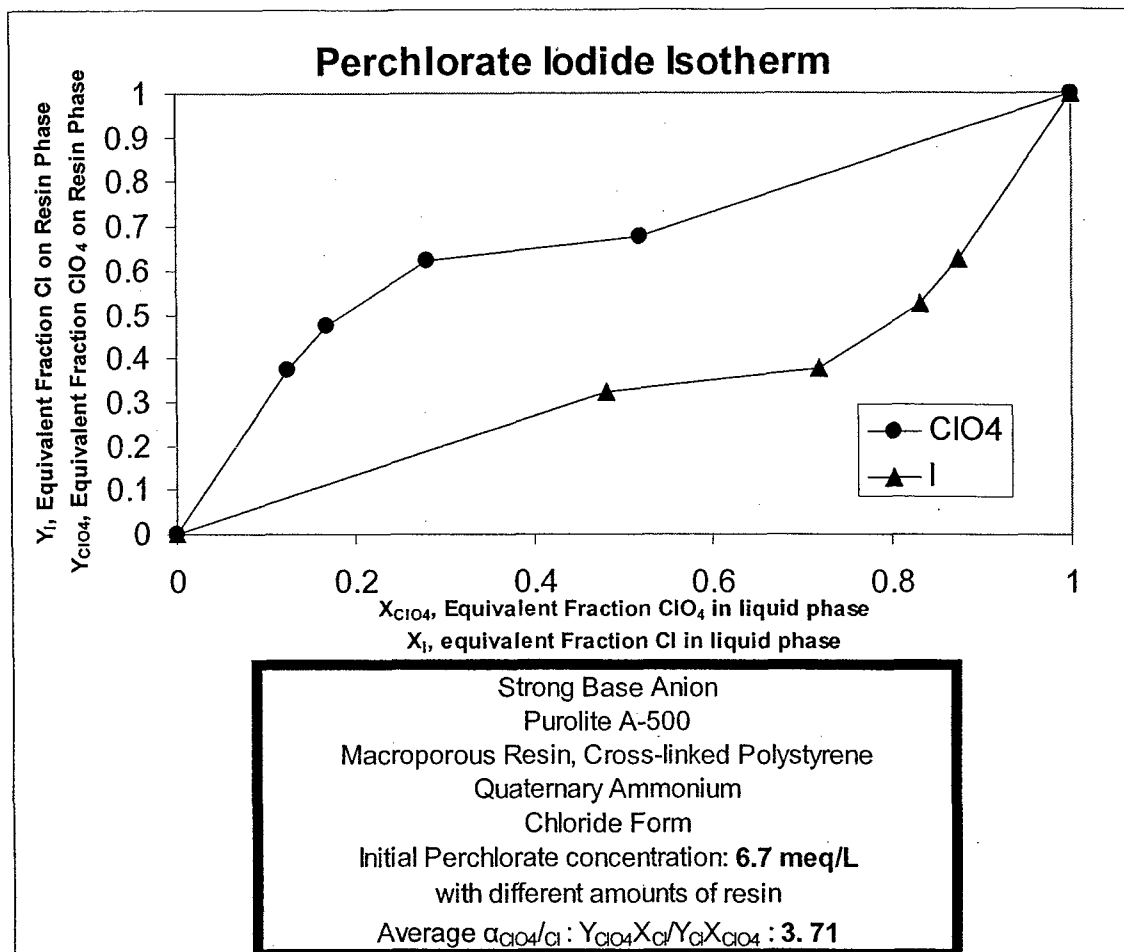


Figure 11: Perchlorate Iodide Isotherm with Resin A500

The A500 perchlorate iodide isotherm resulted in an average separation factor of 3.71. This isotherm was compared to the isotherm from previous isotherm work of the A500 resin with an initial perchlorate concentration of 5 meq/L. This analysis resulted in an average separation factor of perchlorate with respect to iodide of 3.71. This shows that the procedure and analysis for the two studies are comparable and the results for this method are reproducible.

1.5 Comparison of Selectivity

The separation factors were determined from three random samples during the experimentation. These are three random samples from IC analysis. The water dip is at time zero for most of the samples. These separation factors will reflect the separation factor of the resin in the AS16 column because the column allows ions to elute based on their selectivity so the time of elution of ions with respect to each other can be estimated by the ration of elution times.

With all the isotherms created, the separation factors for each resin can be compared (Table 8). The average separation factors for direct determination came from the average separation factor from the perchlorate iodide isotherms. The indirect calculation of the average separation factors came from the perchlorate chloride and iodide chloride isotherms.

Table 8: Separation Factor Comparisons

Resin	$\alpha_{\text{ClO}_4^-/\text{Cl}^-}$	$\alpha_{\text{I}^-/\text{Cl}^-}$	$\alpha_{\text{ClO}_4^-/\text{I}^-}$, calculated, indirect	$\alpha_{\text{ClO}_4^-/\text{I}^-}$, direct	$\alpha_{\text{ClO}_4^-/\text{I}^-}$ = $t_{\text{ClO}_4^-}/t_{\text{I}^-}-t_0$
A400	24.93	6.08	4.10	6.36	2.20
A860	13.05	4.09	3.19	1.69	2.20
A850	8.07	2.03	3.98	3.68	2.14

A separation factor greater than 1 shows that perchlorate is more permeable through semi permeable membranes in relation to iodide. The higher the separation factor the more of a problem perchlorate is if it enters your system. The average $\alpha_{\text{ClO}_4^-/\text{I}^-}$ from calculated indirect and direct determination have the same trend with respect to the resin used. The trend of the average $\alpha_{\text{ClO}_4^-/\text{I}^-}$ shows polystyrene gel resin resulted in the highest perchlorate iodide selectivity of 6.36 calculated directly and 4.10 calculated indirectly. The average direct and indirect $\alpha_{\text{ClO}_4^-/\text{I}^-}$ of 3.98 and 3.68, respectively for the polyacrylic gel resin makes it the next highest ion exchange selectivity. The resin with the lowest ion exchange selectivity in the experiments was the macroporous polyacrylic resin with a direct and indirect separation factor of 1.69 and 3.19, respectively.

From these separation factors, resins with a polystyrene chemical composition show higher separation factors of perchlorate with respect to iodide than polyacrylic resins since when the structure (gel) remained the same the polystyrene resin resulted in a higher separation factor perchlorate with respect to iodide. This would show that polystyrene more readily releases chloride and iodide than it does perchlorate. The macroporous structure is considered a chain of microgels with the space between the gels being the limiting step. This would allow more perchlorate to be adsorbed on the gel resins in the place of iodide than the macroporous resins. The gels should have a higher selectivity than the macroporous resins since they don't have a rate-limiting step as shown by research.

Conclusions

From the separation factors calculated in this study shown in Table 8, the ion exchange resins were less selective for iodide than perchlorate since all of the separation factors of perchlorate with respect to iodide are greater than one. The trend of the average $\alpha_{\text{ClO}_4^-/\text{I}^-}$ shows polystyrene gel resin resulted in the highest perchlorate iodide selectivity followed by the polyacrylic gel resin and then the macroporous polyacrylic resin with the lowest separation factor, which directly correlates with diffusivity through semi permeable membranes. From this trend it is shown that resins with a polystyrene chemical composition show higher separation factors of perchlorate with respect to iodide than polyacrylic resins. This trend also shows that gels should have a higher selectivity for perchlorate with respect to iodide than macroporous resins.

The smaller hydrated radius and higher ion selectivity the higher diffusion coefficient expected. While all of these values could be used to predict permeability, ion exchange separation factors are easier experiments to run. The data is also easily reproducible. Higher diffusion coefficients result in higher permeation through semi permeable membranes. All of the resins show that the separation factor for perchlorate is relatively higher than iodide.

With this knowledge it can be suggested that even if perchlorate is present in the body in only a small amount, it will diffuse preferentially over iodide through membranes. Perchlorate mimics iodide to the sodium iodide symporter (NIS), which allows perchlorate to contact the apical membrane and its higher selectivity compared to iodide shows a mechanism that would allow it to permeate competitively into the thyroid gland. The presence of perchlorate could cause obstacles for the tyrosine to find organic iodide, ultimately causing decrease hormone production. While the gland is triggered to allow more iodide in, since the NIS cannot differentiate between perchlorate and iodide, the presence of perchlorate might not guarantee the amount of thyroid hormones that it triggered to be produced will be produced.

The concentration of perchlorate used in this study are higher than the reference dose of 0.0007 mg/kg per day (USEPA, 2005) but for homovalent isotherms the separation factor is not dependent on initial concentration so the separation factors should be able to be translated to smaller concentrations.

Force Feedback Control for Visually Impaired Wheelchair Users

Project Investigators:

Saeed Niku
Professor
Mechanical Engineering
California Polytechnic State University

Brent Sindorf
Student
Mechanical Engineering
California Polytechnic State University

Abstract

Currently there are no suitable systems available for blind or visually impaired wheelchair users that make travel safe and efficient. In this project, a computer simulation utilizing a force feedback joystick was developed using Simulink. This simulation uses a fuzzy logic control algorithm to determine the forces necessary to properly warn blind and visually impaired wheelchair users of obstacles/hazards in their travel path. With this system, users can "feel" obstacles and hazards through the joystick before collisions occur. This allows users to traverse a virtual scene while avoiding obstacles and hazards. This simulation will be used by Smith-Kettlewell Eye Research Institute in order to develop a prototype wheelchair for blind and visually impaired users. However, the same technology can be applied to autonomous robotic navigation with military and civilian applications.

1 Introduction

According to the National Center for Health Statistics [1], there are approximately 1,057,400 legally blind individuals in the United States. An individual is considered legally blind when visual acuity is 20/200, or worse, in the better eye with the best correction available (i.e., prescription glasses). Of those that are legally blind, approximately 101,600 individuals also use a wheelchair. This is roughly 9.6% of the legally blind population in the United States.

For blind wheelchair users, getting around is a very difficult and slow process. Typically, a long cane is used, but this can only warn the user of objects within a few feet of the wheelchair travel path. Of particular interest to blind wheelchair users are drop-offs. A drop-off can cause the wheelchair to tip over which can seriously injure the user. For a blind wheelchair user with a long cane, when a drop-off is found, the entire length of the drop-off must be explored for a safe passage (i.e., searching for a sidewalk cross slope in order to cross a street). This is a very time consuming and unsafe process. Because of this, many blind wheelchair users are discouraged from traveling outside into unknown and even known areas.

2 Background

Currently Smith-Kettlewell Eye Research Institute (SKI) of San Francisco, California, is developing a wheelchair that will aid blind and visually impaired wheelchair users. SKI has compiled the following list of hazards that need to be overcome in order to make wheelchair use safer for blind and visually impaired users:

1. Drop-offs, curbs and stairs
2. Changes in terrain (such as concrete to grass, dirt to gravel, etc.)
3. Objects in travel path that might catch a wheel
4. Unexpected slopes (such as driveways)
5. Raised objects at side of travel path (such as walls)
6. Lack of visibility of wheelchair to vehicles (especially at street crossings)
7. Crossing open spaces (loss of orientation)
8. Traversing rough terrain (such as cobblestone)

SKI is currently developing sensors to detect/overcome these hazards in order to warn the wheelchair user with enough time to react. These sensors include vision systems (cameras) with laser pointers to detect obstacles, drop-offs, and slopes. By knowing the orientation of the camera relative to the laser, distances, and therefore objects, can be detected and measured through triangulation. In addition, ultrasonic sensors will be used in conjunction with optical sensors for detecting various hazards including obstacles, curbs, etc. Orientation information will be provided through a global positioning system (GPS).

Once all of this information about the wheelchair user's surroundings has been collected, the next problem becomes what to do with all of this information, and more specifically, how this information will be expressed to the wheelchair user. Possible ideas include auditory feedback (noises that represent different hazards), vibratory feedback (an array of vibration devices in contact with the user, either through the back or through the seat of the wheelchair) and tactile feedback in the form of a force feedback in the joystick of a motorized wheelchair.

Continuous auditory feedback, as would be required for detecting all obstacles/hazards is not always reliable due to echo and interfering noise sources [2]. Reliability could be lost if there were a nearby noise source such as a radio or cell phone that happened to produce the same sounds (frequency and pitch) as the feedback. In addition, auditory feedback would be intrusive not only to the wheelchair user, but also to nearby pedestrians [3]. Auditory feedback through headphones would be unsafe to the user. This method would not allow the user to hear other sounds such as sirens, passing cars, speech from others, etc [4]. In addition, auditory feedback can be uncomfortable when in use for long periods.

Vibratory feedback is not as accurate as other types of feedback mentioned since not all people have the same sensitivity to touch. Vibratory feedback is also quite intrusive to the wheelchair user and prolonged use could tend to desensitize the user to certain signals or even cause hand-arm vibration syndrome (also known as vibration white finger) [5].

These methods of feedback have been attempted in the past with varying success [6,7,8,9,10,11]. However, none of these methods were ever developed specifically for blind and visually impaired wheelchair users. In addition, each of these methods is disadvantageous as described above.

Because of this, the most promising way to convey hazard information to a blind and visually impaired wheelchair user is through a tactile or force feedback joystick. This method of feedback would require the least amount of training for current wheelchair users and could prevent the user from encountering various hazards (i.e., colliding with an object or moving over a drop-off). By providing a very large force in the wheelchair-controlling joystick, the user is less likely to cause the wheelchair to move in a potentially dangerous direction since it would be difficult for the user to overcome the resistive force. Force feedback used in conjunction with auditory feedback for special hazards, such as drop-offs and loss of orientation, appears to be the best solution for blind and visually impaired wheelchair users [12].

A force feedback joystick can convey the severity of an obstacle/hazard by varying the amount of force feedback output by the joystick (i.e., a larger force represents a more severe hazard).

This would give the user more information about how dangerous an obstacle/hazard is. For instance, a drop-off is more dangerous to a wheelchair user than a small raised object in the user's travel path. This is because the user will simply bump into a small raised object, while a drop-off could cause the wheelchair to tip over.

3 Project Overview

The purpose of this project was to develop a computer simulation utilizing a force feedback joystick to actively warn visually impaired wheelchair users of obstacles/hazards in their travel path.

The simulation will be used to determine the forces required by the joystick to properly warn the user about various obstacles. These findings will be used to optimize the prototype wheelchair, which will be developed by SKI. This simulation will also be used by SKI to determine the learning curve associated with such a system, since no similar system currently exists. This information will be vital once a prototype is developed and used in the real world. Finally, this simulation will be used by SKI to determine whether a force feedback joystick with a single mode is sufficient for such a wheelchair (as opposed to two switchable modes; one for controlling the wheelchair motion and one mode to give force feedback information about obstacles).

We assumed that all inputs have been received and stored onto an onboard computer since the purpose of this project is to determine feedback as opposed to developing the sensors themselves (all sensors are being developed by SKI). These inputs include the elevations or heights of all objects in the user's environment, and the user's location within the environment. With this data a virtual room will be created that will include such items as walls, drop-offs, slopes and other obstacles. The room will be discretized into finite blocks of a fixed size (i.e., one inch square) and each block will be assigned an elevation. These numbers will be stored as a matrix of elevations where each number represents either the height or amount of drop-off with respect to a chosen datum for each individual point.

During testing, the virtual room remains unknown to the users in order to simulate blind and visually impaired users. The wheelchair begins at an arbitrary location in the virtual room. The position and direction of the wheelchair is continuously modified by the user through the force feedback joystick, which is also the wheelchair control joystick. Sighted and visually impaired users may navigate through the virtual room while data such as obstacles hit, total time traveled, etc., are recorded. SKI will use the data to finalize the prototype design.

The simulation is designed to allow the developer to determine the forces required to send to the force feedback joystick to adequately warn the user(s) of various obstacles/hazards. The output of the simulation is sent to the joystick and perceived by the user.

The simulation was created using Simulink which is an extension of MATLAB used for simulation and modeling of systems. We chose Simulink because it can run in real time and has the ability to communicate with other programs (i.e., the joystick drivers in order to control the joystick). In addition, SKI can use Simulink on its current computer systems without upgrading.

Fuzzy logic is the main control algorithm used to determine the force output for all the various inputs (i.e., distance to object, speed of wheelchair, etc.). This is straightforward to implement within Simulink since Simulink has a *Fuzzy Logic Toolbox* built-in that allows programming using fuzzy logic.

Figure 1 shows the flow chart of the simulation system.

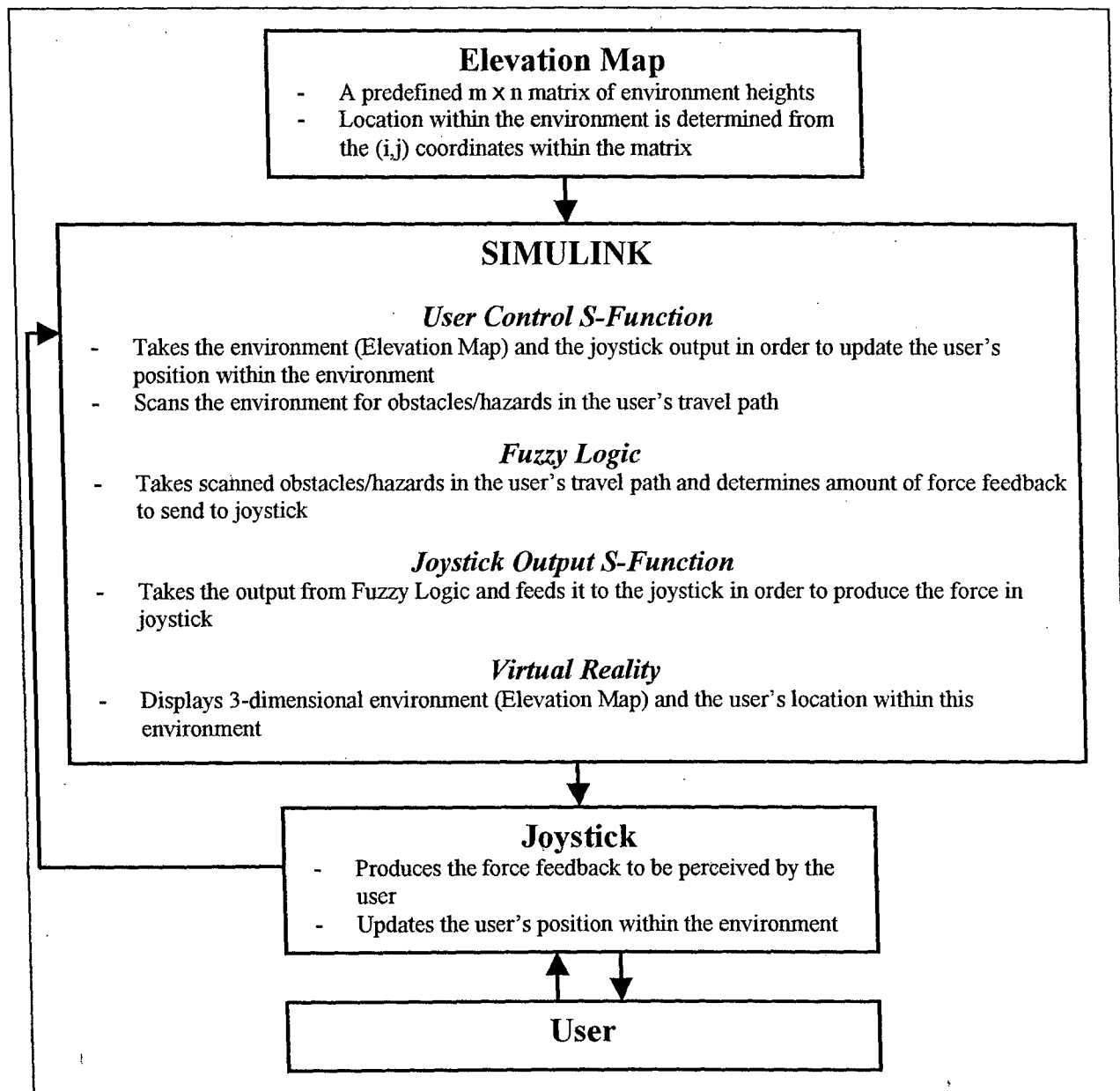


Figure 1: Simulation flow chart

4 Literature Review

Previous research on obstacle avoidance force feedback joystick control for wheelchair users has been done by Brienza et al. Their main design criteria were: (1) ultimate control of the

wheelchair must remain with the driver and not with the control system, and (2) mobility efficiency must be maximized [13,14].

One admitted weakness of this system is the lack of warning for objects to the sides of the wheelchair. When the wheelchair is traveling close to and parallel to an obstacle (i.e., traveling along a hallway) if the user attempts to steer towards the obstacle (i.e., the wall) the joystick should react with a resistive force. However, this system would not react with enough force in time to stop the wheelchair user from colliding with the obstacle.

Another existing obstacle avoidance wheelchair system is the NavChair Assistive Wheelchair Navigation System. Unlike the wheelchair control system described above, this system provides no force feedback. The NavChair is a shared control system in which both the user and the obstacle avoidance subsystem share control of the wheelchair [15].

As mentioned before, this system provides no force feedback, and therefore gives the user no information about the surroundings. In addition, this system does not provide a way for the user to override the control system. The NavChair system also causes the wheelchair to travel at a slower speed than an experienced user would travel without this control system.

5 Project Detail

5.1 Hardware

For this project, we used Microsoft SideWinder Force Feedback 2 joystick due to its low cost and its versatility/programmability (see Figure 2). More information can be found at <http://www.microsoft.com/hardware/sidewinder/FFB2.asp>. Since this is a Microsoft joystick, it uses the Microsoft DirectX drivers. Through the DirectX utilities, nearly any force may be programmed for the joystick, including a constant force, a force that varies with time, a vibration, etc. This joystick allows force feedback along its x-axis and y-axis, and therefore a force may act in any direction as a combination of x- and y-components. Obstacles/hazards are represented as forces acting along a particular direction. This joystick also has the capability to represent texture changes in terrain, such as a change from concrete to gravel, as vibrations at a particular frequency and amplitude depending on the exact texture change.

This joystick has four separate axes: x-axis (side-to-side), y-axis (back-and-forth), z-axis (rotation clockwise and counterclockwise), and throttle axis. This joystick also has eight buttons and a point of view hat switch. Currently, only the x-axis and y-axis are needed by this simulation since these are typically the only features on a joystick-controlled powered wheelchair.



Figure 2: Microsoft SideWinder Force Feedback 2 Joystick

5.2 Software

We used MATLAB version 6.5 R13 (Release 13) which includes Simulink version 5.0 (R13) to create the simulation. Other add-on toolboxes that were needed for this simulation were the *Fuzzy Logic Toolbox* version 2.1.2 (R13) and the *Virtual Reality Toolbox* version 3.0 (R13). In addition, DirectX version 9.0 was used in order to communicate with the joystick.

The simulation was developed as a Simulink model (.mdl file), as this platform provides the most versatility (fuzzy logic, virtual reality, and C++ programming capabilities) and can run in real-time.

5.2.1 Complete Model

Figure 3 shows the complete Simulink model. The model is comprised of the following main subsystems: Elevation Map, Joystick Input, User Control, Fuzzy Logic, Joystick Output, and Virtual Reality. These subsystems are described in detail in the following sections.

5.2.2 Elevation Map

The Elevation Map is an $m \times n$ matrix of surrounding environment heights in the form of a text document. Figure 4 shows an example of an Elevation Map. This file is a representation of an actual environment where the environment is discretized into finite sized blocks (i.e., one inch square) and assigned a value based on the height at each location. The location of each discretized point within the environment is determined from its (i,j) coordinates within the matrix. The value at each (i,j) coordinate is the height at that location. These height values are relative to a predetermined datum (i.e., sea level or the first floor of a house), where a positive value represents a higher elevation and a negative value represents a lower elevation compared to the chosen datum. These values are similar to a topography map. This format allows for the

relatively easy creation of brand new environments for testing purposes and can be duplicated by the data from a scanner or a vision system.

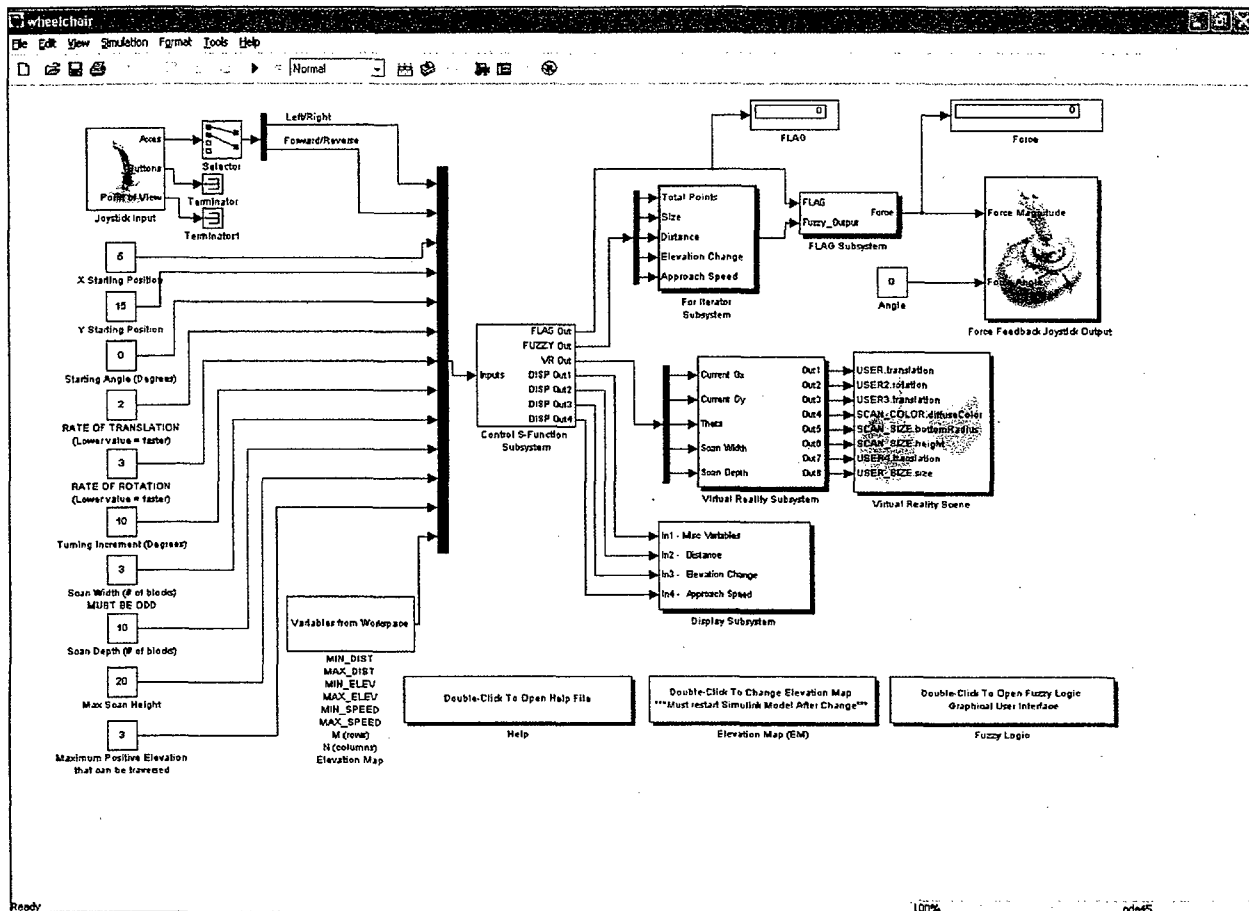


Figure3: Complete Simulink model

5.2.3 Joystick Input

Joystick input is accomplished through the *Joystick Input* block of the *Virtual Reality Toolbox* in Simulink. This block can access any joystick connected to the computer and read the joystick's current parameter values. This block has three output ports: Axes, Buttons, and Point of View. The Axes output port outputs the current values of each joystick axis. The values are normalized to vary from -1 to +1, with zero meaning that the joystick is at the center of that particular axis. These values are used to determine the speed and motion of the user within the virtual environment. The Buttons output port outputs a flag corresponding to the status of each joystick button, zero if the button is released and one if the button is currently pressed. This feature is not used in the current simulation. Finally, the Point of View output port outputs the current status of the point of view selector on the joystick (for appropriate joysticks). This feature is also not used in the current simulation. The size of each of these output ports is automatically scaled for the particular joystick connected to the computer (i.e., a 2-axis joystick will only have two values output from the Axes output port, whereas a 3-axis joystick will output three values).

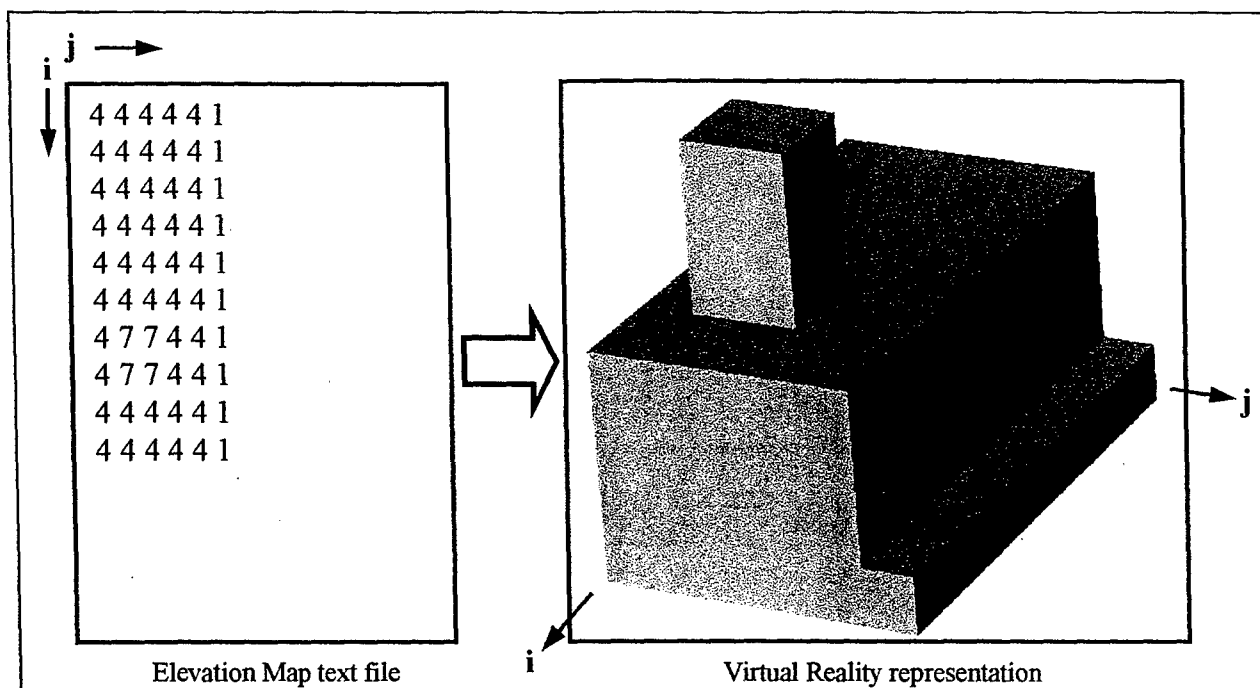


Figure 4: Elevation map text file and corresponding virtual reality representation

5.2.4 User Control

A custom MATLAB S-Function was written in order to control many important aspects of the simulation. A MATLAB S-Function is a customized Simulink block that allows the user to implement custom code/algorithms into a Simulink model. An M-file S-Function is an S-Function written using the MATLAB programming language. M-file S-Functions cause the MATLAB interpreter (application responsible for running non-compiled code) to be called at each time step, which in general is extremely slow compared to using compiled code. C++ S-Functions, on the other hand, are compiled into Dynamic Linked Library (.dll) files. These files are dynamically linked into MATLAB only when needed. This S-Function was written in C++ due to its speed and programmability advantages over M-file S-Functions.

This S-Function does a majority of the work within the simulation. First, this S-Function loads the Elevation Map into memory. It is loaded into memory as a 1-Dimension array. This is done to improve program efficiency since 2-Dimension arrays use large amounts of memory and slow program execution.

In addition, this S-Function keeps track of the user's position and direction within the virtual environment. The scan area is always the same size for a particular simulation and always in the same direction, in front of the user. Therefore, the user and scan area are defined using a local coordinate frame since their relative locations, and therefore distances to one another are constant. These local coordinates must then be transformed into global coordinates (i.e., the elevation map coordinates) using the transformation matrix in order to determine the user's location within the virtual environment.

The global coordinates for any point can be calculated using transformation matrices [16] as shown in Equation 1:

$$^{global}P = ^{global}T_{local} \times ^{local}P \quad (1)$$

This transformation is crucial since all hazards/obstacles are defined in the global coordinate system. Since the user is allowed to translate and rotate simultaneously, the transformation matrix must incorporate transformation matrices for both translation and rotation, as shown in Equations 2 and 3 [16]:

$$Trans(\Delta s, 0, 0) = \begin{bmatrix} 1 & 0 & 0 & \Delta s \\ 0 & 1 & 0 & 0 \\ 0 & 0 & 1 & 0 \\ 0 & 0 & 0 & 1 \end{bmatrix} \quad (2)$$

$$Rot(z, \Delta \theta) = \begin{bmatrix} Cos(\Delta \theta) & -Sin(\Delta \theta) & 0 & 0 \\ Sin(\Delta \theta) & Cos(\Delta \theta) & 0 & 0 \\ 0 & 0 & 1 & 0 \\ 0 & 0 & 0 & 1 \end{bmatrix} \quad (3)$$

The user must be able to rotate around his/her own center (i.e., the local coordinate system origin). Therefore, the motions of the user are relative to the local coordinate system. For transformations relative to a local coordinate system, when an object is first rotated and then translated, the total transformation matrix is:

$$^{global}T_{local} = Rot(z, \Delta \theta) \times Trans(\Delta s, 0, 0) \quad (4)$$

However, if an object is first translated and then rotated with respect to the local coordinate system, the total transformation matrix is:

$$^{global}T_{local} = Trans(\Delta s, 0, 0) \times Rot(z, \Delta \theta) \quad (5)$$

Since this simulation must allow simultaneous rotation and translation with respect to the local coordinate system, equation 6 was used as the transformation matrix [16].

$$^{global}T_{local} = Trans(\Delta s, 0, 0) \times Rot(z, \Delta \theta) = \begin{bmatrix} Cos(\Delta \theta) & -Sin(\Delta \theta) & 0 & \Delta s \\ Sin(\Delta \theta) & Cos(\Delta \theta) & 0 & 0 \\ 0 & 0 & 1 & 0 \\ 0 & 0 & 0 & 1 \end{bmatrix} \quad (6)$$

This equation is valid since the user's motions are broken up into many small paths (i.e., differential motion) with each intermediate position and orientation being continuously recalculated.

The S-Function also prohibits the user from attempting to move forward through obstacles with a larger elevation and keeps the user within the bounds of the virtual environment. However, this simulation does not check for obstacles behind the user. Therefore, if the user travels backwards, no obstacles will be detected. In addition, no force feedback is created in the joystick if the user travels backwards. This is done since the area behind the user is not scanned for obstacles. This is a valid assumption because wheelchair users do not travel backwards for long distances. Typically the user travels backwards to steer around a nearby obstacle and therefore the user knows that there are no obstacles directly behind him/her since s/he has just traveled through that space.

Another feature of the S-Function is that it keeps track of the number of times the user runs into an obstacle. This can be used to improve the simulation through testing of different fuzzy logic rules. A set of rules that results in a smaller number of collisions is better at providing the wheelchair user with appropriate feedback to avoid obstacles. This number can also be used to determine if a user's skills are improving with continued experience with the control system. A user's skills have improved when a user better understands what a specific force means (i.e., how far or how large an obstacle is) and therefore knows how to react in order to avoid collision with an obstacle.

Lastly, the S-Function prepares all inputs needed by the fuzzy logic block. These include the distance from the user to all points in the scan area, the elevation change from the current location to all points in the scan area, and the user's approach speed.

The S-Function has 21 inputs and 16 outputs, as shown in Tables 1 and 2. Many of the output variables were used for program debugging purposes. These variables have not been removed as output variables in case they are needed in future revisions.

Table 1: User control S-Function input variables

Input variable	Description
X-Coordinate	Joystick position coordinate to control user translation
Y-Coordinate	Joystick position coordinate to control user rotation
X Starting Position	User's starting x-coordinate within virtual environment
Y Starting Position	User's starting y-coordinate within virtual environment
Starting Angle	User's starting angle (in degrees) within virtual environment
Rate of Translation	Determines how quickly the user translates in the virtual environment
Rate of Rotation	Determines how quickly the user rotates in the virtual environment
Turning Increment	Increment at which the user rotates within the virtual environment (in degrees)
Scan Width	Total width (in number of block elements) that the program scans for obstacles/hazards in the user's travel path
Scan Depth	Distance from user (in number of block elements) that the program scans for obstacles/hazards in the user's travel path

Max Scan H	Maximum height value that is scanned, any height over this value will be truncated to this value
Max Positive Elevation	Maximum positive height difference that can be successfully traversed by the user
MIN_DIST	Fuzzy logic "Distance" input variable lower limit
MAX_DIST	Fuzzy logic "Distance" input variable upper limit
MIN_ELEV	Fuzzy logic "Elevation Change" input variable lower limit
MAX_ELEV	Fuzzy logic "Elevation Change" input variable upper limit
MIN_SPEED	Fuzzy logic "Approach Speed" input variable lower limit
MAX_SPEED	Fuzzy logic "Approach Speed" input variable upper limit
M (Rows)	Width of the virtual environment
N (Columns)	Depth of the virtual environment
Elevation Map	A row vector containing the entire Elevation Map

Table 2: User control S-Function output variables

Output Variable	Description
Total Points	The total number of points being scanned for obstacles/hazards
Size	The size (total number of points) of the Elevation Map ($M * N$)
Speed	The current speed of the user
Current Gx	The current x-coordinate of the user within the virtual environment
Current Gy	The current y-coordinate of the user within the virtual environment
Current Height	The user's current elevation
T Counter	Counter used to update user's translational motion
R Counter	Counter used to update user's rotational motion
Delta X	Used to recalculate user's position in the virtual environment
Delta Theta	Used to recalculate user's position in the virtual environment
Theta	The current heading of the user within the virtual environment (in degrees)
Distance	A row vector of the distance from the user to every point in the scan area
Elevation Change	A row vector of the elevation change in relation to the user for every point in the scan area
Approach Speed	A row vector of the approach speed of the user to every point in the scan area
Flag	Set equal to 1 if the user is colliding with an obstacle/hazard and used to create maximum force feedback output in joystick
Num Hit	Keeps track of the total number of times the user collides with an obstacle/hazard

5.2.5 Fuzzy Logic

The fuzzy logic algorithm was developed using the Simulink *Fuzzy Logic Toolbox*. This algorithm is used to determine the magnitude of force feedback to be exerted by the joystick in order to warn the user of obstacles and hazards.

Since this algorithm needs to warn blind and visually impaired wheelchair users of obstacles and hazards, the input variables for this simulation were chosen to be:

1. Distance to the obstacle/hazard
2. Elevation Change of obstacle/hazard in relation to user
3. Approach speed of the wheelchair to the obstacle/hazards

The units for the “Distance” input variable are represented by the matrix dimensions. For example, a distance of two would be two matrix dimensions away such as from matrix coordinates (1,2) to (1,4). This makes the system more robust as opposed to designing it with a specific dimension, for example, feet. These matrix dimensions allow the simulation to be compatible with any unit system (i.e., English, metric, etc.).

The units chosen for the “Elevation Change” input variable are defined by the units used in the elevation map. For example, if the elevation map were designed using inches, then the units for the “Elevation Change” input variable are inches. As with the “Distance” input variable units, these user defined units allow the simulation to be compatible with any unit system.

The “Approach Speed” input variable is unitless. Rather than using units, this variable is simply a linear scale with a range from a speed of zero to maximum speed. As with the other two input variables, this allows the simulation to be compatible with any unit system.

The “Distance” input variable range was chosen to be 0-10, however this range is modified by the simulation input variable “Scan Depth” at runtime (see Table 1). This input variable was fuzzified into five fuzzy sets (Figure 5). These sets are:

1. Very-Close
2. Close
3. Average
4. Far
5. Very-Far

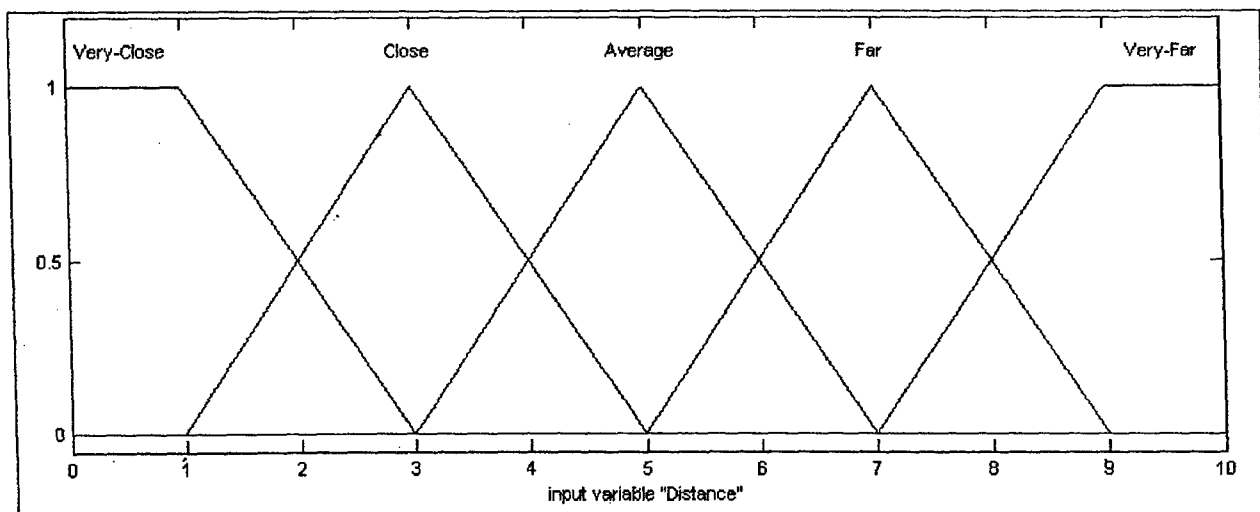


Figure 5: Fuzzy logic set definitions for “Distance” input variable

Similarly, the "Elevation Change" input variable range was chosen to be 0-10, however this range is modified by the simulation input variable "Max Scan H" at runtime (see Table 1). The "Elevation Change" input variable was fuzzified into five fuzzy sets (see Figure 6). These sets are:

1. Large-Negative
2. Negative
3. Level
4. Positive
5. Large-Positive

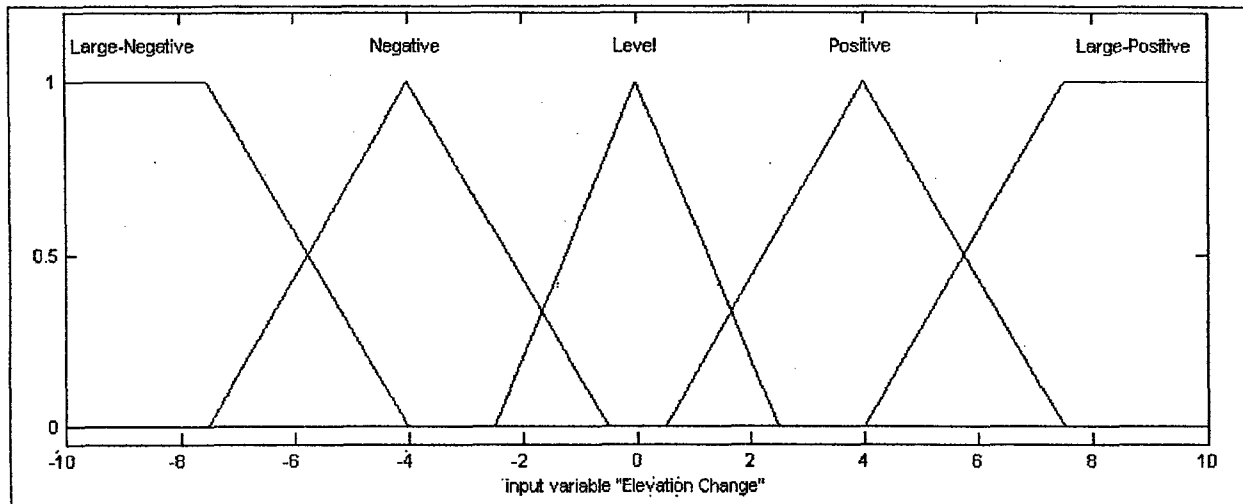


Figure 6: Fuzzy logic set definitions for "Elevation Change" input variable

The "Approach Speed" input variable range was chosen to be 0-10, which as noted previously, is only a linear scale (i.e., unitless). This input variable was fuzzified into six fuzzy sets (see Figure 7). These sets are:

1. Zero
2. Very-Slow
3. Slow
4. Moderate
5. Fast
6. Very-Fast

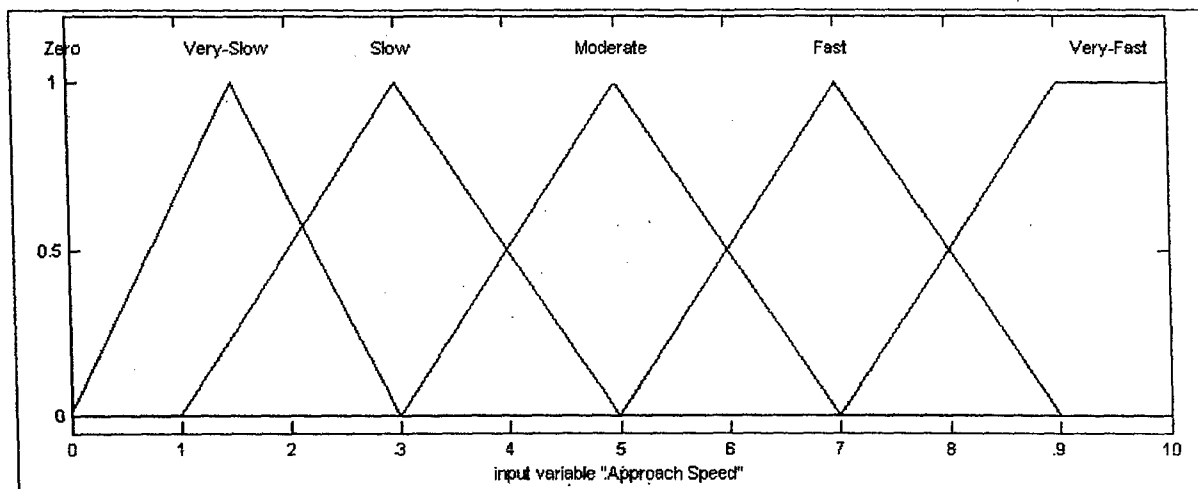


Figure 7: Fuzzy logic set definitions for "Approach Speed" input variable

The "Force Magnitude" output variable range is dependant on the joystick being used. The joystick has a force magnitude range that is pre-defined as 0-10,000. The "Force Magnitude" output variable was fuzzified into six fuzzy sets (see Figure 8). These sets are:

1. Zero
2. Very-Weak
3. Weak
4. Medium
5. Strong
6. Very-Strong

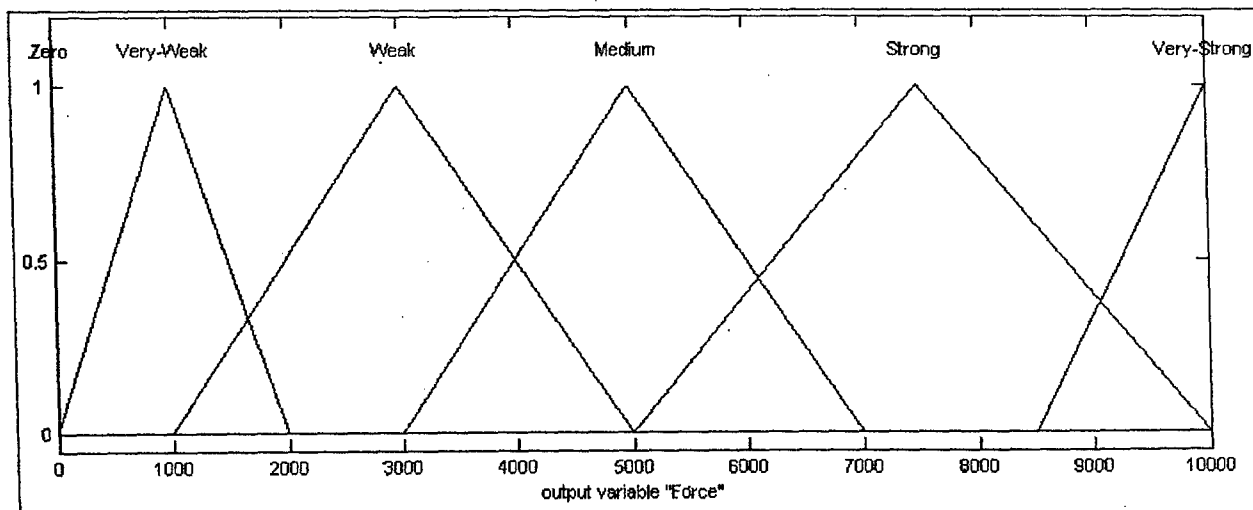


Figure 8: Fuzzy logic set definitions for "Force Magnitude" output variable

For this number of fuzzy sets (five for "Distance", five for "Elevation Change", and six for "Approach Speed"), a total of 150 rules were defined to capture all possible combinations of the input variable sets. The rules were written in the form:

If <VARIABLE 1> and <VARIABLE 2> and <VARIABLE 3> then <Output>

An example of an actual rule used in the fuzzy logic algorithm is:

If (Distance is Very-Far) and (Elevation Change is Large-Negative) and
(Approach Speed is Very-Fast) then (Force is Medium)

The defuzzification method (the process of converting a fuzzy value into a non-fuzzy, or crisp value) used for this fuzzy logic algorithm is the Mamdani fuzzy inference method (16). This is one of the most commonly used defuzzification methods utilized in fuzzy logic systems.

The number of fuzzy sets for each variable, the values associated with each fuzzy set, the range for each variable, and all rules were initially defined based on previous experience with fuzzy logic systems and have been modified with testing of the system.

Since there are three input variables and one output variable, a 4-dimensional plot would be required to show all possible outputs for each set of inputs, which is impossible. Therefore, one of the input variables will be fixed for each output plot. Figure 9 shows the output plot with the "Approach Speed" input variable set to its maximum value of 10, the "Elevation Change" input variable only through its positive range, and the entire range of the "Distance" input variable.

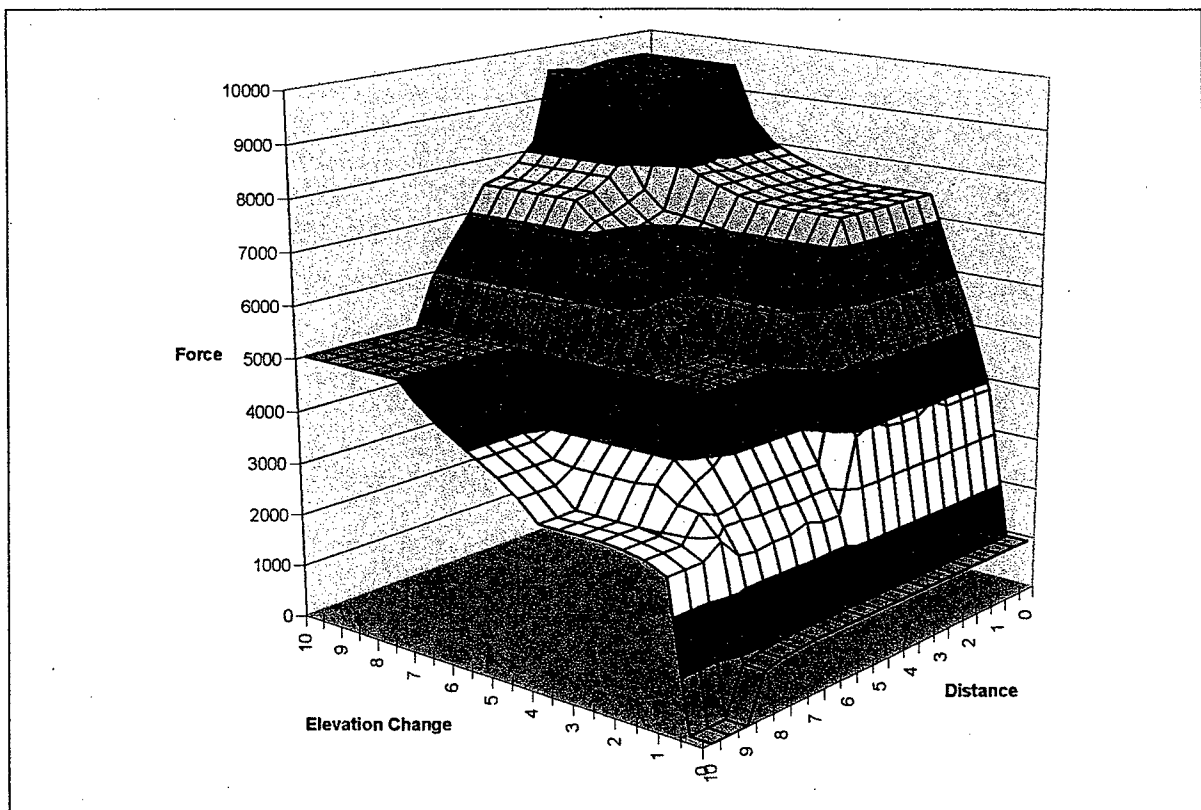


Figure 9: Fuzzy logic output plot for maximum "Approach Speed"

5.2.6 Joystick Output

A custom MATLAB S-Function was written in order to produce the force feedback in the joystick. A custom Simulink block was then created using this S-Function and can be seen in Figure 10. The S-Function was written in C++ to be able to control the force feedback portion of the joystick. The joystick uses Microsoft's DirectX drivers, which can be manipulated using C++.

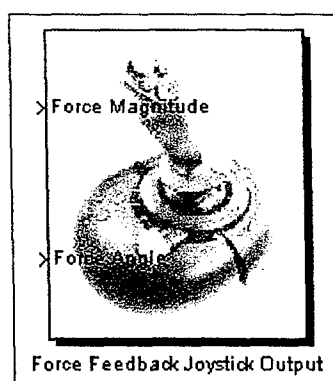


Figure 10: Custom force feedback joystick output block

The Force Feedback Joystick Output block has two inputs: Force Magnitude and Force Angle. The Force Magnitude input is a value between "0" and "10,000", which are predefined for the particular joystick being used. The "10,000" value corresponds to the maximum force magnitude and the "0" value corresponds to no force. This value is the output of the *Fuzzy Logic Controller* block. The Force Angle input is measured in degrees and is the angle at which the force acts (see Figure 11). This value is currently set to act at 0° , which is in the opposite direction as the wheelchair is traveling. This is done because only obstacles in the user's travel path are of importance and therefore the force should push directly backwards (in relation to the user) to warn of upcoming obstacles.

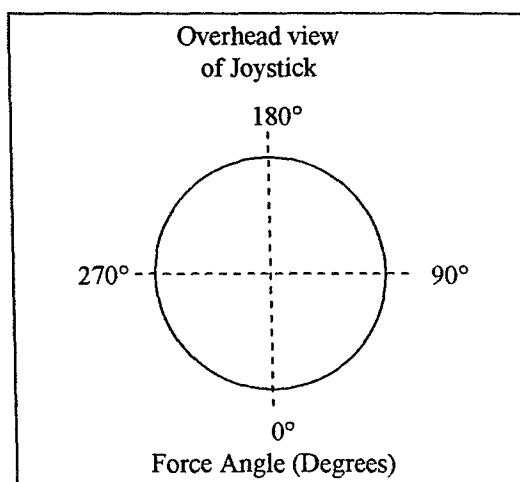


Figure 11: Joystick force angle representation

Currently a "Spring Force" type of output force is used for this simulation. As defined by the Microsoft DirectX drivers, a "Spring Force" is a force that varies linearly from zero at the origin to a maximum value (determined from the hazards/obstacles present) when the joystick is moved to its maximum position away from the origin (Figure 12). This type of force is used so that the force created by the joystick would not cause the wheelchair to move to an undesired location, such as backwards. A "Spring Force" has its neutral point at the origin of the joystick range of motion. When the joystick is at the origin, no force is exerted and therefore the wheelchair remains at rest.

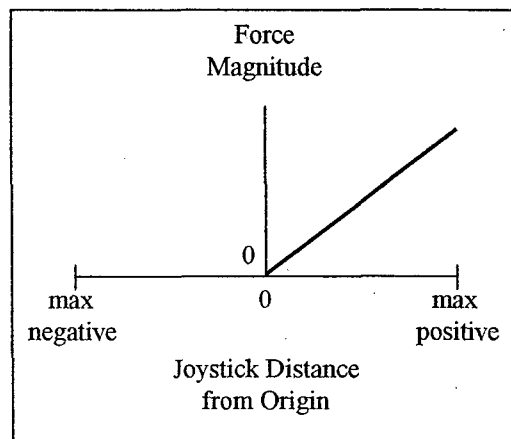


Figure 12: Joystick force magnitude vs. distance relationship for "Spring Force"

A "Constant Force" is defined by the Microsoft DirectX drivers as a force that is constant in a single direction (Figure 13). This type of output force is undesirable for this simulation since the output force itself can cause motion in the direction of the force. For example, a "Constant Force" acting along a direction toward the user (i.e., an obstacle in front of the wheelchair) could cause the wheelchair to move backwards if the user did not resist the joystick force. This is because a "Constant Force" acting along a direction is constant throughout the entire range of the joystick and does not depend on joystick position. Therefore, an unopposed "Constant Force" would cause the joystick to come to rest at its range limit in the direction of the force. This is due to this type of force having no neutral point in the joystick range of motion. Therefore, this type of force was not used for this simulation.

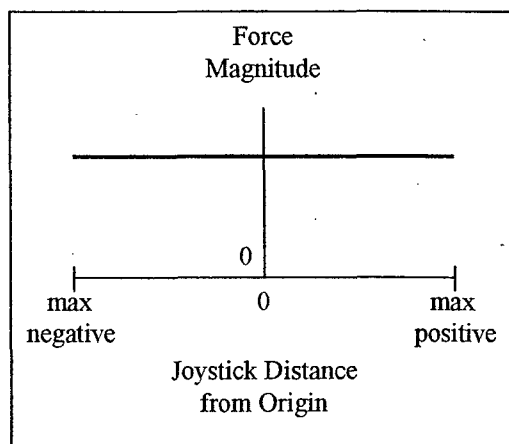


Figure 13: Joystick force magnitude vs. distance relationship for "Constant Force"

5.2.7 Virtual Reality

The virtual reality display allows others to physically see how the user is moving throughout the virtual environment. It is currently used for training purposes and program optimization. No calculations are performed with the virtual display itself. This display is merely an add-on to make it easier to verify the correctness of forces from the joystick for various obstacles/hazards. This will be eliminated in the final prototype by SKI, as this information is useless to a blind or visually impaired wheelchair user. The elimination of the virtual reality display will also increase simulation efficiency and program execution will become faster since much processor power is currently used by the virtual reality display.

The display of the virtual world is accomplished using Virtual Reality Modeling Language (VRML). Simulink R13 has an add-on toolbox, *Virtual Reality Toolbox*, which allows virtual reality world files (.wrl) created using VRML to be displayed and updated.

The simulation needs to be as robust as possible (i.e., work with any number of different virtual environments). Therefore, a custom MATLAB program file (M-file) was written in order to create the VRML virtual world file. The M-file reads in the scene from an external elevation-map file and creates the scene using box nodes (3D cubes). Each box node is a distinct element from the scene with a distinct height determined from the elevation map (Figure 14).

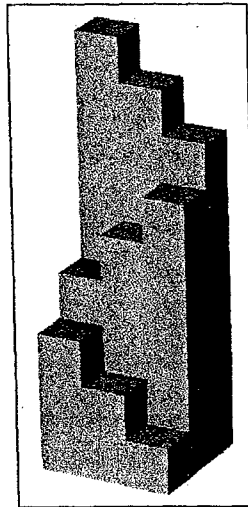


Figure 14: A 3x3 Virtual Reality scene made of 9 individual box nodes

As more box nodes are used to create a virtual reality environment, the resolution of the environment increases and more detail can be achieved. The virtual reality environment can be of any size as long as it is in the form of a matrix (mxn). One of the disadvantages of having a very large virtual reality environment is that the execution of the program is adversely affected. The larger the virtual reality scene, the slower the simulation will execute on a given machine. However, this slowing of execution can be overcome with a faster processor and more RAM.

Figure 15 shows an average sized virtual reality scene. This scene contains several walls and two openings in the walls, such as doorways. The actual size of each virtual reality scene is

completely scalable to the size of the user within the scene. For the scene shown in Figure 15, a 70x45 matrix, if the user were chosen to have a width of five matrix elements within the virtual environment and assuming that a physical wheelchair has a width of three feet, then a 70x45 matrix scene would have approximate dimensions of 14' by 9'. However, if the user width were chosen to be three matrix elements within the virtual environment, then the actual size of the virtual reality scene would be approximately 23.3' by 15'. In this way, a single virtual reality scene is configurable to any size required.

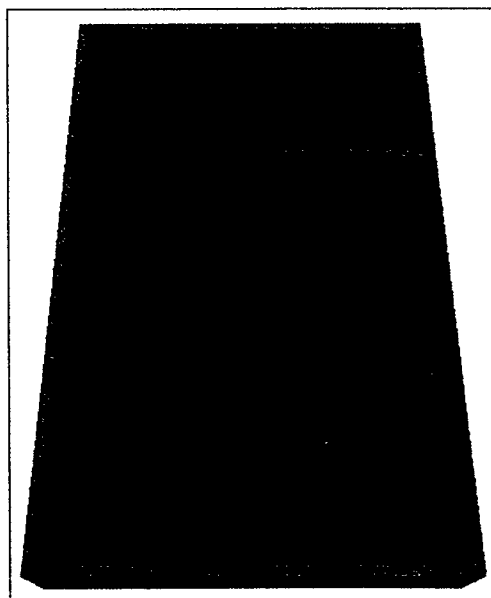


Figure 15: A 70x45 virtual reality scene

The user is represented in the virtual reality scene as a box (Figure 16). A triangle represents the "Scan Area" with dimensions equaling the "Scan Width" and "Scan Depth", even though the actual scan area is rectangular in shape. This was done to better differentiate the user's direction of travel in the virtual scene. In addition, the "Scan Area" blinks in the simulation to indicate to users that this is not a physical object. The "Scan Area" is only the region ahead of the user that is being scanned for obstacles/hazards.

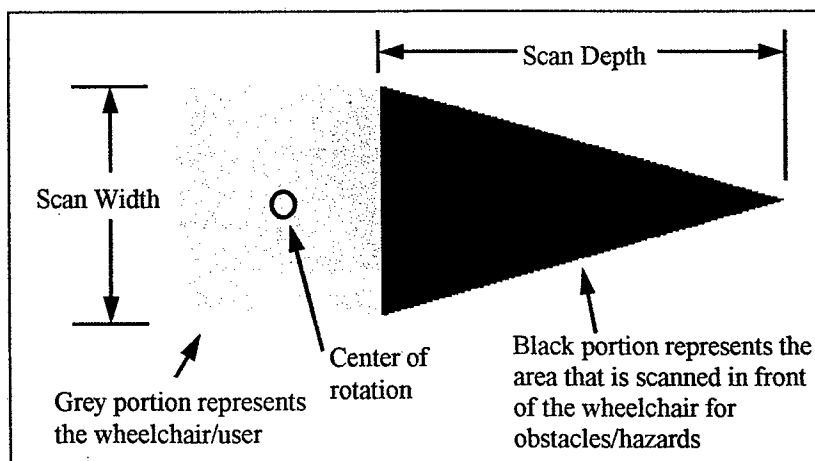


Figure 16: Overhead view of user representation within virtual reality scene

6 Results and Discussion

The program functions as expected. When a virtual environment is entered into the system, a user can try to navigate through the environment by feeling the force feedback from the joystick, even with closed (blind) eyes. As the wheelchair gets close to an obstacle, the user feels a force feedback in the joystick, resisting the forward motion. Turning away from the obstacle will reduce the opposing feedback force on the joystick, allowing the user to move forward. As a result, the user can navigate through an unfamiliar environment with closed eyes.

The simulation was tested by twelve individuals, both viewing the virtual environment and with closed eyes. In most cases, after a few minutes of practice, the user could develop a "feel" for the resistive force and respond accordingly. Since the purpose of the project was to develop the simulation and not training, we only tested the program for proper function and not to train the user.

In its current form, the simulation cannot be fully tested with blind users. This is because the user has no sense of speed within the virtual environment. This includes both translational and rotational speed. This information is available to blind wheelchair users as they can sense how fast they are moving and rotating through the sounds of the wheelchair and the sense of motion. In addition, echoes are not present in a virtual environment. Echoes are important for blind wheelchair users especially for objects to the sides of the wheelchair.

Despite the lack of sound within the virtual environment, testing of this system has yielded promising results. This system is able to warn the user of various hazards in the travel path. Avoidance control is left up to the user. The user has the choice of steering around either side of an obstacle, if possible, or turning around and finding an alternate route.

After being briefed about the virtual environment, each user was allowed to explore throughout the environment. Both sighted and unsighted users were able to "feel" around the environment as they moved. The environment was not revealed to the users as they traversed in order to simulate blind or visually impaired users. Even without knowing their exact surroundings, the users were able to gain valuable information about obstacles/hazards in the environment. Users were able to find doorways and safe passages without colliding with walls.

Even though users had no sense of the speed of translation and rotation due to the virtual environment, they were able to detect obstacles in their travel path. Typically, within 5-10 minutes of exploration, all subjects became acclimated to the system and were able to avoid collisions with obstacles. This time was needed in order for users to learn the meaning of the joystick forces (i.e., the severity of the force versus how close an obstacle was). Therefore, subjects required practice in order to successfully judge how much time they needed before attempting to avoid an obstacle. This, in fact, is one of the major applications for the Smith Kettlewell personnel, who need to train their users to use an actual wheelchair.

When users neared a high-risk hazard (i.e., a drop-off) where the maximum output force was produced by the joystick, it became difficult for them to even continue on the same path. This

feature provides a much safer experience for blind or visually impaired wheelchair users where avoidance of high-risk hazards is critical. If, however, users wish to approach a hazard/obstacle for further examination, they are able to do so by pushing harder on the joystick. This system advises against approaching hazards by producing a larger force until the maximum joystick force has been reached, but cannot completely stop users if they are determined to proceed in the direction of a hazard/obstacle. This is a beneficial feature because it allows the user to be in control of the wheelchair at all times.

Due to the lack of speed information to the users, travel was slower than expected because travel paths needed to be broken up into small segments of exploring for a clear path and then moving. This feature will be solved once the system is incorporated into a prototype wheelchair by SKI.

The fuzzy logic output plots indicate that the rules and variable definitions are well defined, gradually changing for varying input variable values (i.e., no dramatic changes in output for a small change of input except where it is required). In addition, from actual use of the simulation, one can determine that the output ("Force Magnitude") is sufficient to allow the user enough time to react in order to avoid various hazards/obstacles. Moreover, the amount of force gives the user valuable information about the severity of the hazard/obstacle in the wheelchair travel path.

7 Post-Testing System Modification

One major modification that resulted from testing was the creation of a second version of the simulation to be formally tested and compared with the first simulation version (refer to *Complete Model* on page 7). The second version allows for the scanning of obstacles/hazards that are to the sides of the wheelchair user. This was accomplished by changing the rotation degree of freedom (DOF) into a side scan mode, scanning either the left or the right hand side of the user depending on which direction the joystick is moved. The new rotation DOF is now a twisting motion of the joystick (this is a DOF for the particular joystick being used, refer to *Hardware* on page 6). The side scan feature does not scan nearly as far for obstacles as the frontal scan. Instead, the side scan only scans for obstacles in the immediate areas to the side of the wheelchair.

The reasons for these changes were to help the user follow a wall (i.e., along a hallway) and also to warn the user if s/he were to turn in a direction of an obstacle/hazard. In other words, the user can check for obstacles in a particular direction before actually rotating in that direction. This allows the user to move faster through the environment as they can eliminate unnecessary rotations (i.e., rotations that move the user in the path of an obstacle).

8 Conclusion

A haptic (tactile) interface for a wheelchair has been designed and implemented in a virtual environment. Basic testing of this interface has been performed in several designed virtual environments with twelve subjects. All subjects were able to successfully move throughout the virtual environments without collisions, after a brief learning period. This testing has lead to an

alternate simulation version. Final confirmation of the hypothesis for practical applications requires physical testing with a prototype wheelchair – a subject of a future study.

9 Future Work

It is difficult to determine whether this system could be a replacement for the more traditional use of a cane by a blind or visually impaired wheelchair user. This is because a cane cannot be tested in the created virtual environments. The best way to test this system against a traditional cane “system” is to create an actual prototype and then test each version head-to-head. However, the potential is there for the system created to be much better than the cane alternative. With some or all of the improvements listed below, this system could outperform any currently available system for blind or visually impaired wheelchair users.

A pre-proposal has been submitted in response to the Honda Initiation Grant call for proposals to develop a prototype wheelchair based on this system.

9.1 Terrain Changes

Information about terrain changes, changes from one type of terrain to another, could be incorporated through an additional subsystem built into the Simulink model. Terrain changes could be represented as vibrations of the joystick. Each terrain change of interest could be programmed as a vibration with a unique frequency and amplitude. For example, if a user is moving in a direction where the terrain changes to grass, the joystick could have a small vibration feedback amplitude, whereas a terrain change to gravel could have a much larger vibration feedback amplitude. The frequency could also give information about the terrain change. In this way, the roughness and severity of a terrain change could dictate the vibration feedback. This information would give a blind and/or visually impaired wheelchair user a better understanding of their surroundings.

The terrain change information could either be incorporated into the elevation map or be created as its own file that has a one-to-one correspondence with the elevation map (i.e., a particular location i,j is the same point in both the elevation map and terrain change file). This subsystem could work concurrently with the force feedback output subsystem to allow both force feedback and vibration feedback to occur simultaneously.

9.2 Two Modes of Operation

It should also be investigated whether a joystick with two modes of operation is more beneficial than the current one mode. Currently the simulation has one mode of operation. A second mode of operation could be added where one could be used to control the wheelchair motion and a second mode could output the force feedback. The second mode acts in an “investigation” mode, allowing the user to “feel” around the environment for obstacles without actually moving within the environment. Dual mode would also allow for directional feedback, as the directional feedback could not cause the wheelchair to rotate as would occur with the current system. The two modes could be controlled with an on/off switch to allow easy switching between the two

modes. Two modes of operation would be used instead of two joysticks since it is beneficial to leave a blind or visually impaired wheelchair user one free hand for the use of a cane.

10 Acknowledgment

This work was sponsored by the Department of the Navy, Office of Naval Research, under Award # N00014-04-1-0436.

References

1. National Center for Health Statistics, "National Health Interview Survey on Disability, Phase 1 and Phase 2," 1994/1995.
2. Shraga Shoval, Iwan Ulrich and Johann Borenstein, "Computerized Obstacle Avoidance Systems for the Blind and Visually Impaired," *Intelligent Systems and Technologies in Rehabilitation Engineering*, eds. H.N.L. Teodorescu and L.C. Jain (CRC Press, 2000), 414-448.
3. David M. Brienza and Jennifer Angelo, "A Force Feedback Joystick and Control Algorithm for Wheelchair Obstacle Avoidance," *Disability and Rehabilitation* 18, no. 3 (1996): 124.
4. Sylvie Perera, "Tactile Perception and Design," Bionic Project [report online] (Tiresias.org, April 2002, accessed 4 February 2005); available from <http://www.tiresias.org/reports/tpd1.htm>.
5. A.G. Cleary, H. McKendrick and J.A. Sills, "Hand-arm Vibration Syndrome May Be Associated with Prolonged Use of Vibrating Computer Games," *British Medical Journal* 324 (February 2002): 301.
6. N. Pressey, "Mowat Sensor," *Focus* 11, no. 3 (1977): 35-39.
7. Tony Heyes, "Sonic Pathfinder: A programmable guidance aid for the blind," *Electronics and Wireless World* 90, no. 1579 (April 1984): 26-29, 62.
8. Paul Bach-y-Rita et al, "Vision Substitution by Tactile Image Projection," *Nature* 22, no. 184 (March 1969): 963-964.
9. Paul Bach-y-Rita, Kurt Kaczmarek and M. Tyler, "A Tongue-based Tactile Display for Portrayal of Environmental Characteristics," *Virtual and Adaptive Environments: Applications, Implications, and Human Performance*, Vol. 1, eds. Lawrence J. Hettinger and Michael W. Haas (New Jersey: Erlbaum, 2003), 169-186.
10. Leslie Kay, "The Sonic Glasses Evaluated," *The New Outlook for the Blind* 67 (1973): 7-11.
11. Leslie Kay, "Sensory Aids to Spatial Perception for Blind Persons: Their design and evaluation," *Electronic Spatial Sensing for the Blind*, eds. D.H. Warren and E.R. Sterlow (Boston: Martinus Nijhoff, 1985): 125-134.

12. Bernd Petzold et al, "A Study on Visual, Auditory, and Haptic Feedback for Assembly Tasks," Presence 13, no. 1 (February 2004): 16-21.
13. Narayan L. Gehlot and David M. Brienza, "Concept and Implementation of a Force Feedback Active Joystick," Proceedings of the Annual RESNA Conference (Vancouver, British Columbia: RESNA Press, 1995): 325-327.
14. David M. Brienza and Jennifer Angelo, "A Force Feedback Joystick and Control Algorithm for Wheelchair Obstacle Avoidance," Disability and Rehabilitation 18, no. 3 (1996): 123-129.
15. Simon P. Levine et al, "The NavChair Assistive Wheelchair Navigation System," IEEE Transactions on Rehabilitation Engineering 7, no. 4 (December 1999): 443-451
16. Niku, Saeed B., Introduction to Robotics: Analysis, Systems, Applications, Prentice-Hall, New Jersey, 2001.

Effect of Reflow Profile on SnPb and SnAgCu Solder Joint Shear Strength

Project Investigator:

Jianbiao Pan, Ph.D.
Assistant Professor
Industrial & Manufacturing Engineering
Cal Poly State University

Effect of Reflow Profile on SnPb and SnAgCu Solder Joint Shear Strength

Abstract

Reflow profile has significant impact on solder joint performance because it influences wetting and microstructure of the solder joint. The degree of wetting, the microstructure (in particular the intermetallic layer), and the inherent strength of the solder all factor into the reliability of the solder joint. This paper presents experimental results on the effect of reflow profile on both 63%Sn 37%Pb (SnPb) and 96.5%Sn 3.0%Ag 0.5%Cu (SAC 305) solder joint shear strength. Specifically, the effect of the reflow peak temperature and time above solder melting temperature (liquidus) are studied. Nine reflow profiles for SAC 305 and nine reflow profiles for SnPb have been developed with three levels of peak temperature (230°C, 240°C, and 250°C for SAC 305; and 195°C, 205°C, and 215°C for SnPb) and three levels of time above solder melting temperature (30 sec., 60 sec., and 90 sec.). The shear strength data of four different sizes of chip resistors (1206, 0805, 0603, and 0402) are compared across the different profiles. The shear strength of the resistors is measured at both time 0 (right after assembly). In addition to the shear testing the effect of the profiles on the wetting of the solder joint is inspected by optical microscopy.

Introduction

The increasing awareness of health risk associated with lead alloys has pushed the electronics industry toward lead-free. The legislation ban the use of lead is only one of the driving forces. From the business point of view, the lead-free electronic product (green product) is also a market trend.

Effective transition from SnPb soldering to the lead-free soldering requires key implementation issues to be addressed in the electronics industry. One of the critical issues is the effect of reflow profile on lead-free solder joint reliability since reflow profile would influence wetting and microstructure of the solder joint.

Among many proposed lead-free solders, SnAgCu alloy seems to be the leading alternative for the eutectic SnPb solder. The alloy has been recommended by iNEMI (inter-National Electronics Manufacturing Initiative), the European consortium – BRITE-EURAM, and Japan Electronics and Information Technology Industry (JEITA). One of the major differences between SnPb and SnAgCu lead-free solders is that SnAgCu solders require higher reflow temperatures than SnPb. The melting point of SnAg3.8Cu0.7 is 219°C, and that of SnAg3.0Cu0.5 (SAC305) is 217°C. All are higher than eutectic SnPb solder, which has a melting point of 183°C. Note that SnAg3.8Cu0.5 means 3.8 percent in weight Ag, and 0.5 percent in weight Cu, with the leading element Sn making up the balance to 100%.

The high melting temperature not only requires a new reflow profile, but also increases the component stability concerns accompanying with higher temperature. For SnAgCu reflow soldering, a commonly accepted minimum peak temperature of 230°C is necessary to achieve acceptable solder joints. The maximum temperature, on the other hand, depends on the board size, board thickness, component configuration, material thermal mass, oven capability, and etc. These facts result in different temperature delta crossing the board which can sometimes be as high as 20 – 25°C. Moreover, larger components and thicker board leads to higher temperature

delta across the board. In addition, greater complexities of component configuration demands a longer time above liquidus in order to maintain uniform peak temperature across the entire PCB. Some components may not survive at that high reflow temperature.

Solder paste needs adequate reflow temperature to melt, wet, and interact with the copper pad or other board metallization and component metallization to form the solder joint. The intermetallic layers, which act as the bond, will form during the reflow and cooling process. A suitable reflow profile is essential to form a good solder joint.

Research studies show that the peak temperature (PT) and time above liquidus (TAL) during the reflow process are the most critical parameters, impacting solder joints reliability [1, 2]. A good solder joint strength mainly depends on two parts: the microstructure of bulk solder joint and the intermetallic layer. The microstructure of SnAgCu solder joint is different from that of a eutectic SnPb joint due to the presence of Cu_6Sn_5 (note: with SnPb on Cu board this is at the interface) and Ag_3Cu intermetallic compound (IMC) in the bulk solder [2]. Generally speaking, the faster cooling rate would result in finer grain size in the solder joint, which would strengthen solder joint.

The intermetallic layer thickness is another factor that would impact solder joint strength. The intermetallic layer is a critical part of a solder joint because it facilitates bonding between the solder and substrate. With a higher peak temperature and a longer time above liquidus, more solids are dissolved and more intermetallics are formed, which result in thicker intermetallic layer [1]. But too thick intermetallic layer has adversely effect because it is generally the most brittle part of the solder joint. Solder joint strength may be affected by both lack of intermetallic formation as well as excess intermetallics. Hence, an optimum combination of PT and TAL is important to achieve a good solder joint.

The purpose of this experiment is to study the effect of the reflow peak temperature and time above liquidus on solder joint shear strength. Nine reflow profiles for SAC 305 and nine reflow profiles for SnPb have been developed with three levels of peak temperature (230°C, 240°C, and 250°C for SAC 305; and 195°C, 205°C, and 215°C for SnPb) and three levels of time above solder melting temperature (30 sec., 60 sec., and 90 sec.). The shear strength data of four different sizes of chip resistors (1206, 0805, 0603, and 0402) are compared across the different profiles.

Experimental Procedures

Design of experiment

A 2^3 factorial design with three replications was selected in the experiment. The peak temperature and time above liquidus are the two factors and each factor has three levels: PT at 230°C, 240°C, and 250°C for SAC 305 and 195°C, 205°C, and 215°C for SnPb, and TAL at 30 seconds, 60 seconds, 90 seconds, for both, as shown in Table 1. Four different sizes of pure tin plated chip resistors, 1206, 0805, 0603, and 0402 were used in this experiment. 1206 means a component with a nominal length of .12 inch (3.0 mm) in length and .06inch (1.5 mm) in width. This experiment covered both forward compatibility (lead-free component with lead-free solder

paste) case and backward compatibility (lead-free component with SnPb solder paste) case as shown in Table 2.

Table 1. Experiment matrix

Solder paste		Peak temperature (°C)		
Sn-3Ag-0.5Cu	TAL (sec)	230	240	250
	30	A	B	C
	60	D	E	F
	90	G	H	I
Sn-Pb	TAL (sec)	195	205	215
	30	J	K	L
	60	M	N	O
	90	P	Q	R

Table 2. Solder Paste, Components, and Board in the Experiment

	Solder Paste	Components & metallization	Board metallization
Forward compatibility	SAC305	1206, 0805, 0603, 0402, all pure Sn	OSP over Cu pad
Backward compatibility	Sn63Pb37	1206, 0805, 0603, 0402, all pure Sn	HASL SnPb over Cu pad

Test Vehicle

A test vehicle was design as shown in Figure 1. It is a one-layer with the thickness of 62 mils (1.57 mm) and 3.875 x 5.375 inch² in size, FR-4 Board. Both solder pastes, Sn3.0Ag0.5Cu and Sn37Pb (Multicore Brand supplied by Henkel) used in the experiment were type 3 and no-clean flux.

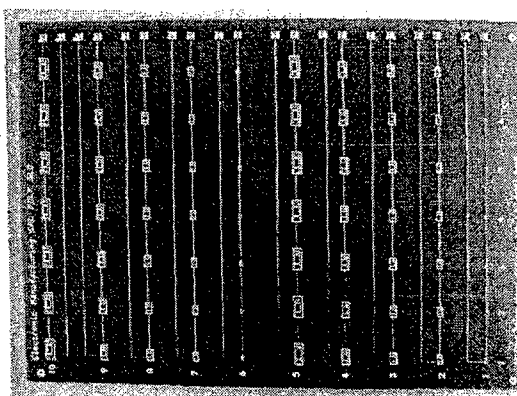


Figure1. Test Vehicle

Printing process

A DEK256 series stencil printer was used to deposit the solder paste on the test vehicles. The standard process recipe developed is showed in Table 3. The printing quality was inspected using microscope and some sample pictures are showed in Figure 2. The stencil was cleaned by dry wiper and vacuum after every three prints.

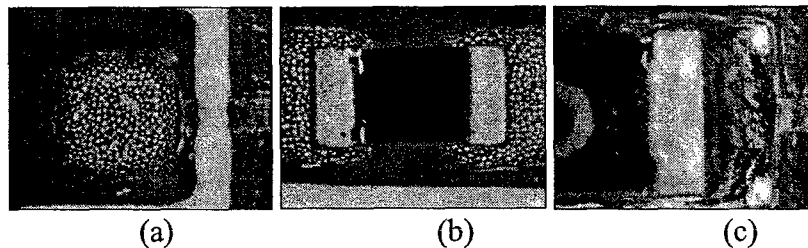


Figure 2 Microscope images (a) after stencil printing (b) after component being placed (c) after reflow

Table 3. Printing setting

Parameters	Details
Stencil thickness	4 mils
Squeegee material	Stainless
Front print speed / Rear print speed	25 mm/sec / 25 mm/sec
Front pressure / Rear pressure	8.0 kg / 8.0 kg
Squeegee length	12 inch
Separation speed	1.0 mm/sec
Separation distance	2.0 mm

Reflow profile development

A Heller 1500 force convection oven with 5 heating-zone and one cooling zone was used to develop the total 18 reflow profiles. Three thermal couples were attached to the test vehicle where covered the diagonal corners of the board and the center as shown in Figure 3.

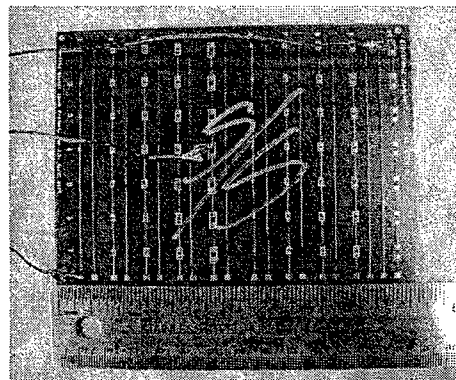


Figure 3 Thermal couple placement

Reflow profiles were developed based on the criteria described in Table 4. A linear ramp-up method was used here (details on linear ramp-up method please refer to [4, 5]). Nine reflow profiles were developed for SnAgCu paste and nine reflow profiles were developed for SnPb paste. The settings including cooling rate for the eighteen reflow profiles are documented in Appendix A. Figure 4 shows a sample lead-free reflow profile used on the experiment.

Table 4. Criteria for Reflow Profile

	SnPb	SnAgCu
Ramp-up	0.5 – 1.0°C/sec until reaching about 170°C	0.5 – 1.0°C/sec until reaching about 204°C
Soak	Between 170 to 183°C for less than 45 seconds	Between 204 to 217°C for less than 45 seconds
Reflow	As described in Table 1	As described in Table 1
Cool rate	4°C /sec	4°C /sec

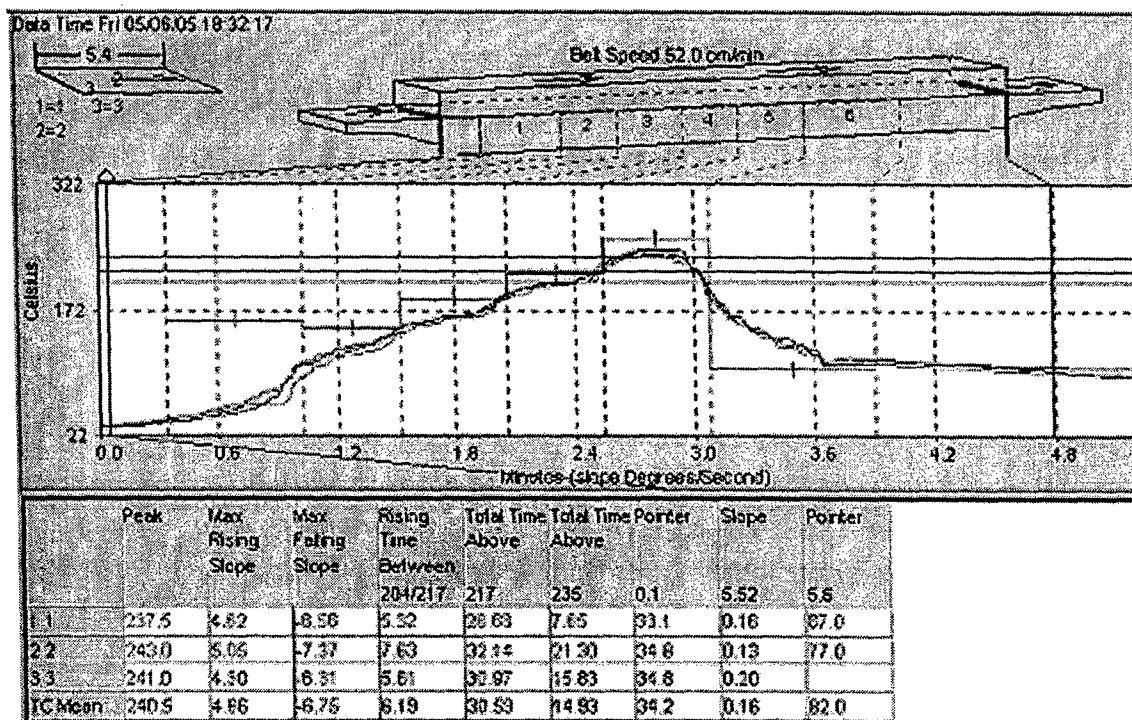


Figure 4 A typical lead-free reflow profile

Assembly

Since it is a 2^3 factorial design with three replications, 27 boards were assembled using SnPb paste and 27 boards were assembled using SAC305 paste. The assembly was conducted over two days, the SnPb boards were assembled in one day and SnAgCu boards were assembled the next day. The assembly sequence in each day was randomized to minimize the nuisance factors such as room temperature, humidity, and other conditions as shown in Appendix B. To be consistent, the process parameters for the stencil printing and pick & place were the same. The only variable is the reflow profile. When moving from one profile to another, the oven settings

were changed and allowed to get to temperature (e.g. wait for green light), and then allowed to stabilize for 5 minutes.

All boards were visually inspected after stencil printing, after pick and place, and after reflow. The only difference observed by visual inspection between SnPb solder joints and SAC305 solder joints after reflow is that SnPb joints look shiny and SAC305 joints look dull.

Shear test

Shear test was performed at Henkel Technologies, Irvine, CA using a Dage-series 4000 shear tester. Table 5 shows the parameters of the shear test machine. Note that the shear strength depends on shear speed [6]. Each board was cut into two identical pieces. The first half of the board was used for the initial time zero after assembly and the other half was used for air-to-air thermal shock testing. For the first half samples, six components of each type (e.g. 0603, 1206, etc.) on one board and each reflow profile were sheared with one component left for SEM analysis. Therefore, 1292 data (6 components x 3 boards x 4 components sizes x 18 reflow profiles) were collected. The peak shear strength and failure mode were recorded.

Table 5. Shear tester parameters

Parameters	Details
Range	20 Kg
Test Speed	8.00 mil/sec
Test Load	0.5 kg
Land speed	19 mil/sec
Shear height	5.00 mil
Over travel	10.00 mil

Results and Discussion

Statistical Analysis

The analysis of solder-joint shear strength data was performed by using ANOVA. As shown in Figures 5 and 6, the residual vs. predicted shear strength plots show that the residual variances are not constant so a transformation is needed. However, it is difficult to decide the numerical level of component size. The component length (such as .12 inch in 1206 component) or component area (such as .12 inch by 0.06 inch in 1206 component) may not be a good variable for transformation since the shear strength of the joint depends on the effective component contact area, not the component length or area. The effective component contact area is difficult to determine. In this study, we did ANOVA for each component size so a transformation is not necessary. The results are listed in Table 6. It should be noted that only two failure modes were observed during the shear testing. They are fracture at bulk solder and component broken. Failure mode of majority samples is fracture at bulk solder. In the data analysis, the shear strength of samples with component broken was not considered. Only the shear strength with solder fracture was analyzed.

The effect of peak temp and TAL on R1206 and R0805 SAC305 solder joint shear strength are shown in Figures 7 -10. It shows that the higher peak temp the higher shear strength, and the

shorter TAL the higher shear strength. But it is not clear to us why the peak temp and TAL do not have significant effect on R0603 and R0402 SAC305 solder joint shear strength.

For SnPb solder joints, the peak temp and TAL have significant effect on R0805 components only. Figure 11 shows that the higher peak temp the higher shear strength. But Figure 12 shows that the longer TAL the higher shear strength. This result is different from SAC305 solder joints.

Table 6. Summary of ANOVA Results

		SAC305	SnPb
1206	Peak Temp	Significant	No (P value = 0.6)
	TAL	Significant	No (P value = 0.1)
0805	Peak Temp	Significant	Significant
	TAL	Significant	Significant
0603	Peak Temp	No (P value = 0.07)	No (P value = 0.27)
	TAL	No (P value = 0.2)	No (P value = 0.66)
0402	Peak Temp	No (P value = 0.1)	No (P value = 0.46)
	TAL	No (P value = 0.06)	No (P value = 0.55)

* Significant at 95% confidence level

Discussion

Since the effects of peak temp and TAL are not consistent to all component size, SEM analysis is necessary to understand the results. Because the failure mode for majority samples is bulk solder fracture, special attention will be paid on the microstructure of bulk solder joint. The intermetallic thickness will be measured also and a relationship between the intermetallic thickness and the TAL will be tried to find.

The shear strength of SnPb solder joints was noticed higher than that of SAC305. That conflicts with the shear strength (force per area) of SnPb bulk solder being lower than that of SAC305. Next, we examined the fracture area of solder joints, it is found that the wetting area of SAC305 is found to be smaller than that of SnPb after visual inspection. Figures 13 and 14 show the difference. Because the peak shear strength (in force) is the multiple of shear strength (in force per area) and contact area, the poor wetting (or small contact area) could explain the experimental results.

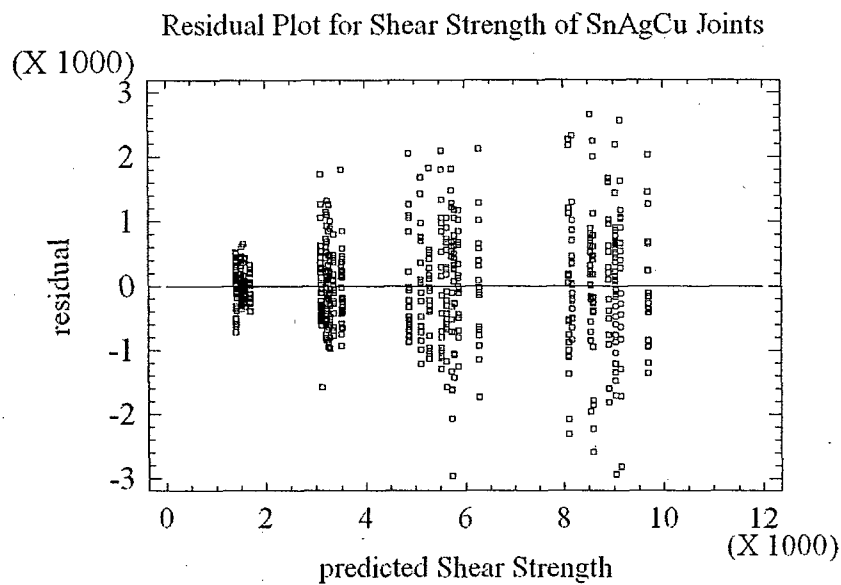


Figure 5. Plot of residuals versus predicted shear strength of SnAgCu joints

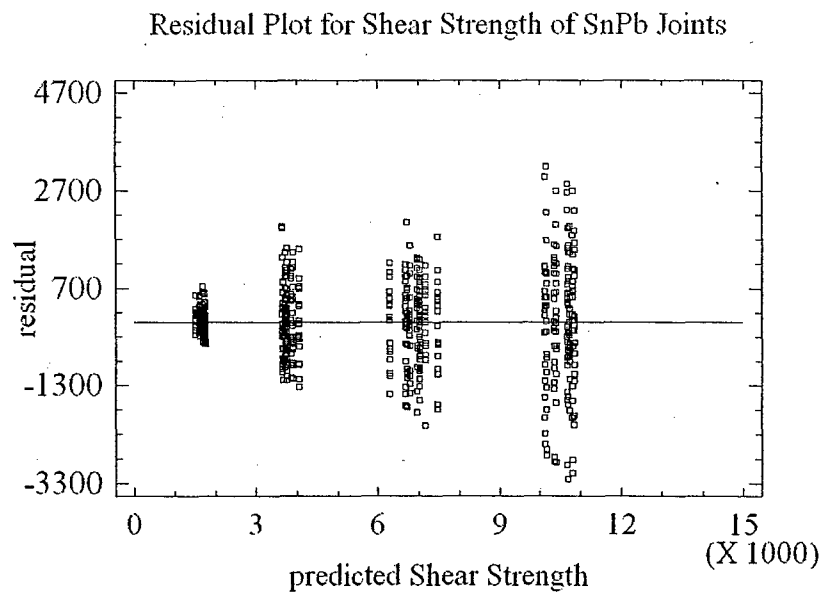


Figure 6. Plot of residuals versus predicted shear strength of SnPb joints

Means and 95.0 Percent LSD Intervals of R1206 SnAgCu Joints

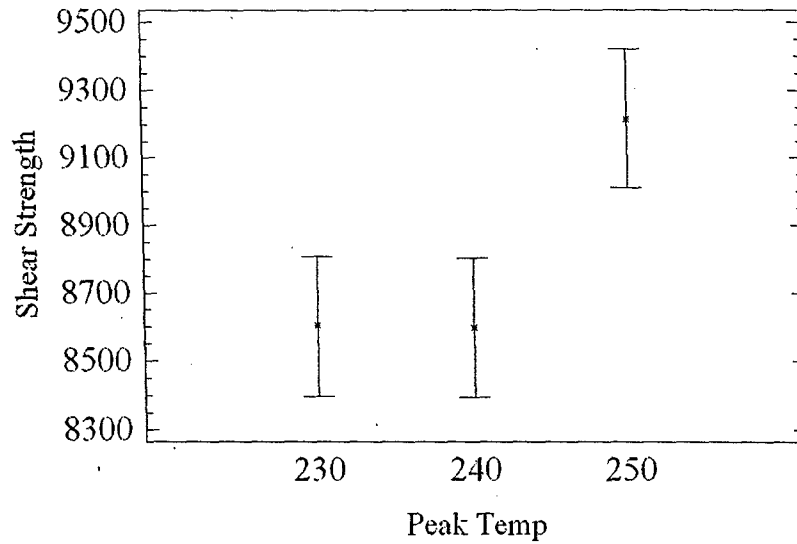


Figure 7. Effect of Peak Temp on SAC305 R1206 Solder Joints

Means and 95.0 Percent LSD Intervals of R1206 SnAgCu Joints

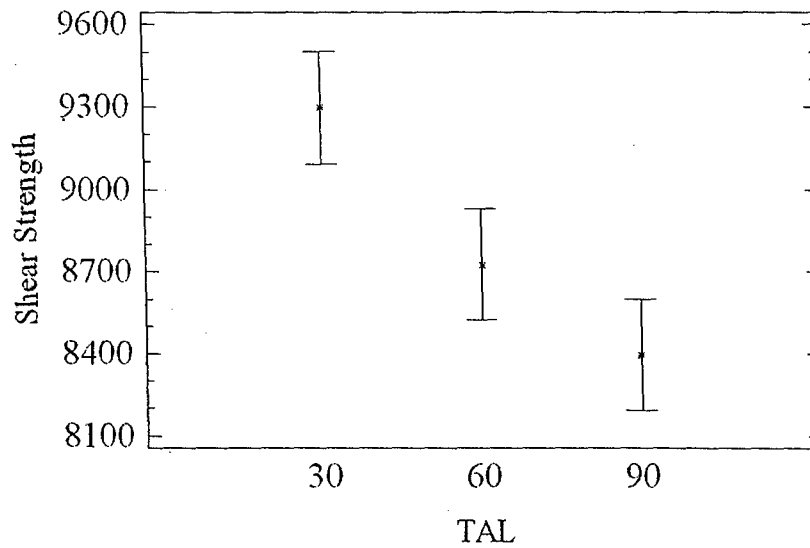


Figure 8. Effect of TAL on SAC305 R1206 Solder Joints

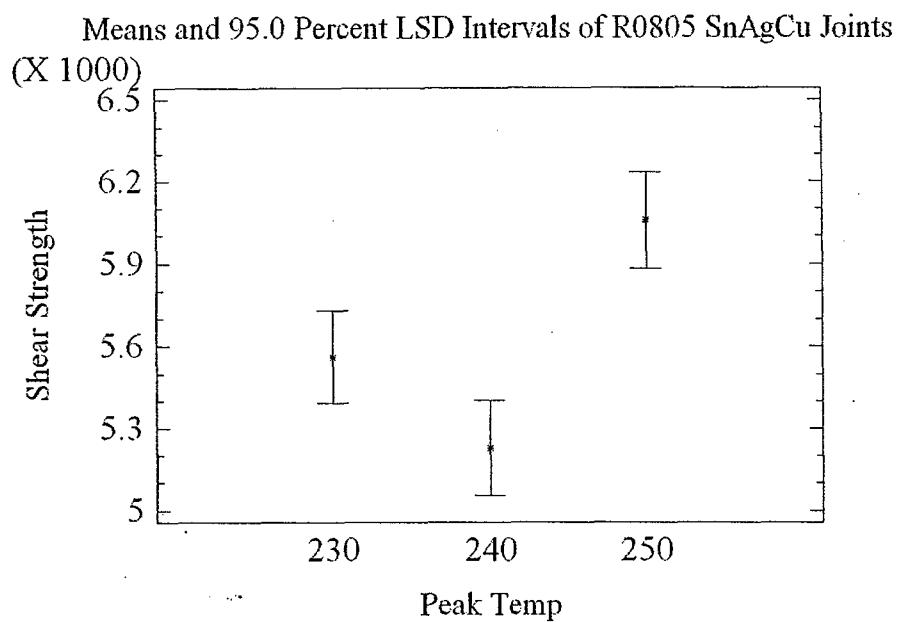


Figure 9. Effect of Peak Temp on SAC305 R0805 Solder Joints

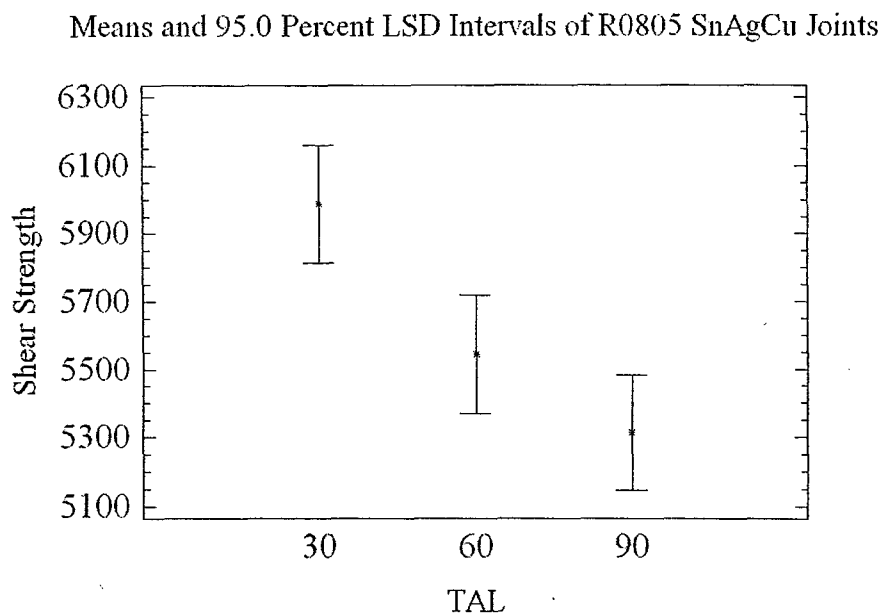


Figure 10. Effect of TAL on SAC305 R0805 Solder Joints

Means and 95.0 Percent LSD Intervals of R0805 SnPb Joints

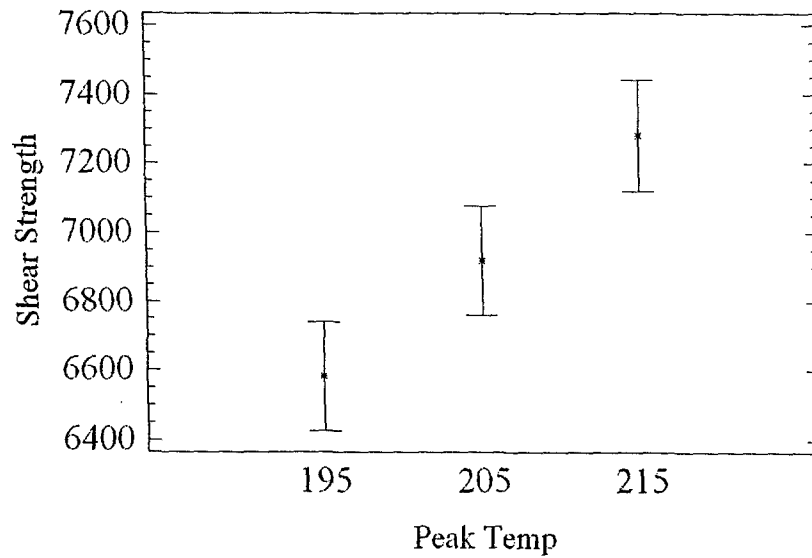


Figure 11. Effect of Peak Temp on SnPb R0805 Solder Joints

Means and 95.0 Percent LSD Intervals of R0805 SnPb Joints

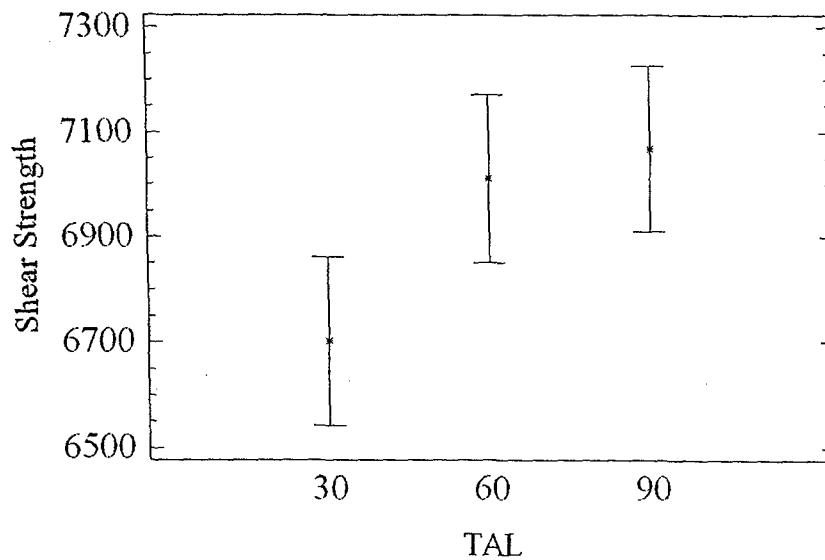


Figure 12. Effect of TAL on SnPb R0805 Solder Joints

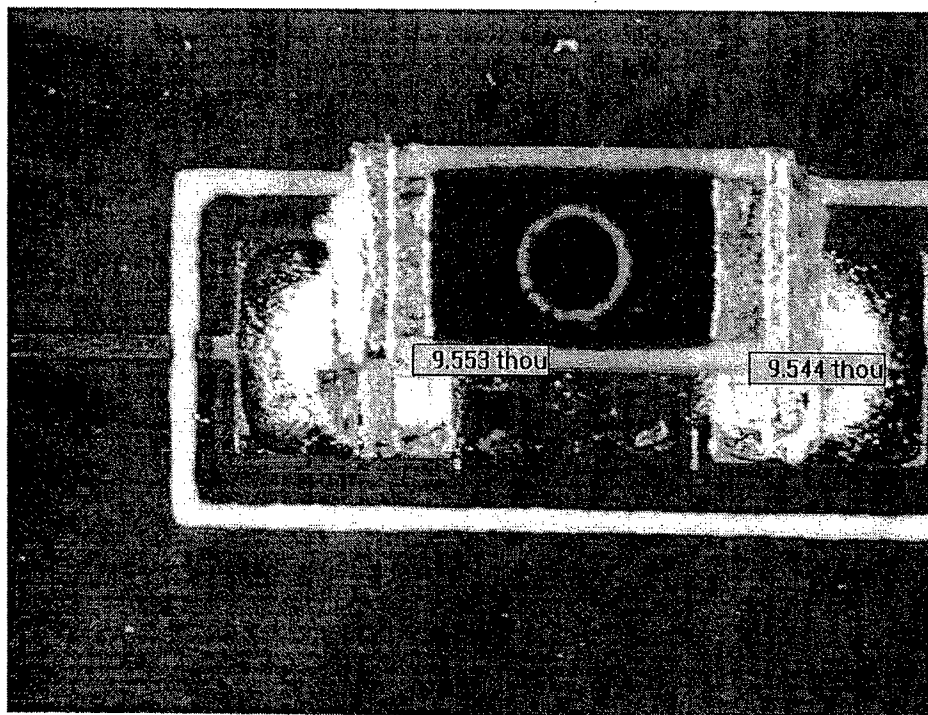


Figure 13. Fracture Area of SAC305 Joint Reflowed at 230C for 30 sec.

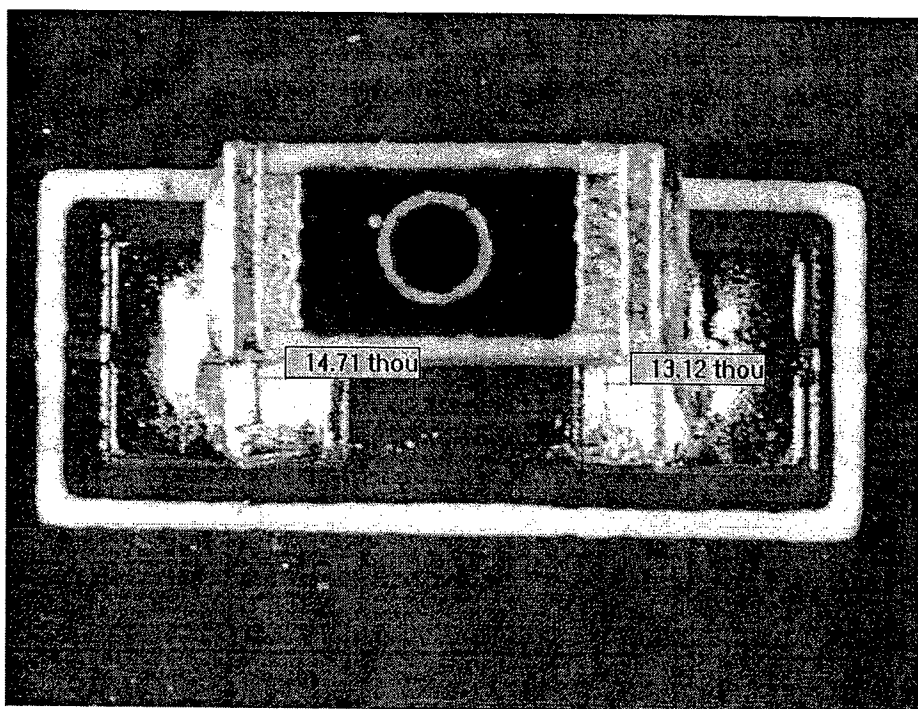


Figure 14. Fracture Area of SnPb Joint Reflowed at 195C for 30 sec.

Further works

The other half of the boards (Phase 2) is undergoing the air-to-air thermal shock cycling from -55°C to +125°C with 30 minutes dwell time (1 hour per cycle) for 1000 cycles at Henkel Technologies, Irvine, CA. The data and analysis will be reported late.

Acknowledgements

The PI would like to acknowledge the research funding by the Department of the Navy, Office of Naval Research, under Award # N00014-04-1-0436. The PI also wants to acknowledge support from Henkel Technologies, Irvine, CA for providing the solder paste, a stencil, and shear testing equipment. The PI would also like to thank DEK, Siemens, and Heller for providing surface mount assembly equipment. Finally the PI wants to thank Dr. Brain Tolendo of Henkel Technologies for good discussion on the project, thank two master students, Tzu-Chien Chou and Wesley Dee for assisting the research project by developing reflow profiles, assembly the boards, and doing shear testing.

References

1. Arra, M., "Effect of Reflow Profile on Wetting and Intermetallic Formation Between Sn/Ag/Cu Solder Components and Printed Circuit Boards," *Soldering and Surface Mount Technology*, Vol. 14 No. 2, pp.18-25, 2002.
2. Salam, B.; Virseda, C.; Da, H.; Ekere, N.N.; and Durairaj, R., "Reflow Profile Study of the Sn-Ag-Cu Solder," *Soldering and Surface Mount Technology*, Vol. 16 No. 1, pp.27-34, 2004.
3. Dahle, B., "Optimizing Your Reflow Profile for Maximum Productivity and Profitability," *IPC Printed Circuits Expo, APEX, and Designers Summit conference*, Anaheim, CA, 2004..
4. Bentzen, B. "Reflow Soldering," *SMT in FOCUS*, Oct 2000, Available at www.smtinfocus.com
5. "Minimizing defects on board assemblies by reflow profile adjustments," TKB-4U, Europe, Available at <http://www.tkb-4u.com/articles/soldering/reflprofadjust/reflprofadjust.php>
6. Newman, K., "BGA brittle fracture alternative solder joint integrity test methods," Proceedings of IEEE/ECTC the 55th Electronic Components and Technology Conference, May 31-June 3, 2005, Lake Buena Vista, FL.
7. Harrison, M.R., "Lead-Free Reflow Soldering for Electronics Assembly," *Soldering and Surface Mount Technology*, 13 No. 3, pp.21-38, 2001.

Appendix A: The settings of the eighteen reflow profiles

Test vehicle – Lead-free

230C-30S	Zone 1	Zone 2	Zone 3	Zone 4	Zone 5	Belt (cm/min)	Exhaust
Top	165	150	185	225	261	50	95
Bottom		150	185	225	261		
	Peak Temp 230 ± 5°C	Max slop °C/sec	25 – 204°C Ramp rate 0.5~1.0°C/sec	204 – 217°C (Sec)	225 – 130°C Cooling rate 2.0~4.0°C/sec	>225C (Sec)	TAL (Sec) 30 ± 3sec
TC1	230.6	4.55	1.31	5.87	-3.01	14.68	27.28
TC2	233.6	4.70	1.31	7.17	-2.96	24.11	29.60
TC3	232.1	3.76	1.29	8.44	-2.86	19.60	28.45
Ave.	232.1	4.34	1.30	7.16	-2.94	19.46	28.45
230C-60S	Zone 1	Zone 2	Zone 3	Zone 4	Zone 5	Belt (cm/min)	Exhaust
Top	165	150	190	225	245	29	95
Bottom	-	150	190	225	245		
	Peak Temp 230 ± 5°C	Max slop °C/sec	25 – 204°C Ramp rate 0.5~1.0°C/sec	204 – 217°C (Sec)	225 – 130°C Cooling rate 2.0~4.0°C/sec	>225C (Sec)	TAL (Sec) 60 ± 3sec
TC1	231.7	2.89	0.80	38.04	-2.58	37.55	58.04
TC2	234.2	3.14	0.80	37.98	-2.64	46.08	61.86
TC3	232.3	2.24	0.80	37.81	-2.35	39.57	59.89
Ave.	232.7	2.76	0.80	37.94	-2.52	41.07	59.93
230C-90S	Zone 1	Zone 2	Zone 3	Zone 4	Zone 5	Belt (cm/min)	Exhaust
Top	160	150	186	221	239	20	95
Bottom	-	150	186	221	239		
	Peak Temp 230 ± 5°C	Max slop °C/sec	25 – 204°C Ramp rate 0.5~1.0°C/sec	204 – 217°C (Sec)	225 – 130°C Cooling rate 2.0~4.0°C/sec	>225C (Sec)	TAL (Sec) 90 ± 3sec
TC1	230.4	2.31	0.56	53.08	-2.08	47.84	85.73
TC2	232.3	2.11	0.56	51.90	-2.09	62.85	96.96
TC3	230.5	1.51	0.55	57.59	-1.83	54.00	89.18
Ave.	231.1	1.97	0.56	54.19	-2.00	54.90	90.62

Appendix A: The settings of the eighteen reflow profiles (Cont.)

Test vehicle – Lead-free

240C-30S	Zone 1	Zone 2	Zone 3	Zone 4	Zone 5	Belt (cm/min)	Exhaust
Top	165	150	185	222	276	52	95
Bottom	-	150	185	222	276		
	Peak Temp 240 ± 5°C	Max slop °C/sec	25 – 204°C Ramp rate 0.5~1.0°C/sec	204 – 217°C (Sec)	225 – 130°C Cooling rate 2.0~4.0°C/sec	>225C (Sec)	TAL (Sec) 30 ± 3sec
TC1	237.5	4.62	1.23	5.32	-2.97	7.65	28.68
TC2	243.0	5.05	1.26	7.63	-3.09	21.30	32.14
TC3	241.0	4.30	1.23	5.61	-3.10	15.83	30.97
Ave.	240.5	4.66	1.24	6.19	-3.05	14.93	30.59

240C-60S	Zone 1	Zone 2	Zone 3	Zone 4	Zone 5	Belt (cm/sec)	Exhaust
Top	165	150	185	220	260	30	95
Bottom	-	150	185	220	260		
	Peak Temp 240 ± 5°C	Max slop °C/sec	25 – 204°C Ramp rate 0.5~1.0°C/sec	204 – 217°C (Sec)	225 – 130°C Cooling rate 2.0~4.0°C/sec	>225C (Sec)	TAL (Sec) 60 ± 3sec
TC1	239.3	3.13	0.77	31.33	-2.42	25.14	58.23
TC2	244.4	3.10	0.78	34.00	-2.63	44.35	63.67
TC3	242.7	2.43	0.77	34.66	-2.46	33.68	59.53
Ave.	242.1	2.89	0.78	33.33	-2.50	34.39	60.48

240C-90S	Zone 1	Zone 2	Zone 3	Zone 4	Zone 5	Belt (cm/min)	Exhaust
Top	165	150	185	220	254	21	95
Bottom	-	150	185	220	254		
	Peak Temp 240 ± 5°C	Max slop °C/sec	25 – 204°C Ramp rate 0.5~1.0°C/sec	204 – 217°C (Sec)	225 – 130°C Cooling rate 2.0~4.0°C/sec	>225C (Sec)	TAL (Sec) 90 ± 3sec
TC1	239.3	2.29	0.54	46.41	-1.95	39.69	89.42
TC2	244.3	2.04	0.53	46.42	-2.05	56.75	98.15
TC3	242.1	1.76	0.53	53.25	-2.03	49.16	90.56
Ave.	241.9	2.03	0.53	48.69	-2.01	48.53	92.71

Appendix A: The settings of the eighteen reflow profiles (Cont.)

Test vehicle – Lead-free

250C-30S	Zone 1	Zone 2	Zone 3	Zone 4	Zone 5	Belt (cm/min)	Exhaust
Top	165	150	185	227	285	52	95
Bottom	-	150	185	227	285		
	Peak Temp 250 ± 5°C	Max slop °C/sec	25 – 204°C Ramp rate 0.5~1.0°C/sec	204 – 217°C (Sec)	225 – 130°C Cooling rate 2.0~4.0°C/sec	>225C (Sec)	TAL (Sec) 30 ± 3sec
TC1	245.9	4.98	1.26	15.94	-3.04	6.61	31.89
TC2	251.8	4.92	1.30	14.75	-2.96	13.82	32.70
TC3	247.5	3.88	1.31	13.90	-3.06	9.51	32.87
Ave.	248.4	4.59	1.29	14.86	-3.02	7.21	32.49
250C-60S	Zone 1	Zone 2	Zone 3	Zone 4	Zone 5	Belt (cm/min)	Exhaust
Top	165	150	185	220	273	31	95
Bottom	-	150	185	220	273		
	Peak Temp 250 ± 5°C	Max slop °C/sec	25 – 204°C Ramp rate 0.5~1.0°C/sec	204 – 217°C (Sec)	225 – 130°C Cooling rate 2.0~4.0°C/sec	>225C (Sec)	TAL (Sec) 60 ± 3sec
TC1	253.5	3.46	0.82	33.42	-2.55	29.85	63.44
TC2	252.6	3.05	0.81	31.51	-2.64	32.25	60.54
TC3	247.6	2.49	0.78	26.91	-2.34	14.33	56.42
Ave.	251.2	3.0	0.80	30.61	-2.51	25.47	60.14
250C-90S	Zone 1	Zone 2	Zone 3	Zone 4	Zone 5	Belt (cm/min)	Exhaust
Top	160	150	185	218	267	22	95
Bottom	-	150	185	218	267		
	Peak Temp 250 ± 5°C	Max slop °C/sec	25 – 204°C Ramp rate 0.5~1.0°C/sec	204 – 217°C (Sec)	225 – 130°C Cooling rate 2.0~4.0°C/sec	>225C (Sec)	TAL (Sec) 90 ± 3sec
TC1	250.0	2.54	0.60	42.56	-2.21	34.34	90.34
TC2	252.0	2.52	0.60	45.63	-2.26	46.23	88.97
TC3	251.0	1.62	0.60	51.90	-2.24	41.36	89.44
Ave.	251.0	2.22	0.60	46.70	-2.24	40.64	89.48

Appendix A: The settings of the eighteen reflow profiles (Cont.)

Test vehicle – Sn-Pb

195C-30S	Zone 1	Zone 2	Zone 3	Zone 4	Zone 5	Belt (cm/min)	Exhaust
Top	140	130	165	183	220	52	95
Bottom	-	130	165	183	220		
	Peak Temp 195 ± 5°C	Max slop °C/sec	25 – 170°C Ramp rate 0.5~1.0°C/sec	170 – 183°C (Sec)	190 – 130°C Cooling rate 2.0~4.0°C/sec	>190C (Sec)	TAL (Sec) 30 ± 3sec
TC1	195.8	4.71	1.01	20.17	-2.78	19.99	28.34
TC2	198.3	5.12	1.00	17.45	-3.14	25.07	28.70
TC3	195.6	3.40	0.99	9.20	-2.19	20.65	29.69
Ave.	196.6	4.41	1.00	15.60	-2.71	21.90	28.91
195C-60S	Zone 1	Zone 2	Zone 3	Zone 4	Zone 5	Belt (cm/min)	Exhaust
Top	125	125	165	185	206	28	95
Bottom	-	125	165	185	206		
	Peak Temp 195 ± 5°C	Max slop °C/sec	25 – 170°C Ramp rate 0.5~1.0°C/sec	170 – 183°C (Sec)	190 – 130°C Cooling rate 2.0~4.0°C/sec	>190C (Sec)	TAL (Sec) 60 ± 3sec
TC1	196.2	2.55	0.63	49.06	-2.21	41.44	59.82
TC2	197.7	2.81	0.62	48.87	-2.42	51.38	63.51
TC3	196.9	1.90	0.62	50.28	-1.95	45.62	64.14
Ave.	196.9	2.42	0.62	49.40	-2.19	45.15	62.49
195C-90S	Zone 1	Zone 2	Zone 3	Zone 4	Zone 5	Belt (cm/min)	Exhaust
Top	130	125	178	190	205	28	95
Bottom	-	125	178	190	205		
	Peak Temp 195 ± 5°C	Max slop °C/sec	25 – 170°C Ramp rate 0.5~1.0°C/sec	170 – 183°C (Sec)	190 – 130°C Cooling rate 2.0~4.0°C/sec	>190C (Sec)	TAL (Sec) 90 ± 3sec
TC1	196.8	3.20	0.66	25.63	-2.15	37.92	85.27
TC2	198.4	2.88	0.66	25.97	-2.56	55.24	93.53
TC3	197.2	2.00	0.66	28.98	-2.20	49.80	94.06
Ave.	197.5	2.69	0.66	26.86	-2.30	47.65	90.95

Appendix A: The settings of the eighteen reflow profiles (Cont.)

Test vehicle – Sn-Pb

205C-30S	Zone 1	Zone 2	Zone 3	Zone 4	Zone 5	Belt (cm/min)	Exhaust
Top	140	130	165	183	232	52	95
Bottom	-	130	165	183	232		
	Peak Temp 205 ± 5°C	Max slop °C/sec	25 – 170°C Ramp rate 0.5~1.0°C/sec	170 – 183°C (Sec)	190 – 130°C Cooling rate 2.0~4.0°C/sec	>190C (Sec)	TAL (Sec) 30 ± 3sec
TC1	202.6	4.75	1.02	21.12	-2.68	13.86	31.34
TC2	205.1	4.80	1.01	15.49	-2.93	17.00	30.73
TC3	201.7	4.30	0.98	7.79	-2.41	9.26	30.29
Ave.	203.1	4.60	1.00	14.8	-2.67	13.37	30.79
205C-60S	Zone 1	Zone 2	Zone 3	Zone 4	Zone 5	Belt (cm/min)	Exhaust
Top	135	125	165	183	221	30	95
Bottom	-	125	165	183	221		
	Peak Temp 205 ± 5°C	Max slop °C/sec	25 – 170°C Ramp rate 0.5~1.0°C/sec	170 – 183°C (Sec)	190 – 130°C Cooling rate 2.0~4.0°C/sec	>190C (Sec)	TAL (Sec) 60 ± 3sec
TC1	204.1	2.63	0.67	39.80	-2.21	28.07	62.63
TC2	207.4	2.86	0.66	42.75	-2.15	39.31	60.18
TC3	206.8	2.14	0.68	45.85	-2.05	38.49	62.99
Ave.	206.1	2.55	0.67	42.80	-2.14	35.29	61.93
205C-90S	Zone 1	Zone 2	Zone 3	Zone 4	Zone 5	Belt (cm/min)	Exhaust
Top	135	125	165	183	219	22	95
Bottom	-	125	165	183	219		
	Peak Temp 205 ± 5°C	Max slop °C/sec	25 – 170°C Ramp rate 0.5~1.0°C/sec	170 – 183°C (Sec)	190 – 130°C Cooling rate 2.0~4.0°C/sec	>190C (Sec)	TAL (Sec) 90 ± 3sec
TC1	207.6	2.51	0.51	52.58	-2.12	48.71	91.81
TC2	209.3	1.89	0.51	52.87	-2.31	58.94	92.48
TC3	208.4	1.49	0.51	56.78	-2.04	54.93	90.05
Ave.	208.4	1.85	0.51	54.07	-2.16	54.19	91.44

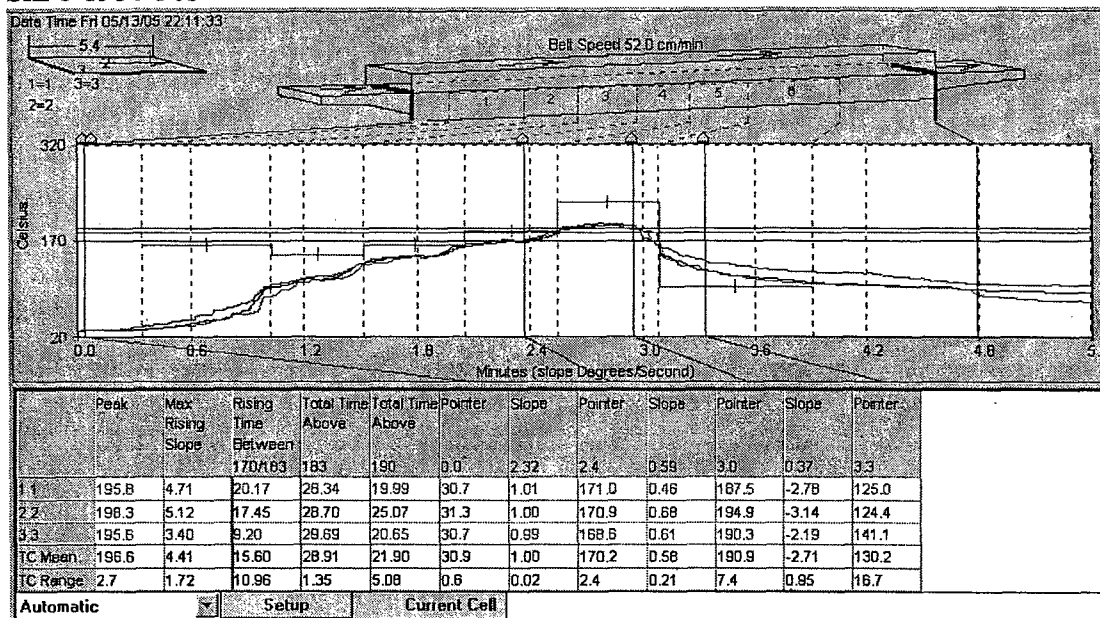
Appendix A: The settings of the eighteen reflow profiles (Cont.)

Test vehicle – Sn-Pb

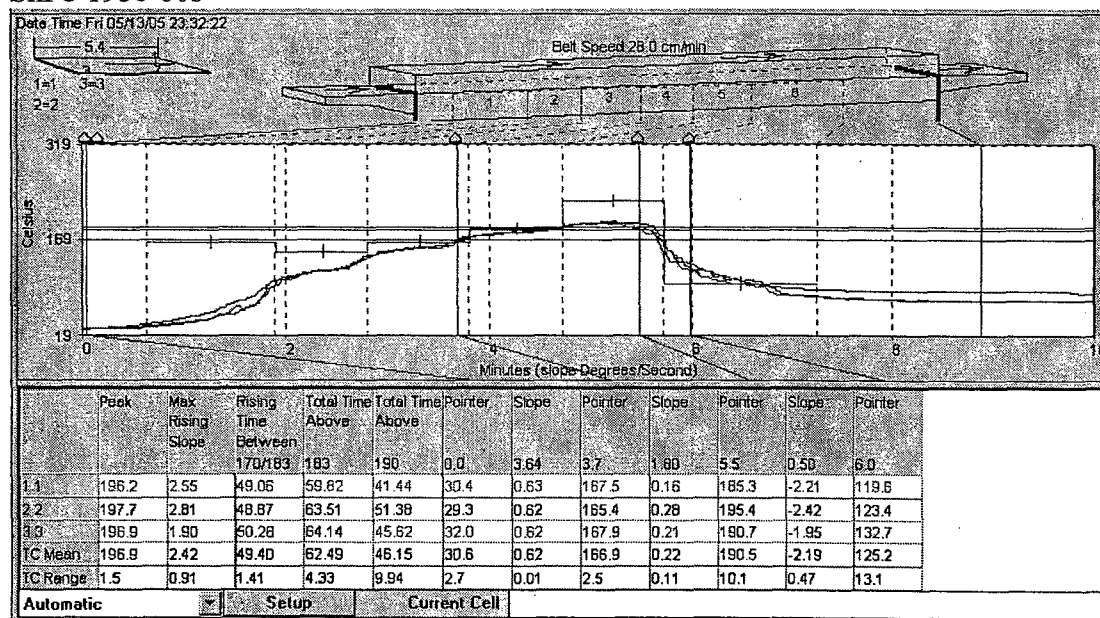
215C-30S	Zone 1	Zone 2	Zone 3	Zone 4	Zone 5	Belt (cm/min)	Exhaust
Top	168	140	171	182	247	52.5	95
Bottom	-	140	171	182	247		
	Peak Temp 215 ± 5°C	Max slop °C/sec	25 – 170°C Ramp rate 0.5~1.0°C/sec	170 – 183°C (Sec)	190 – 130°C Cooling rate 2.0~4.0°C/sec	>190C (Sec)	TAL (Sec) 30 ± 3sec
TC1	213.1	5.29	1.15	19.31	-2.96	8.77	33.77
TC2	214.1	4.91	1.10	16.04	-2.84	15.52	32.96
TC3	213.3	4.33	1.11	15.23	-2.72	9.59	33.39
Ave.	213.5	4.84	1.12	16.86	-2.84	11.29	33.37
215C-60S	Zone 1	Zone 2	Zone 3	Zone 4	Zone 5	Belt (cm/min)	Exhaust
Top	120	145	165	182	235	30	95
Bottom	-	140	150	180	230		
	Peak Temp 215 ± 5°C	Max slop °C/sec	25 – 170°C Ramp rate 0.5~1.0°C/sec	170 – 183°C (Sec)	190 – 130°C Cooling rate 2.0~4.0°C/sec	>190C (Sec)	TAL (Sec) 60 ± 3sec
TC1	214.4	3.35	0.69	36.85	-2.24	25.78	66.90
TC2	217.0	3.55	0.68	39.49	-2.35	35.04	61.80
TC3	214.5	2.76	0.68	41.13	-2.25	26.55	63.99
Ave.	215.3	3.22	0.69	39.15	-2.28	29.12	64.23
215C-90S	Zone 1	Zone 2	Zone 3	Zone 4	Zone 5	Belt (cm/min)	Exhaust
Top	120	145	170	191	236	29	95
Bottom	-	145	165	188	233		
	Peak Temp 215 ± 5°C	Max slop °C/sec	25 – 170°C Ramp rate 0.5~1.0°C/sec	170 – 183°C (Sec)	190 – 130°C Cooling rate 2.0~4.0°C/sec	>190C (Sec)	TAL (Sec) 90 ± 3sec
TC1	217.1	3.30	0.68	22.43	-2.43	33.94	92.58
TC2	218.9	3.27	0.66	24.69	-2.40	42.58	89.40
TC3	217.8	2.59	0.69	26.48	-2.28	37.89	90.41
Ave.	217.9	3.05	0.68	24.53	-2.37	38.14	90.80

Appendix A: The settings of the eighteen reflow profiles (Cont.)

SnPb 195c-30s

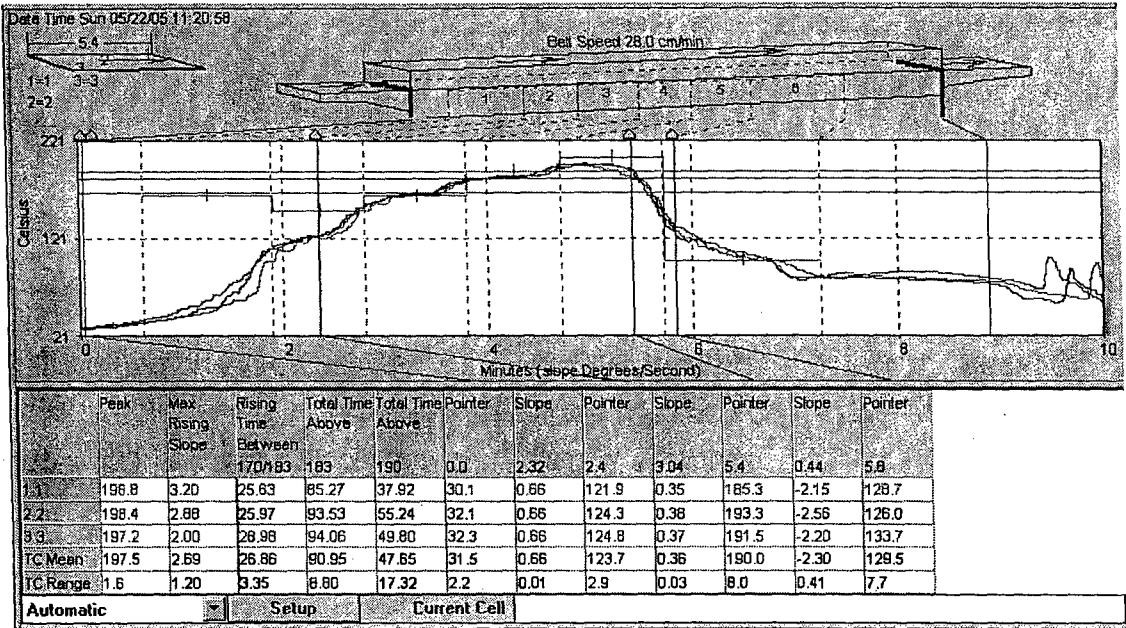


SnPb 195c-60s

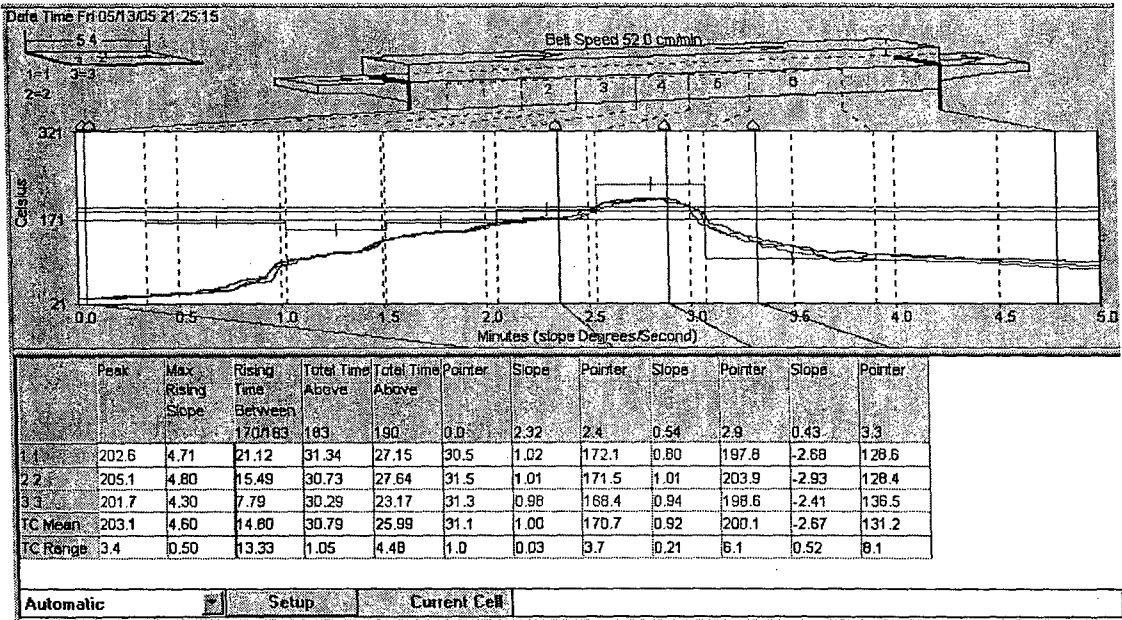


Appendix A: The settings of the eighteen reflow profiles (Cont.)

SnPb 195c-90s

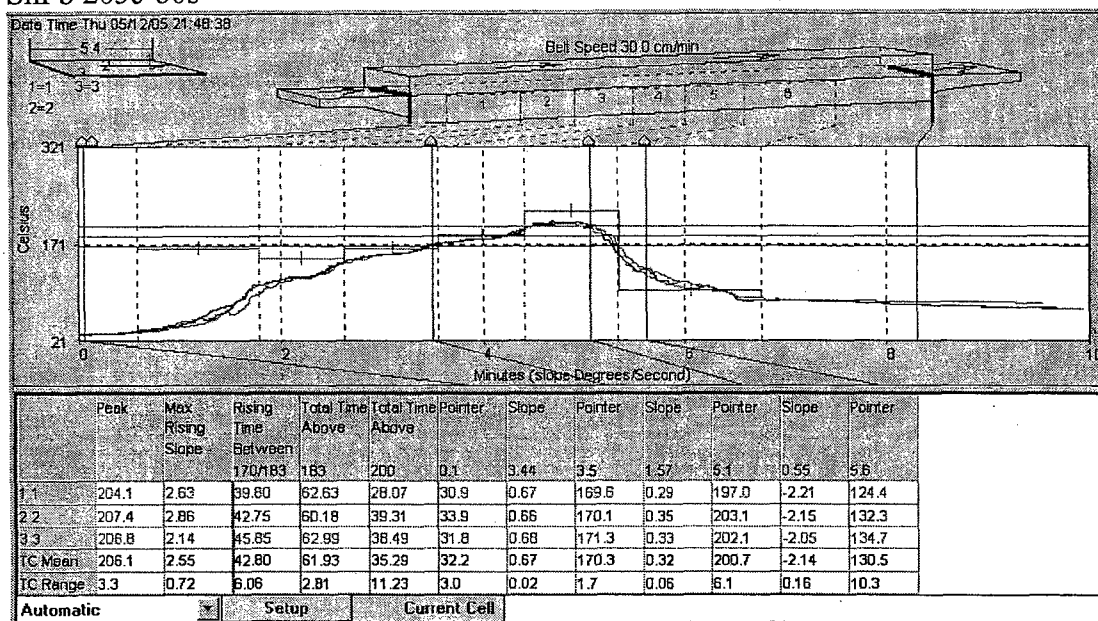


SnPb 205c-30s

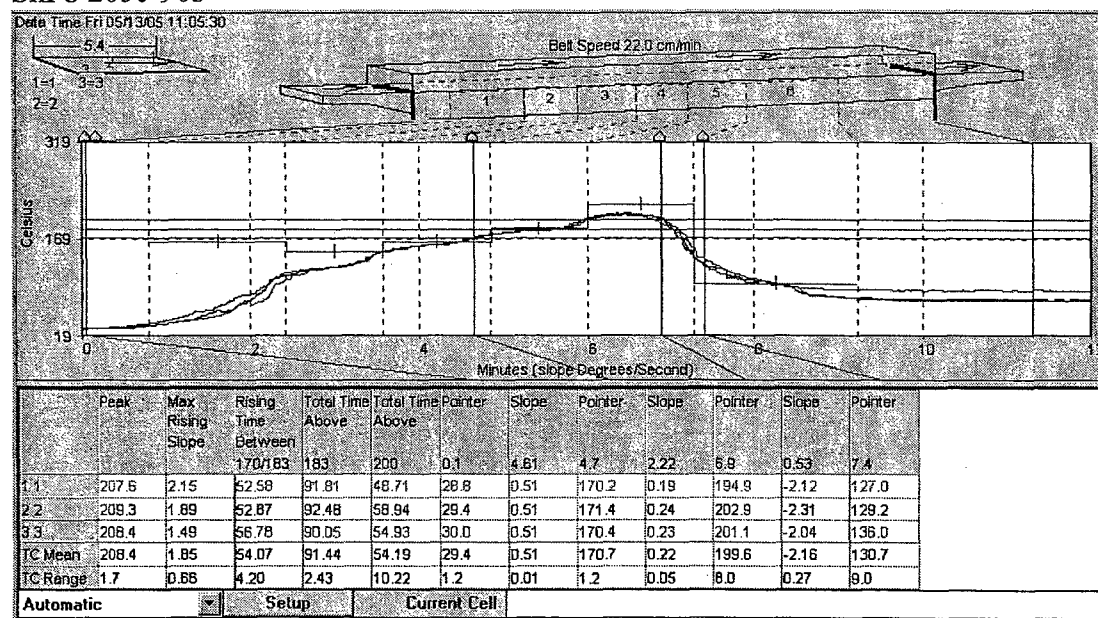


Appendix A: The settings of the eighteen reflow profiles (Cont.)

SnPb 205c-60s

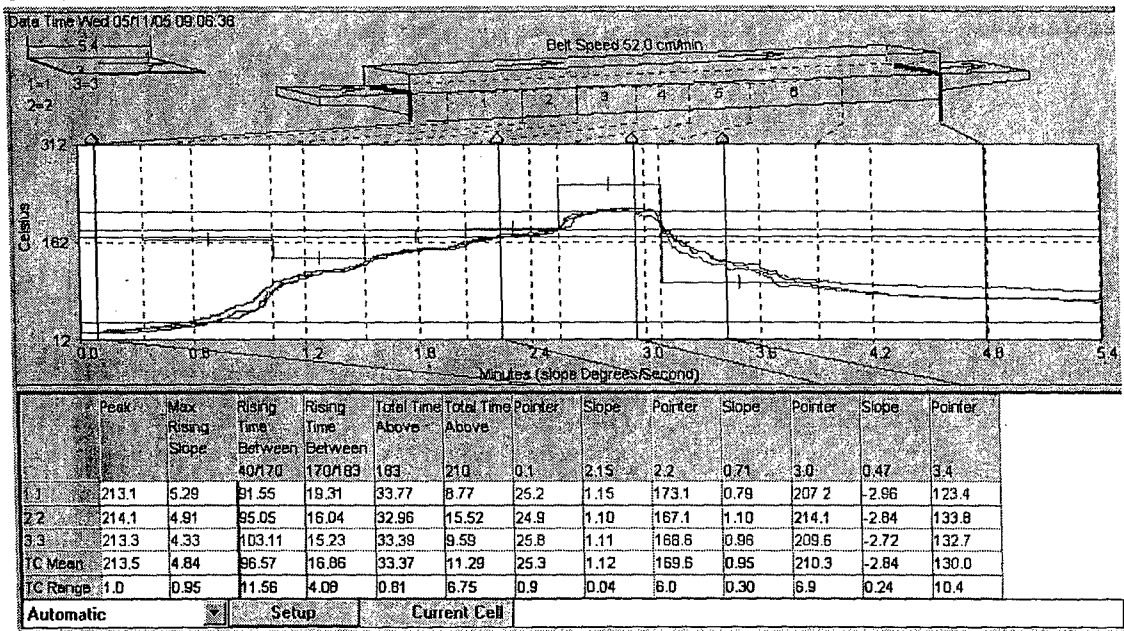


SnPb 205c-90s

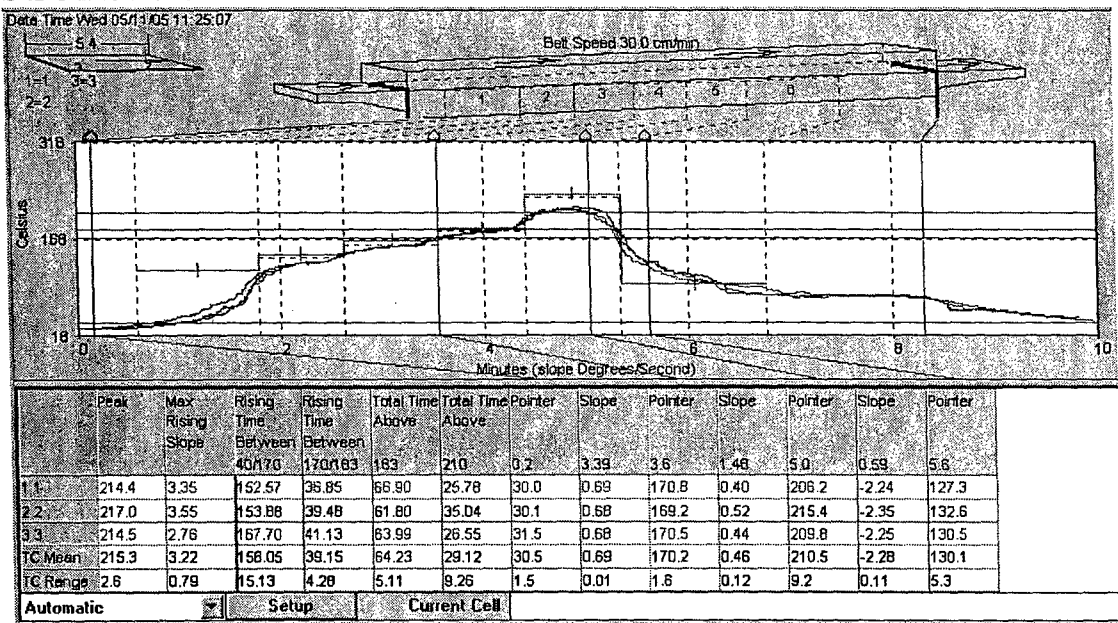


Appendix A: The settings of the eighteen reflow profiles (Cont.)

SnPb 215c-30s

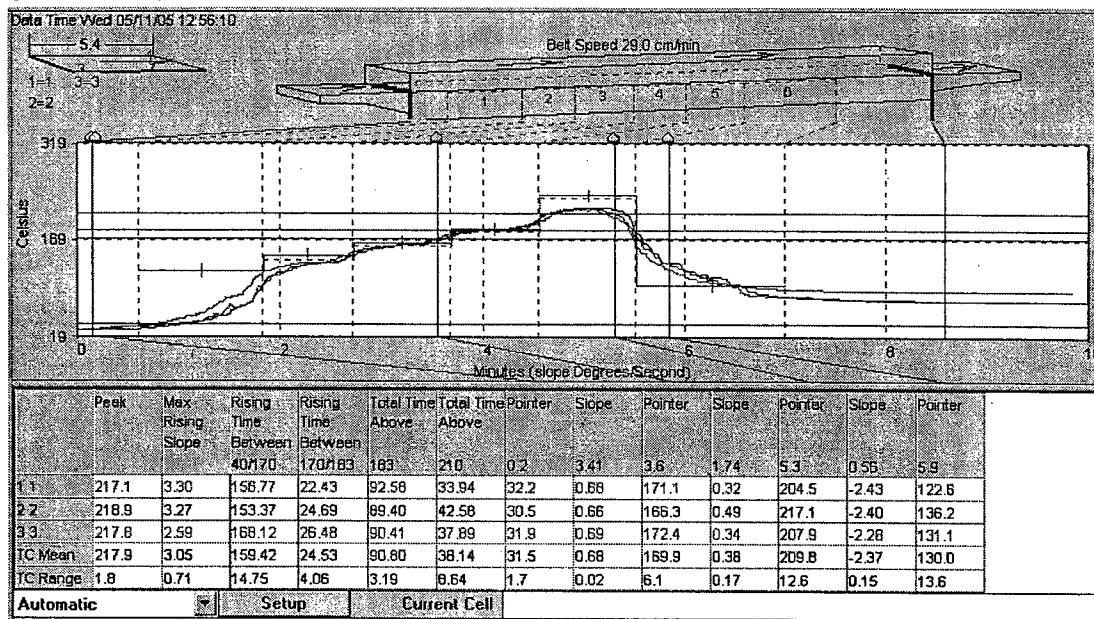


SnPb 215c-60s

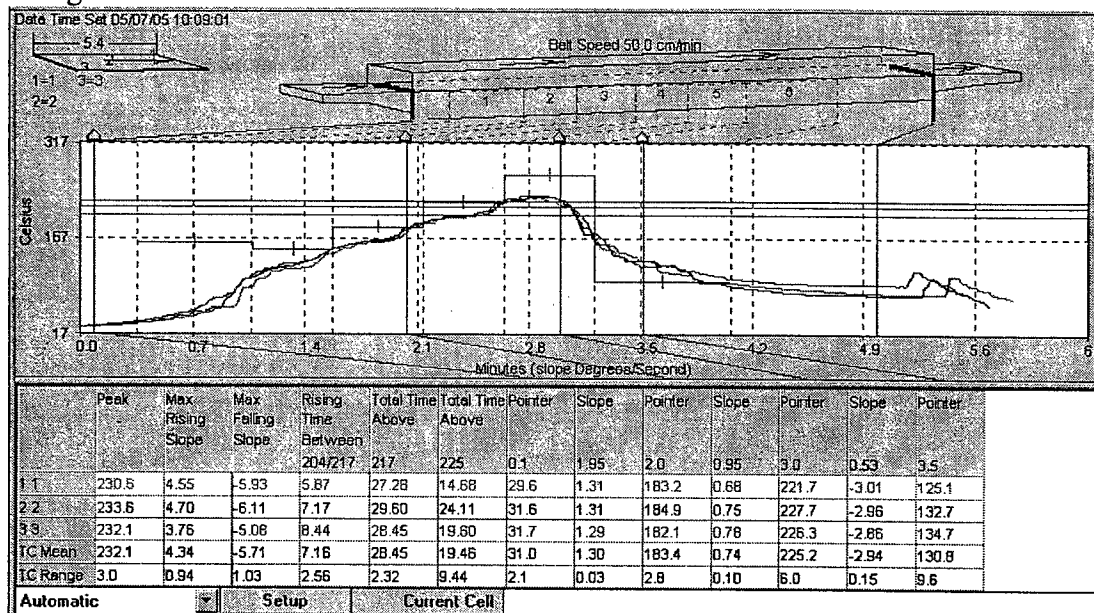


Appendix A: The settings of the eighteen reflow profiles (Cont.)

SnPb 215c-90s

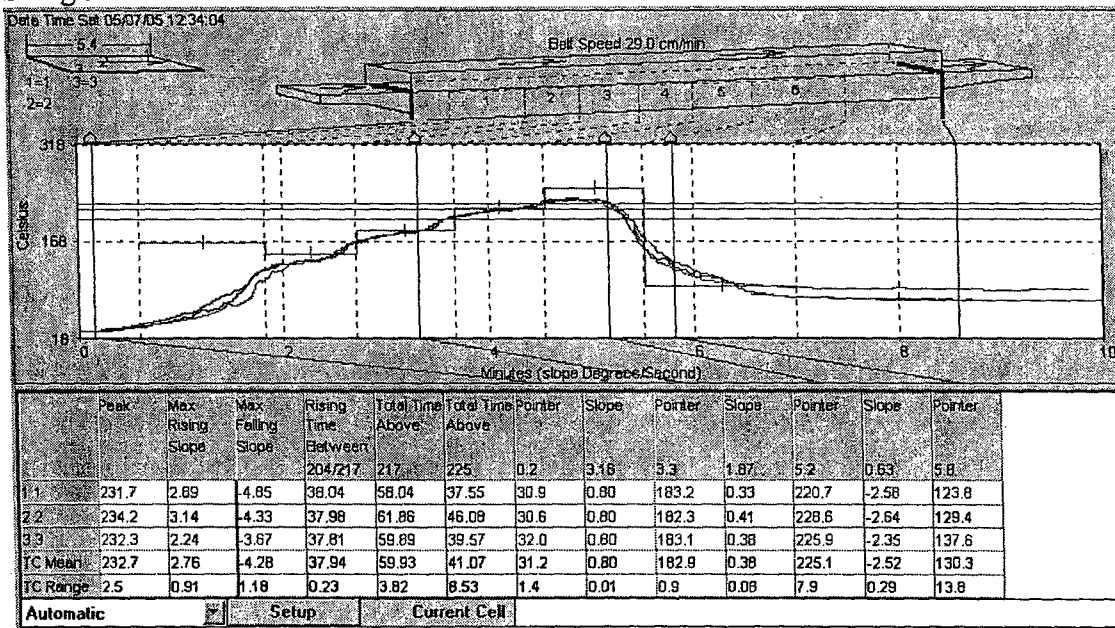


SnAgCu 230c-30s

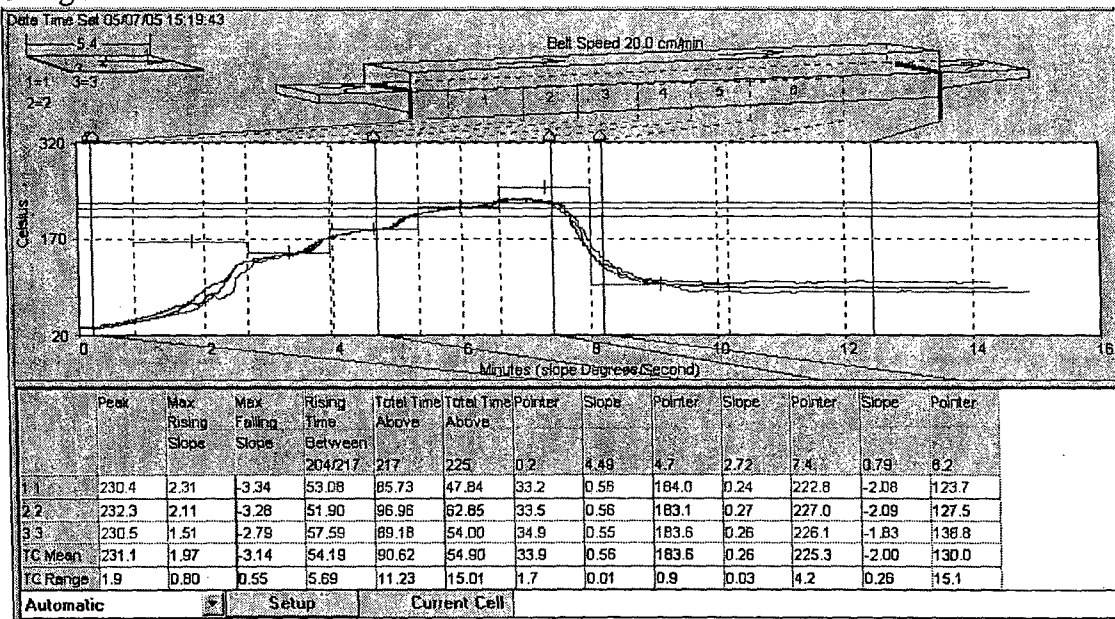


Appendix A: The settings of the eighteen reflow profiles (Cont.)

SnAgCu 230c-60s

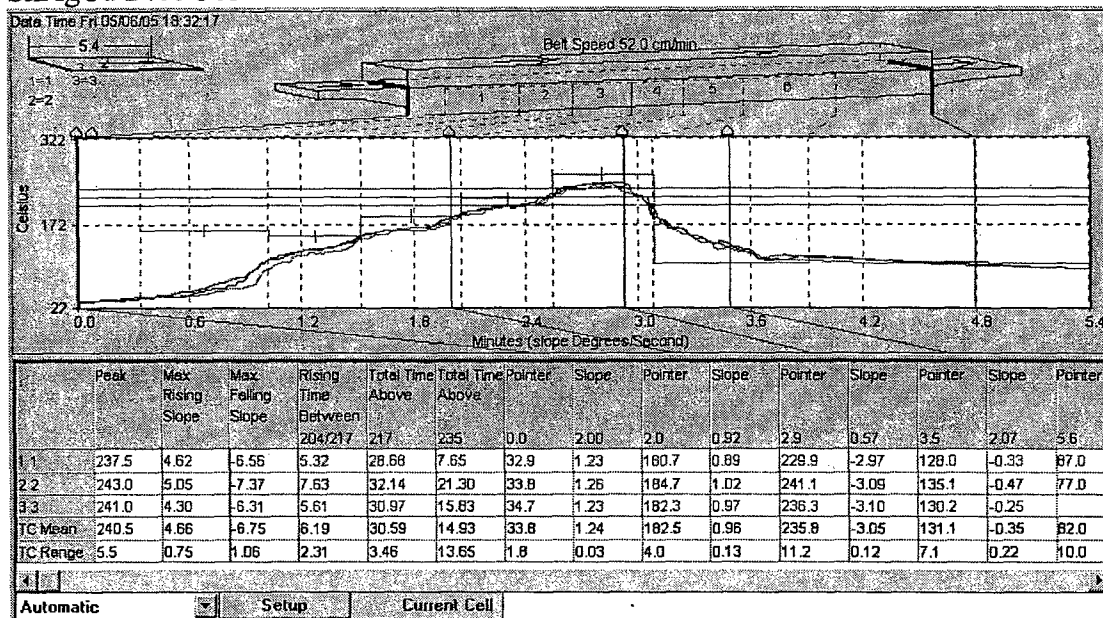


SnAgCu 230c-90s

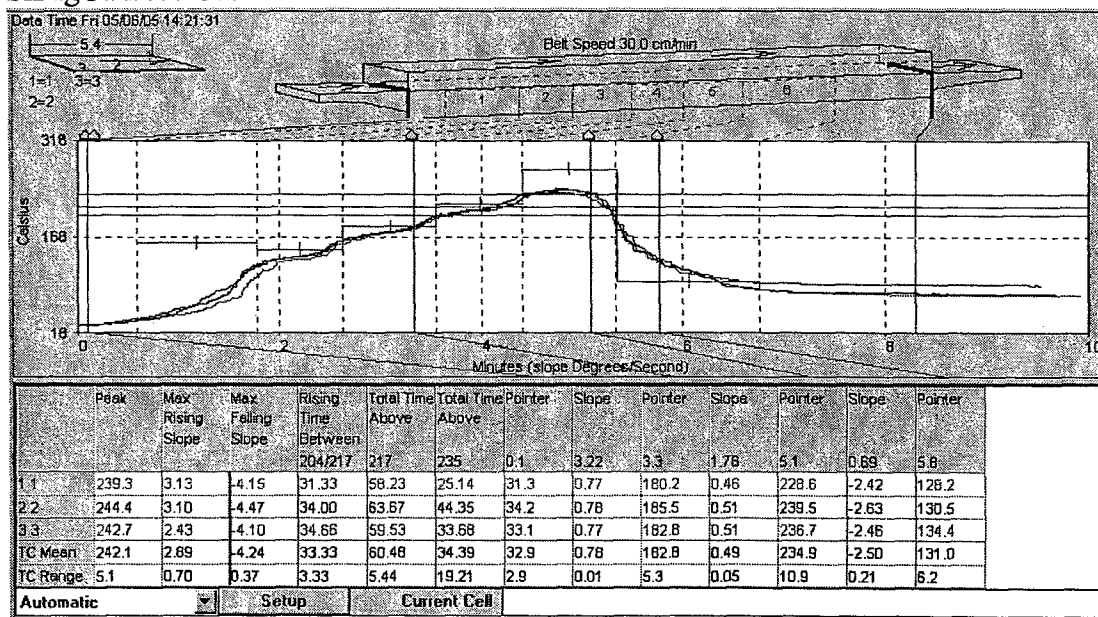


Appendix A: The settings of the eighteen reflow profiles (Cont.)

SnAgCu 240c-30s

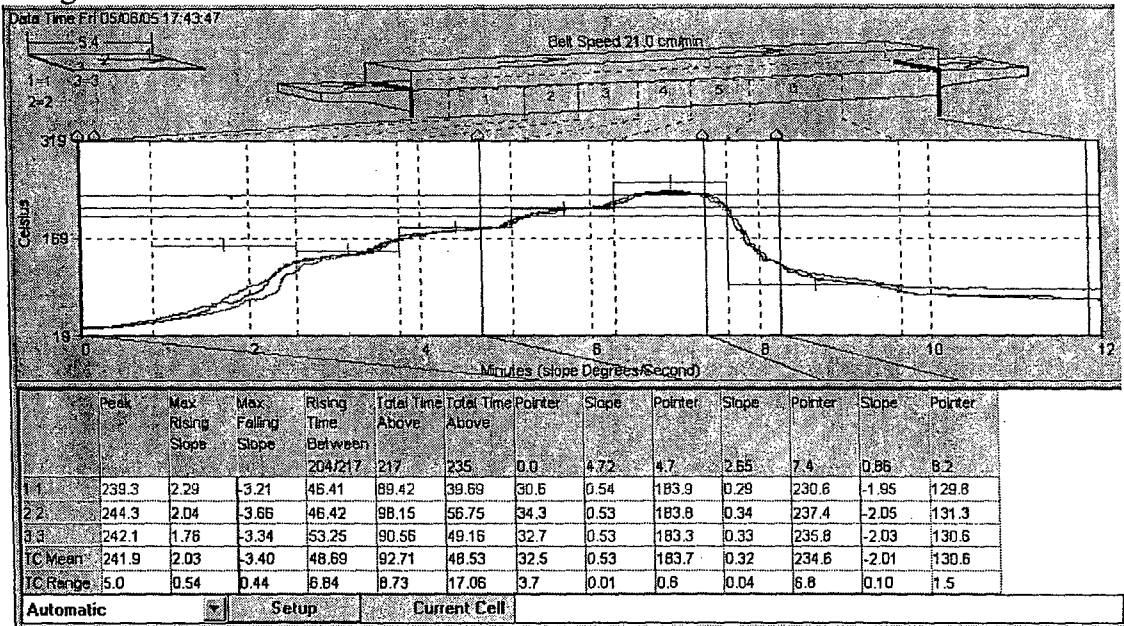


SnAgCu 240c-60s

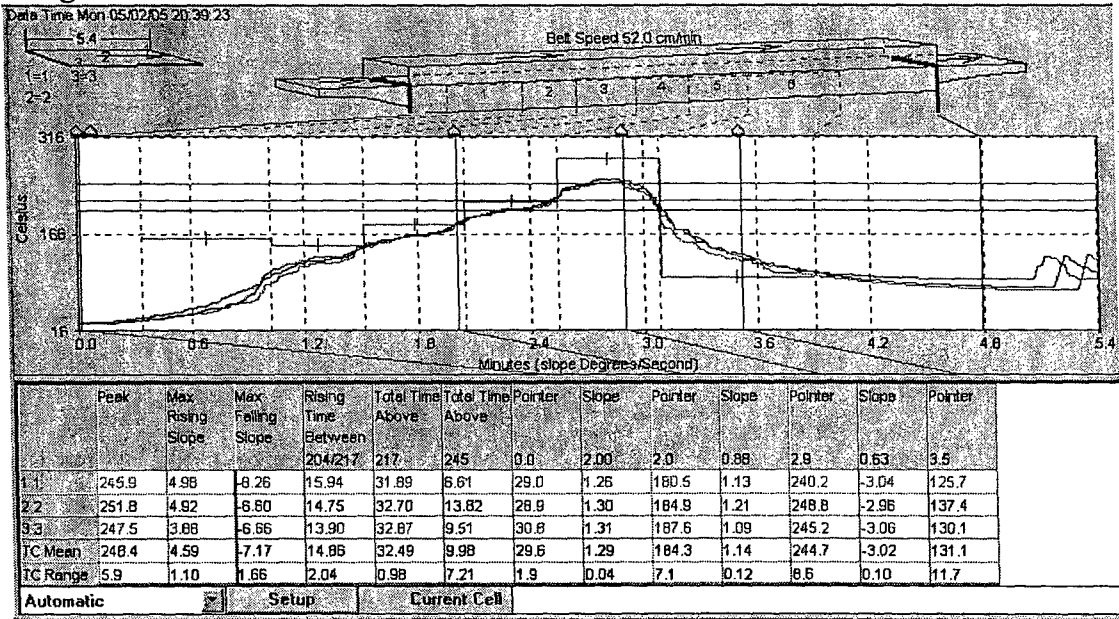


Appendix A: The settings of the eighteen reflow profiles (Cont.)

SnAgCu 240c-90s

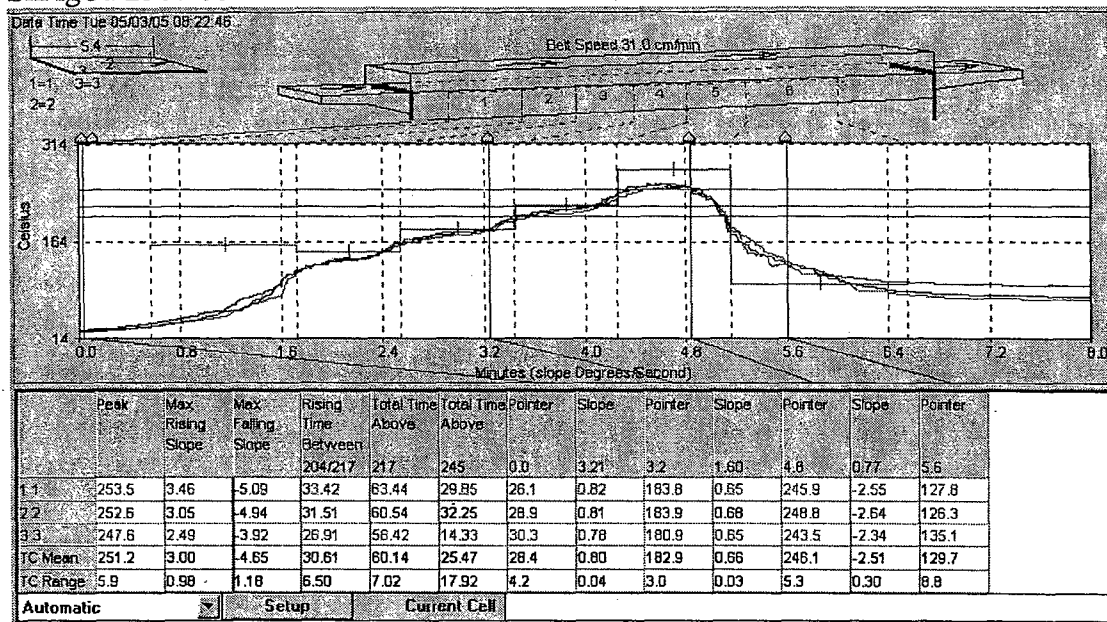


SnAgCu 250c-30s

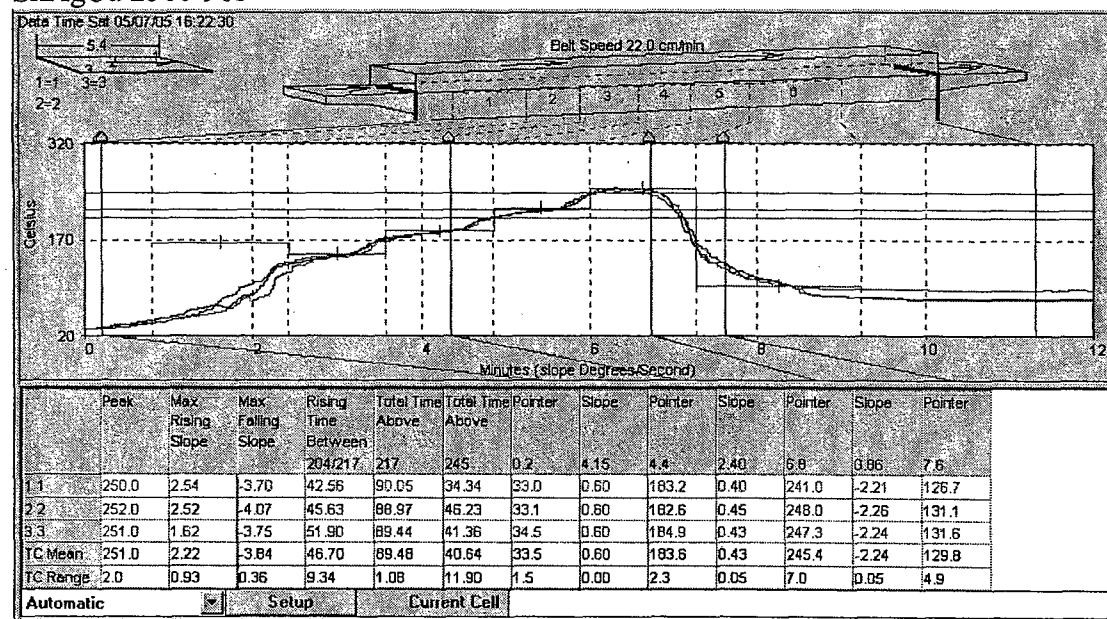


Appendix A: The settings of the eighteen reflow profiles (Cont.)

SnAgCu 250c-60s



SnAgCu 250c-90s



Appendix B: Randomized Experimental Sequences

Run order	Solder Paste	Surface finish	Component finish	Peak temp (°C)	TAL (sec)
1	SAC305	OSP	Pure Sn	240	60
2	SAC305	OSP	Pure Sn	250	60
3	SAC305	OSP	Pure Sn	230	60
4	SAC305	OSP	Pure Sn	230	90
5	SAC305	OSP	Pure Sn	240	60
6	SAC305	OSP	Pure Sn	240	90
7	SAC305	OSP	Pure Sn	240	90
8	SAC305	OSP	Pure Sn	230	60
9	SAC305	OSP	Pure Sn	230	90
10	SAC305	OSP	Pure Sn	240	30
11	SAC305	OSP	Pure Sn	240	30
12	SAC305	OSP	Pure Sn	250	30
13	SAC305	OSP	Pure Sn	240	30
14	SAC305	OSP	Pure Sn	240	60
15	SAC305	OSP	Pure Sn	240	90
16	SAC305	OSP	Pure Sn	230	30
17	SAC305	OSP	Pure Sn	230	90
18	SAC305	OSP	Pure Sn	230	30
19	SAC305	OSP	Pure Sn	250	90
20	SAC305	OSP	Pure Sn	230	30
21	SAC305	OSP	Pure Sn	250	90
22	SAC305	OSP	Pure Sn	230	60
23	SAC305	OSP	Pure Sn	250	60
24	SAC305	OSP	Pure Sn	250	30
25	SAC305	OSP	Pure Sn	250	30
26	SAC305	OSP	Pure Sn	250	90
27	SAC305	OSP	Pure Sn	250	60

Appendix B: Randomized Experimental Sequences (Cont.)

Run order	Solder Paste	Surface finish	Component finish	Peak temp (°C)	TAL (sec)
1	Sn-Pb	HASL	Pure Sn	215	30
2	Sn-Pb	HASL	Pure Sn	195	30
3	Sn-Pb	HASL	Pure Sn	205	60
4	Sn-Pb	HASL	Pure Sn	205	60
5	Sn-Pb	HASL	Pure Sn	215	30
6	Sn-Pb	HASL	Pure Sn	195	60
7	Sn-Pb	HASL	Pure Sn	205	90
8	Sn-Pb	HASL	Pure Sn	215	90
9	Sn-Pb	HASL	Pure Sn	215	60
10	Sn-Pb	HASL	Pure Sn	215	90
11	Sn-Pb	HASL	Pure Sn	205	60
12	Sn-Pb	HASL	Pure Sn	205	30
13	Sn-Pb	HASL	Pure Sn	205	30
14	Sn-Pb	HASL	Pure Sn	195	90
15	Sn-Pb	HASL	Pure Sn	195	90
16	Sn-Pb	HASL	Pure Sn	215	30
17	Sn-Pb	HASL	Pure Sn	195	30
18	Sn-Pb	HASL	Pure Sn	205	90
19	Sn-Pb	HASL	Pure Sn	195	90
20	Sn-Pb	HASL	Pure Sn	215	60
21	Sn-Pb	HASL	Pure Sn	215	90
22	Sn-Pb	HASL	Pure Sn	215	60
23	Sn-Pb	HASL	Pure Sn	205	90
24	Sn-Pb	HASL	Pure Sn	195	60
25	Sn-Pb	HASL	Pure Sn	205	30
26	Sn-Pb	HASL	Pure Sn	195	60
27	Sn-Pb	HASL	Pure Sn	195	30

Lead-free Solder Joint Reliability – State of the Art and Perspectives

Jianbiao Pan*, Ph.D.
Cal Poly State University
San Luis Obispo, CA 93407
Phone: (805) 756-2540
Fax: (805) 756-1420
Email: pan@calpoly.edu

Jyhwen Wang, Ph.D.
Texas A&M University
College Station, TX 77843
Phone: (979) 845-4903
Fax: (979) 862-7969
Email: jwang@tamu.edu
*-Corresponding author

David M. Shaddock
GE Global Research Center,
Niskayuna, NY 12309
Phone: (518) 387-4051
Fax: (518) 387-5442
shaddock@research.ge.com

Abstract

There is an increasing demand for replacing tin-lead (Sn/Pb) solders with lead-free solders in the electronics industry due to health and environmental concerns. The European Union recently passed a law to ban the use of lead in electronic products. The ban will go into effect in July of 2006. The Japanese electronics industry has worked to eliminate lead from consumer electronic products for several years. Although currently there are no specific regulations banning lead in electronics devices in the United States, many companies and consortiums are working on lead-free solder initiatives including Intel, Motorola, Agilent Technologies, General Electric, Boeing, NEMI and many others to avoid a commercial disadvantage. The solder joints reliability not only depends on the solder joint alloys, but also on the component and PCB metallizations. Reflow profile also has significant impact on lead-free solder joint performance because it influences wetting and microstructure of the solder joint. A majority of researchers use temperature cycling for accelerated reliability testing since the solder joint failure mainly comes from thermal stress due to CTE mismatch. A solder joint failure could be caused by crack initiation and growth or by macroscopic solder fracture. There are conflicting views of the reliability comparison between lead-free solders and tin-lead solders. This paper first reviews lead-free solder alloys, lead-free component lead finishes, and lead-free PCB surface finishes. The issue of tin whiskers is also discussed. Next, lead-free solder joint testing methods are presented; finite element modeling of lead-free solder joint reliability is reviewed; and experimental data comparing lead-free and tin-lead solder joint reliability are summarized. Finally the paper gives perspectives of transitions to totally lead-free manufacturing.

Key words Lead free solder, reliability, review

1. INTRODUCTION

There is an increasing demand in replacing tin-lead (Sn/Pb) solders with lead-free solders in the electronics industry due to health and environmental concern. Traditional eutectic tin-lead solder (Sn63/Pb37) has been used in the electronics industry exclusively because of its low cost, excellent physical and chemical properties, and robust reliability. However, electronic products are normally disposed in landfills from which lead can contaminate underground water and endanger humans. The shorter life cycle of today's consumer electronics increases the environmental impact significantly.

The European Union (EU) passed a law to ban the use of lead in electronics on February 13, 2003. The ban goes into effect on July 1, 2006. The Japanese electronics industry has worked to eliminate lead from consumer electronic products for several years. Although currently there are no specific regulations banning lead in electronics devices in the United States, many companies are working on lead-free solder initiatives including Intel [1], Motorola [2], Agilent Technologies [3], General Electric, Boeing [4], and many others to avoid a commercial disadvantage.

To comply with environmental regulations and avoid a marketing disadvantage, many consortium have been formed to conduct research on lead-free solders and lead-free solder joint reliability, for example, National

Electronics Manufacturing Initiative (NEMI) [5], National Center for Manufacturing Sciences (NCMS) [6], High Density Packaging Users Group (HDPUG) [7], Massachusetts Toxics Use Reduction Institute (TURI) [8], Joint Group on Pollution Prevention (JGPP) [9], Computer Aided Life Cycle Engineering (CALCE) in the University of Maryland [10], Tin Technology [11], and EU consortium known as IDEALS (Improved Design Life and Environmentally Aware Manufacturing of Electronic Assemblies by Lead-Free Soldering). Many technical societies are active in organizing activities related to lead-free soldering. These societies include IPC [12], Surface Mount Technology Association (SMTA), International Microelectronics and Packaging Society (IMAPS), and IEEE/CPMT.

This paper first reviews lead-free solder alloys, lead-free component lead finishes, and lead-free Printed Circuit Board (PCB) surface finishes. The issue of tin whiskers is also discussed. Next, lead-free solder joint testing methods are presented; finite element modeling of lead-free solder joint reliability is reviewed; and experimental data comparing lead-free and tin-lead solder joint reliability are summarized. Finally the paper gives perspectives of transitions to totally lead-free manufacturing.

2. LEAD-FREE SOLDER ALLOYS

Lead-free solder is generally defined as a lead (Pb) level in solder less than 0.1% by weight, though there is no standard lead-free definition yet [13]. This definition is adopted by Japanese Electronic Industry Development Association (JEIDA) and European Union End of Life Vehicles Directives (EUELVD), and met ASTM B32-96 and ISO 9453 specifications. However, the Joint Electronic Device Engineering Council (JEDEC) in the United States recommends lead-free as less than 0.2% lead by weight. JEDEC's definition meets ANSI/J-STD-006 specifications.

In the last 10 years, many lead-free solders have been proposed and much research and testing has been done on lead-free solder materials. For example, NCMS recommended SnAg3.5, SnAg3.5Bi4.8, and BiSn42. Note that SnAg3.5Bi4.8 means 3.5 percent in weight Ag, and 4.8 percent in weight Bi, with the leading element Sn making up the balance to 100%. NEMI recommended SnAg3.9Cu0.6 for reflow soldering and SnCu0.7 for wave soldering. Major Japanese electronics manufacturers investigated many lead-free solders including SnAg3.5 and SnAg3.0Cu0.5. A database of solder properties with emphasis on new lead-free solders was developed with the support of National Institute of Standards and Technology (NIST) and Colorado School of Mines [14].

Among the many developed lead-free solders, tin-silver-

copper (SnAgCu or SAC) appears the current best choice as an alternative to SnPb solder for most applications. There are several variations of the SnAgCu alloy. The NEMI in the United States recommends SnAg3.9Cu0.6 for reflow soldering applications [15]. The European consortium – BRITE-EURAM, focused its research and development efforts on SnAg3.8Cu0.7. The standard lead-free solder alloy in Japan is SnAg3Cu0.5 [16], which was recommended by Japan Electronics and Information Technology Industries Association (JEITA).

There are several major differences between SnPb and SnAgCu lead-free solders. First, SnAgCu solders require higher reflow temperatures than the eutectic SnPb. The melting point of SnAg3.8Cu0.7 is 219°C, and that of SnAg3Cu0.5 is 217°C. All are higher than eutectic SnPb solder, which has a melting point of 183°C. Second, the wetting of SnAgCu solders is generally not as good as SnPb alloy [17], although improvement in spreading was observed in lead-free solder when a nitrogen atmosphere was used [18]. Third, SnAgCu solder joints have more voids than SnPb. More voids have been observed when SnAgCu alloy was assembled with SnPb component finishes [19, 61]. Fourth, the appearance between SnAgCu and SnPb is different. SnPb solder joints look shiny and SnAgCu look dull. This difference requires new visual inspection specifications for lead-free solder joints.

3. LEAD-FREE COMPONENT LEAD FINISHES

A component lead finish that has compatibility with solder assembly processes and product life environments has historically been a well defined choice, SnPb. However, the advent of lead-free electronics is changing the component lead finishes offered by component suppliers. This impacts all electronic equipment manufacturers whether or not they need to produce lead-free products. Two considerations when choosing an alternative lead finish are its impact on manufacturing quality and product reliability. Component lead finishes with acceptable manufacturing quality should have intrinsic solderability with lead based and lead-free solders, a reproducible method for its application, and a reproducible method for soldering quality over an economically viable shelf life. A finish with acceptable product reliability is intrinsically stable, has a stable reaction with its neighboring materials and environment, and is durable in the use environment. The component lead finish also must meet the environmental requirements of legislation and be economically viable.

A survey of 72 suppliers responding in the industry found a variety of component lead finishes being proposed [20]. The survey results are shown in Figure 1. *Note that some suppliers offer more than one component lead finishes so that the total percent adds up to more than 100%.* Some

of the finishes being considered are plated Sn, SnBi, SnCu, SnCuAg, and NiPd or NiPdAu. The realistic outlook is that a larger mix of component lead finishes will be represented on a circuit board assembly for consumer and commercial products regardless of lead-free requirements. The soldering process for an assembly will need to be compatible with all these finishes and able to produce a reliable solder joint for the finish with the poorest intrinsic solderability.

The most popular choice is by far plated tin (Sn) as evidenced by 51% of suppliers offer it as component lead finish. This is not surprising since it is a well controlled bath, easily switched from SnPb, low cost, and has good solderability, however it is prone to metal whisker growth as reported by numerous publications such as NASA [21]. Some high reliability applications such as Boeing satellite systems and Raytheon ban pure tin as a component lead finish.

Pure Tin is followed in popularity by tin bismuth (SnBi) and finishes containing nickel palladium (NiPd or NiPdAu). SnBi is offered by some component suppliers responding to the survey. In practice it has been found to solder with acceptable workmanship using SnPb, SnAg3Cu0.5, SnAg4.0Cu0.5, and SnBiAg [22]. A SnBi bath has a higher producer maintenance cost than a Sn bath due to the high standard electrode potential between Sn and Bi causing Bi to immersion plate onto the anode. Nickel Palladium (NiPd) or Nickel Palladium Gold (NiPdAu) has been offered for many years by Texas Instruments (TI). The solderability is slightly less than the other finishes listed but no reports of solder joint failures have been made when used on copper leadframes. NEMI Tin Whisker Users Group recommends NiPdAu as a whisker free alternative but warns that molding compounds do not adhere as well to noble metals (Pd, Au) as they do to Cu [23].

SnCu is another component lead finish. A tin copper (SnCu) bath has a higher maintenance cost than SnBi due to the even greater standard electrode potential between Sn and Cu causing Cu to immersion plate onto the anode. The immersion plate will form a Cu_6Sn_5 intermetallic layer that can degrade solderability. Thickness measurement of SnCu is also difficult when it is plated on a copper lead frame using conventional methods such as X-Ray Fluorescence (XRF). Other lead finishes being offered by a few suppliers are plated SnAg and lead-free solder dipped finishes. Careful control of the SnAg plating process is needed since the melting point of the binary alloy increases rapidly above 5% silver content. SnAgCu solder dipped leads have been produced with acceptable workmanship in SnPb, SnAg3.0Cu0.5, and SnCu0.7 soldering processes [22]. Solder dipped leads after pure tin plating have the risk of whisker formation if the solder dipping does not cover all the tin.

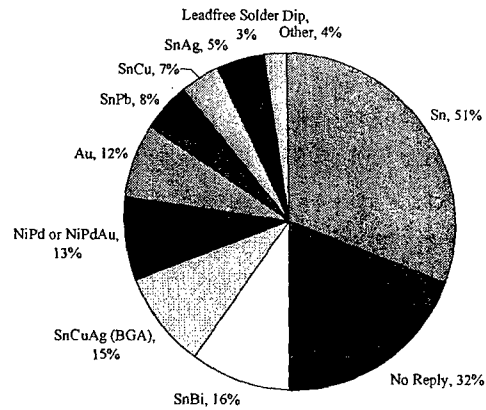


Figure 1 Component Finish Survey [20]

It should be pointed out that the component lead finishes listed above are not available for every package type. Component manufacturers are undergoing extensive qualification testing for all lead-free finishes. At this time, most package styles only have one or two lead-free finishes available. The common component finish for chip resistors and capacitors is pure tin due to its low cost. SnAgCu is by far the choice for Ball Grid Array (BGA) and Chip Scale Package (CSP) components. The popular component lead finishes for leaded packages such as Quad Flat Package (QFP) and Small Outline Package (SOP) are plated tin, SnBi, SnCu, and NiPd or NiPdAu. NiPdAu (or just plain NiPd) is favorable for these leadframe packages due to its whisker free characteristic, especially in fine pitch applications.

There is evidence from published documents that there is variability in the solderability of lead-free component lead finishes. Reliability of solder connections depends on the integrity of the solder joint and the component lead finish is an important constituent. The component lead finish interacts with the solder alloy in a metallurgical reaction to generate a reliable solder joint. The variability of this solderability may lead to variability in solder joint reliability. Component lead finish solderability is a function of preconditioning, temperature, and time. For example, the time a lead is in contact with molten solder in a wave soldering process is on the order of 3 to 5 seconds while for reflow soldering the contact can be for 60 to 90 seconds. Doyle [24] and Fan [25] reported the effects of preconditioning and solder temperature on SnPb, Sn, and SnCu finishes. Variability in wetting among the lead finishes, solder temperature, and the time to wet is noted. A slight increase in wetting time is found when using a lead-free alloy. Other studies on Ni/Pd component lead finishes show comparable results to SnPb.

4. LEAD-FREE PRINTED CIRCUIT BOARD FINISHES

The main function of Printed Circuit Board (PCB) finishes is to enhance the solderability of the substrate or underlying layer so that reliable solder joints will be achieved at the board level assembly. Other important functions of PCB finishes are to create joints that last over a longer period of time as well as being wire bondable.

The most common circuit board finish used for SnPb products is SnPb Hot Air Solder Leveled (HASL) finish. There have been a number of replacements proposed since the early 1990s with the focus of obtaining flatter pads for fine pitch components and a desire by the printed circuit board fabrication industry to eliminate this high maintenance and difficult to control process. These finishes have also been proposed and evaluated for lead-free finishes. The alternatives include organic solderability preservatives (OSP), gold over nickel (electroplated or Electroless Nickel Immersion Gold (ENIG)), immersion silver, immersion tin, and lead-free HASL. The choice of finish has typically been dependent on the process environment (reflow parameters and alloy dependent) and reports for the best performing finish have been varied between testing parties. A rating of PCB finishes by the members of the NEMI Tin Whisker Users Group has shown this variation. Nine participants rated the risk of the five alternatives (lead-free HASL uses SnCu) and the results are reproduced in Table 1. The table is ordered according to preference.

Table 1. NEMI Users Group PCB Finish Rating [23]

Finish	Recommend	Risky	Not Acceptable	No Vote
Immersion Ag	6	2	0	1
Immersion Sn	5	3	0	1
OSP (Entek)	5	2	1	1
ENIG	4	2	2	1
HASL (SnCu)	2	4	0	3

4.1 IMMERSION SILVER

Immersion silver is one of the finishes that has reportedly been used successfully with lead-free solders. Wetting is good, the finish can withstand multiple reflow passes [26], and it has a good shelf life (6-12 months). The surface also is wire bondable. It was originally marketed for its flat surface to be compatible with fine pitch surface mount but is also an option for lead-free assemblies. The thickness is about 0.127 microns with an optimum range of 0.08 to 0.16 microns. Thickness less than 0.04 microns will result in

poor solderability. Silver is a sacrificial layer and must dissolve into the solder joint. Dissolution rate of silver in Sn is slow so soldering processes with short dwell times (such as hand soldering and wave soldering) may lead to incomplete dissolution of silver and the solder joint will be to the silver intermetallic layer rather than the copper surface underneath. This may be tolerable in some cases but with elevated temperature aging and solid-state diffusion, the Ag_3Sn intermetallic can grow at the interface and the mechanical integrity of the solder joint will depend on the brittle Ag_3Sn intermetallic compound and underlying copper bond.

4.2 IMMERSION TIN

Immersion tin is a replacement process. Tin in the immersion tin solution replaces copper in the substrate and the copper goes into the solution. The thickness is on the order of 0.1 to 1.5 μm . Over time, the tin will form an intermetallic compound with Cu at a rate that is dependent on temperature. Cu_6Sn_5 and Cu_3Sn phases can form that reduce the solderability of the surface. Shelf life is estimated to be one year based on storage between 20 and 30°C for the thickness noted [27]. Multiple reflow passes with immersion tin is not recommended due to degradation in solderability after one reflow pass [28]

4.3 ENIG

Electroless Nickel Immersion Gold (ENIG) is a popular lead-free PCB finish because of its good solderability, performance with a number of lead free solders and its ability to withstand multiple soldering passes. Its solderability was rated high compared with the alloys tested as part of the NCMS lead-free study [29]. However, the most popular lead-free solders, SnAgCu, were not included in the NCMS study. ENIG was reported to have the least amount of solder voids in mixed (lead-free and SnPb) and total lead-free area array soldering conditions [30].

One issue with ENIG is called "black pad" or "black nickel". Black pad has given some reservation to its use. Black pad is a phenomenon related to some weak solder joints on ENIG surface finish. After the solder joint interfacial fracture is revealed, the exposed nickel pad is black. Black pad is related to the phosphorous content in the electroless nickel plating bath. High phosphorous content has good corrosion resistance but will induce solder joint embrittlement with the growth of an intermetallic layer through phosphorus enrichment during soldering. Low phosphorous content in the electroless nickel coating has poor corrosion resistance and is attacked by the acidic gold bath, which enriches phosphorus concentration on the surface of the electroless nickel coating. The gold coating dissolves quickly into the solder joint and exposes the poor solderable, phosphor rich nickel surface. Careful

monitoring and process control are needed to produce a quality ENIG finish.

4.4 OSP

Organic Solderability Preservatives (OSP) is proving to be a popular lead-free PCB finish. OSP is widely used in Japan, Saeki and Carano [31] reported that OSP has 69% of the PCB finish market share in 2001 in Japan and Asia, and expect to remain at a similar level (about 67%) in 2006. In the U.S., approximately 26% of PCB finish produced in 2002 used OSP [32]. But it has been reported that OSP didn't work well with lead-free solders with higher melting points. OSP had a higher number of failures during temperature cycling than the immersion Ag and immersion Sn [33]. At high temperatures, OSP is not as robust as the other metal finishes and has a smaller process window. Shear strength tests are found to be comparable to immersion Ag, immersion Sn, and ENIG [34].

4.5 LEAD-FREE HASL (HOT AIR SOLDER LEVELED)

Currently the most popular Sn/Pb finish for printed circuit boards is HASL. Much attention has been paid to alternatives to HASL for lead-free solutions. Studies have been reported on using Castin® (a composition of Sn 93-98%, Ag 1.5-3.5%, Cu .2-2%, and Sb .2-2%) alloy and SnCu0.7 for lead-free HASL [35], [36]. The studies have shown successful coating of circuits with these alloys. For example, a study that included using SnCu0.7 HASL reported good results that are comparable to SnPb HASL. The test was part of a study by Nortel on various board and component lead finishes in a SnCu0.7 soldering process [37]. The primary issues with HASL are the control of finish thickness and the thermal shock that the circuit boards experience during the HASL process. The benefits are that solderability of the finish is excellent and shelf life is longer than the alternatives. Shelf life of 1-2 years is expected from a HASL coated board where OSP and immersion finishes last less than a year.

4.6 SOLDERABILITY OF PCB FINISHES

The wetting behaviors of different lead-free solders on various PWB surface finishes vary. Sattiraju, et al. [18] conducted solder paste spread tests and wetting balance experiments with SnAg3.4Bi4.8, SnAg4.0Cu0.5, SnAg3.5, and SnCu0.7 on Sn, NiAu, Ag, and OSP PCB surface finishes. They concluded that pure Sn is the best surface finish for one reflow cycle, but is not suitable for a process with multiple reflow cycles. OSP has the poorest wetability. They also observed better spreading when a nitrogen atmosphere was used.

A study on five board finishes (HASL, NiAu, immersion Ag, immersion Sn, OSP) on 2512 chip components using the SnAg4.0Cu0.5 solder found that immersion Ag performed about the same as ENIG and immersion Sn [33]. The components were temperature cycled from -55 to 125°C and continuously monitored according to IPC-SM-785. Another comparison of immersion Ag and ENIG in temperature cycling (0 to 100°C) of 2512 chip resistors using SAC405 found that the immersion Ag boards had a higher mean life (5803 cycles) than ENIG (5100 cycles) [38]. However, this study used interval censoring every 250 cycles and the resistance was checked at room temperature, which may result in longer times to indication of failure.

5. TIN WHISKER FORMATION

Components have been commonly provided with terminations (a.k.a leads) that have been typically coated with SnPb to preserve their solderability in storage and suppress tin whisker growth. Plated Sn and high Sn content alloys have been reported to form tin whiskers that may cause electrical shorting. Tin whiskers are spontaneous filaments that grow from plated tin surfaces. Note that tin whisker growth from vapor deposited tin surfaces has also been reported [39]. Tin whiskers can carry more than 20 mA of current with figures as high as 100 mA reported. Tin whiskers have grown long enough to cause an electrical short to adjacent conductors or break off to cause shorts across other connections. The root cause of tin whiskers is not fully understood yet and accelerated test factors have not been established at this time. The problem has been confounded by inconsistent test reports regarding mitigation steps.

Industry groups are in the process of understanding tin whiskering. In the United States, NEMI has formed task groups to address modeling, accelerated testing, and a group in the University of Maryland (CALCE) has formed to investigate risk mitigation steps. The Japan Electronics and Information Technology Industries Association (JEITA) and the International Tin Research Institute (ITRI) in Europe are also contributing to tin whisker research. NEMI has recently proposed an acceptance test requirement for user acceptance of tin or high tin content finishes [40]. It requires that mitigation steps be taken by the component supplier, such as fusing, nickel barriers, or annealing, and are applied to plated Sn finishes. The test regiment includes ambient storage, temperature/humidity, and temperature cycling. Preconditioning is applied to some test groups to represent soldering processes and one test group is biased at 5V. A control group that is expected to whisker and a reference group (i.e. SnPb) are run through the test procedures with the samples. Whiskers must appear on any of the test groups for the test regime to be valid.

Not all lead-free finishes whisker the same. Noble metal finishes do not grow whiskers. A comparison of whisker propensity for several different lead finishes submitted to 60°C/95%RH is listed in Table 2 [41]. Any of the high Sn content finishes have a propensity for producing whiskers. It has been reported that SnCu grows whiskers more rapidly and longer than Sn but Sn grows a greater quantity. Generally it is accepted that SnPb does not form whiskers but the SnPb whisker formation has been reported [21].

Table 2 Tin Whisker Propensity Rank [41]

Ranked By Length (longer to shorter)	Ranked by Quantity (most to least)
SnCu (120 μm)	Sn
Sn (80 μm)	SnCu
SnBi (50 μm)	SnBi
SnPb (40 μm)	SnPb

Whisker formation of SnBi has been reported by Texas Instruments [39]. The whisker lengths are short (50 μm), but it is not known whether they would continue to grow at the same rate. The NEMI Tin Whisker Users Group includes SnBi as a whisker mitigation step in concentrations of 2 to 10% Bi by weight used with lead-free solders [23]. However, used with SnPb solder there is a concern about forming the low melting point (96°C) SnPbBi ternary phase when Bi concentration is greater than 5%. It is recommended that Bi concentration be limited to 3 to 5% by weight in a SnBi plated lead.

6. RELIABILITY OF LEAD FREE SOLDER JOINTS

Although SnAgCu alloy is likely to be the replacement of Sn/Pb solder, a solder joint reliability database has not been established yet. Tonapi [42] stated that the absence of critical data on the reliability of lead-free solder joint assemblies has become of increasing concern but the available data have been improving since his publication.

Reliability of a solder joint is defined as the probability that the solder joint can perform a required function under given conditions for a given time interval. So reliability is application specific and the reliability of a solder joint depends on the component (including size, packaging type, and component surface finish or metallization), the PCB board finish, the solder paste, solder joint geometry and the test conditions. Component size, package type, and test conditions determine the loading condition on the solder joint. Intermetallic layers formed at the interfaces between the solder and the component metallization as well as the PCB metallization will affect the mechanical properties of the joint. Therefore, it is inappropriate to say “lead-free solders in general are more reliable than SnPb, or vice-versa.” We should specify the detailed information on components, boards, solders, and testing conditions. In

addition, the manufacturing assembly processes would contribute to the reliability of the solder joint. For example, reflow profile will influence wetting and microstructure of the solder joint. The reflow profile of SnPb and SnAgCu should be different due to the different melting temperatures. To make the reliability comparison between SnPb and SnAgCu solders meaningful, the reflow profile should be optimized for the specific solder alloy.

A solder joint consists of the solder alloy, the component metallization, and the PCB metallization as shown in Figure 2. Failure of a solder joint can occur at the bulk solder or at the interfacial intermetallic layers between the solder and the component or the PCB. A solder joint failure could be caused by crack initiation and growth (fatigue failure), or by macroscopic solder fracture (fracture failure). The crack initiation and growth is generally the result of grain coarsening, grain boundary sliding, or void formation and growth when solder joints experience stress under the reliability tests or service conditions.

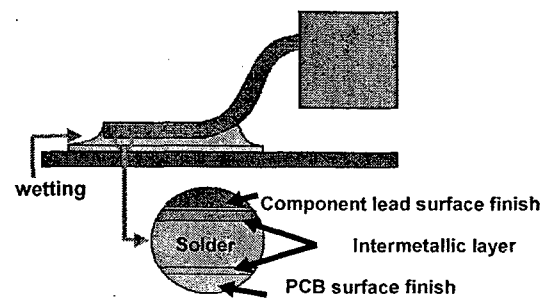


Figure 2. A typical solder joint

Fatigue failure is normally the result of power cycling, temperature cycling, or mechanical vibration. Fracture failure results from bending, twisting, mechanical shock, and free fall drop. The most common reliability threat comes from stress-relaxation based (thermal) fatigue damage [43]. Life prediction of a solder joint can be achieved by mathematical modeling and/or experimental testing.

6.1 RELIABILITY MODELING

The thermal fatigue life of a solder joint is dominated by the joint's creep responses to thermal cycling. The solder joint life can be estimated by the Coffin-Manson equation as reported by Lau et al. [44]:

$$N_f = \psi (\Delta W)^\phi \quad (1)$$

where N_f is the number of thermal cycles to failure, ΔW is the creep strain energy density per cycle, and ψ and ϕ are fatigue crack-growth material constants. Lau et al. [45] further demonstrated that for a given joint structure (geometry), material properties (PCB, IC package, and

solder), and thermal loading cycle, the creep strain energy density per cycle, ΔW , can be determined by creep analysis using Finite Element Analysis (FEA) method. While powerful FEA tools are readily available, the constants in the constitutive equations for FEA input have to be obtained from experiments. The material data such as Young's modulus, coefficient of thermal expansion, and normal creep strain rate of a lead-free solder (95.5Sn-3.9Ag-0.6Cu) were obtained by Vianco and Rejent [46] and can be used for FEA. However, the critical fatigue crack-growth constants (ψ and ϕ in Eq. (1)) for lead-free solder are not currently available for quantitative reliability predictions.

With the same lead-free Sn-Ag-Cu alloy, wave soldering of light-emitting diode (LED) display assembly was tested and analyzed [47]. In the finite element creep analysis, the LED display on a plated through hole (PTH) PCB was modeled as plane strain condition and the creep strain energy density per thermal cycle, ΔW , was calculated. As the quantity of ΔW is very small, it was concluded, qualitatively, that the solder joint should be reliable under normal operating conditions. It should be noted that, in these FEA efforts, the thermal expansion mismatch between materials leads to shear stress and creep shear strain. The joints were analyzed based on continuum models without imperfections. Failure mechanisms such as crack initiation and void growth were not specifically addressed.

6.2 EXPERIMENTAL TESTING METHODS

Experimental evaluation of solder joint reliability is often through accelerated reliability tests though acceleration factors are not well understood yet. The accelerated reliability tests include power cycling, temperature cycling, thermal shock, mechanical vibration, mechanical shock, bend test, and free fall drop test. Which tests should be performed depends on product requirements and service environmental conditions.

The most common accelerated reliability test is temperature cycling because it simulates thermo-mechanical solder fatigue, which is the key failure mechanism in solder joints. During field service, the solder joints are subjected to thermal-mechanical stresses resulting from the coefficient of thermal expansion (CTE) mismatch between the package and the board caused either by power cycling or environmental temperature changes. Two common temperature cycle profiles used in reliability tests are:

- Thermal cycling from -40°C to 125°C per JEDEC JESD22-A104B (July 2000, Condition G)
- Thermal cycling from 0°C to 100°C per IPC-9701 Test Condition 1.

How can we determine whether a solder joint has failed after the accelerated reliability tests? Functions of a solder joint are to provide mechanical interconnection and electrical interconnection. Thus, if the joint is unable to resist enough mechanical load, or the solder joint resistance increases significantly (even electrical open), we say the solder joint has failed. Accordingly, there are two solder joint performance evaluation methods. One is to monitor pull strength or shear strength after every certain number of temperature cycles or other reliability tests [48], [49]. The other is to monitor resistance change after a certain number of temperature cycles or other reliability tests [50] -[52]. Few researchers use visual inspection to evaluate solder joint quality [53]. Visual inspection is highly unreliable and labor intensive. It should be pointed out that the visual inspection specifications for lead-free solder joints should be different from those for the SnPb joints because lead-free solder joints look less shiny than the SnPb solder joints. IPC is revising the IPC-610 standard to revision D for lead-free workmanship. (It should have been released in November 2004).

Pull tests can be used for leadframe packages such as QFP and SOP to evaluate solder joint performance. The pull test is generally performed at a 45° angle as shown in Figure 3 to create a combination of tensile and shear stress on the solder joint [48], [49]. Note that the pull strength at the hook is different from the pull strength at the solder joint. The pull strength at the solder joint can be calculated given the geometry of the lead. For chip resistors and BGA packages shear testing rather than pull testing is used because there is no lead in these packages to pull. One concern of shear testing on BGA packages is that there may be no significant difference in shear strength between good joints and bad joints if only one or two solder joints cracked or failed and all others are still in good shape.

Resistance monitoring is another popular way to evaluate solder joint performance. Based on IPC-9701, the practical definition of solder joint failure is the interruption of electrical continuity (>1000 ohms) for periods greater than 1 microsecond.

An event detector (AnaTech or equivalent conforming to IPC-9701) is used to monitor the resistance of each channel and record the time of each potential failure (resistance exceeds the reference threshold resistor value). Generally daisy-chained dummy components and daisy-chained routed PCBs are used in the test. One form of daisy-chain patterns for dummy components with N leads is as follows: lead 1 is connected to lead 2, lead 3 is connected to lead 4, ..., lead N-3 is connected to lead N-2, lead N-1 is connected to lead N. In order to create a electrical continuity, a corresponding daisy-chain pattern for the PCB has connections as follows: pad for lead 2 is connected to pad for lead 3, pad for lead 4 is connected to pad for lead 5,

..., pad for lead N-2 is connected to pad for lead N-1. Test points should be connected to pad for lead 1 and pad for lead N. Note that different companies may offer dummy components with different daisy-chain patterns.

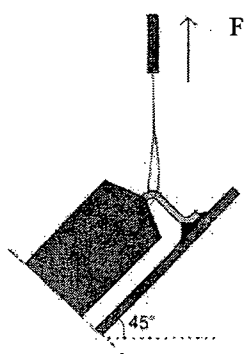


Figure 3. A typical pull test method

To understand how a solder joint fails, the cross-sections of solder joints are commonly characterized by scanning electron microscopy (SEM), or voids or cracks are examined using X-Ray. Through analytical tools, the microscopic structure of solder joints can be revealed.

6.3 EXPERIMENTAL TEST RESULTS

Although many lead-free solder joint reliability studies have been reported, many questions remain. Some researchers reported that the reliability of SnAgCu is equivalent to or better than that of SnPb in terms of cycles to failure in temperature cycling tests, while others reported vice versa. As discussed before, solder joint reliability is application specific, it depends on not only the component lead finish, solder paste, solder joint geometry, and PCB finishes, but also the assembly processes and test conditions. It seems that much of the thermal fatigue experimental data suggest that the SnAgCu alloys outperform SnPb at low strain amplitude applications and vice versa at high strain amplitude applications. Researchers at the CALCE consortium did the reliability study and drew the same conclusion as shown in Figure 4 [54].

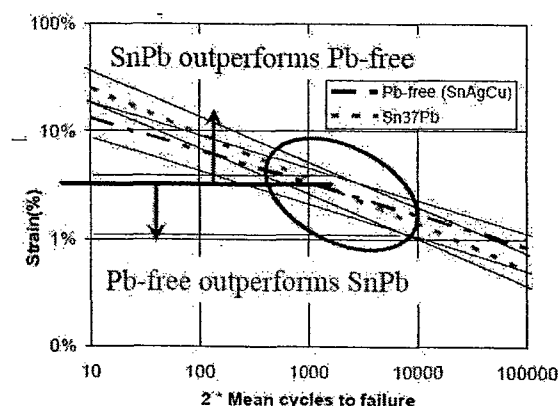


Figure 4. Comparison of Temperature Cycling Mechanical Durability [54]

For chip resistors/capacitors and leadless packages, the applied strain can be approximately (rough first-order) estimated as

$$\gamma = \frac{d\Delta T\Delta\alpha}{h} \quad (2)$$

where γ is the strain imposed to solder joints, d is the distance to the neutral point (DNP), ΔT is the temperature difference, h is the stand-off height and $\Delta\alpha$ is the CTE difference between the package and PCB substrate. Equation 2 assumes the solder takes all the deformation in the joint. But for QFP packages, applied strain on solder joints during temperature cycling is generally much lower than calculated by Equation 2 because of lead compliance. Thus, Equation 2 cannot apply for QFP packages.

For BGA packages, Equation 2 is not appropriate either. Based on Equation 2, the solder joints at the outer perimeter of a BGA package would experience the maximum strain because of the largest DNP and fail first. However, experimental results from Motorola's PBGA packages showed that the solder joints under and proximate to the silicon die perimeter tend to fail first [55]. This is because of the local CTE mismatch between the silicon die and the Bismaleimide Triazine (BT) substrate. BT is a PBGA substrate material. Nonlinear FEA by Lee and Lau [56] confirmed the results. Lau [57] presented stress-strain analysis for various BGA packages.

6.3.1 EXPERIMENTAL RESULTS ON LEADFRAME PACKAGES

Overall, experimental data show that SnAgCu solder joints of QFP packages are as reliable as SnPb. For example, Stam and Davitt [43] reported no failure of solder joints of QFP packages with SnPb15 finish assembled on four board finishes (OSP-Cu, Immersion Sn, Immersion Ag, and NiAu) using three solder alloys (SnPb62Ag, SnAg3.8Cu0.7, and SnAgCuX, where "X" is a proprietary elemental addition) for up to 5000 power cycles from room

temperature to 100°C. They also reported no decrease in pull strength of QFP leads after 5000 cycles. Board level reliability testing on five plating finishes using three different solders was reported by Nakadaira [41]. The plating finishes were Sn, SnBi2, SnCu0.7, Ni/Pd/Au, and SnPb15. The solders were SnPb37, SnAg3.5Cu0.7, and SnAg2.5Bi1.0Cu0.5. Four types of packages (LQFP64, PLCC44, QFP100, and PQFP132) were daisy chained and temperature cycled between -40 to 125°C using IPC-SM-785 guidance. It was concluded that all the finishes performed comparably with no significant failures before 3500 cycles. Since the strain of solder joints of QFP packages is low, the experimental data agree with the conclusion: SnAgCu alloys are as reliable as or better than Sn/Pb alloys.

6.3.2. EXPERIMENTAL RESULTS ON CHIP RESISTORS

Suhling, et al. [58] compared thermal cycling reliability of lead-free solder joints of chip resistors (size 2512). The board finish was ENIG and chip resistor lead finish was pure Sn. Two temperature cycles profiles (-40 to 125°C and -40 to 150°C) were used and 6,000 cycles were completed. They found that the reliability of SnAg3.8Cu0.7 and SnPb37 solder alloys were similar for the temperature range from -40 to 125°C, but SnPb37 outperforms SnAg3.8Cu0.7 for the temperature range from -40 to 150°C. Based on Equation 2, solder joints have lower strain at the temperature range from -40 to 125°C than from -40 to 150°C. Thus, the result is consistent with the earlier conclusion. Woodrow [4] found SnPb outperforms SnAgCu in a reliability study of 1206 chip resistors with SnCu0.7 finish. Three board finishes were tested: immersion Ag, NiAu, and OSP. The temperature cycle was from -55 to 125°C. He also reported that SnAgCu solder joints were slightly stronger than SnPb before temperature cycling. Geiger, et. al [59] did cyclic bending tests and shear tests on 0201 resistors with SnPb10 finish. The board finish was ENIG. They compared SnPb solder and SnAg3.9Cu0.6 solder and found no significant difference in the bending test failures up to 300,000 cycles. They also reported the SnAgCu solder shear strength was about 15% higher than the Sn/Pb solder.

6.3.3 EXPERIMENTAL RESULTS ON BGA PACKAGES

Although Equation 2 is not suitable for calculating the strain of a BGA package, generally speaking, a Ceramic BGA (CBGA) has larger strain than a Plastic BGA (PBGA) because the CTE difference between the CBGA and the FR-4 board is much larger than between the PBGA and the FR-4 board. The strain of BGA solder joints is not only a function of package material, but also a function of package size and standoff height. BGA ball size can have an impact on reliability.

At low strain amplitude application, SnAgCu performs as good as or outperforms SnPb. For example, Syed [59] reported SnAgCu showed better reliability than SnPb. He assembled both PBGA and flexXBGA packages on FR-4 board with OSP finish. Temperature cycling was from -55 to 125°C. Note that flexXBGA uses a polyimide tape substrate, which has a CTE similar to that of an FR-4 board. Lau, [50] reported there were no solder joint failures on the lead-free balled flexBGA with both SnAgCu and SnPb solder pastes on all the Sn-Cu HASL, Ni-Au, and OSP PCBs during temperature cycles from 0 to 100°C for 6,000 cycles.

At high strain amplitude application, SnAgCu has a reliability poorer than SnPb. For example, Lau, [50] reported the test results for the Ceramic Column Grid Array (CCGA) packages with both SnAgCu and SnPb solder paste on PCBs with three finishes: Sn-Cu HASL, Ni-Au, and OSP. They found failures on all the three PCB's with SnAgCu, but no failures with SnPb solder paste.

Though no specific strain value was calculated and compared in published papers, it seems in general that the following conclusion is valid: the reliability of SnAgCu is similar to or better than SnPb at low strain amplitude applications and vice versa at high strain amplitude applications. Note that the conclusion is drawn from thermal fatigue modeling and experimental data.

Several researchers noticed that SnAgCu solder joints have higher pull or shear strength than SnPb before reliability tests. That is easy to understand because SnAgCu alloy has higher yield strength than SnPb.

The authors notice that the component metallization and PCB board metallization may not be as critical as solder alloy in fatigue failure mode. But the metallization may be more critical in fracture failure mode because it determines the intermetallic characteristic. For example, Arra, [49] compared mechanical performance of a SnAuCu solder joint of a QFP208 component with four finishes (Ni/Pd/Au, SnPb15, SnBi2, and Sn100) under the free fall drop test. The PCB finishes were immersion Ag and OSP. They found the intermetallic layer formed between Ni/Pd/Au finish and SnAgCu solder was brittle and resulted in failure earlier in the free fall drop test.

7. TRANSITION TO TOTAL LEAD-FREE MANUFACTURING

There are three routes to convert tin-lead soldering to totally lead-free soldering as shown in Figure 5 [60]. Route A is desirable. However, some lead-free finish components may not be available at this time, so some companies choose route B. For other companies that allow having lead

(Pb) in their electronic equipment until 2010 granted by EU RoHS directive, route C is applicable.

In order to switch to lead-free manufacturing, some surface mount assembly processes must be modified. Surface mount assembly includes solder paste stencil printing, pick and place, and solder reflow processes. Comparing SnPb soldering with lead-free soldering, there is no significant difference in stencil printing and pick and place processes. The key response variable in the stencil printing process is the solder volume deposited. The stencil printing process is solder paste characterization dependant, not solder alloy dependant. But there are significant differences in solder reflow process. These differences include higher reflow temperature and poorer wetting in lead-free soldering. A new reflow profile with different time and temperature parameters is needed for lead-free soldering. The higher reflow temperature may damage sensitive components.

There are many issues in routes B and C transition. Voids in solder joints are of primary concern. More voids have been reported in the solder joints of BGA packages made with SnAgCu solder balls and SnPb solder paste [30] and made with SnPb solder balls and SnAgCu solder paste [61]. How voids will affect long-term solder joint reliability is unknown. It is necessary to establish the relationship between the void (including the size of void, the number of voids, and the location of voids) and long-term reliability. Smetana, [61] summarized other concerns over routes B and C.

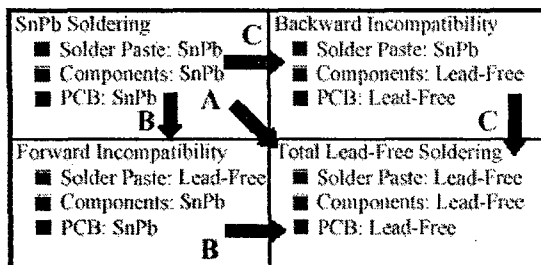


Figure 5. Transition to total lead-free

8. SUMMARY

The Electronics industry has identified lead-free solder alloy consisting of SnAgCu as possible alternates to eutectic SnPb37 solder, though an agreement on the exact composition has not been achieved.

The common lead-free component lead finishes include pure Sn, SnBi, SnCu, NiPdAu, and SnAgCu. At this time, the leading finish available for BGA and CSP packages is SnAgCu, and that for chip resistors is pure tin. Pure Sn, SnBi, SnCu, and NiPdAu are available to QFPs and SOPs, and NiPdAu may be favorable for leadframe packages due to its whisker free characteristic. The leading PCB surface finishes are OSP, ENIG, Immersion Ag, Immersion Sn, and HASL SnCu.

SnAgCu solder joints are generally stronger than SnPb before reliability tests because SnAgCu alloy has a higher yield strength than SnPb. Reliability of SnAgCu is application specific. In low strain amplitude applications, SnAgCu seems to outperform SnPb. In high strain amplitude applications, SnAgCu performance is poorer than SnPb.

ACKNOWLEDGMENT

This work was partially sponsored by the Department of the Navy, Office of Naval Research, under Award # N00014-04-1-0436. The authors would like to thank John Lau of Agilent, Kim Hyland and Dennis Willie of Solelectron, Mark Kessler, Robert Kunz, and Stephen A. McKeown of BAE Systems for their valuable comments and suggestions.

REFERENCES

- [1] Intel webpage: <http://www.intel.com/research/silicon/leadfree.htm>
- [2] K. Gaffney, J. Poarch, and D. Delaney, "Lead-free flip chip process development," *Proceedings of 2000 Electronic Components and Technology Conference*, IEEE, pp. 129-133, 2000.
- [3] J. H. Lau and W. Dauksher, "Creep of Sn-(3.5-3.9)wt%Ag-(0.5-0.8)wt%Cu Lead-Free Solder," *Micromaterials and Nanomaterials*, Edited by B. Michel, Fraunhofer Institute, IZM, Berlin, 2004, pp. 54-62, 2004.
- [4] T. A. Woodrow, "Reliability and Leachate Testing of Lead-Free Solder Joints," *IPC Lead-Free Conference*, San Jose, CA, May 2002.
- [5] National Electronics Manufacturing Initiative (NEMI) webpage <http://www.nemi.org/>
- [6] National Center for Manufacturing Sciences (NCMS) webpage <http://www.ncms.org/>
- [7] High Density Packaging Users Group (HDPUG) webpage <http://www.hdpug.org/>
- [8] Massachusetts Toxics Use Reduction Institute (TURI) webpage <http://www.turi.org/>
- [9] Joint Group on Pollution Prevention (JGPP) webpage <http://www.jgpp.com/>
- [10] Computer Aided Life Cycle Engineering (CALCE) webpage <http://www.calce.umd.edu/>
- [11] Tin Technology webpage <http://www.tintechnology.com/>
- [12] IPC lead-free webpage <http://www.leadfree.org/>
- [13] K. J. Puttlitz, *Handbook of Lead-Free Solder Technology for Microelectronic Assemblies*, Edited by K. J. Puttlitz and K. A. Stalter, Marcel Dekker, Inc., New York, pp. 10, 2004.
- [14] T. Siewert, S. Liu, D. R. Smith, and J. C. Madeni, "Database for Solder Properties with Emphasis on New Lead-free Solders," *NIST & Colorado School of Mines, Release 4.0, Feb. 2002*, <http://www.boulder.nist.gov/div853/lead-free/solders.html>
- [15] E. Bradley, C. Handwerker, and J. E. Sohn, "NEMI Report: A Single Lead-Free Alloy is Recommended," *SMT*, January 2003.
- [16] S. Denda, "Lower Temp Lead-free Solder Needed," *Advancing Microelectronics*, IMAPS, pp. 35, Nov./Dec. 2003.
- [17] T. J. Singler, S. J. Meschter, and J. Spalik, "Soldering Wetting and Spreading," *Handbook of Lead-Free Solder Technology for Microelectronic Assemblies*, Edited by Karl J. Puttlitz and Kathleen A. Stalter, Marcel Dekker, Inc., New York, Chapter 11, pp. 331-429, 2004.
- [18] S. V. Sattiraju, "Wetting Characteristics of Pb-Free Solder Alloys and PWB Finishes," *IEEE Transactions on Electronics Packaging Manufacturing*, Vol. 25, No. 3, pp. 168-184, 2002.
- [19] J. Bath, "A Manufacturable Lead-Free Surface-Mount Process?" *Circuit Assembly*, pp. 26-30, January 2003.
- [20] CALCE EPSC, Component Suppliers' Survey, Available: <http://www.calce.umd.edu/lead-free/tin-whiskers/team/part-suppliers040519.xls>, May 19, 2004.
- [21] NASA Tin Whisker Website, <http://ncpp.nasa.gov/whisker/>
- [22] Experimental results by GE Global Research Center and Soletron.
- [23] NEMI Tin Whisker User Group, "Interim Recommendation on Lead-Free Finishes for Components Used in High-Reliability Products," http://www.nemi.org/projects/ese/tin_whisker_usergroup.html, March 2004.
- [24] C. Doyle, N. Brown, and M. Bardizah, "Factors Influencing the Solderability of Lead-Free Electrodeposits," *Metal Finishing*, January 2002.
- [25] C. Fan, Y. Zhong, and J.A. Alys, "Solderability of lead-free finishes using lead-free solders," *Proceedings of SMTA International Conference*, p. 827, 2001.
- [26] M. Arra, "Aging Mechanisms of Immersion Tin and Silver PCB Surface Finishes in Lead-Free Solder Applications," *IPC/JEDEC 3rd International Lead-free Conference*, San Jose, CA, March 2003.
- [27] D. Ormerod, "Meeting Fine Pitch Assembly Needs with a Solderable Tin Finish," *IPC PCB Expo and APEX*, March 14 -18, 1999.
- [28] M. Arra, D. Shangguan, J. Sundelin, T. Lepisto, E. Ristolainen, "Aging Mechanisms of Immersion Tin and Silver PCB Surface Finishes in Lead-Free Solder Applications," *IPC/JEDEC 3rd International Lead-free Conference*, San Jose, CA, March 2003.
- [29] NCMS Lead Free Solder Project Final Report, NCMS Report 0401RE96.
- [30] G. Echeverria, D. Santos, P. Chouta, and C. Shea, "Effect of Lead-Free Assembly Processing on Solder Joint Voiding," *IPC/JEDEC 5th International Lead-free Conference*, San Jose, CA, March, 2004.
- [31] K. Saeki and M. Carano, "Next Generation Organic Solderability Preservatives (OSP) for Lead-Free Soldering and Mixed Metal Finish PWB's and BGA Substrates," *IPC Printed Circuits Expo, APEX, and Designers Summit conference*, Anaheim, CA, 2004.
- [32] R. Schetty, "Lead-Free Finishes for Printed Circuit Boards and Components," *Handbook of Lead-Free Solder Technology for Microelectronic Assemblies*, Edited by Karl J. Puttlitz and Kathleen A. Stalter, Marcel Dekker, Inc., New York, Chapter 12, pp. 432-464, 2004.
- [33] M. Dusek, and C. Hunt, "Reliability Comparison of Lead-free Solder Joints Formed on Different PCB Finishes," *IPC/JEDEC 3rd International Lead-free Conference*, San Jose, CA, March 2003.
- [34] Y. Zheng, C. Hillman, P. McClusky, "Intermetallic Growth on PWBs Soldered with Sn3.8Ag0.7Cu," *Proceedings of the 52nd IEEE Electronic Components & Technology Conference*, pp. 1226-1231, San Diego, 2002.
- [35] Teledyne, "No-Lead and Horizontal Hot Air Leveling," *Teledyne document HAL-NoLead-004*, <http://www.tet-halco.com/library.asp>
- [36] Cemco, "Overview Report on a Lead Free Electronics Industry," *Cemco report*, 2001. <http://www.cemco.com/Brochures/LeadFreecomplete150301.pdf>
- [37] K. G. Snowdon, C. G. Tanner, and J. R. Thompson, "Lead Free Soldering Electronic Interconnect: Current Status and Future Developments," *2000 Electronic Components and Technology Conference*, IEEE, pp. 1416-1419, 2000.
- [38] A.R. Zbrzezny, P. Snugovsky, and D.D. Perovic, "Reliability of Lead-free Chip Resistor Solder Joints Assembled on Boards with Different Finishes Using Different Reflow Cooling Rates," *IPC-JEDEC 5th International Lead-free Conference*, San Jose, CA, March, 2004.
- [39] D.W. Romm, D.C. Abbott, S. Grenney, and M. Khan, "Whisker Evaluation of Tin-Plated Logic Component Leads," *Texas Instruments Application Report SZZA037A- February 2003*, <http://focus.ti.com/lit/an/szza037a/szza037a.pdf>
- [40] Tin Whisker Acceptance Test Requirements, http://www.nemi.org/projects/ese/tin_whisker_usergroup.html
- [41] Y. Nakadaira, "Pb-free plating for peripheral/leadframe packages," *IEEE Proceedings EcoDesign 2001: 2nd International Symposium on Environmentally Conscious Design and Inverse Manufacturing*, pp. 213-218, 2001.
- [42] S. Tonapi, "Reliability of Lead-Free Solder Interconnects - A Review," *2002 Proceedings Annual Reliability and Maintainability Symposium*, IEEE, pp. 423-428, 2002.
- [43] F. A. Stam, and E. Davitt, "Effects of Thermo-mechanical Cycling on Lead and Lead-Free (SnPb and SnAgCu) Surface Mount Solder Joints," *Microelectronics Reliability*, Vol. 41, pp. 1815-1822, 2001.
- [44] J. H. Lau, et. al., "Creep Analysis and Thermal Fatigue Life Prediction of the Lead-Free Solder Sealing Ring of a Photonic Switch," *ASME Transactions, J. of Electronic Packaging*, vol. 124, pp. 403-410, December 2002.
- [45] J. H. Lau, D. Shangguan, D. Lau, T. Kung, and R. Lee, "Thermal-Fatigue Life Prediction Equation for Wafer-Level Chip Scale Package (WLCSP) Lead-Free Solder Joints on Lead-Free Printed Circuit Board (PCB)," *Proceedings of IEEE Electronic Components and Technology Conferences, Las Vegas*, pp. 1563-1569, May 2004.
- [46] P. Vianco, and J. Rejent, "Compression Deformation Response of 95.5Sn-3.9Ag-0.6Cu Solder," *UCLA Lead-Free Workshop*, October 2002.

- [47] J. H. Lau, "Lead-Free Wave-Soldering and Reliability of Light-Emitting Diode (LED) Display Assembly," *IPC First International Conference on Lead-Free Electronic "Towards Implementation of the RoHS Directive"*, Brussels, Belgium, June 10 - 12, 2003.
- [48] H. Tanaka, Y. Aoki, M. Kitagawa, and Y. Saito, "Reliability Testing and Failure Analysis of Lead-Free Solder Joints under Thermo-Mechanical Stress," *IPC Printed Circuits Expo, APEX, and Designers Summit conference*, Anaheim, CA, 2004.
- [49] M. Arra, T. Castello, D. Shangguan, and E. Ristolainen, "Characterization of Mechanical Performance of Sn/Ag/Cu Solder Joints with Different Component Lead Coatings," *SMTA International Conference*, 2004.
- [50] J. Lau, N. Hoo, R. Horsley, J. Smetana, D. Shangguan, W. Dauksher, D. Love, I. Menis, and B. Sullivan, "Reliability Testing and Data Analysis of Lead-Free Solder Joints for High-density Packages," *Soldering & Surface Mount Technology*, Vol. 16, No. 2, pp.46-68, 2004.
- [51] S. T. Nurmi, J. J. Sundelin, E.O. Ristolainen, and T. Lepisto, "The influence of multiple reflow cycles on solder joint voids for lead-free PBGAs," *Soldering & Surface Mount Technology*, Vol. 15, No. 1, 2003, pp. 31-38.
- [52] J.C. Suhling, H.S. Gale, R.W. Johnson, M.N. Islam, T. Shete, P. Lall, M.J. Bozack, J.L. Evans, P. Seto, T. Gupta, and J.R. Thompson, "Thermal Cycling Reliability of Lead-Free Chip Resistor Solder Joints," *Soldering & Surface Mount Technology*, Vol. 16, No. 2, pp. 77-87, 2004.
- [53] S. Shina, "Lead Free Conversion Analysis for Multiple PWB/Component Materials and Finishes using Quality and Reliability Testing," *IPC Printed Circuits Expo, APEX, and Designers Summit conference*, Anaheim, CA, 2004.
- [54] "Global Transition to Pb-Free/Green Electronics," AIA, May 2004. Available at http://www.calce.umd.edu/lead-free/calcePbfree_AIA.pdf
- [55] A. Mawer, "Plastic Ball Grid Array (PBGA)," *Motorola report AN1231*, Phoenix, AZ, 1996.
- [56] S. Lee and J. H. Lau, "Effect of Chip Dimension and Substrate Thickness on Plastic Ball Grid Array Solder Joint Reliability," *Proceedings of SMI Conference*, Sept. 1996.
- [57] J. H. Lau and Y. Pao, *Solder Joint Reliability of BGA, CSP, Flip Chip, and Fine Pitch SMT Assemblies*, Mc-Graw Hill, New York, 1997, Chapter 5.
- [58] D. Geiger, F. Mattsson, D. Shangguan, M. Ong, P. Wang, T. Castello, and S. Yi, "Process Characterization of PCB Assembly using 0201 Packages with Lead-Free Solder," *Soldering & Surface Mount Technology*, Vol. 15, No. 2, pp. 22-27, 2003.
- [59] A. Syed, "Reliability of Lead-Free Solder Connections for Area-Array Packages," *IPC SMEMA Council APEX conference*, 2001.
- [60] J. Lau and K. Liu, "Global Trends of Lead-Free Soldering," *Advanced Packaging*, Jan. 2004.
- [61] J. Smetana, R. Horsley, J. Lau, K. Snowdon, D. Shangguan, J. Gleason, I. Memis, D. Love, W. Dauksher, and B. Sullivan, "Design, Materials and Process for Lead-Free Assembly of High-density Packages," *Soldering & Surface Mount Technology*, Vol. 16, No. 1, pp.53-62, 2004.

Lead-free Solder Joint Reliability – State of the Art and Perspectives

Jianbiao Pan, Ph.D.
Cal Poly State University
San Luis Obispo, CA 93407
Phone: (805) 756-2540
Fax: (805) 756-1420
Email: pan@calpoly.edu

Jyhwen Wang, Ph.D.
Texas A&M University
College Station, TX 77843
Phone: (979) 845-4903
Fax: (979) 862-7969
Email: jwang@tamu.edu

David M. Shaddock
GE Global Research Center,
Niskayuna, NY 12309
Phone: (518) 387-4051
Fax: (518) 387-5442
shaddock@research.ge.com

Abstract

There is an increasing demand in replacing tin-lead (Sn/Pb) solders with lead-free solders in the electronics industry due to health and environmental concern. The European Union recently passed a law to ban the use of lead in electronic products. The ban will go into effect in July of 2006. The Japanese electronics industry has worked to eliminate lead from consumer electronic products for several years. Although currently there are no specific regulations banning lead in electronics devices in the United States, many companies and consortiums are working on lead-free solder initiatives including Intel, Motorola, Agilent Technologies, General Electric, Boeing, NEMI and many others to avoid a commercial disadvantage.

The solder joints reliability not only depends on the solder joint alloys, but also on the component metallization and PCB metallization. Reflow profile has significant impact on lead-free solder joint performance also because it influences wetting and microstructure of the solder joint. Majority researchers use temperature cycling for accelerated reliability testing since the solder joint failure mainly comes from thermal stress due to CTE mismatch. A solder joint failure could be caused by crack initiation and growth or by macroscopic solder fracture. There are conflicting views of the reliability comparison between lead-free solders and tin-lead solders.

This paper first reviews lead-free solder alloys, lead-free component finishes, and lead-free PCB surface finishes. Tin whisker issue is also discussed. Then the lead-free solder joint testing methods are presented; finite element modeling of lead-free solder joint reliability is reviewed; and experimental data comparing lead-free and tin-lead solder joint reliability are summarized. Finally the paper gives perspectives of transitions to a totally lead-free manufacturing.

Keywords: Lead free solder, reliability, review

1. Introduction

There is an increasing demand in replacing tin-lead (Sn/Pb) solders with lead-free solders in the electronics industry due to health and environmental concern. Traditional eutectic tin-lead solder (Sn63/Pb37) has been used in electronics industry exclusively because of its low cost, excellent physical and chemical properties, and robust reliability. However, electronic products are normally disposed in landfill, from which lead will contaminate underground water and endanger humans. The shorter life cycle of today's consumer electronics increases the environmental impact significantly.

The European Union (EU) passed a law to ban the use of lead in electronics on February 13, 2003. The ban goes into effect on July 1, 2006. The Japanese electronics industry has worked to eliminate lead from consumer electronic products for several years. Although currently there are no specific

regulations banning lead in electronics devices in the United States, many companies are working on lead-free solder initiatives including Intel [1], Motorola [2], Agilent Technologies [3], General Electric, Boeing [4], and many others to avoid a commercial disadvantage.

To comply with environmental regulations and avoid marketing disadvantage, many consortium have been formed to conduct research on lead-free solders and lead-free solder joint reliability, for example, National Electronics Manufacturing Initiative (NEMI) [5], National Center for Manufacturing Sciences (NCMS) [6], High Density Packaging Users Group (HDPUG) [7], Massachusetts Toxics Use Reduction Institute (TURI) [8], Joint Group on Pollution Prevention (JGPP) [9], Computer Aided Life Cycle Engineering (CALCE) in the University of Maryland [10], Tin Technology [11], and EU consortium known as IDEALS (Improved

Design Life and Environmentally Aware Manufacturing of Electronic Assemblies by Lead-Free Soldering). Many technical societies are active in organizing activities related to lead-free soldering. These societies include IPC [12], Surface Mount Technology Association (SMTA), International Microelectronics and Packaging Society (IMAPS), and IEEE/CPMT.

This paper first reviews lead-free solder alloys, lead-free component finishes, and lead-free Printed Circuit Board (PCB) surface finishes. Tin whisker issue is also discussed. Then the lead-free solder joint testing methods are presented; finite element modeling of lead-free solder joint reliability is reviewed; and experimental data comparing lead-free and tin-lead solder joint reliability are summarized. Finally the paper gives perspectives of transitions to a totally lead-free manufacturing.

2. Lead-Free Solder Alloys

The lead-free solder is generally defined as the lead (Pb) level in solder less than 0.1% by weigh, though there is no standard lead-free definition yet [13]. The definition is adopted by Japanese Electronic Industry Development Association (JEIDA) and European Union End of Life Vehicles Directives (EUELVD), and met ASTM B32-96 and ISO 9453 specifications. But the Joint Electronic Device Engineering Council (JEDEC) in the United States recommends lead-free as less than 0.2% lead by weight. The JEDEC's definition meets ANSI/J-STD-006 specifications.

In the last 10 years, many lead-free solders have been proposed and much research and testing has been done on lead-free solder materials. For example, NCMS recommended SnAg3.5, SnAg3.5Bi4.8, and BiSn42. Note that SnAg3.5Bi4.8 means 3.5 percent in weight Ag, and 4.8 percent in weight Bi, with the leading element Sn making up the balance to 100%. NEMI recommended SnAg3.9Cu0.6 for reflow soldering and SnCu0.7 for wave soldering. Major Japanese electronics manufacturers investigated many lead-free solders including SnAg3.5 and SnAg3.0Cu0.5. A database of solder properties with emphasis on new lead-free solders was developed with the support of National Institute of Standards and Technology (NIST) and Colorado School of Mines [14].

Among many developed lead-free solders, tin-silver-copper (SnAgCu or SAC) appears the best choice as an alternative to Sn/Pb solder for most applications. There are several variations of the SnAgCu alloy. The NEMI in the United States recommends SnAg3.9Cu0.6 for reflow soldering application [15]. The European consortium - BRITE-EURAM focused its research and

development efforts on SnAg3.8Cu0.7. The standard lead-free solder alloy in Japan is SnAg3Cu0.5 [16], which was recommended by Japan Electronics and Information Technology Industry (JEITA).

There are several major differences between SnPb and SnAgCu lead-free solders. First, SnAgCu solders require higher reflow temperatures than SnPb. The melting point of SnAg3.8Cu0.7 is 219°C, and that of SnAg3Cu0.5 is 217°C. All are higher than eutectic SnPb solder, which has the melting point of 183°C. Second, the wetting of SnAgCu solders is generally not as good as SnPb alloy [17], although improvement in spreading was observed in lead-free solder when a nitrogen atmosphere was used [18]. Third, SnAgCu solder joints have more voids than SnPb. More voiding was observed when SnAgCu alloy was assembled with SnPb component finishes [19, 61]. Fourth, the appearance between SnAgCu and SnPb is different. SnPb solder joints look shiny and SnAgCu look dull. This difference requires new visual inspection specifications for lead-free solder joints.

3. Lead-Free Component Finishes

A component lead finish that has compatibility with solder assembly processes and product life environments has historically been a well defined choice, SnPb. However, the advent of lead free electronics is changing the component lead finishes offered by component suppliers. This impacts all electronic equipment manufacturers whether or not they need to produce lead free products. Two considerations when choosing an alternative lead finish are its impact on manufacturing quality and product reliability. Component finishes with acceptable manufacturing quality should have intrinsic solderability with lead based and lead free solders, a reproducible method for its application, and a reproducible method for soldering quality over an economically viable shelf life. A finish with acceptable product reliability is intrinsically stable, has a stable reaction with its neighboring materials and environment, and durable in the use environment. The component finish also must meet the environmental requirements of legislation and be economically viable.

A survey of 72 suppliers responding in the industry found a variety of component finishes being proposed [20]. The survey results are shown in Figure 1. Note that some suppliers offer more than one component finishes so that the total percent added up is more than 100%. Some of the finishes being considering are plated Sn, SnBi, SnCu, SnCuAg, and NiPd or NiPdAu. The realistic outlook is that a larger mix of component surface finishes will be represented on a circuit board assembly for

consumer and commercial products regardless of lead-free requirements. The soldering process for an assembly will need to be compatible with all these finishes and able to produce a reliable solder joint for the finish with the poorest intrinsic solderability.

The most popular choice is by far plated tin (Sn) as evidenced by 51% suppliers offer it as component finish. This is not surprising since it is a well controlled bath, easily switched from a SnPb, low cost, and has good solderability, but is prone to metal whisker growth as reported by numerous publications such as NASA [21]. Some high reliability applications such as Boeing satellite systems and Raytheon ban pure tin as a component finish.

Plated Tin is followed in popularity by tin bismuth (SnBi) and finishes containing nickel palladium (NiPd or NiPdAu). SnBi is offered by some component suppliers responding to the survey. It has been found to solder with acceptable workmanship using SnPb, SnAg3Cu0.5, SnAg4.0Cu0.5, and SnBiAg in practice [22]. A SnBi bath has a higher producer maintenance cost than a Sn bath due to the high standard electrode potential between Sn and Bi causing Bi to immersion plate onto the anode. Nickel Palladium (NiPd) or Nickel Palladium Gold (NiPdAu) has been offered for many years by Texas Instruments (TI). The solderability is slightly less than the other finishes listed but no reports of solder joint failures have been made when used on copper leadframes. NEMI Tin Whisker Users Group recommends NiPdAu as a whisker free alternative but warns that molding compounds do not adhere as well to noble metals (Pd, Au) as they do to Cu [23].

SnCu is another component finish. A tin copper (SnCu) bath has a higher maintenance cost than SnBi due to the even higher standard electrode potential between Sn and Cu causing Cu to immersion plate onto the anode. The immersion plate will form a Sn_5Cu_6 intermetallic layer that can degrade solderability. Thickness measurement of SnCu is also difficult when it is plated on a copper lead frame using conventional methods such as X-Ray Fluorescence (XRF). Other finishes that are also offered by a few suppliers are plated SnAg and lead free solder dipped finishes. Careful control of the SnAg plating process is needed since the melting point of the binary alloy increases rapidly above 5% silver content. SnAgCu solder dipped leads have been produced with acceptable workmanship in SnPb, SnAg3.0Cu0.5, and SnCu0.7 soldering processes [22]. Solder dipped leads after tin plating has the risk of whisker formation if the solder dipping does not cover all the tin.

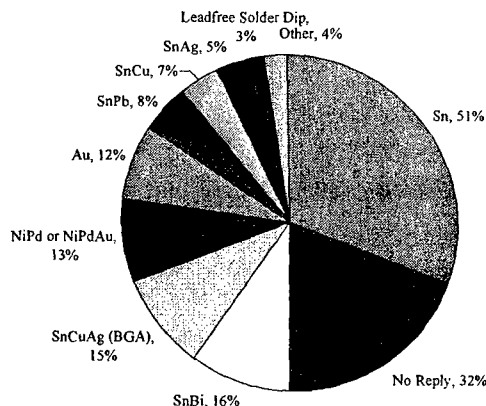


Figure 1 Component Finish Survey

It should be pointed out that the component finishes listed above are not available for every package type. Component manufacturers are undergoing extensive qualification testing for all lead-free finishes. At this time, most package styles only have one or two lead-free finishes available. The common component finish for chip resistors and capacitors is 100% tin due to its low cost. SnAgCu is by far the choice for Ball Grid Array (BGA) and Chip Scale Package (CSP) components. The popular component finishes for leaded packages such as Quad Flat Package (QFP) and Small Outline Package (SOP) are plated tin, SnBi, SnCu, and NiPd or NiPdAu. NiPdAu (or just plain NiPd) is favorable for these leadframe packages due to its whisker free characteristic, especially in fine pitch applications.

There is evidence from published documents that there is variability in the solderability of lead-free component finishes. Reliability of solder connections depends on the integrity of the solder joint and the component finish is an important constituent. The component finish interacts with the solder alloy in a metallurgical reaction to generate a reliable solder joint is indicated by solderability. Component lead finish solderability is a function of preconditioning, temperature, and time. For example, the time a lead is in contact with molten solder in a wave soldering process is on the order of 3 to 5 seconds and 60 to 90 seconds for reflow soldering. Doyle [24] and Fan [25] reported the effects of preconditioning and solder temperature on SnPb, Sn, and SnCu finishes. Variability in wetting among the lead finishes, solder temperature, and the time to wet is noted. A slight increase in wetting time is found when using a lead free alloy. Other studies on NiPd component finishes show comparable results to SnPb.

4. Lead-Free Printed Circuit Board Finishes

The main function of PCB finishes is to enhance the solderability of the substrate or underlying layer so that reliable solder joints will achieve at the board level assembly. Another important function of PCB finishes is to be wire bondable.

The most common circuit board finish used for SnPb products is SnPb Hot Air Solder Leveled (HASL) finish. There have been a number of replacements proposed since the early 1990s with the focus of obtaining flatter pads for fine pitch components and a desire by the printed circuit board fabrication industry to eliminate this high maintenance and difficult to control process. These finishes have also been proposed and evaluated for lead-free finishes. The alternatives include organic solderability preservatives (OSP), gold over nickel (electroplated or Electroless Nickel Immersion Gold (ENIG)), immersion silver, immersion tin, and lead-free HASL. The choice of finish has typically dependent on the process environment (reflow parameters and alloy dependent) and reports for the best performing finish has been varied between testing parties. A rating of circuit board finishes by the members of the NEMI Tin Whisker Users Group members shows this variation. Nine participants rated the risk of the five alternatives (lead-free HASL uses SnCu) and the results are reproduced in Table 1. The table is ordered according to preference.

Table 1. NEMI Users Group PCB Finish Rating [23]

Finish	Recommend	Risky	Not Acceptable	No Vote
Immersion Ag	6	2	0	1
Immersion Sn	5	3	0	1
OSP (Entek)	5	2	1	1
ENIG	4	2	2	1
HASL (SnCu)	2	4	0	3

4.1 Immersion Silver

Immersion silver is one of the finishes that are reported to be used successfully with lead-free solders. Wetting is good, the finish can withstand multiple reflow passes [26], and it has a good shelf life (6-12 months). The surface is wire bondable. It has originally marketed for its flat surface to be compatible with fine pitch surface mount but is also an option for lead free assemblies. The thickness is about 0.127 microns with an optimum range of 0.08 to 0.16 microns. Thickness less than 0.04 microns will result in poor solderability. Silver is a sacrificial layer and must dissolve into the solder joint. Dissolution rate of silver in Sn is slow so soldering processes with short dwell times (such as hand soldering and wave soldering) may lead to

incomplete dissolution of silver and the solder joint will be to the silver coating rather than the copper surface underneath. This may be tolerated in some cases but on elevated temperature aging and solid-state diffusion, the Ag₃Sn intermetallic can grow at the interface and the mechanical integrity of the solder joint will depend on the brittle Ag₃Sn intermetallic compound and underlying copper bond.

4.2 Immersion Tin

Immersion tin is a replacement process. Tin in the immersion tin solution replaces copper in the substrate and the copper goes into solution. The thickness is on the order of 0.1 to 1.5 μ m. Over time, the tin will form an intermetallic compound with Cu at a rate that is dependent on temperature. Cu₆Sn₅ and Cu₃Sn phases can form that reduce the solderability of the surface. Shelf life is estimated to be one year based on storage between 20 and 30°C for the thickness noted [27]. Multiple reflow passes with immersion tin is not recommended due to degradation in solderability after one reflow pass [28]

4.3 ENIG

Electroless Nickel Immersion Gold (ENIG) is a popular lead free printed circuit board finish because of its good solderability performance with a number of lead free solders and ability to withstand multiple soldering passes. Its solderability was rated high on the alloys tested as part of the NCMS lead free study [29]. However, the most popular lead-free solders, SnAgCu, were not included in the NCMS study. ENIG was reported to have the least amount of solder voids in mixed (lead-free and SnPb) and total lead-free area array soldering conditions [30].

One issue with ENIG is called "black pad" or "black nickel". Black pad has given some reservation to its use. Black pad is a phenomenon related to some weak solder joints on ENIG surface finish. After the solder joint interfacial fracture is revealed, the exposed nickel pad is black. Black pad is related to the phosphorous content in the electroless nickel coating bath. High phosphorous content has good corrosion resistance but will induce solder joint embrittlement with the growth of an intermetallic layer through phosphorus enrichment during soldering. Low phosphorous content in the electroless nickel coating has poor corrosion resistance and is attacked by the acidic gold bath, which enriches phosphorus concentration on the surface of the electroless nickel coating. The gold coating dissolves quickly into the solder joint and exposes the poor solderable, phosphor rich nickel surface. Careful monitoring and process control is needed to produce an ENIG quality finish.

4.4 OSP

Organic Solderability Preservatives (OSP) is proving to be a popular lead-free PCB finish. OSP is widely used in Japan as Saeki and Carano [31] reported that OSP has 69% PCB finish market share in 2001 in Japan and Asia, and expect to remain similar level (about 67%) in 2006. In the U.S., approximately 26% of PCB finish produced in 2002 use OSP [32]. But it has been reported that OSP didn't work well with lead-free solders with higher melting points. OSP had a higher number of failures during temperature cycling than compared to immersion Ag and immersion Sn [33]. OSP is not as robust to high temperatures as metal finishes and have a smaller process window. Shear strength tests are found to be comparable to immersion Ag, immersion Sn, and ENIG [34].

4.5 Lead-Free HASL

Currently the most popular Sn/Pb finish for printed circuit boards is HASL. Much attention has been paid to alternatives to HASL for lead-free solutions. Studies have been reported on using the Castin® (a composition of Sn 93-98%, Ag 1.5-3.5%, Cu .2-2%, and Sb .2-2%) alloy and SnCu0.7 for lead-free HASL [35, 36]. The studies have shown successful coating of circuits with these alloys. For example, a study that included using SnCu0.7 HASL reported good results that are comparable to SnPb HASL. The test was part of a study by Nortel on various board and component finishes in a SnCu0.7 soldering process [37]. The primary issues with HASL are controlling thickness and thermal shock the circuit board experiences during the process. The benefits are that solderability is excellent and shelf life is longer compared to the alternatives. Shelf life of 1-2 years is expected from a HASL coated board where OSP and immersion finishes last less than a year.

4.6 Solderability of PCB Finishes

The wetting behaviors of different lead-free solders on various PWB surface finishes vary. Sattiraju, et. al. [18] conducted solder paste spread tests and wetting balance experiments with SnAg3.4Bi4.8, SnAg4.0Cu0.5, SnAg3.5, and SnCu0.7 on Sn, NiAu, Ag, and OSP PCB surface finishes. They concluded that pure Sn is the best surface finishes for reflow only once, but is not suitable for a process with multiple reflow cycles. OSP has the poorest wetability. They also observed better spreading when a nitrogen atmosphere was used.

A study on five board finishes (HASL, NiAu, immersion Ag, immersion Sn, OSP) on 2512 using the SnAg4.0Cu0.5 solder found that immersion

Ag performed about the same as ENIG and immersion Sn [33]. The components were temperature cycled from -55 to 125°C and continuously monitored according to IPC-SM-785. Another comparison of immersion Ag and ENIG in temperature cycling (0 to 100°C) of 2512 chip resistors using SAC405 found that the immersion Ag boards had a higher mean life (5803 cycles) than ENIG (5100 cycles) [38]. However, this study used interval censoring every 250 cycles and the resistance was checked at room temperature, which may result in longer times to indication of failure.

5. Tin Whisker Formation

Components have been commonly provided with terminations (a.k.a leads) that have been typically coated with SnPb to preserve their solderability in storage and suppress tin whisker growth. Plated Sn and high Sn content alloys have been reported to form tin whiskers that may cause electrical shorting. Tin whiskers are spontaneous filaments that grow from plated tin surfaces. Note that tin whiskers grow from vapor deposited tin surfaces has also been reported [39]. Tin whiskers can carry more than 20 mA of current with figures as high as 100 mA reported. The whiskers have grown long enough to cause an electrical short to adjacent conductors or break off to cause shorts across other connections. The root cause of tin whiskers is not fully understood yet and accelerated test factors have not been established at this time. The problem has been confounded by inconsistent test reports regarding mitigation steps.

Industry groups are in the process of understanding tin whiskering. In the United States, NEMI has formed task groups to address modeling, accelerated testing, and a group in the University of Maryland (CALCE) has formed to investigate risk mitigation steps. The Japan Electronics and Information Technology Industries Association (JEITA) and the International Tin Research Institute (ITRI) in Europe are also contributing to tin whisker research. NEMI has recently proposed an acceptance test requirement for user acceptance of tin or high tin content finishes [40]. It requires that mitigation steps be taken by the component supplier, such as fusing, nickel barriers, or annealing, be applied to plated Sn finishes. The test regiment includes ambient storage, temperature/humidity, and temperature cycling. Preconditioning is applied to some test groups to represent soldering processes and one test group is biased at 5V. A control group that is expected to whisker and a reference group (i.e. SnPb) are run through the test procedures with the samples. Whiskers must appear on any of the test groups for the test regime to be valid.

Not all lead free finishes whisker the same. Noble metal finishes do not grow whiskers. A comparison of whisker propensity for several different lead finishes submitted to 60°C/95%RH is listed in Table 2 [41]. Any of the high Sn content finishes have a propensity for producing whiskers. It has been reported that SnCu grows whiskers more rapidly and longer than Sn but Sn grows a greater quantity. Generally it is accepted that SnPb does not form whiskers but there have been reports of SnPb whisker formation [21].

Table 2 Tin Whisker Propensity Rank

Ranked By Length (longer to shorter)	Ranked by Quantity (most to least)
SnCu (120 μm)	Sn
Sn (80 μm)	SnCu
SnBi (50 μm)	SnBi
SnPb (40 μm)	SnPb

Whisker formation of SnBi has been reported in a report from Texas Instruments [39]. The whisker lengths are short (50 μm), but it is not known whether they would continue to grow at the same rate. The NEMI Tin Whisker Users Group includes SnBi as a whisker mitigation step in concentrations of 2 to 10% by weight used with lead-free solders [23]. However, used with SnPb solder there is a concern about forming the low melting point (96°C) SnPbBi ternary phase when Bi concentration is greater than 5%. It is recommended that Bi concentration be limited to 3 to 5% by weight in a SnBi plated lead.

6. Reliability of lead free solder joints

Although SnAgCu alloy is likely to be the replacement of Sn/Pb solder, the solder joint reliability database has not been established yet. Tonapi [42] stated that the absence of critical data on the reliability of lead-free solder joint assemblies has become of increasing concern but the available data has been improving since his publication.

Reliability of a solder joint is defined as the probability that the solder joint can perform a required function under given conditions for a given time interval. So reliability is application specific and the reliability of a solder joint depends on the component (including size, packaging type, and component surface finish or metallization), the PCB board finish, the solder paste, solder joint geometry and test conditions. Component sizes and packaging types, and test conditions determine the loading condition on the solder joint. Intermetallic layers formed at the interfaces between the solder and the component metallization, and between the solder and the PCB metallization will affect the mechanical

performance of the joint. Because of this, it is inappropriate to say "lead-free solders in general are more reliable than SnPb, or vice-versa." We should specify the detailed information on components, boards, solders, and testing conditions. In addition, the manufacturing assembly processes would contribute the reliability of the solder joint. For example, reflow profile will influence wetting and microstructure of the solder joint. The reflow profile of SnPb and SnAgCu should be different due to different melting temperature. To make the reliability comparison between SnPb and SnAgCu solders meaningful, the reflow profile should be optimized for the specific solder alloy.

A solder joint consists of the solder alloy, the component metallization, and the PCB metallization as shown in Figure 2. Failure of a solder joint can occur at the bulk solder or at the interfacial intermetallic layer between the solder and the component or between the solder and the PCB. A solder joint failure could be caused by crack initiation and growth (fatigue failure), or by macroscopic solder fracture (fracture failure). The crack initiation and growth is generally the result of grain coarsening, grain boundary sliding, or void formation and growth when solder joints experience stress under the reliability tests or service conditions.

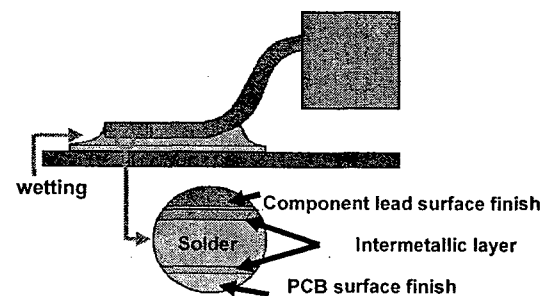


Figure 2. A typical solder joint

Fatigue failure is normally the result of power cycling, temperature cycling, or mechanical vibration. Fracture failure commonly results from bending, twisting, mechanical shock, and free fall drop. The most common reliability threat comes from stress-relaxation based (thermal) fatigue damage [43]. Life prediction of a solder joint can be achieved by mathematical modeling and/or experimental testing.

6.1 Reliability modeling

The thermal fatigue life of a solder joint is dominated by the joint's creep responses to thermal cycling. The solder joint life can be estimated by the Coffin-Manson equation as reported by Lau et al. [44]:

$$N_f = \psi(\Delta W)^\varphi \quad (1)$$

where N_f is the number of thermal cycles to failure, ΔW is the creep strain energy density per cycle, and ψ and φ are fatigue crack-growth material constants. Lau et al. [45] further demonstrated that for a given joint structure (geometry), material properties (PCB, IC package, and solder), and thermal loading cycle, the creep strain energy density per cycle, ΔW , can be determined by creep analysis using Finite Element Analysis (FEA) method. While powerful FEA tools are readily available, the constants in the constitutive equations for FEA input have to be obtained from experiments. The material data such as Young's modulus, coefficient of thermal expansion, and normal creep strain rate of a lead-free solder (95.5Sn-3.9Ag-0.6Cu) were obtained by Vianco and Rejent [46] and can be used for FEA. However, the critical fatigue crack-growth constants (ψ and φ in Eq. (1)) for this lead-free solder are not currently available for quantitative reliability predictions.

With the same lead-free Sn-Ag-Cu alloy, wave soldering of light-emitting diode (LED) display assembly was tested and analyzed [47]. In the finite element creep analysis, the LED display on a plated through hole (PTH) PCB was modeled as plane strain condition and the creep strain energy density per thermal cycle, ΔW , was calculated. As the quantity of ΔW is very small, it was concluded, qualitatively, that the solder joint should be reliable under normal operating conditions. It should be noted that, in these FEA efforts, the thermal expansion mismatch between materials leads to shear stress and creep shear strain. The joints were analyzed based on continuum models without imperfections. Failure mechanisms such as crack initiation and void growth were not specifically addressed.

6.2 Experimental testing methods

Experimental evaluation of a solder joint reliability is often through accelerated reliability tests though acceleration factors are not well understood yet. The accelerated reliability tests include power cycling, temperature cycling, thermal shock, mechanical vibration, mechanical shock, bend test, and free fall drop test. Which tests should be performed depends on product requirements and service environmental conditions.

The most common accelerated reliability test is temperature cycling because it simulates thermo-mechanical solder fatigue, which is the key failure mechanism in solder joints. During field service, the solder joints are subjected to thermal-

mechanical stresses resulting from the coefficient of thermal expansion (CTE) mismatch between the package and the board caused either by power cycling or environmental temperature changes. Two common temperature cycle profiles used in reliability tests are:

1. Thermal cycling from -40°C to 125°C per JEDEC JESD22-A104B (July 2000, Condition G)
2. Thermal cycling from 0°C to 100°C per IPC-9701 Test Condition 1.

How can we determine a solder joint has failed after the accelerated reliability tests? Functions of a solder joint are to provide mechanical interconnection and electrical interconnection. Thus, if the joint is unable to resist enough mechanical load, or the solder joint resistance increases significantly (even electrical open), we say the solder joint fails. Accordingly, there are two solder joint performance evaluation methods. One is to monitor pull strength or shear strength after every certain number of temperature cycles or other reliability tests [48 and 49]. The other is to monitor resistance change after certain number of temperature cycles or other reliability tests [50, 51, and 52]. Few researchers use visual inspection to evaluate the solder joint quality [53]. Visual inspection is highly unreliable and labor intensive. It should be pointed out that the visual inspection specifications for lead-free solder joints should be different from that for SnPb joints because lead-free solder joints look less shiny comparing with SnPb. IPC is revising the IPC-610 standard to revision D for lead-free workmanship. It is expected to release in November 2004.

Pull test can be used for leadframe packages such as QFP and SOP to evaluate solder joint performance. The pull test is generally performed at a 45° angle as shown in Figure 3 to create a combination of tensile and shear stress on the solder joint [48 and 49]. Note that the pull strength at the hook is different from the pull strength at the solder joint. The pull strength at the solder joint can be calculated given the geometry of the lead. For chip resistors and BGA packages, shear test rather than pull test is used because there is no lead in these packages to pull. One concern of shear testing on BGA packages is that there may be no significant difference in shear strength between good joints and bad joints if only one or two solder joints cracked or failed and all others are still in good shape.

Resistance monitoring is another popular way to evaluate solder joint performance. Based on IPC-9701, the practical definition of solder joint failure is the interruption of electrical continuity (>1000 ohms) for periods greater than 1 microsecond.

An event detector (AnaTech or equivalent conforming to IPC-9701) is used to monitor the resistor of each channel and record the time of each potential failure (resistor exceeds the reference threshold resistor value). Generally daisy-chained dummy components and daisy-chained routed PCBs are used in the test. One of daisy-chain patterns for dummy components with N leads is as follows: lead 1 is connected to lead 2, lead 3 is connected to lead 4, ..., lead N-3 is connected to lead N-2, lead N-1 is connected to lead N. In order to create a electrical continuity, a corresponding daisy-chain pattern for the PCB have connections as follows: pad for lead 2 is connected to pad for lead 3, pad for lead 4 is connected to pad for lead 5, ... , pad for lead N-2 is connected to pad for lead N-1. Test points should be connected to pad for lead 1 and pad for lead N. Note that different companies may offer dummy components with different daisy-chain patterns.

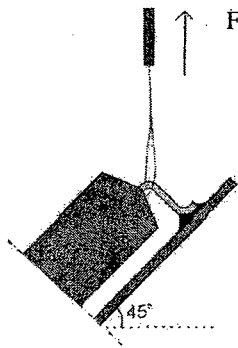


Figure 3. A typical pull test method

To understand how a solder joint fails, the cross-sections of solder joints are commonly characterized by scanning electron microscopy (SEM), or voids or cracks are examined using X-Ray. Through the analytical tools, the microscopic structure of solder joints can be revealed.

6.3 Experimental Testing Results

The lead-free solder joint reliability studies have been reported a lot recently although many questions remain. Some researchers reported the reliability of SnAgCu is equivalent or better than SnPb in terms of cycles to failure in temperature cycling tests, while others reported vice versa. As discussed before, solder joint reliability is application specific. It not only depends on the component finish, the solder paste, solder joint geometry, and PCB finishes, but also depends on the assembly processes and the testing conditions. It seems that many thermal fatigue experimental data suggested a conclusion: SnAgCu alloys outperform SnPb at low

strain amplitude applications and vice versa at high strain amplitude applications. Researchers at the CALCE consortium did the reliability study and drew the same conclusion as shown in Figure 4 [54].

For chip resistors/capacitors and leadless packages, the applied strain can be approximately (rough first-order) estimated

$$\gamma = \frac{d\Delta T\Delta\alpha}{h} \quad (2)$$

where γ is applied strain on solder joints, d is the distance to the neutral point (DNP), ΔT is the temperature difference, and $\Delta\alpha$ is the CTE difference between the package and PCB substrate. Here assume all the deformation is taken by the solder joint. But for QFP packages, applied strain on solder joints during temperature cycles is generally much lower than calculated by Equation 2 because of the compliance lead shape. Thus Equation 2 cannot apply for QFP packages.

For BGA packages, Equation 2 is not appropriate either. If based on Equation 2, the solder joints at the outer perimeter of a BGA package would experience the maximum strain because of the largest DNP and fail first. However, experiments results from Motorola's PBGA packages found that the solder joints under and proximate to the silicon die perimeter tend to fail first [55]. This is because of the local CTE mismatch between the silicon die and the Bismaleimide Triazine (BT) substrate. BT is a PBGA substrate material. Nonlinear FEA by Lee and Lau [56] confirmed the results. Lau [57] presented stress-strain analysis for various BGA packages.

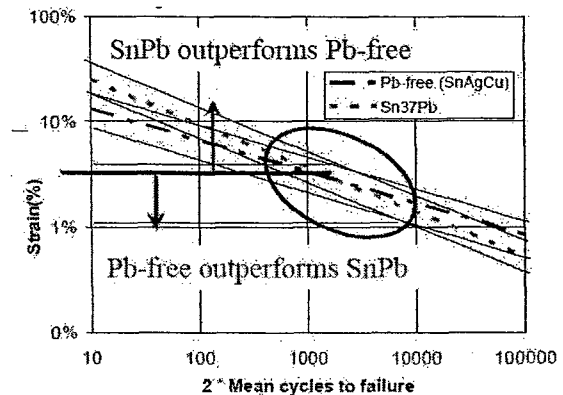


Figure 4. Comparison of Temperature Cycling Mechanical Durability [54]

6.3.1 Experimental results on leadframe packages:

Overall, experimental data show that SnAgCu solder joints of QFP packages are as reliable as SnPb. For example, Stam and Davitt [43] reported no failure of solder joints of QFP packages with SnPb15 finish assembled on four board finishes

(OSP-Cu, Immersion Sn, Immersion Ag, and NiAu) using three solder alloys (SnPb62Ag, SnAg3.8Cu0.7, and SnAgCuX) for up to 5000 power cycles from room to 100°C. They also reported no pull strength of QFP leads decreased after 5000 cycles. Board level reliability testing on five plating finishes using three different solders is reported by Nakadaira [41]. The plating finishes were Sn, SnBi2, SnCu0.7, Ni/Pd/Au, and SnPb15. The solders were SnPb37, SnAg3.5Cu0.7, and SnAg2.5Bi1.0Cu0.5. Four types of packages (LQFP64, PLCC44, QFP100, and PQFP132) were daisy chained and temperature cycled between -40 to 125°C using IPC-SM-785 guidance. It was concluded that all the finishes performed comparably with no significant failures before 3500 cycles. Since the strain of solder joints of QFP packages is low, these experimental data agrees with the conclusion: SnAgCu alloys are as reliable as or better than the Sn/Pb.

6.3.2. Experimental results on chip resistors:

Suhling, et. al. [58] compared thermal cycling reliability of lead-free solder joints of chip resistors 2512. The board finish was ENIG and chip resistor finish was pure Sn. Two temperature cycles profiles (-40 to 125°C and -40 to 150°C) were used and 6,000 cycles each were completed. They found that the reliability of SnAg3.8Cu0.7 and SnPb37 solder alloys were similar at the temperature range from -40 to 125°C, but SnPb37 outperforms SnAg3.8Cu0.7 at the temperature range from -40 to 150°C. Based on Equation 2, solder joints have lower strain at the temperature range from -40 to 125°C than that the temperature range from -40 to 150°C. Thus, the result is consistent with the earlier conclusion. Woodrow [4] found SnPb outperforms SnAgCu in a reliability study of 1206 chip resistors with SnCu0.7 finish. Three board finishes were tested: immersion Ag, NiAu, and OSP. The temperature cycle was from -55 to 125°C. He also reported that SnAgCu solder joints were slightly stronger than SnPb before temperature cycling. Geiger, et. al [59] did cyclic bending tests and shear tests on 0201 resistors with SnPb10 finish. The board finish was ENIG. They compared SnPb solder and SnAg3.9Cu0.6 solder and found no significant difference to the bending test failures up to 300,000 cycles. They also reported the SnAgCu solder shear strength was about 15% higher than the Sn/Pb solder.

6.3.3 Experimental results on BGA packages:

Although Equation 2 is not suitable for calculating the strain of BGA package, generally speaking, Ceramic BGA (CBGA) has larger strain than Plastic BGA (PBGA) because the CTE

difference between the CBGA and the FR-4 board is much larger than between the PBGA and the FR-4 board. The strain of BGA solder joints is not only a function of package material, but also a function of package size and standoff height. BGA ball size can have an impact on reliability.

At low strain amplitude application, SnAgCu seems as good as or outperform SnPb. For example, Syed [59] reported SnAgCu showed better performance in reliability than SnPb. He assembled both PBGA and flexXBGA packages on FR-4 board with OSP finish. Temperature cycling was from -55 to 125°C. Note that flexXBGA uses polyimide tape substrate, which has similar CTE as that of FR-4 board. Lau, et. al. [50] reported there were no solder joint failures on the lead-free balled flexBGA with both SnAgCu and SnPb solder pastes on all the Sn-Cu HASL, Ni-Au, and OSP PCBs during temperature cycles from 0 to 100°C for 6,000 cycles.

At high strain amplitude application, the reliability of SnAgCu seems poorer than SnPb. For example, Lau, et. al. [50] reported the test results for the Ceramic Column Grid Array (CCGA) packages with both SnAgCu and SnPb solder paste on PCBs with three finishes: Sn-Cu HASL, Ni-Au, and OSP. They found failures on all the three PCBs with SnAgCu, but no failures with SnPb solder paste.

Though no specific strain value was calculated and compared in published papers, it seems in general that the following conclusion is valid: the reliability of SnAgCu is similar to or better than SnPb at low strain amplitude applications and vice versa at high strain amplitude applications. Note that the conclusion is drawn from thermal fatigue modeling and experimental data.

Several researchers noticed that SnAgCu solder joints have higher pull or shear strength than SnPb before reliability tests. That is easy to understand because SnAgCu alloy has higher yield strength than SnPb.

The authors notice that the component metallization and PCB board metallization may not be as critical as solder alloy in fatigue failure mode. But the metallization may be more critical in fracture failure mode because it determines the intermetallic characteristic. For example, Arra, et. al. [49] compared mechanical performance of SnAuCu solder joint on QFP208 component with four finishes (Ni/Pd/Au, SnPb15, SnBi2, and Sn100) under the free fall drop test. The PCB finishes were immersion Ag and OSP. They found the intermetallic layer formed between Ni/Pd/Au finish and SnAgCu solder was brittle and resulted in failure earlier in the free fall drop test.

7. Transition to total lead-free manufacturing

There are three routes to convert tin-lead soldering to totally lead-free soldering as shown in Figure 5 [60]. Route A is desirable. However, some lead-free finish components may not be available at this time, so companies choose route B. For other companies that allow having lead (Pb) in their electronic equipment by 2010 granted by EU RoHS directive, route C is applicable.

To switch to lead-free manufacturing, some of surface mount assembly processes needs to be adjusted. Surface mount assembly includes solder paste stencil printing, pick and place, and solder reflow processes. Compared SnPb soldering with lead-free soldering, there is no significant difference in stencil printing and pick and place processes. The key response variable in the stencil printing process is the solder volume deposited. The stencil printing process is solder paste characterization dependant, not solder alloy dependant. But there are significant differences in solder reflow process. These differences include higher reflow temperature and poorer wetting in lead-free soldering. A new reflow profile with different time and temperature is needed for lead-free soldering. The high reflow temperature may damage sensitive components.

There are many issues in routes B and C transition. One of them is the void. More voids have been reported in the solder joints of BGA packages made with SnAgCu solder balled and SnPb solder paste [30] and made with SnPb solder balled and SnAgCu solder paste [61]. How the voids would affect the long-term solder joint reliability is unknown. It is necessary to establish the relationship between the void (including the size of void, the number of voids, and the location of voids) and long-term reliability. Smetana, et. al. [61] summarized other concerns over routes B and C.

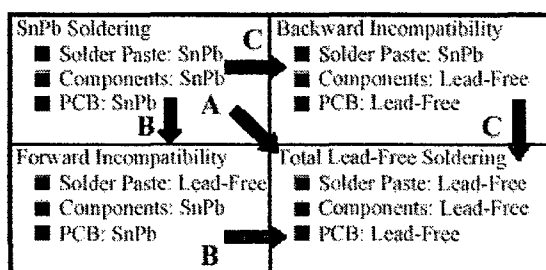


Figure 5. Transition to total lead-free

8. Summary

Electronics industry has identified lead-free solder alloy SnAgCu as possible alternates to eutectic SnPb37 solder, though an agreement on the exact composition has not been achieved.

The common lead-free component finishes include pure Sn, SnBi, SnCu, NiPdAu, and SnAgCu. At this time, the leading finish available for BGA and CSP packages is SnAgCu, and that for chip resistors is pure tin. Pure Sn, SnBi, SnCu, and NiPdAu are available to QFPs and SOPs, and NiPdAu may be favorable for these leadframe packages due to its whisker free characteristic. The leading PCB surface finishes are OSP, ENIG, Immersion Ag, Immersion Sn, and HASL SnCu.

SnAgCu solder joints are generally stronger than SnPb before reliability tests because SnAgCu alloy has higher yield strength than SnPb.

Reliability of SnAgCu is application specific. At low strain amplitude application, SnAgCu seems outperform SnPb. At high strain amplitude application, SnAgCu performance is poorer than SnPb.

Acknowledgment

This work was partially sponsored by the Department of the Navy, Office of Naval Research, under Award # N00014-04-1-0436. The authors would like to thank Dr. John Lau at Agilent, Kim Hyland and Dennis Willie at Soletron, for their valuable comments and suggestions.

References

- [1] Intel webpage <http://www.intel.com/research/silicon/leadfree.htm>
- [2] K. Gaffney, J. Poarch, and D. Delaney, "Lead-free flip chip process development," *Proceedings of 2000 Electronic Components and Technology Conference*, IEEE, pp. 129-133.
- [3] J. H. Lau and W. Dauksher, "Creep of Sn-(3.5-3.9)wt%Ag-(0.5-0.8)wt%Cu Lead-Free Solder," *Micromaterials and Nanomaterials*, Edited by B. Michel, Fraunhofer Institute, IZM, Berlin, 2004, pp. 54-62.
- [4] T. A. Woodrow, "Reliability and Leachate Testing of Lead-Free Solder Joints," *IPC Lead-Free Conference*, San Jose, CA, May 2002.
- [5] National Electronics Manufacturing Initiative (NEMI) webpage <http://www.nemi.org/>
- [6] National Center for Manufacturing Sciences (NCMS) webpage <http://www.ncms.org/>
- [7] High Density Packaging Users Group (HDPUG) webpage <http://www.hdpug.org/>
- [8] Massachusetts Toxics Use Reduction Institute (TURI) webpage <http://www.turi.org/>
- [9] Joint Group on Pollution Prevention (JGPP) webpage <http://www.igpp.com/>
- [10] Computer Aided Life Cycle Engineering (CALCE) webpage <http://www.calce.umd.edu/>
- [11] Tin Technology webpage <http://www.tintechnology.com/>

- [12] IPC lead-free webpage <http://www.leadfree.org/>
- [13] K. J. Puttlitz, "Handbook of Lead-Free Solder Technology for Microelectronic Assemblies," Edited by K. J. Puttlitz and K. A. Stalter, Marcel Dekker, Inc., New York, pp. 10, 2004.
- [14] T. Siewert, S. Liu, D. R. Smith, and J. C. Madeni, "Database for Solder Properties with Emphasis on New Lead-free Solders," NIST & Colorado School of Mines, Release 4.0, Feb. 2002, <http://www.boulder.nist.gov/div853/leadfree/solders.html>
- [15] E. Bradley, C. Handwerker, and J. E. Sohn, "NEMI Report: A Single Lead-Free Alloy is Recommended," *SMT*, January 2003.
- [16] S. Denda, "Lower Temp Lead-free Solder Needed," *Advancing Microelectronics*, IMAPS, pp. 35, Nov./Dec. 2003.
- [17] T. J. Singler, S. J. Meschter, and J. Spalik, "Soldering Wetting and Spreading," *Handbook of Lead-Free Solder Technology for Microelectronic Assemblies*, Edited by Karl J. Puttlitz and Kathleen A. Stalter, Marcel Dekker, Inc., New York, Chapter 11, pp. 331-429, 2004.
- [18] S. V. Sattiraju, et. al., "Wetting Characteristics of Pb-Free Solder Alloys and PWB Finishes," *IEEE Transactions on Electronics Packaging Manufacturing*, Vol. 25, No. 3, pp. 168-184, 2002.
- [19] J. Bath, "A Manufacturable Lead-Free Surface-Mount Process?" *Circuit Assembly*, pp. 26-30, January 2003.
- [20] CALCE EPSC, Component Suppliers' Survey, Available: <http://www.calce.umd.edu/lead-free/tin-whiskers/team/part-suppliers040519.xls>, May 19, 2004.
- [21] NASA Tin Whisker Website, <http://nepp.nasa.gov/whisker/>
- [22] Experimental results by GE Global Research Center and Soletron.
- [23] NEMI Tin Whisker User Group, "Interim Recommendation on Lead-Free Finishes for Components Used in High-Reliability Products", http://www.nemi.org/projects/ese/tin_whisker_usergroup.html, March 2004.
- [24] C. Doyle, N. Brown, and M. Bardizeh, "Factors Influencing the Solderability of Lead-Free Electrodeposits", *Metal Finishing*, January 2002.
- [25] C. Fan, Y. Zhong, and J.A. Abys, "Solderability of lead-free finishes using lead-free solders", *Proceedings of SMTA International Conference*, 9/30/2001, p 827.
- [26] M. Arra, "Aging Mechanisms of Immersion Tin and Silver PCB Surface Finishes in Lead-Free Solder Applications", *IPC/JEDEC 3rd International Lead-free Conference*, San Jose, CA, March 2003.
- [27] D. Ormerod, "Meeting Fine Pitch Assembly Needs with a Solderable Tin Finish", *IPC PCB Expo and APEX*, March 14-18, 1999.
- [28] M. Arra, D. Shangguan, J. Sundelin, T. Lepisto, E. Ristolainen, "Aging Mechanisms of Immersion Tin and Silver PCB Surface Finishes in Lead-Free Solder Applications," *IPC/JEDEC 3rd International Lead-free Conference*, San Jose, CA, March 2003.
- [29] NCMS Lead Free Solder Project Final Report, NCMS Report 0401RE96.
- [30] G. Echeverria, D. Santos, P. Chouta, and C. Shea, "Effect of Lead-Free Assembly Processing on Solder Joint Voiding", *IPC/JEDEC 5th International Lead-free Conference*, San Jose, CA, March, 2004.
- [31] K. Saeki and M. Carano, "Next Generation Organic Solderability Preservatives (OSP) for Lead-Free Soldering and Mixed Metal Finish PWB's and BGA Substrates," *IPC Printed Circuits Expo, APEX, and Designers Summit conference*, Anaheim, CA, 2004.
- [32] R. Schetty, "Lead-Free Finishes for Printed Circuit Boards and Components," *Handbook of Lead-Free Solder Technology for Microelectronic Assemblies*, Edited by Karl J. Puttlitz and Kathleen A. Stalter, Marcel Dekker, Inc., New York, Chapter 12, pp. 432-464, 2004.
- [33] M. Dusek, and C. Hunt, "Reliability Comparison of Lead-free Solder Joints Formed on Different PCB Finishes," *IPC/JEDEC 3rd International Lead-free Conference*, San Jose, CA, March 2003.
- [34] Y. Zheng, C. Hillman, P. McClusky, "Intermetallic Growth on PWBs Soldered with Sn3.8Ag0.7Cu", *Proceedings of the 52nd IEEE Electronic Components & Technology Conference*, pp. 1226-1231, San Diego, 2002.
- [35] Teledyne, "No-Lead and Horizontal Hot Air Leveling", Teledyne document HAL-NoLead-004, <http://www.tet-halco.com/library.asp>
- [36] Cemco, "Overview Report on a Lead Free Electronics Industry", Cemco report, 2001. <http://www.cemco.com/Brochures/LeadFreecomplete150301.pdf>
- [37] K. G. Snowdon, C. G. Tanner, and J. R. Thompson, "Lead Free Soldering Electronic Interconnect: Current Status and Future Developments", *2000 Electronic Components and Technology Conference*, IEEE, p1416-1419.
- [38] A.R. Zbrzezny, P. Snugovsky, and D.D. Perovic, "Reliability of Lead-free Chip Resistor Solder Joints Assembled on Boards with Different Finishes Using Different Reflow Cooling Rates", *IPC/JEDEC 5th International Lead-free Conference*, San Jose, CA, March, 2004.

- [39] D.W. Romm, D.C. Abbott, S. Grenney, and M. Khan, "Whisker Evaluation of Tin-Plated Logic Component Leads", Texas Instruments Application Report SZZA037A- February 2003; <http://focus.ti.com/lit/an/szza037a/szza037a.pdf>
- [40] Tin Whisker Acceptance Test Requirements, http://www.nemi.org/projects/ese/tin_whisker_usergroup.html
- [41] Y. Nakadaira, et. al., "Pb-free plating for peripheral/leadframe packages," *IEEE Proceedings EcoDesign 2001: 2nd International Symposium on Environmentally Conscious Design and Inverse Manufacturing*, 2001, pp. 213-218.
- [42] S. Tonapi, et. al., "Reliability of Lead-Free Solder Interconnects - A Review," *2002 Proceedings Annual Reliability and Maintainability Symposium*, IEEE, pp. 423-428.
- [43] F. A. Stam, and E. Davitt, "Effects of Thermo-mechanical Cycling on Lead and Lead-Free (SnPb and SnAgCu) Surface Mount Solder Joints," *Microelectronics Reliability*, Vol. 41, pp. 1815-1822, 2001.
- [44] J. H. Lau, et. al., "Creep Analysis and Thermal Fatigue Life Prediction of the Lead-Free Solder Sealing Ring of a Photonic Switch," *ASME Transactions, J. of Electronic Packaging*, vol. 124, December 2002, pp. 403-410.
- [45] J. H. Lau, D. Shangguan, D. Lau, T. Kung, and R. Lee, "Thermal-Fatigue Life Prediction Equation for Wafer-Level Chip Scale Package (WLCSP) Lead-Free Solder Joints on Lead-Free Printed Circuit Board (PCB)," *Proceedings of IEEE Electronic Components and Technology Conferences*, Las Vegas, May 2004, pp. 1563-1569.
- [46] P. Vianco, and J. Rejent, "Compression Deformation Response of 95.5Sn-3.9Ag-0.6Cu Solder," *UCLA Lead-Free Workshop*, October 2002.
- [47] J. H. Lau, et. al., "Lead-Free Wave-Soldering and Reliability of Light-Emitting Diode (LED) Display Assembly," *IPC First International Conference on Lead-Free Electronic "Towards Implementation of the RoHS Directive"*, Brussels, Belgium, June 10 - 12, 2003.
- [48] H. Tanaka, Y. Aoki, M. Kitagawa, and Y. Saito, "Reliability Testing and Failure Analysis of Lead-Free Solder Joints under Thermo-Mechanical Stress," *IPC Printed Circuits Expo, APEX, and Designers Summit conference*, Anaheim, CA, 2004.
- [49] M. Arra, T. Castello, D. Shangguan, and E. Ristolainen, "Characterization of Mechanical Performance of Sn/Ag/Cu Solder Joints with Different Component Lead Coatings," *SMTA International Conference*, 2004.
- [50] J. Lau, N. Hoo, R. Horsley, J. Smetana, D. Shangguan, W. Dauksher, D. Love, I. Menis, and B. Sullivan, "Reliability Testing and Data Analysis of Lead-Free Solder Joints for High-density Packages," *Soldering & Surface Mount Technology*, Vol. 16, No. 2, pp.46-68, 2004.
- [51] S. T. Nurmi, J. J. Sundelin, E.O. Ristolainen, and T. Lepisto, "The influence of multiple reflow cycles on solder joint voids for lead-free PBGAs," *Soldering & Surface Mount Technology*, Vol. 15, No. 1, 2003, pp. 31-38.
- [52] J.C. Suhling, H.S. Gale, R.W. Johnson, M.N. Islam, T. Shete, P. Lall, M.J. Bozack, J.L. Evans, P. Seto, T. Gupta, and J.R. Thompson, "Thermal Cycling Reliability of Lead-Free Chip Resistor Solder Joints," *Soldering & Surface Mount Technology*, Vol. 16, No. 2, pp. 77-87, 2004.
- [53] S. Shina, et. al., "Lead Free Conversion Analysis for Multiple PWB/Component Materials and Finishes using Quality and Reliability Testing," *IPC Printed Circuits Expo, APEX, and Designers Summit conference*, Anaheim, CA, 2004.
- [54] "Global Transition to Pb-Free/Green Electronics", AIA, May 2004. Available at http://www.calce.umd.edu/lead-free/calcePbfree_AIA.pdf
- [55] A. Mawer, "Plastic Ball Grid Array (PBGA)," Motorola report AN1231, Phoenix, AZ, 1996.
- [56] S. Lee and J. H. Lau, "Effect of Chip Dimension and Substrate Thickness on Plastic Ball Grid Array Solder Joint Reliability," *Proceedings of SMI Conference*, Sept. 1996.
- [57] J. H. Lau and Y. Pao, *Solder Joint Reliability of BGA, CSP, Flip Chip, and Fine Pitch SMT Assemblies*, Mc-Graw Hill, New York, 1997, Chapter 5.
- [58] D. Geiger, F. Mattsson, D. Shangguan, M. Ong, P. Wang, T. Castello, and S. Yi, "Process Characterization of PCB Assembly using 0201 Packages with Lead-Free Solder," *Soldering & Surface Mount Technology*, Vol. 15, No. 2, pp. 22-27, 2003.
- [59] A. Syed, "Reliability of Lead-Free Solder Connections for Area-Array Packages," *IPC SMEMA Council APEX conference*, 2001.
- [60] J. Lau and K. Liu, "Global Trends of Lead-Free Soldering," *Advanced Packaging*, Jan. 2004.
- [61] J. Smetana, R. Horsley, J. Lau, K. Snowdon, D. Shangguan, J. Gleason, I. Memis, D. Love, W. Dauksher, and B. Sullivan, "Design, Materials and Process for Lead-Free Assembly of High-density Packages," *Soldering & Surface Mount Technology*, Vol. 16, No. 1, pp.53-62, 2004.

**Development of a Micro System Actuator Employing Shape Memory Alloys for
Exploring the Nanotechnology World**

Project Investigator:

Richard N. Savage, Ph.D.
Associate Professor
Materials Engineering
Cal Poly State University

Development of a Micro System Actuator Employing Shape Memory Alloys for Exploring the Nanotechnology World

Summary

The goal of this project was to develop and characterize the process steps required to fabricate a micro actuator based on NiTi shape memory alloy thin films. Micro actuators are a key component of many micro systems, which are capable of detecting bio-hazardous agents, dispensing drugs to combat cancer or improving the success rate of inter-vascular surgery. Moreover, these sensors involve molecular and atomic interactions, which can enable students to explore design elements that bridge into the nanotechnology world.

The project consisted of three phases. The first phase involved designing a process for sputter deposition of NiTi and poly-silicon films onto silicon wafers. The second phase involved testing and characterization of the mechanical properties (stress, yield strength, adhesion, etc.), crystalline structure (x-ray diffraction) and elemental composition (SEM-EDS) of poly-silicon and NiTi thin films. The third phase involved the design and fabrication of test actuator devices using the Coventor MEMS CAD software funded by our industrial partner, Olympus. The first two phases (Design & Test) have been completed and significant progress has been made in the third phase (Implementation).

The **broader impact** of this project is evident in that it has served as a foundation for the formation of a cross-disciplinary Micro Systems Technology (MST) group at Cal Poly with students participating from Electrical Engineering, Materials Engineering and Biomedical Engineering. Two master thesis and four senior projects have been supported by this project. The MST group is also developing several joint undergraduate and graduate level projects between the Electrical Engineering and Materials Engineering departments at Cal Poly. In addition, our industrial partner Olympus has offered to support a summer internship at their Microfabrication Research & Development Center in Tokyo for a Cal Poly student during the summer of 2006. The PI has also secured equipment donations from MKS Instruments, Applied Materials and CLA-Val corporations who have supported the Microfabrication lab in the Materials Engineering department.

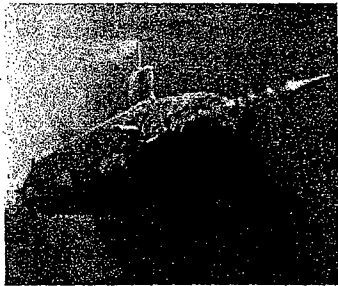
Relevance of the Project

The Technology of Micro Systems

These tiny machines are too small to be seen by the unaided eye but are having a huge impact on the way we live, work and play.¹ One of the first commercial applications of micro systems or micro electro mechanical systems (MEMS) was the airbag. It relies on a micro accelerometer to sense a car crash and signal the deployment of the airbag.

This technology also enabled the fabrication of thousands of micro-mirrors, which produce digital light processing (DLP) arrays; DLP chips are found in most all tabletop PC-projectors today. Recently, IBM has announced that ThinkPad® laptops will contain an

active protection system (APS) that detects if the computer is dropped and safely parks the hard drive to minimize data loss; this APS technology is also based on a MEMS accelerometer.² Inkjet printer heads contain MEMS devices and RF-MEMS devices play a key role in mobile phones, global positioning systems and smart missile targeting systems. Micro systems are found throughout many defense systems, which use MEMS-based digital inertial guidance devices, such as the Predator Missile program, shoulder fired anti-tank weapons and "smart" bombs.



(Note: Figure(s) are from ref.1)

Examples of micro systems are also spreading throughout the medical and health care fields. Pacemakers, retinal implants, hearing aids, blood pressure & glucose monitors for diabetics that require 1/3 the blood sample size as conventional macro instruments, all have MEMS components. Imagine machines so tiny that they can flow through the bloodstream, targeting cancer cells for elimination; you have now entered the nanotechnology world.

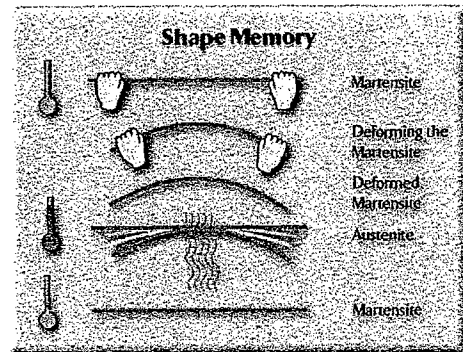
Multiple diseases can be screened with lab-on-a-chip devices that employ micro fluidic channels that are narrower than a human hair, but can quickly separate liquids and gases and allow micro sensors to analyze their properties. These micro sensors utilize thousands of cantilevers (imagine a device shaped like a small diving board) fabricated into detection arrays. Each cantilever is coated with a bio-film that selectively bonds to certain molecules that are associated with specific diseases. The cantilevers bend when the molecules are adsorbed onto their surface, producing a measurable change in their capacity to store electric charge, which can be measured by built-in electronic circuits. The entire device can be mass produced like memory computer chips and sold for a few dollars each making advanced diagnostics available to everyone at a reasonable cost.

Geneticists use these devices to conduct DNA and protein analysis on a chip the size of a dime and get results in 30 minutes, instead of days or weeks from a commercial lab. Soldiers will be able to detect airborne pathogens, such as chemical and biological weapons and instantly identify the threat before it reaches lethal concentrations.

NiTi Shape Memory Alloy Thin Films

Shape memory alloys (SMA) are metals that exhibit two very unique properties: pseudo-elasticity and the shaped memory effect. Ame Olander first observed these unusual properties in 1938 and they have been researched widely for use in many medical applications including vascular stents and endovascular microtools.³ An endovascular micro device consists of an active bending catheter (using SMA materials) and a micro drug infusion device for in-vivo patient testing and treatment.

The process for forming actuators made of SMA metals is as follows: 1) sputter deposit a 50/50 atomic weight percent NiTi thin film on silicon (it will be amorphous or non-crystalline), 2) anneal at a high temperature to form the austenite crystalline structure (rigid), 3) cool the alloy to room temperature and it will undergo a solid-state phase transformation to the martensite crystalline structure (which is relatively soft and ductile), 4) residual stress in the underlying poly-silicon layer will cause the film to deform and bend at room temperature, then 5) heat the film back up to about 100 °C and it will return to the original shape it had when annealed. This cycle can be used to produce actuators.



Actuators using these films demonstrate large force/mass ratios and induce high spatial displacements. This enables them to produce the highest work output of any actuator.⁴ NiTi SMA micro grippers have been fabricated that are capable of 8% recoverable strain and 500 MPa of recoverable stress; they have demonstrated a work density as high as $5 \times 10^7 \text{ J/M}^5$.

Applications to Nanotechnology

Nanotechnology involves materials at the nanometer level (1 billionth of a meter); imagine the thickness of a redwood tree compared to a human hair; that's the difference between a human hair and something one nanometer in size. A good concise definition of nanotechnology would be the creation and application of structures that are 1-100 nanometers or nm (10^{-9} meters) in size. This includes viruses (25nm), hemoglobin (7nm) carbon nanotubes (1.4nm) and a single strand of DNA (2.5nm); in fact, atoms are on the scale of 0.1 nm in diameter. It is beyond the scope of this project proposal to try to discuss all of the applications that fall under the term nanotechnology, but we will focus on some medical areas that intersect with micro systems.

Micro systems can be the platforms that enable scientists to explore biological systems at the molecular level. The study of self-replicating molecular machines is revolutionizing our approach to the detection and dispensing of biological agents. A micro fluidic pump in a MEMS device could deliver dendrimers (tree-like polymers similar to nylon) with cell hunting capabilities that would target and deliver chemical treatments at the molecular level. At 2.5nm, a strand of DNA is about the same size as a carbon nanotube; biochemists may want to take advantage of the similarity of scale and attach therapeutic molecules onto the carrier nanotubes and "program" them to interact with specific cells (e.g. cancerous cells).



Summary of Project Results

The goal of this project was to develop and characterize the process steps required to fabricate a micro actuator based on NiTi shape-memory alloy thin films. The roadmap for the project consisted of three phases (1-Design, 2-Test & 3-Implementation); the first two phases have been completed and the ground-work for the third phase has been laid. To date, the project has completed all of the planned tasks within the assigned budget and the results have been presented at both MRS and ASEE technical society meetings. A strong industrial partnership has been established with Olympus and a summer internship has been approved at their Microfabrication Research & Development Center in Tokyo for a Cal Poly student during the summer of 2006.

Phase 1 – Design

Develop process for sputter deposition of NiTi thin films onto silicon wafers

Through funds provided for the expansion of the Cal Poly Materials Engineering Microfabrication laboratory, an RF&DC powered sputtering system with high temperature vacuum annealing capabilities was procured. Utilizing this system, a process sequence has been established for depositing NiTi on silicon using chromium as an adhesion layer and encapsulant to prevent oxidation of the Ti on the surface, which has been shown to reduce shape-memory performance. The process provides for depositing atomically equal NiTi thin films on <100> silicon wafers by co-sputtering from NiTi and Ti targets at 250 and 75 watts of DC power, respectively. These power settings yielded a deposition rate of 12 angstroms per second and the film stoichiometry was confirmed by SEM-EDS. Pre-sputtering the NiTi and Ti targets effectively cleaned their surfaces and reduced the sputtering systems base pressure to 10^{-7} torr, thereby minimizing the oxygen content of the NiTi films, which is also crucial for shape-memory behavior. It was determined that a 100 nm chromium layer provided excellent adhesion between NiTi layers and silicon. Preliminary investigations into the impact of annealing temperatures on the NiTi film's crystalline structure through x-ray diffraction measurements have been started. In addition, a process for depositing poly-silicon thin films by RF sputtering was developed and the stresses in the as deposited films have been characterized. These results provide the foundation for the design of an actuator.

Phase 2 – Test

Characterize the shape-memory behavior and properties of the NiTi films and formulate a process for fabricating an actuator

In order to complete the next phase of the project, two properties of blank NiTi films were measured on silicon wafers; 1) the force displacement curves for both the martensite and austenite phases (characteristic for shape-memory performance) and 2) the stresses in the thin films. Techniques for measuring both the thickness and stresses within the NiTi and poly-silicon films before and after annealing were developed. It was determined that the NiTi films contain a compressive stress that increase with Ti sputtering target power from

200 \pm 45 MPa to 262 \pm 57 MPa. The poly-silicon films yielded the highest compressive stresses at high Ar pressure and RF power at around 1092 \pm 385 MPa with a 95% confidence interval.

Through funds provided by the project's industrial partner (Olympus), a license for Coventor's MEMS design software was obtained. Utilizing the data provided by the test results and the CAD modeling routines from Coventor, a process sequence and photolithography mask was designed to create test structures. These structures are currently being fabricated and will enable fundamental material properties such as modulus of elasticity, yield strength and tensile strength to be determined for the thin films.

Phase 3 – Implementation

Fabricate a test actuator device

The completion of data collection from the test structures is underway. This will enable a micro actuator to be fabricated and characterized. The design of a process for fabricating an actuator utilizing dual layers of NiTi over poly-silicon will be completed during the extension of the project. As the NiTi layer is thermally cycled through its phase transformation temperature, the residual stresses in the poly-silicon film should cause the cantilever-shaped actuator to deflect. Final testing and characterization of the actuator's performance will be completed at the Olympus research facility during the summer of 2006, where they have an extensive testing facility for measuring actuator deflection characteristics.

Industrial Partnerships & Support

The primary industrial sponsor of this project has been Olympus. They produce medical diagnostic equipment, which employs micro-tactile sensors that utilize active bending with SMA materials to assist physicians and prevent damage to blood vessel walls during surgery.⁶ Olympus has established a Partnership Development Group in San Jose, CA that is connected to their MEMS Technology Division. The PI served as the Chief Technical Officer for Olympus Integrated Technology of America and was involved with the Partnership Development Group. He participated in the establishment of several MEMS research partnership programs in the United States.

An *Industrial Steering Committee* has been formed with the following members: Richard Tauber, Ph.D. Materials Science (over 37 years experience in semiconductor industry & co-authored a textbook entitled "Silicon Processing for the VLSI Era- Process Technology"), John Felts, President & CEO of NanoScale Surface Systems and Larry Wang, Vice President, Olympus Partnership Development Group. These individuals have extensive experience in the micro systems and nanotechnology.

In addition, the PI has also secured *equipment donations* from MKS Instruments, Applied Materials and CLA-Val corporations who have supported the Microfabrication lab in the Materials Engineering department. The donated components have a commercial value of approximately \$75,000 and have been used throughout this project.

The Broader Impact of the Proposed Work

By equipping undergraduate engineering students with the cross-disciplinary tools required to complete this project, they have been enabled to participate in the emerging micro and nano technology-based industries. As students practice engineering in the coming decades, they must be equipped to: 1) understand the impact of scaling on material properties and engineering principles, 2) approach engineering from a systems perspective emphasizing holistic thinking and 3) understand the interdisciplinary nature of micro & nano technologies and 4) apply critical thinking and problem solving skills.

Our goal is to integrate the microfabrication experiences gained from this project into several cross-disciplinary courses being offered at Cal Poly including MATE550 – Micro Systems and Nano Technology and a new course on Nanotechnology in Living Systems⁷ that is being co-developed by faculty from Biology, Physics, Electrical and Materials Engineering. This will broaden student's knowledge of the application of microfabrication techniques beyond just microelectronic devices and provide them with a foundation for engineering micro systems to explore the nanotechnology world of their future. Moreover, with the recent decline in US high-technology graduates and the growing need for interdisciplinary expertise, it is imperative that Cal Poly develops an educational curriculum that will attract and prepare students to participate in the dynamic fields of micro systems and nanotechnology.⁸

This project has enabled the establishment of a Micro Systems Technology (MST) group in Materials Engineering at Cal Poly. To date this project has supported two masters' thesis students and four undergraduate senior projects.⁹⁻¹² Results from this work were presented at the Spring 2005 Materials Research Society Conference¹³ and in part at the recent ASEE Pacific Southwest Conference on Nanotechnology & Preparing Engineers for 2020.¹⁴ A proposal has been submitted to the NSF¹⁵ for a grant to develop a graduate-level MST course that will include some of the microfabrication techniques developed during this project. Some of the photolithography techniques that were developed under this project have also benefited the MATE435 microfabrication-processing course.

References

1. Small Tech 101 – An Introduction to Micro and Nanotechnology, SmallTimes Media Inc. www.smalltimes.com/products
2. SmallTimes: Big News in Small Tech, SmallTimes Media, LLC, Vol 3, No 7, Nov/Dec 2003
3. J. Chang, et.al., "Development of Endovascular Microtools", Journal of Micromechanics and Microengineering, 12, 2002, pgs 824-831
4. P. Krulevitch, et.al., "Thin Film Shape Memory Alloy Microactuators", Journal MEMS, Vol. 5, No.4, 1996, pgs 270-282
5. W. Huang, et.al. "Design, Testing and Simulation of NiTi Shape-memory-alloy Thin-film Based Microgrippers", J. Microlithography, Microfabrication and Microsystems, VI.2, No.3, July 2003, pgs 185-190
6. The Olympus Pursuit, Cover Story: Think Small, Vol. 18, No. 2, 1999

7. NSF Proposal#0532464 for NSF Grant 05-543, "Nanotechnology, Human Biology, Ethics and Society," submitted 4/6/05
8. R.N. Savage & L. Vanasupa, "How Are Universities Preparing Undergraduates for a Nanotechnology World: A Perspective from Cal Poly," Invited talk at Northrop Grumman Technology Symposium, 2/28/2004
9. R. Hosler, "Characterization of Sputter-Deposited NiTi Thin Films Capable of Powering MEMS Devices," Senior Project Report, Materials Engineering, Cal Poly State University, June 2004
10. G. Rom, "Design and Characterization of Sputter-Deposited NiTi Thin Films for MEMS Actuation," Senior Project Report, Materials Engineering, Cal Poly State University, June 2004
11. A. Adams, "Characterization of Polysilicon Thin Films Deposited by Physical Vapor Deposition," Senior Project Report, Materials Engineering, Cal Poly State University, June 2005
12. O. Acton, "Developing Micro System Actuators: Residual Stress and Composition in Co-Sputtered Amorphous Thin Films," Senior Project Report, Materials Engineering, Cal Poly State University, June 2005
13. D. Getchel & R.N. Savage, "Characterization of Structural and Mechanical Properties of NiTi Shape Memory Thin-films for Micro Actuators," MRS Spring Conference, April 2005
14. R.N. Savage, "Micro Systems for Exploring the Nanotechnology World," ASEE-PSW Conference 2005 – Vision of Engineering in Year 2020, Loyola Marymount University, Los Angeles, CA, April 2005
15. NSF Proposal# 0535629 for NSF05-559 CCLI-Phase1: Exploratory, "Micro Systems for Exploring the Nanotechnology World," submitted 5/17/05

Characterization of Structural and Mechanical Properties of NiTi Shape Memory Thin Films for Micro Actuators

David J. Getchel and Richard N. Savage, Ph.D.

Materials Engineering Department, California Polytechnic State University,
San Luis Obispo, CA 93407, U.S.A.

ABSTRACT

Microactuators fabricated with NiTi thin films take advantage of this material's large energy density ($\sim 5\text{-}10\text{ joules/cm}^3$) and high strain recovery ($\sim 8\%$). Microelectromechanical Systems (MEMS) devices designed with these actuators can serve as biosensors, micro-fluidic pumps or optical switches. However, the fundamental mechanical properties stemming from the crystalline structure of these shape memory NiTi films have not been fully characterized with MEMS scale test structures. Understanding the relationship of crystalline structure, film stoichiometry, and phase transformation temperatures is crucial when designing a MEMS actuator. In addition, force displacement curves for both the martensite and austenite phases of NiTi are necessary to know how an actuator will perform.

Atomically equal NiTi thin films were deposited on $\langle 100 \rangle$ silicon wafers by co-sputtering a NiTi and a Ti target at 250W and 75W respectively. These power settings yielded a deposition rate of 12 angstroms per second. Pre-sputtering the NiTi and Ti targets effectively reduced the base pressure and cleaned the target surfaces, which made oxygen undetectable in the films. A 100 nm chromium layer provided excellent adhesion to Si, but poor adhesion to SiO_2 . The films will eventually be used in a cantilever test structure in conjunction with a surface profilometer to measure their mechanical and actuation properties.

INTRODUCTION

The unique shape memory effect (SME) of NiTi films has distinct advantages over traditional actuators when large range of motion and large actuation forces are required [1]. The realization of NiTi actuators requires performance data from test structures that are similar in size to current MEMS devices. Current bulge and diaphragm NiTi test structures provide useful information about film properties, but they are not scale MEMS actuators [2]. NiTi test structures with dimensions similar to today's MEMS structures will test factors such as surface oxides or compositional variation in thickness [3]. Designing, creating, and testing a series of MEMS scale NiTi test structures to examine size effects motivated this study.

An ideal NiTi test structure would use scanning probe microscopy (SPM) instruments to deflect miniature cantilevers etched from thin films. Small cantilevers have been tested with a nanoindenter [4]. Nanoindenters are ideal for force and displacement data from cantilever because they are capable of measuring both tip displacement and tip force continuously during a measurement. Triangular cantilevers with optimized strain profiles [5] and pure tensile fixed beams [6] have also been fabricated for nanoindenter testing. A profilometer is a less expensive alternative with comparable displacement measurement precision. In general, a profilometer is capable of measuring stylus displacement at fixed tip forces. Force displacement measurements of Ni films over silicon trenches have already been taken with a profilometer [7]. NiTi

cantilevers have been made and tested with tiny weights [8], but they were made with very thick trolled sheet (50-95 microns). Small cantilevers, or fixed beams, have provided useful information about various thins films, and could do the same for NiTi thin films.

A prerequisite of a NiTi test structure is quality films with ideal shape memory behavior. Therefore, it is necessary to create atomically equal NiTi thin films. The following experimental procedures describe how DC magnetron sputtering was used to create NiTi thin films that can be used in a MEMS test structure.

EXPERIMENTAL DETAILS

NiTi thin films were deposited with DC magnetron co-sputtering onto room temperature <100> direction 100 mm silicon wafers and subsequently heated in-situ with a non-contact substrate heater. Dual independently controlled 2" diameter targets of 50 at. % Ni, 50 at. % Ti, and pure Ti were chosen to create atomically equal NiTi thin films. Sputtering the pure titanium target buffers the film's composition due to the reactive nature of titanium with oxygen. The substrate is located approximately 10 cm from each sputtering target, and was rotated at 8 rpm during deposition to increase compositional uniformity. Pre-sputtering both targets at 100W for 30 minutes with a shutter covering the substrate removed surface oxidation from the targets. Pre-sputtering the Ti target also acts as a sputter-ion pump, and reduced the system base pressure below 2×10^{-7} Torr. The wafers were cleaned with a piranha etch (9:1, H_2SO_4 : H_2O_2 mixture by volume, at 70°C for 10 minutes), and stripped of there native oxide in a buffered oxide etchant for 1 minute at 25°C. A 100 nm chromium film on top of the clean silicon served as an adhesion promoter and a diffusion barrier. Energy dispersive x-ray spectroscopy (EDS) analysis with pure metal calibration standards verified a sputtering power combination of 250W to the NiTi target and 75W to the pure Ti target at 3.5mTorr argon (99.999%) created atomically equal NiTi films. Profilometer measurements of a film step height showed the deposition rate to be approximately 12Å per second. Temperature lacquer (OMEGALAQ) indicated the substrate reaches temperatures above 550°C when the substrate heater is set to 600°C.

DISCUSSION

The deposition process creates atomically equal NiTi thin films at a reasonable deposition rate. Table I. List the values for Ti-rich and Ni-rich thin films and the power settings. The Ti power settings vs. measured film stoichiometry allows for precise composition control because

Table I. NiTi thin film composition measurements at different Ti target power settings

NiTi Power (W)	Ti Power (W)	At. % Ti	At. % Ni
250	50	48	52
250	75	50	50
250	100	52	48

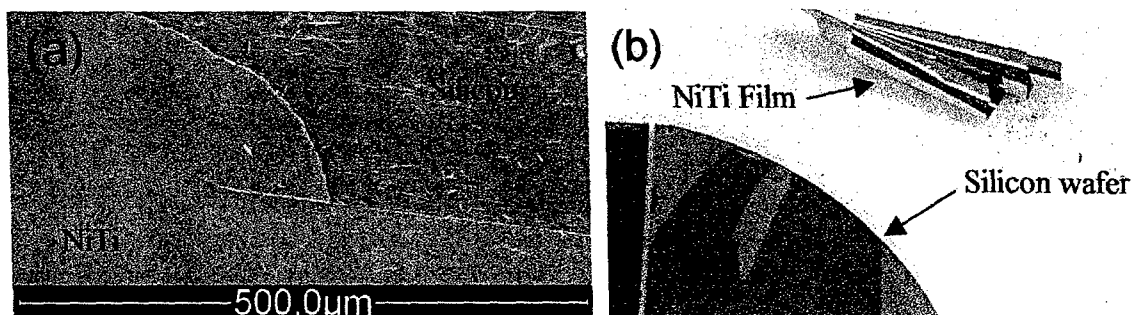


Figure 1. (a) The Cr adhesion layer between the NiTi thin film and silicon substrate was strong enough to remove some of the wafer surface NiTi on an oxidized silicon wafer (b) showed very poor adhesion, which allowed the film to peel off completely.

a variation in titanium composition of two atomic percent requires a large shift of plus or minus 25 watts to the titanium target. The NiTi film adhesion to silicon and Cr is excellent. Figure 1(a), shows the silicon surface after removing the NiTi/Cr film. The excellent adhesion between the NiTi/Cr and silicon was strong enough to remove silicon. Figure 1(b) shows how the poor adhesion between NiTi/Cr and SiO_2 allowed easy removal of the film.

Future experimental work will include shape memory evaluation of the thin films with differential scanning calorimetry (DSC), x-ray diffraction (XRD) and cantilever test structures. DSC analysis will determine the start and finish transition temperature for each crystalline phase. Grazing incidence XRD in conjunction with a temperature stage allows the identification of each NiTi crystal structure as a function of temperature. Finally, test structures will yield the power capabilities of tiny NiTi actuators. Combining all three techniques will give a solid foundation to design NiTi actuators.

CONCLUSIONS

Co-sputtering of NiTi thin films with excellent deposition rate is possible with the current system geometry and sputtering power. Substrate shielding is necessary to depositing pure films. The native oxide on silicon substrate must be removed to ensure good adhesion for subsequent test structure fabrication.

ACKNOWLEDGEMENTS

This work was supported by the Department of the Navy, Office of Naval Research ONR Grant# N00014-04-1-0436.

REFERENCES

1. P. Krulevitch, A. Lee, P. Ramsey, J. Trevino, J. Hamilton, M. Northrup, J. MEMS. Vol. 5 No. 4, 274 (1996)
2. Y. Fu, H. Du, W. Huang, S. Zhang, M. Hu, Sen. & Act. A 112, 397 (2004)
3. A. Ishida, M. Sato, Acta Materialia 51, 5578 (2003)
4. D. Son, J. Jeong, D. Kwon, Thin Solid Films 437, 183 (2003)

5. J. Florando, W. Nix, J. Mech. and Phys. of Solids **53**, 621 (2005)
6. H. Espinosa, B. Prorok, M. Fischer, J. Mech. and Phys. of Solids **51**, 49 (2003)
7. J. Luo, A. Flewitta, S. Spearingb, N. Flecka, W. Milnea, Mate. Lett. **58**, 2307 (2004)
8. M. Kohl, D. Allen, T. Chen, S. Miyazaki, M. Schwörer, Mat. Sci. & Eng. A **270**, 146 (1999)

American Society for Engineering Education

Pacific Southwest Regional Conference

April 7- 8, 2005

Conference Theme: Vision of Engineering Education @ Year 2020

Paper PSW.05-28

Micro Systems for Exploring the Nanotechnology World

**Richard N. Savage, Ph.D.
Cal Poly State University
Materials Engineering
San Luis Obispo, CA 93407 USA**

Abstract

As we prepare students to practice engineering in the coming decades they must be equipped to 1) understand engineering at the nanometer level, 2) approach engineering from a systems perspective and 3) understand the interdisciplinary nature of technology. The study of micro systems can be a perfect forum to accomplish these goals.

Micro systems have been developed for a wider range of applications including accelerometers, digital light processing, RF communications, retinal implants, glucose monitors and DNA analysis. They involve the fabrication of MEMS devices that can be utilized to explore molecular and atomic level reactions. Moreover, the processes employed to fabricate these microscopic devices can be extracted directly from those developed to create micro electronic circuits. As a result, these devices can be produced with affordable material processing equipment that can fit into an undergraduate laboratory environment. Micro cantilever structures are a key component of many micro systems. They can be designed for micro fluidic pumps or to direct light paths for optical switches. By coating the cantilevers with thin films designed to respond to specific organic compounds, they can perform as highly sensitive biological sensors. Micro cantilevers structures can serve as platforms for exploring the behavior of materials at the nanometer level. This paper will explore the approaches being adapted into our curriculum that will enable undergraduate engineers to be prepared to participate in the coming nanotechnology era.

Educating Nano Engineers

Nanotechnology will certainly be a driving force in our society by 2020. Technology has been steadily moving into the micro and nano scale realms since the turn of the century. Today, microelectronic microprocessors and memory devices are manufactured with active components that are less than 100 nm in size. [11] The impact of micro and nano scale technologies on traditional engineering disciplines will lead to revolutionary changes in new product designs. Micro systems are rapidly becoming apart of our everyday lives and nano materials are enabling revolutionary new products like electronic paper, cochlear and retinal implants, portable detectors for chemical and biological agents (e.g. anthrax), self cleaning windows, scratch resistant optical coatings, stain resistant coatings for clothes, and molecular electronics. Molecular tool kits for targeted drug delivery along with lab-on-a-chip devices are having a big impact in the pharmacogenomics field, which enable doctors to tailor medical treatments to a person's individual genetic makeup. [6]

In the United States the National Nanotechnology Initiative [12] has been launched and a network of nanotechnology research centers have been established. NSF, DOD, NIH, etc. are funding graduate research programs and the investment community is supporting a number of startup companies aimed at transferring nanotechnology directly into new products as quickly as possible. This seems to be following the same path that microelectronics blazed in the 1970's and 80's but some of the same pitfalls may force history to repeat itself. For example, there is not much funding being directed at developing undergraduate programs that will train the vast majority of the applied engineers required to support the development and manufacturing of these new nanotech products. This could further exacerbate the problem of outsourcing of high tech jobs from the United States and lead to a serious shortage of adequately trained undergraduate engineers required to support a US based nanotechnology industrial infrastructure. It is imperative that our undergraduate engineering curriculums be modified to meet the nano challenges of the coming decades.

So how do we prepare and enable undergraduate engineers to be ready to practice engineering at the nano scale?

They must of course have a solid foundation in the traditional principles of science, math and engineering, but these principles must focus on the behavior of materials at the nano or atomic level. Atoms and molecules don't always obey the classical laws of physics and instead we enter the quantum zone where the wave-particle duality of nature exists. At this scale mass is so small that gravity is not typically a controlling factor; secondary van der Waals forces can become dominant.

Moreover, engineers must understand the processes required to synthesize structures at atomic and molecular levels. They must be able to approach engineering from a systems perspective and recognize the value of integrating science and engineering throughout the design process. The inter-disciplinary nature of nanotechnology applications require that bioengineering, surface chemistry, solid state physics, photonics, micro fluidics and micro electronics, all be utilized to realize a successful design solution. It is also imperative that we pay attention to the impact that nanotechnology might have on our environment and make sure our efforts as engineers serves to benefit society and not to destroy it.

Micro Systems

Micro systems will probably be engineered as commercial products first and in many cases will serve as the platforms for launching next generation nanotechnology based products. Micro systems are easier to fabricate and require much less expensive material processing equipment, which has been adapted from the microelectronics industry. Such systems are often referred to as Micro-electro-mechanical systems or MEMS devices. They have been designed for a wide range of applications including air bag sensors, digital light projection, RF communications and glucose monitors.

Micro systems typically contain sensors, actuators and some form of logic control. The sensors often detect physical parameters like temperature, pressure or acceleration as well as chemical and optical parameters. Actuators can serve as either sensors or they can perform mechanical or electrical work like dispensing fluids, aligning optical components or forming micro motors. The control logic often employs standard microelectronic circuitry for both analog and digital signal processing. To fabricate entirely autonomous systems, an energy source is also needed which has been a major challenge in the design of micro system. However, recent work at Washington State University on micro thermal powered energy source [5] may provide a solution to this problem and allow for self-powered micro sensor devices. In addition, nano materials are enabling engineers to build micro scale lithium-ion batteries, hydrogen fuel cells and organic polymer based solar cells that can also lead to self-powered renewable energy sources for micro systems.

Actuators and Nano Sensing

Micro systems can serve as an excellent foundation for learning the principles of miniaturization. A key component of many micro systems are actuators. They are often formed in the shape of small diving boards called cantilevers. Cantilever based sensors usually involve measurements of nano scale deflections or nano mechanical resonances. The general idea is that physical, chemical or biological stimuli can affect the behavior of a cantilever in such a way that the resulting change can be measured using optical, electronic or other methods. [7] The measured change in the cantilever can be produced by changes in deformation (static) or resonance frequency of oscillation (dynamic). Although extremely small, cantilevers can be easily micro machined into silicon and other materials. By themselves, they have no intrinsic chemical selectivity. They can only achieve chemical selectivity if they are coated with a thin film composed of a polymer, self-assembled monolayer, antibodies or peptides. Once coated the cantilevers have selective adsorption properties and they can detect a variety of chemical species such as bio-toxins, volatile organic compounds and toxic industrial compounds.

Simplicity, low power consumption, cost effectiveness and the ability to be patterned into arrays make cantilever sensors very practical for a variety of applications. Chemical micro sensors based on ion sensitive field effect transistors can measure the pH [1,2] of solutions. Real-time detection of vapor phase nitroaromatic explosive compounds (TNT & 2,4-DNT) with a LOD of 520 ppt [10] limit of detection have been designed for forensics and anti-

terrorism applications. Bio-chips employing cantilevers have been designed that physically manipulated and detect DNA as it passes through nanopores [3] or by strain induced bending of micro cantilevers as DNA hybridizes on their surfaces [4]. Changes in intrinsic stresses in the cantilever due to mass-loading are developed during interfacial adsorption processes. Cantilevers operating in the dynamic mode are essentially mechanical oscillators and their resonance characteristics depend on the mass attached to their surfaces. The adsorption of analyte molecules changes the mass and hence the resonant frequency, which can be detected by, changes in electromagnetic fields, capacitance or optically deflected signals. These structures have been able to detect changes in mass at the femto (10^{-15}) and atto (10^{-18}) gram levels. [8]. Researchers at Cornell have been able to detect a single *E. coli* bacterium weighing about 665 femto grams using tiny cantilevers made of silicon and silicon nitride that were 4 microns long and 500 nanometers wide; these cantilevers vibrate at radio frequencies in the 1 to 15 megahertz range. Their deflections are measured by hitting them with laser light and observing the changes in reflected light intensity. They have reported that this technique can be extended to measure viruses in the atto gram range. [9]

Micro Systems at Cal Poly

Micro systems can serve as ideal platforms for exploring the nano technology world. Studying their design and characterizing their behavior can provide undergraduate engineers with the opportunity to practice engineering at the micro and nano scales. Currently, our curriculum includes courses on microelectronic processing which can readily be adapted to include micro fabrication techniques for actuators. These courses provide a foundation for material processing techniques such as diffusion, oxidation, photolithography, thin-film deposition and etching. They also introduce students to measurement or metrology techniques like profilometry, electron beam microscopy, x-ray diffraction and optical ellipsometry.

In addition, we are developing a Micro Systems Technology course that will include the educational processes discussed in this paper for learning micro and nano technologies. We have developed a basic process for fabricating micro actuators based on NiTi shape memory alloy (SMA) thin films. There are several senior design projects and masters thesis focused on characterizing the behavior of these materials and their application to micro cantilever structures. SMA based cantilevers function by changing their temperature over a small range, whereby the alloy undergoes a phase transformation from martensite (20 °C) to austenite (100 °C). The cantilever is fabricated with a highly stressed poly-Si film over a SMA NiTi film. As the material undergoes the phase transformation it changes from a ductile state that is bent under the influence of the poly-Si layer to a rigid state that will overcome the stresses in the poly-Si film and return to its original annealed shape. SMA materials can exert a very high force (6 J/cm^3) for their mass but have a low efficiency for converting electrical energy into motion (30 msec time response). The shape memory effect has primarily been studied in bulk materials but there is evidence that SMA nano structures also exhibit the same general behavior.

Conclusions

As technology advances at an ever increasing rate in the 21st century it is imperative that engineers be trained to adapt to changing business environments, think creatively and appreciate the global impact of their efforts. Nanotechnology is truly interdisciplinary in its foundations and will require an interdisciplinary approach to solving problems based on the integration of atomic physics, molecular biochemistry, mechanical, electrical and biomedical engineering along with information systems. At Cal Poly we are adapting a top down approach to learning in our Materials Engineering curriculum. Students are exposed to design problems first and then derive a fishbone diagram that breaks the problem down into detailed technical topics and fundamental principles that must be understood in order to develop a design solution. Through interactive learning exercises students are recognizing that design is basically the integration of science and engineering to solve a problem or create a device according to a plan. We are employing a team teaching format that blends laboratory experiences with lectures and promotes a holistic level of thinking that will be the trademark of the next generation nano engineer.

Biographical Information

References

1. Madou and Morrison, Chemical Sensing with Solid State Devices, Academic Press, Boston, 1989.
2. Bergveld, "Thirty years of ISFETOLOGY", Sensors and Actuators, B: Chemical, Vol. 88, Number 1, 2003, pp1-19.
3. Jiali, et. al., "Ion-beam Sculpting at Nanometer Length Scales", Nature, 412 (6843), 2001, pp166-169.
4. Britton, et. al., "Multiple-input Microcantilever Sensors, » Ultramicroscopy, Vol. 82, 2000, pp 17-21
5. Bahr, et.al., "Electro-Mechanical Coupling And Power Generation In A PZT Micro-Engine," Proceedings of the Materials Research Society, Materials Science of Microelectromechanical Systems (MEMS) Devices IV, vol. 687, 2002, pp 4.3.1-6
6. Forman, "An Overview of Nanotechnology, MEMS and Microsystems," Smalltimes Small Tech 101, 2003, p2
7. Lavrik, "Microsensors, Macrosensitivity," SPIE's oemagezine, February, 2005, pp 22-24
8. Lavrik, Applied Physics Letters, Vol. 82, 2003, p 2697
9. Nanotechnology Now, <http://nanotech-now.com/Cornell-release-04022004.htm>
10. Datskos, Lavrik and Sepaniak, "Detection of Explosive Compounds with the Use of Microcantilevers with Nanoporous Coatings," Sensor Letters, Vol. 1, No. 1, 2003, pp25-31
11. International Technology Roadmap for Semiconductors 2004, <http://public.itrs.net>
12. National Nanotechnology Institute, www.nsf.gov/nano

Biomechanical 'Leg-form' for Pedestrian Impact Tests

Project Investigator:

Peter Schuster
Assistant Professor
Mechanical Engineering Department

C3RP Final Project Report

Biomechanical 'Leg-form' for Pedestrian Impact Tests

Peter Schuster

Mechanical Engineering Department
Cal Poly State University

Abstract

This report summarizes the work completed in this research effort initiated under funding provided by the California Central Coast Research Partnership (C3RP). The goal of this work was the development of a new test device for injury prediction in pedestrian impacts. The project fully met its stated goals. The work consisted of a literature search, design development, materials procurement, leg-form assembly, and testing. The design selected expands upon the latest design trends incorporated in the prototype pedestrian leg-form being developed by the Japanese Automobile Research Institute (JARI). This report provides information on the design, the manufacturing process, the testing, and the next tasks to be performed with the new leg-form.

Beyond the development of the new pedestrian leg-form, there have been several additional key benefits of this project. The new leg-form has been designed and built primarily by a mechanical engineering graduate student, John Davis, with support from a number of undergraduate students. As a result, this project has contributed directly to the education of four mechanical and one manufacturing engineering students. In addition, the development of the device has enabled on-going interactions with industrial partners, which will lead to final impact testing of the system in Detroit. Finally, in addition to the stated goal, the device developed in this research project has been designed to enable prediction of injuries resulting from a variety of impact events (specifically sporting or occupational injuries). This opens a new direction for the next phase of the research.

Introduction

Pedestrian injury accidents are a serious problem globally. In industrialized nations, pedestrians represent 12-25% of all moderate-to-severe traffic injuries, although only 2-4% of minor traffic injuries¹. This means a pedestrian is much more likely to be killed or injured in an impact than a vehicle occupant. In the U.S., 88% of pedestrian accidents result in an injury, versus only 33% of vehicle accidents². This situation is more critical in developing nations, where pedestrians can represent more than half of all traffic casualties.

Lower limb trauma, while rarely fatal, is the most common type of injury resulting from an impact between a pedestrian and a motor vehicle³. Between 60% and 90% of pedestrian accident victims suffer some type of lower limb injury⁴. In pedestrian accidents, the most common lower limb injuries are tibia and femur shaft fractures, followed by knee joint trauma. While simple fractures of the long bones are not typically considered severe injuries, they always present the risk of complex or comminuted fractures and more serious injuries to the blood vessels and nerves in the lower limb. Knee joint injuries require long recovery times or may result in permanent disability. Fractures to the articular bone surfaces, even when healed, typically result in reduced joint motion. Ligament ruptures often cannot be fully repaired or replaced, resulting in some permanent loss of strength. Even soft tissue injuries such as cartilage or meniscus damage can have long-term repercussions, such as degenerative arthritis.

To address these concerns, government-mandated testing of vehicle performance in simulated pedestrian impacts is being conducted in Europe and Japan^{5,6,7}. As a result, major vehicle manufacturers are planning to implement 'pedestrian protection' features on future vehicles. One of the challenges they face is the development of a 'pedestrian-friendly' bumper system that maintains existing performance levels while not degrading styling or packaging. Although manufacturers have been working on pedestrian bumper systems for years and different design concepts have been proposed to meet the pedestrian requirements, these concepts all involve either a compromise in performance, or an increase in bumper packaging, or both.

In July 2002, in recognition of the risk to pedestrians in an impact with a motor vehicle, a 'Negotiated Agreement' was reached between the European Commission and the major automobile manufacturers on the subject of pedestrian protection. As part of this agreement, the major manufacturers committed (in part) that:

- Step I: (July 2005) – meet a minimal set of pedestrian impact criteria.
- Step II: (July 2010) – meet more stringent pedestrian impact criteria. Over the next few years, industry and government will fund research to define the Step II requirements.

¹ EEVC, "Pedestrian Injury Accidents." 9th Conference on Experimental Safety Vehicles, pp. 638-671, 1982.

² *Traffic Safety Facts 1998*, U.S. Department of Transportation, NHTSA, 2000

³ Mizuno K and Kajzer J, "Head Injuries in Vehicle-Pedestrian Impact." SAE Paper # 2000-01-0157, 2000.

⁴ Isenberg RA, Walz M, Chidester C, Kaufman R, "Pedestrian Crash Data Study—an Interim Evaluation." 15th Conference on Enhanced Safety of Vehicles, pp. 1396-1407, 1996.

⁵ "Pedestrian protection: Commitment by the European automobile industry." *Communication from the commission to the council and the European parliament*. Brussels, July 11, 2002.

⁶ "Establishment of Regulation for Pedestrian Safety in Japan." Document 5, 32nd GRSP, December 13, 2002.

⁷ "European New Car Assessment Programme (EuroNCAP): Pedestrian Testing Protocol v. 4." EuroNCAP: www.euroncap.com. January, 2003

Two types of lower limb injuries are addressed in the Step I requirements: Tibia shaft fractures and knee ligament ruptures. Tibia shaft fracture risk is assessed by comparing the peak acceleration of the 'tibia' half of the leg-form to a reference value of 200 g (1961 m/sec²). Knee ligament injury risk is assessed by comparing the 'knee joint' peak bend angle to a reference value of 21°.

A pedestrian 'leg-form' impactor is used to assess Step I performance and current EuroNCAP ratings. This impactor is illustrated in Figure 1, alongside a human lower limb skeleton for comparison. The current leg-form consists of two semi-rigid 70 mm diameter core cylinders connected by a deformable 'knee joint'⁵. This core structure is wrapped in 25 mm of CF-45 Confor™ foam 'flesh,' covered by 6 mm of neoprene 'skin.' The inertial properties are intended to match those of a 50th percentile male human lower extremity, including the foot.

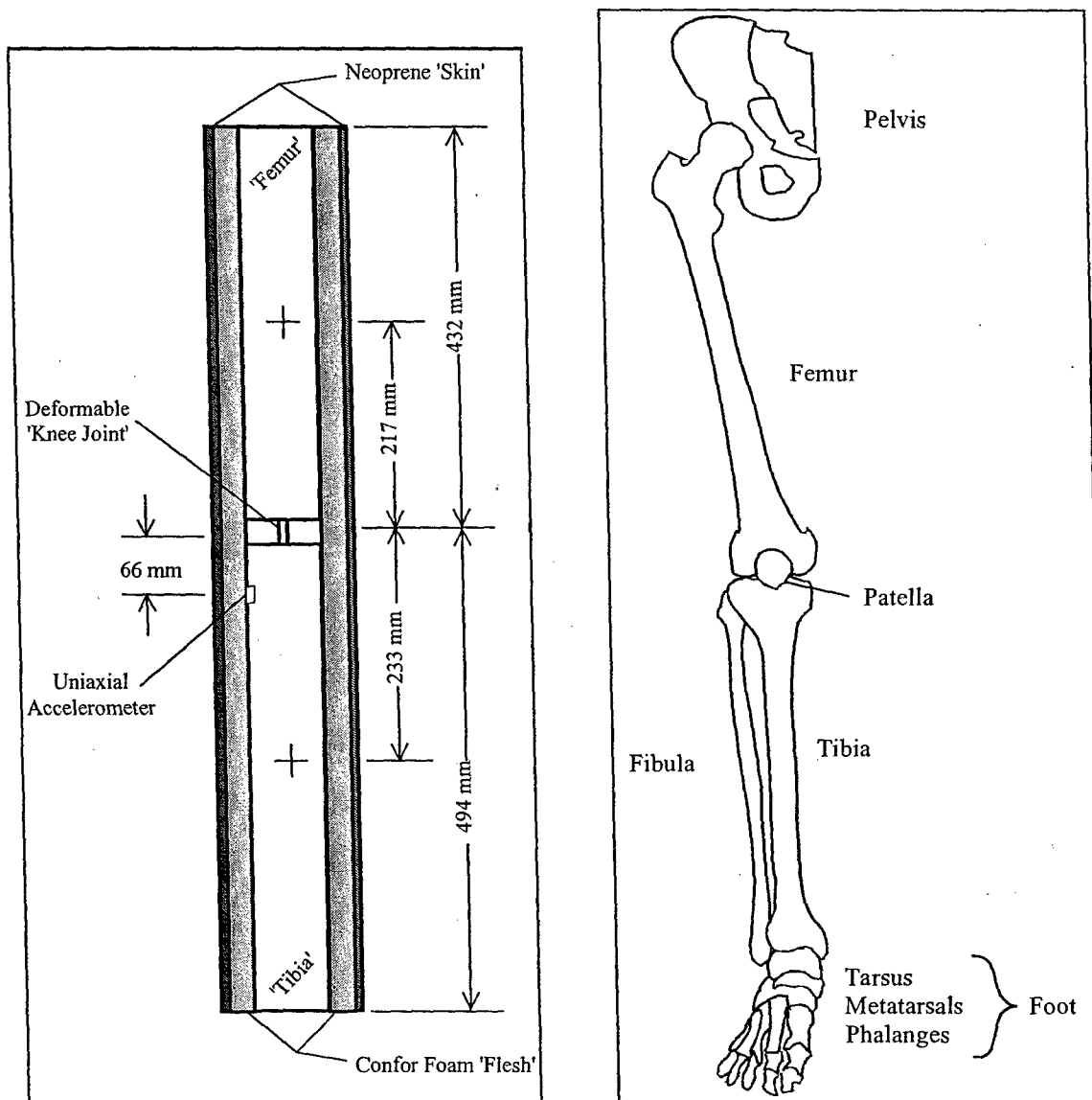


Figure 1: Pedestrian Leg-Form versus Human Lower Limb Bones

In addition to greater protection from tibia shaft fractures and knee ligament ruptures, the Step II European pedestrian requirements are also intended to address intra-articular knee joint fractures. For Step II, the allowable tibia peak acceleration and knee joint peak bend angle are reduced to 150 g (1470-m/sec²) and 15°, respectively. Intra-articular knee joint fracture risk is assessed by comparing the peak shear within the knee joint to a reference value of 6 mm.

A number of recent studies have concluded that the pedestrian 'leg-form' impactor and acceptance criteria have serious shortcomings in predicting lower limb injuries^{8,9,10,11,12}. Use of this device may result in a vehicle meeting the mandated criteria while having limited or even detrimental effect on real-world pedestrian lower limb injuries. The key criticisms are:

- Mass distribution – In a human, 80% of lower limb mass is in flesh, whereas in the current leg-form impactor, 80% is in the 'bones' (rigid core).
- Knee joint response – The impactor is stiffer than a typical knee. Also, the steel joints are damaged in each test, so their bending properties cannot be confirmed independently.
- Soft tissue cushioning – A human knee has little cushion outside the bone, whereas the impactor has the same padding all along its length.
- Knee joint injury tolerance – The test data supporting the bend angle and shear limits are inconclusive. Use of these requirements may result in bumper designs that increase the risk of tibia fracture without influencing knee injuries.
- Tibia shaft fracture tolerance – Peak acceleration is not a good predictor of bone fracture.
- Test reproducibility – Greater than 30% difference in test results on the same vehicle has been observed.

Two new prototype lower limb impactors that address some of these concerns have been constructed, but both still have limitations:

- NHTSA¹⁰ – A clutch plate in the knee replaced the deformable elements, to enable direct measurement of knee joint stiffness. No other improvements.
- JAMA/JARI¹³ – Flexible upper and lower cores were connected by cables, springs, and a geometrically simplified knee joint articular contact, allowing more realistic deformation. Cushioning was reduced around knee joint. Bone fracture risk was assessed using bending moments. However, no changes were made to knee joint injury tolerance assessment or the distribution of mass.

⁸ PJ Schuster, *Evaluation of the Real-World Injury-Reduction Potential of the Proposed European Pedestrian 'Leg-Form' Impact Test Using a Detailed Finite Element Model of the Lower Limb*. Doctoral Dissertation: Michigan Technological University, 2000.

⁹ Y Matsui, A Wittek, A Konosu, "Comparison of pedestrian subsystem safety tests using impactors and full-scale dummy tests." SAE Paper # 2002-01-1021, from SP-1671, 2002.

¹⁰ JR Marous, DB Reynolds, DC Longhitano, RA Saul, "Development of a non-frangible pedestrian legform impactor." Paper # 98-S10-O-06, Proceedings of the 16th Enhanced Vehicle Safety Conference, NHTSA, 1998.

¹¹ D Cesari, H Fontaine, S Lassare, "The validity of the proposed European pedestrian protection procedure and its expected benefits." Paper # 96-S7-O-08, Proceedings of the 15th Enhanced Vehicle Safety Conference, NHTSA, 1996.

¹² J Green, "A technical evaluation of the EEVC proposal on pedestrian protection test methodology." Paper # 98-S10-O-04, *Proceedings of the 16th Enhanced Vehicle Safety Conference*, NHTSA, 1998.

¹³ A Konosu, M Tanahashi, "Development of a Biofidelic Pedestrian Legform Impactor." Paper 378, *Proceedings of the 18th Enhanced Vehicle Safety Conference*, NHTSA, 2003.

Summary of Work Completed

The goal of the project was to develop an improved lower limb test device which addresses most or all of the concerns with the existing 'leg-form' impactor. This goal has been met through completion of the work described in this section.

Literature review

A literature review was conducted to find previous work and understand the state of the art. It was found that the advanced lower limb impactor prototype under development in Japan by JARI represents the best starting point for further work. This device includes flexible upper and lower cores connected by cables, springs, and a geometrically simplified knee joint articular contact, allowing more realistic deformation. Bone fracture risk is assessed using bending moments derived from strain gages. However, no changes were made to knee joint injury tolerance assessment or the distribution of mass. Core geometry does not represent human bones.

In addition to obtaining details of the JARI work so as to build on their experience, the literature search focused on obtaining the most recent information on biological material properties for the purposes of duplicating their response with engineering materials. In particular, flesh, ligament, and bone properties were collected.

Industry contacts for hardware donation and collaboration

To support the development of this project and also address the C3RP objective of increased university-industry interaction, two key industrial partnerships were developed:

- Ford Motor Company
 - Dr. Clifford Chou at Ford has been an advisor to this project from its conception. He has also arranged to loan Ford's production EEVC leg-form test device to MGA for the system validation testing (see below).
- MGA Research Corporation
 - Mike Miller at MGA provided guidance on the selection of accelerometers
 - MGA has also agreed to perform the validation testing of the final lower limb test device along with comparison testing of the current EEVC leg-form.

Design Development

The first step in the design process was to identify specific goals for the new test device. These goals address the specific shortcomings of the JARI prototype while also enhancing its capabilities:

- Reproduce the key enhancements of the JARI prototype.
- Add sensors to enable direct measurement of knee ligament strain.
- Eliminate complexity of the JARI 'bone core' structure.
- Duplicate human bone-flesh mass distribution within test device.
- Adjustability in knee flexion angle to account for test setups in the average gait cycle.

The next step was to implement these goals into a realistic CAD design. Several months were taken developing the CAD geometry to address all of the goals. Figure 2 presents the CAD model and the final assembled knee joint.

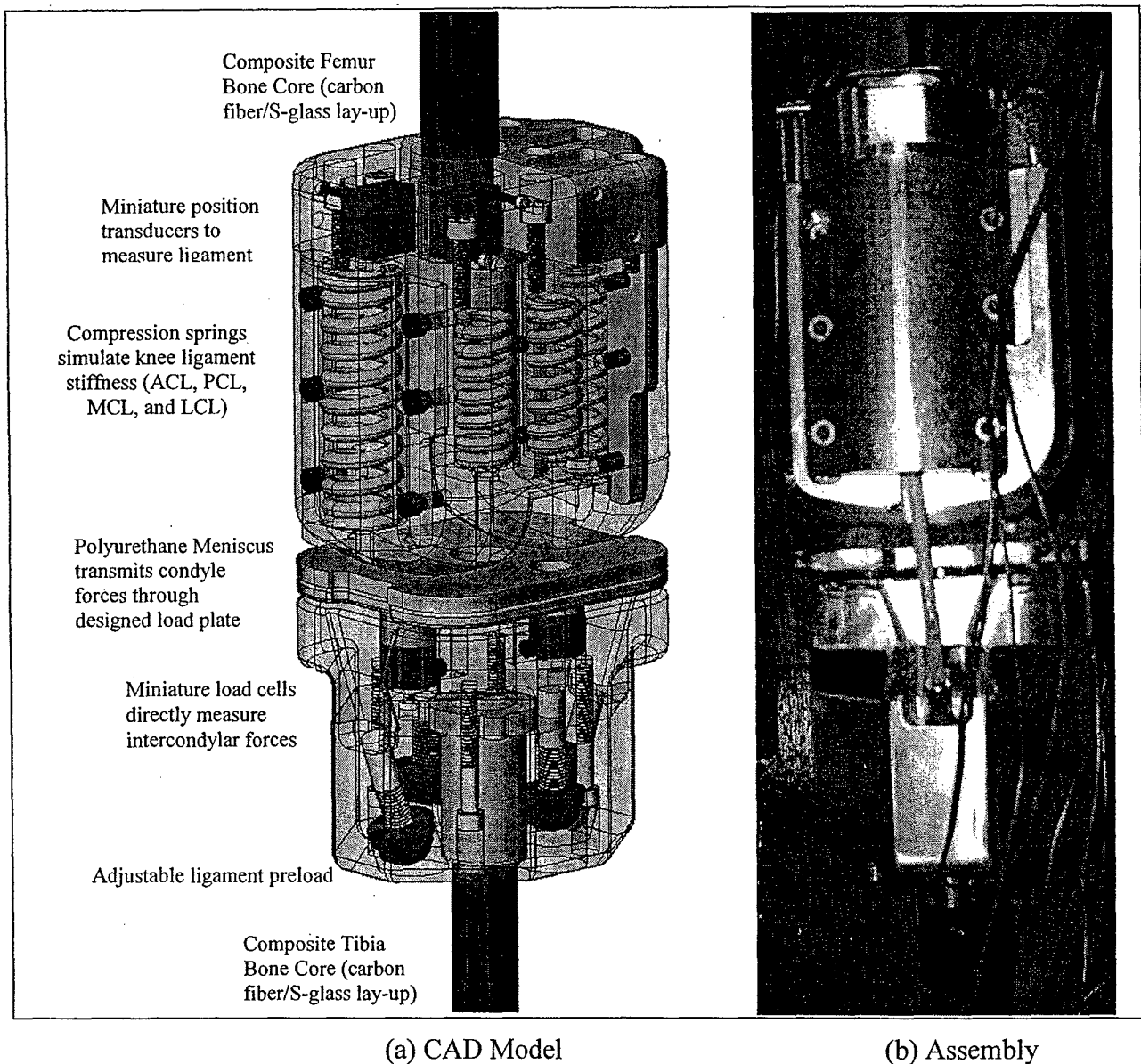


Figure 2: Lower Limb Test Device Knee Joint

Component Acquisition & Manufacturing

Once a final CAD model was completed, the project moved into the prototype construction phase. Most of the components were unavailable for purchase and needed to be manufactured in-house, or in a few cases, ordered from customizers. The main components are:

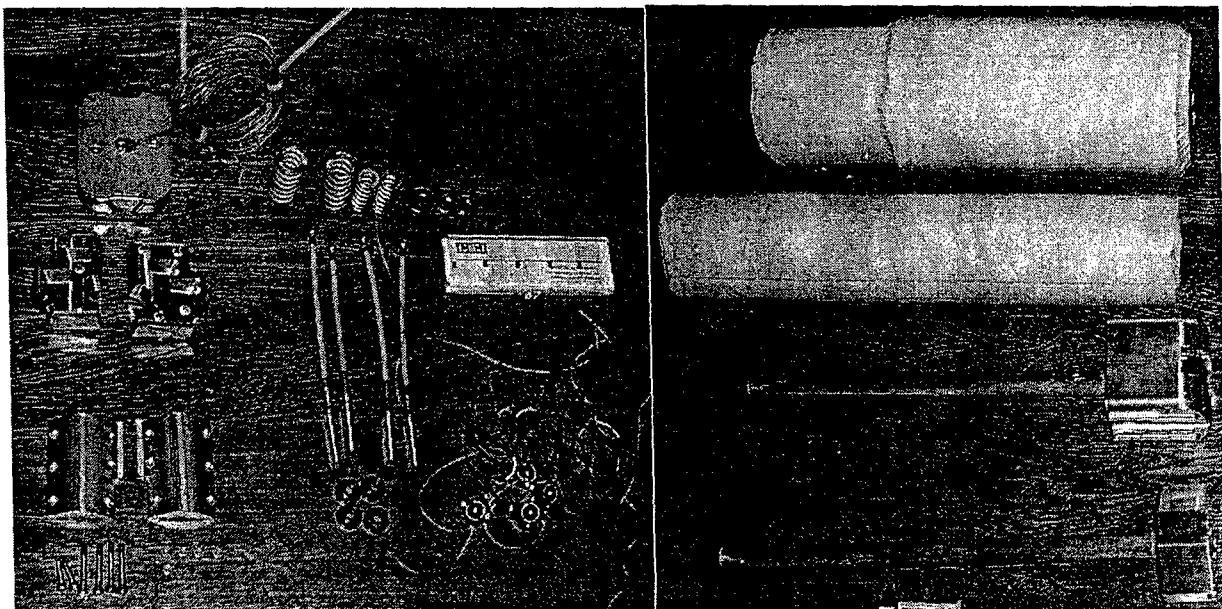
- Knee Joint – The aluminum upper (3-piece) and lower (1-piece) knee joint structures were each manufactured in-house on a CNC milling machine. A steel contact plate and polyurethane damping pad were also cut to enable load sharing between the surfaces.
- Bone Cores – The S-glass composite tibia and femur bone cores were manufactured in-house by RTM (Resin Transfer Molding) using a CNC-milled aluminum mold. Stiffness properties match human bones.

- Muscle/Flesh – Separate silicone components representing the thigh and leg flesh were cast in-house using simple plastic molds. Dimensions and density were selected to match human stiffness and mass properties.
- Skin – A zip-off nylon cover containing Confor polyurethane foam was outsourced. This protects the silicone from damage during an impact.

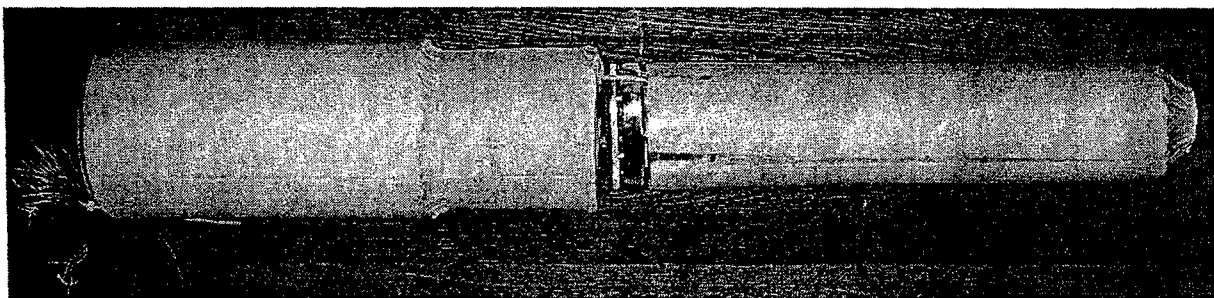
In addition to the manufactured pieces, a number of off-the-shelf hardware and instrumentation components were acquired and integrated in the design:

- 2 uniaxial accelerometers
- 8 uniaxial strain gages
- 4 compact string potentiometers
- 2 uniaxial load cells
- Miscellaneous wiring, nuts, bolts, cables, springs

Figure 3 shows all of the acquired and and manufactured components, together with the assembled leg-form (without nylon cover).



(a) Components



(b) Assembly

Figure 3: Lower Limb Test Device

Quasi-static Testing

- Mass properties of the upper and lower limb segments were measured and confirmed to match a 50th percentile adult male.
- Quasi-static 3-point and 4-point bending tests confirmed that the upper and lower bone cores' stiffness match human bones. However, this testing also revealed that the current bone core strength is insufficient for the desired pedestrian impact test repeatability. A senior project this Fall will develop a new composite layup to address this concern.
- Quasi-static 3-point and 4-point bending tests confirmed that the bending resistance of the knee joint could be adjusted to match a variety of human lateral knee joint stiffness. A specific setting will be determined through more testing before dynamic tests.

Technical Paper Publications

The following paper will be presented to the Society of Automotive Engineers in March 2006:

"Development of a Biofidelic Legform Impactor," John Davis, Peter Schuster [abstract accepted]

Current EuroNCAP test specifications attempt to predict pedestrian leg injury in a lateral impact by measuring deformations in a rigid legform test device developed by the UK's TRL (Transportation Research Lab). Research shows that the measurements taken from this device (knee bending angle, knee shear, and upper tibia acceleration) do not necessarily correspond to accurate injury prediction. Recommendations by several research papers suggest that the primary improvement to the current test device would be a flexible legform, or one that has more biofidelity (simulates actual human leg response).

The work presented in this paper first reviews the current legforms that have been developed for pedestrian impact testing such as the TRL impactor used in EuroNCAP tests, Honda's POLAR II pedestrian dummy, JAMA/JARI's FLEX-PLI legform impactor, and others. Component level testing shows the FLEX-PLI to be the most biofidelic impactor developed to date. However, there are still areas of potential improvement with this design. To address these areas, this research includes the complete development of a new legform impactor by incorporating adjustable ligament pre-load, direct ligament strain measurements, adjustability in knee flexion to account for the gait cycle, tuned composite bone cores that match the force-deflection curves of PMHS testing, and a newly designed condyle load plate. Development techniques include solid modeling, computer-aided manufacturing, composite design and analysis, sensor specifications, and data acquisition. In so doing, the injury specifications set by the EEVC will be modified to account for the more accurate injury assessment of the improved device.

Multi-Disciplinary Project Based Learning

One of the objectives of this project was to foster learning and research at Cal Poly. This was accomplished by involving students from different levels and backgrounds. A mechanical engineering graduate student was the center of the student team. He provided knowledge and skills in mechanical design. In addition three mechanical engineering seniors and one manufacturing engineering senior worked on the project.

The following thesis was a result of this project:

“Development of a Biofidelic Legform Impactor,” John Philip Davis

The following senior project was a result of this project:

“Using Resin Transfer Molding (RTM) to Build a Bone Surrogate,” Anthony Briganti

In addition, aspects of the project have been used as in-class examples in the Mechanical Design classes taught by Professor Schuster.

Recommendations for Future Work

The next phase of the project will include the following:

- Complete leg-form data acquisition setup
- Complete quasi-static testing of full data collection system
- Develop improved bone surrogates
- Perform validation tests and comparison tests at MGA
- Identify industry contacts for alternative uses of test device
- Develop local impact test equipment for future testing
- Publish work in SAE conference

**Construction of Tetrahedral Photonic Bandgap Crystal:
Demonstrating Three-Dimensional Self-Assembly using DNA Linkage**

Project Investigator:

Peter V. Schwartz
Assistant Professor
Physics Department / College of Science and Math

Construction of Tetrahedral Photonic Bandgap Crystal:
Demonstrating Three-Dimensional Self-Assembly using DNA Linkage (Research Summary)
Peter V. Schwartz, Cal Poly Physics Department

Our study of the controlled aggregation of polystyrene beads (diameter = 1 μm) through hybridization of attached strands of DNA reached a successful first step with the acceptance of our first paper to Langmuir: "*Selective, Controllable, and Reversible Aggregation of Polystyrene Latex Microspheres via DNA Hybridization*" Rogers, P. H.; Michel, E.; Bauer, C. A.; Vanderet, S.; Hansen, D.; Roberts, B. K.; Calvez, A.; Crews, J. B.; Lau, K. O.; Wood, A.; Pine, D. J.; Schwartz, P. V., *Langmuir*; **2005**; *21*; 5562-5569. Two authors (Pine and Michel) are collaborators from UCSB. Besides myself, the rest of the authors are present and past undergraduate students in physics and material engineering. In this manuscript, we acknowledge: "Office of Naval Research, under Award # N00014-04-1-0436". Additionally, our findings have been presented at conferences and invited talks:

In talks:

- 1) Columbia University (by Schwartz) July 23, 2004.
- 2) At the American Physical Society meeting in Los Angeles (by student Phil Rogers) March 22, 2005
- 3) At the Materials Research Society meeting in San Francisco (by student Phil Rogers) March 29, 2005
- 4) At the Cal Poly COSAM science conference (By Student Carl Bauer) May 6, 2005

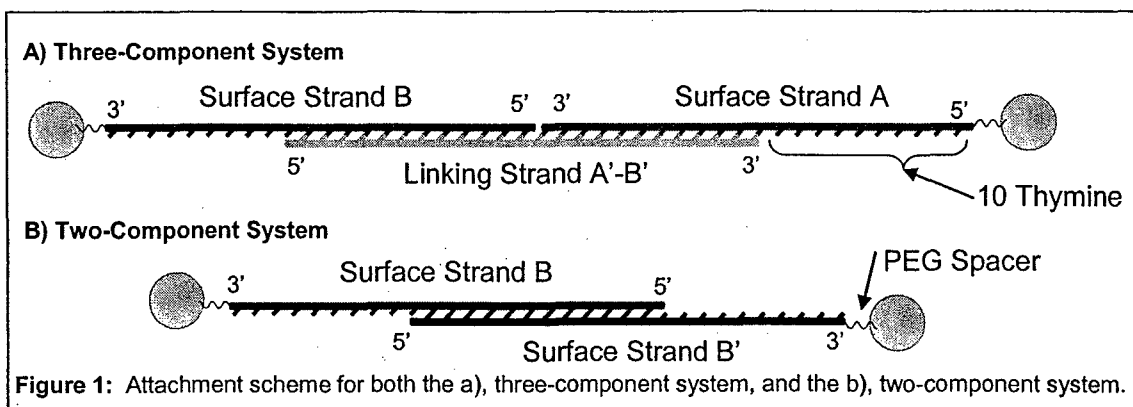
In poster sessions:

- 1) Nanostructure Fabrication Gordon Research Conference in New Hampshire (by Schwartz), July 2004
- 2) At the Materials Research Society meeting in San Francisco (by students Carl Bauer, Daniel Hansen, Steve Vanderet, Phil Rogers) March 29, 2005

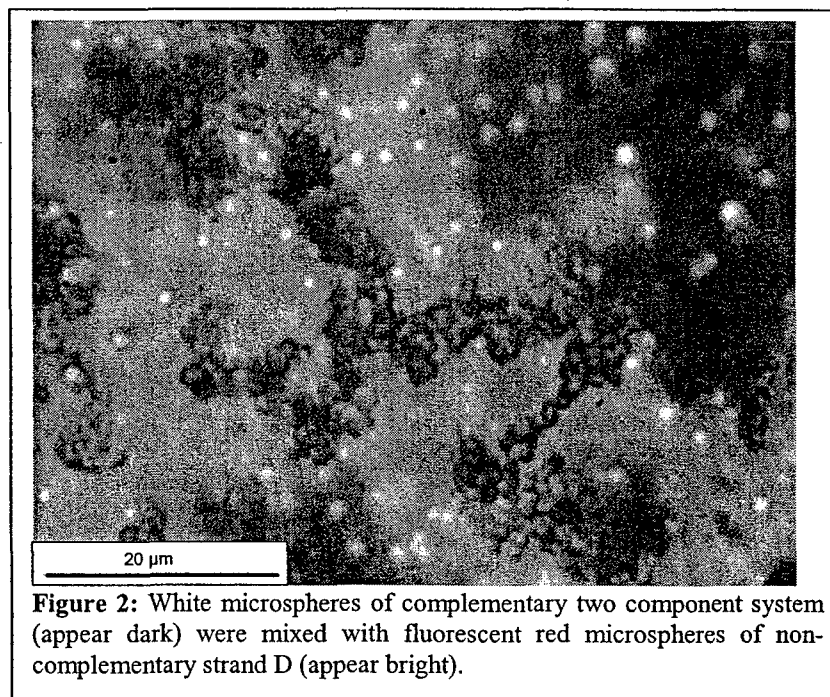
The remainder of this document is a summary of the 30 page manuscript.

Summary of Manuscript:

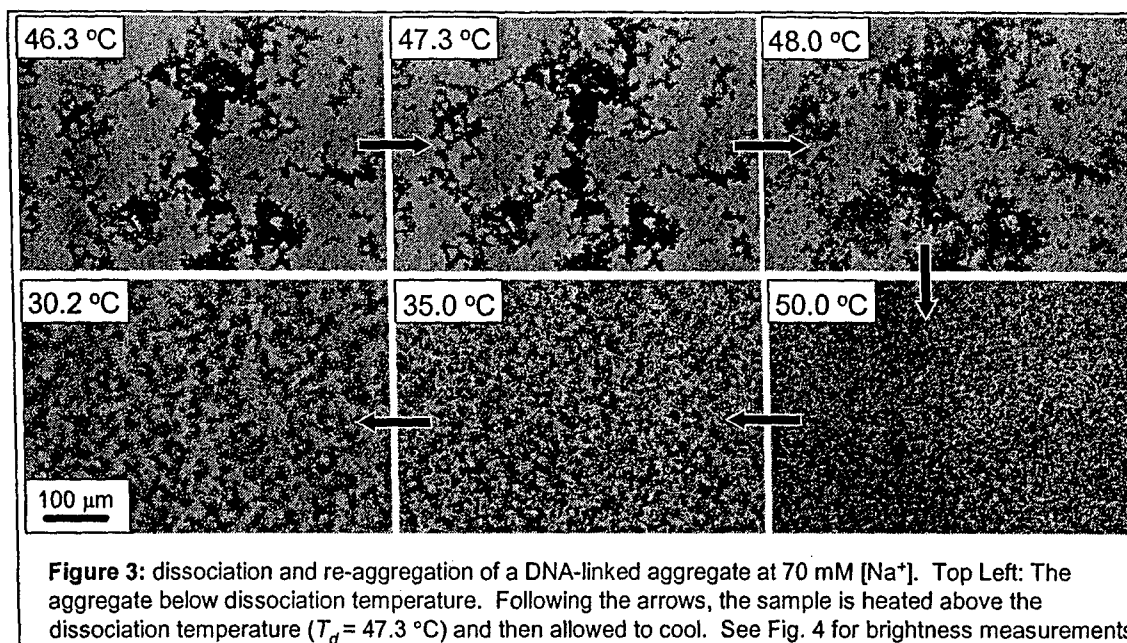
We developed a method to attach DNA to the surface of polystyrene microspheres at surface densities that are 20 to 50 times higher than accomplished by other researchers (corresponding to a molecular footprint of about 5 nm^2). Using fluorescently-labeled DNA, we measured the surface density and the portion of attached DNA that hybridized to complementary DNA in solution (hybridization efficiency). DNA is negatively charged, and the resulting high surface charge was able to prevent the microspheres from clumping up – something that is always a problem with microspheres. We were then able to demonstrate that the microspheres could be controllably and reversibly aggregated through hybridization between complementary strands of attached DNA by either a two component or three component system (Fig. 1). This was done with two experiments and is explained in the following two paragraphs.



Selectivity of DNA attachment. The specificity of the resulting DNA-guided self assembly process was demonstrated by attaching non-complementary DNA to fluorescent microspheres. These fluorescent microspheres were mixed with regular microspheres that were covered with complementary DNA. Non-complementary microspheres remained freely suspended, while the complementary, non-fluorescent microspheres formed large aggregates, as demonstrated in optical micrographs (Fig. 2) and movies.



Thermal Dispersion of Aggregates. Consistent with normal DNA behavior, the DNA-linked aggregates disperse completely when the temperature is raised past a characteristic aggregate dissociation temperature, T_d , and microspheres re-aggregate when the samples are allowed to cool below T_d (Fig. 3). When the aggregates disperse, the average brightness of the screen decreases. This decrease in brightness was used to identify T_d (Fig. 4). Having identified a means to quantify aggregate dispersion, we were able to investigate subtleties of the dispersion process described below.

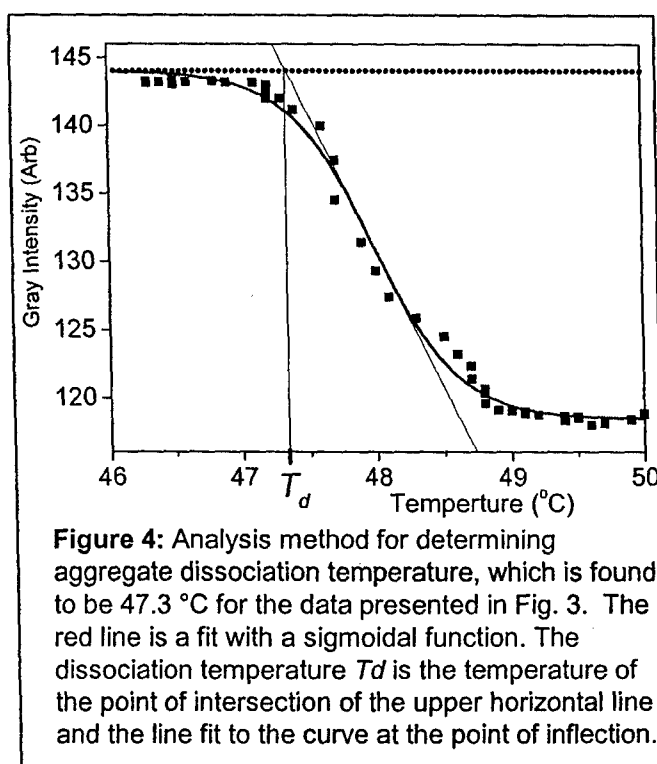


Role of Surfactant in Nonspecific Binding. It was found that the addition of Tween-20 at the end of the conjugation step enhances the ability of the aggregates to disperse upon heating. If Tween-20 is not used, a small core at the center of an aggregate may fail to disperse upon heating; including Tween-20 allows the complete dissociation of the aggregate upon heating. We propose that the Tween-20 coated the hydrophobic patches on the polystyrene surfaces (making them hydrophilic), thus preventing hydrophobic-hydrophobic attraction between microspheres.

Dispersion temperature increases with salt concentration. We discovered that T_d increases with increased concentration of sodium ions, consistent with the melting behavior of free-floating DNA.

Interestingly, we find that the dissociation temperature for the two component system is higher than that of the three component system. We attribute this to the fact that the melting temperature of DNA increases with increased concentration of DNA. The local concentration of DNA (on the microsphere surface) is much greater than the average concentration. However, as the three component DNA melts, the linker strand is released, reducing the local concentration to the average concentration in the solution, and thus reducing the DNA melting temperature.

Dissociation transition is much sharper than DNA melting transition. We also find that the dissociation transition for the aggregates is ten times more abrupt than the melting transition of unattached DNA in solution. Many DNA strands must collectively unbind for two microspheres



to dissociate. Since particles remain bound until all strands collectively unbind, the transition will be sharper (and take place at a higher temperature) when more strands are involved. This is a cooperative effect that is well known: the larger the number of interacting units involved in a transition, the sharper the transition, whether those units are the molecules in a boiling liquid, the base pairs in a DNA chain, or as in this case the hybridizing ssDNA strands themselves.

Conclusions

We have developed a protocol for covalently attaching ssDNA to carboxylated polystyrene latex microspheres that can be used to controllably and reversibly assemble large aggregates of microspheres with excellent selectivity. These results highlight DNA as an excellent selective nanoscopic adhesive to guide the assembly of tailored materials. The wider scope of our work is to understand and control surface interactions through surface functionalities, and applications toward guided self assembly. Our work will prove to be of wide importance in medical, biological, and industrial processes.

Selective, Controllable, and Reversible Aggregation of Polystyrene Latex Microspheres via DNA Hybridization

Phillip H. Rogers,[†] Eric Michel,[‡] Carl A. Bauer,[†] Stephen Vanderet,[†]
Daniel Hansen,[†] Bradley K. Roberts,^{§,||} Antoine Calvez,[†] Jackson B. Crews,[†]
Kwok O. Lau,[§] Alistair Wood,[†] David J. Pine,^{‡,§,||} and Peter V. Schwartz*,[†]

Physics Department, California Polytechnic State University,
San Luis Obispo, California 93407, Chemical Engineering Department,
University of California, Santa Barbara, California 93106-5080, Materials Engineering
Department, California Polytechnic State University, San Luis Obispo, California 93407,
and Materials Department, University of California, Santa Barbara, California 93106

Received December 25, 2004. In Final Form: April 7, 2005

The directed three-dimensional self-assembly of microstructures and nanostructures through the selective hybridization of DNA is the focus of great interest toward the fabrication of new materials. Single-stranded DNA is covalently attached to polystyrene latex microspheres. Single-stranded DNA can function as a sequence-selective Velcro by only bonding to another strand of DNA that has a complementary sequence. The attachment of the DNA increases the charge stabilization of the microspheres and allows controllable aggregation of microspheres by hybridization of complementary DNA sequences. In a mixture of microspheres derivatized with different sequences of DNA, microspheres with complementary DNA form aggregates, while microspheres with noncomplementary sequences remain suspended. The process is reversible by heating, with a characteristic "aggregate dissociation temperature" that is predictably dependent on salt concentration, and the evolution of aggregate dissociation with temperature is observed with optical microscopy.

Introduction

The DNA double helix consists of two negatively charged phosphate-sugar polymer chains held together by hydrogen bonds between the base pairs on each chain. If the sequence of bases on two chains of single-stranded DNA (ssDNA) are complementary (or near complementary), the hydrogen bonding can overcome the electrostatic repulsion and the two ssDNA chains can come together (hybridize) to form double-stranded DNA (dsDNA). The two chains reversibly separate (denature or "melt") above a characteristic melting temperature between approximately 30 and 80 °C. The melting temperature increases with the length of the chain and the concentration of salt in solution and depends to a lesser extent on the specific sequence of base pairs.¹⁻³

The melting and hybridization of DNA oligomers has been extensively investigated for many years,⁴ initially with a focus on genetic detection.⁵ During the past decade,

DNA hybridization has also been exploited to build DNA nanostructures in solution⁶⁻⁹ and to guide the self-assembly of DNA-derivatized nanostructures and microstructures.^{10,11} In particular, DNA-derivatized gold nanoparticles have been assembled onto surfaces¹² or onto other nanoparticles to form nanoparticle aggregates.¹³ The ability to independently control the specificity, strength, and separation of a connection,¹⁴ as well as the melting temperature of bonds, make DNA a versatile tool in the quest for new 'smart' materials, and aggregation of DNA-derivatized gold nanoparticles by hybridization has been well explored. Because of their small size, however, characterization of DNA-only or DNA-gold nanoparticle structures is difficult and indirect: UV-vis absorption spectroscopy only yields averaged measurements, and transmission electron microscopy (TEM) observation is made difficult by the high-vacuum conditions of the measurement.

In this paper, we present a scheme for derivatizing larger polystyrene particles with DNA for the purpose of assembling colloidal aggregates. This larger, polystyrene system is compelling for a number of reasons. First, we can directly follow the dynamics of this larger system using optical microscopy in order to better understand and control the use of hybridization for guiding particle self-

* Author to whom correspondence should be addressed.

[†] Physics Department, California Polytechnic State University.

[‡] Chemical Engineering Department, University of California, Santa Barbara.

[§] Materials Engineering Department, California Polytechnic State University.

^{||} Materials Department, University of California, Santa Barbara.

^{||} Present address: Materials Science and Engineering Department, University of Washington, Seattle, WA 98195.

^{||} Present address: Department of Physics, New York University, 4 Washington Place, New York, New York 10003.

(1) SantaLucia, J. *Proc. Natl. Acad. Sci. U.S.A.* **1998**, *95*, 1460-1465.

(2) Owczarzy, R.; Vallone, P. M.; Gallo, F. J.; Paner, T. M.; Lane, M. J.; Benight, A. S. *Biopolymers* **1997**, *44*, 217-239.

(3) Owczarzy, R.; You, Y.; Moreira, B. G.; Manthey, J. A.; Huang, L. Y.; Behlke, M. A.; Walder, J. A. *Biochemistry* **2004**, *43*, 3537-3554.

(4) Wetmur, J. G. *Crit. Rev. Biochem. Mol.* **1991**, *26*, 227-259.

(5) Chee, M.; Yang, R.; Hubbell, E.; Berno, A.; Huang, X. C.; Stern, D.; Winkler, J.; Lockhart, D. J.; Morris, M. S.; Fodor, S. P. A. *Science* **1996**, *274*, 610-614.

(6) Seeman, N. C. *Nano Lett.* **2001**, *1*, 22-26.

(7) Seeman, N. C. *Sci. Am.* **2004**, *290*, 64-75.

(8) Shih, W. M.; Quispe, J. D.; Joyce, G. F. *Nature* **2004**, *427*, 618-621.

(9) Ekani-Nkodo, A.; Kumar, A.; Fygenon, D. K. *Phys. Rev. Lett.* **2004**, *93*, 268301.

(10) Bashir, R. *Superlattices Microstruct.* **2001**, *29*, 1-16.

(11) Niemeyer, C. M. *Appl. Phys. A: Mater. Sci. Process.* **1999**, *68*, 119-124.

(12) Schwartz, P. V. *Langmuir* **2001**, *17*, 5971-5977.

(13) Storhoff, J. J.; Elghanian, R.; Mucic, R. C.; Mirkin, C. A.; Letsinger, R. L. *J. Am. Chem. Soc.* **1998**, *120*, 1959-1964.

(14) Storhoff, J. J.; Lazarides, A. A.; Mucic, R. C.; Mirkin, C. A.; Letsinger, R. L.; Schatz, G. C. *J. Am. Chem. Soc.* **2000**, *122*, 4640-4650.

assembly. Additionally, microspheres a few hundred nanometers in diameter can aggregate into structures with unique optical properties, such as colloidal crystals having stop band or complete band gaps in the optical range of the spectrum.¹⁵ Last, the ability to tailor the size, shape, and internal chemistry (including the magnetic, optical, and electrical properties) of colloidal microstructures and nanostructures may make this a model system of self-assembling materials with programmable properties.

In 1987, Kremsky et al. reported an efficient two-step covalent process for attaching ssDNA to micrometer-sized polystyrene microspheres.^{16,17} Since then, there have been numerous studies involving microspheres, but most of them have been focused toward biological purposes such as genetic detection, where DNA-coated microspheres in the presence of the target strand of DNA adhere either to DNA on other microspheres^{18–20} or to a DNA-coated surface.²¹

To date, there have been only a few reports focused on using DNA to direct the self-assembly of micrometer-sized colloids for the purpose of developing new materials. Hartmann²² studied the hybridization-mediated selective attachment of DNA-functionalized microspheres onto surface-anchored complementary DNA. Using a similar system, Zhang et al.²¹ studied the effects of shear flow on the detachment of DNA-derivatized microspheres bound to a substrate via DNA hybridization. Some steps have also been taken toward the three-dimensional self-assembly of micrometer-sized particles in solution. Soto et al.²³ recently reported that two sets of ssDNA-coated microspheres with the size ratio properly chosen and linked together by hybridization can create octahedron and tetrahedron structures. Two years ago, Milam²⁴ fabricated and carefully characterized aggregates self-assembled from bi-disperse microspheres coated with complementary ssDNA. The size and shape of the aggregates were studied as a function of the DNA length and the salt concentration by optical and confocal microscopy. Recently, Valignat et al.²⁵ were able to assemble DNA-decorated microspheres into a predetermined arrangement using laser tweezers, and Biancianiello et al.²⁶ reported an annealed crystal of DNA-linked microspheres.

While Milam, Zhang, and Valignat attached the DNA to the microspheres through a NeutrAvidin–biotin link, Soto and Biancianiello chose to covalently attach the DNA onto the microspheres using carboxydimide chemistry. Although technically more difficult and time-consuming, the covalent attachment has several advantages. First, the smaller molecular footprint of the amide linkage permits denser DNA surface coverage than is possible using the NeutrAvidin–biotin link, which has a much

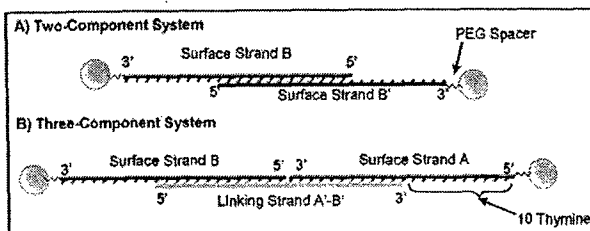


Figure 1. Attachment scheme for (a) the two-component system and (b) the three-component system.

larger footprint due to the steric hindrance of its bulky proteins. Second, the amide linkage is more robust than the NeutrAvidin–biotin link, whose proteins can denature at high temperature and thus compromise the strength of the bonds. Third, an amide bond under tension is stronger than the DNA hybridization bond, in contrast to the NeutrAvidin–biotin link. Zhang reports that the bond made of a succession of NeutrAvidin–biotin and DNA hybridization broke at the NeutrAvidin–biotin connection when the force applied exceeded 2 pN,²¹ whereas the force necessary to separate hybridized strands of antiparallel DNA from opposite ends is approximately 60 pN.^{27,28}

The aim of this paper is to expand the work done with nanoparticles to polystyrene microspheres, promoting microspheres as DNA-guided building blocks. To this end, we functionalize two sets of microspheres with different sequences of ssDNA and subsequently link together the strands and, hence, the microspheres to which they are attached. We use two different DNA-linking motifs (see Figure 1 and Table 1). In the first, two complementary strands of ssDNA are attached to two different sets of identical microspheres; these complementary ssDNA strands are allowed to hybridize so that the microspheres are held together by a “two component” bond. In the second, two noncomplementary strands of ssDNA are attached to two different sets of microspheres. In this case, the ssDNA strands on the different sets of spheres are each complementary to opposite ends of a third free-floating ssDNA “linker”; this linker hybridizes with the ssDNA strands on different microspheres so that the microspheres are held together by a “3 component” bond.

For reasons discussed above, we have chosen to covalently link the DNA to the surface of the microspheres via carboxydimide chemistry. A conjugation process (attachment of DNA to microsphere surface) was developed to minimize the tendency of the microspheres to non-specifically bind (that is, to aggregate through forces other than hybridization of complementary ssDNA).

The method used to attach DNA results in a high surface density of DNA, which electrostatically and sterically stabilizes the microspheres in suspension. The density of DNA on the microsphere surface was estimated to be 20–50 times greater than that achieved with the NeutrAvidin–biotin link.²⁴ Therefore, extra measures taken by others to prevent nonspecific binding were not necessary, such as using microspheres with a high surface density of carboxyl groups that are rather difficult to synthesize (e.g., CML microspheres), or using bulky poly(ethylene glycol) (PEG) polymers.²³

(27) The following reference reports how the DNA rupture force depends logarithmically on the speed of DNA separation and has been measured for 10 bp oligomers to be about 18 and 40 pN for speeds of 1 nm/s and 1 μ m/s, respectively. However, at the higher speeds dictated by the Brownian Motion of our microspheres, the rupture force should approach the asymptotic limit for DNA of 60 pN.

(28) Strunz, T.; Oroszlan, K.; Schafer, R.; Guntherodt, H. J. *P. Natl. Acad. Sci. U.S.A.* 1999, 96, 11277–11282.

(15) Subramanian, G.; Manoharan, V. N.; Thorne, J. D.; Pine, D. J. *Adv. Mater.* 1999, 11, 1261–1265.

(16) Kremsky, J. N.; Wooters, J. L.; Dougherty, J. P.; Meyers, R. E.; Collins, M.; Brown, E. L. *Nucleic Acids Res.* 1987, 15, 2891–2909.

(17) Wolf, S. F.; Haines, L.; Fisch, J.; Kremsky, J. N.; Dougherty, J. P.; Jacobs, K. *Nucleic Acids Res.* 1987, 15, 2911–2926.

(18) Perrin, A.; Martin, T.; Theretz, A. *Bioconjugate Chem.* 2001, 12, 678–683.

(19) Bains, W. *Clin. Chem.* 1998, 44, 876–878.

(20) Bains, W. *Anal. Biochem.* 1998, 260, 252–255.

(21) Zhang, Y.; Eniola, A. O.; Graves, D. J.; Hammer, D. A. *Langmuir* 2003, 19, 6905–6911.

(22) Hartmann, D. M.; Heller, M.; Esener, S. C.; Schwartz, D.; Tu, G. J. *Mater. Res.* 2002, 17, 473–478.

(23) Soto, C. M.; Srinivasan, A.; Ratna, B. R. *J. Am. Chem. Soc.* 2002, 124, 8508–8509.

(24) Milam, V. T.; Hiddessen, A. L.; Crocker, J. C.; Graves, D. J.; Hammer, D. A. *Langmuir* 2003, 19, 10317–10323.

(25) Valignat, M. P.; Theodoly, O.; Crocker, J. C.; Russel, W. B.; Chaikin, P. M. *Proc. Natl. Acad. Sci.* 2005, 102, 4225.

(26) Biancianiello, P.; Kim, A.; Crocker, J. C. *Phys. Rev. Lett.* 2005, 94, 58302.

Table 1. DNA Sequences Used, from the 5' End to the 3' End^a

strand name and function	sequence	T_m (°C)
strand A: surface strand	5'-5AmMC6/iSp18/TTT TTT TTT TCG CAT TCA GGA T-3'	53.8
strand B': surface strand	5'-TAC GAG TTG AGA TTT TTT TTT T/iSp18/3AmMC7/-3'	49.4
strand B: surface strand	5'-TCT CAA CTC GTA TTT TTT TTT T/iSp18/3AmMC7/-3'	49.4
strand A'-B': linking strand	5'-TAC GAG TTG AGA ATC CTG AAT GCG-3'	49.4; 53.8
strand D: noncomplementary strand	5'-5AmMC6/iSp18/TTT TTT TTT TTT GGC TAT GTA T-3'	NA

^a T = thymine, A = adenine, C = cytosine, and G = guanine. iSp18 signifies a PEG spacer used for steric freedom,²⁹ 5AmMC6 is the amine attachment point at the 5' end, and 3AmMC7 is the amine attachment functional group at the 3' end of DNA. Each surface strand sequence contains 10 T bases designed to improve DNA packing and microsphere electrostatic stability.³⁰ The hybridizing sequence of each oligomer is underlined, and its melting temperature in °C \pm 1.4 °C, calculated from the nearest-neighbor method^{1,2} for a 200 μ M DNA concentration and 50 mM NaCl is given in the right column.

The specificity of the resulting DNA-guided self-assembly process is also demonstrated in experiments where spheres are observed to bind only to spheres with complementary strands and not to spheres with noncomplementary strands.

Consistent with normal DNA behavior, the DNA-linked aggregates disperse completely when the temperature is raised past a characteristic aggregate dissociation temperature, T_d . The microspheres reaggregate when the samples are allowed to cool below T_d . The aggregate dissociation temperature, T_d , is determined by optically observing aggregate dissociation and increases with increased concentration of sodium ions, consistent with the melting temperature of free-floating DNA. Interestingly, we find that the dissociation temperature for the two-component system is higher than that of the three-component system. We also find that the dissociation transition for the aggregates is 10 times more abrupt than the melting transition of unattached DNA in solution.^{1,2}

Experimental Methods

Reagents and Equipment. The following solutions were made on site: 10 mM, pH 7.5 phosphate-buffered solution (PBS), 2% Tween-20 PBS solution, 10 mM, pH 7.5; and solutions of 1-ethyl-3-(3-dimethylaminopropyl) carbodiimide hydrochloride (EDC) in 10 mM, pH 4.5 2-morpholinoethanesulfonic acid (MES) buffer with a concentration of 10 mg/mL.

Carboxyl-modified divinylbenzene (DVB) cross-linked polystyrene latex microspheres, with carboxyl functional groups on the surface, were purchased from Interfacial Dynamics Corporation (Portland, OR). White and fluorescent microspheres were ordered with the following identical parameters. Each has a diameter of 0.97 μ m and a surface density of carboxylic groups of 1.075×10^{18} COOH/m² (corresponding to 3.16×10^6 groups per particle and a molecular footprint of about 1 nm²). The fluorescent microspheres have an excitation wavelength of 520 nm and an emission wavelength of 580 nm.

The oligonucleotides are synthesized by Biosearch Technologies (Novato, CA) and Integrated DNA Technologies, Inc. (Coralville, IA). The DNA sequences have been previously used to aggregate gold nanoparticles¹³ and to bind gold nanoparticles to surfaces.¹² Five sequences were used in this study: four 22-base surface-bound strands and a 24-base linker (Table 1).

Microsphere Preparation. The polystyrene spheres come dispersed in distilled deionized water. They were sonicated and vortexed for 15 s and subsequently centrifuged at 2200g for 15 min. The supernatant was then replaced with MES buffer, enough to make the solution 1% solid by volume. The above washing process was repeated and the samples were vortexed and then sonicated repeatedly to disperse any remaining groups of microspheres.

Conjugation of Microspheres. Prior to use, the EDC was stored at -20 °C in a water-free environment. The EDC solution was used immediately, and the excess solution discarded. Microspheres prepared in MES buffer (MES is always 10 mM, pH 4.5) and DNA (178.6 pM/cm² of microsphere surface was typically used. However, we were able to decrease the DNA concentration by a factor of 4 with no measurable decrease in DNA surface density on the microspheres) were placed in a 1.5

mL microfuge tube. Fresh solution (30 μ L) of EDC (10 mg/mL) in MES buffer was added to the sample and incubated at 25 °C for 30 min while being agitated. After 30 min, another 30 μ L of fresh EDC/MES solution was added to the sample and agitated for an additional 30 min. The sample's volume was then doubled by adding the same amount of 2% Tween-20 MES buffer as there was solution. Enough ammonium hydroxide was added to make the solution 4% ammonium hydroxide by volume. Then, the microspheres were washed three times in PBS with the following process: (1) Samples were sonicated and vortexed, each for less than 10 s, and centrifuged at 2200g for 15 min. (2) The supernatant was removed and replaced with PBS to make the solution 1% solid by volume. (3) The samples were sonicated and vortexed (less than 10 s each) until the DNA-covered microspheres were fully dispersed in solution. After the above wash cycle was repeated three times, the resulting DNA-derivatized microspheres, dispersed in PBS to 1% solid by volume, were stored at 7 °C.

Amino-modified ssDNA attaches to carboxyl-modified microspheres by means of an amide bond, activated by water-soluble EDC (Figure 2). In control experiments without EDC, it was found that fluorescently labeled DNA did not attach to the beads, indicating that, when EDC is used, the DNA is covalently attached to the microspheres and not simply physisorbed onto the polystyrene surface. The EDC forms a nucleophile-reactive intermediary with the carboxyl group on the microsphere surface, which subsequently forms an amide bond with the functional amino group on the ssDNA. Urea is produced as a byproduct (not shown in Figure 2).

Prior to being dispersed in the MES buffer solution, the microspheres are stabilized in aqueous suspension at pH 7 through the electrostatic repulsion provided by the surface COO⁻ groups. The pK_a of the COOH on the particles is approximately 5, so the particles lose much of their charge when placed in the pH 4.5 MES buffer solution, causing them to aggregate mildly. The aggregates are readily broken apart by mild agitation or sonication but reaggregate when the agitation ceases. As conjugation of the spheres with DNA proceeds, the aggregates tend to break apart under mild agitation, but in this case, they stay apart when the agitation ceases. The microspheres are thus observed to be better stabilized after conjugation with DNA, which we attribute to the increased charge, as well as the steric repulsion provided by the DNA chains.

Aggregation of Microspheres via DNA Hybridization. All hybridization experiments were carried out in PBS [10 mM, pH 7.5], initially with a sodium ion concentration of $[Na^+] = 62.5$ mM. Two-component aggregates were created by mixing strand B' microspheres and strand B microspheres together at 0.5% volume fraction of solid and left gently vibrating in the dark for at least a day at 7 °C. Three-component aggregates were created by first mixing the A microspheres with an excess of the A'-B' ssDNA linker strands. The samples were left at 7 °C in the dark for 24 h on a vibrating table and then washed in PBS to dispose of excess linker strands. The hybridized spheres were resuspended in PBS at a volume fraction of 1% solid. Then strand A microspheres with hybridized A'-B' linker were mixed with strand B microspheres. After the samples were incubated for only a few hours, aggregates form in both samples and begin to fall out of solution and rest at the bottom of the microfuge tubes. One to four days is allotted for the incubation process allowing for the formation of many macroscopic aggregates containing up to 10⁹ microspheres.

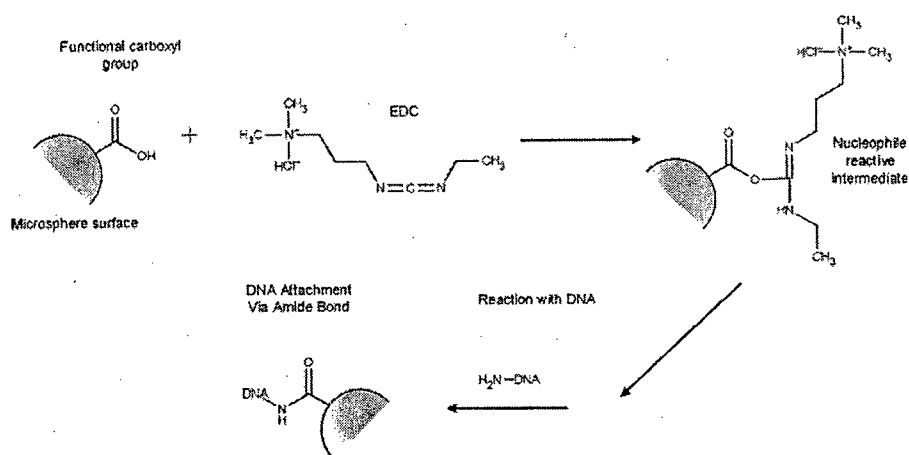


Figure 2. Mechanism for attaching amino-modified oligonucleotide to carboxyl-functionalized microspheres.

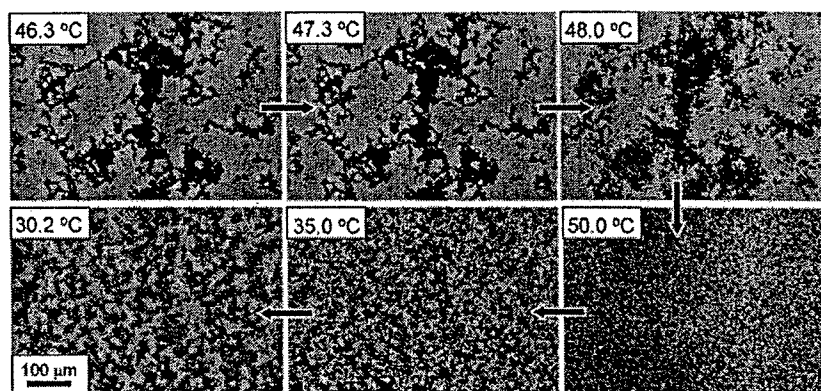


Figure 3. Dissociation and reaggregation of a two-component aggregate at 70 mM $[Na^+]$. Top Left: the beginning aggregate below dissociation temperature. Following the arrows, the sample is heated above the dissociation temperature ($T_d = 47.3^\circ C$) and then allowed to cool. See Figures 4 and 8 for the mean gray intensity measurements and temperatures.

DNA Surface Density and Hybridization Efficiency. Fluorescence measurements and flow cytometry were used to determine the density of attached and/or hybridized DNA on the microsphere surface. For these experiments, DNA oligonucleotides identical to those described in Table 1, but labeled with fluorescent dyes, were purchased. Strand B' was labeled with a Cy5 dye at its 5' end, while the linker strand A'-B' was labeled at its 3' end with a 6FAM dye, a close derivative of fluorescein. For the fluorescence measurements, a calibration curve was first established with the fluorescent DNA in solution (no microspheres). The measurements of the amount of DNA covalently attached to the microspheres were then performed indirectly on the supernatant obtained after each washing step of the conjugation process. The DNA molar concentration obtained was then compared to that added initially to the microspheres. The difference of these two numbers gives the amount of DNA attached to the microspheres.

Direct measurements were performed, using a FACSaria flow cytometer (Becton Dickinson, San Jose, CA). To determine the surface density of DNA, microspheres derivatized with Cy5-dyed B' strand were prepared following the standard protocol described above. To test the hybridization efficiency, a 6FAM dyed linker was hybridized onto microspheres derivatized with DNA (not dyed). The hybridization was performed at 100 mM $[Na^+]$ in PBS buffer. Measurements from both of these samples were compared to reference (negative) samples consisting of microspheres alone and microspheres derivatized with DNA that was not dyed. The fluorescence intensity for each dye was calibrated using Quantum PE-Cy5 and Quantum FITC calibrations beads purchased from Bangs Laboratories. From these calibration curves, the number of molecules of equivalent fluorochrome (MESF, i.e., the mean number of attached or hybridized DNA for each sample) was calculated. It should be noted that these measurements can only yield an estimate of the

DNA loading and efficiency of hybridization because the PE-Cy5 dye of the calibration beads and the Cy5 dye of the DNA are slightly different and because the quantum yield extinction coefficient of a dye almost always changes when it is attached onto a DNA strand.³¹ Nevertheless, the same calibration method has been used by others,²¹ so that our data can be directly compared to that reported in those studies.

Measurement of Dissociation Temperature. The DNA-mediated aggregates dissociate when heated above some characteristic temperature, T_d , which we designate as the aggregate dissociation temperature. This dissociation temperature is closely related to the melting temperature, T_m , of free floating DNA, but is expected to be somewhat higher because of cooperative effects, which we discuss later.

The aggregate dissociation temperature, T_d , was measured as a function of sodium ion concentration $[Na^+]$ using the following procedure: 1.0 μL of aggregate and aqueous buffer was removed from the bottom of the microfuge tube and placed in a cell with 110 μL of PBS of varying ionic strength. Aggregates were observed using an optical microscope, while the temperature was monitored with a submerged thermal couple. Aggregates were then heated until they dissociated (see Figure 3).

The temperature was increased at 0.5 $^\circ C/min$, and images of the dissociation were taken for the entire aggregate dissociation process. Prior to dissociation, the screen appears mostly bright with some black patches where aggregates reside. As the aggregates dissociate, the screen becomes darker as particles

(29) Technical Bulletin: Amino-Modified Custom Oligonucleotides; IDT: Coralville, IA, 2001.

(30) Storhoff, J. J.; Elghanian, R.; Mirkin, C. A.; Letsinger, R. L. *Langmuir* 2002, 18, 6666-6670.

(31) DNA Technical Note: Fluorescence Excitation and Emission; IDT: Coralville, IA, 2001.

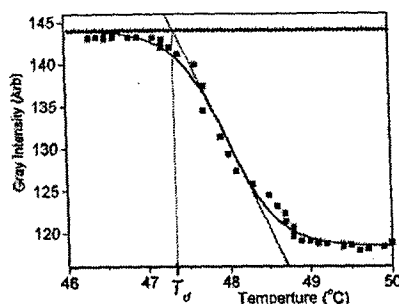


Figure 4. Analysis method for determining aggregate dissociation temperature, which is found to be 47.3 °C for the data presented in Figure 3. The red line is a fit with a sigmoidal function. The dissociation temperature, T_d , is the temperature of the point of intersection of the upper horizontal line determined using the sigmoidal fit and the line fit to the curve at the point of inflection of the sigmoid. Not all data points have been shown in the figure for clarity.

spread out, eventually covering the entire field of view and dimming the overall intensity of the screen. Therefore, a convenient measure of the progression of the dissociation process is the mean gray intensity, i.e., the average pixel brightness across the screen. The mean gray intensity was calculated for each image taken at different temperatures and the points were plotted as a function of temperature (Figure 4).

The data were then fit to a sigmoidal function. The dissociation temperature, T_d , was taken to be the point of intersection between the horizontal line in Figure 4 corresponding to the asymptotic measured intensity at low temperatures and the line fit to the curve at the point of inflection (halfway between the low- and high-temperature asymptotic intensities). Physically, the micrographs show that this is the lowest temperature at which the outermost microspheres of the aggregates start to move away from the aggregates and the dissociation becomes detectable in the low-magnification ($\times 20$) optical micrographs.

The uncertainty in measured temperature is estimated to be 1 °C due partially to the separation (~ 1 cm) between the observed aggregate and the temperature sensor and also due to the time needed for the temperature to reach equilibrium at the center of the circular observation window in the heating stage (diameter ≈ 0.6 mm), which was estimated to be about 1 min. It should also be noted that T_d exhibited a small dependence on the heating rate (T_d increases by 2.75 °C when the heating rate is lowered from 5 to 0.25 °C/min). However, our goal in this study is not to provide a precise measurement of T_d but rather to critically assess the specificity of the interaction that binds the microspheres, as well as to obtain an empirical working dissociation temperature for characterizing annealing experiments.

Results and Discussion

DNA Surface Density and Hybridization Efficiency. The fluorescence measurements yielded a density of DNA on the microsphere surface of $1.9 \times 10^5/\mu\text{m}^2$ with about an 18% uncertainty, corresponding to a DNA molecular footprint of about 5.3 nm² or about 5.5×10^5 DNA strands/bead. The flow cytometry experiments gave numbers that were lower but consistent with this surface coverage: the very sharp peak shown on the count vs fluorescence intensity histogram of Figure 5 corresponds to more than 2×10^5 DNA strands/bead, i.e. a density of $6.7 \times 10^4/\mu\text{m}^2$ or a DNA molecular footprint of about 15 nm². Even using the lower of the two values, the DNA surface density is nearly 20 times greater than that achieved using the Neutravidin–biotin link (3.25×10^3 molecules/ μm^2 reported in ref 24), which presumably was limited by the surface density of active sites of the Neutravidin on the bead surface of $4.6 \times 10^3/\mu\text{m}^2$.

By contrast, the number of hybridized strands, as determined by flow cytometry, is quite low: approximately 6500 strands per bead, which corresponds to a surface

coverage of 2200 linkers/ μm^2 . The distribution of hybridized strands has a broader peak (relative to the mean) than that of the surface-bound DNA (Figure 5), consistent with the expectation that the width of the distribution should scale with the square root of the mean number of hybridized strands. We estimate the hybridization efficiency (fraction of attached DNA hybridized with a linker) to be approximately 3.25%. This number is low but is consistent with the high surface density of attached DNA. Others have reported that the hybridization efficiency of a 25 bp target strand onto its complementary sequence, immobilized onto a gold surface and performed at 1M NaCl, decreases from 70% to 10% when the surface density of attached DNA increases from 2×10^4 to 1.2×10^5 strands/ μm^2 .³² Additionally, it is possible that some DNA strands may be attached to the microsphere surface via a group other than the intended terminal amine, which would render the attached DNA unable to hybridize. This unintended attachment might result from the high reactivity of the acidic environment (pH 4.5) during conjugation.³³

In any case, the DNA-derivatized beads were observed to be excellently stabilized in suspension. The flow cytometry experiments additionally showed that more than 95% of the colloids present in a sample after conjugation are individual microspheres: the beads did not bind to other microspheres unless through hybridization of complementary sequences of DNA.

Selectivity Experiments. The aggregation of DNA-linked microspheres is selective, owing to the sequence sensitivity of DNA hybridization. To investigate the specificity of the bonds between the microspheres in our system, red fluorescent microspheres functionalized with a noncomplementary DNA sequence D were added during the assembly of DNA-linked aggregates made of undyed microspheres using both the two- and three-component systems. The microspheres were mixed in PBS with equal parts dyed and undyed microspheres for a total microsphere concentration of 1 vol%. The mixture was slowly rotated overnight in order to prevent the settling of microspheres on the bottom of the microfuge tubes and the inevitable entrainment and trapping of nonhybridizing red microspheres within the matrix of DNA-linked microspheres. After overnight rotation, the suspension consisted of perfectly dispersed red microspheres (appearing bright in Figure 6) and undyed aggregates (appearing dark) devoid of the red spheres with the noncomplementary DNA sequence. Although it may appear as if some red microspheres are bound to each other, real-time observations reveal that they are moving past each other. Therefore, we conclude that the fraction of non-specifically bound microspheres is essentially zero.

Role of Surfactant in Nonspecific Binding. It was found that the addition of Tween-20 at the end of the conjugation step enhances the ability of the aggregates to disperse upon heating. If Tween-20 is not used, a small core at the center of an aggregate may fail to disperse upon heating; including Tween-20 allows the complete dissociation of the aggregate upon heating. Other than enhancing the dissociation of aggregate cores, we observed no effect of the Tween-20 on aggregate formation or dissociation. For example, flow cytometry measurements showed that nonspecific binding of colloids prior to aggregate formation is insignificant, whether Tween-20 is included or not. The detailed influence of the conjugation

(32) Peterson, A. W.; Heaton, R. J.; Georgiadis, R. M. *Nucleic Acids Res.* 2001, 29, 5163–5168.

(33) Rose, S. IDT, personal communication.

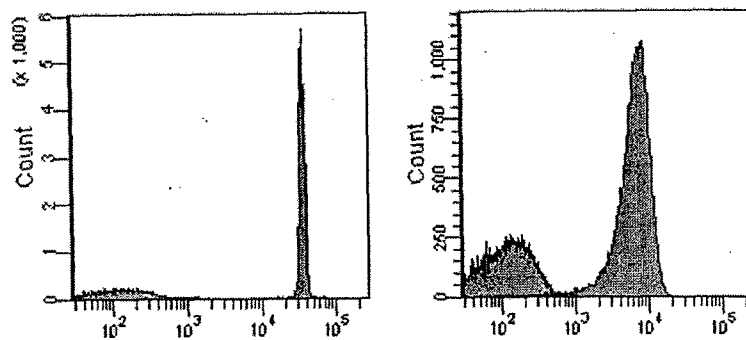


Figure 5. Flow Cytometry histograms: bead count (vertical axis) versus fluorescence intensity (horizontal axis). At left, bead count is shown as a function of the fluorescence intensity of the Cy5-dyed DNA surface strand, B'. The right histogram shows the bead count as a function of the fluorescence intensity of linker A'-B' dyed with 6FAM dye hybridized onto (undyed) DNA covalently bound to the microspheres. Because the fluorescence of Cy5 is not the same as 6FAM, a direct comparison of the intensities of the two graphs does not yield the ratio of the associated populations of DNA on the microsphere surface.

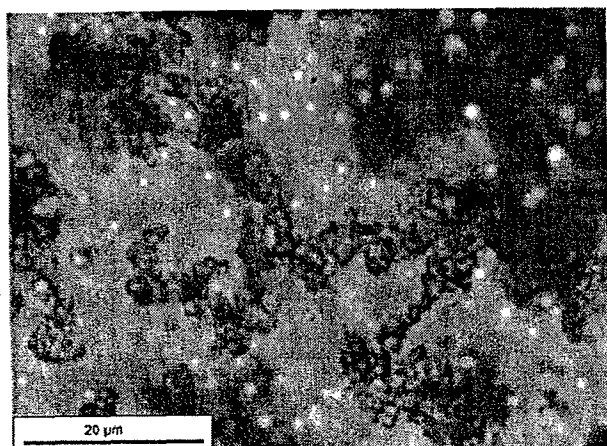


Figure 6. White microspheres of complementary two-component system (appear dark) were mixed with fluorescent red microspheres of noncomplementary strand D (appear bright).

protocol on the prevention of nonspecific binding and on the ability of the aggregates to disperse upon heating is not completely understood and is still under investigation. However, we offer some preliminary observations about nonspecific aggregation and how it may be prevented with Tween-20.

Nonspecific binding can occur when the surfaces of adjacent microspheres come close enough for the electrostatic repulsion to be overcome by van der Waals forces or by the attractive interactions between hydrophobic patches on microsphere surfaces. As observed in our experiments, replacing carboxyl groups with 22-base DNA strands greatly decreases nonspecific binding by both increasing the charge on the microsphere surface and providing steric repulsion by means of the DNA strands. Even this improved stabilization can fail when the microsphere surfaces are compressed together at the center of an aggregate of hybridized microspheres. For samples prepared with Tween-20, however, the aggregates disperse completely upon heating above T_d .

Tween-20 consists of a polar headgroup attached to three strands of PEG (averaging about 3 nm in length) and a hydrophobic 11-carbon alkyl chain. One possibility is that the hydrophobic alkyl chains bind to hydrophobic patches on the microsphere surfaces, effectively rendering those patches hydrophilic because of the PEG strands that are presented to the outside. The floppy PEG arms may also increase steric repulsion, although we note that the PEG strands on the Tween-20 are shorter than the ssDNA strands, so that they do not get in the way of hybridization

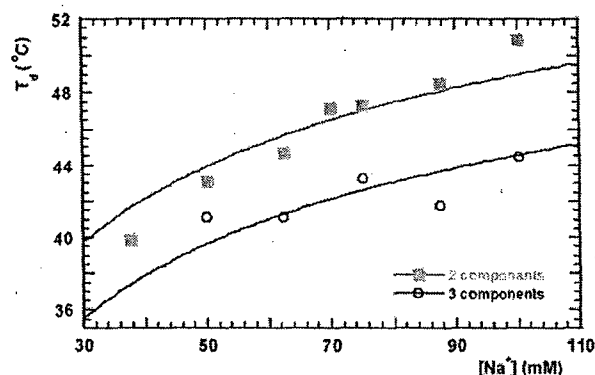


Figure 7. Dissociation temperature versus ionic strength for both three- and two-component aggregates. The full lines are a fit of the data points with eq 1, with one free parameter, the dissociation temperature at 50 mM Na^+ .

between ssDNA strands on different spheres. Others have found³⁴ that PEG alone can stabilize polystyrene microspheres if the chains are more than 30 nm long.

Dependence of Aggregate Dissociation Temperature on Salt Concentration. The specificity of the bonds linking the microspheres was also assessed by heating the aggregates in buffers of varying ionic strength. If they are bound by hybridized DNA, the aggregates should dissociate when the DNA-mediated aggregates are heated above the aggregate dissociation temperature, T_d , as discussed earlier. Moreover, T_d should vary with the sodium ion concentration and exhibit a dependence similar to that observed for the melting of neat DNA. This procedure also allowed us to assess the relative merits of different conjugation and hybridization protocols as discussed in the previous section about surfactant.

Aggregate dissociation temperatures were measured for the three-component aggregates and two-component aggregates for a range of ionic strengths. The experimental data are reported in Figure 7. The figure also shows an empirical relationship describing the variations of T_m with NaCl concentration for free floating oligomers:³

$$\frac{1}{T_{m(1)}} = \frac{1}{T_{m(2)}} + (4.29n_{GC} - 3.95) \times 10^{-5} \ln \left(\frac{[\text{Na}^+]_2}{[\text{Na}^+]_1} \right) + 9.40 \times 10^{-6} (\ln^2 [\text{Na}^+]_2 - \ln^2 [\text{Na}^+]_1) \quad (1)$$

where n_{GC} is the number of G and C bases divided by the

(34) Kim, A.; Manoharan, V. N.; Crocker, J. C. *J. Am. Chem. Soc.* 2005, 127, 1592.

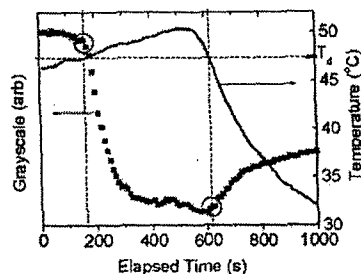


Figure 8. Mean gray intensity (squares) and temperature (line) for the dissociation and reaggregation for the data presented in Figure 3. Circled data points correspond to 47.3 °C, the aggregate dissociation temperature.

total number of bases of the oligomer and $T_{m(i)}$ are the melting temperatures in Kelvin for the corresponding sodium ion molar concentrations $[Na^+]$.

The functional form of eq 1, which gives the temperature dependence of the melting curve that was empirically derived for *free-floating* DNA, fits our data for the dissociation of the microsphere aggregates reasonably well, considering that the precision of the measurement is estimated to be ± 1 °C. The agreement of measured dissociation temperatures of the aggregates in both systems with the general trend of the free-floating DNA melting behavior gives further evidence of the specificity of the force holding the microspheres into aggregates.

The essential difference between the two- and three-component systems is that linker is required to bind spheres together in the three-component system but not in the two-component system. In the three-component system, entropy favors the complete delocalization of the linker molecules throughout the solution, while aggregation requires that the linker molecules be localized between spheres. The entropic penalty associated with confining the linker between two microspheres leads to a dissociation temperature of the three-component system that is lower than that of the two-component system, where no such penalty exists (because all the DNA is permanently bound to the spheres).

Reversibility. Consistent with the reversible nature of DNA hybridization, DNA-linked aggregates, after dispersion, can be reassembled. The sequence of images in Figure 3 and the graph in Figure 8 demonstrate that, after dissociation, the microspheres again reassemble if the temperature is lowered below the aggregate dissociation temperature, T_d . The temperature at which the microspheres start to reaggregate is found to be close to T_d , the temperature at which the aggregates start to dissociate. It should be noted that the rate of microsphere dispersion does not increase with increased ramping rate of the temperature (see Figure 9). Instead, dispersion is controlled by the diffusion rate of the microspheres, which is very slow compared to the diffusion and the dissociation rate of the DNA. So, while the melting of the DNA is an equilibrium process, the dispersion and reaggregation of the microspheres is not at equilibrium at the relatively rapid temperature ramping rates (0.5 °C/min) of these experiments.

Sharpness of Dissociation Profile

The dissociation of DNA-linked microspheres is found to be a much sharper transition than the melting transition of the associated neat DNA dissolved in PBS. The sharpness of the transition can be quantified using the full width at half-maximum (fwhm) of the derivative of the gray scale heating curve. As noted above, the rate of

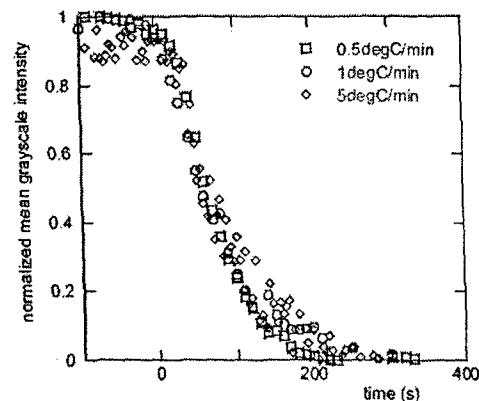


Figure 9. Normalized mean gray intensity versus time for the dissociation of a two-component aggregate at 70 or 75 mM Na^+ concentration. The time $t = 0$ has been set for $T = T_d$. The rate of microspheres dispersion does not increase when the ramping rate of temperature is increased from 0.5 up to 5 °C/min.

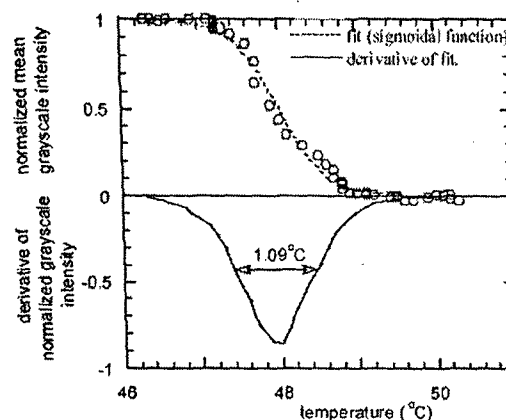


Figure 10. Normalized mean gray intensity versus temperature for the dissociation of a two-component aggregate at 70 mM Na^+ concentration. The dotted line is a fit of the data with a sigmoidal function. The full line is the derivative of this fit, showing the fwhm.

dissociation of an aggregate is limited by the diffusion of microspheres. In an effort to maximize the sharpness of the dissociation transition, the temperature should ramp slowly, so that aggregates dissociate under conditions as close as possible to equilibrium. Figure 10 shows the dissociation of a two-component aggregate where the temperature was increased at 0.5 °C/min. The derivative of the curve is also shown and yields a fwhm of 1.1 °C. Three-component aggregates also displayed a narrow dissociation transition, and within the accuracy of the data, we were not able to distinguish a difference in the fwhm between the two-component and three-component motifs. Other researchers measured a fwhm = 4 °C for the dissociation of gold nanoparticles linked by a three-component system using 15 bp DNA, while the melting curve for the associated *free-floating* DNA had a fwhm = 12 °C.³⁵ A narrower melting transition results in the ability to determine the DNA melting point with greater resolution. As a consequence, a DNA detection scheme based on aggregation of DNA-covered gold nanoparticles would be more selective for single-base mismatches than that of free floating DNA. Similarly, a DNA detection scheme based on aggregation of our DNA-derivatized microspheres should be considerably more selective than the scheme

(35) Elghanian, R.; Storhoff, J. J.; Mucic, R. C.; Letsinger, R. L.; Mirkin, C. A. *Science* 1997, 277, 1078–1081.

based on DNA-derivatized gold nanoparticles. At the same time, this sharp dissociation transition of DNA-derivatized microspheres makes a very challenging task of annealing DNA-derivatized microspheres into a lowest-energy configuration.

The cause of the increased sharpness of the dissociation profile for particles compared to the melting profile of DNA can be understood by considering the number of DNA strands involved in each dissociation process (although recent computer model results³⁶ indicate that modulation in local salt concentration may contribute to the sharpness of the dissociation profile). Many DNA strands must collectively unbind for two microspheres to dissociate, while fewer must unbind for two nanoparticles to dissociate, and fewer still (one, in fact) must unbind for two ssDNA strands to dissociate. Since particles remain bound until all strands collectively unbind, the transition will be sharper (and take place at a higher temperature) when more strands are involved. This is a cooperative effect that is well known: the larger the number of interacting units involved in a transition, the sharper the transition, whether those units are the molecules in a boiling liquid, the base pairs in a DNA chain, or as in this case the hybridizing ssDNA strands themselves. Therefore, we expect the transition to be broadest for two hybridizing strands, narrower for ssDNA attached to nanoparticles, and narrower still for microspheres, which involve the greatest number of hybridizing ssDNA strands.

Conclusions

We have developed a protocol for covalently attaching ssDNA to carboxylated (not CML) polystyrene latex microspheres that can be used to controllably and revers-

ibly assemble large aggregates of microspheres with excellent selectivity. The excellent stability of the microspheres is the result of the high surface density of DNA achieved on the microspheres through carboxydiimide chemistry, which is performed at low pH. The aggregates reversibly and completely dissociate at a characteristic temperature, which increases with increased concentration of $[Na^+]$ consistent with the melting temperature of free DNA in solution. The existence of multiple bonds between microspheres results in a dissociation transition that occurs much more abruptly and at a higher temperature than the melting transition of the associated free-floating DNA in solution. These results highlight DNA as an excellent selective nanoscopic adhesive to guide the assembly of tailored materials.

Acknowledgment. We gratefully acknowledge fruitful conversations with Eric J. Kantorowski (Cal Poly Chemistry), assistance and insight from Khodadad N. Dinyari and Michael Chi-Hang Yeung, and conversations with Richard Owczarzy.^{2,3} We also thank Karen Y. Dane of the Chemical Engineering Department at UCSB who conducted and helped analyze the flow cytometry measurements. This work was supported in part by the Department of the Navy, Office of Naval Research, under Award No. N00014-04-1-0436, in part by the National Science Foundation under Grant No. CTS-0221809, and in part by Raytheon Corporation.

LA046790Y

(36) Jin, R.; Wu, G.; Li, Z.; Mirkin, C. A.; Schatz, G. C. *J. Am. Chem. Soc.* 2003, 125, 1643.

Large Scale Distributed Wireless Networks

Project Investigators:

John Seng
Assistant Professor
Computer Science Department

Diana Franklin
Assistant Professor
Computer Science Department

Abstract

Wireless sensor networks provide an effective tool for acquiring sensor measurements across a large area. Devices in a sensor field can automatically configure themselves into a working network, ready to collect data. The challenge is to collect that data in a timely and power-efficient manner.

In some environments, a data collection device (sink) may need to travel periodically through the field to gather data because keeping a local storage system is impractical. The goal is for this moving sink to gather the most data in the shortest amount of time using the least amount of inter-node communication. Network reconfigure time, memory limitations, and brief radio contact time make this goal challenging.

In this report, we explore three aspects of data retrieval. First, we explore with what nodes the sink should communicate. We present a selection technique for picking target nodes to increase data retrieval rates. We then optimize data collection through message forwarding and exclusion. These two techniques improve data retrieval by 35% on average. Finally, we consider the effect of erratic sink paths on data collection.

1. Introduction

Wireless sensor networks are an effective means of collecting data across a large area. Each node of a sensor network can be placed in locations that are relatively far apart, and the information each node acquires can be relayed through other nodes in the network and collected in a central location. This type of data collection enables many useful applications ranging from monitoring ecological habitats [7] to monitoring the seismic activity over a large area of land [5].

In this report, we study algorithms targeting data retrieval from a wireless sensor network where data collection cannot be performed by routing data to a stationary location. The data must be retrieved by a mobile data collector (sink) which passes through the field of sensor nodes. For example, a vehicle (e.g. car or airplane) may travel through a sensor field to retrieve current measurements from each of the nodes. Often, the vehicle will be moving too quickly to retrieve all the data in a single pass. Additionally, each node's memory may be too small to store data from all its neighbors. Data must either be sent directly to the data sink or routed to a node which is in communication range with the data sink. In this research, we study algorithms to collect data from as many nodes as possible.

The primary challenge of this type of data collection is that the target node, the current node in communication with the data sink, is in communication contact with the data sink only for a finite period of time. Each time the target node changes, the other nodes must reconfigure themselves to send to the new target node, and some must retransmit their data that had not yet reached the sink. Unfortunately, this costs time and power. We attack this problem from several angles - by reducing the number of times the target changes and by optimizing the case in which it changes. The selection of the target node is crucial because each time the target node gets out of range, extra messages and network reconfiguration are required. We present two optimizations for when the target node changes. First, we reduce messages (and thus power) by removing some of the redundant messages from the system. Once this is done, however, the original messages

need to be re-routed to the new target node. Secondly, we present a form of data forwarding which routes data towards the target node, in the presence of target node changes. By utilizing this data forwarding, we are able to increase the amount of data collected from 31% to 66% on average.

Finally, we show that our algorithm works well independently of the path taken. When normalized for total time spent in the field, non-linear paths and linear paths all performed within 8% of each other on average.

This report is organized as follows: Section 2 describes related research and studies, whereas Section 3 describes our work. The simulation methodology, assumptions, and tools are presented in Section 4, followed by results in Section 5. We conclude in Section 6.

2. Related Work

Within the context of sensor networks, there are several interesting problems in transferring information from a field of sensors to a data sink. We focus on how a moving sink collects data and how to maximize data collection given limited radio contact.

TAG [9] creates a language and library for aggregating data from many nodes to a single, stationary sink. It reduces processing and storage by calculating results as the messages propagate through the system. Krishnamachari et al. [8] analyze the problem of data aggregation in terms of energy efficiency and delays. They find that although optimality is NP-hard, special polynomial time cases also exist.

Other groups have looked at quickly and efficiently creating networks between source nodes and sink nodes. Ye et al. [10] propose a cost field that, with few messages, creates a minimum cost forwarding route for each node to a stationary sink. In addition, it requires no centralized information to maintain its routing.

Intanagonwiwat [4] has created a system to allow nodes to pass data with both efficiency and power-management in relation to the path they choose in order to get the data to the sink.

Several projects focus on the MULE (Mobile Ubiquitous LAN Extension) model of communication [6] [1]. This model drives research in routing for delay tolerant networking [3], with scenarios as extreme as a van providing connectivity between South African villages [2].

Finally, there has been some work on collecting data from a network to a non-stationary sink. Zebranet [7] provides nodes with enough memory to store the data from neighboring nodes so that the communication occurs before collection, not during collection. We are assuming simpler nodes that do not have this much memory and may acquire real-time measurements to be transferred to the sink.

3. Non-Stationary Data Retrieval

In this work, we focus on optimizing data collection from a field of sensor nodes via a non-stationary sink node. The sink node is a moving data collector (e.g. an airplane or car) traveling through a field of fixed-location sensors. This sink node is capable of communicating with a given sensor once it is within the radio range of that sensor. The fixed-location sensors may provide either real-time or previously acquired measurements to the sink node, but they have a limited communication range. In any given application, the primary goal is for the sink node to obtain the data from as many of the sensor nodes

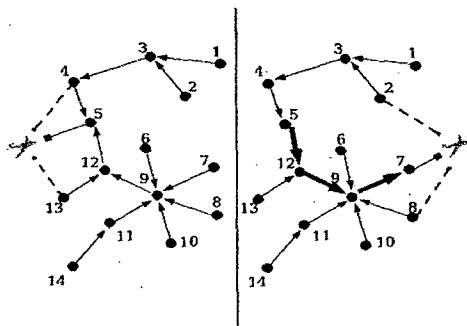


Figure 1. The sensor network as a plane gathers data.

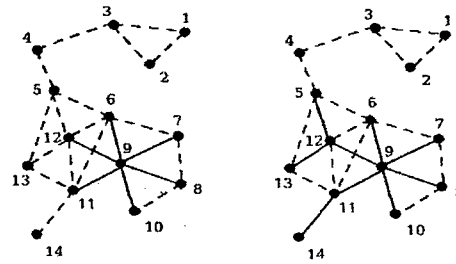


Figure 2. Two steps in linking setup phase. The node with the most neighbors is the start node. As neighboring nodes are added, the nodes with the fewest edges are added first.

as possible in a given pass through the sensor field. A sample scenario is depicted in Figure 1. The figure shows an airplane as it approaches (a) and travels through (b) a sensor network. The numbers represent an individual sensor node. The arrows represent a communication neighbor determined by a linking algorithm to be discussed later. First, the airplane must choose a primary node for initial communication, a target node. Data is routed toward this target node. The target node changes as the airplane comes in and out of communication range with different nodes.

Because the sink node is moving, any one of the sensors may have radio contact with the sink for a brief period of time, and some nodes do not make direct contact with the sink at all. This limits the amount of information that can be collected from the nodes. Collecting all the data is achieved by routing data through other sensor nodes.

In an ideal situation, once the airplane chooses a target node, the nodes would link themselves such that they could pass messages to that target node in the fewest hops possible. Unfortunately, a sink traveling at a high speed will leave the area before such an optimal network is set up, let alone before it has time to receive all messages. We use a linking algorithm for our studies, whereby the sensors form an initial network of bidirectional links at setup time (long before data collection), and only the direction of the links is changed depending on the target node at a given time.

The linking setup algorithm is depicted in Figure 2. Dashed lines represent all possible links, whereas solid lines represent links selected by the algorithm. This algorithm is performed in a distributed manner, without knowing the exact location of any of the nodes. The links are created by first finding the node that is in communication range of the most nodes (node 9 in the example). In order to load-balance messages, the algorithm adds nodes that have the least solid-line links (as opposed to potential links) until all nodes are connected. In the above example, it would link all the neighbors of node 9, and then look for the next set connected to those nodes.

This linking algorithm leads to trees with low depth (assuming the first node selected is the root). This reduces the penalty for new target node selection because the data will not need to be redirected as far. By starting in a high-density area of the field and branching out, it is likely that the next level of nodes will not have many links. By continuing to branch out based on fewest links, it is likely that the nodes with many potential links will not be able to link to all their neighbors because the surrounding nodes will already be linked. Note that this is a tradeoff. We are focusing on speed while sacrificing some power and memory pressure on the first node chosen.

In the end, each node will only receive messages from or send messages to its links; all other messages will be excluded. From this setup, we explore several algorithms for how to choose the target node, how to most efficiently pass data to the sink, and what path the sink should take.

When the sink enters the field and selects the first target node, the bidirectional links are made unidirectional, all leading to the target node. This occurs by the target node sending a message to its links, those sending to their links, etc., until everyone has figured out the direction of the links. Data messages are put in a send queue for each node that sends to their parent node. Each node forwards one message every time the sink sends a message to the target node. Messages are forwarded as long as the sink is within range of the target node. Once the sink is no longer within range, a new target is selected.

This process of target selection and data retrieval is repeated until the sink leaves the sensor field. After the sink has not been in the field for an extended period of time, each node clears its message sending queue.

4. Methodology

For this research, we created Java-based wireless network simulator. The simulator constructs a field with variable number of nodes, communication radius, sink path and sink speed. For each experiment, data was tabulated and averaged on one thousand randomly generated fields. These same thousand random fields were used for each graph.

We simulate a sensor field consisting of a rectangular field with dimensions of 200 by 200 units. Inside this X-Y range, a specified number of nodes are randomly placed in the field, each with a unique x-y coordinate. Each node has a communication radius that determines which nodes can communicate with each other. The default communication radius is 25 units unless otherwise specified. In this work we assume that all nodes are in radio range of at least one other node. Upon construction of the field, all nodes in the field must be connected, and the field will be reconstructed until it meets that requirement.

Once the field is successfully constructed, a receiver sink is constructed and either given a random linear path, or one of three specific nonlinear paths. All paths start from outside of the X-Y range and out of communication range of any node in the field. The sink speed is expressed in the distance covered per message sent.

After a target is selected, the sink will obtain a packet of information for every time "x," which is the send-receive time for node-to-node communication. The default value of x used for all simulations was 40 milli-units of time. The sink sends out a message every x calling for the next packet of data, which is recursively sent down the link tree. Packets are sent back as long as the sink is within range of the node. Once the sink is no longer within range, a new target is selected using the target node selection algorithm.

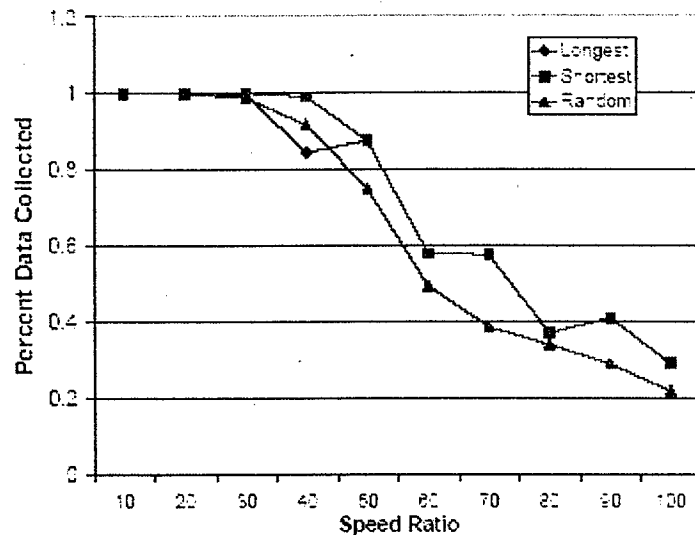


Figure 3. The percent data collected versus sink speed for each of the target node selection algorithms.

5. Results

We present the results of three design decisions when collecting data using a moving sink: how the moving sink determines with which nodes to communicate, how to minimize the number of messages sent while maximizing the amount of data collected, and, whether the sink path through the sensor field affects the system. We present results of optimizations that increase the amount of data collected.

We report our results as a ratio between the speed of the moving data collector to the message latency between sensor nodes. This ratio, not the absolute values of each, will determine how quickly the system must change.

5.1. Target Node Selection

We study three selection mechanisms for choosing the target node from among those nodes in communication range. The sink is assumed to have exponentially more computational power than the nodes, so the sink performs all of the calculations required for each algorithm.

A new target is selected every timer tick (1 unit of simulation time) that the previous target is no longer within communication range. Because the sink is computationally superior, we assume the decision can be made in less than the time to send a message from one node to another. Target selection is quite expensive because it changes the route messages will take, which leads to wasted messages going to the previous target node. Shortest and longest both keep track of how many timer ticks each of the current nodes in communication range have been in range; shortest selects the node that has been in range the fewest ticks, while longest selects the node that has been in range the most ticks. Random target selection randomly selects one of the nodes currently

in communication range.

Figure 3 shows the percent of data collected at different speed ratios with the three configurations. The average percent data collected for longest, shortest, and random is 70%, 71%, and 65% respectively. At higher speeds, longest and shortest both perform well, followed by random. In addition, longest and shortest perform similarly at both very high and very low speeds. It is not surprising that they all perform well at slow speeds - there is sufficient time to get all of the data regardless of the target node.

In order to gain insight into the mid-range and fast speeds, we gathered data on the overlap in nodes chosen between the three algorithms. Regardless of the speed ratio, shortest uses fewer target nodes than the others, so it always has the best performance. At high speeds, the target nodes for shortest are a subset of longest, so they get the same performance. Surprisingly, the set for random had little overlap with the others, even though the others have very different algorithms. Finally, in the mid-range, the longest does poorly at a certain speed ratio due to limited communication range of the nodes. As we increase the communication radius of the nodes, the poorly-performing point shifts to the right but never disappears.

Because shortest always performs as well or better than the longest and random, we will assume the shortest algorithm for the rest of our experiments.

5.2. Optimizing Data Gathering

When a moving sink switches target nodes, there are several efficiency problems. The messages that leaf nodes have sent but did not reach the initial target node may need to be either eliminated or re-routed. Additionally, data that was not collected may need to be retransmitted. We present two complementary techniques which decrease the number of messages in the network and increase the amount of data collected.

5.2.1 Reducing Redundant Messages

When the target node changes, nodes resend their data since the path to the target is different than before. To prevent redundant messages and increase the percent of the overall data that is collected, certain messages are excluded after having been received once. The question is, where do we drop these redundant messages? It is impractical, due to the limited memory of the nodes, for each node to keep track of all messages it has received from all originating nodes. Instead, we have nodes only keep track of messages that originated from neighboring nodes in the network. Figure 4 shows that even with this simple version of exclusion, average packets collected per node reduced from 2.41 to .73, and Figure 5 shows an increase of 19% in the percent data collected. This demonstrates how redundant messages were clogging the network, preventing unique messages from reaching the sink.

5.2.2 Data Forwarding

When a new target node is selected, messages in transit may not be routed to the

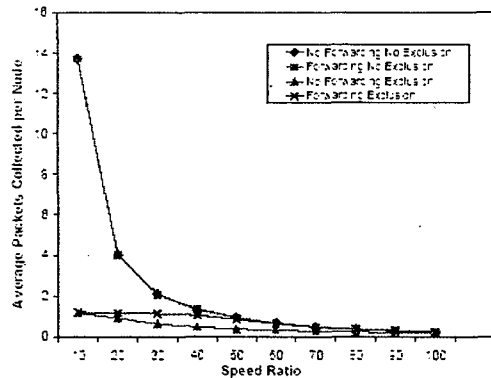


Figure 4. The average number of messages per node with the 4 possible configurations. Reducing redundant messages dramatically reduces the total messages in the system.

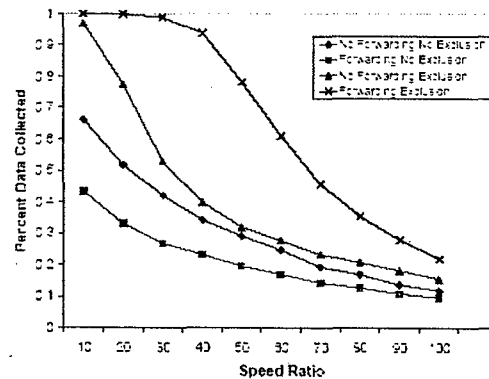


Figure 5. The percent of data received per node, varying data forwarding and message dropping.

new target node. If those messages are not re-routed, they need to be dropped to minimize the traffic through the network. Instead of dropping those messages, we can change the destination of the messages to the new target and continue routing those messages. The intuition is that the message is closer now than it was when it started, so this message forwarding will provide a net gain in data collected, even though there will be more messages total. In concert with the dropping of redundant messages, this becomes the most efficient way to get data to the target nodes.

Figure 5 shows that with data forwarding, we see a dramatic increase in the percent data received. Figure 4 shows that there is only a small increase in total messages - in fact, those are the very messages we needed. The average packets collected per node now follows very closely the percent data collected, so we must be receiving very close to one message per node that gets its data sent, as opposed to many messages from some nodes and none from others.

One interesting configuration is when we have forwarding but no redundant message removal. The percent of data collected actually decreases because those forwarded messages add to an already clogged system without successfully delivering their data.

5.3. Erratic Sink Path Effects

When deployed, it is unknown what path the sink will take. An airplane would take a very linear path, possibly making several passes very far apart in a large field. A smaller object might make more erratic movements. We chose several paths in order to discover whether less regular paths have a negative effect on data collection. We present the results from running multiple nonlinear paths in addition to the linear ones. Figure 7 depicts the three nonlinear paths tested: "L" shape, "U" shape, and a third resembling a "sawtooth."

Figure 6 shows that the U and sawtooth paths actually collect a higher amount of data than L and linear, simply because they are in the field longer. Instead of reducing the amount of data collected, erratic paths actually improve overall data collection because they cause the sink to stay in the field for a longer amount of time total, in some sense "slowing it down." When the time in the field is taken into account, all paths are efficient as long as not all of the data has been gathered. Once the speed is slow enough, the non-

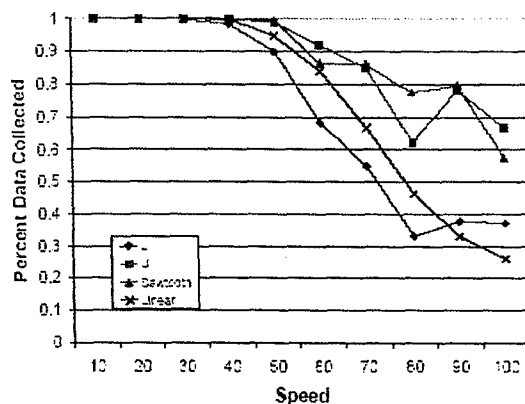


Figure 6. Percent packets collected per node vs. sink speed.

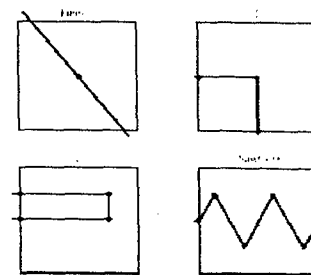


Figure 7. The four paths tested.

linear paths are less efficient because they spend more time in the field for no gain. Due to space limitations, we omit the figure.

6. Conclusion

Data retrieval from a wireless sensor network is a challenging task when the data collector (sink) is moving at high speed. In this work, we look at how the sink should choose a target node for communication, how the data should be routed to the sink in order to maximize the amount of data collected, and how the sink path affects data retrieval.

We find that routing data towards the node that has most recently entered the communication range of the sink produces good results. Selecting the least recent or a random target node did not perform as well, especially for larger communication radii. For the process of actually sending the data, a combination of incremental message forwarding and redundant message exclusion collects 35% more data on average. We find these two techniques to be necessary and complementary. We find exclusion alone only collected 19% more data than the baseline and forwarding collected 10% less data.

Finally, we show that the effectiveness of this algorithm does not depend on the path taken through the field. While any path that is in the field for a longer period of time collects more data, results that were normalized for time spent on the field performed almost equally. Variations in the percent of data collected were within 3% on average, with a maximum of 8%.

References

- [1] The manatee project. <http://www.distlab.dk/manatee>.
- [2] The wizzy project. <http://www.wizzy.org.za/>.
- [3] K. Fall. A delay-tolerant network architecture for challenged internets. In *SIGCOMM '03: Proceedings of the 2003 conference on Applications, technologies, architectures, and protocols for computer communications*, pages 27–34. ACM Press, 2003.
- [4] C. Intanagonwiwat. Impact of network density on data aggregation in wireless sensor networks. In *International Conference on Distributed Computing Systems (ICDCS-22)*, November.
- [5] Intuicom. Urban seismic monitoring network, 2004.
- [6] S. Jain, R. C. Shah, G. Borriello, W. Brunette, and S. Roy. Exploiting Mobility for Energy Efficient Data Collection in Sensor Networks. In *WiOpt*, March 2004.
- [7] P. Juang, H. Oki, Y. Wang, M. Martonosi, L.-S. Peh, and D. Rubenstein. Energy-efficient computing for wildlife tracking: Design tradeoffs and early experiences with zebranet. In *Architectural Support for Programming Languages and Operating Systems, ASPLOS-X*, 2002.
- [8] B. Krishnamachari, D. Estrin, and S. Wicker. Impact of data aggregation in wireless sensor networks. In *Workshop on Distributed Event-Based Systems, DEBS'02*, 2002.
- [9] S. Madden, M. Franklin, J. Hellerstein, and W. Hong. Tag: a tiny aggregation service for ad-hoc sensor networks. In *Symposium on Operating Systems Design and Implementation, OSDI 02*, 2002.
- [10] F. Ye, A. Chen, S. Lu, and L. Zhang. A scalable solution to minimum cost forwarding in large scale sensor networks. In *International Conference on Computer Communications and Networks, ICCCN 2001*, 2001.

**Investigation of Efficiency Improvement in
High-Density Light-Weight DC-DC Converter**

Project Investigator:

Taufik
Associate Professor
Electrical Engineering Department
Cal Poly State University, San Luis Obispo

Executive Summary

Power Electronics is an enabling technology which deals with conversion of electrical energy from one form to another in the most efficient manner. Power Electronic technology encompasses a broad spectrum of applications from the high power transmission controllers to low power dc distribution in hand-held or portable devices.

In the low power domain, more battery-operated electronic systems are becoming more popular than ever before. Hence, the market's shift toward portability and mobility will have far reaching effects on electronic power converter design. With more compact system enclosures, board-level designs become denser. Battery operation demands that the system consume less power to extend the life of the battery. Besides consumer electronics, the thirst for reducing the size of overall products or system with improved efficiency has also been demanded from other electronic industries such as defense, avionics, automotive and aerospace. It is therefore not surprising to observe a growing need for light-weight, high-efficiency and high power density dc-dc converters which is able to support energy-efficient, compact and reliable power conversion systems.

A growing demand for size and weight reduction of portable and on-board power modules has stimulated substantial development and research efforts in high-density, low-profile power supplies. The converters are small and lightweight, facilitating decentralized packaging. They can be PC-Board mounted near the load or installed in a centrally located, multiple output power supply. Their high-efficiency operation conserves power and simplifies thermal design, while delivering tightly regulated DC power under dynamic line and load conditions. The design of high-density, low-profile power supplies typically involves circuit topologies, high switching-frequency operations, magnetic designs, and component selection.

This project proposed an investigation of efficiency improvement in high-density dc-dc converters. In conducting the study, as many as five undergraduate students were involved and each performed a different task. One of the keys in improving any electric circuits, especially of a higher power level is to look into what makes up the circuit, i.e. circuit components. In the high switching frequency environment such that found in high-density converters, the selection of main components can be quite tricky and its driving equations for efficiency may become complex. Based on this observation, the main task of this investigation is to identify critical components in the high-density dc-dc converter under study. Once all the main components which significantly contribute losses to the system have been identified, then a more thorough investigation would have to follow. This part of the task is required to come up with a strategy of component selection that would yield the least amount of power dissipation. To recap, the following is the break down of the task in doing this investigation:

1. Identify "efficiency-sensitive" components
2. Analysis of efficiency equation for every component found in the previous task
3. Model the power loss using Pspice Circuit simulation or MathCAD
4. Provide suggestions on important parameters when selecting the critical components
5. Acquire alternative components to prove the predictions

6. Test and measure new efficiency with the alternative components and compare results to the efficiency obtained from the original components

Since we were using off-the-shelf high-density dc-dc converters, the major challenge in doing this project was to make modifications onto the circuit board, i.e. to replace original component with the alternatives. Hence, in addition to the analytical skill, students felt they have improved their soldering skill as well.

Another key element for improving efficiency is by looking at how the circuit is operated. One student investigated the effect of changing the switching frequency operation of the dc-dc converter to its efficiency. We found that indeed a careful selection of switching frequency would definitely impact overall efficiency of the converter.

To recap, here are the summary of the results of this study:

1. Selection of switch is important in improving the efficiency of high-density dc-dc converters. At higher switching frequency operation, the switching loss contributes most in its loss due to output capacitance of the switch. However, at higher power, the on resistance of the switch will play the major role. Combination of both operations requires careful consideration of the efficiency calculation. The task of placing different switches (MOSFET) was done, and the results show improvement and worsening of the overall efficiency.
2. Selection of main inductor as the energy storage was found to be crucial as well. The main factor in inductor loss is coming from its copper loss. Since this loss is calculated from the rms current flowing through this inductor, therefore a trade-off between lower ripple current and high inductance value (bigger inductor) will have to be dealt with. At high power, the reduction of inductor loss was found to be achievable by introducing parallel winding configurations such as Bifilar and even Trifilar. The use of high quality core is also helpful in improving the overall efficiency of the dc-dc converter. Investigations using several winding configurations along with different cores were conducted and results are presented in this report.
3. Selection of output capacitor is similar to that of inductor. The widely known Equivalent Series Resistance of capacitors contributes significantly to power dissipated in capacitor. Hence strategy such as placing capacitors in parallel will be beneficial since it will enlarge the capacitance value while at the same time suppressing the ESR effect. In addition, different types of capacitor were also investigated. The results show that careful selection of capacitors will improve efficiency.
4. Output Rectifiers plays a major role in power loss in dc-dc converter. This is due to the forward drop that occurs in practical diodes. At high power, this is especially of concern since the product of forward voltage and high forward current would result in high power loss. Therefore, in addition to finding the faster diode, a very important step in selecting diodes is to look through their parameters and predict their power losses.
5. Switching Frequency operation was investigated since in real circuits, we are dealing with stray inductance and stray capacitance. Circuit components may behave 'strangely' at certain frequency. The result of this task shows that the use of different switching frequency can be either advantageous or harmful to the overall efficiency of the converter. The analytical approach to improving efficiency from this angle is to look at the dc-dc converter as a whole

system where we determine complete sets of efficiency equations for all the major parts in the circuit.

This study has been a very challenging and educative experience for the many individuals involved in the project. However, it does not stop here. As many of our EE students are becoming more attracted to power electronics, future internal and external supports will be sought to extend power electronic lab capability to accommodate more student projects in high-density dc-dc converters.

Introduction

With more battery-operated electronic systems than ever before, the market's shift toward portability and mobility will have far reaching effects on electronic power converter design. With more compact system enclosures, board-level designs become denser. Battery operation demands that the system consume less power to extend the life of the battery. Besides consumer electronics, the thirst for reducing the size of overall products or system with improved efficiency has also been demanded from other electronic industries such as defense, avionics, automotive and aerospace. It is therefore not surprising to observe a growing need for light-weight, high-efficiency and high power density dc-dc converters which is able to support energy-efficient, compact and reliable power conversion systems [1].

A growing demand for size and weight reduction of portable and on-board power modules has stimulated substantial development and research efforts in high-density, low-profile power supplies. The converters are small and lightweight, facilitating decentralized packaging. They can be PC-Board mounted near the load or installed in a centrally located, multiple output power supply. Their high-efficiency operation conserves power and simplifies thermal design, while delivering tightly regulated DC power under dynamic line and load conditions. The design of high-density, low-profile power supplies typically involves circuit topologies, high switching-frequency operations, magnetic designs, and component selection.

A major advancement of high density converter was set forward by Vicor in the 1980's. A dc-dc converter module was launched by Vicor where the unit was only ½" thick for a 200 W converter, while running at 1 MHz at full load, with higher efficiencies than any other converters of the time running at lower frequencies of 100 kHz.

Series of research efforts then followed Vicor's wake up call and several examples are worth mentioning here. The Strategic Defense Initiative by the Air Force and NASA has initiated an interagency program to develop a 0.1-kg/kW dc-dc converter technology base [2]. The dc-dc converter will be used for power-conditioning to enable the megawatt-power-level space systems while significantly reducing its weight. Rockwell Collins and Rockwell Science Center have teamed with the Office of Naval Research (ONR) to develop high density, high efficiency, and programmable dc-dc converters for both military and commercial applications [3]. The program aims at the development of two 100W dc-dc converter modules that run off a 50V dc bus and provide 3.3 V and 1.5 V outputs, respectively, at 90-95% efficiency, and with a power density at or higher than 100 W/in³. Another example was reported in [4], where the development of a very

high power density dc-dc converter module for automotive applications was investigated. The 14V/42V converter is specified to operate at a power level of 2.1kW with a water cooled heat sink at 85°C and achieved a final power density of 170 W/in³.

The most recent high density converters are a result of a series of technological improvements for power devices and components over the last 40 years. The milestones in technology steps are listed below:

- High power bipolar devices
- FET devices
- Integrated board magnetics
- Zero-current resonant switching
- Zero-voltage resonant switching
- High-density capacitors
- Low-voltage drop and low-cost synchronous rectification
- New packaging techniques
- New controller techniques

Numerous researches have been done on each of the above listed subject to improve the performance of power converters. However, only a few have been widely accepted by the power electronics industry. Therefore, the next logical step in the development of high-density, light-weight converters will be to investigate the availability and implementation of any of the above recent accomplishment to an existing and marketed dc-dc converter product. This is also important since a fully operational proof-of-concept new technology adaptation into an existing converter module will trigger wider acceptances of these new technologies in the power electronics industry.

A high-density power converter implies high efficiency operation. This means for the same amount of output power, a smaller power converter will be needed since the converter will dissipate less heat, i.e. power losses. A smaller converter implies a more compact power distribution system which eventually leads to a lighter power source. The topic of light-weight power sources has been part of the area of research topic at the ONR Science and Technology Departments. In addition, the proposed investigation will not only attract students in participating in real-world design projects, but it will also generate interaction with local power industry and future collaboration. Therefore, the proposed project indeed relates closely to the technology park initiative and areas of focus or emphasis.

Results

The results of this project will be described in this section and will be organized into the following sub-sections:

1. Impact of Switching Frequency selection to overall efficiency
2. Impact of MOSFET and Inductor Design selections to overall efficiency
3. Impact of Output Capacitor selection to overall efficiency

1. Impact of Switching Frequency

1.a. Background

This project entails the investigation of efficiency improvement in high-density, light-weight 3.3 V 165 W dc-dc converter module. Five areas were chosen for the impact on efficiency performance: switching frequency, power diode, power switch selection, inductor design, and output capacitor. This section emphasized on the impact of switching frequency to the efficiency of dc-dc converter. Results showing converter's performance based on design calculations from computer simulations, and actual lab measurements will be presented.

The forward converter shown in Figure 1 is one of the most studied topologies. Derived from the simple buck converter, the forward converter delivers energy from the input source to the output filter inductor during the on time of the main switch. The single switch forward converter shown in Figure 9 is used for power levels between 100 W and 500W. The advantage of this topology is it provides good cross regulation with coupled inductor. The cost of this topology is moderate compare to other topologies.

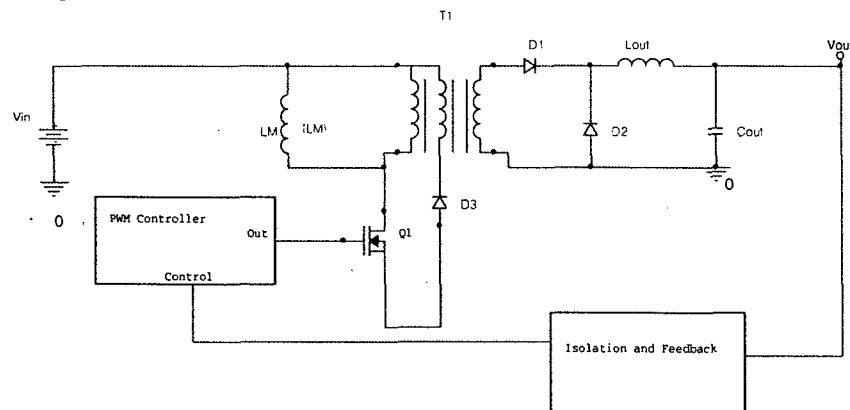


Figure 1. Single Switch Forward Converter

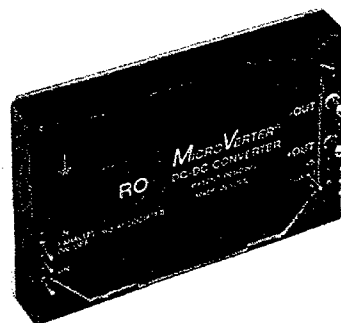


Figure 2. MicroVerter DC-DC Converter [5]

The single switch forward converter is the most elementary form of transformer-isolated buck converter. It is typically used in off-line applications in the 100–300 watt region. A simplified schematic of a single switch forward converter can be seen in Figure 3.

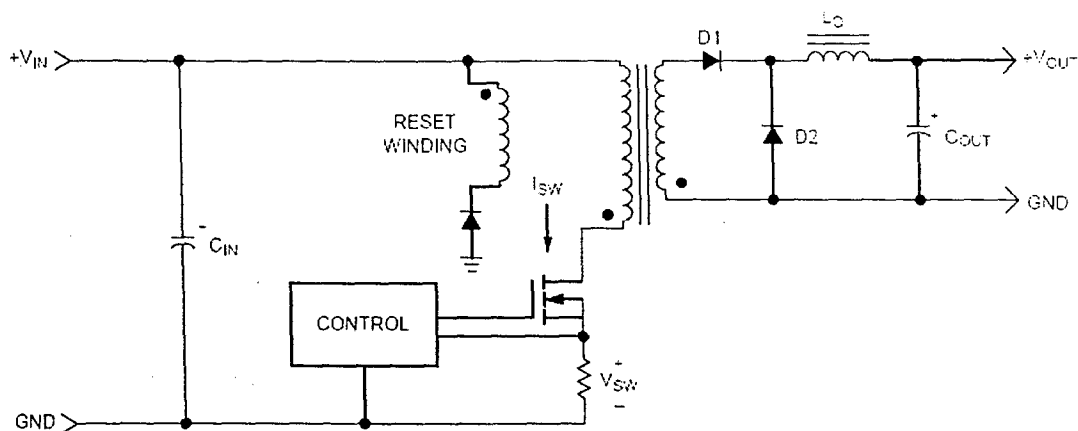


Figure 3. Simplified Schematic of a single switch Forward Converter

In a single switch forward converter, there is a transformer between the input voltage and a buck converter output stage. The power switch (SW) is used to create a rectangular voltage waveform whose amplitude is the input voltage and its duty cycle is the controllable variable. The transformer provides both a step-up or down function and a safety dielectric isolation between the input line and the output load. The major restriction of this topology is the maximum duty cycle must be about 50 percent. Whenever a core is driven in a unidirectional fashion, that is, current only being driven from one direction into the primary, the core must be *reset*. Magnetization energy which serves only to reorient the magnetic domains within the core must be emptied, or else the core will “walk-up” to saturation after a few cycles. Resetting is done by drawing current from a winding during the period when the transformer is unloaded, that is, when the power switch and rectifiers are not conducting. Any winding can provide the reset function, but the higher the voltage on the winding, the quicker the core will reset. Typically, this is the primary winding or a separate reset winding of equal turns to the primary. Current from the reset winding can then be returned to the input capacitor and reused during the next cycle of operation. When the power switch is ON, the switch sees the output filter inductor’s current reflected by through the transformer. The amplitude of the primary current is the output rectifier current times turns ratio of the transformer (N_1/N_2) plus a small amount of magnetization current. During the power switch OFF time, the switch voltage is about twice the input voltage. During this time, the reset winding begins to output magnetization current back to the input capacitor. The output rectification and filter section works identically to the buck converter. The voltage waveform of secondary looks like an inverted primary winding waveform except the zero voltage point is the input voltage point on the primary waveform. The waveform goes positive when the power switch is conducting. The output rectifier also conducts during this time. This presents a unipolar, PWM rectangular voltage signal to the inductor, just as found in a typical buck converter. The diode then operates when the power switch and the output rectifier are OFF. Continuous current is then maintained through the output filter inductor.

1.b. Design/Calculations

For this project, RO’s MicroVerter28V-3 ($\mu V28-3$) (Fig. 2) was used. The summary of specifications of the converter was shown in Table 1. This specific converter is high density

(38W/in³) [5]. Also the maximum efficiency of the MicroVerter28V-3 is 80% as shown in Figure 4.

Table 1: MicroVerter Converter Specifications

		Min	Typical	Max	Units
INPUT	Input Voltage	20	28	32	VDC
OUTPUT	Output Voltage	--	3.3	--	VDC
	Output Current	--	50	--	A
THERMAL	Operating temperature	-40		+100	°C

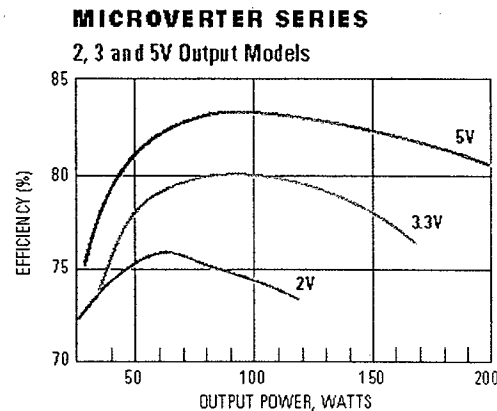


Figure 4. Efficiency Curve for MicroVerter Converter [5]

MathCAD calculations below show efficiency calculation for a single-switch forward converter, 3.3 V 162 W. The calculation contains most main sources of losses but neglects several loss calculations such as those coming from core losses of transformers (main and current sensing if any), snubber circuit, etc. After selecting maximum and minimum duty cycles, the respective duty cycles are calculated assuming linear relationship with the percent load current. Operating conditions such as nominal input and the percent load current are determined from the MicroVerter's datasheet specifications (See Table 1). The turns ratio of the transformer is determined by measuring the inductance of both primary and secondary side of the transformer

and using the relationship of $\left(\frac{N_s}{N_p}\right)^2 = \frac{L_p}{L_s}$. Losses calculations on MOSFET, Diodes, etc. are calculated using the manufacturer's datasheet and Switching Power Supply Design notes [6].

MathCAD Equations

Efficiency Calculations as a function of Switching Frequency

Maximum Output Power: $P_{\text{max}} := 165\text{W}$
 Nominal Output Voltage: $V_{\text{nom}} := 3.3\text{V}$
 Nominal Input Voltage: $V_{\text{in}} := 28\text{V}$
 Transformer Turns Ratio (N_s/N_p): $N := \frac{1}{7}$
 Nominal Input Current: $I_{\text{nominal}} := 50\text{A}$

Definitions

$\text{m}\Omega := 1 \cdot 10^{-3} \Omega$
 $\text{ns} := 1 \cdot 10^{-9} \text{s}$
 $\text{nC} := 1 \cdot 10^{-9} \text{C}$
 $\text{mW} := 1 \cdot 10^{-3} \text{W}$
 $\mu\text{s} := 1 \cdot 10^{-6} \text{s}$
 $\text{mJ} := 1 \cdot 10^{-3} \text{J}$

Load% :=	(10)	Dcycle :=	(0.236)
	15		.275
	20		.319
	25		.355
	30		.379
	35		.416
	40		.422
	45		.426
	50		.426
	55		.433
	60		.434
	65		.439
	70		.442
	75		.448
	80		.449
	85		.452
	90		.456
	95		.461
	100		.465

$D_{\text{nom}} := 0.48$
 $n := 0..18$

$$I_{o_n} := \left(\frac{P_{\text{max}}}{V_{\text{nom}}} \cdot \frac{\text{Load\%}_n}{100} \right)$$

$F_{\text{sw}} := 370\text{kHz}$

$F_{\text{sw}} := 370\text{kHz}$

$P_{o_n} := V_{\text{nom}} \cdot I_{o_n}$

$P_{o_n} := V_{\text{nom}} \cdot I_{o_n}$

$\eta := 0.7$

$$Pin_n := \frac{Po_n}{\eta}$$

$$I_{in_{nom}} := \frac{Pin_n}{Vin_{om} D_{cycle}_n}$$

Output Rectifiers

82CNQ030

$$V_{fwd} := 0.55V$$

$$C_j := 1400pF$$

$$I_r := 500\mu A$$

$$P_{rec}_n := I_{o_n} \cdot V_{fwd} + C_j \cdot V_{on_{om}}^2 \cdot F_{sw} + C_j (V_{in_{om}} N)^2 \cdot F_{sw} + I_r \cdot V_{on_{om}} \cdot D_{nom} + I_r \cdot V_{in_{om}} N \cdot (1 - D_{cycle}_n)$$

Reset Diode

MURD620

$$I_{r_{ww}} := 5\mu A$$

$$C_t := 12pF$$

$$P_{res_{dio}}_n := 2 \left(I_r \cdot V_{in_{om}} D_{cycle}_n + C_t \cdot V_{in_{om}}^2 \cdot F_{sw} \right)$$

MOSFET

IRF3710

$$Q_g := 130nC$$

$$C_{oss} := 410pF$$

$$R_{dson} := 230m\Omega$$

$$T_r := 58ns$$

$$T_f := 47ns$$

$$P_{gd} := Q_g \cdot 12V \cdot F_{sw}$$

$$P_{sw}_n := 0.25 I_{in_{nom}} \cdot V_{in_{om}} (T_f + T_r) F_{sw} + 0.5 C_{oss} \cdot V_{in_{om}}^2 \cdot F_{sw}$$

$$P_{cond}_n := (I_{in_{nom}})^2 \cdot R_{dson} \cdot D_{cycle}_n$$

$$P_{mos}_n := (P_{gd} + P_{sw}_n + P_{cond}_n)$$

Control

$$V_{bias} := 12V$$

$$I_{mic3843} := 17mA$$

Efficiency

$$P_{outloss_n} := Prec_n$$

$$P_{inloss_n} := Presdio_n + P_{mos_n}$$

$$P_{totloss_n} := P_{outloss_n} + P_{inloss_n} + P_{control}$$

$$P_{totout_n} := P_{totloss_n} + P_{o_n}$$

$$P_{total_n} := Prec_n + Presdio_n + P_{mos_n} + P_{control}$$

$$\eta_n := \frac{P_{o_n}}{P_{o_n} + P_{total_n}}$$

EFFICIENCY VS. LOAD CURRENT% AT DIFFERENT SWITCHING FREQUENCIES

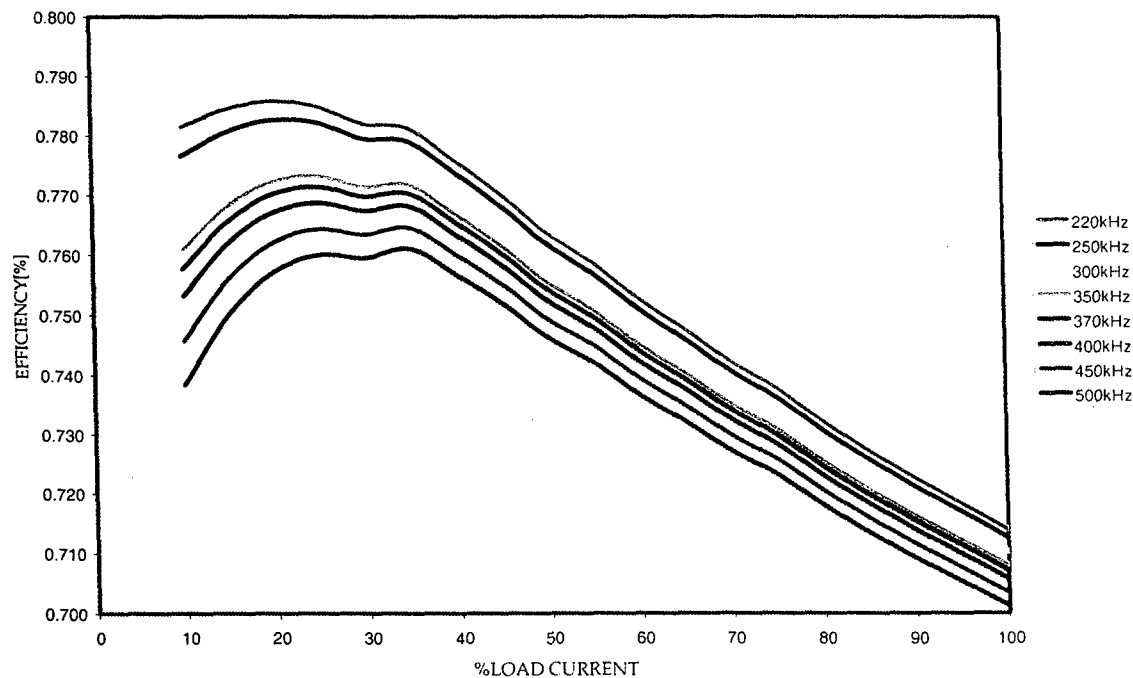


Figure 5. Efficiency Curves for Different Switching Frequencies using MathCAD

From the MathCAD calculations, the efficiency decreases as the switching frequency increases. At 10% load, the efficiency difference is about 4.5% between 220 kHz and 500 kHz. At full load, the efficiency difference is about 1.5% between 220 kHz and 500 kHz.

1.c. Simulation Results

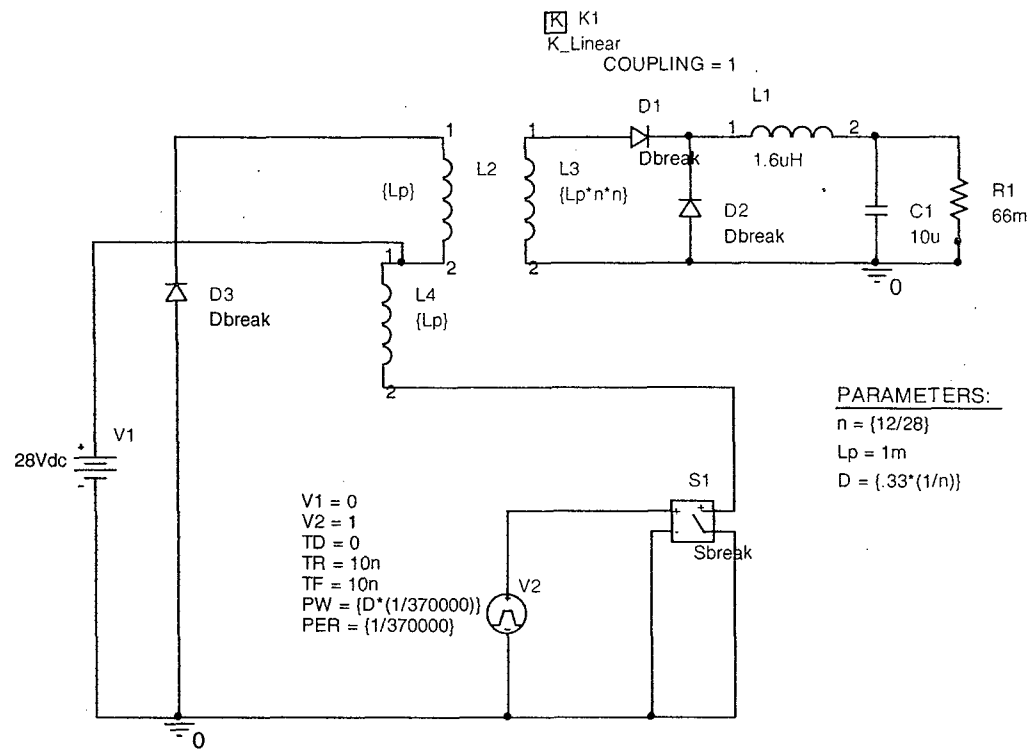


Figure 6. Single Switch Forward Converter with Ideal Components

The single switch forward converter shown in Figure 15 is modeled in OrCAD Capture. The converter is first modeled with ideal switch, Sbreak, and no feedback loop.

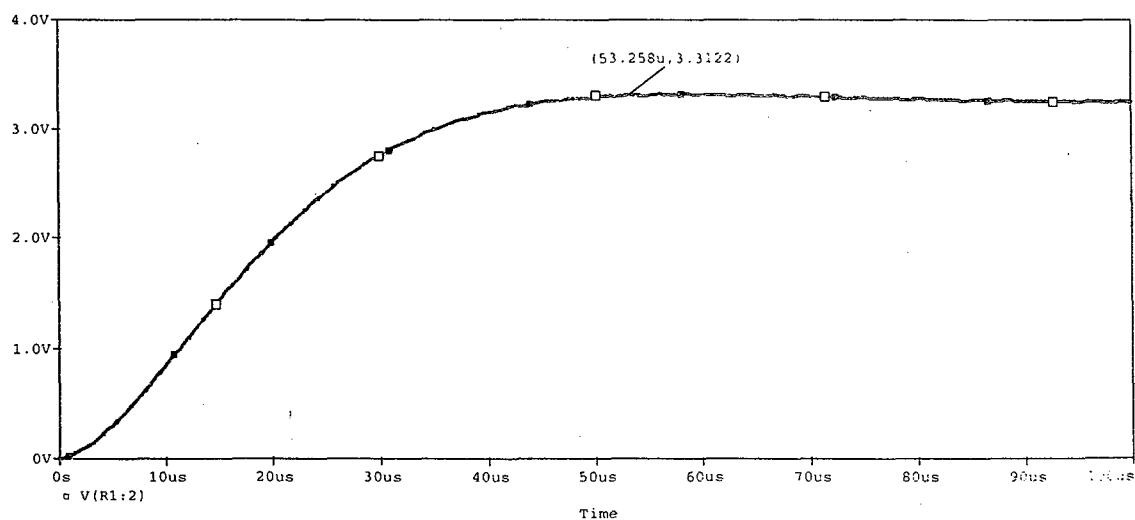


Figure 7. Output Voltage Waveform for Single Switch Forward Converter with Ideal Components

The output voltage waveform from the simulation is shown in Figure 7. The output voltage at steady state (after 50 μ s) is 3.3122 V. Since the nominal output is 3.3 V, the percent difference is less than 1%.

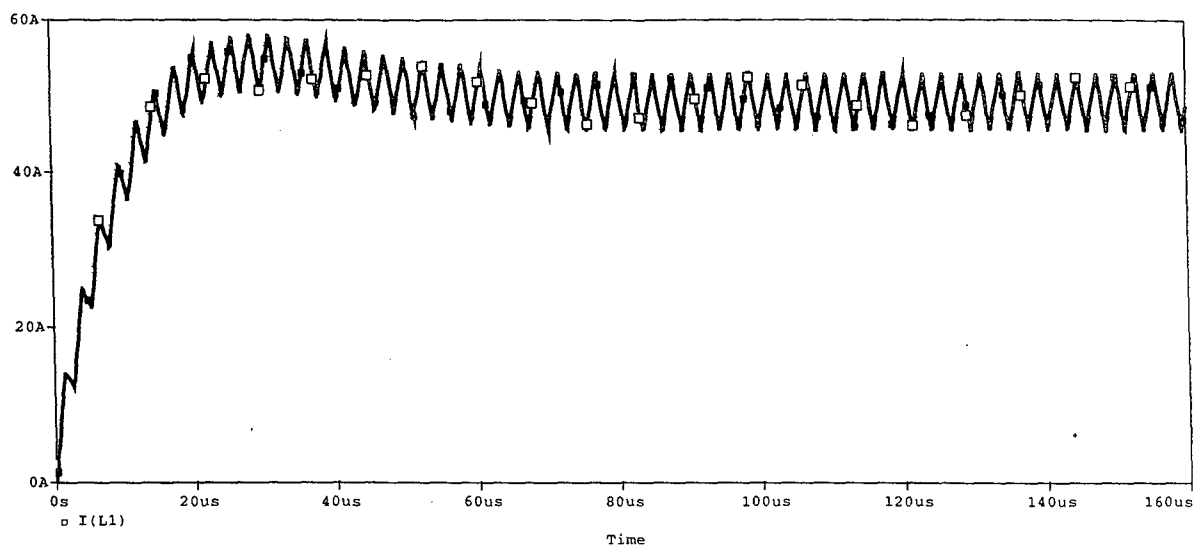


Figure 8. Inductor Current Waveform for Single Switch Forward Converter with Ideal Components

Figure 8 shows the inductor current with its ripple. From the simulation, the peak to peak ripple current of the inductor is about 10A.

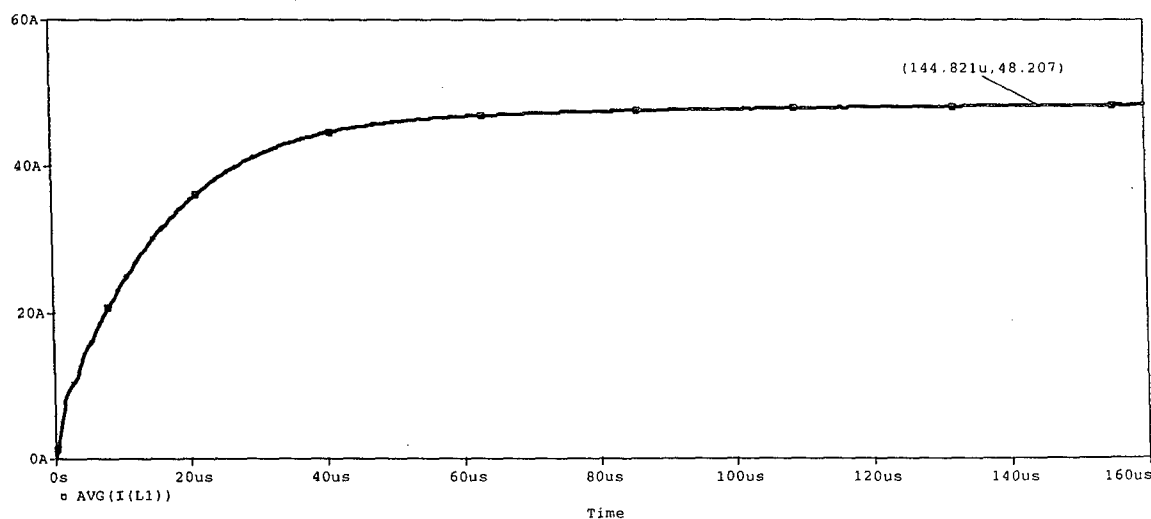


Figure 9. Average Inductor Current Waveform for Single Switch Forward Converter with Ideal Components

From Figure 9, the average inductor current for single switch forward converter with ideal components is 48.207 A. The nominal full load current is 50 A. The percent difference is about 3.6%.

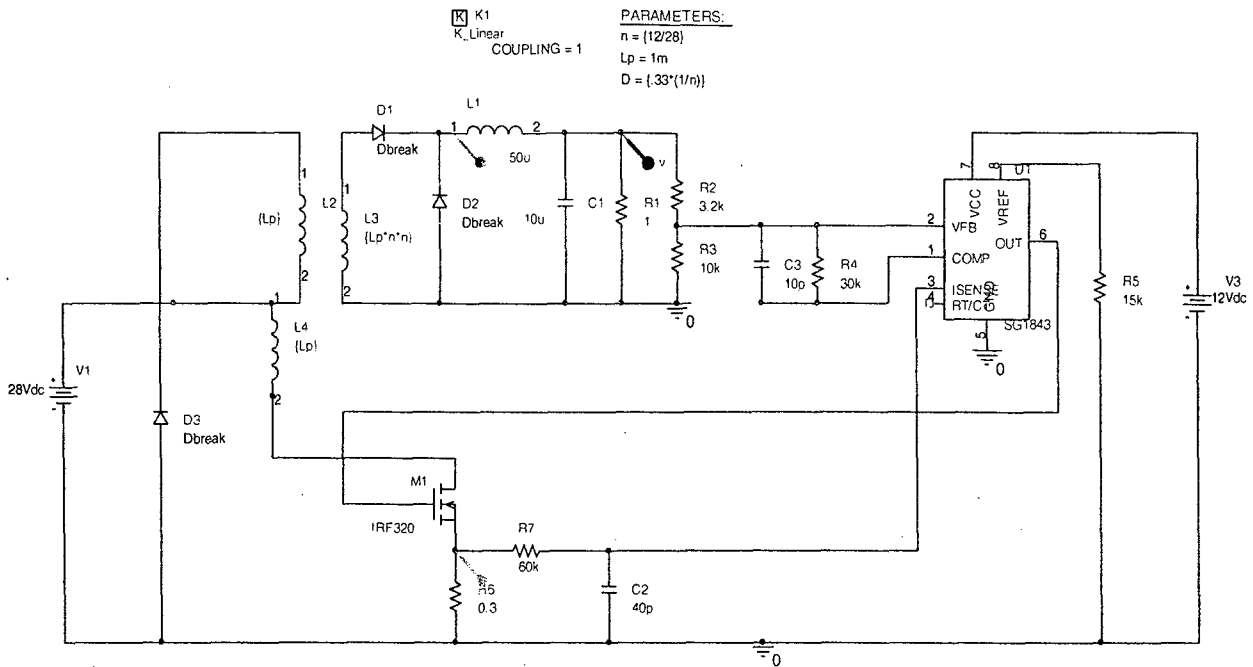


Figure 10: Single Switch Forward Converter with PWM and MOSFET

The single switch forward converter shown in Figure 10 is modeled in OrCAD Capture. The converter is modeled PWM, MOSFET, and feedback loop. The PWM model is SG1843, voltage controlled PWM. The MOSFET is IRF320.

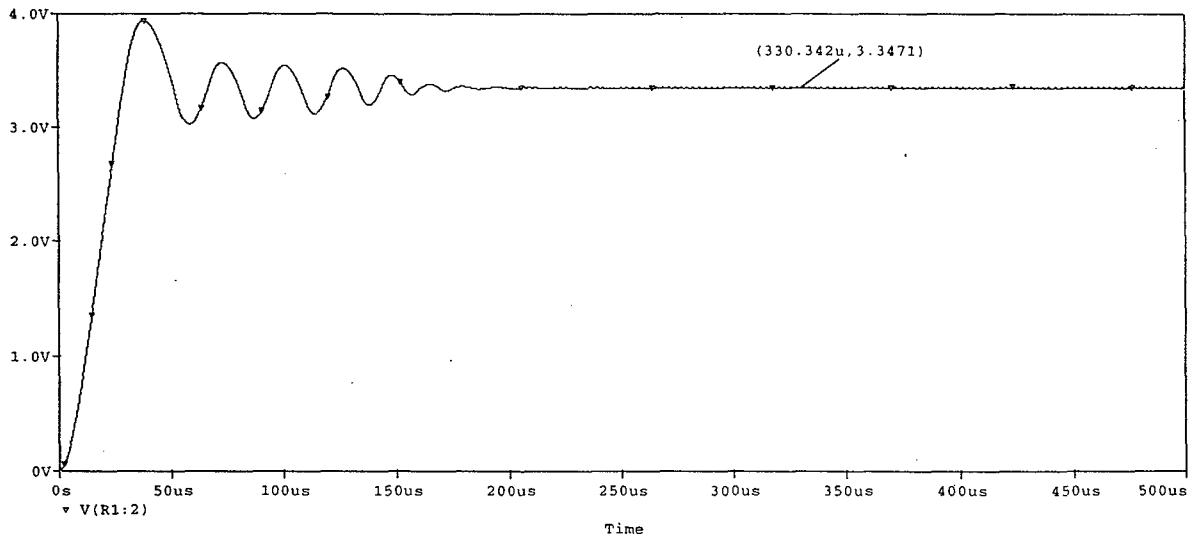


Figure 11. Output Voltage Waveform for Single Switch Forward Converter with PWM and MOSFET

The output voltage waveform from the simulation with feedback loop is shown in Figure 11. The output voltage at steady state (after 200us) is 3.3471 V. Since the nominal output is 3.3V, the percent difference is 1.4%.

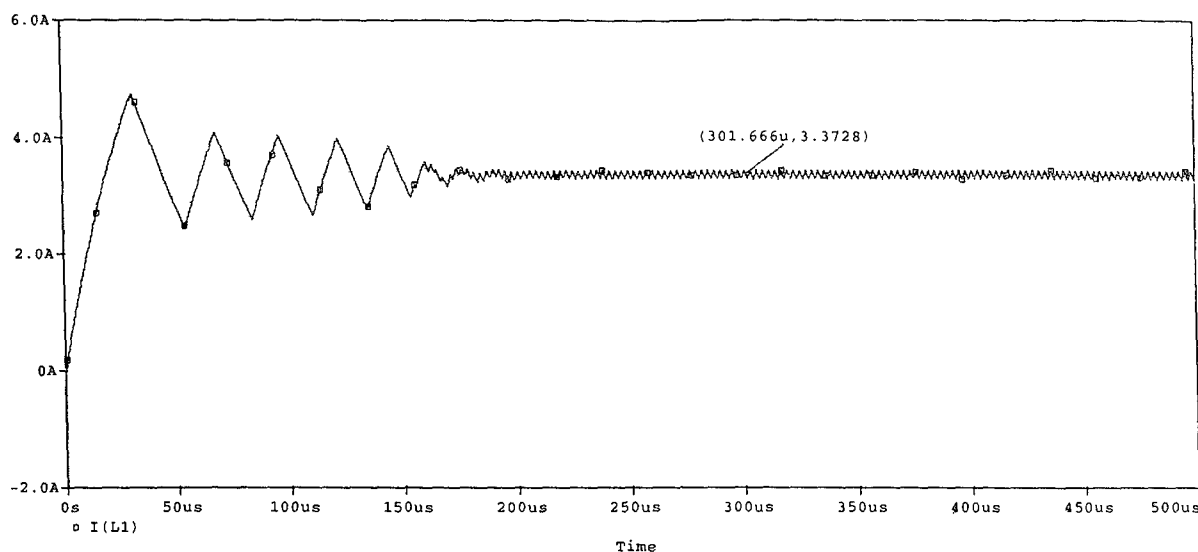


Figure 12. Inductor Current Waveform for Single Switch Forward Converter with PWM and MOSFET

From Figure 12, the average inductor current for single switch forward converter with ideal components is 3.3728 A.

1.d. Empirical Data

The dc converter was carefully unpotted. Then, the controller chip and its timing capacitor and resistor were located. The dc converter was put under testing before making any changes, and the results were recorded. Then, the timing resistor and capacitor were removed from the board and measured. The controller used was 38HC43 of Micrel.

Switching Frequency was determined by Capacitor and Resistor connected to Pin 7 of the controller. (RT/CT pin) Timing Capacitor was 1.1 nF, timing Resistor was 2.26 k Ω , and switching frequency was 370 kHz. Switching frequency can be varied by changing the combination of timing capacitor and resistor. The range of switching frequencies to investigate was from 200 kHz to 700 kHz.

As seen from the following Figure 13, efficiency of the forward converter decreases as the switching frequency is increased from 202 kHz to 704 kHz by changing the timing resistor and capacitor. The decrease in efficiency is more significant in light loads. At 10% load, the efficiency is 73% for 202 kHz switching frequency and 54% for 704 kHz switching frequency. The difference in efficiency is 20%, very significant. At full load, the efficiency is 74.1% for 202 kHz switching frequency and 72% for 704 kHz switching frequency. For full load, the difference is only 2%.

EFFICIENCY VS. LOAD CURRENT% AT DIFFERENT SWITCHING FREQUENCIES

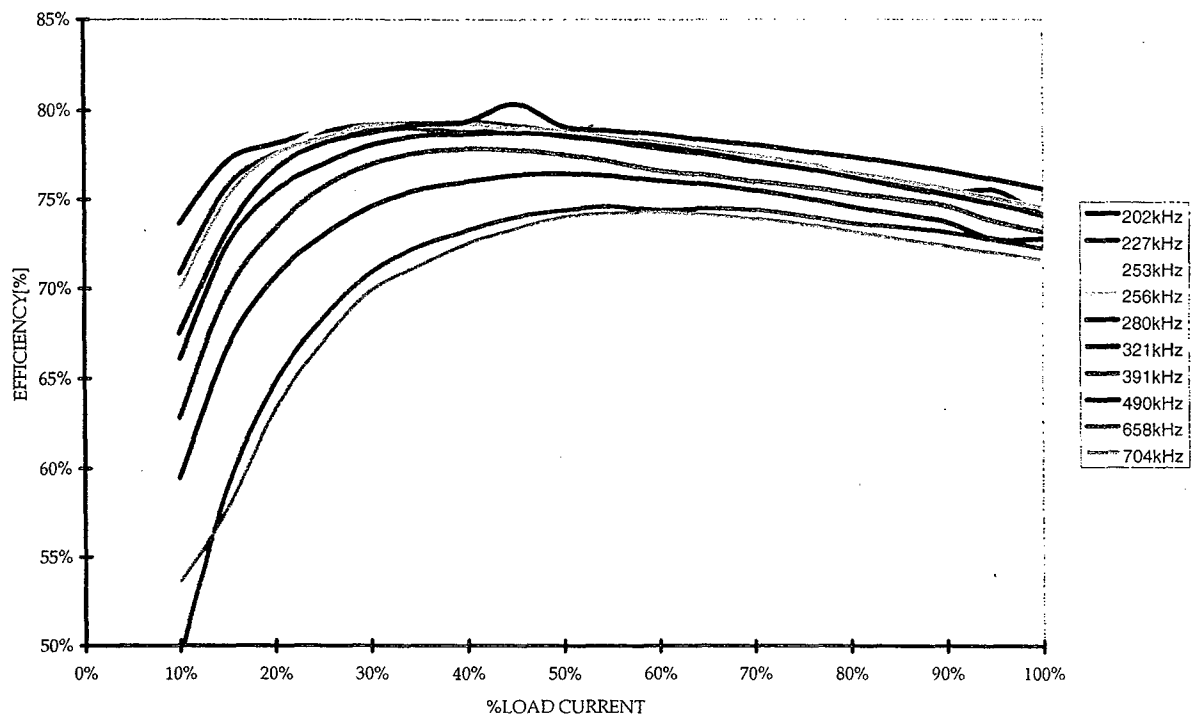


Figure 13: Efficiency curves for different switching frequencies from test data.

2. Impact of Power MOSFET and Power Inductor Selections

This section is about the characteristics and properties of a Single Switch DC-DC forward converter, particularly the effects that the switch and output inductor have on the converter's overall efficiency. The converter used is the μ V28 Microverter -3 model produced by RO Associates. This section also reports the conduction losses involved with the inductor and the switch, and how it affects the efficiency.

2.a. Background

The efficiency of any product is an important factor that many consumers look into before making a wise purchase. The μ V28 Microverter series produced by RO Associates are high density DC-DC converters that have several features, some of which are its miniature size, high density of about 58 Watts per cubic inches, low thermal resistance, and short circuit protection [5]. These converters are better used for high power applications. Some of which are for telecom and switch mode power supplies found in computers, television sets and other electronic equipment. The high voltages are stepped down to a voltage low enough to be useful to run say, a computer. This paper will study the μ V28-3 model that has an output voltage of 3.3 V and an output current of 50 A. The MicroVerter μ V28-3 model is a forward converter that is known to have a maximum efficiency of only eighty percent, when an efficiency of close to one

hundred percent is more desirable. The efficiency curve of the μ V28-3 model, which has an output voltage of 3.3 V, is shown again below in Figure 14.

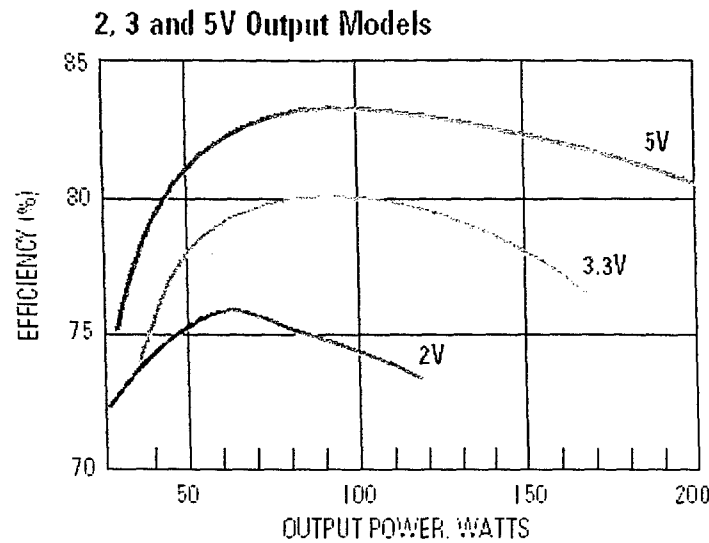


Figure 14. Efficiency Plot of the three MicroVerter DC-DC Converters [5]

The forward, shown in Figure 15, is usually compared to the flyback, shown in Figure 16, due to their similar functions as isolated DC-DC converters. However, one difference between the two converters is that the forward has an output inductor in its circuitry.

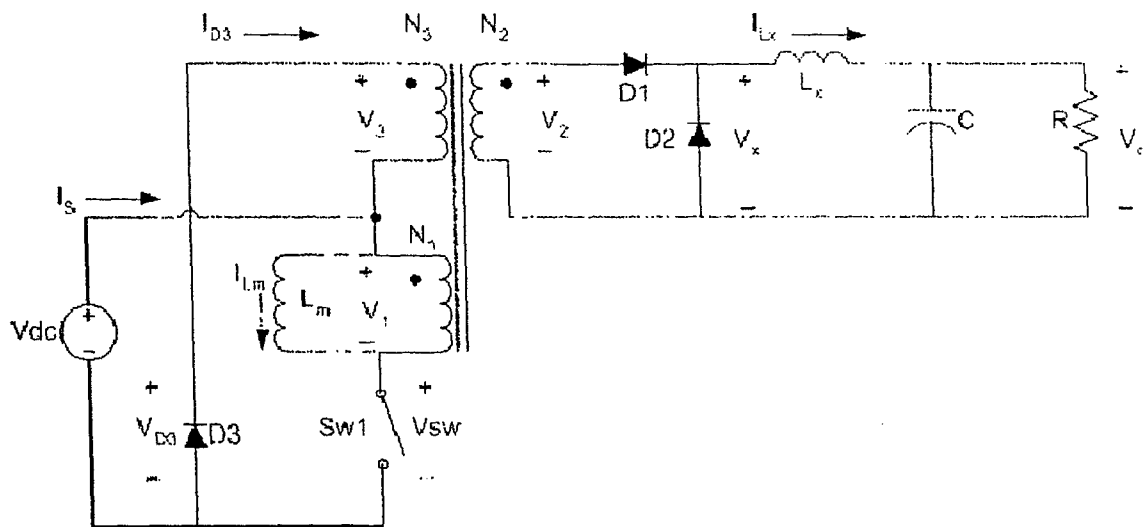


Figure 15. Topology of the Forward Converter [7]

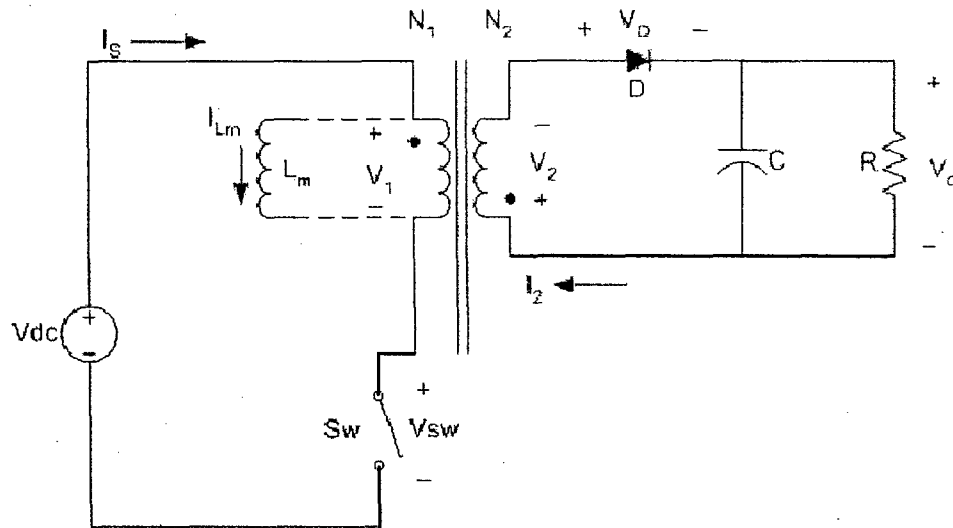


Figure 16. Topology of the Flyback Converter [7]

Not only is the output inductor used to filter out noise and lessen output ripple, it is important in determining the conduction mode of the converter. The minimum inductance of the output inductor is calculated and used to ensure that the converter is operating in continuous conduction mode, meaning the inductor current does not go to zero amps as shown in Figure 17. If the value of the output inductor is less than the minimum required inductance, then the converter will go into discontinuous conduction mode, which may not be desired.

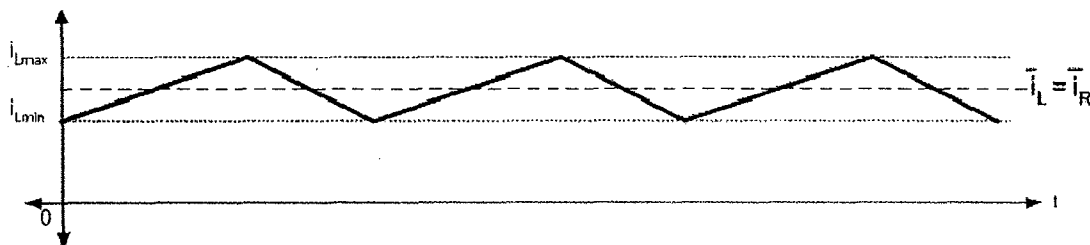


Figure 17. Inductor Current in Continuous Conduction Mode [7]

There are two main types of materials that are used for toroid inductor cores, powder iron cores and ferrite cores. The output inductor in the MicroVerter μ V28-3 model uses a powder iron core. Powder iron cores are better than ferrite cores because "powder cores do not saturate easily and have high temperature stability" [9]. Despite the fact that ferrite cores have high permeability, they saturate easily and become unstable at higher temperatures [9]. Although the powder iron core is more suitable for the MicroVerter μ V28-3 model because its operating temperature may reach one hundred degrees Celsius, the majority of powder iron cores are prone to significant core losses. This occurs when they are exposed to extreme temperatures for long periods of time, which can contribute to a decrease in efficiency [10]. Therefore, certain characteristics of powder iron cores will be considered and discussed in the following section in order to aid in the design of a more efficient output inductor for the MicroVerter μ V28-3 model converter.

2.b. Requirements

In this part of the project, the switch and output inductor are analyzed and somehow improved in order to aim for an increase in the converter's overall efficiency. The switch used in the μ V28-3 model is a fast switching power MOSFET manufactured by International Rectifier. Since the converter has a high switching frequency of 370 kHz, a shorter switching time is preferable. When choosing a better switch for the converter, it is important to make sure the on-state resistance of the MOSFET, $R_{DS(on)}$, should be minimal. A lower $R_{DS(on)}$ will give lower conduction losses [7]. The packaging of the MOSFET is another thing to consider, since different packages have different thermal resistances which affect heat generation and thus, power dissipation. The power MOSFET used in the μ V28-3 model has a TO-220 package. It is important to choose an appropriate size switch for the converter. Also, the values of the drain-to-source breakdown voltage, V_{DSS} , and the continuous drain current, I_D , should not be lower than the values of the original switch, which are 100 V and 57 A, respectively. This is to ensure that the new MOSFET will be able to withstand the given input voltage of 28 V and output current of 50 A.

The original output inductor of the μ V28-3 model has an inductance of $1.6\mu\text{H}$, using a powder iron toroid core and sixteen gauge copper wires, which are wound three in parallel. Since there are no given specifications regarding the output inductor, the size of the powder iron core is estimated to be a T-68 size core, which has an outer diameter of 17.5 mm. In designing a more efficient output inductor, it is important to determine the minimum inductance that is required so that the inductor current does not go to zero. It is not desirable for the converter to go into discontinuous mode of operation. As a safety factor, it is recommended to choose an inductance that is about thirty percent higher than the minimum required inductance. For the coil, a copper wire thick enough to carry the required output current of 50 A should be chosen, preferably sixteen gauge or fourteen gauge wires. To obtain low copper losses in the windings, the DC resistance of the inductor should be minimal, $0.82\text{ m}\Omega$ or less. The size of the core and magnetic flux density should not be very large. Since the original core is fairly small, cores that are much smaller in diameter are not considered because the size of the copper wires is too big to be wounded tightly around the cores. Also, cores with much bigger diameters are not used because they will not be able to fit in the converter. Iron powder cores with low volume and low peak ac flux density reduce the core losses of the inductor, which will help minimize the total inductor losses.

The test equipment that was used for this project was setup in a manner that is shown in Figure 18 below.

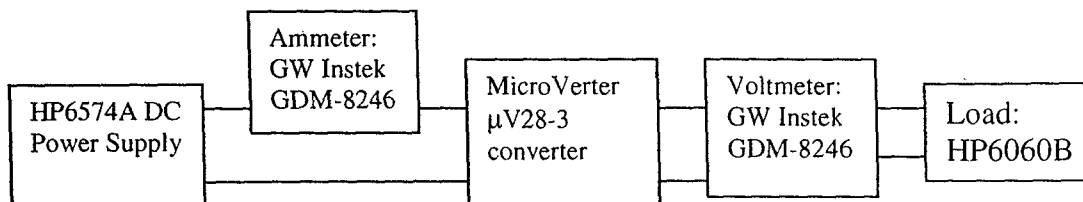


Figure 18. Block diagram of Test-Setup

2.c. Development and Construction

The main objective in this study is a more efficient, less consuming DC-DC converter. The focus is on the power stage, which consists of the power switch, output inductor, transformer, output capacitor, and output diode. Testing will mainly be done on the output inductor and the switch. For the switch, the type was chosen according to the drain to source voltage, V_{ds} , and the drain to source current, I_{ds} , which had to be above or the same as the original values, V_{ds} equals 100 V and I_{ds} equals 57 A given in the IRF3710 data sheet [11]. The on resistance is also an important feature in the switch because the lower the number the lower the loss lost in the package. For the IRF3710, it has a R_{dson} of 23 milli-ohms [11].

The original inductor was a type similar to a T68-2 part from Micrometals, Inc. It is a powder core type material with a dc resistance of 0.82 m Ω and trifilar windings. The core has an inside diameter of 0.3 inches, an outside diameter of 0.5 inches, and a thickness of 0.19 inches. The inductance value was measured to be about 1.6 μ H.

The forward converter was first simulated and tested using the program, Cadence Pspice version 15. The initial tests done were performed using ideal components specifically the switch. These showed what the ideal results are when there are 'ideally' no losses involved. The circuit diagram of this converter is shown in Figure 19 below.

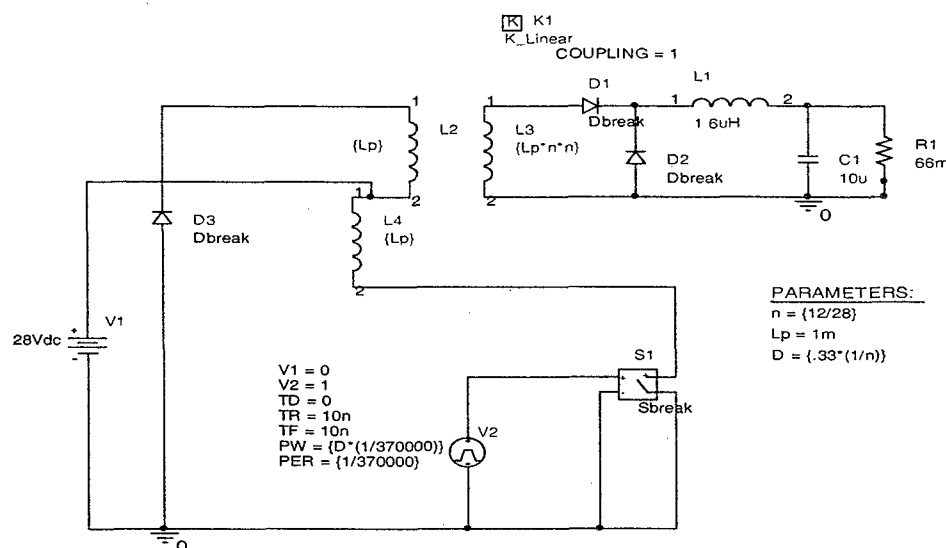


Figure 19. Single Switch Forward Buck converter with Ideal components.

As could be seen in the figure, the switch is controlled by a pulse source, which manually ties in the desired period for the system. The duty cycle affects the output voltage because it is related to the turns-ratio of the transformer. Figures 20 and 21 below show the output voltage waveforms and the ripple voltage. The output voltage is desired to be 3.3 V. It is typically desired that the output ripple voltage be as small as possible. The μ V28-3 model is rated to have 1-3 percent ripple output voltage. In Figure 21, the output voltage ripple was found to be 101 milli-volt. Table II below summarize the data obtained from the plots.

Table II. Max and Min Output Voltage for Circuit with Ideal Components

Vmax (V)	Vmin (V)	Vripple = Vmax – Vmin (V)
3.338	3.237	0.101

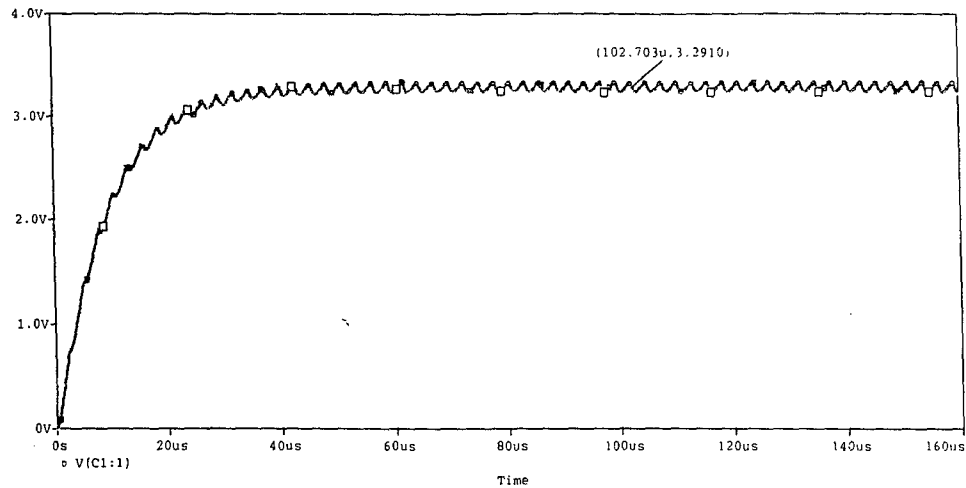


Figure 20. Output Voltage of Ideal Forward Converter with a value of 3.29 V.

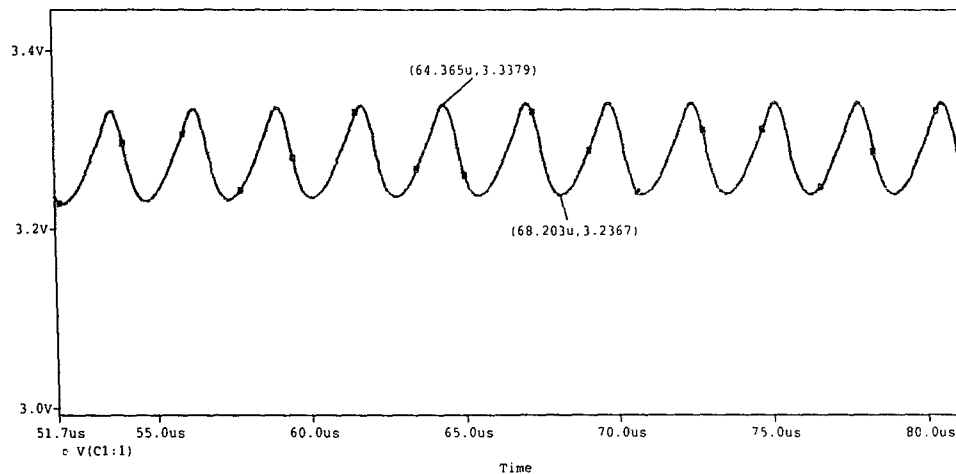


Figure 21. Output Voltage Ripple of Ideal Converter

The average output current, which is also the same as the average current through the inductor, is important in determining the conduction mode and the size of the inductor to use. The conduction mode could either be in continuous or discontinuous mode. It would be discontinuous if the current touches zero. Figure 22 shows that the current is above zero so it is operating in continuous conduction mode.

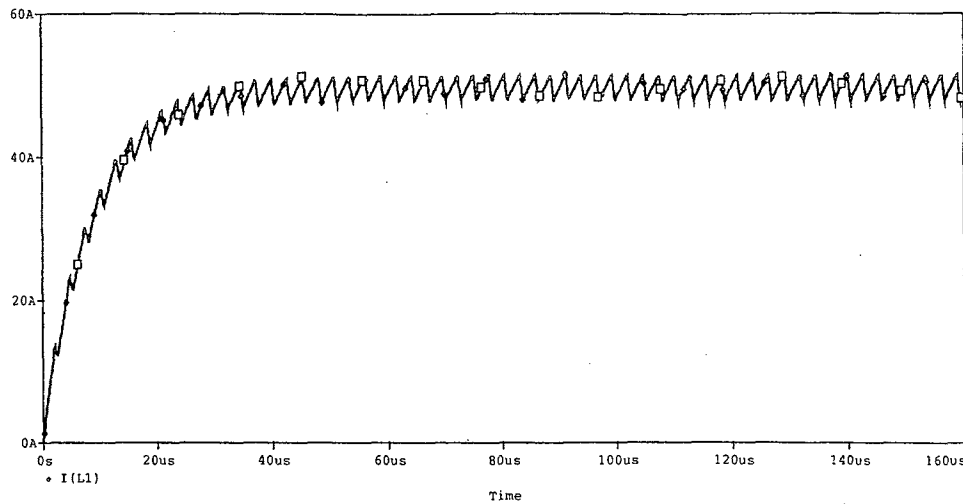


Figure 22. Inductor current showing Continuous Conduction Mode

Finding what the maximum inductor current helps determine a reasonable size for the inductor, and the minimum current determines the conduction mode [7]. An example is shown in Figure 10 below. The maximum current was taken to be 51.37 amps and the minimum to be 47.85 amps.

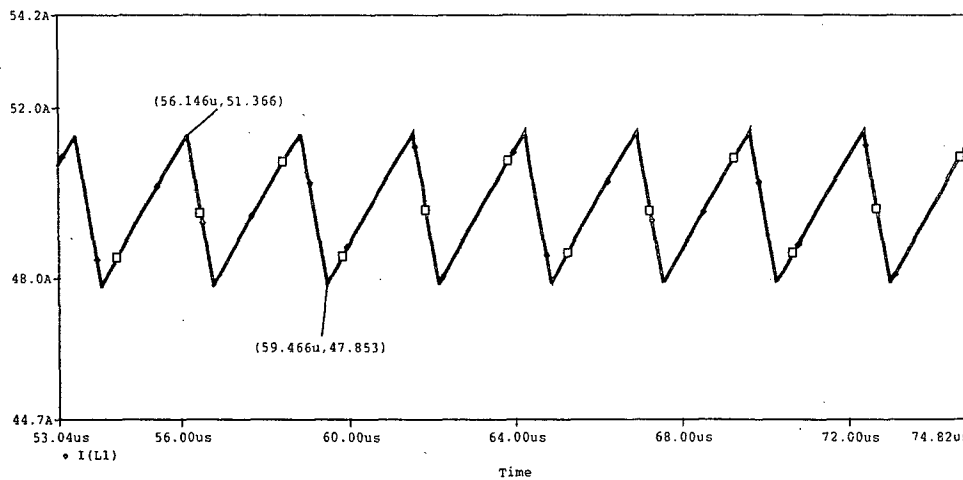


Figure 23. Inductor current showing Maximum and Minimum values.

The average inductor current is theoretically the same as the average output current. In this case, for an output voltage of 3.3 volts and a load resistance of 66 milli-ohms, the output current should be 50 amps. From Figure 24, the simulation showed that the average output current was 46.59 amps, a percent difference of about 6.82 percent.

The peak current in the switch is also important in that it is the same current that goes through the magnetizing inductance and is returned to the supply thus increasing efficiency [12]. It also helps to figure out the maximum voltage in the switch. Figure 25 shows an example.

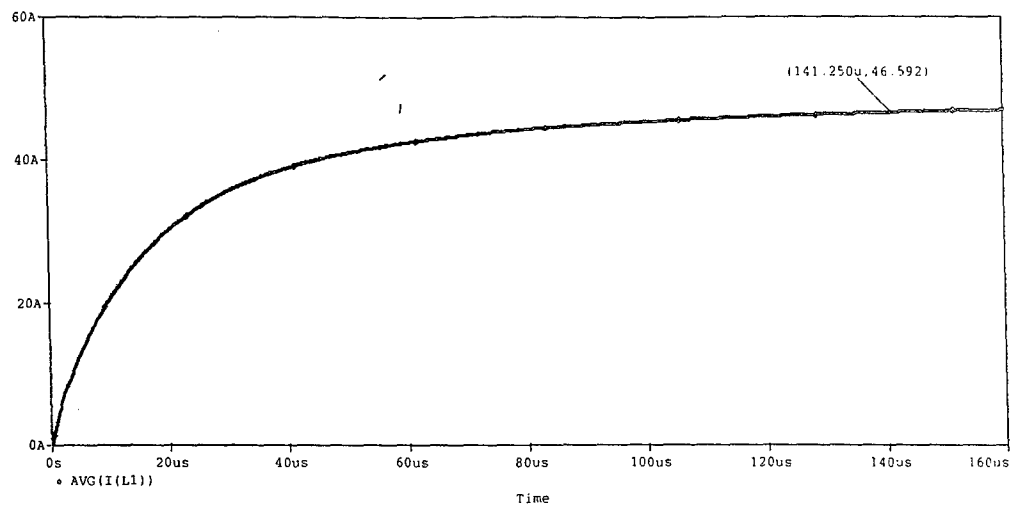


Figure 24. Average Inductor Current of Ideal Converter

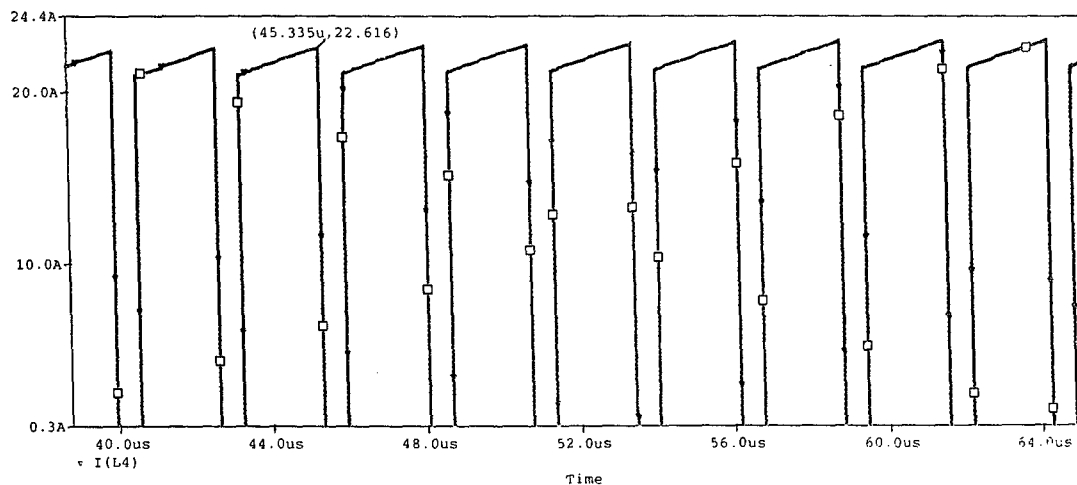


Figure 25. Peak Current in the Switch in Ideal Converter

These simulations and tests were done with the assumption that there are no losses involved in the switch and the generator. However, to observe the practical applications of the forward converter, losses must be accounted for from each part in the circuitry. In the following simulation, a MOSFET, IRF320, (used in place of the ideal switch), and a regulator, UC1843A, (used to drive the switch) are being used to achieve a more realistic model. The switch parameters were changed accordingly. The drain to source voltage, drain to source current, and maximum capacity were manipulated to achieve the desired results. The regulator automatically adjusts to meet the desired voltage and operating frequency. Figure 26 below shows a schematic of the circuitry used.

As could be observed in Figure 27, the output voltage is much closer to the desired 3.3 V with a value of 3.34 V, with only a percent difference of 1.21 percent. The voltage initially looks like it is oscillating but it eventually settles to the average voltage.

Table III. Max and Min Output Voltage with Real Components

Vmax (V)	Vmin (V)	Vripple = Vmax - Vmin (V)
3.355	3.349	0.0055

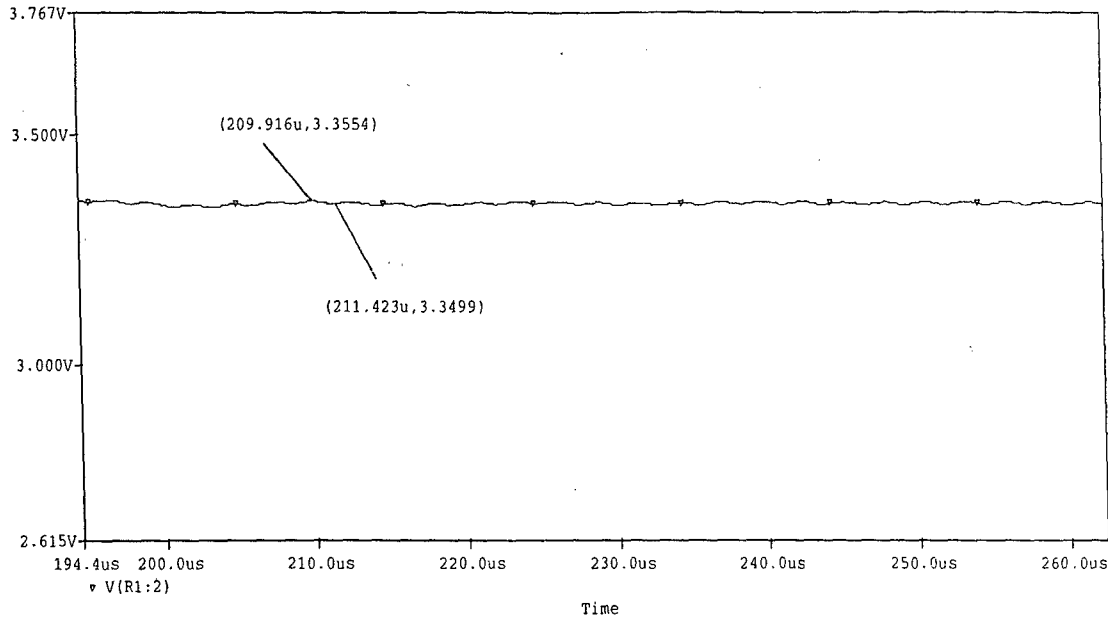


Figure 28. Output Voltage Ripple of 5.5 mV of Real Converter

Figure 29 and 30 below show the inductor current to be above zero, thus allowing for safe operation because it is in the continuous conduction mode. The maximum inductor current is measured to be 3.422 A and the minimum is 3.282 A.

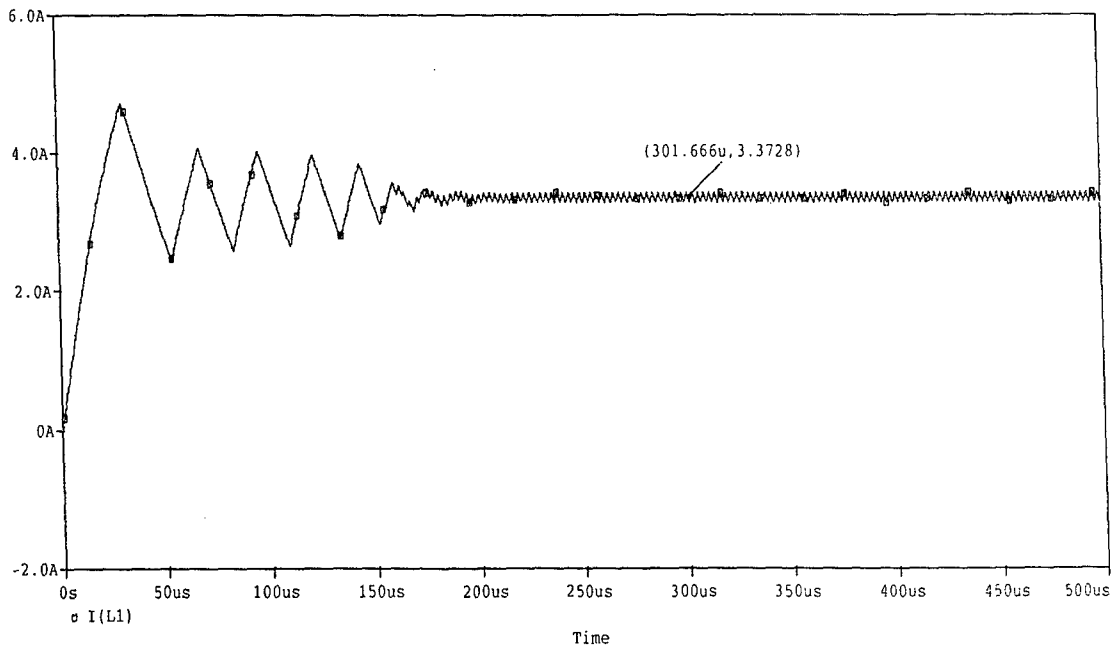


Figure 29. Inductor current showing Continuous Conduction Mode at average of 3.373 A

The difference between the maximum and minimum peak currents is 140 mA, which would help in determining the rms ac value of the current. This could be accounted from the oscillations occurring in the LC tank.

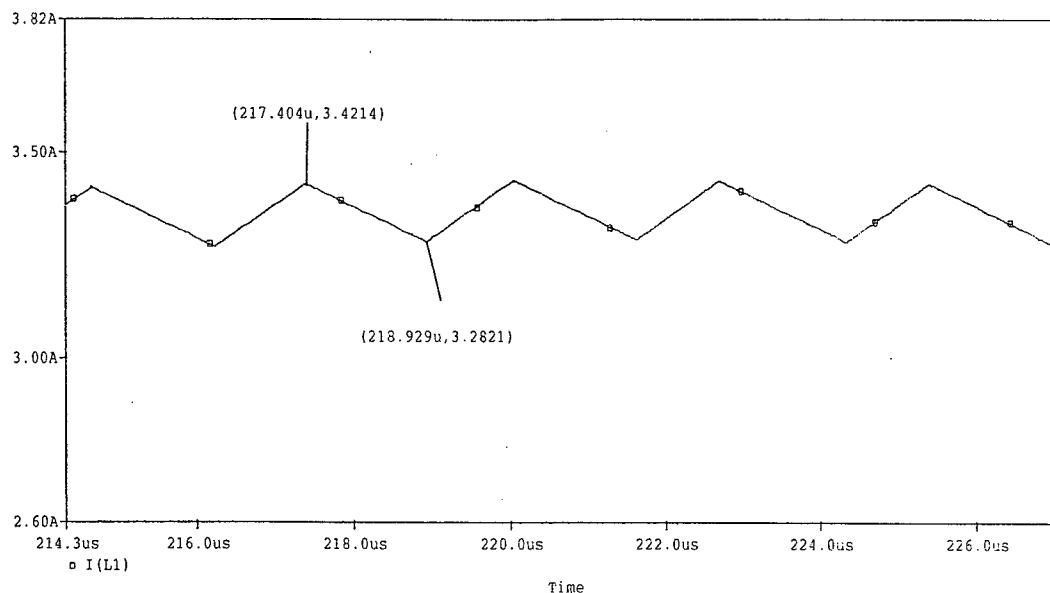


Figure 30. Inductor current showing max and min values of Real converter

The peak current in the switch shown in Figure 31 below is about 57 amps which is twice the value as compared to the ideal switch as shown in Figure 25. This may be due to the output, the value of the inductance, and the duty cycle. The duty cycle was however, observed to be about 50 percent so other factors contributed to the high current.

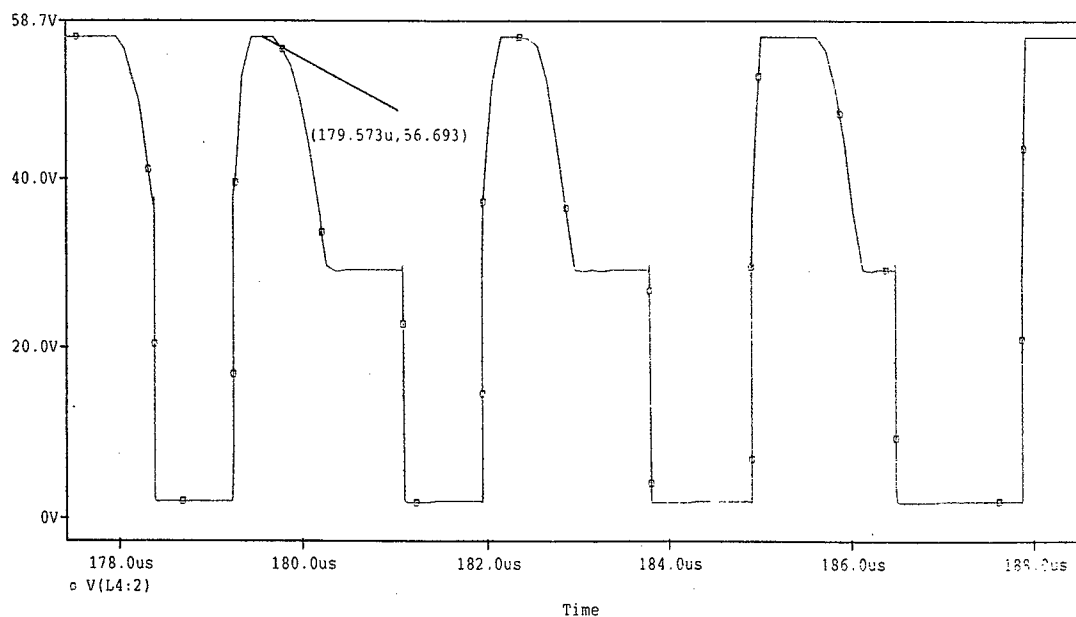


Figure 31. Peak Switch and/or Peak Inductor Current

In using ideal and real components, the waveforms showed the different characteristics of the forward buck converter in conjunction with the inductor current and the output voltage of the converter. The simulations helped to determine a range for choosing the inductance values that would be used in testing the $\mu V28-3$ model.

The following pages are the derivations of the components involved in the total loss of the converter. The components are the power switch, control, inductance, transformer, output capacitor and diode. In these derivations, the power loss of each component is calculated and factored into the total loss to determine the efficiency, which came out to be 73.4 percent. The first set of derivations shown below is in figuring out the rms current and the total rms current.

$$I_{l \max} = \bar{I}_l + \frac{\Delta}{2} = \frac{V_o}{R} + \frac{\left(V_s \left(\frac{N_2}{N_1} \right) - V_o \right)}{2L} * DT$$

$$I_{l \max} = 50 + \frac{28 * 0.5 * \left(\frac{1}{370 * 10^{-3}} \right) * \left(\frac{1}{7} \right)}{2 * 1.6 * 10^{-6}} - \frac{3.3 * 0.5 * \left(\frac{1}{370 * 10^{-3}} \right)}{2 * 1.6 * 10^{-6}} = 50.296 A$$

$$I_{l \min} = \bar{I}_l - \frac{\Delta}{2} = \frac{V_o}{R} - \frac{\left(V_s \left(\frac{N_2}{N_1} \right) - V_o \right)}{2L} * DT$$

$$I_{l \min} = 50 - \frac{28 * 0.5 * \left(\frac{1}{370 * 10^{-3}} \right) * \left(\frac{1}{7} \right)}{2 * 1.6 * 10^{-6}} + \frac{3.3 * 0.5 * \left(\frac{1}{370 * 10^{-3}} \right)}{2 * 1.6 * 10^{-6}} = 49.704 A$$

$$I_{ac} = I_{l \max} - I_{l \min} = 50.296 - 49.704 = 0.5912 A$$

$$I_{l \text{rms}} = \sqrt{I_{dc}^2 + I_{ac}^2} = \sqrt{(20.625)^2 + (0.5912)^2} = 20.634 A$$

Efficiency Calculation Using MathCAD

The following MathCAD file was compiled to calculate the overall efficiency of the converter. The calculations for efficiency considered the losses in the following components: inductor, output rectifier, reset diode, MOSFET, transformer, control switch, and the capacitor

Single Switch Forward Converter

Efficiency Calculations as a function of Inductance and Switch

Metric Definitions

Nominal Input Voltage: $V_{in} := 28 \text{ V}$
 Nominal Output Voltage: $V_{out} := 3.3 \text{ V}$
 Nominal Output Current: $I_{out} := 50 \text{ A}$
 Efficiency: $\eta := 0.8$
 Switching Frequency: $F_{sw} := 370 \text{ kHz}$
 Duty Cycle: $D := 0.5$
 Output Ripple Voltage: $V_{rip} := 99 \text{ mV}$
 Forward Voltage Drop (diode): $V_{drop} := 0.47 \text{ V}$
 Room Temperature(F): $Modtemp_1 := 72$
 Transformer Turns Ratio (N_s/N_p), measured: $\frac{N_s}{N_p} := \frac{1}{7}$

$m\Omega := 1 \cdot 10^{-3} \Omega$ $mJ := 1 \cdot 10^{-3} J$
 $ns := 1 \cdot 10^{-9} s$ $nC := 1 \cdot 10^{-9} C$
 $mW := 1 \cdot 10^{-3} W$ $\mu s := 1 \cdot 10^{-6} s$
 $nH := 1 \cdot 10^{-9} H$ $\mu H := 1 \cdot 10^{-6} H$

$$P_{out} := V_{out} \cdot I_{out}$$

$$P_{out} = 165 \text{ W}$$

$$P_{in} := \frac{P_{out}}{\eta}$$

$$P_{in} = 206.25 \text{ W}$$

$$I_{in} := \frac{P_{in}}{V_{in} \cdot D}$$

$$L_p := \frac{V_{in} \cdot D}{F_{sw} \cdot I_{pp}}$$

$$L_p = 51.368 \times 10^{-6} \text{ H} \quad \text{Magnetizing Inductance}$$

$$P_{diss} := \frac{V_{out} \cdot I_{out}}{\eta} - V_{out} \cdot I_{out}$$

$$P_{diss} = 41.25 \text{ W}$$

Power dissipated in converter

$$V_{ddrop} := 0.75 \text{ V} + (75 - Modtemp) 2 \cdot 10^{-3} \text{ V} \quad V_{ddrop} = 0.756 \text{ V}$$

$$C_{optcu} := 1 + (Modtemp - 25) \cdot 0.0039$$

$$C_{optcu} = 1.185$$

Change of copper resistance with temperature

Output Filter

$$Discon := 0.277245$$

Percentage at which discontinuous

$$L_{out} := \frac{(V_{out} - V_{ddrop}) \cdot (1 - D)}{2 \cdot F_{sw} \cdot Discon \cdot I_{out}}$$

$$L_{out} = 124 \times 10^{-9} \text{ H}$$

$$C_{ou} := \frac{(V_{out} - V_{ddrop}) \cdot (1 - D)}{8 V_{rip} \cdot F_{sw}^2 \cdot L_{out} \cdot 0.5}$$

$$C_{ou} = 189.22 \times 10^{-6} \text{ F}$$

$$\Delta I := \frac{[V_{in} \cdot (N) - V_{out}] \cdot D}{F_{sw} \cdot L_{out}}$$

$$\Delta I = 7.629 \text{ A}$$

Output Inductor

$$I_{dcmax} := I_{out} + \frac{\Delta I}{2}$$

$$I_{dcmax} = 53.814 \text{ A}$$

$$L_{out} \cdot I_{dcmax}^2 = 3.591 \times 10^{-4} \text{ J}$$

Used to choose core from a graph

Core : T80-18

$$l_m := 5.14 \text{ cm}$$

$$A_{\omega} := 0.231 \text{ cm}^2$$

$$\text{Volume} := 1.19 \text{ cm}^3$$

$$SA := 14.7 \text{ cm}^2$$

$$A_l := 31.0 \times 10^{-9} \frac{\text{H}}{\text{N}^2}$$

$$\text{Turns} := \sqrt{\frac{L_{out}}{A_l \cdot N^2}}$$

$$\text{Turns} = 2$$

$$\text{sugdiscon} := \frac{(V_{out} - V_{ddrop}) \cdot (1 - D)}{2 \cdot F_{sw} \cdot (\text{Turns}^2) \cdot A_l \cdot N^2 \cdot I_{out}}$$

$$\text{sugdiscon} = 0.277$$

$$H_{\omega} := \frac{0.4 \cdot \pi \cdot \text{Turns} \cdot I_{dcmax}}{l_m}$$

$$H = 33.066 \text{ Oe}$$

$$B_{max} := 169 \text{ G}$$

Taken from software for Micrometals

DCR

$$R_{dc} := 0.82 \text{ m}\Omega$$

$$P_{cu} := \left(I_{out} + \frac{\Delta I}{2\sqrt{3}} \right)^2 \cdot R_{dc} \cdot C_{optcu}$$

$$P_{cu} = 2.647 \text{ W}$$

$$P_{core} := 0.444 \text{ W}$$

$$P_{inductor} := P_{cu} + P_{core}$$

$$P_{inductor} = 3.091 \text{ W}$$

Temprise := 71.2

Temperature rise of inductor from software

Output Rectifiers

82CNQ030

Vfwd := 0.55 V

Cj := 1400 pF

Ir := 500 μ A

Prect := Iout · Vddrop + Cj · Vout² · Fsw + Cj · (Vin · N)² · Fsw + Ir · Vout · D + Ir · Vin · N · (1 - D)

Prect = 37.816 W

Reset Diode

MURD620

Ir := 5 μ A

Ct := 12 pF

Presdio := 2 · (Ir · Vin · D + Ct · Vin² · Fsw)

Presdio = 7.102×10^{-3} W

MOSFET

IRF3710

Qg := 130 nC

Coss := 410 pF

Rdson := 0.023 Ω

tr := 58 ns

tf := 47 ns

Iprms := 20.634

Calculated from notes

Pgd := Qg · 12 V · Fsw

Pgd = 0.577 W

Psw := 0.25 · Iin · Vin · (tr + tf) · Fsw + 0.5 Coss · Vin² · Fsw

Psw = 4.066 W

Pcond := Iprms² · Rdson · D · $\frac{W}{\Omega}$

Pcond = 4.896 W

Pmos := Pgd + Psw + Pcond

Pmos = 9.539 W

Transformer

$$R_{\text{prim}} := 0.018 \, \Omega$$

$$R_{\text{sec}} := 0.012 \, \Omega$$

$$L_{\text{prim}} := 53 \, \mu\text{H}$$

$$L_{\text{sec}} := 7.4 \, \mu\text{H}$$

$$I_{\text{primrms}} := I_{\text{in}} \cdot \sqrt{D} \cdot \left(1 + \frac{\Delta I}{I_{\text{out}} \cdot 2\sqrt{3}} \right)$$

$$I_{\text{primrms}} = 10.876 \, \text{A}$$

$$P_{\text{cuprim}} := I_{\text{primrms}}^2 \cdot R_{\text{prim}} \cdot \text{Coptcu}$$

$$P_{\text{cuprim}} = 2.522 \, \text{W}$$

$$P_{\text{cusec}} := (I_{\text{primrms}} \cdot N)^2 \cdot R_{\text{sec}} \cdot \text{Coptcl}$$

$$P_{\text{cusec}} = 0.034 \, \text{W}$$

$$P_{\text{trans}} := P_{\text{cuprim}} + P_{\text{cusec}}$$

$$P_{\text{trans}} = 2.557 \, \text{W}$$

Control

$$V_{\text{bias}} := 12 \, \text{V}$$

$$I_{\text{mic3843}} := 17 \, \text{mA}$$

$$P_{\text{control}} := V_{\text{bias}} \cdot (I_{\text{mic3843}})$$

$$P_{\text{control}} = 0.204 \, \text{W}$$

Output Capacitor

$$\text{ESR} := 0.467 \, \Omega$$

$$I_{\text{rms}} := 3.778$$

Calculated from PSpice

$$P_{\text{cap}} := \text{ESR} \cdot I_{\text{rms}}^2 \cdot \frac{\text{W}}{\Omega}$$

$$P_{\text{cap}} = 6.666 \, \text{W}$$

$$P_{\text{total}} := P_{\text{inductor}} + P_{\text{rect}} + P_{\text{resdio}} + P_{\text{mos}} + P_{\text{trans}} + P_{\text{control}} + P_{\text{cap}}$$

$$P_{\text{total}} = 59.88 \, \text{W}$$

Efficiency

$$\eta_{\text{w}} := \frac{V_{\text{out}} \cdot I_{\text{out}}}{V_{\text{out}} \cdot I_{\text{out}} + P_{\text{total}}}$$

$$\eta = 0.734$$

2.d. Integration and Test Results

The results from integrating and testing different power switches and inductors have proved that improving the overall efficiency of the converter is not an easy task. The maximum efficiency of one unmodified MicroVerter μ V28-3 model converter was tested to be 76.7678 %. The original switch is an IRF3710 Power MOSFET with a drain to source voltage of 100 V, drain current of 57 A, and on-state resistance of 23 m Ω . The following figure show the data points recorded during testing and the efficiency plot of the unmodified converter. The figure shows that the efficiency is lower than the actual rated efficiency because it does not reach eighty percent.

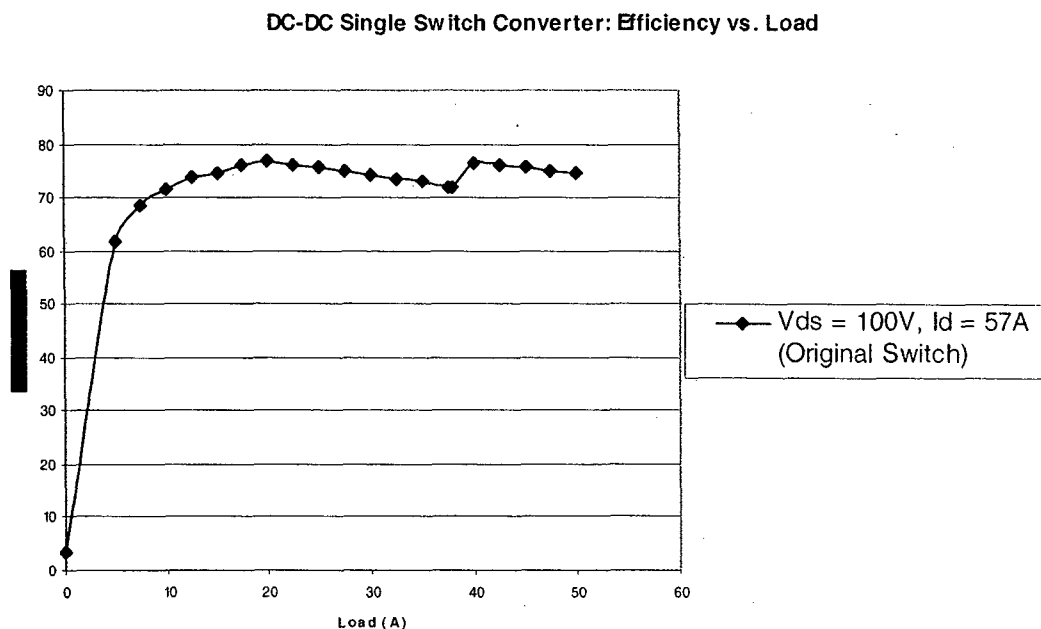


Figure 32. Efficiency plot of unmodified converter (original switch)

Before several MOSFETs were integrated into the MicroVerter μ V28-3 model converter, removing the original switch was one obstacle that had to be taken. The switch could not be easily pulled out of its designated spot on the circuit board. First, the circuit board was placed on a hotplate in order for the bottom of the circuit board to heat up and help loosen the solder beneath the switch. The soldering iron was also used to spread heat throughout the switch in an attempt to loosen and remove it from the circuit board. After several minutes, the switch was detached from the board. In order to easily test different MOSFETs, two sixteen gauge wires were soldered onto the board in order to connect the drain and the back of the MOSFET to the circuit board. By doing so, de-soldering and re-soldering were not as difficult and had saved a lot of time.

Three switches were integrated and tested on the converter. The first switch tested was the IRFB59N10D Power MOSFET with $V_{ds} = 100$ V, $I_d = 59$ A, and $R_{DS(on)} = 25$ m Ω . Below are the results from testing this particular switch. As shown in Figure 33, this switch was able to increase the original maximum efficiency of 76.678 % to 77.678 %, which is a one percent improvement.

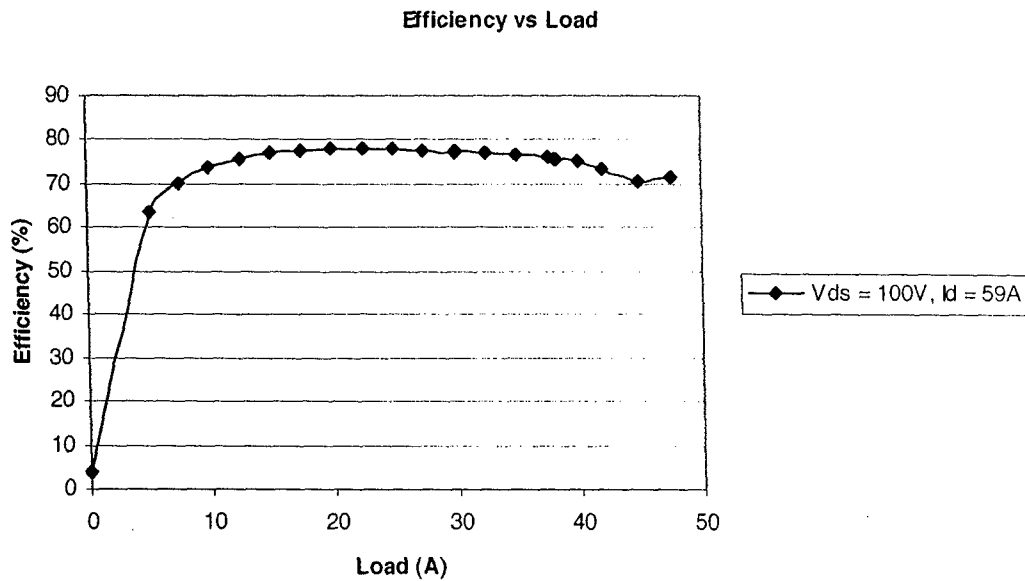


Figure 33. Efficiency plot of the converter with the IRFB59N10D Power MOSFET

The second switch that was integrated into the MicroVerter μ V28-3 model converter was the IRFB61N15 Power MOSFET with $V_{ds} = 150$ V, $I_d = 60$ A, and $R_{DS(on)} = 32$ m Ω . Figure 34 below shows result from testing this particular switch.

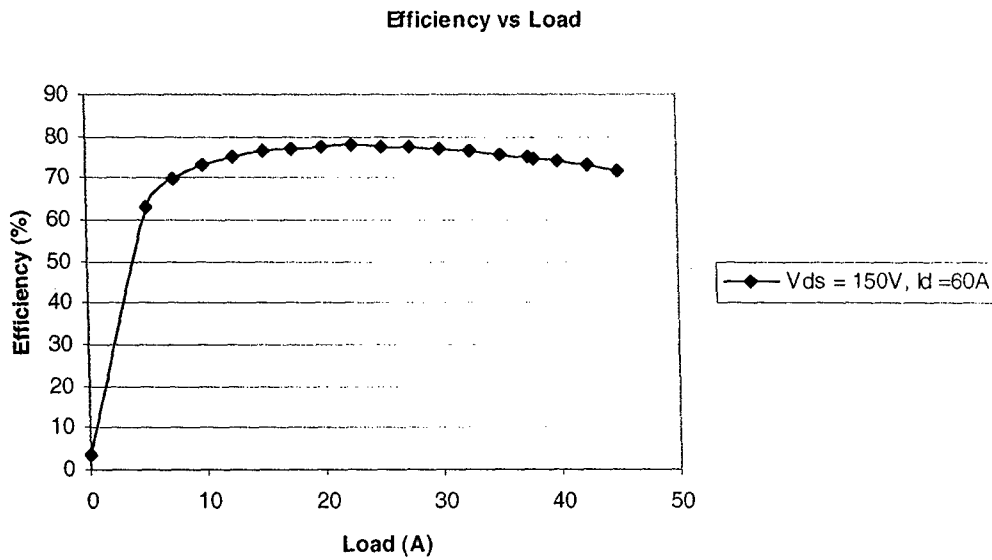


Figure 34. Efficiency plot of the converter with the IRFB61N15 Power MOSFET

The efficiency of the converter with the IRFB61N15 Power MOSFET reaches its maximum of 77.676 % at a load current of 22.51 A. This MOSFET did increase the converter's efficiency by 0.982 %, which is very similar to the affect that the IRFB59N10D Power MOSFET had on the converter's overall efficiency.

The last switch that was tested was the STW60NE10 with $V_{ds} = 100$ V, $I_d = 60$ A, and $R_{DS(on)} = 22$ m Ω . Below is the result from testing this particular switch.

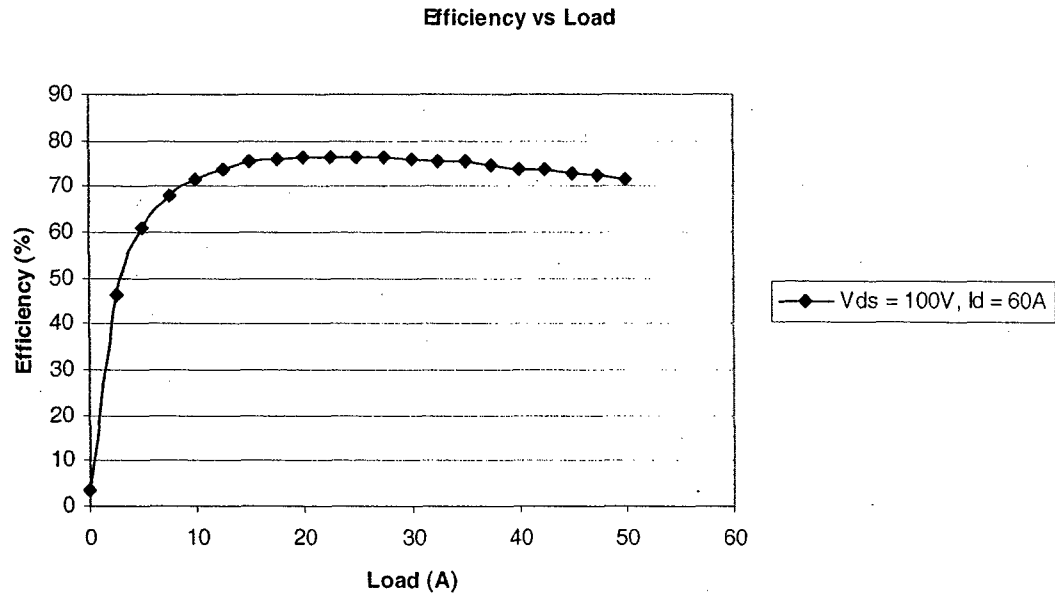


Figure 35. Efficiency plot of the converter with the STW60NE10 Power MOSFET

As shown in Figure 35, the maximum efficiency when integrating the STW60NE10 Power MOSFET into the MicroVerter μ V28-3 model converter was only 76.4198 % at a load current of 25.01 A. This particular switch did not improve the converter's original efficiency. This may be due to the difference in packaging. The original switch with a package of TO-220AB has a low thermal resistance of 0.75 °C/W for the junction to case parameter whereas the STW60NE10 switch with a package of TO-247 has a slightly higher thermal resistance of 0.83 °C/W for the same parameter. Lower thermal resistance due to package size is better because there is less loss.

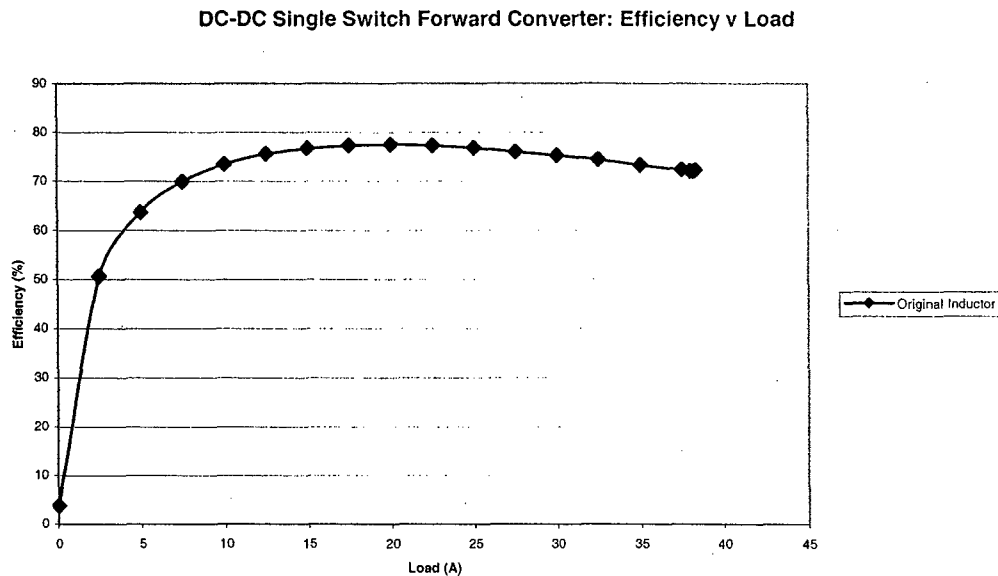


Figure 36. Efficiency plot of unmodified converter (original inductor)

The testing of the power switch and output inductor were performed on two different MicroVerter μ V28-3 model converters. The output inductor of another unaltered converter used a T-68 iron powder core and its measured inductance was $1.6\mu\text{H}$. The highest efficiency with this original output inductor was only 77.467 %, which is about three percent lower than the rated efficiency. The efficiency plot of the unmodified converter can be seen in Figure 36.

Before integrating different output inductors into the unaltered MicroVerter μ V28-3 model converter, the original inductor had to be removed by detaching the coil from the end wires. The end wires were left attached to the circuit board, which were used as connectors when soldering and de-soldering the different inductors onto the converter. All the inductors used in testing consisted of iron powder cores manufactured by Micrometals, Inc. The wire sizes used as coils ranged from fourteen and sixteen gauges. There were several inductor cores with different number of turns that were tested. Below in Table IV are the different inductor cores and their measured inductance values.

Table IV. Data of different output inductors tested

Core Type	Measured Inductance
T68-6	$L=2.03\mu\text{H}$
T68-18	$L=1.01\mu\text{H}$
T68-18	$L=1.17\mu\text{H}$
T80-2	$L=0.89\mu\text{H}$
T80-2	$L=0.92\mu\text{H}$
T80-2	$L=1.02\mu\text{H}$
T80-2	$L=1.13\mu\text{H}$
T80-2	$L=2.0\mu\text{H}$
T80-18	$L=1.49\mu\text{H}$
T80-45	$L=1.15\mu\text{H}$
T80-45	$L=1.69\mu\text{H}$
T130-26	$L=3.84\mu\text{H}$

Although there were several inductors tested, all of them had similar results to the following three output inductors. One output inductor that was integrated into the MicroVerter μ V28-3 model converter was the T80-18 with a measured inductance of $1.49\mu\text{H}$. As shown in Figure 37, the maximum efficiency is 77.3657 %, which is only 0.1013 % lower than the efficiency of the converter with the original inductor.

Another inductor that was integrated into the MicroVerter μ V28-3 model converter was the T68-18 with a measured inductance of $1.17\mu\text{H}$. As shown in Figure 38, the peak efficiency is 76.716 % at an output current of 20.01 A. Compared to the previous inductor, this output inductor had a lower efficiency, which was 0.751 % below the original efficiency.

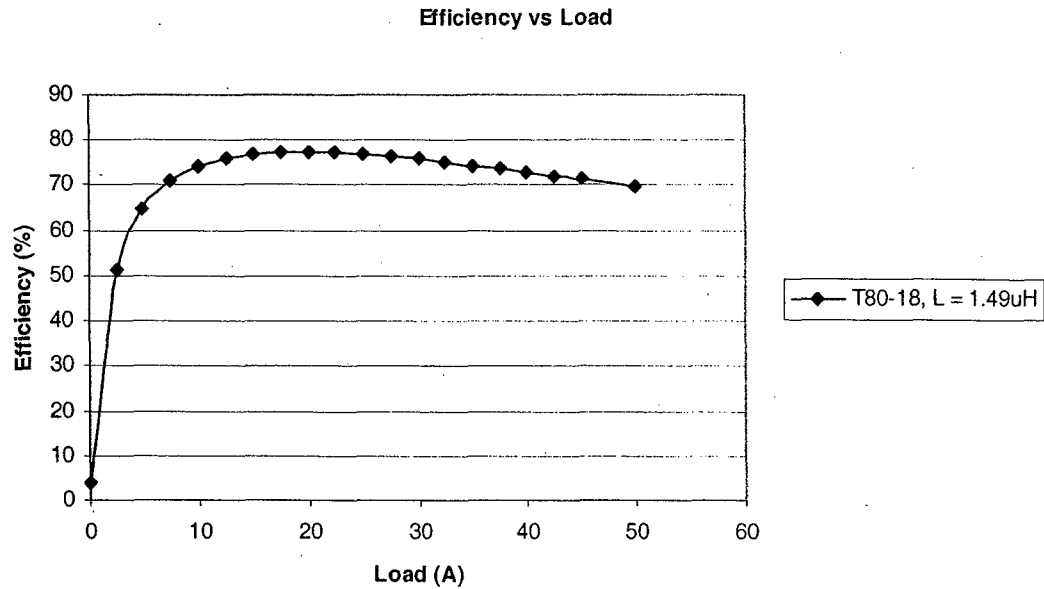


Figure 37. Efficiency of the converter with the T80-10, L = 1.49 μ H output inductor

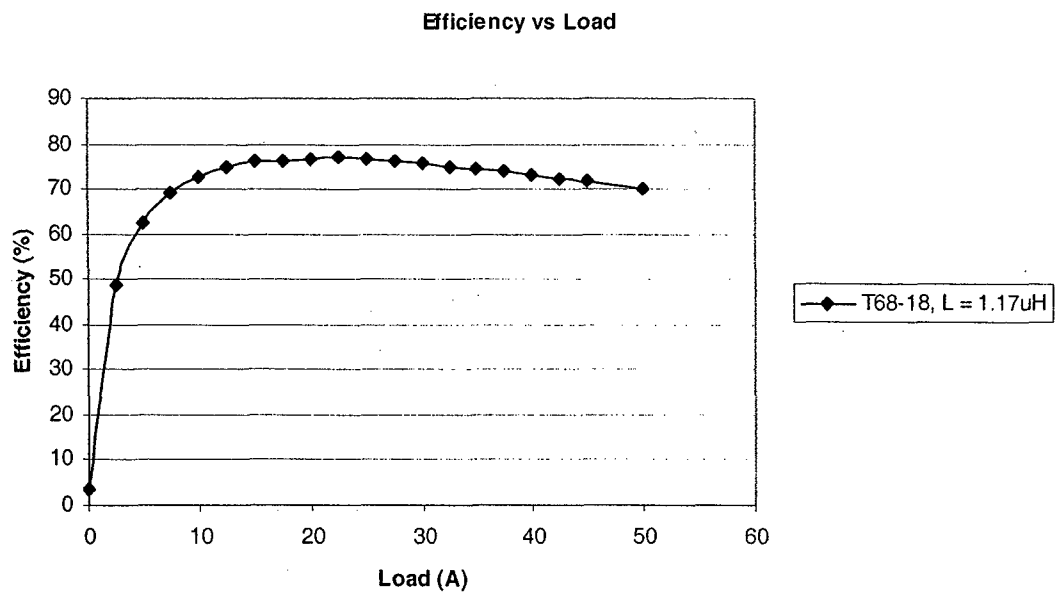


Figure 38. Efficiency of the converter with the T80-10, L = 1.17 μ H output inductor

One other inductor that was tested was the T80-45 with an output inductance of 1.15 μ H. Figure 39 below show results from testing this particular inductor. This inductor had the lowest affect on the efficiency of the MicroVerter μ V28-3 model converter. As seen in Figure 39, the peak efficiency of the converter is only 74.773 %, which is 2.694 % below the original maximum efficiency. This significant drop in efficiency may be due to the fact that the windings were not as tight as with the original inductor, hence more leakage inductance. That may have caused larger inductor losses, resulting in a lower efficiency.

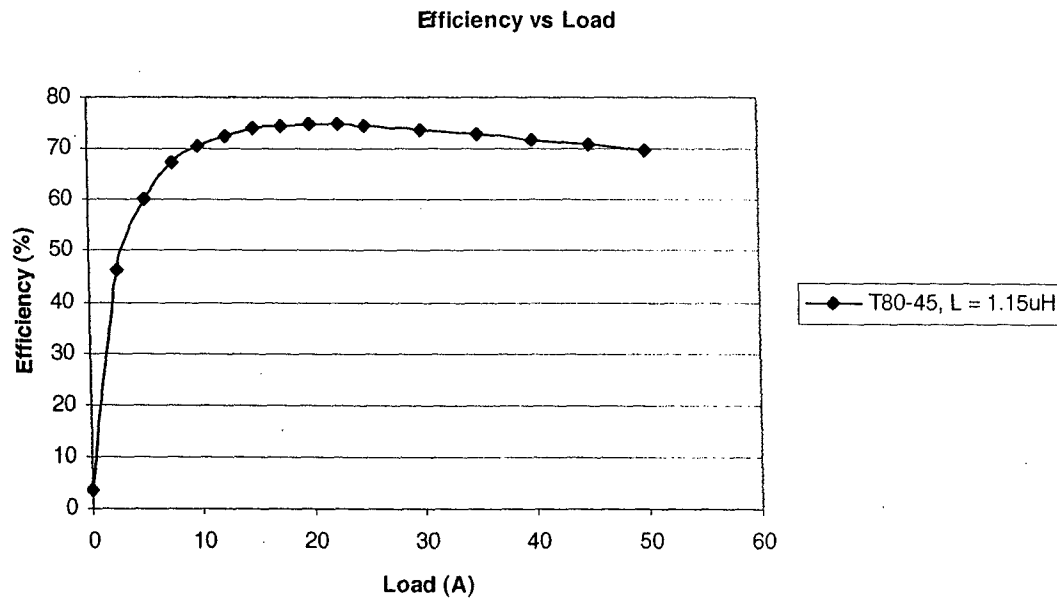


Figure 39. Efficiency of the converter with the T80-45, $L = 1.15 \mu\text{H}$ output inductor

3. Impact of Power MOSFET and Power Inductor Selections

In this section, the impact of output capacitor to converter's efficiency will be discussed. Characteristics of different types of capacitors along with their implementation in the converter under study will be presented. Test results and suggestion for future study will also be included in this report. In the end, all information will be combined and final assessment will be determined.

3.a. Background

RO Associates manufactures series of dc-dc converter that ranges from 40-400W and is highly marketed worldwide. The prototype that we are working with is the MicroVerter28V-3 ($\mu\text{V}28-3$). The model number signifies the nominal input voltage of 28V and the output voltage of 3.3 volts. The converter has an output rating of 150W at 50A. This high-density light-weight design uses metal printed circuit boards, surface mounted components, and planar transformers to produce high wattage output. This is considered extreme considering the package size of the module. The prototype is a single input and single output converter with dimensions of 0.5x2.4x3.6 inches and weighing in at approximately 7 oz.

The drawback in this product design is its efficiency. The data provided by the manufacture gives a peak efficiency of approximately 80% (Figure 14). This plot will later be compared to data obtain at after all tests have been conducted.

There are many factors for the low efficiency rating. The one we are concerned about is the power loss due to the capacitors. The charging and discharging of the capacitor cause energy losses. The energy lost due to a capacitor is linked to the internal parasitic resistance known as

the equivalent series resistance (ESR). This is the easiest loss mechanism to show analytically. Adding the ESR resistance to the circuit and calculating the power dissipated shows the energy loss.

3.b. Calculations

We are interested in the power loss due to the capacitors. The power loss can be calculated with equation shown below.

$$P_{loss} = (\Delta i_{L-rms})^2 (R)$$

The resistance R is simply the ESR values of the capacitors measured with the ESR meter. The Δi_{L-peak} parameter is the peak to peak ripple current and it can be calculated with equation below. The equation following it is simply a conversion to the rms value from the peak-peak value.

$$\Delta i_{L-peak} = \left[\frac{-V_o(1-D)T}{L} \right]$$

$$\Delta i_{L-rms} = \Delta i_{L-peak} \sqrt{\frac{D}{3}}$$

The above equations assume continuous conduction mode which means that the inductor current remains positive throughout the switching period. If the inductor current reaches zero for some time in the switching period that is known as discontinuous mode. The parameter T is the switching period obtained from the switching frequency and L is the inductance value of the inductor in the output circuit of the converter. V_o is the output voltage of the converter. The output voltage of the $\mu V28-3$ is a constant 3.3V. Although it is not needed, equation below is provided to show the relationship between the different formulas. Parameter D is the duty cycle of the converter which is found by multiplying the turns ratio of the transformer ($N1/N2$) and the ratio of the output voltage over the input voltage (V_o/V_s). The formulas for all parameters are provided below.

$$V_o = V_s \left(\frac{N2}{N1} \right) D \quad \text{or,} \quad D = \left(\frac{V_o}{V_s} \right) \left(\frac{N1}{N2} \right)$$

Note that the transformer ratio is inverted in equation on the right side. The power loss will be calculated for each combinations of capacitance used in this test. The switching period, inductance, turns ratio, duty cycle will be the same in this test experiment. Thus throughout the calculation process, there will be a single value for the rms ripple current. The only parameter that is changed is the ESR values. Below is a step by step calculation process to obtain the Δi_{L-rms} value.

The values of known parameters:

$$V_o = 3.3V$$

$$V_s = 28V$$

$$\frac{N_1}{N_2} = \frac{7}{1}$$

$$L = 1.4\mu H$$

$$T = \frac{1}{f} = \frac{1}{370Khz} = 2.7027\mu s$$

$$D = \left(\frac{V_o}{V_s}\right)\left(\frac{N_1}{N_2}\right) = \left(\frac{3.3V}{28V}\right)\left(\frac{7}{1}\right) = 0.825$$

$$V_o = V_s\left(\frac{N_2}{N_1}\right)D = 28V\left(\frac{1}{7}\right)(0.825) = 3.3V$$

$$\Delta i_{L-peak} = \left[\frac{V_o(1-D)T}{L}\right] = \left[\frac{-(3.3)(1-0.825)(2.7027 \times 10^{-6})}{1.4 \times 10^{-6}}\right] = -1.15611A$$

$$\Delta i_{L-rms} = \Delta i_{L-peak} \sqrt{\frac{D}{3}} = -1.15611 \sqrt{\frac{0.8025}{3}} = -0.5979$$

$$P_{loss} = (\Delta i_{L-rms})^2 (ESR) = (-0.5979)^2 (ESR)$$

so,

$$P_{loss} = (0.357484)(ESR)$$

The capacitor will be configured in a parallel fashion as oppose to the series. This configuration will increase the capacitance values and reduce the ESR dramatically. It should be noted that the power loss will decrease as the capacitance value increases. Refer to Table V for the calculated results for each test.

$$C_{total} = C_1 + C_2 + C_3 + + C_n$$

$$\frac{1}{R_{e\ equivalent}} = \frac{1}{ESR_1} + \frac{1}{ESR_2} + \frac{1}{ESR_2} + + \frac{1}{ESR_n}$$

Table V. Summary of the calculated power loss from measured ESR values

Tantalum	ESR Ω	Ploss (W)
9.4uF	0.299350	0.107013
20uF	0.154860	0.055360
94uF	0.105500	0.037715
136uF	0.367017	0.131203
200uF	0.237000	0.084724
440uF	0.233650	0.083526
640uF	0.117657	0.042060
1140uF	0.059038	0.021105
1440uF	0.039406	0.014087

Electrolytic	ESR Ω	Ploss (W)
0.2uF	10.875	3.887639

1.0uF	2.175	0.777528
238uF	0.8815	0.315122
903uF	0.07787	0.027837

Ceramic	ESR Ω	Ploss (W)
44nF	0.323491	0.115643
532nF	0.303066	0.108341
952nF	0.285746	0.102150
1392nF	0.268057	0.095826

3.c. Test Plans

With the understanding of the basic configuration of a forward dc-dc converter; the plan is to vary its critical power components and test each case separately and observe its effect on the output of the converter. There are five individuals participating in this project and each is assigned a different task. The task here is to concentrate on the output capacitor and observe how the different dielectric types and different capacitance values of capacitor affect the overall efficiency of the converter.

There are many types of capacitors in the market. Capacitors are categorized by its internal dielectric material. Dielectrics are insulating materials between the plates of capacitors. The three that will be tested in this investigation are capacitors with dielectric materials known as tantalum, electrolytic, and ceramic. All three will be tested at different capacitance values and the results of each will be compared.

Aside from the values and the dielectric materials of the capacitors, another important parameter that needs to be mentioned is the voltage rating and the classes in which the dielectric belongs. The voltage rating of the original capacitor used inside the converter cannot be determined without identifying the manufacturer; therefore this parameter is disregarded in the experimentation. However, when selecting capacitor replacements it is important that the voltage rating be above the converter output voltage rating which is 3.3V.

Capacitors are generally divided into classes which are defined by the capacitance temperature characteristics over specified temperature ranges [14]. The temperature coefficient are determined by measurement of the capacitance change at various temperature from reference room temperature (25°C), using an environmental chamber. The temperature coefficient (T.C.) is expressed as the percent capacitance change (% ΔC). Class 1 identifies the linear dielectric. These materials display the most stable characteristics, as they are non-ferroelectric formulations with the dielectric constant under 150. The most common class 1 dielectric for chip capacitors is the COG designated class. It possesses the characteristics of °C +/- 30 temperature coefficient, which is the NPO (negative-positive-zero), for flat temperature coefficient. The COG is used in circuitry requiring stability of capacitor with negligible or no change in capacitance or dielectric loss with voltage or frequency [15].

Class 2 dielectrics comprise the ferroelectric materials in that a nonlinear response of charge or polarization versus voltage occurs due to the crystal structure of the material. These materials offer much higher dielectric constants than Class 1 dielectrics, but with less stable properties with temperature, voltage, frequency, and time. The most common chip capacitor in this class is the X7R [15]. The classes are mentioned here for quick references, it was not considered in the process of choosing the capacitors. Before any testing is conducted, each capacitor types were researched and are briefly summarized below.

Tantalum Capacitors

The most interesting property of a tantalum capacitor is its ESR value. Unlike other dielectric materials, tantalum capacitors have a much lower ESR value. The ESR represents the extent to which the capacitor acts like a resistor when charging and discharging and of all the dielectric materials. This value can change with frequency and time. A measure of the total loss range of tantalum capacitors, which includes the leads, electrodes, dielectric losses, leakage and most importantly, the end spray connecting the leads to the metallized film. The lower the ESR value of a capacitor the higher the current carrying capability the capacitor possess. Due to this property, tantalum capacitors are used in smaller electronic devices including portable telephones, personal computers, and automotive electronics. Tantalum capacitors will yield a higher average selling price because of its small dimensions, low leakage current and low dissipation factor [13].

Electrolytic Capacitors

Unlike the other types of capacitor, electrolytic capacitors are large in size. They come in a canister type packaging. They consist of cathode aluminum foil, electrolytic capacitor paper, and a layer of aluminum oxide. The aluminum oxide layer acts as the dielectric and offers rectifying properties. In addition, when in contact with the electrolyte, the dielectric possesses an isolative property, which prevents forward passage, thus making it polarized. If connected in the wrong direction the capacitor can be damaged as well as cause damages in other components. These types are typically used in timing circuits, power supply filters, power signal coupling, motor start and motor run capacitors [13].

Ceramic Capacitors

Ceramic materials have the ability to permit electrostatic attraction and repulsion to take place across it. Ceramics make good dielectric materials due to its poor conducting property and yet it is very effective in supporting electrostatic fields produced between the two plates of capacitors. These types are non-polarized and are typically inexpensive, available in wide voltage rang, posses excellent high frequency characteristics. These types are most suitable for circuits that require timing, tuning applications, noise filtering, spike suppression, and signal coupling [13].

3.d. Test Plans

Step 1.

Test the converter from 0-100% load capacity in increments of 4%. Record the input voltage, input current, output current, and output voltage. Calculate the input power as well as the output power; i.e. (Power in = [input voltage] x [input current]). The ratio of output power over the input power is the efficiency. Obtain efficiency plot of converter as it is without any modification. The efficiency plot is obtained by plotting the efficiency versus the output power in watts.

By observation it has been determined that there are two tantalum capacitors in parallel in the output stage of the converter. Both capacitors have values of 220uF totaling 440uF.

Step 2.

Replace existing capacitor with different combinations of tantalum capacitors providing wide ranges of values as well as the number of capacitor in parallel. Obtain the efficiency plot for each combination of capacitor applied to the converter. Note: With a higher the number of capacitors in parallel, the combined total ESR of the converter will decrease. Theoretically this should allow greater current flow thus improving overall performance. But in this case, other factors are involved and the efficiency is not necessarily improved.

Step 3.

Step 2 is repeated but with electrolytic capacitors.

Step 4.

Step 2 is again repeated but with ceramic capacitors.

3.e. Test Results

Data has been taken and recorded for three different types of capacitor. In analyzing the obtained information each will be compared to its own type before being compared to the original efficiency value of the converter; which consisted of two tantalum capacitors in parallel at a total value of 440uF. Lastly, the best result will be singled out and final recommendations will be discussed in the conclusion.

The first efficiency plot obtained is that of the original converter before any modification was conducted (see Figure 40). When compared to the data sheet provided by the manufacturer, the efficiency obtained is 78% at 80W output power as oppose to 80% at 90W. We are conducting an efficiency test therefore the corresponding power reading is not of importance. It is mentioned here in the report as a reference.

This discrepancy between the data sheet and the actual measurement can be attributed to a number of causes. First, the documented data is in increments of 4%. Perhaps somewhere in between that number is the maximum efficiency of 80%. Second, the test lab at RO Associates' facility is far more suitable with controlled temperature environment for testing than what we posses here in Cal Poly. Thirdly, it is most likely that the published data is the maximum recorded value. Utilizing what we have and obtaining only a 2.5% difference is considered to be acceptable.

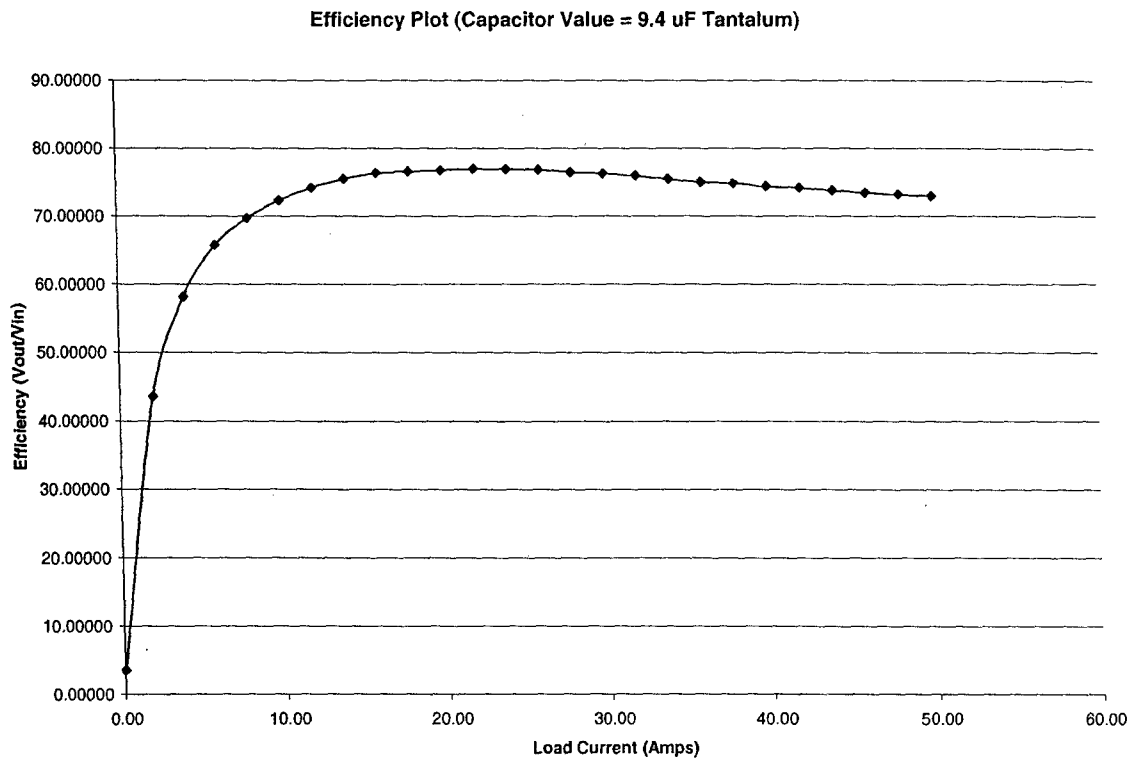


Figure 40. Original Efficiency of the converter

Nine different values were tested using tantalum capacitors with values ranging from 9.4uF to 1440uF. Keep in mind that in most cases the higher the capacitor value tested; the more capacitors were used due to shortage of supply. Two 4.7uF capacitors were in parallel to achieve the 9.4uF value. At the capacitance value of 1440uF, a total of 12 capacitors were aligned in parallel. A table summarizing the result is provided in Table VI. The efficiency plot can be viewed in Figure 41.

Table VI.

Tantalum Results		
Capacitance (uF)	% Efficiency	Power
9.4	76.90	73.00
20	78.00	79.00
94	77.00	73.00
146	77.68	73.00
200	77.76	79.50
440	78.00	79.55
640	78.23	79.54
1140	78.01	79.54
1440	77.77	79.54

Figure C2. Efficiency Plot
(All tantalum results)

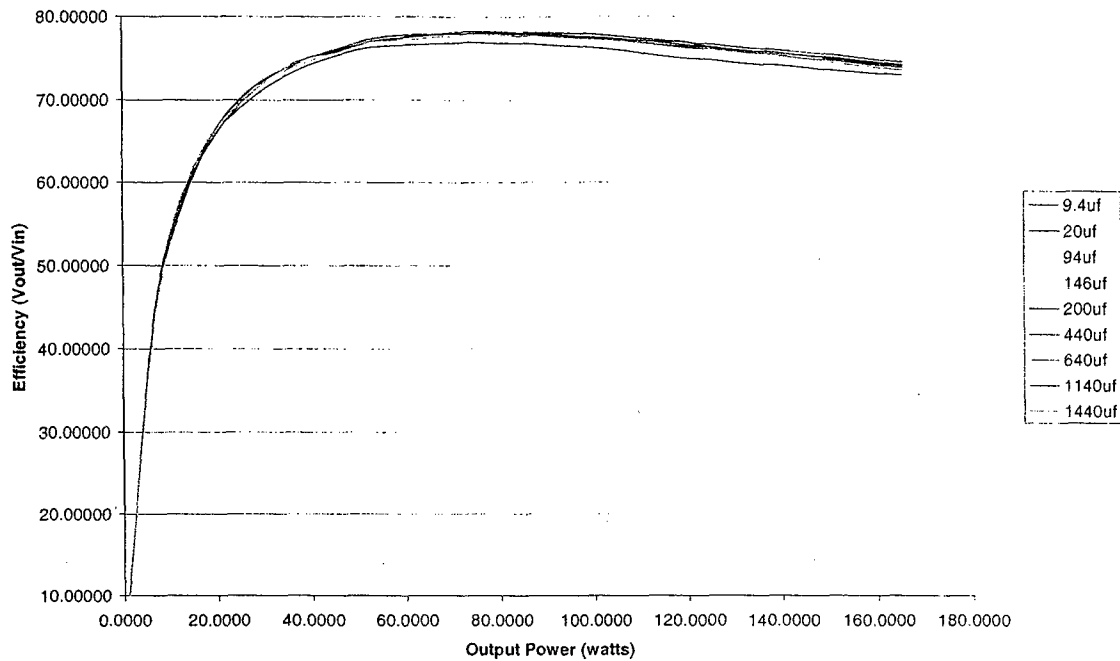


Figure 41. Efficiency of the converter with Tantalum Capacitors

The second capacitor type tested is of electrolytic material. Four values were obtained ranging from 0.2uF to 903uF. The value of 1.0uF appears to give the greatest efficiency of 77.72% at 72.94W. No significant difference was noticed here. The only difference worth mentioning is that of 238uF. At this value, the converter's efficiency drops below 77%, but only to rise again when the capacitor value is at 903uF. No trend was established as the value of the capacitor was increased. The summary of the result is provided in Table VII. The efficiency plot can be viewed in Figure 42.

Table VII.

Electrolytic Results		
Capacitance (uF)	% Efficiency	Power
0.20	77.32	77.23
1.00	77.72	72.94
2.38	76.92	72.90
903.00	77.46	72.93

Similar to electrolytic capacitors, ceramic capacitors were limited. Only four values were tested ranging from 44nF to 1392nF. No significant differences were noticed. Test results indicate that the maximum efficiency obtained is 77.16% at 73.34W. This value is less than that of the tantalum capacitor. A table summarizing the results is provided below in table VIII. The efficiency plot can be view in Figure 43.

Figure C3. Efficiency Plot
(All Electrolytic results)

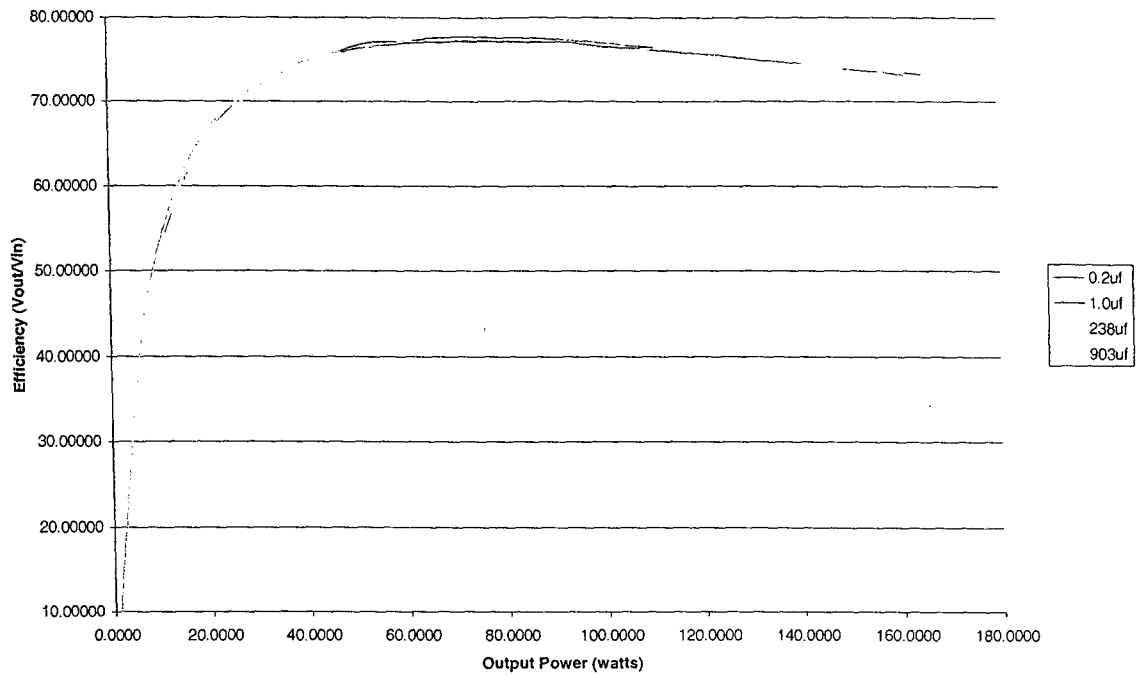


Figure 42. Efficiency of the converter with Electrolytic Capacitors

Figure C4. Efficiency Plot
(All Ceramic results)

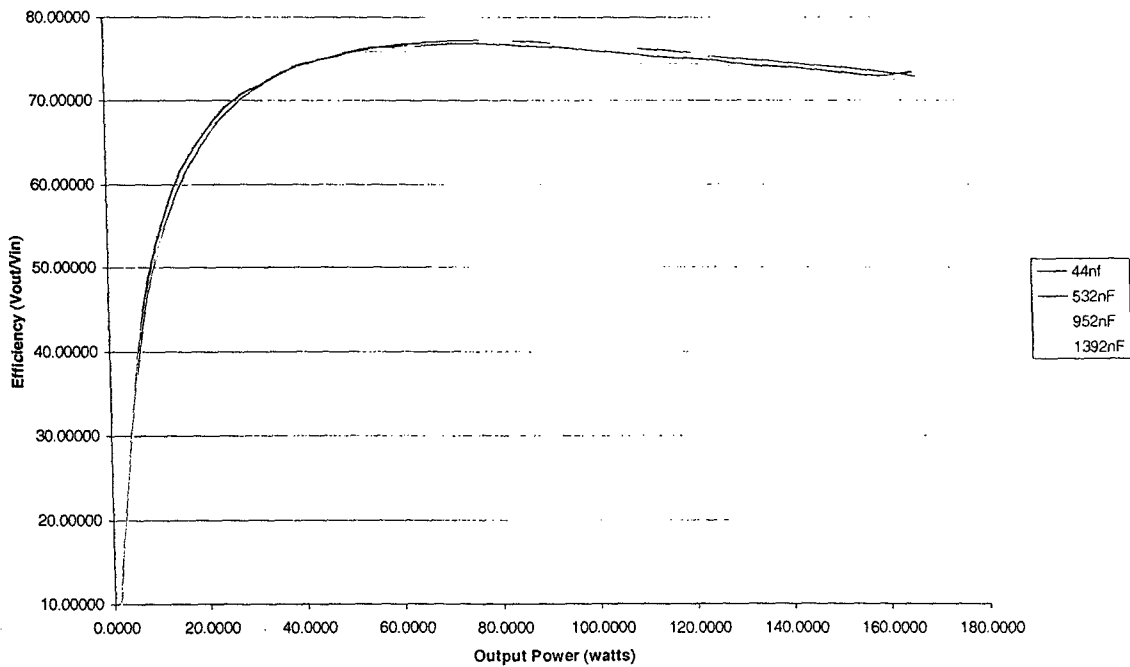


Figure 43. Efficiency of the converter with Ceramic Capacitors

Table VIII.

Ceramic		
Capacitance (nF)	% Efficiency	Power
44	76.78	73.21
532	77.16	73.34
952	77.07	80.20
1392	76.07	73.21

Figure C5. Efficiency Plot
(Comparing all types to the original)

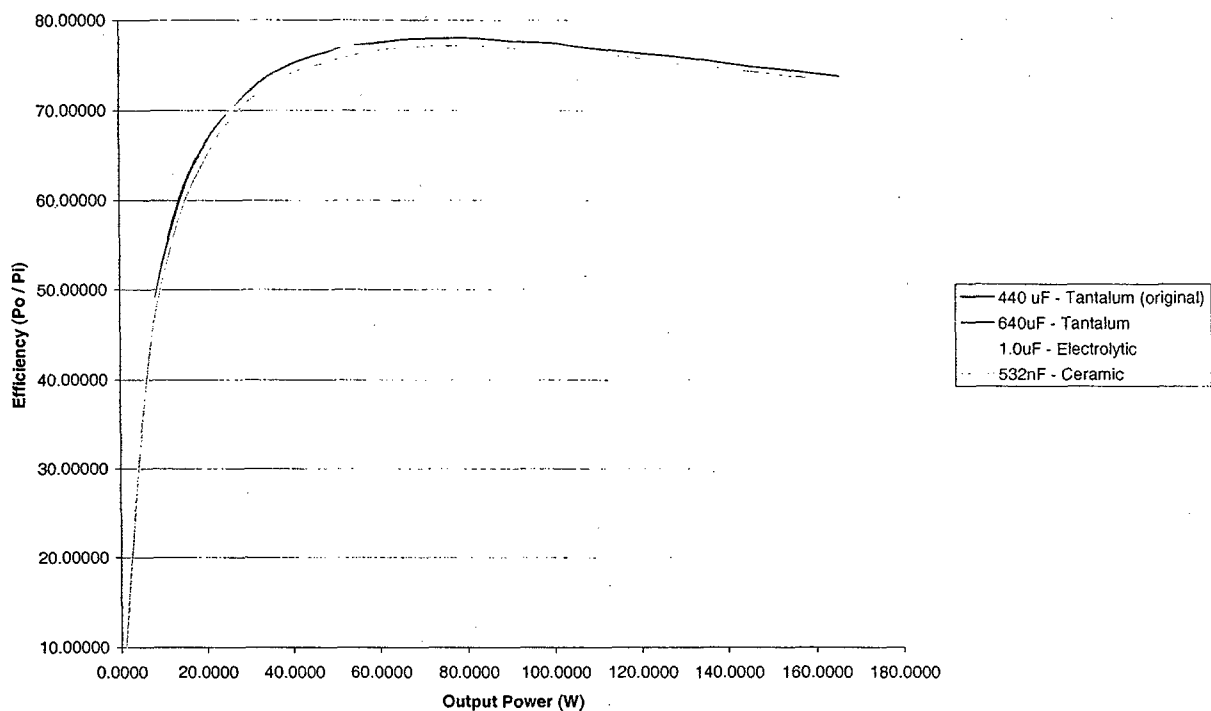


Figure 44. Efficiency of the converter with all types of Capacitors

4. Conclusions and Recommendations

From the data measurements and calculations, the overall efficiency of the converter increases as the switching frequency decreases. It is expected as the switching frequency decreases, the switching losses decreases. The efficiency changes are more significant in lighter load (10%-40% of full load) compared to full load or close to full load. At 10% load, from 704 kHz to 202 kHz, the efficiency difference is about 20%. But the efficiency difference is about 4% at full load between 704 kHz and 202 kHz.

From the above conclusions, it is recommended that the designer engineer should take into account of the switching frequency of the dc-dc converter. Especially, if the converter is not

going to operate at full load most of the time, the switching frequency impacts the efficiency more significantly. Therefore, lower switching frequency is recommended for the dc-dc converter design.

In the switch and output inductor investigations, the forward converter was compared to the flyback converter because of their similarities. The flyback converter does not have an output inductor and only has two transformer windings, whereas the forward has three ideal windings. Despite the smaller size of the flyback, the forward converter is better than the flyback because the transformer in the forward converter typically does not store energy, thus acting as an ideal transformer. The transformer core is reset by reset winding, where the energy stored in the transformer core is returned to the supply and the efficiency is increased.

In a DC-DC forward converter, the transformer helps in increasing efficiency because, ideally, it does not store energy. Instead of absorbing energy, the transformer transfers power directly from the source to the load. However, there will be some power losses due to the windings of the transformer. A way to improve efficiency by means of the transformer is to choose one that is small in size and has a low power density, which will give a low core loss of the transformer. Another way is to reduce the turns-ratio, N_2 / N_1 . This will lessen the copper loss in the secondary winding.

The output inductors that were tested for this project were not successful in the attempt to increase the converter's efficiency. A way to improve on the results is to wind the copper wires more tightly around the toroid cores in order to lessen the core losses. However, the inductor tests performed does show how efficiency could be affected by inductor selection.

The power switch component in the converter also contributes to the effect of the efficiency. The on resistance of a good switch tends to be small as in the IRF3710 which has an on resistance of 23 milli-ohms. Lower on resistance values results in lower conduction losses thus improving efficiency. The total power out is closer to the total power in. The STW60NE10 switch has an on resistance of 22 milli-ohms. This is good except that its packaging is different compared to the original switch. It is not worth it changing the switch component of the converter because the total costs to change the part would be more expensive. The larger size of the STW60NE10 switch would mean the circuit board would have to be made larger and the unit price of the STW60NE10 switch is also more expensive compared to the switches from International Rectifier.

As for the capacitor investigation, although the results show very little variations, careful observation and analysis does show that the values of the capacitor and the dielectric type of capacitor used in the circuit does indeed matter. Perhaps, had this project have been at a much larger scale, had there have been more resources and time; more tests would have been conducted and tests results would have verify that the capacitor have a significant affect on the efficiency of the converter.

RO Associates manufactures great products and although the μ V28-3 is low in the efficiency rating; the manufacturer has only one objective in mind and that is to mass produce a dc-dc converter that can produce 150W output. Its efficiency is apparently not as important as

the power rating in the design consideration. The μ V28-3 is a well designed product and is well suited for applications that require that much power.

While the differences between the three dielectric types are small, the ESR for the electrolytic and the ceramic capacitors are much higher than that of the tantalum capacitor. If the goal is to obtain maximum efficiency out of this converter then the best thing to do is use the highest quality parts available in the market. From the data obtained, tantalum capacitors are the best suited dielectric material because of its low ESR property. When multiple capacitors are connected in parallel, the ESR is reduced exponentially thus reducing the power loss in the circuit.

Overall, this project has successfully shown how careful selection of crucial components of dc-dc converter circuit may indeed improve its overall efficiency. The project also has provided some hands-on learning experience for students and has given them a better understanding on how dc-dc converter is being designed, especially for high-density applications. As many as four undergraduate students took part in this project (Kay Ohn, April Oliver, Yla Alivia, and Kam Insixiengmay), and all have successfully performed the required tasks and gathered useful data to be presented in this report. Also, this project resulted in two conference papers:

- "Recent Experience in Undergraduate Research on High-Density Converter at Cal Poly", Proceedings of 2005 ASEE Conference, Los Angeles, April 2005.
- "Development of Power Electronic Senior Project Bench at Cal Poly", Proceedings of NSF/ONR-Sponsored faculty Workshop on Teaching of First Courses on Power Electronics and Electric Drives, February 2005.

Last but not least, this project allowed us to acquire lab equipment which is now being used frequently for students doing senior design projects. The equipment definitely enhances our lab capability in terms of performing industry standard metering and measurements and has played major role in obtaining industry relationship such as with Texas Instruments and APD Semiconductor. From these relationships, it is hoped that future projects may be generated.

5. References

- [1]. Switching Power Magazine, Volume 4, Issue 1, 2003, pp.7.
- [2]. Kraus, R., Myers, I., Baumann, E., "Light weight, high power, high voltage DC/DC converter technologies", Proceedings of the Intersociety Energy Conversion Engineering Conference, v 1, 1990, p 380-385
- [3]. Sun, J., Mehrotra, V., He, J., "Dual-use development of high density DC/DC converters", Source: Proceedings of the Intersociety Energy Conversion Engineering Conference, v 1, 2000, p 185-192.
- [4]. Gerber, M., Ferreira, J.A., Hofsjager, I.W., Seliger, N., "High density packaging of the passive components in an automotive DC/DC converter", PESC Record - IEEE Annual Power Electronics Specialists Conference, v 2, 2002, p 761-767
- [5]. R.O Associates, Website: <http://www.roassoc.com/products/microv.htm>
- [6]. Taufik, "Switching Power Supply Notes", California Polytechnic State University, San Luis Obispo, CA, 2005.
- [7]. Taufik. "Power Electronics: EE 410 Lecture Notes", California Polytechnic State University, San Luis Obispo, CA, Fall 2004
- [8]. Electus Distribution 2001
http://www1.electusdistribution.com.au/images_uploaded/dcdcconv.pdf.
- [9]. http://www.cwsbytemark.com/cws_catalog/section1/1_01_mag_mtl.pdf
- [10]. Micrometals Catalog Iron Powder Cores for Power Conversions and Line Filter Applications Issue K Feb 2003.
- [11]. International Rectifier Website, www.irf.com/product-info/datasheets/data/irf3710.pdf
- [12]. Rashid, Muhammad. Power Electronics, Circuits, Devices, and Applications. New Jersey: Pearson, 2004.
- [13]. AVX Website, "<http://www.avx.com>"
- [14]. SYFER Website, "<http://www.syfer.com>", March 17, 2005,
- [15]. Novacap Website, "<http://www.novacap.com>"
- [16]. Alexander, Charles K. and Sadiku, Matthew N.O. Fundamentals of Electric Circuits. McGraw-Hill Companies, Inc. U.S.:2000.
- [17]. Foutz, Jerrold, Switching-Mode Power Supply Design, 2004-2005 SMPS Technology Knowledge Base, "<http://www.smpstech.com/index.htm>".

**Establishment of a Field Site for Testing Non-Toxic, Fouling-Release Marine
Coatings to Aid in the Control of Biofouling and Corrosion**

Project Investigators:

**Dean E. Wendt
Assistant Professor
Biological Sciences Department / Center for Coastal Marine Science**

Background

The following report details the activities and accomplishments of work to develop a field site for testing non-toxic, foul-release marine coatings. The original performance period was for one year beginning 15 April 2004. The performance period was subsequently extended to June 2005.

Current technologies for controlling biofouling (i.e., the accumulation of marine organisms on human-made objects), such as the use of toxic paints, are being restricted because of their adverse and often non-discriminate environmental effects. The development of coatings that deter biofouling through non-toxic means is a primary research focus of the US Navy. The work completed under this contract has enabled my research program to expand its current capacity to include field testing of marine coatings. The development of our field site allows my group to offer ONR-supported researchers and private companies a more comprehensive testing facility that involves both laboratory and field-based testing of their experimental coatings. Moreover, the Cal Poly facility is the only field testing site located on the west coast of North America and it is the only ONR-supported site in a cool-water temperate marine environment.

Specific Accomplishments

Our significant accomplishments thus far include: 1) acquisition of the boat used to transport personnel from the Cal Poly pier to the moored floating platform; 2) complete design, construction, and setting of moorings for the platform; and, 3) complete design and construction of the floating platform; and, 4) launch and placement of the floating platform. The boat was purchased as the floating platform is moored approximately 0.5 miles from the end of the Cal Poly pier. The vessel purchased is a 19 ft. inflatable Zodiac with a 90 hp outboard motor. It is small enough to be easily launched from the 1-ton lift on the Cal Poly pier, yet large enough to comfortably transport equipment and several people to and from the floating platform. The floating platform is tethered by two, newly constructed moorings (Fig. 1). The moorings were designed, constructed, and set by the personnel at Port San Luis and they were placed in an area of the bay that receives the least amount of wave action and the greatest growth of fouling organisms. The test platform is a custom-designed floating dock with an open central area for holding between 200 and 600 coated panels, depending on the size of the individual panels (Fig. 2). The panels are placed in submerged racks that attach directly to the floating platform. The floating platform provides plenty of deck space for personnel to perform their duties, and is protected from incursion by sea lions by galvanized fencing, both around the perimeter and over the central open area.

Proposed Work

Our proposed work for next year will include work in two basic areas: 1) quantification of the within-site variability of composition and amount of biofouling at the San Luis Bay testing area; and, 2) development of higher throughput assessment techniques than currently available at other field testing sites. Progress in both of the aforementioned areas will improve our functionality as a premier test facility within the Office of Naval Research biofouling program, through which I am currently receiving funding.

Proper understanding of the within site variability in amount and composition of fouling species at our testing platform is essential to efficient design of future experiments evaluating the efficacy of marine coatings. It is well known that the distribution of fouling organisms can vary over small spatial scales, such as our testing platform. The source of variability under question can arise for two reasons. The first source of potential variability results from the placement of the baskets within the test platform. Because the platform necessarily has fixed orientation to various environmental factors such local currents, light exposure, and swell direction, there is potential for microhabitats to develop over the spatial scale of the field site that will favor the growth and development of certain species of fouling organisms. For example, certain species of barnacles are more likely to thrive in areas with greater exposure to the predominant swell. As such, in this example, the area on the side of the dock facing the mouth of the bay would likely be a better environment for growth of those particular species of barnacles. The second source of variability could result from microhabitats associated with the placement of panels within an individual rack. For similar reasons the panels on the edge of a rack could be in a different microhabitat compared to panels placed within the middle of racks. We are proposing to conduct a series of controlled field experiments to assess the extent to which fouling varies as a result of basket placement within the field site and panel placement within the baskets. Knowledge of this source of variability will aid in the proper design of future experiments.

The second major area of work for the next year will include development of high-throughput methodologies for field testing panels. The current ASTM standard methods are not designed for the rate at which current coatings are being produced through combinatorial techniques. In essence, the technologies associated with coating production have out paced the technologies associated with coatings assessment. As such, a primary focus of our efforts in the coming year will consist of modifying standard practices currently used to assess fouling coverage and fouling release properties of coatings to accommodate the rapid production of coatings.

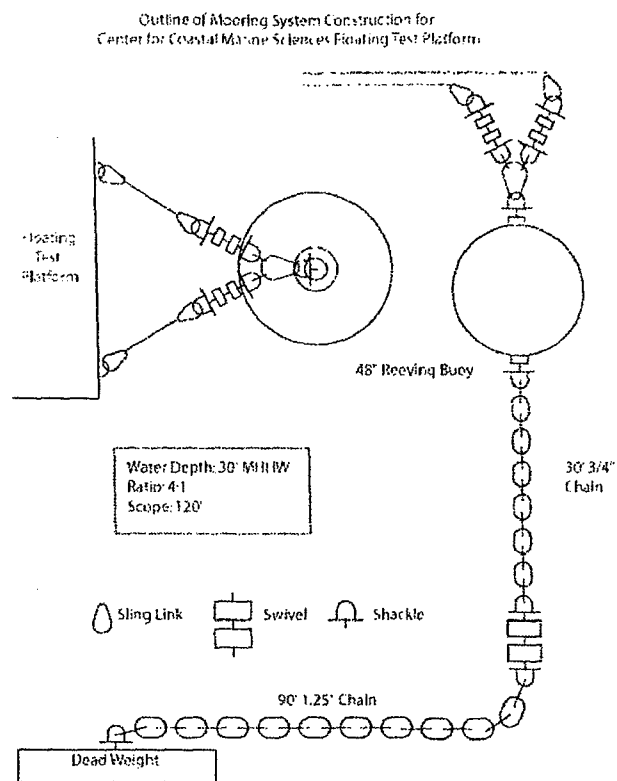


Figure 1. Diagram of mooring system used to secure the Cal Poly floating platform. The floating platform is secured by two moorings to provide for stability in extreme ocean conditions.



Figure 2. Floating platform in place in Port San Luis. Note the open area in the center for holding submerged, coated panels.

3D Digital Data Acquisition and Interaction

Project Investigators:

Zoe J. Wood
Assistant Professor
Computer Science

Lynne A. Slivovsky
Assistant Professor
Computer Engineering, Electrical Engineering

3D Data Acquisition - Structured Light Scanner

Working with a Cal Poly undergraduate student, Professor Wood has set-up an inexpensive, extensible structured light system for range image acquisition and surface reconstruction (Figure 1). The system currently allows for the scanning of approximate range images (Figure 2). The system is comprised of a digital camera, a projector and computer. The Point Grey Research Dragonfly is the camera of choice because it is an affordable research-oriented device of high quality ($1024 \times 768 @ 15\text{Hz}$). The camera is fitted with a Canon TV2714 lens to enlarge and focus variously sized objects. To complement the camera's resolution, the Panasonic PT-L500U LCD projector ($1280 \times 720 @ 60\text{Hz}$) was selected. An extensible software system has been built to drive the camera and projector, programmed in C++ and makes use of third party libraries such as OpenGL and DevIL to integrate image and 3D graphics functionality into the system. All application and project settings are stored in XML and parsed by libxml2. An image of the structured light scanning stage, camera, projector and current system are shown in Figure 1.

The current system is set-up to acquire range images. An example dataset of the 3D data capabilities of the system is shown in Figure 2. Time was spent trying to acquire more accurate depth values for the range images; however, this remains an area of future work for the project. Initial efforts to align images using a genetic algorithm were educational but require more development (Figure 3).

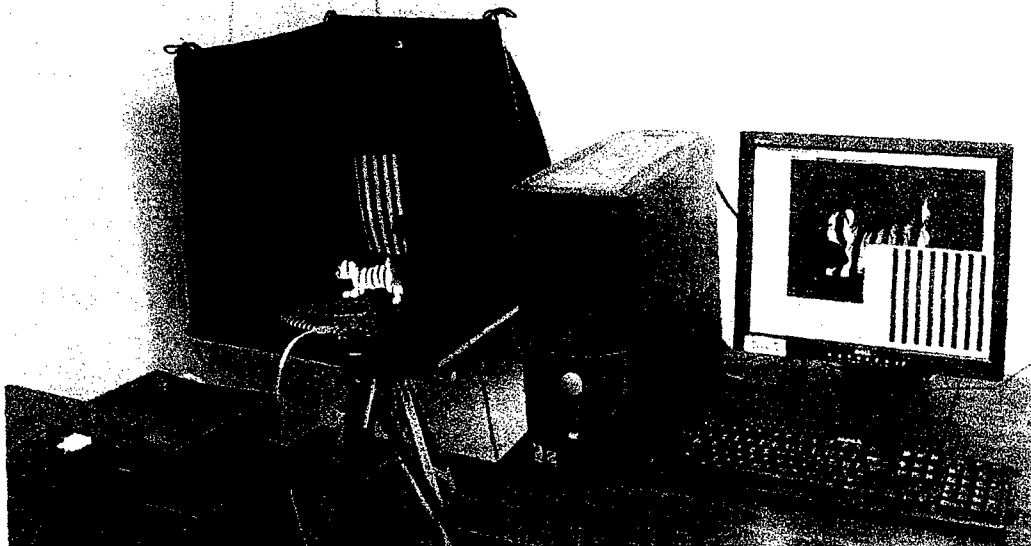


Figure 1. Structured light scanner. A sequence of patterns are projected onto the object, in this case a tiger cub. The camera takes a picture for each pattern as shown on the computer monitor. Finally, a range image is extracted by analyzing the sequence of images.

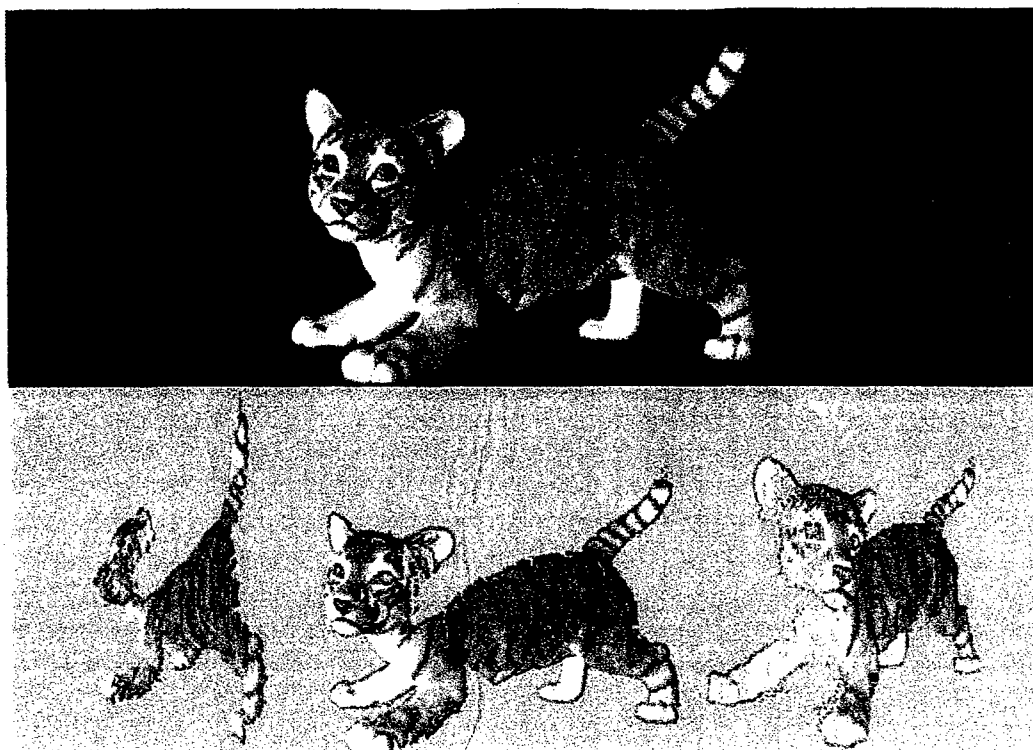


Figure 2. Tiger cub range image. The bottom picture illustrates three viewpoints of the range image drawn as a point cloud. This was extracted from the original viewpoint shown on top. The holes are due to both self occlusions and darker regions that were improperly designated as background pixels.

3D Data acquisition: Future extensions

As the structured light scanner is currently configured to acquire range images, we wish to continue work on the software to complete the 3D surface acquisition capabilities of the system. To do this we will develop the algorithms to acquire more accurate depth values for the range data and more importantly to develop the algorithms to align these range images together to construct complete 3D surface models of real world objects. We have explored initial genetic algorithms to align range images (see Figure 3), however, the results were very preliminary and require improvements.

One of the limitations of the initial attempt to use a genetic algorithm to align the images was the time required to construct an intermediary surface for alignment. The genetic algorithm attempts to align two range images (3D point clouds). In order to measure the accuracy of the current alignment, the algorithm created an initial surface approximation from one range image. The points from one range image were measured against this initial 3D surface to evaluate correctness. The intermediary surface was generated using a 3d Delaunay triangulation, which proved to be prohibitively slow. Future explorations include alternative surface reconstruction algorithms in order to speed up and improve the range image alignment. This includes a system to allow a user to provide a coarse alignment with exact alignment computed algorithmically.

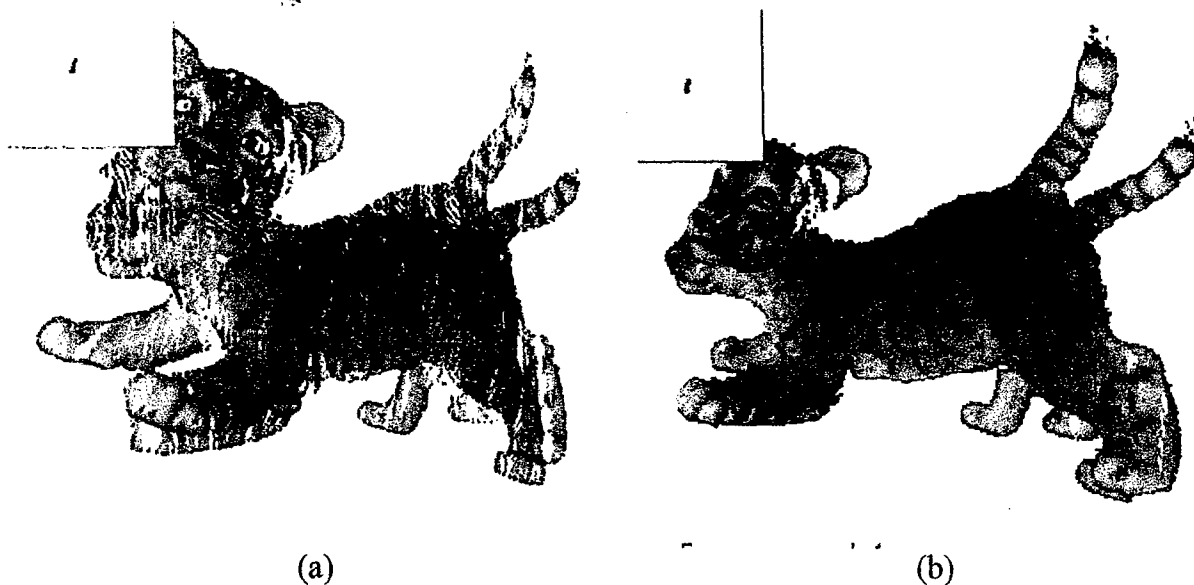


Figure 3. Two stages from the genetic algorithm aligning two range images. Note that the figure on the right (b) is much improved in terms of aligning the two different range images of the tiger dataset, however, the cost of approximating a 3D surface using 3D Delaunay triangulation proved to be prohibitively expensive, stunting the results.

Research Projects

Working with a Cal Poly graduate student, Professor Wood continues to investigate ways to reduce the topological noise present in acquired 3D data, thus improving the final 3D representation acquired by the scanners. Working with existing 3D surface data this project focused on identifying shortest non-separating cuts on surfaces with genus greater than one. These shortest non-separating cuts are then used to simplify the topology of the surface. A software system built in C++ using OpenGL to visualize results has been developed. Initial experiments were conducted to locate short non-separating cuts using Dijkstra's algorithm to identify non-separating cuts that loop across a starting cut once. A modified algorithm was developed to allow these paths to traverse back and forth across the initial cut allowing them to be optimal paths. Initial tests on sample data show an improvement in path length of up to six percent. Figure 4 shows a comparison of the previous algorithm and the improved version.

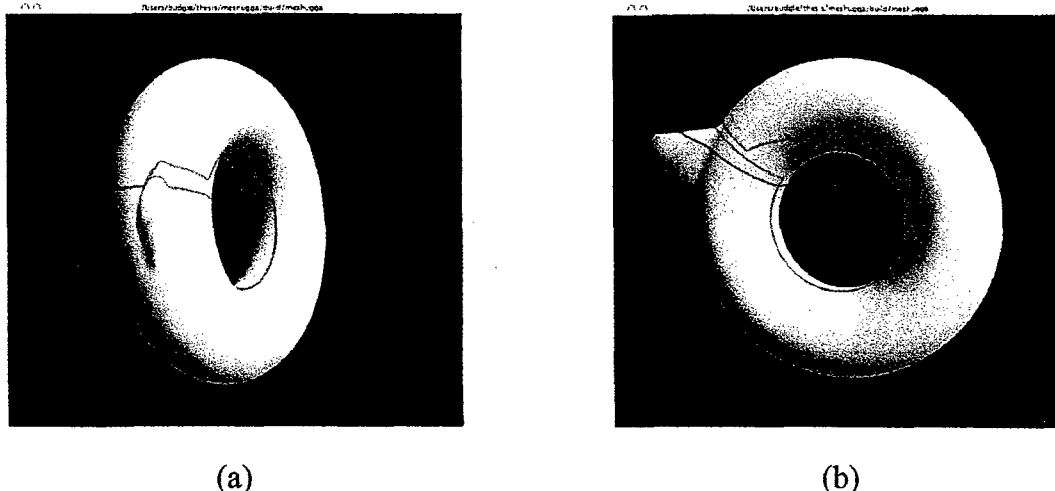


Figure 4. Two cut paths on a torus with a bump. The initial non-separating cut is shown in blue. In figure (a) on the left a path starts from a vertex on the initial cut and is restricted to only cross the cut once (previous algorithm). In contrast in figure (b) on the right, the optimal path is found starting from the same vertex on the initial cut (improved algorithm). The length of the path on the left has a length of 5.587 while the path on the right has a length of 5.960, for a total improvement of six percent.

Sitting Posture Classification

We can extend our notion of intelligent machines beyond the PC to include typically non-computational aspects of our surroundings, such as a room, a chair, a desk, and clothing. Today, systems are being developed that can locate, recognize, and track people; interpret gestures; understand natural language; and use all of this information to predict and assist the needs of a user. These intelligent environments include smart rooms, smart clothes, and smart chairs¹. The majority of these systems use audio and visual cues to interpret their surroundings. The use of haptic (i.e., touch-based) interfaces are driving a new area of machine intelligence research. Those that use pressure sensing devices can be found in the automotive, seating and bedding industries.

The goal of the haptics project using the sensing chair is to enable a computer to track, in real time, the sitting postures of a user through the use of surface-mounted contact sensors. Given the similarity between a pressure distribution map from the contact sensors and a gray-level image, Professor Slivovsky has adapted computer vision and pattern recognition algorithms for the analysis of sitting pressure data. This work involves: (1) data collection for a sitting pressure distribution database, (2) development of real-time sitting posture classification and tracking systems, and (3) performance evaluation of the systems. The realization of a robust,

¹Papers on intelligent environments:

Hong Z. Tan, Lynne A. Slivovsky, and Alex Pentland. "A Sensing Chair Using Pressure Distribution Sensors." In *IEEE/ASME Transactions on Mechatronics*, Vol. 6(3), pp. 261-268, Sept. 2001.

Steve Mann, humanistic Intelligence: Wearcomp as a new framework for intelligent signal processing. *Proceedings of the IEEE*, 86(11):2123-2125, November 1998.

Alex P. Pentland. Smart Rooms. *Scientific American*, 274(4):68-76, April 1996.

real-time tracking system will lead to many exciting applications such as automatic control of airbag deployment forces, ergonomics of furniture design, and biometric authentication for computer security.

Preliminary work has focused on the construction of the Static Posture Classification system. First, a Static Posture Database was established. The database contains a total of 1500 sitting pressure distribution maps from 30 individuals. Second, a real-time multi-user Static Posture Classification system was developed. This system classifies sitting pressure distributions with an overall accuracy of 96% correct for users that contributed training data. When the original system was tested with new data (from users who did not contribute training data, the overall accuracy rate fell below 80%). A system like this is needed in order to represent a person's posture during transitions from one static posture to the next (e.g., from seated upright to sitting with one leg crossed over the other).

The system uses pressure sensors (developed by Tekscan, Inc.) that interface with a PC through a special interface board. They are mounted on an office chair and capture pressure distribution information of a user seated in the chair. The sensor configuration is shown in Figure 5. The pressure information from the sensors is converted to an 8 bit raw digital value that can be treated as a greyscale image. A sample sitting pressure distribution map for posture Seated Upright is also shown. The top half of the image shows the pressure distribution on the back of the chair, and the bottom half shows that of the seatpan. The top, bottom, left and right sides of the image correspond to the shoulder area, knee area, right side and left side of the person, respectively.



Figure 5: Pressure sensing acquisition hardware mounted on an office chair and a sample sitting pressure distribution map.

Classification accuracy of the samples in the posture database was determined using a leave-one-out testing method. All samples went through preprocessing that consisted of one of three options: no preprocessing, cropping to remove background noise of the sensors around chair edges, and peak normalization to factor out subject weight across samples. The samples then underwent a secondary processing phase: no processing, smoothing, whitening, or smoothing and whitening. Finally, the test sample was classified. Table 1 depicts classification results reported by posture and overall classification accuracy for k-nearest neighbor ($k=1,3$) on tests

including the entire pressure distribution map and those that include the seatpan portion. The parameters for this test were: cropping, no smoothing, whitening. Overall classification accuracy ranged in the mid-to-high 80 percentile.

The ultimate selection of an algorithm for sitting posture classification is highly application dependent. Analyzing the trade-offs of various classification algorithms will yield a starting point for application-specific projects in the future.

Postures	1NN seatpan map	1NN full map	3NN seatpan map	3NN full map
Upright	70.67%	69.30%	60.70%	60.00%
Leaning Forward	87.33%	91.30%	86.00%	89.30%
Leaning Right	85.33%	85.33%	84.00%	82.00%
Leaning Left	88.67%	85.33%	90.00%	78.70%
Right Leg Crossed	90.67%	89.33%	88.70%	80.70%
Left Leg Crossed	88.67%	93.33%	88.70%	92.00%
Leaning Left with Right Leg Crossed	89.33%	86.00%	87.30%	86.70%
Leaning Right with Left Leg Crossed	92%	92.00%	85.3%	92.70%
Leaning Back	84.67%	87.33%	82.00%	87.30%
Slouching	94.67%	92.00%	95.30%	95.30%
Average Classification Rate	87.20%	87.10%	84.80%	84.47%

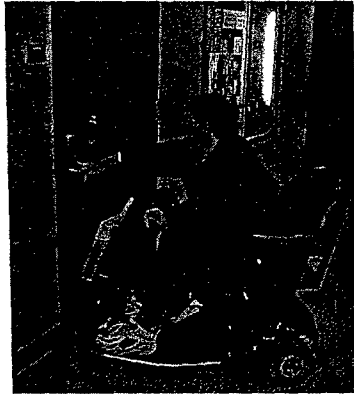
Table 1: Classification accuracy of sitting pressure distribution maps.

Presentations

The work on static posture classification ("Analysis of Pressure Distribution Data for Sitting Posture Classification in a Haptic Chair") was presented at:

- The Stanford – Tohoku Joint Research 100th Anniversary Meeting, May 19, 2005.
- Galatasaray University, Istanbul, Turkey, July 4, 2005.

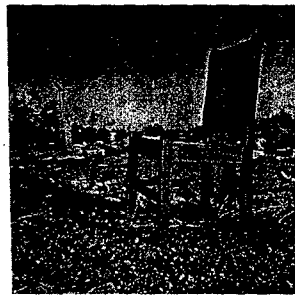
Analysis of Pressure Distribution Data for Sitting Posture Classification in a Haptic Chair

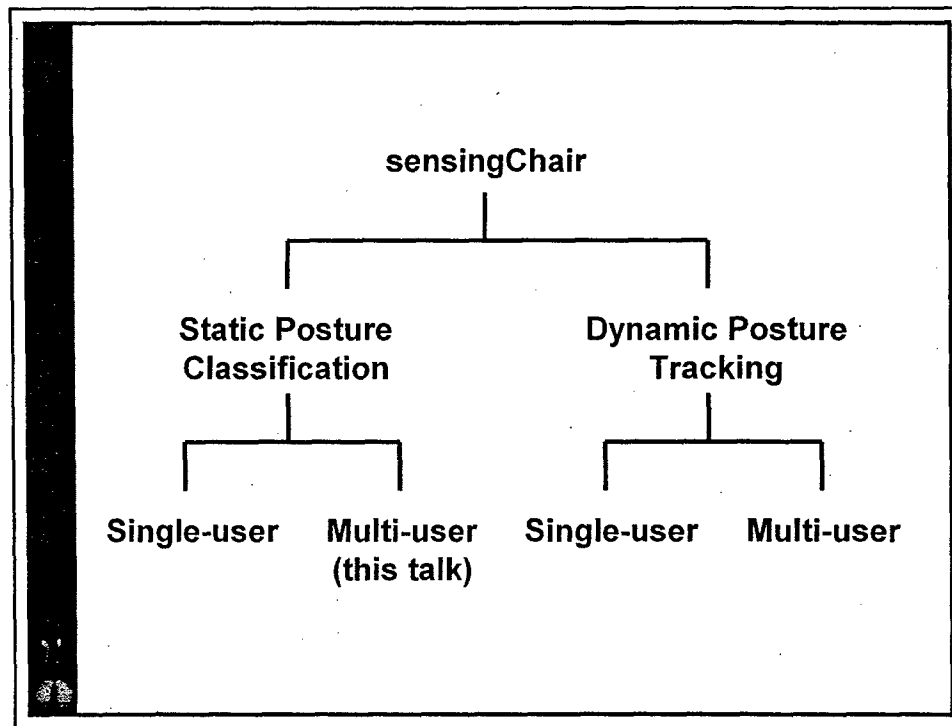


Lynne A. Slivovsky

May 19, 2005

Computer Engineering
Electrical Engineering
California Polytechnic State University
San Luis Obispo, CA





Agenda

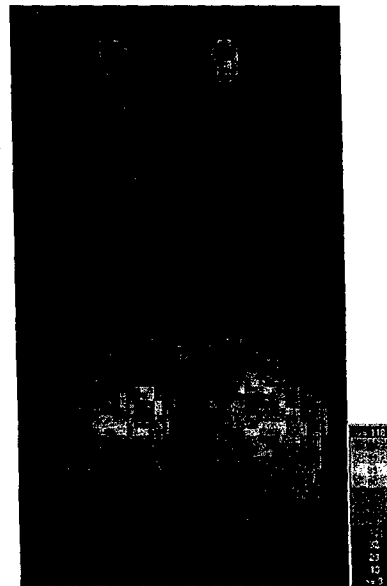
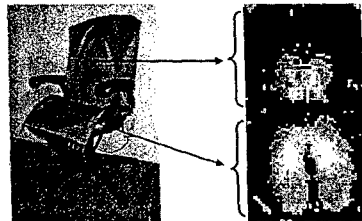
- ☒ Motivation
- ☐ System Configuration
- ☐ Related Work
- ☐ Static Posture Database
- ☐ Posture Classification
- ☐ Conclusion

The Sensing Chair

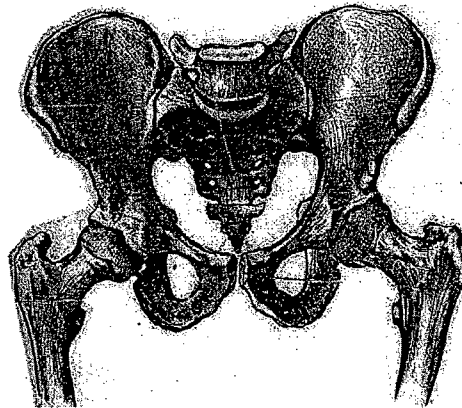
- Tekscan Body Pressure Measurement System
- Sensor Sheet
 - ◆ surface mounted
 - ◆ 0.10 mm thick
 - ◆ 42-by-48 sensels
 - ◆ 10 mm sensel spacing
 - ◆ 8-bit output
 - ◆ 127 Hz throughput
- Two sensor sheets (seatpan & seatback)



Sitting Pressure Distribution Map



Key



Related Work

- **Computer Vision & Pattern Recognition**
- **Haptic (touch-based) Interfaces**
- **Intelligent Environments**
- **Pressure Sensing**
- **Ergonomics**

Agenda

- ☒ **Motivation**
- ☒ **System Configuration**
- ☒ **Related Work**
- ☐ **Static Posture Database**
- ☐ **Posture Classification**
- ☐ **Conclusion**

The Static Posture Database

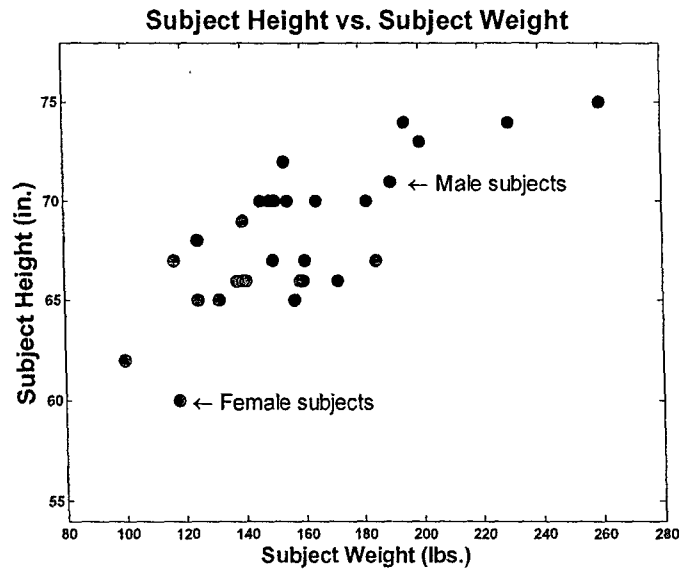
- **50 subjects (25 females, 25 males)**
- **10 common postures**
(e.g., leaning left, slouching)
- **5 samples / posture / subject**
- **2500 sitting pressure distribution maps total**
- **250 samples per posture**
- **Recorded subject anthropometrics**
(e.g., height, weight, paddedness)

Static Postures

Posture Name	Abbreviation
Upright	N
Leaning Forward	LNF
Leaning Left	LNL
Leaning Right	LNR
Right Leg Crossed	RLC
Left Leg Crossed	LLC
Leaning Left with Right Leg Crossed	LLRLC
Leaning Right with Left Leg Crossed	LRLLC
Leaning Back	LNB
Slouching	SL

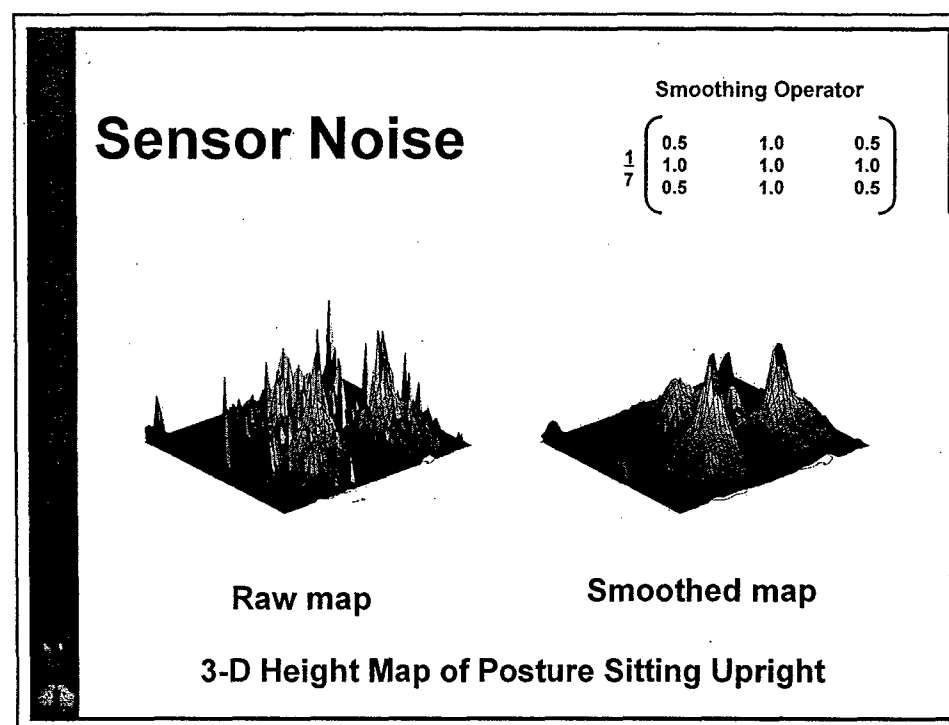
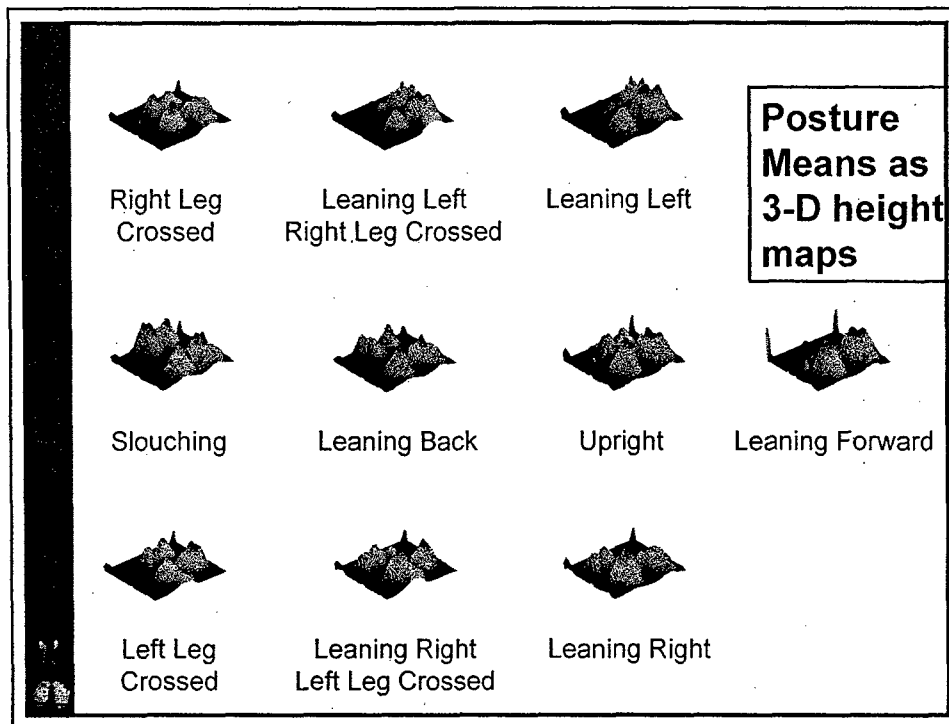
Subject Anthropometrics

Subject Group	Statistic	Subject Height (in)	Subject Weight (lbs)	Subject Age (yrs)	Chair Height (in)	Paddedness
Female	Range	60-70	100-185	18-60	0-3	0-25
	Mean	66	139	30	0.8	11
	StdDev	2.54	21	14	1.1	0.5
Male	Range	66-75	146-260	19-67	0-5	1-3
	Mean	71	177	28	2.3	16
	StdDev	2.7	33	26	1.2	0.8
All	Range	60-75	100-260	18-60	0-5	1-3
	Mean	68	158	29	1.6	15
	StdDev	3.5	36	11	1.4	0.7



Interesting Observations about Pressure Maps

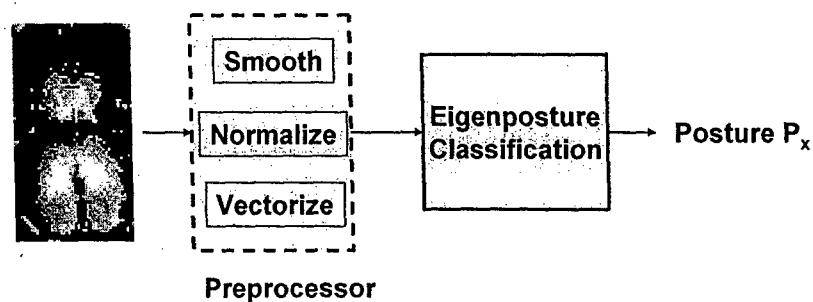
- They are noisy: due to sensor noise and the curved surfaces of the chair
- They are not symmetric
- The pressure data on the seatback is blob-like
- People sit differently for the same posture
- The high dimensionality (4032) of the data inhibits visual examination



Agenda

- ☒ Motivation
- ☒ System Configuration
- ☒ Related Work
- ☒ Static Posture Database
- ☐ Posture Classification
- ☐ Conclusion

Single Stage Classification



Computing Eigenposture Spaces

Eigenvectors of the sample covariance matrix

■ Training

- ◆ Off-line computation
- ◆ 30 database subjects
- ◆ $N=10$ static postures
- ◆ $M=150$ sitting pressure maps for each posture
- ◆ Calculate eigenposture maps for each posture

Classification using Eigenposture Spaces

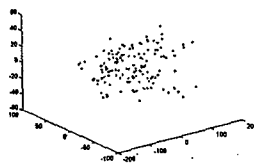
■ Testing

- ◆ On-line computation
- ◆ Let P_{new} be the new pressure map
- ◆ Project P_{new} onto each of the N posture spaces
- ◆ Distance From Feature Space (DFFS) from P_{new} to each posture space
- ◆ The projection closest to P_{new} wins

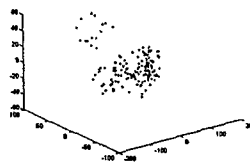
EigenSpace Analysis (*the math*)

- Let P_i be a pressure-map vector of size 4032x1
- Let $\bar{P} = \frac{1}{M} \sum_{i=1}^M P_i$ be the average of M training maps
- Let $\Phi_i = P_i - \bar{P}$ be the mean-adjusted pressure map
- Let $C = \frac{1}{M-1} \sum_{i=1}^{M-1} \Phi_i \Phi_i^T$ be the covariance matrix for Φ_i
- Let u_i be the eigenvectors of C , ordered with descending eigenvalues
- Then u_i , the *EigenPressureMaps (EPM)*, capture the variance in the training data set. ($M \ll 4032$)

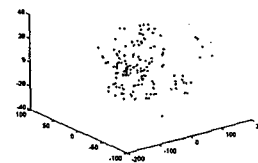
Projection onto the first 3 Eigenvectors



Upright

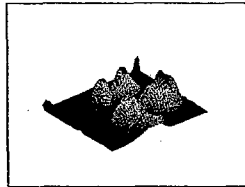


Left Leg
Crossed



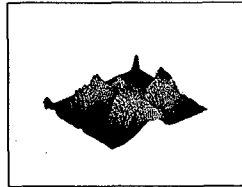
Leaning
Back

Selected Posture Means



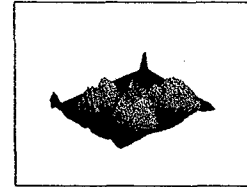
Left Leg
Crossed

94.8 % correct



Leaning Right
Left Leg Crossed

96.5 % correct



Leaning
Right

98.2 % correct

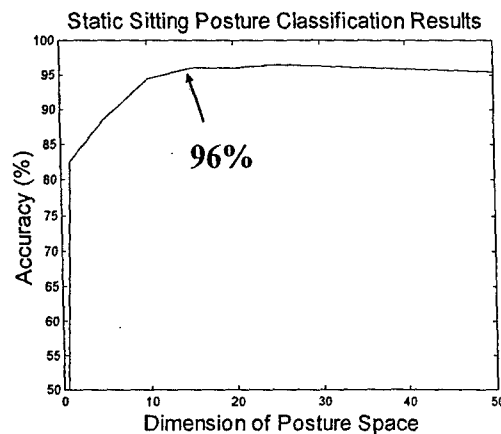
Results

(by Posture on new data from
Training/Familiar subjects)

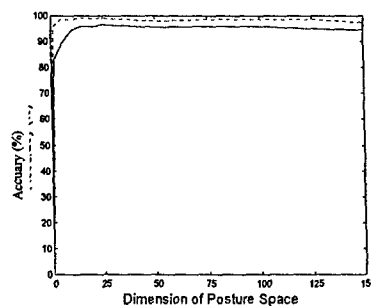
Posture Name	Accuracy
Upright	97.5
Leaning Forward	95.6
Leaning Left	95.2
Leaning Right	98.2
Right Leg Crossed	95.1
Left Leg Crossed	94.8
Leaning Left with Right Leg Crossed	93.5
Leaning Right with Left Leg Crossed	96.5
Leaning Back	90.3
Slouching	99.8

Results

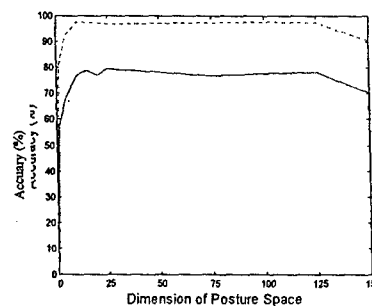
(by Dimension on new data from *Training/Familiar* subjects)



Results on *Familiar* and *New* Subjects using the same model



30 Familiar Subjects



8 New Subjects

Eigenposture Classification: some drawbacks

- New subjects may not be well represented in the Static Posture Database (e.g., data-wise, anthropometrically)
- Performance on new subjects plateaus when the dimension of the eigenposture space is increased.
- Pressure distribution is dependent on seat height

Agenda

- ☒ **Motivation**
- ☒ **System Configuration**
- ☒ **Related Work**
- ☒ **Static Posture Database**
- ☒ **Posture Classification**
- ☐ **Conclusion**

Conclusions

- Built a Static Posture Database containing static sitting pressure distribution maps
 - 2500 samples total
 - 10 static postures
- Developed an eigenposture space-based approach
 - Overall accuracy of 96% correct on familiar subjects
 - 90.3%-99.8% range for different postures

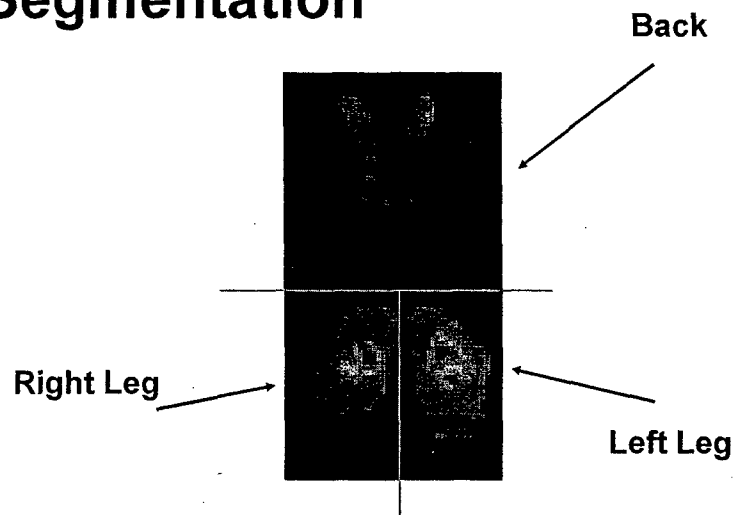
Conclusions (cont.)

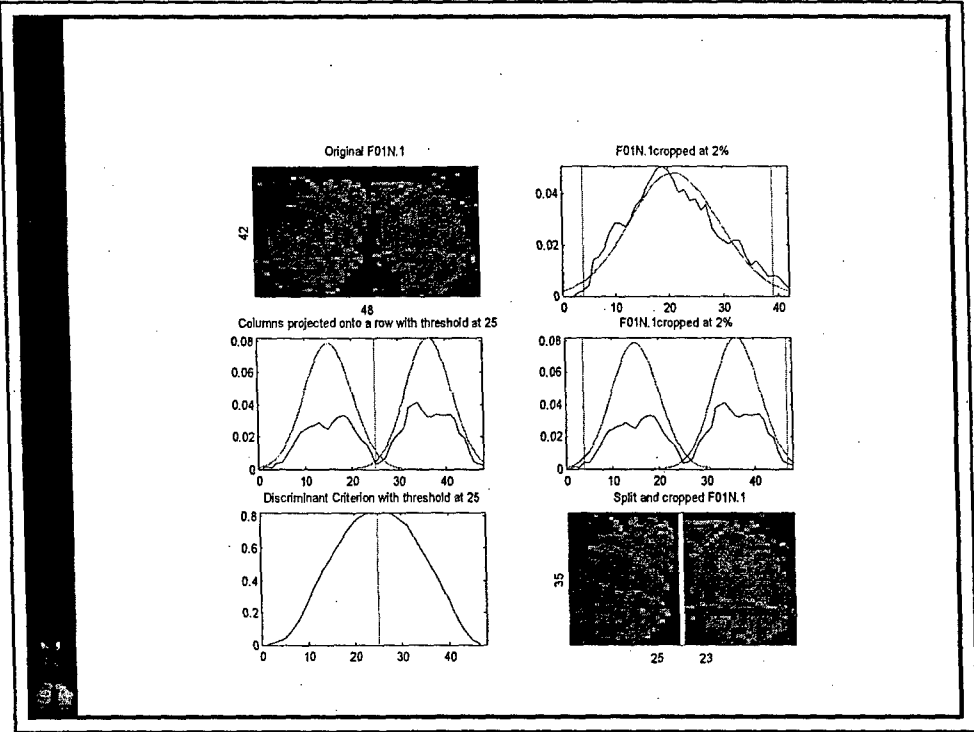
- Observations
 - Gained insight into makeup of sitting pressure distribution maps for each posture
 - *Can use the eigenspace-based approach to generate a set of posture class hypotheses*

Continuing Work

- Current system is application independent.
- Given an application, there can be a speed vs. accuracy tradeoff, can fine tune the algorithm/parameters.
- Apply to different chairs (e.g., wheelchair)
- Sensor size and resolution
- New algorithms that can take advantage of a set of posture class hypotheses

Segmentation





Funding provided by

C³RP – California Central Coast Research Park

Real Time Error Detection Using Artificial Intelligence

Project Investigator:

Xiao-Hua Yu
Assistant Professor
Department of Electrical Engineering
California Polytechnic State University, San Luis Obispo

Abstract

In the studies of rotorcraft flight control and acoustics, the blade vortex interaction (BVI) noise level is an important measure of system performance. This level represents the acoustic noise generated from rotor interaction with the aerodynamic forces generated by previous rotor blade passages, and is a nonlinear function of flight parameters.

Artificial neural networks (ANN) have been successfully applied to system identification and data analysis in recent years. This research focuses on the application of using ANN to model and test the acoustic data gathered from a wind tunnel experiment of a XV-15 tilt-rotorcraft at NASA Ames Research Center. A neural network based model of the blade vortex interaction noise level is developed first; then the modified Z-score method is employed to analyze the residuals between points estimated by the neural network model and the actual BVI noise levels acquired from wind tunnel experiments. Outlier data points were successfully identified using this method.

1. Introduction

A common goal for analyzing experimental data is to identify the relationships between different parameters in the dataset and to find a mathematical model to fully describe it. This knowledge is crucial for the prediction and adaptive control of dynamical systems. However, in most cases the model is non-linear and a closed-form solution is usually not possible.

Artificial neural networks are often used to perform tasks such as machine learning, association, classification, generalization and optimization. An artificial neural network (ANN) is composed of many non-linear adaptive processing elements and is capable of approximating any function under certain conditions. ANN has been widely used in the field of system identification, adaptive control, and statistical modeling.

In aero-acoustic data analysis, an outlier is defined as a data point that is statistically inconsistent with the expectations about this data point, where the expectations are based on the model of the entire data set. Points that deviate greatly from the model could either indicate a fault in the hardware data acquisition system, or may present new information which has not yet incorporated into the model.

In this research, a multi-layer feedforward neural network is employed to model the acoustic data gathered from a wind tunnel test of a XV-15 tilt-rotorcraft at NASA Ames Research Center. To detect outliers in the wind tunnel data, the median-based modified Z-score method is employed. The residuals between the neural network output and the actual wind tunnel values are analyzed using this method to determine the wind tunnel test data whose value is deviated from the neural network model.

2. System Modelling and Outlier Detection using Neural Networks

The experimental data used in this study comes from a wind tunnel test of a XV-15 rotor conducted in the 80 x 120-foot wind tunnel at NASA Ames Research Center at Moffett Field, CA. The purpose of this test was to determine the acoustic noise signature of the XV-15 rotorcraft during simulated flight conditions. The acoustic data is acquired in the wind tunnel by microphones mounted in strategic locations that are estimated to be the locations of maximum

noise relative to the location of the test rotor (Fig. 1). Individual data points are characterized by a set of parameters, including the rotor thrust C_T/σ , a measure of the rotor's lift capability; the advance ratio μ , which is the ratio of true forward airspeed over the wind speed at rotor tip; the rotor tip-path-plane angle α_{TPP} , also commonly known as the angle of attack; and finally, the distance (measured in inches) between the microphone and test rotor x_m .

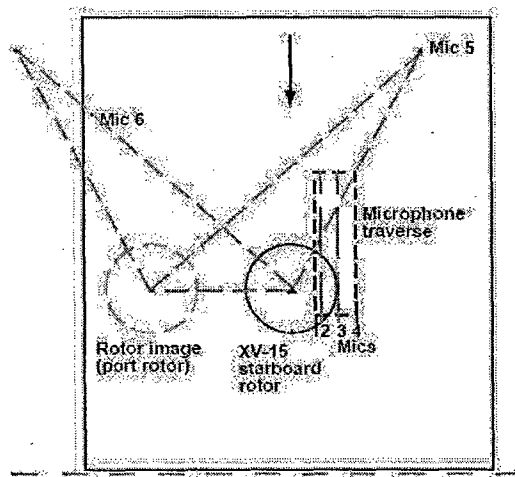


Fig. 1. Schematic of microphone placement in wind tunnel

First, a neural network is trained by the adaptive learning-rate back-propagation algorithm to model the BVI noise level for the traversing microphones. The training set in this case was a random selection of 1/3 of the available test points in the XV-15 database (approximately 360 data points). The neural network was trained for 5,000 iterations with final mean-square-error of 3.30. After training, the neural network is tested using the remaining data in the database. Fig. 2 shows the output of the neural network vs. the values recorded by the microphone in the database. It shows that the neural network can successfully model the BVI noise.

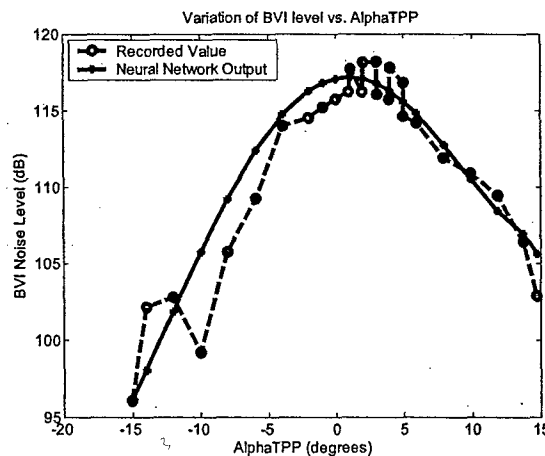


Fig. 2. Output of neural network vs. the measured data

The histogram (Fig. 3) shows that approximately 72% of the residuals (between the estimated and recorded BVI noise levels) are within a range of ± 2 dB where the BVI noise level ranges

from 85 to 120 dB. Again, this indicates that the neural network is capable of modeling the BVI noise level.

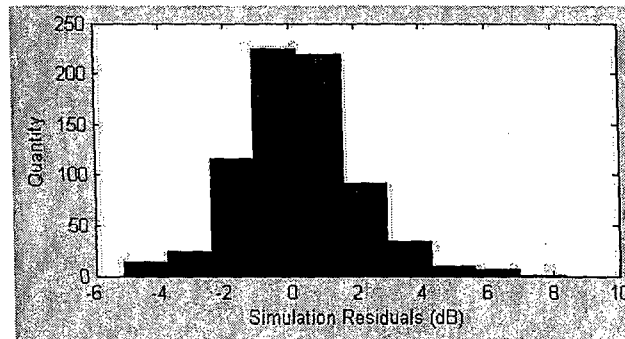


Fig. 3. Histogram of prediction residuals for SCG trained neural network

The modified Z-score method is commonly used in aero-acoustic data analysis for outlier detection. In this research, it is used to find points whose residuals between the estimated neural network output and the recorded BVI noise level are outside the range of the residuals of the entire data set. Among the 740 data points we tested, 7 points were identified as outliers (i.e., 0.95 % of the points were identified as outliers). This indicates that the data overall was of good quality. Four of the outlier data points came from the same set of wind tunnel operating conditions. This set of conditions needs to be further analyzed to see if there was a physical cause as to why the recorded values were outliers or if these points need to be incorporated into the neural network model.

3. Conclusion

In this research, artificial neural networks were successfully applied to aero-acoustic data analysis. Computer simulation results showed that a trained neural network was able to capture the input/output relationship between varying parameters and the corresponding BVI noise level. Outlier detection was also performed using modified Z-scores method. Only a few outliers were detected in the dataset, indicating that the wind tunnel data was overall consistently recorded.

References

- [1] A. Zaknich, *Neural Network for Intelligent Signal Processing* (Singapore: World Scientific, 2003).
- [2] R.J. Schalkoff, *Artificial Neural Networks* (New York: McGraw-Hill, 1997).
- [3] C.F. Lo and F.H. Schmitz, Model-Based Neural Networks for Rotorcraft Ground Noise Prediction. *Proc. 38th AIAA Aerospace Sciences Meeting & Exhibit*, Reno, NV. 2000.
- [4] S. Kottapalli and C. Kitaplioglu, Neural Network Representation of External Tilt-Rotor Noise, *Journal of the American Helicopter Society*, 47(2), 2002, 109-114.
- [5] C. Kitaplioglu, Blade-Vortex Interaction Noise of a Full-Scale XV-15 Rotor Tested in the NASA Ames 80- by 120-Foot Wind Tunnel, NASA Technical Memorandum 208789. Moffett Field: National Aeronautics and Space Administration.

AEROACOUSTIC DATA ANALYSIS WITH ARTIFICIAL NEURAL NETWORKS

Xiao-Hua Yu, Johnny Fu
Dept. of Electrical Engineering
California Polytechnic State University
San Luis Obispo, CA 93407, USA
xhyu@calpoly.edu, jofu@calpoly.edu

ABSTRACT

The blade vortex interaction (BVI) noise level is an important measure in the studies of rotorcraft acoustics. It represents the acoustic noise generated by rotor interaction with the aerodynamic forces generated by previous rotor blade passages, and is a nonlinear function of flight parameters.

In recent years, artificial neural networks (ANN) have been successfully applied to system identification and data analysis. This paper focuses on the application of using ANN to analyze the acoustic data gathered from a wind tunnel test of a XV-15 tilt-rotorcraft at NASA Ames Research Center. Satisfactory simulation results are obtained with two different neural network training algorithms.

KEY WORDS

artificial neural networks, rotorcraft, acoustic data analysis, modeling and simulation, estimation

1. Introduction

A common goal for analyzing experimental data is to identify the relationships between different parameters in the dataset and to find a mathematical model to fully describe it. This knowledge is crucial for the prediction and adaptive control of dynamical systems. However, in most cases the model is non-linear and a closed-form solution is usually not possible.

Artificial neural networks are often used to perform tasks such as machine learning, association, classification, generalization and optimization [1]. An artificial neural networks (ANN) is composed of many non-linear adaptive processing elements and is capable of approximating any function under certain conditions. ANN has been widely used in the field of system identification and adaptive control.

In this research, feedforward neural networks will be employed to analyze the acoustic data gathered from a

wind tunnel test of a XV-15 tilt-rotorcraft at NASA Ames Research Center. Two different training methods are applied, including the adaptive learning-rate back-propagation and the scaled conjugate gradient (SCG) algorithm [2].

2. The Wind Tunnel Acoustic Test

The experimental data used in this study comes from a wind tunnel test of a XV-15 rotor conducted in the 80 x 120-foot wind tunnel at NASA Ames Research Center. The purpose of this test is to find the acoustic noise signature of the XV-15 rotorcraft during simulated flight conditions. Of specific interest is the blade vortex interaction (BVI) noise which occurs when the rotor interacts with the aerodynamic forces generated by previous rotor blade passages. This interaction is known to be a great source of noise disturbance during rotorcraft flight and is a primary concern of both civilian and military rotorcraft use [3].

The acoustic data is acquired in the wind tunnel by microphones mounted in strategic locations that are estimated to be the locations of maximum noise relative to the location of the test rotor. Several of these microphones are also mounted on a traverse array that may be moved horizontally in the wind tunnel. Individual data points are characterized by a set of flight parameters, including the rotor thrust C_T/σ , a measure of the rotor's lift capability; the advance ratio μ , which is the ratio of true forward airspeed over the wind speed at rotor tip; the rotor tip-path-plane angle α_{TPP} , also commonly known as the angle of attack; and finally, the distance between the microphone and test rotor x_m [4] [5]. Figure 1 shows the placement of the microphones used in the XV-15 wind tunnel test. The 4 traversing microphones are moved along the lines bolded to show the traverse path. The data recorded by these traversing microphones will be analyzed using neural networks.

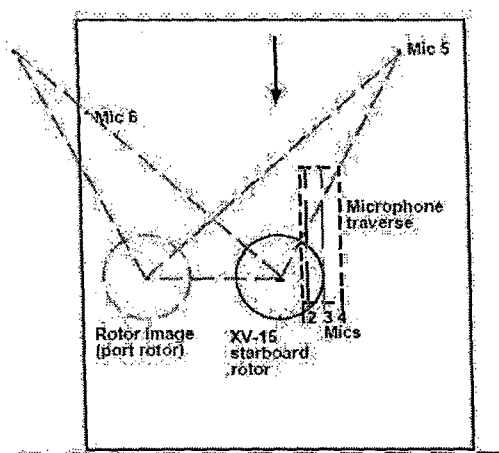


Figure 1: Schematic of microphone placement in wind tunnel

For one set of flight parameters, the acoustic data is sampled and recorded for 16 revolutions of the rotor, at the sampling frequency of 2048 samples per second. The 16 revolutions of data are averaged to obtain an averaged set of data for one rotor revolution. A digital bandpass filter is applied to the averaged data to highlight the BVI noise content. To obtain a single-value representing the overall BVI noise level from one rotor revolution, the time-domain data is transformed into the frequency domain using a FFT. The resulting power spectrum is integrated and converted from units of Pascals² to units of dB to obtain a BVI noise level value that characterizes the acoustic noise from one revolution of the rotor.

3. The Application of Neural Networks

In this section, feedforward artificial neural networks are trained and tested to predict the BVI noise level for a set of flight parameters, including the rotor thrust, the advance ratio, the rotor tip-path-plane angle, and the distance between the microphone and rotor. The trained neural networks are also tested when only one or two flight parameters are changed. Two different training methods are used, including the adaptive learning-rate backpropagation algorithm and scaled conjugate gradient (SCG) algorithm.

The first experiment involves using a neural network trained by the adaptive learning-rate backpropagation algorithm. There are 5 inputs to the neural network; each representing one test condition parameter. The output of the neural network is the BVI level (in dB). There is one hidden layer with 15 neurons in the neural network. The training set in this case is a random selection of 1/3 of the available test points in the XV-15 database (approximately 360 points). The neural network is trained for 5,000 iterations. The final mean-square-error

is 3.30. After training, the neural network is tested using the remaining data in the database. A histogram of the difference between the neural network output and the actual BVI is shown in Figure 2. It shows that about 72% of the error is within a ± 2 dB range; i.e., the neural network is able to predict the BVI level with ± 2 dB accuracy for 72% of the data in the entire database. Meanwhile, 97% of the data is within an error range of ± 5 dB.

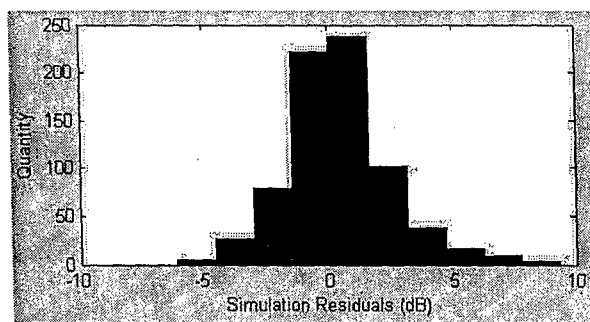


Figure 2: Histogram of prediction residuals for adaptive learning-rate backpropagation trained neural network

An even better result was achieved with the scaled-conjugate-gradient (SCG) algorithm. For a neural network with one hidden layer trained by the SCG algorithm, a mean-square-error (MSE) of 1.59 is reached in just 801 iterations with 78% of the residuals within a ± 2 dB range. Meanwhile, 98% of the residuals were within a ± 5 dB range. The histogram of BVI prediction error for this case is shown in Figure 3.

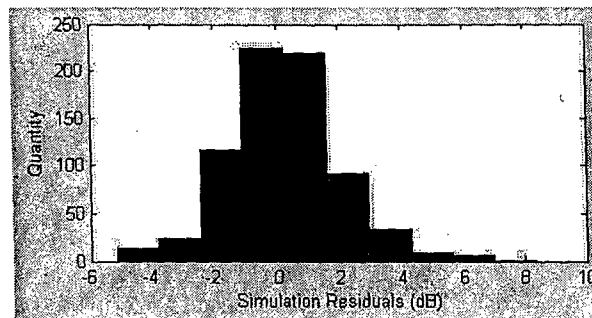


Figure 3: Histogram of prediction residuals for SCG trained neural network

Once the neural network is trained, it is also used to predict the BVI level with respect to the change of one single parameter. That is, instead of testing the neural network on the rest of the dataset, a subset of the data, which contains one varying parameter while the other parameters are kept fixed, is used. Among the five parameters listed at the beginning of this section, one of

the most influential parameters of the BVI noise level is the tip-path-plane angle α_{TPP} . Figure 4 shows the simulation results when α_{TPP} is varied from -15 to 15 degrees while C_T/σ is fixed at 0.0758, μ is set at 0.17, and x_m is fixed at 225 inches. From the figure, the neural network has successfully captured the relationship between varying α_{TPP} and BVI noise level. The neural network used in this case is the neural network that was trained by the SCG algorithm

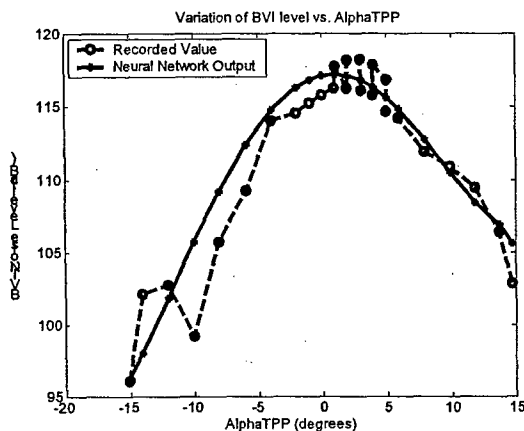


Figure 4: Variation of BVI noise level vs. AlphaTPP

Another influential parameter of BVI noise level is the distance away from the test rotor x_m . The simulation result for this case is shown in Figure 5, with $C_T/\sigma = 0.0845$, $\mu = 0.15$, $\alpha_{TPP} = -1.96$ degrees, and the distance x_m varied from 0 to 300 inches. The neural network in this case is the neural network that was trained by the SCG algorithm.

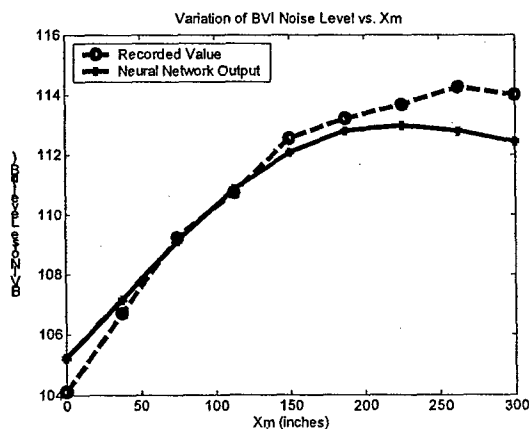


Figure 5: Variation of BVI noise level vs. x_m

When two parameters are varied, the output can be viewed as a contour plot. In such a plot, the x and y axes represent the two varying input parameters and the z-axis contours represents the BVI noise level. Consider the

case when $C_T/\sigma = 0.091$, $x_m = 225$ inches, and microphone number = 4. The varying input parameters are μ (from 0.148 to 0.18) and α_{TPP} (from -4.89 to 4.02 degrees). The experimental wind tunnel database only contains 10 points in this range so a smooth contour plot is not possible, as shown in Figure 6. However, when the output of a neural network is used to interpolate data points that are not included in the original data set, much improved contours can be obtained, as shown in Figure 7. The number of data points used to create the contour plot increased to 60 when using points predicted by the SCG trained neural network.

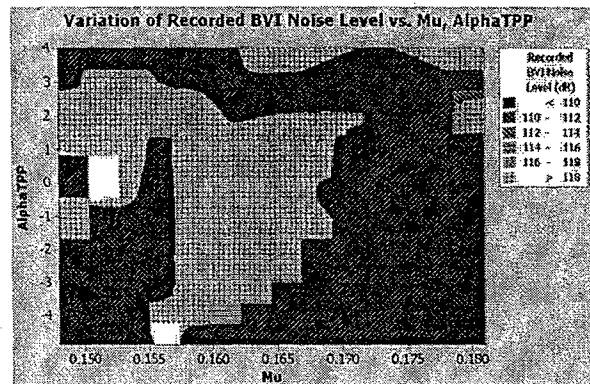


Figure 6: Variation of recorded BVI noise level vs. μ , AlphaTPP

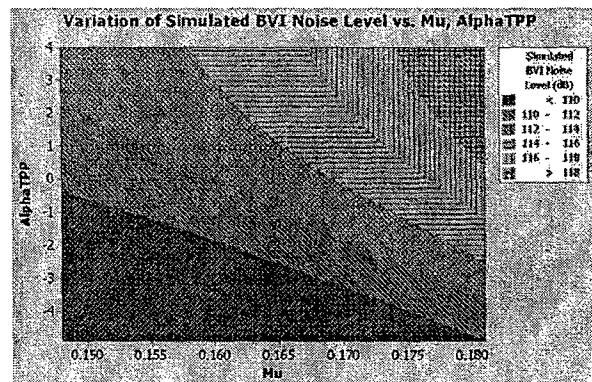


Figure 7: Variation of simulated BVI noise level vs. μ , AlphaTPP

4. Conclusions

The blade vortex interaction (BVI) noise level is an important measure in the studies of rotorcraft flight control and acoustics. In this research, artificial neural networks are successfully applied to analyze acoustic data gathered from wind tunnel tests. The simulation results show that after training with the SCG algorithm, the neural network can predict the BVI level within an accuracy range of ± 2 dB for 78% of the test data and ± 5 dB for 98% of the test data. The trained neural networks

can also be used to identify the relationship between different parameters and the corresponding BVI noise level. The results from this study may be applied to other rotorcraft datasets to determine a model for the acoustic data and also to implement BVI noise level prediction in actual flight.

5. Acknowledgements

The authors would like to thank Dr. William Warmbrodt, Cahit Kitaplioglu, and the other members of the Aeromechanics Branch at NASA Ames Research Center for supporting this work. This work was also partially sponsored by the Department of the Navy, Office of Naval Research, under Award # N00014-04-1-0436.

References:

- [1] A. Zaknich, *Neural Network for Intelligent Signal Processing* (Singapore: World Scientific, 2003).
- [2] R.J. Schalkoff, *Artificial Neural Networks* (New York: McGraw-Hill, 1997).
- [3] C.F. Lo and F.H. Schmitz, Model-Based Neural Networks for Rotorcraft Ground Noise Prediction. *Proc. 38th AIAA Aerospace Sciences Meeting & Exhibit*, Reno, NV. 2000.
- [4] S. Kottapalli and C. Kitaplioglu, Neural Network Representation of External Tilt-Rotor Noise, *Journal of the American Helicopter Society*, 47(2), 2002, 109-114.
- [5] C. Kitaplioglu, Blade-Vortex Interaction Noise of a Full-Scale XV-15 Rotor Tested in the NASA Ames 80-by 120-Foot Wind Tunnel, NASA Technical Memorandum 208789. Moffett Field: National Aeronautics and Space Administration.

Screen Data Compression for Improved VNC

Project Investigator:

Jane (Xiaozheng) Zhang
Assistant Professor
Electrical Engineering Department

Background

VNC [1] stands for Virtual Network Computing. It is a client/server software application that allows one to remotely access a desktop environment from anywhere on the internet. VNC has emerged as a promising technology in distributed computing environment since its invention in the late nineties because it provides great flexibility and convenience in a mobile computing environment. For example, one can use VNC to access his personal Unix or PC desktop from any office on campus and from around the world. A system administrator can use VNC to help troubleshoot a remote computer, or to access and administer server machines without leaving his own computer. VNC can also be very helpful in distance learning. For example a distributed group of students can simultaneously view a computer screen being manipulated by an instructor. It would also be possible for the instructor to take control of the students' computers to provide assistance. There are many programs that provide one with the ability to view the screen on a remote PC. But VNC, besides being free, it is small and simple and has the advantage of being fully cross-platform. Numerous groups [3-6] are currently actively developing VNC and its associated products.

Successful application of VNC requires rapid data transfer from one machine to another over a TCP/IP network connection. However transfer of screen data consumes much network bandwidth and current data encoding schemes for VNC are far from being ideal. When VNC is used over the internet, via a public network, security reasons require the use of encryption, which further exacerbates the bandwidth problem. Finally, mobile computing use of VNC with devices such as Palm Pilot would have to overcome the limitation of a slow network as well as the additional overhead of encryption over the internet.

The original VNC was developed by Olivetti Research Labs in Cambridge in 1998 [1-3]. The technology underlying VNC is a protocol called RFB that stands for Remote Frame Buffer. It supports six different encoding algorithms for pixel data representation. These are: Raw encoding, CopyRect encoding, PRE encoding, CoRRE encoding, Hextile encoding, and ZRLE encoding. It is to note that all these encoding schemes are lossless, i.e. the reconstructed screen image on the client is exactly the same as the image data on the server. The compression algorithm used in the original VNC software is not very efficient and suffers from low performance in low-bandwidth network environments.

TightVNC [4, 7] developed by Kaplinsky is an improved version of the original VNC. Besides the various enhanced features it offers, it implemented a new encoding called "tight". TightVNC incorporates an additional data analyzer to determine statistical properties of pixel data before applying data filters. While TightVNC was shown to outperform standard VNC encoders in compression ratios, the design of the data analyzer is still primitive and leaves much room for improvement.

The new hybrid algorithm

Our newly developed algorithm is hybrid – it considers compression in both still image and a sequence of images and improves coding efficiency in both.

The basic idea in improving compression for a single image is based on the observation that screen image is composed of several distinct regions and no coding technique alone is able to efficiently handle all range of data. In our algorithm we consider four common types of screen images including background with one color, bi-level texts, graphics, and natural images. Figure 1 displays typical images of all four types. Figure 2 shows the flow chart of our segmentation process. Here we employ a simple color counting in combination with edge detection. These two methods are not only efficient in classifying images, but they also have low complexity that requires only minimal processing time, which is very critical in VNC applications.



Figure 1: Examples of four types of images. (a) Background image (one color), (b) Text image (two colors), (c) Graphic image, (d) Natural image.

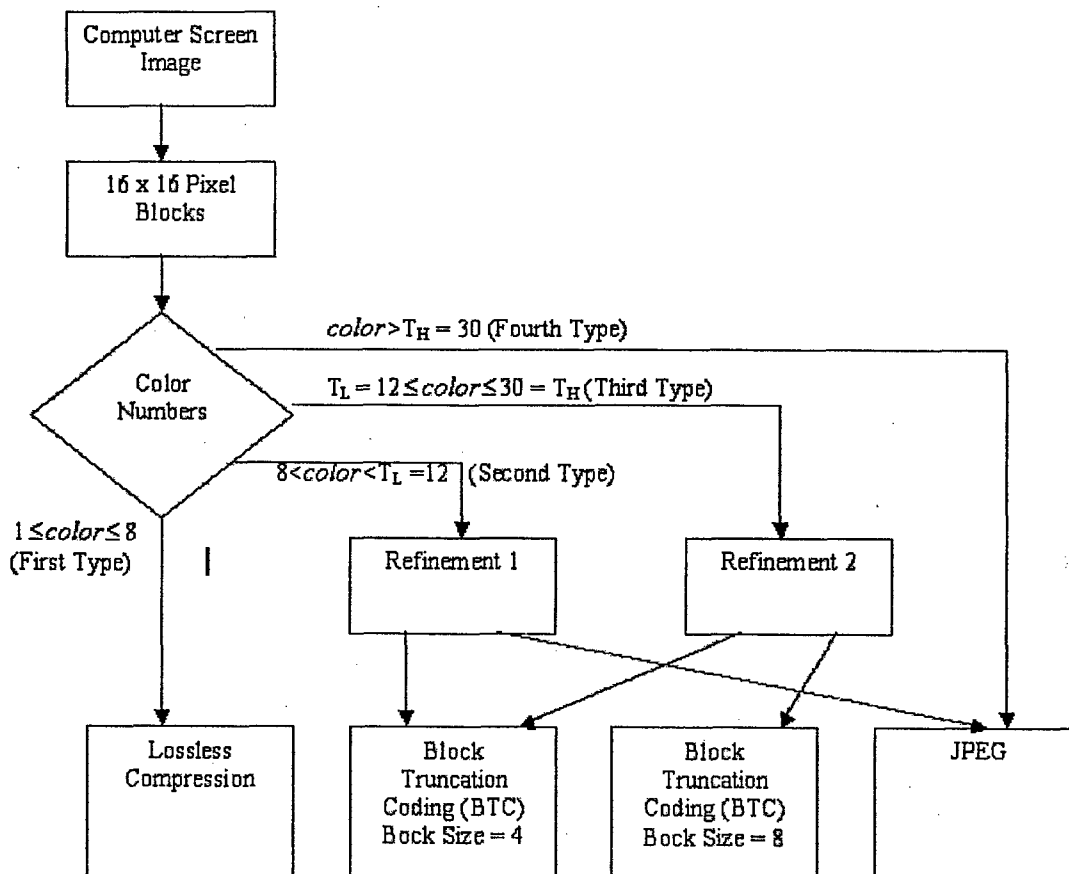


Figure 2: The flow chart of segmentation algorithm.

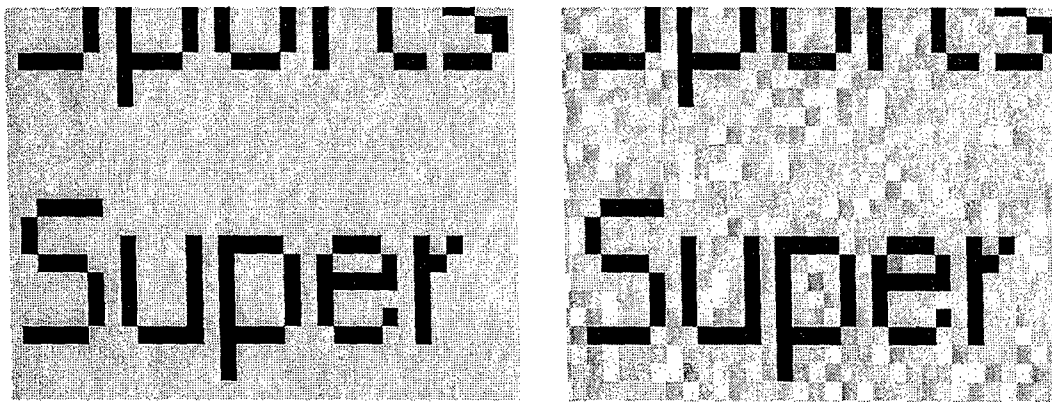


Figure 3: An example of the artifacts introduced by JPEG in a text image.
 (a) Original image (24 bpp), (b) JPEG reconstructed image (4.946 bpp).

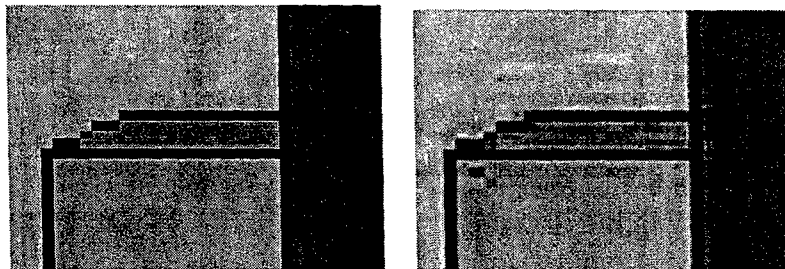


Figure 4: An example of artifacts introduced by JPEG on a graphic image.
 (a) Original image (24 bpp), (b) JPEG reconstructed image (4.946 bpp).

Once the screen image is segmented into predefined areas, the best coding strategy for each region must be identified. We consider JPEG [8] in this work because it is a popular international digital image compression standard for both grayscale and color still image. JPEG is a lossy compression technique and is very efficient in compressing color-rich images. However it introduces noticeable artifacts when it is applied to text and graphic images, as can be seen from Figures 3 and 4. Various psychophysical studies [9] also suggest that higher perceptual importance should be given to the text and edge regions, followed by the smooth and detailed regions. We therefore choose to use lossless technique to encode image blocks with fewer numbers of colors and leave only color-rich images to JPEG.

We apply lossless encoding for image blocks with a color number of eight or less. For an image block with a color number of N (≤ 8), only N color data (requiring $3 \cdot N$ bytes for an RGB color pixel) plus a bitmap are transmitted. The decoder is able to reconstruct the original image from these data. The bitmap requires only 1 bit for each entry when N is 2, 2 bits if N is 3 or 4, and 3 bits if N is from 5 to 8. Note that one-color image does not require any bitmap. Table 1 shows the required bits per pixel (bpp) for a given number of colors in a 16×16 RGB color image. We see that this lossless compression yields the best image quality while keeping the bit rate low.

If the color number in a 16×16 block is more than 30 (this number is determined experimentally), the image is categorized as a natural image and JPEG will be applied. For images in between, we choose BTC for image blocks with strong edges, JPEG for the ones with weak edges. BTC

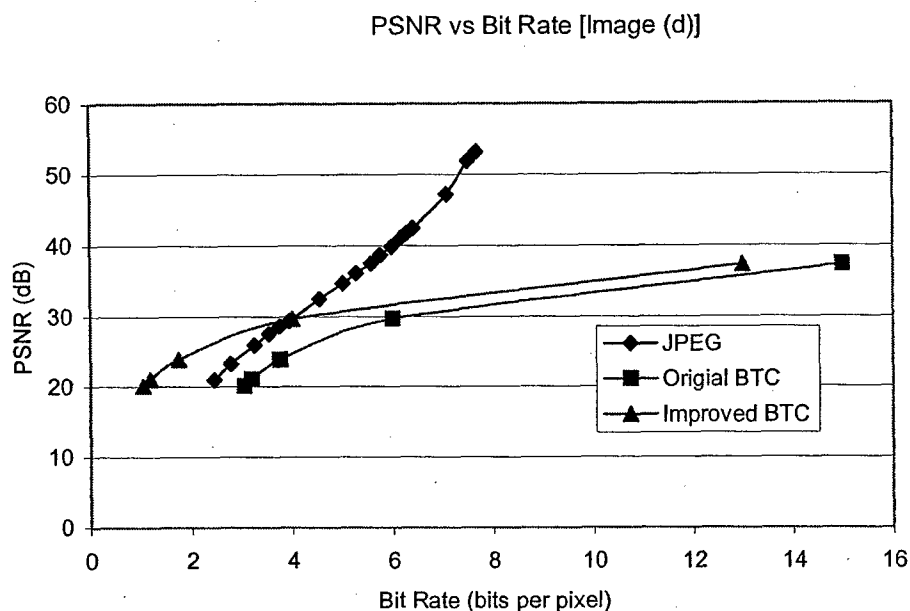


Figure 5: Comparison between JPEG, original BTC, and improved BTC using test image.

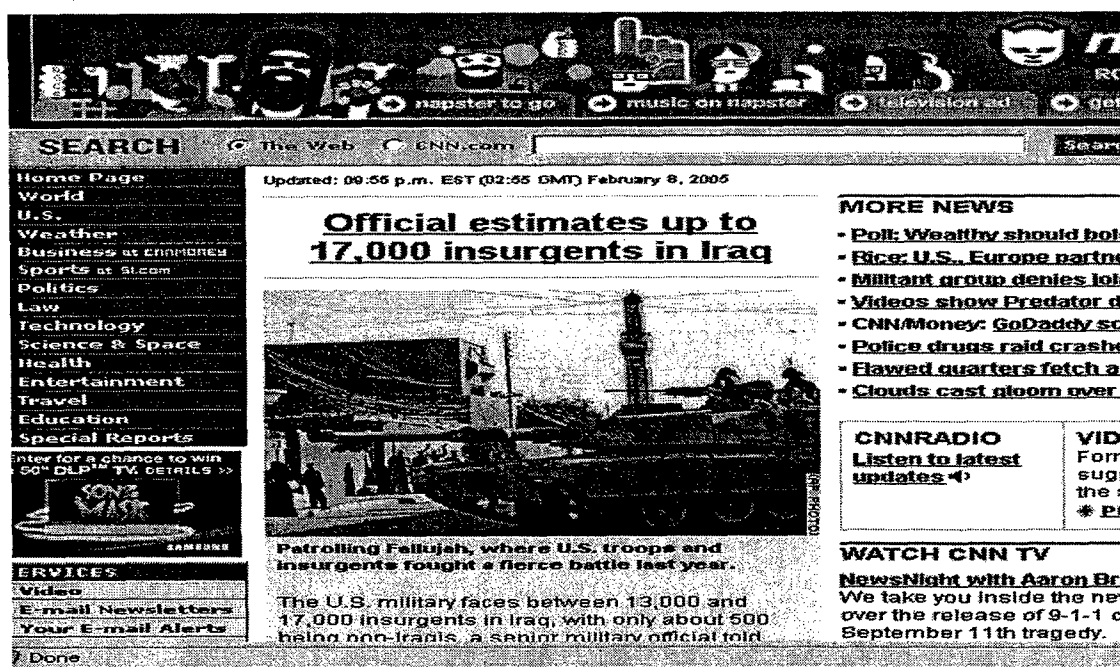


Figure 6: Test image.

(Block Truncation Coding) [10] is a lossy compression technique. The advantage of BTC is that it is relatively easy to implement but still preserves strong edges in an image. We adopted a modified version of BTC [11], where only one bitmap resulting from the sum of three color components is encoded. Figure 5 shows the performance of the improved BTC compared with JPEG and the original BTC on one test image.

Number of Color	Bit Rate (bits per pixel)
1	0.09375
2	1.1875
3	2.281
4	3.375
5	3.469
6	3.563
7	3.656
8	3.750

Table 1: Color number and the corresponding bit rate.

	JPEG			The New Algorithm		
	Bit Rate (bpp)	PSNR (dB)	Time (sec)	Bit Rate (bpp)	PSNR (dB)	Time (sec)
test Image 1	4.25	31.37	146"52	3.01	39.25	73"56
test Image 2	4.81	31.04	149"20	4.73	31.85	99"24
test Image 3	3.45	34.03	140"55	1.87	33.59	86"23
test Image 4	4.89	31.32	149"12	3.57	33.34	76"45
test Image 5	2.75	37.78	132"36	1.62	42.98	76"55

Table 2: Performance comparison between JPEG and the new algorithm.

The performance of presented algorithm is evaluated and compared with JPEG on five test images with a screen size of 560x560. Figure 6 shows a typical test screen image with all considered image types. Table 2 summarizes the results. It shows that in all test images except for the test image 2, the new algorithm produces much better results in all three categories: PSNR, bit rate, and processing time. The new algorithm requires less bits transfer while maintaining a high PSNR (a measurement for image quality). Note also that for all test images, the saving in processing time is almost 50%.

In addition to the improvement on coding a single still image, the hybrid algorithm also exploits correlation of screen data in consecutive frames. Here we notice that in existing VNC encoding schemes each image block is encoded without its relation to adjacent frames. Indeed VNC detects updated region and transmits only those areas. This significantly reduces temporal redundancy between adjacent frames. However further correlation of screen data in consecutive frames can be exploit. For example, it is often observed that during manipulation of a desktop environment, one might scroll up and down the contents in a window, or bring up and hide/cover a window from time to time. The background can also be covered and uncovered over and over. Subsequent occurrences of the same window or background content would be best encoded by reference to its first occurrence. To implement this idea, we create a memory buffer covering up to 250 previously encoded image blocks at both encoder and decoder. Each time a new image is encoded, we first search through the memory buffer. If a good match is found, only the image id

is transmitted. This idea is motivated by PI's previous work [12] on long-term memory motion-compensated prediction, however with the difference that no motion compensation is performed.

In our implementation, we first add a memory prediction encoding and its associated message to the RFB protocol. The message includes frame id, image id, and mode of action that could be either record or playback. The routine is then extended to first ask Memory Buffer for a match to the *rectangle* we are trying to encode. In doing so, we first build a candidate bag including all possible matching rectangles from the Memory Buffer. The most likely candidate is the one that has the same location and size as the *rectangle* to be encoded. This is characterized by a four-edge matching. Following that is three-edge, two-edge, and one-edge matching. Then matching is performed by comparing pixel values between the *rectangle* and the candidate in the bag. If a match is found, the mode of action is set to playback and the frame id and image id of the matched rectangle is transmitted. The decoder will use the id info to retrieve the image stored in its Memory Buffer. If no match is found, the image will be encoded using the original method, and the action is set to record. Both encoder and decoder will save this *rectangle* in their Memory Buffer. An optimization is done whereby we do not look for a perfect match. So long as the *rectangle* "almost" (80% at the moment) matches the image in Memory Buffer we declare a match, and then recursively encode all the rectangles constituting the mismatched portion. For the time being, the algorithm stops once it finds the first good match. An additional optimization does not remember any image smaller than the MINRECTSIZE (currently 900, such as a 30x30 image square). Because we feel that the overhead of recording and then recalling such small rectangles is more than any realized savings, especially once we consider the communication overhead of messages between the client and the server.

Conclusion and future work

In this work we developed a hybrid algorithm that improves the existing software package to enable VNC over slow connections and present a reasonable speed and image quality. The improvement was made in two areas. The proposed method first divides a screen image into several meaningful regions, such as background, text areas, graphics, and natural images. Then by applying encoding schemes to each region according to the region characteristics, better performance in data transfer can be achieved. The second improvement was made in exploiting correlation of screen data in consecutive frames. It is often observed that during manipulation of a desktop environment, the same image content might appear from time to time, or at varying locations. Based on that, we encode multiple occurrences of the same image block by referring to its first occurrence. This leads to further savings in bandwidth.

This algorithm has been tested on several desktop images and during manipulation of desktop environments. Improved image quality and faster transmission speed has been observed visually. However, to objectively evaluate the new algorithm, further work is required. First incorporation of a record/playback mechanism in the original software is necessary so that each VNC session can be reproduced and tested on a variety of algorithms. Furthermore, performance measures need to be built into the original package to allow objective evaluation of our hybrid algorithm with existing techniques. It is our hope that this will justify the usage of our newly developed algorithm and lead to a wider deployment of VNC in the field of mobile computing environment.

References

- [1] T. Richardson, Q. Stafford-Fraser, K. R. Wood and A. Hopper, *Virtual Network Computing*, IEEE Internet Computing, Volume 2, Number 1, January/February 1998.
- [2] T. Richardson, *The RFB Protocol*, RealVNC Ltd, August 2003
- [3] <http://www.realvnc.com>
- [4] <http://www.tightvnc.com>
- [5] <http://ultravnc.sourceforge.net/>
- [6] <http://www.tridiavnc.com/>
- [7] K. V. Kaplinsky, *VNC tight encoder - data compression for VNC*, Modern Techniques and Technology, 2001. Proceedings of the 7th International Scientific and Practical Conference of Students, Post-graduates and Young Scientists, February/March 2001
- [8] W. Pennebaker and J. Mitchell *JPEG Still Image Compression Standard*, Van Nostrand Reinhold, New York, 1992.
- [9] D. Marr, *Vision*, W. H. Freeman and Company, 1982
- [10] O. Mitchell, E. Delp, and S. Calton, *Block Truncation Coding: A New Approach to Image Compression*, IEEE International Conference on Communication, IEEE Press, Piscataway, 1978.
- [11] Y. Wu and D. Coll, *Single Bit-Map Block Truncation Coding of Color Images*, IEEE J. Selected Areas Communication, CA, 1995.
- [12] T. Wiegand, X. Zhang and B. Girod, *Long-Term Memory Motion-Compensated Prediction*, In IEEE Transaction on Circuit and Systems for Video Technology, February 1999.

IV.B.3: Results of Internet2 Pilot Projects

**Utilizing Internet2 to Integrate Multimedia Repositories in an
Adaptive Learning Environment**

Project Investigators:

Dr. Franz Kurfess
Associate Professor
Department of Computer Science, College of Engineering

Meike Muckenhaupt
Graduate Student
Computer Science Department, Cal Poly San Luis Obispo

Final Report

Utilizing Internet2 to Integrate Multimedia Repositories in an Adaptive Learning Environment

Project Director: Franz Kurfess
Computer Science Department, Cal Poly
fkurfess@calpoly.edu

Investigator: Meike Muckenhaupt
Computer Science Department, Cal Poly
meike.muckenhaupt@gmail.com

July 2005

1. Introduction

Adaptive Educational Hypermedia Systems are able to adapt to an individual user, but still allow them to navigate freely through the learning material. Current systems typically are based on adaptation methods and technologies for text but also make use of multimedia components such as interactive applets or flash components. However, there is usually no adaptation within the multimedia components. We altered a taxonomy suggested by Brusilovsky to allow adaptation within multimedia components and adaptive navigation support within multimedia. An Adaptive Educational Hypermedia System (AEHS) was developed to integrate and demonstrate example learning modules with adaptive multimedia components. To allow an integration of the modules and courses into the AEHS and to be able to use the adaptation support of the AEHS the module content files and the course file must be marked up using a newly developed XML markup schema, which describes the structure as well as the semantic content of the documents. This framework allows the integration of components from various sources, and may enable access to resources not available locally. Both for the transfer of multimedia components as well as for the access of remote resources an advanced networking infrastructure such as Internet2 is essential. Adaptive Hypermedia Technologies and the altered taxonomy are discussed and introduced in Section 2. In Section 3 the Adaptive Educational Hypermedia System (AEHS) is described, the major components are illustrated and their realization and implementation is discussed briefly. Section 4 contains the specifications of the Markup Language for Educational Hypermedia. Section 5 is a guide for teachers on authoring and publishing of learning materials.

2. Adaptive Hypermedia Technologies

Two areas of adaptation can be distinguished: adaptive presentation and adaptive navigation support. Adaptive presentation techniques are used to adapt the content of a page to fit the requirements of a user model, that is adapt to the users knowledge, goals and other preferences (Brusilovsky 1996). Common adaptation methods and techniques can be found in Brusilovsky's taxonomy (Brusilovsky 2001) and are summarized in the following Section 2.1. As part of this project we took a look at problems of current utilizations and thereby point out the necessity to extend the taxonomy for adaptive multimedia presentation, and adaptive navigation within multimedia. In the subsequent Section 2.2, we then add on to the taxonomy by introducing two

new branches for granular, component-based adaptation of multimedia presentation and adaptive navigation support within multimedia.

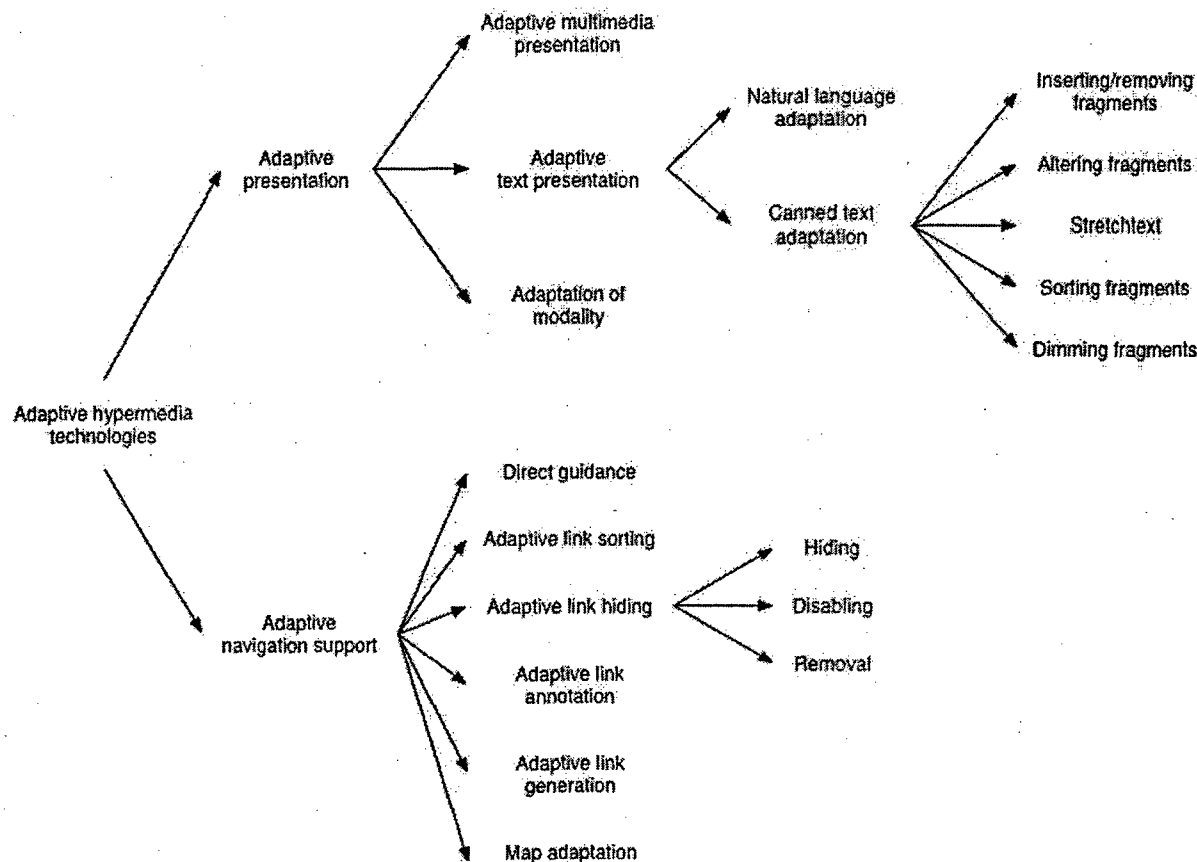


Figure 1: Methods and techniques for adaptive presentation and navigation support (Brusilovsky 2001)

2.1. Taxonomy of adaptive hypermedia technologies

Brusilovsky distinguishes between methods and techniques of adaptive hypermedia. Methods describe adaptation on the conceptual level; techniques refer to implementations of a method in existing Adaptive Hypermedia Systems. One of the most commonly used methods of content adaptation is *additional explanation*: Some of the information is shown if it is relevant, and hidden if it is not relevant to the user. Very similar are *explanation variants*, where several variants of the same information are stored in the system, and the user sees the one that matches his learner model best. The *sorting* method takes into account the user's background and knowledge level and places the fragment of information most relevant to the user toward the front (Brusilovsky 1996). A technique of *additional explanations*, utilized for example in ActiveMath (Melis, et al., 2001), is a *conditional insert of fragments*, e.g. a definition of a concept, if the concept is newly introduced. Goals of adaptive navigation methods are to provide *global and local guidance*, support *global and local orientation* and allow *personalized views* of the link structure. A simple technique for local orientation is *direct guidance* implemented by a "next"-button. In ELM-ART II (Weber 1999) a color bullet system next to available links provides guidance as to which concepts are ready to be learned or have already been learned.

This technique of *link annotation* is used to employ *local guidance* as well as *local* and *global orientation support*. This shows that one technique can implement several methods.

Brusilovsky's taxonomy shown in Figure 1 (Brusilovsky 2001) divides adaptive presentation into three areas: adaptive multimedia presentation, adaptive text presentation and adaptation of modality. Clearly, the taxonomy focuses on textual content, i.e. adaptive text presentation and adaptive navigation support for hypertext. Methods and techniques for the adaptive multimedia presentation sub-branch are not considered. The given areas as well as adaptation of modality are the ones mostly utilized in Adaptive Hypermedia Systems such as ELM-ART II (Weber 1999) and ActiveMath (Melis, et al., 2001). Kobsa, Koenemann and Pohl (1999) state that for adaptation of modality the information content of the different hypermedia components stays the same, while the format changes for example from text to a graph or a map. This method is used in AVANTI (Fink, Kobsa & Nill 1998), a system that presents maps and sights it bases the selection of modalities on the user's physical abilities (Kobsa, et al., 1999). As mentioned earlier, ActiveMath can include multimedia modules like interactive applets in a workbook; however this inclusion can only occur as a whole or not at all. One can see that multimedia components are already present in Adaptive Hypermedia Systems and are becoming more and more dominant. Especially in Adaptive Educational Hypermedia Systems, where a graph or an interactive applet can add significantly to the understanding of the material, and where adaptation to different learning styles occurs, we think the inclusion of multimedia components and their adaptation is important. Depending on the path a user has taken through learning material, different sub-components of a multimedia component as well as different related examples or additional links will be relevant for him. This can not be modeled if an interactive applet, flash component or other multimedia module is included as a whole, with no possibilities to adapt the presentation within the component and to provide adaptive navigation support from within the component. Therefore in the following Section we will introduce an extension to Brusilovsky's taxonomy, which will allow adaptive multimedia presentation as well as adaptive navigation support within multimedia components.

2.2. Multimedia-based taxonomy for adaptive hypermedia technologies

Figure 2 shows our extended version of Brusilovsky's taxonomy; the shaded entries indicate the suggested extensions or changes. The altered adaptive navigation branch allows text-based adaptive navigation support as well as adaptive navigation support within multimedia on a component-based level. The same technologies as for navigation support within text can be used, as explained in Section 2.2.2. For adaptive presentation the branches for text and multimedia presentation are merged and allow adaptation on a component-based level. The technologies to allow both canned text adaptation and adaptation within multimedia are described in Section 2.2.1. These modifications will allow adaptation of multimedia components at a smaller level of granularity. Furthermore, we determined that Natural language adaptation is not only restricted to the text branch, but can also be applied author to video and audio files or can occur within vector-languages such as SVG.

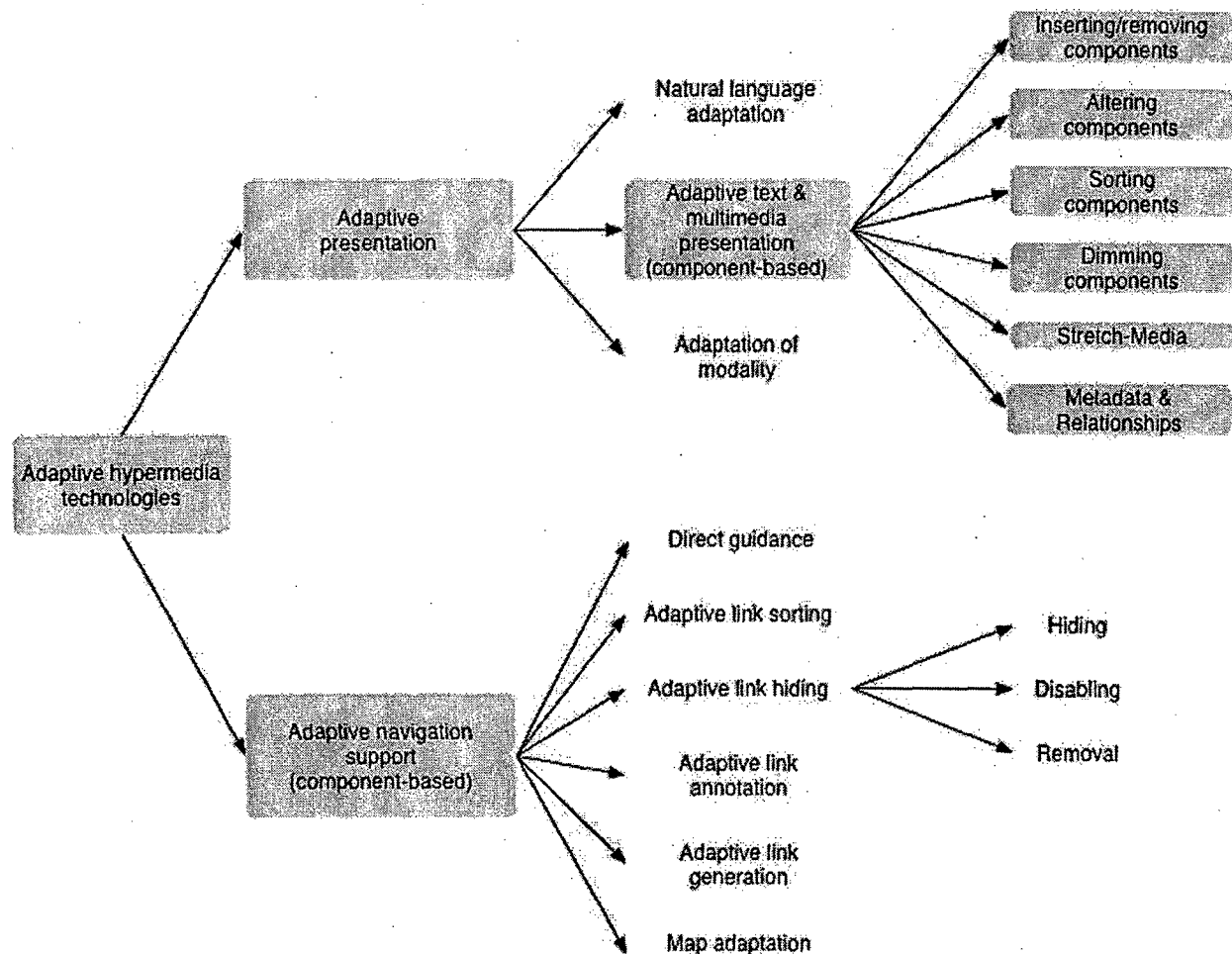


Figure 2: Extended version of Brusilovsky's taxonomy of adaptive hypermedia technologies

For adaptation within multimedia, multimedia components will be considered to be interactive learning objects (ILO), as for example interactive applets or flash components. To allow adaptive navigation support and adaptive presentation within an ILO, the ILO will be divided into several subcomponents. The example applets, for instance, consist of several AWTComponents, which then consist of several GraphicsElements. The ILOs are marked up using the newly developed markup language for educational hypermedia introduced in Section 4. To note is that only a reference to the ILO is included in the module content file the ILO itself can be located on a remote server. Example 1 shows how a reference to an ILO is integrated in the module content file. In the example, an adaptation possibility is provided for one of the GraphicsElements (`<ilo:gfx-item id="id32">`) of the AWTComponent (`<ilo:awt-component id="id30 req="c.ex1">`). The ids specified for the gfx-item and the awt-component have to correspond to the ids of the actual AWTComponent and GraphicsElement in the applet. The requirements specified in the *req* attribute are parsed by the *Adaptation Engine* of the AEHS and then passed to the applet. An AWTComponent of the applet could for example only be displayed, if the user has the required prerequisite knowledge. The parameter passed to the Applet then specifies if the component should be displayed or not. The `<ilo:tip id="t1_app_ex2" req="c.!ex3;u.active">` element represents an additional tip that can be displayed on the applet's Adaptation-Layer. The requirements specified in the *req*

attribute of the tip element are also parsed by the *Adaptation Engine* of the AEHS and if fulfilled, passed to the applet, which then displays the specified annotations on the Adaptation-Layer. Next to the parameters identified by the *req* attributes parameters specifying color and formatting preferences can be passed to the applet and processed by the Adaptation-Layer.

```
<ilo:interaction id="app_ex2" target="applet">
  <ilo:name>DFT</ilo:name>
  <ilo:src>applets.dft.AdMainClass</ilo:src>
  <ilo:codebase>ilo/example2/</ilo:codebase>
  <ilo:archive type="jar">addft.jar</ilo:archive>
  <ilo:width>400</ilo:width>
  <ilo:height>500</ilo:height>
  <ilo:awt-component id="id30" req="c.ex1">
    <ilo:gfx-list>
      <ilo:gfx-item id="id32">
        <ilo:tip id="t1_app_ex2" req="c.!ex3;u.active">
          <ilo:tiptext>
            This is an additinal tip to the Dft Applet,
            shown if ex3 is not known.
          </ilo:tiptext>
        </ilo:tip>
      </ilo:gfx-item>
    </ilo:gfx-list>
  </ilo:awt-component>
```

Example 1: Markup of ILO

The next Sections present possible filtering and presentation methods as well as techniques for the realization of adaptive multimedia presentation and adaptive navigation support within multimedia. Those methods and techniques are adapted and extended from the original taxonomy in order to be suitable for multimedia components. Not all of the presented methods are implemented in the example learning modules with adaptive multimedia components.

2.2.1. Adaptive Multimedia Presentation.

The adaptation methods *inserting/ removing fragments*, *altering fragments*, *sorting fragments* and *dimming fragments* can be adopted with only little alteration from the adaptive text presentation. Methods for *Stretch-Media* and *metadata & relationships* need to be adjusted or developed.

- *Inserting/ removing fragments*

When parsing the ILO's markup and requirements, the Adaptation Engine determines which subcomponents should be inserted or removed to form the complete ILO. The decision can be made depending on the user preferences and data from the User-Model, as for example knowledge of prerequisites. The GRIS/ILO for example includes an applet about color chromatics (Hanisch & Straßer 2003), which can be divided into the following components: change filters, change light and change color. If the user does not yet know the theory of filters, this component would not be included in the ILO. The applet features further components based on different software requirements (Java

packages for advanced imaging – JAI and 3D graphics – Java3D), which can be included or removed according to the system's software installation.

- **Altering fragments**

Similar to inserting/ removing fragments the ILO's subcomponents can be altered depending on the user's preferences and User-Model. For example for different origins or paths through the learning material, different subcomponent might be more relevant and add more to the user's learning experience than another.

- **Sorting fragments**

To accomplish sorting of fragments the ILO display area could be divided into subareas, such as main, center, north, south, or other layouts. The layout of the ILO components can then be determined depending on, e.g. weights or a ranking which is calculated from the ILOs metadata linking of the subcomponents, using the learning style preferences, system requirements and user's knowledge.

- **Dimming fragments**

Dimming fragments implies that a component is not entirely hidden, but dimmed.

This can be achieved by just showing the title of component or making a component transparent. Examples for possible techniques for dimming fragments are:

- Painting the background of the respective component grey.
- Showing the main frame of the ILO with available tabs, as used in web browsers. Clicking a tab will display additional components.
- Displaying the graph structure of the subcomponents that make up the ILO in finder-like, collapsible menu bars.
- Displaying a clickable title or caption of the component and allow the user to expand or collapse the component. This approach is used in a User Modeling Project of the CSC 480 class at Cal Poly (Muckenhaupt, Skorupski & Kaiser 2004).

- **Stretch-media**

Nelson's (1967) definition of Stretchtext is as follows: "Stretchtext consists of ordinary continuous text, which can be 'stretched', or made longer and more detailed. By pointing at specific areas and pulling the throttle in the 'magnify' direction, the reader may obtain a greater detail on a specific subject, ...". We similarly propose stretch-media, focusing on the "magnify" aspect of multi-media. Applying van Dam's clip models (2002), which provide a zoom on the concept level by model components with different granularity, we may turn the presentation zoom into a "what is" zoom. Authors assign a concept to each subcomponent and state, and set up matching concept relationships.

- **Metadata and relationships**

Metadata and information about relationships can be offered for every ILO component according to its current state, i.e. for its model, view, controller, constraints, and scripts. Those can be utilized to provide additional information for an object, as for example done in Tooltips, and actions for an object similar to Microsoft Office SmartTags. Techniques may include this information within the ILO, or separately: while the presentation of additional information within the original module infers further technical issues, exact positioning and interaction can be done easier.

2.2.2. Adaptive Navigation Support

Adaptive navigation support is one of the most frequently occurring adaptations. Following Brusilovsky (Brusilovsky 2001) six technologies can be named: Direct guidance, adaptive link sorting, adaptive link hiding, adaptive link annotation, adaptive link generation and map adaptation. We extended the taxonomy by adding adaptive navigation support within multimedia. To allow the adaptive navigation support within multimedia the ILO has to be marked up as described above. An AWTComponent or GraphicsElements can get internal and external hyperlinks as well as additional tips assigned. The *Adaptation Engine* parses the elements and requirements and depending on the user's prerequisite knowledge, learning style and preferences, passes parameters with the URL or tip text to the applet. In the example applets, the Adaptation-Layer is activated through a "control"-click. The hyperlinks and additional tips are then displayed on a layer above the applet. The *Adaptation Engine* performs the actual adaptation of the links and annotations. Utilizing XSL Transformations the *Adaptation Engine* generates, sorts and annotates the links using the information contained in the markup of the ILO component, depending on the user's prerequisite knowledge, learning style and preferences.

3. Adaptive Educational Hypermedia System (AEHS)

Students come from different backgrounds, have different prerequisite knowledge and prefer different learning styles. An Adaptive Educational Hypermedia System adapts to those differences by tailoring the learning material to the students needs, the system suggests a path through the material but still allows the student to navigate freely.

Figure 3 shows the major components of the AEHS framework, the components are described in Section "3.2. The AEHS Framework". Previously the technologies used for the implementation are presented briefly.

3.1. Methods and Technologies

The AEHS is a web-based framework, a server setup with an Apache HTTP Server with a PHP installation and a connection to a PostgreSQL database form the base. To allow this setup the Cal Poly Computer Science Department provided the Sun Solaris 9 machine *regal* as a server. For evaluation and testing purposes, access from outside of the Cal Poly network to this server is needed. To allow this, Prof. Dr. Kurfess requested a pinhole. The server can be accessed at: <http://regal.csc.calpoly.edu>.

- **Apache HTTP Server** is used as the web server. It stores XML-Learning-Modules and the database containing the User-Model and Lesson-Plan.
- **PHP** is used to implement the Student and Teacher Interface and parts of the Adaptation Engine. PHP is a server-side scripting language, which can be used to develop dynamic web content. Some of its advantages are the platform independence, availability of a large number of libraries, which facilitate for example the interaction with a large number of relational database management systems, such as PostgreSQL, MySQL, IBM DB2 and Oracle, as well as the access of XML documents.
- **PostgreSQL 8.01 database** is used to store the User-Model and Lesson-Plan. PostgreSQL is a free, SQL compliant, open source object-relational database management system. It is available for multiple platforms and several GUI tools to administrate the database and for database design are available. Native interfaces for the

connection to PHP and other programming language are available. The access from Java Servlets or Java Server Pages can be carried out via the ODBC or JDBC interface.

- **XML** is used to write and markup the learning materials. The eXtensible Markup Language (XML) is a meta-language, which can be utilized to create special-purpose markup languages. We used XML-Schema language to define the structure and valid content for the learning modules. This markup language for educational hypermedia allows an easy integration of the learning materials into the AEHS.
- **XSL** is used to display the learning materials and as part of the Adaptation Engine. The eXtensible Stylesheet Language (XSL) consists of three languages, which can be used to describe how an XML document should be formatted or transformed.
 - XSLTransformations (XSLT): for transforming an XML document from one syntax to another. Can be used to transform an XML document in an HTML document.
 - XML Path: to navigate through the tree structure of an XML document.
 - XML Formatting Objects (XSL-FO): to define visual layout and formatting of an XML document.

3.2. The AEHS Framework

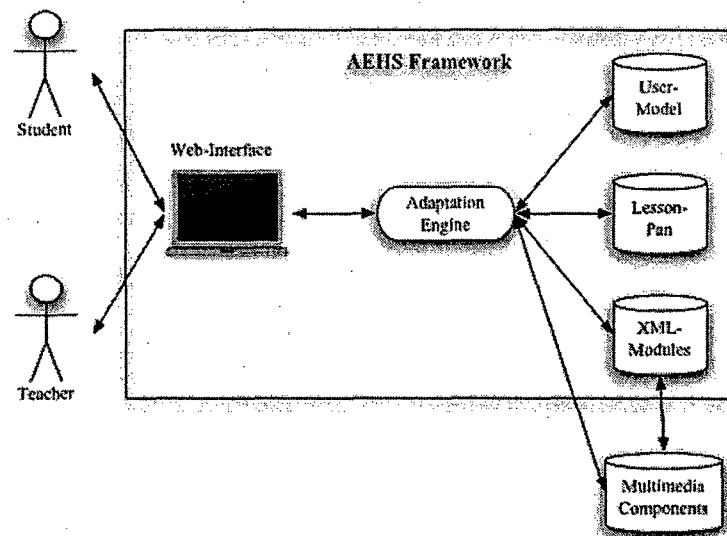


Figure 3: The AEHS Framework

The major components and interactions in the AEHS are illustrated in Figure 3. The two user groups, students and teachers, are presented with different *Web-Interfaces*, implemented in PHP. The *Web-Interface* for teachers is described in Section "5.2 Publishing of Courses and Modules". The *User-Model* stores data about the user, such as his learning style preferences and progress through the learning material. The *Lesson-Plan* stores links to the available modules as well as how the modules are structured into courses. By comparing the knowledge from the *User-Model* with the *Lesson-Plan* the *Adaptation Engine* performs the adaptation of the learning material to the user's needs. The adaptation process is partly implemented in PHP, and partly performed through XSL-Transformations. The *Adaptation Engine* is described in more detail in Section 3.2.3. The learning materials are stored as *XML-Modules* in the file system of the web server. To highlight is thereby, that only the module content file needs to be stored on the server,

accompanying multimedia components, such as audio or video files, applets or flash components do not have to be stored on the server but can be loaded from remote servers. The markup for the educational XML-Modules is introduced and described in Section 4. Section 5 explains the setup of the modules and how to author the module's content.

3.2.1. Student Web-Interface

The *Web-Interfaces* of the AHES can be accessed at

<http://regal.csc.calpoly.edu/~mmuckenb/AdHyMedia/main.php>. To be able to use the AEHS, a user has to be registered in the system. The registration screen appears after clicking the hyperlink "Join" link on the introduction screen seen in Figure 4. To register a username, password, email and the name of the home university have to be entered. The information about the user is stored in the user table of the database.

Login

Username:
Password:

[Join](#)
Send email to the [Admin](#) for a Teacher's Account.

Figure 4: Login Screen

After a student logs in for the first time, he is asked to take the learning style inventory, which determines the learning style of the user. Based on Aase's research (Aase 2002) we chose the Felder-Silverman Learning Style model to determine a student's learning style preferences. In the evaluation of a User Modeling project conducted in the Artificial Intelligence class CSC 480 in Fall 2004, we determined that the 44-item questionnaire used to find out the learning style preferences of a user is too long. In a homework assignment in CSC 484 User-Centered Interface Design and Development in Winter 2005, we developed a 16-item version of the questionnaire, which is now used to determine the learning style preferences of the users in the AEHS. It is not proven, if the shorter version of the questionnaire attains the same results as the original version. For the AEHS it is, however, only necessary to have an approximate classification of the students into the learning style categories. After submitting the learning style inventory the student is presented with list of topics available in the AEHS (Figure 5).

Hello Tina,

Please select one of the following topics:

- [Fourier Theorie](#)
- [Example Course](#)

Figure 5: Topic selection

The concepts assigned to a course (see Figure 6 for concepts of the "Example Course") are displayed on the left side of the screen. The color bullet system next to the links indicates if a concept is already completed (blue), ready to be learned (green) or if the prerequisites for this concept are not known (red). This *link annotation* serves as a guideline for the student, but the student still has the freedom to navigate to the concepts that are not yet recommended for him.

The right side of the screen displays the content file of a learning module. The *Adaptation Engine* performs the formatting and adaptation of the content file through XSL Transformations. The “Done with Concept”-button after the learning material leads to the next concept and thereby implements the *direct guidance* method. The *link annotation* and *direct guidance* are also performed by the *Adaptation Engine*, but are implemented in PHP.

Example Course

Concept: Example Concept 2

- Example Concept 1
- ➡ ● Example Concept 2
- Example Concept 3

Example Concept 2

Definition: For 2π -periodic signals satisfying the Dirichlet conditions $(f, g) := \int_{-\pi}^{\pi} f(x)g(x) dx$ defines a *scalar product*. This is a definition for visual learners.

Definition: This is a definition for visual learners where concept 0.1 should not be known.

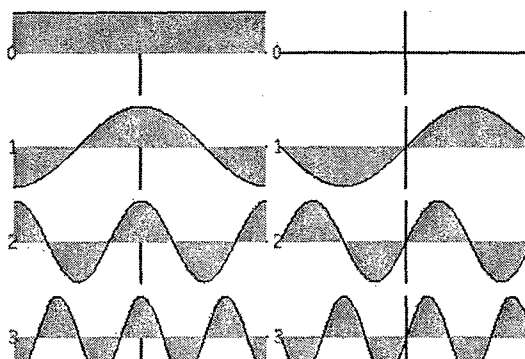


Figure 6: Example Concept 2

3.2.2. User-Model and Lesson-Plan

Figure 7 shows a simplified view of the User-Model and Lesson-Plan database. When uploading a course document as described in Section 5.2, the course topic is automatically stored in the *TOPIC* table, the concept names of the assigned modules are entered into *MASTER_LESSON_PLAN* table. When a module content file is uploaded to the server, the location of the module is entered into the *MEDIA* table. An entry in the *MEDIA* table can then be assigned to a concept name stored in the *MASTER_LESSON_PLAN* table.

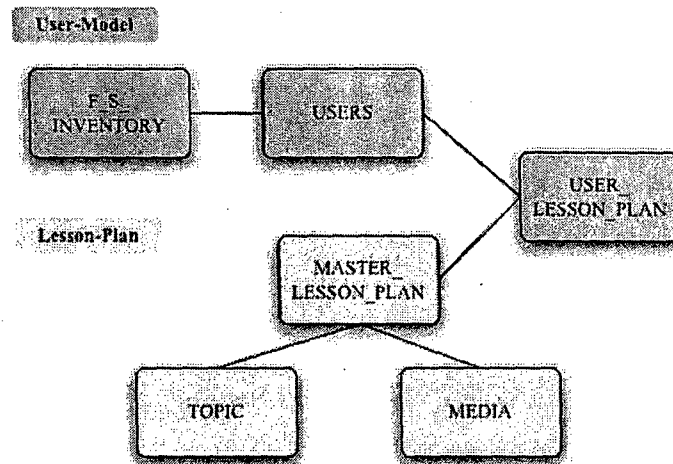


Figure 7: Simplified illustration of User-Model and Lesson-Plan

The User-Model part of the database consists of the following tables: *USERS*, *F_S_INVENTORY* and *USER_LESSON_PLAN*. When a user registers with the AEHS the following data is stored in the *USERS* table: username, password, email and home university. The table furthermore stores information about preferred formatting styles. The preferred color scheme and formatting style can be selected under “Preferences” in the *Student Web-Interface*. The scores from the Felder-Silverman Learning Style questionnaire are stored in the table *F_S_INVENTORY*. Initially it was planned to have four entries for each user in the *F_S_INVENTORY* table. The first entry was intended for the results from the questionnaire. The other three for Felder-Silverman scores from evaluated quiz scores, and active and passive evaluation of the learning material by the user. The three later entries would have been dynamically updated throughout the user’s interaction with the system. This dynamic update of the learning style preferences is currently not implemented for the XML learning modules. The *USER_LESSON_PLAN* table keeps track of the student’s progress. When a student starts to study a new topic all concepts assigned to this topic are entered in the *USER_LESSON_PLAN* table and associated with the student. A flag known indicates if the student has already finished studying this concept. The information stored in the *USER_LESSON_PLAN* and *F_S_INVENTORY* tables are used by the Adaptation Engine to adapt the learning material to the user’s knowledge and preferences.

3.2.3. Adaptation Engine

The adaptation of learning material and adaptive navigation support is partly implemented in PHP and partly realized through XSL Transformations. The two parts together form the Adaptation Engine. The *link annotation* realized through the colored bullet system and the *direct guidance* realized through the “Done with Concept”-button, are implemented in PHP.

The following steps are performed to generate the concept list with the colored bullet system:

- If user studies topic for the first time, enter concept ids assigned to the topic into the table *USER_LESSON_PLAN*.
- For each concept check in table *USER_LESSON_PLAN* if concept is known and generate the corresponding bullet.
- If concept is not known, check if the prerequisite concepts are known and generate the corresponding bullet.

When the “Done with Concept”-button is pressed, the *Adaptation Engine* checks which concept is the next in the sequence of the current course. The user is then forwarded to this concept.

Adaptation of the presentation of the learning material and adaptive navigation support are performed through XSL Transformations.

When calling the XSL Transformations, PHP passes the following parameters:

- **styleparam** Name of the selected color and formatting scheme.
- **knownconcepts** Semicolon (“;”) separated ids of known concepts.
- **learningstyle** Semicolon (“;”) separated learning style values, e.g. visual.
- **tid** Id of current topic.

The following steps are performed to determine, if a component is displayed. Components are thereby all components defined in the markup of the module content file.

- For each component call template *process-display-concept-1*, this checks if the concept requirements specified in the *req* attribute concur with the *knownconcept* parameter. Returns the parameter *cdisp*, which can be true or false.
- For each component call template *process-display-user-1*, this checks if the user requirements specified in the *req* attribute concur with the *learningstyle* parameter. Returns the parameter *udisp*, which can be true or false.
- For each component call template *display*, determines if and how to display the component depending on the values of *cdisp* and *udisp*.

4. XML Markup for Educational Hypermedia

To publish educational hypermedia modules in the Adaptive Educational Hypermedia System (AEHS) the two content component types *modules* and *courses*, are used. Each *module* covers one concept, it consists of a content file and associated files, such as images, applets or other multimedia components. In a *course* the modules are grouped and ordered in a sequence suitable for the teaching of a specific topic. A module can occur in several courses, this allows the reuse of learning materials. To allow an integration of the modules and courses into the AEHS and to be able to use the adaptation support of the AEHS the module content files and the course file must be marked up using the newly developed XML markup. The markup marks up the structure as well as the semantic content of the documents. The basic component structure and the basic structure of the XML markup are adopted from the Connexions Project at the Rice University (Baraniuk, Burrus, Hendricks, et al. 2002). One of the main extensions to the Connexions Markup Language CNXML is the introduction of the attribute *req*, it specifies the requirements for a specific component. The *Adaptation Engine* of the AEHS uses those requirements to adapt the material to the user’s needs. Currently requirements for prerequisite knowledge and user specific requirements, such as learning style preferences are processed. To ensure a standardized markup of the module content files and the course files two XML-Schemas have been developed. The W3C XML-Schema language is not always descriptive enough to depict all restrictions. The specifications described in the subsequent Section should therefore be taken as a guideline for the markup of the course files and module content files.

The XML-Schema *ilo.xsd* defines the structure and valid contents for the module content files and *course.xsd* for course files. A schematic view of the *course* schema is shown in Figure 8. Table 2 specifies the elements allowed in a course document, a short description of the elements

and its attributes is given. Elements that are self-explanatory are not listed to keep clarity. Table 1 lists the annotations for the tree schemas and the specifications tables.

Attributes in tree schema and specification table:		
<u>id</u>	required attribute	
lang	optional attribute	
Occurrence of elements in tree schema:		
*	Description	In XML-Schema
1	Element can occur exactly once	minOccurs="1" maxOccurs="1"
0-1	Element can occur 0 or 1 time	minOccurs="0" maxOccurs="1"
0-n	Element can occur 0 or n times	minOccurs="0" maxOccurs="unbounded"
1-n	Element can occur 1 or n times	minOccurs="1" maxOccurs="unbounded"
Occurrence of elements in specification table:		
element	Element occurs exactly once in the specified order.	
{element}	Element can occur 0, 1 or multiple times.	
{element} ⁺	Element can occur 1 or multiple times.	
[element]	Element can occur 0 or 1 time.	
element1 element2	Element1 or alternatively Element2 can occur.	

Table 1: Annotations for tree schema and specification table

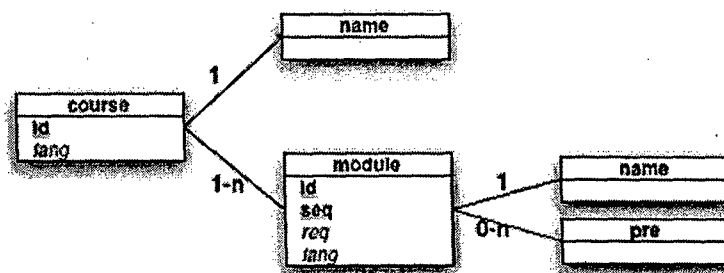


Figure 8: Tree Schema of XML-Schema course.xsd

Tag-Name	Description	Attributes	Children
course	Root element of a course file. id: character string, max length 10. lang: language of course or module.	<u>id</u> lang	name {module} ⁺
module	Specifies a module content file contained in the course. id: Has to correspond to the <i>module id</i> specified in the module's content file. seq: Order of modules. req: To utilize the adaptation support of the AEHS it is important to specify the requirements carefully and to keep to the	<u>id</u> <u>seq</u> req lang	name {pre}

	following description. * Semicolon (";") separated values * Prefixes to differentiate between the types of requirements: c concept prerequisite requirements u user specific requirements, e.g. u.visual => visual learner sw software requirements, e.g java hw hardware requirements env environment requirements,		
pre	Specifies modules from the same course, which should be known before learning this concept in the context of the specified course. The value of a pre element has to correspond to a module id in the same course document.		
The following elements are self-explanatory and not listed to keep clarity: name			

Table 2: Specification of markup language for course file

The markup for the module content files partly extends and partly narrows down version 0.5 of the Connexions Markup Language CNXML (Hendricks & Galvan 2003). Table 3 specifies and describes the allowed elements and attributes of the *ilo* schema. A schematic overview is shown in Figure 9. Like CNXML, the markup for educational hypermedia does not cover all possible markup someone might want to include in a document. Rather, it is designed as a framework defining the structure and semantics of the material, and enabling the use of the adaptation support of the AEHS. For more specific markup, the markup for educational hypermedia can be extended, by combining it with other XML languages. The schema *ilo.xsd* already incorporates the use of MathML, for the markup of mathematical equation and the use of a restricted set of HTML-tags for formatting purposes.

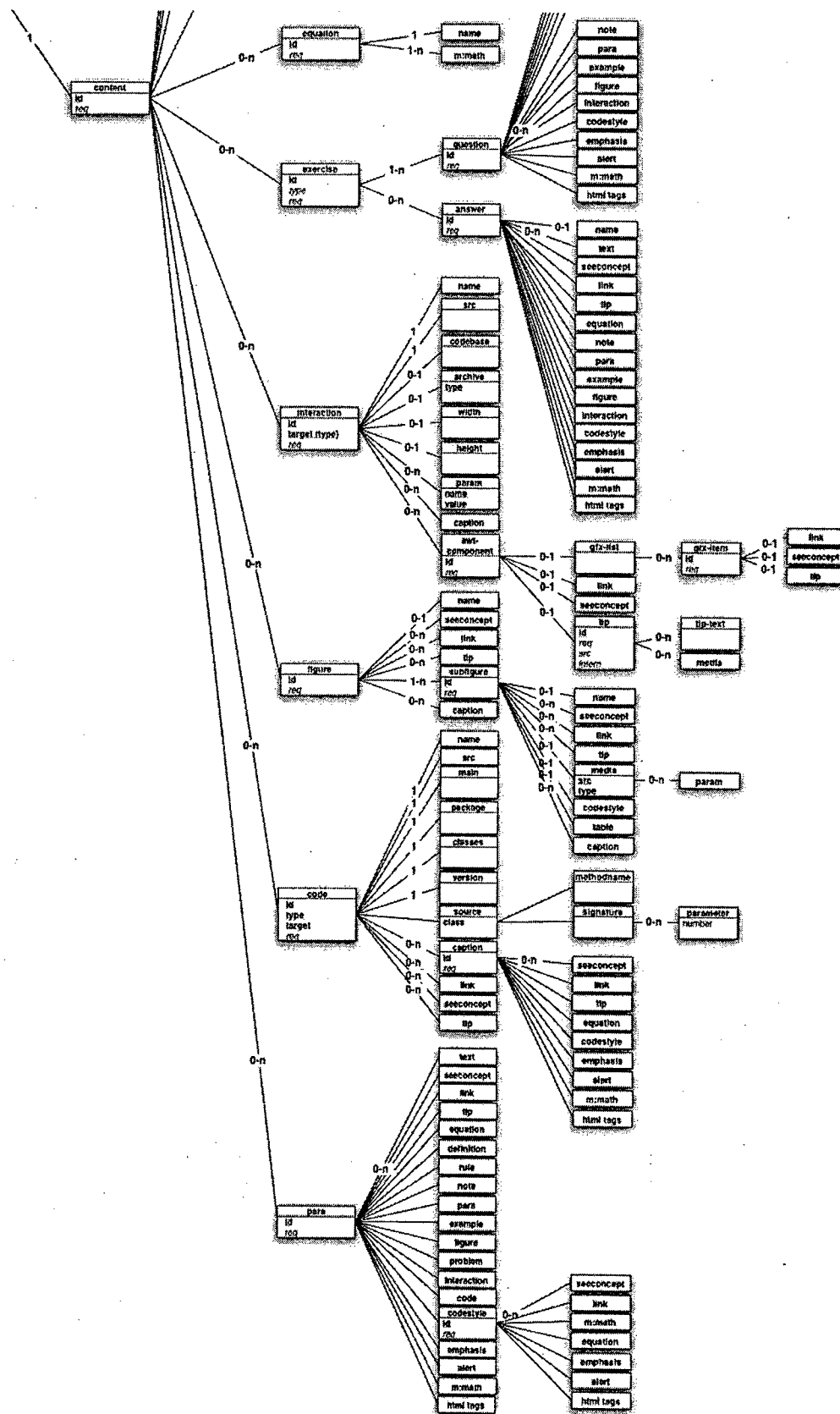


Figure 9: Tree Schema of XML-Schema *ilo.xsd*

Tag-Name	Description	Attributes	Children
module	Root element of a module's content file. id: Has to correspond to the id of the module element as specified in the course file.	<u>id</u> <i>type</i> <i>lang</i> <i>req</i>	{name} ⁺ content
content	Content structured in components. id: Unique identifier	<u>id</u> <i>req</i>	{definition rule note problem example equation exercise interaction figure code para}
definition	Defines a word or term. The meaning element has to occur at least once, the other elements may occur zero times.	<u>id</u> <i>req</i>	term {meaning example seeconcept} ⁺
meaning	Gives one definition for a term defined in a definition element. Multiple meanings can be defined for one term. The actual meaning text is contained in the text-element. This allows the adaptation of the components contained in the meaning element.	<u>id</u> <i>req</i>	{text term seeconcept link tip equation figure interaction codestyle emphasis alert m:math html-tags}
rule	The statement element has to occur at least once, the other elements may occur zero times. type: Best practices: axiom, lemma, proposition. User defined values are allowed.	<u>id</u> <i>type</i> <i>req</i>	{statement proof example seeconcept} ⁺
note	The actual note text is contained in the text-element. This allows the adaptation of the components contained in the note. type: Best practices: note, remark. User defined values are allowed.	<u>id</u> <i>type</i> <i>req</i>	{text seeconcept tip link equation code emphasis alert m:math html-tags}
text	Contains the text of the note, meaning, statement, proof, problem, example, question, answer, and para elements. Encapsulating the text of those elements in the text-element allows the adaptation of the other components contained in the element.		
interaction	Defines interactive components, e.g. applets or flash components. Depending on the type of interaction specified in the target attribute different child-elements might be important. The awt-component element is used for the adaptive navigation support within the interactive multimedia component. target: Type of interaction component,	<u>id</u> <u>target</u> <i>req</i>	name src [codebase] [archive] [width] [height] [param] {caption awt-component}

	e.g. applet.		
src	Location and if applicable startup method of interaction component.		
code base	Specifies the location of necessary classes and libraries.		
archive	Specifies the name of the component archive. Has to be declared if the interaction component is contained in an archive. type: Best practices: jar, zip. User defined values are allowed.	<u>type</u>	
awt-component	Specifies the awt-components of an applet, to which a link, seeconcept or tip is passed to allow adaptive navigation support within the applet. Each awt-component can have an optional gfx-list, and either a link, seeconcept or tip element. Extra awt-component elements are necessary, if more than one of these elements should be passed to the specific AWTComponent of the applet. The id then needs to be encoded with “_x”, $x \in N$. id: Format: element-id[_x]_typY “element-id”, id of the AWTComponent in the applet. “_x”, $x \in N$, encodes the ids if more than one link, seeconcept or tip element are passed to the applet. “_typY”, type of parameter being passed. typ1 - link, typ2 - seeconcept, typ3 - tip.	<u>id</u> req	[gfx-list] [link seeconcept tip]
gfx-list	Contains the GraphicsElements of an AWTComponent..		{gfx-item}
gfx-item	Specifies the GraphicsElements of an AWTComponent, to which a link, seeconcept or tip is passed to allow adaptive navigation support within the applet. Each gfx-item can have either a link, seeconcept or tip element. Extra gfx-item elements are necessary, if more than one of these elements should be passed to the specific GraphicsElement of the AWTComponent. The id then needs to be encoded with “_x”, $x \in N$. See awt-component for description of the format for the id attribute.	<u>id</u> req	[link seeconcept tip]
figure	Each figure is split up in subfigures, which can contain components such as images, tables or graphs, this allows an adaptation within the main figure.	<u>id</u> req	[name] {seeconcept link tip} {subfigure} ⁺ {caption}

subfigure	The elements media, codestyle and table specify the actual figure-media for a subfigure. Only one of those elements can occur in a subfigure element.	<u>id</u> <i>req</i>	[name] {seeconcept link tip} media codestyle table {caption}
main	Contains a string specifying the main class of a code element.		
package	Contains a string specifying the location of necessary classes and libraries.		
classes	Contains a string with all classes needed for the main class. A comma (",") separates multiple class names.		
version	Contains a double specifying the version number of the code element.		
source	class: Class name of code component. The child elements declare the exact methodname and its signature.	<u>class</u>	methodname signature
signature	Groups the parameters to the signature.		{parameter}
parameter	Specifies the type of a parameter passed to the method. number: Positive integer	<u>number</u>	
link	Specifies a hyperlink to an external site. src: URL to site	<u>src</u> <i>req</i>	{m:math equation codestyle emphasis alert}
seeconcept	Specifies a hyperlink to another concept module in the same course context. id: Has to correspond to the id of the module content file it refers to.	<u>id</u> <i>req</i>	{m:math equation codestyle emphasis alert}
tip	Contains additional information to a component. The tip can for example be displayed in a tooltip window. src: URL to site, if tip should also be displayed as a link. intern: 0 -> external URL, 1 -> internal URL	<u>id</u> <i>req</i> <i>src</i> <i>intern</i>	{tip-text media}
tip-text	Contains the text for a tip element.		
equation	Groups one or several m:math elements and a name to an equation.		name {m:math}+
codestyle	Contains code segments. Stylesheets can use this tag to render the text inside using a specific font type. This tag was introduced to allow a distinction between code segments and code blocks that can be uploaded to the server and compiled. The distinction is necessary to allow stronger restrictions in the XML-Schema.	<u>id</u> <i>req</i>	{seeconcept link m:math equation emphasis alert html-tags}
table	Corresponds to the html table tag. Can be placed at the same positions as the allowed html-tags.	<i>id</i> <i>tabstyle</i>	[name] tgroup {caption}

	tabstyle: Specifies the table style.		
list	Corresponds to the html tags for building lists. type: Specifies the type of list used. Allowed values: ol (ordered list), ul (unordered list), dl (definition list) Default: ul	id type	[name] {list-item} ⁺
m:math	MathML is incorporated for the markup of mathematical equations. MathML-tags have to be labeled with the namespace "m", and are allowed where the element m:math is specified.		
html-tags	For formatting purposed a restricted set of HTML-tags is allowed at the specified positions. HTML-tags are labeled with the namespace "h". Allowed tags are: h:br, h:b, h:i, h:sub, h:sup and h:blockquote.		
The following elements are self-explanatory and not listed to keep clarity: name, problem, example, exercise, question, answer, para, caption, term, height, width, param, methodname, emphasis, alert, list-item, tgroup, colspec, spanspec, thead, tfoot, tbody, colspec, row, entry. If not specified otherwise the attribute id defines a unique identifier. Refer to Table 3 for description of the attributes lang and req.			

Table 3: Specification of markup language for module content file

5. Authoring and Publishing of Learning Materials

5.1. Authoring of Learning Materials

The *jEdit Programmer's Text Editor* was chosen as an editor for the XML learning material. jEdit was selected because it is a free software written in Java, therefore it runs on different operating systems such as Mac OS X, Unix and Windows. The basic version of jEdit is just a text editor, but it has an extensible plug-in architecture. After the installation of the plug-ins SideKick, Project Viewer, XInsert, XML, XMLIndenter and XSLT, the editor provides XML-Syntax highlighting, XML-Tag completion and validation of the XML document depending on the given namespaces and included XML-Schema. The XSLT plug-in provides the ability to transform XML documents offline using XSLT stylesheets. Download jEdit from <http://www.jedit.org/index.php>, and follow the installation instructions for your operating system. After successful installation start jEdit and open **Plugins > Plugin Manager**. Select and install the following plugins: *SideKick*, *Project Viewer*, *XInsert*, *XML*, *XMLIndenter*, *XSLT*.

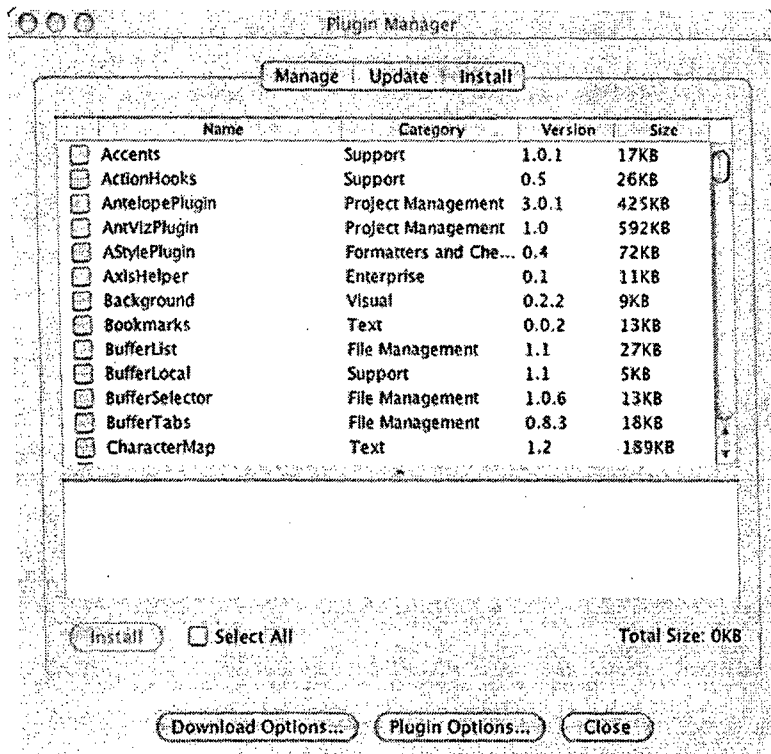


Figure 10: jEdit - Plugin Manager

Unpack ilo.zip in your file system. This will create the following folders and files

- ilo/example_course.xml
- ilo/share/ilo.xsd
- ilo/share/course.xsd
- ilo/stylesheets/ilo.xsl
- ilo/stylesheets/ilo_offline.xsl
- ilo/stylesheets/mathml.xsl
- ilo/stylesheets/cs1.css
- ilo/stylesheets/cs2.css
- ilo/stylesheets/cs3.css
- ilo/stylesheets/teacher.css
- ilo/example1/index.xml
- ilo/example1/nyquist.jar
- ilo/example1/euler.gif

In jEdit select **Plugins > Project Viewer > Projects > New Project Here** and create a new project "ilo", the root directory should be the directory *ilo/* which was created when extracting *ilo.zip*.

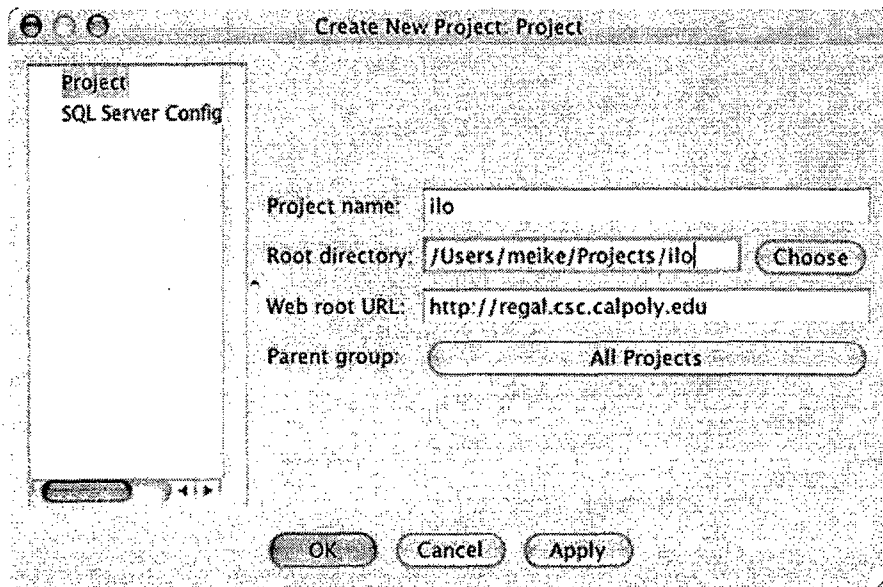


Figure 11 : jEdit Project Viewer - Create New Project

Click “Apply” followed by “OK”. A popup window for the “Initial import” appears, select “Yes, import all files.” This will import all files from the project root directory *ilo/*.

Before creating a new course and modules familiarize yourself with Section “4. XML Markup for Educational Hypermedia” and the example documents *ilo/example_course.xml* (Example 2) and *ilo/example1/index.xml* (Example 3). To create a new course, create a file *<coursename>.xml* in the directory *ilo/*. Add the following root tag to the file:

```
<course xmlns="http://regal.csc.calpoly.edu/"
xmlns:xsi="http://www.w3.org/2001/XMLSchema-instance"
xsi:schemaLocation="http://regal.csc.calpoly.edu/
http://regal.csc.calpoly.edu/~mmuckenh/AdHyMedia/ilo/share/course.xsd"
>
```

The XML-Namespace `xmlns="http://regal.csc.calpoly.edu/"` and the `xsi:schemaLocation` attribute attach the XML-Schema *course.xsd* to the XML document. The XML-Schema *course.xsd* defines the valid contents for the *<coursename>.xml* document. To allow the integration of the new course into the AEHS it is important to follow the structure and specification of the schema *course.xsd* (see 4. XML Markup for Educational Hypermedia). When saving the file *<coursename>.xml* the first time jEdit will ask if the resource <http://regal.csc.calpoly.edu/~mmuckenh/AdHyMedia/ilo/share/course.xsd> should be cached for future use, answer yes to make sure that the *course.xsd* Schema is available when editing the *<coursename>.xml* document.

The jEdit XML-Insert plugin (**Plugins > XML > XML Insert**) lists the XML elements that may be inserted at the current position. The SideKick plugin provides a completion popup, this can be invoked with the **Plugins > SideKick > Show Completion Popup** command. The suggestions from XML Insert and Tag Completion provide a rough guideline of the allowed tags, but they do not always provide the correct suggestions. Check the Error List after saving the *<coursename>.xml* document to make sure the structure corresponds to *course.xsd*. The error message “Invalid content starting with element...” indicates that an element appears at a wrong

position. Note that the schema definition is more lax than the specifications for the markup, this is due to the nature of the W3C schema definition. It is best to follow the specifications described in Section “4. XML Markup for Educational Hypermedia” closely, this helps to develop course and module content files that conform to the specifications and schema definition.

```
<course xmlns="http://regal.csc.calpoly.edu/"
xmlns:xsi="http://www.w3.org/2001/XMLSchema-instance"
xsi:schemaLocation="http://regal.csc.calpoly.edu/
http://regal.csc.calpoly.edu/~mmuckenh/AdHyMedia/ilo/share/course.xsd"
id="ex">
  <name>Example Course</name>
  <module id="ex1" req="u.visual;sw.java11" seq="1">
    <name>Example Concept 1</name>
  </module>
  <module id="ex2" req="c.ex1;u.visual;sw.java11" seq="2">
    <name>Example Concept 2</name>
    <pre>ex1</pre>
  </module>
  <module id="ex3" req="c.ex2;c.ex1;u.visual;sw.java11" seq="3">
    <name>Example Concept 3</name>
    <pre>ex1</pre>
    <pre>ex2</pre>
  </module>
</course>
```

Example 2: XML course document - example_course.xml

A module package has to be created for each module specified in the *<course>.xml* document. To develop a new module, create a directory *<modulename>* in *ilo/*. Create the file *ilo/<modulename>/index.xml* and add it to the Project *ilo* in jEdit. The XML document containing the module definition and text must be called *index.xml*, the documents must follow the structure and specifications of the XML-Schema *ilo.xsd* (see 4. XML Markup for Educational Hypermedia). The following root tag adds necessary namespaces to *index.xml*.

```
<ilo:module xmlns:ilo="http://regal.csc.calpoly.edu/"
xmlns:m="http://www.w3.org/1998/Math/MathML"
xmlns:h="http://www.w3.org/1999/xhtml"
xmlns:xsi="http://www.w3.org/2001/XMLSchema-instance"
xsi:schemaLocation="http://regal.csc.calpoly.edu/
http://regal.csc.calpoly.edu/~mmuckenh/AdHyMedia/ilo/share/ilo.xsd">
```

The namespace *xmlns:ilo="http://regal.csc.calpoly.edu/"* and the *xsi:schemaLocation* attribute attach the XML-Schema *ilo.xsd* to the document. The namespaces *xmlns:m* and *xmlns:h* allow the use of MathML- and HTML-Tags in the *index.xml* document. Follow the specifications and structure of *ilo.xsd* for the allowed locations of MathML and HTML-Tags. A prompt to cache the resources will appear again. Besides the XML-Schema *ilo.xsd* resources for the MathML and XHTML namespace will be cached.

The importance to follow the specifications described in Section “4. XML Markup for Educational Hypermedia” applies for the *<modulename>.xml* document in the same way as for

the <courseName>.xml document. Example shows the document ilo/example1/index.xml. Note not all possible components are used in ilo/example1/index.xml.

```
<?xml version="1.0" encoding="UTF-8"?>
<ilo:module xmlns:ilo="http://regal.csc.calpoly.edu/"
  xmlns:m="http://www.w3.org/1998/Math/MathML"
  xmlns:h="http://www.w3.org/1999/xhtml"
  xmlns:xsi="http://www.w3.org/2001/XMLSchema-instance"
  xsi:schemaLocation="http://regal.csc.calpoly.edu/
http://regal.csc.calpoly.edu/~mmuckenh/AdHyMedia/ilo/share/ilo.xsd"
  id="ex1"
  lang="en">
  <ilo:name>Example Concept 1</ilo:name>
  <ilo:content id="c_ex1">
    <ilo:note type="Note" id="n1_ex1">
      <ilo:text>
        This is a note with an additional tip.
        The tip is only visible when the user does not
        know ex3 and is an active user.
      </ilo:text>
      <ilo:tip id="t1_p1_ex1" req="c.!ex3;u.active"
        src="http://www.google.com" intern="0">
        Put mouse over this text to view tip.
        <ilo:tiptext>
          This is the additional tip, which is
          shown, if concept Example 2. is not known,
          and you are an active user.
        </ilo:tiptext>
        <ilo:media src="ilo/example1/euler.gif"
          type="image/gif">
        </ilo:media>
      </ilo:tip>
    </ilo:note>
    <ilo:figure id="f1_ex1">
      <ilo:name>Complex Numbers</ilo:name>
      <ilo:subfigure id="sf1_ex1">
        <ilo:media src="example1/euler.gif"
          type="image/gif">
        </ilo:media>
      </ilo:subfigure>
      <ilo:caption id="cap1_ex1">
        Graph with the Euler circle.
      </ilo:caption>
    </ilo:figure>
    <ilo:interaction id="app_ex1" target="applet">
      <ilo:name>Nyquist</ilo:name>
      <ilo:src>applets.nyquist.AdMainClass.class</ilo:src>
      <ilo:codebase>ilo/example1</ilo:codebase>
      <ilo:archive type="jar">adnyquist.jar</ilo:archive>
      <ilo:width>600</ilo:width>
      <ilo:height>250</ilo:height>
```

```

        <ilo:awt-component id="ny">
        <ilo:link src="http://www.google.com" req="u.visual">
            Link to google for visual learners.
        </ilo:link>
        </ilo:awt-component>
        <ilo:caption id="cap_ny">
            Press control to activate the Adaptation-Layer.
        </ilo:caption>
    </ilo:interaction>
</ilo:content>
</ilo:module>

```

Example 3: XML module document index.xml

To complete the module package, save the associated files such as images, applet classes or jar-files in the directory *ilo/<modulename>* or suitable subdirectories. Go to the directory *ilo* and create a zip-archive of the directory *<modulename>*:

```
zip -r <modulename>.zip <modulename>/
```

Follow the steps in Section “5.2 Publishing of courses and modules” to publish the course and modules in the AEHS.

5.2 Publishing of Courses and Modules

Teachers can publish the developed courses and module package through the web interface for teachers of the AEHS at <http://regal.csc.calpoly.edu/~mmuckenh/AdHyMedia/main.php>. To be able to use the AEHS, each user has to be registered in the system. After clicking the hyperlink “Join” a registration screen appears. A username, password, email and the name of the home university have to be entered. The information about the user is stored in the user table of the database. The user type can only be specified as “student”. To obtain a teacher account, register just as a student would, then click on the hyperlink “send email to the Admin” on the login page. Include the username and email address in the email, which you used in order to register. The administrator will then verify that you are entitled to register as a teacher and send you an email with a verification of your teacher account.

After successfully logging in as a teacher, the menu shown in Figure 12 is displayed. To upload a new course, click the link “Upload Course”, which will display the course upload page as seen in Figure 13. Select the course XML document you would like to upload. To allow the integration into the AEHS, the course documents have to correspond to the specifications described in Section “4. XML Markup for Educational Hypermedia”. After clicking the “Upload” button the course document is loaded onto the server and course data is saved in the database.

Hello melke,

you are logged in as a "teacher"

List Courses

Upload Course

Change usertype for a user

Figure 12: Main menu for teachers

Please select a course document to upload:

Upload File

Existing Courses:

Course Name	Concept Names	
Fourier Theorie	Sinusoide	ilo/example.zip [Update/Change]

Figure 13: Course upload screen

After a successful upload, the newly added course is displayed (Figure 14).

Added Course:

Please upload the module packages for the concepts!

Course Name	Concept Names	
Example Course	Example Concept 1	[Add Module Package]
	Example Concept 2	[Add Module Package]
	Example Concept 3	[Add Module Package]

Figure 14: Added course screen

A module package must be uploaded for each module specified in the course document. A module package can be uploaded right after a new course is added or later by clicking on the link "List Courses". This will display a list of existing courses as seen in Figure 15. To upload a module package, click on the link "Add Module Package" next to the concept's name. If a module package is already uploaded and assigned to the concept, the module package can be changed or updated by clicking on the link "Update/Change".

Existing Courses:

Course Name	Concept Name	
Example Course	Example Concept 1	[Add Module Package]
	Example Concept 2	[Add Module Package]
	Example Concept 3	[Add Module Package]
Fourier Theorie	Sinusoid	ilo/example.zip [Update/Change]

Figure 15: Existing course List

Figure 16 shows the screen to upload and assign, update or change a module package for a selected concept. To upload a new module package, or update an existing module package click the "Browse" button and select the package. The package must be a zip-package, and the content file *index.xml* must correspond to the specifications of the markup for module content files as described in Section "4. XML Markup for Educational Hypermedia". After clicking the "Upload" button the module package will be uploaded onto the server and unpacked into a directory corresponding to the name of the zip-package. The module name and a link to the module package are saved in the *Lesson Plan* tables of the database and are then available for students to view. Figure 17 shows the screen after successful upload of a module package. An error message is displayed, if a module package is too big, or of the wrong format is uploaded. If a concept occurs in more than one course, the module package is only uploaded and available on the server once. After the module package is uploaded once, it can then be assigned to other concepts, by clicking on the link "Assign Module to Concept ...". Each concept can only have one module package assigned, but each module package can be assigned to several concepts. If the module package is changed and updated the changes are effective for all concepts the module package is assigned to.

Assign new Module to Concept "Example Concept 1":

Upload File

Assign existing Module:

Module	Concept	Assigned to Concept	Assign to Concept
ilo/example.zip	Zip test	Sinusoid	[Assign Module to Concept "Example Concept 1"]

Figure 16: Upload, update, change module package screen

Assigned Module:

Module	Concept	Assigned to Concept
ilo/example1.zip	Example Concept 1	Example Concept 1

Figure 17: New module package assigned

After a course and the corresponding module files are successfully uploaded, the course is available for the students.

6. Conclusion

The newly developed XML markup language for educational hypermedia allows an easy integration of new and existing material in the AEHS and through the web-based AEHS, the learning materials can be made widely available to students at Cal Poly, the University of Tuebingen, as well as other Universities and organizations. Because of the advanced networking structure of Internet2 even large multimedia repositories can be made available.

7. Bibliography

- Aase, M. (2002). *Developing an Interactive Teaching Tutorial utilizing Learning Styles*. Master Thesis, Computer Science Department, California Polytechnic State University.
- Achour, M., Betz, F., Dovgal, A., Lopes, N., Olson, P., Richter, G., Seguy, D., Vrana, J. (2005). PHP Manual. Retrieved Jan. 2005, from <http://www.php.net/manual/en/>
- Baraniuk, R.G., Burrus, C.S., Hendricks, B.M., et al. (2002). Connexions: Education for a Networked World. Presented at the *IEEE International Conference on Acoustics, Speech and Signal Processing (ICASSP 2002)*, Orlando, FL, USA.
- Brusilovsky, P. (1996). Methods and techniques of adaptive hypermedia. *User Modeling and User-Adapted Interaction*, 6(2-3), 87-129.
- Brusilovsky, P. (2001). Adaptive Hypermedia. In A. Kobsa (Ed.), *User Modeling and User-Adapted Interaction, Ten Year Anniversary Issue*, 11(1/2), 87-110.
- Clark, J. (1999). *XSL Transformations (XSLT) Version 1.0*, W3C Recommendation. Retrieved Jan. 2005 from <http://www.w3.org/TR/1999/REC-xslt-19991116>
- Fallside, D.C., Walmsley, P. (2004). *XML Schema Part 0: Primer (Second Edition)*, W3C Recommendation. Retrieved Jan. 2005, from <http://www.w3.org/TR/2004/REC-xmlschema-0-20041028/>
- Fink, J., Kobsa, A., Nill, A. (1998). Adaptable and Adaptive Information Provision for All Users, Including Disabled and Elderly People. *The New Review of Hypermedia and Multimedia* 4, 163-188.
- Hanisch, F., Straßer, W. (2003). Adaptability and interoperability in the field of highly interactive web-based courseware. *Computer & Graphics*, 27(4), 647-655.
- Hanisch, F. (2004). *Highly Interactive Web-Based Courseware*. PhD thesis, Wilhelm Schickard Institute, University of Tübingen, Germany, 2004. Retrieved Oct. 2004 from <http://w210.ub.uni-tuebingen.de/dbt/volltexte/2004/1167>
- Hanisch, F., Görke, J., Straßer, W. (2004). A Visual Scripting Technique for the GRIS/ILO Interactive Learning Objects. In: *Conference on Educational Multimedia, Hypermedia and Telecommunications 2004(1)*, 1347-1350. URL: <http://www.gris.uni-tuebingen.de/projects/ilo>
- Hendricks, B., Galvan, A. (2003). *CNXML 0.5 Language Specification*. Retrieved April 2005, from <http://cnx.rice.edu/technology/cnxml/0.5/spec/>
- Kobsa, A., Koenemann, J., Pohl, W. (1999). *Personalized hypermedia presentation techniques for improving online customer relationships* (Technical report No. 66 GMD). German National Research Center for Information Technology, St. Augustin, Germany.
- Melis, E., Andres, E., Gogouadze, G., Libbrecht, P., Pollet, M., Ullrich, C. (2001).

- ActiveMath: System Description. *International Journal of Artificial Intelligence in Education*, 12, 580-582.
- Muckenhaupt, M., Skorupski, J., Kaiser, M. (2004). *Dynamic User Modeling for Hypermedia Adaptive Learning Systems*. Retrieved Dec. 2004, from http://counties.csc.calpoly.edu/~team_6fk/F04/Final-Documentation.html
- Nelson, T.H. (1967). Stretchtext. *Hypertext Note* 8.
- The PostgreSQL Global Development Group (2005). *PostgreSQL 8.0.3 Documentation*. Retrieved Jan. 2005, from <http://www.postgresql.org/docs/8.0/interactive/index.html>
- van Dam, A. (2002). *Next Generation Educational Software*. Brown University and the NSF STC for Graphics and Visualization. ED-MEDIA 2002 Keynote Presentation, Denver, Colorado, June 2002. Retrieved Nov. 2004, from <http://www.cs.brown.edu/people/avd>
- Weber, G. (1999). *Episodic Learner Model - The Adaptive Remote Tutor (ELM-ART II)*. Retrieved Nov. 2004, from <http://apsymac33.uni-trier.de:8080/Lisp-Course>
- Yergeau, F., Bray, T., Paoli, J., Sperberg-McQueen, C. M. , Maler, E. (2004). *Extensible Markup Language (XML) 1.0* (Third Edition), W3C Recommendation. Retrieved Jan. 2005, from <http://www.w3.org/TR/2004/REC-xml-20040204/>

Redundant Peer to Peer File System

Project Investigators:

Dr. Franz Kurfess
Associate Professor
Department of Computer Science, College of Engineering

Lyle Kozloff
Undergraduate Student
Department of Computer Science, College of Engineering

Cal Poly Internet2 Mini-Grant

Phase III Final Report

Summer 2005

Project Title: Redundant Peer to Peer File System
Project Director: Dr. Franz Kurfess
College and Department: Department of Computer Science, College of Engineering

Introduction

On April 12, 2005 the Recording Industry Association of America (RIAA) generated a buzz in the media by its announcement of 405 lawsuits against individuals attending some 18 colleges and universities across the nation. These lawsuits have arisen due to the distribution of copyrighted materials over the high performance infrastructure of Internet2. Few would argue against the misuse of the collaborative software i2hub (<http://www.i2hub.com>), but fewer still would recognize the need for a more secure environment in which to share information and ideas. This project sought to correct this flaw by launching an investigation into a possible collaboration environment whose very definition is security: FreeNet <http://freenetproject.org/>.

One of FreeNet's main goals is the dissemination of information in an arena free from censorship. To do this an infrastructure that allows complete anonymity in the publishing and consumption of information is required. These unique requirements force an implementation that offers several advantages for its use in a collaborative environment. FreeNet accomplishes its goals through a relatively simple scheme.

FreeNet

All computers connected to FreeNet (nodes) share a portion of their hard drive. FreeNet nodes form a de-centralized network to pass around encrypted chunks of files. Files are only able to be unencrypted upon complete receipt of the file, and much like BitTorrent parity checks are in place to ensure that data integrity is preserved. If chunks have been lost on the network after time, as long as a sufficient number remain the file can be "healed" through the regeneration of missing chunks using the built in checks. The regenerated pieces are then redistributed to the network. Since the network is constantly re-forming, chunks moving between nodes might have been requested by the user, or simply be traffic pushed or pulled by the node itself as the network re-arranges itself. The network ensures that the most popular of these are the most widely available. Since pieces of the complete file may come from several locations, and each piece is essentially useless without the corresponding pieces, communication is completely obfuscated. In this manner both the consumption and publication of information is encapsulated in the same elegant paradigm.

Collaboration and FreeNet

This investigation began with the note that current collaboration techniques could be improved. Communication through current means of telephony, instant messaging, and e-mail seems to work well enough. However the manner in which documents, files and other collaborative materials are distributed amongst peers is not only inefficient, but potentially dangerous. There are essentially two methods; centralized collaboration and distributed collaboration.

Centralized Environment

In the centralized environment documents are kept in a central repository. This repository could store documents in various formats, ranging from a simple file cabinet all members place their material in to a large server with redundant disk arrays. The strength of this method is orderliness. Team members must be authorized to use the resources of the team, so versions are kept in check and everything is kept as it should be. The weakness of the system however lies in its centrality. If materials are all kept in one place, only one place needs to be compromised for a complete loss of data to occur, or worse in some cases the theft of data. In addition, strong restrictions on accessibility may be imposed for documents that exist or are authorized to be used only in limited quantities (e.g. paper documents, or electronic documents subject to Digital Rights Management).

Distributed Environment

In the distributed environment (often the environment student projects are run in) files are passed between members via e-mail, instant-messages, or photo copies. This somewhat chaotic system ensures that there are multiple copies of important data to safe-guard against any losses. The multiple copies however also make for the difficult task of finding the most updated version. While this might safe-guard against data theft, as a potential thief would have to infiltrate all members' machines in order to have access to all pieces of the project, the underlying discord makes this environment unsuitable. Version Control Systems can be used to organize updates in documents in a systematic manner, but they are frequently more suitable for a centralized system, possibly with multiple instances of repositories for easier access or backup purposes.

FreeNet molds these two into what has the potential to be a unique system for collaboration. The advantages of a centralized repository are kept. Files can be published to a place where they can always be reached (centrality), and as long as a sufficient number of nodes carry some portion of the data, it will never be lost (distribution). Since data can only be retrieved with a proper hash key for the files (orderliness), unless the hash is leaked no unauthorized use of the files can occur (security).

FreeNet and Internet2

In its current incarnation with the regular Internet as infrastructure, FreeNet at the time we conducted our experiment (Winter 2005) was so slow as to be practically unusable. Our investigation into using FreeNet on Internet2 was originally incepted to be a hands-on project where data-flow rates would be calculated and the performance benefits imbued by its use on Internet2 would be lauded. The results of the project so far are somewhat different than originally anticipated, however. Our initial idea to port FreeNet to the Internet2 infrastructure turned out to be impractical due to resource constraints. One significant problem, for example,

was the availability of only one single Internet2 node for our experiments. While we did some experiments on a local network whose performance characteristics in terms of bandwidth and latency are probably close to Internet2, the results we obtained were too varied to be of much use. In addition, an extrapolation from a local network to Internet2 seems highly questionable. While the major portions listed in the work plan, such as inspection of FreeNet's source code and the deployment of test nodes over the Internet, were largely completed by the end of the Winter 2005 quarter, another significant result of the project was a deeper understanding of the issues being faced today in collaborative research and teaching. While FreeNet is certainly not a solution in and of itself, with careful use FreeNet can provide a leap forward in the way the existing infrastructure of Internet2 is used in situations where shared repositories of documents are essential.

Conclusions and Future Work

While the results of the initial research into collaborative use of FreeNet over Internet2 were compelling, further investigation regarding the feasibility of such an approach is required. From a purely technical standpoint there does not appear to be a reason that FreeNet nodes could not be placed on computers connected to Internet2. It warrants investigation as to whether or not the high-speeds of Internet2 would make the snails-pace of FreeNet over the Internet quick enough that it could actually be used by a research team. While our team will perform some limited experiments to obtain some results, it is difficult to conduct meaningful tests within the restrictions we face due to our resource constraints, and the lack of a truly distributed test environment.

If these results were in the positive it would also be necessary to construct a collaboration environment that used FreeNet as a base. This project could take on the form of a simple published interface to FreeNet where collaborators could publish their files, or a even more drastic approach of re-writing large portions of FreeNet to include as of yet undetermined features designed to aid in group efforts.

The final step would be to actually have collaborative groups use the new system and discover if this new manner of exchanging information is worthy of further pursuit, or rather to be discarded.

Real-Time searching on I2

Project Investigators:

Dr. Franz Kurfess
Associate Professor
Department of Computer Science, College of Engineering

Foaad Khosmood
Graduate Student
Department of Computer Science, College of Engineering

Cal Poly Internet2 Mini-Grant

Phase II Final Report

Summer 2005

Project Title: Real-Time searching on I2
Project Director: Dr. Franz Kurfess
College and Department: Department of Computer Science, College of Engineering

Introduction and Project Description

Internet2 high speed networks offer great advantages to research into searching technologies for which network speed is a major factor. In the existing market-oriented structure of the Internet, companies like Google and Yahoo offer fast Web-searching. This search is fast because the user can retrieve a list of target matches that correspond to his/her search inquiry in less than a minute depending on connection speeds. However, the pointers returned are based on associations that are not recent. This causes a problem: how do we perform a more meaningful search by having access to a more recent representation of the Web in our search results?

The purpose of this research project is to outline existing mass-usage search technologies prevalent in the current Internet (also referred to as Internet1), examine shortfalls and bottlenecks and identify solutions that could be implemented and tested on Internet2.

Web Searching at a Glance

The World Wide Web represents a large amount of information that is constantly being updated. Users would like to organize or search this knowledge somehow. Classically in information systems, there exist two approaches to such a problem.

The first approach is a centralized indexing. The central index is a repository (often referred to as a data base, although the actual implementation may be different) that contains all meaningful keywords that occur in the documents, together with information that links a particular keyword to all the documents that contain it. In this method, whenever a new piece of information is created or an existing piece is destroyed the central index is informed and altered to reflect the new status. This can be called a “push” approach because data is pushed into the database from the sources. Disk drive file systems, SQL databases or Web-enabled databases such as those employed in Ebay or Amazon.com are examples.

The second approach is when the data is independently updated and an index is created after the fact. This can be called a “pull” approach because the indexer pulls information down from the sources and the sources that are involved in knowledge creation, are not involved in indexing. This is how Windows-non indexed file searching or general Web text or image searching at Google and Yahoo are done.

This dichotomy is almost identical to the classic polling versus interrupt approach in hardware design. Interrupt driven processes are necessary when designing a “real-time” system.

Historically, the development of the World Wide Web has followed a pull approach for several good reasons. First, the pull approach allows for maximum decentralization and minimum coordination. One relatively simple, ubiquitous protocol is sufficient (the Hyper-Text Transfer Protocol, HTTP), and the indexing interface is exactly the same as a regular HTTP access interface. Second, the system wasn't designed with searching in mind. WWW searching came into being after the original WWW protocol and nothing in the protocols themselves are designed for searching and search methods. Only in the recent years, such advances as a "robots.txt" file, or the RSS protocol for news searching and Weblogs has changed the equations just a bit and tilted in the direction of easier searches. The third reason is that the Web itself was not originally designed for up-to-the minute content turnover. The advances in dynamic HTML and streaming media, again, came later.

"Real-Time" Searching

To achieve real-time searching we mean that the gap between generating the index information from the documents being searched and actually retrieving the search results will be as small as possible, ideally in the range of milliseconds or seconds. And the amount of time that a search takes will begin from when the object to be searched for is created or modified, not when the search query itself is made. A more formal definition is the following:

Given a set of networked servers, S , which contain a collection of searchable objects, X ; if a new object, x_1 , is created and added to the searchable collection contained in one member of S , s_1 ; then real-time search is the searching process that can begin the instant x_1 is added to X in s and return s_1 as x_1 's location as soon as mechanically possible.

In other words, real-time searching has no indexing lag time. In fact, it has no *indexing* per se. The index database is constantly updated as soon as new information is created. As mentioned before in Yahoo and Google searching, employing a pull method that creates up to a few weeks of lag time between when the searchable object is first created and when it is available to be returned as a result of a query. Ideally, real-time search finds all instances of documents that contain the keyword(s) in the query, and all of the instances found are up-to-date versions of the documents. Please note that real-time searching does not resolve the problem of semantic search, i.e. finding potentially relevant documents that do not contain the terms used in the search query.

Project Summary

The initial task in our project was the analysis of existing approaches for searching on the Internet. To do this, we formulated an abstract model of an Internet searching architecture, and verified its usefulness against commercial search engines like Google, Yahoo, and MSN. Then we used this model to formulate an idealized system for real-time search, and performed some experiments to determine the advantages of the high-bandwidth and low latency of the Internet2 infrastructure.

Internet Search Architecture

In general the information flows from the source servers to the indexing server which then stores the information in the database. Then this information flows out of the server to the clients who are retrieving search results. The best Internet search services (such as Yahoo, Google, MSN) have divided their tasks and assigned large numbers of parallel computers to performing each one. These tasks can be roughly broken into four groups: Downloading whole HTML pages,

parsing the pages with various algorithms, storage of the keywords and references in a large distributed database, and finally retrieving information out of that database. Of these, only the last one, retrieval, is experienced by the end user when performing the search but the other three tasks contribute to the accuracy and latency of the information.

We present the following table to better profile each of the four major tasks involved in searching a network of N active nodes for a single query string.

Task Name	Abbreviation	Description	Value
Downloading	DL	Time it takes to download an HTML page and cache it.	$N(T_{DL})$
Parsing and Indexing	P	Time it takes to parse a cached page and extract keywords.	$N(T_P)$
Storage Time	S	Time it takes to store the results in a database.	$N(T_S)$
Retrieval Time	R	Time it takes to retrieve one set of results out of the database.	T_R
Total	T		$N(T_{DL} + T_P + T_S) + T_R$

Table 1 Timing on Internet1

These values represent linear operations. As mentioned before, most sophisticated search engines use parallel processing and cluster computation to achieve each of these tasks. In a parallel processing paradigm the N value above will be replaced by N/X where X is the number of concurrent processing units in an ideal situation. The total time value is essentially the amount of time it takes to have a "real-time" response for the system. A real-time response for Web searching can be defined as follows: The amount of time it takes between adding a new piece of information to one or more servers in the network and having that updated information show up in a search result.

The real-time response value for current Web searching services is quite high, on the order of several weeks for Google and Yahoo. However, both services have realized that certain kinds of information, such as news and market information need much faster turn around. The response time for Google News items for example, is now less than an hour and at times 15 minutes. But these specialized news or business services are limited as to the number of sources they track.

Ideal Real-Time Response

The ideal real-time response means that as soon as a new piece of data is created, it is available for searching, save data transportation time. It is easy to see that the only way such a response can be achieved is by using a push approach to upload the right information directly to the search engine. If every node performs this simultaneously (or real-time based on updates occurring), then the ideal real-time response (RTR) would be as follows:

$$RTR = T_{DL} + T_S + T_P + T_R$$

The N element has been eliminated. T_{DL} represents the upload or push time which should be roughly equivalent to the old download time. The ideal real-time response indicates the fastest possible way to search N nodes in a network. This method is essentially equivalent to updating a central database from multiple clients. The data in the database is always up to date because that's where new pieces of information are stored.

Improvement Proposals

Given our aim of approaching real-time performance, we offer the following proposals and consider each for effectiveness and feasibility. These proposals are not necessarily mutually exclusive, but some are more practical than others.

"Push All the Way"

Pushing any new content "all the way" to the search engine databases is the most direct method of approaching real-time. It is however, the least practical in large networks with heterogeneous content. The reason it is not very practical is that fundamental changes to both Web servers and search engines are needed.

The current Web publication paradigms evolved in stages. At its core the modern Web server is simply a piece of middleware passing messages between the networking stack and the previously developed file system. Thus the Web server operations are driven by HTTP requests. Thus, any change in the file system, even the section of the file system that contains Web-accessible material, is not reported to the Web server. This is why an HTTP request for a non-existing object gets processed just like any other HTTP request. The server still attempts to access the object, and if it fails, it reports so to the user. Figure 1 outlines the major dataflow operations in existing Web servers.

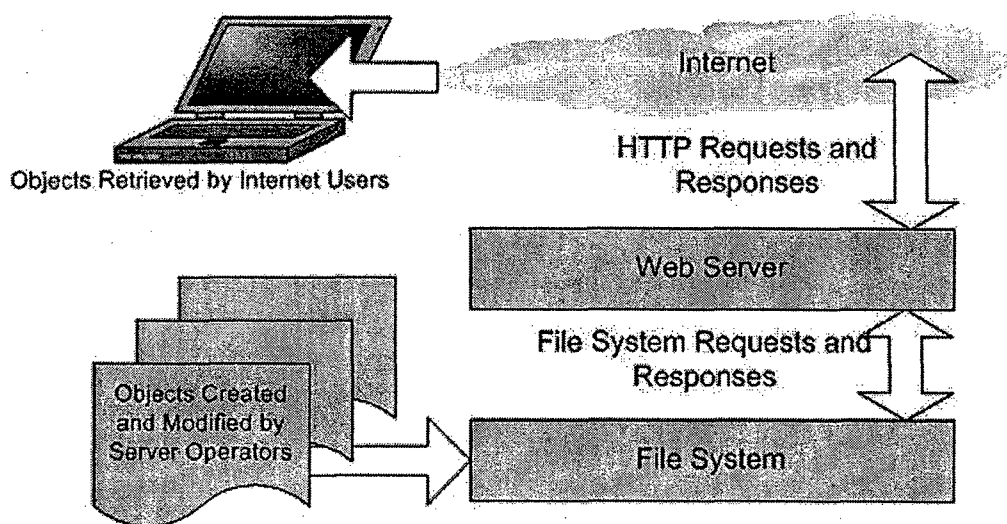


Figure 1 Data Flow in Typical Web Servers

Any kind of a push method requires immediate awareness of any changes to any files accessible on the Web. Existing Web servers are for the most part unaware of the content and the existence of the files they are serving; they themselves make inquiries to the file system to retrieve this information. Existing Web servers are thus unable to implement information pushes.

To implement “push all the way,” a new type of Web server is needed, a content aware Web server. Pushing this material up the stream, “all the way” to the search engine requires that the Web server be directly informed when a new object is created, destroyed or modified. A database of all Web accessible objects, their location and creation and date of modification is needed. Note that this database need not contain the objects themselves. The words inside an HTML file need not necessarily be stored in this case, just the name and the local file name and location. Once a local repository is updated, then the Web server also updates an upstream repository.

To summarize, the enhanced “push” server includes two other modules in addition to the classic server. First a manager of the local repository that accepts update messages from the file system, or from a Web content management system. And second, a push manager that sends actual content upstream to a search engine database. These two major differences are highlighted in Figure 2, the data flow in content-aware Web push servers.

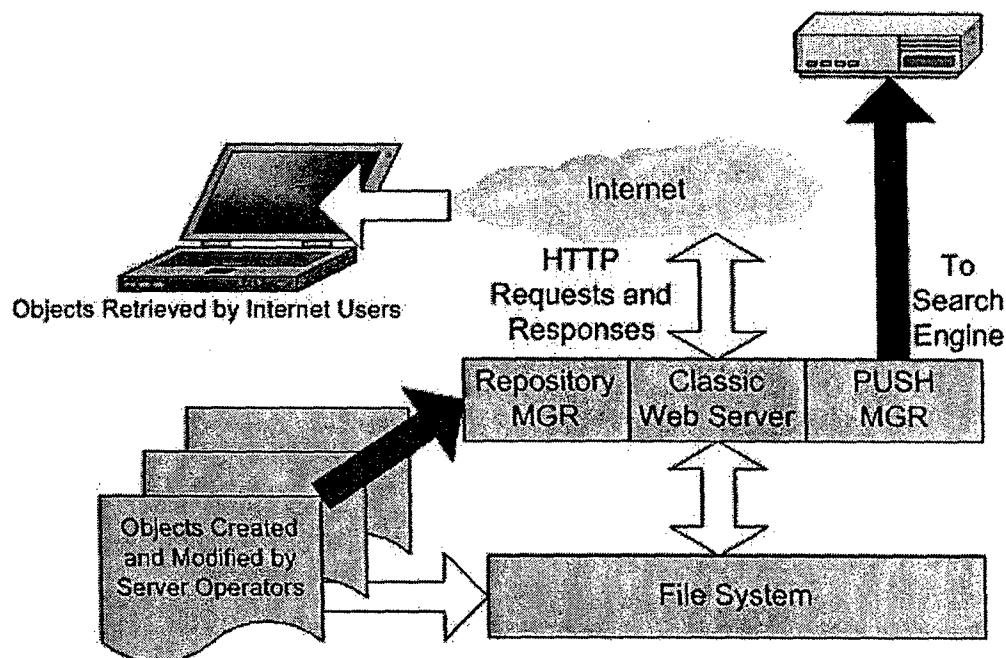


Figure 2 Data Flow in Content-Aware Push Server

The timing advantage of the push method is tremendous. Considering the findings in table 1 and the previous analysis of existing servers, we recall the total search time in classic Web servers:

$$T = (N / X) (T_{DL} + T_P + T_S) + T_R$$

Recalling the discussion on multiprocessing, in ideal conditions the value N is divided by X, where X is the number of processes working on the problem simultaneously. Since the TDL in the push server we discussed does not occur on the server (i.e. there's no indexing) and furthermore, it uses Web server processing resources done by the push manager, then it can be said that the Web servers themselves are acting as a cluster of N computers working on the downloading problem simultaneously. As X approaches N, the value of N/X becomes 1. We can now rewrite the total time equation for the push server as follows:

$$T_{\text{push-all-the-way}} = T_{DL} + 2T_S + N(T_P) + T_R$$

The Web servers are independently and simultaneously doing updates to the search engine database. Thus, the response time becomes nearly insignificant as the large value N is eliminated. Furthermore, even the T_P which represents parsing time can also be similarly distributed. Given the format of the central search engine database, the parsing can also be done at the local Web server as part of the enhanced push manager. The push manager could be updated with the particular parsing algorithm and implement it on the data from local repository and send the results to the corresponding search engine database. Finally, we arrive at this:

$$T_{\text{push-all-the-way}} = T_{DL} + 2T_S + T_P + T_R$$

T_P now occurs at the node level and we assume it can be as fast as when it occurs at the centralized server. Finally, there are two save events, one at the local repository and one at the central search server.

For several reasons this method is impractical in current Internet searching paradigm. While these reasons may not necessarily be valid in an Internet2 network environment, it is important to enumerate them at this point.

Reasons why push methods are impractical for Internet1

- No protocol exists for Web server to search engine communications.
- No service is willing to accept such volume of update requests.
- It is highly sensitive to abuse. The information being pushed cannot be verified easily.
- No uniformity in Web server software or modules.
- No uniformity in Web publishing methods.
- Quality and breadth of the results may suffer as the upload responsibility is transferred to sources and such responsibility cannot be enforced.
- Biggest Technical Obstacle: The search engine has to handle huge amount of near-simultaneous connections of data being pushed, representing changes in the entire network (Internet.)

Internet2 offers a unique opportunity to address these shortcomings. Being a new non-commercialized network, it is possible, now, to circulate standards that Web servers could adopt at this stage. A Web-server push-update protocol could be easily conceived and rolled into a next generation Apache or IIS Web server. Such a server could also have a built in local repository working seamlessly behind the scenes. Every new object will be automatically integrated and index locally. If the server push-update and additional functionality can be done automatically and unobtrusively then the practice would propagate together with the Web server software that features it. Adoption would be easy if these protocols are standardized soon. Lastly, there is no way around the technical obstacle, in a push-all-the-way paradigm. A search engine must be able to accept asynchronous and simultaneous updates as they occur. Most search engine companies such as Yahoo, Google and MSN do have clusters of thousands of computers for various operations, but more research is needed in predicting precisely what kind of resources would be needed to accomplish this.

Push Half-Way

Pushing half-way may be a practical technical compromise solution to the practical shortcomings discussed in the previous section. This technique is very similar to pushing all the way, except that instead of pushing to a central Web search computer, it pushes to a regional database which contains a “partial” index. Such partial-indexers together contain all the information normally found in the central Web-searching index. Implementing a partial indexer solution means that most of the Web-server side changes to the push-server are still necessary, and a consolidating indexer is now needed to collect all the information in all the partial indexers and put them in the central database.

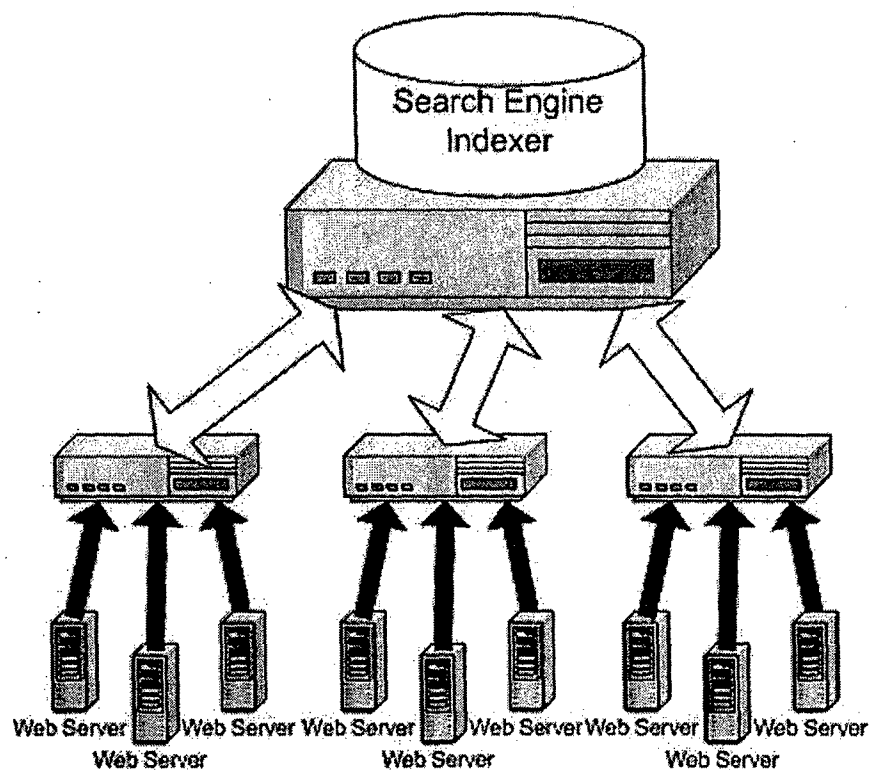


Figure 3 Pushing half-way representation in a 9-node network

In Figure 3, we have a representation of a small 9-node network that we built for the purposes of demonstrating half-way push capability. Each node is a fully functioning Web server with push capability. The middle layer consists of partial-indexers that collect information pushed onto them by their regional servers. Such information is then made available to a classic crawler to go through and collect the information to be placed at the central search engine. As can be seen, pushing is done, but not all the way to the search engine. And the search engine crawls not the entire Internet, but only the partial-indexers. Partial indexers may be pushed complete objects or pre-indexed resource lists from the Web servers. In other words, we can offload the parsing, in addition to the saving capability into the partial indexer machines. To figure out timing for the push-half-way technique, we begin with the time it takes to update a single partial-indexer given server-level parsing and saving.

$$T_{\text{partial-indexer}} = T_{\text{DL}} + 2T_{\text{S}} + T_{\text{P}} + T_{\text{R}}$$

Note that this is identical to the “push-all-the-way” timing for the entire network. We now add to this, the amount of time it takes for the central indexer to crawl through all the partial indexers. We use P to indicate the number of partial indexers and we note that $P \ll N$.

$$T_{\text{half-way-push}} = P(T_S + T_R) + T_{DL} + 2T_S + T_P + T_R$$

Pushing half-way is thus already less efficient than pushing all the way because $P(T_S + T_R)$ or the retrieval and storage time from all the partial-indexers is also considered. Furthermore, both retrieval and storage values are likely much bigger for partial-indexers than they are for Web servers. Thus, to be correct we must add a value, k , representing the proportion of data to be retrieved and stored from a partial-indexer. In the best-case scenario, only one Web server per sub-network has pushed new content into its partial indexer. In this case, $k = 1$. In the worst-case scenario, all the nodes in each sub-network have pushed updates into their partial-indexer. In such a case, $k = N/P$. We rewrite the updated push-half-way timing as follows:

$$T_{\text{half-way-push}} = kP(T_S + T_R) + T_{DL} + 2T_S + T_P + T_R$$

$$1 \leq k \leq N/P$$

The advantage of pushing half-way lies in the fact that no one node in the network overwhelmed by too many access requests. Valuable data could be lost if the indexing server is too busy or unable to handle the load. Under current practices, this is not a problem on the indexing end because the indexing crawler dictates the time and retrieval bandwidth for data. But a situation like “push all the way,” can be unpredictable. “Push half-way” represents a compromise, a way to take the load off a central indexer without completely losing push capability. For real-time reporting purposes, this method is still superior to “pulling” but falls short of the ideal real-time response.

Peer to Peer Indexing

An interesting approach and significant paradigm shift from traditional indexing is peer to peer or P2P indexing. P2P technology is widely used for tasks very similar in nature to Web-searching. These include searching for documents, music or video files. The theory is that every node on the network, in addition to being a user, is also a server and a router for P2P protocols. A number of negative attributes exist that make P2P style Web searching unattractive for Internet1. But we believe that Internet2 will be more capable of implementing a P2P style Web-search.

One of the features that characterize current P2P overlay networks is constantly disappearing nodes. Since most nodes are home computers operated by individuals, they constantly join and disconnect from the overlay network. If we are searching for a few abundant objects (as most often music files are), then this is not such a big problem. If one node disappears, another could be found to complete the transfer. But if instead we have billions and billions of unique Web pages, we cannot afford to have them disappear and reappear all the time. Fortunately, it doesn't have to be this way in Internet2.

For indexing purposes, we propose that the I2 Web servers, and not the clients, be equipped with P2P overlay network software. This means that relatively speaking much fewer machines will be on the P2P network and furthermore, these machines are much more stable and capable than end-user access machines. In other words, we want a meta-peer to meta-peer network of all the Web-servers in Internet2.

The P2P protocol stack and routing functions could be rolled into Web-server software such as Apache as modules. A P2P enabled Web server would have a local repository manager shown in Figure 2. The repository will parse and index all the local objects, but does not push them upstream, as in the previous cases. Also, unlike previous sections, the repository will not be exclusively local. It will represent all the local Web-accessible data but it could also list objects with remote storage locations. The P2P module will accept search queries from clients and respond with operations. First, the local repository is checked for the query in question and results are returned to the requester, and second, a number of query message are sent on to other servers connected to the overlay network. If a server receives a query from a user or from another server, it would repeat the two steps. If a server receives a response to a query, that response will be recorded in some ranked fashion in its local repository.

Compared to push methods, more changes required to the local Web servers. An entire P2P module must be added to handle search messages which are serviced from both end-users and other servers. Figure 4 is a software representation for a P2P enabled Web server. Notice that in this scenario, there is no search engine. Every node in the network is also a search engine as well. Figure 5 is an architectural representation of a typical P2P network. Note that the dotted line represents a multi-query (a query that resulted in one or more other queries) path to the location of the information requested by the client.

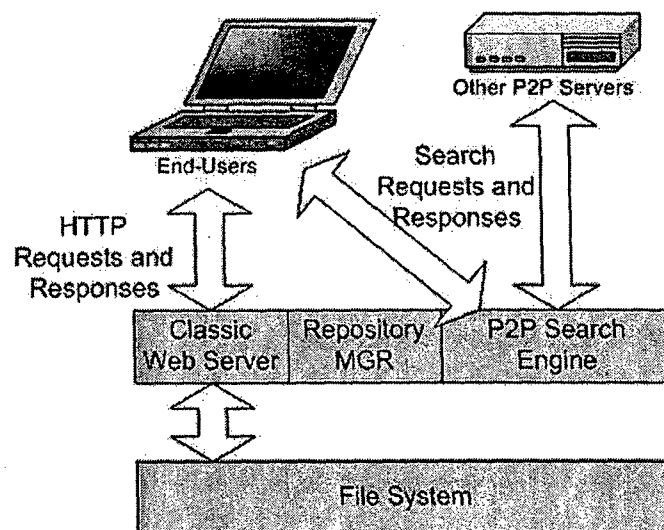


Figure 4 P2P Enabled Web Server

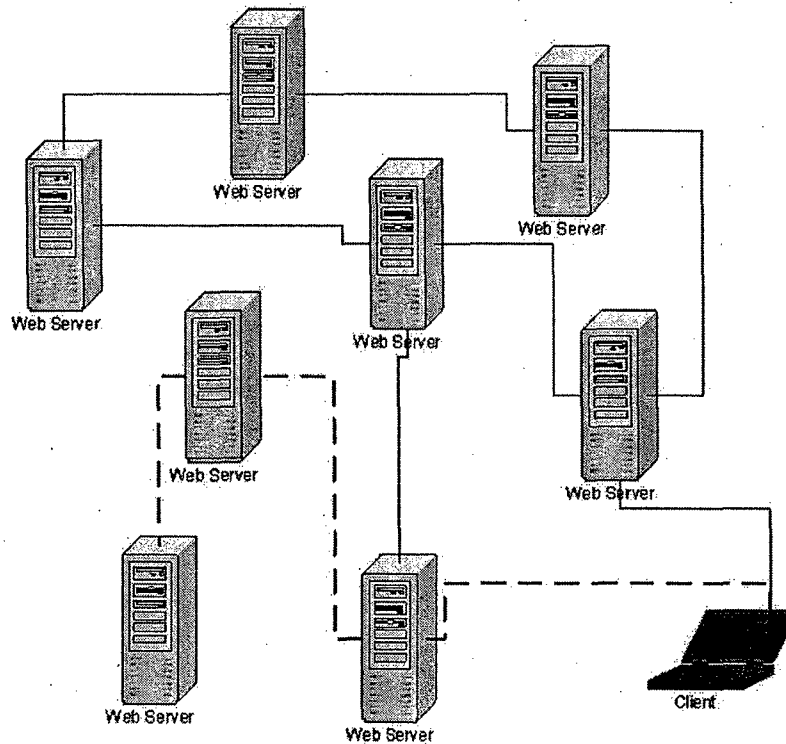


Figure 5 A P2P Network

P2P method timing can be summarized as follows: Given local (and therefore multiprocessing) indexing and parsing, downloading of the Web-accessible objects, we can assume these values are negligible. Retrieval time, too, is near ideal. As soon as the P2P search returns a correct node to the requester, retrieval can begin immediately and reflexively. This only leaves the time it takes for the greater P2P network to figure out which servers contain the requested information and the sorting of the information.

$$T_{p2p} = T_{DL} + T_S + T_P + T_R + T_{\text{messaging}} + T_{\text{sorting}}$$

The messaging time can be greatly unpredictable. Each query generates at least two messages: one for the inquiry itself and one for the return results. Assuming reasonable circular loop checking and other sensible features that are now part of P2P message operations, we will generate at most 2 messages per node for each query to the network. We introduce T_M as the time it takes to send a single P2P message. The equation then becomes:

$$T_{p2p} = T_{DL} + T_S + T_P + T_R + 2N(T_M) + T_{\text{sorting}}$$

A sorting algorithm is a part of every search engine. In methods that require a central database, the sorting time is negligible. Sorting is already conducted as a new piece of information comes in and is almost the same length of time in duration as "storage." But in this case, since search is being done throughout the network and data is being live-inserted into search query results, it is a bottleneck for real-time response.

P2P searching represents another trade-off: comprehensive results versus fast response. P2P query and response messages propagate throughout the network. This means that some nodes

will respond before others. For popular search queries, some responses are given immediately. For less popular searches or ones that have never been done before, one could wait a long time until all local repositories have been checked. The longer one waits in a P2P search, the more results and the more accurate the response of the query becomes. But some responses are certainly available right away, which may be good enough for some users.

Universal Time-stamping

An approach that could significantly reduce network crawling and indexing time is universal time-stamping. If every piece of content (HTML) on the network could have a reliable and universal time stamp, then a remote indexing service can easily recognize whether the content needs to be digested or is still good from the last iteration. This time stamp would be similar to a file system file modified date attribute but it would have to be universally time-zoned.

Such universal time-stamping does not exist in current Web publishing programs. Implementing it would not be easy either. The function will need to be incorporated in the Web server software (which are not universally used) and there are possibilities of abuse as well.

A search appliance device as described above, however, could solve this problem in another way. If the search appliance itself could be securely operated and the time-stamps on IT could be trusted, then additional CPU cycles could be used to physically verify the newly indexed content versus a previous cache. And if such a comparison yields that the content has not changed, then the new content will not be incorporated and consequently need to be pushed up to a central server.

Problems Encountered

This project did not encounter major problems in mathematical research aspects. However, when it came to implementation, some major hurdles were present. Early on we encountered a bottleneck at our local 100BT network interface. A Gigabit network device was purchased for the purposes of this project, which solved that problem.

Timing problems on I2

Our attempts to measure timing responses suffered in several respects. First, we did not have a direct node on I2. We had a secondary connection to Abeline fiber networks. This made measuring effects of message passing between two nodes on the network almost impossible. Second, we only had one end of the I2 network in San Luis Obispo. Our servers on this side of the network could run software and pass messages, but we didn't have corresponding servers on the other side to receive and reply. Third, the network itself is not stable in its timing responses. We encountered wildly differencing speeds and response times on different occasions.

Lack of Time and Resources

Even token implementation of some of our proposals requires alteration of major software such as Apache Web server. Similarly, while we could easily design protocols, we could not implement them between two nodes on the I2 network (we only had write access to the one at Cal Poly).

We only had one student working on the project part time and he was in no position to undertake such projects in their full scope. We thus opted for research, planning, scripting mathematical simulations and derivations instead.

Future Work

The student who did most of the work, Foaad Khosmood, also finished his master's thesis, and won't be available for a continuation. While this project was driven mostly by Foaad's interest, and lies at the border of my own research interests, and I am currently investigating potential continuations with colleagues whose research areas are closer to networking technology.

Recommendations for future work are to obtain a team of 2-3 motivated individuals and pick one aspect within one of the 4 proposals and implement them fully. Some of the work could be done as Senior Projects, possibly coordinated by a graduate student in a Master's Thesis. This way, time and effort can be focused on accomplishing a small project. This phase mainly represented research and ground work for such implementations.

Publication

This work was accepted for publication and presented at the Internet2 Fall 2004 Member Meeting in Austin, Texas, in October 2005; see

http://www.internet2.edu/presentations/fall04/20040930-Teaching-Kurfess2_files/slide0001.htm.

We investigated the potential for more formal publications in scientific journals, but the initial feedback from experts in the field indicated that either a more thorough formal treatment, possibly accompanied by a simulation, or an actual implementation would be needed for that.

Virtual Team Collaboration over Internet2

Project Investigators:

Dr. Franz Kurfess
Associate Professor
Department of Computer Science, College of Engineering

Christopher Shireman
Graduate Student
Department of Computer Science, College of Engineering

Garrett Garcia
Undergraduate Student
Department of Computer Science, College of Engineering

Cal Poly Internet2 Mini-Grant

Phase III Final Report

Summer 2005

Project Title: Virtual Team Collaboration over Internet2
Project Director: Dr. Franz Kurfess
College and Department: Department of Computer Science, College of Engineering

Introduction

The goal of this research is to discover the areas of weakness in the existing collaborative software tools and to determine the amount of benefit that can be obtained by implementing these tools in the more advanced networking environment of Internet2.

The definition and requirements of a virtual team will be examined. A set of criteria for evaluating the existing tools will be formulated with several applications being scored against these criteria. The results of this evaluation will be used to find the weaknesses in the current implementations of this technology which in turn will be used to determine which advantages may be gained by the application of Internet2 technology.

Virtual Teams Defined

Virtual teams are composed of individuals that are dispersed geographically and/or temporally. Whereas traditional, co-located teams rely heavily on face-to-face communications, virtual teams usually rely on recent improvements in communication technology. Virtual teams have arisen for various reasons:

- Academic collaboration
- Corporate Mergers and Acquisitions followed by downsizing
- Increased telecommuting
- Subcontracting work to specialists
- Work moved off-shore to reduce labor costs

Many people (especially project managers) believe that virtual teams function just like traditional teams. There are several key differences. The lack of frequent face-to-face communication has serious consequences on team dynamics. The causes are often psychological in nature, dealing with issues of trust and awareness, stemming from a lack of secondary communication (body language, scent, touch, etc.). Many Internet2 researchers attempt to replicate face-to-face contact using immersive virtual meeting rooms with life-sized multi-wall projection of high definition video and audio.

We feel that this approach alone does not fulfill many of the primary needs of virtual teams. Telecommuters are unlikely to have multi-wall projection systems set up in their home office or

field office. Virtual teams also need to work with team artifacts (documents, source code, designs, etc), outside of the capabilities of video casting. We propose an enhanced virtual team meeting system that marries video conferencing with many of the capabilities of current Web meeting systems (1)

Research Goals

The goal of this research project is to determine if there are any existing applications that can be leveraged to improve virtual team collaboration. Specifically, can the technology be adapted to use the capabilities of Internet2 in order to provide a more productive virtual team environment.

The first step required to accomplish this goal was to evaluate several existing collaboration toolkits to get a sense of the current state of the industry. A set of criteria was determined through careful study of the needs of virtual teams. These needs include a common workspace, real-time meets (formal and informal), asynchronous communication, project awareness, and a reliable infrastructure, just to name a few.

Once these criteria were determined we took a sample of the available collaboration tools from the market and evaluated them using these requirements. Each application was given a score for each area of collaboration technology from 1 to 10 with 10 being perfect; 0 was used to indicate that the respective aspect was not available in the tool.

Due to limited funding, we only could evaluate trial versions of most of the applications. In some ways this hindered our ability to give an accurate score. Some of the applications did not have trial versions or required custom hardware, which prevented us from testing them completely. However, in these cases we used the information that we obtained from their Web sites and white papers to provide as accurate and objective evaluation as we could.

Methods of Testing

When testing the software, we tried to simulate how a normal user would interact with the application. We downloaded the trial from the Web site, filled out the required forms, read the required help documents, and so on. This proved to be more difficult with some of the pieces of software than we had ever expected.

After registering and installing everything, we used a feature matrix to evaluate each application as objectively as possible. We went through and tried each feature to get a feel for how it worked and what it was capable of. We checked for usability, and stability in addition to whether each feature existed.

Our feature matrix covered the following categories. We used the matrix to rate each application that we were able to install on a scale from one to ten. The categories are as follows:

Event Scheduling:

The ability to schedule meetings and other events for multiple participants throughout the virtual

team.

Participant Management:

The ability to add, remove, and limit the types of activities and functions that participants can use in the system.

Instant Messaging (IM):

The overall quality of the instant messaging function included with the system. Whether or not you can have private discussions, buddy lists, custom icons, etc.

Moderated Q&A:

The ability for participants of a meeting to ask questions in an organized manner and for the managers of the meeting to respond to those questions or to allow specific users to post their questions to the group.

Poling/Voting System:

The ability to create a question or set of questions and then post them to all participants of the system. Also, the ease with which the results of the poll can be gathered and displayed to the group.

Remote Window/Desktop Display:

The ability to share the display of an application on one of the participants computers with other computers on the network. Also the ability to manage which users have active control of and which may only view the shared environment.

Shared Whiteboard:

The overall functionality of any shared drawing space which the application may have. This includes the ability to moderate which users have control of the whiteboard, and what features are available.

Remote Window/Desktop Control:

The ability to take control of one participant's computer by an authorized participant in the group. Also, the overall quality of the security that is imposed during this session.

Collaborative Editing:

The ability of two or more people to manage a document or set documents at the same time while maintaining the integrity of the document and providing a record of the changes made by each participant.

File Exchange:

The ability to share files with the members of the group either through a centralized file server or through a peer to peer network.

Audio Conferencing:

The ability to hold an audio conference between various members of the group. Also, the options which are available with such a conference such as private conversations and concurrent group sessions. This feature must be implemented through the software, not through a phone line.

Video Conferencing:

The ability to hold a video conference between various members of the group. Also, the options available with such a conference such as private and concurrent video sessions.

Archive/Media Playback:

The ability of the members to replay the details of meeting, chat sessions, and other features of the system at some future date.

VoIP Integration:

Whether or not Voice over IP (VoIP) was integrated into the software. This is usually present if the audio conferencing feature is present in the application.

Research Results

The table below shows the results of our testing. Each application is given a score between one and ten for each of the evaluation criteria mentioned above. While the assignment of scores is based to some degree on our subjective impressions, we attempted to apply consistent criteria across the different applications. A zero means that the feature was not implemented. A question mark indicates that the feature was unavailable for testing due to the use of a trial version of the software.

	Event Scheduling	Participant Management	IM	Moderated Q & A	Poling/Voting	Remote Window/Desktop Display	Shared Whiteboard	Remote Window/Desktop Control	Collaborative Editing	File Exchange	Audio Conferencing	Video Conferencing	Archive/Meeting Playback	VoIP Integration
WebEx Media Center	?	8	4	0	3	6	7	6	3	0	0	?	?	?
Raindance	4	8	7	0	0	8	9	8	2	0	?	?	5	?
Placeware (MS LiveMeeting)	0	4	6	6	7	3	7	5	2	0	?	?	0	?
Centra														
Genesys	7	6	6	0	8	0	7	0	0	8	0	0	2	0
Latitude	8	8	6	0	0	6	8	6	2	?	8	8	8	6
Radvision Click to Meet 4.1	4	5	5	0	0	3	0	0	0	4	3	4	0	0
VIACK	6	4	5	0	0	6	7	7	9	7	7	7	0	0
Virtual Rooms														
VideoConferencing System (VRVS)	2	0	4	0	0	0	0	0	0	0	2	4	0	0
Groove Workspace	5	6	8	7	7	0	8	0	0	8	6	0	0	0

Table 1 Evaluation of Collaboration Tools

As can be seen in these results, there was no single application that met every one of our criteria. There are some applications that deserve special notes. Raindance is one of the easier applications to use. It has a simple, straightforward interface and a strong set of features. Of all the applications that were evaluated, this one was our favorite.

Another application worth mentioning is Groove Workspace. This application has a comprehensive set of tools, however it came in second mainly because of the size of the application and the amount of resources required for it to function. Other applications were able to accomplish the same functionality without having such a large footprint. Groove also seemed to embed itself deeply in the computer, making it difficult and time consuming to remove.

Also, we came to realize that most of these applications required services from the company to operate, such as special toll free phone numbers or extra bandwidth. Many of them charged a fee either by the month, or per user for the use of their system. This seems to be a significant limiting factor for virtual teams tools to proliferate in the the market of regular home, small business, or student users.

We also noted that many of the applications require third party software in order to function correctly. These third party providers are in some ways hindering the abilities of the collaboration systems by increasing the amount of unneeded processing and the size of the system. This also poses a problem for licensing and distribution of the system on a large scale.

There is also no standard way to implement the features of these systems. Everyone wants to do things their own way and thinks that their way is the best. Some applications even required specialized hardware in order to take advantage of some of their more advanced features. There is no reason to reinvent the wheel every time a system gets built. The establishment of a set of standards will be helpful in the development of the technologies required to create robust collaboration software suites.

Moving Forward With Internet2

In order for these applications to develop into a robust set of tools the advantages of Internet2 need to be leveraged. For instance, the amount of bandwidth available to designers is much greater on Internet2. This frees them to focus on creating a usable tool instead of worrying about squeezing every possible byte out of the existing data stream.

Internet2 also has the innate ability to customize the size and contents of the packets that are sent over the network. This means that the next generation of the collaborative software will be able to set its own rules for data transfer instead of having to rely on the predefined data packets that are available on the current Internet.

Another of the unique features available with Internet2 that will impact the design of collaborative software is multi-cast routing. Such routers are readily available on Internet2, which opens the door for a truly distributed video conferencing session. Figure 1 is an example

of a configuration that will be possible via multi-cast routing.

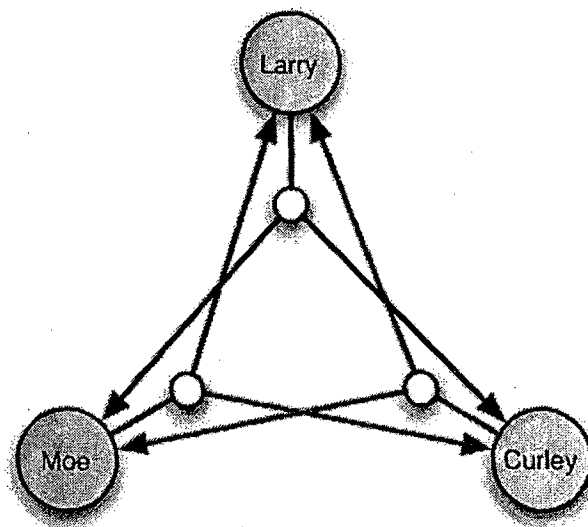


Figure 1 Multi cast Video Conferencing Example

Most of the technology that was reviewed in this research relied on a central server to coordinate all of the communications between the various participants of the system. The primary reason for this is because coordinating multiple conference nodes has required too much bandwidth. Since this limitation is largely eliminated when using the infrastructure provided by Internet2, a more flexible system can be constructed without having to worry about the amount of time required to coordinate distributed nodes of the network.

Conclusions

After having carefully considered the requirements for collaborative software, we have come to the conclusions that there is no single existing tool that will fulfill all of the requirements for a virtual team environment. There are therefore three courses of action in situations where tools for virtual teams are considered:

- to use multiple tools to obtain the functionality that is required,
- to build customized software to incorporate all of the features that are required by the individual virtual team,
- or to build a robust generalized and expandable set of tools that make use of the technology that is best suited to the job of creating a collaborative environment for virtual teams.

Internet2 has the potential to significantly enhance the capabilities of such tools, and hopefully in the near future a better selection will emerge.

Bibliography

- 1) Johnson, Brett and Yano, Derek *Improved Virtual Team Collaboration using Internet2 Technologies* June 06, 2003
- 2) Dr. Franz Kurfess *Cal Poly Internet2 Mini-Grant Phase III Findings* Department of Computer Science, College of Engineering
- 3) Dr. Franz Kurfess *Cal Poly Internet2 Mini-Grant Phase III –Plan of Action* Department of Computer Science, College of Engineering.

**Remote Monitoring and Control of CalPoly Dairy Biogas Pilot Project Using
Internet 2**

Project Investigators:

Shaun Kelly
Project Director
Department of Bioresource and Agricultural Engineering

Doug Williams
Investigator
Department/of
Department of Bioresource and Agricultural Engineering

Mike Lehmkuhl
Investigator
Department of Bioresource and Agricultural Engineering

Final Report

Remote Monitoring and Control of CalPoly Biogas Pilot Project Using Internet 2.

Project Director: Shaun Kelly

Department of Bioresource and Agricultural Engineering, Cal Poly
skelly@calpoly.edu

Investigators: Doug Williams and Mike Lehmkuhl

Department of Bioresource and Agricultural Engineering, Cal Poly
dwwillia@calpoly.edu , mlehmkuh@calpoly.edu

August 1, 2005

Abstract

The CalPoly Biogas Pilot Project demonstrates how electricity may be generated by utilizing gas generated by dairy waste to power a gas turbine. The goal of this Internet 2 project was to facilitate the demonstration of the Biogas Pilot Project to a wider audience by allowing the monitoring and control of the turbine generator to be accessed over the Internet remotely. The gas turbine controls were connected to the internet by establishing an RF radio link from the turbine to a server located in the BRAE department. Remote control software was installed on the server to facilitate control and monitoring of the gas turbine in near real time. Gas pressures, temperatures, speed and voltage output from the turbine generator may be viewed by logging into the server. Further testing will show that the quality of service and reduced latency provided by Internet 2 will allow the turbine generator to be monitored and controlled remotely and provide for demonstration of both Internet 2 capabilities and alternative energy sources to K-12 schools, and other colleges and universities across the U.S and world.

Introduction

Calpoly Biogas Pilot Project

Calpoly operates a working dairy through the College of Agriculture which provides agricultural students the "learn by doing" instruction. Doug Williams, BRAE has utilized the dairy to research sustainable energy systems using biogas generated from the dairy waste. The goal of this project is to facilitate the demonstration of the technologies involved in conversion of dairy waste to energy to a wider audience through remote monitoring and control of the turbine generator utilizing Internet 2.

A brief description of the Biogas Pilot Project at the CalPoly dairy is as follows. Biogas is generated through anaerobic digestion of dairy waste effluent that is collected in lagoons next to the dairy. The lagoons are covered with a large vinyl tarp which facilitates collection of the biogas over the lagoons (Figure 1). The biogas stored under the tarp is pumped from the lagoon to a gas turbine generator (Capstone MicroTurbine Model 330), which burns the biogas to produce electricity. The generator is connected to the electric network to be used by the dairy. The dairy is able to produce "free" electricity utilizing dairy waste that would otherwise be disposed of by spreading on fields.

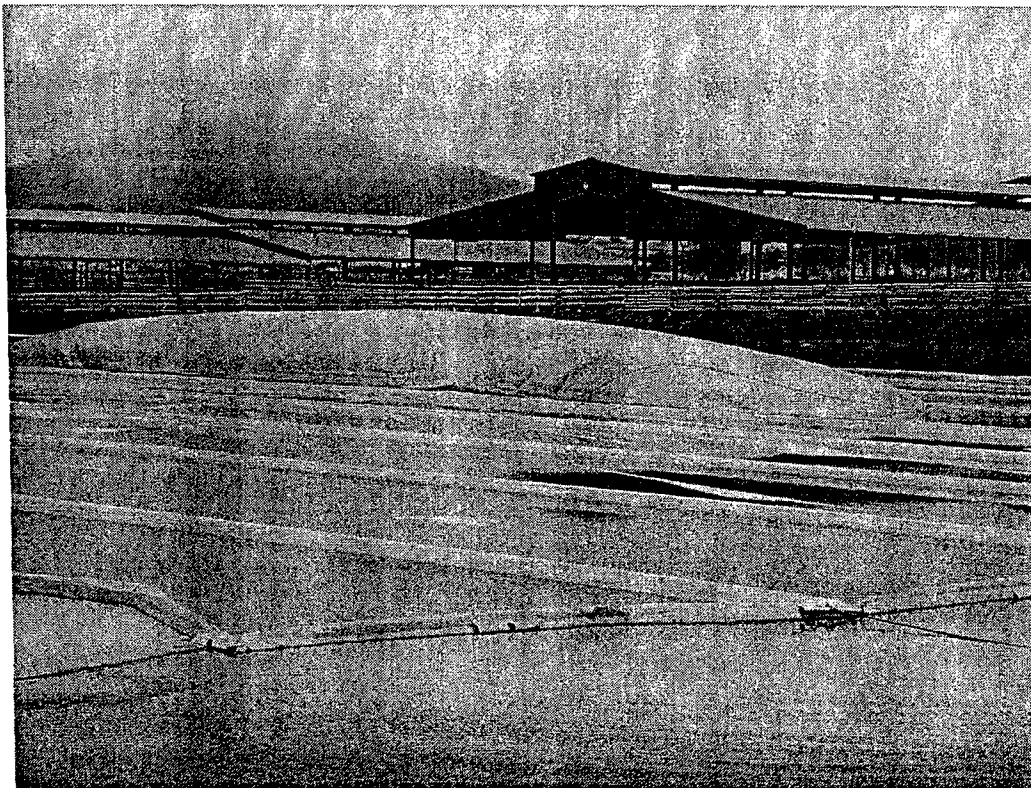


Figure 1. Collection of biogas generated from dairy waste.

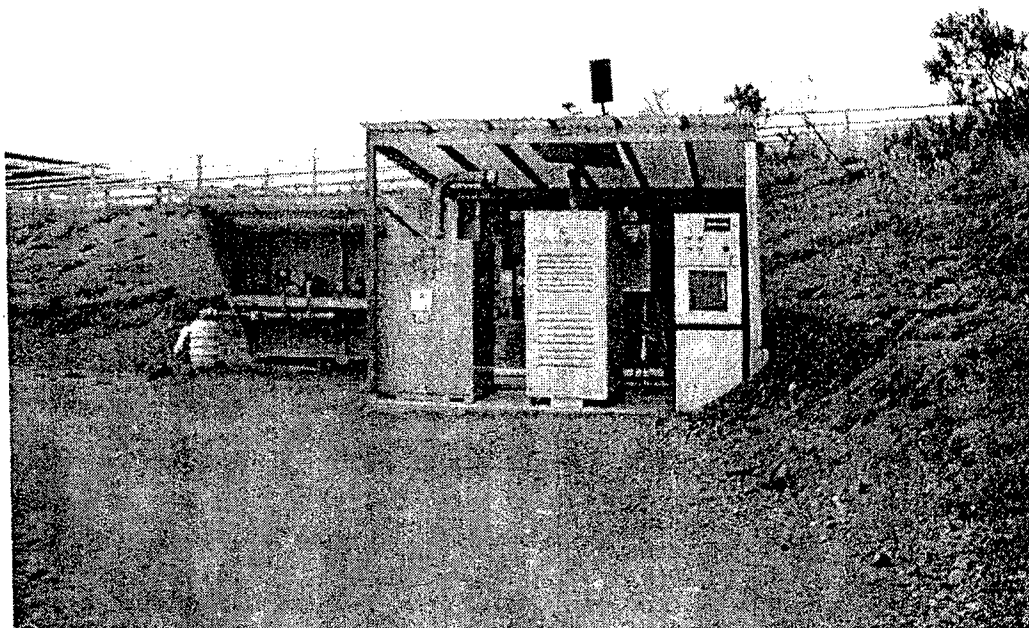


Figure 2. Biogas is pumped from the lagoon to the turbine generator which burns the biogas to generate electricity. The turbine generator is the box in the center.

The turbine comes with a monitoring and control interface program that allows the user complete control of all turbine functions. This interface is available through a serial interface port on the turbine itself. Because the turbine is located next to the dairy waste lagoons at CalPoly it was necessary to establish an RF radio link from the turbine to a server located in the BRAE department.

The server in the BRAE department was connected directly to the RF link to the turbine. The server currently runs Windows Server 2003 and is configured to run as an application server where programs are run remotely from the server using client software. The control and monitoring software was installed on the server and accessed remotely using the client software.

Results and Discussion

Specification, layout and installation fo the RF network

The turbine control electronics did not provide a direct network port, but rather communication for the Capstone control and monitoring software was accessible only through an RS232 serial port on the turbine itself. To provide communication with the turbine via the internet we used 2 standard industrial microwave frequency radios (MDS 500, Microwave Data Systems) to provide the link from the turbine to the server located in the BRAE Lab 08A. These radios provided a secure internet link between turbine and the server without the need to obtain an FCC license. Using existing WiFi technology was not possible because of the distance and security issue as well as the need to interface using the RS232 serial port. To bridge the distance from the dairy to Building 8A it was necessary to utilize a directional Yagi antennae installed at the turbine and an Omni-directional antennae on the roof of Building 8A. Initial tests determined that we would be able to transmit and receive a usable signal through the buildings and trees with a loss of 85dB which although was not great, it was acceptable. The antennae, radios, power supplies and lightning protection for the 2 radio links are shown in Figure 3. The radios and components were mounted inside weatherproof boxes (NEMA 4) and installed outside on the turbine and on Building 08A.

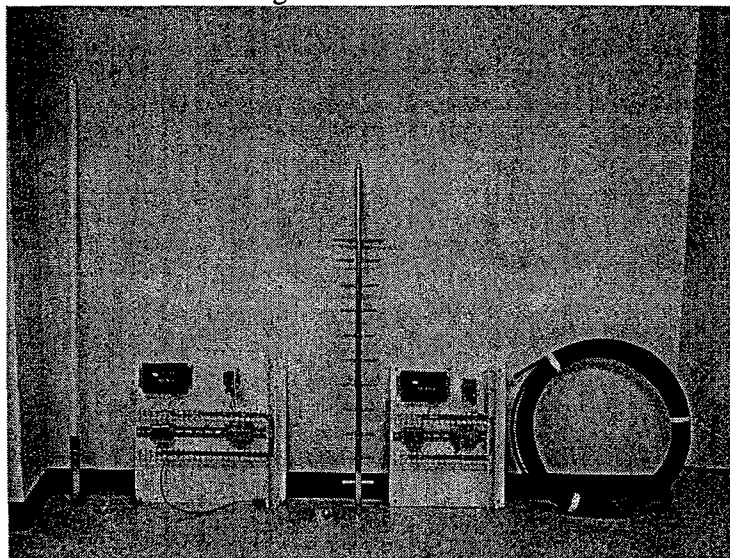


Figure 3. Antennae, radios and other components mounted and ready for installation.

The link was established (see Figure 4) between the turbine and the server. The link runs at a maximum speed of 10 Mbits/sec. Although this speed seems slow, in this link there is not a large quantity of data that is transmitted. It is more important that this link be reliable and error free for monitoring and control of the turbine.

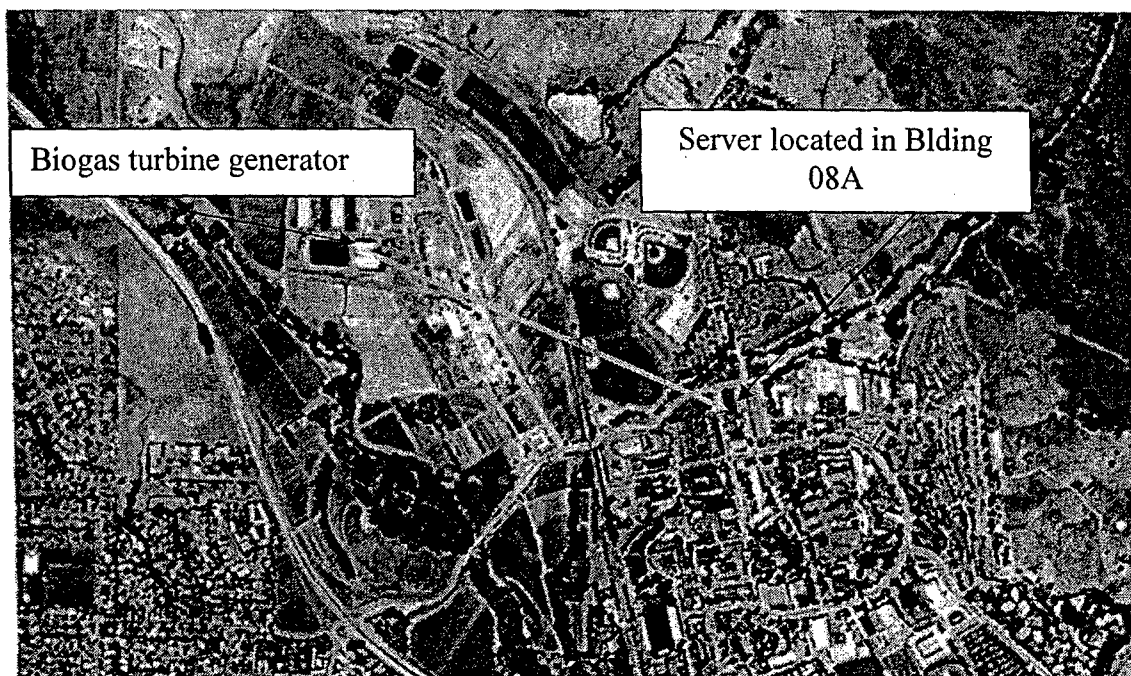


Figure 4. Calpoly campus showing the location of the turbine generator located at the dairy facility and the server located in Bldng 08A. The distance is about 1/4 mile.

Installation of control and monitoring software on server and server upgrades

The server in the BRAE department was be connected directly to the RF link to the turbine. The server currently runs Windows Server 2003 and is configured to run as an application server where programs may be run remotely from the server using client software. The control and monitoring software were installed on the server and can be accessed remotely using the client software. Currently the Capstone remote monitoring and control software is accessible to users with an account on the application server. In the future it would be recommended to build a limited web interface to monitor the operation of the turbine without having the all of the capabilities for operating the turbine.

Testing of network connections from BRAE Lab

Testing of the network connections from the BRAE Lab is ongoing. Monitoring and operation of the turbine from a remote site is theoretically possible, but there have been operation difficulties in the turbine itself. Startup of the turbine is a complex process involving insuring that adequate gas quantity and quality is flowing to the turbine for ignition to take place. Maintenance problems with the turbine currently require the operator to be onsite most of the time for start up.

We are continuing to test the network capabilities using the existing system. Visual and audio feedback from the turbine is important for operating the turbine when starting and stopping. We are currently investigation ways to enhance the remote operation of this complex piece of machinery using Internet 2 capabilities.

Summary and Conclusions

The goal of this Internet 2 project was to facilitate the demonstration of the Biogas Pilot Project to a wider audience by allowing the monitoring and control of the turbine generator to be accessed over the Internet remotely. A network connection was established using an RF link to the turbine located at a remote location. The connection was tested using existing control and monitoring software for the turbine through a server. Monitoring and control of the turbine was possible but difficult due to the complex nature of the system being controlled. Ensuring that the turbine was ready for operation needed more visual site inspections than could be provided by the software alone many times. Further testing from remote sites in I2 still needs to be done, but the basic infrastructure is in place for this testing to occur.

To facilitate the demonstration of the project to a wider audience a monitoring scheme needs to be configured to get operating data from the turbine and when polled through a web interface. This would allow a non-technical user to log onto the site a view the operation of the turbine in real time and demonstrate useful technologies for sustainable power.

Interactive Design and Evaluation of a Learning Environment
For Distributed Collaboration over Internet2:
An Applied Research and Teaching Project

Final Report

Project Investigators:

Mary M. Somerville, Ph.D., Principal Investigator
Assistant Dean, Information and Instructional Services
Robert E. Kennedy Library

Franz Kurfess, Ph.D.
Associate Professor
Computer Science Department
College of Engineering
California Polytechnic State University
San Luis Obispo, California 93402

Anita Mirijamdotter, Ph.D.
Associate Professor and Head, Social Informatics Research
Division of Information Systems Sciences
Department of Business Administration and Social Science
Luleå University of Technology
Luleå, Sweden

Erika Rogers, Ph.D.
Director, University Honors Office
California Polytechnic State University
San Luis Obispo, California 93402

1. Introduction

Between January and June 2005, an international research team investigated the efficacy of an interactive design and evaluation process for technology-enabled collaborative learning. The study involved sixty-two students in four disciplines - computer science, library and information science, social informatics, and computer and systems sciences - on three campuses - California Polytechnic State University (Cal Poly) and San José State University (SJSU) in the United States and Luleå University of Technology (Ltu) in Sweden. Student subjects were enrolled in one of four project-based courses, including two graduate courses in information science and knowledge management and two undergraduate courses in social informatics/computer and systems sciences and human computer interaction (HCI). All four courses focused on a common topic, 'learning commons'. As pedagogical strategy, the faculty research team applied an action research methodology that builds on participation and interaction. We assume that student beneficiaries are able designers and evaluators of the socio-technical elements of student-centered learning spaces and places. In this report, we present the theoretical framework informing this user-centered, user-driven process for co-creation of collaborative physical and virtual 'learning commons'.

1.2 Research Design Context

The 'commons' construct emerges from a three-year Creative University 'arena' initiative at Luleå University of Technology, Sweden (Andersson 2003; Andersson, Jonsson, and Söderlund 2002; Edzén, Holst, and Sandström 2004; Holst 2004; Holst and Mirijamdotter 2004a; 2004b; Sandström 2004). The phrase also acknowledges the contemporary transformation of information commons to 'learning commons', where the focus is on learning rather than technology (Beagle 2004), in North America, Australia, and New Zealand. The convergence of innovative Swedish university practices and international educational computing trends informed the purpose of the project: to promote interdisciplinary, or boundary crossing, exchanges concurrent with advancing team-based knowledge creation proficiencies among student project participants. Faculty researchers sought to concurrently identify what 'learning commons' facilitators/enablers needed to provide in order to embed knowledge enabling processes within student learning communities.

To explore the efficacy of 'learning commons' co-design principles and practices, we introduced selected technology-supported tools for initiating and advancing physical, virtual and mental facets of distributed cooperative and collaborative inquiry. Students also supplemented institutionally supported tools so, consequentially, a wide variety of technology resources were tested. These included two Learning Management Systems (LMSs), two e-meeting software packages, a 3-way video conferencing system, instant messaging (IM), and a wiki, as well as e-mail, facsimile (fax), and telephonic communication. We were also attentive to the social factors affecting tool utility, including cultural expectations, time differences, and role variation among both faculty and student learning groups. Throughout, we employed the lens of interactive design and evaluation (Newman and Lamming 1995; Preece, Rogers, and Sharp 2002) for cultivating and sustaining dynamic technology-enabled, dialogue-driven communities of inquiry (Banathy and Jenlink 2005).

Our interactive evaluation methodology is based on action research principles and practices (Baskerville and Wood-Harper 1996; Checkland and Holwell 1998b). We relied on the work of Nonaka (Nonaka 1994; Nonaka and Konno 1998; Nonaka, Konno, and Toyama 2000; Nonaka and Toyama 2003; von Krogh, Ichijo, and Nonaka 2000) to guide pedagogical decisions on the co-creation of knowledge enabling conditions for course-based learning communities. With the aim to achieve the knowledge-enabling interactions embedded in the concept of *Ba* as advanced by Nonaka and others, these interpretivistic and constructivist theories fueled the co-creation of student-generated insights into 'ideal-making' social exchange conditions and technology infrastructure functionalities. For instance, faculty relied on these foundational concepts and processes in coaching student participants to make tacit information explicit for information sharing and knowledge creation. We were particularly interested in exploring the factors influencing emergence of shared physical, virtual and mental contexts which activate potential learning – through information and knowledge encounters – within and between the four disciplinary course 'learning communities'.

To explore the practical feasibility of constituting and linking learning communities to create new disciplinary knowledge, share it across disciplinary communities, and co-create technology-enabled learning environments supportive of cross-disciplinary discourse, we also employed systems thinking methodology – in this case, Soft Systems Methodology (SSM) (Checkland 1981, 1994, 2000; Checkland and Casar 1986; Checkland and Holwell 1993, 1998a; Checkland and Scholes 1990). SSM involves discourse, dialogue and communication through which faculty and students create shared meanings. 'Intersubjective sense making' discourse serves to identify purposeful actions to be taken in the light of negotiated intentions and resulting accommodations among project participants. With varying degrees of proficiency, the interactive evaluation process became internalized within individuals and embedded within group and inter-group processes. When this happened successfully, participants aligned their decisions with the 'higher level' purposes of disciplinary information exchange and interdisciplinary knowledge production. As context and meaning evolved, 'high performance teams' dynamically modified facets of the distributed technology-enabled learning environment to improve their communication-driven knowledge creation and transfer outcomes. In these cases, systems thinking theories, especially those of Checkland, guided the reflective construction and implementation of design and evaluation processes among faculty and students.

In the following sections, we describe our action research approach for nurturing and implementing user-generated evaluation criteria through iterative and interactive participatory design/redesign and evaluation processes. We begin by outlining the theoretical framework on which we based our research methodology. Following this, we illustrate 'meaning making' processes which shaped discourse on elements of the learning commons environment and advanced 'knowledge making' activities.

2. Interactive Design and Evaluation Methodology

Interactive evaluation contrasts with more traditional methodologies in which researchers assume that evaluation is conducted objectively, independent of social and political context, and where the intention is normally to measure some phenomenon to find out its status. Typically, in the latter context, it is the evaluator who defines what is to be evaluated and how. Moreover, the

evaluation results are oftentimes assumed to be an accurate representation of the actual situation (Guba and Lincoln 1989).

In contrast, the purpose of interactive evaluation is to make the situation of which people are a part more intelligible to them. User-generated results are viewed as 'meaningful constructions' - meaningful to the people involved in the situation. Furthermore, it is assumed that evaluation is a social-political process. Social, cultural, and political factors are viewed as significant aspects of the process - i.e., 'meaning creators', not 'annoying inconveniences' that threaten research validity. Evaluation, within this perspective, is a process to create shared reality and meaning (Guba and Lincoln 1989).

The 'intersubjective sense making' intrinsic to interactive evaluation promotes collaborative learning through social interaction in which individuals construct knowledge and negotiate meaning (Newman and Lamming 1995; Preece et. al. 2002). This requires participants' involvement in both definition and application of evaluation criteria and also interpretation of group observations. During these dialogues, individuals benefit from others' interpretations. They become better able to clarify their own conceptions. Concurrently, community members gain proficiency in identifying the socio-technical design elements necessary to collaborative learning activities.

To manage the implementation of interactive evaluation within a collaborative learning context, we use soft systems design methodology and models (Checkland 1981, 2000; Checkland and Casar 1986; Checkland and Scholes 1990; Vickers 1983). We rely especially on the Processes of Organizational Meanings (POM) (Checkland and Holwell 1993, 1998a; Costello, Crawford, Bentley, and Pollack 2002; Holst 2004; Holst and Mirijamdotter 2004b; Holst and Nidhall 2001; Mirijamdotter and Somerville 2005; Rose 2002). See Figure 1.

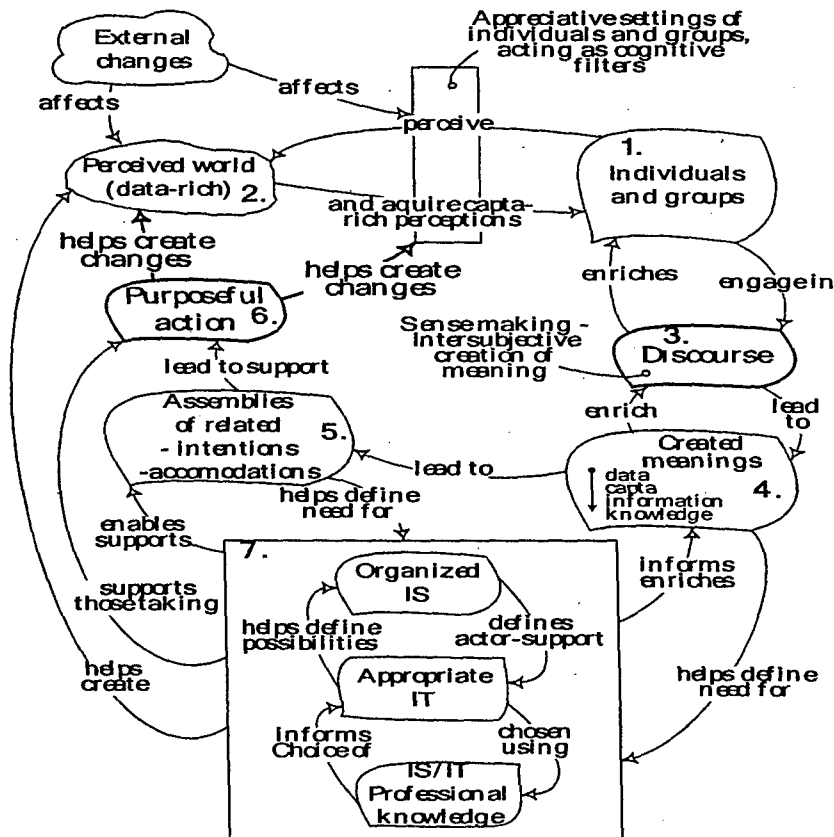


Figure 1: “Processes for Organizational Meanings” (POM) Model. After Checkland and Holwell (1998a: 106).

The POM model reflects information and communication interactions underlying information exchange and knowledge creation. Figure 1 depicts the seven elements derived from Checkland’s Soft Systems Methodology (SSM), as furthered by Vickers’ concept of an appreciative system (Checkland 1994; Checkland and Casar 1986). Both applied theoreticians address the relationship-maintaining aspects of organizations and the underlying social, cultural, and political contexts. Elements 1-2 represent identification of relevant environmental elements, so-called ‘capta’ (Checkland and Holwell 1998a), which both depends upon and extends project participants’ data collection and analysis expertise. The notion is that information exchange drives ongoing processes of creating meaning through dialogue and discourse, as expressed in elements 3-4-5, to affect collaborators’ appreciative settings. It follows then that dialogue and negotiation processes inform purposeful actions (element 6), based on accommodated views. Shared understanding then informs the formally organized distributed information systems (element 7), by means of which needed social and technical support is identified, iteratively, through these recurring processes. POM also provides a textured environmental context for communication and dialogue intended to promote shared reality and meaning.

To deepen reflective insight through dialogue-based collaborative interaction, we draw from Nonaka’s SECI model of the knowledge creation process (Nonaka et. al. 2000; Nonaka and Takeuchi 1995; Nonaka and Toyama 2003). The model delineates four phases, Socialization, Externalization, Combination, and Internalization. These elements characterize effective

information exchange for knowledge creation through dialogue. This conceptualization recognizes that the human activity of knowledge creation requires crossing boundaries (Holst 2004; Nonaka 1994; Nonaka et. al. 2000; von Krogh et. al. 2000) and this occurs through the interaction between individuals in their environment. Over time, through face-to-face – or ‘face-to-face like’ – experiences, individuals develop emotional feelings such as commitment and trust. When fortified by systemic ‘decision making’ and ‘decision taking’ processes, participants build capacity for converting selected data (i.e., *capta*) and information into knowledge. In this exploratory study, we investigate the efficacy of participatory action research processes for co-designing the socio-technical elements of a distributed knowledge enabling environment animated by purposeful intersubjective sense making intentions.

We use the concept of *Ba* (Nonaka and Konno 1998) embedded in the SECI model to connote the context, place and space shared by those who interact successfully – physically, virtually, and mentally – for the purpose of knowledge creation. The concept expands upon the dialogue and interaction represented in elements 3-4-5 of the POM model which, when energized, give energy and quality to the SECI process. Activation depends on the presense of knowledge assets, “the inputs, outputs and moderating factors of the knowledge-creating process” (Nonaka et. al. 2000, p. 20), which, when expressed both tacitly and explicitly, form the base for the knowledge creation process. These enablers include experiential knowledge assets, conceptual knowledge assets, systemic knowledge assets and routine knowledge assets. In our action research study, *Ba*-like conditions epitomize the desired outcome of the learning commons co-design efforts.

3. Action Research Learning Approach

Action research is particularly suitable for situations in which participants aim to simultaneously bring about change while learning from the process of deriving the change. In this case, project participants intended to both explore how to better collaborate in a technology-enabled learning environment and also advance ‘responsive’ improvement in learning pedagogy and environment infrastructure. The emphasis on inquiry-based learning, as well as attention to participation and involvement, emerges out of the action research tradition – which acknowledges the need to investigate practical problems within their real world context concurrently with the need to become involved in their solution. Using action research as an interventionist approach intrinsically and “simultaneously assists in practical problem-solving and expands scientific knowledge, as well as enhancing the competencies of the respective actors” (Hult and Lennung 1980 in Baskerville and Wood-Harper 1996).

This project is also inspired and informed by the Creative University arenas initiative (Andersson 2003; Andersson et. al. 2002; Holst 2004; Holst and Mirijamdotter 2004a; 2004b; Sandström 2004) at Luleå University of Technology (Ltu), Sweden, which explored strategies, from 2001 to 2004, for intentionally constructing collaborative learning environments for interdisciplinary knowledge creation. In studying how to enable naïve users’ abilities to co-construct a distributed learning environment, we draw from Ltu’s action research findings on the efficacy of encouraging boundary crossing knowledge creation through intentional reflection and analysis.

In this exploratory research project, we pose the following guiding questions:

- What are the critical design elements necessary to construction of a collaborative learning environment for boundary-crossing knowledge creation – i.e., a learning commons?

- What processes might faculty researchers embed in curricular strategies to enable students' co-design of collaborative learning spaces, within and between distributed course-defined populations?
- What socio-technical challenges must faculty researchers address to enable students' co-design of technology-enabled collaborative learning environments?

The research project design evolved from the holistic sense making POM model in combination with Nonaka's unified models for knowledge creation, as described above. These concepts and principles were made actionable by Soft Systems Methodology's four constitutive elements of finding out, modeling, comparing, and taking action. SSM inquiry also guided student and faculty exploration of the efficacy of interactive evaluation for co-creation of a shared learning environment. Conveniently, therefore, the 'learning commons' theme provided a shared 'learning object' across courses. Within this contextual framework, students pursued projects aligned with their disciplinary focus. For instance, Ltu students embraced the university's interdisciplinary 'arena' pedagogy, students in library and information science explored implications for information and knowledge management systems, and computer science students designed and developed Internet2 broad bandwidth software applications.

In coaching students on their disciplinary projects, faculty were attentive to the five knowledge creation 'energizers' described by Nonaka et al (2000). In the Ltu case, the project start-up activity provided 'creative chaos' through a presentation delivered through a video conferencing session with one of the U.S. project faculty. The interactive exchange focused on the concept of a learning commons and was followed by distribution of background documents through e-mail attachments. Shortly after that, formal information exchange among Ltu students, international faculty and U.S. students was formally initiated through the first of four video conferencing sessions. However, at no point in that process were Ltu team members and SJSU team members explicitly introduced to one another, an interaction failure which contributed to continuing miscommunication throughout the duration of the project.

During initial project planning activities, Ltu students identified their team's knowledge assets, including proficiencies to be acquired. As their project planning progressed, faculty researchers coached students on enabling processes, including structures and means for ongoing reflection on learning environment elements such as technology mix and social exchange aspects. When students recommended negotiated socio-technical modifications that involved other learning communities, faculty attended closely to those interactions – though they not interfere in the students' interdisciplinary and intercultural communications, choosing instead to observe and thereby learn about 'natural' interaction patterns among 'naïve' learners.

Throughout the semester-long courses, team process and progress was assessed and evaluated collaboratively by students and faculty, as were cross team successes and failures. Insight-driven modifications were made, leading to accommodated decisions on future actions and activities, including the technological dimensions. Faculty researchers coached students to evaluate the emergent holistic design of this dynamic learning environment based on systems thinking and knowledge creation precepts. For instance, Ltu students were obliged to maintain a project diary of the project and record activities, events, plans, and reflections. Additionally, through weekly physical or virtual meetings with faculty, students explored emerging issues and informed responsive redesigns. These interactive evaluation practices reflect common dimensions of

active learning and knowledge creation - i.e., collaborative facilitation of social exchanges among users, where information is transformed into knowledge.

4. Student Data Analysis Highlights

The following highlights provide selected 'snapshots' of students' interactions, as reported to and observed by faculty, on the particularly intense communications efforts among four Ltu students in social informatics/computer and systems sciences and three SJSU students in library and information science. These seven students initiated more frequent information exchanges and interactive evaluations than was typical of other project participants. They also experimented with more technology-enabled exchange strategies. In the following section, we present representative 'snapshots' of the interactive data which faculty researchers continue to analyze.

4.1 Social Implementation Factors

The Ltu students initiated their project through video conferencing communication with faculty from Ltu, SJSU, and Cal Poly in which they discussed the concept of a learning commons and explored the Ltu students' role in this distributed learning experiment. Three students from San José had volunteered to interact with the Ltu students to obtain first hand experience in a distributed international learning commons. However, because of logistical problems, the San José students did not participate in the initial video conferencing session. In hindsight, the inability to interactively communicate early on in 'face-to-face like' circumstances was regrettable and also irreparable. Though students experimented with various communication technology media, such as e-mail, a learning management system, Instant Messenger (IM), and a wiki, their attempts to overcome cultural differences, further compounded by the complications of time differences, remained unsuccessful. They never progressed beyond the first 'intention' phase of forming a viable working group. Admittedly, cultural complications also played a significant factor, as expressed in assumptions about independent versus team action and autonomous versus collaborative work decisions. Lacking the prerequisite rapport building activities, these differences caused presented insurmountable difficulties in reaching an accommodated understanding of common purpose and goals as predicated on the fifth element of energizing *Ba*, i.e., trust.

Work style and discipline-based differences also impacted students' experiences. In the most highly functioning group, the Ltu team, the students assessed team members' knowledge assets, both tacit and explicit, and categorized them according to experiential, conceptual, systemic, and routine. Through this process, they obtained a deeper understanding of one another's competencies and how these could best be utilized in working as a team. At the other end of the continuum, SJSU students continued to function as individuals throughout the duration of the project. In addition to variety in work styles, differences in disciplinary assumptions further complicated communication challenges – while ensuring the presence of the requisite variety necessary to creative thinking.

4.2 Collaboration-Enabling Technology Characteristics

The Ltu and SJSU students explored various software options with only intermittent success during their collaboration attempts. For instance, their early attempts to address significant cultural and disciplinary differences through Learning Management Systems were unsuccessful. Both systems lacked the 'rapport building' elements of 'sight and sound'. Absence of a

designated chat moderator also presented challenges for boundary crossing negotiation and facilitation, as did the physical requirement for 'speed on the keys', given the variability in proficiencies.

Similarly, usage of wikis and blogs was also unsuccessful. When proposed and, though lacking 'buy in', one U.S. student created a wiki, it was ignored, as 'just one more place to go', despite the originator's attempts to 'create traffic' by coaxing others through e-mail solicitations to visit the site.

On the other hand, during the course of the project, participants demonstrated increasing sophistication in articulating their learning needs and also their judgments about potentially useful hardware and software. In addition, they learned that baseline proficiency in 'tech know how' was essential and a common 'tech platform' was desirable. Furthermore, as the project work proceeded, students realized that discussants separated by distance and reliant on information and communication technology (ICT need to come to agreement early on about how and when to communicate.

4. 3 Collaborative Learning Process Considerations

In addition to a wide variety of technology-mediated communication attempts, both successful and unsuccessful, all seven students participated in video conferencing system-enabled information exchange activities intended to support interdisciplinary knowledge creation. The ten hours of shared video conferencing content were archived as digital streaming video to encourage review. However, lacking clear objectives for collaborative learning – and confused by culturally different expectations for collaborative work, students were unable to extract significant benefit from these resources. This led to students' recommendation – and faculty concurrence - that collaboration enablers establish clear protocols and structures, particularly in the formative phase of group work among newly constituted cohorts. Lacking proximity, distributed team members also requested, in hindsight, explicitly moderated discussion of 'leading questions' that could reveal unspoken assumptions and expectations.

5. Technology-Enabled Co-design Processes

In the following section, we report preliminary results from our interactive evaluation study on technology-enabled co-design processes for distributed collaborative learning. To generate generalizable findings according to standard action research methodology practices, we followed a deliberate process of reflective learning in relation to the guiding epistemology. Thus, this project observes the standards for 'academic rigor' established within the action research field through a declared epistemology that guides the recognition of what counts as learning (Checkland and Holwell 1998b). By explicating the epistemology, the research process is made 'recoverable', at least in intellectual terms, which addresses the reliability criterion. The validity of this kind of research is always problematic since the phenomena are not "homogenous through time" (Checkland and Holwell 1998b: 16). Therefore, as action researchers, we are mindful of the potential limitations to our 'claims' to the transferability of our findings. That being said, we do believe our results can benefit other participatory design projects.

The following section first reviews our research framework for interactive evaluation, including our evaluation construct. Following this, we present our preliminary results on the efficacy of our

methodology for student-generated socio-technical design of technology-enabled collaborative environments.

5. 1 Interactive Evaluation Framework

The theoretical framework informing research project design and development integrates the intersubjective meaning making POM processes with the knowledge enabling *Ba* exchange concept. Here we highlight our application of this framework for project design and implementation intended to further knowledge generation.

This holistic construct informed faculty researchers' pedagogical choices for achievement of information exchange and knowledge creation learning outcomes within a course and among courses. In the case of the Ltu students, faculty members' implementation of Nonaka's energizing factors was successful. Despite this, they were unsuccessful in attempts to replicate these conditions in a potential international collaboration, given the 'disablers' previously mentioned. This suggests that while 'creative chaos' (Nonaka et. al. 2000) can be useful, especially within bounded situations, it must be carefully planned and managed, given the 'naturally occurring disablers' intrinsically present in distributed environments. These include and are not limited to variability in experience and expectations for project work, differences in cultural background and time zones, diversity in studying and working conditions, and differences in technological access, awareness and proficiencies. In future applications, we intend be more mindful of combining both POM and *Ba* constructs concurrently.

In a previous course, Ltu students received extensive training in knowledge management techniques for project work and therefore integrated them into course project processes. In the Ltu project, therefore, faculty built on these proficiencies to encourage heightened reflection on systems thinking, feedback processes, knowledge management, and teamwork. As a consequence, these students were better equipped to apply POM and *Ba* processes to reflect not only on their socio-technical environment but also on their learning processes and purposes. On the other hand, the SJSU faculty first concentrated on developing individual student proficiency in making tacit information explicit. When information exchange and teamwork capabilities were introduced in the middle of the course, students found these precepts culturally and experientially unfamiliar. They failed to modify their habits and adopt new conventions, opting instead to continue to work individualistically even within the context of a team assignment. These results raise questions about cultural and disciplinary dispositions that are outside the purview of this study. However, the markedly different outcomes – despite similar pedagogical intentions - do recommend further investigation into the significance of implementation staging.

The POM-inspired aspect of the interactive evaluation framework directed students' iterative reconsideration of tool-specific socio-technical 'solutions' within the holistic context of their technology-enabled socio-technical learning environment. Once again, the Ltu students' proximity relationships, fortified by shared culture, produced relationships that easily energized the trust dimension of *Ba*. Among the distributed communities, however, this essential component of knowledge making proved especially difficult to achieve through 'text-based only' technologies. When we interpret student-generated data in light of the POM model (Figure 1), we notice that technologies weak in 'face-to-face like' communication did not support the discourse crucial for intersubjective sensemaking. This is an especially acute problem when cultural differences already degrade the likelihood of 'naturally' achieving shared appreciative

settings through virtual interactions. In such circumstances, therefore, faculty must be particularly attentive and readily response to participants' concerns and issues by adjusting both social and technology factors promptly. Our 'hindsight' insights suggest that, were we more cognizant of the guidance available by the POM and *Ba* models during implementation, we would have better appreciated where we were at any point and how we might move our inquiry to the next level. Once again, we recommend further research into what we believe is an especially promising line of inquiry.

In addition to assessing the efficacy of this interactive evaluation process approach, we also collected, and continue to analyze, data relevant to core guiding questions. We report on these tentative findings in the next section.

5. 2 Interactive Evaluation Efficacy

In appraising the efficacy of this integrated method for interactive evaluation of technology-enabled distributed learning among distributed learning communities, we concentrated on our three primary research questions. We wished to identify critical design elements necessary to construction of a collaborative learning environment for boundary-crossing knowledge creation – i.e., a 'learning commons'. Relatedly, we wished to investigate processes that faculty enablers might embed in pedagogical strategies to enable students' co-design of collaborative learning spaces, within and between distributed courses. And, finally, we wished to understand what socio-technical challenges must be addressed by faculty responsible for enabling students' co-design of technology-enabled collaborative learning environments.

We continue to analyze project data, so the following are only preliminary findings. Among the highlights is our observation that interactive evaluation experiences underscore the importance of 'rapport building' and 'relationship initiating' processes. Therefore, we are newly mindful of the importance of well orchestrated 'introductions' which lead to viable group work processes, including knowledge assessment activities to 'prime the pump' for knowledge making. We were also reminded that common purposes, structures, and forums for dialogue and interaction are necessary to distributed teamwork, as are enabling technologies appropriate to negotiating and accommodating quickly and efficiently. Throughout all these phases, discourse and dialogue emerges as a means of advancing collective understanding (Banathy and Jenlink 2005) through information exchange, knowledge sharing and meaning creation. Therefore, we are revisiting our interactive evaluation methodology to determine where and how, through dialogue, we might better advance shared agreements on purposes, norms, roles, and expectations, sufficient to support robust cross team 'intersubjective sense making'.

Preliminary findings also suggest that the socialization aspect of *Ba* (Nonaka et. al. 2000) can advance appreciative recognition of other team members' knowledge assets and lead to trust and caring. One emergent diversity issue concerned information and communication technology (ICT) fluency. Although we did not formally assess proficiency, we now recognize the importance of explicitly assessing information and technology proficiencies early on so as to ensure all participants' technical readiness for distributed collaborative work. Similarly, we seek to better embed knowledge asset appraisal into our pedagogical methodology, so as to ensure that through team-enriched interactive evaluation practice, students gain maximum proficiency in this important aspect of the 'socio' dimension of enabling and supporting technologies for distributed virtual learning communities. Relatedly, we are mindful that faculty members' ability

to influence infrastructure modifications is a critically important factor – oftentimes out of their control, particularly because it oftentimes involves other campus stakeholders such as information technology services, with priorities other than instructional design considerations. However, this issue is important, even foundational, as it impacts enablers' ability to become truly enabling of learning through implementing user-driven learning environment modifications.

Results to date suggest significant promise for this user-centered approach to learning environment design and evaluation, which actively engages students in making decisions about both their learning processes as well as the learning outcomes. Our work-in-progress intends to more closely assess the 'value added' benefits of participatory design and evaluation work when it is integral into a larger learning agenda. We believe this approach holds promise for improving socio-technical learning environment design as well as enabling students' heightened experiences of learning, when these processes are ably implemented by a faculty process leader.

6. Research Results Summary

In this report, we present the theoretical framework informing user-centered, user-driven processes for co-creation of collaborative physical and virtual 'learning commons'. The purpose of the project was to promote interdisciplinary, or boundary crossing, exchanges concurrent with advancing team-based knowledge creation proficiencies among student project participants. We therefore combined an interactive and participatory pedagogical course design strategy involving students working in a distributed fashion on a common learning object, the construct of a 'learning commons'. To explore the efficacy of an interactive evaluation design and evaluation method to advance distributed cooperative and collaborative inquiry, we introduced a variety of technology-supported tools and systemic thinking processes. Faculty researchers are now analyzing the resulting data to clarify how learning commons facilitators, or enablers, might successfully embed knowledge enabling processes within student learning communities.

Preliminary results corroborate that student-generated interactive design and evaluation of socio-technical elements for a distributed learning environment requires that participants must commit to active learning. Engagement requires that individuals must evolve common purposes, structures and forums for the dialogue and interaction necessary to distributed teamwork. Reflection plays an important role in reconsideration. In this way, design and evaluation processes as well as actionable results and responsive modification of learning environment conditions contribute to learning and development and design and evaluation activities are integral to the learning agenda. We believe, therefore, that this approach holds promise for improving the socio-technical learning environment characteristics concurrent with advancing participants' collective learning.

We now prepare to implement our research findings in the Cal Poly Learning Commons project scheduled to launch in September 2005. During the pilot year, this joint venture between staff in the Robert E. Kennedy Library, Information Technology Services (ITS), and the Center for Teaching and Learning (CTL) will involve innovative academic faculty in populating the physical and virtual Learning Commons environment. Projects will advance learning through embedded information exchange and knowledge creation processes, concurrent with responsive modification of 'enabling' socio-technical elements driven by user-generated evaluation feedback. At the conclusion of the pilot year activities, we aim to create a conceptual prototype

for faculty members with enabling responsibility for disciplinary and interdisciplinary knowledge making among technology-enabled distributed student learning teams.

References

- Andersson, M. (2003). Drivhusmodellen i teori och praktik - ett verksamhetsintegrerat forsknings- och utvecklingsarbete för integration av utbildning, forskning och samverkan vid Luleå tekniska universitet. Licentiate Thesis, Department of Applied Physics and Mechanical Engineering, Luleå University of Technology.
- Andersson, M., Jonsson, M., and Söderlund, A. (2002). The Greenhouse Learning Concept: a new pedagogical approach. Paper read at 30th SEFI Annual Conference, in Florence.
- Banathy, B., and Jenlink, P. M. (2005). *Dialogue as a Means of Collective Communication*. New York: Kluwer Academic.
- Baskerville R. L. and Wood-Harper, A. T. (1996). A Critical Perspective on Action Research as a Method for Information Systems Research. *Journal of Information Technology* 11: 235-246.
- Beagle, D. (2004). *From Information Commons to Learning Commons* 2004 [cited 2005-01-25]. Available from [http://www.usc.edu/isd/libraries/locations/leavey/news/conference/presentations/presentations_9-16/Beagle Information Commons to Learning.pdf](http://www.usc.edu/isd/libraries/locations/leavey/news/conference/presentations/presentations_9-16/Beagle%20Information%20Commons%20to%20Learning.pdf).
- Checkland, P. (1981). *Systems Thinking, Systems Practice*. Chichester: John Wiley & Sons.
- Checkland, P. (1994). Systems Theory and Management Thinking. *American Behavioural Scientist* 38 (1):75-91.
- Checkland, P. (2000). Soft Systems Methodology: A Thirty Year Retrospective. *Systems Research and Behavioral Science* 17: S11-S58.
- Checkland, P., and Casar, A. (1986). Vickers' Concept of an Appreciative System: A Systemic Account. *Journal of Applied Systems Analysis* 13:3-17.
- Checkland, P., and Holwell, S. (1993). Information Management and Organizational Processes: An Approach through Soft Systems Methodology. *Journal of Information Systems* 3: 3-16..
- Checkland, P., and Holwell, S. (1998a). *Information, Systems and Information Systems - Making Sense of the Field*. Chichester: John Wiley and Sons.
- Checkland P. and Holwell S. (1998b). Action Research: Its Nature and Validity. *Systemic Practice and Action Research* 11: 9-21.
- Checkland, P., and Scholes, J. (1990). *Soft Systems Methodology in Action*. Chichester: John Wiley & Sons.
- Costello, K., Crawford, L., Bentley, L., and Pollack, J. (2002). Connecting Soft Systems Thinking With Project Management Practice: an organizational change case study. In *Systems Theory and Practice in the Knowledge Age*, edited by Ragsdell, G., West, D., & Wilby, J. New York: Kluwer Academic/Plenum Publishers.
- Edzén, S., Holst, M., and Sandström, A. (2004). Answers to Questions About the Creative University. Technical Report. 2004:17. Luleå University of Technology. <http://epubl.luth.se/1402-1536/2004/17/index.html>.
- Guba, Y., and Lincoln, E. (1989). *Fourth generation evaluation*. Newbury Park: Sage Publications Inc.
- Holst, M. (2004). Knowledge Work across Boundaries - Inquiring into the processes of creating a shared context. Licentiate Thesis, Department of Business Administration and Social Sciences, Luleå University of Technology, Sweden.

- Holst, M., and Mirijamdotter, A. (2004a). An Application of Ba - Deconstructing Formative Processes in Multidisciplinary Work Groups. *International Journal of Knowledge, Culture and Change Management* 4:1051-1059.
- Holst, M., and Mirijamdotter, A. (2004b). Interaction in Cross-Functional Team Work: Making Sense through the POM Model. *Systems Research and Behavioural Science* Submitted for Review.
- Holst, M., and Nidhall, L. (2001). Soft Systems Methodology and Organizational Informatics - A Successful Partnership? Master of Science, Industrial Business Administration and Social Science, Luleå University of Technology, Luleå.
- Hult, M. and Lennung, S.-Å. (1980). Towards a definition of action research: a note and bibliography. *Journal of Management Studies*, 17: 241-250. in Baskerville R. L. and Wood-Harper, A. T. (1996).
- Jaramillo, J. (1996). Vygotsky's Sociocultural Theory and Contributions to the Development of the Constructivist Curricula. *Education* 117 (1):113-140.
- Mirijamdotter, A., and Somerville, M. (2005). Dynamic Action Inquiry: A systems approach for knowledge based organizational learning. Paper read at 11th International Conference on Human-Computer Interaction, July, in Las Vegas, Nevada.
- Newman, W., and Lamming, M. (1995). *Interactive System Design*. Cambridge: Addison-Wesley Publishers Ltd.
- Nonaka, I, and Konno, K. (1998). The Concept of "Ba": Building a Foundation for Knowledge Creation. *California Management Review* 40 (3):40-54.
- Nonaka, I, and Takeuchi, H. (1995). *The Knowledge-Creating Company - How Japanese Companies Create the Dynamics of Innovation*. New York: Oxford University Press.
- Nonaka, I, and Toyama, R. (2003). The knowledge-creating theory revisited: knowledge creation as a synthesizing process. *Knowledge Management Research & Practice* 1:2-10.
- Nonaka, I. (1994). A Dynamic Theory of Organizational Knowledge Creation. *Organization Science* 5 (1):14-37.
- Nonaka, I., Konno, N., and Toyama, R. (2000). SECI, Ba and Leadership: a Unified Model of Dynamic Knowledge Creation. *Long Range Planning* 33:5-34.
- Preece, J., Rogers, Y., and Sharp, H. (2002). *Interaction Design: Beyond human-computer interaction*. New York: John Wiley & Sons, Inc.
- Rose, J. (2002). Interaction, transformation and information systems development - an extended application of Soft Systems Methodology. *Information Technology and People* 15 (3):242-268.
- Sandström, A. (2004). Innovative Policy Networks - The relation between structure and performance. Licentiate Thesis, Department of Business Administration and Social Sciences, Luleå University of Technology, Sweden.
- Vickers, G. (1983). *The Art of Judgement*. London: Harper & Row.
- von Krogh, G., Ichijo, K., and Nonaka, I. (2000). *Enabling Knowledge Creation - How to Unlock the Mystery of Tacit Knowledge and Release the Power of Innovation*. New York: Oxford University Press.

July 21, 2005

Cal Poly Internet 2 Mini-Grant Proposal Document - Phase II

FINAL REPORT

6/7/05

**Project Title: Developing a Pest Control Advisor (PCA) Continuing Education
Conference for I2**

Project Director: Neal A. MacDougall

**College and Department: Agribusiness Department and Sustainable Agriculture
Resources Consortium (SARC), College of Agriculture**

Abstract

A study was conducted to assess the feasibility of offering on-line components of an existing professional development conference hosted by the Sustainable Agriculture Resource Consortium (SARC). Feasibility was based on three criteria: 1) is there sufficient interest on the part of the potential attendees?; 2) can the content be accommodated to the web-based approach?; and, 3) can the market be addressed adequately and content transitioned easily enough to make an on-line module workable? Feasibility was assessed through surveys conducted with conference participants, interviews with conference presenters, and consultations with Cal Poly faculty and staff. Trial audio-visual recordings and compilation of surveys, interviews and consultations indicate development of an on-line component to the conference is merited, desired and feasible with slight modifications in strategy.

Narrative

The aim of this proposal was to explore the feasibility of presenting all or part of the annual SARC Sustainable Agriculture PCA conference over the Internet. This conference had been offered twice by the SARC previously (in 2002 and 2003) in traditional, one-day conference format. Provision of the conference electronically in addition to via standard format would allow a more interactive educational experience as well as increased flexibility in terms of conference timing (since the conference would be virtual) and content (since presenters would not be required to all be present in the same place at the same time). As success of electronic offerings would depend on demand for them and the technical practicality of delivering them via the internet, we explored both challenges during the December 2004 PCA Conference as a part of this grant process.

The work for the project was broken down into three sections: Pre-PCA Conference tasks, PCA Conference tasks and post-PCA Conference tasks.

Pre-PCA Conference Tasks:

In collaboration with Cal Poly faculty, the California Certified Organic Farmers (CCOF) organization and the California Agricultural Production Consultants Association (CAPCA), four speakers were selected to participate in the feasibility study: Jake Lewin,

CCOF Director of Marketing and International Programs; Brian McElroy, CCOF Certification Services Manager; Dr. David Headrick, Cal Poly Horticulture and Crop Science Professor; and Dr. Peter Goodell, UCCE IPM Advisor. The latter two speakers presented their work in a joint lecture, thus a total of three one-hour lectures were selected for the purposes of this study. All arrangements necessary for hosting the conference were made with the help of our co-sponsors, and participant survey questions were prepared.

PCA Conference Tasks:

The two-day Conference was successfully offered on December 6-7, 2004 to over 90 paid registrants, and several dozen Cal Poly students and faculty. A total of eight lectures were offered on Day 1 of the conference. All lectures given were audio recorded, and the three lectures involved in the study were video recorded as well. Surveys inquiring about participant interest in an internet based version of the conference were distributed to all in attendance. The surveys requested participants to specify how they heard of the conference, their professional occupation in agriculture, and their impressions of the conference content. Additionally, the conference guests were asked whether they would take advantage of an electronic, web-based conference covering similar topics, how much time they would be willing to spend on educational components, what resources those components should include, and how much they would be willing to pay to access them. Surveys were not distributed to presenters; their comments and impressions were gathered in one-on-one interviews.

Post-PCA Conference Tasks

After completion of the conference, survey results were compiled and summarized. Taped conference presentations were discussed with Cal Poly presenters, and a short presentation on the project to a Cal Poly brown-bag group was made on May 26th. Furthermore, this grant concept was further developed in the form of a written proposal for undertaking an I2-based PCA conference with Cal Poly's information technology personnel, the California Certified Organic Farmers and the California Agricultural Production Consultants Association and submitted to the EPA. Although that grant request was denied in April of 2004, the proposal continued to develop the ideas initiated in this grant. We intend to refine these ideas and resubmit the proposal in future grant competitions, perhaps future I2 rounds, or EPA competitions.

Results & Discussion

Approximately 100 people attended Day 1 of this conference, and 31 surveys successfully administered to attendees. 23 of 31 responses indicated an on-line offering was of interest to them. Willingness to spend time on the Internet ranged from 1 to 5 hours (the December 6th conference ran 8 hours for which up to 8 hours of PCA continuing education credit was granted). The majority of respondents were willing to spend \$50-\$100 on an on-line conference. (The original conference cost was \$125 for Day 1.) As was expected, most in our audience work in orchard and row crop agricultural production industries (as opposed to horticultural) as consultants and growers.

Several lessons from the execution of this grant became immediately apparent. On the upside, attendees were enthusiastic about the idea of being able to access and pay for conference components on-line. We also learned that having speakers prepare PowerPoint presentations opens lots of opportunities for migrating to the Internet platform. On the downside, video and audiotaping were found to be extremely problematic when also trying to run a live conference. If done in the future, professional, outside help would be contracted to assist with recording. Furthermore, trying to adjust presentation materials after the presentation is problematic. Taping the conference live made it hard to avoid unwanted audio and video effects. One unanticipated result was that the greatest response in conference was to the field day the following day (Day 2, not studied in this grant). The success of the field component has led us to propose exploring two separate Internet offerings (described below).

Further review with Cal Poly faculty and staff revealed that straight transfer of video and audio is very complicated and yields visually static presentations. Straight transfer of PowerPoints with no adjustment will lose context in transition to Internet. Dead space in audio is also problematic. Subsequent conversations with presenters also revealed the proposed on-line conference offers the potential of serving multiple audiences because of participant ability to pick and choose modules (e.g. content for orchard or vegetable specialists can be more easily segregated from content for horticultural or even regulatory specialists in the on-line format than in a traditional conference setting).

Is it feasible?

Feasibility in this case encompasses three criteria:

- Is there sufficient interest on the part of the potential attendees? (I.e., is there a market?)
- Can the content be accommodated to the web-based approach?
- Can the market be addressed adequately and can the content be transitioned easily enough to make an on-line module workable?

Results of this study yielded affirmative responses to the first two criteria. Modeling the project to address the needs of the third is where most of the challenge lies.

Can the content be transitioned easily enough to make an on-line module workable? To do this, a restructuring of strategy is needed. PowerPoints of selected presentations need to be required. A recorded narration needs to be inserted before the virtual conference begins (not presented at the live conference). Video-taping should use a basic storyboard approach. Finally, several features were requested by participants in their surveys, and need to be included in an on-line format including: web links, limited self-tests and FAQs which can be incorporated into live conference handouts.

Future Plans

Our team would like to move forward in the development of an internet-based continuing education training series that would make information presented at the annual SARC PCA Conference available online. We would like to expand the scope of the online

format to include information presented in field components of the conference (i.e. components related to the Field Day portion of the standard conference.) The content of the standard PCA conference (Day 1) revolves around issues such as transitioning to organic production in specific crops (with an emphasis on IPM, organic materials and practices, and managing water issues attendant to California's agricultural wastewater discharge waiver). The content of the Field Day events (Day 2) emphasizes soil-based approaches to dealing with organic transition issues. In particular, the Field Day events provide participants with a hands-on approach that is generally absent from more traditional conferences.

We would like to incorporate information presented at these two events into two separate websites. The first website is expected to provide PCAs with ongoing continuing education in a sustainable agriculture program allowing PCAs unable to attend the conferences or wishing to reinforce the lessons of the conference and field days at a later date. The second website is expected to be a more general web page providing information on transitioning to organic agriculture and sustainable agriculture in general. Funds will need to be identified to contract with a web strategist, a web designer and a field day consultant to work with SARC and with CCOF (California Certified Organic Farmers) to eventually develop a full mock-up of the two websites.

Ongoing surveys to gauge the impact of the conferences and the field days as well as provide ongoing guidance as to what material should be incorporated into the websites will need to be conducted. Ultimately, the successful conclusion of the project will allow SARC to pursue money from other funders to formally establish the websites on a permanent basis.

The specific objectives of the next phase of the project are as follows:

- Develop a strategy to design content that incorporates pesticide reduction and IPM issues, related farm water quality management and other issues pertinent to sustainable agriculture;
- Develop a strategy to design Field Day events that emphasize a hands-on approach to reducing pesticide use by focusing on soil-based management approaches;
- Develop a web-based strategy that will allow the development of the following web products in the years following the next phase of the project:
 - A farmer- and PCA-oriented web page providing resources to transition to a certified organic production program; and,
 - A PCA continuing education website emphasizing IPM and pesticide-use reduction based on part of the content of the full-day PCA conferences and the subsequent field days; and,
- Develop a full mock-up of the two web products that will be tested with growers and PCAs.

Funding Objectives

One proposal has already been written to EPA covering the funding of working to put next year's conference in an on-line form – this proposal was rejected but interest was communicated in pursuing the idea in the future.

Proposals will be written to other funders, such as the USDA's Western Sustainable Agriculture Research and Education (SARE) and the USDA's Organic Transitions programs.

Conclusion

This was a successful learning experience.

We will develop a poster for the "Internet 2 day on Campus" and post results on Cal Poly SARC website in Summer 2005.

Thank you.